國立中央大學天文研究所
鹿林天文台年報

2011

No.9

國立中央大學天文研究所 編

目錄

研究報告

工作報告

相關報導

研究報告

A&A 527, A42 (2011)
DOI: 10.1051/0004-6361/201015144

Astronomy & Astrophysics

Photometric and spectroscopic observations of asteroid (21) Lutetia three months before the Rosetta fly-by*
(Research Note)

J. de León,[1], R. Duffard[1], L. M. Lara[1], and Z.-Y. Lin[1]

Instituto de Astrofísica de Andalucía-CSIC, Glorieta de la Astronomía, s/n. 18008 Granada, Spain
e-mail: jleon@iaa.es

Received 3 June 2010 / Accepted 9 December 2010

ABSTRACT

Context. On its journey to comet 67P/Churyumov-Gerasimenko, the International Rosetta Mission (ESA) was planned to fly-by two asteroids: (2867) Steins and (21) Lutetia. Although classified as an M-type asteroid because of its high albedo, its reflectance spectrum in the near and mid-infrared region, suggests a primitive composition, more typical of C-type asteroids. Results from ground-based observations are indicative of compositional variegation and of at least one significantly large crater on the surface of this asteroid.
Aims. We analyse photometric and spectroscopic data of the asteroid, obtained from ground-based observations, to support the data taken by the spacecraft.
Methods. We obtained *uvbyIRi′* photometric measurements covering the complete rotational period of the asteroid (about 8 h), using both the BUSCA instrument at the 2.2 m telescope in Calar Alto Observatory (CSIC-MPIA), and the 1 m telescope at Lulin Observatory (Taiwan, NCU). We also obtained visible and near-infrared spectra, covering the range 0.4–2.5 μm, with CAFOS at the 2.2 m (Calar Alto) and NICS at the 3.6 m telescope TNG ("El Roque de los Muchachos" Observatory). The spectroscopic data were taken at different rotational phases to search for any significant inhomogeneities in the surface of the asteroid.
Results. The simultaneous photometric lightcurves in five filters obtained with the BUSCA instrument, and the lightcurves obtained at Lulin Observatory reveal a brightness variation around a rotational phase 0.1. We took visible and near-infrared spectra at that rotational phase, and a different rotational phase for comparison. Differences in the visible spectral slope among the spectra are indicative of a crater as the most likely cause of this variation.

Key words. minor planets – asteroids: general – methods: observational – techniques: photometric – techniques: spectroscopic

1. Introduction

The International Rosetta Mission, approved in November 1993 by ESA and successfully launched in March 2004, is mainly devoted to the study of the comet 67P/Churyumov-Gerasimenko. The comet will be encountered in May 2014, and during its journey to Rosetta's main target, the spacecraft has flown by two main-belt asteroids: (2867) Steins and (21) Lutetia.

Asteroid (21) Lutetia was encountered on July 10, 2010 at a velocity of 15 km s^{-1} and at a closest approach distance of about 3200 km. Both asteroidal targets of the Rosetta-ESA mission have been extensively investigated by ground-based observational campaigns, to obtain as much information as possible to define the observational strategies of the spacecraft. Asteroid (21) Lutetia, a large object with a diameter of about 100 km, has a visible and infrared spectral behaviour similar to the carbonaceous chondrites (Barucci et al. 2005; Birlan et al. 2006), which are typically associated with C-type asteroids. Alternatively, Vernazza et al. (2009) suggest that (21) Lutetia has physical properties compatible with those of enstatite chondrites. Nedelcu et al. (2007) obtained rotationally resolved near-infrared spectroscopy of (21) Lutetia and interpreted differences in the spectra in terms of the coexistence of several lithologies on its surface. Lazzarin et al. (2009) detected two absorption features centred at 0.43 and 0.51 μm, attributed to the presence of hydrated silicates or carbon-rich compounds, indicative of a primitive composition. However, the infrared data taken with VIRTIS during the fly-by shows that there are no signatures of hydration (Tosi, priv. comm.). Different albedo values have been published for this asteroid: from 0.09 for polarimetric measurements and in agreement with a C-type object, to 0.23 for thermal infrared observations, which is typical of M-type asteroids (Lupisko & Mohamed 1996; Müeller et al. 2006). The most recent value, computed from OSIRIS data during the fly-by, is well constrained between 0.18 and 0.19 (Fornassier et al. 2010). Carvano et al. (2008) suggested that the discrepancies between the albedo and thermal inertia values of Lutetia derived from various thermal-infrared datasets, can be explained by the presence of large craters in its northern hemisphere. While thermal inertia is no longer a problem, as observations by the Spitzer Space Telescope (Lamy et al. 2010) and the onboard Rosetta instruments MIRO and, to a lesser extent, VIRTIS, agree on a very low value (20–30 MKS), fly-by images confirm the presence of numerous craters in the northern hemisphere, observations covering almost all latitudes between +90° and –30°.

All these results indicate that asteroid (21) Lutetia is quite an intriguing object in terms of surface composition, and any additional observational data collected is very valuable to help our understanding.

* Table 2 is only available at CDS via anonymous ftp to cdsarc.u-strasbg.fr (130.79.128.5) or via http://cdsarc.u-strasbg.fr/viz-bin/qcat?J/A+A/527/A42

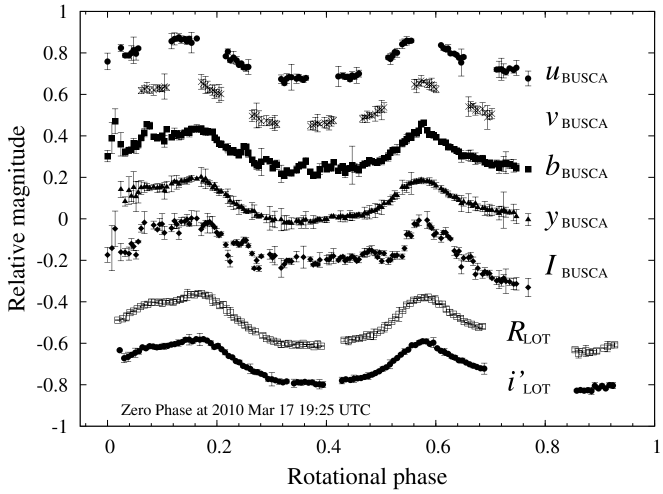

Fig. 1. Lightcurves of asteroid (21) Lutetia obtained at Calar Alto in March 17, using BUSCA instrument. The four Strömgren u, v, b, y and a Cousins-I filters are shown. Additionally, two lightcurves obtained at Lulin Observatory in March 19, using Cousins-R and Sloan i' filters are also shown.

Table 1. Observational details of the photometric and spectroscopic data.

Photometry				
Date (2010)	UT interval	Δ (AU)	α (deg)	Filter
Mar. 17	[20:25–02:42]	1.846	5.9	$uvbyI$
Mar. 19	[12:23–19:48]	1.851	6.6	Ri'
Mar. 20	[11:38–18:47]	1.855	7.0	Ri'
Mar. 21	[11:36–18:59]	1.859	7.4	Ri'

Filters	Central wavelength (μm)
Strömgren u, v, b, y	0.35, 0.41, 0.46, 0.54
Cousins R, I	0.64, 0.81
Sloan i'	0.74

Spectroscopy				
Spec. Id.	UT start	Julian Date	Airmass	Exp. time (s)
V1	Apr. 7 [21:28]	2 455 293.8945	1.101	2×200
V2	Apr. 7 [22:23]	2 455 293.9328	1.109	2×200
V3	Apr. 7 [22:32]	2 455 293.9393	1.115	2×200
V4	Apr. 8 [01:44]	2 455 294.0724	1.878	2×200
V5	Apr. 8 [01:53]	2 455 294.0789	1.981	2×200
V6	Apr. 8 [02:03]	2 455 294.0859	2.107	2×200
V7	Apr. 8 [22:45]	2 455 294.9484	1.132	2×200
V8	Apr. 8 [22:55]	2 455 294.9550	1.144	2×200
V9	Apr. 8 [23:05]	2 455 294.9617	1.158	2×200
V10	Apr. 8 [23:29]	2 455 294.9785	1.204	2×200
IR1	Apr. 5 [21:36]	2 455 291.4006	1.101	4×15
IR2	Apr. 6 [00:01]	2 455 291.5010	1.075	4×15
IR3	Apr. 6 [00:48]	2 455 291.5342	1.156	4×20
IR4	Apr. 6 [00:55]	2 455 291.5389	1.173	4×15
IR5	Apr. 6 [01:01]	2 455 291.5431	1.189	2×15

2. Observations

We performed photometric and spectroscopic observations of asteroid (21) Lutetia during March and April, 2010. We used instruments and telescopes located at three different observatories: Lulin Observatory in Taiwan and the Calar Alto Observatory (CSIC-MPIA) in Almería and the "El Roque de los Muchachos" Observatory in the island of La Palma, both in Spain.

2.1. Photometry

The observations were carried out during March 2010, using both the Lulin's One-meter Telescope (LOT), managed by the Institute of Astronomy of National Central University, and the 2.2 m telescope at Calar Alto. Observations with the 2.2 m telescope were taken on March 17, using the Bonn University Simultaneous CAmera (BUSCA). BUSCA is designed to perform simultaneous observations in four individual bands with a field of view of $11' \times 11'$. It has four individual 4K × 4K CCD systems, which cover the ultra-violet, the blue-green, the yellow-red and the near-infrared part of the spectrum (channels a–d respectively). For our observations, we used Strömgren filters u and v alternately in channel a, Strömgren filter b in channel b, Strömgren filter y in channel c, and a Cousins-I filter in channel d. The exposure time was common to the four channels, so it was selected to both produce enough signal in the ultra-violet and avoid saturation in the near-infrared. Therefore, one single exposure provided four images in four filters, the sequence being $[u, b, y, I]$, $[v, b, y, I]$, $[u, b, y, I]$, and so on. Table 1 shows the time intervals of the observations, the distance to the Earth (Δ), the phase angle (α) and the set of filters used.

At the Lulin Observatory, images were obtained with a PI1300B CCD camera (1340 × 1300 pixels), covering a field of view of $11'.5 \times 11'.52$. We took a series of images using the Cousins-R broadband filter and the Sloan-i' intermediate filter on the nights of March, 19, 20, and 21. Exposure times for each image ranged from 5 to 30 s, depending on the sky conditions, but always avoiding CCD saturation levels. Details of the observing conditions are listed in Table 1.

In both cases, data reduction was performed using IRAF standard procedures (Tody 1993), including bias subtraction and flat field correction. Unfortunately, none of the observations were performed under good photometric conditions, so we were unable to do standard calibration, and no colour information is available. Nevertheless, we performed relative aperture photometry, using several reference stars in the same field on each night, and results were compared to ensure that no intrinsic short-term variability of the stars was introduced. We finally computed the average of the asteroid's relative photometry obtained with all the selected stars. Lightcurves obtained with the BUSCA filters on March 17 and the two filters used for LOT observations (March 19) are shown in Fig. 1. Error bars correspond to 1σ deviation from the computed mean relative magnitude. The lightcurve obtained with filter I seems to be slightly different from the others. We can see a "depression" between rotational phase 0.52 and 0.56, and a significant decrease in brightness beyond 0.7. However, we do not see any of these features in the lightcurves obtained using filter i', so we believe those apparent features should not be interpreted as true variations. Weather conditions were superior during the observations made on March 19, 20, and 21 at Lulin Observatory, so lightcurves with filters R and i' have smaller dispersions.

2.2. Spectroscopy

Visible spectra were obtained with the Calar Alto focal reducer and faint object spectrograph CAFOS on two nights. CAFOS is equipped with a 2048 × 2048 pixel blue-sensitive CCD and a plate scale of 0.53″/pixel. We used the R-400 grism, giving a

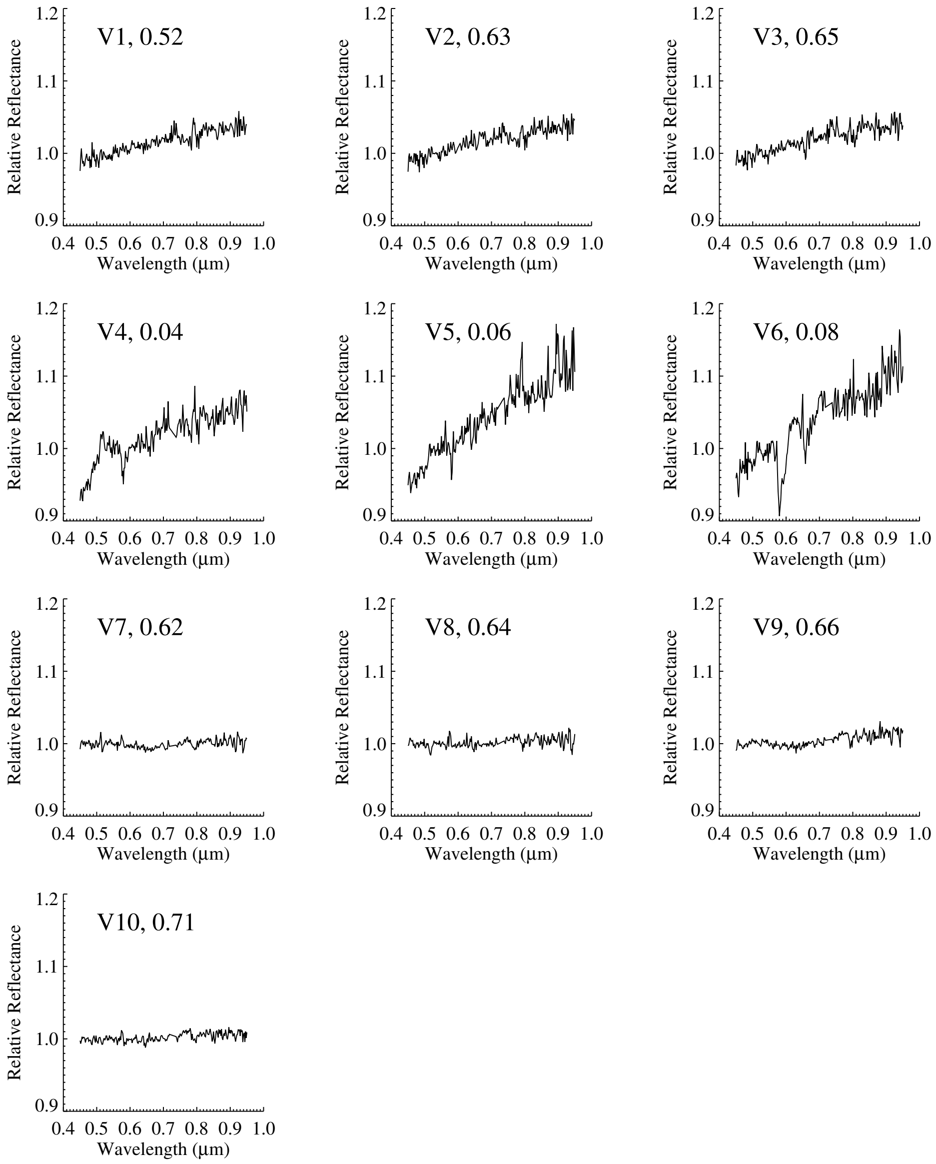

Fig. 2. Reflectance spectra of asteroid (21) Lutetia in the visible, normalised to unity at 0.55 μm. The spectra are labelled as in Table 1. The numbers correspond to the asteroid's rotational phase at which they were taken.

wavelength coverage from about 0.45 to 0.95 μm, and a dispersion of 9.7 Å/ per pixel ($R \sim 400$). A 1.5″ slit was employed, oriented in the parallactic angle to correct for differential refraction effects, and the tracking was at the asteroid's proper motion. Two acquisitions, between which the object was offset in the slit direction (positions A and B), were obtained. Pre-processing of the CCD images included bias and flat field correction. The extraction of 1D spectra from 2D images was carried out after the sky background subtraction ($A - B$), as described in Duffard & Roig (2009). Wavelength calibration was applied using Cd, Hg, and Rb lamps. To obtain the asteroid's reflectance spectra, we observed three solar analogue stars from the Landolt catalogue (Landolt 1992) at similar airmass as the asteroid: SA 105-56, SA 107-684, and SA 110-361. Final reflectance spectra were normalised to unity at 0.55 μm. Observational details can be seen in Table 1, where the starting UT, Julian date (JD), airmass, and total on-object exposure time are indicated. Each spectrum listed in Table 1 corresponds to the sum of two (2x) individual spectra, obtained from one ($A - B$) subtraction, and can be seen in Fig. 2.

Low resolution near-infrared spectra were taken with the 3.6 m Telescopio Nazionale Galileo (TNG) on two nights, using the low resolution mode of NICS (Near Infrared Camera Spectrograph), a multi-mode instrument based on a HgCdTe Hawaii 1024×1024 array. All spectroscopic modes use the large field (LF) camera, which has a plate scale of 0.25″/pixel. We employed a 1.5″ slit, and the Amici prism disperser, covering the 0.8–2.5 μm spectral range. As for the visible observations, the slit was oriented in the parallactic angle, and the tracking was at the asteroid's proper motion. The acquisition consisted of two series of short exposure images, offsetting the object between positions A and B in the slit direction. This process was repeated and a number of $ABBA$ cycles were acquired. The observational method and reduction procedure followed de León et al. (2010). Standard bias and flat field correction were applied to the images. From each $ABBA$ cycle, we obtained two individual AB images, after subtracting consecutive A and B exposures. After the extraction of 1D spectra and wavelength calibration, we divided the asteroid's spectrum by the spectra of the solar analogue

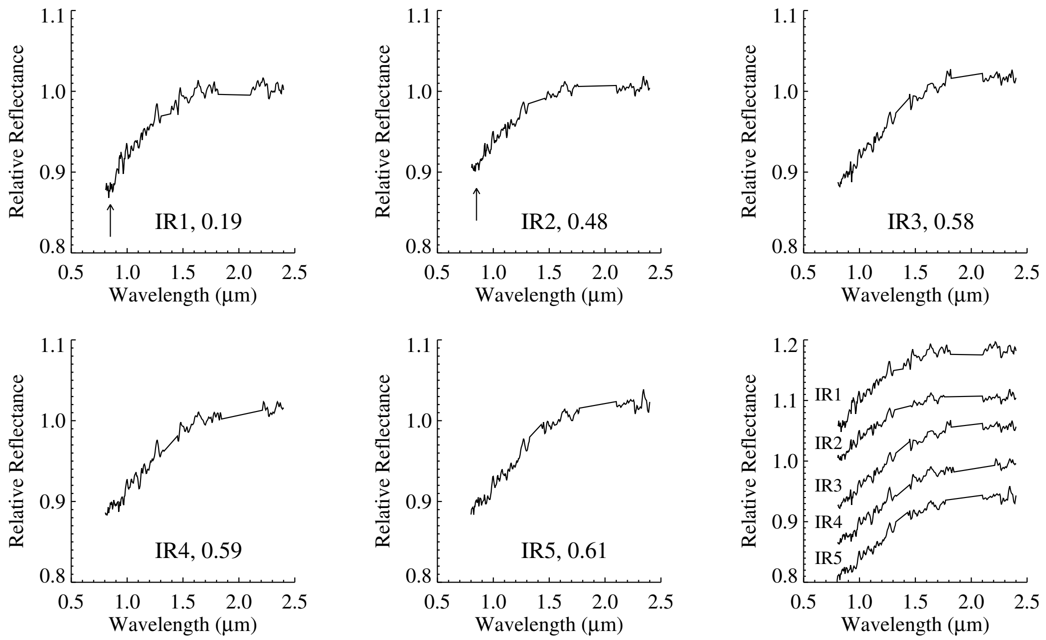

Fig. 3. Same as Fig. 2, but for the near-infrared range. Spectra are normalised to unity at 1.6 μm. Last plot shows all the spectra offset vertically.

stars SA 98-978, SA 102-1081, SA 107-998, and SA 110-361, observed at the same airmass as the object. The final reflectance spectra were normalised to unity at 1.6 μm, and are listed in Table 1, as well as their observational details. Each spectrum was obtained by averaging two (2×) or four (4×) *AB* individual spectra and can be seen in Fig. 3.

3. Results and discussion

We inspected the time-resolved observations in each filter to compute the rotational period of the asteroid, using the Lomb technique (Lomb 1976) as implemented by Press et al. (1979). The highest quality and longer observations, which were those acquired using the Cousins-*R* filter acquired at LOT (19, 20, 21 March), provided a rotational period of 8.16 ± 0.08 h. We also computed the rotational period using observations made with Sloan-i' filter during the same nights, obtaining the same value. Our result is in good agreement with the previously published results, which gave a period of $P = 8.16545$ (Torppa et al. 2003). Figure 4 shows the combined lightcurves used to infer the rotational period, covering a complete rotation. Julian dates, rotational phases, and relative magnitudes for each night are presented in Table 2. It is clearly seen that the asteroid's lightcurve has two asymmetric minima, with a mean peak-to-peak amplitude of 0.25 ± 0.05 mag. The J2000.0 ecliptic coordinates of the latest pole solution, computed from OSIRIS images (Jorda et al. 2010), are $\lambda = 52.^{\circ}2 \pm 1.^{\circ}0$ and $\beta = -7.^{\circ}8 \pm 1.^{\circ}0$. Following this pole solution, our observations were made with an aspect angle of $\xi \sim 72°$, i.e., Lutetia was in a near equatorial aspect. Nedelcu et al. (2007) observed Lutetia with a similar aspect angle and obtained an amplitude of 0.27 mag, in good agreement with our results.

We can see in Fig. 1 that, considering the dispersion in the data of some of the lightcurves, they all have a similar behaviour, and no major differences are found among them. We note that in the combined lightcurve in Fig. 4, and in almost all the lightcurves obtained using different filters, we can observe a "depression", a small-scale magnitude variation marked in the

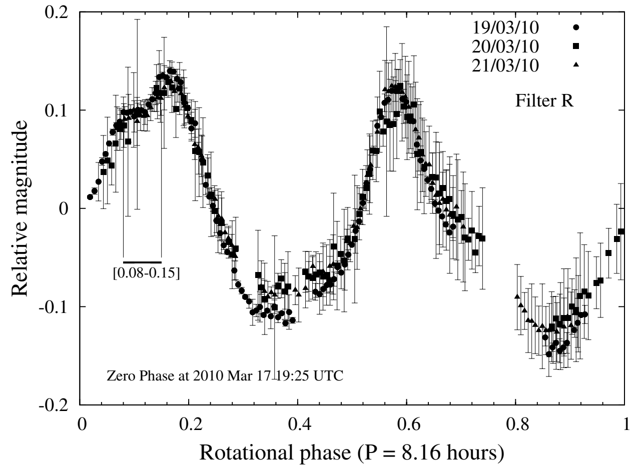

Fig. 4. Combined lightcurve of asteroid (21) Lutetia using photometric data in *R* broadband filter at different observing nights (March 19, 20, and 21, see Table 1). The zero rotational phase was chosen to occur at JD = 2 455 273.3094 (March 17 at 19:25 UTC). The rotational period inferred from this combined lightcurve was derived to be $P = 8.16 \pm 0.08$ h.

figure, between 0.08 and 0.15 rotational phases. This feature can be associated with both a variation in the albedo or a change in the topography (most likely a crater), although the second interpretation is preferred, as albedo spots are rarely detected among asteroids.

With this result in mind, a month after the photometric observations we obtained visible and near-infrared spectra of the asteroid during the rotational phase (around 0.1) when this "depression" was detected. We also took spectra at another rotational phase (around 0.6), for comparison purposes. Each visible and near-infrared spectrum obtained is shown in Figs. 2 and 3, respectively, labelled by their corresponding identifier and rotational phase. For visible spectra, we observe a significant difference between those taken at 0.1 (V4, V5, V6) and the rest

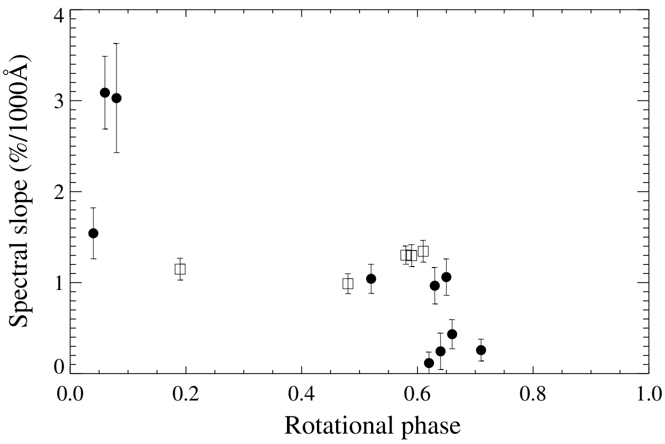

Fig. 5. Spectral slope S' computed in the range 0.5–0.9 μm for the visible spectra (dots), and in the range 0.9–1.8 μm for the near-infrared (open squares) versus rotational phase. Visible and near-infrared spectra are normalised to unity at 0.55 and 1.6 μm respectively.

of spectra. To quantify this variation, we computed the spectral slope S' between 0.5 and 0.9 μm for all the spectra. The obtained values are shown in Table 3 and plotted against rotational phase in Fig. 5. Visible spectra taken around 0.1 have redder slopes. However, they also have a higher dispersion, as they were observed at a higher airmass (see Table 1). Therefore, caution must be taken when interpreting this result, as the effect of differential refraction is higher, and its correction is more critical at visible wavelengths. Nevertheless, the difference in spectral slope at these two rotational phases can be tentatively interpreted in terms of surface inhomogeneities, as we are observing different portions of the surface of the asteroid. These inhomogeneities could be associated with differences in mineralogical composition or be the effect of materials processed to different degrees and then exposed in a crater area.

If we analyse each individual spectrum, we can see an absorption band centred at 0.58–0.60 μm in the V4, V5, and V6 spectra (this last one being significantly deeper). This absorption band has been reported by other authors (Lazzarin et al. 2004; Vernazza et al. 2009; Perna et al. 2010) and detected in the spectra of enstatite chondrites, as well as in minerals produced by aqueous alteration of silicates. Another potential absorption feature centred around 0.78–0.79 μm is seen in V1, V2, and V3 spectra, and is associated with the presence of ferrous and ferric iron in various oxides (crystal field transition Fe^{3+}). These type of features related to oxidation are also observed in the spectra of C and M type asteroids (Busarev 2002). Finally, a broad and shallow absorption band centred around 0.65 μm is marginally present in the series V7-V10, and is also attributable to aqueous altered materials on the surface of the asteroid.

For near-infrared spectra (see Fig. 5), we are unable to discern any significant differences between the data obtained at different rotational phases. As for the visible spectra, we computed the spectral slope S' between 0.9 and 1.8 μm. The values obtained are listed in Table 3 and plotted against rotational phase in Fig. 5 (open squares). We do not see any significant difference in the spectral slopes. Individual spectra are also very similar to each other. Nevertheless, a very weak absorption feature centred around 0.80–0.85 μm, which is barely detectable, can be distinguished in the IR1 and IR2 spectra (see the arrows in Fig. 3). This absorption feature was previously reported

Table 3. Computed spectral slopes in the range 0.5–0.9 μm for visible spectra and 0.9–1.8 for near-infrared spectra.

Spec. Id.	Rot. phase	S' (%/1000 Å)	Spec. Id.	Rot. phase	S' (%/1000 Å)
V1	0.52	1.04 ± 0.16	IR1	0.19	1.15 ± 0.10
V2	0.63	0.97 ± 0.20	IR2	0.48	0.99 ± 0.09
V3	0.65	1.06 ± 0.20	IR3	0.58	1.30 ± 0.08
V4	0.04	1.54 ± 0.28	IR4	0.59	1.28 ± 0.10
V5	0.06	3.09 ± 0.40	IR5	0.61	1.35 ± 0.10
V6	0.08	3.03 ± 0.60			
V7	0.62	0.12 ± 0.12			
V8	0.64	0.24 ± 0.20			
V9	0.66	0.43 ± 0.16			
V10	0.71	0.26 ± 0.12			

by Lazzarin et al. (2004) and Belskaya et al. (2010), and is attributed to charge transfer transitions in oxidised iron.

4. Conclusions

We have compiled photometric lightcurves using several filters and spectra in the visible and near-infrared range for the asteroid (21) Lutetia, just three months before the Rosetta fly-by. Taking into account the results of our data analysis presented here, we have been able to draw some conclusions that support the findings derived from previous observations:

1. From the photometric lightcurves acquired during three consecutive nights, we have obtained a rotational period of 8.16 ± 0.08 h, in good agreement with previous determinations. The rotational lightcurve of the asteroid has two asymmetric minima, with a peak-to-peak amplitude of 0.25 ± 0.05 mag.
2. The lightcurves obtained using different filters have similar properties. We can see a small-scale magnitude variation in all of them, some sort of "depression" around 0.1 rotational phase. This feature could be associated with both variations in mineralogical composition or a shadowing effect caused by the topography of the surface.
3. Visible spectra were taken around 0.1 and 0.6 rotational phases, and spectral slope was computed in the range 0.5–0.9 μm. Spectra taken at a 0.1 rotational phase had redder slopes, which are indicative of differences in mineralogical composition or the level of processing of materials in a crater area. For the near-infrared spectra, we have been unable to discern any significant variation in the spectral slope with rotational phase. Some absorption features were detected in both visible and near-infrared spectra, and were attributed to the action of aqueous alteration on minerals, namely enstatite, phyllosilicates, or oxidised iron. However, infrared data obtained during the fly-by almost exclude the presence of hydrated minerals on the surface of the asteroid.

Acknowledgements. This research has been partially funded by the Ministerio de Ciencia e Innovación through the project AYA 2009-08011. J. de León and Z.-Y. Li. acknowledge a post-doctoral contract by the Junta de Andalucía research project PE07-TIC2744. R. Duffard acknowledges financial support from MICINN (contract Ramón y Cajal). We thank the Centro Astronómico Hispano-Alemán (CAHA) for the facilities and support made available at Calar Alto. We also thank all staff and observers of the Lulin telescope for various arrangements in realizaing this observation. This paper is based on observations made with the Italian Telescopio Nazionale Galileo (TNG) operated on the island of La Palma by the Centro Galileo Galilei of the INAF (Instituto Nazionale di Astrofisica).

Note added in proof Fly-by of asteroid (21) Lutetia was successfully completed on July 10, 2010. Images taken by OSIRIS instrument onboard the spacecraft show that the asteroid is covered with many craters, varying in size. They also show a large crater located close to the asteroid's equator, expanding from -10° to 40° in latitude (Marchi, priv. comm.). That crater could account for the small scale variation in magnitude observed in the ligthcurves presented in this paper.

References

Barucci, M. A., Fulchignoni, M., Fornasier, S., et al. 2005, A&A, 430, 313
Belskaya, I. N., Fornasier, S., Krugly, Yu. N., et al. 2010, A&A, 515, A29
Birlan, M., Vernazza, P., Fulchignoni, M., et al. 2006, A&A, 454, 677
Busarev, V. V. 2002, Sol. Syst. Res., 36, 35
Carvano, J. M., Barucci, A., Delbó, M., et al. 2008, A&A, 479, 241
de León, J., Licandro, J., Serra-Ricart, M., et al. 2010, A&A, 517, A23
Duffard, R., & Roig, F. 2009, Planet. Space Sci., 57, 229
Fornasier, S., Barbieri, C., Barucci, M. A., et al. 2010, BAAS, 42, 1032
Jorda, L., Lamy, P., Besse, S., et al. 2010, BAAS, 42, 1043
Lamy, P. L., Groussin, O., Fornasier, S., et al. 2010, A&A, 516, A74
Landolt, A. U. 1992, AJ, 104, 340
Lazzarin, M., Marchi, S., Magrin, S., et al. 2004, A&A, 425, L25
Lazzarin, M., Marchi, S., Moroz, L. V., & Magrin, S. 2009, A&A, 498, 307
Lomb, N. R. 1976, Ap&SS, 39, L447
Lupishko, D. F., & Mohamed, R. A. 1996, Icarus, 119, 209
Mueller, M., Harris, A. W., Bus, S. J., et al. 2006, A&A, 447, 1153
Nedelcu, D. A., Birlan, M., Vernazza, P., et al. 2007, A&A, 470, 1157
Perna, D., Dotto, E., Lazzarin, M., et al. 2010, A&A, 513, L4
Press, W. H., Teukolsky, S. A., Vetterling, W. T., & Flannery, B. P. 1992, in Numerical Recipes in Fortran: the art of scientific computing, 2nd edn. (London: Cambridge University Press), 569
Tody, D. 1993, in Astronomical Data Analysis Software and Systems II, ed. R. J. Hanisch, R. J. V., Brissenden, & J. Barnes (San Francisco: Astron. Soc. of the Pacific), 173
Torppa, J., Kaasalainen, M., Michalowski, T., et al. 2003, Icarus, 164, 346
Vernazza, P., Brunetto, R., Binzel, R. P., et al. 2009, Icarus, 202, 477

A&A 525, A36 (2011)
DOI: 10.1051/0004-6361/201015515

Astronomy & Astrophysics

67P/Churyumov-Gerasimenko activity evolution during its last perihelion before the Rosetta encounter

L. M. Lara[1], Z.-Y. Lin[1], R. Rodrigo[1], and W.-H. Ip[2]

[1] Instituto de Astrofísica de Andalucía (CSIC), Glorieta de la Astronomía s/n, 18008 Granada, Spain
e-mail: lara@iaa.csic.es
[2] Institute of Astronomy, National Central University, Taiwan
e-mail: wingip@astro.ncu.edu.tw

Received 2 August 2010 / Accepted 23 September 2010

ABSTRACT

Context. The comet 67P/Churyumov-Gerasimenko, target of the Rosetta Mission (ESA) was monitored from January to April 2009 during its last perihelion passage before the Rosetta spacecraft encounters the comet nucleus in May 2014. Photometric data were obtained only from January 25 to March 19, 2009 and they were used to monitor the comet gas and dust activity. Non-photometric data are considered for analysing the evolution of the dust coma morphology.

Aims. The goal of the campaign was to characterize the comet activity evolution as it approaches the Sun. We aimed to assess gas and dust production rates shortly before perihelion and after perihelion, as well as to follow the evolution of the dust coma morphology during this passage.

Methods. Long-slit spectra and optical broadband images were acquired with the instrument CAFOS mounted at the 2.2. m telescope at Calar Alto Observatory (CSIC-MPG), and with the camera at the 1-m telescope of the Lulin Optical Observatory in Taiwan. We investigated the evolution of the dust coma morphology from the R Johnson images with image enhancing techniques. When possible, we studied the dust and gas production rate, the radial profiles of the dust brightness azimuthally averaged and in the Sun-antisunward direction, and the Sun-antisunward profiles of the CN, C_2, C_3, and NH_2 column densities.

Results. The morphological analysis of the dust coma reveals that structures indeed exist. Aside from the dust tail in the SW direction, four more small-scaled structures have been detected by using the adaptive Laplacian filtering, the radial renormalization and the Sekanina-Larson method. These structures are also confirmed by the distortion of the isophotes at the same position angles (PA). During January and February, a faint structure could be seen at PA 330°, whereas this feature seems to have disappeared after perihelion. Additionally, the broad structure at PA $\sim$ 45° seemed to split into two narrower ones on February 26, to become only a considerably fainter one at PA $\sim$ 75° during March. The Afρ values show considerable scatter in the few days we could measure them. There is a clear increase when the comet approaches the perihelion, however it is not possible to conclude where the peak dust activity is reached when the comet is at or beyond the closest distance to the Sun. The CN, C_2, C_3, and NH_2 production rates, Q, have been obtained at r_h 1.25 AU. These Q's are very similar to the ones derived from previous passages around perihelion. The decrease in the perihelion distance in 2009 (1.24 AU in 2009 vs. 1.30 AU in 1982 and 1995) has not induced a noticeable increase either in the gas production rates or in the dust production rates, as measured from the Afρ parameter. The azimuthally averaged surface brightness profiles of the continuum from the broad band images can be well fitted with $-1.92 \leq m \leq -1.35$ in $\log B - \log \rho$ representation for $\rho \leq 100\,000$ km projected cometocentric distance from the R broadband images. On the other hand, when the fit is done in the sun-antisunward direction from the long-slit spectra at $\rho \leq 25\,000$ km, the slope $m \approx -1$.

Key words. comets: general – comets: individual: 67P/Churyumov-Gerasimenko

1. Introduction

On March 2, 2004, the ESA mission Rosetta was launched to explore the comet 67P/Churyumov-Gerasimenko (67P/C-G hereofafter) from May 2014 until December 2014, i.e. the nominal mission duration. The mission target was discovered in 1969 after its perihelion at 1.28 AU, although the comet had several perturbations by Jupiter (1840 and 1959), which have moved the perihelion distance from 2.7 AU prior to 1959 to the current values.

The available data for 67P/C-G is very scarce, because only a few apparitions have provided the ground-based observers with good visibility conditions and a good resulting dataset. There are reported observations during the 1982/83, 1995/96 and 2002/03 perihelion passages (Osip et al. 1992; Weiler et al. 2004; Lara et al. 2005; Schleicher 2006; Ferrín 2010). Results given in Osip et al. (1992) for the 1982/83 apparition conclude that comet 67P/C-G shows a significant asymmetry in both the dust and the gas production rates, with peak productivity occurring in the month after perihelion, and the measured dust-to-gas ratio was considerably high, even higher than for 1P/Halley. During the 1995/96 apparition, Schleicher (2006) obtained data during the pre-perihelion phase and during a few days after the perihelion passage itself. The time range was thus −61 to +118 days from perihelion such that the asymmetry already pointed out by Osip et al. (1992) could be analysed during one more passage. Also, Weiler et al. (2004) analysed spectrophotometric observations of 67P/C-G about 20 days after the 1995/96 perihelion passages, whereas Weiler et al. (2004) and Lara et al. (2005) also studied on the morphological analysis of the dust coma of the comet during the 2003 post-perihelion at r_h = 2.36–2.78. On one hand, Lara et al. (2005) report on dust structures in the inner coma at position angles of 295° and 195°, as well as on a long spike in anti-tail direction reaching 230 000 km identified as a

Table 1. Log of photometric observations and results from R broadband images.

Date 2009	r_h (AU)	Δ (AU)	ΔT^a (days)	PA (deg)	α (deg)	$Af\rho_{10\,000\ km}$ (cm)	m_1	m_2	Location^b
January 25	1.314	1.671	–34	67.8	36.1	245	–1.47	–1.37	LOT
January 30	1.294	1.670	–29	67.5	36.1	252	–1.49	–1.38	LOT
January 31	1.291	1.669	–28	67.4	36.1	250	–1.49	–1.49	LOT
February 23	1.247	1.678	–5	67.5	35.9	344	–1.92	–1.22	LOT
February 25	1.247	1.680	–3	67.5	35.8	257	–1.45	–1.18	LOT
February 26	1.246	1.681	–2	67.5	35.8	373	–1.54	–1.18	LOT
March 12	1.256	1.709	12	69.2	35.1	426	–1.58	–1.09	LOT
March 19	1.269	1.732	19	70.4	34.6	383	–1.35	–1.11	CA

Notes. r_h and Δ are the heliocentric and geocentric distance of the component during the observations, respectively. PA is the position angle of the extended Sun-target radius vector. α is the phase angle Sun-comet-observer. Afρ values are derived for photometric circular aperture with radius 10 000 km from the comet's nucleus. Errors on Afρ are of the order of 10% and are mainly due to absolute flux calibration errors. m_1: slope of the linear fit log B vs. log ρ for $3.5 \leq log\ \rho \leq 5$. Standard deviation of these fits is always lower than 5%. m_2: slope of the linear fit log B vs. log ρ for $3.5 \leq log\ \rho \leq 4.4$. Standard deviation of these fits is always lower than 5%. $^{(a)}$ Days from perihelion; $^{(b)}$ LOT stands for Lulin Optical Telescope (Taiwan) and CA for Calar Alto Observatory (Spain).

neck-line. On the other hand, Weiler et al. (2004) analysed the dust and gas production rate three weeks after the comet passed perihelion on Jan. 17, 1996 and found the same asymmetry as Osip et al. (1992). As a summary, from the data acquired during the last 3 Sun passages, the dust coma of comet 67P/C-G has displayed structures on large and small scales, whereas the gas and dust production rates peaked at about 1 month after perihelion.

The 2009 apparition has not had good visibility for ground-based observers, and usable data were only acquired during few hours in a short interval of time near perihelion, which took place on February 28, 2009. In this paper, we present non-photometric (for coma morphology description), photometric, and spectrophotometric measurements (both for deriving dust and gas production rates, respectively) from the end of January to mid-April 2009. The photometric observations monitor the comet from 1.314 AU pre-perihelion to 1.269 post-perihelion (i.e. −34 to +19 days to perihelion), whereas the non-photometric data follow the comet activity up to r_h = 1.373 AU post-perihelion on April 16, 2009. With this dataset, we have aimed at a global characterization of the Rosetta mission target during its last visit to the inner Solar System before the Rosetta spacecraft encounters the comet nucleus in May 2014.

2. Observations and data reduction

The comet was monitored from the Calar Alto Observatory (CSIC-MPG, near Almería, Spain) from February 22 until April 16, 2009, and from the Lulin Observatory (National Central University, Taiwan) from January 25 until March 22, 2009. Data from both observatories represents a total of 23 observing nights, in which broad-band images and spectroscopic measurements were acquired. However, only ∼30% of the planned data were obtained given the bad weather conditions at Calar Alto Observatory during the first semester of 2009, and not very good target visibility from Lulin Observatory. More concisely, broadband images acquired at either the Calar Alto observatory or Lulin Optical Telescope under non-photometric conditions have only been considered for an indepth morphological analysis (some of them shown and described here), which will be published in a forthcoming paper (Vincent et al. 2011, in prep.). All comet observations were done in service mode at both observatories with telescope tracking at the comet's proper motion. The typical mean seeing was ∼1.0−1.2″ at both observatories.

Imaging. Imaging data were obtained with the central 1k × 1k pixels of the instrument CAFOS (pixel size: 0.″53, FOV 9′ × 9′) mounted at the 2.2 m telescope. The comet was imaged with Johnson R broadband filter by acquiring consecutive series of 5 to 10 images. A considerable data set was also acquired with a CCD at the 1 m optical telescope at the Lulin Observatory, LOT, (1340 × 1300, pixel size 0.515″, FOV 11.0′ × 11.2′). The comet was imaged with B, V, R, and I Asahi filters Appropriate bias, darks and flat field frames were also taken each night, and the usual data reduction was made. If photometric conditions prevailed, photometric stars were observed at an airmass similar to the comet observations for absolute flux calibration. Table 1 only lists the details of the imaging observations acquired during photometric conditions.

Spectroscopy. The spectroscopic measurements were done on February 22−24, and March 19, 2009. We used CAFOS with grism B200 and B400 (see `http://www.caha.es/alises/cafos/cafos22.pdf`) providing us with an observable spectral range between 320 and 880 nm and a wavelength scale of 0.475 nm per pixel, and between 280 and 1000 nm with a wavelength scale of 0.97 nm per pixel, respectively. The slit of the spectrograph is oriented along the Sun-comet direction, as projected on the plane of the sky, giving dust and gas radial profiles in the Sun-antisunward direction. For absolute calibration, observations of appropriate spectrophotometric standard stars were acquired. For the comet observations, the slit width is 2″, whereas the usable selected length is 10.6′, which provides us with radial profiles along selected directions up to cometocentric projected distances of $\geq 10^5$ km. The spectrophotometric standard star was observed with a width of 5″ and the same slit length.

Since the gas emission of 67P/Churyumov-Gerasimenko does not cover the entire length of the slit, it is possible to extract the sky contamination directly from the edges of the frame. More details on the images and spectra reduction and calibration can be found in Lara et al. (2001), Bertini et al. (2009) and Lin et al. (2009).

The images, regardless the sky conditions, have been used to study (i) the dust coma morphology by applying a Laplace filtering technique (Boehnhardt & Birkle 1994), the radial renormalization, and the Sekanina-Larson method (Larson & Sekanina 1984); (ii) the azimuthally averaged profile of surface brightnesses, whereas in photometric sky conditions, the images have

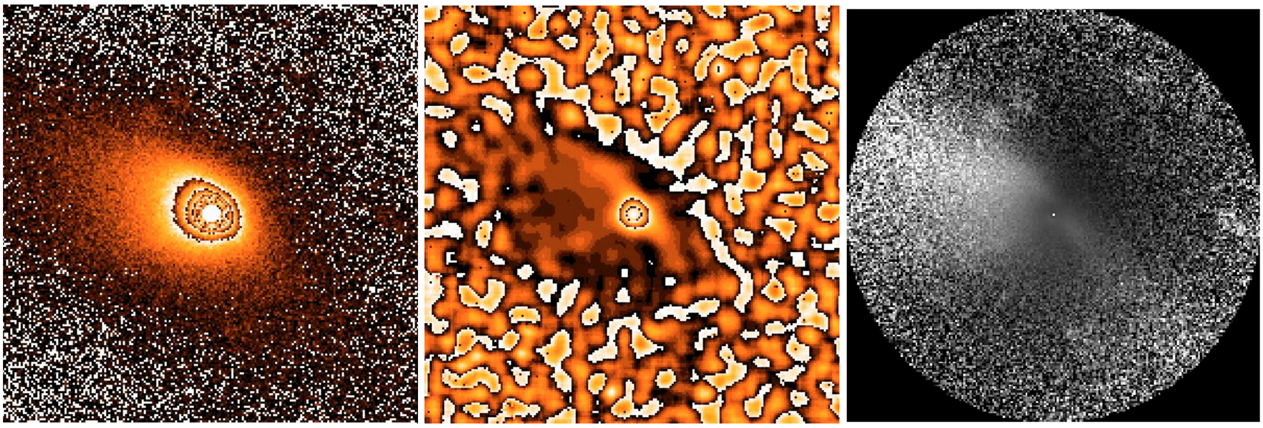

Fig. 1. Image of 67P/Churyumov-Gerasimenko on January 30, 2009, acquired with *R* Johnson filter: **a)** corrected of flat, bias, and sky background, **b)** adaptive Laplace filtered, and **c)** enhanced by the radial renormalization technique. North is up and east to the left. The FOV is 103″ × 103″, meaning 125 000 × 125 000 km at the comet distance.

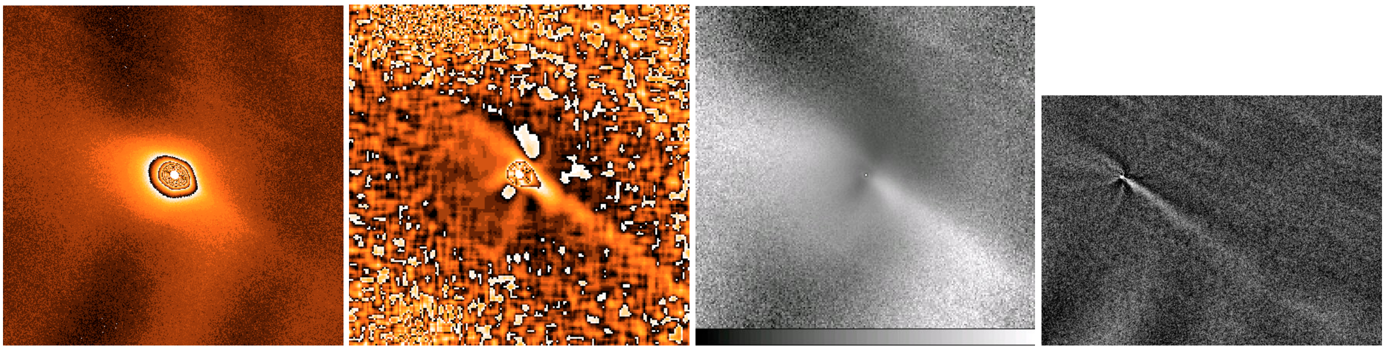

Fig. 2. Image of 67P/Churyumov-Gerasimenko on February 18, 2009, acquired with *R* Johnson filter. *From left to right*: corrected of flat, bias, and sky background; Laplace filtered; radially renormalized; and enhanced by the Sekanina-Larson method. North is up and east to *the left*. The FOV is 212″ × 212″ (192 000 × 192 000 km), 106″ × 106″, 106″ × 106″ (96 000 × 96 000 km), and 208″ × 158″ (189 000 × 143 000 km). The isophotes in the observed image clearly indicate the presence of structures in the inner coma, which are nicely enhanced in the Laplace filtered image, as well as in the resulting frame of the Sekanina-Larson method. However, the radially renormalized image is most suitable for detecting broad and large-scale structures.

been used for analysing the behaviour of Afρ as a function of projected cometocentric distance ρ and of r_h.

On the other hand, the spectra have provided us with CN, C_2, C_3 and NH_2 production rates in the frame of the Haser modelling (Haser 1957), and with dust brightness profiles as a function ρ in the Sun-antisunward direction.

3. Data analysis and results

3.1. Morphology of coma structures

To determine whether some morphological structures are present in the coma 67P/Churyumov-Gerasimenko, we enhanced the *R* filter calibrated images using three different methods: (1) adaptive Laplace filtering as described in Boehnhardt & Birkle (1994) and references therein; (2) radial normalization (A'Hearn et al. 1986) for verification in case there are features after the Laplace filtering; and (3) Sekanina-Larson method (Larson & Sekanina 1984). An independent verification was also done by looking for anisotropies in the isophotes. For this study, we used a sequence of 21 images depicting the evolution of the coma between January 25 and April 16, 2009. This analysis was done on images acquired either under photometric or non-photometric sky conditions as the coma morphology does not depend on them.

The description of coma phenomena is based upon what we found in the Laplace filtered images, and in the Sekanina-Larson processed images, and verified as much as possible in the radially normalized images and in the isophote images

From January 25 to 31, the isophote images show a distorted coma: there is a the long spike in the SW direction (presumably the dust trail) as well as are indications of two more structures, one pointing in approximately the Sun direction, and another at PA ∼ 330°. Both of them become clear after applying any enhancement technique. Figure 1 shows the observed comet image on January 30 after reduction, the Laplace filtered image, and the same image after applying the radial renormalization enhancement technique

During February, the dust coma evolves, the isophotes become more distorted (see Fig. 2), and the structures that are barely seen in January can be undoubtedly detected. On February 18, we can determine three structures at position angles (measured counterclockwise from the north) PA of 40° slightly deviated from the Sun direction, of 115°, and of 170°. A very detailed inspection of the Laplace filtered image in Fig. 2 allows us to infer a fourth short structure, rather close to the dust tail, at PA ∼ 225°. Beside these jets, the long spike in the SW direction is notably enhanced by any of the methods we have used.

Later on, the broad structure at PA 40° seems to split into two narrower ones on February 26, to become only one and much fainter during March. This evolution can be seen in Fig. 3.

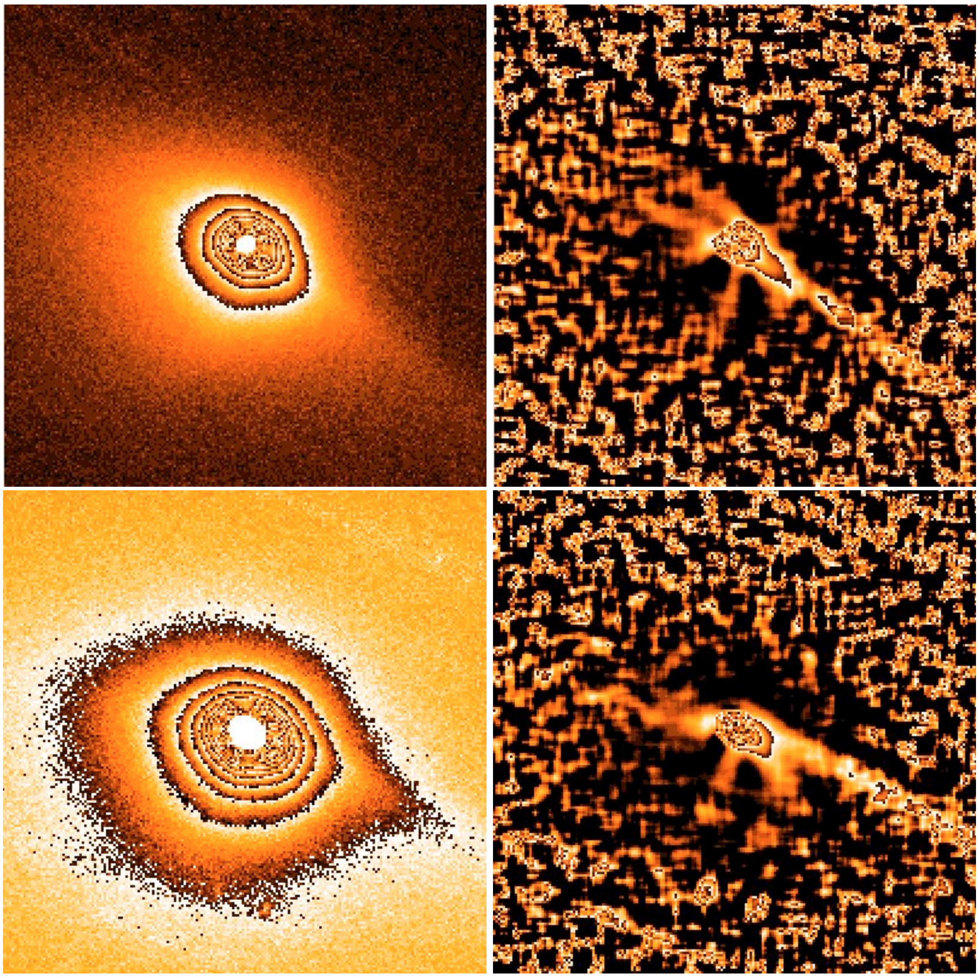

Fig. 3. Evolution of the inner dust coma isophotes and structures of comet 67P/Churyumov-Gerasimenko in 3 weeks. *Top row*: Feb. 26. *Bottom row*: March 19. The FOV is 106″ × 106″ (i.e. 129 300 × 129 300 km and 133 100 × 133 100 km), N is up and E to *the left*. The two structures on Feb. 26 in the NE quadrant only became one and much fainter fainter on March 19, and is slightly curved and is placed at ∼75° counterclockwise from the north.

Additionally, the faint structure at ∼300° visible during January and February disappears in the images of March 12 and 19, whereas on those dates the fourth structure detected in the January and February images have moved more to the south and are now clearly distinguishable from the dust tail.

A more detailed study of the evolution of the dust coma structures, retrieval of the spin axis orientation, and determination of the number and location of active areas will be presented in a forthcoming paper (Vincent et al. 2011, in prep.). Neither Sun-comet-observer angle (i.e. phase angle) nor the position angles of the extended Sun-comet radius vector ("PsAng") has noticeably changed in the period of time covered by our observations, therefore the changes in the dust coma morphology are not due to a different viewing geometry, but intrinsic to the variability in the cometary dust coma.

Beside these structures, i.e. straight jets, the radially renormalized images also show a clear asymmetry in the Sun-antisunward hemisphere, the sunward hemisphere depicting a higher brightness in *R* Johnson filter for every date that we have monitored the comet (see Fig. 4).

The comet also displayed structures in its dust coma at the 1995/96 apparition, whereas during the 1982/83 apparition no available publications on dust coma morphology were found. In fact, Osip et al. (1992), who analysed data pertaining to the 1982/83 perihelion passage, only mention an asymmetry about perihelion in all species with peak productivity occurring in the month following the perihelion. Schleicher (2006) obtained a limited number of images of comet 67P/C-G on January 25, 1996, one week after perihelion. The images were enhanced by removing a $1/\rho$ profile and they detected a strong feature towards the southwest, at a position angle (PA) of about 230−240°, linking this structure with a jet apparently emitted from somewhere on the sunward hemisphere of the nucleus. A second more diffuse feature extends towards the east and is centered at PA of 85° linked to older material within a dust tail. They also reported a general asymmetry with more material towards the southeast than to the northwest. Basically, the structures described by Schleicher (2006) broadly correspond to the ones described in this paper pertaining to the 2009 perihelion passage. However, Schleicher (2006) did not find any additional feature to those mentioned above, whereas our analysis indeed indicates narrow and faint structures at several position angles in the coma whose evolution with time during the 4 months monitoring results in changes of the shape, curvature and number. During March 2003 when the comet was moving outbound from r_h 2.47 to 3.06 AU, Weiler et al. (2004) obtained a series of images in *R*-broadband filter in which an asymmetric coma and an extended neck-line structure could be seen (since the Earth was very close to the comet's orbital plane). In addition to this, two more structures at PA of ∼125° (tentatively identified as part of

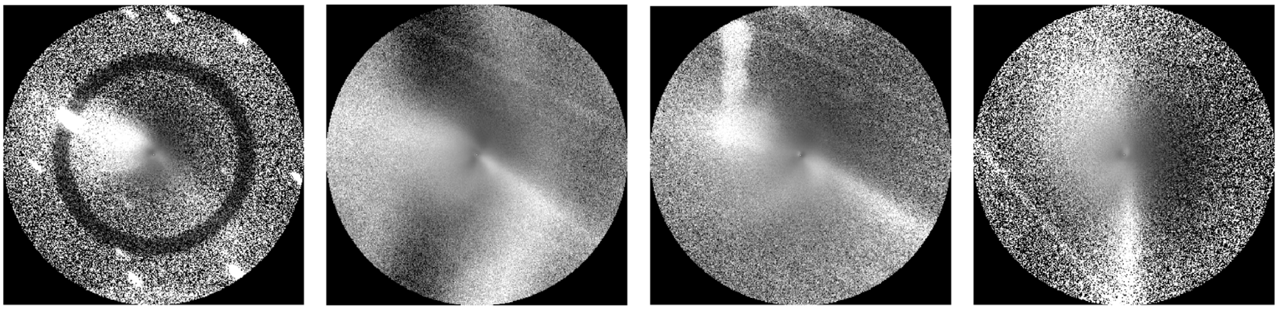

Fig. 4. Radially renormalized images of 67P/Churyumov-Gerasimenko acquired with R Johnson filter on the following dates (*from left to right*): January 25, February 18, March 12, and April 11, 2009. North is up and east to the left. The FOV is 90″ × 90″ for every frame, resulting into 85 600 × 85 600 km, 81 700 × 81 700 km, 81 900 × 81 900 km, and 88 000 × 88 000 km, respectively.

the tail structure) and ~200° were detected. From February 20 to April 20, 2003, Lara et al. (2005) also analysed a series of broadband images of comet 67P/C-G and arrived at the same conclusion, that is, there is asymmetric dust coma, a bright, thin structure at ~294°, and two further jet-like features at position angles ~95° and ~195°. Thus, from the complete available set of observations since 1982, we can conclude the comet 67P/C-G does not show a symmetric dust coma, but a dust coma with structures in it whose size, shape, and number change with the heliocentric distance and with viewing geometry.

3.2. Dust: Afρ and radial profiles

The release of dust from the comet is approximately determined through optical measurements of the parameter Afρ (cm) as a function of the projected cometocentric distance ρ (A'Hearn et al. 1984)

$$\mathrm{Af}\rho = \frac{(2\Delta r_\mathrm{h})^2}{\rho}\frac{F_\mathrm{c}}{F_\mathrm{S}} \tag{1}$$

where Δ (in cm) and r_h (in AU) are the comet's geocentric and heliocentric distances, respectively, F_c is the measured cometary flux in the selected filter (R Johnson in our case), integrated in the radius of aperture ρ, and F_S is the total solar flux in the same filter.

Table 1 contains the Afρ values we were able to measure during our campaign. There is a clear increase when the comet approaches the perihelion on February 28, 2009. Unfortunately, this date is not covered by our observations. As the phase angle barely changes by 2° during our observations, the measured variations in the Afρ parameter do clearly reflect the evolution in dust activity, because the effect of phase angle is not responsible for these variations. Our photometric observation campaign was resumed on March 12, when the Afρ values are very similar to the ones during February 25 and 26 (shortly before the perihelion); therefore, it is impossible to conclude whether the peak dust activity took place close to the perihelion date or afterwards. Compared with previous passages, the Afρ is rather similar to the measurements by Osip et al. (1992) (log (Afρ) between 2.4 and 2.6 to be compared with Fig. 1 in both Osip et al. 1992; Schleicher 2006), and thus slightly higher than the values reported by Schleicher (2006) who claimed an overall decrease in derived Afρ values during the 1995/96 apparition compared to 1982/83. Schleicher (2006) explains those differences between 1982/83 and 1995/96 passages by their different aperture sizes (i.e. larger in the case of the 1995/96 data set) for computing the cometary flux and not to real evolutionary effects. The Afρ values listed in Table 1 were computed within apertures of radius equal 10 000 km at the comet distance, that is, an angular diameter aperture of ~16$''\!.$2, which is in line with the small aperture sizes used by Schleicher (2006) for computing Afρ during the 1982/83 passage.

The behaviour of the continuum intensity, F (flux energy), versus ρ was studied from the azimuthally averaged profiles of every comet image acquired in R broad-band Johnson filter regardless the sky conditions excluding those with low S/N due to passing clouds. The brightness intensity F as a function of the projected cometocentric distance can be fit with a line if expressed in log-log representation. Least-square fits were computed in two different ranges $1'' < \rho \leq 90''$ and $1'' < \rho \leq 20''$, where the lower limit was selected as it is the mean seeing disk in our observations, whereas the upper limit is the distance at which clear comet signal is still well above the sky background for determining m_1, and the inner coma a for determining m_2. The values of the slopes of these fits, $m_{1,2}$ are $-1.58 \leq m \leq -1.09$ between January 25 and March 19 (see Table 1) where the effect of the radiation pressure is clearly seen, giving rise to steeper profiles when considering greater cometocentric distances ρ. The determination of m is characterized by rms errors that are always lower than 5%.

A more thorough study of the dust radial profiles was done by determining the intensity versus ρ at position angles where the structures are clearly visible. For this, we converted the images into polar coordinates and located the angular positions where deviations from a spherical dust coma are more noticeable. For February 23 and March 12, these angles are at about 80° and ~230−240° (see Fig. 5).

Then, the radial profiles log F versus log ρ are computed by azimuthally averaging the measured emission in position angles of (80 ± 30)° and (230 ± 20)° for both dates. The results of this investigation can be seen in Figs. 5 and 6. On March 12, the emission at PA ~ 80°, approximately the Sun direction, was higher than on February 23 even though the comet was receding from the Sun (see also Table 1), whereas the energy intensity at the neck-line angular position is lower after perihelion. Beside this, the slope of the linear fits to log F versus log ρ differ from a position angle of 80° and in the direction of the dust tail as projected on the sky plane (230°). The values of m are −1.50 and −1.57 for Feb. 23 at the azimuthal angles mentioned above, whereas this slope is −1.26 and −1.47 for March 12 at the same angular positions, indicating a higher dust coma anisotropy on March 12 than on Feb. 23.

The spectra also provide us with pure continuum brightness profiles selected from the following spectral ranges: 482−485, 520−525, and 680−690 nm. The slope of linear fit to these log B − log ρ profiles in the range $3000 \leq \rho \leq 63\,100$ km

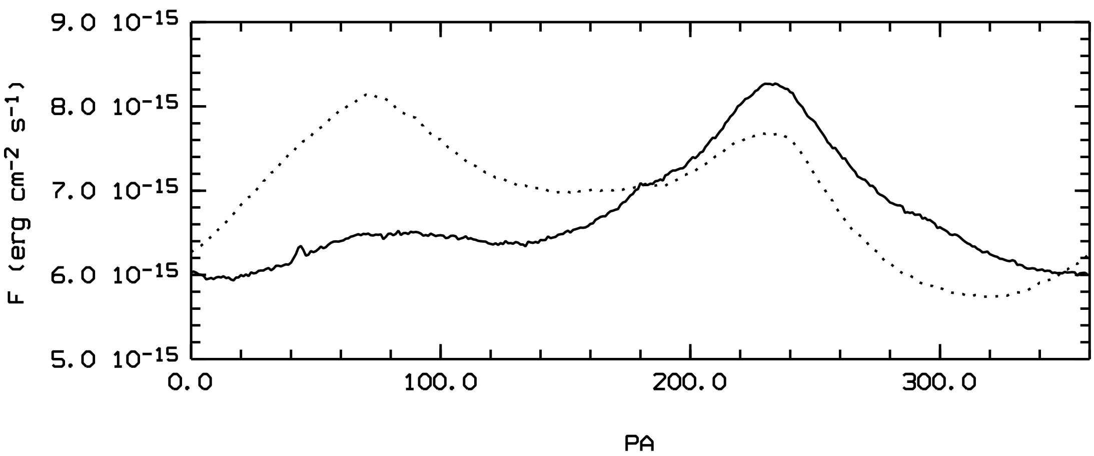

Fig. 5. Azimuthal profile of the brightness intensity for the dust coma of the comet 67P on Feb. 23 (solid line) and March 12 (dashed line) as averaged between the optocentre and 51.5″. The change of the dust coma morphology and of the intensity of the structures from almost perihelion to post-perihelion on March 12. The structure at a position angle of 80° is more pronounced in the post-perihelion than during closest distances to the Sun. On the other hand, the dust tail shows slightly less intensity after the perihelion.

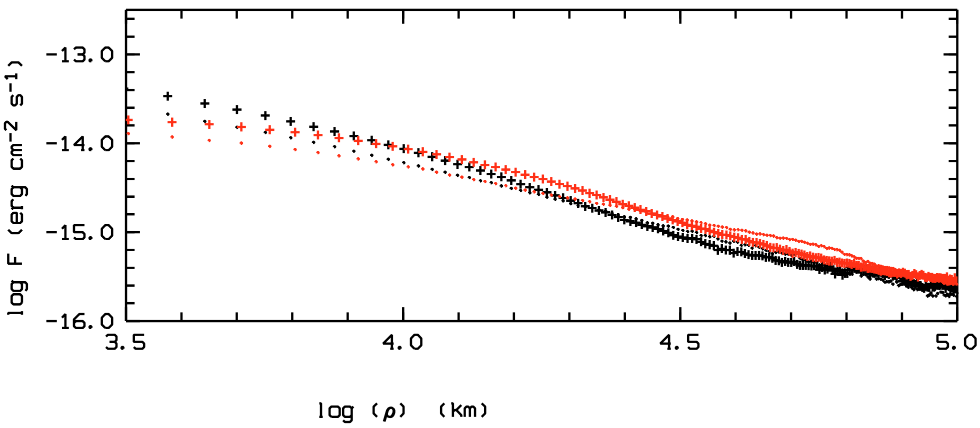

Fig. 6. Dust radial profiles, in log F – log ρ representation at position angles 80° (dots) and 230° (crosses) for Feb. 23 (in black) and March 12 (in red).

provides the values listed in Table 2, which are $m \approx -1$. An example of those profiles on Feb. 23 and March 19 are shown in Fig. 7, together with the best linear fit. At large projected cometocentric distances, the S/N in the spectrophotometric observations is not good enough to obtain a meaningful fit at those distances. In this regard, the values of m_1 listed in Table 1 are more reliable when considering the dust coma up to 100 000 km from the nucleus. Furthermore, the values obtained from the spectra in Sun's direction are closer to the canonical behaviour of $m \approx -1$ of the inner dust coma of long-lived grains expanding at constant speed, whereas in the antisunward direction, m approaches the values listed in Table 1, which are more typical of dust grains already affected by solar radiation pressure and $m \approx -1.5$. In fact, by selecting cometocentric distances in the range 3200–64 000 km from the images, the slope m of the linear fits in log-log representation in Sun-antisunward direction is in very good agreement with results from the long-slit spectrophotometric data.

3.3. Gas production rates

The spectra of the comet are used to investigate the CN, C_2, C_3, and NH_2, and dust continuum profiles in the Sun-antisunward direction. This was possible only on three dates around the comet's perihelion (February 22–24) and on March 19. No further spectra were acquired during the monitoring campaign.

The spectral regions and the subtraction of the underlying continuum in the gas emission bands is done as described by (Lara et al. 2001). The conversion of the emission band fluxes into column densities makes use of constant g-factors for C_2, C_3 and NH_2 (A'Hearn et al. 1995), whereas the g-factor of the CN molecule is calculated for the heliocentric distance and velocity of 67P/C-G on every date from the set of values given by Schleicher (1983). The gas production rates are obtained by means of the Haser (Haser 1957) modelling with parent velocity v_p scaled with r_h ($v_p = 0.86\ r_h^{-0.4}$ km s^{-1}), customary values for the daughter velocity $v_d = 1$ km s^{-1} and scale lengths given in A'Hearn et al. (1995). For the corresponding set of parameters in the Haser modelling, we produced theoretical column density profiles for each species by varying the production rate until the best match between observations and theoretical predictions is achieved.

The production rates obtained that better match the observed column densities and log $[Q(C_2)/Q(CN)]$, log $[Q(C_3)/Q(CN)]$ and log $[Af\rho/Q(CN)]$ are listed in Table 3, whereas as an example, Fig. 8 shows the observed CN and C_3 column density radial profiles in both the anti-sunward and sunward directions together with the best achievable Haser fit.

Table 2. Linear fits to the log B – log ρ profiles obtained form the long-slit spectroscopic measurements.

Date 2009	Direction	Continuum regions 482–485 nm	520–525	680–690 nm	Location
February 22	sunward	–0.93	–1.03	–1.10	CA
	antisunward	–0.92	–1.11	–1.23	CA
February 23	sunward	–1.13	–1.19	–1.20	CA
	antisunward	–1.23	–1.34	–1.36	CA
February 24	sunward	–0.81	–0.91	–1.05	CA
	antisunward	–0.87	–0.98	–1.18	CA
March 19	sunward	–0.96	–1.09	–1.27	CA
	antisunward	–1.00	–1.14	–1.31	CA

Notes. m: slope of the linear fit log B vs. log ρ for $3.0 \leq log\ \rho \leq 4.4$ (i.e. $1000 \leq \rho \leq 25\,000$). Standard deviation of these fits is always lower than 5%.

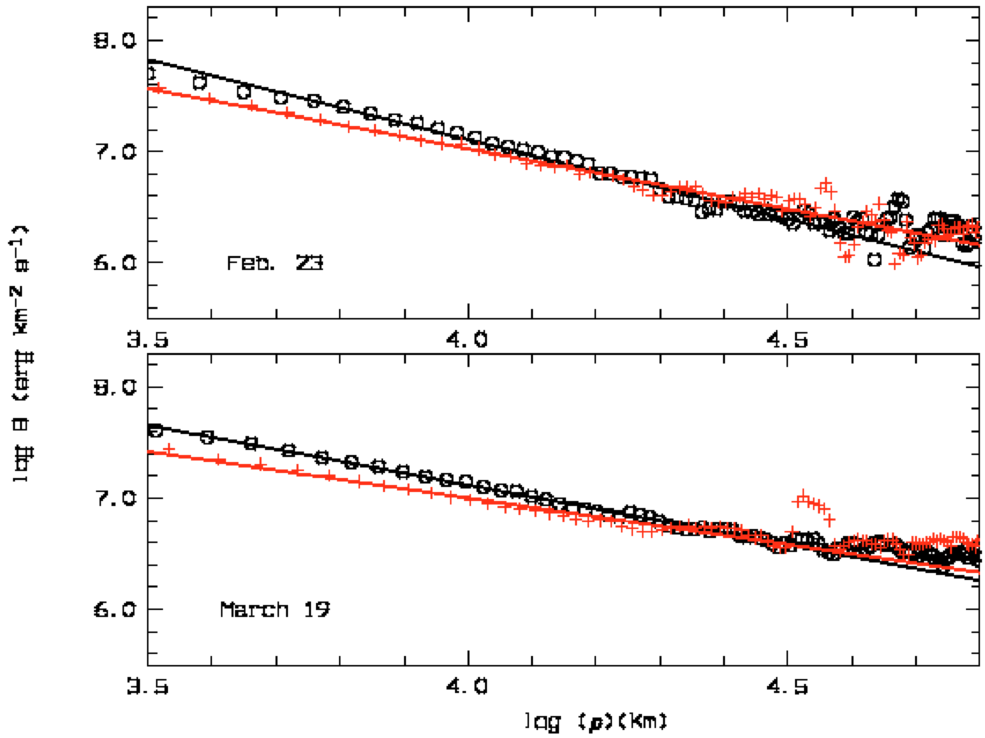

Fig. 7. Dust brightness profiles, in log B – log ρ representation obtained from the spectroscopic measurements on Feb. 23 and March 19, 2009 in Sun (red crosses) – antisunward (black open circles) direction. The selected continuum region is 482−485 nm. Symbols refer to the observational data and solid line refers to the linear fit.

The quotients of the C_2 and CN gas production rates show relatively stable values during the days the spectra were acquired. According to the results listed in Table 3, comet 67P/C-G can be classified as typical following the taxonomic types identified in A'Hearn et al. (1995). The CN, C_3, and NH_2 production rates display rather stable values in that short time span decreasing with increasing heliocentric distance. This trend seems to contradict previous passages results in which the peak activity was reached during the month following the perihelion. Our observations only cover 2 weeks after perihelion, and thus, the minimum measured on March 19, 2009 could be only due to short time variations and not a global decrease in comet activity when receding from perihelion.

The quotient log [Afρ/Q(CN)] has a value of ∼−22 on the only two dates the quotient could be derived. The log [Afρ/Q(CN)] is in the same order of magnitude as reported in previous apparitions around the perihelion (∼−22.3 from Table 1 in Osip et al. 1992; and Table 3 in Schleicher 2006). In spite of the closer heliocentric distance at perihelion during the 2009 passage, the derived gas production rates are very much in the same order of magnitude as during the 1982 (r_h ∼ 1.35 AU) and 1995 (r_h ∼ 1.31 AU in 1995) passages (see Schleicher 2006).

4. Summary

The ground-based observation campaign of the comet 67P/C-G during its last perihelion passage before the Rosetta s/c encounter has provided us with the most recent information about the comet's activity. During the 4 months (mid-January to mid-April 2009) we monitored the comet, we witnessed the development and evolution of several dust structures in the inner coma, as well as the long reported dust trail. The analysis enhancement techniques applied to the whole data set clearly show 3 to 4 structures in the inner dust coma. The evolution of these structures from January to April 2010 is briefly described in this article. A more thorough analysis is being carried out by Vincent et al. (2011, in prep.) and it will allow determination of

Table 3. Gas production rates 67P/Churyumov-Gerasimenko.

Date	r_h	Δ	ΔT	Q(CN)	$Q(C_2)$	$Q(C_3)$	$Q(NH_2)$	log [$Q(C_2)/Q$(CN)]	log [Afρ/Q(CN)]
February 22	1.247	1.678	–6	4.53×10^{24}	3.72×10^{24}	2.82×10^{23}	—	–0.09	—
February 23	1.247	1.678	–5	6.68×10^{24}	5.85×10^{24}	6.19×10^{23}	—	–0.12	–22.29
February 24	1.247	1.679	–4	6.69×10^{24}	5.42×10^{24}	5.96×10^{23}	1.39×10^{26}	–0.09	—
March 19	1.269	1.732	+19	4.97×10^{24}	—	2.18×10^{23}	1.09×10^{26}	—	–22.11

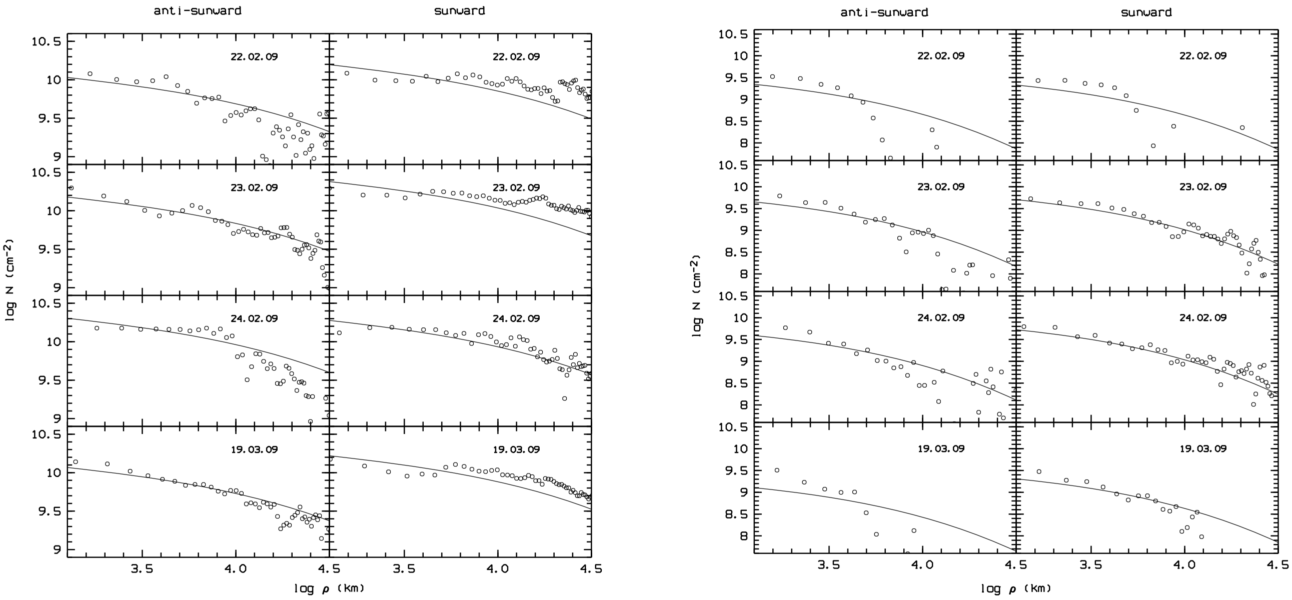

Fig. 8. Observed CN and C_3 column density profiles in cm^{-2} versus ρ (open circles) in log-log representation together with the best achievable fit (solid line) obtained by means of the Haser modelling (Haser 1957) with parameters given in the text and production rates listed in Table 3.

the rotational state, as well as of the location and number of the active areas on the nucleus.

Both the structures in the dust coma and the Afρ parameter, as a proxy of the comet dust activity, show a clear evolution between 1.314 AU pre-perithelion and 1.269 AU post-perihelion. Our dataset allows us to derive a (most likely relative) maximum dust activity, determined through Afρ takes place on March 12, that is, 12 days after perihelion. From an exhaustive analysis of the reported observations during 1982, 1996 and 2002 (Osip et al. 1992; Weiler et al. 2004; Lara et al. 2005; Schleicher 2006), de Almeida et al. (2009) note that 67P/C-G displays an asymmetry in water (or gas) release rates close to perihelion with peak productivity about two months after perihelion. Unfortunately, we monitored the comet until March 19, barely 3 weeks after perihelion, so we cannot confirm that the comet indeed peaks activity two months after the 2009 perihelion on February 28. Our dataset clearly indicates that the dust activity, determined through Afρ, peaked on March 12. However, we cannot conclude whether this maximum is absolute or part of the increasing activity towards a maximum at about two months after perihelion.

The production rates of CN, C_3, C_2, and NH_2 are in the same order of magnitude as during previous apparitions. The closer perihelion distance in 2009 (1.24 AU vs. 1.30 AU in 1982 and 1995) has not induced important changes in the gas sublimation rate. It must be noted that the production rate of the above-mentioned species shortly before the perihelion and about 3 weeks after perihelion is rather similar. This result contrasts with the values of Afρ between February 23 and March 19 when a clear increase in the dust activity occurs, which is not the case for the production rate of gaseous species such as CN, C_3, C_2 and NH_2.

Acknowledgements. The paper is based on observations collected at the Centro Astronómico Hispano Alemán (CAHA) at Calar Alto, operated jointly by the Max-Planck Institut für Astronomie and the Instituto de Astrofisica de Andalucia (CSIC). We are grateful to the service observers J. Aceituno, A. Aguirre, M. Alises, A. Guijarro, and F. Hoyo. Without their engagement and dedication, this programme would not have been successful. The research carried out has been partially supported by the Spanish Ministerio de Educación y Ciencia under contract ESP2006–02934 and by the Ministerio de Ciencia e Innovación under contract AyA 2009-08011. Z.-Y. Lin acknowledges a grant by the Junta de Andalucia under the project JA2007-TIC2744. The work of W.-H. Ip is supported by NSC 97-2112-M-008-001-MY3.

References

A'Hearn, M. F., Schleicher, D. G., Millis, R. L., Feldman, P. D., & Thompson, D. T. 1984, AJ, 89, 579
A'Hearn, M. F., Hoban, S., Birch, P. V., et al. 1986, Nature, 324, 649
A'Hearn, M. F., Millis, R. L., Schleicher, D. G., Osip, D. J., & Birch, P. V. 1995, Icarus, 118, 223
Bertini, I., Lara, L. M., Vincent, J., et al. 2009, A&A, 496, 235
Boehnhardt, H., & Birkle, K. 1994, A&AS, 107, 101
de Almeida, A. A., Trevisan Sanzovo, D., Sanzovo, G. C., Boczko, R., & Miguel Torres, R. 2009, Adv. Space Res., 43, 1993
Ferrín, I. 2010, Planet. Space Sci., 58, 365
Haser, L. 1957, Bull. Soc. R. Sci. Liege, 43, 740
Lara, L. M., Schulz, R., Stüwe, J. A., & Tozzi, G. P. 2001, Icarus, 150, 124
Lara, L. M., de León, J., Licandro, J., & Gutiérrez, P. J. 2005, Earth Moon and Planets, 97, 165
Larson, S. M., & Sekanina, Z. 1984, AJ, 89, 571
Lin, Z., Lin, C., Ip, W., & Lara, L. M. 2009, AJ, 138, 625
Osip, D. J., Schleicher, D. G., & Millis, R. L. 1992, Icarus, 98, 115
Schleicher, D. G. 1983, Ph.D. Thesis, AA, Maryland Univ., College Park
Schleicher, D. G. 2006, Icarus, 181, 442
Weiler, M., Rauer, H., & Helbert, J. 2004, A&A, 414, 749

A&A 525, A145 (2011)
DOI: 10.1051/0004-6361/201015599

Astronomy & Astrophysics

Thermo-physical properties of 162173 (1999 JU3), a potential flyby and rendezvous target for interplanetary missions
(Research Note)

T. G. Müller[1], J. Ďurech[2], S. Hasegawa[3], M. Abe[3], K. Kawakami[3], T. Kasuga[4], D. Kinoshita[5], D. Kuroda[6], S. Urakawa[7], S. Okumura[7], Y. Sarugaku[8], S. Miyasaka[9], Y. Takagi[10], P. R. Weissman[11], Y.-J. Choi[12], S. Larson[13], K. Yanagisawa[6], and S. Nagayama[14]

[1] Max-Planck-Institut für extraterrestrische Physik, Giessenbachstraße, 85748 Garching, Germany
e-mail: tmueller@mpe.mpg.de
[2] Astronomical Institute, Faculty of Mathematics and Physics, Charles University in Prague, V Holešovičkách 2, 180 00, Praha 8, Czech Republic
[3] Institute of Space and Astronautical Science, Japan Aerospace Exploration Agency, 3-1-1 Yoshinodai, Sagamihara, Kanagawa 229-8510, Japan
[4] Department of Physics and Astronomy, The University of Western Ontario, 1151 Richimond St. London, ON, N6A 3K7, Canada
[5] Institute of Astronomy, National Central University, 300 Jhongda RD., Jhongli, Taoyuan 32001, Taiwan
[6] Okayama Astrophysical Observatory, National Astronomical Observatory of Japan, 3037-5 Honjo, Kamogata, Asaguchi, Okayama 719-0232, Japan
[7] Bisei Spaceguard Center, Japan Spaceguard Association, 1716-3 Okura, Bisei, Ibara, Okayama 714-1411, Japan
[8] Kiso Observatory, Institute of Astronomy, The University of Tokyo, 10762-30 Mitake, Kiso, Nagano 397-0101, Japan
[9] Tokyo Metropolitan Government, 2-8-1 Nishishinjyuku, Shinjyuku, Tokyo 163-8001, Japan
[10] Aichi Toho University, 3-11 Heiwagaoka, Meito, Nagoya, Aichi 468-8515, Japan
[11] Jet Propulsion Laboratory, 4800 Oak Grove Drive, MS 183-301, Pasadena, CA 91109, USA
[12] Korea Astronomy and Space Science Institute, 61-1 Hwaam-dong, Yueing-gu, Daejeon, Taejon 305-348, Korea
[13] Lunar and Planetary Laboratory, University of Arizona, Tucson, AZ, 85721-0092, USA
[14] National Astronomical Observatory of Japan, 2-21-1 Osawa, Mitaka, Tokyo 181-8588, Japan

Received 17 August 2010 / Accepted 5 November 2010

ABSTRACT

Context. Near-Earth asteroid 162173 (1999 JU3) is a potential flyby and rendezvous target for interplanetary missions because of its easy-to-reach orbit. The physical and thermal properties of the asteroid are relevant for establishing the scientific mission goals and also important in the context of near-Earth object studies in general.

Aims. Our goal was to derive key physical parameters such as shape, spin-vector, size, geometric albedo, and surface properties of 162173 (1999 JU3).

Methods. With three sets of published thermal observations (ground-based *N*-band, Akari IRC, Spitzer IRS), we applied a thermophysical model to derive the radiometric properties of the asteroid. The calculations were performed for the full range of possible shape and spin-vector solutions derived from the available sample of visual lightcurve observations.

Results. The near-Earth asteroid 162173 (1999 JU3) has an effective diameter of 0.87 ± 0.03 km and a geometric albedo of 0.070 ± 0.006. The χ^2-test reveals a strong preference for a retrograde sense of rotation with a spin-axis orientation of $\lambda_{\rm ecl} = 73°$, $\beta_{\rm ecl} = -62°$ and $P_{\rm sid} = 7.63 \pm 0.01$ h. The most likely thermal inertia ranges between 200 and 600 J m^{-2} s$^{-0.5}$ K^{-1}, about a factor of 2 lower than the value for 25143 Itokawa. This indicates that the surface lies somewhere between a thick-dust regolith and a rock/boulder/cm-sized, gravel-dominated surface like that of 25143 Itokawa. Our analysis represents the first time that shape and spin-vector information has been derived from a combined data set of visual lightcurves (reflected light) and mid-infrared photometry and spectroscopy (thermal emission).

Key words. minor planets, asteroids: individual: 162173 (1999 JU3) – radiation mechanisms: thermal – techniques: photometric – infrared: planetary systems

1. Introduction

Asteroid 162173 (1999 JU3) is currently among the potential targets of future interplanetary exploration missions. The target is relatively easy to reach with state-of-the-art mission capabilities, and it offers high scientific potential (Binzel et al. 2004). This near-Earth asteroid belongs to the C-class objects, which are believed to represent primitive, volatile-rich remnants of the early solar system. Various aspects of this small body have been covered in some detail in the recent works by Hasegawa et al. (2008) and by Campins et al. (2009).

Hasegawa et al. (2008) use a spherical shape model for their radiometric analysis, and alternatively use an ellipsoidal shape model, but without knowing the true spin-vector orientation. The results (radiometric diameter of 0.92 ± 0.12 km, visual geometric albedo of $0.063^{+0.020}_{-0.015}$) which indicate a thermal inertia larger than 500 J m^{-2} s$^{-0.5}$ K^{-1}), were based on a set of photometric

Subaru and *Akari* observations and connected to simplified shape and spin-axis assumptions. Campins et al. (2009) have obtained a single-epoch *Spitzer* infrared spectrograph (IRS) spectrum. They used a spherical shape model, and for the spin-pole orientation they used the extreme case of an equatorial retrograde geometry and a prograde solution published by Abe et al. (2008). Their analysis, based on the single IRS-spectrum and ignoring the data sets published by Hasegawa et al. (2008), yielded a value for the thermal inertia of 700 ± 200 J m^{-2} s$^{-0.5}$ K^{-1}, a diameter estimate of 0.90 ± 0.14 km, and geometric albedo of 0.07 ± 0.01.

Despite the simplifications in shape and spin-vector properties, both sets of published radiometric diameter and albedo values agree within the given uncertainties. Both teams also favoured a relatively high thermal inertia (close to that of 25143 Itokawa). The unknowns of the spin-vector orientation cause a large uncertainty in the thermal properties.

Here we re-analyse all available lightcurve observations to derive (on the basis of standard χ^2 lightcurve inversion techniques) all matching spin-vector and shape solutions (Sect. 2). The full possible range for shape, spin-axis orientation, and rotation period was then used as input for a thermophysical χ^2 analysis of all available thermal observations (Sect. 3) with the goal of deriving radiometric sizes, albedos and thermal inertias. At the same time, we determined the most likely shape-solution, rotation period and spin-axis orientation (Sect. 4).

2. Possible shape and spin-vector solutions

A detailed list of the available photometric observations is presented in Table 1. There are about 40 dedicated visual lightcurve data sets spread over more than 270 days. About half of the lightcurves were calibrated; some of the data sets are very noisy. Based on these data, Abe et al. (2008) found a rotation period of 7.6272 ± 0.0072 h and a spin orientation of $\lambda_{\rm ecl}$ = 331.0°, $\beta_{\rm ecl}$ = +20.0°, indicating a prograde rotation. A more recent analysis by the same authors (priv. communication) resulted in a rotation model with slightly different values: $\lambda_{\rm ecl}$ = 327.3°, $\beta_{\rm ecl}$ = +34.7°, $P_{\rm sid}$ = 7.6273922 h. Both solutions were derived using the epoch and amplitude methods described by Magnusson (1986). These methods are reliable for irregularly shaped bodies and for sufficient lightcurve data covering various aspect angles. 1999 JU3 has a comparatively spherical shape and the available lightcurve data were from restricted directions. Nevertheless, both solutions gave a reasonable match to the observed lightcurves, but it turned out that these solutions are not unique and other parameter sets with different rotation periods, spin-axis orientations and shape models could not be excluded (see Fig. 1).

Since these values are crucial input parameters for our thermophysical model analysis, we repeated the search for possible shape and spin-vector solutions using the lightcurve inversion method developed by Kaasalainen & Torppa (2001). Our goal was to derive a set of the most likely convex shape models that would fit all available lightcurves. Because of the poor quality of some of the data, we were only able to determine the range of the sidereal rotation period to 7.6204–7.6510 h. Different shape models with pole orientations covering almost the entire celestial sphere (without any preference for pro- or retrograde solutions) fit the data equally well. By scanning the period-pole parameter space, we derived 77 shape models that were physically acceptable (rotating around the shortest axis) and for which the χ^2 of the fit was no more than 10% higher than the best-fit χ^2. These models corresponded to local minima in the parameter space.

Table 1. Observation circumstances for the lightcurve measurements.

Mon/Day (2007)	Telescope	Observer
07/8, 09/4	2.2 m/Mauna Kea	T. Kasuga
07/19-23, 12/3,4,6-8, 02/26-28, 04/2,4,5	1.0 m/Lulin	M. Abe, K. Kawakami, D. Kinoshita
08/5,15, 09/6,11,13,15, 10/6,18, 11/13,15	1.0 m/Ishigaki	D. Kuroda, S. Nagayama, K. Yanagisawa
08/9-10,17,20, 09/6,10	1.0 m/Bisei	S. Urakawa, S. Okumura
09/4,5,7,8,10,12,14,15 11/7-9,11,13, 02/5-8, 04/14,15	1.05 m/Kiso	M. Abe, K. Kawakami, Y. Sarugaku, Y. Takagi, S. Miyasaka
09/11-14	1.55 m/Steward	P. R. Weissman, Y.-J. Choi, S. Larson

Notes. See also Table 1 in Abe et al. (2008).

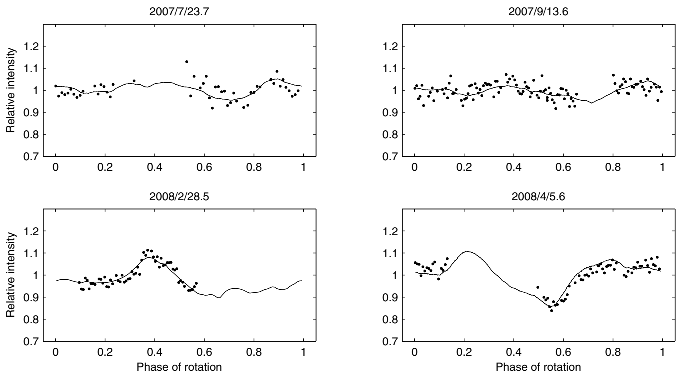

Fig. 1. Match between observed lightcurves and shape/spin-axis model solution "7_1".

In addition, we included both of the original Abe et al. (2008) solutions and added another five with the pole fixed to the two ($\lambda_{\rm ecl}$, $\beta_{\rm ecl}$)-pairs mentioned above and rotation periods in the range given by Abe et al. (2008). Only two of these models pass the χ^2 + 10% limit on the basis of the visual lightcurves, the other five models have higher χ^2-values. Six of these shape models are elongated along the "z" axis and therefore unphysical.

For all 84 models we performed a thermophysical model analysis for a wide range of possible parameters (see Table 3).

3. Thermophysical model analysis

3.1. Model and input parameters

The mid-IR photometric data were already described in Hasegawa et al. (2008). The data set includes 15 *N*-band Subaru observations and two dedicated *Akari* observations at 15 and 24 μm. We binned the single-epoch *Spitzer* IRS data (Campins et al. 2009) into 20 wavelength points (4 for band SL2, 7 for SL1, 4 for LL2, 5 for LL1; see Fig. 5, bottom). The 20 wavelength points were chosen to give about equal weight to the two published data samples in terms of number of observations (17 in Hasegawa et al. (2008) and 20 for the Campins et al. (2009) sample). In this way the derived object properties are better connected to the entire data set, and they do not just match the measurements of one observing epoch. Each observation set also has a mixture of lower and higher quality data: the ground-based Subaru data are of lower quality than the *Akari* data, while the quality of the IRS spectrum changes with wavelength. This again

Table 2. Summary of the avaible thermal observations.

Year/Mon/Day	Wavelength range [μm]	R_h [AU]	Δ [AU]	α [°]	Telescope	Reference
2007/05/16	15.0, 24.0	1.414	0.992	+45.6	Akari	Hasegawa et al. (2008)
2007/08/28	8.8(3×), 9.7(1×), 10.5(1×), 11.7(7×), 12.4(3×)	1.287	0.306	+22.3	Subaru	Hasegawa et al. (2008)
2008/05/02	5.2–8.5, 7.4–14.2, 14.0–21.5, 19.5–38.0	1.202	0.416	+52.6°	Spitzer	Campins et al. (2009)

Notes. R_h is the helio-centric distance and Δ the distance between object and telescope. All observations were taken at positive phase angles α (Sun-object-telescope), i.e., leading the Sun, with a cold terminator for a retrograde rotating body.

Table 3. Summary of general TPM input parameters and applied ranges.

Param.	Value/Range	Remarks
Γ	0...2500	J m^{-2} s$^{-0.5}$ K^{-1}, thermal inertia
ρ	0.4...0.9	rms of the surface slopes
f	0.4...0.9	surface fraction covered by craters
ϵ	0.9	emissivity
H_V-mag.	18.82 ± 0.02 mag	Abe et al. (2008)
G-slope	–0.110 ± 0.007	Abe et al. (2008)
shape	84 models	see Sect. 2
spin-axis	84 solutions	see Sect. 2
P_{sid} [h]	7.6205...7.6510	see Sect. 2

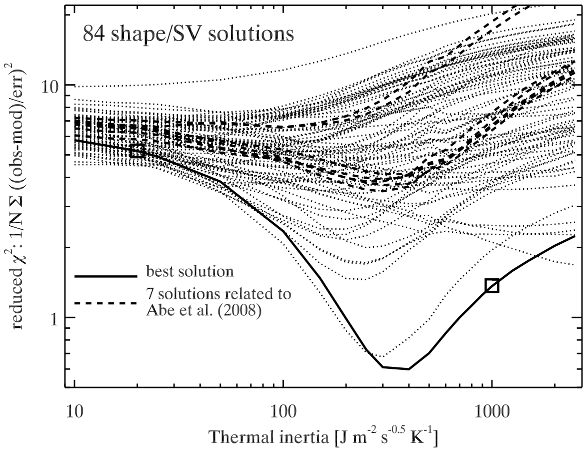

Fig. 2. TPM χ^2-optimization process to find robust solutions for diameter, albedo and thermal inertia simultaneously. Each line represents the reduced χ^2 values for an individual shape/spin-vector solution as a function of thermal inertia. The surface roughness was kept constant using the "default values" of ρ = 0.7 and f = 0.6 as proposed by Müller et al. (1999). Model 7_1 solutions marked with squares on the solid line correspond to the two cases with thermal inertias of 20 and 1000 J m^{-2} s$^{-0.5}$ K^{-1} shown in Fig. 3 (left and middle).

ensures that the final solutions are not biased towards a single measurement. All observations are listed in Table 2.

All 84 possible spin-vector and shape solutions from Sect. 2 have been used in combination with these thermal data.

For our analysis we are using a thermophysical model (TPM) described by Lagerros (1996, 1997, 1998) and Müller & Lagerros (1998). This TPM works with true illumination and observing geometries, accepts irregular shape models and arbitrary spin-vector solutions, works with roughness controlled by the rms of the surface slopes, considers heat-conduction into the surface as well as multiple scattering of both the solar and the thermally emitted radiation. The model has been tested and validated thoroughly for NEAs (e.g., Müller et al. 2005) and MBAs (e.g., Müller & Lagerros 2002). The TPM input parameters and applied variations are listed in Table 3.

3.2. Solving for effective diameter, geometric albedo and thermal inertia

Campins et al. (2009) and Mueller (2007) used a χ^2 or reduced χ^2-test to find solutions for the thermal inertia Γ. Here we follow a modified approach to find the most robust solutions with respect to thermal inertia and allowing for the full range in effective diameter and geometric albedo at the same time. The following procedure was executed for all 84 possible shape and spin-vector solutions separately:

(1) For each value of Γ in a wide range (see Table 3) we calculate the radiometric diameter and albedo solution via the TPM for each individually observed thermal flux (37 individual diameter and albedo solutions). Diameter and albedo are linked by the absolute magnitude H_V which was kept constant (the rotational amplitude is only about 0.1 mag).

(2) We calculate the weighted mean radiometric diameter and albedo solution for each given Γ ($\bar{x} = \frac{\Sigma x_i/\sigma_i^2}{\Sigma 1/\sigma_i^2}$, with diameter/albedo errors σ_i connected to the observational errors).

(3) For each individual observation we predict TPM fluxes based on the given Γ and the corresponding weighted mean radiometric diameter and albedo from step (2).

(4) The most robust solutions occur when the observations and the TPM predictions agree best (taking the uncertainties of the measurements into account in a weighted mean sense, see step 2). This can be expressed as $\frac{1}{N}\Sigma_{i=1}^{N}((\mathrm{obs}_i - \mathrm{mod}_i)/\sigma_i)^2$, a modified reduced χ^2 method. The most likely thermal inertia is found at the smallest χ^2 values; the connected effective diameter and geometric albedo values are the ones calculated at step (2).

In a first round of executing this procedure we kept the surface roughness constant at values which were specified as "default values" for large, regolith-covered asteroids (Müller et al. 1999). The corresponding roughness parameter values are ρ = 0.7, the rms of the surface slopes, and f = 0.6, the fraction of surface covered by craters. The results are shown in Fig. 2.

The best shape and spin-vector solutions (with lowest values for the reduced χ^2 and clear minima in Fig. 2) were then the starting point for further tests:

(i) Are these solutions robust against sub-sets of the thermal data?
(ii) How does the surface roughness influence the solutions?
(iii) Do the solutions explain the thermal behaviour over the observed phase angle range (from ~20° to ~55°)?

Table 4. The shape and spin-vector solutions which produce the lowest χ^2-values in Fig. 2.

model-ID	λ_{ecl} [°]	β_{ecl} [°]	P_{sid} [h]	χ^2-min
7_1[a]	73.1	–62.3	7.6323	0.60
8_2[a]	69.6	–56.7	7.6325	0.68
14_8	77.1	–30.9	7.6510	1.46

Notes. [(a)] Models 7_1 and 8_2 are in the same local minimum in the parameter space for the lightcurve fits.

(iv) Is the TPM match of equal quality at all observed wavelengths?
(v) Are there large discrepancies at certain rotational phases?

4. Results and discussion

4.1. Solution for shape and spin-vector

The shape and spin-vector solutions which produce the lowest χ^2-values in Fig. 2 are listed in Table 4. The model IDs represent a full shape-model, each with more than 2000 surface elements and more than 1000 vertices. The Julian date at zero rotational phase γ_0 is in all cases $T_0 = 2454289.0$.

All three solutions are retrograde solutions and, in fact, the eight best solutions in Fig. 2 are retrograde solutions. The best prograde solutions in the χ^2 picture are models with ID 5_2 and ID 13_5, both have χ^2-minima at 2.3 (almost a factor of 4 higher than the best retrograde solution 7_1) and would require an extremely high thermal inertia (>1000 J m^{-2} s$^{-0.5}$ K^{-1}) to match the observations. Our most likely solution can be summarized as: $\lambda_{ecl} = 73°$, $\beta_{ecl} = -62°$, $P_{sid} = 7.63 \pm 0.01$ h. Figure 3 (left, middle) shows the model-ID 7_1, as seen from *Spitzer* during the IRS-observations and for the two thermal inertias marked in Fig. 2 with boxes. The match between model "7_1" with observed lightcurves is shown in Fig. 1.

We also analysed the thermal data set against the Abe et al. (2008) spin-pole solutions discussed above. The corresponding χ^2-minima are more than a factor five worse than our two best models above (see dashed lines in Fig. 2). Some of these solutions are compatiple with the inertia range given by Campins et al. (2009) and even produced an excellent match to the IRS-spectrum. Nevertheless, these solutions can be excluded with very high confidence:

(i) the match to the rest of the data set (*Akari* and ground-based data) is very poor (reflected in the high χ^2-values);
(ii) the corresponding shape models are unphysical with elongations along the spin axis. Such rotational states would not be stable. The best of these models (in terms of χ^2-minima) is shown in Fig. 3 on the right side (with the rotation along the *z*-axis with the object's largest extension).

4.2. Thermal inertia and surface roughness

The thermal inertia is clearly a key parameter when modelling the mid-IR data for NEAs; it strongly influences the shape of the spectral energy distribution (SED). This can be seen in the *Spitzer* IRS spectrum, especially in the Wien-part of the spectrum. But the thermal inertia also drives the thermal behaviour as a function of phase angle (e.g., Müller 2002), the thermal phase curve. The temperature of the unilluminated fraction of the surface changes strongly with thermal inertia. In Fig. 3 the unilluminated fraction has just rotated out of the solar insolation. In one case (left) we assumed a low thermal inertia of ~20 J m^{-2} s$^{-0.5}$ K^{-1}, which was found to be typical for large MBAs (Müller & Lagerros 2002), while in the second case (middle) the thermal inertia is 1000 J m^{-2} s$^{-0.5}$ K^{-1}, close to the value found by Müller et al. (2005) for 25143 Itokawa.

The importance of the thermal inertia in the modelling is also visible in the χ^2-solutions (Figs. 2 and 4): the χ^2-values change significantly when going through the whole grid of physically meaningful thermal inertias.

But Fig. 4 demonstrates that thermal inertia and surface roughness are not easy to disentangle, at least on the basis of this data set. Both parameters influence the short-wavelength SED-part where the hottest surface temperatures dominate the SED-shape. One way of solving for both parameters would be to obtain data with a larger phase angle coverage and larger wavelength coverage. The roughness plays a much bigger role at small phase angles (beaming effect), but thermal data close to opposition are not available for 162173 (1999 JU3). The thermal inertia is more important at large phase angles and at longer wavelengths where the disk-averaged temperature dominates the SED shape. In general, the larger the coverage in phase angle and wavelength, the more accurate is the determination of diameter, albedo, thermal inertia and roughness.

Figure 4 also shows that similarly low χ^2-values can be reached independent of the surface roughness. This demonstrates that roughness effects are still important for the interpretation of thermal data (via the thermal phase curves), even at these relatively large phase angles (Müller 2002). But the data set does not allow us to constrain the surface roughness which broadens the possible range of thermal inertias as can be seen in Fig. 4. Based on our three best shape/spin-vector solutions and considering the uncertainties due to roughness, we conclude that the thermal inertia is in the range 200–600 J m^{-2} s$^{-0.5}$ K^{-1}. This range is in agreement with the lower limit of 150 J m^{-2} s$^{-0.5}$ K^{-1} given by Campins et al. (2009) but lower than their best fit value of 700 ± 200 J m^{-2} s$^{-0.5}$ K^{-1}. Our value is about a factor of two lower than the one found for 25143 Itokawa (Müller et al. 2005). We expect that the surface of 162173 (1999 JU3) is therefore different in the sense that there might be fewer rocks and boulders and that the surface includes millimetre sized particles (as opposed to the cm-sized gravel on Itokawa). We also find a rigorous lower limit to the thermal inertia of about 100 J m^{-2} s$^{-0.5}$ K^{-1}, similar to Campins et al. (2009). This limit is not compatible with a thick dusty regolith covering the entire surface which would result in a very low thermal conductivity and thermal inertia values well below 100 J m^{-2} s$^{-0.5}$ K^{-1}, which would in principle be possible for an object of that size and the relativly slow rotation rate. For comparison, the Moon's thick regolith gives a value below 40 J m^{-2} s$^{-0.5}$ K^{-1} (Keihm 1984, calculated for $T = 300$ K).

4.3. Radiometric diameter and albedo solution

Our best fit to all observations, as represented in Fig. 2 by the solid line, resulted in a radiometric effective diameter of 0.87 ± 0.02 km and 0.070 ± 0.003 for the visual geometric albedo. Both values are within the error bars of the solutions found by Hasegawa et al. (2008) and by Campins et al. (2009), but now with much smaller errors. The uncertainties are based on the best χ^2-values for model-IDs "7_1" and "8_2" and the full variation in roughness (as shown in Fig. 4). The radiometric effective diameter is connected to the most likely shape model and spin-vector solution from above and corresponds to the size of a

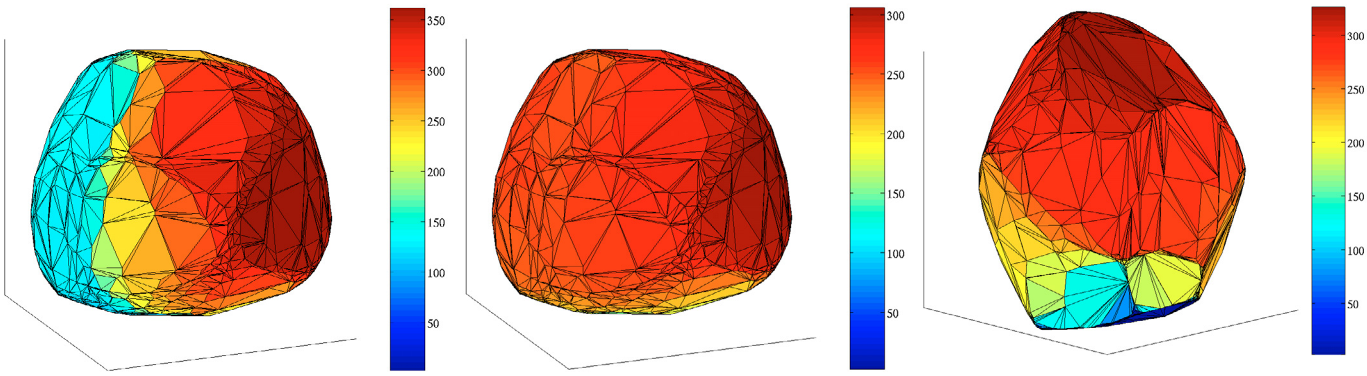

Fig. 3. *Left and middle*: TPM implementation of the shape model 7_1 at the time of the *Spitzer* IRS observations on 2008-May-02 02:01 UT, as seen from *Spitzer* in asteroid-coordinates, i.e., the z-axis goes along the rotation axis. *Left*: low thermal inertia. Middle: high thermal inertia. Both solutions are marked with squares in Fig. 2. *Right*: shape model fixed on the Abe et al. (2008) spin-vector and tuned to match the Campins et al. (2009) findings. The rotation along the largest object extension (z-axis) is unphysical. The surface temperatures are given in Kelvin.

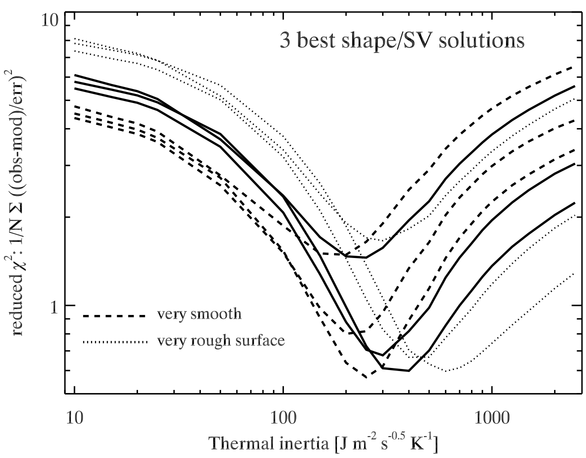

Fig. 4. TPM χ^2-optimization process for the shape and spin-axis solutions with the lowest χ^2-values (models 7_1, 8_2, 14_8). The solid lines are the "default roughness" values derived for MBAs.

spherical object with equal volume. Using the determined possible thermal inertia range of 200–600 J m^{-2} s$^{-0.5}$ K^{-1} and uncertainties in roughness and H_V-magnitude lead to a possible value for the effective diameter of 0.87 ± 0.03 km. The derived geometric albedo provides the best solution between all thermal observations over the full wavelength and phase angle range and the absolute H_V-magnitude. The H_V-magnitude was given with only 0.02 mag error. Using a more realistic H_V-error of ±0.1 mag leads to a final geometric albedo value of 0.070 ± 0.006. The small uncertainties reflect the importance of multi-epoch, multi-wavelength and large phase angle coverage for thermophysical studies of small bodies. In a similar study by Müller et al. (2005), also based on a large thermal data set and a shape model from lightcurve inversion techniques, the derived effective diameter agreed within 2% of the true, in-situ diameter (Müller et al. 2005; Fujiwara et al. 2006). The quoted uncertainties above are formal errors from the χ^2 optimization, including the possible range in thermal inertia, roughness and H_V.

The remaining discrepancy between the *Spitzer* and the *Akari*-flux at 15 μm (seen in Fig. 5 bottom) might be related to an additional error introduced by the flux scaling done by Campins et al. (2009) to match the short-wavelength part of the spectrum (<14 μm) to the long-wavelength part of the spectrum (>14 μm). The mismatch is caused mainly by the placement of the object within the IRS slit and reflected in the specified 10% systematic absolute calibration uncertainty.

Although the Fig. 4 solutions and the model match in Fig. 5 look very convincing, there are some uncertainties remaining: The spin-vector and shape solution from lightcurve inversion techniques is not very robust; more lightcurve observations are needed to improve the quality. The χ^2-test works best if the thermal observations cover a wide range of wavelengths, phase angles (before and after opposition) and rotational phases. But all thermal observations have been taken at pre-opposition (positive) phase angles (leading the Sun) where the unilluminated part of the surface visible to the observer is either warm (prograde rotation) or cold (retrograde rotation); observations after opposition are not yet available. A combined before and after opposition data set would constrain the sense of rotation and the thermal properties much better, observations close to opposition would determine the surface roughness a bit better, hence constrain the thermal inertia further.

It is also important to note here that higher thermal inertias (>600 J m^{-2} s$^{-0.5}$ K^{-1}, Fig. 3 middle) would make a slightly better fit to the *Spitzer* IRS spectrum (improvement mainly at the shortest wavelengths in Fig. 5 bottom), but would cause a significant dependency in the diameter and albedo solutions with phase angle. The measurements taken at around 20° phase angle (Subaru) would then have fluxes that are about 40% higher than the corresponding model predictions (i.e., values >1.4 in Fig. 5, top). The *Akari* fluxes would still be ~20% higher than the model predictions. Our observational data set covering about 30° in phase angle constrains the possible thermal inertia to values below 700 J m^{-2} s$^{-0.5}$ K^{-1}.

5. Conclusions

The radiometric analysis provides the following results: (i) a strong indication of a retrograde sense of rotation; (ii) a spin-vector with $\lambda_{\rm ecl}$ = 73°, $\beta_{\rm ecl}$ = −62°, $P_{\rm sid}$ = 7.63 ± 0.01 h and γ_0 = 0 at T_0 = 2454289.0, derived for the first time based on a combined analysis of visual lightcurve data and thermal observations; (iii) a shape model (here labelled with 7_1) as shown in Fig. 3 (left & middle); (iv) a thermal inertia in the range 200 to 600 J m^{-2} s$^{-0.5}$ K^{-1}; (v) a radiometric effective diameter (of an equal volume sphere) of $D_{\rm eff}$ = 0.87 ± 0.03 km; (vi) a radiometric geometric albedo of p_V = 0.070 ± 0.006; (vii) a lower thermal inertia than for Itokawa, suggesting the presence

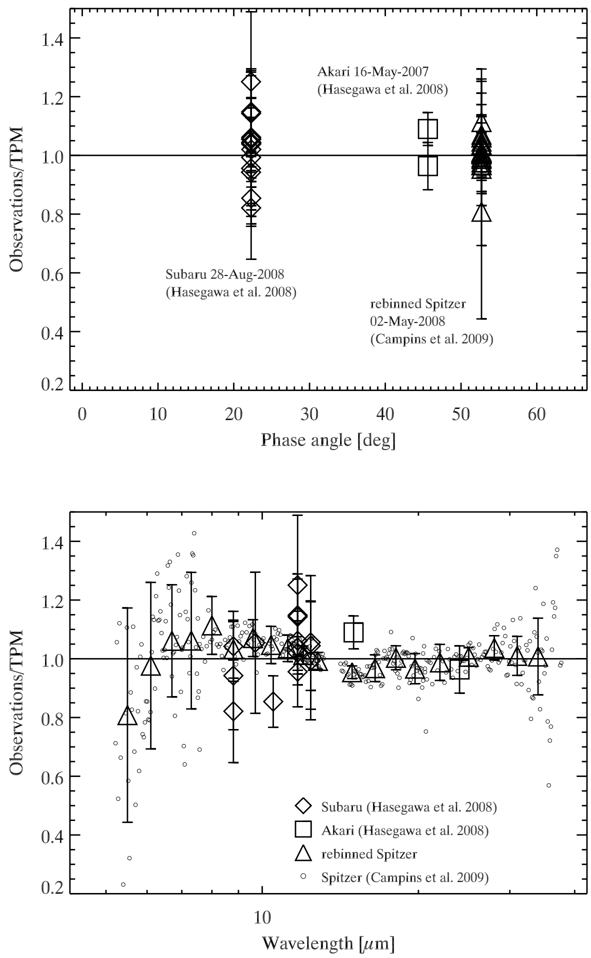

Fig. 5. All observations divided by the corresponding TPM predictions based on our optimized radiometric solution. *Top*: as a function of phase angle. *Bottom*: as a function of wavelength. The full set of *Spitzer* IRS data are shown with little circles (Campins et al. 2009), the triangles are the re-binned data, the *Akari* IRC data are represented by squares; the Subaru-COMICS observations by diamond symbols.

of smaller particles, <cm-sized, in the regolith, though likely not fine dust; (viii) very good agreement in the radiometric solutions between the *Spitzer*, the *Akari* and the *Subaru* observations; (ix) an excellent match of the flux changes with phase angle (the phase angle range covered here is from ~20° to ~55°).

The example of 162173 (1999 JU3) shows that a combination of visual lightcurves (reflected sunlight) and mid-/far-IR photometry or photo-spectroscopy (thermal emission) can improve the quality of shape and spin-vector solutions significantly.

Acknowledgements. J. D. received grants from the Czech Science Foundation (GACR P209/10/0537) and the Research Program MSM0021620860 of the Ministry of education. S. H. was supported by the Space Plasma Laboratory, ISAS, JAXA. We are also grateful to Professor N. Kawai and the gamma-ray bursts project members for furnishing their optical camera at Ishigakijima Astronomical Observatory. Development of the optical CCD camera at Ishigakijima Astronomical Observatory was supported by the Ministry of Education, Science, Sports and Culture, Grant-in-Aid for Creative Scientific Research. T.K. thanks to the JSPS Research Fellowships for Research Abroad for their financial support. This work was supported in part by the NASA Planetary Astronomy Program and performed in part at the Jet Propulsion Laboratory. We thank the Steward Observatory of the University of Arizona for its allocation of telescope time. We also thank the referee Dr. J. Emery for very helpful comments.

References

Abe, M., Kawakami, K., Hasegawa, S., et al. 2008, COSPAR Scientific Assembly, B04-0061-08
Binzel, R. P., Perozzi, E., Rivkin, A. S., Rossi, A., et al. 2004, Meteorit. Planet. Sci., 39, 351
Campins, H., Emery, J. P., Kelley, M., et al. 2009, A&A, 503, L17
Fujiwara, A., Kawaguchi, J., Uesugi, K., et al. 2006, Science, 312, 1330
Hasegawa, S., Müller, T. G., Kawakami, K., et al. 2008, PASJ, 60, 399
Kaasalainen, M., & Torppa, J. 2001, Icarus, 153, 24
Keihm, S. J. 1984, Icarus, 60, 568
Lagerros, J. S. V. 1996, A&A, 310, 1011
Lagerros, J. S. V. 1997, A&A, 325, 1226
Lagerros, J. S. V. 1998, A&A, 332, 1123
Magnusson. P. 1986, Icarus, 68, 1
Müller, T. G., & Lagerros, J. S. V. 1998, A&A, 338, 340
Müller, T. G., Lagerros, J. S. V., Burgdorf, M., et al. 1999, in The Universe as Seen by ISO, ed. P. Cox, & M. F. Kessler, ESA SP-427, 141
Müller, T. G., & Lagerros, J. S. V. 2002, A&A, 381, 324
Müller, T. G. 2002, M&PS, 37, 1919
Müller, T. G., Sekiguchi, T., Kaasalainen, M., Abe, M., & Hasegawa, S. 2005, A&A, 443, 347 (M05)
Mueller, M. 2007, DLR, Thesis FU Berlin (http://www.diss.fu-berlin.de/diss/receive/FUDISS_thesis_000000002596)

A&A 534, A87 (2011)
DOI: 10.1051/0004-6361/201117026

Astronomy & Astrophysics

The long-lasting activity of 3C 454.3

GASP-WEBT and satellite observations in 2008–2010 ⋆,⋆⋆

C. M. Raiteri[1], M. Villata[1], M. F. Aller[2], M. A. Gurwell[3], O. M. Kurtanidze[4], A. Lähteenmäki[5], V. M. Larionov[6,7,8], P. Romano[9], S. Vercellone[9], I. Agudo[10,11], H. D. Aller[2], A. A. Arkharov[7], U. Bach[12], E. Benítez[13], A. Berdyugin[14], D. A. Blinov[6,8], E. V. Borisova[6], M. Böttcher[15], O. J. A. Bravo Calle[6], C. S. Buemi[16], P. Calcidese[17], D. Carosati[18,19], R. Casas[20,21], W.-P. Chen[22], N. V. Efimova[6,7], J. L. Gómez[10], C. Gusbar[15], K. Hawkins[15], J. Heidt[23], D. Hiriart[13], H. Y. Hsiao[24,22], B. Jordan[25], S. G. Jorstad[11,6], M. Joshi[11], G. N. Kimeridze[4], E. Koptelova[22,26], T. S. Konstantinova[6], E. N. Kopatskaya[6], S. O. Kurtanidze[4], E. G. Larionova[6], L. V. Larionova[6], P. Leto[16], Y. Li[15], R. Ligustri[27], E. Lindfors[14], M. Lister[28], A. P. Marscher[11], S. N. Molina[10], D. A. Morozova[6], E. Nieppola[5,29], M. G. Nikolashvili[4], K. Nilsson[29], N. Palma[15,30], M. Pasanen[14], R. Reinthal[14], V. Roberts[15], J. A. Ros[21], P. Roustazadeh[15], A. C. Sadun[31], T. Sakamoto[32], R. D. Schwartz[33], L. A. Sigua[4], A. Sillanpää[14], L. O. Takalo[14], J. Tammi[5], B. Taylor[11,34], M. Tornikoski[5], C. Trigilio[16], I. S. Troitsky[6], G. Umana[16], A. Volvach[35], and T. A. Yuldasheva[6]

(Affiliations can be found after the references)

Received 5 April 2011 / Accepted 24 June 2011

ABSTRACT

Context. The blazar 3C 454.3 is one of the most active sources from the radio to the γ-ray frequencies observed in the past few years.

Aims. We present multiwavelength observations of this source from April 2008 to March 2010. The radio to optical data are mostly from the GASP-WEBT, UV and X-ray data from Swift, and γ-ray data from the AGILE and *Fermi* satellites. The aim is to understand the connection among emissions at different frequencies and to derive information on the emitting jet.

Methods. Light curves in 18 bands were carefully assembled to study flux variability correlations. We improved the calibration of optical-UV data from the UVOT and OM instruments and estimated the Lyα flux to disentangle the contributions from different components in this spectral region.

Results. The observations reveal prominent variability above 8 GHz. In the optical-UV band, the variability amplitude decreases with increasing frequency due to a steadier radiation from both a broad line region and an accretion disc. The optical flux reaches nearly the same levels in the 2008–2009 and 2009–2010 observing seasons; the mm one shows similar behaviour, whereas the γ and X-ray flux levels rise in the second period. Two prominent γ-ray flares in mid 2008 and late 2009 show a double-peaked structure, with a variable γ/optical flux ratio. The X-ray flux variations seem to follow the γ-ray and optical ones by about 0.5 and 1 d, respectively.

Conclusions. We interpret the multifrequency behaviour in terms of an inhomogeneous curved jet, where synchrotron radiation of increasing wavelength is produced in progressively outer and wider jet regions, which can change their orientation in time. In particular, we assume that the long-term variability is due to this geometrical effect. By combining the optical and mm light curves to fit the γ and X-ray ones, we find that the γ (X-ray) emission may be explained by inverse-Comptonisation of synchrotron optical (IR) photons by their parent relativistic electrons (SSC process). A slight, variable misalignment between the synchrotron and Comptonisation zones would explain the increased γ and X-ray flux levels in 2009–2010, as well as the change in the γ/optical flux ratio during the outbursts peaks. The time delays of the X-ray flux changes after the γ, and optical ones are consistent with the proposed scenario.

Key words. galaxies: active – quasars: general – quasars: individual: 3C 454.3 – galaxies: jets

1. Introduction

A relativistic jet pointing at a small angle to the line of sight is most likely responsible for the extreme properties of the active galactic nuclei known as "blazars", i.e. BL Lac objects and flat-spectrum radio quasars (FSRQ). Indeed, the alignment would cause Doppler enhancement of the emission and contraction of its variability time scales. This peculiar orientation would also explain the apparent superluminal motion of radio knots in the jet. Owing to the jet emission beaming, we observe intensified synchrotron radiation from the radio to the UV–X-ray band and inverse-Compton radiation at higher energies, up to the TeV domain. Sometimes, in low brightness states, other contributions are detected, likely because of unbeamed radiation from the blazar nucleus, i.e. the accretion disc and broad line region (BLR). This occurs more often in FSRQ than in BL Lac objects, and indeed the classical distinction between the two classes is based on the equivalent width of their broad emission lines (that has to be greater than 5 Å in the rest frame for FSRQ). One of the main issues concerns the origin of the seed photons that are Comptonised to X- and γ-ray energies: relativistic electrons certainly upscatter the soft photons they have previously produced by synchrotron emission (synchrotron-self-Compton, or SSC, process), but possibly also photons coming from outside the jet (external Compton, or EC, process), in particular from the accretion disc, the BLR, or an obscuring torus (see e.g. Dermer et al. 2009, and references therein).

The quasar-type blazar 3C 454.3 has received particular attention by the international astronomical community since it underwent a major outburst in 2005 (Villata et al. 2006; Giommi et al. 2006; Pian et al. 2006; Fuhrmann et al. 2006). Indeed,

⋆ The radio-to-optical data presented in this paper are stored in the GASP-WEBT archive; for questions regarding their availability, please contact the WEBT President Massimo Villata (villata@oato.inaf.it).

⋆⋆ Table 3 is available in electronic form at http://www.aanda.org after many decades of intense radio, but only mild optical activity, the source began brightening in the optical band in 2001, until in May 2005 it reached the maximum optical level ever observed, $R = 12.0$. The outburst was simultaneously detected also in X-rays, while the millimetric radio flux peaked about one month after, and the 15–43 GHz flux much later (Villata et al. 2007; Raiteri et al. 2008b). According to Villata et al. (2006, 2007) the observed change in behaviour starting from 2001 was a geometric effect, i.e. the motion of a curved jet producing variations in the viewing angle of the different emitting regions.

In the following 2006–2007 observing season the source remained in a faint state, and new features appeared in its spectral energy distribution (SED). Through the analysis of low-energy data from the Whole Earth Blazar Telescope[1] (WEBT) and high-energy data from the *XMM-Newton* satellite, Raiteri et al. (2007) were able to recognise both a little blue bump in the optical, possibly due to emission lines from the BLR, and a UV excess, suggesting a big blue bump likely due to thermal radiation from the accretion disc. Moreover, they argue that the X-ray spectrum may be concave, with spectral softening at lower energies becoming more evident when the source is fainter, maybe revealing the high-frequency tail of the big blue bump. Finally, they ascribed the flux excess in the J band to a prominent broad Hα emission line. Both the UV excess and X-ray spectral curvature were also inferred from further *XMM-Newton* observations, at the beginning of the following observing season, while the contribution of the Hα line was confirmed by near-IR spectroscopy at Campo Imperatore (Raiteri et al. 2008b).

Then, from July 2007 the source began a new activity phase, during which it was detected several times in γ-rays by the AGILE satellite[2], and was monitored from the optical to the radio bands by the WEBT and its GLAST-AGILE Support Program (GASP, Villata et al. 2008). The results of these observations were published in Vercellone et al. (2008), Raiteri et al. (2008a,b), Vercellone et al. (2009), Donnarumma et al. (2009), Villata et al. (2009a), and Vercellone et al. (2010). Rotations of the optical polarisation vector both clockwise and counterclockwise were detected by Sasada et al. (2010). In contrast, observations at very high energies ($E > 100$ GeV) by the Cherenkov telescope MAGIC resulted in only upper limits (Anderhub et al. 2009).

From the theoretical point of view, Ghisellini et al. (2007) compare the source SED of July 2007 with that of May 2005 and infer that the dissipation site in relativistic jets changes, with more compact emitting regions, smaller bulk Lorentz factors, and greater magnetic fields characterising locations closer to the black hole. However, in the Ghisellini et al. (2007) view, the dissipation always occurs in a subparsec zone, where the seed photons for Compton emission are provided by the BLR. In contrast, Sikora et al. (2008) claim that the dissipation region is located much farther, in the millimetric photosphere, at some parsecs from the central engine, so the Compton emission is due to scattering of infrared photons emitted by the hot dust.

In the meanwhile, the *Fermi* satellite[3] was launched, providing an unprecedented monitoring of 3C 454.3 at γ-ray energies (Bonning et al. 2009; Abdo et al. 2009). The data from AGILE and *Fermi* were separately used to study the correlations between flux variations in optical and γ-rays. All results agreed that the time lag of γ-ray flux variations after the optical ones is less than one day (Vercellone et al. 2009; Donnarumma et al. 2009; Bonning et al. 2009; Vercellone et al. 2010). Finke & Dermer (2010) discuss the spectral break at ~2.4 GeV shown by *Fermi* data in August 2008 suggesting that it results from the combination of Compton-scattered disc and BLR radiations.

An analysis of the radio-optical data in 2005–2007, including space observations by *Spitzer* in the infrared, revealed two synchrotron peaks, the primary at IR and the secondary at sub-mm wavelengths, likely arising from distinct regions in the jet (Ogle et al. 2011).

A multiwavelength study of the flaring behaviour of 3C 454.3 during 2005–2008 was performed by Jorstad et al. (2010). These authors suggest that the emergence of a superluminal knot from the core produces a series of optical and high-energy outbursts, and that the millimetre-wave core lies at the end of the jet acceleration and collimation zone.

Suzaku observations of 3C 454.3 in November 2008 analysed by Abdo et al. (2010) confirmed the earlier suggestions by Raiteri et al. (2007, 2008b) that there seems to be a soft X-ray excess, which becomes more important when the source gets fainter. They interpret it as either a contribution of the high-energy tail of the synchrotron component or bulk-Compton radiation produced by Comptonisation of UV photons from the accretion disc by cold electrons in the innermost parts of the relativistic jet.

More recently, Pacciani et al. (2010; see also Striani et al. 2010) have reported on a γ-ray flare of 3C 454.3 detected by AGILE in December 2009, when the peak flux reached 2.0×10^{-5} photons cm^{-2} s^{-1}. The simultaneous flux increase at UV and optical frequencies was by far less dramatic. The authors found that the source behaviour during the flare cannot be accounted for by a simple one-zone model, but an additional particle component is needed. In contrast, Bonnoli et al. (2011) explain the source behaviour in the same period by means of a one-zone model, where the magnetic field is slightly weaker when the overall jet luminosity is higher. A new intense γ-ray flare was detected by *Fermi* in April 2010 ($\approx 1.6 \times 10^{-5}$ photons cm^{-2} s^{-1}, Ackermann et al. 2010), when fast variability on a time scale of a few hours was revealed (Foschini et al. 2010), supporting earlier results by Tavecchio et al. (2010), who claim that the dissipation region must be close to the black hole. The December 2009 and April 2010 γ-ray outbursts detected by *Fermi* were further analysed by Ackermann et al. (2010). These authors in particular discuss the observed spectral break at a few GeV, which they ascribe to a break in the underlying electron spectrum. This feature was also observed during the unprecedented γ-ray outburst of November 2010 (Abdo et al. 2011), when the γ flux rose to $(6.6 \pm 0.2) \times 10^{-5}$ photons cm^{-2} s^{-1} showing clear spectral changes.

In this paper we present the radio-to-optical monitoring results obtained by the GASP-WEBT in 2008–2010, together with UV and X-ray data acquired by Swift and γ-ray observations by the AGILE and *Fermi* satellites. We analyse the flux correlations at different frequencies to derive information on the jet physics and structure. As in several previous WEBT-GASP papers, we focus on an interpretation of the observed light curves in terms of variations in the orientation and curvature of an inhomogeneous emitting jet.

2. GASP-WEBT observations

The GLAST-AGILE Support Program (GASP) was born in 2007 as a project of the WEBT. Its aim is to perform long-term multifrequency monitoring of selected γ-loud blazars during the

[1] http://www.oato.inaf.it/blazars/webt/

[2] http://agile.iasf-roma.inaf.it/

[3] http://fermi.gsfc.nasa.gov/

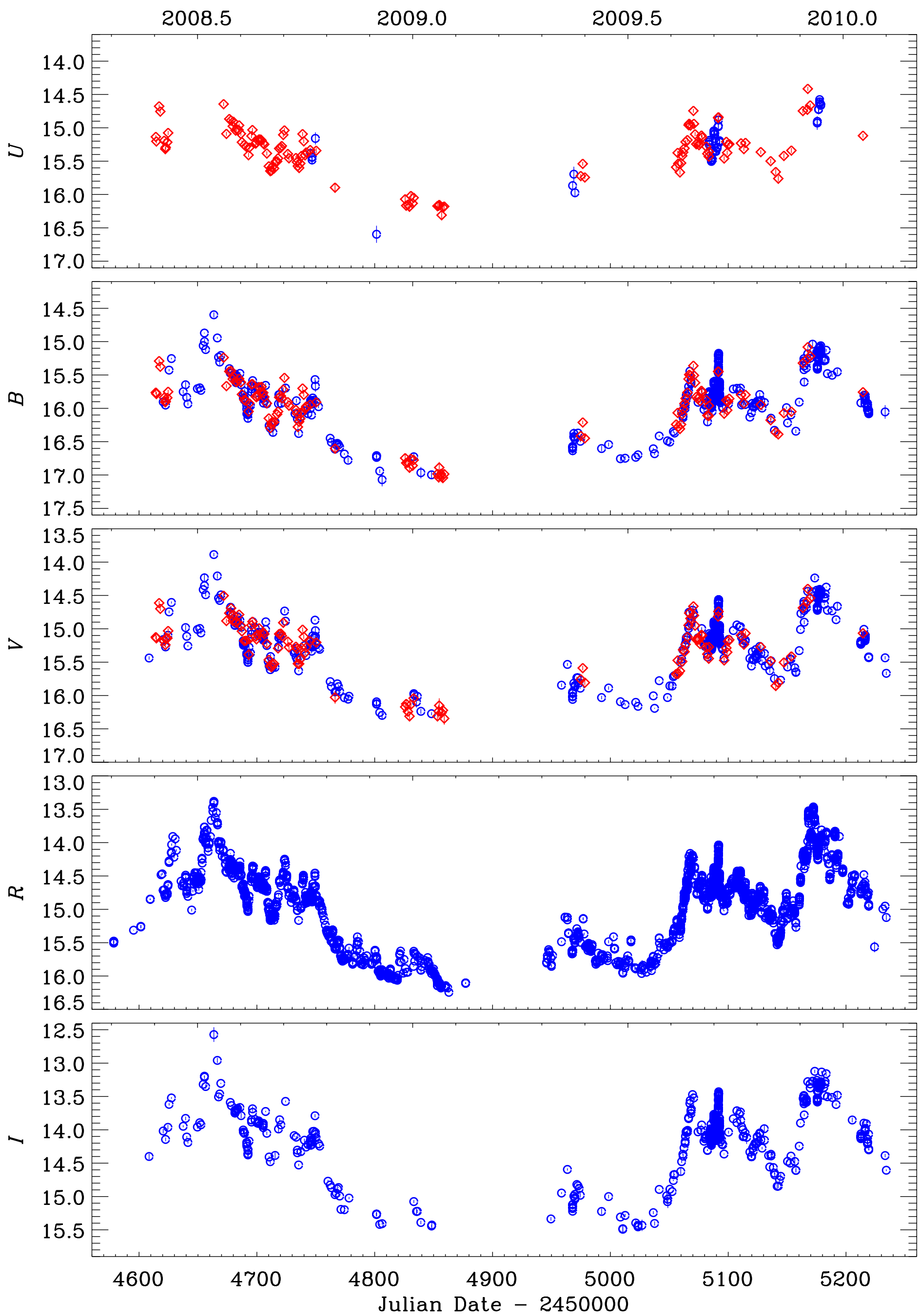

Fig. 1. Optical light curves of 3C 454.3 in 2008–2010 built with GASP-WEBT data (blue circles) and Swift-UVOT data (red diamonds). The UVOT points have been shifted to match the ground-based data (see text for details).

operation of the AGILE and *Fermi* (formerly GLAST) γ-ray satellites. In the optical, data are collected in the *R* band, and photometric calibration of 3C 454.3 is obtained with respect to Stars 1, 2, 3, and 4 by Raiteri et al. (1998). For this paper we also collected data taken by the GASP-WEBT observers in other optical bands to obtain spectral information.

Figure 1 shows the optical light curves of 3C 454.3 in 2008–2010. The 2008–2009 *R*-band light curve has already been published by Villata et al. (2009a). GASP-WEBT observations in 2009–2010 were performed at the following observatories: Abastumani, Calar Alto[4], Crimean, Galaxy View, Goddard (GRT), Kitt Peak (MDM), Lowell (Perkins), Lulin, New Mexico Skies, Roque de los Muchachos (KVA), Sabadell, San Pedro Martir, St. Petersburg, Talmassons, Teide (BRT), Tijarafe, and Valle d'Aosta. The figure also displays optical data acquired by the UVOT instrument onboard the Swift satellite (see Sect. 3).

Both observing seasons are characterised by intense activity, with several flaring episodes superimposed on prominent outbursts. The total variation amplitude is similar in the two seasons and it increases with increasing wavelength, as already noticed in previous works (e.g. Villata et al. 2006; Raiteri et al. 2008b). This feature was interpreted as an effect of an additional, stabler, emission component, mainly contributing to the blue part of the optical spectrum. This radiation likely comes from the accretion disc and BLR (see also Sects. 3 and 4). Noticeable

[4] Calar Alto data were acquired as part of the MAPCAT project: http://www.iaa.es/~iagudo/research/MAPCAT

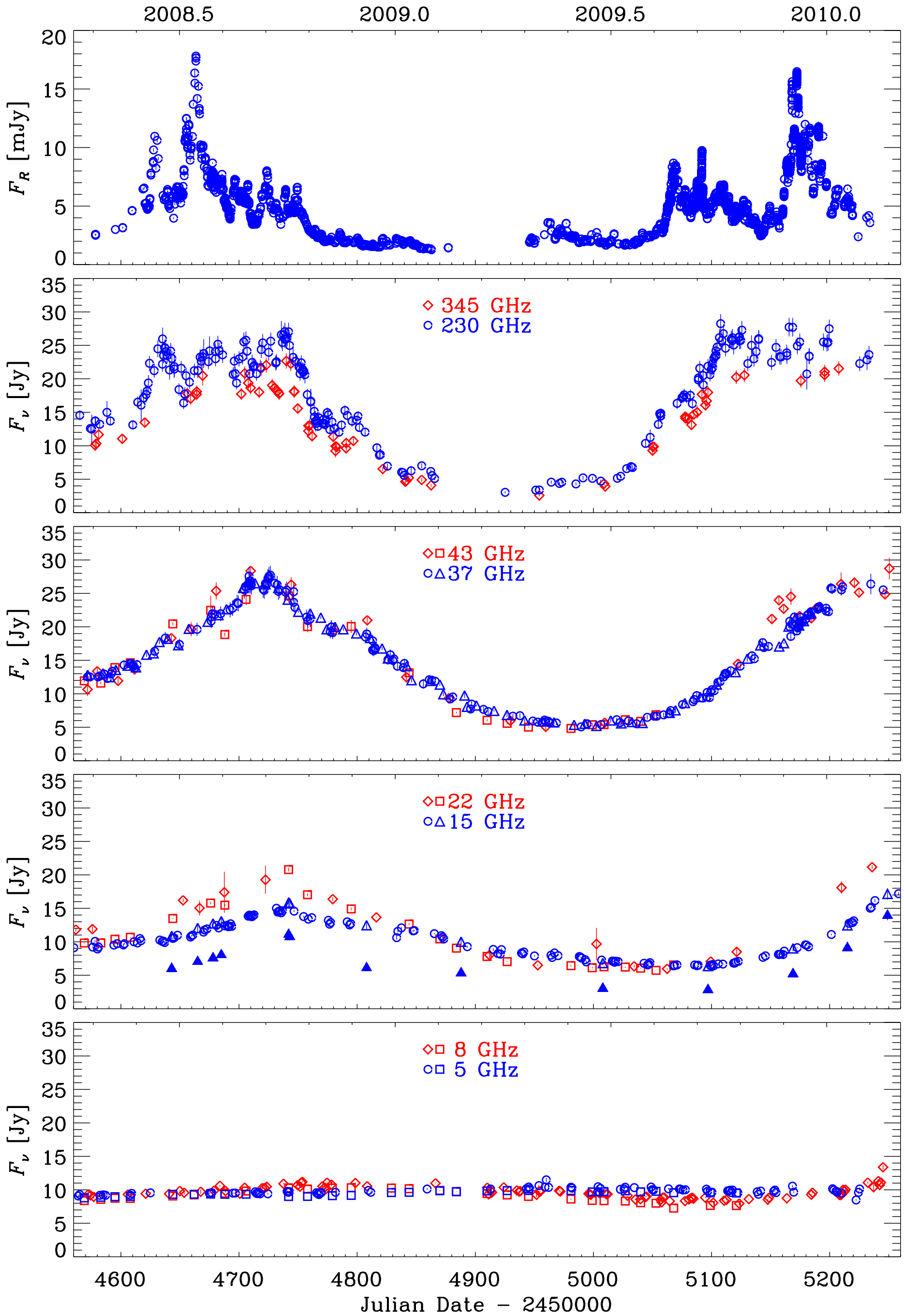

Fig. 2. *R*-band optical flux densities in 2008–2010 (*top*) compared to the radio light curves at different frequencies. The GASP data (blue circles and red diamonds) are complemented with those from the Crimean Observatory at 37 GHz (blue triangles) and with those from the VLA/VLBA Polarization Calibration Database at 43, 22, 8 GHz (red squares), and at 5 GHz (blue squares). Data at 15 GHz from the MOJAVE Program are also included as blue triangles: the filled ones represent the core flux, and the empty ones the total flux.

fast variability episodes are observed; in particular, a 0.3 mag brightening in about six hours on JD = 2 455 066 and 2 455 091, and a 0.5 mag brightening in about 14 h, from JD = 2 455 171.6 to 2 455 172.2.

The radio light curves of 3C 454.3 at different wavelengths in 2008–2010 are displayed in Fig. 2. Observations at 230 and 345 GHz are from the Submillimeter Array (SMA[5]), a radio interferometer including eight dishes of 6 m size located atop Mauna Kea, in Hawaii. Data at longer wavelengths were taken at the radio telescopes of Medicina (5, 8, and 22 GHz), Metsähovi (37 GHz), Noto (43 GHz), and UMRAO (4.8, 8.0, and 14.5 GHz). The Crimean Observatory provided additional observations at 37 GHz. We also included data from the VLA/VLBA Polarization Calibration Database[6] and from the MOJAVE programme[7].

[5] These data were obtained as part of the normal monitoring programme initiated by the SMA (see Gurwell et al. 2007).

[6] http://www.vla.nrao.edu/astro/calib/polar/. Data in the period between JD = 2 455 110 and 2 455 190 at 43 and 22 GHz, and between JD = 2 455 130 and 2 455 190 at 8 and 5 GHz were affected by problems in the automatic reduction procedure (Steven Myers, priv. comm.) and were thus removed.

[7] http://www.physics.purdue.edu/astro/MOJAVE/

In the top panel of Fig. 2 the R-band flux densities are shown for comparison. They were obtained by correcting magnitudes for a Galactic extinction of 0.29 mag and then converting them into fluxes using the absolute fluxes by Bessell et al. (1998).

At 230 GHz two outbursts with flickering superimposed cover the periods of high optical activity. Two outbursts are also visible at 43 and 37 GHz, but they are smoother and clearly delayed with respect to those at higher frequencies.

3. Swift-UVOT observations

The Ultraviolet/Optical Telescope (UVOT; Roming et al. 2005) onboard the Swift spacecraft (Gehrels et al. 2004) acquires data in the optical v, b, and u bands, as well as in the UV filters $uvw1$, $uvm2$, and $uvw2$ (Poole et al. 2008). In the period from 2008 May 27 to 2010 January 17, Swift pointed 173 times at 3C 454.3, acquiring data with the UVOT instrument 168 times. We reduced these data with the HEAsoft package version 6.10, with CALDB updated at the end of March 2010. Multiple exposures in the same filter at the same epoch were summed with `uvotimsum`, and then aperture photometry was performed with the task `uvotsource`. Source counts were extracted from a circular region with 5 arcsec radius, while background counts were estimated in two neighbouring source-free circular regions with 10 arcsec radii. In this way we obtained 147, 143, 165, 128, 126, and 120 photometric data in the $uvw2$, $uvm2$, $uvw1$, u, b, and v bands, respectively.

The UVOT light curves are shown in Fig. 3. The variability amplitude (maximum−minimum magnitude) decreases with increasing frequency: 1.94, 1.95, 1.88, 1.65, 1.48, and 1.46 mag going from the v to the $uvw2$ band. This confirms the trend already noticed for the optical data in Sect. 2 and extends it to the UV.

The UVOT optical data are also reported in Fig. 1. In this case, shifts have been given to the UVOT magnitudes to match the ground-based U, B, and V data taken by the GASP-WEBT observers. We estimated mean offsets $U - u = 0.2$, $B - b = 0.1$, and $V - v = -0.05$, with an uncertainty of a few hundredths of mag. These values are the same as those derived for BL Lacertae by Raiteri et al. (2010). By considering that the average UVOT colour indices of 3C 454.3 are: $u - b \sim -0.7$ and $b - v \sim 0.5$, the UVOT photometric calibrations by Poole et al. (2008) would indicate $U - u \sim 0.2$, $B - b \sim 0$–0.02, and $V - v \sim 0.01$–0.02. While our offset in the u band agrees with their results, the offset we find in the other two bands is larger. This may partly depend on the uncertainties affecting the reference star photometry adopted for the calibration of the ground-based data. Moreover, we must also consider the different spectral shape of our source with respect to the Pickles stars and GRB models used by Poole et al. (2008) to make the UVOT calibrations. As a result, following Raiteri et al. (2010) we checked the calibrations for our source, calculating effective wavelengths, $\lambda_{\rm eff}$, and count rate to flux conversion factors, CF_Λ, by folding them with both the blazar spectrum and the effective areas of the UVOT filters. The same folding procedure was also applied to evaluate the amount of Galactic extinction for each band, A_Λ, starting from the Cardelli et al. (1989) laws. This is an important point, because the average extinction curve shows a bump at about 2175 Å, which makes the usual calculation of extinction at the filter $\lambda_{\rm eff}$ dangerous in the UV bands for very absorbed objects, as shown by Raiteri et al. (2010) for BL Lacertae. Galactic reddening towards 3C 454.3 is smaller than in the BL Lacertae case, so we expect that deviations from

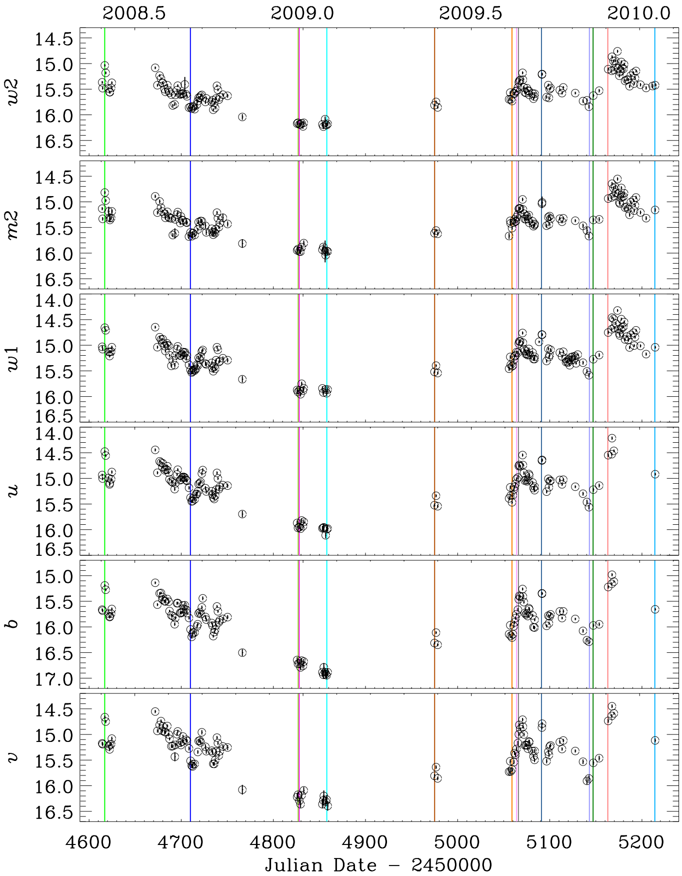

Fig. 3. Optical and UV light curves of 3C 454.3 in the 2008–2009 and 2009–2010 observing seasons. All data were acquired with the UVOT instrument onboard the Swift satellite. Vertical lines indicate the epochs selected for the calibration procedure.

both the Poole et al. (2008) calibrations and the Galactic extinction evaluated at the filter $\lambda_{\rm eff}$ are milder. To verify this we selected a number of epochs where UVOT data were available in all filters and which represented different brightness levels of the source, and we built an average observed spectrum of 3C 454.3 (see Fig. 4, top panel). Then we fitted this mean spectrum with a log-cubic curve and used this fit in the folding procedure. We checked the stability of the results by iterating the procedure twice.

The new $\lambda_{\rm eff}$, CF_Λ, and A_Λ are reported in Table 1. For comparison, the corresponding "standard" values ($\lambda_{\rm eff}$ and CF_Λ by Poole et al. 2008; and A_Λ calculated at the $\lambda_{\rm eff}$ of Poole et al. 2008) are shown in brackets. We then obtained recalibrated flux densities from count rates using the new CF_Λ, and corrected for Galactic extinction according to the new A_Λ. In the bottom-left panel of Fig. 4 we show the resulting SEDs corresponding to the selected observing epochs, together with their average. This average is compared to that obtained from the average spectrum shown in the top panel after applying standard calibrations and de-reddening. The main differences are in the UV, where the recalibrated spectral shape is smoother.

As expected, there is a change in the spectral slope when going from bright to faint states, as the ratio between the optical and UV fluxes decreases, leading to the already noticed smaller flux-density variation at higher frequencies. This reveals the presence of another emission component, likely coming from the accretion disc and BLR. Indeed, BLR contributions to the source SED in the near-IR (Hα line), in the optical band (Mg II, Fe II, and Balmer lines), and in the UV (Lyα) have already

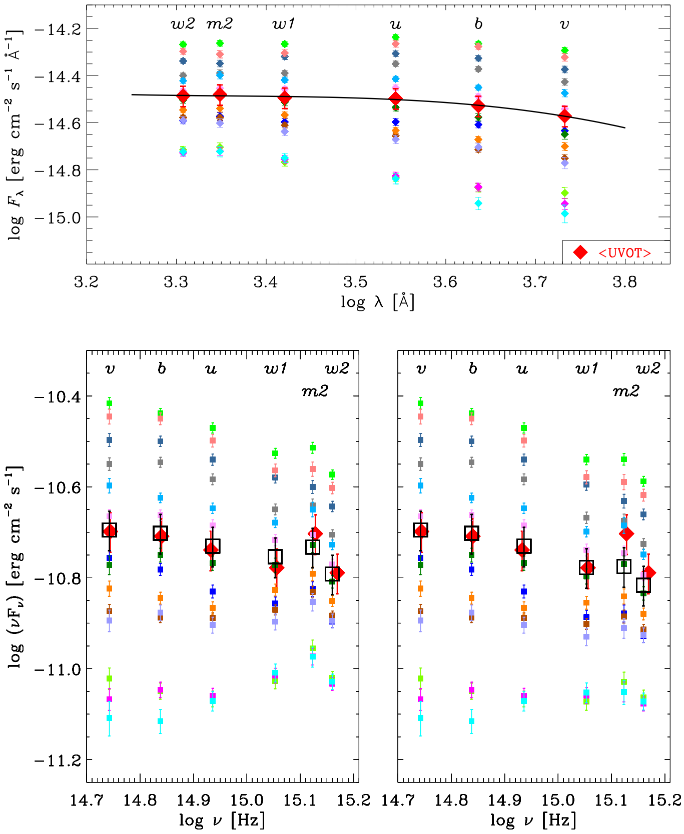

Fig. 4. *Top*: observed spectra of 3C 454.3 in the optical-UV band obtained from different epochs of UVOT observations analysed in this paper. Red diamonds refer to the mean UVOT observed spectrum. The solid line is the log-cubic fit used in the calibration procedure. *Bottom-left*: optical-UV SEDs of 3C 454.3 corresponding to the observed spectra shown in the top panel. Red diamonds are derived from the UVOT average spectra shown in the top panel by using standard prescriptions to obtain de-reddened flux densities. Black squares represent the mean UVOT SED after recalibration as explained in the text. *Bottom-right*: the same SEDs shown on the left, after correction for the emission lines contribution.

Table 1. Results of the UVOT recalibration procedure for 3C 454.3.

Filter	$\lambda_{\rm eff}$ Å	CF$_\Lambda$ 10^{-16} erg cm^{-2} s^{-1} Å^{-1}	A_Λ mag
v	5423 (5402)	2.61 (2.614)	0.36 (0.35)
b	4352 (4329)	1.47 (1.472)	0.47 (0.46)
u	3472 (3501)	1.65 (1.63)	0.57 (0.55)
*uvw*1	2652 (2634)	4.18 (4.00)	0.79 (0.73)
*uvm*2	2256 (2231)	8.42 (8.50)	0.99 (1.07)
*uvw*2	2074 (2030)	6.24 (6.2)	0.94 (1.02)

Notes. Values in brackets represent "standard" values, i.e. effective wavelengths $\lambda_{\rm eff}$ and count rate to flux conversion factors CF$_\Lambda$ from Poole et al. (2008), and Galactic extinction calculated from the Cardelli et al. (1989) laws at the $\lambda_{\rm eff}$ by Poole et al. (2008).

been recognised (Raiteri et al. 2007, 2008b; Benítez et al. 2010; Bonnoli et al. 2011). Subtraction of the Lyα flux would clarify to what extent a further contribution, possibly from the accretion disc, is needed. We used the publicly available UV spectrum acquired by the Galaxy Evolution Explorer[8] (GALEX) on 2008 September 30 to estimate the Lyα flux, finding $\sim 1.8 \times 10^{-14}$ erg cm^{-2} s^{-1}, about 30% lower than the value derived by Wills et al. (1995). By folding the line profile with the effective areas of the UV filters, we found contributions of 1.1, 3.1, and 1.2×10^{-16} erg cm^{-2} s^{-1} Å^{-1} in the *uvw*1, *uvm*2, and *uvw*2 bands, respectively. This means that in the *uvm*2 band the Lyα accounts for about 6% of the source flux density in the brightest state shown in Fig. 4, and for 17% in the faintest state. However, the Lyα line is not the only emission line to affect the UV spectrum of 3C 454.3. The *Hubble* Space Telescope (HST) spectra acquired in 1991 and analysed by Bahcall et al. (1993), Wills et al. (1995), and Evans & Koratkar (2004) also show prominent C IV and O VI + Lyβ lines, which are expected to mainly affect the flux in the *uvw*1 and *uvw*2 bands, respectively. We made a rough estimate of these further BLR contributions, finding that they are about one half of the Lyα ones. The bottom-right panel of Fig. 4 shows the source SEDs already displayed in the bottom-left panel, after correction for the emission line flux contribution. A UV excess still remains, likely indicating thermal emission from the accretion disc, as suggested by Raiteri et al. (2007, 2008b) and Bonnoli et al. (2011).

4. Spectral behaviour from the near-IR to the UV band

In the 2008–2009 observing season, near-IR monitoring in *J*, *H*, and *K* bands was performed at Campo Imperatore. L'Aquila earthquake that occurred on 2009 April 6 prevented the acquisition of data in the following season. Figure 5 shows four near-IR-to-UV SEDs obtained with simultaneous near-IR and optical GASP-WEBT data and the Swift-UVOT data treated as explained in the previous section, but without subtraction of the emission line contributions. To add information on the source behaviour at even fainter levels, we reconsidered the two SEDs corresponding to the *XMM-Newton* observations of July and December 2006, which were published by Raiteri et al. (2007). The corresponding near-IR and optical data were acquired by the WEBT collaboration, and they show the flux excess in the *J* band owing to the Hα emission line (see also Raiteri et al. 2008b) and the little bump in the optical, probably caused by Mg II, Fe II, and Balmer lines. The OM data shown in Fig. 6 of Raiteri et al. (2007) were treated in a standard way by converting magnitudes into fluxes according to the general method based on the Vega flux scale[9] and by correcting for Galactic extinction calculated from the Cardelli et al. (1989) law at the effective wavelength of the OM filters. We checked the reliability of those results by applying the same calibration procedure used in the previous section to check the UVOT calibrations.

Table 2 shows the results we obtained by folding the quantities of interest with both the source spectrum and the effective areas of the OM filters. The most noticeable difference between the new and the standard $\lambda_{\rm eff}$ is a blueshift in the *B* band, which makes the new value more like to the UVOT one. We also notice a 15% increase in the CF$_\Lambda$ in the *U* band over Vega and a 10% decrease in the Galactic extinction in the *UVW*2 band over the value we got from the Cardelli et al. (1989) law at the standard effective wavelength.

The main effect of the OM recalibration procedure is that the *U* points in Fig. 5 are shifted to a higher flux level than in Fig. 6 of Raiteri et al. (2007), confirming what we have already found for the UVOT data, i.e. that the satellite data are much brighter

[8] http://www.galex.caltech.edu/

[9] http://xmm.esa.int/sas/current/watchout/Evergreen_tips_and_tricks/uvflux.shtml

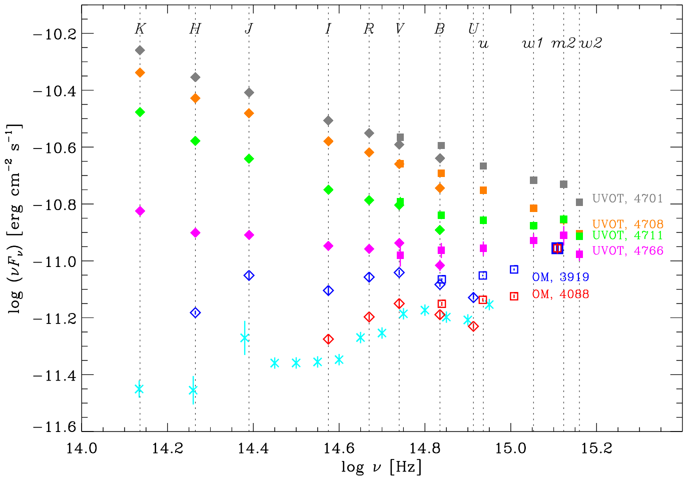

Fig. 5. SEDs of 3C 454.3 from the near-IR to the UV band at different brightness levels. The four SEDs plotted with filled symbols correspond to epochs of Swift observations: recalibrated UVOT data are displayed with squares, simultaneous optical and near-IR data from the GASP-WEBT with diamonds. The two SEDs shown with empty symbols correspond to the two *XMM-Newton* observations of July (blue) and December (red) 2006 (see Raiteri et al. 2007): recalibrated OM data are plotted with squares and WEBT data with diamonds. The epochs of satellite observations (JD – 2 450 000) are indicated on the right. Error bars only take measure errors into account. Cyan crosses represent observations by Neugebauer et al. (1979).

Table 2. Results of the OM recalibration procedure for 3C 454.3.

Filter	$\lambda_{\rm eff}$ Å	CF_Λ 10^{-16} erg cm^{-2} s^{-1} Å^{-1}	A_Λ mag
V	5423 (5430)	2.53 (2.50)	0.36 (0.35)
B	4340 (4500)	1.35 (1.34)	0.47 (0.46)
U	3483 (3440)	1.96 (1.70)	0.56 (0.54)
*UVW*1	2945 (2910)	4.76 (4.86)	0.67 (0.65)
*UVM*2	2334 (2310)	21.8 (21.9)	0.96 (0.98)
*UVW*2	2146 (2120)	56.5 (58.8)	1.00 (1.10)

Notes. Values in brackets represent, respectively, "standard" effective wavelengths $\lambda_{\rm eff}$, count rate to flux conversion factors CF_Λ based on Vega, and Galactic extinction calculated from the Cardelli et al. (1989) laws at the standard $\lambda_{\rm eff}$.

than the ground-based one in the *U* band. The recalibration of the OM data confirms the sharp rise of the SED in the UV when the source is in a faint state.

5. Swift-XRT observations

In the period from 2008 May 27 to 2010 January 17 (see Sect. 3) the XRT instrument onboard Swift (Burrows et al. 2005) performed 173 observations of 3C 454.3 in different observing modes. We processed the event files acquired in pointing mode, using the HEASoft package version 6.10 with CALDB updated as 2010 September 30. We considered the observations with exposure time longer than five minutes, including 111 observations in photon-counting (PC) mode and 59 in windowed-timing (WT) mode. The task `xrtpipeline` was run with standard filtering and screening criteria. For the PC mode, we selected event grades 0–12. Source counts were extracted from a 30 pixel circular region (~71 arcsec) centred on the source, and background counts were derived from a surrounding annular region with radii 110 and 160 pixels. When the count rate was greater than 0.5 counts/s, we punctured the source-extracting region, discarding the inner 3-pixel radius circle to correct for pile-up. The `xrtmkarf` task was used to generate ancillary response files (ARF), which account for different extraction regions, vignetting, and PSF corrections. The last in particular correct for the loss of counts caused by the central hole of the source extracting region in the pile-up case.

For the data acquired in WT mode, we selected event grades 0–2. We used the same circular region of 30 pixel radius centred on the source to extract the source counts, and a similar region shifted away from the source along the window to extract the background counts. When in the same observation the windows corresponding to different orbits overlapped with different position angles, we both created event files and extracted source and background counts separately for each orbit[10]. For each event file we then generated the exposure map with the task `xrtexpomap`, which was used to obtain the ARF for the corresponding source spectrum. Finally, we recombined the information from all the orbits of a single observation by summing the source spectra and the background spectra. The ARFs were summed by weighting them according to their orbit contribution to the total counts of the observation.

The task `grppha` was used to group the spectra and bin them to have more than 20 counts in each bin. These spectra were then analysed with the `xspec` task, version 12.6.0q. We applied an absorbed single power-law model, where absorption is modelled according to Wilms et al. (2000). Table 3 presents the result of the spectral analysis in the case where the hydrogen column is fixed to $N_{\rm H} = 1.34 \times 10^{21}$ cm^{-2}, as determined by the *Chandra* observations in 2005 (Villata et al. 2006). Column 1 gives the ObsID, Col. 2 the start time (UT), and Col. 3 the total exposure time, often distributed over several orbits. Column 4 gives the observing mode: an asterisk following "PC" means that the count rate was greater than 0.5 counts/s, and the data were thus corrected for pile-up, while a number following "WT" indicates how many misaligned windows were present in the total event file. Column 5 gives the photon index Γ, Col. 6 the 1 keV flux, Col. 7 the value of the reduced χ^2, while the number of degrees of freedom ν appears in brackets.

Some observations resulted in a low number of counts, and the corresponding χ^2/ν values were mostly small, indicating that the model is "over-fitting" the data. Indeed, the χ^2 statistic is not appropriate for a low number of counts, so that we refitted the spectra with either $\nu < 10$ or $\chi^2/\nu < 0.5$ adopting the Cash's C-statistic, which was developed to address this problem (Cash 1979; Nousek & Shue 1989). When in Col. 7 of Table 3 the label "Cash" appears, it means that the results of the spectral fit were obtained with the C-statistic. The photon index Γ ranges from 1.38 to 1.85, with an average value $\langle\Gamma\rangle = 1.59$, and a standard deviation $\sigma = 0.09$. However, the mean square uncertainty $\delta^2 = 0.18$ is greater than the variance σ^2, so that the mean fractional variation (Peterson 2001) $F_{\rm var} = \sqrt{\sigma^2 - \delta^2}/\langle\Gamma\rangle$ is not even real. This means that the spectral variations are dominated by noise and cannot be ascribed to real changes in the source spectrum. The lack of a trend of Γ with the source flux favours this interpretation.

6. Flux correlations

Figure 6 shows the multiwavelength behaviour of 3C 454.3 from May 2008 to January 2010. The top panel displays the

[10] We did not separate orbits if the misalignment was less than a few degrees.

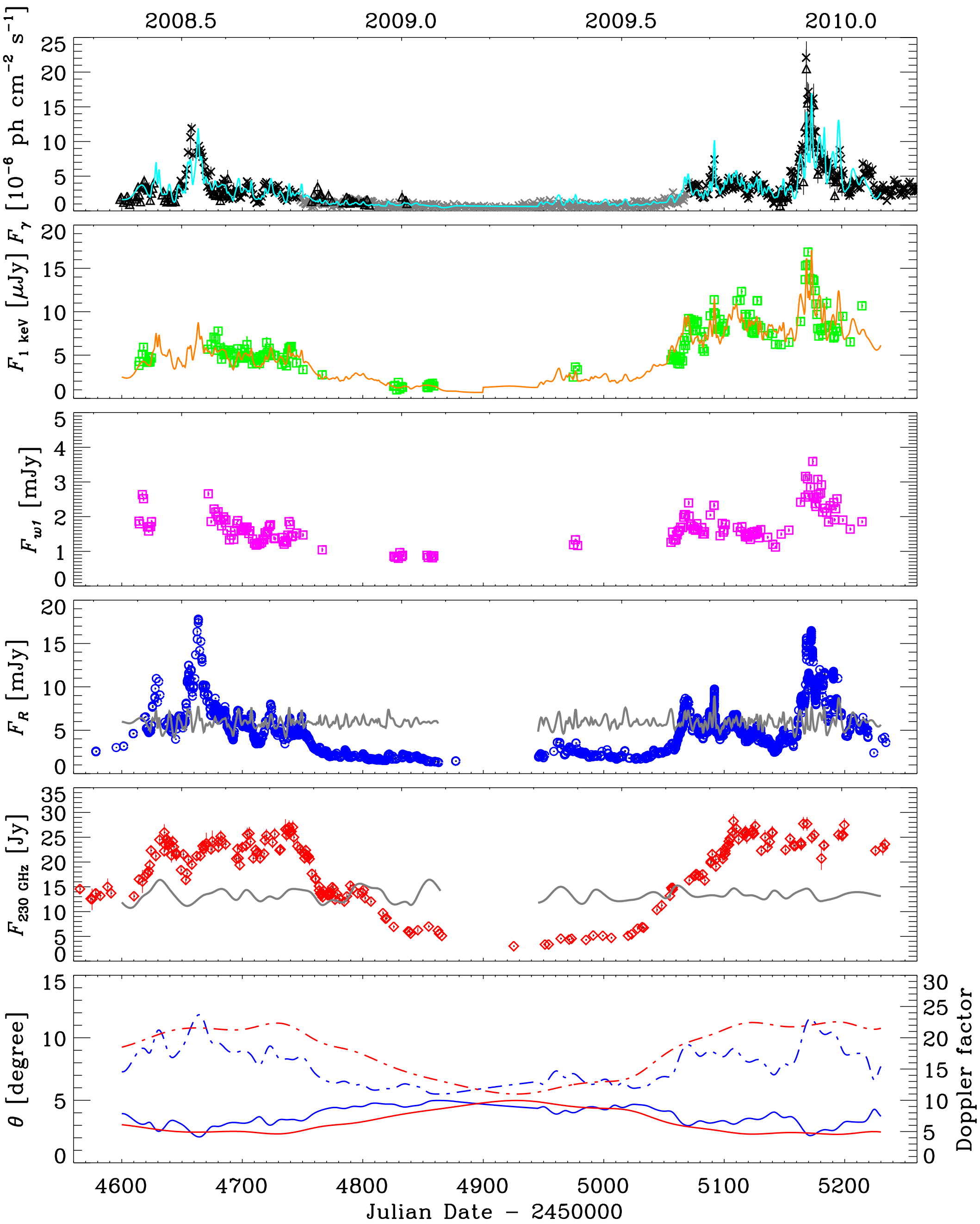

Fig. 6. Light curves of 3C 454.3 from May 2008 to January 2010 at different frequencies. The γ-ray data are 0.1–300 GeV fluxes; black triangles are from AGILE (Vercellone et al. 2010; Pacciani et al. 2010) and crosses from *Fermi* (the black ones from Abdo et al. 2009; and Ackermann et al. 2010, and the grey ones from the public light curve of the LAT monitored sources). The 1 keV flux densities are derived from Swift-XRT spectra fitted with an absorbed power law with $N_H = 1.34\times10^{21}$ cm^{-2} (see Sect. 5 and Table 3). De-reddened UV flux densities in the $w1$ band are obtained as explained in Sect. 3. The optical R-band dereddened flux densities are derived from GASP data (see Sect. 2). The mm light curve is from the SMA. The cyan and orange curves superposed on the γ- and X-ray light curves, respectively, are obtained by combining cubic spline interpolations through the 1-day binned optical and the 7-day binned mm light curves as explained in the text. The *bottom panel* displays the evolution of the Doppler factors (dot-dashed lines) affecting the optical (blue) and mm (red) fluxes, and the viewing angles of the corresponding emitting regions (solid lines). Grey lines superposed on the optical and mm light curves represent intrinsic flux variations as would be observed under a constant Doppler factor $\delta = 18$.

0.1–300 GeV γ-ray light curve; the 2008–2009 AGILE data have already been published by Vercellone et al. (2010), and the 2009–2010 ones by Pacciani et al. (2010). *Fermi*-LAT data corresponding to the 2008 outburst are presented by Abdo et al. (2009), and those starting from August 2009 by Ackermann et al. (2010). For the period in between we downloaded the public *Fermi* light curve from HEASARC as 3C 454.3 is part of the *Fermi* LAT Monitored Source List[11]. The 1 keV flux densities plotted in the second panel are the result of the Swift-XRT spectral fitting with an absorbed power law with fixed absorption discussed in Sect. 5 and reported in Table 3. The

[11] http://heasarc.gsfc.nasa.gov/W3Browse/fermi/fermilasp.html

following ultraviolet (*uvw*1 band), optical (*R* band), and millimetric (230 GHz) light curves have already been shown in Figs. 1–3. We notice a rough correlation among the fluxes at all wavelengths, but the variability amplitude decreases from the higher to the lower frequencies, with the ultraviolet the only exception. Indeed, the maximum variation in the γ-ray flux is a factor ~214, while it is ~17 at 1 keV, ~14 in the optical *R* band, and ~9 at ~1 mm. The total change of the *uvw*1 flux density is only a factor ~5, and this is the consequence of the dilution of the variable synchrotron emission with the less variable disc and BLR radiation (see Sects. 3 and 4).

It is interesting to notice that the flux level reached by the optical light curve is similar in the two seasons; the same is true for the mm light curve, while in the X-ray and γ-ray bands there is a clear general flux increase in the second period. We miss information in the infrared, but can guess that the source behaviour would be intermediate between those in the optical and mm bands.

One possible interpretation of the observed long-term flux variations of 3C 454.3 at low frequencies (radio to UV) assumes that the jet is both inhomogeneous, with radiation of increasing wavelength being produced in progressively outer regions (e.g. Ghisellini & Maraschi 1989; Maraschi et al. 1992), and curved and that the alignment of the various emitting regions with the line of sight changes in time (Villata et al. 2006, 2007, 2009a). Because the Doppler factor $\delta = [\Gamma(1-\beta\cos\theta)]^{-1}$, where Γ is the bulk Lorentz factor of the jet plasma and $\beta = v/c$ its bulk velocity, depends on the viewing angle θ, the flux at a given wavelength will be Doppler-enhanced according to the orientation of the corresponding emitting zone. In the bottom panel of Fig. 6, we show the variation in the Doppler factors affecting the optical and mm fluxes under the hypothesis that their long-term trend is due to variations in the viewing angle alone and that the observed flux is proportional to δ^3 (see e.g. Urry & Padovani 1995; Villata & Raiteri 1999), so that $\delta(t) = \delta_{\min}[F(t)/F_{\min}]^{1/3}$. We set $\delta_{\min} = 11$, in the range of the values estimated by Abdo et al. (2009) and Ackermann et al. (2010) to avoid pair production, hence self-absorption, of γ-ray radiation. To reproduce the long-term trends we tentatively used cubic spline interpolations through the 7-d binned optical light curve and 30-d binned mm light curve[12]. In the bottom panel of Fig. 6 we also show the evolution of the corresponding viewing angles, obtained as $\theta(t) = \arccos\{[\Gamma\,\delta(t) - 1]/[\sqrt{\Gamma^2 - 1}\,\delta(t)]\}$, where we put $\Gamma = 15.6$, in agreement with the value derived by long-term Very Long Baseline Interferometry (VLBI) monitoring (Jorstad et al. 2005). This produces maximum Doppler factors of ~23.7 for the optical and ~22.5 for the mm, and corresponding minimum viewing angles of about 2.1° and 2.3°, respectively, at the time of flux maxima. The minimum Doppler factor of 11, corresponding to a maximum angle of about 5.0°, was reached during the flux minima. The above picture would explain the long/mid-term flux variations (see also Villata et al. 2002, 2004), while the short-term flares (see below) would be due either to perturbations moving downstream in the jet or to a finer geometrical structure, as proposed for BL Lacertae by Larionov et al. (2010).

As mentioned in the Introduction, the high-energy emission is commonly believed to come from inverse-Comptonisation of low-energy radiation according to either an SSC or an EC process, or a combination of both. In an SSC scenario, the dependence of the synchrotron emissivity on the density of relativistic particles is linear, while the dependence of the self-Compton emissivity is quadratic. However, that the increase of the flux levels of the γ and X-ray light curves in the second observing season does not correspond to a rise of the optical and mm flux levels seems to rule out a variation in the electron density. The most straightward explanation is therefore that there has been a growth of the number of Comptonised seed photons, i.e. of the Comptonisation rate.

We investigate the matter in an SSC framework and we roughly divide the emitting jet in three zones, where radiation at different frequencies is produced through the synchrotron process: the UV to near-IR region, which we will call the "optical" region, the IR region, and the mm region[13]. We assume that the variation in time of the number of both synchrotron (seed) photons and target electrons in the various zones is represented by the *R*-band light in the first region, by a linear combination of the *R*-band and mm light curves in the second region, and by the mm flux density variations in the third region. We therefore try to fit the γ and X-ray light curves in Fig. 6 with the following general expression:

$$[s_R\,F_R(t)/\delta_R^3(t) + s_{\rm mm}\,F_{\rm mm}(t)/\delta_{\rm mm}^3(t)] \times [e_R\,F_R(t) + e_{\rm mm}\,F_{\rm mm}(t)]$$

where the first factor refers to the seed photons in the jet rest frame, the second factor to the Comptonising electrons, $F_R(t)$ and $F_{\rm mm}(t)$ represent cubic spline interpolations through the 1-d binned *R*-band and 7-d binned mm light curves, respectively, $\delta_R(t)$ and $\delta_{\rm mm}(t)$ are the Doppler factors affecting the optical and mm emissions, respectively, which are plotted in the bottom panel of Fig. 6, and $s_R, s_{\rm mm}, e_R, e_{\rm mm}$ are coefficients that regulate the relative contributions of the jet zones. The functions $F'_R(t) = F_R(t)/\delta_R^3(t)$ and $F'_{\rm mm}(t) = F_{\rm mm}(t)/\delta_{\rm mm}^3(t)$ represent the intrinsic optical and mm flux density changes, respectively, since δ^{-3} corrects for the variability due to the Doppler boosting. To better clarify this point, we superposed, on the optical and mm light curves in Fig. 6, those intrinsic changes that would be observed in case of a constant Doppler factor $\delta = 18$, i.e. if there were no viewing angle variations. As one can see, ascribing the long-term trends to viewing angle variations on the chosen time scales (one week for the optical, one month for the mm) reveals intrinsic variations of similar amplitude, which in turn supports the initial assumption.

The fit to the γ-ray light curve shown in the top panel of Fig. 6 is obtained by setting $s_{\rm mm} = e_{\rm mm} = 0$, suggesting that the γ-ray emission comes from the Comptonisation of synchrotron optical photons in the optical emitting region. However, due to the photon's mean free path before upscattering and to the fact that the synchrotron radiation is relativistically beamed forward, the bulk of the γ-ray radiation is expected to come from a region slightly downstream from the region responsible for the bulk of the optical emission. To fit the X-ray light curve, we set $s_R = e_R$ and $s_{\rm mm} = e_{\rm mm}$, meaning that the X-ray emission is obtained by upscattering of IR photons on their parent relativistic electrons. Also in this case we can imagine that the bulk of the X-ray radiation is produced a bit downstream from the bulk of the IR radiation.

The increase in the γ and X-ray flux levels from the first to the second observing season can thus be explained as a growth in the number of seed photons that are Comptonised. In particular, to explain the higher γ flux in the second season, we need to increase the number of Comptonising interactions by about 60%, while we need to increase it by a factor 1.6–1.8 to explain the

[12] The mm emitting region is expected to be much wider than the optical one, so that its variability time scales would be longer.

[13] Indeed, in our inhomogeneous jet model the synchrotron emission at each frequency mainly comes from the jet region where that frequency is close to self absorption.

higher X-ray flux. This may be due to a variable misalignment between the zone responsible for the bulk of the synchrotron emission and the one responsible for the bulk of the respective inverse-Compton one. In the second observing season, the regions would be better aligned, so that more seed photons can enter the corresponding Comptonisation zone.

In summary, we imagine a scenario where the variation in the angle between our line of sight and the optical emitting region in the 2008–2009 observing season is similar to the variation in the following 2009–2010 season, implying similar flux density levels. The same is true for the mm region. At the same time, the γ and X-ray production zones become more aligned with the optical and IR regions in the second period, explaining the increased γ and X-ray flux levels.

6.1. Short-term correlation between the optical and γ-ray fluxes

The correlation between the γ-ray and optical fluxes of 3C 454.3 has been analysed in a number of papers including AGILE or *Fermi* data. Using AGILE and WEBT data, Vercellone et al. (2009) find a mild correlation with no evident time delay in November 2007, while the increased optical activity in December allowed Donnarumma et al. (2009) to constrain the γ-optical time lag to $-0.6^{+0.7}_{-0.5}$ d, indicating that the γ-ray flux variations follow the optical ones by ~0–1 d, even if a very fast γ and optical flare on December 12 seemed to constrain the delay within 12 h. When considering 18 months of AGILE and GASP-WEBT observations (2007 July–2009 January), Vercellone et al. (2010) found a time lag of $-0.4^{+0.6}_{-0.8}$ d of the γ-ray variations after the optical ones, consistent with the earlier results. The cross-correlation study performed by Bonning et al. (2009) on γ-ray data from *Fermi* and optical/IR data from SMARTS in 2008 found no detectable lag between IR/optical and γ-ray fluxes.

Figure 7 shows an enlargement of the γ and optical light curves of Fig. 6 around the brightest phase of the 2008 outburst. The γ-ray flare appears double-peaked, the flux of the first maximum being 27% higher than that of the second one. The shape of the optical flare seems more complex, but we notice that there is an optical minor peak corresponding to the first γ maximum, just before or simultaneous to it, and there is a major optical peak just before or simultaneous to the second γ peak. It is not clear whether there are really more optical events than γ ones, or if other γ peaks are hidden by insufficient sampling and precision. Moreover, it is not easy to understand why a minor (major) optical flare corresponds to a major (minor) event at γ energies.

The period of most intense activity in late 2009 is shown in Fig. 8. We can recognise some features similar to those noticed in the light curves of mid 2008. The dense optical monitoring performed by the GASP collaboration allowed us to detect a sharp peak on JD = 2 455 168, simultaneous to the major γ-ray one. Then, a second major fast optical flare at JD = 2 455 172 found the γ-ray flux at a much lower level, possibly in between two little γ bumps. We again notice a difference in the flux ratios: the second optical peak is brighter than the first one, whereas the opposite is true in γ-rays. Moreover, a well-sampled optical minimum is visible at JD = 2 455 176, while the minimum is reached 1–2 days later at γ frequencies. Finally, the optical flares peaking at JD = 2 455 183 and JD = 2 455 190 have no evident γ-ray counterparts.

In summary, when inspecting the γ-optical correlation on short time scales, sometimes the optical and γ flux variations are simultaneous, whereas in other cases the latter seem to be lacking or to possibly be delayed.

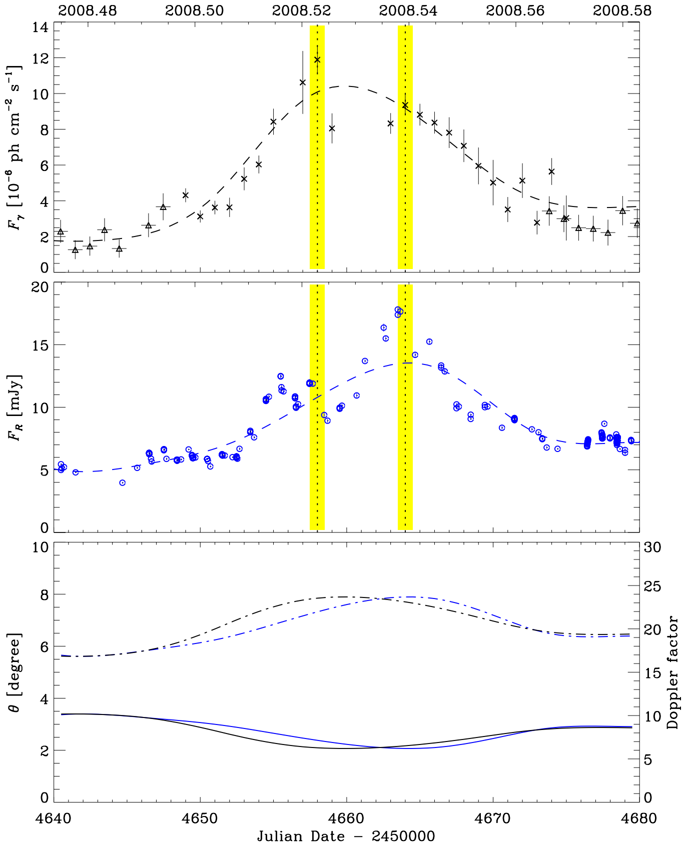

Fig. 7. Flux variations of 3C 454.3 at γ-ray (*top*) and optical (*middle*) frequencies in mid 2008. The γ-ray light curve is built with *Fermi* data (crosses) from Abdo et al. (2009) and AGILE data (triangles) from Vercellone et al. (2010). Vertical dotted lines indicate the position of the two γ peaks, the yellow stripes highlighting the data integration interval. Cubic spline interpolations through the 7-day binned optical (blue dashed line) and γ (black dashed line) light curves are also shown. They represent the variations due to geometrical changes. The evolution of the Doppler factor δ (dot-dashed lines) and viewing angle θ (solid lines) is shown in the bottom panel for both the γ-ray (black) and optical (blue) bands.

In the geometrical scenario proposed above to explain the long-term flux variations of the optical and mm light curves, as well as the increased γ and X-ray fluxes in 2009–2010, a slight misalignment between the regions responsible for the production of the optical and γ-ray radiations can also account for the variation in the γ/optical flux ratio. In the bottom panels of Figs. 7 and 8 we show the evolution of the Doppler factors δ and viewing angles θ affecting the optical and γ fluxes in the considered periods. The trends of the optical δ and θ have already been presented in the bottom panel of Fig. 6. To obtain the γ-ray ones we used cubic spline interpolations through the 7-d binned *Fermi* light curve and rescaled it to the optical one to take into account that we are comparing fluxes deriving from different processes. We therefore constructed a new γ-ray spline as $F_{\rm res} = a F^b$, which has the same flux maximum and minimum as the optical one. We got $a = 3.53$ and $b = 0.57$ in the period shown in Fig. 7, while $a = 1.70$ and $b = 0.73$ in the period plotted in Fig. 8[14]. In both periods one can see that the γ-emitting region acquires the minimum θ, corresponding to the maximum δ, slightly before

[14] This means that in the considered periods the total long-term variation in the γ flux is less than quadratic with respect to the optical one, as expected, because the quadratic dependence of the intrinsic fluxes is "diluted" by the Doppler factor variation.

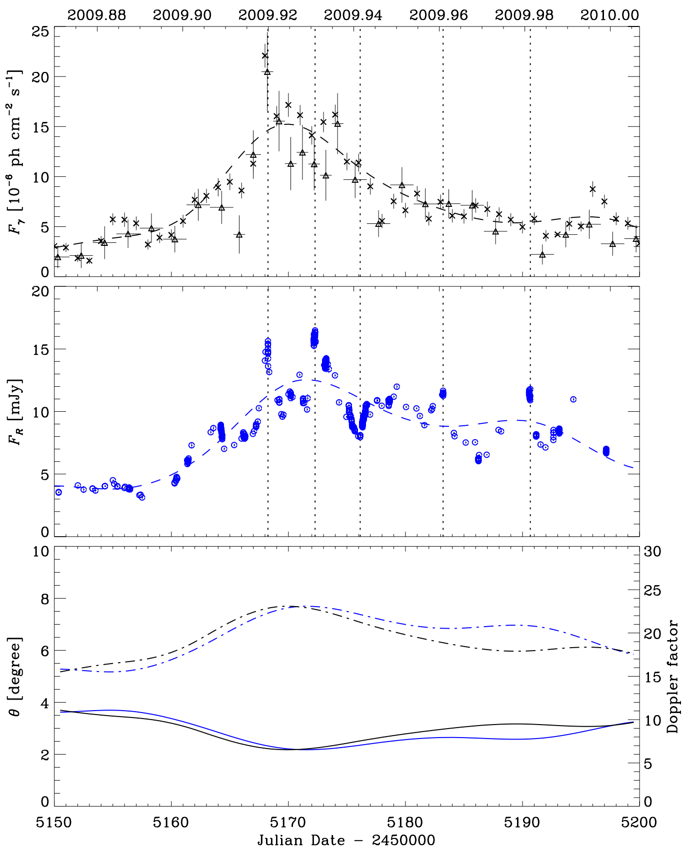

Fig. 8. Flux variations of 3C 454.3 at γ-ray (*top*) and optical (*middle*) frequencies in late 2009. The γ-ray light curve is built with *Fermi* data (crosses) from Ackermann et al. (2010) and AGILE data (triangles) from Pacciani et al. (2010). Vertical dotted lines indicate remarkable optical events. Cubic spline interpolations through the 7-day binned optical (blue dashed line) and γ (black dashed line) light curves are also shown. They represent the variations due to geometrical changes. The evolution of the Doppler factor δ (dot-dashed lines) and viewing angle θ (solid lines) is shown in the bottom panel for both the γ-ray (black) and optical (blue) bands.

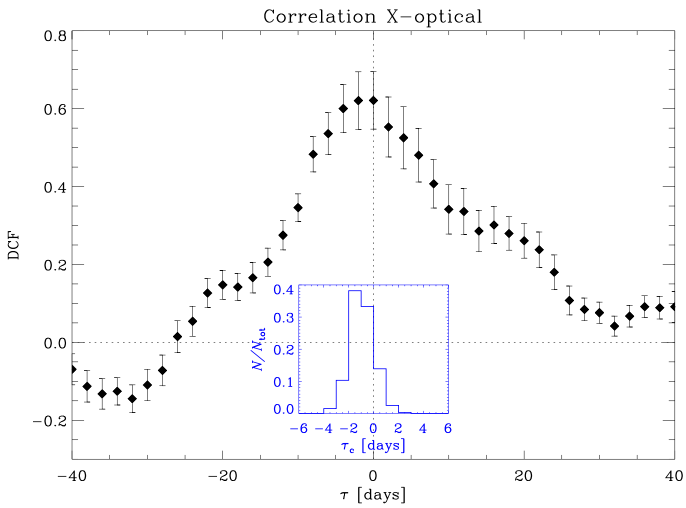

Fig. 9. Discrete correlation function (DCF) between the 1 keV flux densities from XRT and the GASP R-band flux densities. The inset shows the results of 1000 Monte Carlo simulations.

than the optical zone. We suggest that in both periods, because of the different orientation of the emitting regions, the γ-ray flux was more relativistically boosted than the optical one at the time of the first γ peak, while the opposite occurred at the time of the second peak. Moreover, we can see that, in the rising part of the 2009 outburst, the two regions are better aligned, yielding more comparable optical and γ flares than in the rising part of the 2008 outburst. The maximum misalignment between the optical and γ emitting regions is quite small: $\sim 0.4°$ in mid 2008 and $\sim 0.6°$ in late 2009.

6.2. Short-term correlation between the X-ray and optical/γ fluxes

The X-ray light curve is less sampled than the γ-ray one, so that a detailed analysis of correlation like the one performed in the previous section is not possible. We thus investigate the optical-X correlation by analysing the entire long-term light curves shown in Fig. 6 by means of the discrete correlation function (DCF; Edelson & Krolik 1988; Hufnagel & Bregman 1992), which was specifically designed to study unevenly sampled data sets. In Fig. 9 we show the DCF obtained by cross-correlating the 1 keV with the R-band flux densities. Both light curves have previously been binned over 12 h, while the DCF bin was set to two days. The curve peaks at a time lag τ between -2 and 0 d, with a DCF value of 0.62, which indicates mild correlation, and flux variations in the optical band leading or being simultaneous to those in the X-ray one. In general, a more precise measure of the time lag can be obtained by calculating the centroid of the DCF, $\tau_c = (\sum_i \tau_i \mathrm{DCF}_i)/(\sum_i \mathrm{DCF}_i)$, where sums run over the points which have a DCF value close to the peak one. In our case the calculation of the centroid using all points with DCF $> 0.8\,\mathrm{DCF_{peak}}$ (6 points) yields $\tau_c = -1.0$ d, i.e. an X-ray lag of 1 d. The same result is obtained by lowering the threshold for the centroid calculation to 0.75 and 0.70 of the $\mathrm{DCF_{peak}}$ (8 points). To estimate the uncertainty on this time lag, we performed Monte Carlo simulations following the technique known as "flux redistribution/random subset selection" (FR/RSS; Peterson et al. 1998; see also Raiteri et al. 2003), which allows testing the influence of both sampling and errors on the results. We randomly selected subsets of the X-ray and optical light curves, discarding redundant points, and adding to the fluxes random Gaussian deviates constrained by the flux errors. The X-ray and optical subsets are then cross-correlated and the resulting DCF centroids stored. A measure of the lag uncertainty can then be derived from the centroid distribution, by considering the range of τ_c values containing 68.27% of the realisations. The inset in Fig. 9 displays the τ_c distribution obtained from 1000 Monte Carlo realisations: τ_c is in the range -2–0 d in 71% of cases ($\gtrsim 1\sigma$). This allows us to conclude in a more precise way that the time lag of the X-ray flux variations after the optical ones is $\tau = 1.0 \pm 1.0$ d.

The finding of a time delay of the X-ray variations after the optical ones agrees with the picture proposed above, where the X-ray radiation is produced in the IR region, downstream of the optical one. In the proposed scenario we would also expect the X-ray emission to be slightly delayed with respect to the γ-ray one, which is supposed to be very close to the optical one. Cross-correlation of the γ-ray light curve with the X-ray one, with the same choice of binning parameters as in the X-ray/optical case, yields a highly significant peak ($\mathrm{DCF_{peak}} \sim 1$) at zero time lag, while $\tau_c = 1.0$ d. The result of the Monte Carlo method described above is $\tau = 0.5 \pm 1.0$ d, confirming a possible slight delay in the X-ray flux variations.

7. Conclusions

In this paper we have presented multifrequency observations of 3C 454.3 from April 2008 to March 2010. Radio-to-optical data are mainly from the GASP-WEBT, and UV and X-ray data are from Swift and γ-ray data from AGILE and *Fermi*. In these two observing seasons, the source showed prominent outbursts at frequencies greater than 8 GHz, with rapid flares superposed in the optical-to-γ light curves.

We have reanalysed the question of the nature of the optical-UV emission, deriving more accurate calibrations for both the UVOT instrument onboard Swift and the OM detector onboard *XMM-Newton*, and estimating the contribution of the emission lines (mainly Lyα) in the UV. We confirmed that the observed decrease of the variability amplitude with increasing frequency from the near-IR to the UV band is due to the contribution of radiation from both the BLR and the accretion disc. The long-term flux variations from the optical to the γ-ray frequencies appear roughly correlated. The mm flux remained high during the whole optical flaring period.

By comparing the multiwavelength behaviour in the 2008–2009 and 2009–2010 observing seasons, we noticed that the optical flux reached nearly the same levels (i.e. minimum and maximum brightness) in both seasons. The same thing occurred in the mm band, whereas the γ-ray and X-ray flux levels increased in the second period.

We interpreted the observations in terms of an inhomogeneous jet model, where synchrotron radiation of increasing wavelength is produced in progressively larger regions farther away from the emitting jet apex. The jet is supposed to be a curved (possibly in a helical shape) and flexible (maybe rotating) structure, where different emitting zones have different alignments with the line of sight, and their viewing angle can change in time. A similar model has been adopted to explain the multiwavelength behaviour of Mkn 501 (Villata & Raiteri 1999), S4 0954+65 (Raiteri et al. 1999), BL Lacertae (Villata et al. 2002, 2004, 2009b; Raiteri et al. 2009, 2010; Larionov et al. 2010), AO 0235+164 (Ostorero et al. 2004), along with 3C 454.3 (Villata et al. 2006, 2007, 2009a).

We assumed that the long-term flux density variations, with a tentative time scale of one week in the optical and of one month in the mm band, are due to changes of the viewing angles of the corresponding emitting regions, while variability on shorter time scales can be ascribed either to intrinsic flaring activity or to a finer geometrical structure (as suggested by Larionov et al. 2010, for BL Lacertae). Then, under the further assumption that the γ and X-ray emissions are produced by inverse-Compton scattering of synchrotron photons and that the behaviour of the IR light curve is intermediate between the optical and mm ones, we combined the optical and mm fluxes to fit the γ and X-ray light curves. In this scenario the multiwavelength observations presented in this paper suggest that the γ-ray radiation comes from inverse-Comptonisation of "optical" (actually UV to-near-IR) synchrotron photons produced in the inner emitting jet region by their parent relativistic electrons (SSC process). However, depending on the mean free path before upscattering, the bulk of the γ-ray radiation is produced in a region slightly downstream of the one responsible for the bulk of the optical emission. The jet curvature then implies that the γ and optical regions are slightly misaligned. A reduction of this misalignment, allowing more optical seed photons to enter the Comptonisation zone, could thus be at the origin of the γ-ray flux increase in 2009–2010. Moreover, the variation in the γ/optical flux ratio during the outburst peaks of mid 2008 and late 2009 can be explained by the fact that the γ zone acquires the minimum viewing angle, hence the maximum Doppler boosting, some days before the optical zone.

The X-ray light curve is not as well sampled as the optical and γ-ray ones, which makes a detailed analysis more difficult. However, the above-mentioned fit suggests that the X-ray radiation comes from a downstream region, where relativistic electrons produce and upscatter synchrotron IR photons (SSC process). The rise in the X-ray flux levels in the 2009–2010 season would then be explained similarly to the case of the γ flux, with a better alignment between the zones responsible for the bulk of the synchrotron and inverse-Compton emissions. The mean delay of about 1 d of the X-ray flux variations after the optical ones and of about 0.5 d after the γ-ray ones, found by cross-correlation analysis, are consistent with this picture.

Acknowledgements. C.M.R. is grateful to Stefania Rasetti from the Torino Observatory Computer Centre for her assistance. We thank the *Fermi*-LAT team for providing *Fermi* data. We acknowledge the use of public data from the Swift data archive. We acknowledge financial contribution from the agreement ASI-INAF I/009/10/0. St.-Petersburg University team acknowledges support from Russian RFBR foundation via grant 09-02-00092. Abastumani Observatory team acknowledges financial support by the Georgian National Science Foundation through grant GNSF/ST08/4-404. The Metsähovi team acknowledges the support from the Academy of Finland to our observing projects (numbers 212656, 210338, 121148, and others). The University of Michigan team acknowledges financial support through the NASA *Fermi* grants NNX09AU16G, NNX10AP16G, and NSF grant AST-0607523. The operation of UMRAO is funded by the University of Michigan. This paper is partly based on observations carried out at the German-Spanish Calar Alto Observatory, which is jointly operated by the MPIA and the IAA-CSIC. Acquisition of the MAPCAT data is supported in part by MICIIN (Spain) grant and AYA2010-14844, and by CEIC (Andalucía) grant P09-FQM-4784. Partly based on observations with the Medicina and Noto telescopes operated by INAF – Istituto di Radioastronomia. This research has made use of NASA's Astrophysics Data System and of the XRT Data Analysis Software (XRTDAS) developed under the responsibility of the ASI Science Data Center (ASDC), Italy. This research has made use of data from the MOJAVE database that is maintained by the MOJAVE team (Lister et al. 2009). The Submillimeter Array is a joint project between the Smithsonian Astrophysical Observatory and the Academia Sinica Institute of Astronomy and Astrophysics and is funded by the Smithsonian Institution and the Academia Sinica. The research at Boston U. was supported by NSF grant AST-0907893 and NASA *Fermi* GI grants NNX08AV65G, NNX08AV61G, and NNX09AT99G. The PRISM camera at Lowell Observatory was developed by K. Janes et al. at BU and Lowell Observatory, with funding from the NSF, BU, and Lowell Observatory.

References

Abdo, A. A., Ackermann, M., Ajello, M., et al. 2009, ApJ, 699, 817
Abdo, A. A., Ackermann, M., Ajello, M., et al. 2010, ApJ, 716, 835
Abdo, A. A., Ackermann, M., Ajello, M., et al. 2011, ApJ, 733, L26
Ackermann, M., Ajello, M., Baldini, L., et al. 2010, ApJ, 721, 1383
Anderhub, H., Antonelli, L. A., Antoranz, P., et al. 2009, A&A, 498, 83
Bahcall, J. N., Bergeron, J., Boksenberg, A., et al. 1993, ApJS, 87, 1
Benítez, E., Chavushyan, V. H., Raiteri, C. M., et al. 2010, in Accretion and Ejection in AGN: a Global View, ed. L. Maraschi, G. Ghisellini, R. Della Ceca, & F. Tavecchio, ASP Conf. Ser., 427, 291
Bessell, M. S., Castelli, F., & Plez, B. 1998, A&A, 333, 231
Bonning, E. W., Bailyn, C., Urry, C. M., et al. 2009, ApJ, 697, L81
Bonnoli, G., Ghisellini, G., Foschini, L., Tavecchio, F., & Ghirlanda, G. 2011, MNRAS, 410, 368
Burrows, D. N., Hill, J. E., Nousek, J. A., et al. 2005, Space Sci. Rev., 120, 165
Cardelli, J. A., Clayton, G. C., & Mathis, J. S. 1989, ApJ, 345, 245
Cash, W. 1979, ApJ, 228, 939
Dermer, C. D., Finke, J. D., Krug, H., & Böttcher, M. 2009, ApJ, 692, 32
Donnarumma, I., Pucella, G., Vittorini, V., et al. 2009, ApJ, 707, 1115
Edelson, R. A., & Krolik, J. H. 1988, ApJ, 333, 646
Evans, I. N., & Koratkar, A. P. 2004, ApJS, 150, 73
Finke, J. D., & Dermer, C. D. 2010, ApJ, 714, L303
Foschini, L., Tagliaferri, G., Ghisellini, G., et al. 2010, MNRAS, 408, 448
Fuhrmann, L., Cucchiara, A., Marchili, N., et al. 2006, A&A, 445, L1
Gehrels, N., Chincarini, G., Giommi, P., et al. 2004, ApJ, 611, 1005

Ghisellini, G., & Maraschi, L. 1989, ApJ, 340, 181
Ghisellini, G., Foschini, L., Tavecchio, F., & Pian, E. 2007, MNRAS, 382, L82
Giommi, P., Blustin, A. J., Capalbi, M., et al. 2006, A&A, 456, 911
Gurwell, M. A., Peck, A. B., Hostler, S. R., Darrah, M. R., & Katz, C. A. 2007, in From Z-Machines to ALMA: (Sub)Millimeter Spectroscopy of Galaxies, ed. A. J. Baker, J. Glenn, A. I. Harris, J. G. Mangum, & M. S. Yun, ASP Conf. Ser., 375, 234
Hufnagel, B. R., & Bregman, J. N. 1992, ApJ, 386, 473
Jorstad, S. G., Marscher, A. P., Lister, M. L., et al. 2005, AJ, 130, 1418
Jorstad, S. G., Marscher, A. P., Larionov, V. M., et al. 2010, ApJ, 715, 362
Larionov, V. M., Villata, M., & Raiteri, C. M. 2010, A&A, 510, A93
Lister, M. L., Aller, H. D., Aller, M. F., et al. 2009, AJ, 137, 3718
Maraschi, L., Ghisellini, G., & Celotti, A. 1992, ApJ, 397, L5
Neugebauer, G., Oke, J. B., Becklin, E. E., & Matthews, K. 1979, ApJ, 230, 79
Nousek, J. A., & Shue, D. R. 1989, ApJ, 342, 1207
Ogle, P. M., Wehrle, A. E., Balonek, T., & Gurwell, M. A. 2011, ApJS, 195, 19
Ostorero, L., Villata, M., & Raiteri, C. M. 2004, A&A, 419, 913
Pacciani, L., Vittorini, V., Tavani, M., et al. 2010, ApJ, 716, L170
Peterson, B. M. 2001, in Advanced Lectures on the Starburst-AGN Connection, ed. I. Aretxaga, D. Kunth, & R. Mújica (Singapore: World Scientific), 3
Peterson, B. M., Wanders, I., Horne, K., et al. 1998, PASP, 110, 660
Pian, E., Foschini, L., Beckmann, V., et al. 2006, A&A, 449, L21
Poole, T. S., Breeveld, A. A., Page, M. J., et al. 2008, MNRAS, 383, 627
Raiteri, C. M., Villata, M., Lanteri, L., Cavallone, M., & Sobrito, G. 1998, A&AS, 130, 495
Raiteri, C. M., Villata, M., Tosti, G., et al. 1999, A&A, 352, 19
Raiteri, C. M., Villata, M., Tosti, G., et al. 2003, A&A, 402, 151
Raiteri, C. M., Villata, M., Larionov, V. M., et al. 2007, A&A, 473, 819
Raiteri, C. M., Villata, M., Chen, W. P., et al. 2008a, A&A, 485, L17
Raiteri, C. M., Villata, M., Larionov, V. M., et al. 2008b, A&A, 491, 755
Raiteri, C. M., Villata, M., Capetti, A., et al. 2009, A&A, 507, 769
Raiteri, C. M., Villata, M., Bruschini, L., & Capetti, A. 2010, A&A, 524, A43
Roming, P. W. A., Kennedy, T. E., Mason, K. O., et al. 2005, Space Sci. Rev., 120, 95
Sasada, M., Uemura, M., Arai, A., et al. 2010, PASJ, 62, 645
Sikora, M., Moderski, R., & Madejski, G. M. 2008, ApJ, 675, 71
Striani, E., Vercellone, S., Tavani, M., et al. 2010, ApJ, 718, 455
Tavecchio, F., Ghisellini, G., Bonnoli, G., & Ghirlanda, G. 2010, MNRAS, 405, L94
Urry, C. M., & Padovani, P. 1995, PASP, 107, 803
Vercellone, S., Chen, A. W., Giuliani, A., et al. 2008, ApJ, 676, L13
Vercellone, S., Chen, A. W., Vittorini, V., et al. 2009, ApJ, 690, 1018
Vercellone, S., D'Ammando, F., Vittorini, V., et al. 2010, ApJ, 712, 405
Villata, M., & Raiteri, C. M. 1999, A&A, 347, 30
Villata, M., Raiteri, C. M., Kurtanidze, O. M., et al. 2002, A&A, 390, 407
Villata, M., Raiteri, C. M., Kurtanidze, O. M., et al. 2004, A&A, 421, 103
Villata, M., Raiteri, C. M., Balonek, T. J., et al. 2006, A&A, 453, 817
Villata, M., Raiteri, C. M., Aller, M. F., et al. 2007, A&A, 464, L5
Villata, M., Raiteri, C. M., Larionov, V. M., et al. 2008, A&A, 481, L79
Villata, M., Raiteri, C. M., Gurwell, M. A., et al. 2009a, A&A, 504, L9
Villata, M., Raiteri, C. M., Larionov, V. M., et al. 2009b, A&A, 501, 455
Wills, B. J., Thompson, K. L., Han, M., et al. 1995, ApJ, 447, 139
Wilms, J., Allen, A., & McCray, R. 2000, ApJ, 542, 914

[1] INAF, Osservatorio Astronomico di Torino, Italy
e-mail: raiteri@oato.inaf.it
[2] Department of Astronomy, University of Michigan, MI, USA
[3] Harvard-Smithsonian Center for Astrophysics, Cambridge, MA, USA
[4] Abastumani Observatory, Mt. Kanobili, Abastumani, Georgia
[5] Aalto University Metsähovi Radio Observatory, Kylmälä, Finland
[6] Astron. Inst., St.-Petersburg State Univ., Russia
[7] Pulkovo Observatory, St.-Petersburg, Russia
[8] Isaac Newton Institute of Chile, St.-Petersburg Branch, Russia
[9] INAF-IASF Palermo, Italy
[10] Instituto de Astrofísica de Andalucía, CSIC, Granada, Spain
[11] Institute for Astrophysical Research, Boston University, MA, USA
[12] Max-Planck-Institut für Radioastronomie, Bonn, Germany
[13] Instituto de Astronomía, Universidad Nacional Autónoma de México, Mexico
[14] Tuorla Observatory, Univ. of Turku, Piikkiö, Finland
[15] Astrophysical Inst., Department of Physics and Astronomy, Ohio Univ., Athens OH, USA
[16] INAF, Osservatorio Astrofisico di Catania, Italy
[17] Osservatorio Astronomico della Regione Autonoma Valle d'Aosta, Italy
[18] EPT Observatories, Tijarafe, La Palma, Spain
[19] INAF, TNG Fundación Galileo Galilei, La Palma, Spain
[20] Institut de Ciències de l'Espai (CSIC-IEEC), Spain
[21] Agrupació Astronòmica de Sabadell, Spain
[22] Graduate Institute of Astronomy, National Central University, Taiwan
[23] ZAH, Landessternwarte Heidelberg-Königstuhl, Germany
[24] Lulin Observatory, National Central University, Taiwan
[25] School of Cosmic Physics, Dublin Institute For Advanced Studies, Ireland
[26] Department of Physics, National Taiwan University, Taipei, Taiwan
[27] Circolo Astrofili Talmassons, Italy
[28] Department of Physics, Purdue University, West Lafayette, IN, USA
[29] Finnish Centre for Astronomy with ESO (FINCA), University of Turku, Piikkiö, Finland
[30] Facultad de Ciencias Espaciales, Univ. Nacional Autonoma de Honduras, Tegucigalpa M.D.C., Honduras
[31] Department of Physics, Univ. of Colorado Denver, CO, USA
[32] Center for Research and Exploration in Space Science and Technology, NASA/GSFC, Greenbelt, MD, USA
[33] Galaxy View Observatory, Sequim, Washington, USA
[34] Lowell Observatory, Flagstaff, AZ, USA
[35] Radio Astronomy Laboratory of Crimean Astrophysical Observatory, Ukraine

Pages 14 to 16 are available in the electronic edition of the journal at http://www.aanda.org

Table 3. Results of the analysis of the XRT observations.

ObsID	START	JD −2 450 000	Exp [s]	Mode	Γ	$F_{1\ \mathrm{keV}}$ [μJy]	$\chi^2/\nu\,(\nu)$
00031216001	2008-05-27 16:45:01	4614.19793	3982	PC*	1.54 ± 0.07	3.81 ± 0.22	0.95 (65)
00031216002	2008-05-28 04:08:01	4614.67223	2023	PC*	1.57 ± 0.08	4.26 ± 0.29	1.16 (45)
00031216003	2008-05-30 12:18:00	4617.01250	2144	PC*	1.56 ± 0.07	5.09 ± 0.33	0.99 (53)
00031216004	2008-05-31 12:22:01	4618.01529	2144	PC*	1.47 ± 0.06	5.90 ± 0.35	1.12 (68)
00031216005	2008-06-03 18:45:10	4621.28137	1995	PC*	1.57 ± 0.10	4.16 ± 0.37	1.19 (32)
00031216006	2008-06-04 18:50:57	4622.28538	1995	PC*	1.56 ± 0.09	4.20 ± 0.31	0.68 (40)
00031216007	2008-06-05 01:35:00	4622.56597	2137	PC*	1.59 ± 0.08	4.82 ± 0.33	0.66 (46)
00031216008	2008-06-06 00:19:01	4623.51321	2079	PC*	1.59 ± 0.09	4.21 ± 0.31	0.71 (42)
00031216009	2008-06-07 02:03:01	4624.58543	1807	PC*	1.59 ± 0.09	4.66 ± 0.35	1.29 (41)
00031216010	2008-07-24 00:10:01	4671.50696	1952	PC*	1.55 ± 0.07	5.68 ± 0.35	0.81 (57)
00031216011	2008-07-26 14:43:01	4674.11321	1969	PC*	1.47 ± 0.06	6.23 ± 0.36	1.31 (69)
00031216012	2008-07-29 00:32:00	4676.52222	1769	WT	1.65 ± 0.05	7.07 ± 0.30	0.99 (117)
00031216013	2008-07-30 11:52:00	4677.99444	1939	PC*	1.49 ± 0.07	6.88 ± 0.42	0.81 (61)
00031216014	2008-08-01 00:25:01	4679.51737	1963	PC*	1.54 ± 0.07	5.56 ± 0.34	0.98 (58)
00031216017	2008-08-01 11:37:30	4679.98438	1999	WT	1.61 ± 0.07	7.77 ± 0.44	1.50 (84)
00031216015	2008-08-03 10:34:01	4681.94029	2043	PC*	1.54 ± 0.08	5.83 ± 0.38	0.82 (55)
00031216016	2008-08-04 07:19:01	4682.80487	1915	PC*	1.53 ± 0.09	4.53 ± 0.34	1.23 (44)
00031216018	2008-08-05 21:41:01	4684.40348	380	PC*	1.64 ± 0.20	$5.59^{+0.91}_{-0.82}$	Cash
00031216019	2008-08-06 07:19:01	4684.80487	2276	PC*	1.60 ± 0.08	5.04 ± 0.33	1.02 (54)
00031216020	2008-08-07 20:44:01	4686.36390	1803	PC*	1.61 ± 0.09	5.20 ± 0.39	1.02 (38)
00031216021	2008-08-08 12:47:01	4687.03265	4217	PC*	1.64 ± 0.06	5.34 ± 0.26	1.17 (89)
00031216022	2008-08-10 01:47:01	4688.57432	2753	PC*	1.62 ± 0.09	5.56 ± 0.43	1.08 (35)
00031216023	2008-08-12 06:32:01	4690.77223	2190	PC*	1.55 ± 0.07	5.31 ± 0.32	1.18 (62)
00031216024	2008-08-14 04:52:00	4692.70278	1355	PC*	1.52 ± 0.13	4.10 ± 0.44	1.38 (21)
00031216025	2008-08-15 01:47:01	4693.57432	1649	PC*	1.63 ± 0.10	4.22 ± 0.34	0.98 (33)
00031216026	2008-08-16 21:07:01	4695.37987	1969	PC*	1.59 ± 0.08	5.19 ± 0.35	1.04 (50)
00031216027	2008-08-17 16:43:00	4696.19653	2425	PC*	1.61 ± 0.07	5.72 ± 0.32	0.80 (66)
00031216029	2008-08-20 08:59:01	4698.87432	1846	PC*	1.40 ± 0.07	4.72 ± 0.33	0.90 (51)
00031216030	2008-08-21 02:20:01	4699.59723	2095	PC*	1.61 ± 0.08	4.90 ± 0.34	1.08 (44)
00031216031	2008-08-22 10:28:01	4700.93612	1975	PC*	1.54 ± 0.08	4.64 ± 0.32	1.13 (46)
00031216032	2008-08-23 08:58:01	4701.87362	2155	PC*	1.57 ± 0.07	5.68 ± 0.34	1.41 (63)
00031216033	2008-08-24 14:20:01	4703.09723	538	PC*	$1.58^{+0.21}_{-0.20}$	$4.97^{+0.78}_{-0.76}$	1.30 (11)
00031216034	2008-08-25 09:37:01	4703.90071	335	PC*	1.52 ± 0.18	$6.20^{+0.97}_{-0.89}$	Cash
00031216035	2008-08-26 20:45:00	4705.36458	1059	PC*	1.55 ± 0.12	4.91 ± 0.50	0.81 (23)
00031216036	2008-08-27 17:39:00	4706.23542	1957	PC*	1.53 ± 0.08	4.78 ± 0.35	0.86 (43)
00031216038	2008-08-29 19:22:01	4708.30696	1885	PC*	1.46 ± 0.09	3.99 ± 0.33	1.12 (37)
00031216039	2008-08-31 14:36:01	4710.10834	1597	PC*	1.51 ± 0.09	4.39 ± 0.34	1.19 (37)
00031216040	2008-09-01 19:41:01	4711.32015	1730	PC*	1.54 ± 0.09	4.64 ± 0.37	0.78 (37)
00031216041	2008-09-02 18:05:01	4712.25348	2863	PC*	1.52 ± 0.07	4.05 ± 0.26	1.05 (59)
00031216042	2008-09-03 05:15:01	4712.71876	2052	PC*	1.65 ± 0.08	4.59 ± 0.31	0.79 (44)
00031216043	2008-09-04 16:54:46	4714.20470	346	PC*	1.59 ± 0.22	$4.02^{+0.76}_{-0.68}$	Cash
00031216044	2008-09-05 01:00:01	4714.54168	1711	PC*	1.62 ± 0.09	4.83 ± 0.36	1.50 (42)
00031216046	2008-09-07 15:27:40	4717.14421	470	PC*	1.54 ± 0.16	$4.96^{+0.72}_{-0.66}$	Cash
00031216047	2008-09-08 10:33:00	4717.93958	2501	PC*	1.54 ± 0.07	5.03 ± 0.32	0.63 (52)
00090023001	2008-09-09 01:20:01	4718.55557	1815	PC*	1.51 ± 0.09	4.73 ± 0.37	1.22 (38)
00031216048	2008-09-10 17:32:01	4720.23057	1046	PC*	1.53 ± 0.12	6.44 ± 0.66	0.98 (23)
00031216049	2008-09-11 12:58:00	4721.04028	2001	PC*	1.56 ± 0.08	5.32 ± 0.35	1.04 (53)
00031216050	2008-09-12 20:58:01	4722.37362	1973	PC*	1.66 ± 0.08	5.80 ± 0.39	0.76 (47)
00031216051	2008-09-13 20:55:02	4723.37155	411	PC*	1.38 ± 0.16	$5.13^{+0.77}_{-0.70}$	Cash
00031216052	2008-09-16 15:03:00	4726.12708	837	PC*	1.51 ± 0.13	4.93 ± 0.52	0.98 (21)
00031216053	2008-09-17 16:29:01	4727.18682	894	PC*	1.56 ± 0.12	4.98 ± 0.52	0.99 (22)
00031216054	2008-09-23 05:36:01	4732.73334	3103	PC*	1.58 ± 0.08	3.93 ± 0.24	0.89 (61)
00031216055	2008-09-24 09:14:01	4733.88473	1387	PC*	1.66 ± 0.12	4.74 ± 0.44	0.89 (26)
00031216056	2008-09-25 02:34:01	4734.60696	2786	PC*	1.60 ± 0.07	4.43 ± 0.27	1.13 (58)
00031216057	2008-09-26 04:16:01	4735.67779	2725	PC*	1.55 ± 0.07	4.11 ± 0.25	0.70 (57)
00031216058	2008-09-27 04:22:00	4736.68194	2725	PC*	1.62 ± 0.08	3.75 ± 0.25	1.11 (48)
00031216059	2008-09-28 04:27:01	4737.68543	1797	PC*	1.57 ± 0.08	5.23 ± 0.35	0.93 (46)
00031216060	2008-09-29 03:08:01	4738.63057	2759	PC*	1.59 ± 0.06	5.81 ± 0.32	1.09 (73)
00031216061	2008-09-30 03:06:01	4739.62918	2594	PC*	1.60 ± 0.06	5.92 ± 0.32	1.29 (71)
00031216062	2008-10-01 04:42:00	4740.69583	3108	PC*	1.66 ± 0.06	6.00 ± 0.29	1.04 (86)
00031216063	2008-10-02 04:47:01	4741.69932	3107	PC*	1.64 ± 0.06	5.12 ± 0.27	1.20 (75)
00035030028	2008-10-05 13:06:01	4745.04584	1221	PC*	1.62 ± 0.13	4.09 ± 0.40	0.61 (23)
00035030029	2008-10-10 20:26:01	4750.35140	807	PC*	1.78 ± 0.16	$3.32^{+0.42}_{-0.38}$	Cash
00035030030	2008-10-26 20:25:01	4766.35071	428	PC*	$1.69^{+0.24}_{-0.23}$	$2.72^{+0.54}_{-0.47}$	Cash
00090023002	2008-12-25 04:53:00	4825.70347	1493	PC	1.62 ± 0.15	$1.39^{+0.16}_{-0.17}$	0.93 (16)

Table 3. continued.

ObsID	START	JD $-2\,450\,000$	Exp [s]	Mode	Γ	$F_{1\ \mathrm{keV}}$ [μJy]	$\chi^2/\nu\,(\nu)$
00090023003	2008-12-26 05:15:01	4826.71876	1522	PC	1.54 ± 0.13	$1.49^{+0.17}_{-0.16}$	0.66 (19)
00090023004	2008-12-27 16:31:01	4828.18821	1682	PC	1.77 ± 0.20	$0.99^{+0.16}_{-0.14}$	Cash
00090023005	2008-12-29 00:27:01	4829.51876	1331	PC	1.68 ± 0.16	$1.85^{+0.25}_{-0.23}$	Cash
00090023006	2008-12-30 05:24:00	4830.72500	1276	PC	1.46 ± 0.18	$1.10^{+0.16}_{-0.17}$	1.24 (12)
00090023007	2008-12-31 16:42:01	4832.19584	707	PC	$1.58^{+0.21}_{-0.22}$	1.37 ± 0.23	Cash
00090023008	2009-01-01 12:01:00	4833.00069	1131	PC	1.57 ± 0.21	1.28 ± 0.21	1.72 (10)
00035030031	2009-01-21 17:05:01	4853.21182	1436	PC	$1.59^{+0.19}_{-0.18}$	$1.34^{+0.22}_{-0.19}$	Cash
00035030032	2009-01-22 17:17:10	4854.22025	857	PC	$1.73^{+0.25}_{-0.23}$	$1.24^{+0.22}_{-0.21}$	Cash
00035030033	2009-01-23 06:10:01	4854.75696	634	PC	$1.70^{+0.27}_{-0.25}$	$1.58^{+0.31}_{-0.28}$	Cash
00035030034	2009-01-24 15:46:01	4856.15696	485	PC	$1.80^{+0.25}_{-0.24}$	$1.66^{+0.31}_{-0.29}$	Cash
00035030035	2009-01-25 06:32:00	4856.77222	927	PC	1.70 ± 0.16	$1.44^{+0.20}_{-0.18}$	Cash
00035030036	2009-01-26 08:14:01	4857.84307	924	PC	1.78 ± 0.19	$1.75^{+0.24}_{-0.25}$	1.26 (11)
00035030037	2009-01-27 11:32:01	4858.98057	991	PC	1.67 ± 0.18	$1.43^{+0.22}_{-0.21}$	0.96 (10)
00035030038	2009-05-23 03:25:01	4974.64237	4137	PC*	1.56 ± 0.07	2.46 ± 0.16	1.05 (52)
00035030039	2009-05-24 22:38:01	4976.44307	3805	PC*	1.62 ± 0.07	3.62 ± 0.20	0.92 (70)
00035030040	2009-05-26 16:30:00	4978.18750	4061	PC*	1.58 ± 0.06	3.31 ± 0.19	1.17 (67)
00031018009	2009-08-12 07:42:01	5055.82084	837	PC*	1.65 ± 0.14	4.45 ± 0.50	1.20 (16)
00090081001	2009-08-13 12:55:01	5057.03821	2101	PC*	1.75 ± 0.08	5.09 ± 0.33	1.17 (46)
00035030041	2009-08-14 00:09:01	5057.50626	1033	PC*	1.74 ± 0.12	$4.58^{+0.47}_{-0.46}$	1.39 (20)
00035030042	2009-08-15 01:47:02	5058.57433	1961	PC*	1.70 ± 0.09	4.88 ± 0.34	0.73 (41)
00035030043	2009-08-16 11:17:01	5059.97015	451	PC*	$1.85^{+0.19}_{-0.18}$	$4.73^{+0.68}_{-0.63}$	Cash
00035030044	2009-08-17 09:55:00	5060.91319	1783	PC*	1.70 ± 0.10	4.36 ± 0.35	0.71 (32)
00035030045	2009-08-18 00:19:01	5061.51321	2178	PC*	1.54 ± 0.08	4.04 ± 0.29	1.06 (43)
00035030046	2009-08-19 08:27:01	5062.85209	1367	PC*	1.76 ± 0.12	4.59 ± 0.43	0.68 (24)
00035030047	2009-08-19 13:30:00	5063.06250	812	PC*	1.62 ± 0.14	3.96 ± 0.49	1.31 (15)
00035030048	2009-08-20 06:55:01	5063.78821	1923	PC*	1.66 ± 0.08	4.70 ± 0.34	0.75 (40)
00035030049	2009-08-21 21:33:00	5065.39792	1096	PC*	1.68 ± 0.13	4.33 ± 0.45	0.92 (21)
00035030050	2009-08-22 19:57:52	5066.33185	1826	PC*	1.51 ± 0.08	5.71 ± 0.38	1.20 (49)
00035030051	2009-08-23 08:47:00	5066.86597	2066	PC*	1.51 ± 0.07	6.70 ± 0.40	1.01 (63)
00035030052	2009-08-24 08:55:01	5067.87154	2021	PC*	1.51 ± 0.06	6.11 ± 0.36	1.20 (63)
00035030053	2009-08-25 08:48:00	5068.86667	1517	PC*	1.51 ± 0.09	7.02 ± 0.51	1.05 (47)
00035030054	2009-08-26 21:59:00	5070.41597	1559	PC*	1.47 ± 0.06	9.22 ± 0.53	0.68 (71)
00035030055	2009-08-27 09:01:01	5070.87571	1573	PC*	1.38 ± 0.07	8.25 ± 0.53	0.75 (64)
00035030056	2009-08-28 09:15:01	5071.88543	1637	PC*	1.39 ± 0.07	8.85 ± 0.54	1.08 (67)
00035030057	2009-08-29 09:10:01	5072.88196	1692	PC*	1.57 ± 0.06	9.06 ± 0.48	0.98 (75)
00035030058	2009-08-30 15:42:01	5074.15418	2601	PC*	1.45 ± 0.05	7.80 ± 0.36	1.06 (102)
00035030059	2009-08-31 15:47:01	5075.15765	2074	PC*	1.50 ± 0.06	8.56 ± 0.43	1.01 (91)
00035030060	2009-09-01 14:17:00	5076.09514	2003	PC*	1.52 ± 0.06	7.82 ± 0.40	1.13 (82)
00035030061	2009-09-02 17:55:42	5077.24701	2124	PC*	1.52 ± 0.06	8.66 ± 0.43	0.94 (91)
00035030062	2009-09-03 06:54:01	5077.78751	963	PC*	1.55 ± 0.09	8.86 ± 0.72	0.91 (37)
00035030063	2009-09-06 19:51:01	5081.32709	1647	PC*	1.63 ± 0.07	7.11 ± 0.44	0.86 (54)
00035030064	2009-09-07 18:23:01	5082.26598	1467	PC*	1.44 ± 0.09	5.71 ± 0.47	1.14 (38)
00035030065	2009-09-08 23:15:01	5083.46876	1442	PC*	1.45 ± 0.08	7.68 ± 0.55	0.93 (46)
00035030066	2009-09-09 00:56:01	5083.53890	2116	PC*	1.49 ± 0.08	5.44 ± 0.40	0.84 (44)
00090081002	2009-09-13 20:33:47	5088.35679	1993	PC*	1.55 ± 0.06	9.53 ± 0.53	1.22 (70)
00035030067	2009-09-16 22:15:01	5091.42709	1503	PC*	1.61 ± 0.06	9.89 ± 0.54	1.04 (71)
00031493001	2009-09-17 04:29:43	5091.68730	1999	WT	1.51 ± 0.04	11.38 ± 0.36	1.00 (211)
00031493003	2009-09-18 03:15:00	5092.63542	2509	PC*	1.58 ± 0.05	9.75 ± 0.40	1.16 (118)
00031493004	2009-09-19 13:06:00	5094.04583	2542	PC*	1.71 ± 0.05	8.02 ± 0.36	1.32 (94)
00031493005	2009-09-20 17:59:00	5095.24931	2389	WT2	1.65 ± 0.04	7.96 ± 0.28	1.08 (185)
00031493007	2009-09-22 00:26:01	5096.51807	1819	WT2	1.68 ± 0.05	9.11 ± 0.35	1.08 (157)
00031493008	2009-09-23 19:51:01	5098.32709	1578	WT	1.72 ± 0.05	8.36 ± 0.34	0.99 (116)
00031493009	2009-09-24 13:12:01	5099.05001	2109	WT3	1.66 ± 0.05	8.64 ± 0.34	1.19 (132)
00031493010	2009-09-25 06:52:00	5099.78611	2149	WT3	1.62 ± 0.05	7.66 ± 0.31	1.22 (137)
00031493011	2009-09-26 06:58:00	5100.79028	2144	WT3	1.64 ± 0.05	7.85 ± 0.33	1.00 (126)
00031493012	2009-10-06 03:08:00	5110.63056	3422	WT6	1.58 ± 0.03	11.28 ± 0.28	1.15 (285)
00031493013	2009-10-08 14:55:01	5113.12154	3416	WT5	1.63 ± 0.03	11.31 ± 0.27	1.12 (282)
00031493014	2009-10-09 21:28:00	5114.39444	2917	WT5	1.58 ± 0.03	12.33 ± 0.32	1.06 (265)
00090077001	2009-10-12 20:05:02	5117.33683	1958	WT4	1.64 ± 0.04	9.70 ± 0.36	0.95 (158)
00090077002	2009-10-13 00:32:01	5117.52223	1783	WT4	1.63 ± 0.04	9.41 ± 0.36	1.17 (148)
00090077003	2009-10-14 00:41:00	5118.52847	1838	WT5	1.66 ± 0.04	8.54 ± 0.39	1.01 (110)
00090077004	2009-10-15 00:43:01	5119.52987	1854	WT3	1.65 ± 0.04	8.38 ± 0.33	0.87 (130)
00090077005	2009-10-16 04:02:01	5120.66807	2114	WT3	1.65 ± 0.04	8.38 ± 0.33	0.87 (130)
00090077006	2009-10-17 00:55:01	5121.53821	1964	WT3	1.67 ± 0.04	9.70 ± 0.33	1.16 (185)
00090077007	2009-10-18 11:03:01	5122.96043	2119	WT2	1.64 ± 0.05	7.66 ± 0.30	1.22 (147)

Table 3. continued.

ObsID	START	JD $-2\,450\,000$	Exp [s]	Mode	Γ	$F_{1\ \mathrm{keV}}$ [μJy]	$\chi^2/\nu\,(\nu)$
00090077008	2009-10-19 02:44:00	5123.61389	539	WT2	1.70 ± 0.09	7.60 ± 0.58	1.20 (41)
00090077009	2009-10-20 06:21:01	5124.76459	1868	WT4	1.62 ± 0.05	7.51 ± 0.31	0.96 (134)
00090077010	2009-10-21 15:55:01	5126.16321	495	WT	1.68 ± 0.09	8.82 ± 0.63	1.16 (44)
00090077011	2009-10-22 19:25:01	5127.30904	2054	WT2	1.75 ± 0.04	11.27 ± 0.35	1.23 (191)
00090077012	2009-10-23 00:27:01	5127.51876	4922	WT6	1.68 ± 0.02	11.27 ± 0.23	1.18 (318)
00090077013	2009-10-24 00:01:01	5128.50071	1638	WT4	1.67 ± 0.05	8.41 ± 0.34	0.87 (125)
00090077014	2009-10-25 19:41:00	5130.32014	2124	WT2	1.67 ± 0.04	8.15 ± 0.30	1.01 (155)
00035030068	2009-10-31 12:08:01	5136.00557	1429	WT2	1.65 ± 0.06	7.25 ± 0.34	0.76 (99)
00035030069	2009-11-04 17:38:02	5140.23475	801	WT4	1.78 ± 0.09	7.48 ± 0.48	1.29 (57)
00035030070	2009-11-06 23:56:00	5142.49722	1015	WT	1.64 ± 0.08	6.23 ± 0.39	0.95 (66)
00035030071	2009-11-11 17:45:00	5147.23958	1080	WT	1.78 ± 0.08	6.20 ± 0.37	1.00 (66)
00035030072	2009-11-18 02:33:01	5153.60626	1144	WT	1.62 ± 0.07	6.48 ± 0.37	0.79 (75)
00035030073	2009-11-27 20:49:01	5163.36737	940	WT	1.52 ± 0.06	8.87 ± 0.48	1.03 (88)
00035030074	2009-12-01 16:35:01	5167.19098	1065	WT	1.56 ± 0.05	13.71 ± 0.54	1.11 (138)
00035030075	2009-12-02 00:28:01	5167.51946	1174	WT	1.53 ± 0.04	15.30 ± 0.53	1.20 (166)
00035030076	2009-12-03 15:22:01	5169.14029	985	WT	1.56 ± 0.05	15.42 ± 0.60	1.10 (139)
00035030077	2009-12-04 00:39:01	5169.52709	2759	WT2	1.49 ± 0.02	16.88 ± 0.37	1.09 (328)
00035030078	2009-12-05 13:37:38	5171.06780	645	WT	1.50 ± 0.05	13.83 ± 0.67	1.07 (92)
00035030079	2009-12-06 00:54:01	5171.53751	1079	WT2	1.62 ± 0.05	13.79 ± 0.59	1.00 (117)
00035030080	2009-12-07 23:23:01	5173.47432	1114	WT	1.51 ± 0.04	13.73 ± 0.52	1.36 (145)
00035030081	2009-12-08 21:53:01	5174.41182	1164	WT2	1.59 ± 0.04	13.58 ± 0.51	1.16 (143)
00035030082	2009-12-09 23:35:01	5175.48265	1100	WT	1.48 ± 0.04	12.43 ± 0.50	1.32 (130)
00035030083	2009-12-10 14:17:01	5176.09515	990	WT	1.60 ± 0.06	10.90 ± 0.51	0.92 (104)
00035030084	2009-12-11 09:20:01	5176.88890	1369	WT2	1.54 ± 0.05	9.68 ± 0.40	1.24 (126)
00035030085	2009-12-12 03:05:01	5177.62848	879	WT2	1.59 ± 0.08	8.07 ± 0.57	1.03 (57)
00035030086	2009-12-12 23:59:01	5178.49932	1325	WT2	1.57 ± 0.06	7.19 ± 0.37	0.87 (90)
00035030087	2009-12-14 01:35:01	5179.56598	1344	WT3	1.62 ± 0.05	8.00 ± 0.37	0.94 (106)
00035030088	2009-12-15 03:18:01	5180.63751	924	WT2	1.56 ± 0.07	7.81 ± 0.50	1.24 (68)
00035030089	2009-12-16 03:23:01	5181.64098	1194	WT2	1.56 ± 0.06	7.37 ± 0.40	1.14 (93)
00035030090	2009-12-18 00:22:01	5183.51529	1374	WT	1.59 ± 0.06	8.17 ± 0.39	0.86 (110)
00035030091	2009-12-19 11:45:01	5184.98959	1255	WT	1.73 ± 0.08	10.98 ± 0.73	0.86 (61)
00035030093	2009-12-21 02:15:01	5186.59376	1104	WT	1.52 ± 0.06	8.38 ± 0.42	1.49 (98)
00035030094	2009-12-22 10:22:00	5187.93194	1110	WT	1.61 ± 0.06	8.44 ± 0.42	1.09 (95)
00035030095	2009-12-25 07:46:01	5190.82362	1220	WT	1.62 ± 0.09	6.98 ± 0.56	1.08 (47)
00035030096	2009-12-26 01:06:00	5191.54583	1154	WT	1.48 ± 0.08	7.16 ± 0.51	1.08 (60)
00035030097	2009-12-26 23:59:01	5192.49932	869	WT	1.62 ± 0.08	8.12 ± 0.53	0.79 (64)
00035030098	2009-12-28 01:37:01	5193.56737	1200	WT	1.63 ± 0.06	7.73 ± 0.41	1.04 (88)
00035030099	2010-01-01 20:56:01	5198.37223	1109	WT2	1.67 ± 0.06	9.47 ± 0.45	1.02 (98)
00035030100	2010-01-08 01:02:01	5204.54307	1065	WT	1.60 ± 0.08	6.52 ± 0.43	0.94 (64)
00035030102	2010-01-17 19:11:01	5214.29932	2394	WT3	1.63 ± 0.03	10.68 ± 0.31	0.95 (221)

The Astrophysical Journal, 726:43 (14pp), 2011 January 1 doi:10.1088/0004-637X/726/1/43

MULTI-WAVELENGTH OBSERVATIONS OF THE FLARING GAMMA-RAY BLAZAR 3C 66A IN 2008 OCTOBER

A. A. Abdo[1,2], M. Ackermann[3], M. Ajello[3], L. Baldini[4], J. Ballet[5], G. Barbiellini[6,7], D. Bastieri[8,9], K. Bechtol[3], R. Bellazzini[4], B. Berenji[3], R. D. Blandford[3], E. Bonamente[10,11], A. W. Borgland[3], A. Bouvier[3], J. Bregeon[4], A. Brez[4], M. Brigida[12,13], P. Bruel[14], R. Buehler[3], S. Buson[8,9], G. A. Caliandro[15], R. A. Cameron[3], P. A. Caraveo[16], S. Carrigan[9], J. M. Casandjian[5], E. Cavazzuti[17], C. Cecchi[10,11], Ö. Çelik[18,19,20], E. Charles[3], A. Chekhtman[1,21], C. C. Cheung[1,2], J. Chiang[3], S. Ciprini[11], R. Claus[3], J. Cohen-Tanugi[22], J. Conrad[23,24,118], L. Costamante[3], S. Cutini[17], D. S. Davis[18,20], C. D. Dermer[1], F. de Palma[12,13], S. W. Digel[3], E. do Couto e Silva[3], P. S. Drell[3], R. Dubois[3], D. Dumora[25,26], C. Favuzzi[12,13], S. J. Fegan[14], P. Fortin[14], M. Frailis[27,28], L. Fuhrmann[29], Y. Fukazawa[30], S. Funk[3], P. Fusco[12,13], F. Gargano[13], D. Gasparrini[17], N. Gehrels[18], S. Germani[10,11], N. Giglietto[12,13], P. Giommi[17], F. Giordano[12,13], M. Giroletti[31], T. Glanzman[3], G. Godfrey[3], I. A. Grenier[5], J. E. Grove[1], L. Guillemot[25,26,29], S. Guiriec[32], D. Hadasch[15], M. Hayashida[3], E. Hays[18], D. Horan[14], R. E. Hughes[33], R. Itoh[30], G. Jóhannesson[3], A. S. Johnson[3], T. J. Johnson[18,34], W. N. Johnson[1], T. Kamae[3], H. Katagiri[30], J. Kataoka[35], J. Knödlseder[36], M. Kuss[4], J. Lande[3], L. Latronico[4], S.-H. Lee[3], F. Longo[6,7], F. Loparco[12,13], B. Lott[25,26], M. N. Lovellette[1], P. Lubrano[10,11], A. Makeev[1,21], M. N. Mazziotta[13], J. E. McEnery[18,34], J. Mehault[22], P. F. Michelson[3], T. Mizuno[30], A. A. Moiseev[19,34], C. Monte[12,13], M. E. Monzani[3], A. Morselli[37], I. V. Moskalenko[3], S. Murgia[3], T. Nakamori[35], M. Naumann-Godo[5], I. Nestoras[29], P. L. Nolan[3], J. P. Norris[38], E. Nuss[22], T. Ohsugi[39], A. Okumura[40], N. Omodei[3], E. Orlando[41], J. F. Ormes[38], M. Ozaki[40], D. Paneque[3], J. H. Panetta[3], D. Parent[1,21], V. Pelassa[22], M. Pepe[10,11], M. Pesce-Rollins[4], F. Piron[22], T. A. Porter[3], S. Rainò[12,13], R. Rando[8,9], M. Razzano[4], A. Reimer[42,3], O. Reimer[42,3], L. C. Reyes[43], J. Ripken[23,24], S. Ritz[44], R. W. Romani[3], M. Roth[45], H. F.-W. Sadrozinski[44], D. Sanchez[14], A. Sander[33], J. D. Scargle[46], C. Sgrò[4], M. S. Shaw[3], P. D. Smith[33], G. Spandre[4], P. Spinelli[12,13], M. S. Strickman[1], D. J. Suson[47], H. Takahashi[39], T. Tanaka[3], J. B. Thayer[3], J. G. Thayer[3], D. J. Thompson[18], L. Tibaldo[5,8,9,119], D. F. Torres[15,48], G. Tosti[10,11], A. Tramacere[3,49,50], T. L. Usher[3], J. Vandenbroucke[3], V. Vasileiou[19,20], N. Vilchez[36], V. Vitale[37,51], A. P. Waite[3], P. Wang[3], B. L. Winer[33], K. S. Wood[1], Z. Yang[23,24], T. Ylinen[24,52,53], M. Ziegler[44]

(The Fermi-LAT Collaboration)

V. A. Acciari[54], E. Aliu[55], T. Arlen[56], T. Aune[57], M. Beilicke[58], W. Benbow[54], M. Böttcher[59], D. Boltuch[60], S. M. Bradbury[61], J. H. Buckley[58], V. Bugaev[58], K. Byrum[62], A. Cannon[63], A. Cesarini[64], J. L. Christiansen[65], L. Ciupik[66], W. Cui[67], I. de la Calle Perez[68], R. Dickherber[58], M. Errando[55], A. Falcone[69], J. P. Finley[67], G. Finnegan[70], L. Fortson[66], A. Furniss[57], N. Galante[54], D. Gall[67], G. H. Gillanders[64], S. Godambe[70], J. Grube[66], R. Guenette[71], G. Gyuk[66], D. Hanna[71], J. Holder[60], C. M. Hui[70], T. B. Humensky[72], A. Imran[73], P. Kaaret[74], N. Karlsson[66], M. Kertzman[75], D. Kieda[70], A. Konopelko[76], H. Krawczynski[58], F. Krennrich[73], M. J. Lang[64], S. LeBohec[70], G. Maier[71,120], S. McArthur[58], A. McCann[71], M. McCutcheon[71], P. Moriarty[77], R. Mukherjee[55], R. A. Ong[56], A. N. Otte[57], D. Pandel[74], J. S. Perkins[54], A. Pichel[78], M. Pohl[73,121], J. Quinn[63], K. Ragan[71], P. T. Reynolds[79], E. Roache[54], H. J. Rose[61], M. Schroedter[73], G. H. Sembroski[67], G. Demet Senturk[80], A. W. Smith[62], D. Steele[66,122], S. P. Swordy[72], G. Tešić[71], M. Theiling[54], S. Thibadeau[58], A. Varlotta[67], V. V. Vassiliev[56], S. Vincent[70], S. P. Wakely[72], J. E. Ward[63], T. C. Weekes[54], A. Weinstein[56], T. Weisgarber[72], D. A. Williams[57], S. Wissel[72], M. Wood[56]

(The VERITAS Collaboration)

M. Villata[81], C. M. Raiteri[81], M. A. Gurwell[82], V. M. Larionov[83,84,85], O. M. Kurtanidze[86], M. F. Aller[87], A. Lähteenmäki[88], W. P. Chen[89], A. Berduygin[90], I. Agudo[91], H. D. Aller[87], A. A. Arkharov[84], U. Bach[92], R. Bachev[93], P. Beltrame[94], E. Benítez[95], C. S. Buemi[96], J. Dashti[97], P. Calcidese[98], D. Capezzali[99], D. Carosati[99], D. Da Rio[94], A. Di Paola[100], C. Diltz[97], M. Dolci[101], D. Dultzin[95], E. Forné[102], J. L. Gómez[91], V. A. Hagen-Thorn[83,85], A. Halkola[90], J. Heidt[103], D. Hiriart[104], T. Hovatta[88], H.-Y. Hsiao[89], S. G. Jorstad[105], G. N. Kimeridze[86], T. S. Konstantinova[83], E. N. Kopatskaya[83], E. Koptelova[89], P. Leto[96], R. Ligustri[94], E. Lindfors[90], J. M. Lopez[104], A. P. Marscher[105], M. Mommert[103,106], R. Mujica[107], M. G. Nikolashvili[86], K. Nilsson[108], N. Palma[97], M. Pasanen[90], M. Roca-Sogorb[91], J. A. Ros[102], P. Roustazadeh[97], A. C. Sadun[109], J. Saino[90], L. A. Sigua[86], A. Sillanää[90], M. Sorcia[95], L. O. Takalo[90], M. Tornikoski[88], C. Trigilio[96], R. Turchetti[94], G. Umana[96]

(The GASP-WEBT Consortium)

and

T. Belloni[110], C. H. Blake[111], J. S. Bloom[112], E. Angelakis[113], M. Fumagalli[114], M. Hauser[115], J. X. Prochaska[114,116], D. Riquelme[117], A. Sievers[117], D. L. Starr[112], G. Tagliaferri[110], H. Ungerechts[117], S. Wagner[115], J. A. Zensus[113]

[1] Space Science Division, Naval Research Laboratory, Washington, DC 20375, USA
[2] National Research Council Research Associate, National Academy of Sciences, Washington, DC 20001, USA
[3] W. W. Hansen Experimental Physics Laboratory, Kavli Institute for Particle Astrophysics and Cosmology, Department of Physics and SLAC National Accelerator Laboratory, Stanford University, Stanford, CA 94305, USA
[4] Istituto Nazionale di Fisica Nucleare, Sezione di Pisa, I-56127 Pisa, Italy
[5] Laboratoire AIM, CEA-IRFU/CNRS/Université Paris Diderot, Service d'Astrophysique, CEA Saclay, F-91191 Gif sur Yvette, France

[6] Istituto Nazionale di Fisica Nucleare, Sezione di Trieste, I-34127 Trieste, Italy
[7] Dipartimento di Fisica, Università di Trieste, I-34127 Trieste, Italy
[8] Istituto Nazionale di Fisica Nucleare, Sezione di Padova, I-35131 Padova, Italy
[9] Dipartimento di Fisica "G. Galilei," Università di Padova, I-35131 Padova, Italy
[10] Istituto Nazionale di Fisica Nucleare, Sezione di Perugia, I-06123 Perugia, Italy
[11] Dipartimento di Fisica, Università degli Studi di Perugia, I-06123 Perugia, Italy
[12] Dipartimento di Fisica "M. Merlin" dell'Università e del Politecnico di Bari, I-70126 Bari, Italy
[13] Istituto Nazionale di Fisica Nucleare, Sezione di Bari, I-70126 Bari, Italy
[14] Laboratoire Leprince-Ringuet, École polytechnique, CNRS/IN2P3, Palaiseau, France
[15] Institut de Ciencies de l'Espai (IEEC-CSIC), Campus UAB, E-08193 Barcelona, Spain
[16] INAF-Istituto di Astrofisica Spaziale e Fisica Cosmica, I-20133 Milano, Italy
[17] Agenzia Spaziale Italiana (ASI) Science Data Center, I-00044 Frascati (Roma), Italy
[18] NASA Goddard Space Flight Center, Greenbelt, MD 20771, USA
[19] Center for Research and Exploration in Space Science and Technology (CRESST) and NASA Goddard Space Flight Center, Greenbelt, MD 20771, USA
[20] Department of Physics and Center for Space Sciences and Technology, University of Maryland Baltimore County, Baltimore, MD 21250, USA
[21] George Mason University, Fairfax, VA 22030, USA
[22] Laboratoire de Physique Théorique et Astroparticules, Université Montpellier 2, CNRS/IN2P3, Montpellier, France
[23] Department of Physics, Stockholm University, AlbaNova, SE-106 91 Stockholm, Sweden
[24] The Oskar Klein Centre for Cosmoparticle Physics, AlbaNova, SE-106 91 Stockholm, Sweden
[25] CNRS/IN2P3, Centre d'Études Nucléaires Bordeaux Gradignan, UMR 5797, F-33175 Gradignan, France
[26] Université de Bordeaux, Centre d'Études Nucléaires Bordeaux Gradignan, UMR 5797, F-33175 Gradignan, France
[27] Dipartimento di Fisica, Università di Udine and Istituto Nazionale di Fisica Nucleare, Sezione di Trieste, Gruppo Collegato di Udine, I-33100 Udine, Italy
[28] Osservatorio Astronomico di Trieste, Istituto Nazionale di Astrofisica, I-34143 Trieste, Italy
[29] Max-Planck-Institut für Radioastronomie, Auf dem Hügel 69, D-53121 Bonn, Germany
[30] Department of Physical Sciences, Hiroshima University, Higashi-Hiroshima, Hiroshima 739-8526, Japan
[31] INAF Istituto di Radioastronomia, I-40129 Bologna, Italy
[32] Center for Space Plasma and Aeronomic Research (CSPAR), University of Alabama in Huntsville, Huntsville, AL 35899, USA
[33] Department of Physics, Center for Cosmology and Astro-Particle Physics, The Ohio State University, Columbus, OH 43210, USA
[34] Department of Physics and Department of Astronomy, University of Maryland, College Park, MD 20742, USA
[35] Research Institute for Science and Engineering, Waseda University, 3-4-1, Okubo, Shinjuku, Tokyo, 169-8555 Japan
[36] Centre d'Étude Spatiale des Rayonnements, CNRS/UPS, BP 44346, F-30128 Toulouse Cedex 4, France
[37] Istituto Nazionale di Fisica Nucleare, Sezione di Roma "Tor Vergata," I-00133 Roma, Italy
[38] Department of Physics and Astronomy, University of Denver, Denver, CO 80208, USA
[39] Hiroshima Astrophysical Science Center, Hiroshima University, Higashi-Hiroshima, Hiroshima 739-8526, Japan
[40] Institute of Space and Astronautical Science, JAXA, 3-1-1 Yoshinodai, Sagamihara, Kanagawa 229-8510, Japan
[41] Max-Planck Institut für extraterrestrische Physik, D-85748 Garching, Germany
[42] Institut für Astro- und Teilchenphysik and Institut für Theoretische Physik, Leopold-Franzens-Universität Innsbruck, A-6020 Innsbruck, Austria
[43] Kavli Institute for Cosmological Physics, University of Chicago, Chicago, IL 60637, USA; lreyes@kicp.uchicago.edu
[44] Santa Cruz Institute for Particle Physics, Department of Physics and Department of Astronomy and Astrophysics, University of California at Santa Cruz, Santa Cruz, CA 95064, USA
[45] Department of Physics, University of Washington, Seattle, WA 98195-1560, USA
[46] Space Sciences Division, NASA Ames Research Center, Moffett Field, CA 94035-1000, USA
[47] Department of Chemistry and Physics, Purdue University Calumet, Hammond, IN 46323-2094, USA
[48] Institució Catalana de Recerca i Estudis Avançats (ICREA), Barcelona, Spain
[49] Consorzio Interuniversitario per la Fisica Spaziale (CIFS), I-10133 Torino, Italy
[50] INTEGRAL Science Data Centre, CH-1290 Versoix, Switzerland
[51] Dipartimento di Fisica, Università di Roma "Tor Vergata," I-00133 Roma, Italy
[52] Department of Physics, Royal Institute of Technology (KTH), AlbaNova, SE-106 91 Stockholm, Sweden
[53] School of Pure and Applied Natural Sciences, University of Kalmar, SE-391 82 Kalmar, Sweden
[54] Fred Lawrence Whipple Observatory, Harvard-Smithsonian Center for Astrophysics, Amado, AZ 85645, USA
[55] Department of Physics and Astronomy, Barnard College, Columbia University, NY 10027, USA
[56] Department of Physics and Astronomy, University of California, Los Angeles, CA 90095, USA
[57] Santa Cruz Institute for Particle Physics and Department of Physics, University of California, Santa Cruz, CA 95064, USA
[58] Department of Physics, Washington University, St. Louis, MO 63130, USA
[59] Astrophysical Institute, Department of Physics and Astronomy, Ohio University, Athens, OH 45701, USA
[60] Department of Physics and Astronomy and the Bartol Research Institute, University of Delaware, Newark, DE 19716, USA
[61] School of Physics and Astronomy, University of Leeds, Leeds LS2 9JT, UK
[62] Argonne National Laboratory, 9700 S. Cass Avenue, Argonne, IL 60439, USA
[63] School of Physics, University College Dublin, Belfield, Dublin 4, Ireland
[64] School of Physics, National University of Ireland Galway, University Road, Galway, Ireland
[65] Physics Department, California Polytechnic State University, San Luis Obispo, CA 94307, USA
[66] Astronomy Department, Adler Planetarium and Astronomy Museum, Chicago, IL 60605, USA
[67] Department of Physics, Purdue University, West Lafayette, IN 47907, USA
[68] European Space Astronomy Centre (INSA-ESAC), European Space Agency (ESA), Satellite Tracking Station, P.O. Box Apdo 50727, E-28080 Villafranca del Castillo, Madrid, Spain
[69] Department of Astronomy and Astrophysics, 525 Davey Lab, Pennsylvania State University, University Park, PA 16802, USA
[70] Department of Physics and Astronomy, University of Utah, Salt Lake City, UT 84112, USA
[71] Physics Department, McGill University, Montreal, QC H3A 2T8, Canada
[72] Enrico Fermi Institute, University of Chicago, Chicago, IL 60637, USA
[73] Department of Physics and Astronomy, Iowa State University, Ames, IA 50011, USA
[74] Department of Physics and Astronomy, University of Iowa, Van Allen Hall, Iowa City, IA 52242, USA
[75] Department of Physics and Astronomy, DePauw University, Greencastle, IN 46135-0037, USA
[76] Department of Physics, Pittsburg State University, 1701 South Broadway, Pittsburg, KS 66762, USA
[77] Department of Life and Physical Sciences, Galway-Mayo Institute of Technology, Dublin Road, Galway, Ireland
[78] Instituto de Astronomia y Fisica del Espacio, Casilla de Correo 67, Sucursal 28, (C1428ZAA) Ciudad Autnoma de Buenos Aires, Argentina
[79] Department of Applied Physics and Instrumentation, Cork Institute of Technology, Bishopstown, Cork, Ireland

[80] Columbia Astrophysics Laboratory, Columbia University, New York, NY 10027, USA
[81] INAF, Osservatorio Astronomico di Torino, Italy
[82] Harvard-Smithsonian Center for Astrophysics, MA, USA
[83] Astronomical Institute, St. Petersburg State University, Russia
[84] Pulkovo Observatory, Russia
[85] Isaac Newton Institute of Chile, St. Petersburg Branch, Russia
[86] Abastumani Observatory, Mt. Kanobili, 0301 Abastumani, Georgia
[87] Department of Astronomy, University of Michigan, MI, USA
[88] Metsähovi Radio Observatory, Helsinki University of Technology TKK, Finland
[89] Institute of Astronomy, National Central University, Taiwan
[90] Tuorla Observatory, Department of Physics and Astronomy, University of Turku, Finland
[91] Instituto de Astrofísica de Andalucía, CSIC, Spain
[92] Max-Planck-Institut für Radioastronomie, Germany
[93] Institute of Astronomy, Bulgarian Academy of Sciences, Bulgaria
[94] Circolo Astrofili Talmassons, Italy
[95] Instituto de Astronomía, Universidad Nacional Autónoma de Mexico, Apdo. Postal 70-265, CP 04510, Mexico DF, Mexico
[96] INAF, Osservatorio Astrofisico di Catania, Italy
[97] Astrophysical Institute, Department of Physics and Astronomy, Ohio University, OH, USA
[98] Osservatorio Astronomico della Regione Autonoma Valle d'Aosta, Italy
[99] Armenzano Astronomical Observatory, Italy
[100] INAF, Osservatorio Astronomico di Roma, Italy
[101] INAF, Osservatorio Astronomico di Collurania Teramo, Italy
[102] Agrupació Astronòmica de Sabadell, Spain
[103] ZAH, Landessternwarte Heidelberg, Königstuhl, D-69117 Heidelberg, Germany
[104] Instituto de Astronomía, Universidad Nacional Autónoma deMexico, Apdo. Postal 877, CP 22800, Ensenada, B. C., Mexico
[105] Institute for Astrophysical Research, Boston University, MA, USA
[106] DLR, Institute of Planetary Research, Rutherfordstr. 2, D-12489 Berlin, Germany
[107] INAOE, Apdo. Postal 51 & 216, 72000 Tonantzintla, Puebla, Mexico
[108] Finnish Centre for Astronomy with ESO (FINCA), University of Turku,Väisäläntie 20, FI-21500 Piikkiö, Finland
[109] Department of Physics, University of Colorado Denver, CO, USA
[110] INAF-Osservatorio Astronomico di Brera, via E. Bianchi 46, I-23807 Merate, Italy
[111] Department of Astrophysical Sciences, Princeton University, Princeton, NJ 08544, USA
[112] Department of Astronomy, University of California, Berkeley, CA 94720-3411, USA
[113] Max-Planck-Institut für Radioastronomie, Auf dem Hügel 69, D-53121 Bonn, Germany
[114] Department of Astronomy and Astrophysics, University of California, 1156 High Street, Santa Cruz, CA 95064, USA
[115] Landessternwarte, Universität Heidelberg,Königstuhl 12, D-69117 Heidelberg, Germany
[116] UCO/Lick Observatory, University of California, 1156 High Street, Santa Cruz, CA 95064, USA
[117] Institut de Radio Astronomie Millimétrique, Avenida Divina Pastora 7, Local 20, E-18012 Granada, Spain
Received 2010 June 17; accepted 2010 October 29; published 2010 December 14

ABSTRACT

The BL Lacertae object 3C 66A was detected in a flaring state by the *Fermi* Large Area Telescope (LAT) and VERITAS in 2008 October. In addition to these gamma-ray observations, F-GAMMA, GASP-WEBT, PAIRITEL, MDM, ATOM, *Swift*, and *Chandra* provided radio to X-ray coverage. The available light curves show variability and, in particular, correlated flares are observed in the optical and *Fermi*-LAT gamma-ray band. The resulting spectral energy distribution can be well fitted using standard leptonic models with and without an external radiation field for inverse Compton scattering. It is found, however, that only the model with an external radiation field can accommodate the intra-night variability observed at optical wavelengths.

Key words: BL Lacertae objects: individual (3C 66A) – galaxies: active – gamma rays: galaxies

1. INTRODUCTION

The radio source 3C 66 (Bennett 1962) was shown by Mackay (1971) and Northover (1973) to actually consist of two unrelated radio sources separated by $0\overset{\circ}{.}11$: a compact source (3C 66A) and a resolved galaxy (3C 66B). 3C 66A was subsequently identified as a quasi-stellar object by Wills & Wills (1974), and as a BL Lacertae object by Smith et al. (1976) based on its optical spectrum. 3C 66A is now a well-known blazar which, like other active galactic nuclei (AGNs), is thought to be powered by accretion of material onto a supermassive black hole located in the central region of the host galaxy (Urry & Padovani 1995). Some AGNs present strong relativistic outflows in the form of jets, where particles are believed to be accelerated to ultra-relativistic energies and gamma rays are subsequently produced. Blazars are the particular subset of AGNs with jets aligned to the observer's line of sight. Indeed, the jet of 3C 66A has been imaged using very long baseline interferometry (VLBI; Taylor et al. 1996; Jorstad et al. 2001; Marscher et al. 2002; Britzen et al. 2007) and superluminal motion has been inferred (Jorstad et al. 2001; Britzen et al. 2008). This is indicative of the relativistic Lorentz factor of the jet and its small angle with respect to the line of sight.

BL Lacs are known for having very weak (if any) detectable emission lines, which makes determination of their redshift quite difficult. The redshift of 3C 66A was reported as $z = 0.444$ by Miller et al. (1978) and also (although tentatively) by Kinney et al. (1991). Each measurement, however, is based on the

[118] Royal Swedish Academy of Sciences Research Fellow, funded by a grant from the K. A. Wallenberg Foundation.
[119] Partially supported by the International Doctorate on Astroparticle Physics (IDAPP) program.
[120] Now at DESY, Platanenallee 6, D-15738 Zeuthen, Germany.
[121] Now at Institut für Physik und Astronomie, Universität Potsdam, D-14476 Potsdam-Golm,Germany; DESY, Platanenallee 6, D-15738 Zeuthen, Germany.
[122] Now at Los Alamos National Laboratory, MS H803, Los Alamos, NM 87545, USA.

measurement of a single line and is not reliable (Bramel et al. 2005). Recent efforts (described in Section 2.5) to provide further constraints have proven unsuccessful.

Similar to other blazars, the spectral energy distribution (SED) of 3C 66A has two pronounced peaks, which suggests that at least two different physical emission processes are at work (e.g., Joshi & Böttcher 2007). The first peak, extending from radio to soft X-ray frequencies, is likely due to synchrotron emission from high-energy electrons, while different emission models have been proposed to explain the second peak, which extends up to gamma-ray energies. Given the location of its synchrotron peak ($\lesssim 10^{15}$ Hz), 3C 66A is further sub-classified as an intermediate synchrotron peaked (ISP) blazar (Abdo et al. 2010c).

The models that have been proposed to explain gamma-ray emission in blazars can be roughly categorized into leptonic or hadronic, depending on whether the accelerated particles responsible for the gamma-ray emission are primarily electrons and positrons (hereafter "electrons") or protons. In leptonic models, high-energy electrons produce gamma rays via inverse Compton (IC) scattering of low-energy photons. In synchrotron self-Compton (SSC) models, the same population of electrons responsible for the observed gamma rays generates the low-energy photon field through synchrotron emission. In external Compton (EC) models, the low-energy photons originate outside the emission volume of the gamma rays. Possible sources of target photons include accretion-disk photons radiated directly into the jet (Dermer & Schlickeiser 1993), accretion-disk photons scattered by emission-line clouds or dust into the jet (Sikora et al. 1994), synchrotron radiation re-scattered back into the jet by broad-line emission clouds (Ghisellini & Madau 1996), jet emission from an outer slow jet sheet (Ghisellini et al. 2005), or emission from faster or slower portions of the jet (Georganopoulos & Kazanas 2004). In hadronic models, gamma rays are produced by high-energy protons, either via proton synchrotron radiation (Mücke et al. 2003), or via secondary emission from photo-pion and photo-pair-production reactions (see Böttcher (2007) and references therein for a review of blazar gamma-ray emission processes).

One of the main obstacles in the broadband study of gamma-ray blazars is the lack of simultaneity, or at least contemporaneousness, of the data at the various wavelengths. At high energies, the situation is made even more difficult due to the lack of objects that can be detected by MeV/GeV and TeV observatories on comparable timescales. Indeed, until recently the knowledge of blazars at gamma-ray energies had been obtained from observations performed in two disjoint energy regimes: (1) the high-energy range (20 MeV$< E <$ 10 GeV) studied in the 1990s by EGRET (Thompson et al. 1993) and (2) the very high energy (VHE) regime ($E >$ 100 GeV) observed by ground-based instruments such as imaging atmospheric Cherenkov telescopes (IACTs; Weekes 2000). Only[123] Markarian 421 was detected by both EGRET and the first IACTs (Kerrick et al. 1995). Furthermore, blazars detected by EGRET at MeV/GeV energies are predominantly flat-spectrum radio quasars (FSRQs), while TeV blazars are, to date, predominantly BL Lacs. It is important to understand these observational differences since they are likely related to the physics of the AGN (Cavaliere & D'Elia 2002) or to the evolution of blazars over cosmic time (Böttcher & Dermer 2002).

[123] Markarian 501 was marginally detected by EGRET only during a few months in 1996 (Kataoka et al. 1999).

The current generation of gamma-ray instruments (AGILE, *Fermi*, H.E.S.S., MAGIC, and VERITAS) is closing the gap between the two energy regimes due to improved instrument sensitivities, leading us toward a deeper and more complete characterization of blazars as high-energy sources and as a population (Abdo et al. 2009b). An example of the successful synergy of space-borne and ground-based observatories is provided by the joint observations of 3C 66A by the *Fermi* LAT and the Very Energetic Radiation Imaging Telescope Array System (VERITAS) during its strong flare of 2008 October. The flare was originally reported by VERITAS (Swordy 2008; Acciari et al. 2009) and soon after contemporaneous variability was also detected at optical to infrared wavelengths (Larionov et al. 2008) and in the *Fermi*-LAT energy band (Tosti 2008). Follow-up observations were obtained at radio, optical, and X-ray wavelengths in order to measure the flux and spectral variability of the source across the electromagnetic spectrum and to obtain a quasi-simultaneous SED. This paper reports the results of this campaign, including the broadband spectrum and a model interpretation of this constraining SED.

2. OBSERVATIONS AND DATA ANALYSIS

2.1. VERITAS

VERITAS is an array of four 12 m diameter imaging Cherenkov telescopes in southern Arizona, USA (Acciari et al. 2008b). 3C 66A was observed with VERITAS for 14 hr from 2007 September through 2008 January and for 46 hr between 2008 September and 2008 November. These observations (hereafter 2007 and 2008 data) add up to ~32.8 hr of live time after data quality selection. The data were analyzed following the procedure described in Acciari et al. (2008b).

As reported in Acciari et al. (2009), the average spectrum measured by VERITAS is very soft, yielding a photon index Γ of 4.1 $\pm 0.4_{\rm stat} \pm 0.6_{\rm sys}$ when fitted to a power law $dN/dE \propto E^{-\Gamma}$. The average integral flux above 200 GeV measured by VERITAS is $(1.3 \pm 0.1) \times 10^{-11}$ cm^{-2} s^{-1}, which corresponds to 6% of the Crab Nebula's flux above this threshold. In addition, a strong flare with night-by-night VHE-flux variability was detected in 2008 October. For this analysis, the VERITAS spectrum is calculated for the short time interval 2008 October 8–10 (MJD 54747–54749; hereafter *flare* period), and for a longer period corresponding to the *dark run*[124] where most of the VHE emission from 3C 66A was detected (MJD 54734–54749). It should be noted that the *flare* and *dark run* intervals overlap and are therefore not independent. Table 1 lists the relevant information from each data set.

As shown in Figure 1, the *flare* and *dark run* spectra are very soft, yielding nearly identical photon indices of $4.1 \pm 0.6_{\rm stat} \pm 0.6_{\rm sys}$, entirely consistent with that derived from the full 2007 and 2008 data set. The integral flux above 200 GeV for the *flare* period is $(2.5 \pm 0.4) \times 10^{-11}$ cm^{-2} s^{-1}, while the average flux for the *dark run* period is $(1.4 \pm 0.2) \times 10^{-11}$ cm^{-2} s^{-1}. The extragalactic background light (EBL) de-absorbed spectral points for the *dark run* calculated using the optical depth values of Franceschini et al. (2008) and assuming a nominal redshift of $z = 0.444$ are also shown in Figure 1. These points are well fitted by a power-law function with $\Gamma = 1.9 \pm 0.5$.

[124] IACTs like VERITAS do not operate on nights with bright moonlight. The series of nights between consecutive bright moonlight periods is usually referred to as a *dark run*.

Table 1
Results from VERITAS Observations of 3C 66A

Interval	Live Time (hr)	$N_{\rm on}$	$N_{\rm off}$	Alpha	Excess	Significance (σ)
Flare	6.0	1531	7072	0.121	678.3	18.0
Dark run	21.2	3888	20452	0.125	1331.5	22.2
2007 and 2008	28.1	7257	31201	0.175	1791	21.1

Notes. Live time corresponds to the effective exposure time after accounting for data quality selection. $N_{\rm on}$ ($N_{\rm off}$) corresponds to the number of on (off)-source events passing background-rejection cuts. Alpha is the normalization of off-source events and the excess is equal to $N_{\rm on} - \alpha N_{\rm off}$. The significance is expressed in number of standard deviations and is calculated according to Equation (17) of Li & Ma (1983). See Acciari et al. (2009) for a complete description of the VERITAS analysis.

2.2. *Fermi*-LAT

The LAT on board the *Fermi* Gamma-ray Space Telescope is a pair-conversion detector sensitive to gamma rays with energies between 20 MeV and several hundred GeV (Atwood et al. 2009). Since launch the instrument has operated almost exclusively in sky survey mode, covering the whole sky every 3 hr. The overall coverage of the sky is fairly uniform, with exposure variations of $\leqslant$ 15% around the mean value. The LAT data are analyzed using ScienceTools v9r15p5 and instrument response functions P6V3 (available via the *Fermi* science support center[125]). Only photons in the *diffuse* event class are selected for this analysis because of their reduced charged-particle background contamination and very good angular reconstruction. A zenith angle $<105^\circ$ cut in instrument coordinates is used to avoid gamma rays from the Earth limb. The diffuse emission from the Galaxy is modeled using a spatial model (`gll_iem_v02.fit`) which was refined with *Fermi*-LAT data taken during the first year of operation. The extragalactic diffuse and residual instrumental backgrounds are modeled as an isotropic component and are included in the fit.[126] The data are analyzed with an unbinned maximum likelihood technique (Mattox et al. 1996) using the likelihood analysis software developed by the LAT team.

Although 3C 66A was detected by EGRET as source 3EG J0222+4253 (Hartman et al. 1999), detailed spatial and timing analyses by Kuiper et al. (2000) showed that this EGRET source actually consists of the superposition of 3C 66A and the nearby millisecond pulsar PSR J0218+4232 which is $0\overset{\circ}{.}96$ distant from the blazar. This interpretation of the EGRET data is verified by *Fermi*-LAT, whose improved angular resolution permits the clear separation of the two sources as shown in Figure 2. Furthermore, the known pulsar period is detected with high confidence in the *Fermi*-LAT data (Abdo et al. 2009a). More importantly for this analysis, the clear separation between the pulsar and the blazar enables studies of each source independently in the maximum likelihood analysis, and thus permits an accurate determination of the spectrum and localization of each source, with negligible contamination.

Figure 2 also shows the localization of the *Fermi* and VERITAS sources with respect to blazar 3C 66A and radio galaxy 3C 66B (see caption in Figure 2 for details). It is clear from the map that the *Fermi*-LAT and VERITAS localizations are consistent and that the gamma-ray emission is confidently associated with the blazar and not with the radio galaxy. Some small contribution in the *Fermi*-LAT data from radio galaxy 3C 66B as suggested by Aliu et al. (2009) and Tavecchio & Ghisellini (2009) cannot be excluded, given the large spillover of low-energy photons from 3C 66A at the location of 3C 66B. This is due to the long tails of the *Fermi*-LAT point-spread function at low energies as described in Atwood et al. (2009). Nevertheless, considering only photons with energy $E > 1$ GeV, the upper limit (95% confidence level) for a source at the location of 3C 66B is 2.9×10^{-8} cm^{-2} s^{-1} for the *dark run* period (with a test statistic[127] (TS) = 1.3). For the 11 months of data corresponding to the first *Fermi*-LAT catalog (Abdo et al. 2010a), the upper limit is 4.9×10^{-9} cm^{-2} s^{-1} (TS = 5.8).

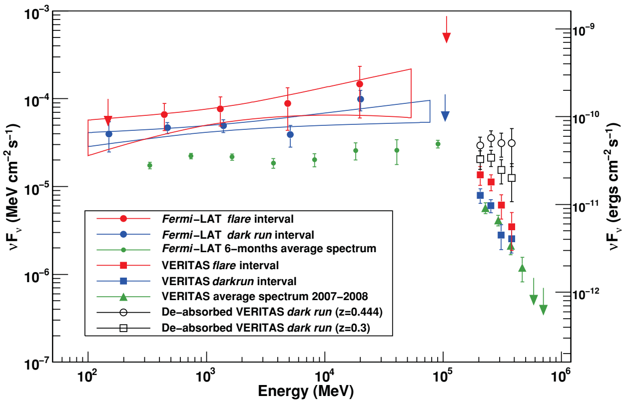

Figure 1. Gamma-ray SED of 3C 66A including *Fermi*-LAT and VERITAS data for the *flare* (red symbols) and *dark run* (blue symbols) intervals. The *Fermi*-LAT spectra are also shown here as "butterfly" contours (solid lines) describing the statistical error on the spectrum (Abdo et al. 2009b). The previously reported *Fermi*-LAT six-month-average spectrum (Abdo et al. 2010b) is also shown here (green circles) and is lower than the spectrum obtained during the campaign. The average 2007–2008 VERITAS spectrum originally reported in Acciari et al. (2009) is displayed with green triangles. In all cases, the upper limits are calculated at 95% confidence level. The de-absorbed *dark run* spectra obtained using the optical depth values of Franceschini et al. (2008) are also shown as open circles and open squares for redshifts of 0.444 and 0.3, respectively.

As in the analysis of the VERITAS observations, the *Fermi*-LAT spectrum is calculated for the *flare* and for the *dark run* periods. The *Fermi flare* period flux $F(E > 100\ {\rm MeV}) = (5.0 \pm 1.4_{\rm stat} \pm 0.3_{\rm sys}) \times 10^{-7}$ cm^{-2} s^{-1} is consistent within errors with the *dark run* flux of $(3.9 \pm 0.5_{\rm stat} \pm 0.3_{\rm sys}) \times 10^{-7}$ cm^{-2} s^{-1}. In both cases, the *Fermi*-LAT spectrum is quite hard and can be described by a power law with a photon index Γ of $1.8 \pm 0.1_{\rm stat} \pm 0.1_{\rm sys}$ and $1.9 \pm 0.1_{\rm stat} \pm 0.1_{\rm sys}$ in the *flare* period and *dark run* intervals, respectively. Both spectra are shown in the high-energy SED in Figure 1.

2.3. *Chandra*

3C 66A was observed by the *Chandra* observatory on 2008 October 6 for a total of 37.6 ks with the Advanced CCD Imaging Spectrometer (ACIS), covering the energy band between 0.3 and 10 keV. The source was observed in the continuous clocking mode to avoid pile-up effects. Standard analysis tools (CIAO 4.1) and calibration files (CALDB v3.5.0) provided by the *Chandra* X-ray center[128] are used.

The time-averaged spectrum is obtained and re-binned to ensure that each spectral channel contains at least 25 background-subtracted counts. This condition allows the use of the χ^2

[125] http://fermi.gsfc.nasa.gov/ssc/data/analysis/scitools/overview.html.
[126] http://fermi.gsfc.nasa.gov/ssc/data/access/lat/BackgroundModels.html.
[127] The test statistic (TS) value quantifies the probability of having a point source at the location specified. It is roughly the square of the significance value: a TS of 25 corresponds to a signal of approximately 5 standard deviations (Abdo et al. 2010a).
[128] http://cxc.harvard.edu/ciao/.

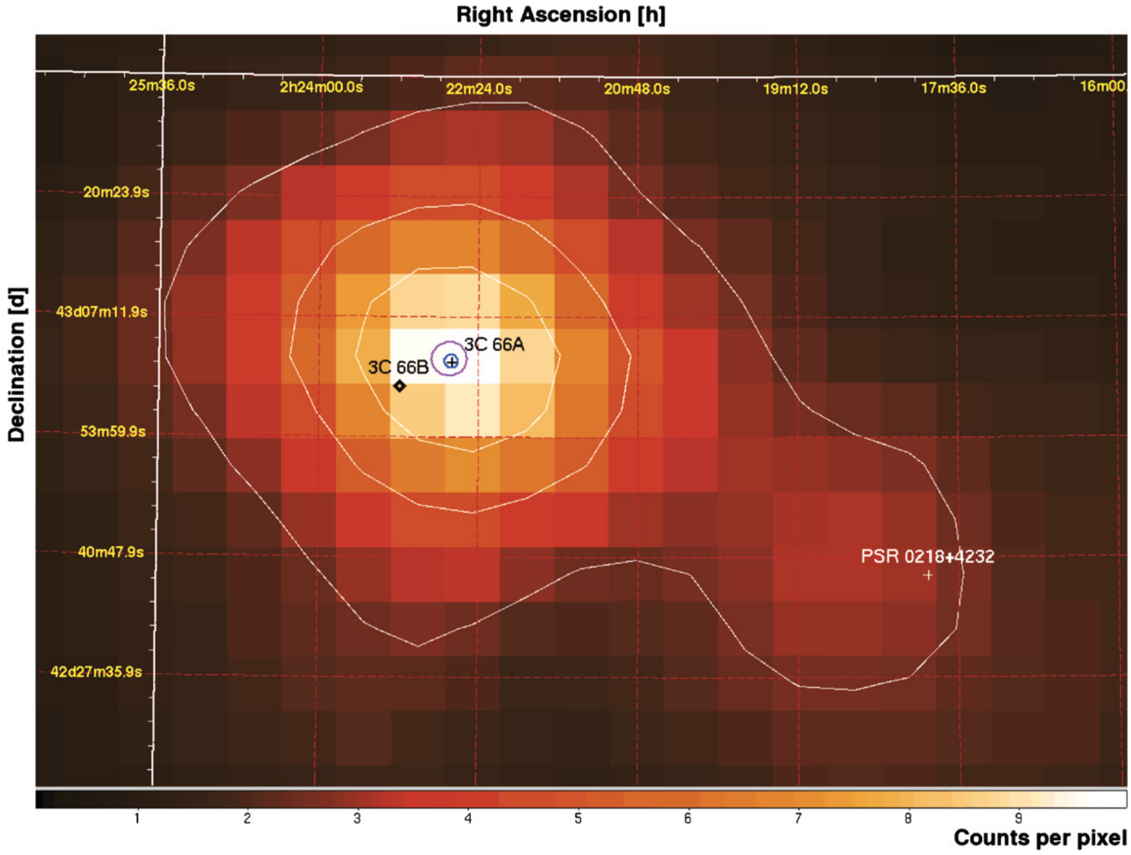

Figure 2. Smoothed count map of the 3C 66A region as seen by *Fermi*-LAT between 2008 September 1 and December 31 with $E > 100$ MeV. The color bar has units of counts per pixel and the pixel dimensions are $0\overset{\circ}{.}1 \times 0\overset{\circ}{.}1$. The contour levels have been smoothed and correspond to 2.8, 5.2, and 7.6 counts per pixel. The locations of 3C 66A and 3C 66B (a radio galaxy that is $0\overset{\circ}{.}11$ away) are shown as a cross and as a diamond, respectively. The location of millisecond pulsar PSR 0218+4232 is also indicated with a white cross. The magenta circle represents the VERITAS localization of the VHE source (RA; DEC) = ($2^{h}22^{m}41\overset{s}{.}6 \pm 1\overset{s}{.}7_{stat} \pm 6\overset{s}{.}0_{sys}$; $43°02'35\overset{''}{.}5 \pm 21''_{stat} \pm 1'30''_{sys}$) as reported in Acciari et al. (2009). The blue interior circle represents the 95% error radius of the *Fermi*-LAT localization (RA; DEC) = ($02^{h}22^{m}40\overset{s}{.}3 \pm 4\overset{s}{.}5$; $43°02'18\overset{''}{.}6 \pm 42\overset{''}{.}1$) as reported in the *Fermi*-LAT first source catalog (Abdo et al. 2010a). All positions are based on the J2000 epoch.

quality-of-fit estimator to find the best-fit model. XSPEC v12.4 (Arnaud 1996) is used for the spectral analysis and fitting procedure. Two spectral models have been used to fit the data: single power law and broken power law. Each model includes galactic H I column density ($N_{H,Gal} = 8.99 \times 10^{20}$ cm^{-2}) according to Dickey & Lockman (1990), where the photoelectric absorption is set with the XSPEC model *phabs*.[129] An additional local H I column density was also tried but in both cases the spectra were consistent with pure galactic density. Consequently, the column density has been fixed to the galactic value in each model, and the results obtained are presented in Table 2. An *F*-test was performed to demonstrate that the spectral fit improves significantly when using the extra degrees of freedom of the broken power-law model. Table 2 also contains the results of the *F*-test.

2.4. *Swift XRT and UVOT*

Following the VERITAS detection of VHE emission from 3C 66A, Target of Opportunity (ToO) observations of 3C 66A with *Swift* were obtained for a total duration of ∼10 ks. The *Swift* satellite observatory comprises an UV–Optical telescope (UVOT), an X-ray telescope (XRT), and a Burst Alert Telescope (Gehrels et al. 2004). Data reduction and calibration of the XRT data are performed with *HEASoft* v6.5 standard tools. All XRT data presented here are taken in photon counting mode with negligible pile-up effects. The X-ray spectrum of each observation is fitted with an absorbed power law using a fixed Galactic column density from Dickey & Lockman (1990), which gives good χ^2 values for all observations. The measured photon spectral index ranges between 2.5 and 2.9 with a typical statistical uncertainty of 0.1.

UVOT obtained data through each of six color filters, *V*, *B,* and *U* together with filters defining three ultraviolet passbands *UVW1*, *UVM2,* and *UVW2* with central wavelengths of 260 nm, 220 nm, and 193 nm, respectively. The data are calibrated using standard techniques (Poole et al. 2008) and corrected for Galactic extinction by interpolating the absorption values from Schlegel et al. (1998) ($E_{B-V} = 0.083$ mag) with the galactic spectral extinction model of Fitzpatrick (1999).

2.5. *Optical to Infrared Observations*

The *R* magnitude of the host galaxy of 3C 66A is ∼ 19 in the optical band (Wurtz et al. 1996). Its contribution is negligible compared to the typical AGN magnitude of $R \lesssim 15$; therefore, host-galaxy correction is not necessary.

GASP-WEBT. 3C 66A is continuously monitored by telescopes affiliated to the GLAST-AGILE support program of the Whole Earth Blazar Telescope (GASP-WEBT; see Villata et al.

[129] http://heasarc.gsfc.nasa.gov/docs/software/lheasoft/xanadu/xspec/manual/XSmodelPhabs.html.

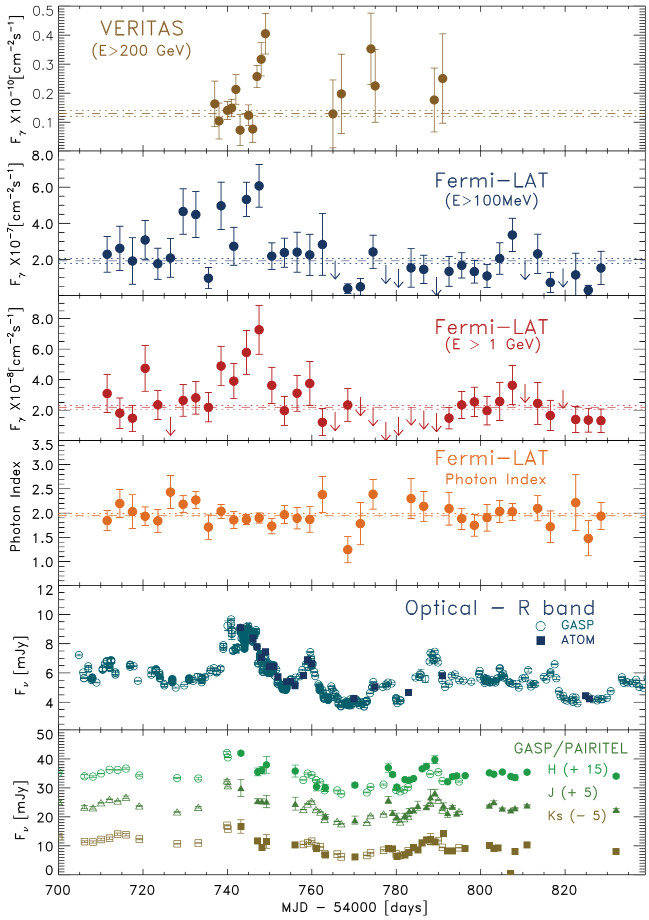

Figure 3. 3C 66A light curves covering 2008 August 22 to December 31 in order of increasing wavelength. The VERITAS observations are combined to obtain nightly flux values and the dashed and dotted lines represent the average flux measured from the 2007 and 2008 data and its standard deviation. The *Fermi*-LAT light curves contain time bins with a width of 3 days. The average flux and average photon index measured by *Fermi*-LAT during the first six months of science operations are shown as horizontal lines in the respective panels. In all cases, the *Fermi*-LAT photon index is calculated over the 100 MeV to 200 GeV energy range. The long-term light curves at optical and infrared wavelengths are presented in the two bottom panels. In the bottom panel, GASP-WEBT and PAIRITEL observations are represented by open and solid symbols, respectively.

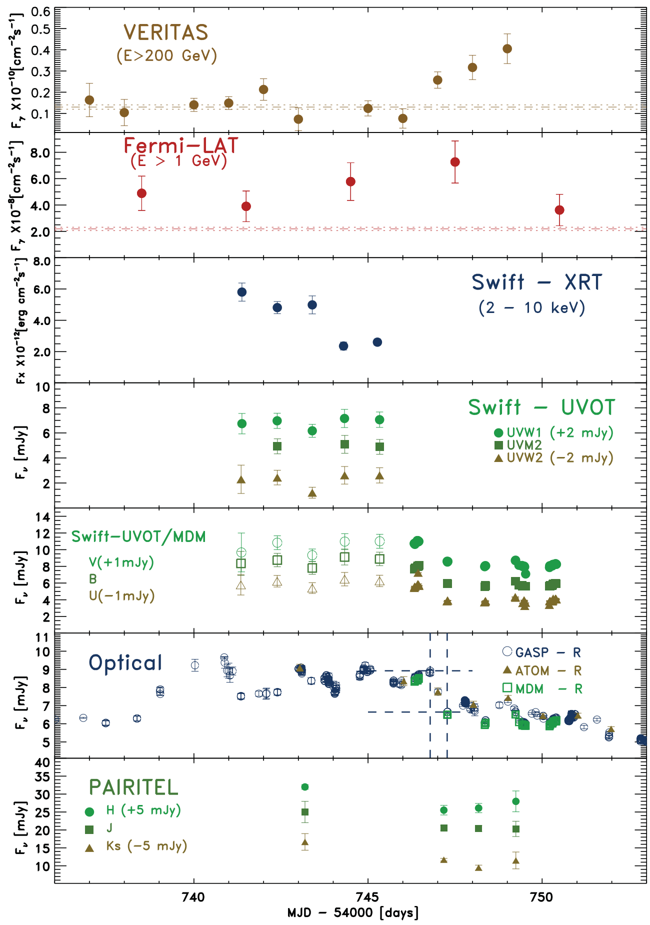

Figure 4. 3C 66A light curves covering the period centered on the gamma-ray flare (2008 October 1–10). The VERITAS and *Fermi*-LAT panels were already described in the caption of Figure 3. *Swift* Target-of-Opportunity (ToO) observations (panels 3–5 from the top) were obtained following the discovery of VHE emission by VERITAS (Swordy 2008). *Swift*-UVOT and MDM observations are represented by open and solid symbols, respectively. The optical light curve in panel 6 from the top displays intra-night variability. An example is identified in the plot, when a rapid decline of the optical flux by $\Delta F/\Delta t \sim -0.2$ mJy hr^{-1} is observed on MJD 54747.

2008, 2009). These observations provide a long-term light curve of this object with complete sampling as shown in Figure 3. During the time interval in consideration (MJD 54700–54840), several observatories (Abastumani, Armenzano, Crimean, El Vendrell, L'Ampolla, Lulin, New Mexico Skies, Roque de los Muchachos (KVA), Rozhen, Sabadell, San Pedro Martir, St. Petersburg, Talmassons, Teide (BRT), Torino, Tuorla, and Valle d' Aosta) contributed photometric observations in the *R* band. Data in the *J*, *H,* and *K* bands were taken at the Campo Imperatore observatory. A list of the observatories and their locations is available in Table 3.

MDM. Following the discovery of VHE emission, 3C 66A was observed with the 1.3 m telescope of the MDM Observatory during the nights of 2008 October 6–10. A total of 290 science frames in *U*, *B*, *V*, and *R* bands (58 each) were taken throughout the entire visibility period (approx. 4:30 – 10:00 UT) during each night. The light curves, which cover the time around the flare, are presented in Figure 4.

ATOM. Optical observations for this campaign in the *R* band were also obtained with the 0.8 m optical telescope ATOM in Namibia, which monitors this source periodically. Twenty photometric observations are available starting on MJD 54740 and are shown in Figures 3 and 4.

PAIRITEL. Near-infrared observations in the *J*, *H,* and K_s were obtained following the VHE flare with the 1.3 m Peters Automated Infrared Imaging Telescope (PAIRITEL; see Bloom et al. 2006) located at the Fred Lawrence Whipple Observatory. The resulting light curves using differential photometry with four nearby calibration stars are shown in Figure 4.

Keck. The optical spectrum of 3C 66A was measured with the LRIS spectrometer (Oke et al. 1995) on the Keck I telescope on the night of 2009 September 17 under good conditions. The instrument configuration resulted in a full width half-maximum of ∼250 km s^{-1} over the wavelength range 3200–5500 Å (blue side) and ∼200 km s^{-1} over the range 6350–9000 Å (red side). A series of exposures totaling 110 s (blue) and 50 s (red) were obtained, yielding a signal-to-noise (S/N) per resolution element of ∼250 and 230 for the blue and red cameras, respectively. The data were reduced with the LowRedux[130] pipeline and calibrated using a spectrophotometric star observed on the same night.

[130] http://www.ucolick.org/∼xavier/LowRedux/index.html.

Table 2
Best-fit Model Parameters for a Fit Performed to the *Chandra* Data in the 1–7 keV Energy Range

Single Power-law Model		
Γ	Flux (10^{-12} erg cm^{-2} s^{-1})	χ^2/dof
2.99 ± 0.03	3.47 ± 0.06	1.21 (232.6/193)

Broken Power-law Model					
Γ_1	Γ_2	Flux (10^{-12} erg cm^{-2} s^{-1})	Break (keV)	χ^2/dof	F-test Probability
$3.08^{+0.3}_{-0.5}$	$2.24^{+0.23}_{0.37}$	$3.58^{+0.07}_{-0.08}$	$3.3^{+0.5}_{-0.3}$	0.97 (185.2/191)	3.47×10^{-10}

Notes. The galactic $N_{H,Gal}$ value is fixed to 8.99×10^{20} cm^{-2}, the value of the galactic H I column density according to Dickey & Lockman (1990). Errors indicate the 90% confidence level.

Table 3
List of Ground-based Observatories that Participated in This Campaign

Observatory	Location	Web Page
Radio Observatories		
Crimean Radio Obs.	Ukraine	www.crao.crimea.ua
Effelsberg	Germany	www.mpifr.de/english/radiotelescope
IRAM	Spain	www.iram-institute.org/EN/30-meter-telescope.php
Medicina	Italy	www.med.ira.inaf.it
Metsähovi	Finland	www.metsahovi.fi/en
Noto	Italy	www.noto.ira.inaf.it
UMRAO	Michigan, USA	www.astro.lsa.umich.edu/obs/radiotel
Infrared Observatories		
Campo Imperatore	Italy	www.oa-teramo.inaf.it
PAIRITEL	Arizona, USA	www.pairitel.org
Optical Observatories		
Abastumani	Georgia	www.genao.org
Armenzano	Italy	www.webalice.it/dcarosati
ATOM	Namibia	www.lsw.uni-heidelberg.de/projects/hess/ATOM/
Crimean Astr. Obs.	Ukraine	www.crao.crimea.ua
El Vendrell	Spain	
Kitt Peak (MDM)	Arizona, USA	www.astro.lsa.umich.edu/obs/mdm
L'Ampolla	Spain	
Lulin	Taiwan	www.lulin.ncu.edu.tw/english
New Mexico Skies Obs.	New Mexico, USA	www.nmskies.com
Roque (KVA)	Canary Islands, Spain	www.otri.iac.es/eno/nt.htm
Rozhen	Bulgaria	www.astro.bas.bg/rozhen.html
Sabadell	Spain	www.astrosabadell.org/html/es/observatoriosab.htm
San Pedro Mártir	México	www.astrossp.unam.mx/indexspm.html
St. Petersburg	Russia	www.gao.spb.ru
Talmassons	Italy	www.castfvg.it
Teide (BRT)	Canary Islands, Spain	www.telescope.org
Torino	Italy	www.to.astro.it
Tuorla	Finland	www.astro.utu.fi
Valle d' Aosta	Italy	www.oavda.it/english/osservatorio
Gamma-ray Observatory		
VERITAS	Arizona, USA	www.veritas.sao.arizona.edu

Inspection of the 3C 66A spectrum reveals no spectral features aside from those imposed by Earth's atmosphere and the Milky Way (Ca H+K). Therefore, these new data do not offer any insight on the redshift of 3C 66A and in particular are unable to confirm the previously reported value of $z = 0.444$ (Miller et al. 1978).

2.6. Radio Observations

Radio observations are available thanks to the F-GAMMA (Fermi-Gamma-ray Space Telescope AGN Multi-frequency Monitoring Alliance) program, which is dedicated to monthly monitoring of selected *Fermi*-LAT blazars (Fuhrmann et al. 2007; Angelakis et al. 2008). Radio flux density measurements were conducted with the 100 m Effelsberg radio telescope at 4.85, 8.35, 10.45, and 14.60 GHz on 2008 October 16. These data are supplemented with an additional measurement at 86 GHz conducted with the IRAM 30 m telescope (Pico Veleta, Spain) on 2008 October 8. The data were reduced using standard procedures described in Fuhrmann et al. (2008). Additional radio observations taken between 2008 October 5 and 15 (contemporaneous to the *flare* period) are provided by the Medicina, Metsähovi, Noto, and UMRAO observatories, all of which are members of the GASP-WEBT consortium.

3. DISCUSSION

3.1. Light Curves

The resulting multi-wavelength light curves from this campaign are shown in Figure 3 for those bands with long-term coverage and in Figure 4 for those observations that were obtained shortly before and after the gamma-ray flare. The VERITAS observations are combined to obtain nightly ($E > 200$ GeV) flux values since no evidence for intra-night variability is observed. The highest flux occurred on MJD 54749 and significant variability is observed during the whole interval (χ^2 probability less than 10^{-4} for a fit of a constant flux).

The temporal dependence of the *Fermi*-LAT photon index and integral flux above 100 MeV and 1 GeV are shown with time bins with width of 3 days in Figure 3. For those time intervals with no significant detection, a 95% confidence flux upper limit is calculated. The flux and photon index from the *Fermi*-LAT first source catalog (Abdo et al. 2010a) are shown as horizontal lines for comparison. These values correspond to the average flux and photon index measured during the first 11 months of *Fermi* operations, and thus span the time interval considered in the figures. It is evident from the plot that the VHE flare detected by VERITAS starting on MJD 54740 is coincident with a period of high flux in the *Fermi* energy band. The photon index during this time interval is consistent within errors with the average photon index $\Gamma = 1.95 \pm 0.03$ measured during the first six months of the *Fermi* mission (Abdo et al. 2010b).

Long-term and well-sampled light curves are available at optical and near-infrared wavelengths thanks to observations by GASP-WEBT, ATOM, MDM, and PAIRITEL. Unfortunately, radio observations were too limited to obtain a light curve and no statement about variability in this band can be made. The best sampling is available for the R band, for which variations with a factor of $\gtrsim 2$ are observed in the long-term light curve. Furthermore, variability on timescales of less than a day is observed, as indicated in Figure 4, and as previously reported by Böttcher et al. (2009) following the WEBT (Whole Earth Blazar Telescope) campaign on 3C 66A in 2007 and 2008.

The increase in gamma-ray flux observed in the *Fermi* band seems contemporaneous with a period of increased flux in the optical, and to test this hypothesis, the discrete correlation function (DCF) is used (Edelson & Krolik 1988). Figure 5 shows the DCF of the $F(E > 1$ GeV) gamma-ray band with respect to the R band with time-lag bins of 3, 5, and 7 days. The profile of the DCF is consistent for all time-lag bins, indicating that the result is independent of bin size. The DCF with time-lag bins of 3 days was fitted with a Gaussian function of the form $\mathrm{DCF}(\tau) = \mathrm{C}_{\max} \times \exp{(\tau - \tau_0)^2/\sigma^2}$, where $C_{\max}$ is the peak value of the DCF, τ_0 is the delay timescale at which the DCF peaks, and σ parameterizes the Gaussian width of the DCF. The best-fit function is plotted in Figure 5 and the best-fit parameters are $C_{\max} = 1.1 \pm 0.3$, $\tau_0 = (0.7 \pm 0.7)$ days and $\sigma = (3.3 \pm 0.7)$ days. An identical analysis was also performed between the $F(E > 100$ MeV) and the R optical band with consistent results. This indicates a clear correlation between the *Fermi*-LAT and optical energy bands with a time lag that is consistent with zero and not greater than ∼5 days. Despite the sparsity of the VERITAS light curve (due in part to the time periods when the source was not observable due to the full Moon), the DCF analysis was also performed to search for correlations with either the *Fermi*-LAT or optical data. Apart from the overall increase in flux, no significant correlations can be established. The onset of the $E > 200$ GeV flare seems delayed by about ∼5 days with respect to the optical–GeV flare but given the coverage gaps no firm conclusion can be drawn (e.g., the flare could have been already underway when the observations took place). No such lag is expected from the homogeneous model described in the next section but could arise in models with complex energy stratification and geometry in the emitting region.

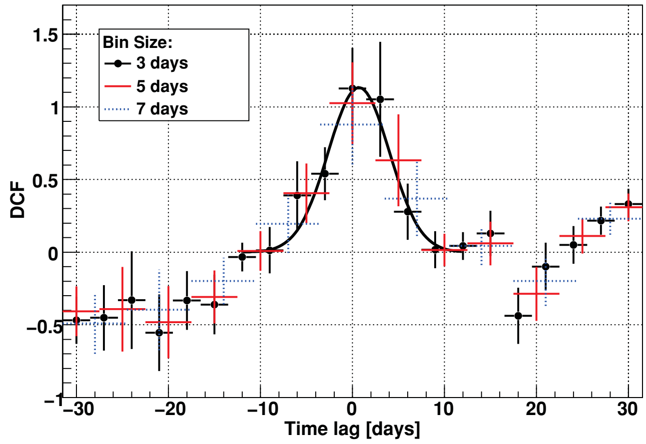

Figure 5. Discrete correlation function (DCF) of the $F(E > 1$ GeV) gamma-ray light curve with respect to the R-band light curve. A positive time lag indicates that the gamma-ray band leads the optical band. Different symbols correspond to different bin sizes of time lag as indicated in the legend. The profile of the DCF is independent of bin size and is well described by a Gaussian function of the form $\mathrm{DCF}(\tau) = \mathrm{C}_{\max} \times \exp{(\tau - \tau_0)^2/\sigma^2}$. The fit to the 3-day bin size distribution is shown in the plot as a solid black line and the best-fit parameters are $C_{\max} = 1.1 \pm 0.3$, $\tau_0 = (0.7 \pm 0.7)$ days, and $\sigma = (3.3 \pm 0.7)$ days.

3.2. SED and Modeling

The broadband SED derived from these observations is presented in Figure 6 and modeled using the code of Böttcher & Chiang (2002). In this model, a power-law distribution of ultra-relativistic electrons and/or pairs with lower and upper energy cutoffs at $\gamma_{\min}$ and $\gamma_{\max}$, respectively, and power-law index q is injected into a spherical region of comoving radius R_B. The injection rate is normalized to an injection luminosity L_e, which is a free input parameter of the model. The model assumes a temporary equilibrium between particle injection, radiative cooling due to synchrotron and Compton losses, and particle escape on a time $t_{\mathrm{esc}} \equiv \eta_{\mathrm{esc}} R_B/c$, where η_{esc} is a scale parameter in the range ∼250–500. Both the internal synchrotron photon field (SSC) and external photon sources (EC) are considered as targets for Compton scattering. The emission region is moving with a bulk Lorentz factor Γ along the jet. To reduce the number of free parameters, we assume that the jet is oriented with respect to the line of sight at the superluminal angle so that the Doppler factor is equal to $D = (\Gamma\,[1 - \beta\, \cos\theta_{\mathrm{obs}}])^{-1} = \Gamma$, where θ_{obs} is the angle of the jet with respect to the line of sight. Given the uncertainty in the redshift determination of 3C 66A, a range of plausible redshifts, namely $z = 0.1, 0.2, 0.3$, and the generally used catalog value $z = 0.444$, are considered for the modeling. All model fits include EBL absorption using the optical depth values from Franceschini et al. (2008).

Most VHE blazars known to date are high synchrotron peaked (HSP) blazars, whose SEDs can often be fitted satisfactorily with pure SSC models. Since the transition from HSP to ISP is continuous, a pure SSC model was fitted first to the radio through VHE gamma-ray SED. Independently of the model under consideration, the low-frequency part of the SED ($<10^{20}$ Hz) is well fitted with a synchrotron component, as shown in Figure 6.

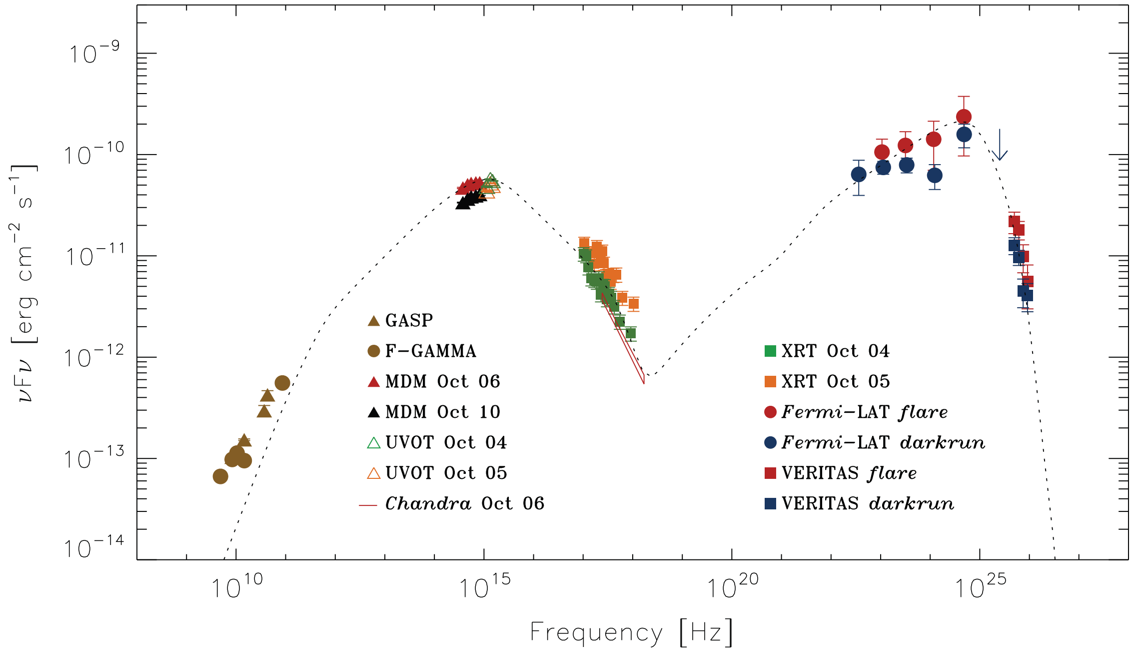

Figure 6. Broadband SED of 3C 66A during the 2008 October multi-wavelength campaign. The observation that corresponds to each set of data points is indicated in the legend. As an example, the EBL-absorbed EC+SSC model for $z = 0.3$ is plotted here for reference. A description of the model is provided in the text.

For clarity, only the high-frequency range is shown in Figures 7 and 8, where the different models are compared. As can be seen from the figures, a reasonable agreement with the overall SED can be achieved for any redshift in the range explored. The weighted sum of squared residuals has been calculated for the *Fermi*-LAT and VERITAS *flare* data (8 data points in total) in order to quantify the scatter of the points with respect to the model and is shown in Table 4. The best agreement is achieved when the source is located at $z \sim 0.2$–0.3. For lower redshifts, the model spectrum is systematically too hard, while at $z = 0.444$ the model spectrum is invariably too soft as a result of EBL absorption. It should be noted that the EBL model of Franceschini et al. (2008) predicts some of the lowest optical depth values in comparison to other models (Finke et al. 2010; Gilmore et al. 2009; Stecker et al. 2006). Thus, a model spectrum with redshift of 0.3 or above would be even harder to reconcile with the observations when using other EBL models.

A major problem of the SSC models with $z \gtrsim 0.1$ is that R_B is of the order of $\gtrsim 5 \times 10^{16}$ cm. This does not allow for variability timescales shorter than $\lesssim 1$ day, which seems to be in contrast with the optical variability observed on shorter timescales. A smaller R_B would require an increase in the electron energy density (with no change in the magnetic field in order to preserve the flux level of the synchrotron peak) and would lead to internal gamma–gamma absorption. This problem could be mitigated by choosing extremely high Doppler factors, $D \gtrsim 100$. However, these are significantly larger than the values inferred from VLBI observations of *Fermi*-LAT blazars (Savolainen et al. 2010).[131] Moreover, all SSC models require very low magnetic fields, far below the value expected from equipartition ($\epsilon_B = L_B/L_e \sim 10^{-3} \ll 1$), where L_B is the Poynting flux derived from the magnetic energy density and L_e is the energy flux of the electrons propagating along the jet. Table 4 lists the parameters used for the SSC models displayed in Figure 7.

Subsequently, an external infrared radiation field with ad hoc properties was included as a source of photons to be Compton scattered. For all SSC+EC models shown in Figure 8, the peak frequency of the external radiation field is set to $\nu_{\mathrm{ext}} = 1.4 \times 10^{14}$ Hz, corresponding to near-IR. This adopted value is high enough to produce $E \gtrsim 100$ GeV photons from IC scattering off the synchrotron electrons and at the same time is below the energy regime in which Klein–Nishina effects take place. Although the weighted sums of squared residuals for EC+SSC models are generally worse than for pure SSC models, reasonable agreement with the overall SED can still be achieved for redshifts $z \lesssim 0.3$. Furthermore, all SSC+EC models are consistent with a variability timescale of $\Delta t_{\mathrm{var}} \sim 4$ hr. This is in better agreement with the observed variability at optical wavelengths than the pure SSC interpretation. Also, while the SSC+EC interpretation still requires sub-equipartition magnetic fields, the magnetic fields are significantly closer to equipartition than in the pure SSC case, with $L_B/L_e \sim 0.1$. The parameters of the SSC+EC models are listed in Table 5.

Models with and without EC component yield the best agreement with the SED if the source is located at a redshift $z \sim 0.2$–0.3. Of course, this depends on the EBL model used in the analysis. An EBL model that predicts higher attenuation than Franceschini et al. (2008) would lead to a lower redshift range and make it even more difficult to have agreement between the SED models and the data when the source is located at redshifts $z \gtrsim 0.4$. Finally, it is worth mentioning that the redshift range $z \sim 0.2$–0.3 is in agreement with previous estimates by Finke et al. (2008), who estimate the redshift of 3C 66A to be $z = 0.321$ based on the magnitude of the host galaxy, and by Prandini et al. (2010) who use an empirical relation between the previously reported *Fermi*-LAT and IACTs spectral slopes of blazars and their redshifts to estimate the redshift of 3C 66A to be below $z = 0.34 \pm 0.05$.

[131] As a caveat, jet models with a decelerating flow (Georganopoulos & Kazanas 2003; Piner et al. 2008) or with inhomogeneous transverse structure (Ghisellini et al. 2005; Henri & Saugé 2006) can accommodate very high Doppler factors in the gamma-ray emitting region and still be consistent with the VLBI observations of the large scale jet.

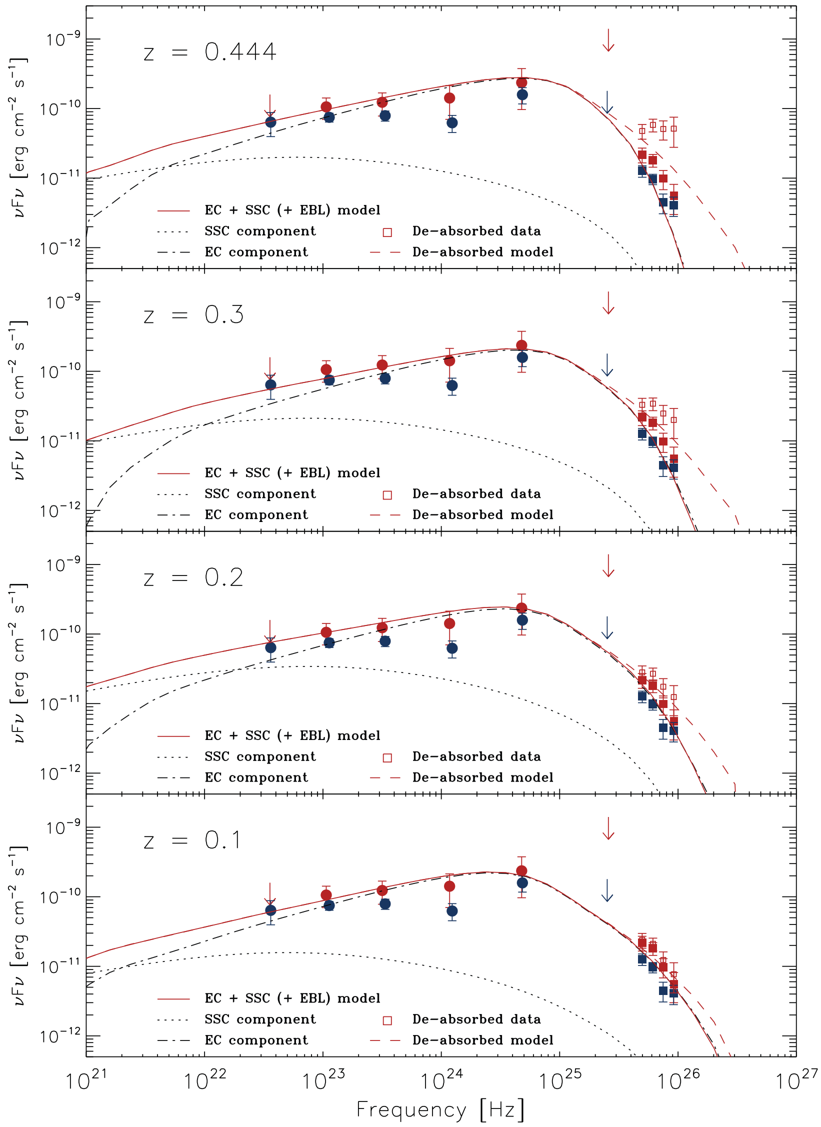

Figure 7. SSC models for redshifts $z = 0.444$, 0.3, 0.2, and 0.1 from top to bottom. The *Fermi*-LAT and VERITAS data points follow the same convention used in Figures 1 and 6 to distinguish between *flare* (red) and *dark run* (blue) data points. In each panel, the EBL-absorbed model is shown as a solid red line and the de-absorbed model as a red dashed line. De-absorbed VERITAS *flare* points are shown as open squares. In all cases, the optical depth values from Franceschini et al. (2008) are used. The best agreement between the model and the data is achieved when the source is located at $z = 0.2$–0.3. For lower redshifts, the model spectrum is systematically too hard, while at $z = 0.444$ the model spectrum is too soft.

A detailed study of hadronic versus leptonic modeling of the 2008 October data will be published elsewhere, but it is worth mentioning that the synchrotron proton blazar (SPB) model has been used to adequately reproduce the quasi-simultaneous SED observed during the 2003–2004 multi-wavelength campaign (Reimer et al. 2008). On that occasion rapid intra-day variations down to a 2 hr timescale were observed, while during the 2008 campaign presented here these variations seem less rapid. Qualitatively, the longer timescale variations may be due to a lower Doppler beaming at the same time that a strongly reprocessed proton synchrotron component dominates the high energy output of this source.

4. SUMMARY

Multi-wavelength observations of 3C 66A were carried out prompted by the gamma-ray outburst detected by the VERITAS and *Fermi* observatories in 2008 October. This marks the first occasion that a gamma-ray flare is detected by GeV and TeV instruments in comparable timescales. The light curves obtained show strong variability at every observed wavelength and, in particular, the flux increase observed by VERITAS and *Fermi* is coincident with an optical outburst. The clear correlation between the *Fermi*-LAT and *R* optical light curves permits one to go beyond the source association reported in the first *Fermi*-LAT source catalog (Abdo et al. 2010a) and finally identify the gamma-ray source 1FGL J0222.6+4302 as blazar 3C 66A.

For the modeling of the overall SED, a reasonable agreement can be achieved using both a pure SSC model and an SSC+EC model with an external near-infrared radiation field as an additional source for Compton scattering. However, the pure SSC model requires (1) a large emission region, which is inconsistent with the observed intra-night scale variability at optical wavelengths, and (2) low magnetic fields, about a factor $\sim 10^{-3}$ below equipartition. In contrast, an SSC+EC interpretation allows for variability on timescales of a few hours,

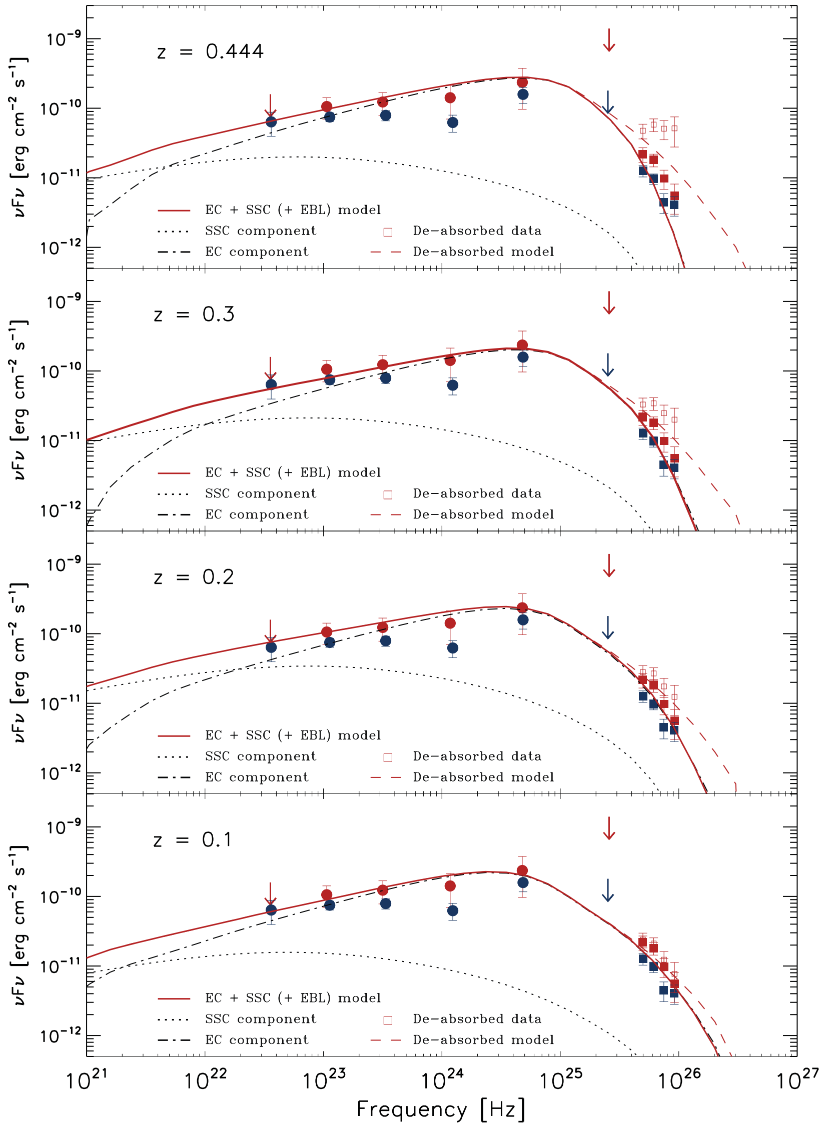

Figure 8. EC+SSC model for redshifts z =0.444, 0.3, 0.2, and 0.1 from top to bottom. The individual EBL-absorbed EC and SSC components are indicated as dash-dotted and dotted lines, respectively. The sum is shown as a solid red line (dashed when de-absorbed). The best agreement between the model and the data is achieved when the source is located at $z \sim 0.2$.

Table 4
Parameters Used for the SSC Models Displayed in Figure 7

Model Parameter	$z = 0.1$	$z = 0.2$	$z = 0.3$	$z = 0.444$
Low-energy cutoff, $\gamma_{\rm min}$	1.8×10^4	2.0×10^4	2.2×10^4	2.5×10^4
High-energy cutoff, $\gamma_{\rm max}$	3.0×10^5	4.0×10^5	4.0×10^5	5.0×10^5
Injection index, q	2.9	2.9	3.0	3.0
Injection luminosity, L_e (10^{45} erg s^{-1})	1.3	3.3	5.7	12.8
Comoving magnetic field, B (G)	0.03	0.02	0.02	0.01
Poynting flux, L_B (10^{42} erg s^{-1})	1.1	4.9	8.5	13.7
$\epsilon_B \equiv L_B/L_e$	0.9×10^{-3}	1.5×10^{-3}	1.5×10^{-3}	1.1×10^{-3}
Doppler factor (D)	30	30	40	50
Plasmoid radius, R_B (10^{16} cm)	2.2	6.0	7.0	11
Variability timescale, $\delta t_{\rm var}^{\rm min}$ (hr)	7.4	22.1	21.1	29.4
Weighted sum of squared residuals to VERITAS *flare* data	7.1	0.9	0.7	6.2
Weighted sum of squared residuals to *Fermi*-LAT *flare* data	1.6	1.6	1.3	1.4
Total weighted sum of squared residuals	8.7	2.5	1.9	7.6

Notes. All SSC models require very low magnetic fields, far below the value expected from equipartition (i.e., $\epsilon_B \ll 1$). The weighted sum of squared residuals to the VERITAS and *Fermi*-LAT data and the total value for the combined data set are included at the bottom of the table. The best agreement between the model and the data is obtained when the source is at redshift $z = 0.2$–0.3.

Table 5
Parameters Used for the EC+SSC Model Fits Displayed in Figure 8

Model Parameter	$z = 0.1$	$z = 0.2$	$z = 0.3$	$z = 0.444$
Low-energy cutoff, $\gamma_{\rm min}$	5.5×10^3	7.0×10^3	6.5×10^3	6.0×10^3
High-energy cutoff, $\gamma_{\rm max}$	1.2×10^5	$1.51.2 \times 10^5$	$1.51.2 \times 10^5$	$1.51.2 \times 10^5$
Injection index, q	3.0	3.0	3.0	3.0
Injection luminosity, L_e (10^{44} erg $\rm s^{-1}$)	1.1	4.2	6.0	10.4
Comoving magnetic field, B (G)	0.35	0.22	0.21	0.23
Poynting flux, L_B (10^{43} erg $\rm s^{-1}$)	1.0	2.4	6.0	11.2
$\epsilon_B \equiv L_B/L_e$	0.10	0.06	0.10	0.11
Doppler factor, D	30	30	40	50
Plasmoid radius, R_B (10^{16} cm)	0.5	1.2	1.5	1.5
Variability timescale, $\delta t_{\rm var}^{\rm min}$ (hr)	1.7	4.4	4.5	4.0
Ext. radiation energy density (10^{-6} erg $\rm cm^{-3}$)	5.4	2.4	1.2	1.3
Weighted sum of squared residuals to VERITAS *flare* data	4.8	3.6	7.9	15.7
Weighted sum of squared residuals to *Fermi*-LAT *flare* data	1.0	1.2	0.8	1.5
Total weighted sum of squared residuals	5.8	4.8	8.7	17.2

Notes. These model fits require magnetic fields closer to equipartition and allow for the intra-night variability observed in the optical data. The weighted sum of squared residuals to the VERITAS and *Fermi*-LAT data and the total value for the combined data set are included at the bottom of the table.

and for magnetic fields within about an order of magnitude of, though still below, equipartition. It is worth noting that the results presented here agree with the findings following the ($E > 200$ GeV) flare of blazar W Comae (also an ISP) in 2008 March (Acciari et al. 2008a). In both cases, the high optical luminosity is expected to play a key role in providing the seed population for IC scattering.

Intermediate synchrotron peaked blazars like 3C 66A are well suited for simultaneous observations by *Fermi*-LAT and ground-based IACTs like VERITAS. Relative to the sensitivities of these instruments, ISPs are bright enough to allow for time-resolved spectral measurements in each band during flaring episodes. These types of observations coupled with extensive multi-wavelength coverage at lower energies will continue to provide key tests of blazar emission models.

The *Fermi*-LAT Collaboration acknowledges generous ongoing support from a number of agencies and institutes that have supported both the development and the operation of the LAT as well as scientific data analysis. These include the National Aeronautics and Space Administration and the Department of Energy in the United States, the Commissariat à l'Energie Atomique and the Centre National de la Recherche Scientifique/Institut National de Physique Nucléaire et de Physique des Particules in France, the Agenzia Spaziale Italiana and the Istituto Nazionale di Fisica Nucleare in Italy, the Ministry of Education, Culture, Sports, Science and Technology (MEXT), High Energy Accelerator Research Organization (KEK) and Japan Aerospace Exploration Agency (JAXA) in Japan, and the K. A. Wallenberg Foundation, the Swedish Research Council and the Swedish National Space Board in Sweden. Additional support for science analysis during the operations phase is gratefully acknowledged from the Istituto Nazionale di Astrofisica in Italy and the Centre National d'Études Spatiales in France.

The VERITAS collaboration acknowledges the generous support from the US Department of Energy, the US National Science Foundation, and the Smithsonian Institution, by NSERC in Canada, by Science Foundation Ireland, and by STFC in UK. The VERITAS collaboration also acknowledges the excellent work of the technical support staff at the FLWO and the collaborating institutions in the construction and operation of the instrument, as well as support from the NASA/*Swift* guest investigator program (grant NNX08AU13G) for the *Swift* observations.

PAIRITEL is operated by the Smithsonian Astrophysical Observatory (SAO) and was made possible by a grant from the Harvard University Milton Fund, a camera loan from the University of Virginia, and continued support of the SAO and UC Berkeley. The PAIRITEL project is further supported by NASA/*Swift* Guest Investigator grant NNG06GH50G. This research is partly based on observations with the 100 m telescope of the MPIfR (Max-Planck-Institut für Radioastronomie) at Effelsberg and has also made use of observations with the IRAM 30 m telescope. The Metsähovi team acknowledges the support from the Academy of Finland. The Abastumani Observatory team acknowledges financial support by the Georgian National Science Foundation through grant GNSF/ST08/4-404. The St. Petersburg University team acknowledges support from Russian RFBR foundation via grant 09-02-00092. AZT-24 observations are made within an agreement between Pulkovo, Rome, and Teramo observatories.

L. C. Reyes acknowledges the support by the Kavli Institute for Cosmological Physics at the University of Chicago through grants NSF PHY-0114422 and NSF PHY-0551142 and an endowment from the Kavli Foundation and its founder Fred Kavli. M. Böttcher acknowledges support from NASA through *Chandra* Guest Investigator Grant GO8-9100X. Some of the VERITAS simulations used in this work have been performed on the joint Fermilab-KICP supercomputing cluster, supported by grants from Fermilab, the Kavli Institute for Cosmological Physics, and the University of Chicago.

REFERENCES

Abdo, A. A., et al. 2009a, Science, 325, 848
Abdo, A. A., et al. 2009b, ApJ, 707, 1310
Abdo, A. A., et al. 2010a, ApJS, 188, 405
Abdo, A. A., et al. 2010b, ApJ, 710, 1271
Abdo, A. A., et al. 2010c, ApJ, 716, 30
Acciari, V. A., et al. 2008a, ApJ, 684, L73

Acciari, V. A., et al. 2008b, ApJ, 679, 1427
Acciari, V. A., et al. 2009, ApJ, 693, L104
Aliu, E., et al. 2009, ApJ, 692, L29
Angelakis, E., Fuhrmann, L., Marchili, N., Krichbaum, T. P., & Zensus, J. A. 2008, Mem. Soc. Astron. Ital., 79, 1042
Arnaud, K. A. 1996, in ASP Conf. Ser. 101, Astronomical Data Analysis Software and Systems V, ed. G. H. Jacoby & J. Barnes (San Francisco, CA: ASP), 17
Atwood, W. B., et al. 2009, ApJ, 697, 1071
Bennett, A. S. 1962, Mem. R. Astron. Soc, 68, 163
Bloom, J. S., Starr, D. L., Blake, C. H., Skrutskie, M. F., & Falco, E. E. 2006, in ASP Conf. Ser. 351, Astronomical Data Analysis Software and Systems XV, ed. C. Gabriel, C. Arviset, D. Ponz, & S. Enrique (San Francisco, CA: ASP), 751
Böttcher, M. 2007, Ap&SS, 309, 95
Böttcher, M., & Chiang, J. 2002, ApJ, 581, 127
Böttcher, M., & Dermer, C. D. 2002, ApJ, 564, 86
Böttcher, M., et al. 2009, ApJ, 694, 174
Bramel, D. A., et al. 2005, ApJ, 629, 108
Britzen, S., et al. 2007, A&A, 472, 763
Britzen, S., et al. 2008, A&A, 484, 119
Cavaliere, A., & D'Elia, V. 2002, ApJ, 571, 226
Dermer, C. D., & Schlickeiser, R. 1993, ApJ, 416, 458
Dickey, J. M., & Lockman, F. J. 1990, ARA&A, 28, 215
Edelson, R. A., & Krolik, J. H. 1988, ApJ, 333, 646
Finke, J. D., Razzaque, S., & Dermer, C. D. 2010, ApJ, 712, 238
Finke, J. D., Shields, J. C., Böttcher, M., & Basu, S. 2008, A&A, 477, 513
Fitzpatrick, E. L. 1999, PASP, 111, 63
Franceschini, A., Rodighiero, G., & Vaccari, M. 2008, A&A, 487, 837
Fuhrmann, L., Zensus, J. A., Krichbaum, T. P., Angelakis, E., & Readhead, A. C. S. 2007, in AIP Conf. Proc. 921, The First GLAST Symposium, ed. S. Ritz, P. Michelson, & C. A. Meegan (Melville, NY: AIP), 249
Fuhrmann, L., et al. 2008, A&A, 490, 1019
Gehrels, N., et al. 2004, ApJ, 611, 1005
Georganopoulos, M., & Kazanas, D. 2003, ApJ, 594, L27
Georganopoulos, M., & Kazanas, D. 2004, ApJ, 604, L81
Ghisellini, G., & Madau, P. 1996, MNRAS, 280, 67
Ghisellini, G., Tavecchio, F., & Chiaberge, M. 2005, A&A, 432, 401
Gilmore, R. C., Madau, P., Primack, J. R., Somerville, R. S., & Haardt, F. 2009, MNRAS, 399, 1694
Hartman, R. C., et al. 1999, ApJS, 123, 79
Henri, G., & Saugé, L. 2006, ApJ, 640, 185
Jorstad, S. G., Marscher, A. P., Mattox, J. R., Wehrle, A. E., Bloom, S. D., & Yurchenko, A. V. 2001, ApJS, 134, 181
Joshi, M., & Böttcher, M. 2007, ApJ, 662, 884
Kataoka, J., et al. 1999, Astropart. Phys., 11, 149
Kerrick, A. D., et al. 1995, ApJ, 452, 588
Kinney, A. L., Bohlin, R. C., Blades, J. C., & York, D. G. 1991, ApJS, 75, 645
Kuiper, L., Hermsen, W., Verbunt, F., Thompson, D. J., Stairs, I. H., Lyne, A. G., Strickman, M. S., & Cusumano, G. 2000, A&A, 359, 615
Larionov, V. M., et al. 2008, ATel, 1755, 1
Li, T.-P., & Ma, Y.-Q. 1983, ApJ, 272, 317
Mackay, C. D. 1971, MNRAS, 154, 209
Marscher, A. P., Jorstad, S. G., Mattox, J. R., & Wehrle, A. E. 2002, ApJ, 577, 85
Mattox, J. R., et al. 1996, ApJ, 461, 396
Miller, J. S., French, H. B., & Hawley, S. A. 1978, Proc. Pittsburgh Conf. on BL Lac Objects, ed. A. M. Wolfe, 176
Mücke, A., Protheroe, R. J., Engel, R., Rachen, J. P., & Stanev, T. 2003, Astropart. Phys., 18, 593
Northover, K. J. E. 1973, MNRAS, 165, 369
Oke, J. B., et al. 1995, PASP, 107, 375
Piner, B. G., Pant, N., & Edwards, P. G. 2008, ApJ, 678, 64
Poole, T. S., et al. 2008, MNRAS, 383, 627
Prandini, E., Bonnoli, G., Maraschi, L., Mariotti, M., & Tavecchio, F. 2010, MNRAS, 405, L76
Reimer, A., Joshi, M., & Böttcher, M. 2008, in AIP Conf. Ser. 1085, High Energy Gamma-Ray Astronomy, ed. F. A. Aharonian, W. Hofmann, & F. Rieger (Melville, NY: AIP), 502
Savolainen, T., Homan, D. C., Hovatta, T., Kadler, M., Kovalev, Y. Y., Lister, M. L., Ros, E., & Zensus, J. A. 2010, A&A, 512, A24
Schlegel, D. J., Finkbeiner, D. P., & Davis, M. 1998, ApJ, 500, 525
Sikora, M., Begelman, M. C., & Rees, M. J. 1994, ApJ, 421, 153
Smith, H. E., Smith, E. O., & Spinrad, H. 1976, PASP, 88, 621
Stecker, F. W., Malkan, M. A., & Scully, S. T. 2006, ApJ, 648, 774 (erratum 658, 1392 [2007])
Swordy, S. 2008, ATel, 1753, 1
Tavecchio, F., & Ghisellini, G. 2009, MNRAS, 394, L131
Taylor, G. B., Vermeulen, R. C., Readhead, A. C. S., Pearson, T. J., Henstock, D. R., & Wilkinson, P. N. 1996, ApJS, 107, 37
Thompson, D. J., et al. 1993, ApJS, 86, 629
Tosti, G. 2008, ATel, 1759, 1
Urry, C. M., & Padovani, P. 1995, PASP, 107, 803
Villata, M., et al. 2008, A&A, 481, L79
Villata, M., et al. 2009, A&A, 504, L9
Weekes, T. C. 2000, in AIP Conf. Ser. 515, GeV–TeV Gamma Ray Astrophysics Workshop: Towards a Major Atmospheric Cherenkov Detector VI, ed. B. L. Dingus, M. H. Salamon, & D. B. Kieda (Melville, NY: AIP), 3
Wills, B. J., & Wills, D. 1974, ApJ, 190, L97
Wurtz, R., Stocke, J. T., & Yee, H. K. C. 1996, ApJS, 103, 109

The Astronomical Journal, 141:32 (8pp), 2011 February
doi:10.1088/0004-6256/141/2/32

BVRI PHOTOMETRY OF 53 UNUSUAL ASTEROIDS

Q.-z. Ye[1]
Department of Atmospheric Sciences, School of Environmental Science and Engineering, Sun Yat-sen University, Guangzhou, China; tom6740@gmail.com
Received 2010 July 4; accepted 2010 November 3; published 2010 December 29

ABSTRACT

We present the results of *BVRI* photometry and classification of 53 unusual asteroids, including 35 near-Earth asteroids (NEAs), 6 high eccentricity/inclination asteroids, and 12 recently identified asteroid-pair candidates. Most of these asteroids were not classified prior to this work. For the few asteroids that have been previously studied, the results are generally in agreement. In addition to observing and classifying these objects, we merge the results from severalphotometric/spectroscopic surveys to create the largest-ever sample with 449 spectrally classified NEAs for statistical analysis. We identify a "transition point" of the relative number of C/X-like and S-like NEAs at $H \sim 18 \Leftrightarrow D \sim 1$ km with confidence level at ~95% or higher. We find that the C/X-like:S-like ratio for $18 \leqslant H < 22$ is about twice as high as that of $H < 18$ (0.33 ± 0.04 versus 0.17 ± 0.02), virtually supporting the hypothesis that smaller NEAs generally have less weathered surfaces (therefore less reddish appearance) due to younger collision ages.

Key words: minor planets, asteroids: general – techniques: photometric

1. INTRODUCTION

The origin of unusual asteroid groups, such as the near-Earth asteroids (NEAs) and paired-asteroid candidates (Vokrouhlický & Nesvorný 2008; Pravec & Vokrouhlický 2009), has attracted much research interest in recent years. A good way to understand this phenomenon is to spectrally classify as many individuals as possible (e.g., Binzel et al. 1996). Since the 1980s, around a dozen photometric and spectroscopic surveys aimed at determining taxonomic distributions of asteroids of different categories have been carried out (Table 1) and spectral classifications for a few hundred NEAs have been derived as a result. However, among the >7,500 known NEAs, high eccentricity/inclination asteroids, and a few dozen proposed paired-asteroid candidates, the fraction of classified objects is still small (around 5%), and it is even lower (~1%) for those with measured physical characteristics (albedo, diameter, mineralogy, etc.).

Recent studies have suggested that the characteristics of sub-kilometer-size NEAs may be very different from those of kilometer-size NEAs (see Trilling et al. 2010, for an overview), and for a decade an overabundance of C/X-like (or neutral colored) asteroids among small NEAs has been noted (Rabinowitz 1998). Compared with other investigations that generally require fine spectroscopic information and albedo measurement, the issue of overabundance of small C/X-like asteroids is relatively easy to address, since only crude classification is required. However, previous studies (such as Dandy et al. 2003; Binzel et al. 2004) could not reach any firm conclusions due to the lack of data on sub-kilometer-size NEAs.

On the other hand, the recently identified paired-asteroid candidates are likely to be of common origin (Pravec & Vokrouhlický 2009). Convincing evidence to support this hypothesis would be if both components within a pair were proven to have identical classification. However, physical observations of almost all paired-asteroid candidates have been unavailable until now.

A method that combines visual/near-infrared spectroscopy and thermal infrared measurement is preferred among all practical ground-based methods as it provides the highest accuracy as well as the most complete information on a target in most cases, but it is also very time consuming and generally requires medium-sized or large telescopes. In contrast, broadband *BVRI* photometry may only allow crude classification, but it is more efficient than spectroscopy as it does not require as much time and effort as the latter, and the results are useful for preliminary diagnostic purposes. In this study, we employed this method to investigate some unusual asteroids. Most of these asteroids had not been classified prior to the observational phase of this work. A description of the observation procedure, data reduction, and details of the classification are presented in Sections 2 and 3. We then compare and merge our results with other reported studies to assess the consistency between our and others' results (Section 4.1) and investigate the degree of consistency with theoretical expectations (Sections 4.2 and 4.3).

2. OBSERVATION

The Lulin One-meter Telescope (LOT) at Lulin Observatory, Taiwan, was employed for this study, except for one asteroid, 2008 EV5, which was observed with the 0.41 m telescope at the same observatory. The 0.41 m telescope observations for 2008 EV5 were made in 2009 January with the 2048 × 2048 U42 CCD, while the LOT observations were all made during the observation runs in the dark period of 2010 January except (143651) 2003 QO104, which was observed in 2009 April, with the 1340 × 1300 PI-1300B CCD and a 0.5 × focal reducer. A broadband Bessell *BVRI* filter system was used on both telescopes, with wavelengths centered at 442, 540, 647, and 786 nm, respectively.

Landolt standard stars (Landolt 1992) are preferred in optical photometry because they guarantee the highest accuracy (better than 0.01–0.02 mag) in most cases. However, as Landolt standard stars are only available to a very limited region, in most situations one needs to know the atmospheric extinction coefficient by observing standard stars in different airmass to work on targets located far from Landolt fields. As we were unable to observe enough Landolt standard stars to obtain a secure extinction coefficient throughout each observing night, an alternative approach, introduced by Warner (2007), was employed. Warner applied third-order polynomials on his

[1] Current address: 404, 12 Huasheng Street, Guangzhou, China.

Table 1
Photometric/Spectroscopic NEA Surveys Conducted Over the Last Decade

Publication	Observation Period	NEA Sample Size	Method
de León et al. (2010)	2002–2007	77	VIS/NIR[a] spectroscopy
Fevig & Fink (2007)	1997–1998, 2004	55	VIS[b] spectroscopy
Michelsen et al. (2006)	2003	12	VIS spectroscopy
SINEO (Lazzarin et al. 2005)	2002–2004	36	VIS/NIR spectroscopy
SMASS (Binzel et al. 2004; Bus & Binzel 2002)	1994–2002	310	VIS spectroscopy
Dandy et al. (2003)	2000–2001	56	Broadband *BVRIZ* photometry
S^3OS^2 (Angeli & Lazzaro 2002)	1996–2001	12	VIS spectroscopy

Notes.
[a] VIS stands for visual channel (about 390–750 nm) while NIR stands for near-infrared channel (about 700–3000 nm).
[b] Although the study is labeled as visual and near-infrared spectroscopy in that publication, it only covers the near-infrared channel to 1000 nm, so it is considered as visual spectroscopy in this summary.

Table 2
Comparison of *VRI* Photometry of M67 (NGC 2682) between This Work and Taylor et al. (2008)

Star	$V-R$ of Taylor et al.	$V-I$ of Taylor et al.	Date Observed	Airmass	$V-R$ by This Study	$V-I$ by This Study
NGC 2682 F132	0.350 ± 0.003	0.679 ± 0.006	2010 Jan 12	1.69	0.336 ± 0.011	0.676 ± 0.023
			2010 Jan 13	1.34	0.342 ± 0.003	0.677 ± 0.007
NGC 2682 I51	0.336 ± 0.003	0.671 ± 0.007	2010 Jan 12	1.69	0.331 ± 0.016	0.651 ± 0.024
			2010 Jan 13	1.34	0.334 ± 0.007	0.655 ± 0.010

optical observations of 128 carefully chosen Landolt standard stars to find the conversion terms between the Two Micron All Sky Survey (2MASS) *JHK* system (Skrutskie et al. 2006) and the Landolt system. The errors in Warner's method are 0.034 for $B-V$ and $V-I$ and 0.021 for $V-R$. The fields of view for the LOT and the 0.41 m telescope are $22' \times 22'$ and $47' \times 47'$, respectively, which are large enough to include enough 2MASS catalog stars for setting up a good in-field transformation. To assess the accuracy of Warner's method, we observed a few stars in M67 (NGC 2682) and derived their colors following the procedure described by Warner, then compared them once results from another high-precision *VRI* photometric procedure (Taylor et al. 2008). The resulting accuracy was better than 0.02 mag in $V-R$ and $V-I$ (Table 2).

The targets were all observed in an airmass of $X \leqslant 2$ with predicted visual magnitude brighter than 19.0. Observational details and basic information for each target are given in Tables 3 and 4 for NEAs/high eccentricity (inclination) objects and paired-asteroid candidates. The exposure sequence for all targets was $B-R-V-I$ to minimize the error produced by significant brightness variation. Image frames were then bias-subtracted and flat-fielded, and the fringing effects in the *I*-band images were also removed.

The raw observations were then inspected manually to exclude bad cases, such as the target asteroid crossing over or passing very close to background stars, or low signal-to-noise ratio (S/N) caused by unstable weather conditions. Photometric measurements were then performed with Warner's software *MPO Canopus*. At least 10 background stars with known 2MASS magnitudes were used to derive the transformation coefficient between instrumental magnitude and standard magnitude for each field. In a very few cases, the limited number of background stars could not guarantee derivation of a good transform, so coefficients derived from observations obtained on the same night with a similar airmass ($\Delta X \lesssim 0.05$) were used instead. Although each target was planned to be observed 3–5 times, various factors (such as target/star encounter, unstable weather, and/or instrument problems) prevented us from doing so, and for some targets only one observation of each filter was obtained. These results need to be treated with caution.

3. CLASSIFICATION

Observations of 53 asteroids were obtained and reduced following the procedure described in Section 2, including 35 NEAs,[2] 6 high eccentricity/inclination asteroids, and 12 main-belt paired-asteroid candidates. The objects were then classified using Dandy et al.'s (2003) derivation of the Tholen taxonomy (Tholen 1984), intentded for optical broadband photometry.[3] We note that the spectral appearances of C-, B-, F-, G-, and X-class are fairly close, making it difficult to classify them uniquely by broadband photometry, so all objects with colors similar to these classes were considered as X-class. The only exception is that the object shown to be particularly blue ($B-V \ll 0.75$) can be considered as B-class with some confidence.

For each object, the second central moment about the $B-V$, $V-R$, and $V-I$ magnitudes from the typical colors for each taxonomic class was computed, and the class with minimum second central moment was assigned as the object's class. In some cases, the error range of the colors covered more than one class and/or the second central moment of several classes was very close, so multiple classes were assigned to this object with the first class being the most probable. In two cases, (13732) Woodall and (228747) 2002 VH3, only a very crude classification (C/X-like or S-like) could be made due to low-quality observations (see Section 4.3 for details). When the second central moment of the most probable class for a particular object was large ($\gtrsim 0.003$), a "(u)" was appended to indicate that this classification may be uncertain.

[2] We also obtained the *BV* magnitude for (143947) 2003 YQ117 and *BVRI* magnitude for (214088) 2004 JN13, suggesting R/S and A-type classification for these two objects, but as the raw images suffered from bad seeing conditions, resulting in uncertainty at the level of 0.2 mag, these two measurements are excluded in our formal result.

[3] It should be noted that Dandy et al.'s derivation was used for their KPNO *B* and Harris *VRI* filter system, which is slightly different (the differences in wavelength centers are up to 2.5%) from the Bessell *BVRI* system applied in this study.

Table 3
Observational Details of the Observed NEAs and High Eccentricity/Inclination Objects

Object	H	Orbit	Date Observed	V_{obs}	Exp. Time	Cycle	Tot. Time
(5604) 1992 FE	16.4	ATE	2010 Jan 13	19.4	60 s	5	40 minutes
(5653) Camarillo	15.4	AMO	2010 Jan 13	18.5	60 s	5	40 minutes
(16868) 1998 AK8	16.6	UNU	2010 Jan 13	17.3	30 s	3	16 minutes
(20898) Fountainhills	11.0	UNU	2010 Jan 8	14.7	60 s	5	39 minutes
(21088) 1992 BL2	14.2	AMO	2010 Jan 8, 13	17.4, 17.4	60 s, 60 s	5, 5	39 minutes, 40 minutes
(24761) Ahau	17.4	APO	2010 Jan 8	15.6	20 s	3	15 minutes
(35432) 1998 BG9	19.3	AMO	2010 Jan 13	18.9	30 s	3	24 minutes
(38086) Beowulf	17.1	APO	2010 Jan 13	18.2	30 s	2	11 minutes
(54789) 2001 MZ7	14.8	AMO	2010 Jan 8	14.6	30 s	5	30 minutes
(66251) 1999 GJ2	17.0	AMO	2010 Jan 13	18.2	90 s	2	18 minutes
(68216) 2001 CV26	16.3	APO	2010 Jan 8	17.6	30 s	3	22 minutes
(86067) 1999 RM28	16.4	AMO	2010 Jan 8	17.1	30 s	3	17 minutes
(96177) 1984 BC	16.0	UNU	2010 Jan 13	17.7	2 minutes	5	58 minutes
(99248) 2001 KY66	16.2	APO	2010 Jan 13	19.0	90 s	4	39 minutes
(103067) 1999 XA143	16.6	APO	2010 Jan 8	16.8	30 s	5	30 minutes
(122180) 2001 KV43	17.3	AMO	2010 Jan 10, 12	18.1, 18.3	3 minutes, 3 minutes	5, 2	56 minutes, 37 minutes
(137805) 1999 YK5	16.6	ATE	2010 Jan 8	17.5	30 s	5	30 minutes
(137925) 2000 BJ19	15.8	APO	2010 Jan 10, 12	19.0, 18.7	60 s	5, 5	22 minutes, 14 minutes
(138937) 2001 BK16	17.3	APO	2010 Jan 10, 12	17.4, 17.7	30 s, 30 s	5, 3	22 minutes, 7 minutes
(143651) 2003 QO104	16.0	AMO	2009 Apr 24	16.6	60 s	9	59 minutes
(152742) 1998 XE12	19.1	ATE	2010 Jan 10, 12	18.2, 18.0	30 s, 30 s	5, 5	22 minutes, 14 minutes
(159402) 1999 AP10	16.0	AMO	2010 Jan 8	15.7	30 s	5	30 minutes
(162566) 2000 RJ34	15.2	AMO	2010 Jan 12	18.9	60 s	5	39 minutes
(162998) 2001 SK162	17.9	AMO	2010 Jan 10	18.6	60 s	3	17 minutes
(230111) 2001 BE10	19.1	ATE	2010 Jan 10, 12	17.7, 17.7	20 s, 20 s	1, 3	2 minutes, 28 minutes
2002 LV	16.6	APO	2010 Jan 9	18.1	60 s	5	40 minutes
2003 SM4	15.4	UNU	2010 Jan 9	19.0	90 s	3	28 minutes
2004 NZ8	16.1	UNU	2010 Jan 9	18.3	2 minutes	5	58 minutes
2004 TB18	17.8	APO	2010 Jan 12	18.2	20 s	4	21 minutes
2004 XD50	18.5	AMO	2010 Jan 9	17.6	30 s	4	24 minutes
2005 EN36	17.2	UNU	2010 Jan 8, 9	17.5, 17.5	2 minutes, 2 minutes	1, 5	6 minutes, 58 minutes
2005 MC	16.6	AMO	2010 Jan 8	16.5	30 s	3	18 minutes
2006 UR	19.4	AMO	2010 Jan 8	16.4	30 s	2	11 minutes
2006 YT13	18.4	APO	2010 Jan 10	18.1	20 s	5	20 minutes
2007 MK13	20.0	APO	2010 Jan 8	17.2	30 s	3	43 minutes
2007 UR3	21.2	AMO	2010 Jan 9	17.7	60 s	5	39 minutes
2008 EV5	20.0	ATE	2009 Jan 4	14.7	20 s	5	10 minutes
2008 YZ32	20.1	APO	2010 Jan 9	17.3	20 s	5	15 minutes
2009 UV18	16.0	AMO	2010 Jan 9	18.3	30 s	5	30 minutes
2009 XR2	18.6	AMO	2010 Jan 9	16.5	30 s	3	17 minutes
2010 AE30	23.6	APO	2010 Jan 9	18.5	60 s	2	39 minutes

Notes. The absolute magnitude H for each object is obtained from the Minor Planet Center Orbit Database (MPCORB). The orbit types are classified as follows: main-belt asteroids (MBA), Atens (ATE), Apollos (APO), and Amors (AMO). Asteroids with $e > 0.4$ and/or $i > 40°$ but which do not fall into the category of NEAs ($q < 1.3$) are classified as unusual objects (UNU). The visual magnitude V_{obs} given here is the mean value of the V-band observations.

Table 4
Observational Details of the Observed Paired-asteroid Candidates

Object	H	Companion	Date Observed	V_{obs}	Exp. Time	Cycle	Tot. Time
(1979) Sakharov	13.5	(13732) Woodall[a]	2010 Jan 12, 13	18.8, 18.8	90 s, 90 s	1, 1	7 minutes, 5 minutes
(2110) Moore-Sitterly	13.8	(44612) 1999 RP27	2010 Jan 10	18.4	2 minutes	5	42 minutes
(4765) Wasserburg	14.1	2001 XO105	2010 Jan 9	16.9	60 s	3	23 minutes
(5026) Martes	12.9	2005 WW113	2010 Jan 10	18.6	60 s	1	11 minutes
(11842) Kap'bos	13.8	(228747) 2002 VH3[a]	2010 Jan 9	18.5	60 s	5	39 minutes
(13732) Woodall	14.4	(1979) Sakharov[a]	2010 Jan 10	18.7	90 s	4	29 minutes
(15107) Toepperwein	14.3	2006 AL54	2010 Jan 10, 12	18.5, 18.5	2 minutes, 2 minutes	5, 2	43 minutes, 9 minutes
(25884) 2000 SQ4	14.6	(48527) 1993 LC1	2010 Jan 10	18.5	150 s	2	14 minutes
(52852) 1998 RB75	14.6	2003 SC7	2010 Jan 12	18.7	5 minutes	5	115 minutes
(54041) 2000 GQ113	14.5	2002 TO134	2010 Jan 10	18.6	2 minutes	2	12 minutes
(56048) 1998 XV39	15.0	(76148) 2000 EP17	2010 Jan 10, 12	17.4, 18.4	3 minutes, 3 minutes	5, 5	54 minutes, 37 minutes
(228747) 2002 VN3	16.5	(11842) Kap'bos[a]	2010 Jan 9	18.8	2 minutes	3	33 minutes

Notes. The absolute magnitude H for each object is obtained from the Minor Planet Center Orbit Database (MPCORB). The visual magnitude V_{obs} given here is the mean value of the V-band observations.
[a] The companion of this object is also observed in this study.

Table 5
Photometry and Classification Results of Observed NEAs and High Eccentricity/Inclination Objects

Object	Date Observed	V_{obs}	Class (This Work)	Previous Class	$B-V$	$V-R$	$V-I$	Albedo
(5604) 1992 FE	2010 Jan 13	19.4	VQXR	V[a]		0.439 ± 0.077	0.679 ± 0.083	0.38–0.69[b]
(5653) Camarillo	2010 Jan 13	18.5	S	Sq[c]	0.985 ± 0.062	0.465 ± 0.050	0.893 ± 0.048	
(16868) 1998 AK8	2010 Jan 13	17.3	S		0.908 ± 0.031	0.443 ± 0.014	0.857 ± 0.002	
(20898) Fountainhills	2010 Jan 8	14.7	X		0.767 ± 0.008	0.428 ± 0.010	0.826 ± 0.008	
(21088) 1992 BL2	2010 Jan 8	17.4	S	Sl[c]	0.972 ± 0.048	0.490 ± 0.006	0.913 ± 0.015	
	2010 Jan 13	17.4			0.919 ± 0.055	0.438 ± 0.014	0.907 ± 0.028	
(24761) Ahau	2010 Jan 8	15.6	S		0.835 ± 0.023	0.469 ± 0.008	0.872 ± 0.002	
(35432) 1998 BG9	2010 Jan 13	18.9	A			0.547 ± 0.030	0.913 ± 0.045	
(38086) Beowulf	2010 Jan 13	18.2	R(u)		0.999 ± 0.020	0.447 ± 0.018	0.645 ± 0.098	0.37[b]
(54789) 2001 MZ7	2010 Jan 8	14.6	X	X[d], G[e]	0.707 ± 0.011	0.389 ± 0.004	0.711 ± 0.002	
(66251) 1999 GJ2	2010 Jan 13	18.2	S	Sa[c], Sa[e]	0.976 ± 0.088	0.448 ± 0.036	0.844 ± 0.021	
(68216) 2001 CV26	2010 Jan 8	17.6	R		0.916 ± 0.036	0.479 ± 0.007	0.811 ± 0.025	
(86067) 1999 RM28	2010 Jan 8	17.1	S(u)		0.996 ± 0.069	0.499 ± 0.018	0.881 ± 0.021	
(96177) 1984 BC	2010 Jan 13	17.7	S		0.864 ± 0.045	0.484 ± 0.018	0.921 ± 0.019	
(99248) 2001 KY66	2010 Jan 13	19.0	ST		0.865 ± 0.048	0.455 ± 0.041	0.998 ± 0.072	
(103067) 1999 XA143	2010 Jan 8	16.8	S		0.925 ± 0.029	0.458 ± 0.011	0.878 ± 0.009	
(122180) 2001 KV43	2010 Jan 10	18.1	S		0.894 ± 0.067	0.508 ± 0.036		
	2010 Jan 12	18.3					0.915 ± 0.072	
(137805) 1999 YK5	2010 Jan 8	17.5	RQ	X[a]	0.908 ± 0.035	0.390 ± 0.051	0.704 ± 0.036	
(137925) 2000 BJ19	2010 Jan 10	19.0	STD	Q[a]	0.756 ± 0.135	0.508 ± 0.079		
	2010 Jan 12	18.7					0.915 ± 0.072	
(138937) 2001 BK16	2010 Jan 10	17.4	X		0.648 ± 0.067	0.369 ± 0.034		0.21[b]
	2010 Jan 12	17.7					0.565 ± 0.082	
(143651) 2003 QO104	2009 Apr 24	16.6	R	RS[e]	0.903 ± 0.008	0.454 ± 0.011	0.797 ± 0.019	
(152742) 1998 XE12	2010 Jan 10	18.2	RS		0.898 ± 0.100	0.460 ± 0.062		
	2010 Jan 12	18.0					0.825 ± 0.043	
(159402) 1999 AP10	2010 Jan 8	15.7	S(u)	S[f]	0.983 ± 0.023	0.485 ± 0.007	0.868 ± 0.009	0.34[b]
(162566) 2000 RJ34	2010 Jan 12	18.9	X		0.755 ± 0.136	0.400 ± 0.032	0.836 ± 0.047	
(162998) 2001 SK162	2010 Jan 10	18.6	XV	T[a]	0.822 ± 0.139	0.386 ± 0.018		
(230111) 2001 BE10	2010 Jan 10	17.7	R		0.929	0.420		
	2010 Jan 12	17.7			0.982 ± 0.087	0.496 ± 0.035	0.870 ± 0.095	
2002 LV	2010 Jan 9	18.1	QX		0.772 ± 0.144	0.425 ± 0.039	0.719 ± 0.046	0.15[b]
2003 SM4	2010 Jan 9	19.0	V			0.387 ± 0.052	0.602 ± 0.055	
2004 NZ8	2010 Jan 9	18.3	X		0.704 ± 0.085	0.404 ± 0.027	0.707 ± 0.028	
2004 TB18	2010 Jan 12	18.2	AS			0.510 ± 0.084	1.000 ± 0.138	
2004 XD50	2010 Jan 9	17.6	R		0.927 ± 0.030	0.458 ± 0.005	0.791 ± 0.025	
2005 EN36	2010 Jan 8	17.5	X		0.701	0.356	0.697	
	2010 Jan 9	17.5			0.737 ± 0.016	0.369 ± 0.010	0.681 ± 0.014	
2005 MC	2010 Jan 8	16.5	X		0.752 ± 0.022	0.413 ± 0.010	0.766 ± 0.010	
2006 UR	2010 Jan 8	16.4	R		0.969 ± 0.097	0.434 ± 0.060	0.754 ± 0.053	
2006 YT13	2010 Jan 10	18.1	AR		1.042 ± 0.088	0.475 ± 0.057		
2007 MK13	2010 Jan 8	17.2	XT	C[f]	0.783 ± 0.016	0.414 ± 0.010	0.838 ± 0.019	
2007 UR3	2010 Jan 9	17.7	X		0.631 ± 0.054	0.381 ± 0.025	0.603 ± 0.044	
2008 EV5	2009 Jan 4	14.7	X		0.722 ± 0.033	0.363 ± 0.010	0.702 ± 0.010	
2008 YZ32	2010 Jan 9	17.3	B		0.535 ± 0.032	0.207 ± 0.055	0.507 ± 0.012	
2009 UV18	2010 Jan 9	18.3	A		0.967 ± 0.094	0.520 ± 0.019	0.957 ± 0.052	
2009 XR2	2010 Jan 9	16.5	R		0.908 ± 0.017	0.484 ± 0.008	0.724 ± 0.031	
2010 AE30	2010 Jan 9	18.5	S		0.862 ± 0.090	0.461 ± 0.010	0.845 ± 0.011	

Notes. The visual magnitude V_{obs} given here is the mean value of the V-band observations. Albedos given by reference b all have uncertainties around a factor of two.
[a] Bus & Binzel (2002); Binzel et al. (2004).
[b] Trilling et al. (2010).
[c] de León et al. (2010).
[d] Lazzarin et al. (2005).
[e] Betzler et al. (2010).
[f] Hicks & Somers (2010).

The colors and classifications for the observed NEAs/high eccentricity (inclination) asteroids and paired-asteroid candidates observed in this study are shown in Tables 5 and 6, respectively. Classification and/or albedo measurement from previous work is also given if available. We note that a total of four objects were observed on different nights; color measurements across these nights with different calibration stars were found to be consistent. Measurements from each night are listed separately and illustrate the accuracy and consistency of our work.

4. DISCUSSION

4.1. Comparisons with Previous Works on NEA Colors

Following the procedure described in Sections 2 and 3, we derived color indices and classifications for 35 NEAs, including

Table 6
Photometry and Classification Results of Observed Paired-asteroid Candidates

Object	Companion	Date Observed	V_{obs}	Class (This Work)	$B - V$	$V - R$	$V - I$
(1979) Sakharov	**(13732) Woodall**	**2010 Jan 12**	**18.8**	**S(u)**		0.407	0.922
		2010 Jan 13	**18.8**		1.086	0.411	
(13732) Woodall	**(1979) Sakharov**	**2010 Jan 10**	**18.7**	**S-like**	0.864 ± 0.147	0.468 ± 0.068	
(2110) Moore-Sitterly	(44612) 1999 RP27	2010 Jan 10	18.4	R	0.956 ± 0.034	0.517 ± 0.033	
(4765) Wasserburg	2001 XO105	2010 Jan 9	16.9	R	0.852 ± 0.043	0.456 ± 0.023	0.813 ± 0.040
(5026) Martes	2005 WW113	2010 Jan 10	18.6	SRQV	0.863 ± 0.042	0.440 ± 0.047	
(11842) Kap'bos	**(228747) 2002 VH3**	**2010 Jan 9**	**18.5**	**R**	1.011 ± 0.088	0.453 ± 0.013	0.792 ± 0.027
(228747) 2002 VH3	**(11842) Kap'bos**	**2010 Jan 9**	**18.8**	**S-like**	0.704 ± 0.154	0.480 ± 0.057	0.829 ± 0.111
(15107) Toepperwein	2006 AL54	2010 Jan 10	18.5	A(u)	0.876 ± 0.079	0.492 ± 0.027	
		2010 Jan 12	18.5				1.016 ± 0.021
(25884) 2000 SQ4	(48527) 1993 LC1	2010 Jan 10	18.5	XT	0.709 ± 0.055	0.432 ± 0.014	
(52852) 1998 RB75	2003 SC7	2010 Jan 12	18.7	S	0.891 ± 0.083	0.488 ± 0.035	0.908 ± 0.079
(54041) 2000 GQ113	2002 TO134	2010 Jan 10	18.6	SRQ	0.871 ± 0.073	0.459 ± 0.027	
(56048) 1998 XV39	(76148) 2000 EP17	2010 Jan 10	17.4	R	0.874 ± 0.039	0.476 ± 0.035	
		2010 Jan 12	18.4				0.770 ± 0.045

Notes. The visual magnitude V_{obs} given here is the mean value of the V-band observations. The pairs with both companions observed are listed in bold characters.

17 Amors, 13 Apollos, and 5 Atens. Among the sample, a total of eight NEAs were classified by previous surveys; it is found that our classifications are generally consistent with them. In addition, we note that a total of six NEAs in our sample were also observed by a recently conducted Warm-Spitzer program (Trilling et al. 2010), with uncertainties around a factor of two unless otherwise specified (see Section 5.3.4 of their paper). Although Warm-Spitzer derives an albedo of the NEAs and does not classify them directly, its observation is a good addition to broadband photometry, especially when the classification is ambiguous. Each case of these cross-observed NEAs is discussed below.

(5604) 1992 FE. The $V - R$ and $V - I$ colors measured from our observation suggested V-, Q-, C-, or R-type classification, with V-type the most likely. This is consistent with the classification made by Binzel et al. (2004) from spectroscopy. Albedo measurement by Delbó et al. (2003) and Warm-Spitzer observation (Trilling et al. 2010) also suggests a high albedo, which that supports a V-type classification.

(5653) Camarillo. The S- and Sq-type classifications suggested by Dandy et al. and de León et al. (2010) are consistent with the S-type classification suggested by our observation.

(21088) 1992 BL2. de León et al. suggested an Sl-type classification which is consistent with the S-type classification suggested by our observation.

(38086) Beowulf. Warm-Spitzer reported an albedo of 0.37 for this object. This is a rough match to our R-type classification according to the debiased mean albedo estimates for R-type NEAs given by Stuart & Binzel (2004), which is 0.340. However, we need to point out that Stuart & Binzel were actually using the average albedo of main-belt asteroids derived from the work of Tedesco et al. (2002), as no albedo measurements of any R-type NEA had been reported (see Section 1.4, Paragraph 3 and Footnote 1 in their paper for details), hence this comparison can be misleading.

(54789) 2001 MZ7. Near-infrared spectroscopy by Lazzarin et al. (2005) reported (54789) 2001 MZ7 to be an X-complex asteroid, while *BVRI* photometry by Betzler et al. (2010) suggested G-type classification. These two results are consistent with the X-type classification made in this study, since the degenerate X-type includes the C and G types. The color indices we measured also match with Betzler et al.'s within 0.03 mag.

(56048) 1998 XV39. Our observation suggested an R-type classification while Sa-type was suggested both by Lazzarin et al. and de León et al. using spectroscopy. We note that (56048) 1998 XV39 appears redder than typical S-type asteroids in our observation (0.770 ± 0.045 in the $V - I$ magnitude versus the criterion of 0.889). As the redness of an Sa-type asteroid iscloser to that of an R-type asteroid than to that of a typical S-type asteroid (see DeMeo et al. 2009, Figure 15), it can be considered that our observation is consistent with the two spectroscopic observations.

(137805) 1999 YK5. Our observation suggested an R- or Q-type classification which is inconsistent with the X-type classification by Binzel et al. using spectroscopy.

(137925) 2000 BJ19. Our observation of this object suffered from low S/N, so the colors we measured couldnot distinguish it from S-, T-, or D-type classification, with S-type the most likely. Binzel et al. suggested a Q-type classification for this object from by spectroscopy, which is consistent with our suggestion, of S-type.

(138937) 2001 BK16. Our observation showed (138937) 2001 BK16 to be slightly blue, with $B - V = 0.648 \pm 0.067$. Since the upper limit allowed by our error is $B - V = 0.71$, which is within the range of X-class, we classify this object as X- rather than the rare B-type. The Warm-Spitzer observation yielded an albedo of 0.2, which can barely be matched with the albedo estimates for C- or X-type (debiased mean albedo of 0.101 for C-type and 0.072 for X-type as given by Stuart & Binzel).

(143651) 2003 QO104. Our observation suggested an R-type classification for (143651) 2003 QO104, which is consistent with the S-type suggested by Hicks and R- or S-type suggested by Betzler et al. (2010). The color indices we measured matched Betzler et al.'s to within 0.02 mag. On the other hand, the Warm-Spitzer observation indicated an albedo of 0.13 for this object. Considering the debiased mean albedo for R- and S-type NEAs given by Stuart & Binzel as 0.340 and 0.239, respectively, an S-type classification for this object might be more appropriate. However, as mentioned earlier, we do not know the true mean albedo for R-type NEAs, so the exact classification for this object is still an open question.

(159402) 1999 AP10. Our observation suggested an S-type classification for this object, but there is a ~0.1 mag difference in the $B - V$ magnitude from the typical color. Meanwhile, it has been reported that (159402) 1999 AP10 is an L- or S-type asteroid (Betzler et al. 2010) using spectroscopy and broadband photometry. The difference between our and Betzler et al.'s observation of the $B - V$ magnitude is about 0.12 mag, while $V - R$ and $V - I$ colors matched to within 0.02 mag. The Warm-Spitzer program gave an albedo estimate of 0.34, which does not oppose our S-type suggestion since the mean albedo for S-type NEAs was found to be 0.239 by Stuart & Binzel. In addition, the error bar σ for mean albedo determination of S-type NEAs is ± 0.044 as given by the authors, corresponding to an average dispersion of ± 0.15. Considering there are 12 S-type NEAs used to determine the mean,[4] we can see that the Warm-Spitzer measurement mostly overlaps the albedo range of S-type NEAs.

(162998) 2001 SK162. The $B - V$ and $V - R$ magnitudes derived from our observation suggested an X- or V-type classification, with X-type the more likely. There is a rough consistency between our X-type suggestion and Binzel et al.'s T-type classification.

2002 LV. Our observation suggests an X- or Q-type classification for this object, with Q-type the more likely. On the other hand, observation from Warm-Spitzer suggested an albedo of 0.15. This does not resolve the ambiguity, since the uncertainty range covers the mean albedos for C-, X-, and Q-type NEAs by Stuart & Binzel, which are 0.101, 0.072, and 0.247, respectively. However, considering that the average dispersions for each of the three complexes are 0.06, 0.06, and 0.15, respectively, we may conclude that a Q-type classification is the most probable classification for this object, since the uncertainties from both sources could have the largest intersection under such a justification.

2007 MK13. Colors derived from our observation fall between the typical colors of X- and T-type asteroids, with X-type classification the more likely. Considering we have combined the C- and X-class together, our classification is consistent with Hicks & Somers' (2010) C-type classification.

4.2. Statistical Analysis with Results from Other Photometric and Spectroscopic Surveys

To compare the similarities and differences between the results of some recently conducted photometric and spectroscopic NEA surveys, we include the results from several surveys as listed in Table 1, including de León et al. (2010), SINEO (Lazzarin et al. 2005), SMASS (Bus & Binzel 2002; Binzel et al. 2004), Dandy et al. (2003), and Angeli & Lazzaro (2002).[5] The classification results are first consolidated into several taxonomic complexes based on the scheme suggested by Binzel et al. (2004) to allow the fractional abundances detected by each survey to be comparable (Table 7). The taxonomic complexes are further consolidated into two general categories, "C/X-like"[6] and "S-like," in order to determine the ratio of C/X-like and S-like observed by each survey. Considering the definition by Morbidelli et al. (2002),[7] we consider the asteroids of class A, O, Q, R, S, U, and V as "S-like," and the asteroids of class C and D as "C/X-like." The degeneracy of X-complex is a problem since it includes members with diverse physical properties. As we do not have the fine physical data for each X-complex member, we consider the assumption of a dark-to-bright ratio (equivalent to our C/X-like:S-like ratio, as we have argued and presumed above) of 0.45 among X-complex NEAs as given by Binzel et al. (2004) based on the albedo–taxonomy correlation of 22 X-complex NEAs. For the two photometric surveys (ours and Dandy et al.'s), matters are more complicated since C- and X-complex cannot be distinguished, so we consider the relative number of C- and X-complex members among NEAs to be ~ 0.5 as determined by Binzel et al., resulting a C/X-like:S-like ratio of $(0.5 + 0.45)/(1–0.45) \approx 1.73$ in the combined C- and X-complex for the two photometric surveys. Finally, objects with several possible classifications are excluded to avoid inducing further uncertainty.

Table 7
Summary of Consolidated Taxonomic Classes Based on the Works of Binzel et al. (2004) and Stuart & Binzel (2004)

Taxonomic Complex	Includes
A	A
C	C, Cb, Cg, Cgh, Ch, B, F, G
D	D, T
O	O
Q	Q, Sq
R	R
S	S, Sa, Sk, Sl, Sr, Sv, K, L, Ld
U	U
V	V
X	X, Xc, Xe, Xk, E, M, P

As illustrated in Table 8, the surveys agree on a dominant position of silicate-composed asteroids (Q-, R-, S-, and V-type). The fractions of each complex tend to be close on a larger sample n, suggesting that the fraction differences among the surveys are primarily caused by random errors in observational sampling.

An interesting observation is that the C/X-like:S-like ratio appeared to be magnitude-dependent. The surveys with $\overline{H} < 17$ (de León et al.'s, Michelsen et al.'s, and Angeli & Lazzaro's) all have a ratio smaller than 0.1, while all others have a ratio larger than 0.1, suggesting a trend of more C/X-like asteroids at a larger H (smaller size). This phenomenon has been noted by Rabinowitz (1998), Morbidelli et al. (2002), Dandy et al. (2003), and Binzel et al. (2004), but no decisive conclusion was reached owing to the lack of data among large H (small size) asteroids. By contrast, Morbidelli et al. suggested that the ratio should slightly decrease with larger H due to observational bias effects and based on model prediction (see Section 2 of their paper), which is contrary to the implication of Table 8.

To investigate this matter further, we merge all the data together, creating a large data set with 449 NEAs (with 434 NEAs with $H \leqslant 22$ and 382 NEAs with $H \leqslant 20$), and grouped them into one-magnitude-wide bins. For each magnitude bin, the C/X-like:S-like ratio is computed based on the scheme described above. The result is listed in Table 9.

4 As calculated by $D(x) = \sigma\sqrt{N-1}$, where $D(x)$ is the average dispersion.

5 The result of Fevig & Fink (2007) is excluded as they used a different taxonomy from Tholen's or Bus–DeMeo's.

6 We see the need to use the "C/X-like" concept, instead of the "C-like" concept as used in many other papers to date, to avoid interference over the "dark/bright" issue (which should primarily rely on albedo information), although these two concepts are, in fact, equivalent to each other.

7 The classification method applied by Morbidelli et al. actually divides the asteroids into "dark" (corresponding to the "C/X-like" group in our study) and "bright" (corresponding to the "S-like" group in our study). However, some NEAs in their sample were classified based on taxonomic classification rather than real albedo. As the correlation between spectroscopic information and the target's albedo is still not well understood, we still apply a "C/X-like versus S-like" pattern that emphasizes the trend in color rather than a "dark–bright" pattern that emphasizes albedo. To simplify our subsequent discussions, we also consider results coming from a "dark–bright" pattern (as applied by studies mainly based on spectroscopic data, such as Morbidelli et al.'s and Binzel et al.'s) to be quantitatively equivalent with the results from "C/X-like versus S-like" pattern.

Table 8
Fractional Abundances of each Taxonomic Complex and Apparent C/X-like:S-like Ratio as Analyzed from the Results of Several Photometric/Spectroscopic Studies

Taxonomic Complex	This Work	de León et al. (2010)[a]	Michelsen et al. (2006)	Lazzarin et al. (2005)	Binzel et al. (2004)[a]	Dandy et al. (2003)	Angeli & Lazzaro (2002)
Method	Photometry	Spectroscopy	Spectroscopy	Spectroscopy	Spectroscopy	Photometry	Spectroscopy
Sample n	25	77	12	36	310	51	12
$\overline{H}$	17.2	16.1	15.7	17.6	17.8	17.4	14.6
A	8%	3%	0%	3%	∼0%	0%	8%
C	···	1%	0%	11%	7%	34%[b]	0%
D	0%	0%	8%	0%	3%	0%	0%
O	0%	4%	0%	0%	2%	0%	0%
Q	0%	25%	0%	8%	26%	25%	17%
R	28%	0%	0%	0%	∼0%	14%	0%
S	36%	58%	92%	58%	40%	22%	58%
U	0%	0%	0%	0%	1%	0%	0%
V	0%	8%	0%	0%	5%	2%	8%
X	24%[b]	3%	0%	11%	15%	···	8%
C/X-like:S-like ratio	0.14	0.01	0.09	0.27	0.21	0.21	0.04

Notes.
[a] Mars-crossers in the sample have been removed in this comparison.
[b] The fraction of C-complex includes the contribution from B-, C-, E-,and X-complex.

Table 9
Counts of C/X-like, S-like, or X-complex Categories in each Magnitude Bin and the Corresponding C/X-like:S-like Ratio

Mag Bin	C/X-like	S-like	X-complex (Numbers Assigned to C/X-like)	C/X-like:S-like Ratio
<14.00	1	11	0(0)	0.09
14.00–14.99	3	19	5(2)	0.23
15.00–15.99	1	43	3(1)	0.04
16.00–16.99	14	65	4(2)	0.24
17.00–17.99	6	61	10(5)	0.17
18.00–18.99	12	44	15(7)	0.37
19.00–19.99	10	39	9(4)	0.32
20.00–20.99	9	21	7(3)	0.48
21.00–21.99	1	15	5(2)	0.17
⩾22.00	1	12	3(1)	0.14

Comparing the result with Morbidelli et al.'s study, which included 183 NEAs with $H < 20$, the ratio variation from magnitude to magnitude between the two studies is similar: a lower C/X-like:S-like ratio on $H < 18$ and a higher ratio on $H \geqslant 18 \Leftrightarrow D \leqslant 1$ km, which agrees with the implication of Table 8. To check the statistical significance of this phenomenon, we divide the whole sample into two groups with an $H = 18$ cutoff, with the sample n of each group being 246 ($H < 18$) and 203 ($H \geqslant 18$), respectively, and perform a χ^2 test on the two groups. It is found that the distributions of two groups are different at a confidence level of 99.5%, which is large enough to be considered statistically significant. Although our treatment of the C/X-like:S-like ratio of the X-complex may induce some uncertainty, we note that even when we consider a 1σ uncertainty of the numbers of X-complex members to be "C/X-like" (assuming random observation errors) for both $H < 18$ and $H \geqslant 18$, for which the numbers of X-complex members considered as "C/X-like" would be 10 ± 3 and 17 ± 4, respectively, the minimum possible confidence level is still shown to be ∼95%. Furthermore, we note that the C/X-like:S-like ratio we derived is 0.17 ± 0.02 for NEAs with $H < 18$, which is a good match with the model prediction of 0.18 according to Morbidelli et al., implying that our treatment of the X-complex members with $H < 18$ would lead to a good match with the model. However, this is no longer the case when we take an $H < 20$ cutoff line, for which our estimate of the C/X-like:S-like ratio is shown to be 0.22 ± 0.02, about 3%–7% higher than Morbidelli et al.'s model prediction (0.17). It is noteworthy that we have to consider all X-complex members with $18 \leqslant H < 20$ to be "S-like" as an extreme situation for a compatible ratio with the model prediction (0.18 versus the model's 0.165 ± 0.015). In addition, our estimate of the C/X-like:S-like ratio for $18 \leqslant H < 22$ (sample $n = 187$ compared with $n \sim 50$ for $18 \leqslant H < 20$ in Morbidelli et al.'s sample) is 0.33 ± 0.04. In all, it is plausible to say that a transition point of the C/X-like:S-like ratio exists at $H = 18$ in our sample, which is consistent with the hypothesis that small asteroids generally have younger collision age and tend to be less weathered (thus, less reddish/neutral colored) than large ones (Binzel et al. 1998), hence leading to an overabundance of C/X-like asteroids in small NEAs.

Morbidelli et al. suggested a factor of ∼1.4 between the observed and true C/X-like:S-like ratio caused by the phase angle effect at discovery. Assuming that this number remains quasi-constant for different H, we will get a true C/X-like:S-like ratio of 0.24 for asteroids with $H < 18$, which is a good match with Morbidelli et al.'s model (0.25 ± 0.02). However, for $H \geqslant 18$, the true ratio can be as high as 0.5 in our sample.

4.3. Discussion of the Paired-asteroid Candidate Observations

Because of the constraints on the target observability, only two pairs with both components were observed: (1979)

Sakharov versus (13732) Woodall and (11842) Kap'bos versus (228747) 2002 VH3. Unfortunately, we were unable to obtain complete color indices for either pair; for the first pair, (13732) Woodallsuffered from instrument problems so the $V - I$ magnitude is missing, while (228747) 2002 VH3 was just passing close to a 4.5 mag star when the observation was taken for the second pair, so we were only able to make a very crude classification for these two objects. In general, both components of both pairs are classified as an S-like asteroid, providing weak evidence for the common-origin hypothesis as expected.

5. CONCLUSION

Our work has provided spectral data of some tens of interesting asteroids. For the few asteroids that had been previously classified, our results are generally in agreement. Further to observing and classifying the asteroids, we also examined the matter of overabundance of C/X-like (neutral colored) asteroids among small NEAs, a phenomenon that had previously been noted by several studies without a decisive conclusion. In the largest-ever sample we created from merging results from several photometric/spectroscopic surveys with 449 spectrally classified NEAs in total, we identified a "transition point" of the C/X-like:S-like ratio among NEAs at $H \sim 18 \Leftrightarrow D \sim 1$ km with statistical confidence level at 95% or higher. The C/X-like:S-like ratio for NEAs with $H < 18$ is estimated to be 0.17 ± 0.02 as measured in this sample, which is in good agreement with a previous model prediction by Morbidelli et al. The ratio for NEAs with $18 \leqslant H < 22$ is estimated to be 0.33 ± 0.04, about twice as high as that for $H < 18$ inconsistent with the model prediction. However, this finding supports the hypothesis that asteroids with less reddish appearance are more abundant among small NEAs than large ones due to younger collision age and less weathered surface.

The author is very grateful to Alan Harris for his valuable help and constructive comments, which have led to an advancement of this work. The author is also very grateful to Alberto Betzler, Wing-Huen Ip, Timothy Spahr, and Jin Zhu for their help and encouragement to the author in initiating this work; and to Johnson Lau, Petr Pravec, Brian Warner, and Linjiong Zhou for their help with data processing and manuscript preparation. In addition, the author thanks Hung-Chin Lin, Chi Sheng Lin, and Hsiang-Yao Hsiao from Lulin Observatory, on behalf of the Graduate Institute of Astronomy, National Central University, for providing assistance in obtaining the observational data and granting permission to use their licensed copy of *MPO Canopus* for data processing. This work is supported by a 2007 Gene Shoemaker NEO Grant from the Planetary Society. The LOT and 0.41 m telescope are operated with support from the Graduate Institute of Astronomy, National Central University.

REFERENCES

Angeli, C. A., & Lazzaro, D. 2002, A&A, 391, 757

Betzler, A. S., Noaves, A. B., Santos, A. C. P., & Sobral, E. G. 2010, Minor Planet Bull., 37, 95

Binzel, R. P., Bus, S. J., & Burbine, T. H. 1998, in 29th Annual Lunar Planet. Sci. Conf. (Houston, TX), 1222

Binzel, R. P., Bus, S. J., Burbine, T. H., & Sunshine, J. M. 1996, Science, 273, 946

Binzel, R. P., Rivkin, A. S., Stuart, J. S., Harris, A. W., Bus, S. J., & Burbine, T. H. 2004, Icarus, 170, 259

Bus, S. J., & Binzel, R. P. 2002, Icarus, 158, 146

Dandy, C. L., Fitzsimmons, A., & Collander-Brown, S. J. 2003, Icarus, 163, 363

Delbó, M., Harris, A. W., Binzel, R. P., Pravec, P., & Davies, J. K. 2003, Icarus, 166, 116

de León, J., Licandro, J., Serra-Ricart, M., Pinilla-Alonso, N., & Campins, H. 2010, A&A, 517, A23

DeMeo, F. E., Binzel, R. P., Slivan, S. M., & Bus, S. J. 2009, Icarus, 202, 160

Fevig, R. A., & Fink, U. 2007, Icarus, 188, 175

Hicks, M., & Somers, J. 2010, ATel, 2372

Landolt, A. U. 1992, AJ, 104, 340

Lazzarin, M., Marchi, S., Magrin, S., & Licandro, J. 2005, MNRAS, 359, 1575

Michelsen, R., Nathues, A., & Lagerkvist, C. I. 2006, A&A, 451, 331

Morbidelli, A., Jedicke, R., Bottke, W. F., Michel, P., & Tedesco, E. F. 2002, Icarus, 158, 329

Pravec, P., & Vokrouhlický, D. 2009, Icarus, 204, 580

Rabinowitz, D. L. 1998, Icarus, 134, 342

Skrutskie, M. F., et al. 2006, AJ, 131, 1163

Stuart, J. S., & Binzel, R. P. 2004, Icarus, 170, 295

Taylor, B. J., Joner, M. D., & Jeffery, E. J. 2008, ApJS, 176, 262

Tedesco, E. F., Noah, P. V., Noah, M., & Price, S. D. 2002, AJ, 123, 1056

Tholen, D. 1984, PhD thesis, Arizona Univ., Tucson

Trilling, D. E., et al. 2010, AJ, 140, 770

Vokrouhlický, D., & Nesvorný, D. 2008, AJ, 136, 280

Warner, B. D. 2007, Minor Planet Bull., 34, 113

The Astrophysical Journal, 736:131 (22pp), 2011 August 1 doi:10.1088/0004-637X/736/2/131

FERMI LARGE AREA TELESCOPE OBSERVATIONS OF MARKARIAN 421: THE MISSING PIECE OF ITS SPECTRAL ENERGY DISTRIBUTION

A. A. Abdo[1,110], M. Ackermann[2], M. Ajello[2], L. Baldini[3], J. Ballet[4], G. Barbiellini[5,6], D. Bastieri[7,8], K. Bechtol[2], R. Bellazzini[3], B. Berenji[2], R. D. Blandford[2], E. D. Bloom[2], E. Bonamente[9,10], A. W. Borgland[2], A. Bouvier[11], J. Bregeon[3], A. Brez[3], M. Brigida[12,13], P. Bruel[14], R. Buehler[2], S. Buson[7,8], G. A. Caliandro[15], R. A. Cameron[2], A. Cannon[16,17], P. A. Caraveo[18], S. Carrigan[8], J. M. Casandjian[4], E. Cavazzuti[19], C. Cecchi[9,10], Ö. Çelik[16,20,21], E. Charles[2], A. Chekhtman[22,110], J. Chiang[2], S. Ciprini[10], R. Claus[2], J. Cohen-Tanugi[23], J. Conrad[24,25,111], S. Cutini[19], A. de Angelis[26], F. de Palma[12,13], C. D. Dermer[27], E. do Couto e Silva[2], P. S. Drell[2], R. Dubois[2], D. Dumora[28], L. Escande[28,29], C. Favuzzi[12,13], S. J. Fegan[14], J. Finke[27], W. B. Focke[2], P. Fortin[14], M. Frailis[26,30], L. Fuhrmann[31], Y. Fukazawa[32], T. Fukuyama[33], S. Funk[2], P. Fusco[12,13], F. Gargano[13], D. Gasparrini[19], N. Gehrels[16], M. Georganopoulos[21], S. Germani[9,10], B. Giebels[14], N. Giglietto[12,13], P. Giommi[19], F. Giordano[12,13], M. Giroletti[34], T. Glanzman[2], G. Godfrey[2], I. A. Grenier[4], S. Guiriec[35], D. Hadasch[15], M. Hayashida[2], E. Hays[16], D. Horan[14], R. E. Hughes[36], G. Jóhannesson[37], A. S. Johnson[2], W. N. Johnson[27], M. Kadler[20,38,39,40], T. Kamae[2], H. Katagiri[32], J. Kataoka[41], J. Knödlseder[42], M. Kuss[3], J. Lande[2], L. Latronico[3], S.-H. Lee[2], F. Longo[5,6], F. Loparco[12,13], B. Lott[28], M. N. Lovellette[27], P. Lubrano[9,10], G. M. Madejski[2], A. Makeev[22,110], W. Max-Moerbeck[43], M. N. Mazziotta[13], J. E. McEnery[16,44], J. Mehault[23], P. F. Michelson[2], W. Mitthumsiri[2], T. Mizuno[32], C. Monte[12,13], M. E. Monzani[2], A. Morselli[45], I. V. Moskalenko[2], S. Murgia[2], T. Nakamori[41], M. Naumann-Godo[4], S. Nishino[32], P. L. Nolan[2], J. P. Norris[46], E. Nuss[23], T. Ohsugi[47], A. Okumura[33], N. Omodei[2], E. Orlando[2,48], J. F. Ormes[46], M. Ozaki[33], D. Paneque[2,49], J. H. Panetta[2], D. Parent[22,110], V. Pavlidou[43], T. J. Pearson[43], V. Pelassa[23], M. Pepe[9,10], M. Pesce-Rollins[3], M. Pierbattista[4], F. Piron[23], T. A. Porter[2], S. Rainò[12,13], R. Rando[7,8], M. Razzano[3], A. Readhead[43], A. Reimer[2,50], O. Reimer[2,50], L. C. Reyes[51], J. L. Richards[43], S. Ritz[11], M. Roth[52], H. F.-W. Sadrozinski[11], D. Sanchez[14], A. Sander[36], C. Sgrò[3], E. J. Siskind[53], P. D. Smith[36], G. Spandre[3], P. Spinelli[12,13], Ł. Stawarz[33,54], M. Stevenson[43], M. S. Strickman[27], D. J. Suson[55], H. Takahashi[47], T. Takahashi[33], T. Tanaka[2], J. G. Thayer[2], J. B. Thayer[2], D. J. Thompson[16], L. Tibaldo[4,7,8,112], D. F. Torres[15,56], G. Tosti[9,10], A. Tramacere[2,57,58], E. Troja[16,113], T. L. Usher[2], J. Vandenbroucke[2], V. Vasileiou[20,21], G. Vianello[2,57], N. Vilchez[42], V. Vitale[45,59], A. P. Waite[2], P. Wang[2], A. E. Wehrle[60], B. L. Winer[36], K. S. Wood[27], Z. Yang[24,25], Y. Yatsu[61], T. Ylinen[25,62,63], J. A. Zensus[31], M. Ziegler[11]

(The Fermi-LAT Collaboration)

J. Aleksić[64], L. A. Antonelli[65], P. Antoranz[66], M. Backes[67], J. A. Barrio[68], J. Becerra González[69,70], W. Bednarek[71], A. Berdyugin[72], K. Berger[70], E. Bernardini[73], A. Biland[74], O. Blanch[64], R. K. Bock[49], A. Boller[74], G. Bonnoli[65], P. Bordas[75], D. Borla Tridon[49], V. Bosch-Ramon[75], D. Bose[68], I. Braun[74], T. Bretz[76], M. Camara[68], E. Carmona[49], A. Carosi[65], P. Colin[49], E. Colombo[69], J. L. Contreras[68], J. Cortina[64], S. Covino[65], F. Dazzi[26,114], A. de Angelis[26], E. De Cea del Pozo[15], C. Delgado Mendez[69,77], B. De Lotto[78], M. De Maria[78], F. De Sabata[78], A. Diago Ortega[69,70], M. Doert[67], A. Domínguez[79], D. Dominis Prester[80], D. Dorner[74], M. Doro[7,8], D. Elsaesser[76], D. Ferenc[80], M. V. Fonseca[68], L. Font[81], R. J. García López[69,70], M. Garczarczyk[69], M. Gaug[69], G. Giavitto[64], N. Godinovi[80], D. Hadasch[15], A. Herrero[69,70], D. Hildebrand[74], D. Höhne-Mönch[76], J. Hose[49], D. Hrupec[80], T. Jogler[49], S. Klepser[64], T. Krähenbühl[74], D. Kranich[74], J. Krause[49], A. La Barbera[65], E. Leonardo[66], E. Lindfors[72], S. Lombardi[7,8], M. López[7,8], E. Lorenz[49,74], P. Majumdar[73], E. Makariev[82], G. Maneva[82], N. Mankuzhiyil[26], K. Mannheim[76], L. Maraschi[83], M. Mariotti[7,8], M. Martínez[64], D. Mazin[64], M. Meucci[66], J. M. Miranda[66], R. Mirzoyan[49], H. Miyamoto[49], J. Moldón[75], A. Moralejo[64], D. Nieto[68], K. Nilsson[84], R. Orito[49], I. Oya[68], R. Paoletti[66], J. M. Paredes[75], S. Partini[66], M. Pasanen[72], F. Pauss[74], R. G. Pegna[66], M. A. Perez-Torres[79], M. Persic[26,85], J. Peruzzo[7,8], J. Pochon[69], F. Prada[79], P. G. Prada Moroni[66], E. Prandini[7,8], N. Puchades[64], I. Puljak[80], T. Reichardt[64], W. Rhode[67], M. Ribó[75], J. Rico[56,64], M. Rissi[74], S. Rügamer[76], A. Saggion[7,8], K. Saito[49], T. Y. Saito[49], M. Salvati[65], M. Sánchez-Conde[69,70], K. Satalecka[73], V. Scalzotto[7,8], V. Scapin[26], C. Schultz[7,8], T. Schweizer[49], M. Shayduk[49], S. N. Shore[3,86], A. Sierpowska-Bartosik[71], A. Sillanpää[72], J. Sitarek[49,71], D. Sobczynska[71], F. Spanier[76], S. Spiro[65], A. Stamerra[66], B. Steinke[49], J. Storz[76], N. Strah[67], J. C. Struebig[76], T. Suric[80], L. O. Takalo[72], F. Tavecchio[83], P. Temnikov[82], T. Terzić[80], D. Tescaro[64], M. Teshima[49], H. Vankov[82], R. M. Wagner[49], Q. Weitzel[74], V. Zabalza[75], F. Zandanel[79], R. Zanin[64]

(The MAGIC Collaboration)

and

M. Villata[87], C. Raiteri[87], H. D. Aller[88], M. F. Aller[88], W. P. Chen[89], B. Jordan[90], E. Koptelova[89], O. M. Kurtanidze[91], A. Lähteenmäki[92], B. McBreen[17], V. M. Larionov[93,94,95], C. S. Lin[89], M. G. Nikolashvili[91], R. Reinthal[72], E. Angelakis[31], M. Capalbi[19], A. Carramiñana[96], L. Carrasco[96], P. Cassaro[97], A. Cesarini[98], A. Falcone[99], M. A. Gurwell[100], T. Hovatta[92], Yu. A. Kovalev[101], Y. Y. Kovalev[31,101], T. P. Krichbaum[31], H. A. Krimm[20,40], M. L. Lister[102], J. W. Moody[103], G. Maccaferri[104], Y. Mori[61], I. Nestoras[31], A. Orlati[104], C. Pace[103], C. Pagani[105], R. Pearson[103], M. Perri[19], B. G. Piner[106], E. Ros[31,107], A. C. Sadun[108], T. Sakamoto[16], J. Tammi[92], and A. Zook[109]

[1] National Research Council Research Associate, National Academy of Sciences, Washington, DC 20001, USA
[2] W. W. Hansen Experimental Physics Laboratory, Kavli Institute for Particle Astrophysics and Cosmology, Department of Physics and SLAC National Accelerator Laboratory, Stanford University, Stanford, CA 94305, USA; dpaneque@mppmu.mpg.de, anita.reimer@uibk.ac.at
[3] Istituto Nazionale di Fisica Nucleare, Sezione di Pisa, I-56127 Pisa, Italy
[4] Laboratoire AIM, CEA-IRFU/CNRS/Université Paris Diderot, Service d'Astrophysique, CEA Saclay, 91191 Gif sur Yvette, France
[5] Istituto Nazionale di Fisica Nucleare, Sezione di Trieste, I-34127 Trieste, Italy
[6] Dipartimento di Fisica, Università di Trieste, I-34127 Trieste, Italy
[7] Istituto Nazionale di Fisica Nucleare, Sezione di Padova, I-35131 Padova, Italy
[8] Dipartimento di Fisica "G. Galilei," Università di Padova, I-35131 Padova, Italy
[9] Istituto Nazionale di Fisica Nucleare, Sezione di Perugia, I-06123 Perugia, Italy
[10] Dipartimento di Fisica, Università degli Studi di Perugia, I-06123 Perugia, Italy
[11] Santa Cruz Institute for Particle Physics, Department of Physics and Department of Astronomy and Astrophysics, University of California at Santa Cruz, Santa Cruz, CA 95064, USA
[12] Dipartimento di Fisica "M. Merlin" dell'Università e del Politecnico di Bari, I-70126 Bari, Italy
[13] Istituto Nazionale di Fisica Nucleare, Sezione di Bari, 70126 Bari, Italy
[14] Laboratoire Leprince-Ringuet, École polytechnique, CNRS/IN2P3, Palaiseau, France
[15] Institut de Ciencies de l'Espai (IEEC-CSIC), Campus UAB, 08193 Barcelona, Spain
[16] NASA Goddard Space Flight Center, Greenbelt, MD 20771, USA
[17] University College Dublin, Belfield, Dublin 4, Ireland
[18] INAF-Istituto di Astrofisica Spaziale e Fisica Cosmica, I-20133 Milano, Italy
[19] Agenzia Spaziale Italiana (ASI) Science Data Center, I-00044 Frascati (Roma), Italy
[20] Center for Research and Exploration in Space Science and Technology (CRESST) and NASA Goddard Space Flight Center, Greenbelt, MD 20771, USA
[21] Department of Physics and Center for Space Sciences and Technology, University of Maryland Baltimore County, Baltimore, MD 21250, USA; georgano@umbc.edu
[22] College of Science, George Mason University, Fairfax, VA 22030, USA
[23] Laboratoire de Physique Théorique et Astroparticules, Université Montpellier 2, CNRS/IN2P3, Montpellier, France
[24] Department of Physics, Stockholm University, AlbaNova, SE-106 91 Stockholm, Sweden
[25] The Oskar Klein Centre for Cosmoparticle Physics, AlbaNova, SE-106 91 Stockholm, Sweden
[26] Dipartimento di Fisica, Università di Udine and Istituto Nazionale di Fisica Nucleare, Sezione di Trieste, Gruppo Collegato di Udine, I-33100 Udine, Italy
[27] Space Science Division, Naval Research Laboratory, Washington, DC 20375, USA; justin.finke@nrl.navy.mil
[28] Université Bordeaux 1, CNRS/IN2p3, Centre d'Études Nucléaires de Bordeaux Gradignan, 33175 Gradignan, France
[29] CNRS/IN2P3, Centre d'Études Nucléaires Bordeaux Gradignan, UMR 5797, Gradignan, 33175, France
[30] Osservatorio Astronomico di Trieste, Istituto Nazionale di Astrofisica, I-34143 Trieste, Italy
[31] Max-Planck-Institut für Radioastronomie, Auf dem Hügel 69, 53121 Bonn, Germany
[32] Department of Physical Sciences, Hiroshima University, Higashi-Hiroshima, Hiroshima 739-8526, Japan
[33] Institute of Space and Astronautical Science, JAXA, 3-1-1 Yoshinodai, Chuo-ku, Sagamihara, Kanagawa 252-5210, Japan
[34] INAF Istituto di Radioastronomia, 40129 Bologna, Italy
[35] Center for Space Plasma and Aeronomic Research (CSPAR), University of Alabama in Huntsville, Huntsville, AL 35899, USA
[36] Department of Physics, Center for Cosmology and Astro-Particle Physics, The Ohio State University, Columbus, OH 43210, USA
[37] Science Institute, University of Iceland, IS-107 Reykjavik, Iceland
[38] Dr. Remeis-Sternwarte Bamberg, Sternwartstrasse 7, D-96049 Bamberg, Germany
[39] Erlangen Centre for Astroparticle Physics, D-91058 Erlangen, Germany
[40] Universities Space Research Association (USRA), Columbia, MD 21044, USA
[41] Research Institute for Science and Engineering, Waseda University, 3-4-1, Okubo, Shinjuku, Tokyo, 169-8555 Japan
[42] Centre d'Étude Spatiale des Rayonnements, CNRS/UPS, BP 44346, F-30128 Toulouse Cedex 4, France
[43] Cahill Center for Astronomy and Astrophysics, California Institute of Technology, Pasadena, CA 91125, USA
[44] Department of Physics and Department of Astronomy, University of Maryland, College Park, MD 20742, USA
[45] Istituto Nazionale di Fisica Nucleare, Sezione di Roma "Tor Vergata," I-00133 Roma, Italy
[46] Department of Physics and Astronomy, University of Denver, Denver, CO 80208, USA
[47] Hiroshima Astrophysical Science Center, Hiroshima University, Higashi-Hiroshima, Hiroshima 739-8526, Japan
[48] Max-Planck Institut für extraterrestrische Physik, 85748 Garching, Germany
[49] Max-Planck-Institut für Physik, D-80805 München, Germany
[50] Institut für Astro- und Teilchenphysik and Institut für Theoretische Physik, Leopold-Franzens-Universität Innsbruck, A-6020 Innsbruck, Austria
[51] Kavli Institute for Cosmological Physics, University of Chicago, Chicago, IL 60637, USA
[52] Department of Physics, University of Washington, Seattle, WA 98195-1560, USA
[53] NYCB Real-Time Computing Inc., Lattingtown, NY 11560-1025, USA
[54] Astronomical Observatory, Jagiellonian University, 30-244 Kraków, Poland
[55] Department of Chemistry and Physics, Purdue University Calumet, Hammond, IN 46323-2094, USA
[56] Institució Catalana de Recerca i Estudis Avançats (ICREA), Barcelona, Spain
[57] Consorzio Interuniversitario per la Fisica Spaziale (CIFS), I-10133 Torino, Italy
[58] *INTEGRAL* Science Data Centre, CH-1290 Versoix, Switzerland
[59] Dipartimento di Fisica, Università di Roma "Tor Vergata," I-00133 Roma, Italy
[60] Space Science Institute, Boulder, CO 80301, USA
[61] Department of Physics, Tokyo Institute of Technology, Meguro City, Tokyo 152-8551, Japan
[62] Department of Physics, Royal Institute of Technology (KTH), AlbaNova, SE-106 91 Stockholm, Sweden
[63] School of Pure and Applied Natural Sciences, University of Kalmar, SE-391 82 Kalmar, Sweden
[64] Institut de Física d'Altes Energies (IFAE), Edifici Cn, Universitat Autònoma de Barcelona (UAB), E-08193 Bellaterra (Barcelona), Spain; diegot@ifae.es
[65] INAF National Institute for Astrophysics, I-00136 Roma, Italy
[66] Università di Siena and INFN Pisa, I-53100 Siena, Italy
[67] Technische Universität Dortmund, D-44221 Dortmund, Germany
[68] Universidad Complutense, E-28040 Madrid, Spain
[69] Instituto de Astrofísica de Canarias, E38205 - La Laguna (Tenerife), Spain
[70] Departamento de Astrofisica, Universidad de La Laguna, E-38205 La Laguna, Tenerife, Spain

[71] University of Łódź, PL-90236 Łódź, Poland
[72] Tuorla Observatory, University of Turku, FI-21500 Piikkiö, Finland
[73] Deutsches Elektronen Synchrotron DESY, D-15738 Zeuthen, Germany
[74] ETH Zurich, CH-8093 Zurich, Switzerland
[75] Universitat de Barcelona (ICC/IEEC), E-08028 Barcelona, Spain
[76] Institut für Theoretische Physik and Astrophysik, Universität Würzburg, D-97074 Würzburg, Germany
[77] Centro de Investigaciones Energéticas, Medioambientales y Tecnológicas (CIEMAT), Madrid, Spain
[78] Istituto Nazionale di Fisica Nucleare, Sezione di Trieste, and Università di Trieste, I-34127 Trieste, Italy
[79] Instituto de Astrofísica de Andalucía, CSIC, E-18080 Granada, Spain
[80] Croatian MAGIC Consortium, Institute R. Bošković, University of Rijeka and University of Split, HR-10000 Zagreb, Croatia
[81] Universitat Autónoma de Barcelona, E-08193 Bellaterra, Spain
[82] Institute for Nuclear Research and Nuclear Energy, BG-1784 Sofia, Bulgaria
[83] INAF Osservatorio Astronomico di Brera, I-23807 Merate, Italy
[84] Finnish Centre for Astronomy with ESO (FINCA), University of Turku, FI-21500 Piikiiö, Finland
[85] INAF Osservatorio Astronomico di Trieste, I-34143 Trieste, Italy
[86] Dipartimento di Fisica "Enrico Fermi," Università di Pisa, Pisa I-56127, Italy
[87] INAF, Osservatorio Astronomico di Torino, I-10025 Pino Torinese (TO), Italy
[88] Department of Astronomy, University of Michigan, Ann Arbor, MI 48109-1042, USA
[89] Graduate Institute of Astronomy, National Central University, Jhongli 32054, Taiwan
[90] School of Cosmic Physics, Dublin Institute for Advanced Studies, Dublin, 2, Ireland
[91] Abastumani Observatory, Mt. Kanobili, 0301 Abastumani, Georgia
[92] Aalto University Metsähovi Radio Observatory, FIN-02540 Kylmala, Finland
[93] Isaac Newton Institute of Chile, St. Petersburg Branch, St. Petersburg, Russia
[94] Pulkovo Observatory, 196140 St. Petersburg, Russia
[95] Astronomical Institute, St. Petersburg State University, St. Petersburg, Russia
[96] Instituto Nacional de Astrofísica, Óptica y Electrónica, Tonantzintla, Puebla 72840, Mexico
[97] INAF Istituto di Radioastronomia, Sezione di Noto,Contrada Renna Bassa, 96017 Noto (SR), Italy
[98] Physics Department, National University of Ireland Galway, Ireland
[99] Department of Astronomy and Astrophysics, Pennsylvania State University, University Park, PA 16802, USA
[100] Harvard-Smithsonian Center for Astrophysics, Cambridge, MA 02138, USA
[101] Astro Space Center of the Lebedev Physical Institute, 117997 Moscow, Russia
[102] Department of Physics, Purdue University, West Lafayette, IN 47907, USA
[103] Department of Physics and Astronomy, Brigham Young University, Provo, Utah 84602, USA
[104] INAF Istituto di Radioastronomia, Stazione Radioastronomica di Medicina, I-40059 Medicina (Bologna), Italy
[105] Department of Physics and Astronomy, University of Leicester, Leicester, LE1 7RH, UK
[106] Department of Physics and Astronomy, Whittier College, Whittier, CA, USA
[107] Universitat de València, 46010 València, Spain
[108] Department of Physics, University of Colorado, Denver, CO 80220, USA
[109] Department of Physics and Astronomy, Pomona College, Claremont CA 91711-6312, USA
Received 2010 November 25; accepted 2011 May 19; published 2011 July 15

ABSTRACT

We report on the γ-ray activity of the high-synchrotron-peaked BL Lacertae object Markarian 421 (Mrk 421) during the first 1.5 years of *Fermi* operation, from 2008 August 5 to 2010 March 12. We find that the Large Area Telescope (LAT) γ-ray spectrum above 0.3 GeV can be well described by a power-law function with photon index $\Gamma = 1.78 \pm 0.02$ and average photon flux $F(>0.3 \text{ GeV}) = (7.23 \pm 0.16) \times 10^{-8}$ ph cm^{-2} s^{-1}. Over this time period, the *Fermi*-LAT spectrum above 0.3 GeV was evaluated on seven-day-long time intervals, showing significant variations in the photon flux (up to a factor $\sim$3 from the minimum to the maximum flux) but mild spectral variations. The variability amplitude at X-ray frequencies measured by *RXTE*/ASM and *Swift*/BAT is substantially larger than that in γ-rays measured by *Fermi*-LAT, and these two energy ranges are not significantly correlated. We also present the first results from the 4.5 month long multifrequency campaign on Mrk 421, which included the VLBA, *Swift*, *RXTE*, MAGIC, the F-GAMMA, GASP-WEBT, and other collaborations and instruments that provided excellent temporal and energy coverage of the source throughout the entire campaign (2009 January 19 to 2009 June 1). During this campaign, Mrk 421 showed a low activity at all wavebands. The extensive multi-instrument (radio to TeV) data set provides an unprecedented, complete look at the quiescent spectral energy distribution (SED) for this source. The broadband SED was reproduced with a leptonic (one-zone synchrotron self-Compton) and a hadronic model (synchrotron proton blazar). Both frameworks are able to describe the average SED reasonably well, implying comparable jet powers but very different characteristics for the blazar emission site.

Key words: acceleration of particles – BL Lacertae objects: general – BL Lacertae objects: individual (Mrk 421) – galaxies: active – gamma rays: general – radiation mechanisms: non-thermal

Online-only material: color figures

1. INTRODUCTION

Blazars are active galaxies believed to have pairs of relativistic jets flowing in opposite directions closely aligned to our line of

[110] Resident at Naval Research Laboratory, Washington, DC 20375, USA.
[111] Royal Swedish Academy of Sciences Research Fellow, funded by a grant from the K. A. Wallenberg Foundation.
[112] Partially supported by the International Doctorate on Astroparticle Physics (IDAPP) program.
[113] NASA Postdoctoral Program Fellow, USA.
[114] Supported by INFN Padova.

sight. Their spectral energy distributions (SEDs) are dominated by beamed jet emission and take the form of two broad non-thermal components, one at low energies, peaking in the radio through optical, and one at high energies, peaking in the γ-rays. Some blazars have been well monitored for decades and along a wide range of wavelengths. Although there is ample evidence for the electron synchrotron origin of the low-energy bump, the existing data do not allow an unambiguous identification of the radiation mechanism responsible for the high-energy bump. One reason for this is that the high-energy bump is poorly constrained due to the lack of observations at energies between ~0.1 MeV and 0.3 TeV. This gap was filled to some extent by EGRET on board the *Compton Gamma-Ray Observatory* (Hartman et al. 1999). However, its moderate sensitivity and limited observing time precluded detailed cross-correlation studies between γ-ray and lower-energy wavebands. On the other hand, the current generation of TeV imaging atmospheric Cherenkov telescopes (IACTs)—the High Energy Stereoscopic System, the Major Atmospheric Gamma Imaging Cherenkov telescope (MAGIC), and the Very Energetic Radiation Imaging Telescope Array System, which have good sensitivity at energies as low as 0.1 TeV—did not start scientific operation until 2004, that is, well after EGRET had stopped operating.

This has changed with the launch of the *Fermi Gamma-ray Space Telescope* in 2008 June. In science operation since 2008 August, its Large Area Telescope (LAT) instrument (Atwood et al. 2009) views the entire sky in the 20 MeV to greater than 300 GeV range every three hours. The one-year First LAT Active Galactic Nuclei Catalog (1LAC; Abdo et al. 2010b) contains around 600 blazars, a factor of ~10 greater than EGRET detected during its entire operational lifetime. For the first time, simultaneous observations of *Fermi* with the latest generation of IACTs can cover the entire high-energy bump. Combining this with simultaneous low-energy observations gives an unprecedented multiwavelength view of these enigmatic objects.

Blazars found in low states are particularly poorly studied. This is due in part to the lower sensitivity of previous instruments, and in part to the fact that multiwavelength monitoring programs, including space-based instruments, are mostly triggered when an object enters a particularly bright state, as observed by ground-based optical telescopes and all-sky monitors such as the *RXTE* (Bradt et al. 1993) All Sky Monitor (ASM) or the *Swift* (Gehrels et al. 2004) Burst Alert Telescope (BAT). Having a well-measured low-state SED will be useful for constraining models and as a baseline to which other, flaring states can be compared. This will be crucial for answering many of the questions regarding these objects.

Markarian 421 (Mrk 421; R.A. = $11^{\mathrm{h}}\,4^{\mathrm{m}}\,27\overset{\mathrm{s}}{.}31$, decl. = $38^\circ\,12'\,31\overset{''}{.}8$, J2000, redshift $z = 0.031$) is a high-synchrotron-peaked (HSP) BL Lac object (according to the classification presented in Abdo et al. (2010c)) that is one of the brightest sources in the extragalactic X-ray/TeV sky. Mrk 421 was actually the first extragalactic object to be discovered as a TeV emitter (Punch et al. 1992), and one of the fastest varying γ-ray sources (Gaidos et al. 1996). During the last decade, there were a large number of publications on the very high energy (VHE) γ-ray spectrum of this source, which has been measured with almost all the existing IACTs (Krennrich et al. 2002; Aharonian et al. 2002, 2003, 2005; Albert et al. 2007a; Acciari et al. 2009). Among other things, we learned that the source shows evidence for a spectral hardening with increasing flux. The SED and the multifrequency correlations of Mrk 421 have also been intensively studied in the past through dedicated multifrequency observations of the source (Katarzyński et al. 2003; Błażejowski et al. 2005; Revillot et al. 2006; Fossati et al. 2008; Horan et al. 2009), which showed a positive but very complex relation between X-rays and VHE γ-rays, and that a simple one-zone synchrotron self-Compton (SSC) model with an electron distribution parameterized with one or two power laws seemed to describe the collected SED well during the observing campaigns. During a strong flare in 2008 June, the source was also detected with the gamma-ray telescope *AGILE* and, for the first time, a hint of correlation between optical and TeV energies was reported by Donnarumma et al. (2009).

Despite the large number of publications on Mrk 421, the details of the physical processes underlying the blazar emission are still unknown. The main reasons for this are the sparse multifrequency data during long periods of time, and the moderate sensitivity available in the past to study the γ-ray emission of this source. In addition, as occurs often with studies of blazars, many of the previous multifrequency campaigns were triggered by an enhanced flux level at X-rays and/or γ-rays, and hence many of the previous studies of this source are biased toward "high-activity" states, where perhaps distinct physical processes play a dominant role. Moreover, we have very little information from the MeV–GeV energy range: nine years of operation with EGRET resulted in only a few viewing periods with a signal significance of barely five standard deviations (σ hereafter; Hartman et al. 1999), which precluded detailed correlation studies with other energy bands.

We took advantage of the new capabilities provided by *Fermi*-LAT and the new IACTs, as well as the existing capabilities for observing at X-ray and lower frequencies, and organized a multifrequency (from radio to TeV) campaign to observe Mrk 421 over 4.5 months. The observational goal for this campaign was to sample Mrk 421 every two days, which was accomplished at optical, X-ray, and TeV energies whenever the weather and/or technical operations allowed. *Fermi*-LAT operated in survey mode and thus the source was constantly observed at γ-ray energies.

In this paper, we report the overall SED averaged over the duration of the observing campaign. A more in-depth analysis of the multifrequency data set (variability, correlations, and implications) will be given in a forthcoming paper.

This work is organized as follows: In Section 2 we introduce the LAT instrument and report on the data analysis. In Section 3 we report the flux/spectral variability in the γ-ray range observed by *Fermi*-LAT during the first 1.5 years of operation, and compare it with the flux variability obtained with *RXTE*/ASM and *Swift*/BAT, which are also all-sky instruments. In Section 4 we report on the spectrum of Mrk 421 measured by *Fermi*, and Section 5 reports on the overall SED collected during the 4.5 month long multiwavelength campaign organized in 2009. Section 6 is devoted to SED modeling of the multifrequency data with both a hadronic and a leptonic model, and in Section 7 we discuss the implications of the experimental and modeling results. Finally, we conclude in Section 8.

2. *FERMI*-LAT DATA SELECTION AND ANALYSIS

The *Fermi*-LAT is a γ-ray telescope operating from 20 MeV to >300 GeV. The instrument is an array of 4×4 identical towers, each one consisting of a tracker (where the photons are pair-converted) and a calorimeter (where the energies of the pair-converted photons are measured). The entire instrument is covered with an anticoincidence detector to reject the

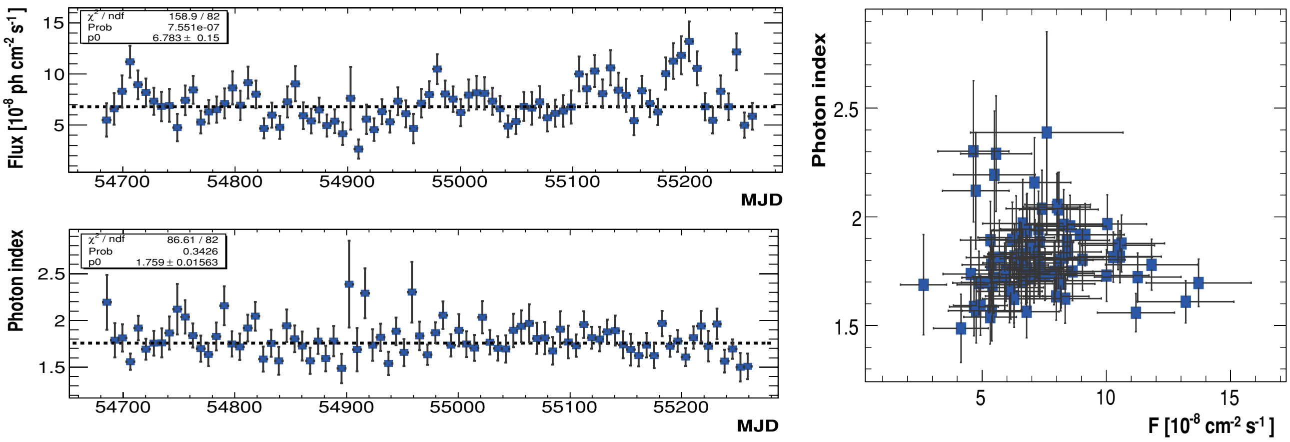

Figure 1. Left: γ-ray flux at photon energies above 0.3 GeV (top) and spectral photon index from a power-law fit (bottom) for Mrk 421 for seven-day-long time intervals from 2008 August 5 (MJD 54683) to 2009 March 12 (MJD 55248). Vertical bars denote 1σ uncertainties and the horizontal error bars denote the width of the time interval. The black dashed line and legend show the results from a constant fit to the entire data set. Right: scatter plot of the photon index vs. flux.

(A color version of this figure is available in the online journal.)

charged-particle background. LAT has a large peak effective area (0.8 m^2 for 1 GeV photons), an energy resolution typically better than 10%, and a field of view of about 2.4 sr with an angular resolution (68% containment angle) better than 1° for energies above 1 GeV. Further details on the description of LAT are given by Atwood et al. (2009).

The LAT data reported in this paper were collected from 2008 August 5 (MJD 54683) to 2010 March 12 (MJD 55248). During this time, the *Fermi*-LAT instrument operated almost entirely in survey mode. The analysis was performed with the Science Tools software package version v9r15p6. Only events having the highest probability of being photons, those in the “diffuse” class, were used. The LAT data were extracted from a circular region with a 10° radius centered at the location of Mrk 421. The spectral fits were performed using photon energies greater than 0.3 GeV, where the effective area of the instrument is large (>0.5 m^2) and the angular resolution relatively good (68% containment angle smaller than 2°). The spectral fits using energies above 0.3 GeV are less sensitive to possible contamination from non-accounted (transient) neighboring sources, and have smaller systematic errors, at the expense of reducing somewhat the number of photons from the source. In addition, a cut on the zenith angle (<105°) was also applied to reduce contamination from the Earth limb γ-rays, which are produced by cosmic rays interacting with the upper atmosphere.

The background model used to extract the γ-ray signal includes a Galactic diffuse emission component and an isotropic component. The model that we adopted for the Galactic component is given by the file gll_iem_v02.fit, and the isotropic component, which is the sum of the extragalactic diffuse emission and the residual charged particle background, is parameterized by the file isotropic_iem_v02.[115] The normalization of both components in the background model was allowed to vary freely during the spectral point fitting. The spectral analyses (from which we derived spectral fits and photon fluxes) were performed with the post-launch instrument response functions `P6_V3_DIFFUSE` using an unbinned maximum likelihood method. The systematic uncertainties in the flux were estimated as 10% at 0.1 GeV, 5% at 560 MeV and 20% at 10 GeV and above.[116]

3. FLUX AND SPECTRAL VARIABILITY

The sensitivity of *Fermi*-LAT is sufficient to accurately monitor the γ-ray flux of Mrk 421 on short timescales (a few days).[117] The measured γ-ray flux above 0.3 GeV and the photon index from a power-law (PL) fit are shown in Figure 1. The data span the time from 2008 August 5 (MJD 54683) to 2009 March 12 (MJD 55248) and they are binned on time intervals of 7 days. The Test Statistic (TS) values[118] for the 81 time intervals are typically well in excess of 100 ($\sim 10\sigma$). The number of intervals with TS $<$ 100 is only nine (11%). The lowest TS value is 30, which occurs for the time interval MJD 54899–54906. This low signal significance is due to the fact that the *Fermi*-LAT instrument did not operate during the time interval MJD 54901–54905[119] and hence only three out of the seven days of the interval contain data. The second lowest TS value is 40, which occurred for the time interval 54962–54969. During the first 19 months of *Fermi* operation, Mrk 421 showed relatively mild γ-ray flux variations, with the lowest photon flux $F(>0.3\ \mathrm{GeV}) = (2.6 \pm 0.9) \times 10^{-8}\ \mathrm{cm}^{-2}\ \mathrm{s}^{-1}$ (MJD 54906–54913; TS = 53) and the highest $F(>0.3\ \mathrm{GeV}) = (13.2 \pm 1.9) \times 10^{-8}\ \mathrm{cm}^{-2}\ \mathrm{s}^{-1}$ (MJD 55200–55207; TS = 355). A constant fit to the flux points from Figure 1 gave a $\chi^2 = 159$ for 82 degrees of freedom (probability that the flux was constant is 8×10^{-7}), hence indicating the existence of statistically significant flux variability. On the other hand, the photon index measured in seven-day-long time intervals is statistically compatible with being constant, as indicated by the results of the constant fit to all the photon index values, which gave $\chi^2 = 87$ for 82 degrees of freedom (NDF; probability of no variability is 0.34). The scatter

[115] http://fermi.gsfc.nasa.gov/ssc/data/access/lat/BackgroundModels.html.

[116] See http://fermi.gsfc.nasa.gov/ssc/data/analysis/LAT_caveats.html.

[117] The number of photons from Mrk 421 (above 0.3 GeV) detected by LAT in one day is typically about six.

[118] The Test Statistic TS = 2Δ log(likelihood) between models with and without the source is a measure of the probability of having a point γ-ray source at the location specified. The TS value is related to the significance of the signal (Mattox et al. 1996).

[119] The LAT did not operate during the time interval MJD 54901–54905 due to an unscheduled shutdown.

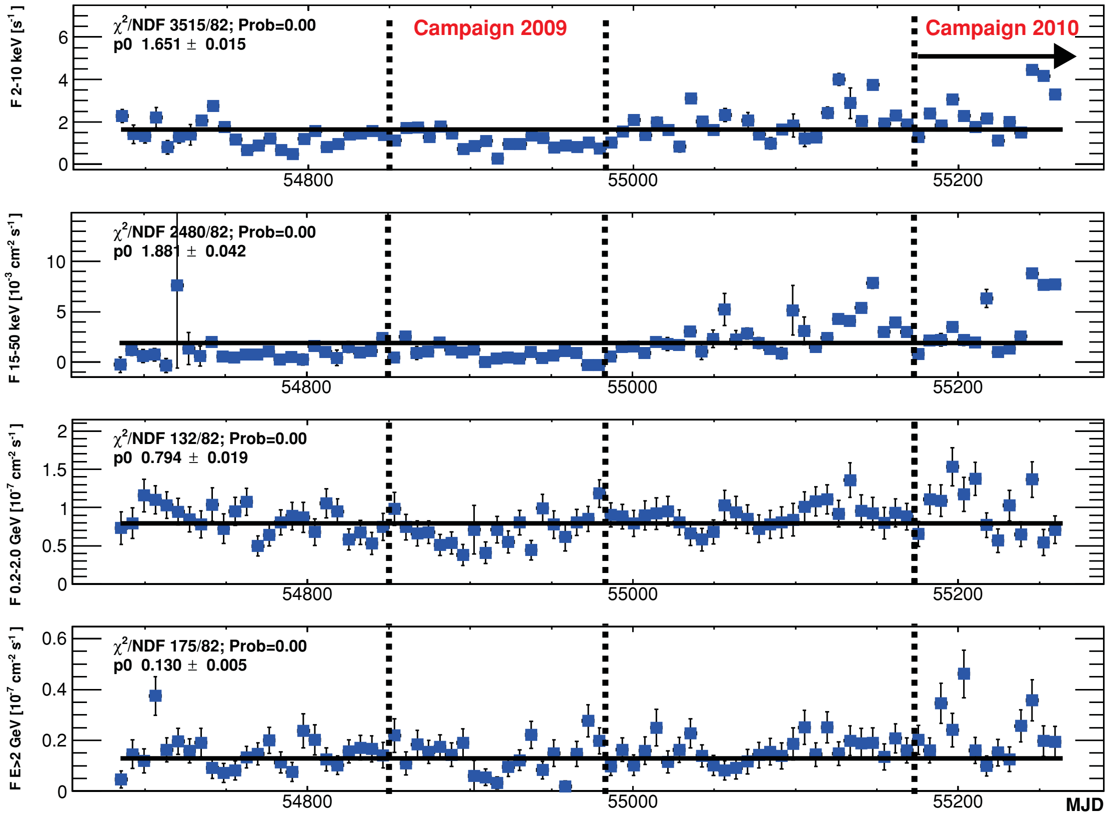

Figure 2. Multifrequency light curves of Mrk 421 with seven-day-long time bins obtained with three all-sky-monitoring instruments: *RXTE*/ASM (2–10 keV, top), *Swift*/BAT (15–50 keV, second from top), and *Fermi*-LAT for two different energy ranges (0.2–2 GeV, third from top, and >2 GeV, bottom). The light curves cover the period from 2008 August 5 (MJD 54683) to 2009 March 12 (MJD 55248). Vertical bars denote 1σ uncertainties and horizontal error bars show the width of the time interval. The black dashed lines and legends show the results from constant fits to the entire data set. The vertical dashed lines denote the time intervals with the extensive multifrequency campaigns during the 2009 and 2010 seasons.

(A color version of this figure is available in the online journal.)

plot with Flux versus Index in Figure 1 shows that there is no obvious relation between these two quantities. We quantified the correlation as prescribed in Edelson & Krolik (1988), obtaining a discrete correlation function DCF $= 0.06 \pm 0.11$ for a time lag of zero.

It is interesting to compare the γ-ray fluxes measured by *Fermi* with those historical ones recorded by EGRET. From the third EGRET catalog (Hartman et al. 1999), one can see that the highest and lowest significantly measured (TS > 25) photon fluxes are $F^{\rm Max}(>0.1~{\rm GeV}) = (27.1 \pm 6.9) \times 10^{-8}~{\rm cm}^{-2}~{\rm s}^{-1}$ (TS = 32) and $F^{\rm Min}(>0.1~{\rm GeV}) = (10.9 \pm 2.8) \times 10^{-8}~{\rm cm}^{-2}~{\rm s}^{-1}$ (TS = 26), respectively, where $F(>0.1~{\rm GeV})$ is the flux above 0.1 GeV. These values do not deviate by more than 2σ from the P1234 average, $F(>0.1~{\rm GeV}) = (13.8 \pm 1.8) \times 10^{-8}~{\rm cm}^{-2}~{\rm s}^{-1}$ (TS = 100), and hence EGRET did not detect significant variability in the flux from Mrk 421. We can easily obtain the *Fermi* $F(>0.1~{\rm GeV})$ fluxes by using the flux (F) index (Γ) values reported in Figure 1 ($E > 0.3$ GeV): $F(>0.1~{\rm GeV}) = F(>0.3~{\rm GeV}) \times (0.3/0.1)^{\Gamma-1}$. Applying this simple formalism one gets, for the maximum and minimum fluxes from Figure 1, $F^{\rm Max}(>0.1~{\rm GeV}) = (25.7 \pm 4.7) \times 10^{-8}~{\rm cm}^{-2}~{\rm s}^{-1}$ and $F^{\rm Min}(>0.1~{\rm GeV}) = (5.6 \pm 2.4) \times 10^{-8}~{\rm cm}^{-2}~{\rm s}^{-1}$, respectively. The maximum flux measured by EGRET and LAT are similar, although the *minimum* fluxes are not. LAT's larger effective area compared to EGRET permits detection of lower γ-ray fluxes. In any case, the EGRET and LAT fluxes are comparable, which may indicate that Mrk 421 is not as variable in the MeV/GeV range as at other wavelengths, particularly X-rays and TeV γ-rays (e.g., Wagner 2008).

The *Fermi*-LAT capability for constant source monitoring is nicely complemented at X-ray energies by *RXTE*/ASM and *Swift*/BAT, the two other all-sky instruments that can probe the X-ray activity of Mrk 421 in seven-day-long time intervals. Figure 2 shows the measured fluxes by ASM in the energy range 2–10 keV, by BAT at 15–50 keV, and by LAT in two different energy bands: 0.2–2 GeV (low energy) and >2 GeV (high energy).[120] The low and high *Fermi*-LAT energy bands were chosen (among other reasons) to produce comparable flux errors. This might seem surprising at first glance, given that the number of detected photons in the low energy band is about five times larger than in the high energy band (for a differential energy spectrum parameterized by a PL with photon index of 1.8, which is the case of Mrk 421). Hence the number of detected γ-rays decreases from about 50 down to about 10 for time intervals of seven days. The main reason for having comparable flux errors in these two energy bands is that the diffuse background, which follows a PL with index 2.4 for the high galactic latitude of Mrk 421, is about 25 times smaller in the high energy band. Consequently, signal to noise $\sim N_S/\sqrt{(N_B)}$ remains approximately equal.

[120] The fluxes depicted in the light curves were computed fixing the photon index to 1.78 (average index during the first 1.5 years of *Fermi* operation) and fitting only the normalization factor of the PL function.

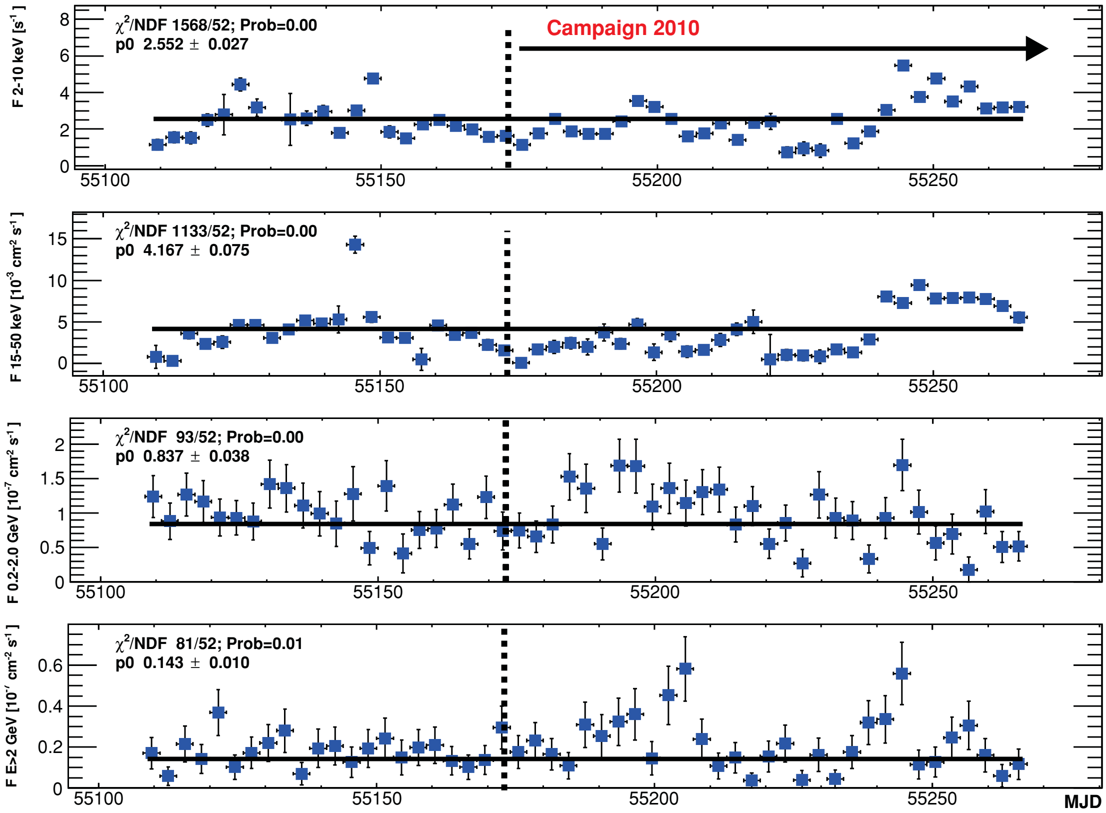

Figure 3. Multifrequency light curves of Mrk 421 with three-day-long time bins obtained with three all-sky-monitoring instruments: *RXTE*/ASM (2–10 keV, top), *Swift*/BAT (15–50 keV, second from top), and *Fermi*-LAT for two different energy ranges (0.2–2 GeV, third from top, and >2 GeV, bottom). The light curves cover the period from 2009 October 4 to 2010 March 12. Vertical bars denote 1σ uncertainties and horizontal error bars show the width of the time interval. The black dashed lines and legends show the results from constant fits to the entire data set. The vertical dashed lines denote the beginning of the extensive multifrequency campaign on Mrk 421 during the 2010 season.

(A color version of this figure is available in the online journal.)

We do not see variations in the LAT hardness ratio (i.e., $F(>2\ \mathrm{GeV})/F(0.2\text{–}2\ \mathrm{GeV})$ with the γ-ray flux, but this is limited by the relatively large uncertainties and the low γ-ray flux variability during this time interval. The data from *RXTE*/ASM were obtained from the ASM Web site.[121] We filtered out the data according to the provided prescription on the ASM Web site, and made a weighted average of all the dwells (scan/rotation of the ASM Scanning Shadow Cameras lasting 90 s) from the seven-day-long time intervals defined for the *Fermi* data. The data from *Swift*/BAT were gathered from the BAT Web site.[122] We retrieved the daily averaged BAT values and produced a weighted average for all the seven-day-long time intervals defined for the *Fermi* data.

The X-ray flux from Mrk 421 was $\sim$1.7 counts s^{-1} in ASM and $\sim 1.9 \times 10^{-3}$ counts s^{-1} cm^{-2} in BAT. These fluxes correspond to $\sim$22 mCrab in ASM (1 Crab = 75 counts s^{-1}) and 9 mCrab in BAT (1 Crab = 0.22 counts s^{-1} cm^{-2}), although given the recent reports on flux variability from the Crab Nebula (see Wilson-Hodge et al. 2011; Abdo et al. 2011a; Tavani et al. 2011), the flux from the Crab Nebula is not a good absolute standard candle any longer and hence those numbers need to be taken with caveats. One may note that the X-ray activity was rather low during the first year of *Fermi* operation. The X-ray activity increased around MJD 54990 and then increased even more around MJD 55110. The γ-ray activity seemed to follow some of the X-ray activity, but the variations in the γ-ray range are substantially smoother than those observed in X-rays.

Figure 3 shows the same light curves as Figure 2, but only during the period of time after MJD 55110 (when Mrk 421 showed high X-ray activity) with a time bin of only three days. During this time period the ASM and BAT flux (integrated over three days) went beyond 5 counts s^{-1} and 8×10^{-3} counts s^{-1} cm^{-2}, respectively, which implies a flux increase by a factor of five to eight with respect to the average fluxes during the first year. It is worth noting that these large flux variations do not have a counterpart at γ-ray energies measured by *Fermi*-LAT. The MeV/GeV flux measured by LAT remained roughly constant, with the exception of a flux increase by a factor of about two for the time intervals around MJD 55180–55210 and around MJD 55240–55250, which was also seen by *RXTE*/ASM and (to some extent) by *Swift*/BAT.

We quantified the correlation among the light curves shown in Figures 2 and 3 following the prescription from Edelson & Krolik (1988). The results are shown in Table 1 for a time lag of zero, which is the one giving the largest DCF values. There is no indication of correlated activity at positive/negative time lags in the DCF versus time plot for any of the used X-ray/γ-ray bands. The advantage of using the DCF instead of the Pearson's correlation coefficient is that the latter does not consider the error in the individual flux points, while the former does. In this particular situation it is relevant to consider these errors because they are sometimes comparable

[121] See http://xte.mit.edu/ASM_lc.html.
[122] See http://swift.gsfc.nasa.gov/docs/swift/results/transients/.

Table 1
Discrete Correlation Function (DCF)

Interval	ASM-BAT	ASM-LAT$_{<2\,\mathrm{GeV}}$	ASM-LAT$_{>2\,\mathrm{GeV}}$	BAT-LAT$_{<2\,\mathrm{GeV}}$	BAT-LAT$_{>2\,\mathrm{GeV}}$	LAT$_{<2\,\mathrm{GeV}}$–LAT$_{>2\,\mathrm{GeV}}$
7 days	0.73 ± 0.20	0.28 ± 0.15	0.35 ± 0.14	0.20 ± 0.13	0.26 ± 0.13	0.31 ± 0.14
3 days	0.65 ± 0.13	0.01 ± 0.18	0.15 ± 0.19	-0.03 ± 0.13	0.01 ± 0.13	0.29 ± 0.17

Note. Computed using the flux values reported in Figure 2 (seven-day-long time intervals, first 1.5 years of *Fermi* operation) and Figure 3 (three-day-long time intervals during the last five months, where the X-ray activity was high). The DCF values are given for time lag zero. The DCF was computed as prescribed in Edelson & Krolik (1988).

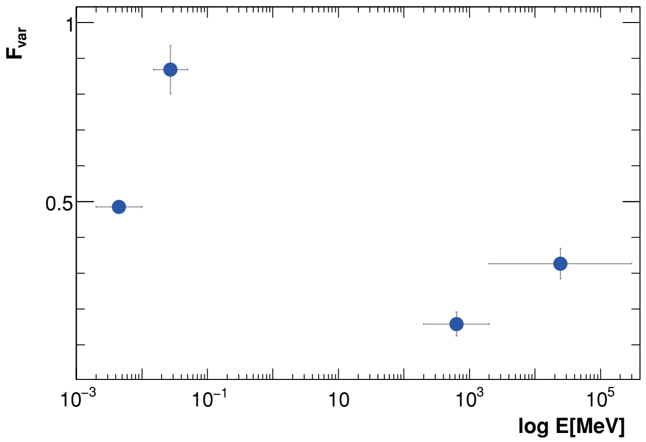

Figure 4. Fractional variability parameter for 1.5 year data (2008 August 5–2009 March 12) from three all-sky-monitoring instruments: *RXTE*/ASM (2–10 keV, first), *Swift*/BAT (15–50 keV, second) and *Fermi*-LAT for two energy ranges 0.2–2 GeV and 2–300 GeV. The fractional variability was computed according to Vaughan et al. (2003) using the light curves from Figure 2. Vertical bars denote 1σ uncertainties and horizontal bars indicate the width of each energy bin.

(A color version of this figure is available in the online journal.)

to the magnitude of the measured flux variations. The main result is a clear (DCF/DCF$_{\mathrm{error}}$ $\sim$ 4) correlation between ASM and BAT, while there is no indication of X-ray/γ-ray correlation (DCF/DCF$_{\mathrm{error}}$ $\lesssim$ 2). The correlation between the *Fermi*-LAT fluxes below and above 2 GeV is not significant (DCF $= 0.31 \pm 0.14$), which is probably due to the low variability at γ-rays, together with the relatively large flux errors for the individual seven-day-long and three-day-long time intervals.

We followed the prescription given in Vaughan et al. (2003) to quantify the flux variability by means of the fractional variability parameter, F_{var}, as a function of energy. In order to account for the individual flux measurement errors ($\sigma_{\mathrm{err},i}$), we used the "excess variance" (Nandra et al. 1997; Edelson et al. 2002) as an estimator of the intrinsic source variance. This is the variance after subtracting the expected contribution from measurement errors. For a given energy range, the F_{var} is calculated as

$$F_{\mathrm{var}} = \sqrt{\frac{S^2 - \langle\sigma^2_{\mathrm{err}}\rangle}{\langle F\rangle^2}},$$

where $\langle F\rangle$ is the mean photon flux, S the standard deviation of the N flux points, and $\langle\sigma^2_{\mathrm{err}}\rangle$ the average mean square error, all determined for a given energy bin.

Figure 4 shows the derived F_{var} values for the four energy ranges and the time window covered by the light curves shown in Figure 2. The fractional variability is significant for all energy ranges, with the X-rays having a substantially higher variability than the γ-rays.

It is interesting to note that while the PL photon index variations from Figure 1 were not statistically significant ($\chi^2/NDF = 87/82$), Figure 4 shows that the fractional variability for photon energies above 2 GeV is higher than that below 2 GeV; specifically, $F_{\mathrm{var}}(E < 2\ \mathrm{GeV}) = 0.16 \pm 0.04$ while $F_{\mathrm{var}}(E > 2\mathrm{GeV}) = 0.33 \pm 0.04$. This apparent discrepancy between the results reported in Figure 1 and the ones reported in Figure 4 (produced with the flux points from Figure 2) might be due to the fact that, on timescales of seven days, the photons below 2 GeV dominate the determination of the PL photon index in the unbinned likelihood fit. In other words, the source is bright enough in the energy range 0.3–2 GeV such that the (relatively few) photons above 2 GeV do not have a large (statistical) weight in the computation of the PL photon index. Consequently, we are more sensitive to spectral variations when doing the analysis separately for these two energy ranges.

One may also note that, besides the larger variability in the *Fermi* fluxes above 2 GeV with respect to those below 2 GeV, the variability in the BAT fluxes (15–50 keV) is also higher than that of ASM (2–10 keV). The implications of this experimental result will be further discussed in Section 7.3, in light of the modeling results presented in Section 6.2.

4. SPECTRAL ANALYSIS UP TO 400 GeV

The LAT instrument allows one to accurately reconstruct the photon energy over many orders of magnitude. Figure 5 shows the spectrum of Mrk 421 in the energy range 0.1–400 GeV. This is the first time that the spectrum of Mrk 421 can be studied with this level of detail over this large a fraction of the electromagnetic spectrum, which includes the previously unexplored energy range 10–100 GeV. The spectrum was computed using the analysis procedures described in Section 2. In order to reduced systematics, the spectral fit was performed using photon energies greater than 0.3 GeV, where the LAT instrument has good angular resolution and large effective area. The black line in Figure 5 is the result of a fit with a single PL function over the energy range 0.3–400 GeV, and the red contour is the 68% uncertainty of the fit. The data are consistent with a pure PL function with a photon index of 1.78 ± 0.02. The black data points are the result of performing the analysis on differential energy ranges (2.5 bins per decade of energy).[123] The points are well within 1σ–2σ from the fit to the overall spectrum (black line), which confirms that the entire *Fermi* spectrum is consistent with a pure PL function.

However, it is worth noticing that the error bars at the highest energies are relatively large due to the low photon count. In the

[123] Because of the analysis being carried out in small energy ranges, we fixed the spectral index to 1.78, which is the value obtained when fitting the entire energy range. We repeated the same procedure fixing the photon indices to 1.5 and 2.0, and found no significant change. Therefore, the results from the differential energy analysis are not sensitive to the selected photon index used in the analysis.

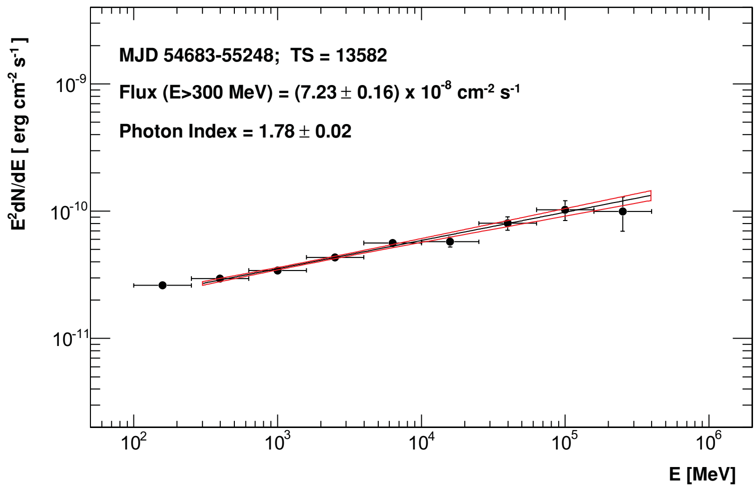

Figure 5. *Fermi* spectrum of Mrk 421 during the period from 2008 August 5 to 2010 February 20. The black line is the likelihood PL fit, the red contour is the 68% uncertainty of the fit, and the black data points show the energy fluxes computed on differential energy ranges. The inlay summarizes the unbinned likelihood PL fit in the energy range 0.3–400 GeV.

(A color version of this figure is available in the online journal.)

energy bins 60–160 GeV and 160–400 GeV, the predicted (by the model for Mrk 421) numbers of photons detected by LAT are 33 and 11, respectively. Even though the low background makes those signals very significant (TS values of 562 and 195, respectively), the statistical uncertainties in the energy flux values are naturally large and hence they could hide a potential turnover in the spectrum of Mrk 421 at around 100 GeV. Indeed, when performing the likelihood analysis on LAT data above 100 GeV, one obtains a photon flux above 100 GeV of $(5.6\pm1.1)\times10^{-10}$ ph cm^{-2} s^{-1} with a photon index of 2.6 ± 0.6, which might suggest a turnover in the spectrum, consistent with the TeV spectra determined by past observations with IACTs (Krennrich et al. 2002; Aharonian et al. 2003, 2005; Albert et al. 2007a). In order to make a statistical evaluation of this possibility, the LAT spectrum (in the range 0.3–400 GeV) was fit with a broken power law (BPL) function, obtaining the indices of 1.77 ± 0.02 and 2.9 ± 1.0 below and above the break energy of 182 ± 39 GeV, respectively. The likelihood ratio of the BPL and the PL gave 0.7, which, given the two extra degrees of freedom for the BPL function, indicates that the BPL function is not statistically preferred over the PL function. Therefore, the statistical significance of the LAT data above 100 GeV is not sufficiently high to evaluate the potential existence of a break (peak) in the spectrum.

5. SPECTRAL ENERGY DISTRIBUTION OF MRK 421 DURING THE 4.5 MONTH LONG MULTIFREQUENCY CAMPAIGN FROM 2009

As mentioned in Section 1, we organized a multifrequency (from radio to TeV photon energies) campaign to monitor Mrk 421 during a time period of 4.5 months. The observing campaign started on 2009 January 19 (MJD 54850) and finished on 2009 June 1 (MJD 54983). The observing strategy for this campaign was to sample the broadband emission of Mrk 421 every two days, which was accomplished at optical, X-ray, and TeV energies when the weather and/or technical limitations allowed. The main goal of this project was to collect an extensive multifrequency data set that is simultaneous and representative of the average/typical SED from Mrk 421. Such a data set can provide additional constraints that will allow us to refine the emission models, which in turn will provide new insights into the processes related to the particle acceleration and radiation in this source. In this section we describe the source coverage during the campaign, the data analysis for several of the participating instruments, and finally we report on the averaged SED resulting from the whole campaign.

5.1. *Details of the Campaign: Participating Instruments and Temporal Coverage*

The list of all the instruments that participated in the campaign is reported in Table 2, and the scheduled observations can be found online.[124] We note that in some cases the planned observations could not be performed due to bad observing conditions, while on other occasions the observations were performed but the data could not be properly analyzed due to technical problems or rapidly changing weather conditions. Figure 6 shows the time coverage as a function of the energy range for the instruments/observations used to produce the SED shown in Figure 8. Apart from the unprecedented energy coverage (including, for the first time, the GeV energy range from *Fermi*-LAT), the source was sampled very uniformly with the various instruments participating in the campaign and, consequently, it is reasonable to consider the SED constructed below as the actual average (typical) SED of Mrk 421 during the time interval covered by this multifrequency campaign. The largest non-uniformity in the sampling of the source comes from the Cherenkov telescopes, which are the instruments most sensitive to weather conditions. Moreover, while there are many radio/optical instruments spread all over the globe, in this observing campaign only two Cherenkov telescope observatories participated, namely MAGIC and the Fred Lawrence Whipple Observatory. Hence, the impact of observing conditions was more important to the coverage at the VHE γ-ray energies. During the time interval MJD 54901–54905, the *Fermi* satellite did not operate due to a spacecraft technical problem. The lack of *Fermi*-LAT data during this period is clearly seen in Figure 6.

We note that Figure 6 shows the MAGIC and Whipple coverage in VHE γ-ray energies, but only the MAGIC observations

[124] See https://confluence.slac.stanford.edu/display/GLAMCOG/Campaign+on+Mrk421+(Jan+2009+to+May+2009) maintained by D. Paneque.

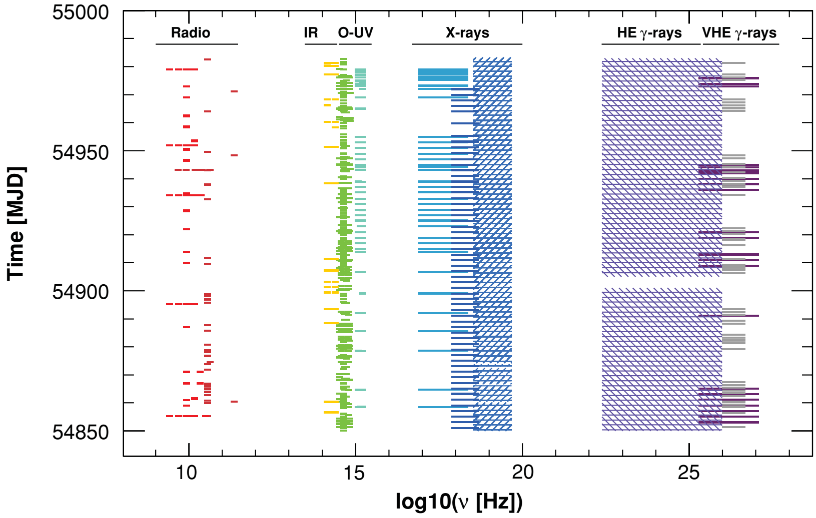

Figure 6. Time and energy coverage during the multifrequency campaign. For the sake of clarity, the minimum observing time displayed in the plot was set to half a day.

Table 2
List of Instruments Participating in the Multifrequency Campaign and Used in the Compilation of the SED Shown in Figure 8

Instrument/Observatory	Energy Range Covered	Web Site
MAGIC	0.08–5.0 TeV	http://wwwmagic.mppmu.mpg.de/
Whipple[a]	0.4–2.0 TeV	http://veritas.sao.arizona.edu/content/blogsection/6/40/
Fermi-LAT	0.1–400 GeV	http://www-glast.stanford.edu/index.html
Swift/BAT	14–195 keV	http://heasarc.gsfc.nasa.gov/docs/swift/swiftsc.html/
RXTE/PCA	3–32 keV	http://heasarc.gsfc.nasa.gov/docs/xte/rxte.html
Swift/XRT	0.3–9.6 keV	http://heasarc.gsfc.nasa.gov/docs/swift/swiftsc.html
Swift/UVOT	UVW1, UVM2, UVW2	http://heasarc.gsfc.nasa.gov/docs/swift/swiftsc.html
Abastumani (through GASP-WEBT program)	R band	http://www.oato.inaf.it/blazars/webt/
Lulin (through GASP-WEBT program)	R band	http://www.oato.inaf.it/blazars/webt/
Roque de los Muchachos (KVA; through GASP-WEBT program)	R band	http://www.oato.inaf.it/blazars/webt/
St. Petersburg (through GASP-WEBT program)	R band	http://www.oato.inaf.it/blazars/webt/
Talmassons (through GASP-WEBT program)	R band	http://www.oato.inaf.it/blazars/webt/
Valle d'Aosta (through GASP-WEBT program)	R band	http://www.oato.inaf.it/blazars/webt/
GRT	V, R, B, I bands	http://asd.gsfc.nasa.gov/Takanori.Sakamoto/GRT/index.html
ROVOR	B, R, V bands	http://rovor.byu.edu/
New Mexico Skies	R, V bands	http://www.nmskies.com/equipment.html/
MITSuME	g, Rc, Ic bands	http://www.hp.phys.titech.ac.jp/mitsume/index.html
OAGH	H, J, K bands	http://astro.inaoep.mx/en/observatories/oagh/
WIRO	J, K bands	http://physics.uwyo.edu/chip/wiro/wiro.html
SMA	225 GHz	http://sma1.sma.hawaii.edu/
VLBA	4.8, 8.3, 15.4, 23.8, 43.2 GHz	http://www.vlba.nrao.edu/
Noto	8.4, 22.3 GHz	http://www.noto.ira.inaf.it/
Metsähovi (through GASP-WEBT program)	37 GHz	http://www.metsahovi.fi/
VLBA (through MOJAVE program)	15 GHz	http://www.physics.purdue.edu/MOJAVE/
OVRO	15 GHz	http://www.ovro.caltech.edu/
Medicina	8.4 GHz	http://www.med.ira.inaf.it/index_EN.htm
UMRAO (through GASP-WEBT program)	4.8, 8.0, 14.5 GHz	http://www.oato.inaf.it/blazars/webt/
RATAN-600	2.3, 4.8, 7.7, 11.1, 22.2 GHz	http://w0.sao.ru/ratan/
Effelsberg (through F-GAMMA program)	2.6, 4.6, 7.8, 10.3, 13.6, 21.7, 31 GHz	http://www.mpifr-bonn.mpg.de/div/effelsberg/index_e.html/

Notes. The energy range shown in Column 2 is the actual energy range covered during the Mrk 421 observations, and not the instrument nominal energy range, which might only be achievable for bright sources and in excellent observing conditions.
[a] The Whipple spectra were not included in Figure 8. See the text for further comments.

were used to produce the spectra shown in Figure 8. The more extensive, but less sensitive, Whipple data (shown as gray boxes in Figure 6) were primarily taken to determine the light curve (Pichel et al. 2009) and a re-optimization was required to derive the spectrum, which will be reported elsewhere.

In the following paragraphs we briefly discuss the procedures used in the analysis of the instruments participating in the campaign. The analysis of the *Fermi*-LAT data was described in Section 2 and the results obtained will be described in detail in Section 5.2.

5.1.1. Radio Instruments

Radio data were taken for this campaign from single-dish telescopes, one millimeter interferometer, and one very long baseline interferometry (VLBI) array, at frequencies between 2.6 GHz and 225 GHz (see Table 2). The single-dish telescopes were the Effelsberg 100 m radio telescope, the Medicina 32 m radio telescope, the Metsähovi 14 m radio telescope, the Noto 32 m radio telescope, the Owens Valley Radio Observatory (OVRO) 40 m telescope, the 26 m radio telescope at the University of Michigan Radio Astronomy Observatory (UMRAO), and the 600 meter ring radio telescope RATAN-600. The millimeter interferometer was the Submillimeter Array (SMA). The NRAO Very Long Baseline Array (VLBA) was used for the VLBI observations. For the single-dish instruments and SMA, Mrk 421 is pointlike and unresolved at all observing frequencies. Consequently, the single-dish measurements denote the total flux density of the source integrated over the whole source extension. Details of the observing strategy and data reduction are given by Fuhrmann et al. (2008); Angelakis et al. (2008; F-GAMMA project), Teräsranta et al. (1998; Metsähovi), Aller et al. (1985; UMRAO), Venturi et al. (2001; Medicina and Noto), Kovalev et al. (1999; RATAN-600), and Richards et al. (2011; OVRO).

The VLBA data were obtained at various frequencies (5, 8, 15, 24, and 43 GHz) through various programs (BP143, BK150, and Monitoring of Jets in Active galactic nuclei with VLBA Experiments (MOJAVE)). The data were reduced following standard procedures for data reduction and calibration (see, for example, Lister et al. 2009; Sokolovsky et al. 2010, for a description of the MOJAVE and BK150 programs, respectively). Since the VLBA angular resolution is smaller than the radio source extension, measurements were performed for the most compact core region, as well as for the total radio structure at parsec scales. The core is partially resolved by our 15, 24 and 43 GHz observations according to the resolution criterion proposed by Kovalev et al. (2005) and Lobanov (2005). The VLBA core size was determined with two-dimensional Gaussian fits to the measured visibilities. The FWHM size of the core was estimated to be in the range of 0.06–0.12 mas at the highest observing frequencies, 15, 24 and 43 GHz. Both the total and the core radio flux densities from the VLBA data are shown in Figure 8.

5.1.2. Optical and Near-infrared Instruments

The coverage at optical frequencies was provided by various telescopes around the globe, and this decreased the sensitivity to weather and technical difficulties and provided good overall coverage of the source, as depicted in Figure 6. Many of the observations were performed within the GASP-WEBT program (e.g., Villata et al. 2008, 2009); this is the case for the data collected by the telescopes at Abastumani, Lulin, Roque de los Muchachos (KVA), St. Petersburg, Talmassons, and Valle d'Aosta observatories (R band). In addition, the Goddard Robotic Telescope (GRT), the Remote Observatory for Variable Object Research (ROVOR), the New Mexico Skies telescopes, and the Multicolor Imaging Telescopes for Survey and Monstrous Explosions (MITSuME) provided data with various optical filters, while the Guillermo Haro Observatory (OAGH) and the Wyoming Infrared Observatory (WIRO) provided data at near-IR wavelengths. See Table 2 for further details.

All the optical and near-IR instruments used the calibration stars reported in Villata et al. (1998), and the Galactic extinction was corrected with the coefficients given in Schlegel et al. (1998). The flux from the host galaxy (which is significant only below $\nu \sim 10^{15}$ Hz) was estimated using the flux values at the R band from Nilsson et al. (2007) and the colors reported in Fukugita et al. (1995), and then subtracted from the measured flux.

5.1.3. *Swift*/UVOT

The *Swift* Ultraviolet and Optical Telescope (UVOT; Roming et al. 2005) data set includes all the observations performed during the time interval MJD 54858–54979, which amounts to 46 single pointing observations that were requested to provide UV coverage during the Mrk 421 multifrequency campaign. The UVOT telescope cycled through each of three ultraviolet passbands (UVW1, UVM2, and UVW2). Photometry was computed using a five-arcsecond source region around Mrk 421 using a custom UVOT pipeline that performs the calibrations presented in Poole et al. (2008). Moreover, the custom pipeline also allows for separate, observation-by-observation corrections for astrometric misalignments (Acciari et al. 2011). A visual inspection was also performed on each of the observations to ensure proper data quality selection and correction. The flux measurements obtained have been corrected for Galactic extinction $E_{B-V} = 0.019$ mag (Schlegel et al. 1998) in each spectral band (Fitzpatrick 1999).

5.1.4. *Swift*/XRT

All the *Swift* X-Ray Telescope (XRT; Burrows et al. 2005) Windowed Timing observations of Mrk 421 carried out from MJD 54858 to 54979 were used for the analysis; this amounts to a total of 46 observations that were performed within this dedicated multi-instrument effort. The XRT data set was first processed with the XRTDAS software package (v.2.5.0) developed at the ASI Science Data Center (ASDC) and distributed by HEASARC within the HEASoft package (v.6.7). Event files were calibrated and cleaned with standard filtering criteria with the *xrtpipeline* task using the latest calibration files available in the *Swift* CALDB. The individual XRT event files were then merged together using the XSELECT package and the average spectrum was extracted from the summed event file. Events for the spectral analysis were selected within a circle with a 20 pixel ($\sim 47''$) radius, which encloses about 95% of the point-spread function (PSF), centered on the source position. The background was extracted from a nearby circular region with a 40 pixel radius. The source spectrum was binned to ensure a minimum of 20 counts per bin to utilize the χ^2 minimization fitting technique. In addition, we needed to apply a small energy offset ($\sim$40 eV) to the observed energy spectrum. The origin of this correction is likely to be CCD charge traps generated by radiation and high-energy proton damage (SWIFT-XRT-CALDB-12), which affect mostly the lowest energies (first 1–2 bins) of the spectrum. The ancillary response files were generated with the *xrtmkarf* task applying corrections for the PSF losses and CCD defects using the cumulative exposure map. The latest response matrices (v.011) available in the *Swift* CALDB were used.

The XRT average spectrum in the 0.3–10 keV energy band was fitted using the XSPEC package. We adopted a log-parabolic model of the form $F(E) = K \times (\frac{E}{\mathrm{keV}})^{-(\Gamma+\beta\times\log(\frac{E}{\mathrm{keV}}))}$ (Massaro et al. 2004a, 2004b) with an absorption hydrogen-equivalent column density fixed to the Galactic value in the direction of the source, which is 1.61×10^{20} cm^{-2} (Kalberla et al. 2005). We found that this model provided a good description of the observed spectrum, with the exception of the 1.4–2.3 keV energy band where spectral fit residuals were present. These residuals are due to known XRT calibration uncertainties (SWIFT-XRT-CALDB-12[125]) and hence we decided to exclude the 1.4–2.3 keV energy band from the analysis. The resulting spectral fit gave the following parameters: $K = (1.839 \pm 0.002) \times 10^{-1}$ ph cm^{-2} s^{-1} keV^{-1}, $\Gamma = 2.178 \pm 0.002$, and $\beta = 0.391 \pm 0.004$. The XRT SED data shown in Figure 8 were corrected for the Galactic absorption and then binned in 16 energy intervals.

5.1.5. RXTE/PCA

The *Rossi X-Ray Timing Explorer* (*RXTE*; Bradt et al. 1993) satellite performed 59 pointing observations of Mrk 421 during the time interval MJD 54851–54972. These observations amount to a total exposure of 118 ks, which was requested through a dedicated Cycle 13 proposal to provide X-ray coverage for this multi-instrument campaign on Mrk 421.

The data analysis was performed using `FTOOLS` v6.9 and following the procedures and filtering criteria recommended by the *RXTE* Guest Observer Facility[126] after 2007 September. The average net count rate from Mrk 421 was about 25 counts s^{-1} per pcu (in the energy range 3–20 keV) with flux variations typically much smaller than a factor of two. Consequently, the observations were filtered following the conservative procedures for faint sources: Earth elevation angle greater than 10°, pointing offset less than 0°.02, time since the peak of the last SAA (South Atlantic Anomaly) passage greater than 30 minutes, and electron contamination less than 0.1. For further details on the analysis of faint sources with *RXTE*, see the online Cook Book.[127] In the data analysis, in order to increase the quality of the signal, only the first xenon layer of PCU2 was used. We used the package `pcabackest` to model the background and the package `saextrct` to produce spectra for the source and background files and the script[128] `pcarsp` to produce the response matrix.

The Proportional Counter Array (PCA) average spectrum in the 3–32 keV energy band was fitted using the XSPEC package using a PL function with an exponential cutoff (cutoffpl) with a non-variable neutral hydrogen column density $N_{\rm H}$ fixed to the Galactic value in the direction of the source (1.61×10^{20} cm^{-2}; Kalberla et al. 2005). However, since the PCA bandpass starts at 3 keV, the value for $N_{\rm H}$ used does not significantly affect our results. The resulting spectral fit provided a good representation of the data for the following parameters: normalization parameter $K = (2.77 \pm 0.03) \times 10^{-1}$ ph cm^{-2} s^{-1} keV^{-1}, photon index $\Gamma = 2.413 \pm 0.015$, and cutoff energy $E_{\rm exp} = 22.9 \pm 1.3$ keV. The obtained 23 energy bins' PCA average spectrum is shown in Figure 8.

5.1.6. Swift/BAT

The *Swift*/BAT (Barthelmy et al. 2005) analysis results presented in this paper were derived with all the available data during the time interval MJD 54850–54983. The spectrum was extracted following the recipes presented in Ajello et al. (2008, 2009b). This spectrum is constructed by weight averaging the source spectra extracted over short exposures (e.g., 300 s) and it is representative of the averaged source emission over the time range spanned by the observations. These spectra are accurate to the mCrab level and the reader is referred to Ajello et al. (2009a) for more details. The *Swift*/BAT spectrum in the 15–200 keV energy range is consistent with a PL function with normalization parameter $K = 0.46 \pm 0.27$ ph cm^{-2} s^{-1} keV^{-1} and photon index $\Gamma = 3.0 \pm 0.3$. The last two flux points are within one standard deviation from the above-mentioned PL function, and hence the apparent upturn given by these last two data points in the spectrum is not significant.

5.1.7. MAGIC

MAGIC is a system of two 17 m diameter IACTs for VHE γ-ray astronomy located on the Canary Island of La Palma, at an altitude of 2200 m above sea level. At the time of the observation, MAGIC-II, the new second telescope of the current array system, was still in its commissioning phase so that Mrk 421 was observed in stand-alone mode by MAGIC-I, which has been in scientific operation since 2004 (Albert et al. 2008). The MAGIC observations were performed in the so-called wobble mode (Daum 1997). In order to have a low energy threshold, only observations at zenith angles less than 35° were used in this analysis. The bad weather and a shutdown for a scheduled hardware system upgrade during the period MJD 54948–54960 (April 27–May 13) significantly reduced the amount of time that had initially been scheduled for this campaign. The data were analyzed following the prescription given by Albert et al. (2008) and Aliu et al. (2009). The data surviving the quality cuts amounted to a total of 27.7 hr. The preliminary reconstructed photon fluxes for the individual observations gave an average flux of about 50% that of the Crab Nebula, with relatively mild (typically less than a factor of two) flux variations. The derived spectrum was unfolded to correct for the effects of the limited energy resolution of the detector and possible bias (Albert et al. 2007c). The resulting spectrum was fit satisfactorily with a single log-parabola function: $F(E) = K \times (E/0.3\,{\rm TeV})^{-(\Gamma + \beta \cdot \log(E/0.3\,{\rm TeV}))}$. The resulting spectral fit gave the following parameters: $K = (6.50 \pm 0.13) \times 10^{-10}$ ph cm^{-2} s^{-1} erg^{-1}, $\Gamma = 2.48 \pm 0.03$, and $\beta = 0.33 \pm 0.06$, with $\chi^2/NDF = 11/6$. A fit with a simple PL function gives $\chi^2/NDF = 47/7$, which confirmed the existence of curvature in the VHE spectrum.

5.2. Fermi-LAT Spectra during the Campaign

The Mrk 421 spectrum measured by *Fermi*-LAT during the period covered by the multifrequency campaign is shown in panel (b) of Figure 7. The spectrum can be described with a single PL function with photon index 1.75 ± 0.03 and photon flux $F(>0.3\ {\rm GeV}) = (6.1 \pm 0.3) \times 10^{-8}$ ph cm^{-2} s^{-1}, which is somewhat lower than the average spectrum over the first 1.5 years of *Fermi*-LAT operation (see Figure 5).

For comparison purposes, we also computed the spectra for the time periods before and after the multifrequency campaign (the time intervals MJD 54683–54850 and MJD 54983–55248, respectively). These two spectra are shown in panels (a) and (c) of Figure 7. The two spectra can be described very satisfactorily with single PL functions of photon indices 1.79 ± 0.03 and 1.78 ± 0.02 and photon fluxes $F(>0.3\ {\rm GeV}) = (7.1 \pm 0.3) \times 10^{-8}$ ph cm^{-2} s^{-1} and $F(>0.3\ {\rm GeV}) = (7.9 \pm 0.2) \times 10^{-8}$ ph cm^{-2} s^{-1}. Therefore, during the multifrequency campaign, Mrk 421 showed a spectral shape that is compatible with the periods before and after the campaign, and a photon flux which is about 20% lower than before the campaign and 30% lower than after the campaign.

[125] http://heasarc.gsfc.nasa.gov/docs/heasarc/caldb/swift/docs/xrt/SWIFT-XRT-CALDB-09_v12.pdf
[126] http://www.universe.nasa.gov/xrays/programs/rxte/pca/doc/bkg/bkg-2007-saa/
[127] http://heasarc.gsfc.nasa.gov/docs/xte/recipes/cook_book.html
[128] The CALDB files are located at http://heasarc.gsfc.nasa.gov/FTP/caldb.

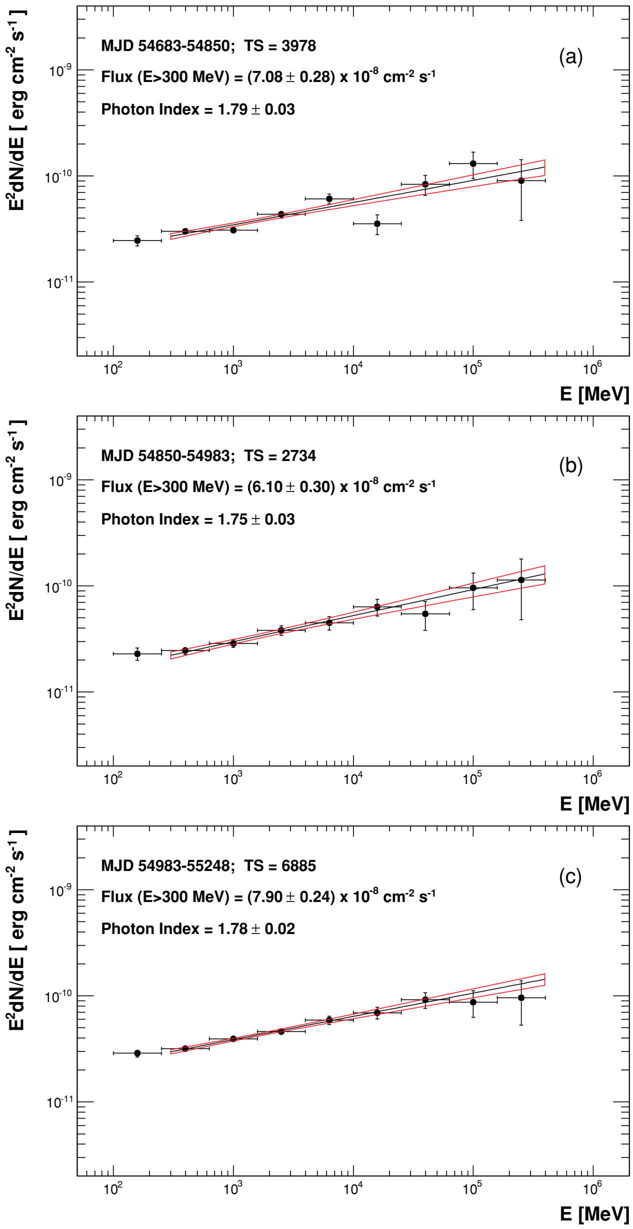

Figure 7. *Fermi* spectra of Mrk 421 for several time intervals of interest. Panel (a) shows the spectrum for the time period before the multifrequency campaign (MJD 54683–54850), panel (b) for the time interval corresponding to the multifrequency campaign (MJD 54850–54983), and panel (c) for the period after the campaign (MJD 54983–55248). In all panels, the black line depicts the result of the unbinned likelihood PL fit and the red contours denote the 68% uncertainty of the PL fit. The legend reports the results from the unbinned likelihood PL fit in the energy range 0.3–400 GeV.

(A color version of this figure is available in the online journal.)

5.3. The Average Broadband SED during the Multifrequency Campaign

The average SED of Mrk 421 resulting from our 4.5 month long multifrequency campaign is shown in Figure 8. This is the most complete SED ever collected for Mrk 421 or for any other BL Lac object (although an SED of nearly similar quality was reported in Abdo et al. 2011b for Mrk 501). At the highest energies, the combination of *Fermi*-LAT and MAGIC allows us to measure, for the first time, the high energy bump without any gap; both the rising and falling segments of the components are precisely determined by the data. The low energy bump is also measured very well: *Swift*/BAT and *RXTE*/PCA describe its falling part, *Swift*/XRT describes the peak, and the *Swift*/UV and the various optical and IR observations describe the rising part. The rising tail of this peak was also measured with various radio instruments. Especially important are the observations from SMA at 225 GHz, which help connect the bottom (radio) to the peak (optical/X-rays) of the synchrotron bump (in the νF_ν representation). The flux measurements by VLBA, especially the ones corresponding to the core, provide us with the radio flux density from a region that is presumably not much larger than the blazar emission region. Therefore, the radio flux densities from interferometric observations (from the VLBA core) are expected to be close upper limits to the radio continuum of the blazar emission component. On the other hand, the low frequency radio observations performed with single dish instruments have a relatively large contamination from the non-blazar emission and are probably considerably above the energy flux from the blazar emission region. The only spectral intervals lacking observations are 1 meV–0.4 eV, and 200 keV–100 MeV, where the sensitivity of the current instruments is insufficient to detect Mrk 421. We note, however, that the detailed GeV coverage together with our broadband, one-zone SSC modeling strongly constrains the expected emission in the difficult-to-access 1 meV–0.4 eV bandpass.

During this campaign, Mrk 421 showed low activity and relatively small flux variations at all frequencies (Paneque 2009). At VHE (>100 GeV), the measured flux is half the flux from the Crab Nebula, which is among the lowest fluxes recorded by MAGIC for this source (Albert et al. 2007a; Aleksić et al. 2010). At X-rays, the fluxes observed during this campaign are about 15 mCrab, which is about three times higher than the lowest fluxes measured by *RXTE*/ASM since 1996. Therefore, because of the low flux, low (multifrequency) variability, and the large density of observations, the collected data during this campaign can be considered an excellent proxy for the low/quiescent state SED of Mrk 421. It is worth stressing that the good agreement in the overlapping energies of the various instruments (which had somewhat different time coverages during the campaign) supports this hypothesis.

6. SED MODELING

We turn now to modeling the multifrequency data set collected during the 4.5 month campaign in the context of homogeneous hadronic and leptonic models. The models discussed below assume emission mainly from a single, spherical, and homogeneous region of the jet. This is a good approximation to model flaring events with observed correlated variability (where the dynamical timescale does not exceed the flaring timescale significantly), although it is an oversimplification for quiescent states, where the measured blazar emission might be produced by the radiation from different zones characterized by different values of the relevant parameters. There are several models in the literature along those lines (e.g., Ghisellini et al. 2005; Katarzyński et al. 2008; Graff et al. 2008; Giannios et al. 2009) but at the cost of introducing more free parameters that are, consequently, less well constrained and more difficult to compare between models. This is particularly problematic if a “limited” data set (in time and energy coverage) is employed in the modeling, although it could work well if the amount of multifrequency data is extensive enough to substantially constrain the parameter space. In this work, we adopted the one-zone homogeneous models for their simplicity as well as for being able to compare

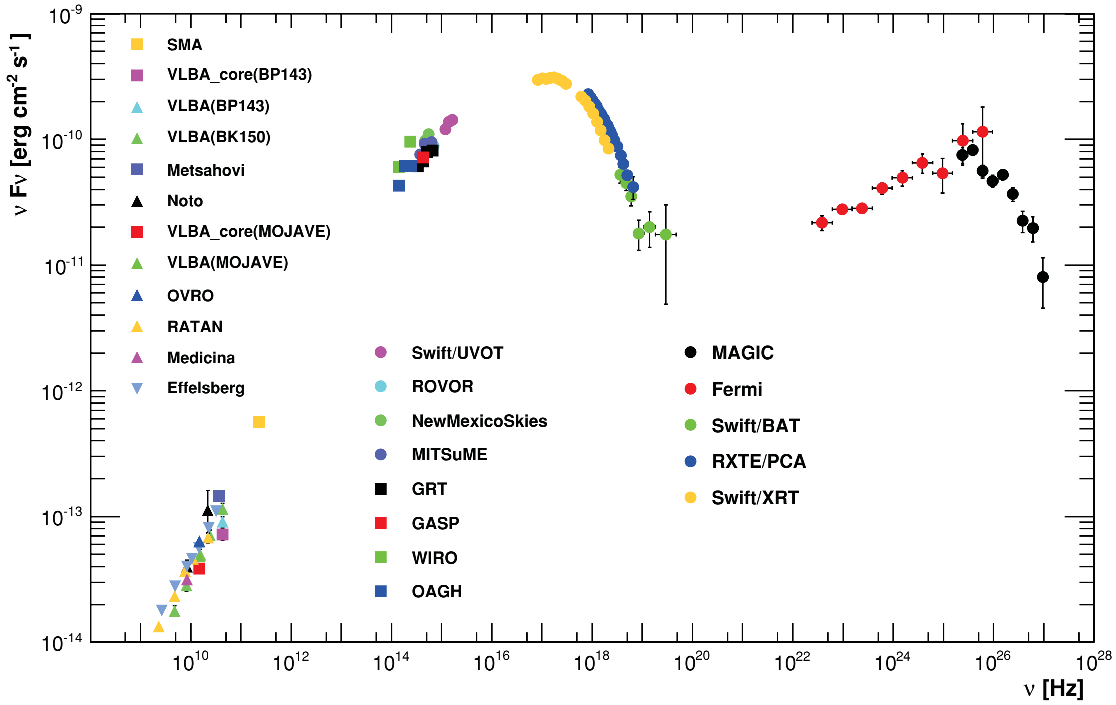

Figure 8. Spectral energy distribution of Mrk 421 averaged over all the observations taken during the multifrequency campaign from 2009 January 19 (MJD 54850) to 2009 June 1 (MJD 54983). The legend reports the correspondence between the instruments and the measured fluxes. The host galaxy has been subtracted, and the optical/X-ray data were corrected for the Galactic extinction. The TeV data from MAGIC were corrected for the absorption in the EBL using the prescription given in Franceschini et al. (2008).

with previous works. The one-zone homogeneous models are the most widely used models to describe the SED of high-peaked BL Lac objects. Furthermore, although the modeled SED is averaged over 4.5 months of observations, the very low observed multifrequency variability during this campaign, and in particular the lack of strong keV and GeV variability (see Figures 1 and 2) in these timescales, suggests that the presented data are a good representation of the average broadband emission of Mrk 421 on timescales of a few days. We therefore feel confident that the physical parameters required by our modeling to reproduce the average 4.5 month SED are a good representation of the physical conditions at the emission region down to timescales of a few days, which is comparable to the dynamical timescale derived from the models we discuss. The implications (and caveats) of the modeling results are discussed in Section 7.

Mrk 421 is at a relatively low redshift ($z = 0.031$), yet the attenuation of its VHE MAGIC spectrum by the extragalactic background light (EBL) is non-negligible for all models and hence needs to be accounted for using a parameterization for the EBL density. The EBL absorption at 4 TeV, the highest energy bin of the MAGIC data (absorption will be less at lower energies), varies according to the model used from $e^{-\tau_{\gamma\gamma}} = 0.29$ for the "Fast Evolution" model of Stecker et al. (2006) to $e^{-\tau_{\gamma\gamma}} = 0.58$ for the models of Franceschini et al. (2008) and Gilmore et al. (2009), with most models giving $e^{-\tau_{\gamma\gamma}} \sim 0.5$–$0.6$, including the model of Finke et al. (2010) and the "best fit" model of Kneiske et al. (2004). We have de-absorbed the TeV data from MAGIC with the Franceschini et al. (2008) model, although most other models give comparable results.

6.1. Hadronic Model

If relativistic protons are present in the jet of Mrk 421, hadronic interactions, if above the interaction threshold, must be considered for modeling the source emission. For the present modeling, we use the hadronic Synchrotron-Proton Blazar (SPB) model of Mücke et al. (2001, 2003). Here, the relativistic electrons (e) injected in the strongly magnetized (with homogeneous magnetic field with strength B) blob lose energy predominantly through synchrotron emission. The resulting synchrotron radiation of the primary e component dominates the low energy bump of the blazar SED, and serves as target photon field for interactions with the instantaneously injected relativistic protons (with index $\alpha_p = \alpha_e$) and pair (synchrotron-supported) cascading.

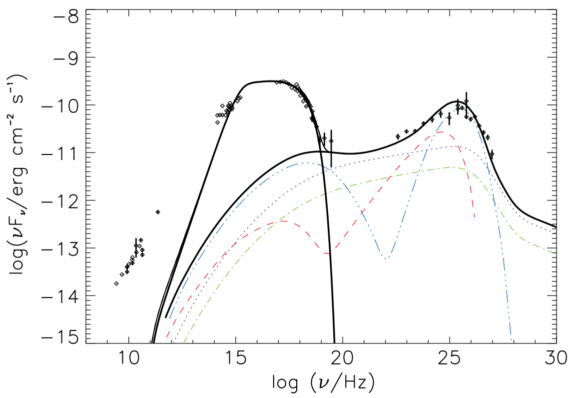

Figure 9. Hadronic model fit components: π^0-cascade (black dotted line), $\pi^\pm$ cascade (green dash-dotted line), μ-synchrotron and cascade (blue triple-dot-dashed line), and proton synchrotron and cascade (red dashed line). The black thick solid line is the sum of all emission components (which also includes the synchrotron emission of the primary electrons at optical/X-ray frequencies). The resulting model parameters are reported in Table 3.

Figures 9 and 10 show a satisfactory (single zone) SPB model representation of the data from Mrk 421 collected during the

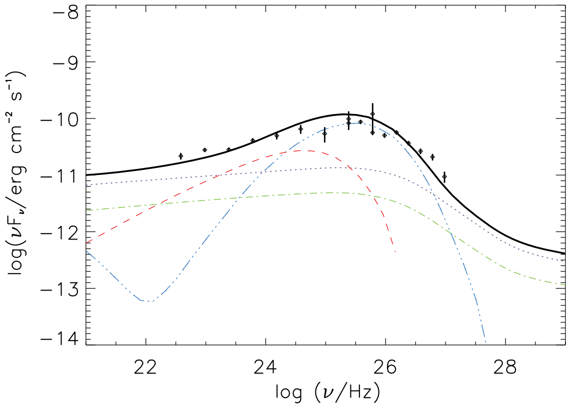

Figure 10. Expanded view of the high energy bump of the SED data and model presented in Figure 9.

Table 3
Parameter Values from the SPB Model Fit to the SED from Mrk 421 Shown in Figure 9

Parameter	Symbol	Value
Doppler factor	δ	12
Magnetic field (G)	B	50
Comoving blob radius (cm)	R	4×10^{14}
Power-law index of the injected electron distribution[a]	α_e	1.9
Power-law index of the injected proton distribution[a]	α_p	1.9
Minimum electron Lorentz factor	$\gamma_{e,\min}$	7×10^2
Maximum electron Lorentz factor	$\gamma_{e,\max}$	4×10^4
Minimum proton Lorentz factor[b]	$\gamma_{p,\min}$	1
Maximum proton Lorentz factor	$\gamma_{p,\max}$	2.3×10^9
Energy density in protons (erg cm^{-3})	u'_p	510
Ratio of number of electrons with respect to protons	e/p	90
Jet power (erg s^{-1})	$P_{\rm jet}$	4.5×10^{44}

Notes.
[a] The model assumes $\alpha_e = \alpha_p$, hence only one free parameter.
[b] The parameter $\gamma_{p,\min}$ was fixed to the lowest possible value, 1, and hence this is actually not a free parameter.

campaign. The corresponding parameter values are reported in Table 3. In order to fit the optical data, the lowest energy of the injected electrons is required to be maintained as $\gamma_{e,\min} \approx 700$ through the steady state. This requires a continuous electron injection rate density of at least $\gtrsim 1.4$ cm^{-3} s^{-1} to balance the synchrotron losses at that energy, and is a factor of ∼100 larger than the proton injection rate. The radio fluxes predicted by the model are significantly below the observed 8–230 GHz radio fluxes. This is related to the model being designed to follow the evolution of the jet emission during γ-ray production where radiative cooling dominates over adiabatic cooling. Here, the emission region is optically thick up to ∼100 GHz frequencies, and the synchrotron cooling break ($\gamma_e \sim 10$) would be below the synchrotron-self-absorption turnover. The introduction of additional, poorly constrained components would be necessary to account for the subsequent evolution of the jet through the expansion phase where the synchrotron radiation becomes gradually optically thin at centimeter wavelengths. This is omitted in the following modeling.

The measured spectra in the γ-ray band (>1 GeV) is dominated by synchrotron radiation from short-lived muons (produced during photomeson production) as well as proton synchrotron radiation, with significant overall reprocessing, while below this energy the π-cascade dominates. The interplay between muon and proton synchrotron radiation together with appreciable cascade synchrotron radiation initiated by the pairs and high energy photons from photomeson production, is responsible for the observed MeV–GeV flux. The TeV emission is dominated by the high energy photons from the muon synchrotron component. The source intrinsic model SED predicts >10 TeV emission on a level of two to three orders of magnitude below the sub-TeV flux, which will be further weakened by γ-ray absorption by the EBL.

The overall required particle and field energy density are within a factor of five of equipartition, and a total jet power (as measured in the galaxy rest frame) of 4×10^{44} erg s^{-1} in agreement with expectations for a weakly accreting disk of a BL Lac object (see Cao 2003).

Alternative model fits are possible if the injected electron and proton components do not have the same PL index. This "relaxation" of the model would add one extra parameter and so would allow for improvement in the data-model agreement, especially around the synchrotron peak and the high energy bump. It would also allow a larger tolerance on the size region R, which is considered to be small in the SPB model fit presented here.

6.2. Leptonic Model

The simplest leptonic model typically used to describe the emission from BL Lac objects is the one-zone SSC model. Within this framework, the radio through X-ray emission is produced by synchrotron radiation from electrons in a homogeneous, randomly oriented magnetic field (B) and the γ-rays are produced by inverse Compton scattering of the synchrotron photons by the same electrons which produce them. For this purpose, we use the one-zone SSC code described in Finke et al. (2008). The electron distribution from one-zone SSC models is typically parameterized with one or two PL functions (that is, zero breaks or one break) within an electron Lorentz factor range defined by $\gamma_{\min}$ and $\gamma_{\max}$ (where the electron energy is $\gamma m_e c^2$). We use the same approach in this work. However, we find that, in order to properly describe the shape of the measured broadband SED during the 4.5 month long campaign, the model requires an electron distribution parameterized with three PL functions (and hence two breaks). In other words, we must add two extra free parameters to the model: the second break at $\gamma_{\rm brk,2}$ and the index of the third PL function p_3. Note that a second break was also needed to describe the SED of Mrk 501 in the context of the synchrotron/SSC model (Abdo et al. 2011b). An alternative possibility might be to use an electron distribution parameterized with a curved function such as that resulting from episodic particle acceleration (Perlman et al. 2005) or the log-parabolic function used in Tramacere et al. (2009). However, we note that such a parameterization might have problems describing the highest X-ray energies, where the current SED data (*RXTE*/PCA and *Swift*/BAT) do not show a large spectrum curvature.

Even though the very complete SED constrains the shape of the electron distribution quite well, there is still some degeneracy in the range of allowed values for the general source parameters R (comoving blob radius), B, and δ (doppler factor). For a given break in the measured low energy (synchrotron) bump, the break in the electron distribution $\gamma_{\rm brk}$ scales as $1/\sqrt{B\delta}$. In order to minimize the range of possible parameters, we note that the emitting region radius is constrained by the variability time, t_v,

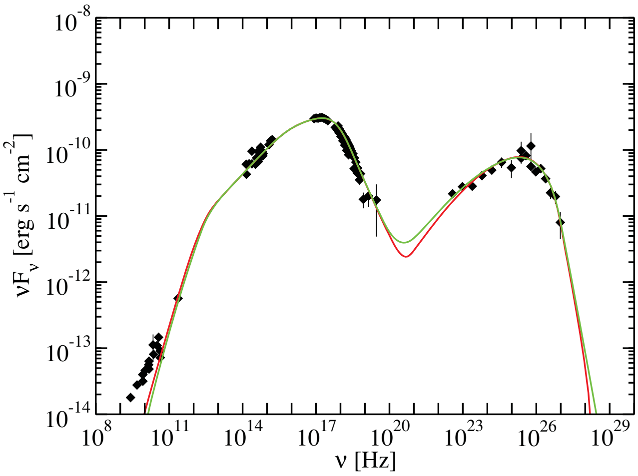

Figure 11. SED of Mrk 421 with two one-zone SSC model fits obtained with different minimum variability timescales: $t_{\rm var} = 1$ day (red curve) and $t_{\rm var} = 1$ hr (green curve). The parameter values are reported in Table 4. See the text for further details.

Table 4
Parameter Values from the One-zone SSC Model Fits to the SED from Mrk 421 Shown in Figure 11

Parameter	Symbol	Red Curve	Green Curve
Variability timescale (s)[a]	$t_{v,\rm min}$	8.64×10^4	3.6×10^3
Doppler factor	δ	21	50
Magnetic field (G)	B	3.8×10^{-2}	8.2×10^{-2}
Comoving blob radius (cm)	R	5.2×10^{16}	5.3×10^{15}
Low-energy electron spectral index	p_1	2.2	2.2
Medium-energy electron spectral index	p_2	2.7	2.7
High-energy electron spectral index	p_3	4.7	4.7
Minimum electron Lorentz factor	$\gamma_{\rm min}$	8.0×10^2	4×10^2
Break1 electron Lorentz factor	$\gamma_{\rm brk1}$	5.0×10^4	2.2×10^4
Break2 electron Lorentz factor	$\gamma_{\rm brk2}$	3.9×10^5	1.7×10^5
Maximum electron Lorentz factor	$\gamma_{\rm max}$	1.0×10^8	1.0×10^8
Jet power in magnetic field (erg s^{-1})[b]x	$P_{j,B}$	1.3×10^{43}	3.6×10^{42}
Jet power in electrons (erg s^{-1})	$P_{j,e}$	1.3×10^{44}	1.0×10^{44}
Jet power in photons (erg s^{-1})[b]	$P_{j,ph}$	6.3×10^{42}	1.1×10^{42}

Notes.
[a] The variability timescale was not derived from the model fit, but rather used as an input (constrain) to the model. See the text for further details.
[b] The quantities $P_{j,B}$ and $P_{j,ph}$ are derived quantities; only $P_{j,e}$ is a free parameter in the model.

so that

$$R = \frac{\delta c t_{v,\rm min}}{1+z} \leqslant \frac{\delta c t_v}{1+z}. \tag{1}$$

During the observing campaign, Mrk 421 was in a rather low activity state, with multifrequency flux variations occurring on timescales larger than one day (Paneque 2009), so we used $t_{v,\rm min} = 1$ day in our modeling. In addition, given that this only gives an upper limit on the size scale, and the history of fast variability detected for this object (e.g., Gaidos et al. 1996; Giebels et al. 2007), we also performed the SED model using $t_{v,\rm min} = 1$ hr. The resulting SED models obtained with these two variability timescales are shown in Figure 11, with the parameter values reported in Table 4. The blob radii are large enough in these models that synchrotron self-absorption (SSA) is not important; for the $t_{v,\rm min} = 1$ hr model, $\nu_{\rm SSA} = 3 \times 10^{10}$ Hz, at which frequency a break is barely visible in Figure 11. It is worth stressing the good agreement between the model and the data: the model describes very satisfactorily the entire measured broadband SED. The model goes through the SMA (225 GHz) data point, as well as through the VLBA (43 GHz) data point for the partially resolved radio core. The size of the VLBA core of the 2009 data from Mrk 421 at 15 GHz and 43 GHz is $\simeq$0.06–0.12 mas (as reported in Section 5.1.1) or using the conversion scale 0.61 pc mas^{-1} $\simeq$ 1–2 $\times 10^{17}$ cm. The VLBA size estimation is the FWHM of a Gaussian representing the brightness distribution of the blob, which could be approximated as 0.9 times the radius of a corresponding spherical blob (Marscher 1983). That implies that the size of the VLBA core is comparable (a factor of about two to four times larger) than that of the model blob for $t_{\rm var} = 1$ day ($\sim 5 \times 10^{16}$ cm). Therefore, it is reasonable to consider that the radio flux density from the VLBA core is indeed dominated by the radio flux density of the blazar emission. The other radio observations are single dish measurements and hence integrate over a region that is orders of magnitude larger than the blazar emission. Consequently, we treat them as upper limits for the model.

The powers of the different jet components derived from the model fits (assuming $\Gamma = \delta$) are also reported in Table 4. Estimates for the mass of the supermassive black hole in Mrk 421 range from $2 \times 10^8\, M_\odot$ to $9 \times 10^8\, M_\odot$ (Barth et al. 2003; Wu et al. 2002), and hence the Eddington luminosity should be between 2.6×10^{46} and 1.2×10^{47} erg s^{-1}, that is, well above the jet luminosity.

It is important to note that the parameters resulting from the modeling of our broadband SED differ somewhat from the parameters obtained for this source of previous works (Krawczynski et al. 2001; Błażejowski et al. 2005; Revillot et al. 2006; Albert et al. 2007b; Giebels et al. 2007; Fossati et al. 2008; Finke et al. 2008; Horan et al. 2009; Acciari et al. 2009). One difference, as already noted, is that an extra break is required. This could be a feature of Mrk 421 in all states, but we only now have the simultaneous high quality spectral coverage to identify it. For the model with $t_{\rm var} = 1$ day (which is the time variability observed during the multifrequency campaign), additional differences with previous models are in R, which is an order of magnitude larger, and B, which is an order of magnitude smaller. This mostly results from the longer variability time in this low state. Note that using a shorter variability ($t_{\rm var} = 1$ hr; green curve) gives a smaller R and bigger B than most models of this source.

Another difference in our one-zone SSC model with respect to previous works relates to the parameter $\gamma_{\rm min}$. This parameter has typically not been well constrained because the single-dish radio data can only be used as upper limits for the radio flux from the blazar emission. This means that the obtained value for $\gamma_{\rm min}$ (for a given set of other parameters R, B, and δ) can only be taken as a lower limit: a higher value of $\gamma_{\rm min}$ is usually possible. In our modeling we use simultaneous *Fermi*-LAT data as well as SMA and VLBA radio data, which we assume are dominated by the blazar emission. We note that the size of the emission from our SED model fit (when using $t_{\rm var}$ $\sim$1 day) is comparable to the partially resolved VLBA radio core and hence we think this assumption is reasonable. The requirement that the model SED fit goes through those radio points further constrains the model, and in particular the parameter $\gamma_{\rm min}$: a decrease in the value of $\gamma_{\rm min}$ would overpredict the radio data, while an increase of $\gamma_{\rm min}$ would underpredict the SMA and VLBA core radio data, as well as the *Fermi*-LAT spectrum below 1 GeV if the increase in $\gamma_{\rm min}$ would be large. We explored model fits with different $\gamma_{\rm min}$ and p_1, and found that, for the SSC model fit with $t_{\rm var} = 1$ day

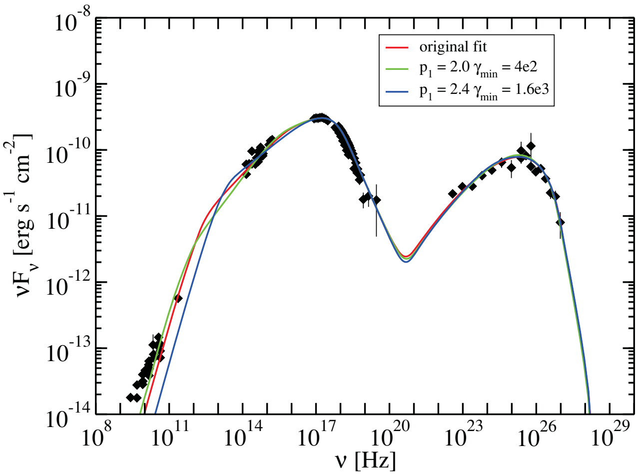

Figure 12. SSC model fit of the SED from Mrk 421 presented in Figure 11 (for $t_{\rm var}$ ∼1 day), with variations by a factor of two of the parameter $\gamma_{\rm min}$, together with adjustments in the parameter p_1 in order to match the experimental data. See the text for further details.

(red curve in Figure 11), $\gamma_{\rm min}$ is well constrained within a factor of two to the value of 8×10^2 (see Figure 12). In the case of the SSC model with $t_{\rm var} = 1$ hr (green curve in Figure 11), if we make the same assumption that the SMA and VLBA core emission is dominated by the blazer emission,[129] $\gamma_{\rm min}$ can be from 2×10^2 up to 10^3, and still provide a good match to the SMA/VLBA/optical data and the *Fermi*-LAT spectrum. In any case, for any variability timescale, the electron distribution does not extend down to $\gamma_{\rm min} \sim 1$ to a few, and is constrained within a factor of two. This is particularly relevant because, for PL distributions with index $p > 2$, the jet power carried by the electrons is dominated by the low energy electrons. Therefore, the tight constraints on $\gamma_{\rm min}$ translate into tight constraints on the jet power carried by the electrons. For instance, in the case of the model with $t_{\rm var} = 1$ hr, using $\gamma_{\rm min} = 10^3$ (instead of $\gamma_{\rm min} = 4 \times 10^2$) would reduce the jet power carried by electrons from $P_{j,e} \approx 10^{44}$ erg s^{-1} down to $P_{j,e} \approx 8 \times 10^{43}$ erg s^{-1}.

Another parameter where the results presented here differ from previous results in the literature is the first PL index p_1. This parameter is dominated by the optical and UV data points connecting with the *Swift*/XRT, as well as by the necessity of matching the model with the *Fermi*-LAT GeV data. Note that our model fit also goes over the SMA and VLBA (partially resolved) core fluxes. Again, since these constraints did not exist (or were not used) in the past, most of the one-zone SSC model results (for Mrk 421) in the literature report a p_1 value that differs from the one reported in this work. We note, however, that the values for the parameters p_2 and p_3 from our model fits, which are constrained mostly by the X-ray/TeV data, are actually quite similar to the parameters p_1 and p_2 from the previous one-zone SSC model fits to Mrk 421 data.

7. DISCUSSION

In this section of the paper, we discuss the implications of the experimental and SED modeling results presented in the previous sections. As explained at the beginning of Section 6, for simplicity and for the sake of comparison with previously published results, we modeled the SED with scenarios based on one-zone homogeneous emitting regions, which are commonly used to parameterize the broadband emission in blazars. We note that this is a simplification of the problem; the emission in blazar jets could be produced in an inhomogeneous or stratified region, as well as in N independent regions. An alternative and quite realistic scenario could be a standing shock where particle acceleration takes place and radiation is being produced as the jet flow or superluminal knots cross it (e.g., Komissarov & Falle 1997; Marscher et al. 2008). The Lorentz factor of the plasma, as it flows through the standing (and by necessity oblique) shock, is the Lorentz factor (and through setting the angle, the Doppler factor) of the model. We note, however, that, as discussed in Sikora et al. (1997), the steady-state emission could also be parameterized by N moving blobs that only radiate when passing through the standing shock. If at any given moment only one of these blobs were visible at the observer frame, the one-zone homogeneous model could be a plausible approximation of the standing-shock scenario.

In any case, the important thing is that, in the proposed physical scenario, the stability timescale of the particle accelerating shock front is not connected to the much shorter cooling times that give rise to spectral features. For as long as the injection of particles in the blob and the dynamics of the blob remain unchanged, the SED, along with the breaks due to radiative cooling and due to the value of $\gamma_{\rm min}$ where *Fermi* acceleration presumably picks up, will remain unchanged. The lack of (substantial) multifrequency variability observed during this campaign suggests that this is the case, and hence that the 4.5 month averaged SED is also representative of the broadband emission of SED during much shorter periods of time that are comparable to the dynamical timescales derived from the models.

7.1. What are the Spectral Breaks Telling Us?

In our homogenous leptonic model, we reproduce the location of the νf_ν peaks by fitting the Lorentz factors $\gamma_{\rm brk,1}$ and $\gamma_{\rm brk,2}$ (as well as the values of B and δ) where the electron energy distribution breaks. There is, however, a Lorentz factor where one typically (in blazar modeling) expects a break in the electron energy distribution (EED), and this is the Lorentz factor $\gamma_c = 3\pi m_e c^2/(\sigma_\tau B^2 R)$ where the escape time from the source equals the radiative (synchrotron) cooling time. The fact that the values of the second break, $\gamma_{\rm brk,2}$, fit by our leptonic models ($\gamma_{\rm brk,2} = 3.9 \times 10^5$, 1.7×10^5) are similar to the Lorentz factors ($\gamma_c = 1.6 \times 10^5$, 3.3×10^5), where a cooling break in the EED is expected, strongly suggests that the second break in the EED derived from the modeling is indeed the cooling break.

The observed spectral shape in both the low and high energy SED components are reproduced in our homogenous model by a change of electron index $\Delta p = p_3 - p_2 = 2.0$. Such a large break in the EED is in contrast to the canonical cooling break $\Delta p = p_3 - p_2 = 1.0$ that produces a spectral index change of $\Delta\alpha = 0.5$, as predicted for homogenous models (e.g., Longair 1994). An attempt to model the data fixing $\Delta p = p_3 - p_2 = 1.0$ gave unsatisfactory results, and hence this is not an option; a large spectral break is needed. It would be tempting to speculate that what we observe is not a cooling break, but rather something that results from a characteristic of the acceleration process which is not understood and that, therefore, does not bind us to the $\Delta p = 1.0$ constraint. But we would then have to attribute to shear fortuity the fact that the Lorentz factors where this break

[129] In the case of $t_{\rm var} \sim 1$ hr, the size of the emission region derived from the SSC model is one order of magnitude smaller than the size of the VLBA core and hence the assumption used is somewhat less valid than for the model with $t_{\rm var} \sim 1$ day.

takes place are very close to the Lorentz factors where cooling is actually expected.

The question that naturally arises is why, although the EED break postulated by the homogeneous model is at nearly the same energy as the expected cooling break, the spectral break observed is stronger. Such strong breaks are the rule rather than the exception in some non-thermal sources like pulsar-wind nebulae and extragalactic jets (see Reynolds 2009) and the explanations that have been given relax the assumption of a homogenous emitting zone, invoking gradients in the physical quantities describing the system (Marscher 1980). In all inhomogeneous models, electrons are injected at an inlet and are advected downstream, suffering radiative losses that result in the effective size of the source declining with increasing frequency for a given spectral component. In sources where the beaming of the emitted radiation is the same throughout the source (this is the case for non-relativistic flows or for relativistic flows with small velocity gradients), the spectral break formed is stronger than the canonical $\Delta\alpha = 0.5$ if the physical conditions change in such a way that the emissivity at a given frequency increases downstream (Wilson 1975; Coleman & Bicknell 1988; Reynolds 2009).

If, in addition to these considerations, we allow for significant relativistic velocity gradients, either in the form of a decelerating flow (Georganopoulos et al. 2003) or the form of a fast spine and slow sheath flow (Ghisellini et al. 2005), the resulting differential beaming of the emitted radiation can result in spectral breaks stronger that $\Delta\alpha \approx 0.5$. Studies of the SEDs of sources with different jet orientations (e.g., radio galaxies and blazars) can help to understand the importance of differential beaming, and therefore of relativistic velocity gradients in these flows. Because in all these models the volume of the source emitting at a given frequency is connected to the predicted spectral break, it should be possible to use the variability timescale at different frequencies to constrain the physics of the inhomogeneous flow.

7.2. Physical Properties of Mrk 421

As mentioned in Section 5.3, the SED emerging from the multifrequency campaign is the most complete and accurate representation of the low/quiescent state of Mrk 421 to date. This data provided us with an unprecedented opportunity to constrain and tune state-of-the-art modeling codes. In Section 6 we modeled the SED within two different frameworks: a leptonic and a hadronic scenario. Both models are able to represent the overall SED. As can be seen in Figures 9 and 11, the leptonic model fits describe the observational data somewhat better than the hadronic model fits; yet we also note here that, in this paper, the leptonic model has one more free parameter than the hadronic model. A very efficient way of discriminating between the two scenarios would be through multiwavelength variability observations. It is, however, interesting to discuss the differences between the two model descriptions we presented above.

7.2.1. Size and Location of the Emitting Region

The characteristic size to which the size of the emitting region must be compared is the gravitational radius of the Mrk 421 black hole. For a black hole mass of $\sim$2–9 $\times 10^8\,M_\odot$ (Barth et al. 2003; Wu et al. 2002), the corresponding size is $R_g \approx$ 0.5–2.0 $\times 10^{14}$ cm. In the hadronic model the source size can be as small as $R = 4 \times 10^{14}$ cm (larger source sizes cannot be ruled out though; see Section 6.1), within one order of magnitude of the gravitational radius. The consequence is a dense synchrotron photon energy density that facilitates frequent interactions with relativistic protons, resulting in a strong reprocessed/cascade component which leads to a softening of the spectrum occurring mostly below 100 MeV. The *Fermi*-LAT analysis presented in this paper (which used the instrument response function given by `P6_V3_DIFFUSE`) is not sensitive to these low energies and hence the evaluation of this potential softening in the spectrum will have to be done with future analyses (and more data). This will potentially allow the accurate determination of spectra down to photon energies of $\sim$20 MeV with LAT.

The leptonic model can accommodate a large range of values for R, as long as it is not so compact that internal $\gamma\gamma$ attenuation becomes too strong and absorbs the TeV γ-rays. In the particular case of $t_{\mathrm{var}} = 1$ day, which is supported by the low activity and low multifrequency variability observed during the campaign, $R = 5 \times 10^{16}$ cm, that is two to three orders of magnitude larger than the gravitational radius. Under the assumption that the emission comes from the entire (or a large fraction of the) cross-section of the jet, and assuming a conical jet, the location of the emitting region would be given by $L \sim R/\theta$, where $\theta \sim 1/\Gamma \sim 1/\delta$. Therefore, under these assumptions, which are valid for large distances ($L \gg R_g$) when the outflow is fully formed, the leptonic model would put the emission region at $L \sim 10^3$–$10^4 R_g$. We note, however, that since the R for the leptonic model is considered an upper limit on the blob size scale (see Equation (1)), this distance should be considered as an upper limit as well.

7.2.2. Particle Content and Particle Acceleration

The particle contents predicted by the hadronic and leptonic scenarios are different by construction. In the hadronic scenario presented in Section 6.1, the dominantly radiating particles are protons, secondary electron/positron pairs, muons, and pions, in addition to the primary electrons. In the leptonic scenario, the dominantly radiating particles are the primary electrons only. In both cases, the distribution of particles is clearly non-thermal and acceleration mechanisms are required.

In the leptonic scenario, the PL index $p_1 = 2.2$, which is the canonical particle spectral index from efficient first-order *Fermi* acceleration at the fronts of relativistic shocks, suggests that this process is at work in Mrk 421. For electrons to be picked up by first-order *Fermi* acceleration in perpendicular shocks, their Larmor radius is required to be significantly larger than the width of the shock, which for electron–proton plasmas is set by the Larmor radius of the dynamically dominant particles (electrons or protons). The large γ_{min} $(= 8 \times 10^2)$ provided by the model implies that electrons are efficiently accelerated by the *Fermi* mechanism only above this energy and that below this energy they are accelerated by a different mechanism that produces an extremely hard electron distribution. Such pre-acceleration mechanisms have been discussed in the past (e.g., Hoshino et al. 1992). The suggestion that the *Fermi* mechanism picks up only after γ_{min} $(= 8 \times 10^2)$ suggests a large thickness of the shock, which would imply that the shock is dominated by (cold) protons. We refer the reader to the *Fermi*-LAT paper on Mrk 501 (Abdo et al. 2011b) for more detailed discussion on this topic. In addition, in Sections 6.2 and 7.1 we argued that the second break $\gamma_{\mathrm{brk,2}} m_e c^2$ ($\sim$200 GeV) is probably due to synchrotron cooling (the electrons radiate most of their energy before exiting the region of size R), but the first break $\gamma_{\mathrm{brk,1}} m_e c^2$ ($\sim$25 GeV) must be related to the acceleration mechanism; and hence the leptonic model also requires that electrons above the first break are accelerated less efficiently. At this point it is interesting to note that the one-zone SSC model of Mrk 501 in 2009 (where the source was also observed mostly in a quiescent state), returned $\gamma_{\mathrm{brk},1} m_e c^2 \sim 20$ GeV with essentially the same spectral change (0.5) in the electron distribution (Abdo et al. 2011b). Therefore, the first break (presumably related to the acceleration mechanism) is of the same magnitude and located approximately at the same energy for both Mrk 421 and Mrk 501, which might suggest a common property in the quiescent state of HSP BL Lac objects detected at TeV energies.

The presence of intrinsic high energy breaks in the EED electron energy distribution has been observed in several of the *Fermi*-LAT blazars (see Abdo et al. 2009, 2010a). As reported in Abdo et al. (2010a), this characteristic was observed on several FSRQs, and it is present in some low-synchrotron-peaked BL Lac objects, and a small number of intermediate-synchrotron-peaked BL Lac objects; yet it is absent in all 1LAC HSP BL Lac objects. In this paper (as well as in Abdo et al. 2011b), we claim that such a feature is also present in HSP BL Lac objects like Mrk 421 and Mrk 501, yet for those objects, the breaks in the EED can only be accessed through proper SED modeling because they are smaller in magnitude, and somewhat smoothed in the high energy component. We note that, for HSP BL Lac objects, the high energy bump is believed to be produced by the EED upscattering seed photons from a wide energy range (the synchrotron photons emitted by the EED itself) and hence all the features from the EED are smoothed out. On the other hand, in the other blazar objects like FSRQs, the high energy bump is believed to be produced by the EED upscattering (external) seed photons which have a "relatively narrow" energy range. In this latter case (external Compton), the features of the EED may be directly seen in the gamma-ray spectrum. Another interesting observation is that, at least for one of the FSRQs, 3C 454.3, the location and the magnitude of the break seems to be insensitive to flux variations (Ackermann et al. 2010). If the break observed in Mrk 421 and Mrk 501 is of the same nature as that of 3C 454.3, we should also expect to see this break at the same location ($\sim$20 GeV) regardless of the activity level of these sources.

In the hadronic scenario of Figure 9, the blazar emission comes from a compact ($R \sim$ a few R_g) highly magnetized emission region, which should be sufficiently far away from the central engine so that the photon density from the accretion disk is much smaller than the density of synchrotron photons. The gyroradius of the highest energy protons ($R_L = \gamma_{p,\max} m_p c^2/(eB)$ in Gaussian-cgs units) is $\sim 1.4 \times 10^{14}$ cm, which is a factor of about three times smaller than the radius of the spherical region responsible for the blazar emission ($R = 4 \times 10^{14}$ cm), hence (barely) fulfilling the Hillas criterium. The small size of the emitting region, the ultra-high particle energies and the somewhat higher (by factor of about five) particle energy density with respect to the magnetic energy density imply that this scenario requires extreme acceleration and confinement conditions.

7.2.3. Energetics of the Jet

The power of the various components of the flow differs in the two models. In the SPB model, the particle energy density is about a factor of $\sim$5 higher than the magnetic field energy density and the proton energy density dominates over that of the electrons by a factor of $\sim$40. In the leptonic model, the electron energy density dominates over that of the magnetic field by a factor of 10. By construction, the leptonic model does not constrain the proton content and hence we need to make assumptions about the number of protons. It is reasonable to use charge neutrality to justify a comparable number of electrons and protons. Under this assumption, the leptonic model predicts that the energy carried by the electrons (which is dominated by the parameter $\gamma_{\min} \sim 10^3$) is comparable to that carried by the (cold) protons.

The overall jet power determined by the hadronic model is $P_{\mathrm{jet}} = 4.4 \times 10^{44}$ erg s^{-1}. For the day variability timescale leptonic model, assuming one cold proton per radiating electron, the power carried by the protons would be 4.4×10^{43} erg s^{-1}, giving a total jet power of $P_{\mathrm{jet}} = 1.9 \times 10^{44}$ erg s^{-1}. In both cases, the computed jet power is a small fraction ($\sim 10^{-2}$ to 10^{-3}) of the Eddington luminosity for the supermassive black hole in Mrk 421 ($2 \times 10^8\ M_\odot$), which is $L_{\mathrm{Edd}} \sim 10^{46}$–$10^{47}$ erg s^{-1}.

7.3. Interpretation of the Reported Variability

In Section 3 we reported the γ-ray flux/spectral variations of Mrk 421 as measured by the *Fermi*-LAT instrument during the first 1.5 years of operation. The flux and spectral index were determined on seven-day-long time intervals. We showed that, while the γ-ray flux above 0.3 GeV flux changed by a factor of about three, the PL photon index variations are consistent with statistical fluctuations (Figure 1) and the spectral variability could only be detected when comparing the variability in the γ-ray flux above 2 GeV with the one from the γ-ray flux below 2 GeV. It is worth pointing out that, in the case of the TeV blazar Mrk 501, the γ-ray flux above 2 GeV was also found to vary more than the γ-ray flux below 2 GeV. Yet unlike Mrk 421, Mrk 501 was less bright at γ-rays and the flux variations above 2 GeV seem to be larger, which produced statistically significant changes in the photon index from the PL fit in the energy range 0.3–400 GeV (see Abdo et al. 2011b). In any case, it is interesting to note that in these two (classical) TeV objects, the flux variations above a few GeV are larger than the ones below a few GeV, which might suggest that this is a common property in HSP BL Lac objects detected at TeV energies.

In Section 3 we also showed (see Figures 2–4) that the X-ray variability is significantly higher than that in the γ-ray band measured by *Fermi*-LAT. In addition, we also saw that the 15–50 keV (BAT) and the 2–10 keV (ASM) fluxes are positively correlated, and that the BAT flux is more variable than the ASM flux. In other words, when the source flares in X-rays, the X-ray spectrum becomes harder.

In order to understand this long baseline X-ray/γ-ray variability within our leptonic scenario, we decomposed the γ-ray bump of the SED into the various contributions from the various segments of the EED, according to our one-zone SSC model, in a similar way as it was done in Tavecchio et al. (1998). This is depicted in Figure 13. The contributions of different segments of the EED are indicated by different colors. As shown, the low-energy electrons, $\gamma_{\min} \leqslant \gamma < \gamma_{br,1}$, which are emitting synchrotron photons up to the observed frequencies $\simeq 5.2 \times 10^{15}$ Hz, dominate the production of γ-rays up to the observed photon energies of $\sim$20 GeV (green line). The contribution of higher energy electrons with Lorentz factors $\gamma_{br,1} \leqslant \gamma < \gamma_{br,2}$ is pronounced within the observed synchrotron range 5×10^{15}–10^{17} Hz, and at γ-ray energies from $\sim$20 GeV up to $\sim$ TeV (blue line). Finally, the highest energy tail of the electron energy distribution, $\gamma \geqslant \gamma_{br,2}$, responsible for the production of the observed X-ray synchrotron continuum ($>$0.5 keV) generates the bulk of γ-rays with the observed energies $>$TeV (purple line). Because of the electrons upscattering the broad energy range of synchrotron photons, the emission

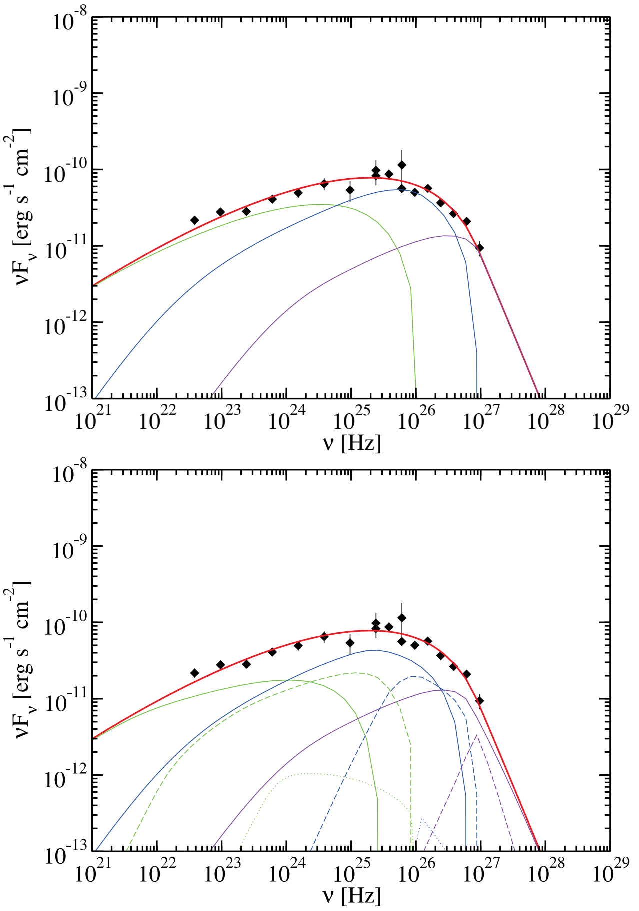

Figure 13. Decomposition of the high energy bump of the SSC continuum for Mrk 421. The data points are the same as in the high energy bump from Figure 11. The SSC fit to the average spectrum is denoted by the red solid curve. Top: contributions of the different segments of electrons Comptonizing the whole synchrotron continuum (green curve: $\gamma_{\rm min} < \gamma < \gamma_{br,1}$; blue curve: $\gamma_{br,1} < \gamma < \gamma_{br,2}$; purple curve: $\gamma_{br,2} < \gamma$). Bottom: contributions of the different segments of electrons (as in the top panel) Comptonizing different segments of the synchrotron continuum (solid curves: $\nu < \nu_{br,1} \simeq 5.3 \times 10^{15}$ Hz; dashed curves: $\nu_{br,1} < \nu < \nu_{br,2} \simeq 1.3 \times 10^{17}$ Hz; dotted curves, corresponding to $\nu > \nu_{br,2}$).

of the different electron segments are somewhat connected, as shown in the bottom plot of Figure 13. Specifically, the low energy electrons have also contributed to the TeV photon flux through the emitted synchrotron photons which are being upscattered by the high energy electrons. Hence, changes in the number of low energy electrons should also have an impact on the TeV photon flux. However, note that the synchrotron photons emitted by the high energy electrons, which are upscattered in the Klein–Nishina regime, do not have any significant contribution to the gamma-ray flux, thus changes in the number of high energy electrons (say $\gamma > \gamma_{br,2}$) will not significantly change the MeV/GeV photon flux.

Within our one-zone SSC scenario, the γ-rays measured by *Fermi*-LAT are mostly produced by the low energy electrons ($\gamma \leqslant \gamma_{br,1}$) while the X-rays seen by ASM and BAT are mostly produced by the highest energy electrons ($\gamma \geqslant \gamma_{br,2}$). In this scenario, the significantly higher variability in the X-rays with respect to that of γ-rays suggests that the flux variations in Mrk 421 are dominated by changes in the number of the highest energy electrons. Note that the same trend is observed in the X-rays (ASM versus BAT) and γ-rays (below versus above 2 GeV); the variability in the emission increases with the energy of the radiating electrons.

The greater variability in the radiation produced by the highest energy electrons is not surprising. The cooling timescales of the electrons from synchrotron and inverse Compton (in the Thomson regime) losses scale as $t \propto \gamma^{-1}$, and hence it is expected that the emission from higher energy electrons will be the most variable. However, since the high energy electrons are the ones losing their energy fastest, in order to keep the source emitting in X-rays, injection (acceleration) of electrons up to the highest energies is needed. This injection (acceleration) of high energy electrons could well be the origin of the flux variations in Mrk 421. The details of this high energy electron injection could be parameterized by changes in the parameters $\gamma_{br,2}$, p_3, and $\gamma_{\rm max}$ within the framework of the one-zone SSC model that could result from episodic acceleration events (Perlman et al. 2005). The characterization of the SED evolution (and hence SSC parameter variations) will be one of the prime subjects of the forthcoming publications with the multi-instrument variability and correlation during the campaigns in 2009[130] and 2010.[131] We note here that SSC models, both one-zone and multizone (e.g., Graff et al. 2008), predict a positive correlation between the X-rays and the TeV γ-rays measured by IACTs. Indeed, during the 2010 campaign the source was detected in a flaring state with the TeV instruments (see ATel 2443). Such an X-ray/TeV correlation has been established in the past for this object (see Maraschi et al. 1999), although the relation is not simple. Sometimes it is linear and at other times it is quadratic (e.g., Fossati et al. 2008). The complexity of this correlation is also consistent with our one-zone SSC model; the X-rays are produced by electrons with $\gamma > \gamma_{br,2}$, while the TeV photons are produced by electrons with $\gamma > \gamma_{br,1}$, and is indirectly affected by the electrons with $\gamma < \gamma_{br,1}$ through the emitted synchrotron photons that are used as seed photons for the inverse Compton scattering (see the bottom plot of Figure 13).

We also note that the one-zone SSC scenario presented here predicts a direct correlation on the basis of simultaneous data sets between the low energy gamma-rays (from *Fermi*) and the SMA and optical frequencies, since both energy bands are produced by the lowest energy electrons in the source. On the other hand, our SPB model fit does not require such a strict correlation, but there could be a loose correlation if electrons and protons are accelerated together. In particular, a direct correlation with zero time lag between the millimeter radio frequencies and the γ-rays is not expected in our SPB model because the radiation at these two energy bands are produced at different sites. The radiation in the X-ray and γ-ray bands originates from the primary electrons, and from the protons and secondary particles created by proton-initiated processes, respectively. Consequently, although a loose correlation between the X-ray and γ-ray bands can be expected if protons and electrons are accelerated together, a strict correlation with zero time lag is rather unlikely in our model fit.

During the 2009 and 2010 campaigns, Mrk 421 was very densely sampled during a very long baseline (4.5 and 6 months for the 2009 and 2010 campaigns, respectively) and hence these data sets will provide excellent information for performing a

[130] For details of the 2009 campaign, see the URL https://confluence.slac.stanford.edu/display/GLAMCOG/Campaign+on+Mrk421+(Jan+2009+to+May+2009).

[131] For details of the 2010 campaign, see the URL https://confluence.slac.stanford.edu/display/GLAMCOG/Campaign+on+Mrk421+%28December+2009+to+December+2010%29.

very detailed study of these multiband relations. In particular, during the campaign in 2010, there were regular observations with VLBA and SMA, which will allow us to study with a greater level of detail the relationship between the rising parts of the low energy and high energy bumps, where the predictions from the leptonic and hadronic models differ.

8. CONCLUSIONS

In this work, we reported on the γ-ray activity of Mrk 421 as measured by the LAT instrument on board the *Fermi* satellite during its first 1.5 years of operation, from 2008 August 5 (MJD 54683) to 2009 March 12 (MJD 55248). Because of the large leap in capabilities of LAT with respect to its predecessor, EGRET, this is the most extensive study of the γ-ray activity of this object at GeV photon energies to date. The *Fermi*-LAT spectrum (quantified with a single PL function) was evaluated for seven-day-long time intervals. The average photon flux above 0.3 GeV was found to be $(7.23 \pm 0.16) \times 10^{-8}$ ph cm^{-2} s^{-1}, and the average photon index 1.78 ± 0.02. The photon flux changed significantly (up to a factor of about three) while the spectral variations were mild. The variations in the PL photon index were not statistically significant, yet the light curves and variability quantification below and above 2 GeV showed that the high γ-ray energies vary more than the low energy γ-rays. We found $F_{\mathrm{var}}(E < 2\ \mathrm{GeV}) = 0.16 \pm 0.04$ while $F_{\mathrm{var}}(E > 2\ \mathrm{GeV}) = 0.33 \pm 0.04$. We compared the LAT γ-ray activity in these two energy ranges (0.2–2 GeV and >2 GeV) with the X-ray activity recorded by the all-sky instruments *RXTE*/ASM (2–10 keV) and *Swift*/BAT (15–50 keV). We found that X-rays are significantly more variable than γ-rays, with no significant ($\lesssim 2\sigma$) correlation between them. We also found that, within the X-ray and γ-ray energy bands, the variability increased with photon energy. The physical interpretation of this result within the context of the one-zone SSC model is that the variability in the radiation increases with the energy of the electrons that produce them, which is expected given the radiating timescales for synchrotron and inverse Compton emission.

We also presented the first results from the 4.5 month long multifrequency campaign on Mrk 421, which lasted from 2009 January 19 (MJD 54850) to 2009 June 1 (MJD 54983). During this time period, the source was systematically observed from radio to TeV energies. Because of the low activity and low variability shown during this campaign, the compiled data provided us with the best SED yet of Mrk 421 in the low/quiescent state.

The broadband SED was modeled with two different scenarios: a leptonic (one-zone SSC) model and a hadronic model (SPB). Both frameworks are able to describe reasonably well the average SED, implying comparable powers for the jet emission, which constitute only a small fraction ($\sim 10^{-2}$ to 10^{-3}) of the Eddington luminosity. However, those models differ on the predicted environment for the blazar emission: the leptonic scenario constrains the size to be $R \lesssim 10^4 R_g$, the magnetic field to $B \sim 0.05$ G and particles (electrons) with energies up to $\sim 5 \times 10^{13}$ eV while, if $\alpha_e = \alpha_p$, our hadronic scenario implies a size of the emitting region of a few R_g, a magnetic field $B \sim 50$ G and particles (protons) with energies up to $\sim 2 \times 10^{18}$ eV, which requires extreme conditions for particle acceleration and confinement.

The leptonic scenario suggests that the acceleration of the radiating particles (electrons) is through diffusive shock acceleration in relativistic shocks mediated by cold protons, and that this mechanism accelerates particles (electrons) less efficiently above an energy of $\sim$25 GeV, which is comparable to what was reported in Abdo et al. (2011b) for another classical TeV blazar, Mrk 501. In addition, unlike what was observed for Mrk 501, in the case of Mrk 421 a stronger-than-canonical electron cooling break was required to reproduce the observed SED, which might suggest that the blazar emitting region is inhomogeneous.

Within the SSC model (Figure 11), the observed X-ray/γ-ray variability during the first 1.5 years of *Fermi* operation indicates that the flux variations in Mrk 421 are produced by acceleration of the highest energy electrons, which radiate in the X-ray and TeV bands, and lose energy, radiating as they do so in the optical and GeV range. In our hadronic model (Figure 9), a rather loose correlation between the X-ray and γ-ray bands is expected if electrons and protons are accelerated together. A forthcoming publication will report on whether these emission models can reproduce the multiband flux variations observed during the intensive campaigns on Mrk 421 performed in 2009 and 2010. Those studies should help us distinguish between the hadronic and the leptonic scenarios and eventually lead to a better understanding of one of the fundamental mysteries of blazars: how flux variations are produced.

The authors of the paper thank the anonymous referee for very well-organized and constructive comments that helped improve the quality and clarity of this publication.

The *Fermi*-LAT Collaboration acknowledges the generous support of a number of agencies and institutes that have supported the *Fermi*-LAT Collaboration. These include the National Aeronautics and Space Administration and the Department of Energy in the United States, the Commissariat à l'Energie Atomique and the Centre National de la Recherche Scientifique/Institut National de Physique Nucléaire et de Physique des Particules in France, the Agenzia Spaziale Italiana and the Istituto Nazionale di Fisica Nucleare in Italy, the Ministry of Education, Culture, Sports, Science and Technology (MEXT), High Energy Accelerator Research Organization (KEK), and Japan Aerospace Exploration Agency (JAXA) in Japan, and the K. A. Wallenberg Foundation, the Swedish Research Council and the Swedish National Space Board in Sweden. Additional support for science analysis during the operations phase is gratefully acknowledged from the Istituto Nazionale di Astrofisica in Italy and the Centre National d'Études Spatiales in France.

The MAGIC Collaboration thanks the Instituto de Astrofísica de Canarias for the excellent working conditions at the Observatorio del Roque de los Muchachos in La Palma. The support of the German BMBF and MPG, the Italian INFN, the Swiss National Fund SNF, and the Spanish MICINN is gratefully acknowledged. This work was also supported by the Marie Curie program, by the CPAN CSD2007-00042 and MultiDark CSD2009-00064 projects of the Spanish Consolider-Ingenio 2010 programme, by grant DO02-353 of the Bulgarian NSF, by grant 127740 of the Academy of Finland, by the YIP of the Helmholtz Gemeinschaft, by the DFG Cluster of Excellence "Origin and Structure of the Universe," and by the Polish MNiSzW Grant N N203 390834.

We acknowledge the use of public data from the *Swift* and *RXTE* data archives. The Metsähovi team acknowledges the support from the Academy of Finland for the observing projects (numbers 212656, 210338, among others). This research has made use of data obtained from the National Radio Astronomy Observatory's Very Long Baseline Array (VLBA), projects BK150, BP143, and BL149 (MOJAVE). The National

Radio Astronomy Observatory is a facility of the National Science Foundation operated under cooperative agreement by Associated Universities, Inc. The St. Petersburg University team acknowledges support from the Russian RFBR foundation via grant 09-02-00092. AZT-24 observations are made within an agreement between Pulkovo, Rome and Teramo observatories. This research is partly based on observations with the 100 m telescope of the MPIfR (Max-Planck-Institut für Radioastronomie) at Effelsberg, as well as with the Medicina and Noto telescopes operated by INAF–Istituto di Radioastronomia. RATAN-600 observations were supported in part by the RFBR grant 08-02-00545 and the OVRO 40 m program was funded in part by NASA (NNX08AW31G) and the NSF (AST-0808050). The Submillimeter Array is a joint project between the Smithsonian Astrophysical Observatory and the Academia Sinica Institute of Astronomy and Astrophysics and is funded by the Smithsonian Institution and the Academia Sinica. M. Villata organized the optical-to-radio observations by GASP-WEBT as the president of the collaboration. The Abastumani Observatory team acknowledges financial support by the Georgian National Science Foundation through grant GNSF/ST07/4-180.

REFERENCES

Abdo, A. A., et al. 2009, ApJ, 699, 817
Abdo, A. A., et al. 2010a, ApJ, 710, 1271
Abdo, A. A., et al. 2010b, ApJS, 188, 405
Abdo, A. A., et al. 2010c, ApJ, 716, 30
Abdo, A. A., et al. 2011a, Science, 331, 739
Abdo, A. A., et al. 2011b, ApJ, 727, 129
Acciari, V. A., et al. 2009, ApJ, 703, 169
Acciari, V. A., et al. 2011, ApJ, in press (arXiv:1106.1210)
Ackermann, M., et al. 2010, ApJ, 721, 1383
Aharonian, F., et al. 2002, A&A, 393, 89
Aharonian, F., et al. 2003, A&A, 410, 813
Aharonian, F., et al. 2005, A&A, 437, 95
Ajello, M., et al. 2008, ApJ, 673, 96
Ajello, M., et al. 2009a, ApJ, 690, 367
Ajello, M., et al. 2009b, ApJ, 699, 603
Albert, J., et al. 2007a, ApJ, 663, 125
Albert, J., et al. 2007b, ApJ, 669, 862
Albert, J., et al. 2007c, Nucl. Instrum. Methods, A583, 494
Albert, J., et al. 2008, ApJ, 674, 1037
Aleksić, J., et al. 2010, A&A, 519, A32
Aliu, E., et al. 2009, Astropart. Phys., 30, 293
Aller, H. D., Aller, M. F., Latimer, G. E., & Hodge, P. E. 1985, ApJS, 59, 513
Angelakis, E., Fuhrmann, L., Marchili, N., Krichbaum, T. P., & Zensus, J. A. 2008, Mem. Soc. Astron. Ital., 79, 1042
Atwood, W. B., et al. 2009, ApJ, 697, 1071
Barth, A. J., Ho, L. C., & Sargent, W. L. W. 2003, ApJ, 583, 134
Barthelmy, S. D., et al. 2005, Space Sci. Rev., 120, 143
Błażejowski, M., et al. 2005, ApJ, 630, 130
Bradt, H. V., Rothschild, R. E., & Swank, J. H. 1993, A&AS, 97, 355
Burrows, D. N., et al. 2005, Space Sci. Rev., 120, 165
Cao, X. 2003, ApJ, 599, 147
Coleman, C. S., & Bicknell, G. V. 1988, MNRAS, 230, 497
Daum, A., et al. 1997, Astropart. Phys., 8, 1
Donnarumma, I., et al. 2009, ApJ, 691, L13
Edelson, R. A., & Krolik, J. H. 1988, ApJ, 333, 646
Edelson, R., et al. 2002, ApJ, 568, 610
Finke, J. D., Dermer, C. D., & Böttcher, M. 2008, ApJ, 686, 181
Finke, J. D., Razzaque, S., & Dermer, C. D. 2010, ApJ, 712, 238
Fitzpatrick, E. L. 1999, PASP, 111, 63
Fossati, G., et al. 2008, ApJ, 677, 906
Franceschini, A., et al. 2008, A&A, 487, 837
Fuhrmann, L., et al. 2008, A&A, 490, 1019
Fukugita, M., Shimasaku, K., & Ichikawa, T. 1995, PASP, 107, 945
Gaidos, J. A., et al. 1996, Nature, 383, 319
Gehrels, N., et al. 2004, ApJ, 611, 1005
Georganopoulos, M., & Kazanas, D. 2003, ApJ, 594, L27
Ghisellini, G., Tavvechio, F., & Chiaberge, M. 2005, A&A, 432, 401
Giannios, D., Uzdensky, D. A., & Begelman, M. C. 2009, MNRAS, 395, L29
Giebels, B., Dubus, G., & Khélifi, B. 2007, A&A, 462, 29
Gilmore, R. C., Madau, P., Primack, J. R., Somerville, R. S., & Haardt, F. 2009, MNRAS, 399, 1694
Graff, P. B., Georganopoulos, M., Perlman, E. S., & Kazanas, D. 2008, ApJ, 689, 68
Hartman, R. C., et al. 1999, ApJS, 123, 79
Horan, D., et al. 2009, ApJ, 695, 596
Hoshino, M., Arons, J., Gallant, Y. A., & Langdon, A. B. 1992, ApJ, 390, 454
Kalberla, P. M. W., et al. 2005, A&A, 440, 775
Katarzyński, K., Lenain, J.-P., Zech, A., Boisson, C., & Sol, H. 2008, MNRAS, 390, 371
Katarzyński, K., Sol, H., & Kus, A. 2003, A&A, 410, 101
Kneiske, T. M., Bretz, T., Mannheim, K., & Hartmann, D. H. 2004, A&A, 413, 807
Komissarov, S. S., & Falle, S. A. E. G. 1997, MNRAS, 288, 833
Kovalev, Y. Y., Nizhelsky, N. A., Kovalev, Y. A., Berlin, A. B., Zhekanis, G. V., Mingaliev, M. G., & Bogdantsov, A. V. 1999, A&AS, 139, 545
Kovalev, Y. Y., et al. 2005, AJ, 130, 2473
Krawczynski, H., et al. 2001, ApJ, 559, 187
Krennrich, F., et al. 2002, ApJ, 575, L9
Lister, M. L., et al. 2009, AJ, 137, 3718
Lobanov, A. P. 2005, arXiv:astro-ph/0503225
Longair, M. S. 1994, High Energy Astrophysics (Cambridge: Cambridge Univ. Press)
Maraschi, L., et al. 1999, ApJ, 526, L81
Marscher, A. P. 1980, ApJ, 235, 386
Marscher, A. P. 1983, ApJ, 264, 296
Marscher, A. P., et al. 2008, Nature, 452, 966
Massaro, E., Perri, M., Giommi, P., & Nesci, R. 2004a, A&A, 413, 489
Massaro, E., Perri, M., Giommi, P., Nesci, R., & Verrecchia, F. 2004b, A&A, 422, 103
Mattox, J. R., et al. 1996, ApJ, 461, 396243
Mücke, A., & Protheroe, R. J. 2001, Astropart. Phys., 15, 121
Mücke, A., Protheroe, R. J., Engel, R., Rachen, J. P., & Stanev, T. 2003, Astropart. Phys., 18, 593
Nandra, K., et al. 1997, ApJ, 476, 70
Nilsson, K., et al. 2007, A&A, 475, 199
Paneque, D. 2009, in ASP Conf. Ser. 427, Accretion and Ejection in AGNs: A Global View, ed. L. Maraschi et al. (San Francisco, CA: ASP), 277
Perlman, E. S., et al. 2005, ApJ, 625, 727
Pichel, A. (VERITAS Collaboration) 2009, Proc. 31st ICRC (Łódż) arXiv:0908.0010
Poole, T. S., et al. 2008, MNRAS, 383, 627
Punch, M., et al. 1992, Nature, 358, 477
Rebillot, P. F., et al. 2006, ApJ, 641, 740
Reynolds, S. P. 2009, ApJ, 703, 662
Richards, J., et al. 2011, ApJS, 194, 29
Roming, P. W. A., et al. 2005, Space Sci. Rev., 120, 95
Schlegel, D. J., Finkbeiner, D. P., & Davis, M. 1998, ApJ, 500, 525
Sikora, M., Madejski, G., Moderski, R., & Poutanen, J. 1997, ApJ, 484, 108
Sokolovsky, K. V., Kovalev, Y. Y., Lobanov, A. P., Savolainen, T., Pushkarev, A. B., & Kadler, M. 2010, arXiv:1001.2591
Stecker, F. W., Malkan, M. A., & Scully, S. T. 2006, ApJ, 648, 774
Tavani, M., et al. 2011, Science, 331, 736
Tavecchio, F., Maraschi, L., & Ghisellini, G. 1998, ApJ, 509, 608
Teräsranta, H., et al. 1998, A&AS, 132, 305
Tramacere, A., Giommi, P., Perri, M., Verrecchia, F., & Tosti, G. 2009, A&A, 501, 879
Vaughan, S., et al. 2003, MNRAS, 345, 1271
Venturi, T., et al. 2001, A&A, 379, 755
Villata, M., Raiteri, C. M., Lanteri, L., Sobrito, G., & Cavallone, M. 1998, A&AS, 130, 305
Villata, M., et al. 2008, A&A, 481, L79
Villata, M., et al. 2009, A&A, 504, L9
Wagner, R. M. 2008, MNRAS, 385, 119
Wilson, A. S. 1975, A&A, 43, 1
Wilson-Hodge, C. A., et al. 2011, ApJ, 727, L40
Wu, X.-B., Liu, F. K., & Zhang, T. Z. 2002, A&A, 389, 742

The Astrophysical Journal, 727:129 (26pp), 2011 February 1 doi:10.1088/0004-637X/727/2/129

INSIGHTS INTO THE HIGH-ENERGY γ-RAY EMISSION OF MARKARIAN 501 FROM EXTENSIVE MULTIFREQUENCY OBSERVATIONS IN THE *FERMI* ERA

A. A. Abdo[1,2], M. Ackermann[3], M. Ajello[3], A. Allafort[3], L. Baldini[4], J. Ballet[5], G. Barbiellini[6,7], M. G. Baring[8], D. Bastieri[9,10], K. Bechtol[3], R. Bellazzini[4], B. Berenji[3], R. D. Blandford[3], E. D. Bloom[3], E. Bonamente[11,12], A. W. Borgland[3], A. Bouvier[3], T. J. Brandt[13,14], J. Bregeon[4], A. Brez[4], M. Brigida[15,16], P. Bruel[17], R. Buehler[3], S. Buson[9,10], G. A. Caliandro[18], R. A. Cameron[3], A. Cannon[19,20], P. A. Caraveo[21], S. Carrigan[10], J. M. Casandjian[5], E. Cavazzuti[22], C. Cecchi[11,12], Ö. Çelik[19,23,24], E. Charles[3], A. Chekhtman[1,25], C. C. Cheung[1,2], J. Chiang[3], S. Ciprini[12], R. Claus[3], J. Cohen-Tanugi[26], J. Conrad[27,28,133], S. Cutini[22], C. D. Dermer[1], F. de Palma[15,16], E. do Couto e Silva[3], P. S. Drell[3], R. Dubois[3], D. Dumora[29], C. Favuzzi[15,16], S. J. Fegan[17], E. C. Ferrara[19], W. B. Focke[3], P. Fortin[17], M. Frailis[30,31], L. Fuhrmann[32], Y. Fukazawa[33], S. Funk[3], P. Fusco[15,16], F. Gargano[16], D. Gasparrini[22], N. Gehrels[19], S. Germani[11,12], N. Giglietto[15,16], F. Giordano[15,16], M. Giroletti[34], T. Glanzman[3], G. Godfrey[3], I. A. Grenier[5], L. Guillemot[29,32], S. Guiriec[35], M. Hayashida[3], E. Hays[19], D. Horan[17], R. E. Hughes[14], G. Jóhannesson[3], A. S. Johnson[3], W. N. Johnson[1], M. Kadler[23,36,37,38], T. Kamae[3], H. Katagiri[33], J. Kataoka[39], J. Knödlseder[13], M. Kuss[4], J. Lande[3], L. Latronico[4], S.-H. Lee[3], M. Lemoine-Goumard[29], F. Longo[6,7], F. Loparco[15,16], B. Lott[29], M. N. Lovellette[1], P. Lubrano[11,12], G. M. Madejski[3], A. Makeev[1,25], W. Max-Moerbeck[40], M. N. Mazziotta[16], J. E. McEnery[19,41], J. Mehault[26], P. F. Michelson[3], W. Mitthumsiri[3], T. Mizuno[33], A. A. Moiseev[23,41], C. Monte[15,16], M. E. Monzani[3], A. Morselli[42], I. V. Moskalenko[3], S. Murgia[3], M. Naumann-Godo[5], S. Nishino[33], P. L. Nolan[3], J. P. Norris[43], E. Nuss[26], T. Ohsugi[44], A. Okumura[45], N. Omodei[3], E. Orlando[46], J. F. Ormes[43], D. Paneque[3,47,134], J. H. Panetta[3], D. Parent[1,25], V. Pavlidou[40], T. J. Pearson[40], V. Pelassa[26], M. Pepe[11,12], M. Pesce-Rollins[4], F. Piron[26], T. A. Porter[3], S. Rainò[15,16], R. Rando[9,10], M. Razzano[4], A. Readhead[40], A. Reimer[3,48], O. Reimer[3,48], J. L. Richards[40], J. Ripken[27,28], S. Ritz[49], M. Roth[50], H. F.-W. Sadrozinski[49], D. Sanchez[17], A. Sander[14], J. D. Scargle[51], C. Sgrò[4], E. J. Siskind[52], P. D. Smith[14], G. Spandre[4], P. Spinelli[15,16], Ł. Stawarz[45,53,134], M. Stevenson[40], M. S. Strickman[1], K. V. Sokolovsky[32,54], D. J. Suson[55], H. Takahashi[44], T. Takahashi[45], T. Tanaka[3], J. B. Thayer[3], J. G. Thayer[3], D. J. Thompson[19], L. Tibaldo[5,9,10,135], D. F. Torres[18,56], G. Tosti[11,12], A. Tramacere[3,57,58], Y. Uchiyama[3], T. L. Usher[3], J. Vandenbroucke[3], V. Vasileiou[23,24], N. Vilchez[13], V. Vitale[42,59], A. P. Waite[3], P. Wang[3], A. E. Wehrle[60], B. L. Winer[14], K. S. Wood[1], Z. Yang[27,28], T. Ylinen[28,61,62], J. A. Zensus[32], M. Ziegler[49]

(The *Fermi*-LAT collaboration)

J. Aleksić[63], L. A. Antonelli[64], P. Antoranz[65], M. Backes[66], J. A. Barrio[67], J. Becerra González[68,69], W. Bednarek[70], A. Berdyugin[71], K. Berger[69], E. Bernardini[72], A. Biland[73], O. Blanch[63], R. K. Bock[47], A. Boller[73], G. Bonnoli[64], P. Bordas[74], D. Borla Tridon[47], V. Bosch-Ramon[74], D. Bose[67], I. Braun[73], T. Bretz[75], M. Camara[67], E. Carmona[47], A. Carosi[64], P. Colin[47], E. Colombo[68], J. L. Contreras[67], J. Cortina[63], S. Covino[64], F. Dazzi[30,136], A. de Angelis[30], E. De Cea del Pozo[18], B. De Lotto[76], M. De Maria[76], F. De Sabata[76], C. Delgado Mendez[68,77], A. Diago Ortega[68,69], M. Doert[66], A. Domínguez[78], D. Dominis Prester[79], D. Dorner[73], M. Doro[9,10], D. Elsaesser[75], D. Ferenc[79], M. V. Fonseca[67], L. Font[80], R. J. García López[68,69], M. Garczarczyk[68], M. Gaug[68], G. Giavitto[63], N. Godinovi[79], D. Hadasch[18], A. Herrero[68,69], D. Hildebrand[73], D. Höhne-Mönch[75], J. Hose[47], D. Hrupec[79], T. Jogler[47], S. Klepser[63], T. Krähenbühl[73], D. Kranich[73], J. Krause[47], A. La Barbera[64], E. Leonardo[65], E. Lindfors[71], S. Lombardi[9,10], M. López[9,10], E. Lorenz[73,47], P. Majumdar[72], E. Makariev[81], G. Maneva[81], N. Mankuzhiyil[30], K. Mannheim[75], L. Maraschi[82], M. Mariotti[9,10], M. Martínez[63], D. Mazin[63], M. Meucci[65], J. M. Miranda[65], R. Mirzoyan[47], H. Miyamoto[47], J. Moldón[74], A. Moralejo[63], D. Nieto[67], K. Nilsson[71], R. Orito[47], I. Oya[67], R. Paoletti[65], J. M. Paredes[74], S. Partini[65], M. Pasanen[71], F. Pauss[73], R. G. Pegna[65], M. A. Perez-Torres[78], M. Persic[30,83], J. Peruzzo[9,10], J. Pochon[68], P. G. Prada Moroni[65], F. Prada[78], E. Prandini[9,10], N. Puchades[63], I. Puljak[79], T. Reichardt[63], R. Reinthal[71], W. Rhode[66], M. Ribó[74], J. Rico[56,63], M. Rissi[73], S. Rügamer[75], A. Saggion[9,10], K. Saito[47], T. Y. Saito[47], M. Salvati[64], M. Sánchez-Conde[68,69], K. Satalecka[72], V. Scalzotto[9,10], V. Scapin[30], C. Schultz[9,10], T. Schweizer[47], M. Shayduk[47], S. N. Shore[4,84], A. Sierpowska-Bartosik[70], A. Sillanpää[71], J. Sitarek[70,47], D. Sobczynska[70], F. Spanier[75], S. Spiro[64], A. Stamerra[65], B. Steinke[47], J. Storz[75], N. Strah[66], J. C. Struebig[75], T. Suric[79], L. O. Takalo[71], F. Tavecchio[82], P. Temnikov[81], T. Terzić[79], D. Tescaro[63], M. Teshima[47], H. Vankov[81], R. M. Wagner[47], Q. Weitzel[73], V. Zabalza[74], F. Zandanel[78], R. Zanin[63]

(The MAGIC collaboration)

V. A. Acciari[85], T. Arlen[86], T. Aune[49], W. Benbow[85], D. Boltuch[87], S. M. Bradbury[88], J. H. Buckley[89], V. Bugaev[89], A. Cannon[20], A. Cesarini[90], L. Ciupik[91], W. Cui[92], R. Dickherber[89], M. Errando[93], A. Falcone[94], J. P. Finley[92], G. Finnegan[95], L. Fortson[91], A. Furniss[49], N. Galante[85], D. Gall[92], G. H. Gillanders[90], S. Godambe[95], J. Grube[91], R. Guenette[96], G. Gyuk[91], D. Hanna[96], J. Holder[87], D. Huang[97], C. M. Hui[95], T. B. Humensky[98], P. Kaaret[99], N. Karlsson[91], M. Kertzman[100], D. Kieda[95], A. Konopelko[97], H. Krawczynski[89], F. Krennrich[101], M. J. Lang[90], G. Maier[72,96], S. McArthur[89], A. McCann[96], M. McCutcheon[96], P. Moriarty[102], R. Mukherjee[93], R. Ong[86], A. N. Otte[49], D. Pandel[99], J. S. Perkins[85], A. Pichel[103], M. Pohl[72,104], J. Quinn[20], K. Ragan[96], L. C. Reyes[105], P. T. Reynolds[106], E. Roache[85], H. J. Rose[88], A. C. Rovero[103], M. Schroedter[101], G. H. Sembroski[92], G. D. Senturk[107], D. Steele[91,108], S. P. Swordy[98,137], G. Tešić[96], M. Theiling[85], S. Thibadeau[89], A. Varlotta[92], S. Vincent[95], S. P. Wakely[98], J. E. Ward[20],

T. C. Weekes[85], A. Weinstein[86], T. Weisgarber[98], D. A. Williams[49], M. Wood[86], B. Zitzer[92]
(The VERITAS collaboration)
M. Villata[109], C. M. Raiteri[109], H. D. Aller[110], M. F. Aller[110], A. A. Arkharov[111], D. A. Blinov[111], P. Calcidese[112], W. P. Chen[113], N. V. Efimova[111,114], G. Kimeridze[115], T. S. Konstantinova[114], E. N. Kopatskaya[114], E. Koptelova[113], O. M. Kurtanidze[115], S. O. Kurtanidze[115], A. Lähteenmäki[116], V. M. Larionov[111,114,117], E. G. Larionova[114], L. V. Larionova[114], R. Ligustri[118], D. A. Morozova[114], M. G. Nikolashvili[114], L. A. Sigua[115], I. S. Troitsky[114], E. Angelakis[32], M. Capalbi[22], A. Carramiñana[119], L. Carrasco[119], P. Cassaro[120], E. de la Fuente[121], M. A. Gurwell[122], Y. Y. Kovalev[32,54], Yu. A. Kovalev[54], T. P. Krichbaum[32], H. A. Krimm[23,38], P. Leto[123], M. L. Lister[92], G. Maccaferri[124], J. W. Moody[125], Y. Mori[126], I. Nestoras[32], A. Orlati[124], C. Pagani[127], C. Pace[125], R. Pearson III[125], M. Perri[22], B. G. Piner[128], A. B. Pushkarev[32,111,129], E. Ros[32,130], A. C. Sadun[131], T. Sakamoto[19], M. Tornikoski[116], Y. Yatsu[126], and A. Zook[132]

[1] Space Science Division, Naval Research Laboratory, Washington, DC 20375, USA
[2] National Research Council Research Associate, National Academy of Sciences, Washington, DC 20001, USA
[3] W. W. Hansen Experimental Physics Laboratory, Kavli Institute for Particle Astrophysics and Cosmology, Department of Physics and SLAC National Accelerator Laboratory, Stanford University, Stanford, CA 94305, USA; dpaneque@mppmu.mpg.de
[4] Istituto Nazionale di Fisica Nucleare, Sezione di Pisa, I-56127 Pisa, Italy
[5] Laboratoire AIM, CEA-IRFU/CNRS/Université Paris Diderot, Service d'Astrophysique, CEA Saclay, 91191 Gif sur Yvette, France
[6] Istituto Nazionale di Fisica Nucleare, Sezione di Trieste, I-34127 Trieste, Italy
[7] Dipartimento di Fisica, Università di Trieste, I-34127 Trieste, Italy
[8] Rice University, Department of Physics and Astronomy, MS-108, P. O. Box 1892, Houston, TX 77251, USA
[9] Istituto Nazionale di Fisica Nucleare, Sezione di Padova, I-35131 Padova, Italy
[10] Dipartimento di Fisica "G. Galilei," Università di Padova, I-35131 Padova, Italy
[11] Istituto Nazionale di Fisica Nucleare, Sezione di Perugia, I-06123 Perugia, Italy
[12] Dipartimento di Fisica, Università degli Studi di Perugia, I-06123 Perugia, Italy
[13] Centre d'Étude Spatiale des Rayonnements, CNRS/UPS, BP 44346, F-30128 Toulouse Cedex 4, France
[14] Department of Physics, Center for Cosmology and Astro-Particle Physics, The Ohio State University, Columbus, OH 43210, USA
[15] Dipartimento di Fisica "M. Merlin" dell'Università e del Politecnico di Bari, I-70126 Bari, Italy
[16] Istituto Nazionale di Fisica Nucleare, Sezione di Bari, 70126 Bari, Italy
[17] Laboratoire Leprince-Ringuet, École polytechnique, CNRS/IN2P3, Palaiseau, France
[18] Institut de Ciencies de l'Espai (IEEC-CSIC), Campus UAB, 08193 Barcelona, Spain
[19] NASA Goddard Space Flight Center, Greenbelt, MD 20771, USA
[20] University College Dublin, Belfield, Dublin 4, Ireland
[21] INAF-Istituto di Astrofisica Spaziale e Fisica Cosmica, I-20133 Milano, Italy
[22] Agenzia Spaziale Italiana (ASI) Science Data Center, I-00044 Frascati (Roma), Italy
[23] Center for Research and Exploration in Space Science and Technology (CRESST) and NASA Goddard Space Flight Center, Greenbelt, MD 20771, USA
[24] Department of Physics and Center for Space Sciences and Technology, University of Maryland Baltimore County, Baltimore, MD 21250, USA
[25] George Mason University, Fairfax, VA 22030, USA
[26] Laboratoire de Physique Théorique et Astroparticules, Université Montpellier 2, CNRS/IN2P3, Montpellier, France
[27] Department of Physics, Stockholm University, AlbaNova, SE-106 91 Stockholm, Sweden
[28] The Oskar Klein Centre for Cosmoparticle Physics, AlbaNova, SE-106 91 Stockholm, Sweden
[29] Université Bordeaux 1, CNRS/IN2p3, Centre d'Études Nucléaires de Bordeaux Gradignan, 33175 Gradignan, France
[30] Dipartimento di Fisica, Università di Udine and Istituto Nazionale di Fisica Nucleare, Sezione di Trieste, Gruppo Collegato di Udine, I-33100 Udine, Italy
[31] Osservatorio Astronomico di Trieste, Istituto Nazionale di Astrofisica, I-34143 Trieste, Italy
[32] Max-Planck-Institut für Radioastronomie, Auf dem Hügel 69, 53121 Bonn, Germany
[33] Department of Physical Sciences, Hiroshima University, Higashi-Hiroshima, Hiroshima 739-8526, Japan
[34] INAF Istituto di Radioastronomia, 40129 Bologna, Italy
[35] Center for Space Plasma and Aeronomic Research (CSPAR), University of Alabama in Huntsville, Huntsville, AL 35899, USA
[36] Dr. Remeis-Sternwarte Bamberg, Sternwartstrasse 7, D-96049 Bamberg, Germany
[37] Erlangen Centre for Astroparticle Physics, D-91058 Erlangen, Germany
[38] Universities Space Research Association (USRA), Columbia, MD 21044, USA
[39] Research Institute for Science and Engineering, Waseda University, 3-4-1, Okubo, Shinjuku, Tokyo 169-8555, Japan
[40] Cahill Center for Astronomy and Astrophysics, California Institute of Technology, Pasadena, CA 91125, USA
[41] Department of Physics and Department of Astronomy, University of Maryland, College Park, MD 20742, USA
[42] Istituto Nazionale di Fisica Nucleare, Sezione di Roma "Tor Vergata," I-00133 Roma, Italy
[43] Department of Physics and Astronomy, University of Denver, Denver, CO 80208, USA
[44] Hiroshima Astrophysical Science Center, Hiroshima University, Higashi-Hiroshima, Hiroshima 739-8526, Japan
[45] Institute of Space and Astronautical Science, JAXA, 3-1-1 Yoshinodai, Sagamihara, Kanagawa 229-8510, Japan; stawarz@astro.isas.jaxa.jp
[46] Max-Planck Institut für extraterrestrische Physik, 85748 Garching, Germany
[47] Max-Planck-Institut für Physik, D-80805 München, Germany
[48] Institut für Astro- und Teilchenphysik and Institut für Theoretische Physik, Leopold-Franzens-Universität Innsbruck, A-6020 Innsbruck, Austria
[49] Santa Cruz Institute for Particle Physics, Department of Physics and Department of Astronomy and Astrophysics, University of California at Santa Cruz, Santa Cruz, CA 95064, USA
[50] Department of Physics, University of Washington, Seattle, WA 98195-1560, USA
[51] Space Sciences Division, NASA Ames Research Center, Moffett Field, CA 94035-1000, USA
[52] NYCB Real-Time Computing Inc., Lattingtown, NY 11560-1025, USA
[53] Astronomical Observatory, Jagiellonian University, 30-244 Kraków, Poland
[54] Astro Space Center of the Lebedev Physical Institute, 117810 Moscow, Russia
[55] Department of Chemistry and Physics, Purdue University Calumet, Hammond, IN 46323-2094, USA
[56] Institució Catalana de Recerca i Estudis Avançats (ICREA), Barcelona, Spain
[57] Consorzio Interuniversitario per la Fisica Spaziale (CIFS), I-10133 Torino, Italy
[58] INTEGRAL Science Data Centre, CH-1290 Versoix, Switzerland
[59] Dipartimento di Fisica, Università di Roma "Tor Vergata," I-00133 Roma, Italy
[60] Space Science Institute, Boulder, CO 80301, USA

[61] Department of Physics, Royal Institute of Technology (KTH), AlbaNova, SE-106 91 Stockholm, Sweden
[62] School of Pure and Applied Natural Sciences, University of Kalmar, SE-391 82 Kalmar, Sweden
[63] Institut de Física d'Altes Energies (IFAE), Edifici Cn, Universitat Autònoma de Barcelona (UAB), E-08193 Bellaterra (Barcelona), Spain
[64] INAF National Institute for Astrophysics, I-00136 Roma, Italy
[65] Università di Siena and INFN Pisa, I-53100 Siena, Italy
[66] Technische Universität Dortmund, D-44221 Dortmund, Germany
[67] Universidad Complutense, E-28040 Madrid, Spain
[68] Instituto de Astrofísica de Canarias, E38205 - La Laguna (Tenerife), Spain
[69] Departamento de Astrofisica, Universidad de La Laguna, E-38205 La Laguna, Tenerife, Spain
[70] University of Łódź, PL-90236 Łódź, Poland
[71] Tuorla Observatory, University of Turku, FI-21500 Piikkiö, Finland
[72] Deutsches Elektronen Synchrotron DESY, D-15738 Zeuthen, Germany
[73] ETH Zurich, CH-8093 Zurich, Switzerland
[74] Universitat de Barcelona (ICC/IEED), E-08028 Barcelona, Spain
[75] Institut für Theoretische Physik and Astrophysik, Universität Würzburg, D-97074 Würzburg, Germany
[76] Istituto Nazionale di Fisica Nucleare, Sezione di Trieste, and Università di Trieste, I-34127 Trieste, Italy
[77] Centro de Investigaciones Energéticas, Medioambientales y Tecnológicas (CIEMAT), Madrid, Spain
[78] Instituto de Astrofísica de Andalucía, CSIC, E-18080 Granada, Spain
[79] Croatian MAGIC Consortium, Institute R. Bošković, University of Rijeka and University of Split, HR-10000 Zagreb, Croatia
[80] Universitat Autónoma de Barcelona, E-08193 Bellaterra, Spain
[81] Institute for Nuclear Research and Nuclear Energy, BG-1784 Sofia, Bulgaria
[82] INAF Osservatorio Astronomico di Brera, I-23807 Merate, Italy
[83] INAF Osservatorio Astronomico di Trieste, I-34143 Trieste, Italy
[84] Dipartimento di Fisica "Enrico Fermi," Università di Pisa, Pisa I-56127, Italy
[85] Fred Lawrence Whipple Observatory, Harvard-Smithsonian Center for Astrophysics, Amado, AZ 85645, USA
[86] Department of Physics and Astronomy, University of California, Los Angeles, CA 90095-1547, USA
[87] Department of Physics and Astronomy and the Bartol Research Institute, University of Delaware, Newark, DE 19716, USA
[88] School of Physics and Astronomy, University of Leeds, Leeds LS2 9JT, UK
[89] Department of Physics, Washington University, St. Louis, MO 63130, USA
[90] National University of Ireland Galway, University Road, Galway, Ireland
[91] Adler Planetarium and Astronomy Museum, Chicago, IL 60605, USA
[92] Department of Physics, Purdue University, West Lafayette, IN 47907, USA
[93] Department of Physics and Astronomy, Barnard College, Columbia University, New York, NY 10027, USA
[94] Department of Astronomy and Astrophysics, Pennsylvania State University, University Park, PA 16802, USA
[95] Department of Physics and Astronomy, University of Utah, Salt Lake City, UT 84112, USA
[96] Department of Physics, McGill University, Montreal, PQ, Canada H3A 2T8
[97] Department of Physics, Pittsburg State University, Pittsburg, KS 66762, USA
[98] Enrico Fermi Institute, University of Chicago, Chicago, IL 60637, USA
[99] Department of Physics and Astronomy, University of Iowa, Iowa City, IA 52242, USA
[100] Department of Physics and Astronomy, DePauw University, Greencastle, IN 46135-0037, USA
[101] Department of Physics and Astronomy, Iowa State University, Ames, IA 50011-3160, USA
[102] Department of Life and Physical Sciences, Galway-Mayo Institute of Technology, Galway, Ireland
[103] Instituto de Astronomía y Fisica del Espacio, Parbellón IAFE, Cdad. Universitaria, Buenos Aires, Argentina
[104] Institut für Physik und Astronomie, Universität Potsdam, 14476 Potsdam, Germany
[105] Kavli Institute for Cosmological Physics, University of Chicago, Chicago, IL 60637, USA
[106] Department of Applied Physics and Instrumentation, Cork Institute of Technology, Bishopstown, Cork, Ireland
[107] Columbia Astrophysics Laboratory, Columbia University, New York, NY 10027, USA
[108] Los Alamos National Laboratory, Los Alamos, NM 87545, USA
[109] INAF, Osservatorio Astronomico di Torino, I-10025 Pino Torinese (TO), Italy
[110] Department of Astronomy, University of Michigan, Ann Arbor, MI 48109-1042, USA
[111] Pulkovo Observatory, 196140 St. Petersburg, Russia
[112] Osservatorio Astronomico della Regione Autonoma Valle d'Aosta, Italy
[113] Graduate Institute of Astronomy, National Central University, Jhongli 32054, Taiwan
[114] Astronomical Institute, St. Petersburg State University, St. Petersburg, Russia
[115] Abastumani Observatory, Mt. Kanobili, 0301 Abastumani, Georgia
[116] Aalto University Metsähovi Radio Observatory, FIN-02540 Kylmälä, Finland
[117] Isaac Newton Institute of Chile, St. Petersburg Branch, St. Petersburg, Russia
[118] Circolo Astrofili Talmassons, I-33030 Campoformido (UD), Italy
[119] Instituto Nacional de Astrofísica, Óptica y Electrónica, Tonantzintla, Puebla 72840, Mexico
[120] INAF Istituto di Radioastronomia, Sezione di Noto, Contrada Renna Bassa, 96017 Noto (SR), Italy
[121] Instututo de Astronomia y Meteorologia, Dpto. de Fisica, CUCEI, Universidad de Guadalajara, Jalisco, Mexico
[122] Harvard-Smithsonian Center for Astrophysics, Cambridge, MA 02138, USA
[123] Osservatorio Astrofisico di Catania, 95123 Catania, Italy
[124] INAF Istituto di Radioastronomia, Stazione Radioastronomica di Medicina, I-40059 Medicina (Bologna), Italy
[125] Department of Physics and Astronomy, Brigham Young University, Provo Utah 84602, USA
[126] Department of Physics, Tokyo Institute of Technology, Meguro City, Tokyo 152-8551, Japan
[127] Department of Physics and Astronomy, University of Leicester, Leicester, LE1 7RH, UK
[128] Department of Physics and Astronomy, Whittier College, Whittier, CA, USA
[129] Crimean Astrophysical Observatory, 98409 Nauchny, Crimea, Ukraine
[130] Universitat de València, 46010 València, Spain
[131] Department of Physics, University of Colorado, Denver, CO 80220, USA
[132] Department of Physics and Astronomy, Pomona College, Claremont CA 91711-6312, USA
Received 2010 August 18; accepted 2010 November 19; published 2011 January 12

ABSTRACT

We report on the γ-ray activity of the blazar Mrk 501 during the first 480 days of *Fermi* operation. We find that the average Large Area Telescope (LAT) γ-ray spectrum of Mrk 501 can be well described by a single power-law function with a photon index of 1.78 ± 0.03. While we observe relatively mild flux variations with the *Fermi*-LAT (within less than a factor of two), we detect remarkable spectral variability where the hardest observed spectral index within the LAT energy range is 1.52 ± 0.14, and the softest one is 2.51 ± 0.20. These unexpected spectral changes do not correlate with the measured flux variations above 0.3 GeV. In this paper, we also present the first results from the 4.5 month long multifrequency campaign (2009 March 15—August 1) on Mrk 501, which included the Very Long Baseline Array (VLBA), *Swift*, *RXTE*, MAGIC, and VERITAS, the F-GAMMA, GASP-WEBT, and other collaborations and instruments which provided excellent temporal and energy coverage of the source throughout the entire campaign. The extensive radio to TeV data set from this campaign provides us with the most detailed spectral energy distribution yet collected for this source during its relatively low activity. The average spectral energy distribution of Mrk 501 is well described by the standard one-zone synchrotron self-Compton (SSC) model. In the framework of this model, we find that the dominant emission region is characterized by a size $\lesssim$0.1 pc (comparable within a factor of few to the size of the partially resolved VLBA core at 15–43 GHz), and that the total jet power ($\simeq 10^{44}$ erg s^{-1}) constitutes only a small fraction ($\sim 10^{-3}$) of the Eddington luminosity. The energy distribution of the freshly accelerated radiating electrons required to fit the time-averaged data has a broken power-law form in the energy range 0.3 GeV–10 TeV, with spectral indices 2.2 and 2.7 below and above the break energy of 20 GeV. We argue that such a form is consistent with a scenario in which the bulk of the energy dissipation within the dominant emission zone of Mrk 501 is due to relativistic, proton-mediated shocks. We find that the ultrarelativistic electrons and mildly relativistic protons within the blazar zone, if comparable in number, are in approximate energy equipartition, with their energy dominating the jet magnetic field energy by about two orders of magnitude.

Key words: acceleration of particles – BL Lacertae objects: general – BL Lacertae objects: individual (Mrk 501) – galaxies: active – gamma rays: general – radiation mechanisms: non-thermal

Online-only material: color figures

1. INTRODUCTION

Blazars constitute a subclass of radio-loud active galactic nuclei (AGNs), in which a jet of magnetized plasma assumed to emanate with relativistic bulk velocity from close to a central supermassive black hole points almost along the line of sight. The broadband emission spectra of these objects are dominated by non-thermal, strongly Doppler-boosted, and variable radiation produced in the innermost part of the jet. Most of the identified extragalactic γ-ray sources detected with the EGRET instrument (Hartman et al. 1999) on board the *Compton Gamma Ray Observatory* belong to this category. Blazars include flat-spectrum radio quasars (FSRQs) and BL Lacertae objects (BL Lac objects). Even though blazars have been observed for several decades at different frequencies, the existing experimental data did not permit unambiguous identification of the physical mechanisms responsible for the production of their high-energy (γ-ray) emission. Given the existing high-sensitivity detectors which allow detailed study of the low-energy (synchrotron) component of blazar sources (extending from radio up to hard X-rays), one of the reasons for the incomplete understanding of those objects was only the moderate sensitivity of previous γ-ray instruments. This often precluded detailed cross-correlation studies between the low- and high-energy emission and did not provide enough constraints on the parameters of the theoretical models. Some of the open and fundamental questions regarding blazar sources are (1) the content of their jets, (2) the location and structure of their dominant emission zones, (3) the origin of their variability, observed on timescales from minutes to tens of years, (4) the role of external photon fields (including the extragalactic background light, EBL) in shaping their observed γ-ray spectra, and (5) the energy distribution and the dominant acceleration mechanism for the underlying radiating particles.

The Large Area Telescope (LAT) instrument (Atwood et al. 2009) on board the *Fermi Gamma-ray Space Telescope* satellite provides a large improvement in the experimental capability for performing γ-ray astronomy, and hence it is shedding new light on the blazar phenomenon. In this paper, we report on the *Fermi* observations of the TeV-emitting high-frequency-peaked—or, according to a more recent classification (Abdo et al. 2010c), high-synchrotron-peaked (HSP)—BL Lac object Markarian 501 (Mrk 501; R.A. = $16^{h}45^{m}52\overset{s}{.}22$, decl. = $39^{\circ}45'36\overset{''}{.}6$, J2000, redshift $z = 0.034$), which is one of the brightest extragalactic sources in the X-ray/TeV sky. Mrk 501 was the second extragalactic object (after Markarian 421) identified as a very high energy (hereafter VHE) γ-ray emitter (Quinn et al. 1996; Bradbury et al. 1997). After a phase of moderate emission lasting for about a year following its discovery (1996), Mrk 501 went into a state of surprisingly high activity and strong variability, becoming >10 times brighter than the Crab Nebula at energies >1 TeV, as reported by various instruments/groups (Catanese et al. 1997; Samuelson et al. 1998; Aharonian et al. 1999a, 1999b, 1999c; Djannati-Ataï et al. 1999). In 1998–1999, the mean VHE γ-ray flux dropped by an order of magnitude, and the overall VHE spectrum softened significantly (Piron 2000; Aharonian et al. 2001). In 2005, γ-ray flux variability on minute timescales was observed in the VHE band, thus establishing Mrk 501 as one of the sources with the fastest γ-ray

[133] Royal Swedish Academy of Sciences Research Fellow, funded by a grant from the K. A. Wallenberg Foundation.
[134] Author to whom any correspondence should be addressed.
[135] Partially supported by the International Doctorate on Astroparticle Physics (IDAPP) program.
[136] Supported by INFN Padova.
[137] Deceased.

flux changes (Albert et al. 2007a). During the 2005 VHE flux variations (when Mrk 501 was three to four times dimmer than it was in 1997), significant spectral variability was detected as well, with a clear "harder when brighter" behavior. Those spectral variations are even more pronounced when compared with the spectrum measured during the low-activity level recently reported in Anderhub et al. (2009).

The spectral energy distribution (SED) and the multifrequency correlations of Mrk 501 have been intensively studied in the past (e.g., Pian et al. 1998; Villata & Raiteri 1999; Krawczynski et al. 2000; Sambruna et al. 2000; Tavecchio et al. 2001; Katarzyński et al. 2001; Ghisellini et al. 2002; Gliozzi et al. 2006; Anderhub et al. 2009), but the nature of this object is still far from being understood. The main reasons for this lack of knowledge are the sparse multifrequency data during long periods of time, and the moderate sensitivity available in the past to study the γ-ray emission of this source. Besides, most of the previous multifrequency campaigns were triggered by an enhanced flux level in some energy band, and hence much of our information about the source is biased toward "high-activity" states, where perhaps distinct physical processes play a dominant role. In addition, until now we knew very little about the GeV emission of Mrk 501. The only detection reported at GeV energies before *Fermi* was in Kataoka et al. (1999), but the significance of this detection was too low to include Mrk 501 in the third EGRET catalog (Hartman et al. 1999). Moreover, Mrk 501 was not detected by EGRET during the large X-ray and VHE γ-ray flare which lasted for several months in 1997 (Pian et al. 1998).

The large improvement in the performance provided by the *Fermi*-LAT compared with its predecessor, EGRET, provides us with a new perspective for the study of blazars like Mrk 501. However, it is important to emphasize that blazars can vary their emitted power by one or two orders of magnitude on short timescales, and that they emit radiation over the entire observable electromagnetic spectrum (from $\sim 10^{-6}$ eV up to $\sim 10^{13}$ eV). For this reason, the information from *Fermi*-LAT alone is not enough to understand the broadband emission of Mrk 501, and hence simultaneous data in other frequency ranges are required. In particular, the frequency ranges where the low- and high-energy spectral components peak in the SED representation are of major importance. In the case of Mrk 501, those peaks are typically located around 1 keV (low-energy bump) and 100 GeV (high-energy bump), and hence simultaneous UV/X-ray and GeV/TeV observations are essential for the proper reconstruction of the overall SED of Mrk 501. At TeV energies there has been a substantial improvement in the instrumental capability as a result of the deployment of a new generation of imaging atmospheric Cherenkov telescopes (IACTs). In particular, for the study of Mrk 501, the new telescope systems MAGIC and VERITAS provide greater sensitivity, wider energy range, and improved energy resolution compared with the previous generation of instruments. Simultaneous observations with *Fermi*-LAT and IACTs like MAGIC or VERITAS (potentially covering six decades in energy, from 20 MeV to 20 TeV) can, for the first time, significantly resolve both the rising and the falling segments of the high-energy emission component of Mrk 501, with the expected location of the SED peak in the overlapping energy range between those instruments. Because of the smaller collection area, and the self-veto problem,[138] the sensitivity of EGRET to detect γ-rays with energies larger than 10 GeV was about two orders of magnitude lower than that of *Fermi*-LAT.[139] Besides, during the period of operation of EGRET, the sensitivity of the previous generation of IACTs was only moderate, with relatively low sensitivity below 0.5 TeV. Therefore, the higher sensitivity and larger energy range of the newer γ-ray instruments have become a crucial tool for studying Mrk 501, and the blazar phenomenon in general.

In order to exploit the performance of *Fermi*-LAT and the new IACTs, as well as the capabilities of several existing instruments observing at radio-to-X-ray frequencies, a multifrequency (from radio to TeV photon energies) campaign was organized to monitor Mrk 501 during a period of 4.5 months, from 2009 mid-March to August. The scientific goal was to collect a very complete, simultaneous, multifrequency data set that would allow current theoretical models of broadband blazar emission to be tested. This, in turn, should help us to understand the origin of high-energy emission of blazar sources and the physical mechanisms responsible for the acceleration of radiating particles in relativistic jets in general. In this paper, the only reported result from the multifrequency observations is the overall SED averaged over the duration of the observing campaign. A more in-depth analysis of the multifrequency data set will be given in a forthcoming paper. The scientific results from the data collected during the two-day time interval 2009 March 23–25 (which includes extensive observations with the *Suzaku* X-ray satellite) will be reported in a separate paper (V. A. Acciari et al. 2011, in preparation). The paper is organized as follows. In Section 2, we introduce the LAT instrument and describe the LAT data analysis. In Section 3, we report on the flux/spectral variability of Mrk 501 observed during the first 16 months of *Fermi*-LAT operation, and compare it with the flux variability observed in X-rays by the all-sky instruments *Rossi X-Ray Timing Explorer* (*RXTE*; Bradt et al. 1993) All Sky Monitor (ASM) and the *Swift* (Gehrels et al. 2004) Burst Alert Telescope (BAT). In Section 4, we analyze the γ-ray spectrum of Mrk 501 measured by *Fermi*-LAT in the energy range 0.1–400 GeV. Section 5 reports on the overall SED obtained during the 4.5 month long multifrequency campaign organized in 2009. Section 6 is devoted to SED modeling, the results of which are further discussed in Section 7. Conclusions are presented in Section 8.

2. *FERMI*-LAT DATA SELECTION AND ANALYSIS

The *Fermi*-LAT is an instrument that performs γ-ray astronomy above 20 MeV. The instrument is an array of 4×4 identical towers, each one consisting of a tracker (where the photons are pair-converted) and a calorimeter (where the energies of the pair-converted photons are measured). The entire instrument is covered with an anticoincidence detector to reject charged-particle background. The LAT has a peak effective area of 0.8 m^2 for 1 GeV photons, an energy resolution typically better than 10%, and an FoV of about 2.4 sr, with an angular resolution (68% containment angle) better than 1° for energies above 1 GeV. Further details on the LAT can be found in Atwood et al. (2009).

The LAT data reported in this paper were collected from 2008 August 5 (MJD 54683) to 2009 November 27 (MJD 55162). During this time, the *Fermi*-LAT instrument operated

[138] The self-veto problem in EGRET is the degradation of the effective area at high energies (>5 GeV) due to backsplash of secondary particles from the calorimeter causing the anticoincidence system to veto the event. This problem is substantially reduced in the LAT by using a segmented anticoincidence detector.

[139] This estimate includes the larger exposure from *Fermi*-LAT due to the four times larger field of view (FoV).

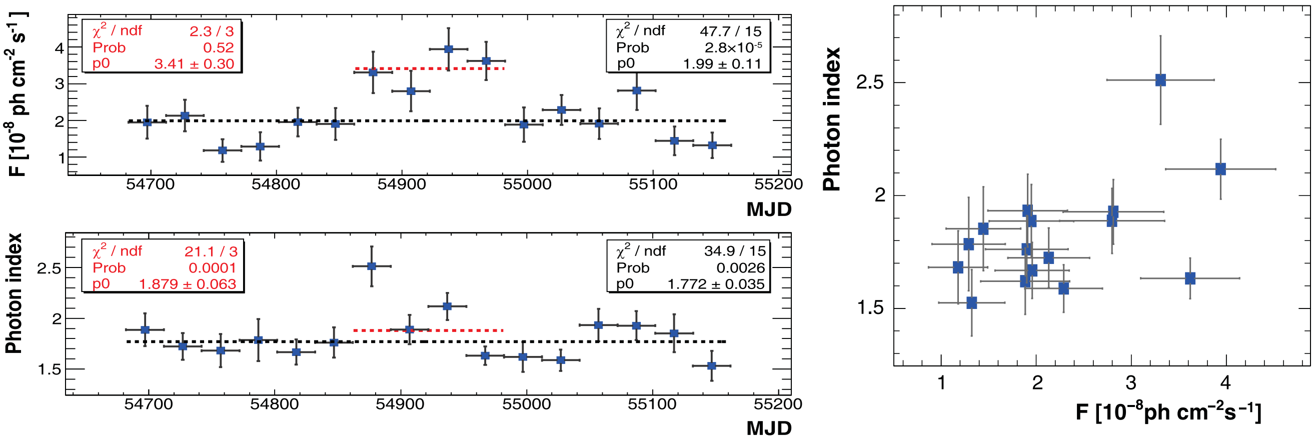

Figure 1. Left: *FERMI*-LAT γ-ray flux in the energy range 0.3–400 GeV (top panel) and spectral photon index from a power-law fit (bottom panel) for Mrk 501 for 30-day time intervals from 2008 August 5 (MJD 54683) to 2009 November 27 (MJD 55162). Vertical bars denote 1σ uncertainties and the horizontal bars denote the width of the time interval. The red dashed line and the red legend show the results from a constant fit to the time interval MJD 54862–54982, while the black dashed line and black legend show the results from a constant fit to the entire 480-day data set. Right: the scatter plot of the photon index vs. flux values.

mostly in survey mode. The analysis was performed with the Fermi Science Tools software package version `v9r15p6`. Only events with the highest probability of being photons—those in the "diffuse" class—were used. The LAT data were extracted from a circular region of 10° radius centered at the location of Mrk 501. The spectral fits were performed using photon energies in the energy range 0.3–400 GeV. At photon energies above 0.3 GeV, the effective area of the instrument is relatively large (>0.5 m^2) and the angular resolution relatively good (68% containment angle smaller than 2°). In particular, because of the better angular resolution, the spectral fits using energies above 0.3 GeV (instead of 0.1 GeV) are less sensitive to possible contamination from unaccounted (perhaps transient), neighboring γ-ray sources and hence have smaller systematic errors, at the expense of reducing somewhat the number of photons from the source. In addition, a cut on the zenith angle (>105°) was applied to reduce contamination from Earth-albedo γ-rays, which are produced by cosmic rays interacting with the upper atmosphere.

The background model used to extract the γ-ray signal includes a Galactic diffuse emission component and an isotropic component. The model that we adopted for the Galactic component is `gll_iem_v02.fit`.[140] The isotropic component, which is the sum of the extragalactic diffuse emission and the residual charged-particle background, is parameterized here with a single power-law function. To reduce systematic uncertainties in the analysis, the photon index of the isotropic component and the normalization of both components in the background model were allowed to vary freely during the spectral point fitting. Owing to the relatively small size of the region analyzed (radius 10°) and the hardness of the spectrum of Mrk 501, the high-energy structure in the standard tabulated isotropic background spectrum isotropic_iem_v02.txt does not dominate the total counts at high energies. In addition, we find that for this region a power-law approximation to the isotropic background results in somewhat smaller residuals for the overall model, possibly because the isotropic term, with a free spectral index, compensates for an inaccuracy in the model for the Galactic diffuse emission, which is also approximately isotropic at the high Galactic latitude of Mrk 501 ($b \sim 39°$). In any case, the resulting spectral fits for Mrk 501 are not significantly different if isotropic_iem_v02.txt is used for the analysis. In addition, the model also includes five nearby sources from the 1FGL catalog (Abdo et al. 2010b): 1FGL J1724.0+4002, 1FGL J1642.5+3947, 1FGL J1635.0+3808, 1FGL J1734.4+3859, and 1FGL J1709.6+4320. The spectra of those sources were also parameterized by a power-law functions, whose photon index values were fixed to the values from the 1FGL catalog, and only the normalization factors for the single sources were left as free parameters. The spectral analysis was performed with the post-launch instrument-response functions `P6_V3_DIFFUSE` using an unbinned maximum-likelihood method (Mattox et al. 1996). The systematic uncertainties on the flux were estimated as 10% at 0.1 GeV, 5% at 560 MeV and 20% at 10 GeV and above.[141]

3. FLUX AND SPECTRAL VARIABILITY

The high sensitivity and survey-mode operation of *Fermi*-LAT permit systematic, uninterrupted monitoring of Mrk 501 in γ-rays, regardless of the activity level of the source. The measured γ-ray flux above 0.3 GeV and the photon index from a power-law fit are shown in the left panel of Figure 1. The data span the time from 2008 August 5 (MJD 54683) to 2009 November 27 (MJD 55162), binned in time intervals of 30 days. The Test Statistic (TS) values[142] for the 16 time intervals are all in excess of 50 (i.e., ∼7 standard deviations, hereafter σ), with three-quarters of them greater than 100 (i.e., $\sim 10\sigma$). During this 480-day period, Mrk 501 did not show any outstanding flaring activity in the *Fermi*-LAT energy range, but there appear to be flux and spectral variations on timescales of the order of 30 days. During the 120-day period MJD 54862–54982, the photon flux above 0.3 GeV was $(3.41 \pm 0.28) \times 10^{-8}$ ph cm^{-2} s^{-1}, which is about twice as large as the averaged flux values before and after that time period, which are $(1.65 \pm 0.16) \times 10^{-8}$ ph cm^{-2} s^{-1} and $(1.84 \pm 0.17) \times 10^{-8}$ ph cm^{-2} s^{-1}, respectively. Remarkably, the photon index changed from 2.51 ± 0.20 for the first 30-day interval of this "enhanced-flux period" to 1.63 ± 0.09 for the last 30-day interval. As shown in the red legend of the bottom plot in the left panel of Figure 1, a constant fit to the photon

[140] http://fermi.gsfc.nasa.gov/ssc/data/access/lat/BackgroundModels.html

[141] http://fermi.gsfc.nasa.gov/ssc/data/analysis/LAT_caveats.html

[142] The TS value quantifies the probability of having a point γ-ray source at the location specified. It is roughly the square of the significance value: a TS of 25 would correspond to a signal of approximately five standard deviations (Mattox et al. 1996).

index values of this 120-day period gives a null probability of 10^{-4}, hence a deviation of 4σ. A constant fit to the entire 16-month period gives a null probability of 2.6×10^{-3}; hence, spectral variability is detected for the entire data set at the level of 3σ. It is worth stressing that the spectral variability in the 480-day time interval is entirely dominated by the spectral variability occurring during the 120-day time interval of MJD 54862–54982, with no significant spectral variability before or after this "enhanced-flux period." The right plot in Figure 1 does not show any clear correlation between the flux and the spectral variations. The discrete correlation function (DCF) computed as prescribed in Edelson & Krolik (1988) gives DCF $= 0.5 \pm 0.3$ for a time lag of zero.

Mrk 501 is known for showing spectral variability at VHE γ-ray energies. During the large X-ray/γ-ray flare in 1997, Whipple and (especially) CAT observations showed evidence of spectral curvature and variability (Samuelson et al. 1998; Djannati-Ataï et al. 1999). The spectral changes are larger when comparing the measurements from 1997 with the low states from 1998 and 1999, as reported by CAT and HEGRA (Piron 2000; Aharonian et al. 2001). The MAGIC telescope, with lower energy threshold and higher sensitivity than the Whipple, HEGRA, and CAT telescopes, observed remarkable spectral variability in 2005, when the γ-ray activity of Mrk 501 was significantly smaller than that observed in 1997 (Albert et al. 2007a). The spectral variability is even larger when comparing the MAGIC measurements from 2005 with those from 2006 when the source was in an even lower state (Anderhub et al. 2009). However, despite the measured spectral variability at VHE γ-ray energies, the outstanding spectral steepening at GeV energies observed during the time interval MJD 54862–54892 was not envisioned in any of the previous works in the literature; the modeled spectrum of Mrk 501 at GeV energies was always assumed to be hard (photon indices $\sim$1.5–1.8). This observational finding, further discussed in Sections 4 and 7, shows the importance of having a γ-ray instrument capable of long-term, uninterrupted, high-sensitivity monitoring of Mrk 501 and other HSP BL Lac objects, and it points to the important role *Fermi*-LAT will play in improving our understanding of the physics behind the blazar phenomenon.

The *Fermi*-LAT capability for continuous source monitoring is complemented at X-ray frequencies by *RXTE*-ASM and *Swift*-BAT, the two all-sky instruments that can probe the X-ray activity of Mrk 501 on a 30-day timescale. Figure 2 shows the fluxes measured by the ASM in the energy range 2–10 keV, by the BAT in the energy range 15–50 keV, and by the LAT in two different energy bands: 0.2–2 GeV (low-energy band) and >2 GeV (high-energy band).[143] The data from *RXTE*-ASM were obtained from the ASM Web site.[144] The data were filtered according to the prescription provided there, and the weighted average over all of the dwells[145] was determined for the 30-day time intervals defined for the Fermi data. The data from *Swift*-BAT were gathered from the BAT Web site.[146] We retrieved the daily averaged BAT values and made the weighted average over all the days from the 30-day time intervals defined for the *Fermi* data. The X-ray intensity from Mrk 501, averaged over the 16 months, is 0.25 ± 0.01 count s^{-1} per Scanning Shadow Camera in the ASM, and $(0.52 \pm 0.05) \times 10^{-3}$ count s^{-1} cm^{-2} in the BAT (close to the BAT 30-day detection limit). This X-ray activity is compatible with that recorded in recent years, but quite different from the activity of the source during 1997, when the ASM flux was above 1 count s^{-1} per Scanning Shadow Camera during most of the year, with a peak well above 2 count s^{-1} around 1997 June.

As noted previously (Section 1), Mrk 501 is not in the third EGRET catalog, although there was a marginally significant EGRET detection during the γ-ray outburst (with no clear X-ray counterpart) in 1996 (Kataoka et al. 1999). At that time, the source was detected at a level of 4.0σ at energies above 0.1 GeV and at 5.2σ above 0.5 GeV. The flux from the EGRET 1996 flare above 0.5 GeV was $(6 \pm 2) \times 10^{-8}$ ph cm^{-2} s^{-1}, which is about five times higher than the average flux observed by *Fermi* from 2008 August 5 (MJD 54683) to 2009 November 27 (MJD 55162), namely $(1.39 \pm 0.07) \times 10^{-8}$ ph cm^{-2} s^{-1} (also above photon energy 0.5 GeV). The *Fermi*-LAT flux measured during the 120 days with the "enhanced" γ-ray activity (MJD 54862–54982) is $(2.03 \pm 0.18) \times 10^{-8}$ ph cm^{-2} s^{-1} (above photon energy 0.5 GeV), about a factor of three lower than that detected by EGRET in 1996.

In spite of the relatively low activity, the ASM and BAT fluxes show some flux variations and a positive correlation between the fluxes measured by these two instruments. The discrete correlation function for the ASM/BAT data points shown in Figure 2 is DCF $= 0.73 \pm 0.17$ for a time lag of zero. On the other hand, the X-ray ASM/BAT fluxes are not significantly correlated with the γ-ray LAT fluxes. We found, for a time lag of zero, DCF $= 0.32 \pm 0.22$ for the ASM/LAT (<2 GeV) and DCF $= 0.43 \pm 0.30$ for the ASM/LAT (>2 GeV) flux data points shown in Figure 2. It is also interesting to note that the largest flux variations occur at the highest *Fermi* energies (>2 GeV), where the γ-ray flux increased by one order of magnitude during the 120-day interval MJD 54862–54892. This trend is consistent with the photon index hardening revealed by the spectral analysis reported above (see Figure 1).

We followed the description given in Vaughan et al. (2003) to quantify the flux variability by means of the fractional variability parameter, $F_{\rm var}$, as a function of photon energy. In order to account for the individual flux measurement errors ($\sigma_{\rm err,\,i}$), we used the "excess variance" as an estimator of the intrinsic source variance (Nandra et al. 1997; Edelson et al. 2002). This is the variance after subtracting the expected contribution from the measurement errors. For a given energy range, $F_{\rm var}$ is calculated as

$$F_{\rm var} = \sqrt{\frac{S^2 - \langle\sigma^2_{\rm err}\rangle}{\langle F_\gamma\rangle^2}}, \qquad (1)$$

where $\langle F_\gamma\rangle$ is the mean photon flux, S is the standard deviation of the N flux points, and $\langle\sigma^2_{\rm err}\rangle$ is the average mean square error, all determined for a given energy bin.

Figure 3 shows the $F_{\rm var}$ values derived for the four different energy ranges and the time window covered by the light curves shown in Figure 2. The source is variable at all energies. The uncertainty in the variability quantification for the *Swift*-BAT energies is large due to the fact that Mrk 501 is a relatively weak X-ray source, and is therefore difficult to detect above 15 keV in exposure times as short as 30 days. In contrast, the variability at the *RXTE*-ASM and, especially, *Fermi*-LAT energies, is significant (>3σ level). The amplitude variability in the two X-ray bands is compatible within errors, and the same holds for

143 The fluxes depicted in the *Fermi*-LAT light curves were computed fixing the photon index to 1.78 (average index during the first 480 days of *Fermi* operation) and fitting only the normalization factor of the power-law function.
144 http://xte.mit.edu/ASM_lc.html
145 A dwell is a scan/rotation of the ASM Scanning Shadow Camera lasting 90 s.
146 http://swift.gsfc.nasa.gov/docs/swift/results/transients/

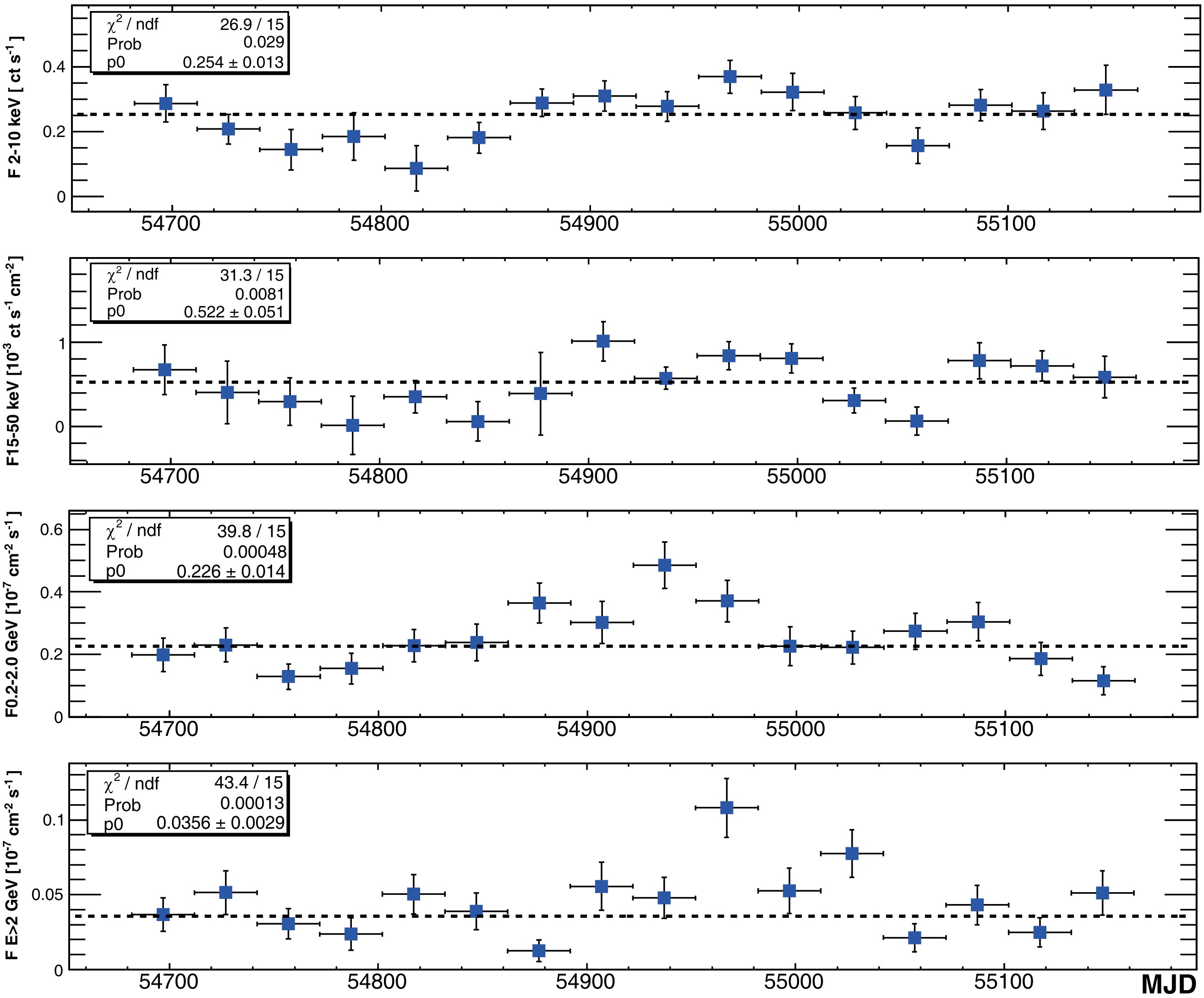

Figure 2. Multifrequency light curves of Mrk 501 with 30-day time bins obtained with three all-sky-monitoring instruments: *RXTE*-ASM (2–10 keV, first from the top); *Swift*-BAT (15–50 keV, second), and *Fermi*-LAT for two different energy ranges (0.2–2 GeV, third, and >2 GeV, fourth). The light curves cover the period from 2008 August 5 (MJD 54683) to 2009 November 27 (MJD 55162). Vertical bars denote 1σ uncertainties and horizontal bars show the width of the time interval. The horizontal dashed lines and the legends (for all the plots) show the results from a constant fit to the entire 480-day data set.

(A color version of this figure is available in the online journal.)

the variability in the two γ-ray bands. As shown in Figure 3, for the hypothesis of a constant $F_{\rm var}$ over the four energy bands, one obtains $\chi^2 = 3.5$ for three degrees of freedom (probability of 0.32), implying that the energy-dependent variability is not statistically significant. It is worth noticing that the limited sensitivity of the ASM and (particularly) BAT instruments to detect Mrk 501 in 30-day time intervals, as well as the relatively stable X-ray emission of Mrk 501 during the analyzed observations, precludes any detailed X-ray/γ-ray variability and correlation analysis.

4. SPECTRAL ANALYSIS UP TO 400 GeV

The large effective area of the *Fermi*-LAT instrument permits photon energy reconstruction over many orders of magnitude. As a result, the spectrum of Mrk 501 could be resolved within the energy range 0.1–400 GeV, as shown in Figure 4. This is the first time the spectrum of Mrk 501 has been studied with high accuracy over this energy range. The fluxes were computed using the analysis procedures described in Section 2. The black line in Figure 4 is the result of an unbinned likelihood fit with a single power-law function in the energy range 0.3–400 GeV,[147] and the red contour is the 68% uncertainty of the fit. The data are consistent with a pure power-law function with a photon index of 1.78 ± 0.03. The black data points result from the analysis in differential energy ranges[148] ($\log \Delta E = 0.4$). The points are well within 1σ–2σ from the fit to the overall spectrum (black line), which confirms that the entire *Fermi* spectrum is consistent with a pure power-law function. Note, however, that, due to the low photon count, the error bars for the highest energy data points are

[147] The unbinned likelihood fit was performed on photon energies above 0.3 GeV in order to reduce systematics. See Section 2 for further details.

[148] Because the analysis was carried out in small energy ranges, we decided to fix the spectral index at 1.78 (the value obtained from fitting the entire energy range) and fit only the normalization factor. We repeated the same procedure fixing the photon indices to 1.5 and 2.0 and found no significant change. Therefore, the results from the differential energy analysis are not sensitive to the photon index used in the analysis.

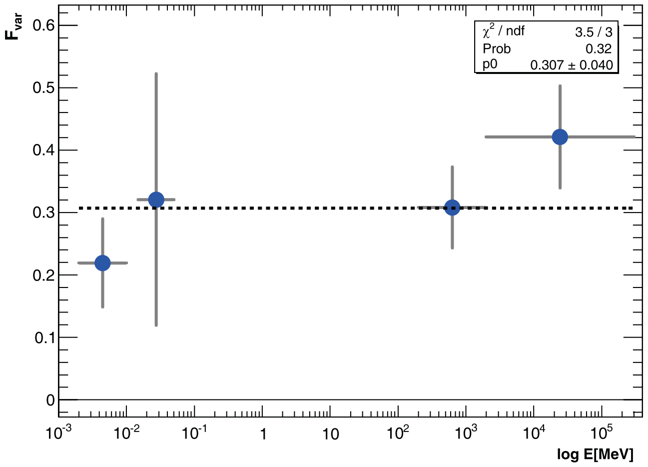

Figure 3. Fractional variability parameter for 16 months data (2008 August 5–2009 November 27) from three all-sky-monitoring instruments: *RXTE*-ASM (2–10 keV); *Swift*-BAT (15–50 keV), and *Fermi*-LAT (two energy ranges 0.2–2 GeV and 2–300 GeV). The fractional variability was computed according to Vaughan et al. (2003) using the light curves from Figure 2. Vertical bars denote 1σ uncertainties and horizontal bars indicate the width of each energy bin. The horizontal dashed line and the legend show the results from a constant fit.

(A color version of this figure is available in the online journal.)

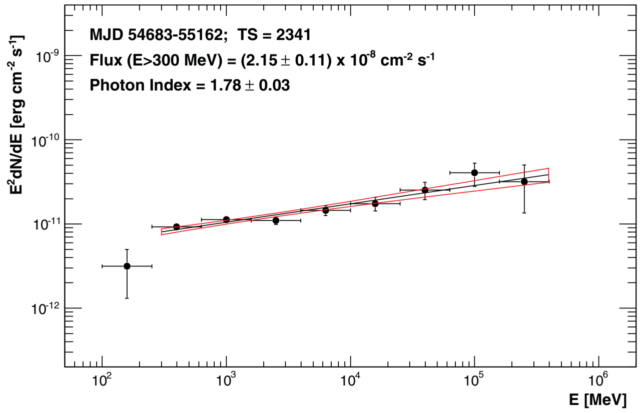

Figure 4. SED for Mrk 501 from *Fermi*-LAT during the period from 2008 August 5 (MJD 54683) to 2009 November 27 (MJD 55162). The black line depicts the result of the unbinned likelihood power-law fit, the red contour is the 68% uncertainty of the fit, and the black data points show the energy fluxes in differential energy ranges. The legend reports the results from the unbinned likelihood power-law fit in the energy range 0.3–400 GeV.

(A color version of this figure is available in the online journal.)

rather large. The predicted (by the model for Mrk 501) numbers of photons detected by the LAT in the energy bins 60–160 GeV and 160–400 GeV are only 11 and 3, respectively. Therefore, even though the signal significance in the highest energy bins is very high due to the very low background (the TS values for the two highest-energy ranges is 162 and 61, respectively), the large statistical uncertainties could hide a potential turnover in the spectrum of Mrk 501 around 100 GeV photon energies. As we know from past observations, the VHE spectrum is significantly softer than the one observed by *Fermi* (e.g., Aharonian et al. 2001; Anderhub et al. 2009), and hence the spectrum of Mrk 501 must have a break around the highest *Fermi*-LAT energies.

In Section 3, we reported remarkable spectral variability during the 120-day time interval MJD 54862–54982, when Mrk 501 was characterized by a photon flux (at >0.3 GeV) twice as large as during the rest of the exposure. In order to understand better the behavior of the source during that time, we produced SED plots (analogous to that of Figure 4) for each of the 30-day time intervals from the period with the enhanced flux level. These are shown in Figure 5, together with the SED plots from the 30-day time intervals before and after this 120-day epoch, which are representative of the average source behavior during the other 360 days. The variability of the SED data points below a few GeV is rather mild (factor of two), but above a few GeV the spectra vary substantially (factor of 10). The γ-ray signal at the highest energies is suppressed during MJD 54862–54982, while it increases by a large factor during MJD 54952–54982, where the analysis model for Mrk 501 predicts 2.0 photons in the energy range 160–400 GeV. It is worth stressing that for the SED from Figure 4, which corresponds to the total exposure of 480 days, the analysis model for Mrk 501 predicts only 3.2 photons in the highest energy bin. Hence, the time interval MJD 54952–54982 holds almost all the signal detected by the LAT in the energy range 160–400 GeV during 16 months. The situation changes somewhat for the lower energy bin 60–160 GeV, for which the analysis model for Mrk 501 predicts 2.4 photons for the time interval MJD 54952–54982, while it does predict 11.3 photons for the entire 16-month time interval. Fortunately, the 30-day time interval characterized by hard spectrum is covered by the 4.5-month campaign that we organized, and hence simultaneous multifrequency observations (radio to TeV) are available for this particular period, as discussed further below.

5. BROADBAND SPECTRAL ENERGY DISTRIBUTION OF Mrk 501

As mentioned in Section 1, we organized a multifrequency campaign (from radio to TeV photon energies) to monitor Mrk 501 during a time period of 4.5 months. The observing campaign started on 2009 March 15 (MJD 54905) and finished on 2009 August 1 (MJD 55044). The observing goal for this campaign was to sample the broadband emission of Mrk 501 every five days, which was largely accomplished whenever the weather and/or technical limitations allowed. The underlying scientific goal has already been outlined in Section 1. A detailed analysis of the multifrequency variability and correlations, as well as the evolution of the overall SED with time, will be reported in a forthcoming paper. In this section of the manuscript, we describe the source coverage during the campaign and the data analysis for several of the participating instruments, and we report on the averaged SED resulting from the campaign. The modeling of these data and the physical implications are given in Sections 6 and 7, respectively.

5.1. Details of the Campaign: Participating Instruments and Temporal Coverage

The list of all the instruments that participated in the campaign is given in Table 1, and the scheduled observations can be found online.[149] In some cases, the planned observations could not be performed due to bad observing conditions, while in some other occasions the observations were performed but the data could not be properly analyzed due to technical problems or rapidly changing weather conditions. In order to quantify the actual time and energy coverage during the campaign on Mrk 501, Figure 6 shows the exposure time as a function of the

[149] https://confluence.slac.stanford.edu/display/GLAMCOG/Campaign+on+Mrk501+(March+2009+to+July+2009)

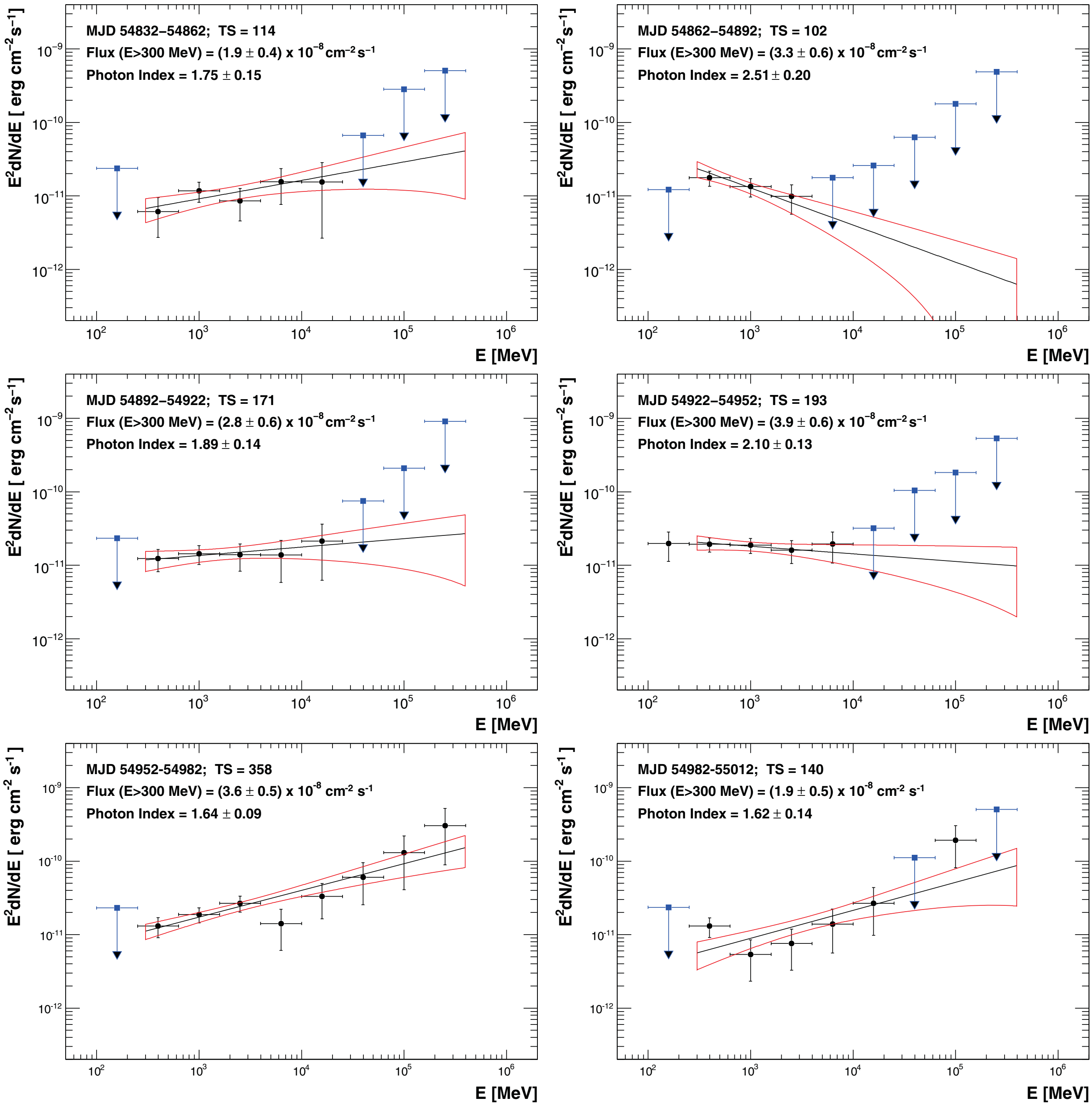

Figure 5. SED for Mrk 501 from *Fermi*-LAT for six 30-day time intervals: MJD 54832–54862 (top left), MJD 54862–54892 (top right), MJD 54892–54922 (middle left), MJD 54922–54952 (middle right), MJD 54952–54982 (bottom left), and MJD 54982–55012 (bottom right). In all the panels, the black line depicts the result of the unbinned likelihood power-law fit, the red contour denotes the 68% uncertainty of the fit, and the black data points show the energy fluxes computed for differential energy ranges. The blue arrows denote 95% upper limits, which were computed for the differential energy ranges with a signal of $TS < 4$ or less than two photons predicted by the analysis model for Mrk 501. The legend reports the results from the unbinned likelihood power-law fit in the energy range 0.3–400 GeV.

(A color version of this figure is available in the online journal.)

energy range for the instruments/observations used to produce the SED shown in Figure 8. Apart from the unprecedented energy coverage (including, for the first time, the GeV energy range from *Fermi*-LAT), the source was sampled quite uniformly with the various instruments participating in the campaign and, consequently, it is reasonable to consider the SED constructed below as the actual average (typical) SED of Mrk 501 during the time interval covered by this multifrequency campaign. The largest non-uniformity in the sampling of the source comes from the Cherenkov Telescopes, which are the instruments most sensitive to weather conditions. Moreover, while there are many radio/optical instruments spread all over the globe, there are only three Cherenkov Telescope observatories in the northern hemisphere we could utilize (MAGIC, VERITAS, Whipple). Hence, the impact of observing conditions was more important to the coverage at the VHE γ-ray energies.

We note that Figure 6 shows the MAGIC, VERITAS, and Whipple coverage at VHE γ-ray energies, but only the MAGIC

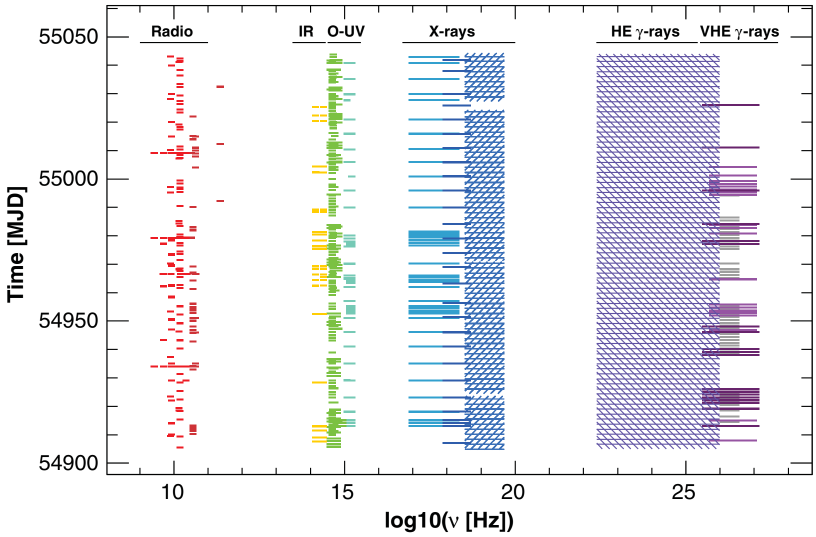

Figure 6. Time and energy coverage during the multifrequency campaign. For the sake of clarity, the minimum observing time displayed in the plot was set to half a day.

Table 1
List of Instruments Participating in the Multifrequency Campaign and Used in the Construction of the SED in Figure 8

Instrument/Observatory	Energy Range Covered	Web Page
MAGIC	0.12–5.8 TeV	http://wwwmagic.mppmu.mpg.de/
VERITAS	0.20–5.0 TeV	http://veritas.sao.arizona.edu/
Whipple[a]	0.4–1.5 TeV	http://veritas.sao.arizona.edu/content/blogsection/6/40/
Fermi-LAT	0.1–400 GeV	http://www-glast.stanford.edu/index.html
Swift-BAT	14–195 keV	http://heasarc.gsfc.nasa.gov/docs/swift/swiftsc.html
RXTE-PCA	3–28 keV	http://heasarc.gsfc.nasa.gov/docs/xte/rxte.html
Swift-XRT	0.3–9.6 keV	http://heasarc.gsfc.nasa.gov/docs/swift/swiftsc.html
Swift-UVOT	V, B, U, UVW1, UVM2, UVW2	http://heasarc.gsfc.nasa.gov/docs/swift/swiftsc.html
Abastumani (through GASP-WEBT program)	*R* band	http://www.oato.inaf.it/blazars/webt/
Lulin (through GASP-WEBT program)	*R* band	http://www.oato.inaf.it/blazars/webt/
Roque de los Muchachos (KVA) (through GASP-WEBT program)	*R* band	http://www.oato.inaf.it/blazars/webt/
St. Petersburg (through GASP-WEBT program)	*R* band	http://www.oato.inaf.it/blazars/webt/
Talmassons (through GASP-WEBT program)	*R* band	http://www.oato.inaf.it/blazars/webt/
Valle d'Aosta (through GASP-WEBT program)	*R* band	http://www.oato.inaf.it/blazars/webt/
GRT	*V*, *R*, *B* bands	http://asd.gsfc.nasa.gov/Takanori.Sakamoto/GRT/index.html
MitSume	*g*, *Rc*, *Ic* bands	http://www.hp.phys.titech.ac.jp/mitsume/index.html
ROVOR	*B*, *R*, *V*, *I* bands	http://rovor.byu.edu/
Campo Imperatore (through GASP-WEBT program)	*H*, *J*, *K* bands	http://www.oato.inaf.it/blazars/webt/
OAGH	*H*, *J*, *K* bands	http://astro.inaoep.mx/en/observatories/oagh/
WIRO	*J*, *K* bands	http://physics.uwyo.edu/~chip/wiro/wiro.html
SMA	225 GHz	http://sma1.sma.hawaii.edu/
VLBA	4.8, 8.3, 15.4, 23.8, 43.2 GHz	http://www.vlba.nrao.edu/
Noto	8.4, 43 GHz	http://www.noto.ira.inaf.it/
Metsähovi (through GASP-WEBT program)	37 GHz	http://www.metsahovi.fi/
VLBA (through MOJAVE program)	15 GHz	http://www.physics.purdue.edu/MOJAVE/
OVRO	15 GHz	http://www.astro.caltech.edu/ovroblazars
Medicina	8.4, 22.3 GHz	http://www.med.ira.inaf.it/index_EN.htm
UMRAO (through GASP-WEBT program)	4.8, 8.0, 14.5 GHz	http://www.oato.inaf.it/blazars/webt/
RATAN-600	2.3, 4.8, 7.7, 11.1, 22.2 GHz	http://w0.sao.ru/ratan/
Effelsberg (through F-GAMMA program)	2.6, 4.6, 7.8, 10.3, 13.6, 21.7, 31 GHz	http://www.mpifr-bonn.mpg.de/div/effelsberg/index_e.html

Notes. The energy range shown in Column 2 is the actual energy range covered during the Mrk 501 observations, and not the instrument's nominal energy range, which might only be achievable for bright sources and excellent observing conditions.
[a] The Whipple spectra were not included in Figure 8. The energy range given in the table is based on a very conservative estimate given before performing the spectral analysis of the data. See the text for further comments.

and VERITAS observations were used to produce the spectra shown in Figure 8. The more extensive (120 hr), but less sensitive, Whipple data (shown as gray boxes in Figure 6) were primarily taken to determine the light curve (Pichel et al. 2009) and a re-optimization was required to derive the spectrum which will be reported elsewhere.

In the following paragraphs, we briefly discuss the procedures used in the data analysis of the instruments participating in the campaign. The analysis of the *Fermi*-LAT data was described in Section 2, and the results obtained will be described in detail in Section 5.2.

5.1.1. Radio Instruments

Radio data were taken for this campaign from single-dish telescopes, 1 mm interferometer, and one VLBI array, at frequencies between 2.6 GHz and 225 GHz (see Table 1). The single-dish telescopes were the Effelsberg 100 m radio telescope, the 32 m Medicina radio telescope, the 14 m Metsähovi radio telescope, the 32 m Noto radio telescope, the Owens Valley Radio Observatory (OVRO) 40 m telescope, the 26 m University of Michigan Radio Astronomy Observatory (UMRAO) and the 600 m ring radio telescope RATAN-600. The millimeter-interferometer is the Submillimeter Array (SMA). The NRAO VLBA was used for the VLBI observations. For the single-dish instruments and SMA, Mrk 501 is point-like and unresolved at all observing frequencies. Consequently, the single-dish measurements denote the total flux density of the source integrated over the whole source extension. Details of the observing strategy and data reduction can be found in Fuhrmann et al. (2008), Angelakis et al. (2008, F-GAMMA project), Teräsranta et al. (1998, Metsähovi), Aller et al. (1985, UMRAO), Venturi et al. (2001, Medicina and Noto), Kovalev et al. (1999, RATAN-600), and Richards et al. (2011, OVRO).

In the case of the VLBA, the data were obtained at various frequencies from 5 GHz to 43 GHz through various programs (BP143, BK150, and MOJAVE). The data were reduced following standard procedures for data reduction and calibration (see, for example, Lister et al. 2009, for a description of the MOJAVE program which provided the 15 GHz data). Since the VLBA angular resolution is smaller than the radio source extension, measurements were performed for the most compact core region, as well as for the total radio structure at parsec scales. The VLBA core size was determined with two-dimensional circular or elliptical Gaussian fits to the measured visibilities. The FWHM size of the core was estimated to be in the range 0.14–0.18 mas at the highest observing frequencies, 15–43 GHz. Both the total and the core radio flux densities from the VLBA data are depicted in Figure 8.

5.1.2. Optical and Near-IR Instruments

The coverage at optical frequencies was obtained through various telescopes around the globe, and this decreased the sensitivity to weather/technical difficulties and provided good overall coverage of the source, as depicted in Figure 6. Many of the observations were performed within the GASP-WEBT program (e.g., Villata et al. 2008, 2009); that is the case for the data collected by the telescopes at Abastumani, Lulin, Roque de los Muchachos (KVA), St. Petersburg, Talmassons, and Valle d'Aosta observatories (*R* band), and also for Campo Imperatore (near-infrared frequencies, *JHK* bands). In addition, the telescopes GRT, ROVOR, and MitSume provided data with various optical filters, while OAGH and WIRO provided data at near-infrared wavelengths. See Table 1 for further details.

All the instruments used the calibration stars reported in Villata et al. (1998), and the Galactic extinction was corrected with the coefficients given in Schlegel et al. (1998). On the other hand, the flux from the host galaxy, which in the *R* band accounts for about two-thirds of the overall measured optical flux (Nilsson et al. 2007), was not subtracted. As can be seen from Figure 8, the host galaxy contribution shows up as an additional (narrow) bump in the SED with the peak located at infrared frequencies and the flux decreasing rapidly with increasing frequency. At frequencies above 10^{15} Hz, the blazar emission again dominates the radiative output of Mrk 501.

5.1.3. Swift-UVOT

The *Swift*-Ultra-Violet/Optical Telescope (UVOT; Roming et al. 2005) data used in this analysis include all the observations performed during the time interval MJD 54905 and 55044, which amounts to 41 single pointing observations that were requested to provide UV coverage during the Mrk 501 multifrequency campaign. The UVOT telescope cycled through each of six optical and ultraviolet passbands (*V*, *B*, *U*, *UVW1*, *UVM2*, and *UVW2*). Photometry was computed using a 5 arcsec source region around Mrk 501 using a custom UVOT pipeline that obtains similar photometric results to the public pipeline (Poole et al. 2008). The custom pipeline also allows for separate, observation-by-observation corrections for astrometric misalignments (Acciari et al. 2011). A visual inspection was also performed on each of the observations to ensure proper data quality selection and correction. The flux measurements obtained have been corrected for Galactic extinction $E_{B-V} = 0.019$ mag (Schlegel et al. 1998) in each spectral band (Fitzpatrick 1999).

5.1.4. Swift-XRT

All the *Swift*-X-ray Telescope (XRT; Burrows et al. 2005) Windowed Timing observations carried out from MJD 54905 to 55044 were used for the analysis: this amounts to a total of 41 observations performed within this dedicated multi-instrument effort to study Mrk 501. The XRT data set was first processed with the `XRTDAS` software package (v.2.5.0) developed at the ASI Science Data Center (ASDC) and distributed by HEASARC within the `HEASoft` package (v.6.7). Event files were calibrated and cleaned with standard filtering criteria with the `xrtpipeline` task using the latest calibration files available in the *Swift* CALDB. The individual XRT event files were then merged together using the `XSELECT` package and the average spectrum was extracted from the summed event file. Events for the spectral analysis were selected within a circle of 20-pixel (∼47 arcsec) radius centered at the source position and enclosing about 95% of the point-spread function (PSF) of the instrument. The background was extracted from a nearby circular region of 40-pixel radius. The source spectrum was binned to ensure a minimum of 20 counts per bin to utilize the χ^2 minimization fitting technique. The ancillary response files were generated with the `xrtmkarf` task applying corrections for the PSF losses and CCD defects using the cumulative exposure map. The latest response matrices (v.011) available in the *Swift* CALDB were used.

The XRT average spectrum in the 0.3–10 keV energy band was fitted using the `XSPEC` package. We adopted a log-parabolic model for the photon flux spectral density (Massaro et al. 2004a, 2004b) of the form $\log[\mathcal{F}(E)] = \log K - a \log[E/\mathrm{keV}] - b \log^2[E/\mathrm{keV}]$, with an absorption hydrogen-equivalent column density fixed to the Galactic value in the direction of the source, namely 1.56×10^{20} cm^{-2} (Kalberla et al. 2005). This model provided a good description of the observed spectrum, with the exception of the 1.4–2.3 keV energy band where spectral fit residuals were present. These residuals are due to known XRT calibration uncertainties (SWIFT-XRT-CALDB-12)[150] and hence we decided to exclude the 1.4–2.3 keV

[150] http://heasarc.gsfc.nasa.gov/docs/heasarc/caldb/swift/docs/xrt/SWIFT-XRT-CALDB-09_v12.pdf

energy band from the analysis. In addition, we had to apply a small energy offset (∼40 eV) to the observed energy spectrum. The origin of this correction is likely to be CCD charge traps generated by radiation and high-energy proton damage (SWIFT-XRT-CALDB-12), which affects mostly the lowest energies (first one or two bins) in the spectrum. The resulting spectral fit gave the following parameters: $K = (3.41 \pm 0.03) \times 10^{-2}$ ph cm^{-2} s^{-1} keV^{-1}, $a = 1.96 \pm 0.04$, and $b = 0.308 \pm 0.010$. The XRT SED data shown in Figure 8 were corrected for the Galactic absorption and then binned into 10 energy intervals.

5.1.5. RXTE-PCA

The *Rossi*-X-ray Timing Explorer (*RXTE*; Bradt et al. 1993) satellite performed 29 pointing observations of Mrk 501 during the time interval MJD 54905 and 55044. These observations amount to a total exposure of 52 ks, which was requested through a dedicated Cycle 13 proposal to provide X-ray coverage for our campaign. We did not find a significant signal in the *RXTE*-HEXTE data and hence we only report on the data from *RXTE*-Proportional Counter Array (*RXTE*-PCA), which is the main pointing instrument on board *RXTE*. The data analysis was performed using `FTOOLS` v6.5 and following the procedures and filtering criteria recommended by the *RXTE* Guest Observer Facility[151] after 2007 September. In particular, the observations were filtered following the conservative procedures for faint sources[152]: Earth elevation angle greater than 10°, pointing offset less than 0°.02, time since the peak of the last South Atlantic Anomaly (SAA) passage greater than 30 minutes, and electron contamination less than 0.1. For further details on the analysis of faint sources with *RXTE*, see the online Cook Book.[153] In the data analysis, in order to increase the quality of the signal, only the first xenon layer of PCU2 was used. We used the package `pcabackest` to model the background and the package `saextrct` to produce spectra for the source and background files and the script[154] `pcarsp` to produce the response matrix.

The PCA average spectrum in the 3–28 keV energy band was fitted using the XSPEC package with a single power-law function $\log[\mathcal{F}(E)] = \log K - a \log[E/\mathrm{keV}]$ with a constant neutral hydrogen column density N_{H} fixed at the Galactic value in the direction of the source, namely 1.56×10^{20} cm^{-2} (Kalberla et al. 2005). However, since the PCA bandpass starts at 3 keV, the value used for N_{H} does not significantly affect our results. The resulting spectral fit provided a good representation of the data for the following parameters: $K = (4.34 \pm 0.11) \times 10^{-2}$ ph cm^{-2} s^{-1} keV^{-1}, and $a = 2.28 \pm 0.02$. The PCA average spectrum obtained using 23 energy bins is shown in Figure 8.

5.1.6. Swift-BAT

The *Swift*-BAT (Barthelmy et al. 2005) analysis results presented in this paper were derived with all the available data during the time intervals MJD 54905 and 55044. The spectrum was extracted following the recipes presented in Ajello et al. (2008, 2009b). This spectrum is constructed by weighted averaging of the source spectra extracted from short exposures (e.g., 300 s) and is representative of the averaged source emission over the time range spanned by the observations. These spectra are accurate to the mCrab level and the reader is referred to Ajello et al. (2009a) for more details. The *Swift*-BAT spectrum is consistent with a power-law function with the normalization parameter $K = 0.24 \pm 0.16$ ph cm^{-2} s^{-1} keV^{-1} and photon index a $= 2.8 \pm 0.4$.

5.1.7. MAGIC

MAGIC is a system of two 17 m diameter IACTs for VHE γ-ray astronomy located on the Canary Island of La Palma, at an altitude of 2200 m above sea level. At the time of the observation, MAGIC-II, the new second telescope of the current array system, was still in its commissioning phase so that Mrk 501 was observed in standalone mode by MAGIC-I, which is in scientific operation since 2004 (Albert et al. 2008). The MAGIC telescope monitored the VHE activity of Mrk 501 in the framework of the organized multifrequency campaign. The observations were performed in the so-called wobble mode (Daum 1997). In order to have a low-energy threshold, only observations at zenith angles less than 35° were used in this analysis. Bad weather and a shutdown for a scheduled hardware system upgrade during the period MJD 54948–54960 (April 27–May 13) significantly reduced the actual amount of observing time compared to what had initially been scheduled for this campaign. The data were analyzed following the prescription given in Albert et al. (2008) and Aliu et al. (2009). The data surviving the quality cuts amount to a total of 16.2 hr. The preliminary reconstructed photon fluxes for the individual observations gave an average activity of about 30% the flux of the Crab Nebula, with small (typically much less than a factor of two) flux variations. The derived spectrum was unfolded to correct for the effects of the limited energy resolution of the detector and of possible bias (Albert et al. 2007b). The resulting spectrum was fitted satisfactorily with a single power-law function of the form $\log[\mathcal{F}(E)] = \log K - a \log[E/\mathrm{TeV}]$, giving the normalization parameter $K = (0.90 \pm 0.05) \times 10^{-11}$ph cm^{-2} s^{-1} TeV^{-1} and photon index $a = 2.51 \pm 0.05$.

5.1.8. VERITAS

VERITAS is a state-of-the-art TeV γ-ray observatory consisting of four 12 m diameter IACTs. VERITAS is located at the base camp of the F. L. Whipple Observatory in southern Arizona, USA, at an altitude of 1250 m above sea level, and the system has been fully operational since fall 2007 (Acciari et al. 2010). VERITAS observed Mrk 501 as part of the long-term monitoring campaign between 2009 March and June. The observations were performed in "wobble" mode (Daum 1997) at relatively low zenith angle (<40°). These data were analyzed following the prescription reported in Acciari et al. (2008). After removal of data runs with poor observing conditions, a total of 9.7 hr of good quality data were obtained between MJD 54907 and MJD 55004. Due to the long-term nature of these observations, several factors had to be taken into account when analyzing the data. The initial portion of the campaign includes data taken under standard four-telescope operating conditions. Two nights of data were taken with only two operational telescopes due to technical difficulties. For the latter portion of the campaign, data were taken over several nights with three operational telescopes because one of the telescopes was being relocated as part of an upgrade to the array (Perkins et al. 2009). The effective collection areas for the array in these three configurations

[151] http://www.universe.nasa.gov/xrays/programs/rxte/pca/doc/bkg/bkg-2007-saa/

[152] The average net count rate from Mrk 501 was about 7 counts s^{-1} pcu^{-1} (in the energy range 3–20 keV) with flux variations typically much smaller than a factor of two.

[153] http://heasarc.gsfc.nasa.gov/docs/xte/recipes/cook_book.html

[154] The CALDB files are located at http://heasarc.gsfc.nasa.gov/FTP/caldb.

were calculated using Monte Carlo simulations of extensive air showers passed through the analysis chain with detector configurations corresponding to the respective data-taking conditions.

An initial analysis of the VHE activity showed an increase in the flux by a factor of about five during MJD 54953–54956. Because of the large difference in the VHE flux, we decided to analyze this three-day data set (corresponding to a "flaring" state of Mrk 501) separately from the rest of the collected data (non-flaring). The "flaring" epoch consists of 2.4 hr of data taken during MJD 54953–54956. The "non-flaring" epoch consists of 7.3 hr of data taken during the remaining portion of the campaign. The spectra from these two data sets were each fitted with a single power-law function of the form $\log[\mathcal{F}(E)] = \log K - a \log[E/\mathrm{TeV}]$. The resulting fit parameter values are $K = (4.17 \pm 0.24) \times 10^{-11}$ ph cm^{-2} s^{-1} TeV^{-1} with $a = 2.26 \pm 0.06$ for the "flaring" state, and $K = (0.88 \pm 0.06) \times 10^{-11}$ ph cm^{-2} s^{-1} TeV^{-1} with the photon index $a = 2.48 \pm 0.07$ for the "non-flaring" state.

5.2. *Fermi*-LAT Spectra During the Campaign

The Mrk 501 spectrum measured by *Fermi*-LAT, integrated during the time interval of the multifrequency campaign, is shown in the panel (b) of Figure 7. The spectrum can be described by a power-law function with the photon index 1.74 ± 0.05. The flux data points resulting from the analysis in differential energy ranges are within 1σ–2σ of the power-law fit result; this is an independent indication that a single power-law function is a good representation of the spectrum during the multifrequency campaign. On the other hand, the shape of the spectrum depicted by the differential energy flux data points suggests the possibility of a concave spectrum. As was discussed in Sections 3 and 4 (see Figures 1 and 5), Mrk 501 showed substantial spectral variability during the time period covered by the multifrequency campaign, with some 30-day time intervals characterized by relatively soft spectra (photon index $\sim$2 for the 30-day intervals MJD 54892–54922 and MJD 54922–54952) and others by relatively hard spectra (photon index $\sim$1.6 for the 30-day intervals MJD 54952–54982, MJD 54982–55012, and MJD 55012–55042). Panel (b) of Figure 7 presents the average spectrum over those time intervals, and hence it would not be surprising to see two slopes (instead of one) in the spectrum. In order to evaluate this possibility, a broken power-law fit was applied, yielding indices of 1.86 ± 0.08 and 1.44 ± 0.14 below and above a break energy of 10 ± 3 GeV, respectively. The likelihood ratio of the broken power law and the power law is 2.2. Given that the broken power law has two additional degrees of freedom, this indicates that the broken power law is not statistically preferred over the single power-law function.

For comparison purposes we also computed the spectra for time intervals before and after the multifrequency campaign (MJD 54683–54901 and MJD 55044–55162).[155] These two spectra, shown in panels (a) and (c) of Figure 7, can both be described satisfactorily by single power-law functions with photon indices 1.82 ± 0.06 and 1.80 ± 0.08. Note that the two spectra are perfectly compatible with each other, which is consistent with the relatively small flux/spectral variability shown in Figures 1 and 2 for those time periods.

155 Technical problems prevented the scientific operation of the *Fermi*-LAT instrument during the interval MJD 54901–54905.

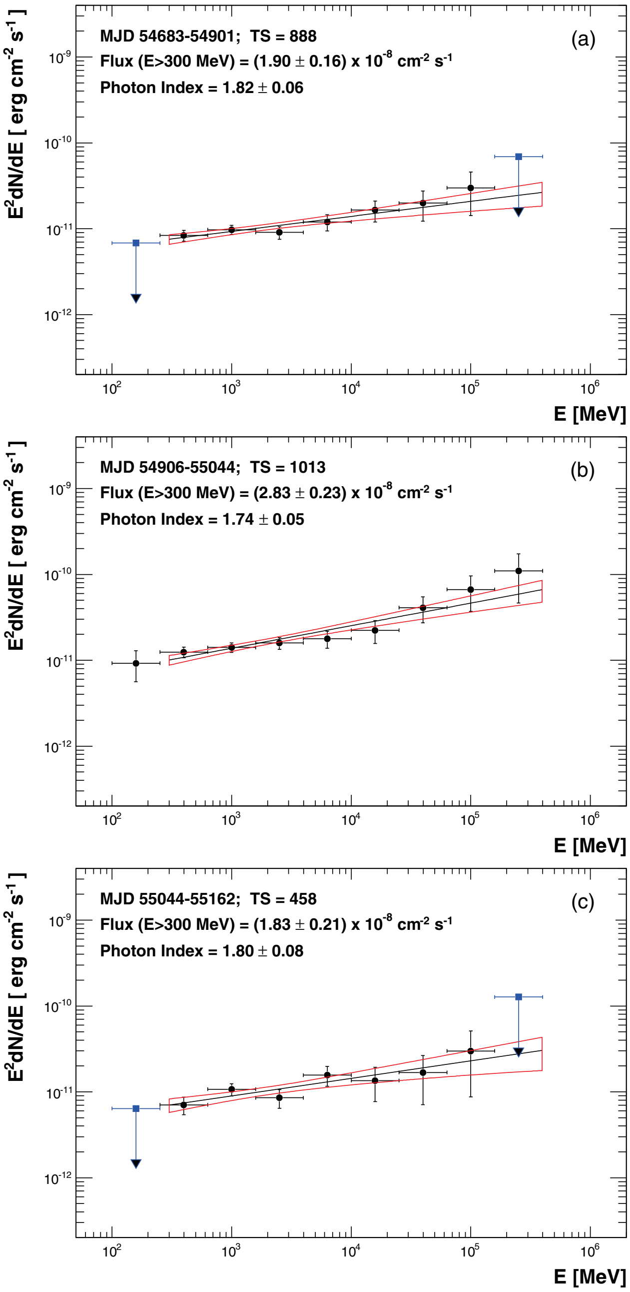

Figure 7. SED for Mrk 501 from *Fermi*-LAT for several time intervals of interest. Panel (a) shows the SED for the time period before the multifrequency campaign (MJD 54683–54901), panel (b) for the time interval corresponding to the multifrequency campaign (MJD 54905–55044), and panel (c) for the period after the campaign (MJD 55044–55162). In all panels, the black line depicts the result of the unbinned likelihood power-law fit, the red contours denote the 68% uncertainty of the power-law fit, and blue arrows denote upper limits at 95% confidence level, which were computed for the differential energy ranges with a signal of $TS < 4$ or less than two photons predicted by the analysis model for Mrk 501. The legend reports the results from the unbinned likelihood power-law fit in the energy range 0.3–400 GeV.

(A color version of this figure is available in the online journal.)

5.3. The Average Broadband SED During the Campaign

The average broadband SED of Mrk 501 resulting from our 4.5 month long multifrequency campaign is shown in Figure 8. The TeV data from MAGIC and VERITAS have been corrected for the absorption in the EBL using the particular EBL model

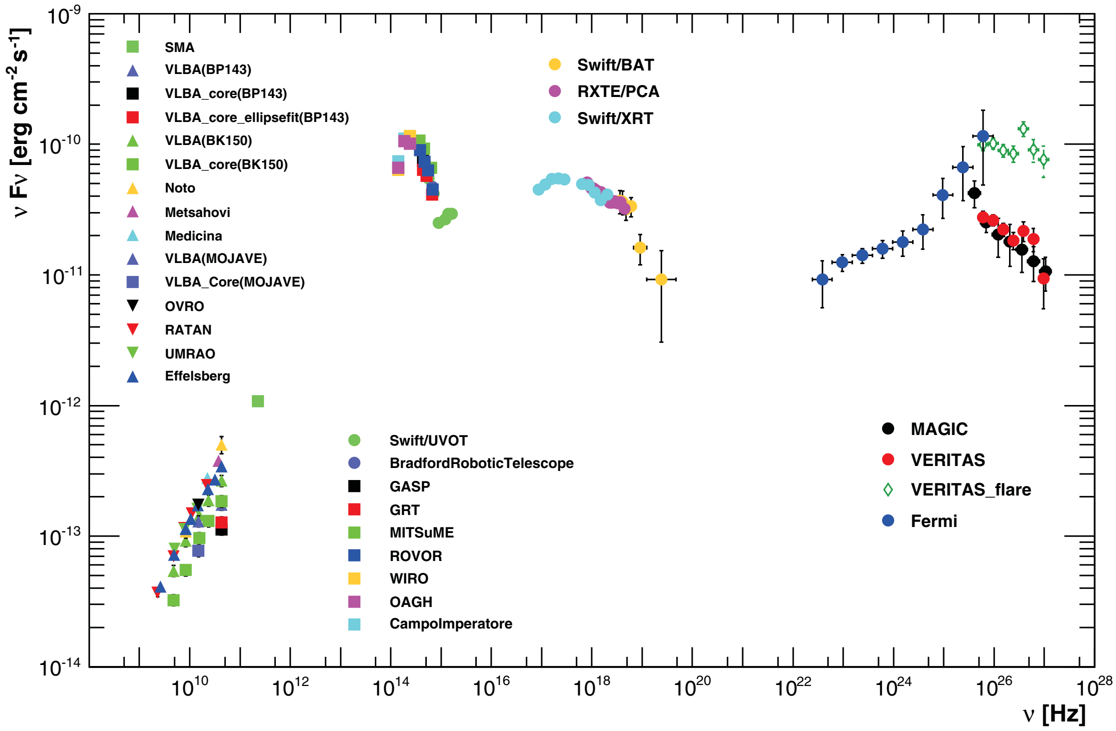

Figure 8. SED for Mrk 501 averaged over all observations taken during the multifrequency campaign performed between 2009 March 15 (MJD 54905) and 2009 August 1 (MJD 55044). The legend reports the correspondence between the instruments and the measured fluxes. Further details about the instruments are given in Section 5.1. The optical and X-ray data have been corrected for Galactic extinction, but the host galaxy (which is clearly visible at the IR/optical frequencies) has not been subtracted. The TeV data from MAGIC and VERITAS have been corrected for the absorption in the EBL using the model reported in Franceschini et al. (2008). The VERITAS data from the time interval MJD 54952.9–54955.9 were removed from the data set used to compute the average spectrum, and are depicted separately in the SED plot (in green diamonds). See the text for further details.

by Franceschini et al. (2008). The corrections given by the other low-EBL-level models (Kneiske et al. 2004; Gilmore et al. 2009; Finke et al. 2010) are very similar for the low redshift of Mrk 501 ($z = 0.034$). The attenuation factor at a photon energy of 6 TeV (the highest energy detected from Mrk 501 during this campaign) is in the range $e^{-\tau_{\gamma\gamma}} \simeq 0.4$–0.5, and smaller at lower energies.

During the campaign, as already noted above, the source did not show large flux variations like those recorded by EGRET in 1996, or those measured by X-ray and TeV instruments in 1997. Nevertheless, significant flux and spectral variations at γ-ray energies occurred in the time interval MJD 54905–55044. The largest flux variation during the campaign was observed at TeV energies during the time interval MJD 54952.9–54955.9, when VERITAS measured a flux about five times higher than the average one during the campaign. Because of the remarkable difference with respect to the rest of the analyzed exposure, these observations were excluded from the data set used to compute the average VERITAS spectrum for the campaign; the three-day "flaring-state" spectrum (2.4 hr of observation) is presented separately in Figure 8. Such a remarkable flux enhancement was not observed in the other energy ranges and hence Figure 8 shows only the averaged spectra for the other instruments.[156]

The top panel in Figure 9 shows a zoom of the high-energy bump depicted in Figure 8. The last two energy bins from *Fermi* (60–160 and 160–400 GeV) are systematically above (1σ–2σ) the measured/extrapolated spectrum from MAGIC and VERITAS. Even though this mismatch is not statistically significant, we believe that the spectral variability observed during the 4.5 month long campaign (see Sections 4 and 5.2) could be the origin of such a difference. Because *Fermi*-LAT operates in a survey mode, Mrk 501 is constantly monitored at GeV energies,[157] while this is not the case for the other instruments which typically sampled the source for $\leqslant$1 hr every five days approximately. Moreover, because of bad weather or moonlight conditions, the monitoring at the TeV energies with Cherenkov telescopes was even less regular than that at lower frequencies. Therefore, *Fermi*-LAT may have measured high activity that was missed by the other instruments. Indeed, the 2.4 hr high-flux spectrum from VERITAS depicted in Figure 8 (which was obtained during the three-day interval MJD 54952.9–54955.9) demonstrates that, during the multifrequency campaign, there were time periods with substantially (factor of five) higher TeV activity. It is possible that the highest energy LAT observations ($\geqslant$50 GeV) include high TeV flux states which occurred while the IACTs were not observing.

If the flaring activity occurred only at the highest photon energies, then the computed *Fermi*-LAT flux (>0.3 GeV) would not change very much and the effect might only be visible in the measured power-law photon index. This seems to be the case in the presented data set. As was shown in Figure 5, the 30-day intervals MJD 54922–54952 and MJD 54952–54982 have photon fluxes above 0.3 GeV of $(3.9 \pm 0.6) \times 10^{-8}$ ph cm^{-2} s^{-1} and $(3.6 \pm 0.5) \times 10^{-8}$ ph cm^{-2} s^{-1}, while their photon indices are 2.10 ± 0.13 and 1.63 ± 0.09, respectively. Therefore, the spectral information (together with the enhanced photon flux) indicates

[156] The MAGIC telescope did not operate during the time interval MJD 54948–54965 due to a drive system upgrade.

[157] For every three hours of *Fermi* operation, Mrk 501 is in the LAT FoV for about 0.5 hr.

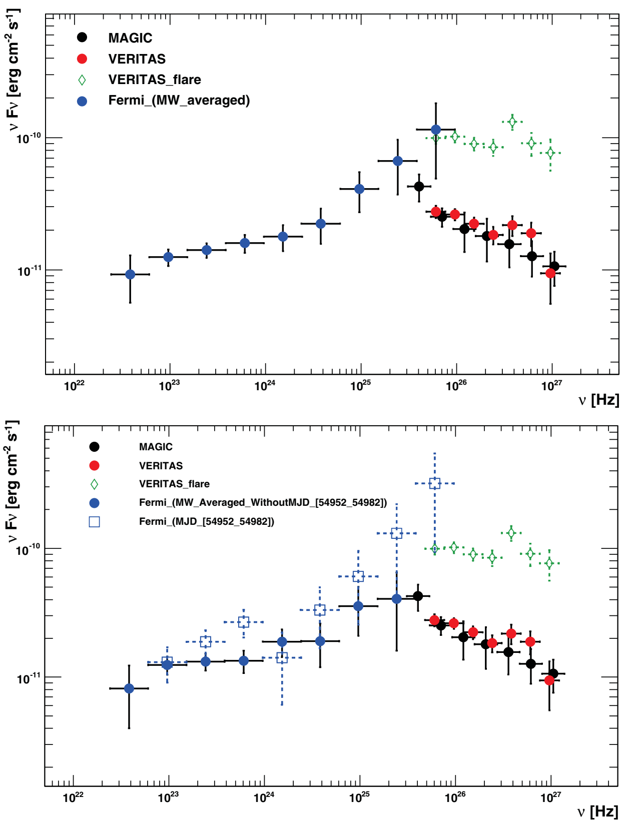

Figure 9. Top panel: enlargement of the γ-ray energy range from Figure 8. Bottom panel: same SED as in the top panel, but with the *Fermi*-LAT data from the multifrequency campaign split in two data sets: MJD 54952–54982 (open blue squares) and the rest (filled blue circles).

the presence of flaring activity at the highest γ-ray energies during the second 30-day time period. Besides the factor $\sim$5 VHE flux enhancement recorded by VERITAS and Whipple at the beginning of the time interval MJD 54952–54982, MAGIC, and Whipple also recorded a factor $\sim$2 VHE flux enhancement at the end of this 30-day time interval (see preliminary fluxes reported in Paneque 2009; Pichel et al. 2009). This flux enhancement was measured for the time interval MJD 54975–54977, but there were no VHE measurements during the period MJD 54970.5–54975.0. Thus, the average *Fermi*-LAT spectrum could have been affected by elevated VHE activity during the 30-day time interval MJD 54952–54982, which was only partly covered by the IACTs participating in the campaign.

For illustrative purposes, in the bottom panel of Figure 9, we show separately the *Fermi*-LAT spectra for the 30-day time interval MJD 54952–54982 (high photon flux and hard spectrum), and for the rest of the campaign. It is interesting to note that the *Fermi*-LAT spectrum without the 30-day time interval MJD 54952–54982 (blue data points in the bottom panel of Figure 9) agrees perfectly with the VHE spectrum measured by IACTs. We also want to point out that the power-law fit to the *Fermi*-LAT spectrum without the 30-day interval MJD 54952–54982 gave a photon flux above 0.3 GeV of $(2.62 \pm 0.25) \times 10^{-8}$ ph cm^{-2} s^{-1} with a photon index of 1.78 ± 0.07, which is statistically compatible with the results for the power-law fit to the *Fermi*-LAT data from the entire campaign (see panel (b) in Figure 7). As discussed above, the flaring activity occurred mostly at the highest energies, where the (relatively) low photon count has little impact on the overall power-law fit performed above 0.3 GeV.

This is the most complete quasi-simultaneous SED ever collected for Mrk 501, or for any other TeV-emitting BL Lac object (see also A. A. Abdo et al. 2011, in preparation). At the highest energies, the combination of *Fermi* and MAGIC/VERITAS data allows us to measure, for the first time, the high-energy bump without any spectral gap. The low-energy spectral component is also very well characterized with *Swift*-UVOT, *Swift*-XRT, and *RXTE*-PCA data, covering the peak of the synchrotron continuum. The only (large) region of the SED with no available data corresponds to the photon energy range 200 keV–100 MeV, where the sensitivity of current instruments is not good enough to detect Mrk 501. It is worth stressing that the excellent agreement in the overlapping energies among the various instruments (which had somewhat different time coverages) indicates that the collected data are representative of the truly average SED during the multi-instrument campaign.

6. MODELING THE SPECTRAL ENERGY DISTRIBUTION OF Mrk 501

The simultaneous broadband data set resulting from the multifrequency campaign reported above offers an unprecedented opportunity of modeling the emission of an archetypal TeV blazar in a more robust way than in the past. It is widely believed that the radio-to-γ-ray emission of the BL Lac class of an AGN is produced predominantly via the synchrotron and SSC processes, and hence the homogeneous one-zone approximation of the SSC scenario is the simplest model to consider. Here, we therefore adopt the "standard" one-zone SSC model, which has had moderate success in accounting for the spectral and temporal properties of the TeV-emitting BL Lac objects analyzed so far (e.g., Finke et al. 2008; Ghisellini et al. 2009b, and references therein). We also note that one-zone SSC analyses have been widely applied before to the particular case of Mrk 501 (e.g., Bednarek & Protheroe 1999; Katarzyński et al. 2001; Tavecchio et al. 2001; Kino et al. 2002; Albert et al. 2007a). However, it is important to stress that the modeling results from the previous works related almost exclusively to the high-activity state of Mrk 501. In the more recent work by Anderhub et al. (2009), the source was studied also during its low-activity state, yet the simultaneous observations used in the modeling covered only the X-ray and TeV photon energies. In this paper, we study Mrk 501 during a relatively low-activity state, and the modeling is applied to a more complete broadband SED extending from radio to TeV energies, including the previously unavailable GeV data from *Fermi*. This constitutes a substantial difference with respect to previous works. The resulting constraints on the physical parameters of the source, together with several limitations of the applied scenario, are discussed further down in the following sections.

We want to note that modeling of the average blazar SED based on a scenario assuming a steady-state homogenous emission zone could be an oversimplification of the problem. The blazar emission may be produced in an inhomogeneous region, involving stratification of the emitting plasma both along and across a relativistic outflow. In such a case, the observed radiative output of a blazar could be due to a complex superposition of different emission zones characterized by very different parameters and emission properties. Some first attempts to approach this problem in a more quantitative way have been already discussed in the literature (e.g., Ghisellini et al. 2005; Katarzyński et al. 2008; Graff et al. 2008; Giannios et al. 2009). The main drawback of the proposed models, however, is the increased number of free parameters (over the simplest homogeneous one-zone scenario), which reduces considerably the predictive power of the modeling. That is particularly problematic if a "limited" (in time and energy coverage) data set is considered in the modeling. Only a truly simultaneous multifrequency data set covering a large fraction of the available electromagnetic spectrum and a wide range of timescales—like the one collected during this and future campaigns which will be further exploited in forthcoming publications—will enable us to test such more sophisticated and possibly more realistic blazar emission models in a time-dependent manner.

6.1. SSC Modeling

Let us assume that the emitting region is a homogeneous and roughly spherically symmetric moving blob, with radius R and comoving volume $V' \simeq (4\pi/3)\,R^3$. For this, we evaluate the comoving synchrotron and SSC emissivities, $\nu' j'_{\nu'}$, assuming isotropic distributions of ultrarelativistic electrons and synchrotron photons in the rest frame of the emitting region. Thus, we use the exact synchrotron and inverse-Compton kernels (the latter one valid in both Thomson and Klein–Nishina regimes), as given in Crusius & Schlickeiser (1986) and Blumenthal & Gould (1970), respectively. The intrinsic monochromatic synchrotron and SSC luminosities are then $\nu' L'_{\nu'} = 4\pi\, V'\, \nu' j'_{\nu'}$, while the observed monochromatic flux densities (measured in erg cm^{-2} s^{-1}) can be found as

$$\nu F_\nu = \frac{\delta^4}{4\pi\, d_L^2}\,[\nu' L'_{\nu'}]_{\nu'=\nu\,(1+z)/\delta} \simeq \frac{4\pi\,\delta^4 R^3}{3\,d_L^2}\,[\nu' j'_{\nu'}]_{\nu'=\nu\,(1+z)/\delta}\,, \tag{2}$$

where δ is the jet Doppler factor, $z = 0.034$ is the source redshift, and $d_L = 142$ Mpc is the luminosity distance to Mrk 501. In order to evaluate the comoving emissivities $\nu' j'_{\nu'}$, the electron energy distribution $n'_e(\gamma)$ has to be specified. For this, we assume a general power-law form between the minimum and maximum electron energies, $\gamma_{\rm min}$ and $\gamma_{\rm max}$, allowing for multiple spectral breaks in between, as well as for an exponential cut-off above $\gamma_{\rm max}$. In fact, the broadband data set for Mrk 501 requires two different electron break energies, and hence we take the electron energy distribution in the form

$$n'_e(\gamma) \propto \begin{cases} \gamma^{-s_1} & \text{for} \quad \gamma_{\rm min} \leqslant \gamma < \gamma_{\rm br,\,1} \\ \gamma^{-s_2} & \text{for} \quad \gamma_{\rm br,\,1} \leqslant \gamma < \gamma_{\rm br,\,2} \\ \gamma^{-s_3}\,\exp[-\gamma/\gamma_{\rm max}] & \text{for} \quad \gamma_{\rm br,\,2} \leqslant \gamma, \end{cases} \tag{3}$$

with the normalization expressed in terms of the equipartition parameter (the ratio of the comoving electron and magnetic field energy densities), namely

$$\eta_e \equiv \frac{U'_e}{U'_B} = \frac{\int \gamma\, m_e c^2\, n'_e(\gamma)\, d\gamma}{B^2/8\pi}\,. \tag{4}$$

The measured SED is hardly compatible with a simpler form of the electron distribution with only one break and an exponential cutoff. However, some smoothly curved spectral shape might perhaps be an alternative representation of the electron spectrum (e.g., Stawarz & Petrosian 2008; Tramacere et al. 2009).

The model adopted is thus characterized by four main free parameters (B, R, δ, and η_e), plus seven additional ones related to the electron energy distribution ($\gamma_{\rm min}$, $\gamma_{\rm br,\,1}$, $\gamma_{\rm br,\,2}$, $\gamma_{\rm max}$, s_1, s_2, and s_3). These seven additional parameters are determined by the spectral shape of the non-thermal emission continuum probed by the observations, predominantly by the spectral shape of the synchrotron bump (rather than the inverse-Compton bump), and depend only slightly on the particular choice of the magnetic field B and the Doppler factor δ within the allowed range.[158] There is a substantial degeneracy regarding the four main free parameters: the average emission spectrum of Mrk 501 may be fitted by different combinations of B, R, δ, and η_e with little variation in the shape of the electron energy distribution. Note that, for example, $[\nu F_\nu]_{\rm syn} \propto R^3\,\eta_e$, but at the same time $[\nu F_\nu]_{\rm ssc} \propto R^4\,\eta_e^2$. We can attempt to reduce this degeneracy by assuming that the observed main variability timescale is related to the size of the emission region and its Doppler factor according to the formula

$$t_{\rm var} \simeq \frac{(1+z)\,R}{c\,\delta}\,. \tag{5}$$

The multifrequency data collected during the 4.5 month campaign (see Section 5) allow us to study the variability of Mrk 501 on timescales from months to a few days. We found that, during this time period, the multifrequency activity typically varied on a timescale of 5–10 days, with the exception of a few particular epochs when the source became very active in VHE γ-rays, and flux variations with timescales of a day or shorter were found at TeV energies. Nevertheless, it is important to stress that several authors concluded in the past that the dominant emission site of Mrk 501 is characterized by variability timescales longer than one day (see Kataoka et al. 2001, for a comprehensive study of the Mrk 501 variability in X-rays), and that the power in the intraday flickering of this source is small, in agreement with the results of our campaign. Nevertheless, one should keep in mind that this object is known for showing sporadic but extreme changes in its activity that can give flux variations on timescales as short as a few minutes (Albert et al. 2007a). In this work, we aim to model the average/typical behavior of Mrk 501 (corresponding to the 4.5 month campaign) rather than specific/short periods with outstanding activity, and hence we constrained the minimum (typical) variability timescale $t_{\rm var}$ in the model to the range 1–5 days.

Even with $t_{\rm var}$ fixed as discussed above, the reconstructed SED of Mrk 501 may be fitted by different combinations of B, R, δ, and η_e. Such a degeneracy between the main model parameters is an inevitable feature of the SSC modeling of blazars (e.g., Kataoka et al. 1999), and it is therefore necessary to impose additional constraints on the physical parameters of the dominant emission zone. Here, we argue that such constraints follow from the requirement for the electron energy distribution to be in agreement with the one resulting from the simplest prescription of the energy evolution of the radiating electrons within the emission region, as discussed below.

The idea of separating the sites for the particle acceleration and emission processes is commonly invoked in modeling different astrophysical sources of high-energy radiation, and blazar jets in particular. Such a procedure is not always justified, because interactions of ultrarelativistic particles with the magnetic field (leading to particle diffusion and convection in momentum space) are generally accompanied by particle radiative losses (and vice versa). On the other hand, if the characteristic timescale for energy gains is much shorter than the timescales for radiative cooling ($t'_{\rm rad}$) or escape ($t'_{\rm esc}$) from the system, the particle acceleration processes may be indeed approximated as

[158] For example, for a given critical (break) synchrotron frequency in the observed SED, the corresponding electron break Lorentz factor scales as $\gamma_{\rm br} \propto 1/\sqrt{B\,\delta}$.

Table 2
Parameters of the Blazar Emission Zone in Mrk 501

Parameter	Main SSC Fit Considered	Alternative SSC Fit
Magnetic field	$B = 0.015$ G	$B = 0.03$ G
Emission region size	$R = 1.3 \times 10^{17}$ cm	$R = 0.2 \times 10^{17}$ cm
Jet Doppler and bulk Lorentz factors	$\Gamma = \delta = 12$	$\Gamma = \delta = 22$
Equipartition parameter	$\eta_e \equiv U'_e/U'_B = 56$	$\eta_e \equiv U'_e/U'_B = 130$
Minimum electron energy	$\gamma_{\rm min} = 600$	$\gamma_{\rm min} = 300$
Intrinsic electron break energy	$\gamma_{\rm br,\,1} = 4 \times 10^4$	$\gamma_{\rm br,\,1} = 3 \times 10^4$
Cooling electron break energy	$\gamma_{\rm br,\,2} = 9 \times 10^5$	$\gamma_{\rm br,\,2} = 5 \times 10^5$
Maximum electron energy	$\gamma_{\rm max} = 1.5 \times 10^7$	$\gamma_{\rm max} = 0.3 \times 10^7$
Low-energy electron index	$s_1 = 2.2$	$s_1 = 2.2$
High-energy electron index	$s_2 = 2.7$	$s_2 = 2.7$
Electron index above the cooling break	$s_3 = 3.65$	$s_3 = 3.5$
Mean electron energy	$\langle\gamma\rangle \simeq 2400$	$\langle\gamma\rangle \simeq 1200$
Main variability timescale	$t_{\rm var} \simeq 4$ days	$t_{\rm var} \simeq 0.35$ day
Comoving electron energy density	$U'_e \simeq 0.5 \times 10^{-3}$ erg cm^{-3}	$U'_e \simeq 4.6 \times 10^{-3}$ erg cm^{-3}
Comoving magnetic field energy density	$U'_B \simeq 0.9 \times 10^{-5}$ erg cm^{-3}	$U'_B \simeq 3.6 \times 10^{-5}$ erg cm^{-3}
Comoving energy density of synchrotron photons	$U'_{\rm syn} \simeq 0.9 \times 10^{-5}$ erg cm^{-3}	$U'_{\rm syn} \simeq 3.1 \times 10^{-5}$ erg cm^{-3}
Comoving electron number density	$N'_e \simeq 0.3$ cm^{-3}	$N'_e \simeq 4.6$ cm^{-3}
Luminosity of the host galaxy	$L_{\rm star} \simeq 3 \times 10^{44}$ erg s^{-1}	$L_{\rm star} \simeq 3 \times 10^{44}$ erg s^{-1}
Jet power carried by electrons	$L_e \simeq 1.1 \times 10^{44}$ erg s^{-1}	$L_e \simeq 0.85 \times 10^{44}$ erg s^{-1}
Jet power carried by magnetic field	$L_B \simeq 2 \times 10^{42}$ erg s^{-1}	$L_B \simeq 0.65 \times 10^{42}$ erg s^{-1}
Jet power carried by protons[a]	$L_p \simeq 3 \times 10^{43}$ erg s^{-1}	$L_p \simeq 4.2 \times 10^{43}$ erg s^{-1}
Total jet kinetic power	$L_j \simeq 1.4 \times 10^{44}$ erg s^{-1}	$L_j \simeq 1.3 \times 10^{44}$ erg s^{-1}
Total emitted power	$L_{em} \simeq 9.7 \times 10^{42}$ erg s^{-1}	$L_{em} \simeq 2.7 \times 10^{42}$ erg s^{-1}
Isotropic synchrotron luminosity	$L_{\rm syn} \simeq 10^{45}$ erg s^{-1}	$L_{\rm syn} \simeq 10^{45}$ erg s^{-1}
Isotropic SSC luminosity	$L_{\rm ssc} \simeq 2 \times 10^{44}$ erg s^{-1}	$L_{\rm ssc} \simeq 2 \times 10^{44}$ erg s^{-1}

Note. [a] Assuming one electron–proton pair per electron–positron pair, and mean proton Lorentz factor $\langle\gamma_p\rangle \sim 1$.

being "instantaneous," and may be modeled by a single injection term $\dot{Q}(\gamma)$ in the simplified version of the kinetic equation

$$\frac{\partial n'_e(\gamma)}{\partial t} = -\frac{\partial}{\partial\gamma}\left[\frac{\gamma\, n_e(\gamma)}{t'_{\rm rad}(\gamma)}\right] - \frac{n_e(\gamma)}{t'_{\rm esc}} + \dot{Q}(\gamma), \qquad (6)$$

describing a very particular scenario for the energy evolution of the radiating ultrarelativistic electrons.

It is widely believed that the above equation is a good approximation for the energy evolution of particles undergoing diffusive (first-order Fermi) shock acceleration, and cooling radiatively in the downstream region of the shock. In such a case, the term $\dot{Q}(\gamma)$ specifies the energy spectrum and the injection rate of the electrons freshly accelerated at the shock front and not affected by radiative losses, while the escape term corresponds to the energy-independent dynamical timescale for the advection of the radiating particles from the downstream region of a given size R, namely $t'_{\rm esc} \simeq t'_{\rm dyn} \simeq R/c$. The steady-state electron energy distribution is then very roughly $n'_e(\gamma) \sim t'_{\rm dyn}\, \dot{Q}(\gamma)$ below the critical energy for which $t'_{\rm rad}(\gamma) = t'_{\rm dyn}$, and $n'_e(\gamma) \sim t'_{\rm rad}(\gamma)\, \dot{Q}(\gamma)$ above this energy. Note that in the case of a power-law injection $\dot{Q}(\gamma) \propto \gamma^{-s}$ and a homogeneous emission region with dominant radiative losses of the synchrotron type, $t'_{\rm rad}(\gamma) \propto \gamma^{-1}$, the injected electron spectrum is expected to steepen by $\Delta s = 1$ above the critical "cooling break" energy. This provides us with the additional constraint on the free model parameters for Mrk 501: namely, we require that the position of the second break in the electron energy distribution needed to fit the reconstructed SED, $\gamma_{\rm br\,2}$, should correspond to the location of the cooling break for a given chosen set of the model free parameters.

Figure 10 (black curves) shows the resulting SSC model fit (summarized in Table 2) to the averaged broadband emission

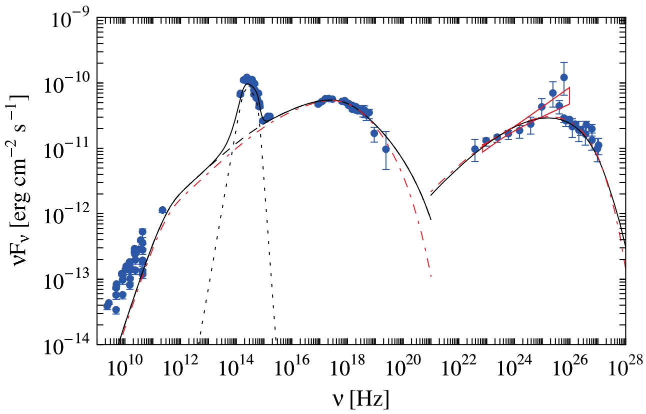

Figure 10. SSC model fits to the broadband emission spectrum of Mrk 501, averaged over all the observations made during the multifrequency campaign performed between 2009 March 15 (MJD 54905) and 2009 August 1 (MJD 55044). The red bow-tie in the figure corresponds to the 68% containment of the power-law fit to the average *Fermi*-LAT spectrum (photon index 1.74 ± 0.05). The dotted black curve denotes the fit to the starlight emission of the host galaxy assuming a template of a luminous elliptical as given in Silva et al. (1998). The details of the model are given in Section 6. The black curves correspond to the main set of the model parameters considered (variability timescale $t_{\rm var} \simeq 4$ days), while the red dot-dashed curves to the alternative set of the model parameters with the emission region size decreased by an order of magnitude ($t_{\rm var} \simeq 0.35$ days). See the text for further discussion.

spectrum of Mrk 501, which was obtained for the following parameters: $B = 0.015$ G, $R = 1.3 \times 10^{17}$ cm, $\delta = 12$, $\eta_e = 56$, $\gamma_{\rm min} = 600$, $\gamma_{\rm br,\,1} = 4 \times 10^4$, $\gamma_{\rm br,\,2} = 9 \times 10^5$, $\gamma_{\rm max} = 1.5 \times 10^7$, $s_1 = 2.2$, $s_2 = 2.7$, and $s_3 = 3.65$. The overall good agreement of the model with the data is further discussed in Section 6.2. Here, we note that, for these model parameters, synchrotron self-absorption effects are important only below 1 GHz, where we do not have observations.[159] We also emphasize that with all the aforementioned constraints and for a given spectral shape of the synchrotron continuum (including all the data points aimed to be fitted by the model, as discussed below), and thus for a fixed spectral shape of the electron energy distribution (modulo critical electron Lorentz factors scaling as $\propto 1/\sqrt{B\,\delta}$), the allowed range for the free parameters of the model is relatively narrow. Namely, for the variability timescale between one and five days, the main model parameters may change within the ranges $R \simeq (0.35–1.45) \times 10^{17}$ cm, $\delta \simeq 11–14$, and $B \simeq 0.01–0.04$ G. The parameter η_e depends predominantly on the minimum Lorentz factor of the radiating electrons. Hence, it is determined uniquely as $\eta_e \simeq 50$ with the submillimeter flux included in the fitted data set. Only with a different prescription for the spectral shape of the electron energy distribution could the main free parameters of the model be significantly different from those given above.

Despite the absence of any fast variability during this multi-frequency campaign (apart from the already discussed isolated three-day-long flare), Mrk 501 is known for the extremely rapid flux changes at the highest observed photon energies (e.g., Albert et al. 2007a). Hence, it is interesting to check whether any shorter than few-day-long variability timescales can be accommodated in the framework of the simplest SSC model applied here for the collected data set. In order to do that, we decreased the minimum variability time scale by one order of magnitude (from four days to 0.4 days), and tried to model the data. A satisfactory fit could be obtained with those modified parameters, but only when we relaxed the requirement for the electron energy distribution to be in agreement with the one following from the steady-state solution to Equation (6), and in particular the resulting constraint for the second break in the electron spectrum to be equal to the cooling break. This "alternative" model fit is shown in Figure 10 (red curves) together with the "best" model fit discussed above. The resulting model parameters for the "alternative" fit are $B = 0.03$ G, $R = 2 \times 10^{16}$ cm, $\delta = 22$, $\eta_e = 130$, $\gamma_{\rm min} = 300$, $\gamma_{\rm br,\,1} = 3 \times 10^4$, $\gamma_{\rm br,\,2} = 5 \times 10^5$, $\gamma_{\rm max} = 3 \times 10^6$, $s_1 = 2.2$, $s_2 = 2.7$, and $s_3 = 3.5$. This particular parameter set—which should be considered as an illustrative one only—would be therefore consistent with a minimum variability timescale of 0.36 days, but at the price of much larger departures from the energy equipartition ($\eta_e > 100$). The other source parameters, on the other hand, would change only slightly (see Table 2). Because of the mismatch (by a factor $\sim$3) between the location of the cooling break and the second break in the electron distribution, we consider this "alternative" fit less consistent with the hypothesis of the steady-state homogeneous one-zone SSC scenario, which is the framework with which we chose to model the broadband SED of Mrk 501 emerging from the campaign.

6.2. *Notes on the Spectral Data Points*

The low-frequency radio observations performed with single-dish instruments have a relatively large contamination from non-blazar emission due to the underlying extended jet component, and hence they only provide upper limits for the radio flux density of the blazar emission zone. On the other hand, the flux measurements by the interferometric instruments (such as VLBA), especially the ones corresponding to the core, provide us with the radio flux density from a region that is not much larger than the blazar emission region.

The radio flux densities from interferometric observations (from the VLBA core) are expected to be close upper limits to the radio continuum of the blazar emission component. The estimated size of the partially resolved VLBA core of Mrk 501 at 15 GHz and 43 GHz is $\simeq$0.14–0.18 mas $\simeq$2.9–3.7 $\times 10^{17}$ cm (with the appropriate conversion scale 0.67 pc mas^{-1}). The VLBA size estimation is the FWHM of a Gaussian representing the brightness distribution of the blob, which could be approximated as 0.9 times the radius of a corresponding spherical blob (Marscher 1983). That implies that the size of the VLBA core is only a factor of two to three larger than the emission region in our SSC model fit ($R = 1.3 \times 10^{17}$ cm). Therefore, it is reasonable to assume that the radio flux density from the VLBA core is indeed dominated by the radio flux density of the blazar emission. Forthcoming multi-band correlation studies (in particular VLBA and SMA radio with the γ-rays from *Fermi*-LAT) will shed light on this particular subject. Interestingly, the magnetic field claimed for the partially resolved radio core of Mrk 501 (which has a size of $\lesssim$0.2 mas) and its submilliarcsec jet, namely $B \simeq (10–30)$ mG (Giroletti et al. 2004, 2008), is in very good agreement with the value emerging from our model fits (15 mG), assuring self-consistency of the approach adopted.

In addition to this, in the modeling we also aimed at matching the submillimeter flux of Mrk 501, given at the observed frequency of 225 GHz, assuming that it represents the low-frequency tail of the optically thin synchrotron blazar component. One should emphasize in this context that it is not clear if the blazar emission zone is in general located deep within the millimeter photosphere or not. However, the broadband variability of luminous blazars of the FSRQ type indicates that there is a significant overlap of the blazar zone with a region where the jet becomes optically thin at millimeter wavelengths (as discussed by Sikora et al. 2008, for the particular case of the blazar 3C 454.3). We have assumed that the same holds for BL Lac objects.

The IR/optical flux measurements in the range $\sim(1–10) \times 10^{14}$ Hz represent the starlight of the host galaxy and hence they should be excluded when fitting the non-thermal emission of Mrk 501. We modeled these data points with the template spectrum of an elliptical galaxy instead (including only the dominant stellar component due to the evolved red giants, as discussed in Silva et al. 1998), obtaining a very good match (see the dotted line in Figure 10) for the bolometric starlight luminosity $L_{\rm star} \simeq 3 \times 10^{44}$ erg s^{-1}. Such a luminosity is in fact expected for the elliptical host of a BL Lac object. The model spectrum of the galaxy falls off very rapidly above 5×10^{14} Hz, while the three UV data points (above 10^{15} Hz) indicate a prominent, flat power-law UV excess over the starlight emission. Therefore, it is reasonable to assume that the observed UV fluxes correspond to the synchrotron (blazar-type) emission of Mrk 501 and, consequently, we used them in our model fit. However, many elliptical galaxies do reveal in their spectra the so-called UV upturn, or UV excess, whose origin is not well known, but which is presumably related to the starlight continuum (most likely due to young stars from the residual star-forming activity within the central region of a galaxy) rather than to non-thermal (jet-related) emission processes (see, e.g., Code & Welch 1979; Atlee et al. 2009). Hence, it is possible that the UV data points

[159] The turnover frequency related to the synchrotron self-absorption may be evaluated using the formulae given in Ghisellini & Svensson (1991) and the parameter values from our SSC model fit as $\nu'_{\rm ssa} \simeq 60$ MHz, which in the observer frame reads $\nu_{\rm ssa} = \delta\,\nu'_{\rm ssa}/(1+z) \simeq 0.7$ GHz.

provided here include some additional contamination from the stellar emission, and as such might be considered as upper limits for the synchrotron radiation of the Mrk 501 jet.

The observed X-ray spectrum of Mrk 501 agrees very well with the SSC model fit, except for a small but statistically significant discrepancy between the model curve and the first two data points provided by *Swift*-XRT, which correspond to the energy range 0.3–0.6 keV. As pointed out in Section 5.1, the *Swift*-XRT data had to be corrected for a residual energy offset which affects the lowest energies. The correction for this effect could introduce some systematic differences with respect to the actual fluxes detected at those energies. These low-energy X-ray data points might also be influenced by intrinsic absorption of the X-ray photons within the gaseous environment of Mrk 501 nucleus, as suggested by the earlier studies with the *ASCA* satellite (see Kataoka et al. 1999). As a result, the small discrepancy between the data and the model curve within the range 0.3–0.6 keV can be ignored in the modeling.

The agreement between the applied SSC model and the γ-ray data is also very good. In particular, the model returns the γ-ray photon index 1.78 in the energy range 0.3–30 GeV, which can be compared with the one resulting from the power-law fit to the *Fermi*-LAT data above 0.3 GeV, namely 1.74 ± 0.05. However, the last two energy bins from *Fermi* (60–160 and 160–400 GeV) are systematically above (2σ) the model curves, as well as above the averaged spectrum reported by MAGIC and VERITAS. A possible reason for mismatch between the average *Fermi*-LAT spectrum and the one from MAGIC/VERITAS was discussed in Section 5.3.

7. DISCUSSION

In this section, we discuss some of the implications of the model results presented above. After a brief analysis of the global parameters of the source resulting from the SSC fits (Section 7.1), the discussion focuses on two topics. First (Section 7.2), we show that the characteristics of the electron energy distribution emerging from our modeling can be used to constrain the physical processes responsible for the particle acceleration in Mrk 501, processes which may also be at work in other BL Lac-type objects. Second (Section 7.3), we examine the broadband variability of Mrk 501 in the framework of the model.

7.1. Main Characteristics of the Blazar Emission Zone in Mrk 501

The values for the emission region size $R = 1.3 \times 10^{17}$ cm and the jet Doppler factor $\delta = 12$ emerging from our SSC model fit give a minimum (typical) variability timescale of $t_{\rm var} \simeq (1+z)\, R/c\,\delta \sim 4$ days, which is consistent with the variability observed during the campaign and with previous studies of the X-ray activity of Mrk 501 (Kataoka et al. 2001). At this point, it is necessary to determine whether an emission region characterized by these values of R and δ is optically thin to internal two-photon pair creation $\gamma\gamma \rightarrow e^+e^-$ for the highest TeV energies observed during the campaign. We now affirm pair transparency due to insufficient density of soft target photons.

Since Mrk 501 is a cosmologically local object, pair conversion in the EBL is not expected to prevent its multi-TeV photons from reaching the Earth, although the impact of this process is not negligible, as mentioned in Section 5. Therefore, dealing with a nearby source allows us to focus mostly on the intrinsic absorption processes, rather than on the cosmological, EBL-related, attenuation of the γ-ray emission. Moreover, because of the absence (or weakness) of accretion-disk-related circumnuclear photon fields in BL Lac objects like Mrk 501, we only need to consider photon–photon pair production involving photon fields internal to the jet emission site. The analysis is therefore simpler than in the case of FSRQs, where the attenuation of high-energy γ-ray fluxes is dominated by interactions with photon fields external to the jet—such as those provided by the broad line regions or tori—for which the exact spatial distribution is still under debate.

Pair-creation optical depths can be estimated as follows. Using the δ-function approximation for the photon–photon annihilation cross-section (Zdziarski & Lightman 1985), $\sigma_{\gamma\gamma}(\varepsilon_0', \varepsilon_\gamma') \simeq 0.2\, \sigma_T\, \varepsilon_0'\, \delta[\varepsilon_0' - (2m_e^2c^4/\varepsilon_\gamma')]$, the corresponding optical depth for a γ-ray photon with observed energy $\varepsilon_\gamma = \delta\, \varepsilon_\gamma'/(1+z)$ interacting with a jet-originating soft photon with observed energy

$$\varepsilon_0 = \frac{\delta\, \varepsilon_0'}{1+z} \simeq \frac{2\,\delta^2 m_e^2 c^4}{\varepsilon_\gamma\,(1+z)^2} \simeq 50\, \left(\frac{\delta}{10}\right)^2 \left(\frac{\varepsilon_\gamma}{\rm TeV}\right)^{-1} {\rm eV}\,, \quad (7)$$

may be found as

$$\tau_{\gamma\gamma} \simeq \int^R ds \int_{m_e c^2/\varepsilon_0} d\varepsilon_0\, n_0'(\varepsilon_0)\, \sigma_{\gamma\gamma}(\varepsilon_0, \varepsilon_\gamma) \sim 0.2\, \sigma_{\rm T}\, R\, \varepsilon_0'\, n_0'(\varepsilon_0)\,, \quad (8)$$

where $n_0'(\varepsilon_0')$ is the differential comoving number density of soft photons. Noting that $\varepsilon_0'^2\, n_0'(\varepsilon_0') = L_0'/4\pi\, R^2 c$, where L_0' is the intrinsic monochromatic luminosity at photon energy ε_0', we obtain

$$\tau_{\gamma\gamma} \simeq \frac{\sigma_{\rm T}\, d_L^2\, F_0\, \varepsilon_\gamma (1+z)}{10\, R\, m_e^2 c^5\, \delta^5} \simeq 0.001\, \left(\frac{\varepsilon_\gamma}{\rm TeV}\right) \times \left(\frac{F_0}{10^{-11}\, {\rm erg\ cm^{-2}\ s^{-1}}}\right) \left(\frac{R}{10^{17}\, {\rm cm}}\right)^{-1} \left(\frac{\delta}{10}\right)^{-5}, \quad (9)$$

where $F_0 = L_0/4\pi d_L^2$ is the observed monochromatic flux energy density as measured at the observed photon energy ε_0. Thus, for 5 TeV γ-rays and the model parameters discussed (implying the observed $\varepsilon_0 = 15$ eV flux of Mrk 501 roughly $F_0 \simeq 3.2 \times 10^{-11}$ erg s^{-1} cm^{-2}), one has $\tau_{\gamma\gamma}(5\,{\rm TeV}) \simeq 0.005$. Therefore, the values of R and δ from our SSC model fit do not need to be adjusted to take into account the influence of spectral modifications due to pair attenuation. Note that such opacity effects, studied extensively in the context of γ-ray bursts, generally yield a broken power law for the spectral form, with the position and magnitude of the break fixed by the pair-production kinematics (e.g., Baring 2006 and references therein). The broad-band continuum of Mrk 501, and in particular its relatively flat spectrum VHE γ-ray segment, is inconsistent with such an expected break. This deduction is in agreement with the above derived transparency of the emitting region for high-energy γ-ray photons.

Next we evaluated the "monoenergetic" comoving energy density of ultrarelativistic electrons for a given electron Lorentz factor,

$$\gamma\, U_e'(\gamma) \equiv \gamma^2 m_e c^2\, n_e'(\gamma)\,, \quad (10)$$

and this is shown in Figure 11 (solid black line). The total electron energy density is then $U_e' = \int U_e'(\gamma)\, d\gamma \simeq 5 \times$

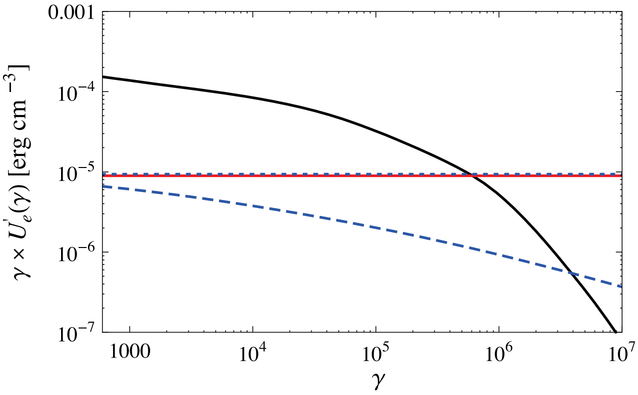

Figure 11. Jet comoving energy density of ultrarelativistic electrons per logarithmic energy bin, $\gamma U'_e(\gamma)$, as a function of the electron Lorentz factor γ (solid black curve). For comparison, the comoving energy density of the magnetic field U'_B (solid red line) and synchrotron photons U'_{syn} (dotted blue line) are shown. The dashed blue curve denotes the comoving energy density of synchrotron photons which are inverse-Compton upscattered in the Thomson regime, $U'_{syn/T}$, for a given electron Lorentz factor γ (see equation 12).

10^{-4} erg cm^{-3}. As shown, most of the energy is stored in the lowest energy particles ($\gamma_{\rm min} \simeq 600$). For comparison, the comoving energy density of the magnetic field and that of the synchrotron photons are plotted in the figure as well (horizontal solid red line and dotted blue line, respectively). These two quantities are approximately equal, namely $U'_B = B^2/8\pi \simeq 0.9 \times 10^{-5}$ erg cm^{-3} and

$$U'_{\rm syn} = \frac{4\pi\, R}{3\, c} \int j'_{\nu',\,{\rm syn}}\, d\nu' \simeq 0.9 \times 10^{-5}\, {\rm erg\, cm^{-3}}\,. \quad (11)$$

In Figure 11, we also plot the comoving energy density of synchrotron photons which are inverse-Compton upscattered in the Thomson regime for a given electron Lorentz factor γ,

$$U'_{\rm syn/T}(\gamma) = \frac{4\pi\, R}{3\, c} \int^{\nu'_{KN}(\gamma)} j'_{\nu',\,{\rm syn}}\, d\nu' \quad (12)$$

(dashed blue line), where $\nu'_{KN}(\gamma) \equiv m_e c^2/4\gamma\, h$. Because of the well-known suppression of the inverse-Compton scattering rate in the Klein–Nishina regime, the scattering in the Thomson regime dominates the inverse-Compton energy losses.[160] Hence, one may conclude that even though the total energy density of the synchrotron photons in the jet rest frame is comparable to the comoving energy density of the magnetic field ($U'_{\rm syn} \simeq U'_B$), the dominant radiative cooling for all the electrons is due to synchrotron emission, since $U'_{\rm syn/T} < U'_B$ for any γ.

The timescale for synchrotron cooling may be evaluated as

$$t'_{\rm syn} \simeq \frac{3 m_e c}{4\sigma_T \gamma\, U'_B} \simeq 4 \left(\frac{\gamma}{10^7}\right)^{-1} {\rm days}\,. \quad (13)$$

Hence, $t'_{\rm rad} \simeq t'_{\rm syn}$ equals the dynamical timescale of the emitting region, $t'_{\rm dyn} \simeq R/c$, for electron Lorentz factor $\gamma \simeq 8 \times 10^5$, i.e., close to the second electron break energy $\gamma_{\rm br,\,2}$. Also, the difference between the spectral indices below and above the break energy $\gamma_{\rm br,\,2}$ determined by our modeling, namely $\Delta s_{3/2} = s_3 - s_2 = 0.95$, is very close to the "classical" synchrotron cooling break $\Delta s = 1$ expected for a uniform emission region, as discussed in Section 6.1. This agreement, which justifies at some level the assumed homogeneity of the emission zone, was in fact the additional constraint imposed on the model to break the degeneracy between the main free parameters. Note that in such a case the first break in the electron energy distribution around electron energy $\gamma_{\rm br,\,1} = 4 \times 10^4$ is related to the nature of the underlying particle acceleration process. We come back to this issue in Section 7.2,

Another interesting result from our model fit comes from the evaluation of the mean energy of the electrons responsible for the observed non-thermal emission of Mrk 501. In particular, the mean electron Lorentz factor is

$$\langle\gamma\rangle \equiv \frac{\int \gamma\, n'_e(\gamma)\, d\gamma}{\int n'_e(\gamma)\, d\gamma} \simeq 2400. \quad (14)$$

This value, which is determined predominantly by the minimum electron energy $\gamma_{\rm min} = 600$ and by the position of the first break in the electron energy distribution, is comparable to the proton-to-electron mass ratio m_p/m_e. In other words, the mean energy of ultrarelativistic electrons within the blazar emission zone of Mrk 501 is comparable to the energy of non-relativistic/mildly-relativistic (cold) protons. This topic will be discussed further in Section 7.2 as well.

The analysis presented allows us also to access the global energetics of the Mrk 501 jet. In particular, with the given energy densities U'_e and U'_B, we evaluate the total kinetic powers of the jet stored in ultrarelativistic electrons and magnetic field as

$$L_e = \pi R^2 c \Gamma^2\, U'_e \simeq 10^{44}\, {\rm erg\, s^{-1}}\,, \quad (15)$$

and

$$L_B = \pi R^2 c \Gamma^2\, U'_B \simeq 2 \times 10^{42}\, {\rm erg\, s^{-1}}\,, \quad (16)$$

respectively. In the above expressions, we have assumed that the emission region analyzed occupies the whole cross-sectional area of the outflow, and that the jet propagates at sufficiently small viewing angle that the bulk Lorentz factor of the jet equals the jet Doppler factor emerging from our modeling, $\Gamma = \delta$. These assumptions are justified in the framework of the one-zone homogeneous SSC scenario. Moreover, assuming one electron–proton pair per electron–positron pair within the emission region (see Celotti & Ghisellini 2008), or equivalently $N'_p \simeq N'_e/3$, where the total comoving number density of the jet leptons is

$$N'_e = \int n'_e(\gamma)\, d\gamma \simeq 0.26\, {\rm cm^{-3}}\,, \quad (17)$$

we obtain the comoving energy density of the jet protons $U'_p = \langle\gamma_p\rangle\, m_p c^2 N'_e/3$, and hence the proton kinetic flux $L_p = \pi R^2 c \Gamma^2\, U'_p \simeq 0.3\, \langle\gamma_p\rangle\, 10^{44}$ erg s^{-1}. This is comparable to the kinetic power carried out by the leptons for mean proton Lorentz factor $\langle\gamma_p\rangle \simeq 4$ (see Equation (15)). It means that, within the dominant emission zone of Mrk 501 (at least during non-flaring activity), ultrarelativistic electrons and mildly relativistic protons, if comparable in number, are in approximate energy equipartition, and their energy dominates that of the jet magnetic field by two orders of magnitude. It is important to compare this result with the case of powerful blazars of the FSRQ type, for which the relatively low mean energy of the radiating electrons, $\langle\gamma\rangle \ll 10^3$, assures dynamical domination of cold protons even for a smaller proton content $N'_p/N'_e \lesssim 0.1$ (see the discussion in Sikora et al. 2009 and references therein).

[160] The inverse-Compton cross-section goes as $\sigma_{ic} \simeq \sigma_T$ for $\nu' < \nu'_{KN}(\gamma)$, and roughly as $\sigma_{ic} \sim \sigma_T\, (\nu'/\nu'_{KN})^{-1}\, \ln[\nu'/\nu'_{KN}]$ for $\nu' > \nu'_{KN}(\gamma)$ (e.g., Coppi & Blandford 1990).

Assuming $\langle\gamma_p\rangle \sim 1$ for simplicity, we find that the implied total jet power $L_j = L_e + L_p + L_B \simeq 1.4 \times 10^{44}$ erg s^{-1} constitutes only a small fraction of the Eddington luminosity $L_{\rm Edd} = 4\pi\, G M_{\rm BH}\, m_p c/\sigma_T \simeq (1.1\text{–}4.4) \times 10^{47}$ erg s^{-1} for the Mrk 501 black hole mass $M_{\rm BH} \simeq (0.9\text{–}3.5) \times 10^9 M_\odot$ (Barth et al. 2002). In particular, our model implies $L_j/L_{\rm Edd} \sim 10^{-3}$ in Mrk 501. In this context, detailed investigation of the emission-line radiative output from the Mrk 501 nucleus by Barth et al. (2002) allowed for an estimate of the bolometric, accretion-related luminosity as $L_{\rm disk} \simeq 2.4 \times 10^{43}$ erg s^{-1}, or $L_{\rm disk}/L_{\rm Edd} \sim 10^{-4}$. Such a relatively low luminosity is not surprising for BL Lac objects, which are believed to accrete at low, sub-Eddington rates (e.g., Ghisellini et al. 2009a). For a low-accretion rate AGN (i.e., those for which $L_{\rm disk}/L_{\rm Edd} < 10^{-2}$) the expected radiative efficiency of the accretion disk is $\eta_{\rm disk} \equiv L_{\rm disk}/L_{\rm acc} < 0.1$ (Narayan & Yi 1994; Blandford & Begelman 1999). Therefore, the jet power estimated here for Mrk 501 is comfortably smaller than the available power of the accreting matter $L_{\rm acc}$.

Finally, we note that the total emitted radiative power is

$$L_{\rm em} \simeq \Gamma^2\,(L'_{\rm syn}+L'_{\rm ssc}) = 4\pi\, R^2 c\, \Gamma^2\,(U'_{\rm syn}+U'_{\rm ssc}) \sim 10^{43}\ {\rm erg\ s^{-1}}\,, \tag{18}$$

where $U'_{\rm syn}$ is given in Equation (11) and the comoving energy density of γ-ray photons, $U'_{\rm ssc}$, was evaluated in an analogous way as $\simeq 1.7 \times 10^{-6}$ erg cm^{-3}. This implies that the jet/blazar radiative efficiency was at the level of a few percent ($L_{\rm em}/L_{\rm j} \simeq 0.07$) during the period covered by the multifrequency campaign. Such a relatively low radiative efficiency is a common characteristic of blazar jets in general, typically claimed to be at the level of 1%–10% (see Celotti & Ghisellini 2008; Sikora et al. 2009). On the other hand, the isotropic synchrotron and SSC luminosities of Mrk 501 corresponding to the observed average flux levels are $L_{\rm syn} = \delta^4 L'_{\rm syn} \simeq 10^{45}$ erg s^{-1} and $L_{\rm ssc} = \delta^4 L'_{\rm ssc} \simeq 2 \times 10^{44}$ erg s^{-1}, respectively.

7.2. Electron Energy Distribution

The results of the SSC modeling presented in the previous sections indicate that the energy spectrum of freshly accelerated electrons within the blazar emission zone of Mrk 501 is of the form $\propto E_e^{-2.2}$ between electron energy $E_{e,\,\rm min} = \gamma_{\rm min} m_e c^2 \sim 0.3$ GeV and $E_{e,\,br} = \gamma_{\rm br,\,1} m_e c^2 \sim 20$ GeV, steepening to $\propto E_e^{-2.7}$ above 20 GeV, such that the mean electron energy is $\langle E_e\rangle \equiv \langle\gamma\rangle\, m_e c^2 \sim 1$ GeV. At this point, a natural question arises: is this electron distribution consistent with the particle spectrum expected for a diffusive shock acceleration process? Note in this context that the formation of a strong shock in the innermost parts of Mrk 501 might be expected around the location of the large bend (change in the position angle by 90°) observed in the outflow within the first few parsecs (projected) from the core (Edwards & Piner 2002; Piner et al. 2009). This distance scale could possibly be reconciled with the expected distance of the blazar emission zone from the center for the model parameters discussed, $r \sim R/\theta_j \sim 0.5$ pc, for jet opening angle $\theta_j \simeq 1/\Gamma \ll 1$.

In order to address this question, let us first discuss the minimum electron energy implied by the modeling, $E_{e,\,\rm min} \sim 0.3$ GeV. In principle, electrons with lower energies may be present within the emission zone, although their energy distribution has to be very flat (possibly even inverted), in order not to overproduce the synchrotron radio photons and to account for the measured *Fermi*-LAT γ-ray continuum. Therefore, the constrained minimum electron energy marks the injection threshold for the main acceleration mechanism, meaning that only electrons with energies larger than $E_{e,\,\rm min}$ are picked up by this process to form the higher-energy (broken) power-law tail. Interestingly, the energy dissipation mechanisms operating at the shock fronts do introduce a particular characteristic (injection) energy scale, below which the particles are not freely able to cross the shock front. This energy scale depends on the shock microphysics, in particular on the thickness of the shock front. The shock thickness, in turn, is determined by the operating inertial length, or the diffusive mean free path of the radiating particles, or both. Such a scale depends critically on the constituents of the shocked plasma. For pure pair plasmas, only the electron thermal scale enters, and this sets $E_{e,\,\rm min} \sim \Gamma m_e c^2$. In contrast, if there are approximately equal numbers of electrons and protons, the shock thickness can be relatively large. Diffusive shock acceleration can then operate on electrons only above a relatively high energy, establishing $E_{e,\,\rm min} \sim \epsilon\, \Gamma m_p c^2$. Here, ϵ represents some efficiency of the equilibration in the shock layer between shocked thermal protons and their electron counterparts, perhaps resulting from electrostatic potentials induced by charge separation of species of different masses (Baring & Summerlin 2007). Our multifrequency model fits suggest that $\epsilon \sim 0.025$, providing an important blazar shock diagnostic.

At even lower electron energies, other energization processes must play a dominant role (e.g., Hoshino et al. 1992), resulting in formation of very flat electron spectra (see the related discussion in Sikora et al. 2009). Which of these energy dissipation mechanisms are the most relevant, as well as how flat the particle spectra could be, are subjects of ongoing debates. Different models and numerical simulations presented in the literature indicate a wide possible range for the lowest-energy particle spectral indices (below $E_{e,\,\rm min}$), from $s_{\rm inj} \simeq 1.0$–1.5 down to $s_{\rm inj} \simeq -2$, depending on the particular shock conditions and parameters (Amato & Arons 2006; Sironi & Spitkovsky 2009).

All in all, we argue that the relatively high minimum energy of the radiating electrons implied by the SSC modeling of the Mrk 501 broadband spectrum and the overall character of the electron energy evolution in this source are consistent with a proton-mediated shock scenario. In addition, the fact that the mean energy of the ultrarelativistic electrons is of the order of the proton rest energy, $\langle E_e\rangle \sim m_p c^2$, can be reconciled with such a model. Moreover, the constrained power-law slope of the electrons with energies $E_{e,\,\rm min} \leqslant E_e \leqslant E_{e,\,br}$, namely $s_1 = 2.2$, seems to suggest a dominant role for diffusive shock acceleration above the injection energy $E_{e,\,\rm min}$, as this value of the spectral index is often claimed in the literature for particles undergoing first-order Fermi acceleration at relativistic shock (Bednarz & Ostrowski 1998; Kirk et al. 2000; Achterberg et al. 2001). The caveat here is that this result for the "universal" particle spectral index holds only for particular conditions (namely, for ultrarelativistic shock velocities with highly turbulent conditions downstream of the shock: see the discussion in Ostrowski & Bednarz 2002), whereas in general a variety of particle spectra may result from the relativistic first-order Fermi mechanism, depending on the local magnetic field and turbulence parameters at the shock front, and the speed of the upstream flow (Kirk & Heavens 1989; Niemiec & Ostrowski 2004; Lemoine et al. 2006; Sironi & Spitkovsky 2009; Baring 2010). Nevertheless, the evidence for ultrarelativistic electrons with spectral index $s_1 = 2.2$ in the jet of Mrk 501 may be considered as an indication that the plasma conditions within the blazar emission zone allow for efficient diffusive shock acceleration (at least in this source), as described by the simplest asymptotic test-particle models, though only in a relatively narrow electron energy range.

If the relativistic shock acceleration plays a dominant role in the blazar Mrk 501 (as argued above), the observations and the model results impose important constraints on this mechanism, many aspects of which are still not well understood. Firstly, this process must be very efficient in the sense that all the electrons pre-accelerated/preheated to the energy $E_{e,\,\mathrm{min}} \sim 0.3$ GeV are picked up by the acceleration process so that a single electron component is formed above the injection threshold and there is no Maxwellian-like population of particles around $E_{e,\,\mathrm{min}}$ outnumbering the higher energy ones from the power-law tail.[161] The second constraint is due to the presence of the spectral break $\Delta s_{2/1} = s_2 - s_1 \simeq 0.5$ around electron energies $E_{e,\,br} \sim 20$ GeV. As discussed in the previous section, this break cannot be simply a result of cooling or internal pair-attenuation effects, and hence must be accounted for by the acceleration mechanism. The discussion regarding the origin of this break—which may reflect variations in the global field orientation or turbulence levels sampled by particles of different energy—is beyond the scope of this paper. However, the presence of high-energy breaks in the electron energy distribution (intrinsic to the particle spectrum rather than forming due to cooling or absorption effects) seems to be a common property of relativistic jet sources observed by *Fermi*-LAT, such as the FSRQ objects 3C 454.3 and AO 0235+164 (Abdo et al. 2009, 2010a).

7.3. Variability

In Sections 3–4, we reported on the γ-ray flux and spectral variability of Mrk 501 as measured by the *Fermi*-LAT instrument during the first 16 months of operation. In this section, we discuss whether the observed spectral evolution can be accounted for by our simple one-zone SSC model.

Figure 12 (top panel) presents in more detail the GeV–TeV γ-ray spectrum of Mrk 501, together with the decomposition of the SSC model continuum. Here the contributions of different segments of the electron energy distribution are indicated by different colors. As shown, the low-energy electrons, $\gamma_{\mathrm{min}} \leqslant \gamma < \gamma_{\mathrm{br},\,1}$, which emit synchrotron photons up to $\simeq 10^{15}$ Hz, dominate the production of γ-rays up to a few GeV (red line). The contribution of higher energy electrons with Lorentz factors $\gamma_{\mathrm{br},\,1} \leqslant \gamma < \gamma_{\mathrm{br},\,2}$ is pronounced within the observed synchrotron range $10^{15} - 10^{18}$ Hz, and at γ-ray energies from a few GeV up to $\sim$TeV (green line). Finally, the highest energy tail of the electron energy distribution, $\gamma \geqslant \gamma_{\mathrm{br},\,2}$, responsible for the observed hard-X-ray synchrotron continuum (>2 keV) in the fast cooling regime, generates the bulk of γ-rays with observed energies > TeV (blue line). Interestingly, even though any sharp breaks in the underlying electron energy distribution are "smeared out" into a smoothly curved spectral continuum due to the nature of the SSC emission, the average data set does support the presence of distinct low-energy and high-energy segments in the electron spectrum.

It therefore seems reasonable to argue that the spectral variability of Mrk 501 observed by *Fermi*-LAT may be explained by postulating that the low-energy segment of the electron energy distribution ($\gamma < \gamma_{\mathrm{br},\,1}$) is characterized by only small flux variations, while the high-energy electron tail ($\gamma > \gamma_{\mathrm{br},\,1}$) varies more substantially. In such a scenario, some correlation might be expected between the fluxes in the UV-to-soft-X-ray photon energies from the synchrotron bump and the GeV–TeV fluxes from the inverse-Compton bump. This expectation is not inconsistent with the fact that we do not see any obvious relation between the ASM/BAT fluxes and the LAT (>2 GeV) fluxes (see Figure 2), because the electrons producing X-ray synchrotron photons above 2–3 keV contribute to the SSC emission mostly at the highest photon energies in the TeV range (see Figure 12). This issue will be studied in detail (on timescales of 1 month down to 5 days) in a forthcoming publication using the data from this multifrequency campaign.

The X-ray/TeV connection has been established in the past for many BL Lac objects (and for Mrk 501 in particular). However, the exact character of the correlation between the X-ray and TeV fluxes is known to vary from object to object, and from epoch to epoch in a given source, as widely discussed in, e.g., Krawczynski et al. (2004), Błazejowski et al. (2005), Gliozzi et al. (2006), and Fossati et al. (2008). Note that the data analyzed in those papers were obtained mostly during periods of high activity. Consequently, the conclusions presented were somewhat biased towards flaring activity, and hence they might not apply to the typical (average) behavior of the source, which is the main focus of this paper. Moreover, the data set from

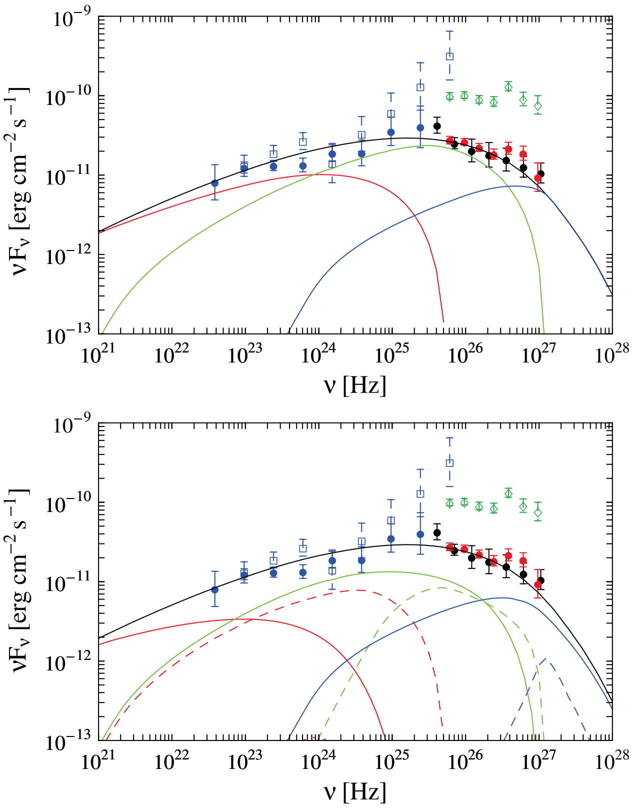

Figure 12. Decomposition of the SSC continuum for Mrk 501. The data points are the same as in the bottom panel of Figure 9. The SSC fit to the average spectrum is denoted by the solid black curve. Top: contributions of the different segments of the electron spectrum Comptonizing the whole synchrotron continuum (red curve: $\gamma_{\mathrm{min}} < \gamma < \gamma_{\mathrm{br},\,1}$; green curve: $\gamma_{\mathrm{br},\,1} < \gamma < \gamma_{\mathrm{br},\,2}$; blue curve: $\gamma_{\mathrm{br},\,2} < \gamma$). Bottom: contributions of the different segments of the electron spectrum (as in the top panel) Comptonizing different segments of the synchrotron continuum (solid curves: $\nu < \nu_{br,\,1} \simeq 10^{15}$ Hz; dashed curves: $\nu_{br,\,1} < \nu < \nu_{br,\,2} \simeq 6 \times 10^{17}$ Hz; curves for $\nu > \nu_{br,\,2}$ do not appear in the plot because the corresponding flux levels are all less than 10^{-13} erg cm^{-1} s^{-1}).

[161] Note that due to low accretion rates and thus low luminosities of the accretion disks in BL Lac objects, the number of non-relativistic/mildly relativistic electrons (Lorentz factors $\gamma \sim 1$) cannot be constrained by analyzing "bulk-Compton" spectral features in the observed SED of Mrk 501, in contrast to the situation in FSRQs (see Sikora & Madejski 2000).

our campaign includes UV fluxes, soft-X-ray fluxes (down to 0.3 keV; Swift), and γ-ray fluxes spanning a very wide photon energy range (0.1 GeV−10 TeV; *Fermi*-LAT combined with MAGIC and VERITAS). This unique data set allows us to evaluate the multifrequency variability and correlations for Mrk 501 over an unprecedented range of photon energies.

Considering only the data set presented in this paper, we note that by steepening the high-energy electron continuum above the intrinsic break energy $\gamma_{\rm br,\,1}$ (and only slightly adjusting the other model parameters), one can effectively remove photons above 10 GeV in the SSC component, leaving a relatively steep spectrum below 10 GeV, similar to the one observed by *Fermi*-LAT during the time interval MJD 54862–54892 (see Section 4). Such a change should be accompanied by a decrease in the UV-to-soft-X-ray synchrotron fluxes by a factor of a few, but the data available during that time interval are not sufficient to detect this effect.[162] This statement is further justified by the bottom panel in Figure 12, where the contributions of the different segments of electrons Comptonizing the different segments of the synchrotron bump to the average γ-ray emission of Mrk 501 are shown. Note that the lowest-energy electron population ($\gamma < \gamma_{\rm br,\,1}$) inverse-Compton upscattering only synchrotron photons emitted by the same population ($\nu < \nu_{br,\,1} \sim 10^{15}$ Hz; solid red line) may account for the bulk of the observed steep-spectrum γ-ray emission.

Another important conclusion from this figure is that Comptonization of the highest-energy synchrotron photons ($\nu > \nu_{br,\,2} \sim 6 \times 10^{17}$ Hz) by electrons with arbitrary energies produces only a negligible contribution to the average γ-ray flux of Mrk 501 due to the Klein–Nishina suppression. Thus, the model presented here explains in a natural way the fact that the X-ray and TeV fluxes of TeV-emitting BL Lac objects are rarely correlated according to the simple scaling $F_{\rm TeV} \propto F^2_{\rm keV}$ which would be expected from the class of SSC models in which the highest-energy electrons upscatter (in the Thomson regime) their own synchrotron photons to the TeV band (see, e.g., Gliozzi et al. 2006; Fossati et al. 2008). In addition, it opens a possibility for accommodating short-timescale variability ($t_{\rm var} < 4$ days) at the highest synchrotron and inverse-Compton frequencies (hard X-rays and TeV photon energies, respectively). The reason for this is that, in the model considered here, these high-energy tails of the two spectral components are produced by the highest-energy electrons which are deep in the strong cooling regime (i.e., for which $t'_{\rm rad} \ll R/c$), and thus the corresponding flux changes may occur on timescales shorter than $R/c\,\delta$ (see in this context, e.g., Chiaberge & Ghisellini 1999; Kataoka et al. 2000).

A more in-depth analysis of the multifrequency data set (including correlation studies of the variability in different frequency ranges) will be presented in a forthcoming paper. The epoch of enhanced γ-ray activity of Mrk 501 (MJD 54952–54982; see Section 4) may be more difficult to explain in the framework of the one-zone SSC model, because a relatively flat *Fermi*-LAT spectrum above 10 GeV, together with an increased TeV flux as measured by the VERITAS and Whipple 10 m telescopes around this time, may not be easy to reproduce with a set of model parameters similar to that discussed in previous sections. This is mostly due to Klein–Nishina effects, which tend to steepen the high-energy tail of the SSC component, thus precluding the formation of a flat power law extending beyond the observed TeV energies. Hence, detailed modeling and data analysis will be needed to determine whether the enhanced VHE γ-ray activity period can be accommodated within a one-zone SSC model, or whether it will require a multi-zone approach.

8. CONCLUSIONS

We have presented a study of the γ-ray activity of Mrk 501 as measured by the LAT instrument on board the *Fermi* satellite during its first 16 months of operation, from 2008 August 5 (MJD 54683) to 2009 November 27 (MJD 55162). Because of the large leap in capabilities of LAT with respect to its predecessor, EGRET, this is the most extensive study to date of the γ-ray activity of this object at GeV–TeV photon energies. The *Fermi*-LAT spectrum (fitted with a single power-law function) was evaluated for 30-day time intervals. The average photon flux above 0.3 GeV was found to be $(2.15 \pm 0.11) \times 10^{-8}$ ph cm^{-2} s^{-1}, and the average photon index 1.78 ± 0.03. We observed only relatively mild (factor less than 2) γ-ray flux variations, but we detected remarkable spectral variability. In particular, during the four consecutive 30-day intervals of the "enhanced γ-ray flux" (MJD 54862–54982), the photon index changed from 2.51 ± 0.20 (for the first interval) down to 1.63 ± 0.09 (for the fourth one). During the whole period of 16 months, the hardest spectral index within the LAT energy range was 1.52 ± 0.14, and the softest one was 2.51 ± 0.20. Interestingly, this outstanding (and quite unexpected) variation in the slope of the GeV continuum did not correlate with the observed flux variations at energies above 0.3 GeV.

We compared the γ-ray activity measured by LAT in two different energy ranges (0.2–2 GeV and >2 GeV) with the X-ray activity recorded by the all-sky instruments *RXTE*-ASM (2–10 keV) and *Swift*-BAT (15–50 keV). We found no significant difference in the amplitude of the variability between X-rays and γ-rays, and no clear relation between the X-ray and γ-ray flux changes. We note, however, that the limited sensitivity of the ASM and (particularly) the BAT instruments to detect Mrk 501 in a 30-day time interval, together with the relatively stable X-ray emission of Mrk 501 during the observations, precludes any detailed X-ray/γ-ray variability or correlation analysis.

In this paper we also presented the first results from a 4.5 month multifrequency campaign on Mrk 501, which lasted from 2009 March 15 (MJD 54905) to 2009 August 1 (MJD 55044). During this period, the source was systematically observed with different instruments covering an extremely broad segment of the electromagnetic spectrum, from radio frequencies up to TeV photon energies. In this manuscript, we have focused on the average SED emerging from the campaign. Further studies on the multifrequency variability and correlations will be covered in a forthcoming publication.

We have modeled the average broadband spectrum of Mrk 501 (from radio to TeV) in the framework of the standard one-zone SSC model, obtaining a satisfactory fit to the experimental data. We found that the dominant emission region in this source can be characterized by a size of $R \simeq 10^3\, r_g$, where $r_g \sim 1.5 \times 10^{14}$ cm is the gravitational radius of the black hole ($M_{BH} \simeq 10^9 M_\odot$) hosted by Mrk 501. The intrinsic (i.e., not affected by cooling or absorption effects) energy distribution of the radiating electrons required to fit the data was found to be of a broken power-law form in the energy range 0.3 GeV−10 TeV, with spectral indices 2.2 and 2.7 below and above the break energy of $E_{e,\,br} \sim 20$ GeV, respectively. In addition, the model parameters

[162] The 4.5 month multifrequency campaign started 13 days after the end of the 30-day time interval MJD 54862–54892. Therefore, for this epoch, the only additional multifrequency data are from *RXTE*-ASM and *Swift*-BAT, which have only moderate ability to detect Mrk 501 on short timescales.

imply that all the electrons cool predominantly via synchrotron emission, forming a cooling break at 0.5 TeV. We argue that the particular form of the electron energy distribution emerging from our modeling is consistent with the scenario in which the bulk of the energy dissipation within the dominant emission zone of Mrk 501 is related to relativistic, proton-mediated shock waves. The low-energy segment of the electron energy distribution ($E_e < E_{e,br}$) formed thereby, which dominates the production of γ-rays observed below a few GeV, seems to be characterized by low and relatively slow variability. On the other hand, the high-energy electron tail ($E_e > E_{e,br}$), responsible for the bulk of the γ-rays detected above a few GeV, may be characterized by more significant variability.

Finally, we found that ultrarelativistic electrons and mildly-relativistic protons within the blazar zone of Mrk 501, if comparable in number, are in approximate energy equipartition, with their energy dominating the energy in the jet magnetic field by about two orders of magnitude. The model fit implies also that the total jet power, $L_j \simeq 10^{44}$ erg s^{-1}, constitutes only a small fraction of the Eddington luminosity, $L_j/L_{\rm Edd} \sim 10^{-3}$, but is an order of magnitude larger than the bolometric, accretion-related luminosity of the central engine, $L_j/L_{\rm disk} \sim 10$. Finally, we estimated the radiative efficiency of the Mrk 501 jet to be at the level of a few percent, $L_{em}/L_j \lesssim 0.1$, where L_{em} is the total emitted power of the blazar. The results from this study could perhaps be extended to all HSP BL Lac objects.

The *Fermi*-LAT Collaboration acknowledges the generous support of a number of agencies and institutes that have supported the *Fermi*-LAT Collaboration. These include the National Aeronautics and Space Administration and the Department of Energy in the United States, the Commissariat à l'Energie Atomique and the Centre National de la Recherche Scientifique / Institut National de Physique Nucléaire et de Physique des Particules in France, the Agenzia Spaziale Italiana and the Istituto Nazionale di Fisica Nucleare in Italy, the Ministry of Education, Culture, Sports, Science and Technology (MEXT), High Energy Accelerator Research Organization (KEK) and Japan Aerospace Exploration Agency (JAXA) in Japan, and the K. A. Wallenberg Foundation, the Swedish Research Council and the Swedish National Space Board in Sweden. Additional support for science analysis during the operations phase is gratefully acknowledged from the Istituto Nazionale di Astrofisica in Italy and the Centre National d'Études Spatiales in France.

The MAGIC collaboration would like to thank the Instituto de Astrofísica de Canarias for the excellent working conditions at the Observatorio del Roque de los Muchachos in La Palma. The support of the German BMBF and MPG, the Italian INFN, the Swiss National Fund SNF, and the Spanish MICINN is gratefully acknowledged. This work was also supported by the Marie Curie program, by the CPAN CSD2007-00042 and MultiDark CSD2009-00064 projects of the Spanish Consolider-Ingenio 2010 programme, by grant DO02-353 of the Bulgarian NSF, by grant 127740 of the Academy of Finland, by the YIP of the Helmholtz Gemeinschaft, by the DFG Cluster of Excellence "Origin and Structure of the Universe," and by the Polish MNiSzW Grant N N203 390834.

VERITAS is supported by grants from the US Department of Energy, the US National Science Foundation, and the Smithsonian Institution, by NSERC in Canada, by Science Foundation Ireland, and by STFC in the UK. The VERITAS Collaboration also acknowledges the support of the *Fermi*/LAT team through the Guest Investigator Program Grant NNX09AT86G.

We acknowledge the use of public data from the *Swift* and *RXTE* data archive. The Metsähovi team acknowledges the support from the Academy of Finland to the observing projects (numbers 212656, 210338, among others). This research has made use of data obtained from the National Radio Astronomy Observatory's Very Long Baseline Array (VLBA), projects BK150, BP143, and MOJAVE. The National Radio Astronomy Observatory is a facility of the National Science Foundation operated under cooperative agreement by Associated Universities, Inc. St. Petersburg University team acknowledges support from Russian RFBR foundation via grant 09-02-00092. AZT-24 observations are made within an agreement between Pulkovo, Rome and Teramo observatories. This research is partly based on observations with the 100-m telescope of the MPIfR (Max-Planck-Institut für Radioastronomie) at Effelsberg, as well as with the Medicina and Noto telescopes operated by INAF–Istituto di Radioastronomia. The Submillimeter Array is a joint project between the Smithsonian Astrophysical Observatory and the Academia Sinica Institute of Astronomy and Astrophysics and is funded by the Smithsonian Institution and the Academia Sinica. M. Villata organized the optical-to-radio observations by GASP-WEBT as the president of the collaboration. Abastumani Observatory team acknowledges financial support by the Georgian National Science Foundation through grant GNSF/ST07/4-180. The OVRO 40 m program was funded in part by NASA (NNX08AW31G) and the NSF (AST-0808050).

REFERENCES

Abdo, A. A., et al. 2009, ApJ, 699, 817
Acciari, V. A. 2011, ApJ, in press (arXiv:1012.2200)
Abdo, A. A., et al. 2010a, ApJ, 710, 1271
Abdo, A. A., et al. 2010b, ApJS, 188, 405
Abdo, A. A., et al. 2010c, ApJ, 716, 30
Acciari, V. A., et al. 2008, ApJ, 679, 1427
Acciari, V. A., et al. 2010, ApJ, 714, 163A
Achterberg, A., Gallant, Y. A., Kirk, J. G., & Guthmann, A. W. 2001, MNRAS, 328, 393
Aharonian, F. A., et al. 1999a, A&A, 342, 69
Aharonian, F. A., et al. 1999b, A&A, 349, 11
Aharonian, F. A., et al. 1999c, A&A, 349, 29
Aharonian, F. A., et al. 2001, ApJ, 546, 898
Ajello, M., et al. 2008, ApJ, 673, 96
Ajello, M., et al. 2009a, ApJ, 690, 367
Ajello, M., et al. 2009b, ApJ, 699, 603
Albert, J., et al. 2007a, ApJ, 669, 862
Albert, J., et al. 2007b, Nucl. Instrum. Methods A, 583, 494
Albert, J., et al. 2008, ApJ, 674, 1037
Aliu, E., et al. 2009, Astropart. Phys., 30, 293
Aller, H. D., Aller, M. F., Latimer, G. E., & Hodge, P. E. 1985, ApJS, 59, 513
Amato, E., & Arons, J. 2006, ApJ, 653, 325
Anderhub, H., et al. 2009, ApJ, 705, 1624
Angelakis, E., Fuhrmann, L., Marchili, N., Krichbaum, T. P., & Zensus, J. A. 2008, Mem. Soc. Astron. Ital., 79, 1042
Atlee, D. W., Assef, R. J., & Kochanek, C. S. 2009, ApJ, 694, 1539
Atwood, W. B., et al. 2009, ApJ, 697, 1071
Baring, M. G. 2006, ApJ, 650, 1004
Baring, M. G. 2010, Adv. Space Res., in press (arXiv:1002.3848)
Baring, M. G., & Summerlin, E. J. 2007, Ap&SS, 307, 165
Barth, A. J., Ho, L. C., & Sargent, W. L. W. 2002, ApJ, 566, L13
Barthelmy, S. D., et al. 2005, Space Sci. Rev., 120, 143
Bednarek, W., & Protheroe, R. J. 1999, MNRAS, 310, 577
Bednarz, J., & Ostrowski, M. 1998, Phys. Rev. Lett., 80, 3911
Blandford, R. D., & Begelman, M. C. 1999, MNRAS, 303, L1
Błazejowski, M., et al. 2005, ApJ, 630, 130
Blumenthal, G. R., & Gould, R. J. 1970, Rev. Mod. Phys., 42, 237
Bradbury, S. M., et al. 1997, A&A, 320, L5
Bradt, H. V., Rothschild, R. E., & Swank, J. H. 1993, A&AS, 97, 355
Burrows, D. N., et al. 2005, Space Sci. Rev., 120, 165
Catanese, M., et al. 1997, ApJ, 487, L143

Celotti, A., & Ghisellini, G. 2008, MNRAS, 385, 283
Chiaberge, M., & Ghisellini, G. 1999, MNRAS, 306, 551
Code, A. D., & Welch, G. A. 1979, ApJ, 228, 95
Coppi, P. S., & Blandford, R. D. 1990, MNRAS, 245, 453
Crusius, A., & Schlickeiser, R. 1986, A&A, 164, L16
Daum, A., et al. 1997, Astropart. Phys., 8, 1
Djannati-Ataï, A., et al. 1999, A&A, 350, 17
Edelson, R. A., & Krolik, J. H. 1988, ApJ, 333, 646
Edelson, R., et al. 2002, ApJ, 568, 610
Edwards, P. G., & Piner, B. G. 2002, ApJ, 579, L67
Finke, J. D., Dermer, C. D., & Böttcher, M. 2008, ApJ, 686, 181
Finke, J. D., Razzaque, S., & Dermer, C. D. 2010, ApJ, 712, 238
Fitzpatrick, E. L. 1999, PASP, 111, 63
Fossati, G., et al. 2008, ApJ, 677, 906
Franceschini, A., et al. 2008, A&A, 487, 837
Fuhrmann, L., et al. 2008, A&A, 490, 1019
Gehrels, N., et al. 2004, ApJ, 611, 1005
Ghisellini, G., Maraschi, L., & Tavecchio, F. 2009a, MNRAS, 396, L105
Ghisellini, G., & Svensson, R. 1991, MNRAS, 252, 313
Ghisellini, G., Tavecchio, F., Bodo, G., & Celotti, A. 2009b, MNRAS, 393, L16
Ghisellini, G., Tavecchio, F., & Chiaberge, M. 2005, A&A, 432, 401
Ghisellini, G., et al. 2002, A&A, 386, 833
Giannios, D., Uzdensky, D. A., & Begelman, M. C. 2009, MNRAS, 395, L29
Gilmore, R. C., Madau, P., Primack, J. R., Somerville, R. S., & Haardt, F. 2009, MNRAS, 399, 1694
Giroletti, M., et al. 2004, ApJ, 600, 127
Giroletti, M., et al. 2008, A&A, 488, 905
Gliozzi, M., et al. 2006, ApJ, 646, 61
Graff, P. B., Georganopoulos, M., Perlman, E. S., & Kazanas, D. 2008, ApJ, 689, 68
Hartman, R. C., et al. 1999, ApJS, 123, 79
Hoshino, M., Arons, J., Gallant, Y. A., & Langdon, A. B. 1992, ApJ, 390, 454
Kalberla, P. M. W., et al. 2005, A&A, 440, 775
Kataoka, J., et al. 1999, ApJ, 514, 138
Kataoka, J., et al. 2000, ApJ, 528, 243
Kataoka, J., et al. 2001, ApJ, 560, 659
Katarzyński, K., Lenain, J.-P., Zech, A., Boisson, C., & Sol, H. 2008, MNRAS, 390, 371
Katarzyński, K., Sol, H., & Kus, A. 2001, A&A, 367, 809
Kino, M., Takahara, F., & Kusunose, M. 2002, ApJ, 564, 97
Kirk, J. G., Guthmann, A. W., Gallant, Y. A., & Achterberg, A. 2000, ApJ, 542, 235
Kirk, J. G., & Heavens, A. F. 1989, MNRAS, 239, 995
Kneiske, T. M., Bretz, T., Mannheim, K., & Hartmann, D. H. 2004, A&A, 413, 807
Kovalev, Y. Y., Nizhelsky, N. A., Kovalev, Y. A., Berlin, A. B., Zhekanis, G. V., Mingaliev, M. G., & Bogdantsov, A. V. 1999, A&AS, 139, 545
Krawczynski, H., et al. 2000, A&A, 353, 97
Krawczynski, H., et al. 2004, ApJ, 601, 151
Lemoine, M., Pelletier, G., & Revenu, B. 2006, ApJ, 645, L129
Lister, M. L., et al. 2009, AJ, 137, 3718
Marscher, A. P. 1983, ApJ, 264, 296
Massaro, E., Perri, M., Giommi, P., & Nesci, R. 2004, A&A, 413, 489
Massaro, E., Perri, M., Giommi, P., Nesci, R., & Verrecchia, F. 2004, A&A, 422, 103
Mattox, J. R., et al. 1996, ApJ, 461, 396
Nandra, K., et al. 1997, ApJ, 476, 70
Narayan, R., & Yi, I. 1994, ApJ, 428, L13
Niemiec, J., & Ostrowski, M. 2004, ApJ, 610, 851
Nilsson, K., Pasanen, M., Takalo, L. O., Lindfors, E., Berdyugin, A., Ciprini, S., & Pforr, J. 2007, A&A, 475, 199
Ostrowski, M., & Bednarz, J. 2002, A&A, 394, 1141
Paneque, D. 2009, in ASP Conf. Ser. 427, Accretion and Ejection in AGNs: A Global View, ed. L. Maraschi et al. (San Francisco, CA: ASP), 277
Perkins, J. S., et al. 2009, 2009 Fermi Symposium, eConf Proceedings C091122, arXiv:0912.3841v1
Pian, E., et al. 1998, ApJ, 492, L17
Pichel, A. (for the VERITAS Collaboration) 2009, Proc. 31st ICRC (Łodz), arXiv:0908.0010
Piner, B. G., Pant, N., Edwards, P. G., & Wiik, K. 2009, ApJ, 690, L31
Piron, F. 2000, in AIP Conf. Proc. 515, Gev–Tev Gamma Ray Astrophysics Workshop: Towards a Major Atmospheric Cherenkov Detector VI, ed. B. L. Dingus, M. H. Salamon, & D. B. Kieda (Melville, NY: AIP), 113
Poole, T. S., et al. 2008, MNRAS, 383, 627
Quinn, J., et al. 1996, ApJ, 456, L83
Richards, J. L. 2011, ApJS, submitted (arXiv:1011.3111)
Roming, P. W. A., et al. 2005, Space Sci. Rev., 120, 95
Sambruna, R., et al. 2000, ApJ, 538, 127
Samuelson, F. W., et al. 1998, ApJ, 501, L17
Schlegel, D. J., Finkbeiner, D. P., & Davis, M. 1998, ApJ, 500, 525
Sikora, M., & Madejski, G. 2000, ApJ, 534, 109
Sikora, M., Moderski, R., & Madejski, G. M. 2008, ApJ, 675, 71
Sikora, M., Stawarz, Ł., Moderski, R., Nalewajko, K., & Madejski, G. M. 2009, ApJ, 704, 38
Silva, L., Granato, G. L., Bressan, A., & Danese, L. 1998, ApJ, 509, 103
Sironi, L., & Spitkovsky, A. 2009, ApJ, 698, 1523
Stawarz, Ł., & Petrosian, V. 2008, ApJ, 681, 1725
Tavecchio, F., et al. 2001, ApJ, 554, 725
Teräsranta, H., et al. 1998, A&AS, 132, 305
Tramacere, A., Giommi, P., Perri, M., Verrecchia, F., & Tosti, G. 2009, A&A, 501, 879
Vaughan, S., Edelson, R., Warwick, R. S., & Uttley, P. 2003, MNRAS, 345, 1271
Venturi, T., et al. 2001, A&A, 379, 755
Villata, M., & Raiteri, C. M. 1999, A&A, 347, 30
Villata, M., Raiteri, C. M., Lanteri, L., Sobrito, G., & Cavallone, M. 1998, A&AS, 130, 305
Villata, M., et al. 2008, A&A, 481, L79
Villata, M., et al. 2009, A&A, 504, L9
Zdziarski, A. A., & Lightman, A. P. 1985, ApJ, 294, L79

Astron. Nachr. / AN **332**, No. 6, 547 – 561 (2011) / **DOI** 10.1002/asna.201111573

The Young Exoplanet Transit Initiative (YETI)

R. Neuhäuser[1,⋆], **R. Errmann**[1], **A. Berndt**[1], **G. Maciejewski**[1,2], **H. Takahashi**[3], **W.P. Chen**[4], **D.P. Dimitrov**[5], **T. Pribulla**[6,1], **E.H. Nikogossian**[7], **E.L.N. Jensen**[8], **L. Marschall**[9], **Z.-Y. Wu**[10], **A. Kellerer**[11,12], **F.M. Walter**[13], **C. Briceño**[14], **R. Chini**[15,16], **M. Fernandez**[17], **St. Raetz**[1], **G. Torres**[18], **D.W. Latham**[18], **S.N. Quinn**[18], **A. Niedzielski**[2], **Ł. Bukowiecki**[2], **G. Nowak**[2], **T. Tomov**[2], **K. Tachihara**[19,20], **S.C.-L. Hu**[4], **L.W. Hung**[4], **D.P. Kjurkchieva**[21], **V.S. Radeva**[21], **B.M. Mihov**[5], **L. Slavcheva-Mihova**[5], **I.N. Bozhinova**[5], **J. Budaj**[6], **M. Vaňko**[6], **E. Kundra**[6], **Ľ. Hambálek**[6], **V. Krushevska**[6,22], **T. Movsessian**[7], **H. Harutyunyan**[7], **J.J. Downes**[14], **J. Hernandez**[14], **V.H. Hoffmeister**[15], **D.H. Cohen**[8], **I. Abel**[8], **R. Ahmad**[8], **S. Chapman**[8], **S. Eckert**[8], **J. Goodman**[8], **A. Guerard**[8], **H.M. Kim**[8], **A. Koontharana**[8], **J. Sokol**[8], **J. Trinh**[8], **Y. Wang**[8], **X. Zhou**[10], **R. Redmer**[23], **U. Kramm**[23], **N. Nettelmann**[23], **M. Mugrauer**[1], **J. Schmidt**[1], **M. Moualla**[1], **C. Ginski**[1], **C. Marka**[1], **C. Adam**[1], **M. Seeliger**[1], **S. Baar**[1], **T. Roell**[1], **T.O.B. Schmidt**[1], **L. Trepl**[1], **T. Eisenbeiß**[1], **S. Fiedler**[1], **N. Tetzlaff**[1], **E. Schmidt**[1], **M.M. Hohle**[1,24], **M. Kitze**[1], **N. Chakrova**[25], **C. Gräfe**[1,26], **K. Schreyer**[1], **V.V. Hambaryan**[1], **C.H. Broeg**[27], **J. Koppenhoefer**[24,28], and **A.K. Pandey**[29]

1 Astrophysikalisches Institut und Universitäts-Sternwarte, FSU Jena, Schillergäßchen 2-3, D-07745 Jena, Germany
2 Toruń Centre for Astronomy, Nicolaus Copernicus University, Gagarina 11, PL87-100 Toruń, Poland
3 Gunma Astronomical Observatory, 6860-86 Nakayama, Takayama-mura, Agatsuma-gun, Gunma 377-0702 Japan
4 Graduate Institute of Astronomy, National Central University, Jhongli City, Taoyuan County 32001, Taiwan (R.O.C.)
5 Institute of Astronomy and NAO, Bulg. Acad. Sc., 72 Tsarigradsko Chaussee Blvd., 1784 Sofia, Bulgaria
6 Astronomical Institute, Slovak Academy of Sciences, 059 60, Tatranská Lomnica, Slovakia
7 Byurakan Astrophysical Observatory, 378433 Byurakan, Armenia
8 Dept. of Physics and Astronomy, Swarthmore College, Swarthmore, PA 19081-1390, USA
9 Gettysburg College Observatory, Department of Physics, 300 North Washington St., Gettysburg, PA 17325, USA
10 Key Laboratory of Optical Astronomy, NAO, Chinese Academy of Sciences, 20A Datun Road, Beijing 100012, China
11 Institute of Astronomy, University of Hawaii, 640 N. A'ohoku Place, Hilo, Hawaii 96720
12 Big Bear Solar Observatory, 40386 North Shore Lane, Big Bear City, CA 92314-9672, USA
13 Department of Physics and Astronomy, Stony Brook University, Stony Brook, NY 11794-3800, USA
14 Centro de Investigaciones de Astronomia, Apartado Postal 264, Merida 5101, Venezuela
15 Astronomisches Institut, Ruhr-Universität Bochum, Universitätsstr. 150, D-44801 Bochum, Germany
16 Facultad de Ciencias, Universidad Católica del Norte, Antofagasta, Chile
17 Instituto de Astrofisica de Andalucia, CSIC, Apdo. 3004, 18080 Granada, Spain
18 Harvard-Smithsonian Center for Astrophysics, 60 Garden St., Mail Stop 20, Cambridge MA 02138, USA
19 Joint ALMA Observatory, Alonso de Córdova 3107, Vitacura, Santiago, Chile
20 National Astronomical Observatory of Japan, ALMA project office, 2-21-1 Osawa Mitaka Tokyo 181-8588 Japan
21 Shumen University, 115 Universitetska str., 9700 Shumen, Bulgaria
22 Main Astronomical Observatory of NAS of Ukraine, 27 Akademika Zabolotnoho St., 03680 Kyiv, Ukraine
23 Institut für Physik, Universität Rostock, D-18051 Rostock, Germany
24 MPI für Extraterrestrische Physik, Gießenbachstraße 1, D-85740 Garching, Germany
25 Institute for Applied Physics, FSU Jena, Max-Wien Platz 1, D-07743 Jena, Germany
26 Christian-Albrechts-Universität Kiel, Leibnizstraße 15, D-24098 Kiel, Germany
27 Physikalisches Institut, University of Bern, Sidlerstraße 5, CH-3012 Bern, Switzerland
28 Universitäts-Sternwarte München, Scheinerstraße 1, D-81679 München, Germany
29 Aryabhatta Research Institute of Observational Science, Manora Peak, Naini Tal, 263 129, Uttarakhand, India

Received 2011 Apr 20, accepted 2011 Jun 15
Published online 2011 Jul 11

Key words planetary systems – surveys – techniques: photometric – techniques: spectroscopic

We present the Young Exoplanet Transit Initiative (YETI), in which we use several 0.2 to 2.6-m telescopes around the world to monitor continuously young ($\leq$100 Myr), nearby ($\leq$1 kpc) stellar clusters mainly to detect young transiting planets (and to study other variability phenomena on time-scales from minutes to years). The telescope network enables us to observe the targets continuously for several days in order not to miss any transit. The runs are typically one to two weeks long, about three runs per year per cluster in two or three subsequent years for about ten clusters. There are thousands of stars detectable in each field with several hundred known cluster members, e.g. in the first cluster observed, Tr-37, a typical cluster for the YETI survey, there are at least 469 known young stars detected in YETI data down to $R = 16.5$ mag with sufficient precision of 50 millimag rms (5 mmag rms down to $R = 14.5$ mag) to detect transits, so that we can expect at least about one young transiting object in this cluster. If we observe $\sim$10 similar clusters, we can expect to detect $\sim$10 young transiting planets with radius determinations. The precision given above is for a typical telescope of the YETI network, namely the 60/90-cm Jena telescope (similar brightness limit, namely within $\pm$1 mag, for the others) so that planetary transits can be detected. For targets with a periodic transit-like light curve, we obtain spectroscopy to ensure that the star is young and that the transiting object can be sub-stellar; then, we obtain Adaptive Optics infrared images and spectra, to exclude other bright eclipsing stars in the (larger) optical PSF; we carry out other observations as needed to rule out other false positive scenarios; finally, we also perform spectroscopy to determine the mass of the transiting companion. For planets with mass and radius determinations, we can calculate the mean density and probe the internal structure. We aim to constrain planet formation models and their time-scales by discovering planets younger than $\sim$100 Myr and determining not only their orbital parameters, but also measuring their true masses and radii, which is possible so far only by the transit method. Here, we present an overview and first results.

1 Introduction: Extrasolar planets

Beginning with the discovery of planets around a neutron star (Wolszczan & Frail 1992; Wolszczan 1994) and around

⋆ Corresponding author: rne@astro.uni-jena.de

© 2011 WILEY-VCH Verlag GmbH & Co. KGaA, Weinheim

normal stars (Latham et al. 1989; Mayor & Queloz 1995; Marcy & Butler 1996), it has become possible to study planetary systems and their formation outside the Solar System.

The most successful of the detection methods (the spectroscopic or radial velocity (RV) technique) yields only a lower limit $m \sin i$ on the mass m of the companions, because the orbital inclination i is unknown. RV companions could be planets, brown dwarfs, or even low-mass stars. Combined with other observational techniques (e.g. astrometry, Benedict et al. 2002), one can determine the orbital inclination i and the true mass m.

The very existence of a transit requires that $\sin i$ is close to 1, hence it confirms an RV planet candidate to be really below some upper mass limit of planets (see below for the definition of planets). The transit technique can then even give the planetary radius and, together with the mass (from RV and transit data), also the mean density (e.g. Torres, Winn & Holman 2008). Modeling can then constrain the chemical composition and the mass of a solid core (e.g. Guillot et al. 2006; Burrows et al. 2007; Nettelmann et al. 2010). The first transiting extrasolar planet identified was the planet candidate HD 209458b found by RV by Mazeh et al. (2000) and confirmed to be a planet with 0.7 Jupiter masses by transit observations (Charbonneau et al. 2000; Henry et al. 2000); it is also the first RV planet candidate confirmed by another technique. For transiting planets, one can also obtain spectral information by transmission spectroscopy (e.g. Charbonneau et al. 2002). One can also indirectly determine the brightness of the planet by detecting the secondary eclipse (e.g. Deming et al. 2005). The Rossiter-McLaughlin effect can provide information about spin axis-orbital plane alignment and, hence, dynamics in the system (e.g. Queloz et al. 2000; Triaud et al. 2010; Winn et al. 2010).

The direct imaging technique can detect planets or candidates at wide separations from the star, for which one can then often also take spectra, e.g. GQ Lup b (Neuhäuser et al. 2005) or CT Cha b (Schmidt et al. 2008). The mass is difficult to determine and model-dependent, so that all or most directly imaged planets (or planet candidates) can be either planets or brown dwarfs. The upper mass limit of planets is also not yet defined and can be either the deuterium burning mass limit ($\sim$13 $M_{\rm Jup}$, Burrows et al. 1997) or the mass range of the brown dwarf desert ($\sim$35 $M_{\rm Jup}$, Grether & Lineweaver 2006).

Some additional planets or planet candidates detected by microlensing or timing have not yet been confirmed (see, e.g, exoplanet.eu for references).

The detectability of a planet depends on its mass, radius, or luminosity (depending on the technique) *relative* to the host star. Since all detection techniques are biased towards more massive (or larger) planets, it is not surprising that Earth-mass planets have not yet been discovered. Low-mass planets in the so-called habitable zone can possibly be detected by the RV technique around low-mass stars like M dwarfs (e.g. GJ 1214 by Charbonneau et al. 2009). The RV and transit techniques are also biased towards close-in planets, while direct imaging is biased towards wide separations. The RV technique has led to the discovery of $\sim$500 planet candidates, of which some 20 % are confirmed by either the astrometry or transit technique (see e.g. exoplanet.eu for updates). The latter method has detected $\sim$100 planets, all of which have been confirmed by RV data (or transit timing, see Lissauer et al. 2011). Many more transit candidates are reported by Borucki et al. (2011) with the Kepler satellite.

Almost 50 planet host stars are already known to be surrounded by more than one planet (e.g. Fischer et al. 2002; Lovis et al. 2011), e.g. most recently Kepler-11 with six transiting planets, where the transit timing variations (TTV) could be used to determine the masses of the planets (Lissauer et al. 2011) instead of radial velocity follow-up; several planet host stars are multiple stars themselves (Cochran et al. 1997; Mugrauer, Neuhäuser & Mazeh 2007). Planetary systems can also be discovered (indirectly) by TTV (Maciejewski et al. 2010, 2011a; Holman et al. 2010). One can also observe in several cases dust debris disks around planet host stars, which are produced by colliding planetesimals (e.g. Krivov 2010), e.g. the probably planetary mass companions around the A0-type star HR 8799 discovered by Marois et al. (2008, 2010) and studied in detail by Reidemeister et al. (2009) with a debris disk resolved by Su et al. (2010).

Stellar activity can be a problem for the RV, transit, TTV, and astrometric techniques, but not for direct imaging. Most of the planet host stars are main-sequence G-type stars, few planets are also discovered around more or less massive stars including giants (Frink et al. 2002; Niedzielski et al. 2007) and M-type dwarfs (Marcy et al. 1998; Charbonneau et al. 2009), respectively. The MEarth project is searching for transiting planets around M-type dwarfs (see, e.g., Charbonneau et al. 2009). Almost all the planets (and host stars) are, however, Gyr old, so that it might be difficult to study planet formation from this sample. Among the important overall statistical results is the fact that many planets orbit their stars on much shorter orbits than in the Solar System; hence, planets may migrate inwards after formation further outwards (Goldreich & Tremaine 1980; Lin et al. 1996), e.g. beyond the ice line if they did not form in-situ. In addition, many more planets have been detected around metal-rich stars than around metal-poor stars (e.g. Marcy et al. 2005; Butler et al. 2006), which may suggest that planets are more likely to form when there is a more abundant supply of dust.

Planets (or planet candidates) around pre-main sequence (PMS) stars or stars significantly younger than 100 Myr (the maximal PMS time-scale for very low-mass stars) have been discovered so far only with the direct imaging technique, so that the mass and, hence, the planetary status of those objects are model-dependent and still uncertain. The youngest known planetary system – except maybe HR 8799 (Marois et al. 2008, 2010, four planets by direct imaging) – may be WASP-10bc, where WASP-10b was discovered by the transit technique and confirmed by RV (Christian et al. 2009) and WASP-10c by transit timing (Maciejewski et al. 2011a), still to be confirmed independently; the age of WASP-10 was inferred from the 12 day rotation period using gyro-chronology to be only 200 to 350 Myr (Maciejewski et al. 2011a). In addition, there were also RV surveys for planets among young, PMS stars, e.g. Guenther & Esposito (2007) have monitored 85 young pre- and zero-age main sequence stars with ESO 3.6-m HARPS without planet discoveries; Joergens (2006) observed 12 very low-mass PMS stars and brown dwarfs in Cha I and found one companion with 25 ± 7 to 31 ± 8 Jupiter mass lower mass limits around Cha Hα 8 (Joergens & Müller 2007; Joergens, Müller & Reffert 2010); and Setiawan et al. (2008) monitored young stars including PMS stars and published an RV planet candidate around TW Hya, which was not confirmed by Huélamo et al. (2008).

To study planet formation (planets younger than 100 Myr, partly even younger than $\sim$10 Myr), measuring their ages, masses, radii, and orbital elements, studying their internal structure) and possible secular effects (by comparing the architecture, i.e. the number and properties of planets including their semi-major axes, of young planetary systems with the Solar System and other old systems), we started a project to monitor young stellar clusters (age $\leq$ 100 Myr) in order to find young transiting planets (called YETI for Young Exoplanet Transit Initiative[1]) and also to study other variability in general in the young stars. A first brief presentation of the project was given in Maciejewski et al. (2011b).

In this paper, we first summarize previous and/or ongoing searches for young planets in clusters (Sect. 2) and then describe the YETI target selection criteria and list the first few clusters being observed (Sect. 3). In Sect. 4 we present the telescope network put together for continuous monitoring and follow-up observations. We mention other science projects to be studied with the same data sets in Sect. 5. Finally, we present in Sect. 6 the YETI data reduction technique and then also a few preliminary YETI results from the Trumpler 37 (Tr-37) cluster observed in 2009 and 2010.

2 Previous searches for young transit planets

We know of two other previous and/or ongoing searches for planetary transits in young clusters: CoRoT's survey of NGC 2264 and the MONITOR project.

The French-European satellite CoRoT with its 30 cm mirror continuously monitored the young cluster NCG 2264 for 24 days in March 2008, the PI being F. Favata. NGC 2264 is $\sim$3 Myr old at $\sim$760 pc (Dahm 2008). Some first preliminary results (rotation periods of member stars, but no transit candidates) were presented by Favata et al. (2010). Because of the unprecedented precision of a space telescope like CoRoT, we will not observe NGC 2264 in the YETI survey.

The MONITOR project aims at observing ten young clusters (1–200 Myr) also mainly to detect transiting planets (Hodgkin et al. 2006; Aigrain et al. 2007), including h and χ Per, also potential target clusters for the YETI survey. So far, rotation periods of hundreds of member stars have been reported for the clusters M34 (Irwin et al. 2006), NGC 2516 (Irwin et al. 2007), NGC 2362 (Irwin et al. 2008a), NGC 2547 (Irwin et al. 2008b), and M50 (Irwin et al. 2009). Results for the planet transit search have been published so far only for NGC 2362, where no planet was found among 475 member stars observed for a total of 100 hours spread over 18 nights within 362 days (Miller et al. 2008); the non-detection of transiting planets was not surprising given the expectation value for this cluster: Aigrain et al. (2007) expected that there are in total 11.3 transiting planets in NGC 2362 – however, only 0.0 of them were expected to be detectable by their survey. This non-detection is for planets with 1.5 Jupiter radii and periods between 1 and 10 days (Miller et al. 2008).

With the $\sim$50 mmag rms precision down to $R = 16.5$ mag (5 mmag rms down to $R = 14.5$ mag, both for Jena), we can detect (young large) planets down to $\sim$1 Jupiter radius, given the typical radii and brightness of the YETI targets stars. Given the YETI approach to observe a certain field continuously for several days (24 hours per day), e.g. continuously for up to $\sim$2 weeks (e.g. the Tr-37 run 2010 August 26 to September 13), we would be able to detect all planets down to $\sim$1 Jupiter radius with periods up to $\sim$14 days. Hence, even if we would not detect any planets, we would be able to place limits (for the frequency of young planets) lower than the current limits for either the solar neighbourhood or the NGC 2362 cluster (Miller et al. 2008).

To justify the YETI project, it is important that we understand why no transiting planets have been reported by the MONITOR survey so far. It is possible that this is due to the fact that the telescopes used in the MONITOR project do not cover all longitudes on Earth (being located in Europe and America only), so that continuous coverage is not possible. Hence, transits can be missed; the light curves of stars from the MONITOR project as published in the papers listed above also show that the phase coverage is not complete.

3 YETI target selection criteria and transit planet detection expectations

For successful detection of a planetary transit it is very important to choose regions on the sky where there is a high probability to observe this event.

An interesting environment is represented by stars in a cluster. Open cluster surveys should help to clarify the factors that control the formation and survival of planets by characterizing hot Jupiter populations as a function of age, metallicity and crowding. A significant fraction of stars in the solar vicinity form in clusters (Lada & Lada 2003). Stars in clusters also have the advantage that their age and dis-

[1] www.astro.uni-jena.de/YETI.html

tance is known, which is otherwise often difficult to obtain precisely for isolated stars.

Wide-field CCD cameras on 1–2 m telescopes with $\sim 1^\circ$ field-of-view (FoV) are suitable for surveying stars in open clusters fields. An estimate of the number of expected transiting planets, N_p, can be parameterized as

$$N_\mathrm{p} = N_* \cdot f_\mathrm{p} \cdot \rho_\mathrm{t} \cdot \rho_\mathrm{eff}. \quad (1)$$

Here N_* is the number of stars included in the transit search, f_p is the fraction of stars with close-in planets within 0.1 AU (~ 0.012, Butler et al. 2006), ρ_t is the probability to view the orbit nearly edge-on (~ 0.1 for close-in planets), and ρ_eff is a measure of the efficiency of the observation.

The number of stars, N_*, depends on the FoV of the telescope, the magnitude limits (excluding the brightest earliest stars and the faintest latest stars), and the photometric precision. In wide-field transit searches or deep searches with large telescopes, usually thousands of stars are covered in the FoV. However, only the number of stars with sufficiently high S/N for detecting transits are relevant in Eq. (1). For typical giant planets around solar-type stars, this means the S/N must provide a detection limit of ~ 0.5 % dimming of the stellar light, or ~ 5 millimag (mmag) rms for a significant detection. For young 10 Jupiter-mass planets that are still contracting (hence, large), the transit depth can be as large as ~ 80 mmag (Burrows et al. 1997; Baraffe et al. 1998, 2000, 2001, 2002, 2003, 2008), see below for details.

Target stars must not be too faint, so that high-resolution spectroscopic follow-up for determining the mass of the transiting companion from radial velocities is possible with current-generation telescopes (8 to 10 meter mirrors), i.e. down to about 16.5 mag (see e.g. the OGLE-TR-56 transit planet, Konacki et al. 2003). The first observations with the Jena 90/60-cm telescope (90-cm mirror reduced to 60-cm effective mirror diameter in Schmidt mode) in 2009 show that we can reach sufficient photometric precision down to $R = 16.5$ mag and 5 mmag rms down to $R = 14.5$ mag (Fig. 5). The limiting sensitivity of other telescopes for the Tr-37 cluster campaigns, from 0.4 to 2.6 m, are similar within ± 1 mag. Hence, the number of stars, N_*, in Eq. (1) in the FoV should be the number of stars brighter than $R = 16.5$ mag (the number of stars being too bright so that they saturate the CCD are negligible).

The parameter ρ_eff in Eq. (1) depends on many observational factors, e.g. weather, coordinates of targets and observatories; in Rauer et al. (2004), who have observed with only one telescope (the Berlin Exoplanet Search telescope, BEST) at Tautenburg near Jena for 3 years, this factor was 0.7 – limited by weather and the fact that only one telescope was used; this factor is a period-dependent variable only calculable after the fact as done for the BEST survey at Tautenburg by Rauer et al. (2004). We can assume a larger number for the YETI survey, because we will use several telescopes at many different longitudes on Earth to observe continuously. Hence, we can use $\rho_\mathrm{eff} \simeq 1$ for our calculations (the factor should definitely lie between 0.7 and 1.0; if it would be 0.7 only, the number of expected observable transits listed in Table 1 would decrease by only 30 %, ~ 1.0 is a good approximation for planet periods up to ~ 14 days, detectable by us completely down to ~ 1 Jupiter radius given the continuous observations.

See Table 1 for the clusters being observed so far and the expected number of transiting planets in the whole FoV (including old field stars and among young members in the YETI clusters). For young planets around young stars, we may assume a larger fraction of transiting planets than for old planets around old stars: If planets form partly by contraction, they are larger than old planets (Burrows et al. 1997; Baraffe et al. 1998, 2000, 2001, 2002, 2003, 2008). E.g., ~ 3 Myr young planets with 1 to 10 Jupiter masses are expected to have radii of 1.4 times the radius of Jupiter, hence are a factor of 2 larger than old Gyr old 1 to 10 Jupiter mass planets (Burrows et al. 1997).

For planets with 1 to 12 Jupiter masses (radii from Baraffe et al. 2003, COND models) transiting stars with 1 or 0.5 $M_\odot$ (radii from Baraffe et al. 1998, 2002), the transit depth will have a maximum of ~ 15 to 80 mmag at ~ 50 to ~ 100 Myr, respectively; for 40 Jupiter mass brown dwarfs (radii from Baraffe et al. 2003) eclipsing such stars, the transit depth will have a maximum of ~ 60 to 100 mmag at ~ 5 Myr, respectively; see Fig. 2.

For planets with 10 to 13 Jup masses (radii from Baraffe et al. 2000, 2001, DUSTY models) transiting stars with 1 or 0.5 $M_\odot$ (radii from Baraffe et al. 1998, 2002), the transit depth will have a maximum of ~ 20 to 80 mmag at ~ 50 to ~ 200 Myr, respectively; for 40 Jupiter mass brown dwarfs (radii from Baraffe et al. 2000, 2001) eclipsing such stars, the transit depth will have a maximum of ~ 70 to 100 mmag at ~ 10 to 20 Myr, respectively.

For planets with 1 to 10 Jupiter masses (radii from Baraffe et al. 2008, both radiated and non-irradiated models) transiting stars with 1 or 0.5 $M_\odot$ (radii from Baraffe et al. 1998, 2002), the transit depth will have a maximum of ~ 20 to 70 mmag at ~ 50 to 200 Myr, respectively.

Even though these models may still be uncertain, in particular for young ages and low masses, they tend to show that the transit depth reaches a maximum at ~ 10 to 200 Myr (for 40 to 1 Jupiter-mass companions and 1 to 0.5 $M_\odot$ stars), see Fig. 2. After that maximum, the transit depth decreases only slowly with age. If the models are correct, we can use for young planets a factor of roughly 2 larger than for old planets (for number of expected detectable planets).

Through its first four months of operation, NASA's Kepler mission (Koch et al. 2010) detected 83 transit candidates with transit depths of at least 5 mmag and periods shorter than 10 days (Borucki et al. 2011). Given the Kepler target list of $\sim 160\,000$ stars (Koch et al. 2010), this is an occurrence rate of 0.00052 short period transiting planets of this size per star. If we can assume that the rate of planet occurrence is the same for the Kepler target list and the YETI Tr-37 sample, then we can estimate the rate of planets detectable in Tr-37: The Kepler target list has been carefully selected using the Kepler Input Catalog, and the

Table 1 First two target clusters.

Cluster Name	Central Coordinates RA J2000.0 [h : m : s]	Dec J2000.0 [° : ′ : ″]	Age [Myr]	Distance [pc]	No. of Stars with $R \leq 16.50$ mag Members in Total	Members in Jena FoV	Stars in Jena FoV (b)	Expect. No. of Transit Planets in the Jena FoV (a) (and Among Members)
Tr-37	21:38:09	+57:26:48	7	870	614	≥469	6762	∼8.1 (∼1.1)
25 Ori	05:24:45	+01:50:47	7–10	323	179	≥108	1045	∼1.3 (∼0.3)

Remarks: (a) According to Eq. (1) and Sect. 3; (b) Jena FoV is $53' \times 53'$ for STK, see Table 2.
References for coordinates, age, distance, and members: 25 Ori – Kharchenko et al. (2005), Briceño et al. (2005, 2007); Trumpler 37 – see Sect. 6.

Kepler targets are nearly all on or near the main sequence (MS); the Kepler target list is dominated by F and G dwarfs, similar to the sample of Tr-37 members; the Tr-37 members are of course younger (pre-MS) and, hence, larger than the Kepler MS targets; the Kepler target list is, however, probably not a good match to a magnitude-limited sample in the Tr-37 FoV (field stars), which will have heavy contamination by giants; however, we can apply the Kepler planet rate to the Tr-37 members.

Nevertheless, if we apply this estimate to Tr-37 (6762 stars in the Jena FoV, including 469 young members), and also correct for the size of young stars with young planets compared to old systems in the Kepler field, we expect ∼0.5 short-period planets among the known cluster members (and ∼3.8 short-period planets total for the Tr-37 FoV). If we include periods out to 30 days, the number of candidates with transits deeper than 5 mmag detected by Kepler is 131, corresponding to ∼0.8 expected planets among the known Tr-37 cluster members (and 5.9 total in the Tr-37 FoV).

This estimate (∼0.8 transiting planets) is consistent with our other estimate (derived differently) given in Table 1. The estimates of expected detectable planets in Table 1 are upper limits in the sense, that we may still miss some planets, if we always would have problems with weather and/or technical issues, i.e. would never reach a truly contiuous monitoring, or due to the activity and, hence, intrinsic variability of the young targets (however, ∼10 to 100 Myr old stars like weak-line T Tauri stars and zero-age main sequence stars already show much lower variability amplitudes compared to ∼1 Myr young classical T Tauri stars). The estimates for planets in Table 1 are also lower limits, because the number of young members in the clusters known (and given in Table 1) are also lower limits; in the YETI survey, we will find new members by photometric variability and follow-up spectroscopy. Using the monitoring campaigns with three one- to two-week runs in three consecutive months, repeated in two or three consecutive years, it will be possible to detect most of the transiting planets with periods up to ∼30 days.

We show in Fig. 6 below that we are indeed able to combine the photometric data points from different telescopes (with different mirror sizes, different detectors, and different weather conditions) with sufficient precision to detect transits: Fig. 6 shows a preliminary light curve for an eclipsing double-lined spectroscopic binary in the Tr-37 field; this is probably not a young member of Tr-37, but still to be confirmed.

Even though transiting planets have not yet been found in clusters (most of the clusters surveyed for transits are several Gyr old), it is not yet known, whether the occurrence rate of (transiting) planets is lower in clusters compared to non-cluster field stars. If hot (transiting) Jupiters do not survive as long as the cluster age, then young clusters may still have more planets than old clusters. On the other hand, stars in young clusters are more active than in old clusters, which makes it more difficult to detect and confirm young transiting planets. It is also not yet known how long planet formation (and migration) lasts, i.e. whether planet formation is possible during the (small) age of the YETI clusters. In this project, we aim to clarify those questions.

We argue that the fraction of transiting planets expected and found in the MONITOR survey is lower than expected in the YETI survey, because we obtain continuous monitoring with telecopes covering all longitudes on Earth, i.e. 24 hours per day for several consecutive days. With such continuous observations, we will be able to detect any transit with a depth of at least about 5 mmag rms (down to 14.5 mag), the mean YETI sensitivity, for every planet with an orbital period lower than the survey – or, in order to detect the periodicity of the candidate, lower than about half the survey duration (somewhere between a few days and a few months).

The YETI cluster target selection criteria to study planet formation by transit observations are therefore as follows:

– Young age: at least one Myr, so that planets may already exist, and younger than ∼100 Myr, the PMS time-scale of the lowest mass stars.
– Intermediate distance: neither too close (otherwise the field with enough stars would be too large on the sky) nor too distant (otherwise the stars would be too faint), roughly 50 to 1000 pc.
– Size of the cluster on sky: roughly $1° \times 1°$, i.e. well suited to the typical field sizes set be the YETI telescope optics and CCD sizes; in case of smaller FoVs and mosaicing, the cadence should still be high enough to obtain sufficient data points during the typical transit duration.
– Clusters not studied before with similar or better observations, e.g. like NGC 2264 with CoRoT.

– As many young stars as possible in a useful magnitude range in VRI: Not too bright (fainter than ∼10 mag) to avoid saturation and not too faint (brighter than 16.5 mag) not to lose sensitivity (even if different exposure times are used for stars of different brightness) and to be able to do RV follow-up spectroscopy of transit candidates (the faintest host star where this was successfully done is OGLE-TR-56 with $V = 16.6$ mag, Konacki et al. 2003).
– Location on sky, so that many telescopes can observe and monitor it continuously.

The number of confirmed transit planet detections is 134 (e.g. exoplanet.eu), relatively small when compared with early predictions (Horne 2003). The origin of this discrepancy may have several causes: (i) simplifying assumptions in the noise properties that govern the detection limits in previous predictions – in many cases red instead of white noise may be dominating (Pont et al. 2006), (ii) unaccounted errors in aperture photometry on non-auto- guided telescopes, (iii) overestimates of the fraction of stars that are suitable as targets for transit surveys, and (iv) underestimates of the need for continuous observations.

Another topic whose consequences have only been recognized during the course of the first transit searches is the problem of false alarms caused by other stellar combinations that may produce transit-like light curves. Of these, the most notorious case may be that of an eclipsing binary star located within the point spread function (PSF) of a brighter star (Brown 2003). An increasing number of tools are now available to recognize false alarms: (i) precise analysis of transit shapes or durations, (ii) color signatures, and (iii) variations in the positioning of the stellar PSF. The effectiveness of several of these tools depends strongly on the information (e.g., temperature, radius) that is available for the host star, and underlines the need for auxiliary observations in transit detection experiments.

In practice, it is not always possible from the light curve alone to exclude false positives, such as background eclipsing binaries blended with the target. We obtain follow-up spectroscopy to aid in examining these possibilities, as well as to measure the stellar properties temperature, rotational velocity, gravity, and metallicity, and to measure the mass of the companion. Except when TTV signals are observed, one always needs follow-up spectroscopy to determine the mass of the companion.

4 The YETI telescope network for continuous monitoring

Given the target selection criteria listed above, we have selected the clusters Tr-37 and 25 Ori (Table 1) as the first two clusters to be observed, several more will follow later in order to cover the full age range to study formation and early evolution of planets. Additional clusters to be observed fully or partly in future years are Pleiades, NGC 2244, α Per, h and χ Per, Collinder 69, σ Ori, IC 2602, etc. If we will observe approximately ten clusters in the project, each cluster for 2 or 3 years, and not more than two different clusters per year, then the whole YETI project will last for more than ten years. Most of the observatories participating can allocate their telescopes for all nights in all runs for the whole duration of the YETI project (mostly already guaranteed, partly by internal proposals), while for some of the participating telescopes, we have to apply for time (e.g. Sierra Nevada, Calar Alto, Mauna Kea).

The clusters Tr-37 (Fig. 1) and 25 Ori have been observed since 2009. The cluster Tr-37 was observed by most of the participating telescopes in 2010 during the three runs August 3/4 to 12/13, August 26/27 to September 12/13, and September 24/25 to September 30/October 1, i.e. 35 nights in total. The cluster 25 Ori was observed simultaneously and continuously by most of the participating telescopes 2010 December 10/11 to 17/18, 2011 January 13/14 to 23/24, and February 16/17 to 27/28. Additional nights for the 2011 and subsequent observing seasons are expected to be allocated on all the YETI telescopes, 34 nights for Tr-37 in 2011 and 29 nights for 25 Ori in the (northern) winter 2011/12. We also observed a field at the edge of the Pleiades cluster (Eisenbeiss et al. 2009; Moualla 2011). First results from Tr-37 are reported below.

Given the problems listed in the previous section and in order not to miss a transit and to determine the periodicity in the transit-like variability, it is important to monitor the targets (almost) continuously, i.e. 24 hours per day for the whole run of at least several days. Therefore, we established a network of several observatories around the world covering many longitudes, to that we can observe the YETI targets continuously.

The participating observatories are listed in Table 2 with their telescopes and instruments.

5 Additional science projects

Although the main thrust of this project is the search for young transiting planets, the observations we are collecting also lend themselves to studies of variability phenomena on different time-scales, and can be co-added as well to provide very deep imaging of the YETI target clusters. An additional component of the project is a theoretical study of the interiors of young transiting planets to provide a framework for interpreting the YETI discoveries. We describe these topics below.

5.1 Other variability phenomena

The precise and nearly continuous time series photometry gathered for this project enables us to investigate rotational periods for cluster members and field stars (see, e.g., Fig. 3; first results on Tr-37 data from Jena from 2009 can be found in Berndt et al. 2011), longer-term cycles (Fig. 4), and irregular variability like flares. We can also detect eclipsing bina-

Table 2 Telescope network (1) (sorted by longitude).

Observatory	Long. [°]	Lat. [°]	Mirror Diameter [m]	CCD Type (Camera)	No. of Pixels	Size of Field [′×′]	Ref.
Gunma/Japan	139.0 E	36.6 N	1.50	Andor DW432	1250×1152	12.5×12.5	(2)
Lulin/Taiwan	120.5 E	23.3 N	1.00	Marconi CCD36-40 PI1300B	1340×1300	22×22	
			0.41	E2V 42-40 (U42)	2048×2048	28×28	
Xinglong/China	117.6 E	40.4 N	0.90 (3)	E2V CCD203-82	4096×4096	94×94	Wu07
Nainital/India	79.5 E	29.4 N	1.04	TK2048E	2000×2000	13×13	
Byurakan/Armenia	44.3 E	40.3 N	2.60	SCORPIO Loral	2058×2063	14×14	
Rozhen/Bulgaria	24.7 E	41.7 N	0.60	FLI ProLine 09000	3056×3056	17×17	(4)
			0.60 (5)	FLI ProLine 09000	3056×3056	27×27	(4)
			0.70 (6)	FLI ProLine 16803	4096×4096	73×73	(4)
			2.00	Princ. Instr. VersArray:1300B	1340×1300	6×6	(4)
Stará Lesná	20.3 E	49.2 N	0.50	SBIG ST10 MXE	2184×1472	20×14	
(Slovak Rep.)			0.60	SITe TK1024	1024×1024	11×11	
			0.25	SBIG ST10 MXE	2184×1472	43×29	
Toruń/Poland	18.6 E	53.1 N	0.90 (3)	SBIG STL-11000	4008×2672	48×72	
Jena/Germany	11.5 E	50.9 N	0.90 (3)	E2V CCD42-10 (STK)	2048×2048	53 x 53	Mug10
			0.25 (7)	SITe TK1024 (CTK)	1024×1024	38×38	Mug09
			0.25 (8)	E2V CCD47-10 (CTK-II)	1056×1027	21×20	Mug11a
			0.20	Kodak KAF-0402ME (RTK)	765×510	8×5	Mug11b
Sierra Nevada/Spain	3.4 W	37.1 N	1.50	EEV VersArray:2048B	2048×2048	8×8	
Calar Alto/Spain	2.5 W	37.2 N	2.20 (9)	SITe1d (CAFOS)	2048×2048	16×16	(10)
Armazones/Chile	70.2 W	24.6 S	0.15	Apogee U16M KAF-16803	4096×4096	162×162	(11)
CIDA/Venezuela	70.9 W	8.8 N	1.00	Quest-I CCD Mosaic	8000×8000	138×138	Ba02
			1.00 (5)	FLI Proline E2V42-40	2048×2048	19×19	
Stony Brook/USA	73.1 W	40.9 N	0.37	SBIG ST1001E KAF-1001E	1024×1024	17×17	
Swarthmore/USA	75.4 W	39.9 N	0.62	Apogee U16M KAF-16803	4096×4096	26×26	
Gettysburg/USA	77.2 W	39.8 N	0.40	SITe 003B	1024×1024	18×18	(12)
Tenagra II/USA	110.5 W	31.3 N	0.81	SITe SI003 AP8p	1024×1024	15×15	
Mauna Kea/Hawaii	155.5 W	19.8 N	2.20	8 CCD chips for mosaic	8×2048×4096	33×33	

Remarks: (1) Listed are only those from which we have obtained (or proposed) photometric monitoring data so far; (2) www.astron.pref.gunma.jp/e/inst_ldsi.html; (3) 0.60 m in Schmidt mode; (4) www.nao-rozhen.org/telescopes.fr_en.htm; (5) with focal reducer; (6) 0.50 m in Schmidt mode; (7) until July 2010; (8) since August 2010; (9) by open time observing proposals; (10) w3.caha.es/CAHA/Instruments/CAFOS/cafos_overview.html; (11) www.astro.ruhr-uni-bochum.de/astro/oca/vysos6.html; (12) www3.gettysburg.edu/∼marschal/clea/obshome.html.
Ref.: Mug09 – Mugrauer 2009; Mug10 – Mugrauer & Berthold 2010; Mug11a,b – Mugrauer 2011a,b (in prep); Wu07 – Wu et al. 2007; Ba02 – Baltay et al. 2002.

ries comprised of two stars, or two brown dwarfs, or a brown dwarf orbiting a star. From eclipsing binaries among young cluster members, we can derive mass-luminosity relations, which are one of the main uncertainties in obtaining luminosity and mass functions and of pre-main sequence populations as well as ages and masses of individual stars. We plan to use multi-color photometry to refine age, distance, and extinction measurements for the clusters, e.g. from the color-magnitude or color-color diagrams.

5.2 Deep imaging

We can add up many images obtained per cluster to get much deeper photometry. We have already tested this using a field at the edge of the Pleiades, where we could find several brown dwarf candidates by $RIJHK$ colors (Eisenbeiss et al. 2009), for which we have recently obtained follow-up optical and infrared spectra with the ESO VLT (Seeliger 2011). We also applied this technique very successfully by combining co-added optical I-band data of ∼180 square degrees across the Orion OB1 region, with 2MASS JHK data (Downes et al. 2008; Downes et al., in preparation), to identify several thousand young very low-mass stars and brown dwarfs, for many of which we have confirmed membership through follow-up spectroscopy (Downes et al., in preparation).

Co-added individual frames from the larger telescopes will also provide a more sparsely sampled, but much deeper time series, which will allow us to carry out systematic variability studies amongst the young brown dwarfs of the YETI target clusters.

Similar studies can be done for all clusters observed by YETI. Such a study can reveal the very low-mass population including massive brown dwarfs, i.e. the low-mass end of the mass function. We can re-determine cluster distance, age, and mass function based on a larger set of photometric and spectroscopic data obtained for a larger sample of

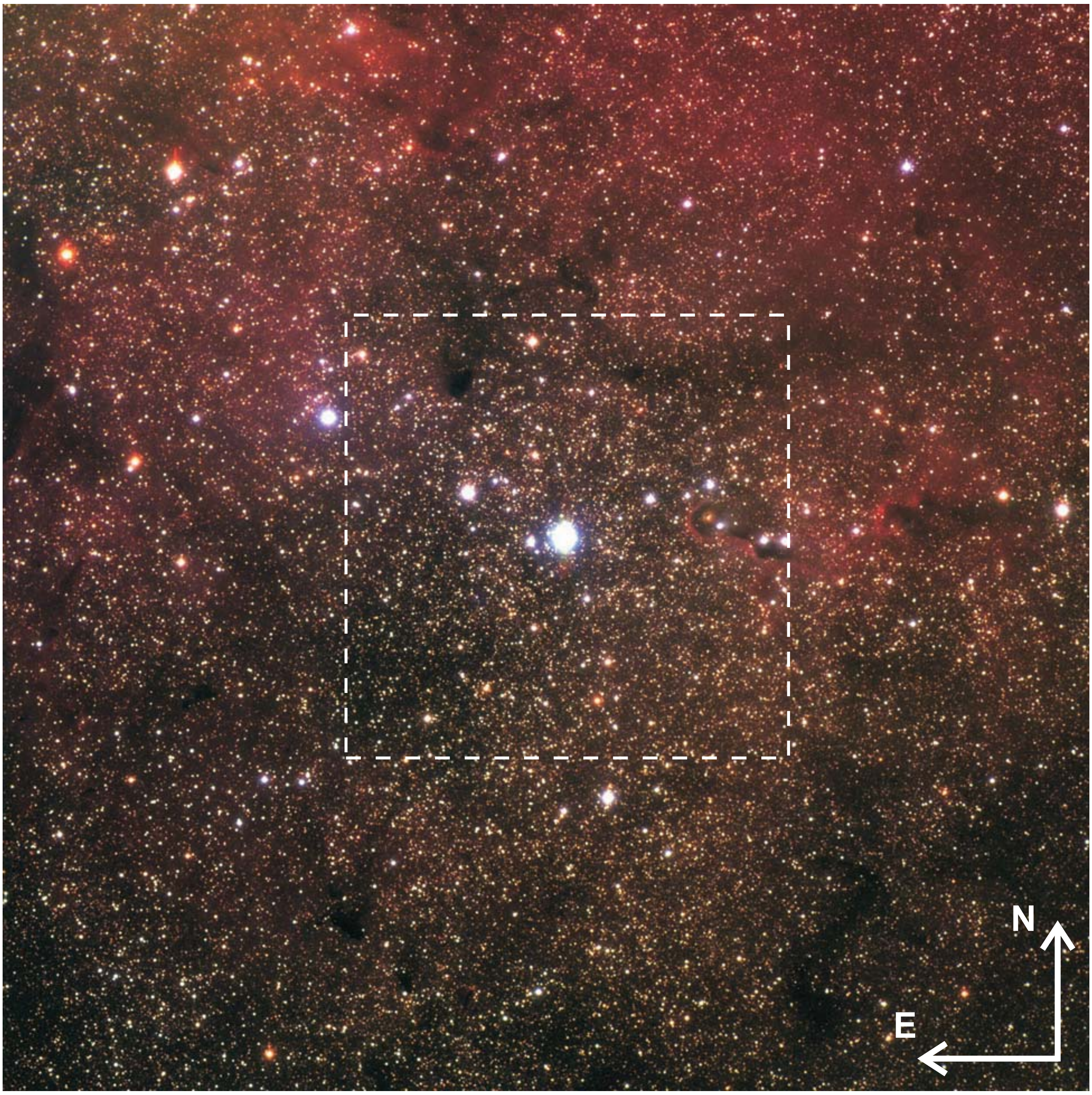

Fig. 1 (online colour at: www.an-journal.org) A BVR three-color composite image of the Tr-37 cluster as observed with STK at University Observatory Jena in July 2009. The image is a mosaic of nine STK images, each the composite of three 60 s integrations taken in the B, V, and R band. The total FoV shown is $2\overset{\circ}{.}1 \times 2\overset{\circ}{.}1$ (North is up, and East to the left). The central dashed box indicates the STK $53' \times 53'$ FoV monitored in Jena only in 2009 and with the YETI consortium in 2010.

cluster members. Given the large FoV, we can probe possible variations of the mass function and brown dwarf density with the distance to the center of the cluster.

Deep images can also be used to study the proper motion compared to previous images, hence to detect new cluster members. We note that for deep imaging, we do not plan to add up all data from all different telescopes together into just one deep image, because of differences in FoV size, pixel scales, seeing, etc., but we will use the data from the largest telescope(s) (and also the one with the largest FoV) to add up all images from that telescope(s) into one deep image (one per detector).

5.3 Interior models for giant planets

Widely accepted models for giant planets assume three layer structures composed of a central core of rock or ices and two fluid envelopes above (Guillot 1999 a,b). The location of the layer boundaries and the composition within the layers are subject of an optimization procedure with respect to observational constraints, e.g. gravitational moments for the solar giant planets and possibly the Love number (Kramm et al. 2011), if known for an extrasolar giant planet.

The main input in interior models is the equation of state (EoS) for H, He, H_2O, NH_3, CH_4, or rock material for the respective extreme conditions (up to several 10 Mbar and several 10 000 K). We perform ab initio molecular dynamics simulations which yield accurate EoS data and electrical conductivities for H (Holst et al. 2008, Lorenzen et al. 2010), He (Kietzmann et al. 2007), H-He mixtures (Lorenzen et al. 2009), and water (French et al. 2009, 2010). Besides the generation of wide range EoS data tables, we study the high-pressure phase diagram, nonmetal-to-metal transitions, and demixing phenomena which are important for interior models.

Based on these results, we have determined the structure of giant planets and calculated their cooling history: Jupiter (Nettelmann et al. 2008), the hot Neptune GJ436b (Nettelmann et al. 2010; Kramm et al. 2011), and for Uranus and Neptune (Fortney & Nettelmann 2010; Redmer et al. 2011).

Within the YETI project we plan to develop interior models especially for young planets that are detected within the observational campaigns. Then, we can study the formation and early evolution of giant planets.

6 First results for Trumpler 37

The open cluster Trumpler 37 (Tr-37), first studied by Trumpler (1930) and Markarian (1952), is embedded in the H II region IC 1396, and is the nucleus of the Cep OB2 association (Simonson 1968). The $V = 4$ mag M2 Ia super giant μ Cep is a probable member of the cluster, but outside of the Jena FoV (and outside the mosaic in Fig. 1). Comparison of the Tr-37 main sequence to that of Upper Scorpius yielded a distance modulus of 9.9 to 10 mag, i.e. $\sim$1000 pc (Garrison & Kormendy 1976); from the MS life-time of the earliest member, the O6e type star HD 206267 ($V = 5.6$ mag), they conclude an age of 2 to 4 Myr. Marschall & van Altena (1987) studied the proper motions of $\sim$1400 stars within $1\overset{\circ}{.}5$ of HD 206267 down to $V = 15$ mag and found $\sim$500 kinematic members. Marschall et al. (1990) then determined the age of the cluster by the MS contraction time of those members which just have reached the zero-age main-sequence (ZAMS), to be $\sim$6.7 Myr; later, an age range from 3 to 10 Myr was considered (Contreras et al. 2002; Sicilia-Aguilar et al. 2004b, 2005). The current best age estimate is $\sim$4 Myr (Kun, Kiss & Balog 2008), and the latest distance estimate is 870 ± 70 pc (Contreras et al. 2002).

A three-color BVR composite image of the Tr-37 cluster obtained with the STK CCD camera at the Jena 60-cm Schmidt telescope is shown in Fig. 1.

A total of 732 members or member candidates of the cluster were found by Hα emission, ZAMS or pre-MS location, lithium absorption, X-ray emission, infrared excess emission, proper motion, or radial velocity (Marschall & van Altena 1987; Marschall et al. 1990; Contreras et al. 2002; Sicilia-Aguilar et al. 2004a,b; Sicilia-Aguilar et al. 2005; Sicilia-Aguilar et al. 2006a,b; Mercer et al. 2009). Some of the candidates may not be members, e.g. stars with either radial velocity or proper motion consistent with membership, but no or very weak lithium absorption, while true members may still be missing, e.g. faint very low-mass members. We are taking low- and high-resolution spectra of hundreds of stars in the YETI $\sim 1^\circ \times 1^\circ$ FoV with MMT/Hectochelle, in particular of suggested but uncertain member candidates, in order to confirm or reject them as members based on radial velocity and lithium absorption (Errmann et al., in prep.).

Table 3 Observations log from 2009 for Tr-37 (Jena only).

Date (a)	Begin [UT]	End [UT]	Filter	Exp. [s] (b)
07/29	21:32	01:53	R	7790
07/31	01:08	02:07	R	2660
08/01	20:32	02:07	R	14650
08/04	20:46	02:39	R	15260
08/05	20:27	02:24	R	14160
08/06	20:16	01:24	R	5840
08/13	21:48	00:49	R	7070
08/15	20:07	21:58	R	4980
08/17	21:38	22:54	R	3430
08/18	19:43	03:14	R	16720
08/19	20:22	02:35	R	14220
08/21	00:26	01:30	R	2380
08/22	20:00	02:22	R	17260
08/23	19:32	03:05	R	16000
08/24	20:50	02:23	R	14870
08/26	22:07	03:01	R	9460
08/27	22:18	02:56	R	10290
08/29	21:37	02:26	R	12810
08/30	21:07	02:00	R	12810
08/31	23:16	02:54	R	9530
09/05	20:33	03:05	R	9360
09/07	19:00	03:27	R	18790
09/08	19:08	01:52	R	16440
09/09	19:00	01:50	R	14880
09/18	18:58	00:08	R	12530
09/19	18:20	23:29	R	13880
09/21	21:40	22:05	$BVRI$	1560
09/22	18:49	03:54	R	19190
09/25	19:54	03:16	R	19080
09/26	18:04	23:07	R	13520
09/27	23:07	04:17	R	13650
10/20	21:27	01:50	R	11900
11/06	19:59	23:38	R	1110

Remarks: (a) Dates (month/day) for the beginning of the observing nights, all in the year 2009; (b) total exposure of all images in that night, split roughly half and half into individual exposures of 10 s and 60 s.

We present here preliminary results including a few exemplary light curves from the 2009 data, obtained in Jena only with the 90/60-cm telescope. In 2009, we observed only from Jena. The observations log from 2009 (Jena only) is given in Table 3. Only in Fig. 6, we also show a preliminary light curve from the 2010 campaign. In addition, in Fig. 7, we show a spectrum obtained with the Jena 90-cm telescope and a fiber-fed spectrograph; we can take spectra of bright stars (90-cm mirror) also simultaneously with optical CCD photometry with the small 25-cm telescope, which can be quite interesting for variable young active stars. The

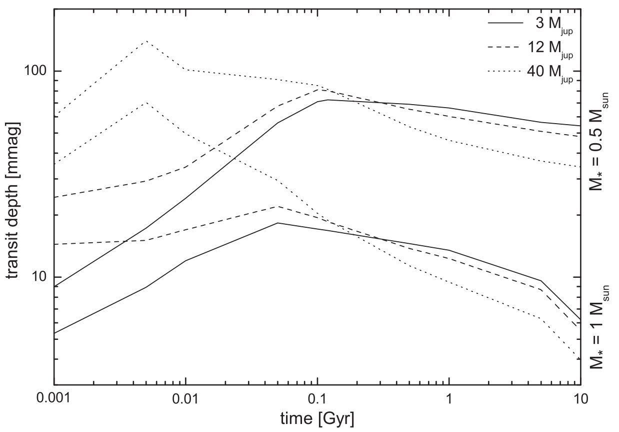

Fig. 2 Expected transit depth (in millimag) versus ages (in Gyr) for 40 Jupiter-mass brown dwarfs (dotted lines) as well as 12 and 3 Jupiter-mass planets (dashed and full lines, respectively) transiting 0.5 (*top*) and 1 $M_\odot$ (*bottom*) stars according to Baraffe et al. (1998, 2002, 2003). These theoretical calculations show that the transit depth reaches a maximum at 5 to 100 Myr due to different contraction time-scales of stars and sub-stellar objects – hence, our target cluster selection.

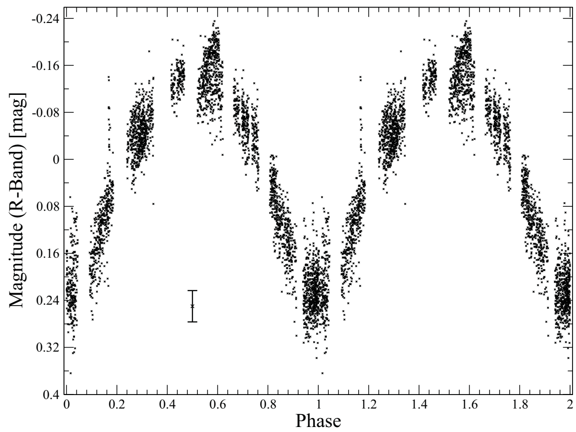

Fig. 3 Phase-folded R-band light curve from Jena STK data from July to November 2009 for the star 2MASS J21353021 +5731164. The error bar in the lower left is the typical (mean) photometric error. The star is a classical T Tauri member of Tr-37 with spectral type K6 according to optical spectra (Sicilia-Aguilar et al. 2005, 2006b). We find $R = 15.8$ mag and $V = 16.9$ mag, consistent with K6, and a rotation period of $\sim$3.5 days, it has a relatively large peak-to-peak amplitude of $\Delta R \simeq 0.5$ mag, which has been observed also in a few other classical T Tauri stars before.

Tr-37 was observed for three runs in 2010 and will also be observed for three runs in 2011 and 2012 by most telescopes of the network. Final results including follow-up observations will be presented later.

Basic data reduction of the Jena data from 2009 shown in the figures here includes bias, dark, flat-field, illumination, and bad pixel corrections. Relative photometry follows the procedure described in Broeg et al. (2005): We compare each star in the FoV with all other stars to investigate its variability, then we construct an artifical comparison star, then iterate by giving variable stars less weight; the final artifical comparison star is then very constant. We do this not only for one particular program star, as in Broeg et al. (2005), but for all stars in the field. For details, see Broeg et al. (2005). Finally, we also test de-trending (Tamuz, Mazeh & Zucker 2005).

Periodic variability can then be detected by typical period search procedures like Stringlength, Lomb-Scargle, or Fourier analysis (see, e.g., Berndt et al. 2011 for rotation periods of members of Tr-37). We are currently implementing a Bayesian transit detection routine (Hambaryan et al., in prep.) to search for the exact type of the signal (planetary transit), even if not strictly periodic, as in the case of TTV signals or very long periods (so that only one transit is observed).

The first few planetary transit observations with a 25-cm telescope of the University of Jena Observatory near the village of Großschwabhausen near Jena of the objects TrES-1, TrES-2, and XO-1 (Raetz et al. 2009a; Vaňko et al. 2009; Raetz et al. 2009b, 2009c) show that transits can be detected from the Jena observatory, but they do not prove that we can find new transiting planets. Since early 2009, we also use the 90-cm mirror of the Jena observatory in its 60-cm Schmidt mode ($53' \times 53'$ FoV) with the CCD called Schmidt-Teleskop-Kamera (STK), see Mugrauer & Bertold (2009) for details. With that telescope and camera, we could also re-detect known planetary transits with a precision of $\sim$1 mmag rms scatter and $\pm$27 s transit timing precision (Maciejewski et al. 2010, 2011a).

We reached 5 mmag rms precision for all un-saturated stars down to $R = 14.5$ mag with the Jena 90-cm telescope in the 60-cm Schmidt mode (see Fig. 5). For the other telescopes of the network with similar mirror size and similar CCD detectors, we can reach a similar precision: 50 mmag rms down to $R = 17.7$ mag for Byurakan 2.6 m, as well as down to $R = 17.8$ mag for Lulin 1 m, down to $R = 15.4$ mag for Swarthmore 0.6 m, and to $R = 16.9$ mag for Xinglong 0.9 m; also 5 mmag rms down to $R = 14.9$ mag for Byurakan 2.6 m, as well as down to $R = 15.4$ mag for Lulin 1 m, and down to $R = 13.4$ mag for Swarthmore 0.6 m: the data for the other telescopes are still being reduced.

We show a few preliminary results in figures 2 to 6: light curves from the 2009 monitoring only at the Jena telescope, e.g. a 3.5 day rotation period of a classical T Tauri star (Fig. 3) – but also light curves with obvious gaps (e.g. Fig. 4), motivating the collaboration with many other observatories (YETI). We show the sensitivity obtained with the Jena 90/60 cm in Fig. 5. In Fig. 6, we show a preliminary light-curve with data combined from several telescopes from the 2010 Tr-37 campaign. We also show a spectrum obtained with the 90-cm telescope in Jena (Fig. 7), namely for the brightest member of Tr-37 (HD 206267), together with a light curve for this star with high time resolution with 5 s exposures (Fig. 8). In Fig. 9, we show the light curve for an apparently non-variable member star ($\pm$2.7 mmag).

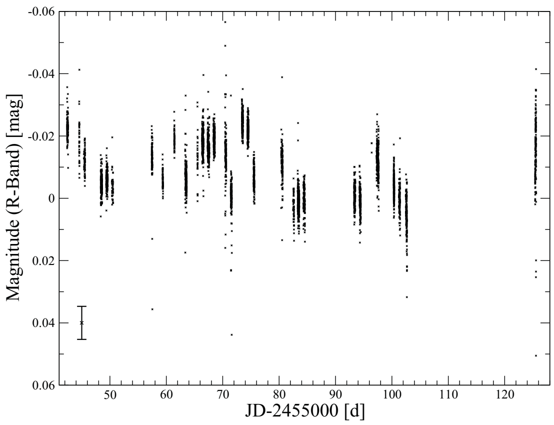

Fig. 4 R-band light curve from Jena STK data from July to October 2009 for the star MVA 1312, spectral type B4 (Contreras et al. 2002; Sicilia-Aguilar et al. 2005), it has a proper motion membership probability of 0.84 (Marschall & van Altena 1987). The observing date is given in JD since 2009 June 17. The error bar in lower left is the typical (mean) photometric error. We find $R = 10.60$ mag and $V = 10.3$ mag, consistent with early B. The star shows variability on short (nightly) and longer time-scales (days to weeks), but we also have strong gaps in the light curve from one observatory (Jena). This shows the need for continuous monitoring.

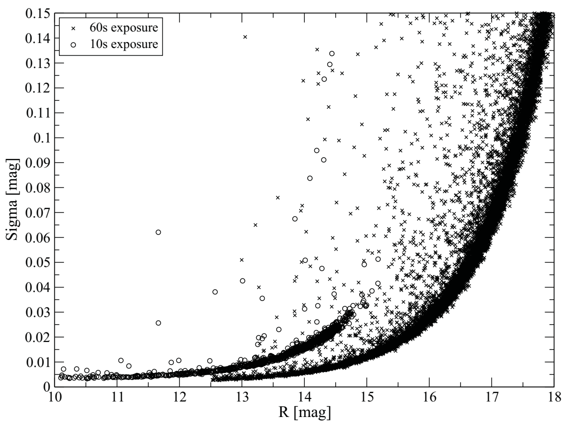

Fig. 5 Photometric precision achieved (in mag) versus apparent photometric brightness (in mag in the R band with Jena 90/60-cm telescope in the night 2009 Sept 9/10) with 6762 stars in the Tr-37 field. A precision of better than 50 millimag rms (sufficient to detect transits) is achieved for all stars brighter than 16.5 mag, and a precision of 5 millimag rms for all stars brighter than $R = 14.5$ mag.

We also found a few new eclipsing binaries, both member candidates and field stars. For the member candidates, low-resolution spectra have been obtained at Calar Alto with CAFOS, see below, to confirm membership; high-resolution spectra were obtained at Keck with HIRES to measure the masses of the companions (Errmann et al., in prep.). Since the FIASCO spectrograph at the 90-cm Jena telescope is useful only down to about 11th mag, we also use the Calar Alto 2.2 m/CAFOS for low-resolution and the 1.5-m Tillinghast Reflector for high-resolution spectra.

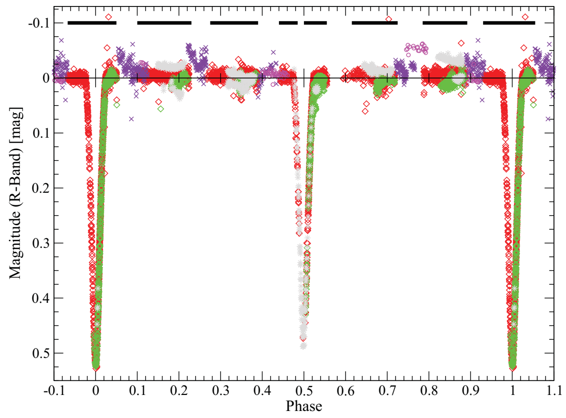

Fig. 6 (online colour at: www.an-journal.org) A preliminary light curve of an eclipsing star in the Tr-37 field phased to a 6.005 day orbital period. Data from Jena are shown as red and green diamonds (for 10 s and 60 s exposures, respectively). From Jena alone, we could not fully cover the secondary (shallower) eclipse (phase 0.5). The bars on the figure top show the phases covered from Jena. The other (colored) symbols show the data from four other telescopes: brown plusses from Byurakan/Armenia (60 s), pink crosses from Xinglong/China (10 s), grey stars from Swarthmore/USA (60 s), and pink circles from Lulin/Taiwan (10 s). This example shows how important it is to cover all longitudes on Earth, hence the YETI telescope network. Follow-up spectroscopy has shown that this star is a double-lined spectroscopic binary. This particular star is probably not a young member of the Tr-37 cluster, but follow-up observations are still ongoing. Final results will be reported later in Errmann et al. (in prep.). This figure shows that we can successfully combine data from different telescopes with different CCDs and different ambient conditions.

The optical spectra of HD 206267A+B ($V = 5.6$ mag), C ($V = 8.1$ mag), and D ($V = 7.9$ mag) were obtained with the fiber-fed spectrograph FIASCO (Mugrauer & Avila 2009) operated at the Nasmyth port of the 90-cm telescope of the University Observatory Jena. The data were taken on 2010 June 7, using three exposures with 600 s exposure time each for HD 206267A+B and four such 600 s exposures for HD 206267C and D. Standard calibration was done (dark and flat-field correction, removal of bad pixels). Flux correction was performed by using a Vega spectrum from the same night and airmass, standard spectra are from Le Borgne et al. (2003). The de-reddened spectrum of HD 206267A+B is consistent with a spectral type of O6 (as in Simbad and Sota et al. 2011) and the spectra of HD 206267C and D show spectral type B0V (as in Simbad and Sota et al. 2011), all spectra show Hα and He absorption as well as telluric oxygen, all as expected.

For transit candidates, i.e. stars showing a light curve with periodic, small, transit-like, flat-bottom dips, we will do the usual follow-up observations: First, a high-precision photometric light curve is obtained with a larger telescope to confirm that the dip is consistent with a planet transit,

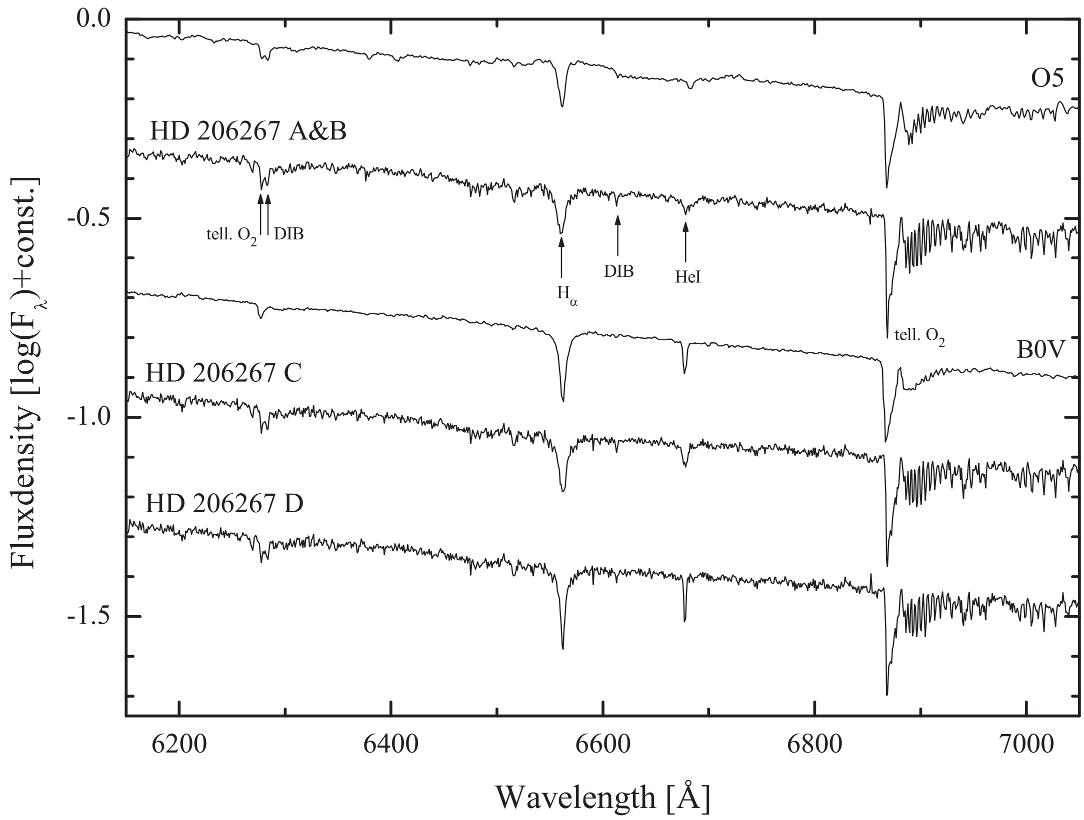

Fig. 7 An optical spectra of HD 206267A+B (together), C, and D, all obtained with the FIASCO spectrograph at the Jena 90-cm telescope on 2010 June 7, shown together with template spectra (O5 star HD 93250 and B0V star HD 36512 from Le Borgne et al. 2003). The spectrum of HD 206267A+B is consistent with a spectral type of O6 (as in Simbad and Sota et al. 2011), and the spectra of both HD 206267 C and D are consistent with a spectral type of B0V (as in Simbad and Sota et al. 2011); HD 206267A+B as well as C and D show Hα and He absorption as well as diffuse interstellar absorption bands and telluric oxygen.

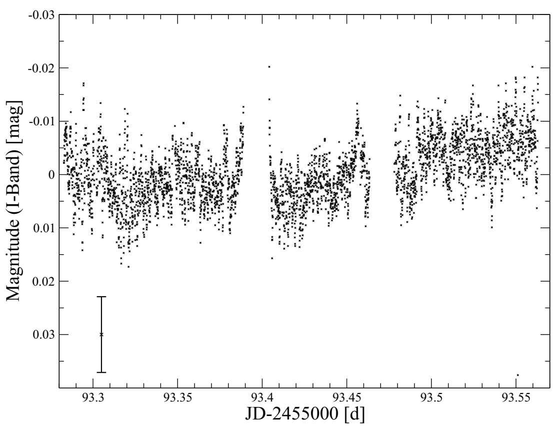

Fig. 8 I-band light curve from Jena RTK data from 2009 September 18 for the star HD 206267A+B (spectroscopic binary), the brightest member of Tr-37 in the Jena FoV, $I = 5.6$ mag, $V = 5.6$ mag, and spectral type O6 (Simbad, Sota et al. 2011, and our Fig. 7). The error bar in the lower left is the typical (mean) photometric error. The membership probability of this star to Tr-37 is 0.67 (Marschall & van Altena 1987). The time resolution is 40 s, because each data point plotted is a mean of eight exposures of 5 s each.

i.e. shows a flat-bottom light curve. Then, low- to high-resolution spectroscopic reconnaissance spectra are taken, e.g. with the 2.2-m Calar Alto CAFOS spectrograph or the 1.5-m Tillinghast Reflector at the Whipple Observatory, the latter giving a resolution of 6.5 km/s down to $V = 14$ mag. If the object is still not found to be a binary star, then we obtain high-angular resolution follow-up imaging with Adaptive Optics (AO, large telescope mirror, small PSF, e.g. Subaru) to check whether there are background eclipsing binaries in the larger optical PSF (from imaging photometry with a smaller telescope mirror), which could mimic a transit-like periodic event. Then, we can also consider to obtain high-resolution infrared spectra, to check for background eclipsing binaries even closer to the target star, i.e. within the AO PSF (not yet done). If the transit-like event can still only be explained by a sub-stellar object transiting the star, then the last follow-up observation is time-critical high-resolution spectroscopy, to measure the mass of the transiting companion. With the RV data, we can then also use the Rossiter-McLaughlin effect to show that a body of small radius orbits the observed star, excluding a faint eclipsing binary hidden in the system PSF.

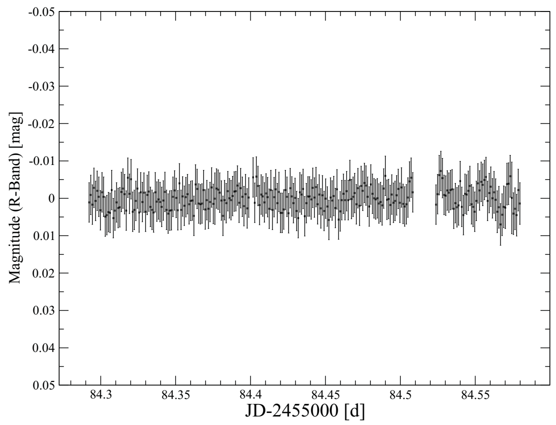

Fig. 9 R-band light curve from Jena STK CCD from 2009 September 9 for the star MVA 497, spectral type A1 (Sicilia-Aguilar et al. 2005). It has a proper motion membership probability of 0.92 (Marschall & van Altena 1987). We obtained $R = 12.8$ mag and $V = 12.8$ mag, consistent with early A spectral type. This is the most constant member star in the Jena STK data from the best night (lowest scatter in photometric data of whole ensemble, excluding nights with observations lasting less than 3 hours). The scatter of this star is ± 2.7 millimag. The observation in the night ended due to clouds, which arrived at UT 2:00 h. The first cloud ridge arrived earlier, therefore the scatter at the end of the night is slightly worse. There were two stars in the FoV with even slightly smaller scatter, but for those it is not yet known whether they are members or non-members.

We have done most of those follow-up observations so far for one transit candidate (Errmann et al., in prep.). This first candidate was detected in the 2009 data of the Jena 90/60-cm telescope only. Hence, after combining the data from all telescopes from the 2010 campaign, we can expect to detect several more candidates.

We will report results of the photometric monitoring campaigns and the follow-up observations in the near future.

7 Summary

We presented the motivation, observing strategy, target cluster selection, and first results of the new international multi-site project YETI with its main goal being the discovery and study of young exoplanets. The photometric precision is 50 mmag rms down to $R = 16.5$ mag (5 mmag rms down to $R = 14.5$ mag, both values for Jena 90/60 cm, similar brightness limit within about ± 1 mag also for the other telescopes of the network), i.e. sufficient to detect planetary transits. We use several telescopes around the world to observe continuously for 24 hours per day for several days in order not to miss a transit.

For young transiting exoplanets, we can determine mass and radius, hence also the density and possibly the internal structure and composition. With young exoplanets, one can constrain planet formation models, e.g. whether they form by gravitational contraction (disk instability) or by core accretion (nucleated instability), during which time-scale and at which separations from the star planets can form. By comparing different planets found within one cluster, one can determine the role of stellar parameters like mass on planet formation; by comparing the planet population between the different clusters, we can study the impact of environmental conditions on planet formation like metallicity and density of the cluster.

Acknowledgements. All the participating observatories appreciate the logistic and financial support of their institutions and in particular their technical workshops. We would like to thank F. Gießler, H. Gilbert, I. Häusler, D. Keeley, and S. Fitzpatrick for participating in some of the observations at the Jena telescope. RN would like to thank DLN for long-term support and many good ideas and questions. RN would like to acknowledge financial support from the Thuringian government (B 515-07010) for the STK CCD camera used in this project. RN would like to thank the German National Science Foundation (Deutsche Forschungsgemeinschaft, DFG) for general support in various projects. RN, RE, SR, and CA would like to thank DFG for support in the Priority Programme SPP 1385 on the "First Ten Million Years of the Solar System" in projects NE 515 / 34-1, NE 515 / 33-1, and NE 515 / 35-1. RN, GM, TP, and MV would like to thank the European Union in the Framework Programme FP6 Marie Curie Transfer of Knowledge project MTKD-CT-2006-042514 for support. SF thanks the State of Thuringia for a scholarship. RN, GM, AN, LB, TT, GN, MaMu, SR, and TP would like to thank DAAD PPP-MNiSW in project no. 50724260-2010/2011 for support. RR and UK would like to thank DFG for support in the Priority Programme SPP 1385 in project RE 882 / 12-1. AB would like to thank DFG for support in project NE 515 / 32-1. MoMo would like to thank the Tishreen University in Lattakia, Syria for a scholarship. TE, NT, MMH, LT, and VVH would like to thank the DFG for support from the SFB-TR 7. TR would like to thank DFG for support in project NE 515 / 33-1. CM and KS would like to thank DFG for support in project SCHR 665 / 7-1. TOBS, ChGi, LT, TE, and TR would like to thank DFG for support in project NE 515 / 30-1. MS would like to thank DFG for support in project NE 515 / 36-1. NT would like to acknowledge a scholarship. RN, RE, TP, TOBS, UK, and MS would like to thank DFG for travel support to Calar Alto runs in projects NE 515 / 38-1 and 39-1. RN and RE would like to thank DFG for financial support for a Keck run in project NE 515 / 42-1. ELNJ and his colleagues from Swarthmore acknowledge support from the US National Science Foundation grant, AST-0721386. Osservatorio Cerro Armazones (OCA) is supported as a project of the Nordrhein-Westfälische Akademie der Wissenschaften und der Künste in the framework of the academy program by the Federal Republic of Germany and the state Nordrhein-Westfalen. ZYW is supported by the National Natural Science Foundation of China, No. 10803007. JB, TP, and MV thank VEGA grants 2/0094/11, 2/0078/10, 2/0074/09. DPD, DPK, and VSR would like to acknowledge for financial support to the National Science Foundation of the Bulgarian Ministry of Education and Science (project DO 02-362). We used Simbad, ViziR, 2MASS, and WEBDA. We would like to thank an anonymous referee for good suggestions.

References

Aigrain, S., Hodgkin, S., Irwin, J., et al.: 2007, MNRAS 375, 29
Baltay, C., Snyder, J.A., Andrews, P., et al.: 2002, PASP 114, 780
Baraffe, I., Chabrier, G., Allard, F., Hauschildt, P.H.: 1998, A&A 337, 403
Baraffe, I., Chabrier, G., Allard, F., Hauschildt, P.H.: 2000, ApJ 542, 464
Baraffe, I., Chabrier, G., Allard, F., Hauschildt, P.H.: 2001, A&A 382, 563
Baraffe, I., Chabrier, G., Allard, F., Hauschildt, P.H.: 2002, A&A 382, 563
Baraffe, I., Chabrier, G., Barman, T., Allard, F., Hauschildt, P.H.: 2003, A&A 402, 701
Baraffe, I., Chabrier, G., Barman, T.: 2008, A&A 482, 315
Benedict, G.F., McArthur, B.E., Forveille, T., et al.: 2002, ApJ 581, L115
Berndt, A., Errmann, R., Maciejewski, G., et al.: 2011, in: C. Johns-Krull, M. Browning, A. West (eds.), *Cool Stars, Stellar Systems, and the Sun*, ASPC, in press
Borucki, W.J., Koch, D.G., Basri, G., et al.: 2011, ApJ, subm., astro-ph/1102.0541
Briceño, C., Calvet, N., Hernandez, J., Vivas, A.K., Hartmann L., Downes, J.J., Berlind, P.: 2005, AJ 129, 907
Briceño, C., Hartmann L., Hernandez, J., Calvet, N., Vivas, A.K., Furesz, G., Szentgyorgyi, A.: 2007, ApJ 661, 1119
Broeg, C., Fernandez, M., Neuhäuser, R.: 2005, AN 326, 134
Burrows, A., Marley, M., Hubbard, W.B., et al.: 1997, ApJ 491, 856
Burrows, A., Hubeny, I., Budaj, J., Hubbard, W.B.: 2007, ApJ 661, 502
Butler, R.P., Wright, J.T., Marcy, G.W., et al.: 2006, ApJ 646, 505
Charbonneau, D., Brown, T.M., Latham, D.W., Mayor, M.: 2000, ApJ 529, L45
Charbonneau, D., Brown, T.M., Noyes, R.W., Gilliland, R.L.: 2002, ApJ 568, 377
Charbonneau, D., Berta, Z.K., Irwin, J., et al.: 2009, Nature 462, 891
Christian, D., Gibson, N., Simpson, E., et al.: 2009, MNRAS 392, 1585
Cochran, W.D., Hatzes, A.P., Butler, R.P., Marcy, G.W.: 1997, ApJ 483, 457
Contreras, M.E., Sicilia-Aguilar, A., Muzerolle, J., Calvet, N., Berlind, P., Hartmann, L.: 2002, AJ 124, 1585
Dahm, S.E.: 2008, in: B. Reipurth (ed.), *Handbook of Star Forming Regions, Vol. 1: The Northern Sky*, p. 966
Deming, D., Seager, S., Richardson, L.J., Harrington, J.: 2005, Nature 434, 740
Downes, J.J., Briceno, C., Hernandez, J., Calvet, N., Hartmann, L., Ponsot Balaguer, E.: 2008, AJ 136, 51
Eisenbeiss, T., Moualla, M., Mugrauer, M., et al.: 2009, AN 330, 439
Favata, F., Micela, G., Alencar, S., Aigrain, S., Zwintz, K.: 2010: Highlights in Astronomy 15, 752
Fischer, D., Marcy, D., Butler, P., Laughlin, G., Vogt, S.: 2002, ApJ 564, 1028
Fortney, J.J., Nettelmann, N.: 2010, Space Sci. Rev. 152, 423
French, M., Mattsson, T.R., Nettelmann, N., Redmer, R.: 2009, Phys. Rev. B 79, 054107
French, M., Mattsson, T.R., Redmer, R.: 2010, Phys. Rev. B 82, 174108
Frink, S., Mitchell, D.S., Quirrenbach, A., Fischer, D.A., Marcy, G.W., Butler, R.P.: 2002, ApJ 576, 478
Garrison, R.F., Kormendy, J.: 1976: PASP 88, 865
Goldreich, P., Tremaine, S.: 1980, ApJ 241, 425
Grether, D., Lineweaver, C.H.: 2006, ApJ 640, 1051
Guenther, E.W., Esposito, E.: 2007, astro-ph/0701293
Guillot, T.: 1999a, Sci 286, 27
Guillot, T.: 1999b, Planet. Space Sci. 47, 1183
Guillot, T., Santos, N., Iro, N., Melo, C., Ribas, I.: 2006, A&A 453, L21
Henry, G.W., Marcy, G.W., Butler, R.P., Vogt, S.S.: 2000, ApJ 529, L41
Hodgkin, S., Irwin, J., Aigrain, S., Hebb, L., Moraux, E., Irwin, M.: 2006, AN 327, 9
Holman, M., Fabrycky, D., Rogozzine, D., et al.: 2010, Sci 330, 51
Holst, B., Redmer, R., Desjarlais, M.P.: 2008, Phys. Rev. B 77, 184201
Horne, K.: 2003: in: D. Deming, S. Seager (eds.), *Scientific Frontiers in Research on Extrasolar Planets*, ASPC 294, p. 361
Huélamo, N., Figueira, P., Bonfils, X., et al.: 2008, A&A 489, L9
Irwin, J., Aigrain, S., Hodgkin, S., et al.: 2006, MNRAS 370, 954
Irwin, J., Hodgkin, S., Aigrain, S., et al.: 2007, MNRAS 377, 741
Irwin, J., Hodgkin, S., Aigrain, S., Bouvier, J., Hebb, L., Irwin, M., Moraux, E.: 2008a, MNRAS 384, 675
Irwin, J., Hodgkin, S., Aigrain, S., Bouvier, J., Hebb, L., Moraux, E.: 2008b, MNRAS 383, 1588
Irwin, J., Aigrain, S., Bouvier, J., Hebb, L., Hodgkin, S., Irwin, M., Moraux, E.: 2009, MNRAS 392, 1456
Joergens, V.: 2006, A&A 446, 1165
Joergens, V., Müller, A.: 2007, ApJ 666, L113
Joergens, V., Müller, A., Reffert, S.: 2010, A&A 521, 24
Kharchenko, N.V., Piskunov, A.E., Röser, S., Schilbach, E., Scholz, R.-D.: 2005, A&A 440, 403
Kietzmann, A., et al.: 2007, Phys. Rev. Lett. 98, 190602
Koch, D.G., Borucki, W.J., Basri, G., et al.: 2010, ApJ 713, L79
Konacki, M., Torres, G., Jha, S., Sasselov, D.: 2003, Nature 421, 507
Kramm, U., Nettelmann, N., Redmer, R., Stevenson, D.J.: 2011, A&A 528, 18
Krivov, A.V.: 2010, Res. A&A 10, 383
Kun, M., Kiss, Z.T., Balog, Z.: 2008, in: B. Reipurth (ed.), *Handbook of Star Forming Regions, Vol. 1: The Northern Sky*, p. 136
Lada, C., Lada, E.: 2003, ARA&A 41, 57
Latham, D., Stefanik, R.P., Mazeh, T., Mayor, M., Burki, G.: 1989, Nature 339, L38
Le Borgne, J.F., Bruzual, G., Pello, R., et al.: 2003, A&A 402, L433
Lin, D.N.C., Bodenheimer, P., Richardson, D.C.: 1996, Nature 380, 606
Lissauer, J.J., Fabrycky, D.C., Ford, E.B., et al.: 2011, Nature 470, 53
Lorenzen, W., Holst, B., Redmer, R.: 2009, Phys. Rev. Lett. 102, 115701
Lorenzen, W., Holst, B., Redmer, R.: 2010, Phys. Rev. B 82, 195107
Lovis, C., Segransan, D., Mayor, M., et al.: 2011, A&A 528, L112
Maciejewski, G., Dimitrov, D., Neuhäuser, R., et al.: 2010, MNRAS 407, 2625
Maciejewski, G., Dimitrov, D., Neuhäuser, R., et al.: 2011a, MNRAS 411, 1204
Maciejewski, G., Neuhäuser, R., Errmann, R., et al.: 2011b, in: F. Bouchy, R.F. Diaz, C. Moutou (eds.), *Detection and Dynamics of Transiting Exoplanets*, EPJ Web of Conferences 11, 04006
Marcy, G.W., Butler, R.P.: 1996, ApJ 464, L147

Marcy, G.W., Butler, R.P., Vogt, S., Fischer, D., Lissauer, J.: 1998, ApJ 505, L147
Marcy, G.W., Butler, R.P., Fischer, D., Vogt, S., Wright, J.T., Tinney, C.G., Jones, H.R.A.: 2005, Progress Theoret. Physics Suppl. 158, 24
Markarian, B.E.: 1952, Proc. Acad. Sci. Armenian SSR 15, 11
Marois, C., MacIntosh, B., Barman, T., et al.: 2008, Sci 322, 1348
Marois, C., Zuckerman, B., Konopacky, Q.M., Macintosh, B., Barman, T.: 2010, Nature 468, 1080
Marschall, L.A., van Altena, W.F.: 1987, AJ 94, 71
Marschall, L.A., Karshner, G.B., Comins, N.F.: 1990, AJ 99, 1536
Mayor, M., Queloz, D.: 1995, Nature 378, 355
Mazeh, T., Naef, D., Torres, G., et al.: 2000, ApJ 532, L55
Mercer, E.P., Miller, J.M., Calvet, N., Hartmann, L., Hernandez, J., Sicilia-Aguilar, A., Gutermuth, R.: 2009, AJ 138, 7
Miller A.A., Irwin, J., Aigrain, S., Hodgkin, S., Hebb, L.: 2008, MNRAS 387, 349
Moualla, M.: 2011: PhD Thesis, University Jena
Mugrauer, M.: 2009, AN 330, 419
Mugrauer, M., Avila, G.: 2009 AN 330, 430
Mugrauer, M., Berthold, T.: 2010, AN 331, 449
Mugrauer, M., Neuhäuser, R., Mazeh, T.: 2007, A&A 469, 755
Nettelmann, N., Holst, B., Kietzmann, A., French, M., Redmer, R., Blaschke, D.: 2008, ApJ 683, 1217
Nettelmann, N., Kramm, U., Redmer, R., Neuhäuser, R.: 2010, A&A 523, 26
Neuhäuser, R., Guenther, E.W., Wuchterl, G., Mugrauer, M., Bedalov, A., Hauschildt, P.H.: 2005, A&A 435, L13
Niedzielski, A., Konacki, M., Wolszczan, A., Nowak, G., Maciejewski, G., et al.: 2007, ApJ 669, 1354
Queloz, D., Eggenberger, A., Mayor, M.: 2000, A&A 359, L13
Raetz, St., Mugrauer, M., Schmidt, T.O.B., et al.: 2009a, in: F. Pont, D.D. Sasselov, M.J. Holman (eds.), *Transiting Planets*, IAU Symp. 253, p. 436
Raetz, St., Mugrauer, M., Schmidt, T.O.B., et al.: 2009b, AN 330, 459
Raetz, St., Mugrauer, M., Schmidt, T.O.B., et al.: 2009c, AN 330, 475
Rauer, H., Eisloeffel, J., Eriksen, A., Guenther E., Hatzes, A.P., Michaelis, H., Voss, H.: 2004, PASP 116, 38
Redmer, R., Mattsson, T.R., Nettelmann, N., French, M.: 2011, Icarus 211, 798
Reidemeister, M., Krivov, A.V., Schmidt, T.O.B., Fiedler, S., Müller, S., Löhne, T., Neuhäuser, R.: 2009, A&A 503, 247
Schmidt, T., Neuhäuser, R., Seifahrt, A., et al.: 2008, A&A 491, 311
Seeliger, M.: 2011: Diploma Thesis, University Jena
Setiawan, J., Henning, T., Launhardt, R., Müller, A., Weise, P., Kürster, M.: 2008, Nature 451, 38
Sicilia-Aguilar, A., Hartmann, L.W., Briceño, C., Muzerolle, J., Calvet, N.: 2004a, AJ 128, 805
Sicilia-Aguilar, A., Hartmann, L.W., Briceño, C., Contreras, M.E., Muzerolle, J., Calvet, N.: 2004b, Ap&SS 292, 457
Sicilia-Aguilar, A., Hartmann, L.W., Hernandes, J., Briceño, C., Calvet, N.: 2005, AJ 130, 188
Sicilia-Aguilar, A., Hartmann, L.W., Calvet, N., et al.: 2006a, ApJ 638, 897
Sicilia-Aguilar, A., Hartmann, L.W., Füresz, G., Henning, T., Dullemond, C., Brandner, W.: 2006b, AJ 132, 2135
Simonson, S.C.: 1968, ApJ 154, 923
Sota, A., Maiz Apellaniz, J., Walborn, N.R., et al.: 2011, ApJS 193, 24
Su, K., Rieke, G., Stapelfeldt, K., et al.: 2009, ApJ 705, 314
Tamuz, O., Mazeh, T., Zucker, S.: 2005, MNRAS 356, 1466
Torres, G., Winn, J.N., Holman, M.J.: 2008, ApJ 677, 1324
Triaud, A.H.M.J., Collier Cameron, A., Queloz, D., et al.: 2010, A&A 524, 25
Trumpler, R.J.: 1930, Lick Obs. Bull. 14, 420
Vaňko, M., Raetz, St., Mugrauer, M., et al.: 2009, in: F. Pont, D.D. Sasselov, M.J. Holman (eds.), *Transiting Planets*, IAU Symp. 253, p. 440
Winn, J.N., Fabrycky, D., Albrecht, S., Johnson, J.A.: 2010, ApJ 718, L145
Wolszczan, A.: 1994, Sci 264, 538
Wolszczan, A., Frail, D.: 1992, Nature 355, 145
Wu, Z.-Y., Zhou, X., Ma, J., Jiang, Z.-J., Chen, J.-S., Wu, J.-H.: 2007, AJ 133, 2061

Icarus 215 (2011) 17–26

Contents lists available at ScienceDirect

Icarus

journal homepage: www.elsevier.com/locate/icarus

Photometric observations of 107P/Wilson–Harrington

Seitaro Urakawa [a,*], Shin-ichiro Okumura [a], Kota Nishiyama [a], Tsuyoshi Sakamoto [a], Noritsugu Takahashi [a], Shinsuke Abe [b], Masateru Ishiguro [c], Kohei Kitazato [d], Daisuke Kuroda [e], Sunao Hasegawa [f], Kouji Ohta [g], Nobuyuki Kawai [h], Yasuhiro Shimizu [e], Shogo Nagayama [i], Kenshi Yanagisawa [e], Michitoshi Yoshida [j], Makoto Yoshikawa [a,f]

[a] *Bisei Spaceguard Center, Japan Spaceguard Association, 1716-3 Okura, Bisei, Ibara, Okayama 714-1411, Japan*
[b] *Institute of Astronomy, National Central University, 300 Jhongda Road, Jhongli, Taoyuan 32001, Taiwan*
[c] *Department of Physics and Astronomy, Seoul National University, 599 Gwanak-ro, Gwanak-gu, Seoul 151-742, Republic of Korea*
[d] *Research Center for Advanced Information Science and Technology, University of Aizu, Aizu-Wakamatsu, Fukushima 965-8580, Japan*
[e] *Okayama Astrophysical Observatory, NAOJ, 3037-5 Honjo, Kamogata, Asakuchi, Okayama 719-0232, Japan*
[f] *Institute of Space and Astronautical Science, Japan Aerospace Exploration Agency, 3-1-1 Yoshinodai, Chuo-ku, Sagamihara, Kanagawa 252-5210, Japan*
[g] *Department of Astronomy, Kyoto University, Sakyo-ku, Kyoto 606-8502, Japan*
[h] *Department of Physics, Tokyo Institute of Technology, 2-12-1 Ookayama, Meguro-ku, Tokyo 152-8551, Japan*
[i] *National Astronomical Observatory of Japan, 2-21-1 Osawa, Mitaka, Tokyo 181-8588, Japan*
[j] *Department of Physical Science, Hiroshima University, 1-3-1 Kagamiyama, Higashi-Hiroshima, Hiroshima 739-8526, Japan*

ARTICLE INFO

Article history:
Received 8 April 2011
Revised 17 June 2011
Accepted 21 June 2011
Available online 18 July 2011

Keywords:
Asteroids, Rotation
Comets
Photometry
Satellites of asteroids

ABSTRACT

We present lightcurve observations and multiband photometry for 107P/Wilson–Harrington using five small- and medium-sized telescopes. The lightcurve has shown a periodicity of 0.2979 day (7.15 h) and 0.0993 day (2.38 h), which has a commensurability of 3:1. The physical properties of the lightcurve indicate two models: (1) 107P/Wilson–Harrington is a tumbling object with a sidereal rotation period of 0.2979 day and a precession period of 0.0993 day. The shape has a long axis mode (LAM) of L_1:L_2:L_3 = 1.0:1.0:1.6. The direction of the total rotational angular momentum is around $\lambda = 310°$, $\beta = -10°$, or $\lambda = 132°$, $\beta = -17°$. The nutation angle is approximately constant at 65°. (2) 107P/Wilson–Harrington is not a tumbler. The sidereal rotation period is 0.2979 day. The shape is nearly spherical but slightly hexagonal with a short axis mode (SAM) of L_1:L_2:L_3 = 1.5:1.5:1.0. The pole orientation is around $\lambda = 330°$, $\beta = -27°$. In addition, the model includes the possibility of binary hosting. For both models, the sense of rotation is retrograde. Furthermore, multiband photometry indicates that the taxonomy class of 107P/Wilson–Harrington is C-type. No clear rotational color variations are confirmed on the surface.

1. Introduction

Asteroids and comets are primordial bodies that formed in the earliest stage of the Solar System. Their rotational states, shapes, and material reflect the collisions, disruptions, and chemical processes since then to the present. Some small Solar System bodies exhibit behavior such as that shown by both comets and asteroids (so-called, comet-asteroid transition objects). As an example, near-earth object (NEO) (3200) Phaethon shows signs of past cometary activity because it is thought to be associated with the Geminid (Gustafson, 1989). Dynamical numerical simulations and spectral observations for (3200) Phaethon support (2) Pallas, which is outer main belt asteroids, is the most likely parent body of (3200) Phaethon (Clark et al., 2010; de León et al., 2010). Meanwhile, objects that display cometary activities in the main-belt asteroid (MBA) region have recently been discovered. They are classified as main-belt comets (MBCs) (Hsieh and Jewitt, 2006); the MBCs are 133P/Elst-Pizzaro (Elst et al., 1996), P/2005 U1 (Read et al., 2005), 176P/LINEAR (Hsieh et al., 2011), P/2008 R1 (Garrad) (Jewitt et al., 2009), P/2010 A2 (LINEAR) (Birtwhistle et al., 2010), P/2010 R2 (La Sagra) (Marsden et al., 2010), and (596) Scheila (Bodewits et al., 2011; Jewitt et al., 2011). One possible activation mechanism for MBCs is impacts with small (e.g., meter-sized) objects (Toth, 2000; Díaz and Gil-Hutton, 2008; Jewitt et al., 2010; Snodgrass et al., 2010; Bodewits et al., 2011; Jewitt et al., 2011). The other activation mechanisms are rotational-fissions due to the spin-up by Yarkovsky–O'Keefe–Radzievskii–Paddack (YORP) effects (Jewitt et al., 2010), and thermal influences (Jewitt et al., 2009). Interesting properties of MBCs are their dynamical origin and possible function as reservoirs for water–ice and organics. A numerical integration by Haghighipour (2009) states that the origin of 133P/Elst-Pizarro, 176P/LINEAR, and P/2005 U1 (Read) is concordant with the Themis family of asteroids. Compared with all asteroids, the Themis family of asteroids

* Corresponding author.
E-mail address: urakawa@spaceguard.or.jp (S. Urakawa).

0019-1035/$ - see front matter © 2011 Elsevier Inc. All rights reserved.
doi:10.1016/j.icarus.2011.06.044

includes B-type asteroids at a relatively high population rate. Some B-type asteroids in the Themis family seem to have experienced aqueous alterations (Yang and Jewitt, 2010; Clark et al., 2010). (3200) Phaethon is also a B-type asteroid and shows the existence of aqueous alteration materials (Licandro et al., 2007). In addition, water–ice and organics are detected on the surface of (24) Themis (Rivkin and Emery, 2010) and (65) Cybele, which orbits along the outer edge of the main belt (Licandro et al., 2011). The study of comet–asteroid transition objects provides keys to the dynamical origin and evolution of NEOs, the mutual collisions of small Solar System bodies, the material differences between asteroids and comets, and the origin of Earth's water.

This study's purpose is to obtain the rotational states, shape model, and rotational color variations for 107P/Wilson–Harrington (also know as (4015) Wilson–Harrington; hereafter 107P), which is a representative comet-asteroid transition object. 107P was discovered accompanied by a faint cometary tail at Palomar Observatory in 1949 (Fernandez et al., 1997). The object, however, could not be tracked because of insufficient observations to determine an accurate orbit. Later, a near-earth Asteroid 1979VA (=4015) was discovered. Subsequent observations identified Asteroid (4015) 1979VA and 107P as the same object. Despite a devoted search, no cometary activity has been detected since the initial observation of 107P (Chamberlin et al., 1996; Lowry and Weissman, 2003; Ishiguro et al., 2011). 107P is an Apollo asteroid whose orbital parameters are a = 2.639 AU, e = 0.624, i = 2.785°, and the Tisserand parameters (T_J) = 3.08. A numerical simulation by Bottke et al. (2002) mentions that there is a 4% chance that 107P has a JFC origin and a 65% chance it has an origin in the outer main-belt region. Taxonomically, it is categorized as a CF-type (Tholen, 1989). The reflectance spectrum in the region 3800–6200 Å is similar to (3200) Phaethon (Chamberlin et al., 1996). The thermal properties of 107P have been investigated by mid-infrared photometry with NASA's Spitzer Telescope (Licandro et al., 2009). These observations show that the beaming parameter, the diameter, and the albedo are $\eta = 1.39 \pm 0.26$, $D = 3.46 \pm 0.32$ km, and $p_v = 0.059 \pm 0.011$, respectively. The rotational period of 107P has been reported to be 3.556 h and 6.10 ± 0.05 h by Harris and Young (1983) and Osip et al. (1995), respectively. Osip et al. (1995) ascribes the difference of the two reports to the noisy data of Harris and Young (1983) because of the weather conditions. The few days' observation in both reports, however, is not enough to determine the correct rotational period. Longer observations are required to derive the correct rotational period and other physical properties.

We hypothesize that 107P migrates to the NEO region from the outer main-belt region inhabited by six of seven known MBCs, and impacts with small objects could eject dust and/or expose sub-surface ice that then trigger 107P's cometary activity. Post-MBC, 107P is capable of becoming host to water–ice, organics, and aqueous alteration materials. In this hypothesis, the impacts' influence would be apparent in the rotational states and/or the surface color variations.

We had an opportunity to observe 107P from August 2009 to March 2010. Our long observation campaigns enable us to derive the rotational states, shape model, and rotational color variations. Furthermore, the orbit of 107P makes it accessible by spacecraft. A more advanced sample return mission from a D-type asteroid or an asteroid–comet transition object is envisioned in Japan. One candidate is 107P (Yoshikawa et al., 2008). Clarification of the physical properties of 107P is important to the design of the future mission. If we are able to obtain 107P's physical properties, the data will be useful to revise the physical model of Licandro et al. (2009), similar to the Hayabusa-2 target 162173 (1999JU3) whose physical model was reconstructed by both thermal observations and the lightcurve (Müller et al., 2011). This paper is organized as follows. In Section 2, we describe the observations made and the data reduction. In Section 3, we mention the rotational states and shape model of 107P. In Section 4, we focus on the possibility of tumbling motion and the existence of a binary. Finally, we summarize the physical model of 107P and discuss the feasibility of a sample return mission.

2. Observations and data reduction

2.1. Observations

We conducted the photometric observation campaigns of 107P with five small- and medium-sized telescopes. The observational circumstances and the states of 107P are listed in Tables 1 and 2, respectively. All telescopes were operated with the non-sidereal tracking mode. The longest-term observation of this campaign was carried out using the 1.0 m f/3 telescope at the Bisei Spaceguard Center (BSGC[1]) from September 6, 2009 to March 11, 2010. The detector consisted of four CCD chips with 4096 × 2048 pixels. We used one CCD chip to obtain as many images as possible by shortening the processing time. The field of view (FOV) for one CCD chip is 1.14° × 0.57° with a pixel resolution of 1.0″. The exposure time varied from 30 s to 600 s according to the observational situations. Individual images were taken with a commercially available short-pass (long-wavecut) filter, the effective wavelength of which ranged from 490 nm to 910 nm. We denote the filter as W in Table 1. In order to investigate rotational color variations, multiband photometry was conducted using a Sloan Digital Sky Survey (SDSS) g', r', i', z' filter on December 17, 2009. One set of observations was made using three consecutive images for each filter. The filters were changed in the following sequence: three g' images → three r' images → three i' images → three z' images. We repeated this sequence four times.

The second-longest-term observation used the 0.5 m f/6.5 Multicolor Imaging Telescope for Survey and Monstrous Explosions (MITSuME) (Kotani et al., 2005) at Okayama Astrophysical Observatory (OAO) from November 7, 2009 to December 21, 2009. The telescope is capable of obtaining a three-color (SDSS g', Johnson–Cousins R_c and I_c) image simultaneously. The detector is 1024 × 1024 pixels CCD with FOV of 26′ × 26′ (1.52″/pixel). The images were taken with an exposure time of 120 s. To search for the rotational color variation, we used the data of December 17 because they could be compared with the observations of the BSGC and the photometric precision of the other day's data was not sufficient to detect the color variation.

The third observation was carried out using a 1.05 m f/3.1 Schmidt telescope with 2048 × 2048 pixels CCD at Kiso Observatory on August 17, 19, and 20 and December 12, 2009. This instrument provides a FOV of 50′ × 50′ (1.46″/pixel). The images were obtained using a Kron–Cousins R_c filter with an exposure time of 120–300 s.

The fourth observation was made using the Lulin One-meter Telescope (LOT) (Huang et al., 2005) in Taiwan on December 7–10, 2009. The CCD consists of a 1340 × 1300 array, and the FOV covers the area of 11.5′ × 11.2′. The pixel resolution and f-number are 0.51″/pixel and 8, respectively. The images were obtained using a Johnson–Cousins R_c filter with an exposure time of 90 s.

The last, observation was made using the University of Hawaii 2.24 m f/10 telescope (UH88) on December 19, 2009, with a 2048 × 2048 pixels CCD. The FOV of the instrument is 7.5′ × 7.5′ with a pixel resolution of 0.44″. Almost all images were obtained using a Kron–Cousins R_c filter with an exposure time of 60 s.

2.2. Data reduction

All images were bias and flat-field corrected. When using the data of OAO for the derivation of lightcurve, we stacked four

[1] BSGC is administrated by the Japan Space Forum.

Table 1
Observation states.

Observatory	Year/Mon/Day	Exp. time (s)	Filter
BSGC	2009/12/17	300	g', r', i', z'
BSGC[†]	2009/09/6,7,9,10,15,16,19, 2009/10/8,10,28	30–180	W
BSGC	2009/11/3,5–7,11,14, 2009/12/5,7–9,19,22	60–300	W
BSGC	2010/01/3,6–8,14–18,22,23	180–300	W
BSGC[a]	2010/02/3–5,7,9,16,18,19, 2010/03/11	240–600	W
OAO	2009/11/7,14,15,18–21,23,	120	g', R_c, I_c
OAO	2009/12/1,2,6,7,14,16–21	120	g', R_c, I_c
KISO[a]	2009/08/17,19,20, 2009/12/12	120–300	R_c
LOT	2009/12/7–10	90	R_c
UH88	2009/12/19	60	R_c

[a] A sufficient number of data was not obtained from August to October because the altitude of 107P fell below 25° about 30 min from the observation start and 107P overlapped stars of the galactic plane. The photometric precision was insufficient after February 7, 2010. We did not use these data for the estimation of rotational periods and shape models. These data were utilized for the trend confirmation of lightcurves that were obtained from the other day's data and the monitoring of cometary activity.

Table 2
States of 107P in each month.

Year/Mon/Day	Δ[a] (AU)	R[b] (AU)	α[c] (°)	Sky motion (″/min)	m[d]
2009/08/17–20	0.687–0.684	1.309–1.286	49.8–51.4	0.45–0.55	17.7–17.7
2009/09/6–19	0.653–0.612	1.162–1.084	59.9–66.0	1.09–1.49	17.9–17.9
2009/10/8–28	0.529–0.434	1.008–0.995	73.8–77.2	2.18–3.26	17.3–17.5
2009/11/3–23	0.410–0.382	1.006–1.083	76.3–65.4	3.65–4.52	17.1–16.7
2009/12/1–22	0.401–0.543	1.130–1.277	59.2–46.3	4.31–2.96	16.6–17.0
2010/01/3-23	0.670–0.936	1.373–1.539	42.0–37.8	2.32–1.70	17.4–18.4
2010/02/3–19	1.105–1.372	1.632–1.767	36.1–33.8	1.51–1.34	18.8–19.7
2010/03/11	1.732	1.932	30.8	1.22	20.0

[a] Object to observer distance.
[b] Heliocentric distance.
[c] Phase angle (Sun–107P–observer).
[d] Apparent magnitude. This value is estimated using UCAC 2 catalog stars that are taken in the same field with 107P.

images to compensate for the poor flux. All observation times were corrected using the light travel time from 107P to the Earth. By using the IRAF/APPHOT[2] package, we measured the raw magnitude of 107P and from three to seven reference stars that were bright enough compared with 107P. We set aperture radius to 1.5× FWHM for 107P and reference stars images, respectively. Since the reference star images are slightly elongated by the non-sidereal tracking, the aperture radius is larger than that of 107P. We calibrated the magnitude fluctuations due to the change of atmospheric conditions as follows:

$$F_c^i(t) = F_o^i(t) - \overline{F_r^i(t)}. \tag{1}$$

Here, $F_c^i(t)$ is the lightcurve by rotation of 107P in ith observation day, $F_o^i(t)$ is the raw magnitude of 107P, $\overline{F_r^i(t)}$ is the averaged raw magnitude of reference stars and represents the change of atmospheric conditions, and t is the observational time. Next, we define the averaged magnitude of $F_c^i(t)$ in each night as the normalized (zero) magnitude. The lightcurve by rotation of 107P can be rewritten as

$$F_{wh}^i(t) = F_c^i(t) - \overline{F_c^i}, \tag{2}$$

where $\overline{F_c^i}$ is the averaged magnitude of $F_c^i(t)$. Since the averaged magnitude is normalized to zero magnitude for all nights, we can connect the different night's lightcurve with little regard for the difference of absolute magnitude. In addition, the difference of reference stars each night does not affect the periodicity of lightcurve. The problem of this procedure could include the offset between different nights when the short observation time per day poses the detection of a specific peak (bottom) in the lightcurve. However, the peaks and bottoms in the lightcurve have been detected evenly (see Fig. 3) because the observation time per day is long enough from November 2009 to February 2010 when the data are utilized for the analysis. Thus, the offset is negligible. Furthermore, the apparent magnitude change of 107P is gradual up to 1.0 magnitude per month (Table 2). The change does not act on the derivation of rotational period that is expected to be from 3 to 7 h according to past reports.

In contrast to the relative photometry of the lightcurve, more photometric precision is required to detect the rotational color variation by multiband photometry. In order to improve the photometric precision, we averaged three consecutive images of 107P for the BSGC's data and 14–16 consecutive images of 107P for the OAO's data. We also measured the flux of ten standard stars from SDSS data Release 7 (Abazajian et al., 2009), whose stars were imaged simultaneously in the same frame as 107P (Table 3). These objects have magnitudes of about 14–16 mag in the r'-band and classification code 1 (=primary), quality flag 3 (=good), and object class 6 (=star). We evaluated atmospheric extinction coefficients and conversion factors to standardize the SDSS system for each filter. The atmospheric extinction coefficient was calculated by the magnitude variations of the standard stars for the change in airmass. Extra-atmospheric instrumental magnitudes of both 107P and the standard stars were derived using the obtained atmospheric extinction coefficient. The conversion factors were estimated by comparing the extra-atmospheric instrumental magnitudes with the magnitude of standard stars. In BSGC's observation, the multi-color images were not obtained simultaneously. The brightness of 107P by the rotation changes inevitably during the filter switch. We defined the time of the third r' images in each

[2] IRAF is distributed by the National Optical Astronomy Observatory, which is operated by the Association of Universities for Research in Astronomy (AURA) under cooperative agreement with the National Science Foundation.

Table 3
Standard stars in SDSS-7.

Ra (°)	Dec (°)	g′	r′	i′	z′
12.051081	8.615352	15.891 ± 0.003	15.279 ± 0.003	15.057 ± 0.003	14.913 ± 0.005
12.246608	8.604861	15.209 ± 0.003	14.756 ± 0.003	14.598 ± 0.003	14.525 ± 0.004
12.073952	8.515561	14.536 ± 0.003	14.215 ± 0.003	14.115 ± 0.003	14.074 ± 0.004
12.011267	8.489718	15.766 ± 0.004	14.891 ± 0.004	14.587 ± 0.003	14.444 ± 0.004
12.275938	8.545386	16.158 ± 0.003	15.566 ± 0.003	15.349 ± 0.004	15.230 ± 0.005
11.898784	8.539119	14.947 ± 0.003	14.554 ± 0.003	14.418 ± 0.003	14.366 ± 0.004
12.365509	8.569521	14.587 ± 0.003	14.037 ± 0.003	13.839 ± 0.003	13.713 ± 0.003
12.374946	8.538940	16.005 ± 0.003	15.555 ± 0.003	15.396 ± 0.004	15.307 ± 0.005
11.796300	8.569376	15.308 ± 0.003	14.641 ± 0.003	14.413 ± 0.003	14.287 ± 0.004
12.371825	8.478789	15.763 ± 0.004	15.298 ± 0.004	15.156 ± 0.004	15.099 ± 0.005

sequence as a standard time, and then calibrated the amount of brightness change for the standard time. The amount of brightness change was estimated by the fitting curve of the lightcurve. In order to compare the OAO's data with BSGC's, the R_c and I_c magnitudes obtained at OAO were converted to r' and i' magnitudes using the conversion equations proposed by Jordi et al. (2006).

3. Results

3.1. Rotational states

Since the "Standard Feature (*SF*)" that is, the flux peaks and/or bottoms in lightcurves, shifts along the phase of lightcurves due to changes in the geometric relationship between the Earth, 107P, and the Sun during the long-term observations, the estimation of the sidereal rotation period for 107P requires a short-term observation within a few weeks. We use the data from December 7 to 22, when the phase-shift is small. The photometric precision of 107P and the observational implementation time per day are enough to make clear the sidereal rotational period during the term. Assuming double-peak lightcurves, a period analysis is carried out with a Lomb–Scargle periodgram (Lomb, 1976; Scargle, 1982). The power spectrum from the period analysis shows four period candidates of 0.0993 day, 0.2294 day, 0.2591 day and 0.2979 day (Fig. 1). A typical error of 0.0002 day corresponds to ±0.005 h. Though the most significant candidate is 0.2591 day, we conclude that 0.2979 day ($\simeq$7.15 h) is the sidereal rotation period of 107P for the following reasons. First, the amount of the amplitude in the folded lightcurve with 0.2591 day is not stable in the same phase. That is to say, the different amplitudes overlap on a specific phase. For example, the lightcurve peaks and bottoms overlap around the phase of 0.2–0.4 in the folded lightcurve with 0.2591 day (Fig. 2: Top). In the case of the folded lightcurve with 0.2979 day, the same amplitudes appear periodically (Fig. 2: Bottom. A few lightcurves each night are also shown in Fig. 3). The periods of 0.2591 day and 0.2979 day correspond approximately to 3.86 and 3.36 cycles per day, respectively. The difference is just 0.5 cycles per day. Lightcurves mainly represent the light scattering cross section of objects. When we assume that an object is a symmetric ellipsoidal body, almost the same cross section appears in every half rotation. Therefore, it is difficult to distinguish the difference of the half rotation using the short observation time, which is comparable with the sidereal rotation period. We call the indistinctive period a pseudo-period. The periods of 0.2591 day and 0.2294 day (=4.36 cycles per day) are the pseudo-period of 0.2979 day. Second, the period of 0.2979 day is able to explain the previous reports about the sidereal rotation period of 107P. Since the period of 0.2979 day is around twice the period of Harris and Young (1983) (0.1482 day $\simeq$ 3.556 h), their data show enough periodicity in 0.2979 day. Needless to say, assuming the lightcurve of 107P has a triple-peak, the period of 0.1490 day ($\simeq$3.58 h) is also a candidate

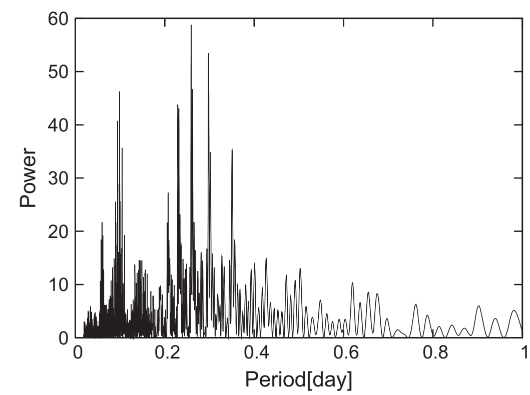

Fig. 1. Power spectrum for the sidereal rotation period of 107P by assuming the double-peak lightcurve. The calculation is carried out on data obtained from December 7 to 22.

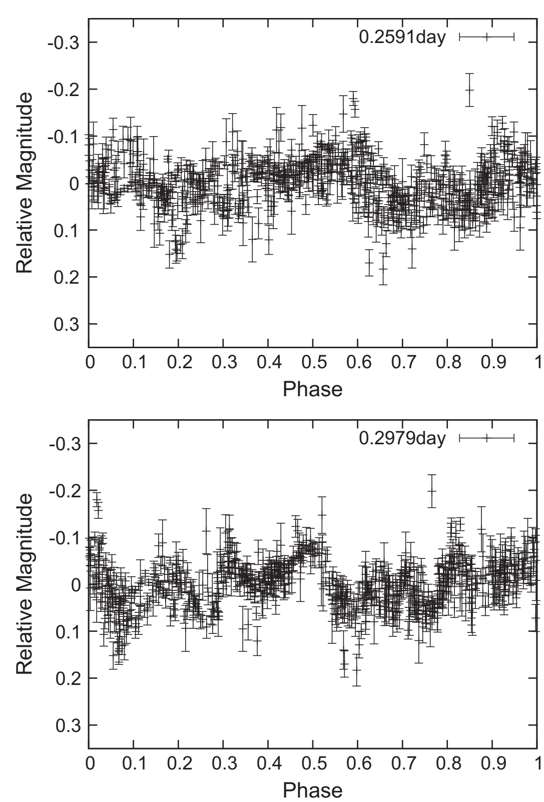

Fig. 2. Lightcurve of 107P. (Top) The lightcurve is folded with 0.2591 day. The peak and bottom of the lightcurve overlap around the phase between 0.2 and 0.4. (Bottom) The lightcurve is folded with 0.2979 day. The same amplitudes appear periodically.

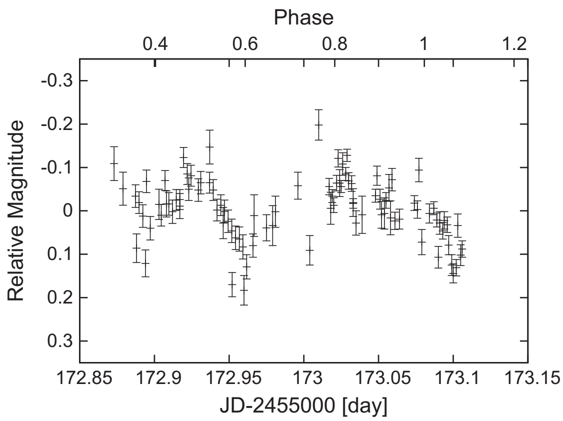

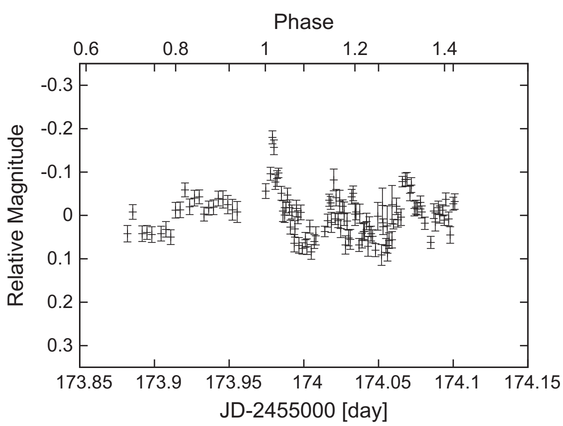

Fig. 3. (Top) Lightcurve in December 7, 2009. (Bottom) Lightcurve in December 8, 2009. The phase corresponding to Fig. 2 is added to the top scale of the figures.

for the sidereal rotation period. However, the possibility of 0.1490 day is eliminated by the inconsistency with the data of Osip et al. (1995). Harris and Young (1983) would recognize their lightcurve as the typical double-peak with the period of 3.556 h, because the third amplitude of flux in their lightcurve was not detected. Moreover, the period of Osip et al. (1995) (0.2542 day = 6.1 ± 0.05 h) is approximately the same as 0.2591 day ($\simeq$6.22 h). Our data set also has a sufficiently high significance level around the period of 0.2542 day. As we mentioned above, however, the period of around 0.2591 day is a pseudo-period. Since the observation term of Osip et al. (1995) was only 2 days, the demarcation of a pseudo-period would have been difficult. Third, we focus on the lightcurve of 0.2979 day as having an unusual six peaks. The period of 0.0993 day is just one-third that of 0.2979 day. If 107P has a typical double-peak lightcurve, the period of 0.0993 day is the sidereal rotation period. However, the amplitudes overlap the different three peaks and bottoms in the folded lightcurve with a period of 0.0993 day. Thus, we exclude the period of 0.0993 day as the sidereal rotation period.

On the other hand, the period of 0.0993 day may be the precession period. If an object has tumbling motions, the lightcurve is dominated by two periods: one, P_ψ, for the rotation about the extremal axis of the object as an inertia ellipsoid, and the other, P_ϕ, for the precession about the total rotational angular momentum vector. When frequencies are defined as $2f_\psi = P_\psi^{-1}$ and $2f_\phi = P_\phi^{-1}$, the lightcurve periodicity of tumbling objects appears at frequencies that are a linear combination of f_ψ and f_ϕ (Kaasalainen, 2001). When we assume that P_ψ is 0.2979 day and P_ϕ is 0.0993 day, the frequency $4f_\psi = 2(f_\phi - f_\psi) = 6.713\ \mathrm{day}^{-1}$ approximately corresponds to the inverse of period of Harris and Young (1983) and one half of our rotational period of 0.2979 day. The existence of periodicity of the linear combination of two periods shows circumstantial evidence for tumbling. We make the shape model of 107P in the following subsection and discuss the feasibility of tumbling motion in Section 4.1.

3.2. Direction of total rotational angular momentum and shape model

Above, we suggested the possibility of tumbling motion. If 107P is a tumbler, the pole orientation does not accord with the direction of total rotational angular momentum and is not stable. What we can obtain is not the pole orientation but the direction of total rotational angular momentum. The direction of total rotational angular momentum of 107P can be estimated using the "epoch method" (Magnusson, 1986) or the "lightcurve inversion method" (Kaasalainen and Torppa, 2001; Kaasalainen et al., 2001, 2002). The "amplitude method" is also proposed as an alternative method (Magnusson, 1986). However, we cannot adopt the amplitude method because of the small amplitude change during the observational term. The epoch method determines the direction of total rotational angular momentum by minimizing the phase-shift of the *SF* in lightcurves. We select a lightcurve peak around the phase of 0.01 at the bottom of Fig. 2 as the *SF* because the peak is better observed than any other feature. Moreover, we use the data obtained from November 5, 2009 to February 5, 2010. The identification of the lightcurve peak is difficult from the data of another term because of the photometric error. The phase-shift can be written as

$$\frac{T_i - T_0}{P_\psi} - n_i = \frac{\theta_i - \theta_0}{2\pi}, \tag{3}$$

where T_0 is the time at the first *SF*, T_i is the time at the *i*th *SF*,P_ψ is the sidereal rotational period, and n_i is the number of rotations between T_0 and T_i. θ_0 and θ_i are the projected directions of the phase angle bisector (*PAB*) in the plane that is perpendicular to the direction of total rotational angular momentum at T_0 and T_i, respectively. Table 4 shows the epoch of *SFs*. The left hand of Eq. (3) is estimated from the observations; the right hand is theoretically calculated from the tentative direction of total rotational angular momentum and the orbital information of 107P. We define δ with the following equation

$$\delta = \sum_i^N \sqrt{\left(\frac{T_i - T_0}{P_\psi} - n_i - \frac{\theta_i - \theta_0}{2\pi}\right)^2 / (N-1)}, \tag{4}$$

where N is the number of the epoch; here $N = 4$. We can estimate the direction of total rotational angular momentum by seeking the minimum of δ. Fig. 4 shows the δ map that is obtained by scanning the celestial sphere with a trial axis in steps of 1° in ecliptic longitude and latitude. Two candidates are found near the directions, A ($\lambda = 310°$, $\beta = -10°$) and B ($\lambda = 132°$, $\beta = -17°$). Since the epoch method generally derives two solutions with around the same significance level, we cannot determine a unique solution.

The lightcurve inversion method derives the most adequate shape model and the corresponding direction of total rotational angular momentum. When carrying out the lightcurve inversion method, we set the initial conditions for the direction of total rota-

Table 4
Epoch of Standard Feature (*SF*) and the amount of phase-shift.

Year/Mon/Day	Ecliptic longitude (PAB) [°]	Ecliptic latitude (PAB) [°]	Amount of phase-shift ($\times 10^{-2}$)
2009/11/5	341.958	4.611	0
2009/12/10	30.902	2.805	−5.305
2009/12/20	54.706	1.094	−6.113
2010/01/3	57.829	0.879	−7.794
2010/02/5	76.114	−0.202	−8.506

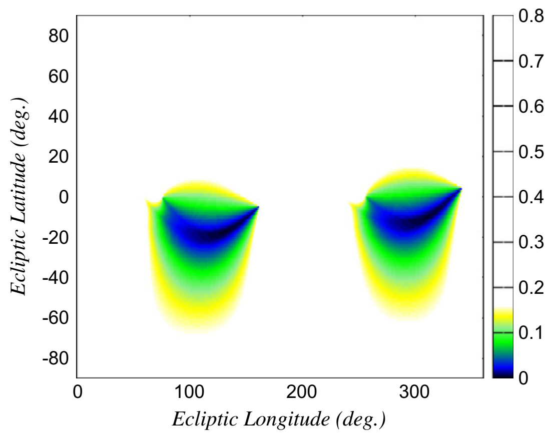

Fig. 4. δ maps for the direction of total rotational angular momentum by the epoch method.

tional angular momentum and the sidereal rotation period to that of 0.2979 day. We seek the least deviation between the observational lightcurve and the reconstructed lightcurve from the shape model by scanning the direction of total rotational angular momentum in steps of 1° in ecliptic longitude and latitude. We use the data of November 16, 1979 (Harris and Young, 1983); December 1–2, 1992 (Osip et al., 1995); and our high photometric precision data (the error is less than 0.05 mag), which was obtained from November 7, 2009 to January 18, 2010. Fig. 5 shows the deviation map of the direction of total rotational angular momentum using the lightcurve inversion method. In addition to the candidates of the epoch method, we have found three other candidates: C ($\lambda = 330°$, $\beta = -27°$), D ($\lambda = 328°$, $\beta = -61°$), and E ($\lambda = 167°$, $\beta = 7°$). However, we exclude the candidates D and E because they are less compatible with the epoch method. Note that the observational data was obtained in the phase angle from 21° to 77°. There is no data in a low phase angle. Furthermore, the direction of rotational angular momentum has an uncertainty of typically more than 5°. For example, though the ground-based observation of Itokawa showed that the pole orientation was $\lambda = 355°, \beta = -84°$ (Kaasalainen et al., 2003), the Hayabusa spacecraft revealed that the pole orientation of Itokawa was $\lambda = 128.5°$, $\beta = -89.66°$ (Demura et al., 2006). Moreover, we can see from Table 4 that the *SF* in the lightcurve shifts to the negative direction with time. As a corollary, the direction of total rotational angular momentum of the three candidates is south of the ecliptic plane.

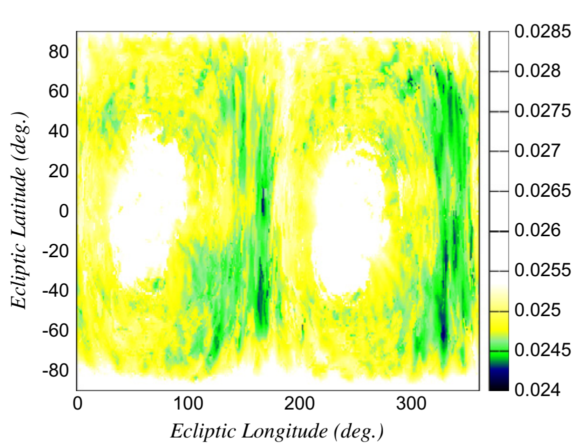

Fig. 5. Deviation maps for the direction of total rotational angular momentum by the lightcurve inversion method.

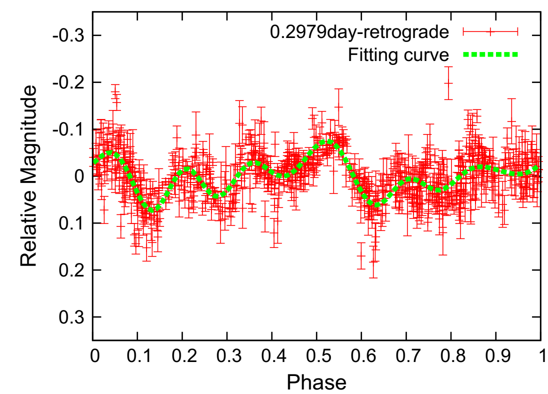

Fig. 6. Calibrated lightcurve for phase-shift. The fitting curve is described by two-order two-dimensional Fourier series.

This indicates that the sense of sidereal rotation is retrograde. The lightcurve of Fig. 6 has been calibrated for the phase-shift. The six peaks and the periodicity in the lightcurve become clearer than in the lightcurve of 0.2979 day period in Fig. 2. This result adds to the evidence of the retrograde rotation.

Next, we make the three shape models of 107P for the directions of total rotational angular momentum A, B and C. The shape model A is shown in Fig. 7. Here, L_1, L_2, and L_3 are defined as the normalized axis length when 107P is a triaxial ellipsoid body. The axes satisfy the relationship $L_1 \leqslant L_2 \leqslant L_3$. L_3 is a sidereal rotation axis of the shape model A. We have found that the normalized axis lengths L_1, L_2, and L_3 are around 1.0, 1.0, and 1.6, respectively. The axis ratio of the shape model B is around the same as that of the shape model A. The shape model A and B indicate a so-called long axis mode (LAM). Some previous studies have described the motion of a force-free asymmetric rigid body (Samarasinha and A'Hearn, 1991; Kaasalainen, 2001). Now, $L_1 \simeq L_2$ indicates that the equations of force-free precession are simplified to the following:

$$\dot{\psi} = \cos\theta\left(\frac{M}{I_3} - \dot{\phi}\right), \tag{5}$$

$$\dot{\phi} = \frac{M}{I_1}, \tag{6}$$

$$I_1 = \frac{\mu}{20}\left(L_2^2 + L_3^2\right), \tag{7}$$

$$I_3 = \frac{\mu}{20}\left(L_1^2 + L_2^2\right). \tag{8}$$

Here, ψ, ϕ, θ are the Euler angles of sidereal rotation, precession, and nutation, respectively. M is the total rotational angular momentum in an inertial frame. I_1 and I_3 express the inertia moment of a triaxial ellipsoid by using mass μ. Moreover, the equations show that the motion of the external axis about M occurs as a constant rate. From these equations and $\dot{\phi} = 3\dot{\psi}$, the nutation is negligible, and the angle θ is constant around 65°. A tilted, rugby-ball-shaped body rotates with a period of 0.0993 day about the total rotational angular momentum, and with a period of 0.2979 day about the external axes of 107P itself. Alternatively, we can assume a case that has the sidereal rotation of 0.0993 day and the precession period of 0.2979 day. Substituting $\dot{\psi} = 3\dot{\phi}$, there is no solution for the nutation angle. Therefore, the assumption is not adequate.

Meanwhile, as we show in Fig. 8, the normalized axis lengths for the shape model C are around 1.5, 1.5, and 1.0. Here, the axes satisfy the relationship $L_1 \geqslant L_2 \geqslant L_3$. L_3 is a sidereal rotation axis. Thus, the shape model C is a short axis mode (SAM). The rotation and precession of a SAM are in opposite direction from $I_1 < I_3$. We calculate the nutation angle by assuming $\dot{\phi} = -3\dot{\psi}$. However, there

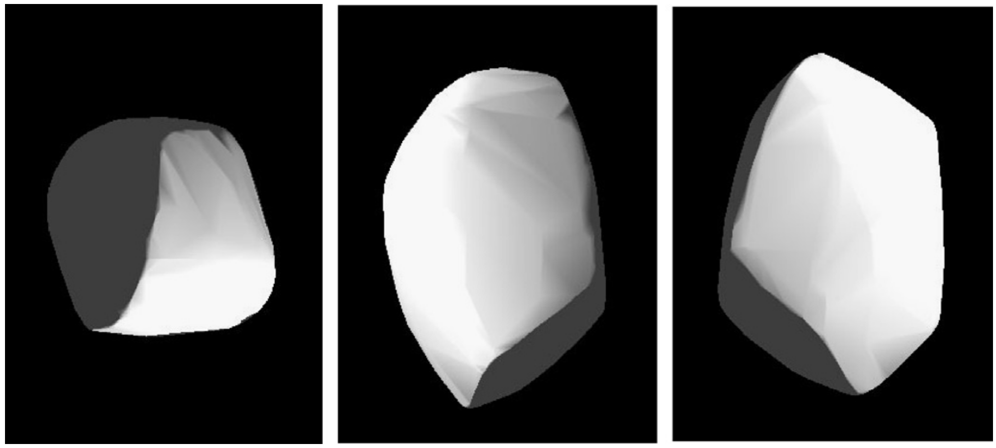

Fig. 7. Shape model A of 107P. (Left) Pole-on view. (Center) Equatorial view from the right side of the pole-on image. (Right) Equatorial view from the bottom of the pole-on image.

Fig. 8. Shape model C of 107P. (Left) Pole-on view. (Center) Equatorial view from the right side of the pole-on image. (Right) Equatorial view from the bottom of the pole-on image.

is no solution for the nutation angle. To obtain the solution for the nutation angle, $\dot{\phi}$ should be less than $-3.62\dot{\psi}$ if the axis lengths of the shape model C are correct, or the axis lengths of L_1 and L_2 should be longer than $\sqrt{3}L_3$ if $\dot{\phi} = -3\dot{\psi}$ and $L_1 \simeq L_2$ are correct. These situations are inconsistent with our results. Therefore, 107P of the shape model C is a non-precession object rather than a precessional object.

3.3. Taxonomic class and rotational color variations

The taxonomic class and rotational color variations for 107P were investigated by a color–color diagram. We note that the classification of subclasses, such as B, F, or G-type, is difficult using multiband photometry. We conducted the multiband photometry eight times (*Phase*-1 to -8). The obtained color–color diagram and the color index are shown in Fig. 9 and Table 5. We utilized the z' images of *Phase*-6 for those of *Phase*-7 due to the poor weather conditions in *Phase*-7. The color–color diagram macroscopically shows that 107P is a C-type (including B, F, G-type) asteroid. The colors of *Phase*-2 and *Phase*-6 indicate typical C-type features in the three color indices. The others are slightly reddish features like an X-type asteroid in the color index of $r'–i'$. Though only the $g'–r'$ of *Phase*-3 barely exceed the one-sigma of mean color index in Table 5, it is difficult to assert the detection of the rotational color variation due to the photometric error. In addition to it, the long observation term of ~0.15 in phase (~1.0 h) for each sequence obscures the detection of rotational color variation. In order to confirm the color variations, follow-up observations and/or exploration by spacecraft are needed.

4. Discussion

4.1. Tumbling

We discuss the possibility of tumbling. There were some reports in which asteroid lightcurves indicated tumbling, e.g., (253) Mathilde (Mottola et al., 1995), (3288) Seleucus (Harris et al., 1999), and (4179) Toutatis (Spencer et al., 1995; Kryszczyńska et al., 1999). Pravec et al. (2005) assessed the validity of tumbling for these asteroids based on whether the lightcurves could be approximated with two-dimensional Fourier series and the physical model of tumbling could be constructed. The two-dimensional Fourier series is described in the following form:

$$F^m(t) = C_0 + \sum_{j=1}^{m}\left[C_{j0}\cos\frac{2\pi j}{P_\psi}t + S_{j0}\sin\frac{2\pi j}{P_\psi}t\right] + \sum_{k=1}^{m} \times \sum_{j=-m}^{m}\left[C_{jk}\cos\left(\frac{2\pi j}{P_\psi}+\frac{2\pi k}{P_\phi}\right)t + S_{jk}\sin\left(\frac{2\pi j}{P_\psi}+\frac{2\pi k}{P_\phi}\right)t\right], \quad (9)$$

where m is the order, C_0 is the mean reduced light flux, C_{jk} and S_{jk} are the Fourier coefficients for the linear combination of the two frequencies P_ψ^{-1} and P_ϕ^{-1}, respectively, and t is the time. Substituting $m = 2$, $P_\psi = 0.2979$ day, and $P_\phi = 0.0993$ day for 107P, we obtain a fitting curve, as shown in Fig. 6. The fitting curve adequately reconstructs the trend of the lightcurve. However, since the sidereal rotation period and the processing period have a commensurability of 3:1, the lightcurve can also be reconstructed using the one-dimensional Fourier series of sixth order. As we mentioned in Section 3.2,

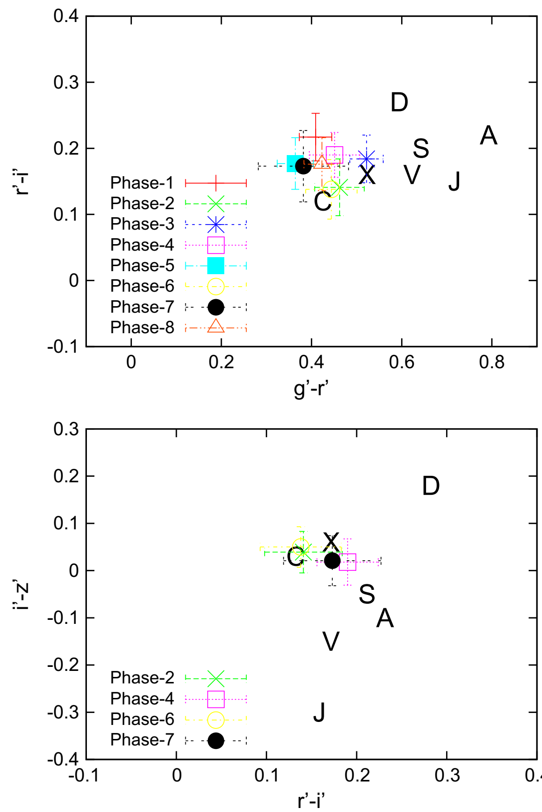

Fig. 9. Color–color diagram of 107P. Letters in the figure represent the taxonomic classes of asteroids on the color–color diagram (Ivezić et al., 2001). X-type asteroids include E, M, and P-type asteroids. The case of low-albedo asteroids indicates P-type.

the physical model is possibly constructed using a LAM of L_1:L_2:L_3 = 1.0:1.0:1.6,(λ = 310°, β = −10°) or (λ = 132°, β = −17°), θ = 65°, P_ψ = 0.2979 day, and P_ϕ = 0.0993 day. Although Pravec et al. (2005) mentions that a tumbling asteroid generally does not return to the same orientation in any single period, the approximately equal length of L_1 and L_2 for 107P suggests a negligible change for the nutation angle. Therefore, 107P can return to the same orientation every 0.2979 day. These circumstances imply that 107P might be a tumbling object.

Assuming 107P is a tumbler, external forces are required to trigger the motion. Impacts of small objects, tidal encounters with planets, and YORP effects are suggested by Pravec et al. (2005). Though 107P is a NEO, the object did not have an encounter with Earth in 1949. In the case of km-size objects, the efficient onset of tumbling by YORP requires a longer timescale than that of collision with small objects (Vokrouhlický et al., 2007). Therefore, we propose the impact of small objects as a probable cause for tumbling of 107P. The orbital origin of 107P has a high possibility of being from the outer MBA region inhabited by MBCs. One possibility is that the cometary activities of MBCs are caused by impacts of small objects. We can consider that 107P is originally an object like an MBC and impacts with small objects in the NEO region could eject dust and/or expose sub-surface ice that then trigger 107P's cometary activity. When we suppose that the collisional excitation happened in 1949, the damping timescale (Harris, 1994) is expressed as

$$\tau = \frac{P_\psi^3}{C^3 D^2}, \tag{10}$$

where D is the mean diameter of tumblers in kilometer units and C is a constant of about 17 (uncertain by about a factor of 2.5). The units of P_ψ and τ are hours and billion (10^9) of years, respectively. Since the damping timescale of around 6.2×10^6 yr is long enough, 107P would continue tumbling even if the impact occurred before 1949.

4.2. Binary asteroids

We describe the situation in which 107P hosts a binary. In order to confirm the existence of a binary, the detection of mutual eclipse events is required in the lightcurve. The mutual eclipse events were not detected in the observations of Harris and Young (1983) and Osip et al. (1995) because of the viewing angle, the lower photometric precision, or the absence of the binary. On the other hand, we detected the around same flux decrease in every 0.50 phase. Therefore, the existence of the binary is conceivable as the other interpretation of the shape model C. If we define the flux decrease around the phase of 0.15 (or 0.30, 0.45) and 0.65 (or 0.80, 0.95) in Fig. 6 as the primary (secondary) eclipse and the secondary (primary) eclipse, respectively, the orbital period of the binary is 0.2979 day. Supposing a circular orbit and negligible mass for the binary, the semi-major axis is described as

$$a = \left(\frac{GMP_{orb}^2}{4\pi^2}\right)^{\frac{1}{3}}, \tag{11}$$

where G is the gravitational constant, M is the mass of 107P, and P_{orb} is the orbital period of the binary. For the sake of simplicity, when assuming that 107P is spherical with the diameter of 3.46 km (Licandro et al., 2009) and a typical density of 2 g/cm^3, the semi-major axis is around 3.65 km. In the case of the same albedo for 107P and the binary, the flux decrease of the total eclipse (A_{mut}) satisfies the following relationship (Polishook et al., 2011)

$$A_{mut} = 2.5 log\left[1 + \left(\frac{R_s}{R_p}\right)^2\right], \tag{12}$$

where R_s is the radius of the binary and R_p is the radius of 107P. Since the typical flux decrease is ~0.05 mag in Fig. 6, the radius of the binary is around 0.4 km. When we assume the orbital plane of

Table 5
Color index of 107P. The observation term (Obs term) of each sequence is expressed as the rotational phase in the lightcurve. Since the data of the OAO are obtained with three bands, there is no color index of i'–z'. Mean shows the arithmetic average and standard deviation of each color index.

	Obs term (Phase)	Observatory	$g' - r'$	r'–i'	i'–z'
Phase-1	0.0365–0.1221	OAO	0.409 ± 0.036	0.217 ± 0.036	
Phase-2	0.0048–0.1590	BSGC	0.462 ± 0.055	0.141 ± 0.043	0.039 ± 0.044
Phase-3	0.1348–0.2177	OAO	0.522 ± 0.037	0.184 ± 0.036	
Phase-4	0.1941–0.3335	BSGC	0.451 ± 0.056	0.190 ± 0.034	0.018 ± 0.049
Phase-5	0.2345–0.3177	OAO	0.364 ± 0.040	0.177 ± 0.039	
Phase-6	0.3461–0.5045	BSGC	0.444 ± 0.057	0.138 ± 0.045	0.050 ± 0.043
Phase-7	0.4662–0.5426	BSGC	0.382 ± 0.100	0.173 ± 0.054	0.021 ± 0.053
Phase-8	0.9590–1.0239	OAO	0.423 ± 0.040	0.176 ± 0.040	
Mean	–	–	0.432 ± 0.050	0.175 ± 0.026	0.032 ± 0.015

107P accords with the line of sight from an observer, the inclination of the binary as an occulter satisfies

$$\sin i < \frac{R_p + R_s}{a}. \tag{13}$$

Here, i is the inclination of the binary for the orbital plane of 107P is less than 36° in the 107P system. If i is zero, the eclipse duration is estimated to be ~0.05 day. The term is around one-sixth of the orbital period and consistent with the interval of lightcurve peaks of Fig. 6. Moreover, the binary hypothesis indicates that the double-peak period of the lightcurve without the eclipse becomes 0.1490 day. As we mentioned in Section 3.1, the period of 0.1490 day as the sidereal rotation of 107P is not likely. Alternatively, the lightcurve without the eclipse might be a quadruple-peak lightcurve whose period is 0.2979 day. Though the quadruple-peak lightcurve is rare, the period could compatibly account for all the past reports. In addition, the situation shows that the sidereal rotation of 107P and the orbital periods of the binary are locked with 0.2979 day. The period of 0.0993 day is explained by the period between the egress time of the primary (secondary) eclipse and the ingress time of the secondary (primary) eclipse.

The promising mechanisms for formation of asteroid binaries are the rotational-fission due to the spin-up by YORP effects (Scheeres, 2007; Pravec and Harris, 2007; Walsh et al., 2008), tidal encounter with planets (Richardson et al., 1998; Bottke et al., 1999; Walsh and Richardson, 2006), and the escaping ejecta by the collisions (Durda et al., 2004; Polishook et al., 2011). The mechanisms have a lot in common with the cause of tumbling. Fissions and collisions in every mechanism can trigger 107P's cometary activity. The possible existence of a binary is consistent with the past cometary activity.

5. Summary

This study revealed the physical properties of 107P by a photometric observation campaign. We detected the lightcurve periodicity to be 0.2979 day and 0.0993 day with a commensurability of 3:1. The multiband photometry indicates that the taxonomy class of 107P is C-type. No clear rotational color variations are confirmed on the surface. We suggested two models to explain the different interpretations of the lightcurve periodicity.

1. The commensurability reflects tumbling with the sidereal rotation period of 0.2979 day and the precession period of 0.0993 day. The shape is a LAM of L_1:L_2:L_3 = 1.0:1.0:1.6. Around the same length of L_1 and L_2 shows the nutation angle is approximately constant at 65°. The direction of total rotational angular momentum is around λ = 310°, β = −10°, or λ = 132°, β = −17°. 107P returns to the same orientation every 0.2979 day by retrograde motion. Impacts of small objects are suggested as a cause for the tumbling and comet activity. Alternatively, the past comet activity itself is thought to be a cause of the tumbling, like a 1P/Halley (Samarasinha and A'Hearn, 1991).
2. 107P is not a tumbler. The sidereal rotation period is 0.2979 day. The shape is roughly spherical but slightly hexagonal with a SAM of L_1:L_2:L_3 = 1.5:1.0:1.0. The pole orientation is around λ = 330°, β = −27°. The sense of rotation is retrograde. The lightcurve of commensurability would reflect a discriminative appearance like (2867) Steins, which has been explored by the Rosetta spacecraft (Keller et al., 2010). Otherwise, the lightcurve also indicates the possibility of hosting a binary whose orbital period is 0.2979 day. The existence of a binary is also consistent with the past cometary activity.

Finally, we describe the mission feasibility for 107P. The orbit accessible by spacecraft makes 107P a promising target for a sample-return mission. If 107P is not a tumbling object, the moderate rotational period of 0.2979 day would enable us to obtain a sample by the touchdown of a spacecraft, whereas touchdown on 107P would require a difficult maneuver if 107P is a tumbler. In that case, a multi-fly-by mission that combines with the sample return mission for another target would become a hopeful plan.

Acknowledgments

We appreciate the observational campaign participants, especially Dr. Ryosuke Nakamura and Dr. Masanao Abe, for their dedicated coordination of the campaign and encouragement. We also acknowledge the Japan Space Forum. This work was financially supported in part by a Grant-in-Aid for Scientific Research (KAKENHI) from the Ministry of Education, Culture, Sports, Science and Technology of Japan (Nos. 22916007, 14GS0211, and 1947003). Sunao Hasegawa was supported by the Space Plasma Laboratory, ISAS, JAXA.

Funding for the SDSS and SDSS-II has been provided by the Alfred P. Sloan Foundation, the Participating Institutions, the National Science Foundation, the US Department of Energy, the National Aeronautics and Space Administration, the Japanese Monbukagakusho, the Max Planck Society, and the Higher Education Fund- ing Council for England. The SDSS Web Site is http://www.sdss.org/.

The SDSS is managed by the Astrophysical Research Consortium for the Participating Institutions. The Participating Institutions are the American Museum of Natural History, Astrophysical Institute Potsdam, University of Basel, University of Cambridge, Case Western Reserve University, University of Chicago, Drexel University, Fermilab, the Institute for Advanced Study, the Japan Participation Group, Johns Hopkins University, the Joint Institute for Nuclear Astrophysics, the Kavli Institute for Particle Astrophysics and Cosmology, the Korean Scientist Group, the Chinese Academy of Sciences (LAMOST), Los Alamos National Laboratory, the Max-Planck-Institute for Astronomy (MPIA), the Max-Planck-Institute for Astrophysics (MPA), New Mexico State University, Ohio State University, University of Pittsburgh, University of Portsmouth, Princeton University, the United States Naval Observatory, and the University of Washington.

References

Abazajian, K.N. et al., 2009. The seventh data release of the Sloan digital sky survey. Astrophys. J. Suppl. Ser. 182, 543–558.
Birtwhistle, P., Ryan, W.H., Sato, H., Beshore, E.C., Kadota, K., 2010. Comet P/2010 A2 (LINEAR). IAU Circ. 9105, 1.
Bodewits, D. et al., 2011. Collisional excavation of Asteroid (596) Scheila. Astrophys. J. Lett. 733, L3.
Bottke, W.F., Richardson, D.C., Michel, P., Love, S.G., 1999. 1620 Geographos and 433 Eros: Shaped by planetary tides? Astron. J. 117, 1921–1928.
Bottke, W.F. et al., 2002. Debiased orbital and absolute magnitude distribution of the near-Earth objects. Icarus 156, 399–433.
Chamberlin, A.B., McFadden, L.A., Schulz, R., Schleicher, D.G., Bus, S.J., 1996. 4015 Wilson–Harrington, 2201 Oljato, and 3200 Phaethon: Search for CN emission. Icarus 119, 173–181.
Clark, B.E. et al., 2010. Spectroscopy of B-type asteroids: Subgroups and meteorite analogs. J. Geophys. Res. 115, E06005.
de León, J., Campins, H., Tsiganis, K., Morbidelli, A., Licandoro, J., 2010. Origin of the near-Earth Asteroid Phaethon and the Geminids meteor shower. Astron. Astrophys. 513, A26.
Demura, H. et al., 2006. Pole and global shape of 25143 Itokawa. Science 312, 1347–1349.
Díaz, C.G., Gil-Hutton, R., 2008. Collisional activation of asteroids in cometary orbits. Astron. Astrophys. 487, 363–367.
Durda, D.D. et al., 2004. The formation of asteroid satellites in large impacts: Results from numerical simulations. Icarus 170, 243–257.
Elst, E.W. et al., 1996. Comet P/1996 N2 (Elst–Pizarro). IAU Circ. 6456, 1.
Fernandez, Y.R., McFadden, L.A., Lisse, C.M., Helin, E.F., Chamberlin, A.B., 1997. Analysis of POSS images of comet–asteroid transition object 107P/1949 W1 (Wilson–Harrington). Icarus 128, 114–126.
Gustafson, B.A.S., 1989. Geminid meteoroids traced to cometary activity on Phaethon. Astron. Astrophys. 225, 533–540.

Haghighipour, N., 2009. Dynamical constraints on the origin of Main Belt comets. Meteor. Planet. Sci. 44, 1863–1869.
Harris, A.W., Young, J.W., 1983. Asteroid rotation. IV. Icarus 54, 59–109.
Harris, A.W., 1994. Tumbling asteroids. Icarus 107, 209–211.
Harris, A.W., Young, J.W., Bowell, E., Tholen, D.J., 1999. Asteroid lightcurve observations from 1981 to 1983. Icarus 142, 173–201.
Hsieh, H.H., Jewitt, D., 2006. A population of comets in the main asteroid belt. Science 312, 561–563.
Hsieh, H.H., Ishiguro, M., Lacerda, P., Jewitt, D., 2011. Physical properties of main-belt Comet 176P/LINEAR. Astron. J. 142, 29–41.
Huang, K.Y. et al., 2005. GRBs optical follow-up observation at Lulin observatory, Taiwan. Il Nuovo Cimento C 28, 731–734.
Ishiguro, M. et al., 2011. Search for the comet activity of 107P/(4015) Wilson–Harrington during 2009/2010 apparition. Astrophys. J. 726, 101–110.
Ivezić, Z. et al., 2001. Solar System objects observed in the Sloan digital sky survey commissioning data. Astron. J. 122, 2749–2784.
Jewitt, D., Yang, B., Haghighipour, N., 2009. Main-belt Comet P/2008 R1 (Garradd). Astron. J. 137, 4313–4321.
Jewitt, D., Weaver, H., Agarwal, J., Mutchler, M., Drahus, M., 2010. A recent disruption of the main-belt Asteroid P/2010 A2. Nature 467, 817–819.
Jewitt, D., Weaver, H., Mutchler, M., Larson, S., Agarwal, J., 2011. Hubble space telescope observations of main-belt Comets (596) Scheila. Astrophys. J. Lett. 733, L4.
Jordi, K., Grebel, E.K., Ammon, K., 2006. Empirical color transformations between SDSS photometry and other photometric system. Astron. Astrophys. 460, 339–347.
Kaasalainen, M., 2001. Interpretation of lightcurves of precessing asteroids. Astron. Astrophys. 376, 302–309.
Kaasalainen, M., Torppa, J., 2001. Optimization methods for asteroid lightcurve inversion. I. Shape determination. Icarus 153, 24–36.
Kaasalainen, M., Torppa, J., Muinonen, K., 2001. Optimization methods for asteroid lightcurve inversion. II. The complete inverse problem. Icarus 153, 37–51.
Kaasalainen, M., Mottola, S., Fulchignoni, M., 2002. Asteroid models from disk-integrated data. In: Bottke., W.F., Cellino, A., Paolicchi, P., Binzel, R.P. (Eds.), Asteroid III. University of Arizona Press, Tucson, pp. 139–150.
Kaasalainen, M. et al., 2003. CCD photometry and model of MUSES-C target (25143) 1998 SF36. Astron. Astrophys. 405, 29–32.
Keller, H.U. et al., 2010. E-type Asteroid (2867) Steins as imaged by OSIRIS on Board Rosetta. Science 327, 190–193.
Kotani, T. et al., 2005. MITSuME—Multicolor Imaging Telescopes for Survey and Monstrous Explosions. Il Nuovo Cimento C 28, 755–758.
Kryszczyńska, A., Kwiatkowski, T., Breiter, S., Michałowski, T., 1999. Relation between rotation and lightcurve of 4179 Toutatis. Astron. Astrophys. 345, 643–645.
Licandro, J., Campins, H., Mothé-Diniz, T., Pinilla-Alonso, N., de León, J., 2007. The nature of comet–asteroid transition object (3200) Phaethon. Astron. Astrophys. 461, 751–757.
Licandro, J. et al., 2009. Spitzer observations of the asteroid–comet transition object and potential spacecraft target 107P (4015) Wilson–Harrington. Astron. Astrophys. 507, 1667–1670.
Licandro, J. et al., 2011. (65) Cybele: Detection of small silicate grains, water–ice, and organics. Astron. Astrophys. 525, A34.
Lomb, N.R., 1976. Least-squares frequency analysis of unequally spaced data. Astrophys. Space Sci. 39, 447–462.
Lowry, S.C., Weissman, P.R., 2003. CCD observations of distant comets from Palomar and Steward Observatories. Icarus 164, 492–503.
Magnusson, P., 1986. Distribution of spin axes and senses of rotation for 20 large asteroids. Icarus 68, 1–39.
Marsden, B.G. et al., 2010. Comet P/2010 R2 (la Sagra). IAU Circ. 9169, 1.
Mottola, S. et al., 1995. The slow rotation of 253 Mathilde. Planet. Space Sci. 43, 1609–1613.
Müller, T.G. et al., 2011. Thermo-physical properties of 162173 (1999 JU3), a potential flyby and rendezvous target for interplanetary missions. Astron. Astrophys. 525, A145.
Osip, D., Campins, H., Schleicher, D.G., 1995. The rotation state of 4015 Wilson–Harrington: Revisiting origins for the near-Earth asteroids. Icarus 114, 423–426.
Polishook, D., Brosch, N., Prialnik, 2011. Rotation periods of binary asteroids with large separations – Confronting the Escaping Ejecta Binaries model with observations. Icarus 212, 167–174.
Pravec, P. et al., 2005. Tumbling asteroids. Icarus 173, 108–131.
Pravec, P., Harris, A.W., 2007. Binary asteroid population. 1. Angular momentum content. Icarus 190, 250–259.
Read, M.I., Bressi, T.H., Gehrels, T., Scotti, J.V., Christensen, E.J., 2005. Comet P/2005 U1 (Read). IAU Circ. 8624, 1.
Richardson, D.C., Bottke, W.F., Love, S.G., 1998. Tidal distortion and disruption of Earth-crossing asteroids. Icarus 134, 47–76.
Rivkin, A.S., Emery, J.P., 2010. Detection of ice and organics on an asteroidal surface. Nature 464, 1322–1323.
Samarasinha, N.H., A'Hearn, M.F., 1991. Observational and dynamical constraints on the rotation of comet P/Halley. Icarus 93, 194–225.
Scargle, D.J., 1982. Studies in astronomical time series analysis. II – Statistical aspects of spectral analysis of unevenly spaced data. Astrophys. J. 263, 835–853.
Scheeres, D.J., 2007. Rotational fission of contact binary asteroids. Icarus 189, 370–385.
Snodgrass, C. et al., 2010. A collision in 2009 as the origin of the debris trail of Asteroid P/2010 A2. Nature 467, 814–816.
Spencer, J.R. et al., 1995. The lightcurve of 4179 Toutatis: Evidence for complex rotation. Icarus 117, 71–89.
Tholen, D.J., 1989. Asteroid taxonomic classifications. In: Binzel, R.P., Gehrels, T., Matthews, M.S. (Eds.), Asteroid II. University of Arizona press, Tucson, pp. 1139–1150.
Toth, I., 2000. Impact-generated activity period of the Asteroid 7968 Elst–Pizarro in 1996: Identification of the Asteroid 427 Galene as the most probable parent body of the impactors. Astron. Astrophys. 360, 375–380.
Vokrouhlický, D., Breiter, S., Nesvorný, D., Bottke, W.F., 2007. Generalized YORP evolution: Onset of tumbling and new asymptotic states. Icarus 191, 636–650.
Walsh, K.J., Richardson, D.C., 2006. Binary near-Earth asteroid formation: Rubble pile model of tidal disruptions. Icarus 180, 201–216.
Walsh, K.J., Richardson, D.C., Michel, P., 2008. Rotational breakup as the origin of small binary asteroids. Nature 454, 188–191.
Yang, B., Jewitt, D., 2010. Identification of magnetite in B-type asteroids. Astron. J. 140, 692–698.
Yoshikawa, M., Yano, H., Kawaguchi, J., Hayabusa-2 Pre-Project Team., Small Bosy Exploration Wg., 2008. Japan's Future Plans for Missions to Primitive Bodies: Hayabusa-2, Hayabusa-Mk2, and Marco Polo. Lunar. Planet. Sci. XXXIX, 1747 (abstract).

Monthly Notices of the ROYAL ASTRONOMICAL SOCIETY

Mon. Not. R. Astron. Soc. **412,** 371–390 (2011) doi:10.1111/j.1365-2966.2010.17912.x

Whole Earth Telescope observations of the subdwarf B star KPD 1930+2752: a rich, short-period pulsator in a close binary

M. D. Reed,[1⋆†] S. L. Harms,[1] S. Poindexter,[1,2] A.-Y. Zhou,[1,3] J. R. Eggen,[1] M. A. Morris,[1,4] A. C. Quint,[1] S. McDaniel,[1] A. Baran,[5] N. Dolez,[6] S. D. Kawaler,[7] D. W. Kurtz,[8] P. Moskalik,[9] R. Riddle,[7,10] S. Zola,[5,11] R. H. Østensen,[12,13] J.-E. Solheim,[14] S. O. Kepler,[15] A. F. M. Costa,[16] J. L. Provencal,[17] F. Mullally,[18] D. W. Winget,[18] M. Vuckovic,[7,13] R. Crowe,[19] D. Terry,[19] R. Avila,[19,20] B. Berkey,[19,21] S. Stewart,[19] J. Bodnarik,[19,22] D. Bolton,[19] P.-M. Binder,[19] K. Sekiguchi,[23] D. J. Sullivan,[24] S.-L. Kim,[25] W.-P. Chen,[26] C.-W. Chen,[26] H.-C. Lin,[26] X.-J. Jian,[27] H. Wu,[27] J.-P. Gou,[27] Z. Liu,[27] E. Leibowitz,[28] Y. Lipkin,[28] C. Akan,[29] O. Cakirli,[29] R. Janulis,[30] R. Pretorius,[31] W. Ogloza,[5] G. Stachowski,[5] M. Paparo,[32] R. Szabo,[32] Z. Csubry,[32] D. Zsuffa,[32] R. Silvotti,[33] S. Marinoni,[34,35] I. Bruni,[35] G. Vauclair,[6] M. Chevreton,[36] J. M. Matthews,[37] C. Cameron[37] and H. Pablo[7]

[1]*Department of Physics, Astronomy, and Materials Science, Missouri State University, Springfield, MO 65897, USA*
[2]*Department of Astronomy, The Ohio State University, 140 W. 18th Ave., Columbus, OH 43210, USA*
[3]*National Astronomical Observatories, Chinese Academy of Sciencies, Beijing 100012, China*
[4]*School of Earth and Space Exploration, Arizona State University, PO Box 871404, Tempe, AZ 85287-1404, USA*
[5]*Mt Suhora Observatory of the Pedagogical University, ul. Podchorąży 2, PL-30-084 Kracow, Poland*
[6]*Laboratoire d'Astrophysique de Toulouse-Tarbes, Université de Toulouse, CNRS, 14 Av. Ed. Belin, 31400 Toulouse, France*
[7]*Department of Physics and Astronomy, Iowa State University, Ames, IA 50011, USA*
[8]*Centre for Astrophysics, University of Central Lancashire, Preston PR1 2HE*
[9]*Nicolaus Copernicus Astronomical Center, ul. Bartycka 18, 00-716 Warsaw, Poland*
[10]*California Institute of Technology, 1200 E. California Blvd MC 11-17, Pasadena, CA 91125, USA*
[11]*Astronomical Observatory, Jagiellonian University, ul. Orla 171, 30-244 Cracow, Poland*
[12]*Isaac Newton Group of Telescopes, 37800 Santa Cruz de La Palma, Spain*
[13]*Instituut voor Sterrenkunde, Katholieke Universiteit Leuven, Celestijnenlaan 200 D, 3001 Leuven, Belgium*
[14]*Institutt for Teoretisk Astrofysikk, Universitetet i Oslo, 0212 Blindern-Oslo, Norway*
[15]*Instituto de Fisica, UFRGS, CP 15051, 91501-970 Porto Alegre, RS, Brazil*
[16]*Universidade do Estado de Santa Catarina, CAV, CP 88520-000 Lages, SC, Brazil*
[17]*Mount Cuba Observatory and University of Delaware, Newark, DE 19716, USA*
[18]*McDonald Observatory, and Department of Astronomy, University of Texas, Austin, TX 78712, USA*
[19]*Department of Physics and Astronomy, University of Hawaii-Hilo, 200 West Kawili Street, Hilo, HI 96720-4091, USA*
[20]*Department of Astronomy, New Mexico State University, Box 30001, Las Cruces, NM 88003, USA*
[21]*W. M. Keck Observatory, Kamuela, HI 96743, USA*
[22]*Gemini Observatory, 670 North A'ohoku Place, Hilo, HI 96720, USA*
[23]*Subaru Observatory, National Astronomical Observatory of Japan, 650 North A'ohoku Place, Hilo, HI 96720, USA*
[24]*School of Chemical and Physical Sciences, Victoria University of Wellington, PO Box 600, Wellington, New Zealand*
[25]*Korea Astronomy Observatory, Daejeon 305-348, Korea*
[26]*Graduate Institute of Astronomy, National Central University, Chung-Li 32054, Taiwan*
[27]*National Astronomical Observatories and Joint Laboratory of Optical Astronomy, Chinese Academy of Sciences, Beijing 100012, China*
[28]*Wise Observatory, Tel-Aviv University, Tel Aviv 69978, Israel*
[29]*Ege University Observatory, TR-35100 Bornova, İzmir, Turkey*
[30]*Institute of Theoretical Physics & Astronomy of Vilnius University. A. Go tauto St. 12, 01108 Vilnius, Lithuania*
[31]*South African Astronomical Observatory, PO Box 9, Observatory 7935, South Africa*
[32]*Konkoly Observatory, Box 67, H-1525 Budapest XII, Hungary*
[33]*INAF–Osservatorio Astronomico di Torino, strada dell'Osservatorio 20, 10025 Pino Torinese, Italy*
[34]*Dipartimento di Astronomia, Universitádi Bologna, via Ranzani 1, 40127 Bologna, Italy*
[35]*INAF-Osservatorio Astronomico di Bologna, via Ranzani 1, 40127 Bologna, Italy*

⋆E-mail: mikereed@missouristate.edu
†Visiting Astronomer, Kitt Peak National Observatory, National Optical Astronomy Observatory, which is operated by the Association of Universities for Research in Astronomy (AURA) under cooperative agreement with the National Science Foundation.

[36]*LESIA, Observatoire de Paris-Meudon, Meudon 92190, France*
[37]*Department of Physics and Astronomy, University of British Columbia, 6224 Agricultural Road, Vancouver, BC V6T1Z1, Canada*

Accepted 2010 October 22. Received 2010 October 22; in original form 2010 August 13

ABSTRACT

KPD 1930+2752 is a short-period pulsating subdwarf B (sdB) star. It is also an ellipsoidal variable with a known binary period of 2.3 h. The companion is most likely a white dwarf and the total mass of the system is close to the Chandresekhar limit. In this paper, we report the results of Whole Earth Telescope (WET) photometric observations during 2003 and a smaller multisite campaign of 2002. From 355 h of WET data, we detect 68 pulsation frequencies and suggest an additional 13 frequencies within a crowded and complex temporal spectrum between 3065 and 6343 μHz (periods between 326 and 157 s). We examine pulsation properties including phase and amplitude stability in an attempt to understand the nature of the pulsation mechanism. We examine a stochastic mechanism by comparing amplitude variations with simulated stochastic data. We also use the binary nature of KPD 1930+2752 for identifying pulsation modes via multiplet structure and a tidally induced pulsation geometry. Our results indicate a complicated pulsation structure that includes short-period (≈16 h) amplitude variability, rotationally split modes, tidally induced modes and some pulsations which are geometrically limited on the sdB star.

Key words: binaries: close – stars: general – stars: oscillations – subdwarfs – oscillations: individual: KPD 1930+2752.

1 INTRODUCTION

Subdwarf B (sdB) stars are thought to have masses of about 0.5 $M_\odot$ with thin ($<10^{-2}\,M_\odot$) hydrogen shells and temperatures from 22 000 to 40 000 K (Heber et al. 1984; Saffer et al. 1994). Shell hydrogen burning cannot be supported by such thin envelopes, and it is likely that they proceed directly to the white dwarf cooling track without reaching the asymptotic giant branch (Saffer et al. 1994).

Pulsating sdB stars with periods of a few minutes (officially V361 Hya, and also known as EC 14026 or sdBV stars) were first observed by Kilkenny et al. (1997), nearly simultaneous to their predicted existence by Charpinet et al. (1996, 1997). The sdBV stars have pulsation periods ranging from 90 to 600 s with amplitudes typically near or below 1 per cent. The pulsations are likely p modes driven by the κ mechanism due to a diffusive iron-group opacity bump in the envelope (Charpinet et al. 1997; Jeffery & Saio 2007). Subdwarf B pulsators are typically found among the hotter sdB stars, with $T_{\rm eff} \approx 34\,000$ K and $\log g \approx 5.8$. Reviews of this pulsation class include an observational review by Reed et al. (2007a) for an of 23 resolved class members and by Charpinet, Fontaine & Brassard (2001) who described the pulsation mechanism. Another class of pulsating sdB stars have periods longer than 45 min, are likely g-mode pulsations and are designated V1093 Her, but commonly known as PG 1716 stars (Green et al. 2003; Reed et al. 2004a). General reviews of sdB stars and pulsators are of Heber (2009) and Østensen (2009). Our target is a p-mode, sdBV-type pulsator.

KPD 1930+2752 (also V2214 Cyg and hereafter KPD 1930) was discovered to be a variable by Billéres et al. (2000, hereafter B00), who obtained data during four nights within one week. Their longest run was 5 h, yet within this limited data set, they detected 45 separate frequencies, which indicate that KPD 1930 is an interesting and complex pulsator. A velocity study confirmed the $2^{\rm h}17^{\rm m}$ binary period and, using the canonical sdB mass of 0.5 $M_\odot$, determined the companion mass to be $0.97 \pm 0.01\,M_\odot$ (Maxted, Marsh & North 2000). As the companion is not observed either photometrically or spectroscopically, it is likely a white dwarf, placing the mass of the system over the Chandrasekhar limit. A study by Ergma, Fedorova & Yungelson (2001) suggested that the binary will shed sufficient mass to avoid a Type Ia supernova and will merge to form a massive white dwarf. With a rich, unresolved pulsation spectrum and the opportunity to learn some very interesting physics via asteroseismology, KPD 1930 was chosen for observation by the Whole Earth Telescope (WET). KPD 1930 also has an infrared companion ≈0.5 arcsec away (Østensen, Heber & Maxted 2005).

2 OBSERVATIONS

KPD 1930 was the target of the WET run Xcov 23. Nearly 355 h of data were collected at 17 observatories from 2003 August 15 to September 9. The individual runs are provided in Table 1. Overall, these data have an observational duty cycle of 36 per cent which is less than typical WET campaigns. Because of the crowded field, most of the data were obtained with CCD photometers whereas some were obtained with photoelectric (photomultiplier tube) photometers. The photoelectric data were reduced in the usual manner as described by Kleinman, Nather & Phillips (1996). The standard procedures of CCD image reduction, including bias subtraction, dark correction and flat-field correction, were followed using IRAF packages. Differential intensities were determined via aperture photometry with the aperture optimized for each individual run with varying numbers of comparison stars depending on the field of view. Lightcurves are shown in Fig. 1.

We will also examine a small multisite campaign that obtained data during 2002 July. In total, almost 45 h of data were obtained from McDonald (the 2.1-m Otto Struve Telescope), San

Table 1. WET observations of KPD 1930+2752 during XCov23 in 2003.

Run	Length (h)	Date UT	Observatory	Run	Length (h)	Date UT	Observatory
t081403	5.5	Aug. 15	Mt Cuba 0.4 m	loi2708	3.0	Aug. 27	Loiano 1.5 m
phot081503	6.4	Aug. 16	Mt Cuba 0.4 m	gv30808	5.8	Aug. 27	OHP 1.9 m
phot081703	0.7	Aug. 18	Mt Cuba 0.4 m	a0688	2.0	Aug. 28	McDonald 2.1 m
hunaug18	3.1	Aug. 18	Piszkesteto 1.0 m	mdr245	0.9	Aug. 28	KPNO 2.1 m
NOT_Aug19	7.8	Aug. 19	NOT 2.6 m	haw28aug	3.0	Aug. 28	Hawaii 0.6 m
phot081903	6.5	Aug. 19	Mt Cuba 0.4 m	lulin28aug	7.5	Aug. 28	Lulin 1.0 m
hunaug19	4.3	Aug. 19	Piszkesteto 1.0 m	turkaug28	2.5	Aug. 28	Turkey 1.5 m
NOT_Aug20	8.6	Aug. 20	NOT 2.6 m	jr0828	3.7	Aug. 28	Moletai 1.65 m
lna20aug	4.4	Aug. 20	LNA 0.6 m	retha-0031	3.4	Aug. 28	SAAO 1.9 m
phot082003	6.9	Aug. 20	Mt Cuba 0.4 m	phot082903	4.9	Aug. 29	Mt Cuba
hunaug20	4.6	Aug. 20	Piszkesteto 1.0 m	a0690	0.2	Aug. 29	McDonald 2.1 m
hunaug21	4.8	Aug. 21	Piszkesteto 1.0 m	mdr246	3.8	Aug. 29	KPNO 2.1 m
NOT_Aug21	8.8	Aug. 21	NOT 2.6 m	haw29aug	3.0	Aug. 29	Hawaii 0.6 m
lna21aug	4.5	Aug. 21	LNA 0.6 m	turkaug29	5.5	Aug. 29	Turkey 1.5 m
lulin21aug	7.0	Aug. 21	Lulin 1.0 m	retha-0041	3.9	Aug. 29	SAAO 1.9 m
NOT_Aug22	8.7	Aug. 22	NOT 2.6 m	gv30809	5.7	Aug. 29	OHP 1.9 m
lna22aug	1.3	Aug. 22	LNA 0.6 m	mdr247	6.8	Aug. 30	KPNO 2.1 m
haw22aug	1.0	Aug. 22	Hawaii 0.6 m	haw30aug	2.4	Aug. 30	Hawaii 0.6 m
lulin22aug	2.4	Aug. 22	Lulin 1.0 m	turkaug30	4.3	Aug. 30	Turkey 1.5 m
suh-114	3.9	Aug. 22	Suhora 0.6 m	retha-0051	3.9	Aug. 30	SAAO 1.9 m
gv30801	2.5	Aug. 22	OHP 1.9 m	loi0830	0.1	Aug. 30	Loiano 1.5 m
NOT_Aug23	6.5	Aug. 23	NOT 2.6 m	mdr248	6.5	Aug. 31	KPNO 2.1 m
lna23aug	3.1	Aug. 23	LNA 0.6 m	haw31aug	2.9	Aug. 31	Hawaii 0.6 m
haw23aug	3.6	Aug. 23	Hawaii 0.6 m	turkaug31	5.5	Aug. 31	Turkey 1.5 m
lulin23aug	6.8	Aug. 23	Lulin 1.0 m	se0103q1	2.6	Sep. 01	SSO 1.0 m
gv30803	1.1	Aug. 23	OHP 1.9 m	turksep01	5.0	Sep. 01	Turkey 1.5 m
lna24aug	4.8	Aug. 24	LNA 0.6 m	mdr249	3.6	Sep. 02	KPNO 2.1 m
phot082403	6.9	Aug. 24	Mt Cuba 0.4 m	se0203q1	4.6	Sep. 02	SSO 1.0 m
haw24aug	0.5	Aug. 24	Hawaii 0.6 m	turksep02	4.9	Sep. 02	Turkey 1.5 m
gv30805	3.5	Aug. 24	OHP 1.9 m	haw03sep	2.3	Sep. 03	Hawaii 0.6 m
phot082503	3.8	Aug. 25	Mt Cuba 0.4 m	se0303q1	4.5	Sep. 03	SSO 1.0 m
haw25aug	0.7	Aug. 25	Hawaii 0.6 m	wise03sep	6.0	Sep. 03	Wise 1.0 m
lulin25aug	0.2	Aug. 25	Lulin 1.0 m	haw04sep	2.4	Sep. 04	Hawaii 0.6 m
suh-116	3.1	Aug. 25	Suhora 0.6 m	se0403q1	4.6	Sep. 04	SSO 1.0 m
gv30806	4.5	Aug. 25	OHP 1.9 m	wise04sep	3.8	Sep. 04	Wise 1.0 m
phot082603	6.6	Aug. 26	Mt Cuba 0.4 m	hunsep04	1.7	Sep. 04	Piszkesteto 1.0 m
a0684	0.5	Aug. 26	McDonald 2.1 m	haw05sep	2.5	Sep. 05	Hawaii 0.6 m
a0685	0.3	Aug. 26	McDonald 2.1 m	wise05sep	7.0	Sep. 05	Wise 1.0 m
lulin26aug	7.0	Aug. 26	Lulin 1.0 m	haw06sep	2.2	Sep. 06	Hawaii 0.6 m
retha-0020	0.7	Aug. 26	SAAO 1.9 m	wise06sep	7.0	Sep. 06	Wise 1.0 m
gv30807	4.9	Aug. 26	OHP 1.9 m	hunsep06	4.8	Sep. 06	Piszkesteto 1.0 m
lna27aug	3.5	Aug. 27	LNA 0.6 m	haw07sep	1.2	Sep. 07	Hawaii 0.6 m
lulin27aug	7.4	Aug. 27	Lulin 1.0 m	hunsep07	4.6	Sep. 07	Piszkesteto 1.0 m
retha-0021	3.7	Aug. 27	SAAO 1.9 m	hunsep09	0.7	Sep. 09	Piszkesteto 1.0 m

Table 2. Observations of KPD 1930+2752 during 2002.

Run	Length (h)	Date UT	Observatory	Run	Length (h)	Date UT	Observatory
20710	3.5	July 10	Suhora 0.6 m	A0302	4.0	July 14	McDonald 2.1 m
20711	1.8	July 11	Suhora 0.6 m	A0304	3.9	July 15	Suhora 0.6 m
A0296	2.0	July 11	McDonald 2.1 m	20717	5.9	July 15	McDonald 2.1 m
20712	5.3	July 12	Suhora 0.6 m	sp1	2.4	July 17	Suhora 0.6 m
A0300	0.3	July 13	McDonald 2.1 m	20720	2.2	July 17	S.P. Martir 1.5 m
A0301	4.5	July 13	McDonald 2.1 m	sp2	2.4	July 20	Suhora 0.6 m
20714	1.4	July 14	Suhora 0.6 m	20715	4.2	July 20	S.P. Martir 1.5 m

Pedro-Martir (1.5 m) and Suhora (0.6 m) observatories. Specifics of these runs are given in Table 2.

As sdB stars are substantially hotter than typical field stars, differential light curves are not flat due to atmospheric reddening. A low-order polynomial was fitted to remove nightly trends from the data. Finally, the light curves were normalized by their average flux and centred around zero, so the reported differential intensities are $\Delta I = (I/\langle I\rangle) - 1$. Amplitudes are given as milli-modulation

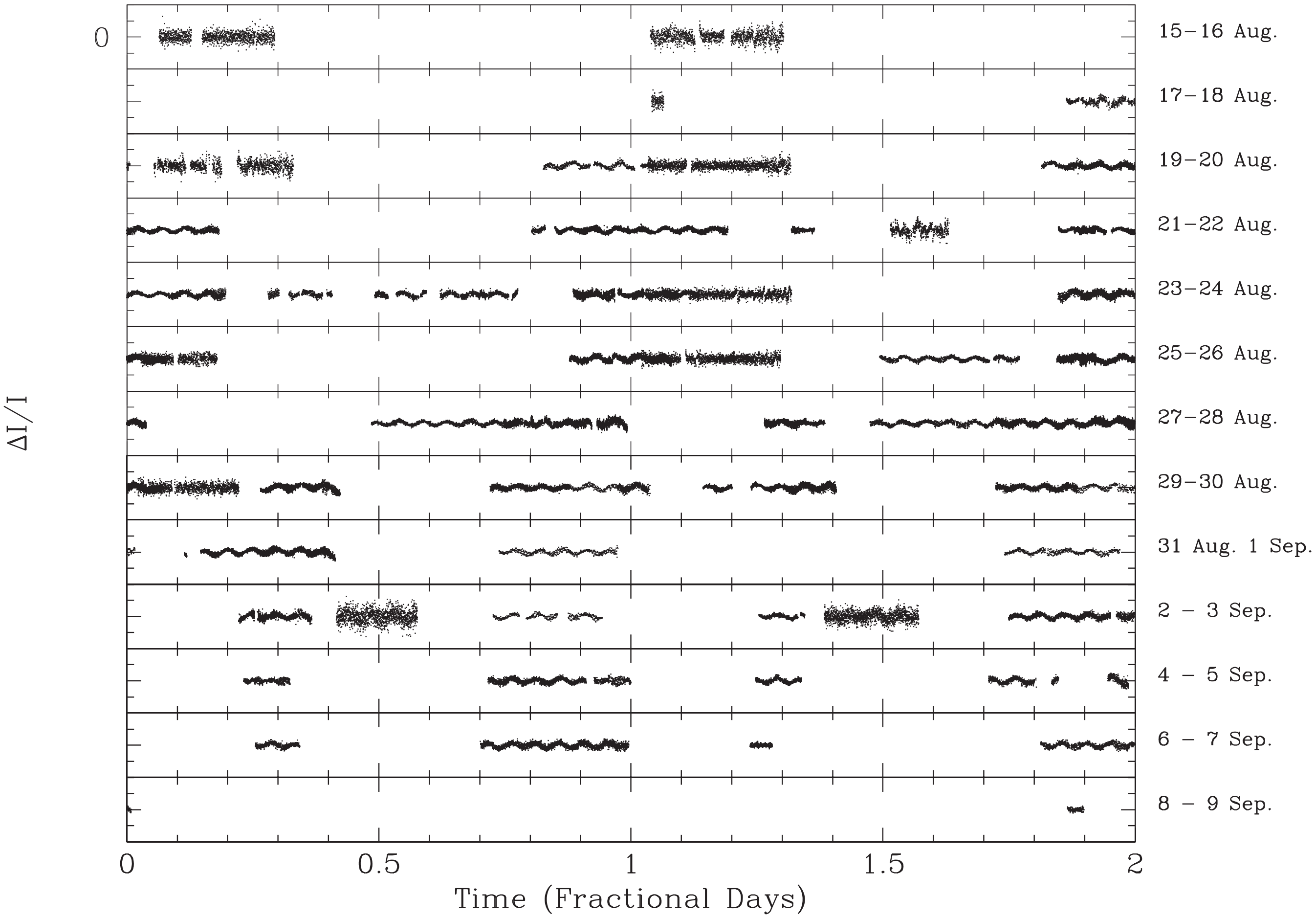

Figure 1. Light curves showing all data obtained during Xcov 23. Each panel is 2 d with the dates given on the right-hand side.

amplitudes (mma), with 10 mma corresponding to 1.0 per cent or 9.2 mmag.

3 ANALYSIS

3.1 Orbital parameters

The largestvariation in the light curve is caused by an ellipsoidal variation of the sdB star. In removing this variation to examine the pulsations, we can deduce some of the orbital properties. We defer attempting a complete binary solution to a work in progress (Pablo et al., private communication), but provide some basic information here that is obvious from the data. Non-linear least-squares (NLLS) fitting to the data (2002 and 2004) provides a frequency of ellipsoidal variation of $243.369\,87 \pm 0.000\,07$ μHz. The binary period is twice that at 8217.994 ± 0.002 s or $0.095\,115\,67 \pm 0.000\,000\,03$ d. Our value is within that found by B00 but outside the errors of the period determined by Geier et al. (2007, hereafter G07). G07 had 2900 spectroscopic data points unevenly scattered throughout 4 yr while we had 36 per cent coverage during 26 d in 2003 and ~45 h spanning 7 d in 2002. As the epochs of our data overlap, period change can be ruled out and it is most likely that one (or both) of us is underestimating our errors. Fig. 2 shows modified XCov 23 data folded over the binary period. The pulsations make the light curve very broad and it even appears that a pulsation frequency is an integer multiple of the binary period. However that is not the case, but rather that there are many pulsation frequencies between 33 and 34 times the orbital frequency (see Section 3.2). To transform the broad pulsation-included light curve into a narrower, pre-whitened form, we used our best data (Group II), pre-whitened by all 61 pulsation frequencies. Then we phase-folded the data over the orbital period, did a 60-point (≈11.5-s) smoothing and fitted an additional three frequencies. We then pre-whitened these three frequencies from the original, non-phase-folded data, phase folded again and smoothed by 60 (≈11.5 s), 168 (≈30 s) and 335 (≈60 s) points. The differently smoothed data did not affect the maxima and minima of the orbital variations, and so we used the 335-point smoothed data, shown as a solid line in Fig. 2, to examine the ellipsoidal variations.

Using radial velocity data, G07 estimate the orbital inclination as $i \sim 80^\circ$. At this inclination, the white dwarf companion should eclipse the sdB star. An eclipse is shown for $i = 80^\circ$ in fig. 8 of G07 and using the orbital parameters of G07, we produced a simulated light curve with BINARY MAKER 3 (Fig. 3).[1] Our simulation was not intended to fit the actual data, but rather to illustrate the eclipse shape. From the simulation, the eclipse duration would be ≈164 s or nearly three of our binned data points (at a binning of 335 points) with a depth of 0.2 per cent. While the observed minima are uneven, the shape and depth do not match those of an eclipse. We can therefore rule out inclinations for which an eclipse should occur, namely $i \geq 78\overset{\circ}{.}5$, based on G07. The uneven minima indicate what would

[1] See www.binarymaker.com.

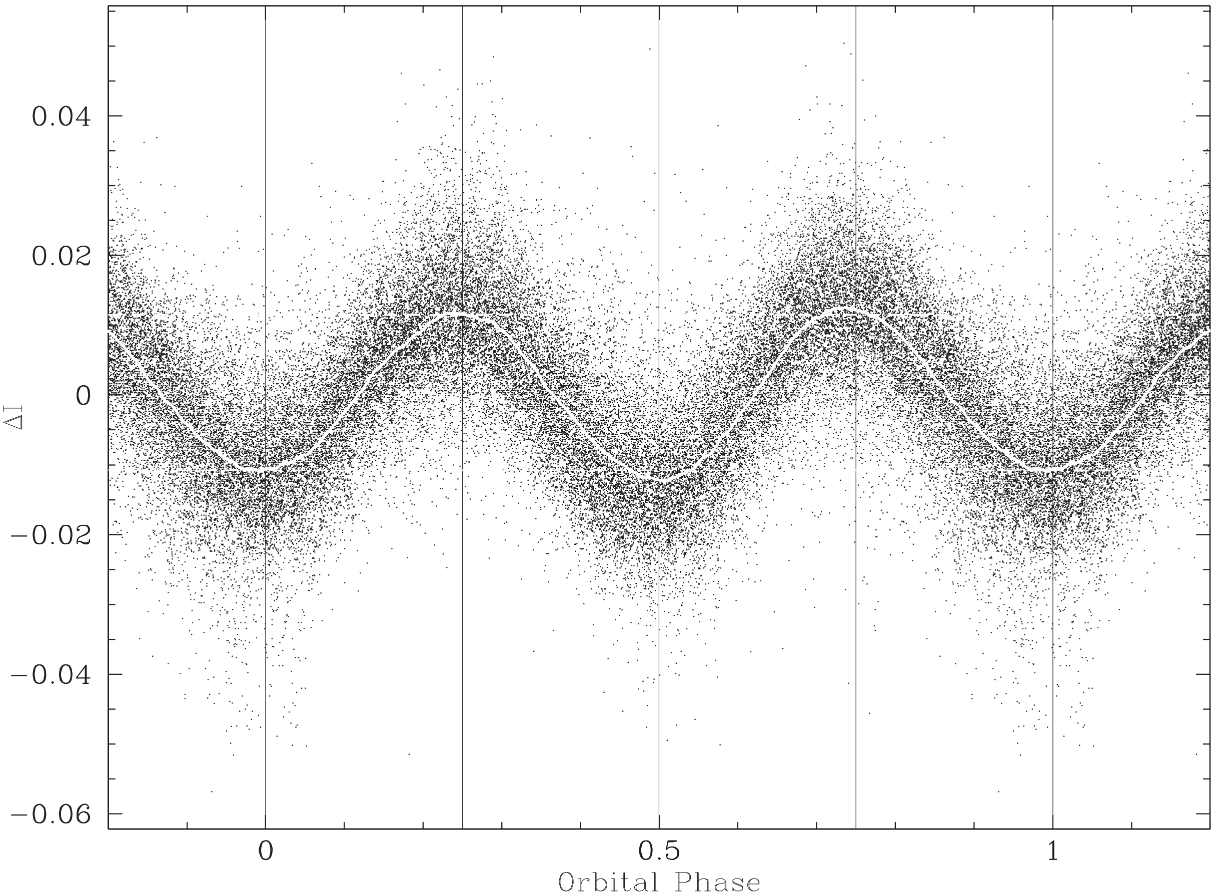

Figure 2. XCov 23 data folded over the binary period. The solid line is a result of pre-whitening the data and smoothing over 335 points (60 s in time) and the dashed horizontal lines indicate one maximum and minimum. For clarity, slightly more than one orbit is shown.

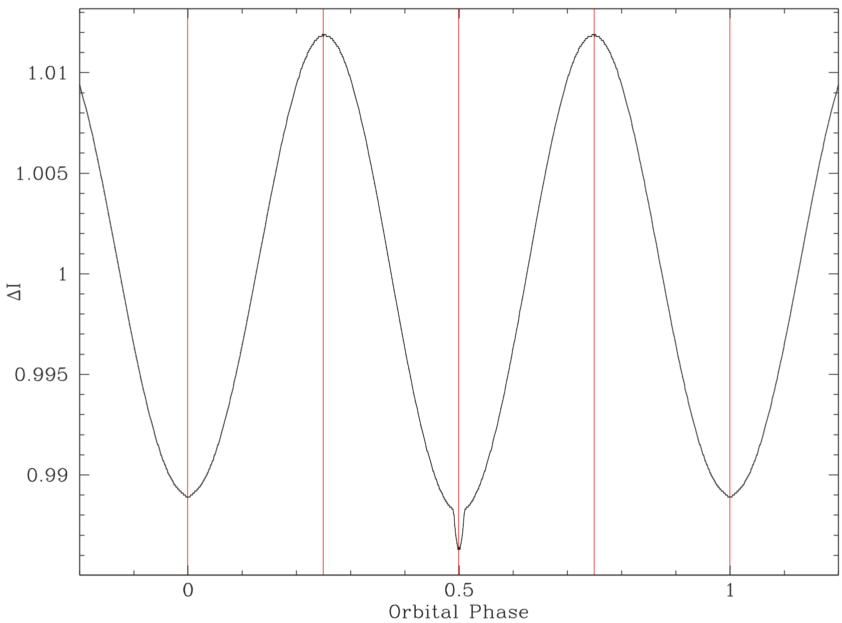

Figure 3. Simulated data showing the eclipse shape for $i = 80°$.

be expected based on the tidal distortion (gravity darkening). The gravity of the white dwarf makes the sdB star slightly egg-shaped. When the marginally sharper end faces us, the line-of-sight angle does not go as deep at one optical depth as it does when the blunter end faces us. This produces a fainter minimum when the sdB is farthest from us, and we view the slightly sharper end. A vastly exaggerated schematic of this is shown in Fig. 4 (a reconstructed image based on fig. 2 of Veen, van Genderen & van der Hucht

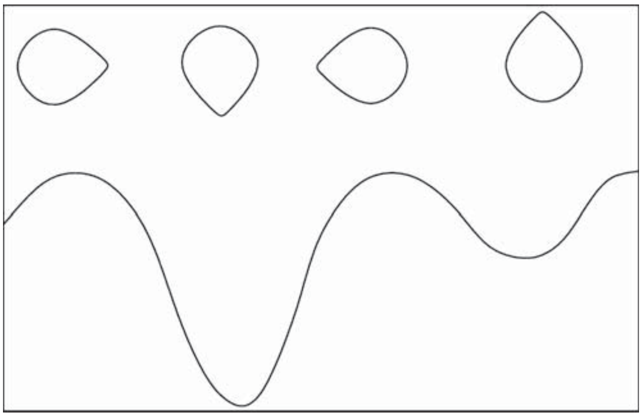

Figure 4. Exaggerated simulated data showing how limb darkening, combined with ellipsoidal variation, causes uneven minima.

2002). We fitted regions spanning 0.2 in phase with Gaussians to determine each maximum and minimum. The minimum at $\phi = 0.5$ is 0.18 ± 0.03 per cent fainter than the other mininum and using detailed models, this information, along with the amplitude of the ellipsoidal variation, should be sufficient to constrain the shape and limb darkening of KPD 1930. The uneven minima allow us to define the closest approach of the sdB star, and like Maxted et al. (2000), we define this as the zero-point of the orbital phase.

The light-curve maxima are also not quite even. Using the same Gaussian fitting technique, the maximum at $\phi_{\rm orb} = 0.75$, which is when the sdB component is travelling towards us, is 0.06 ± 0.05 per cent brighter than at 1.25, when the star is travelling away from us. Doppler boosting and Doppler shifting affect the flux by a factor of $(1 - v(t)/c)$ (Maxted et al. 2000; G07) which, using K1 from G07, should result in a Doppler brightening semi-amplitude of 0.11 per cent. This is at the 1σ upper limit of our measurement. Instead of using the measured velocity to deduce flux differences in maxima, two of us (SDK and HP) attempted to constrain the velocity from the light curve itself. Using low-pass filtering of the light curve, we obtained approximate values for the flux increase and converted those to velocity. The estimate of the maximum radial velocity is $529.76 \pm 16\,{\rm km\,s^{-1}}$ which is of the same order as the radial velocity measurements of G07. The error estimate is the error of the fit to the light curve and does not include the (large) systematic error of the spectrum estimate. [More details about this measurement and its effects on the binary will be discussed in Pablo et al. (in preparation).] So Doppler effects could be responsible for the difference in maxima. Interestingly, such special-relativistic effects have been detected in another sdB binary at the expected level (Bloemen et al. 2011).

3.2 Pulsation analysis

In a standard manner for long time-series data (i.e. Kilkenny et al. 1999; Reed et al. 2004b, 2007b), we analysed the data in several different groupings. We can use these groups to examine frequency and amplitude stability, look for consistent frequencies and amplitude variations. The groups are provided in Table 3, and pertinent sections of their temporal spectra [Fourier transforms (FTs)] are shown in Figs 5 and 6. Table 3 also lists the temporal resolution (defined as $1/t$, where t is the run duration) and the 4σ detection limit determined for ranges of 1000–3000 and 8000–10 000 μHz. Group I data include all of the XCov 23 data. Group II excludes

Table 3. Various groups of data used in our pulsation analysis. Columns 3 and 4 indicate the temporal resolution (in μHz) and 4σ detection limit (in mma).

Group	Inclusive dates	Resolution	Limit
I	Aug. 15–Sep. 9	0.45	0.44
II	Aug. 18–Sep. 7	0.60	0.31
III	Aug. 19–23	2.69	0.44
IV	Aug. 27–31	2.58	0.52
V	Sep. 3–6	3.75	0.77
VI	2002 July 10–21	1.87	0.59

noisy data, which is defined as a 4σ limit above 2 mma and has been trimmed so that for any overlapping data, only the best quality data were kept. Groups III, IV and V contain data obtained over 4 or 5 d of relatively good coverage during three different weeks of the 2003 campaign. Group VI is the 2002 small multisite campaign. Figure insets show the window functions, which are a single sine wave temporally sampled as the actual data. The central peak is the input frequency while other peaks are aliases which can complicate the data. Groups I and II are relatively well sampled, with alias peaks less than 40 per cent of the input amplitude whereas the remaining groups have obvious aliases that will contribute to the overall noise of the data.

A glance at the figures provides two simple observations as follows: (i) KPD 1930 is multiperiodic, pulsating in several tens of modes, confirming what was found in the discovery data (B00) and (ii) the pulsation frequencies are short-lived. This is evident from the fact that the highest amplitude peaks change between the shortest data sets (Groups III through VI) and the groups with the longest data sets (Groups I and II) have the lowest amplitudes.

As peak amplitudes in FTs show a mixture of the *median* amplitude and effects of phase stability, pre-whitening of the combined data sets could not be expected to accurately remove variations in amplitudes and/or phases (see Reed et al. 2007a; Koen 2009). However, because of the frequency density shorter duration data sets would likely have unresolved frequencies. This does not mean that least-squares fitting and pre-whitening are not of use; it is just that they need to be used with caution. We did the usual method of simultaneously fitting and pre-whitening the data using NLLS software independently for all the groups in Table 3 until we could not discern peaks (as in Fig. 7). However, because of the rich pulsation spectrum, we added an additional step. When searching the FT for pulsation peaks, we also plotted a window function made from the pre-whitening information gathered for all fitted frequencies. In this manner, we could view cumulative windowing effects and better judge the impact of pre-whitening on the FT. (A pre-whitening sequence of Group IV's data is provided as Fig. S1 in the online Supporting Information.)

Frequencies were deemed intrinsic to the star if they were detected in at least two groups above the 4σ detection limits. Table 4 provides a list of detected pulsation frequencies. The first column lists a designation, the second gives the frequency from the highest temporal-resolution group and the NLLS error is given in parentheses. Subsequent columns list the fitted amplitude from each group (NLLS error in parentheses) along with any pertinent notes: NF indicates that the frequency was not NLLS fitted, and frequencies fitted, but off by a daily alias, are noted as + or − for 1 daily alias away or ++ or −− for 2 daily aliases away. The last

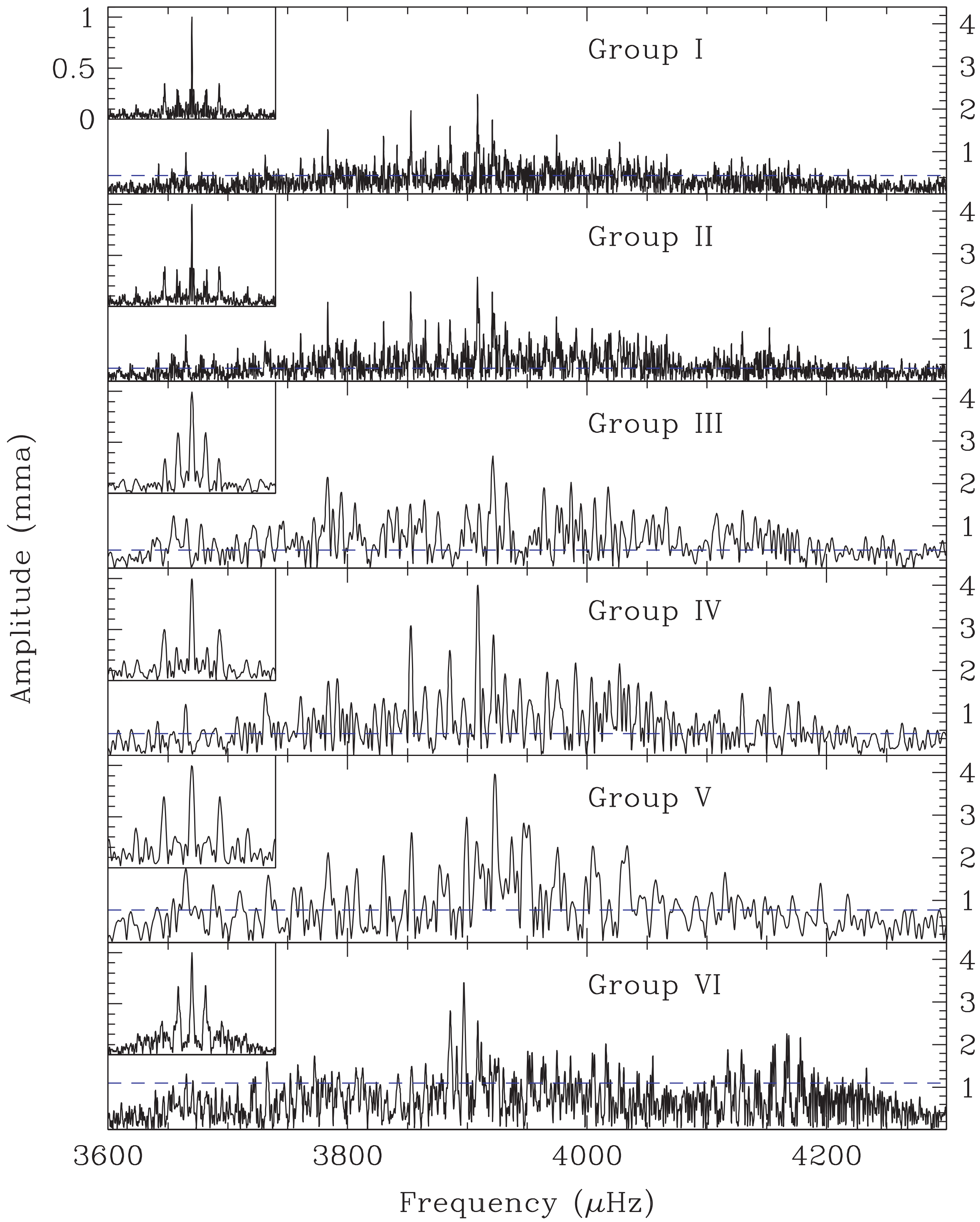

Figure 5. Plot of the temporal spectra and window functions (inset) for the groupings of data in Table 3 for the frequency range from 3600 to 4250 μHz. Dashed lines are the 4σ detection limit.

column notes other frequencies that are within 1 μHz of the daily alias as this could make pre-whitening difficult, depending on the window function. Table 5 lists other frequencies that we *suspect* are intrinsic to the star but did not meet our requirements. Fig. 7 is an expanded FT for Group II's data. Each panel shows the original FT and the residuals after pre-whitening. The dashed (blue) line is the 4σ detection limit. There are regions where the residuals remain higher than the 4σ detection limit because either NLLS fitting and pre-whitening did not effectively remove all of the amplitude (most likely caused by amplitude and/or phase variations or another, unresolved frequency) or remaining peaks were not observable in the original FT.

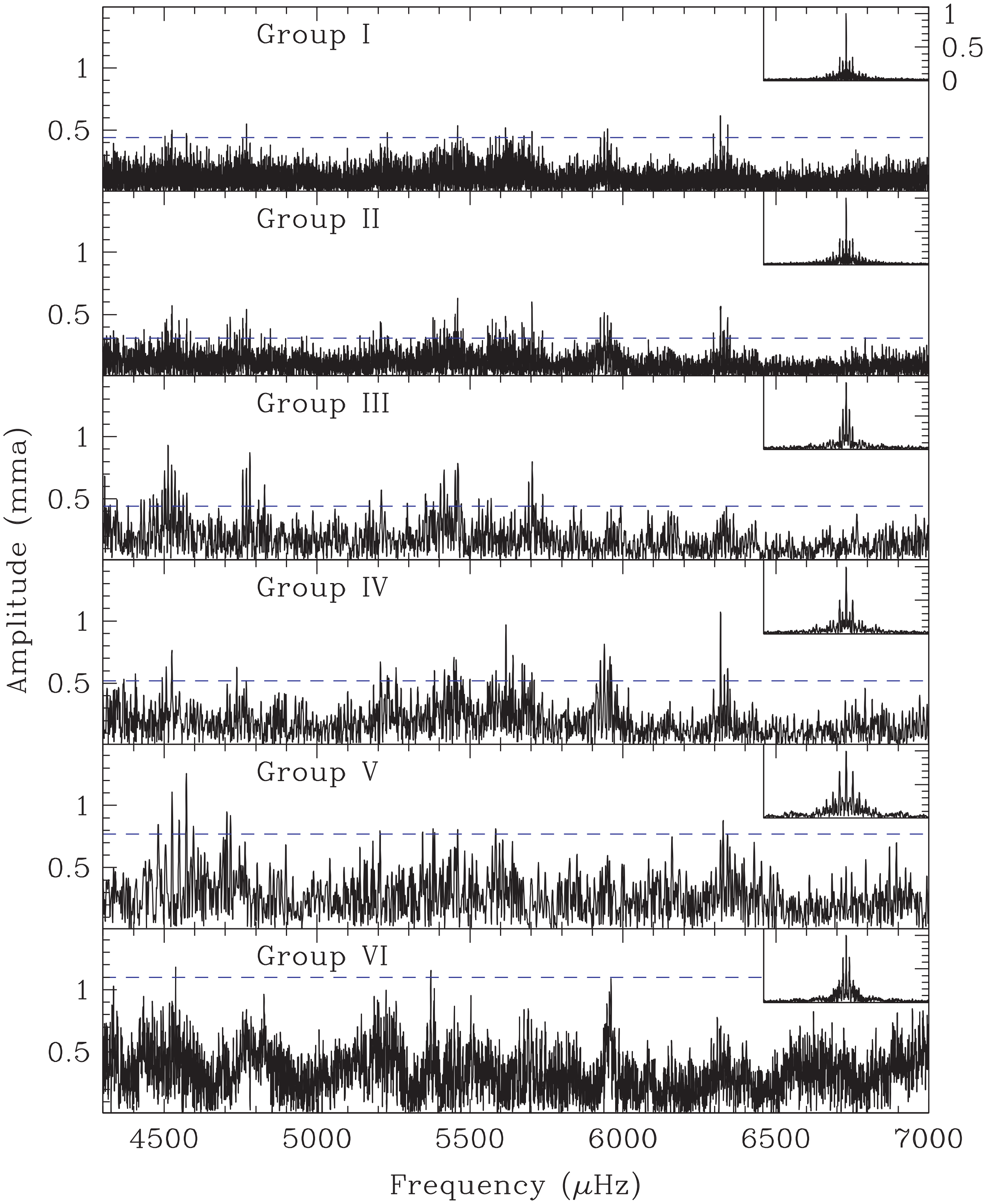

Figure 6. Same as Fig. 5 but for the frequency range from 4300 to 7000 μHz.

3.3 The frequency content

In total, we detected 68 independent pulsation frequencies and 13 suspected ones. Here we summarize some generalities which will be used in subsequent sections. Only three frequencies are detected in all six data groups. Six other frequencies are detected in five data groups and 13 are detected in four data groups. 38 frequencies are within a 650-μHz region between 3650 and 4300 μHz. Unlike most sdBV stars, which contain several frequencies above 3 mma, KPD 1930 does not have any in the integrated data (Groups I and II). Only *f*17 has an amplitude of >2 mma in all detections, though it is only detected in four groups. 11 of the 68

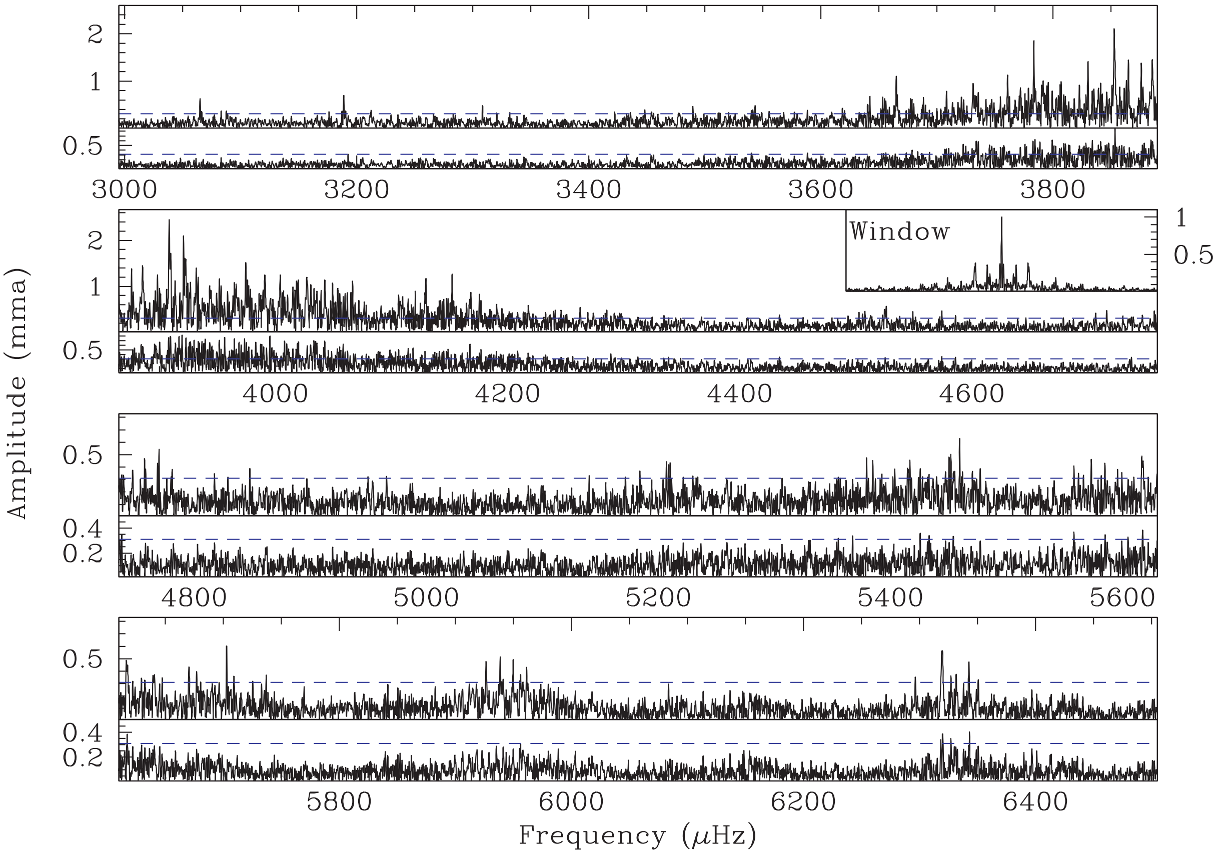

Figure 7. A detailed FT of Group II data showing the residuals after pre-whitening by 61 frequencies. Each panel shows the same frequency resolution, but the amplitudes in the top two panels differ from the bottom two. The dashed (blue) line is the 4σ detection limit.

frequencies have Group I amplitudes of >1 mma and these always have higher amplitudes in the shorter data sets (Groups III through VI), if detected. These simple observations again lead to the conclusion that pulsations of KPD 1930 are highly variable in amplitude and/or phase over the course of our observations. Combining this with the density in the main region of pulsations will make accurate deciphering of the temporal spectrum difficult. Additionally, the pulsations in uncrowded regions have low amplitudes which will make them difficult to detect in short data sets.

4 DISCUSSION

4.1 Comparison with the discovery data

By combining their four nights of data, B00 obtained a resolution of 1.89 μHz and their estimate of a mean noise level is 0.021 per cent, giving their data a 4σ detection limit of 0.84 mma. By comparison, our XCov 23 data have 4.2 × better resolution and our detection limit is about half. Frequencies that match those of B00 are marked with a ⋄ in Tables 4 and 5 while those that are a daily alias away are marked with a ⋆. 26 of our 81 frequencies are related to the 44 frequencies listed in B00. Of the eight frequencies listed in B00 with amplitudes greater than 2 mma, seven are detected in our data. For comparison, there are 21 frequencies which we have detected in at least five of our groups or have amplitudes of >1 mma in at least two groups (one of which must be Group I or II), and of these, eight are related to frequencies detected in B00. This also indicates a substantial amount of amplitude and/or phase change since the B00 observations.

4.2 Amplitude and phase stability

KPD 1930 shows characteristics similar to the sdBV star PG 0048+091 (Reed et al. 2007b), which has pulsation properties normally associated with stochastic oscillations. These properties include frequencies that are inconsistent between data sets and lower amplitudes in longer duration data. Of the 69 frequencies in Table 4, only $f10$, $f11$ and $f24$ are detected in all six groups of data, while $f2$ is detected in five groups, with a peak just below 4σ in the sixth. Six more frequencies are detected and fitted in five of the six groups. Unfortunately, unlike PG 0048+091's well-spaced frequencies, most of those in KPD 1930 are packed tightly between 3600 and 4200 μHz. Outside of this main region of power, the amplitudes are quite low, making detection difficult.

Despite these complications, we analysed data sets of varying lengths with the goal of reaching time-scales shorter than the time-scale of amplitude and/or phase variations. Such data would be free of the resultant complications, allowing the amplitudes and phases to be more accurately measured. These could then be examined over the duration of our observations for changes. For the shortest possible time-scale, we examined every individual run for which the 4σ detection limit was better than 2.0 mma, totalling 32 runs. We also created 13 daily data sets combining low-noise runs that were contiguous or nearly so. The lengths of the daily data ranged from 7 to 27 h, with a median value of 16.5 h. Including the data for Groups III, IV and V, we have data sets sampling time-scales near 0.25, 0.67 and 4 d.

To resolve frequencies from individual runs and daily data sets, we selected frequencies isolated by at least 30 μHz from Table 4

Table 4. Frequencies and amplitudes detected in various groupings of data. The temporal resolution of 1/(run length) and the 4σ detection limit are provided in the first two rows. Frequencies are in μHz and amplitudes in mma with NLLS fitting errors given by the last digits in parentheses. The last column indicates other frequencies that are within 1 μHz of the daily alias.

ID	Group	I	II	III	IV	V	VI	Alias
	4σ limit	0.44	0.31	0.44	0.52	0.77	0.59	
	resolution	0.45	0.60	2.69	2.58	3.75	1.87	
	frequency				Amplitudes			
$f1$	3065.085 (49)	0.70 (8)	0.62 (8)	0.56 (13)	0.75 (13)	–	0.79 (14)	
$f2^{\star}$	3188.864 (44)	0.68 (8)	0.69 (8)	0.62 (13)	0.88 (13)	$<4\sigma$	0.61 (14)	
$f3$	3308.382 (66)	0.44 (8)	0.45 (8)	NF	$<4\sigma$	$<4\sigma$+	0.63 (14)+	
$f4$	3422.386 (92)	–	0.32 (8)	–	–	–	0.56 (14)+	
$f5$	3489.608 (80)	0.48 (8)	0.38 (8)	–	$<4\sigma$	–	–	
$f6$	3543.258 (60)	0.52 (8)	0.50 (8)	–	0.75 (13)	–	–	
$f7$	3653.074 (54)	0.55 (8)	0.59 (9)	1.13 (14)	–	–	–	$f8$
$f8$	3664.968 (29)	≈0.92 (9)	1.10 (9)	–	1.09 (14)	1.91 (24)	1.25 (15)	$f7$
$f9$	3683.269 (63)	0.41 (8)	–	≈0.95 (14)	–	–	1.17 (16)	
$f10^{\diamond}$	3731.065 (38)	0.84 (9)	0.79 (8)	1.40 (14)+	1.08 (15)	1.15 (24) ++	1.06 (16)−	
$f11^{\diamond}$	3783.460 (17)	1.51 (9)	1.88 (9)	2.35 (14)	1.84 (15)	1.52 (26)	1.55 (19)	
$f12$	3791.545 (41)	NF	0.79 (9)	–	NF	–	1.15 (19)+	
$f13^{\diamond}$	3804.693 (41)	–	0.79 (9)	–	–	–	1.67 (17)	
$f14$	3822.646 (39)	0.70 (9)	NF	1.28 (14)+NF	0.90 (15)++	≈1.96 (26)	–	
$f15^{\star}$	3852.709 (19)	1.64 (9)	1.90 (9)	1.63 (14)	2.27 (15)	NF	–	$f16$
$f16$	3862.952 (34)	–	1.06 (9)	NF	–	–	1.57 (16)	$f15$
$f17^{\star}$	3908.614 (17)	2.26 (11)	2.09 (9)	–	3.76 (15)	–	2.85 (17)−	$f18$
$f18$	3920.717 (27)	1.07 (10)	1.40 (10)	NF	NF	NF	1.04 (16)[a]	$f17$
$f19$	3921.901 (28)	1.22 (9)	1.29 (9)	2.40[a] (14)	–	–	–	
$f20$	3924.426 (26)	1.30 (9)	1.24 (9)	–	–	3.94 (25)[a]	–	
$f21$	3926.008 (25)	1.11 (9)	–	–	–	–	1.77 (16)	
$f22$	3958.804 (35)	∼0.66 (9)	0.94 (9)	–	–	–	–	
$f23$	3964.686 (30)	0.93 (9)	–	1.72 (15)	–	–	–	$f24$
$f24^{\diamond}$	3974.320 (19)	1.60 (9)	1.68 (9)	≈1.29 (15)	1.97 (15)	3.16 (25)	1.76 (16)	$f23$
$f25^{\diamond}$	3990.848 (29)	0.65 (9)	1.12 (9)	≈1.04 (16)	1.99 (15)	≈1.74 (25)	–	
$f26$	4004.192 (25)	–	1.31 (9)	–	–	2.01 (25)	–	
$f27$	4018.289 (27)	1.22 (9)	1.19 (9)	1.85 (14)	1.51 (15)	–	2.11 (16)	$s72$
$f28$	4027.241 (27)	1.04 (9)	–	NF	2.19 (16)	–	–	
$f29$	4034.710 (31)	0.90 (9)	–	–	1.37 (16)	–	–	
$f30$	4049.223 (29)	0.86 (9)	1.12 (9)	1.23 (14)	1.27 (15)	–	–	
$f31^{\star}$	4066.443 (33)	0.84 (9)	0.98 (9)	1.21 (14)	–	NF	–	
$f32^{\diamond}$	4120.459 (48)	0.78 (9)	0.65 (8)	–	NF	≈1.57 (24)	1.41 (16)−	
$f33$	4129.667 (32)	0.69 (9)	0.95 (9)	1.34 (13)	–	–	1.59 (16)	
$f34^{\star}$	4152.155 (33)	0.55 (9)	0.92 (9)	≈1.02 (13)	1.42 (14)	–	–	
$f35$	4168.331 (36)	0.92 (9)	0.85 (8)	–	1.19 (14)	–	1.81 (15)+	
$f36^{\diamond}$	4195.364 (51)	0.65 (9)	0.59 (8)	–	0.75 (14)	1.03 (22)	0.98 (14)	
$f37^{\diamond}$	4262.566 (69)	–	0.44 (8)	–	0.57 (14)	–	–	
$f38$	4297.849 (58)	0.44 (8)	0.43 (8)−	0.76 (17)	0.57 (13)	–	–	$s75$
$f39^{\diamond}$	4453.34 (31)	–	–	0.66 (13)	–	–	0.62 (14)−	
$f40$	4480.61 (57)	–	–	–	–	0.78 (22)	0.89 (14)	
$f41$	4507.884 (62)	–	0.48 (8)	0.50 (13)−	–	NF	0.57 (15)+	
$f42$	4524.708 (56)	0.66 (8)	0.53 (8)	0.99 (13)−	0.70 (13)	–	0.61 (14)	
$f43$	4549.152 (69)	–	0.44 (8)	0.49 (13)	–	–	–	
$f44$	4572.412 (42)	0.61 (8)	NF	0.51 (13)−	–	1.2 (22)	–	
$f45$	4716.271 (67)	NF	0.45 (8)	–	0.60 (13)++NF	0.98 (22)	NF−	
$f46$	4769.657 (67)	0.53 (8)	0.45 (8)	0.58 (14)−	–	–	–	$f47$
$f47^{\diamond}$	4781.042 (94)	–	0.31 (8)	0.67 (14)	–	–	–	$f46$
$f48$	4847.885 (84)	–	0.35 (8)	0.55 (13)−−	–	–	0.65 (14)−	
$f49$	5184.009 (86)	–	0.34 (8)	–	–	–	0.64 (14)	
$f50$	5207.451 (68)	NF	0.44 (8)	NF	0.67 (13)[a]	$<4\sigma$[a]	–	
$f51^{\star}$	5210.203 (78)	–	0.38 (8)	0.50 (13)[a]	–	–	–	
$f52$	5230.003 (41)	0.63 (8)	–	–	–	NF++	0.51 (14)++	
$f53^{\star}$	5379.426 (79)	–	0.38 (8)	0.57 (13)−−	–	–	–	
$f54$	5384.750 (83)	–	0.36 (8)	–	0.57 (13)	0.71 (22)	0.93 (14)+NF	
$f55^{\diamond}$	5416.641 (74)	–	0.40 (8)	0.72 (13)	≈0.65 (14)++	–	–	
$f56$	5451.930 (57)	–	0.53 (8)	0.72 (17)	0.73 (14)	NF	≈0.58 (15)	
$f57$	5459.529 (47)	0.51 (8)	0.64 (8)	≈0.56 (17)	–	$<4\sigma$	0.57 (15)	
$f58^{\star}$	5529.22 (37)	–	–	0.54 (13)	–	–	–	

Table 4 – *continued*

ID	Frequency	I	II	III	IV	V	VI
$f59$	5572.909 (74)	–	0.40 (8)	≈0.51 (13)	–	0.72 (22)+	–
$f60$	5616.391 (65)	0.51 (8)	0.46 (8)	–	0.94 (13)	NF	–
$f61$	5670.540 (79)	–	0.38 (8)	–	0.64 (13)	–	≈0.61 (14)
$f62$	5702.901 (51)	NF	0.59 (8)	0.98 (13)	–	–	0.79 (15)
$f63$	5709.319 (79)	–	0.38 (8)	–	–	–	0.56 (15)+
$f64^{\diamond}$	5737.037 (83)	$<4\sigma$	0.35 (8)	0.47 (13)+	–	–	–
$f65$	5938.582 (60)	0.42 (9)	0.54 (8)	–	0.74 (13)	–	0.51 (14)−
$f66^{\diamond}$	5950.308 (68)	0.44 (9)	–	$<4\sigma$+	≈0.61 (13)	–	≈0.74 (15)
$f67$	6319.148 (69)	0.54 (9)	0.44 (8)	–	1.03 (13)	0.83 (22)+	1.40 (22)+
$f68$	6342.994 (62)	0.52 (9)	0.49 (8)	$<4\sigma$-	–	–	0.75 (22)

Note. + indicates that the frequency fit using NLLS was one daily alias (11.5 μHz) larger than that listed. Likewise, ++, − and −− indicate frequencies that are +2 daily, −1 daily and −2 daily aliases from those listed, respectively. ≈ indicates that frequencies were slightly more than 1σ away from that shown, $<4\sigma$ indicates frequencies that had power in the FT which was below the 4σ detection limit; NF indicates frequencies above the 4σ limit that could not be fitted using our NLLS programme. ◇ indicates frequencies that match B00 while ⋆ indicates those that are a daily alias away.
[a]Unresolved frequencies. Amplitudes of unresolved frequencies do not reflect the intrinsic amplitudes of each frequency.

Table 5. Same as Table 5 for suspected frequencies.

	Group	I	II	III	IV	V	VI	Alias
$s69$	3448.361 (85)	–	0.35 (8)	–	–	–	–	
$s70^{\diamond}$	3885.715 (28)	1.03 (10)	–	–	–	≈NF	–	
$s71$	3995.235 (27)	1.01 (9)	–	–	–	NF	–	
$s72$	4030.437 (29)	1.09 (9)	–	–	NF	NF	–	$f27$
$s73$	4232.67 (25)	–	–	0.91 (14)	–	–	–	
$s74$	4246.23 (31)	–	–	0.74 (14)	–	–	–	
$s75^{\star}$	4307.84 (29)	–	–	0.87 (17)	–	–	–	$f38$
$s76$	4897.000 (78)	–	0.38 (8)	–	–	–	–	
$s77$	4949.582 (94)	–	0.31 (8)	–	–	–	–	
$s78$	4965.63 (10)	–	0.36 (8)	–	–	–	–	
$s79^{\diamond}$	5140.42 (12)	–	0.25 (8)	–	–	–	–	
$s80$	5769.48 (11)	–	0.28 (8)	–	–	–	≈0.55 (14)	
$s81^{\star}$	6083.547 (83)	–	0.35 (8)	$<4\sigma$+	–	–	–	

which included $f1$ through $f6$, $f44$, $f45$, $f48$, $f58$ through $f61$, $f67$ and $f68$. We then attempted to fit amplitudes and phases for each of the frequencies for all of the data subsets. As expected, most of the fits failed as the pulsation amplitudes were well below the detection limits. Only for five frequencies were we able to fit phases and amplitudes to some of the shorter data sets. From the 48 data subsets, we fitted 52 of the possible 480 phases and amplitudes for the five frequencies. Phases are determined as the time of the first maximum amplitude after BJD = 245 2871.5 and converted to fractional phases by dividing by the period. In this manner, an error of 0.1 represents a 10 per cent change in phase. The fractional phases and amplitudes are shown in Figs 8 and 9 (and provided in Table S1 in the online Supporting Information). Horizontal bars indicate the time-span of the data for the daily and group sets. Note that some of the amplitudes are just below the 4σ detection limit. We include them because the peaks were fairly obvious in the FT and since the frequency is known, a lower detection limit is not unreasonable.

Table 6 examines the amplitude and phase properties organized by the time domain. While $f1$ is not detected in any individual runs, the phase is stable to within the error bars. $f2$ shows deviations of 12 per cent and $f44$, $f60$ and $f67$ have deviations all near 18 per cent. Phase errors for individual measurements are under 10 per cent (except for one) with an average of 5.0 per cent. Phase variations are provided in Table 6 labelled as σ_{ϕ} (per cent). While the deviations appear similar for $f44$, $f60$ and $f67$, $f44$ has one discrepant value while $f60$ and $f67$ appear as a phase variable, particularly from the individual runs (black circles in Fig 8). However none of the phases appear randomly distributed nor do they appear bimodal, which would be an indicator of unresolved frequencies.

The amplitudes show a larger variety. $f1$ and $f2$ are the most stable (the smallest $\sigma A/\langle A\rangle$), but the amplitudes for $f1$ are so small that it is not detected in any individual runs and only three of 13 daily runs. As such, it is clear that the number of detections will significantly affect amplitude stability as smaller and therefore more deviant amplitudes will not have been measured. For these five frequencies, none is detected more than 30 per cent of the time. Therefore our measure of amplitude variability, $\sigma A/\langle A\rangle$, should be considered a lower limit. Likewise, the variations for $f44$, $f60$ and $f67$ must be higher than what we report as they have some relatively high amplitudes yet are not detected in all runs. For the amplitudes, temporally nearby runs can have different amplitudes and consistently longer time domains have lower amplitudes. As these frequencies are reasonably separated from others for all of the time-scales considered and their amplitudes do not appear bimodal, it is unlikely that beating plays a role in the amplitude variations. They are most likely intrinsic to the pulsations.

The original goal of this subsection was to determine the time-scale of phase and amplitude variations. Indicators of this time-scale are the standard deviations, the ratios between of the average

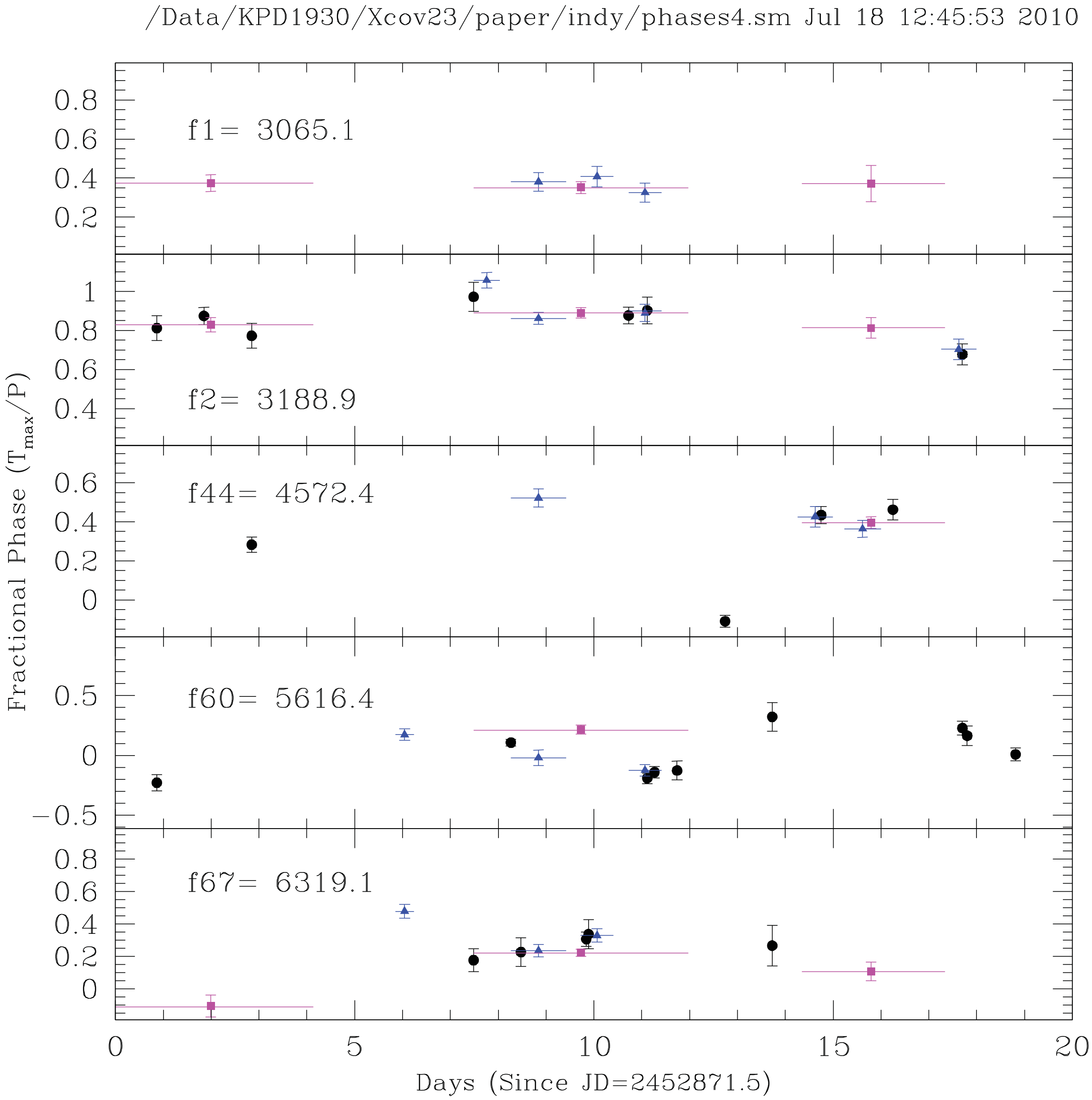

Figure 8. Phases of frequencies resolvable from short data sets. Circles (black) indicate individual runs, triangles (blue) are from daily runs and squares (magenta) are for Groups III to V. Horizontal lines indicate the time-span of the data used in the phase determination for the daily and group sets.

to maximum amplitudes and comparison these between the sets. For example, if the time-scale of variation is longer than a day, then the average and maximum values of the daily runs and the individual ones should be similar and should have $\langle A\rangle/A_{\max}$ near 1. For $f2$, the average daily amplitude is slightly larger than that for the individual runs while that for the group sets is significantly smaller. This indicates that the time-scale for amplitude variations is near to or longer than 16 h but shorter than 72 h.

4.3 Stochastic properties

An indicator for stochastic pulsations in solar-like oscillators is a $\sigma_A/\langle A\rangle$ ratio near 0.52 (Christensen-Dalsgaard, Kjeldsen & Mattei 2001). Pereira & Lopes (2005) also derived this ratio and were the first to apply it in testing whether pulsating sdB stars could be stochastically excited. Their results for the pulsating sdB star PG 1605+072, based on seven nights of data, indicated that those pulsations were driven rather than stochastically excited. The ratios for $f60$ and $f67$ are near to this value. However in solar-like oscillators the amplitude decay time-scale is long compared to the re-excitation time-scale, and so this ratio may not be a good indicator for sdBV stars. Other features that could indicate stochastic oscillations include significant amplitude variability, amplitudes that are reduced in longer duration data sets (caused by phase variations) and match with simulated stochastic data.

Similar to what was done for PG 0048+091, we produced Monte Carlo simulations for stochastic oscillations with varying decay and re-excitation time-scales appropriate for the various data sets and groups we had for KPD 1930. As there are many amplitude ratios to work with from Table 6, it was hoped that tight constraints for amplitude variations could be deduced by matching the simulations with the observations. However, such was not the case and the

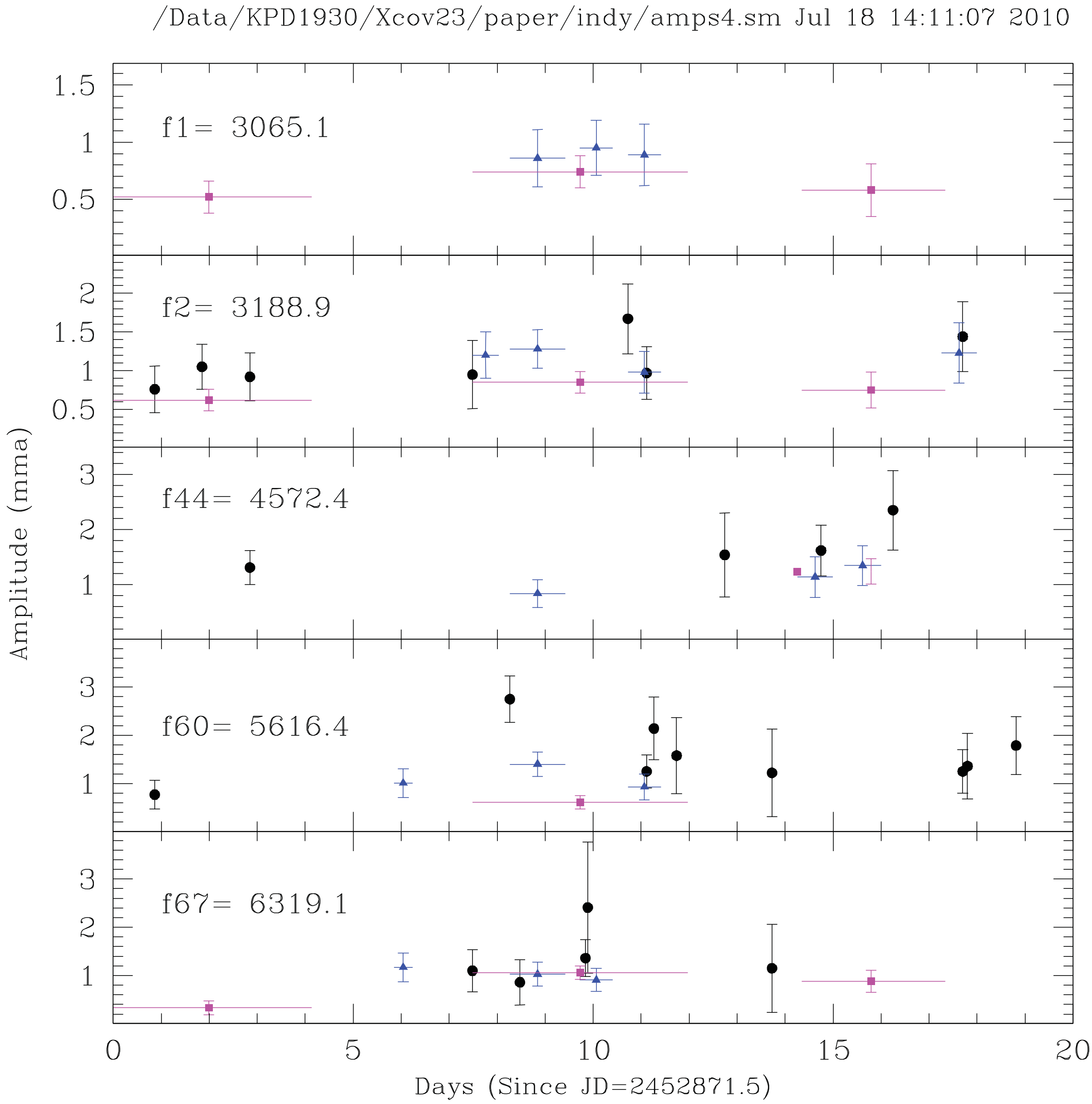

Figure 9. Pulsation amplitudes corresponding to the phases shown in Fig. 8.

best we could do was produce loose time-scales. The best results for *f*1 indicate short amplitude decay time-scales (4–6 h) and long re-excitation time-scales (20–30 h), those for *f*2 indicate medium decay time-scales (9–15 h) and medium to long re-excitation time-scales (12–27 h), those for *f*44 indicate short decay time-scales (4–9 h) and medium re-excitation time-scales (8–16 h), those for *f*60 indicate short to medium decay time-scales (4–15 h) and long re-excitation time-scales (25–40 h), and those for *f*67 indicate short to medium decay time-scales (4–20 h) and long re-excitation time-scales (15–28 h). The resultant time-scales are fairly consistent in that the decays are always short compared to the re-excitations, but they are not nearly as clear as for PG 0048+091, certainly owing to the complexity of KPD 1930's pulsation spectrum. However, the pulsation phases do not appear randomly distributed, as would be expected for stochastic oscillations. So we are left with some indications that stochastic processes may be present and some information contrary to stochastic oscillations. From these data, we cannot discern between them.

4.4 Observed multiplets

From the ellipsoidal variations in KPD 1930, we can strongly infer it to be tidally locked, which means that we also know the rotation period. In standard spherical harmonics, each ℓ can produce $2\ell + 1$ m azimuthal values separated by the orbital frequency and the Ledoux constant (which is very small for p modes in sdB stars). We can search for multiplets to impose observational constraints on the mode degrees (ℓ). Table 7 lists multiplets detected to splittings of four times the orbital frequency of 121.7 μHz. As there are many pulsation frequencies related by a multiple of the rotation/orbital frequency, the order of the frequencies is the same as in Table 4 with the numbers in parentheses indicating the multiple of the rotation/orbital frequency between it and the previous (smaller) frequency. The leftmost frequency is just the lowest for each multiplet but has no significance otherwise.

Table 6. Properties of pulsation phases and amplitudes for frequencies separated by >30 μHz. Pulsation amplitudes are compared in a number of ways including by standard deviations (σ), average ($\langle\,\rangle$) and maximum ($_{\max}$) amplitudes for various groupings of data. The number of possible detections is in parentheses next to the category (All, Individual, Daily or Groups).

	$f1$	$f2$	$f44$	$f60$	$f67$
			All (54)		
$\#_{\rm det}$	7	16	8	14	16
$\langle A\rangle$	0.79	1.07	1.43	1.33	1.04
σ_A	0.19	0.27	0.45	0.60	0.45
$\sigma_A/\langle A\rangle$	0.24	0.25	0.31	0.45	0.43
$A_{\rm GI-II}/\langle A\rangle$	0.78	0.64	0.43	0.35	0.42
σ_ϕ (per cent)	4.3	12.4	19.7	17.8	17.1
			Individual runs (37)		
$\#_{\rm det}$	0	8	4	10	9
$\langle A\rangle$	–	1.11	1.72	1.47	1.20
σ_A	–	0.29	0.45	0.64	0.51
$\sigma_A/\langle A\rangle$	–	0.26	0.26	0.44	0.43
$A_{\max}$	–	1.67	2.35	2.75	2.41
$\langle A\rangle/A_{\max}$	–	0.66	0.73	0.53	0.50
$A_{\rm GI-II}/\langle A\rangle$	–	0.62	0.35	0.31	0.37
$\langle A_d\rangle/\langle A\rangle$	–	1.05	0.65	0.76	0.87
$\langle A_{\rm GIII-VI}\rangle/\langle A\rangle$	–	0.79	0.72	0.41	0.59
$A_{\rm GI-II}/A_{\max}$	–	0.41	0.26	0.17	0.18
$\langle A_d\rangle/A_{\max}$	–	0.70	0.47	0.40	0.43
$\langle A_{\rm GIII-VI}\rangle/A_{\max}$	–	0.53	0.53	0.22	0.29
σ_ϕ (per cent)	–	14.6	26.0	19.2	13.6
			Daily runs (13)		
$\#_{\rm det}$	3	4	3	3	3
$\langle A\rangle$	0.90	1.17	1.11	1.11	1.04
σ_A	0.05	0.13	0.26	0.25	0.13
$\sigma_A/\langle A\rangle$	0.06	0.11	0.23	0.23	0.13
$A_{\max}$	0.95	1.28	1.35	1.40	1.17
$\langle A\rangle/A_{\max}$	0.95	0.91	0.82	0.79	0.89
$A_{\rm GI-II}/\langle A\rangle$	0.69	0.59	0.55	0.41	0.42
$\langle A_{\rm GIII-VI}\rangle/\langle A\rangle$	0.79	0.75	1.12	0.55	0.68
$A_{\rm GI-II}/A_{\max}$	0.65	0.54	0.45	0.33	0.38
$\langle A_{\rm GIII-VI}\rangle/A_{\max}$	0.75	0.69	0.92	0.44	0.61
σ_ϕ (per cent)	4.0	14.5	8.0	15.2	12.2
			Groups III–VI		
$\#_{\rm det}$	4	4	1	1	4
$\langle A\rangle$	0.71	0.88	1.24	0.61	0.71
σ_A	0.22	0.29	–	–	0.33
$\sigma_A/\langle A\rangle$	0.31	0.33	–	–	0.46
$A_{\max}$	1.01	1.28	1.24	0.61	1.06
$\langle A\rangle/A_{\max}$	0.70	0.69	–	–	0.67
$A_{\rm GI-II}/\langle A\rangle$	0.87	0.78	0.49	0.75	0.62
$A_{\rm GI-II}/A_{\max}$	0.61	0.54	0.49	0.75	0.42
σ_ϕ (per cent)	4.9	3.4	–	–	14.0

4.4.1 *Classical interpretation*

In total, 61 of our 81 frequencies are related by a multiple of the rotation/orbital frequency. In a classical asteroseismological interpretation, we would assume that the spin axis is aligned with the orbital axis and the stars are tidally locked. As such, we are viewing the spin axis close to equator-on, or an inclination near 80° and the multiplets are caused by stellar rotation.

As each degree can have $2\ell+1$ azimuthal orders, m, the number of orbital splittings provides a minimum ℓ value and constrains where the $m=0$ is. For example, the $f1$, $f2$, $f3$ triplet is best interpreted as an $\ell=1$ triplet with $m=0$ at $f2$. The multiplet beginning with $f4$ has sufficient frequencies to warrant an $\ell=3$ interpretation. However, $\ell=3$ modes have low amplitudes caused by geometric cancellation, making such an interpretation unlikely. More feasible is the fact that there are two $\ell=1$ multiplets with their outside components at a chance separation of nearly $2f_{\rm orb}$. Column 1 of Table 7 gives the minimum ℓ degree based on the number of orbital splittings. For entries with multiple possibilities, the most likely is given first. (The online Supporting Information includes a colour-coded figure showing the multiplets and a figure showing just the $m=$ components with their corresponding degrees; Figs S2 and S3.)

Table 7. Pulsation frequencies split by a multiple of the rotation/orbital frequency. The pulsation frequencies refer to those in Tables 4 and 5. The frequencies are in ascending order and the number in parentheses indicates the multiple of the orbital frequency between itself and the previously listed frequency. Column 1 lists the minimum degree for the multiplet using the classical interpretation.

$\ell_{\min}$	Des.	Designations of related frequencies
1	$f1$:	$f2$ (1), $f3$ (1)
1, 1 or 3	$f4$:	$f6$ (1), $f8$ (1), $f17$ (2), $s72$ (1), $f34$ (1)
2	$f5$:	$f10$ (2), $f15$ (1), $f24$ (1)
2 or 4	$f7$:	$f27$ (3), $f37$ (2), $f41$ (2)
2	$f9$:	$f13$ (1), $f21$ (1), $f30$ (1), $f35$ (1)
1	$f11$:	$f28$ (2)
1	$f12$:	$f29$ (2)
3	$f14$:	$f31$ (2), $s75$ (2), $f43$ (2)
1	$s70$:	$f33$ (2)
1 or 3	$f23$:	$f39$ (4), $f44$ (1)
2	$f25$:	$s73$ (2)
3 or 5	$s71$:	$f40$ (4), $f48$ (3), $f51$ (3)
1	$f26$:	$s74$ (2)
1	$f42$:	$f46$ (2)
2	$s76$:	$s79$ (2), $f55$ (2)
4 or 3	$s78$:	$f50$ (2), $f56$ (2), $f59$ (1), $f65$ (3)
2	$f49$:	$f61$ (4)
1	$f57$:	$f62$ (2)
1	$f60$:	$f64$ (1)
1	$f63$:	$f66$ (2)

We can also use the pulsation amplitudes to place some constraints on the modal degrees. Using Groups I and II as a guide, all of the amplitudes are within a factor of 7 of each other, while most are within a factor of 4. Table 8 lists the geometric cancellation factors for azimuthal orders $\ell, m = 1, 0$ through 4, 4 for rotation axes of $i_{\rm r} = 70°$ and 80°. These factors indicate how much a pulsation amplitude would be reduced relative to a radial mode, which suffers no geometric cancellation. As Column 2 indicates, for the classical interpretation, all of the $\ell \le 2$ modes have amplitudes reduced by factors less than 5–8, depending on orientation. This is roughly in agreement with the observed amplitude range. By contrast, all $\ell \ge 3$ modes have amplitudes reduced by factors of $\ge$20 (except for $\ell, m = 4, |1|$ depending on the viewing angle). Since we do not observe this range of amplitudes in KPD 1930, it is unlikely that these multiplets are being observed.

Ignoring high-degree modes, there remains multiplets as evidence of 12 $\ell=1$ and four $\ell=2$ modes. There are also 20 frequencies which show *no* relations to other frequencies via an orbital overtone. These are all candidates for radial modes. As there is no geometric cancellation for radial modes, they would be expected to have some of the higher amplitudes. $f16$, $f18$, $f19$ and $f20$ all have amplitudes greater than 1 mma for all of their detections. Yet none of these has amplitudes significantly higher than the other frequencies.

Table 8. Geometric cancellation (pulsation amplitude reduction) factors for $i_r = 80°$ ($i_r = 70°$ in parentheses).

ℓ, m	Classical	Tipped
1, 0	4.81 (2.44)	1.69 (1.77)
1, |1|	1.20 (1.26)	2.40 (2.52)
2, 0	3.35 (4.70)	4.18 (4.59)
2, |1|	7.28 (3.87)	5.15 (5.65)
2, |2|	2.57 (2.82)	5.48 (7.67)
3, 0	48.2 (28.9)	39.9 (45.9)
3, |1|	32.9 (70.6)	860 (72.6)
3, |2|	51.7 (28.9)	73.0 (57.8)
3, |3|	22.3 (25.7)	68.1 (51.8)
4, 0	32.9 (7,911)	34.6 (41.8)
4, |1|	41.7 (4.81)	7.46 (8.04)
4, |2|	30.0 (151)	55.0 (45.9)
4, |3|	173 (21.4)	64.2 (57.2)
4, |4|	81.4 (98.1)	282 (218)

Therefore, it is also possible they are $\ell > 0$ modes with only one frequency visible.

4.4.2 *Tipped-axis interpretation*

Another interpretation would be that the pulsation axis is aligned with the tidal force of the companion. As described by Reed, Brondel & Kawaler (2005), such a pulsation geometry would precess, completing a revolution every orbital period. The change in viewing pulsation geometry incorporates three additional pieces of information into the light curve which can be used to uniquely identify the pulsation degree ℓ and the absolute value of the azimuthal order $|m|$. These are a pattern of peaks in the FT of the integrated light curve, two or more 180° flips in the pulsation phase over an orbital period and recovery of the 'true' peak in the FT of the phase-separated data. As in Reed et al. (2005), we will not seek analytic solutions, but will use simulated data of precessing pulsation geometries to guide us. These simulations and any tipped-axis analysis make the assumption that spherical harmonics apply.

We begin by searching for patterns in the FT of the integrated data of KPD 1930. To guide our search, we produced simulated data for modes from $\ell = 0$ to 4 for an orbital/rotation axis of $i_r = 70°$ and a pulsation axis of $i_p = 85°$ relative to the rotation axis. This geometry seems reasonable for what we know of the orbital inclination and with tidal forces larger than the maximum Coriolis force. Changes of 5°–10° in either axis make little difference in the patterns. The simulated FTs are shown in Fig. 10. The amplitudes are relative to the $\ell = 0$ (radial) mode and along with the geometric cancellation factors of Table 8 indicate that high-degree modes are unlikely to be observed. The frequency patterns of Fig. 10 are what we are looking for in the observed data.

18 of the multiplets from Table 4 match patterns from simulated tipped-axis pulsations.[2] The next step is to divide the data into orbital regions of like and opposing pulsation phases [Reed et al. (2005) showed this procedure in detail] for the different modes. If the intrinsic frequencies predicted by the tipped-axis model are recovered, and their phases are opposite in appropriate data sets, this would be a reasonable indicator of a tipped pulsation axis. As can be seen in Fig. 10, the intrinsic frequency for tipped modes $\ell, m = 1, 1; 2, 0; 2, 2; 3, 1$ and $3, 3$ will have a corresponding frequency in the combined data. As such, recovering the peak in the divided data is less important but detecting a phase shift of 0.5 will be vitally important for associating these frequency patterns with tipped pulsation modes.

We separated the data for Groups I through V into orbital regions of like and opposing phases appropriate for modes $\ell, m = 1, 0$ through 4, 4 and searched each group not only for the frequencies predicted from the observed multiplets, but for any previously unobserved frequencies above the noise.[3] The simplest data sets are those for $\ell = 1$ as the orbit is divided into halves, with set A of $\ell, m = 1, 1$ going from an orbital phase of 0.0 to 0.5 and set B covering the other half. Those for $\ell, m = 1, 0$ are shifted by -0.25 in phase. Table 9 provides the results of the search. Column 1 provides a unique mode identifier (with a corresponding identifier from Table 4 in parentheses, if there is any), Column 2 the frequency, Column 3 indicates the mode the data were phase-separated for and the remaining columns give the phase difference (set A − set B) for each group.

As anticipated considering the complexity of the data, the results are not straightforward. In the split data sets, the aliasing is significantly worse and the pulsation amplitudes are very low. Evidence also suggests that amplitudes and phases are changing throughout the campaign. Most of the predicted frequencies are not detected. Those that are detected have amplitudes only marginally above the noise. But the strongest evidence will be consistent phase differences of one-half in the various data sets. Frequency $t10\,(f15)$ shows no phase shift between the sets for all groups and so cannot be a tipped pulsation mode. Frequencies $t11$ and $t14$ have intermediate values, again indicating that they are likely not tipped pulsation modes, but rather that their phases are not stable over the course of the observations. Frequencies $t2$ and $t12$ are only detected in two of the five data sets, and while one phase difference is near one-half, the other has an intermediate value. As $t2$ is also detected in the integrated light curve, but should not be for an $\ell, m = 1, 0$ mode, it is unlikely a tipped mode. Frequencies $t5$, $t8$ and $t9$ do fit what we expect for tipped pulsations. $t9$ is detected with a similar phase difference in all five groups, $t8$ has consistent phase differences for the three data sets in which it can be detected and $t5$ has consistent phase differences in three of four detections. Additionally, $t5$ is not detected in the integrated data, as should be the case. More surprising are the results for $t17$ and $t19$, both of which are only detected in two of the five groups but have phase differences near to one-half. These modes are unlikely to be observed because the geometric cancellation factors are very high (73 and 282, respectively), meaning the intrinsic amplitudes would need to be much higher than the others. Monte Carlo simulations were produced with random phases between data sets. This could be appropriate for purely stochastic pulsations, but for driven pulsations, the phases should not be random at all, but rather close to a fixed number. As tipped pulsations have a phase shift of 0.5 which is very unexpected for driven pulsations, the significance of the simulations is somewhat startling. Our phase detections for $t8$ and $t9$ only occur in 0.1 per cent of our simulations while those for $t5$ occur 1.0 per cent of the time. Those for $t17$ and $t19$ occur 6.7 and 4.9 per cent of the time, respectively.

[2] These are shown schematically in Fig. S2 of the online Supporting Information.

[3] The phased data sets for Group II with $\ell, m = 1, 0$ and 1, 1 are shown in Fig. S5 of the online Supporting Information.

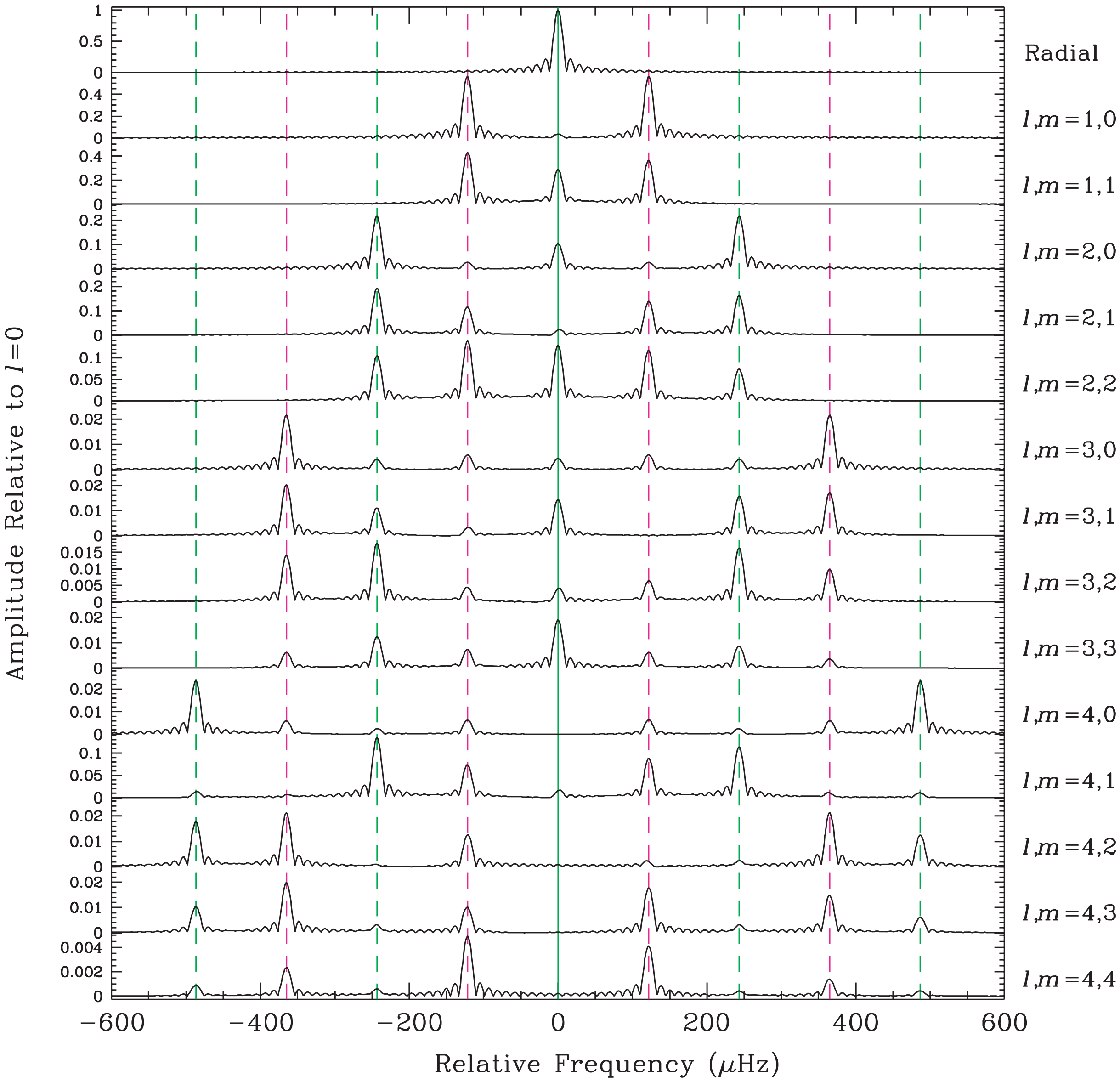

Figure 10. Pulsation spectra of simulated data where the pulsation pole points 5° off the orbital axis, which has an inclination of 70°. The input frequency is at the centre (solid green line) and the dashed lines indicate orbital aliases. The amplitudes are relative to the radial mode and the mode is indicated on the right-hand side.

Of the 18 frequency multiplets in the combined data sets, three possess indicators for tipped pulsation modes. Nine have no detections at all, two have phase differences near zero and two more have marginally appropriate phase differences, but would indicate modes that are unlikely to be detected because of geometric cancellation. Still, particularly for $t5$, which is not observed in the integrated data, the phase difference is a precise indicator for tipped pulsation modes. The chance of this occurring randomly is quite small.

4.5 Orbital dependence

While searching for tipped-axis pulsations, we stumbled upon the unexpected finding that some frequencies appeared to only occur for some stellar orientations.[4] So we divided the data into four, eight and 10 subsets according to the orbital phase and examined the pulsation spectra of each. We found that quadrants, centred around the orbital phases 0 (QI), 0.25 (QII), 0.5 (QIII) and 0.75 (QIV) sufficiently differentiated the orbital dependence of the frequencies. Temporal spectra of Group II's data, split into four quadrants, are shown in Fig. 11. The dashed lines indicate likely intrinsic frequencies while the dotted lines are more likely aliases, with the arrows indicating which frequency they are an alias of.

It is obvious that there is an orbital dependence on some frequencies, particularly $o3$, which is clearly and only seen in QI. This most likely means that the pulsation geometry, as normally described by spherical harmonics, is more complex for these frequencies. Describing the pulsation geometry for such modes is beyond the scope of this paper, but we provide frequencies which have a detectable orbital dependence in Table 10. Outside of the main area of power, there is little sign of this uniqueness other than the fact that $f57$ (5459) has a slightly higher amplitude in quadrant $\phi = 0.25$ and

[4] These can be seen in Fig. S5 of the online Supporting Information.

Table 9. Phase differences (A−B) for possible tipped pulsation frequencies. NLLS errors are in parentheses. Differences near ±0.5 indicate tippled-axis modes.

ID	Frequency	Mode	GI	GII	GIII	GIV	GV
$t1(f17)$	3913	1, 0	–	–	–	–	–
$t2(f26)$	4008	1, 0	−0.50 (2)	0.82 (2)	–	–	–
$t3(f32)$	4113	1, 0	–	–	–	–	–
$t4(f33)$	4126	1, 0	–	–	–	–	–
$t5$	4647	1, 0	0.55 (6)	−0.45 (5)	0.27 (4)	−0.43 (6)	–
$t6$	5581	1, 0	–	–	–	–	–
$t7$	5831	1, 0	–	–	–	–	–
$t8(f2)$	3187	1, 1	−0.55 (3)	0.49 (5)	–	0.46 (4)	–
$t9(f6)$	3543	1, 1	−0.67 (3)	−0.64 (3)	−0.51 (4)	0.39 (4)	0.41 (4)
$t10(f15)$	3853	1, 1	−0.08 (3)	−0.07 (2)	−0.16 (3)	−0.01 (2)	−0.13 (3)
$t11(f28/29)$	4030	1, 1	−0.25 (2)	−0.26 (2)	–	−0.39 (2)	−0.26 (3)
$t12(f37)$	4263	2, 0	–	0.51 (2)	–	−0.31 (4)	–
$t13$	5140	2, 0	–	–	–	–	–
$t14(f10)$	3731	2, 2	−0.22 (2)	–	–	−0.27 (2)	–
$t15(f21)$	3926	2, 2	–	–	–	–	–
$t16(f50)$	5207	3, 1	–	–	–	–	–
$t17$	4210	3, 2	−0.54 (5)	–	–	−0.63 (3)	–
$t18$	4188	4, 3	–	–	–	–	–
$t19$	4188	4, 4	0.61 (4)	–	−0.47 (5)	–	–

$f67$ (6319) is higher in quadrants $\phi = 0$ and 0.5. Undoubtedly, the lack of other detections is caused by low amplitudes combined with severe aliasing.

5 RESULTS

We have analysed WET data spanning 26 d in 2003 August and September, supplemented by 45 h of multisite data obtained in 2002 July. These data were used to examine the orbital properties and the pulsation spectrum of the sdB+WD binary KPD 1930. We used the ellipsoidal variation to affirm the orbital period and folded the data over that period. No signs of eclipse were detected, constraining the inclination to $<78\overset{\circ}{.}5$. Additionally, we noted that the minima are uneven, indicating that KPD 1930 is very slightly asymmetric and marginally detect anticipated Doppler effects from possibly uneven maxima.

As implied from the discovery data (B00), we have found KPD 1930 to be an extremely complex pulsator with frequencies and amplitudes that can vary on a daily time-scale. In these data, we confidently detect 68 pulsation frequencies and suggest a further 13. Of these, only 26 are related to frequencies observed by B00, a surprisingly small number that attests to KPD 1930's pulsational complexity. Our WET data, which covered more than three weeks during 2003, have over four times better temporal resolution and one-half the detection limit of B00.

We examined amplitude and phase stability by analysing subsets of data over several time-scales for well-separated frequencies. Unfortunately, the low amplitude of these frequencies hampered our investigation and we were unable to detect them in most of the subsets. For the times we could detect them, we found the pulsation amplitudes to be fairly variable, although all $\sigma_A/\langle A\rangle$ ratios are short of the value of 0.52 used in solar-like oscillators to indicate stochastic oscillations (Christensen-Dalsgaard et al. 2001). The low ratio could be an artefact of only a few amplitude detections or caused by an amplitude decay time-scale shorter than the re-excitation time-scale. To investigate time-scales, we compared the observed amplitude ratios for several subsets with simulated stochastic oscillations. The simulations could easily fit the observed ratios and broadly found decay time-scales near 12 h and re-excitation time-scales near 25 h. As such, the pulsations do have some qualities normally associated with stochastic oscillations; however, the phases are relatively stable which argue against stochastic oscillations. Hence, it is possible that the amplitude variations have a different cause.

We have found 20 separate multiplets including up to 61 frequencies. Assuming the classical interpretation which aligns the pulsation axis with the rotation axis, these would indicate 12 $\ell = 1$, four $\ell = 2$ and/or possibly (but unlikely) four $\ell = 3$, two $\ell = 4$ and one $\ell = 5$ modes. We also searched for indicators of a tidally induced tipped pulsation axis which would precess with each orbit. While the complexities of the pulsations made searching for tipped modes difficult, three frequencies were found which indicated that tipped modes are present.

Two further modes have indications of tipped modes, but these would indicate $\ell = 3$ and 4, which are unlikely to be observed. We also detected frequencies which only appeared during certain orbital phases, which indicate that some frequencies are affected by the slight asymmetry of the star. Fig. 12 schematically shows these results with the height of the arrows indicating the degree (except as noted below). Classically interpreted multiplet $m = 0$ components are shown as solid arrows (with multiple possible $m = 0$ frequencies connected by a horizontal line as in Fig. 10 and colour-coded in the electronic version); modes from the tipped-axis interpretation are shown as dashed arrows, with the m value above the arrow; and frequencies which only appear during certain orbital phases are shown as dotted arrows (at an arbitrary height of 1.5 since we have no indication of their degree). Any frequencies that were not involved in the above cases were (somewhat arbitrarily) deemed to be $\ell = 0$ modes and are indicated in the figure with solid arrows. Note that the classically interpreted $\ell = 1$ mode which could have its $m = 0$ component at 4453 or 4572 is marked with a question mark. This is part of the tipped $l, m = 3, 2$ multiplet and so *if* the tipped mode is correct, then the classical mode would be invalid. The small '3' and '2' under the axes are to indicate that there are three and two closely spaced frequencies, all of which fit the conditions we ascribe to $\ell = 0$ modes that would be unresolvable in the figure.

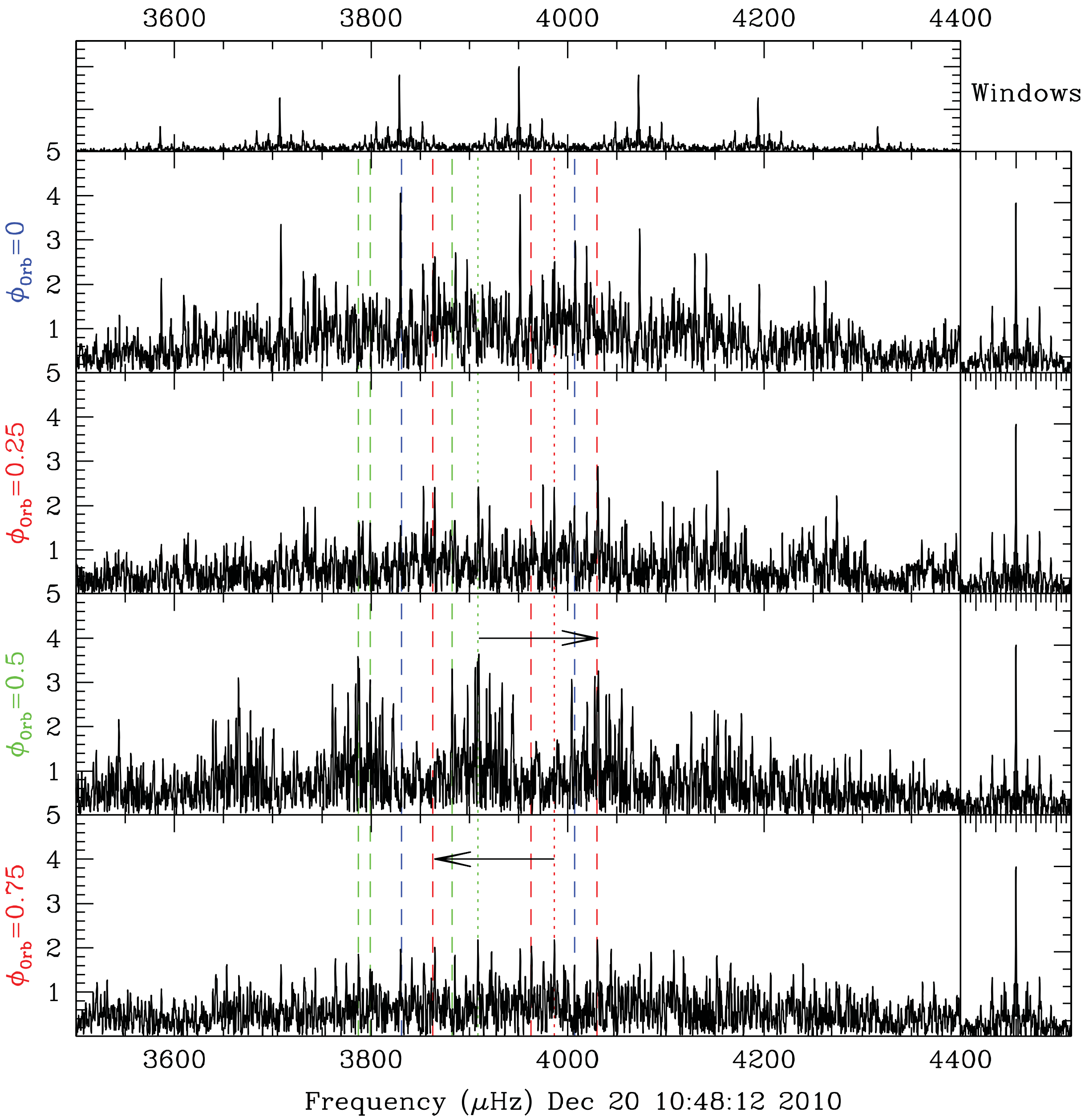

Figure 11. Pulsation spectra of Group II's data, separated into four subsets based on the orbital phase. Dashed lines indicate frequencies which show an orbital dependence and dotted lines indicate frequencies that are an orbital alias away from the most likely frequency (indicated with an arrow and colour-coded in the online version). The top and right-hand panels are window functions.

In the end, KPD 1930 is a star that incorporates a little bit of everything, many pulsation frequencies, multiplets, indications of a tidally induced pulsation geometry, non-sphericity, relativistic Doppler effects, amplitude variations and ellipsoidal variations, all wrapped up in a likely pre-Type Ia supernova binary. Unfortunately, all these effects complicate the analysis, making it a bit of an unruly mess. While we have tried to unravel it, our results indicate that even the WET fails to fully resolve the complexity of the pulsation spectrum and we can only imagine that perhaps Microvariability and Oscillations of Stars or Kepler-like data[5] would be required to improve this situation. Unfortunately, the Kepler field just misses KPD 1930. KPD 1930 remains a fascinating star that warrants further attempts to understand its complexities.

[5] For information, see http://www.astro.ubc.ca/MOST/ and http://astro.phys.au.dk/KASC/

ACKNOWLEDGMENTS

This material is based upon work supported by the National Science Foundation under grant no. 0307480. Any opinions, findings, and conclusions or recommendations expressed in this material are those of the author(s) and do not necessarily reflect the views of the National Science Foundation. This research was supported in part by NASA through the American Astronomical Society's Small Research Grant Program. MDR was partially funded by a Summer Faculty Fellowship provided by Missouri State University and

Table 10. Pulsation frequencies that have an orbital dependence. o− and o+ indicate frequencies detected an orbital alias away while d+ indicates a frequency a daily alias away.

ID	Freq.	QI	QII	QIII	QIV
*o*1	3787			X	
*o*2	3799			X	
*o*3	3831	X			
*o*4 (*f*16)	3865		X		o−
*o*5	3882			X	
*o*6 (*f*23)	3963		d+		X
*o*7	4008	X			
*o*8	4031		X	o−	X

would like to acknowledge HELAS travel funding and Dr. Conny Aerts for helpful discussions. MAM, SLH, SP, JRE and ACQ were supported by the Missouri Space Grant Consortium, funded by NASA. We would also like to thank several other observers who assisted with observing, including E. Brassfield, D. McLemore, J. Peacock, R. Knight, T. Kawasaki, E. Hart, N. Purves, A. Nishimura, M. Hyogo and E. Rau.

REFERENCES

Billéres M., Fontaine G., Brassard P., Charpinet S., Liebert J., Saffer R. A., 2000, ApJ, 530, 441 (B00)
Bloemen S. et al., 2011, MNRAS, 410, 1787
Charpinet S., Fontaine G., Brassard P., Dorman B., 1996, ApJ, 471, L103
Charpinet S., Fontaine G., Brassard P., Chayer P., Rogers F. J., Iglesias C. A., Dorman B., 1997, ApJ, 483, L123
Charpinet S., Fontaine G., Brassard P., 2001, PASP, 113, 775
Christensen-Dalsgaard J., Kjeldsen H., Mattei J. A., 2001, ApJ, 562, L141
Ergma E., Fedorova A. V., Yungelson L. R., 2001, A&A, 376, 9
Geier S., Nesslinger S., Heber U., Przybilla N., Napiwotzki R., Kudritzki R.-P., 2007, A&A, 464, 299 (G07)
Green E. M. et al., 2003, ApJ, 583, L31
Heber U., 2009, ARA&A, 47, 211
Heber U., Hunger K., Jonas G., Kudritzki R. P., 1984, A&A, 130, 119
Jeffery C. S., Saio H., 2007, MNRAS, 378, 379
Kilkenny D., Koen C., O'Donoghue D., Stobie R. S., 1997, MNRAS, 285, 640
Kilkenny D. et al., 1999, MNRAS, 303, 525
Kleinman S. J., Nather R. E., Phillips T., 1996, PASP, 108, 356
Koen C., 2009, MNRAS, 392, 190
Maxted P. F. L., Marsh T. R., North R. C., 2000, MNRAS, 317, 41
Pereira T. M. D., Lopes I. P., 2005, ApJ, 622, 1068
Reed M. D. et al., 2004a, ApJ, 607, 445
Reed M. D. et al., 2004b, MNRAS, 348, 1164

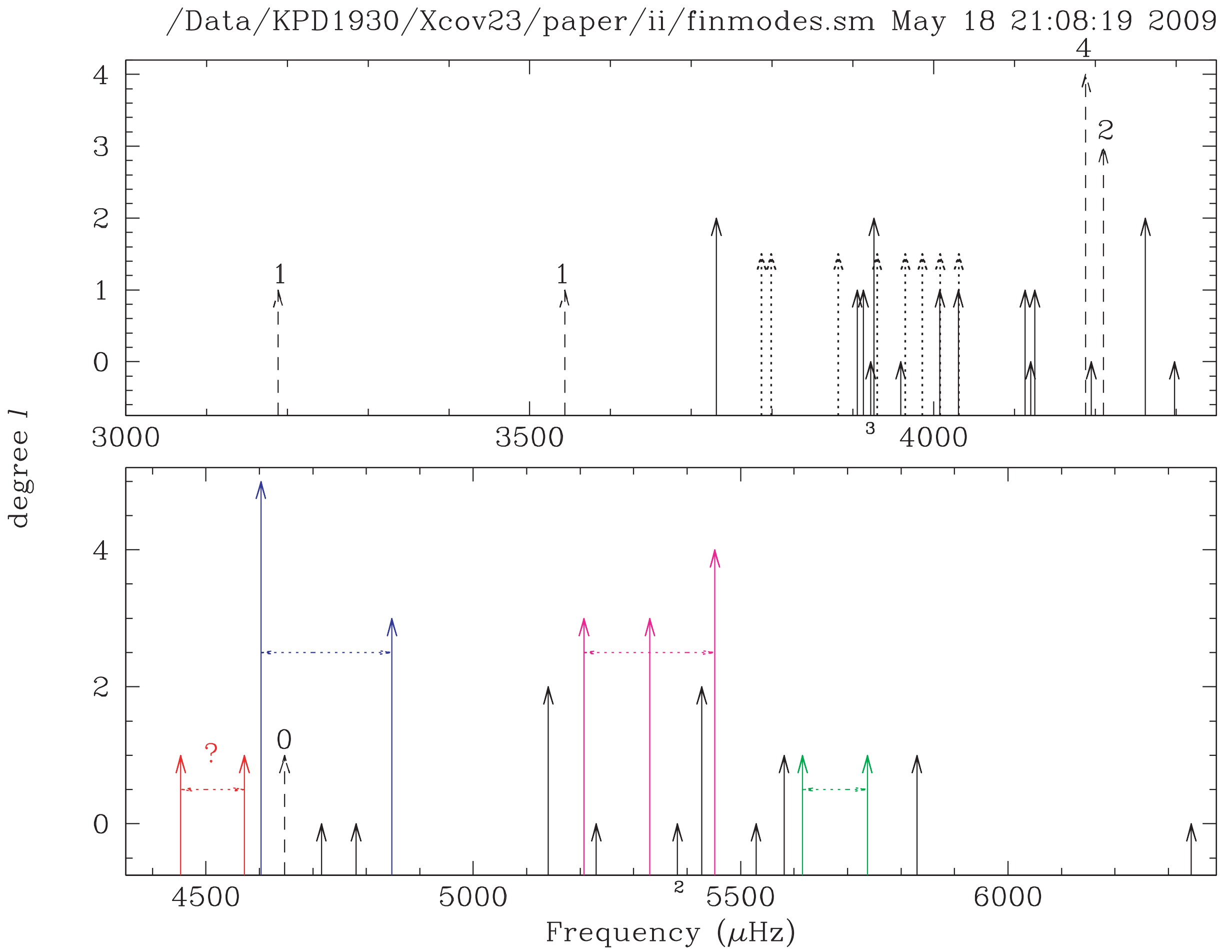

Figure 12. Schematic of modes for KPD 1930. The modal degree (ℓ) is indicated by the height of the arrow. Solid lines indicate the $m = 0$ component of classically interpreted multiplets. For those multiplets with more than one possible $m = 0$ frequency, they are connected by a dotted horizontal line. (They are also colour-coded in the electronic version.) The dashed lines indicate tipped-axis modes, with the m index above the arrow, and the dotted lines indicate frequencies which show a dependence on the orbital phase (set to an arbitrary amplitude of 1.5, as no degree was ascertained for these frequencies).

Reed M. D., Brondel B. J., Kawaler S. D., 2005, ApJ, 634, 602
Reed M. D., Terndrup D. M., Zhou A.-Y., Unterborn C. T., An D., Eggen J. R., 2007a, MNRAS, 378, 1049
Reed M. D. et al., 2007b, ApJ, 664, 518
Saffer R. A., Bergeron P., Koester D., Leibert J., 1994, ApJ, 432, 351
Veen P. M., van Genderen A. M., van der Hucht K. A., 2002, A&A, 385, 619
Østensen R., 2009, Communications Asteroseismology, 159, 75
Østensen R., Heber U., Maxted P., 2005, in Koester D., Moehler S., eds, ASP Conf. Ser. Vol. 334, 14th European Workshop on White Dwarfs. Astron. Soc. Pac., San Francisco, p. 435

SUPPORTING INFORMATION

Additional Supporting Information may be found in the online version of this article:

Figure S1. Detailed pre-whitening sequence of Group IV data between 3600 and 4250 μHz.
Figure S2. Schematic of frequency spacings commensurate with the orbital frequency.
Figure S3. Schematic associating pulsation frequencies with modes for traditionally interpreted multiplets.
Figure S4. Schematic associating pulsation frequencies with possible tipped modes.
Figure S5. Pulsation spectra of Group II's data, separated into opposing phases appropriate for $\ell, m = 1, 0$ and $1, 1$ tipped pulsation axis modes.
Table S1. Pulsation phases and amplitudes for frequencies separated by >30 μHz for individual runs, daily combined runs and groups of data.

Please note: Wiley-Blackwell are not responsible for the content or functionality of any supporting materials supplied by the authors. Any queries (other than missing material) should be directed to the corresponding author for the article.

This paper has been typeset from a TEX/LATEX file prepared by the author.

Monthly Notices
of the
ROYAL ASTRONOMICAL SOCIETY

Mon. Not. R. Astron. Soc. **413,** 2709–2720 (2011) doi:10.1111/j.1365-2966.2011.18342.x

Cepheid investigations using the *Kepler* space telescope

R. Szabó,[1★] L. Szabados,[1] C.-C. Ngeow,[2] R. Smolec,[3] A. Derekas,[1,4†] P. Moskalik,[5] J. Nuspl,[1] H. Lehmann,[6] G. Fűrész,[7] J. Molenda-Żakowicz,[8] S. T. Bryson,[9] A. A. Henden,[10] D. W. Kurtz,[11] D. Stello,[12] J. M. Nemec,[13] J. M. Benkő,[1] L. Berdnikov,[14,15] H. Bruntt,[16] N. R. Evans,[17] N. A. Gorynya,[18] E. N. Pastukhova,[18] R. J. Simcoe,[14] J. E. Grindlay,[19] E. J. Los,[19] A. Doane,[19] S. G. Laycock,[19] D. J. Mink,[17] G. Champine,[19] A. Sliski,[19] G. Handler,[3] L. L. Kiss,[1] Z. Kolláth,[1] J. Kovács,[20] J. Christensen-Dalsgaard,[21] H. Kjeldsen,[21] C. Allen,[22] S. E. Thompson[23] and J. Van Cleve[23]

[1] *Konkoly Observatory of the Hungarian Academy of Sciences, Konkoly Thege Miklós út 15-17, H-1121 Budapest, Hungary*
[2] *Graduate Institute of Astronomy, National Central University, Jhongli City, Taoyuan County 32001, Taiwan*
[3] *Institut für Astronomie, Universität Wien, Türkenschanzstrasse 17, A-1180 Wien, Austria*
[4] *Department of Astronomy, Eötvös University, Budapest, Hungary*
[5] *Copernicus Astronomical Center, ul. Bartycka 18, 00-716 Warsaw, Poland*
[6] *Thüringer Landessternwarte Tautenburg, Karl-Schwarzschild-Observatorium, 07778 Tautenburg, Germany*
[7] *Harvard–Smithsonian Center for Astrophysics, MS 20, 60 Garden Street, Cambridge, MA 02138, USA*
[8] *Astronomical Institute, University of Wrocław, ul. Kopernika 11, 51-622 Wrocław, Poland*
[9] *NASA Ames Research Center, Moffett Field, CA 94035, USA*
[10] *American Association of Variable Star Observers, Cambridge, MA 02138, USA*
[11] *Jeremiah Horrocks Institute of Astrophysics, University of Central Lancashire, Preston PR1 2HE*
[12] *Sydney Institute for Astronomy, School of Physics, The University of Sydney, Sydney, 2006 NSW, Australia*
[13] *Department of Physics & Astronomy, Camosun College, Victoria, British Columbia V8P 5J2, Canada*
[14] *Sternberg Astronomical Institute, Moscow University, Moscow, Russia*
[15] *Isaac Newton Institute of Chile, Moscow Branch, Universitetskij Pr. 13, Moscow 119992, Russia*
[16] *LESIA, UMR 8109, Observatoire de Paris, 92195 Meudon Cedex, France*
[17] *Smithsonian Astrophysical Observatory, MS 4, 60 Garden Street, Cambridge, MA 02138, USA*
[18] *Institute of Astronomy, Russian Academy of Sciences, 48 Pyatnitskaya Street, Moscow 109017, Russia*
[19] *Harvard College Observatory, 60 Garden Street, Cambridge, MA 02138, USA*
[20] *Gothard Astrophysical Observatory, H-9707 Szombathely, Hungary*
[21] *Department of Physics and Astronomy, Aarhus University, DK-8000 Aarhus C, Denmark*
[22] *Orbital Sciences Corporation/NASA Ames Research Center, Moffett Field, CA 94035, USA*
[23] *SETI Institute/NASA Ames Research Center, Moffett Field, CA 94035, USA*

Accepted 2011 January 12. Received 2010 December 31

ABSTRACT

We report results of initial work done on selected candidate Cepheids to be observed with the *Kepler* space telescope. Prior to the launch, 40 candidates were selected from previous surveys and data bases. The analysis of the first 322 d of *Kepler* photometry, and recent ground-based follow-up multicolour photometry and spectroscopy allowed us to confirm that one of these stars, V1154 Cyg (KIC 7548061), is indeed a 4.9-d Cepheid. Using the phase lag method, we show that this star pulsates in the fundamental mode. New radial velocity data are consistent with previous measurements, suggesting that a long-period binary component is unlikely. No evidence is seen in the ultraprecise, nearly uninterrupted *Kepler* photometry for non-radial or stochastically excited modes at the micromagnitude level. The other candidates are not Cepheids, but an interesting mix of possible spotted stars, eclipsing systems and flare stars.

Key words: techniques: photometric – techniques: spectroscopic – stars: individual: V1154 Cygni, KIC 7548061 – stars: individual: V2279 Cygni, KIC 8022670 – stars: oscillations – stars: variables: Cepheids.

★E-mail: rszabo@konkoly.hu
†Magyary Zoltán Postdoctoral Research Fellow.

1 INTRODUCTION

The *Kepler*[1] space mission is designed to detect Earth-like planets around solar-type stars with the transit method (Borucki et al. 2010) by monitoring continuously over 150 000 stars with an unprecedented photometric precision. The lifetime of at least 3.5 yr and the quasi-continuous observations make *Kepler* an ideal tool to measure stellar photometric variability with a precision that is unachievable from the ground (see e.g. Gilliland et al. 2010a).

Ground-based photometric observations of Cepheids usually consist of a few (typically one or two) observations per night. Until now it has not been possible to adequately cover many consecutive pulsational cycles with ground-based photometry. Ground-based studies of several types of variable stars – such as δ Sct stars, DOV, DBV and DAV white dwarfs, sdBV stars and roAp stars – have benefited from multisite photometric observations. But because of their longer period, Cepheids have not been the target of such concerted efforts, with the notable exception of V473 Lyr (Burki et al. 1986).

Space-based Cepheid observations were conducted earlier with the star tracker of the *WIRE* satellite and the Solar Mass Ejection Imager (SMEI) instrument onboard the *Coriolis* satellite (Bruntt et al. 2008; Spreckley & Stevens 2008; Berdnikov 2010). The lengths of these data sets ($\sim$1000–1600 d) are comparable to the nominal lifetime of the *Kepler* mission. The *WIRE* and SMEI data of Polaris (α UMi, $V = 2.005$) confirmed that the pulsation amplitude of Polaris has been increasing again, after a long period of decrease. *Kepler* is capable of delivering comparably accurate photometric observations for the much fainter Cepheid, V1154 Cyg ($V = 9.19$).

The Kepler Asteroseismic Science Consortium (KASC)[2] was set up to exploit the *Kepler* data for studying stellar pulsations. KASC working group number 7 (WG7) is dedicated to the investigation of Cepheids. In compliance with one of the original KASC proposals submitted before the launch of the space telescope, we searched for Cepheids among a list of 40 targets, including the only previously known Cepheid V1154 Cyg (KIC 7548061) in the field. In this paper, we describe the first results from *Kepler* observations of a Cepheid and a couple of not confirmed Cepheids, complemented by extended ground-based follow-up observations.

2 TARGET SELECTION

Being supergiants, Cepheids are rare and the number of Cepheids in the *Kepler*-fixed 105-deg^2 field of view (FOV) is expected to be low. Due to telemetry bandwidth constraints, *Kepler* cannot observe all stars in the field. The first 10 months of operation (observing quarters Q0–Q4) were therefore dedicated to a survey phase to find the best candidates, which would then be observed during the rest of the mission.

We used two different approaches to find Cepheid candidates for the survey phase. First, all known, possible or suspected variable stars in the relevant pulsational period range were selected from all available data bases containing variability information, such as the GCVS (Samus et al. 2002), ASAS North (Pigulski et al. 2009), ROTSE (Akerlof et al. 2000) and HAT catalogues (Hartman et al. 2004). Light-curve shapes and the log P versus $J - H$ diagram (Pojmanski & Maciejewski 2004) were also utilized for further selection. Finally, stars with close (bright) companions were excluded.

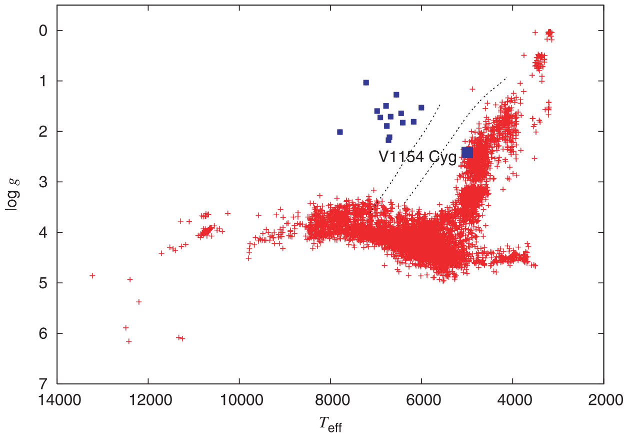

Figure 1. Selection of Cepheid candidates based on KIC effective temperature and log g values (small squares). The plot contains 5987 KASC targets (red plus signs); the selected Cepheid candidates are shown by the full (blue) squares. V1154 Cyg, the only confirmed Cepheid, is denoted by a large (blue) square. The linear Cepheid instability strip is denoted by the dashed lines.

This procedure resulted in a list of 26 stars. We note that these catalogues are not complete in the coverage of the field, nor in the relevant magnitude range.

As a second approach, we searched for stars lying inside or close to the Cepheid instability strip based on the Kepler Input Catalog (KIC)[3] effective temperature and log g values. Stars fainter than $Kp = 16.0$ mag were excluded, where Kp denotes the *Kepler* magnitude system (see Section 3 for more details on the *Kepler* magnitudes). Candidates with a contamination index (CI) larger than 0.5 were also omitted, where CI = 0 means that all the flux in the aperture comes from the target and in the case of CI = 1 the flux entirely comes from surrounding sources. This resulted in 14 additional targets as shown in Fig. 1. The linear Cepheid instability strip, denoted by the dashed lines in the figure, was calculated with the Florida–Budapest code (Szabó, Buchler & Bartee 2007).

We note that the process followed to derive the KIC parameters was optimized to find main-sequence stars with high probability and to distinguish them from cool giants (Batalha et al. 2010). The precision of the parameters is therefore limited for our purposes. This is illustrated in Fig. 1 by the fact that the KIC parameters of V1154 Cyg (the only previously known Cepheid in the field) put it outside the computed instability strip by several hundred Kelvins.

Consequently, we proposed to observe the above-mentioned 40 stars by *Kepler* during the 'survey period'.

3 *KEPLER* OBSERVATIONS

Kepler was launched on 2009 March 6 into a 372-d solar orbit and is observing a 105-deg^2 area of the sky in between the constellations of Cygnus and Lyra (Koch et al. 2010). After a 9.7-d commissioning phase (Q0), the regular observations started on 2009 May 12. In order to ensure optimal solar illumination of the solar panels, a 90° roll of the telescope is performed at the end of each quarter of its solar orbit. The first quarter lasted only for 33.5 d (Q1), while subsequent quarters are all 3 months long. In each of the four quarters annually, the *Kepler* targets fall on different CCDs.

[1] http://kepler.nasa.gov

[2] http://astro.phys.au.dk/KASC/

[3] http://archive.stsci.edu/kepler

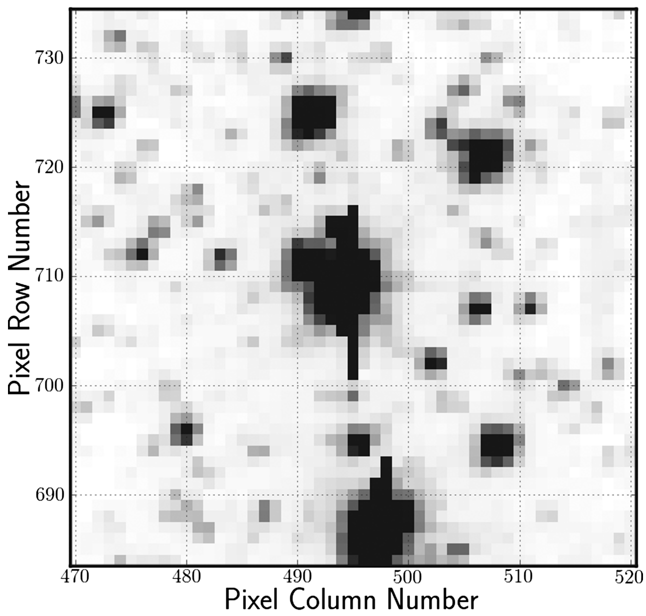

Figure 2. Vicinity of V1154 Cyg from one of the full-frame images. The star is slightly saturated as indicated by its brightness and the elongated shape.

The *Kepler* magnitude system (*Kp*) refers to the wide passband (430–900 nm) transmission of the telescope and detector system. Note that the *Kepler* magnitudes (*Kp*) were derived before the mission launch and are only approximate values. Currently, *Kepler* processing does not provide calibrated *Kepler* magnitudes *Kp* (Kolenberg et al. 2010). Both long-cadence (LC, 29.4 min, Jenkins et al. 2010b) and short-cadence (SC, 58.9 s, Gilliland et al. 2010b) observations are based on the same 6-s integrations which are summed to form the LC and SC data onboard. In this work, we use BJD-corrected, raw LC data (Jenkins et al. 2010a) spanning from Q0 to Q4, that is, 321.7 d of quasi-continuous observations. Some of our targets (V1154 Cyg among them) were observed in SC mode as well. We exploit this opportunity to compare LC and SC characteristics and investigate the frequency spectrum to a much higher Nyquist frequency (733.4 d^{-1} versus 24.5 d^{-1}).

The saturation limit is between $Kp \simeq 11$–12 mag depending on the particular chip the star is observed; brighter than this, accurate photometry can be performed up to $Kp \simeq 7$ mag with judiciously designed apertures (Szabó et al. 2010). Since V1154 Cyg is much brighter than the saturation limit, it required special treatment, as can be seen in Fig. 2, which shows a 50-pixel box centred on V1154 Cyg. The plot was made using KEPLERFFI[4] written by M. Still.

To illustrate some of the common characteristics of the data, we show in Fig. 3 the raw *Kepler* light curve of V1154 Cyg after normalizing the raw flux counts and converting the fluxes to the magnitude scale. The small gaps in the light curve are due to unplanned safe-mode and loss-of-fine-point events, as well as regular data downlink periods. This LC data set spanning Q0–Q4 data contains 14 485 points. Fig. 4 shows a 33.5-d segment (Q1) where SC data are available for V1154 Cyg, containing 49 032 data points.

The varying amplitude seen in Fig. 3 is of instrumental origin. It is a result of the small drift of the telescope, coupled with different pixel sensitivities. In addition, different aperture masks are assigned to the targets quarterly which result in small changes in the measured flux. The most notable amplitude change is seen towards the end of Q2, which was noted to be due to the flux flowing outside the optimal aperture (bleeding), affecting the measured brightness. Fortunately, in Q2, a larger mask was also downloaded besides the standard optimal aperture assigned to this star, which allowed us to investigate the variation in the flux outside the optimal aperture. This confirmed that the total flux was indeed captured within the larger aperture and hence that the star shows no intrinsic amplitude variation within the current accuracy of the data. Without further information, we cannot make a choice between a possible slight amplitude variation and instrumental effects in other quarters.

[4] http://keplergo.arc.nasa.gov/ContributedSoftwareKeplerFFI.shtml

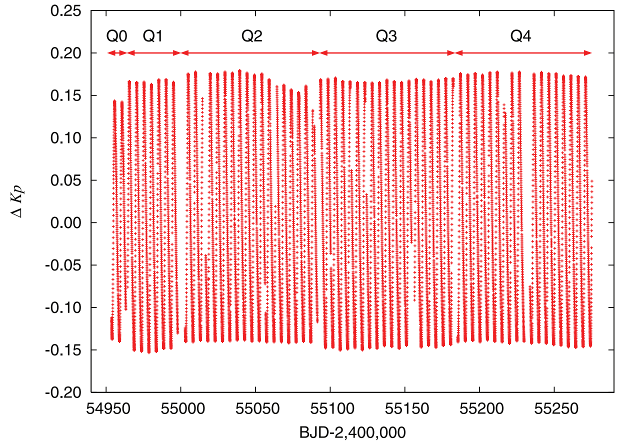

Figure 3. Raw *Kepler* light curve of V1154 Cyg. The varying amplitude is instrumental in origin; see text for more details.

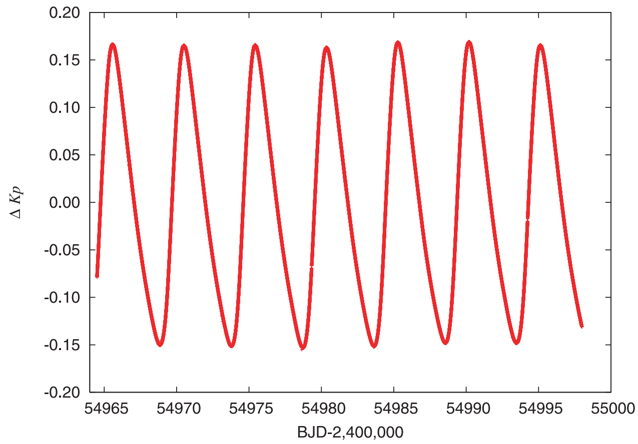

Figure 4. Q1 SC *Kepler* light curve of V1154 Cyg. It is almost indistinguishable from LC data taken during the same time-interval. Note the essentially uninterrupted sampling.

4 TARGET CLASSIFICATION

After the release of the first *Kepler* light curves to the KASC, it turned out that only a few stars showed Cepheid-like variability. The properties of these *Kepler* Cepheid candidates are listed in Table 1. Periods were determined for the *Kepler* LC light curves using the PERIOD04 program (Lenz & Breger 2005).

Apart from these candidates, a number of other variable stars were included in the initial sample of 40 stars. Based on their light curves and the automatic classification (Blomme et al. 2010), we classify these as eclipsing binaries (eight stars), ellipsoidal variables (six),

Table 1. Main properties of the observed *Kepler* Cepheid and Cepheid candidates. The uncertainty of the period is given in parentheses and refers to the last digit(s) of the period. Q3.1 means the first month of Q3. See text for the definition of the CI.

KIC ID	Other name	α (J2000)	δ (J2000)	Kp (mag)	Period (d)	Contamination index	Runs
7548061	**V1154 Cyg**	**19 48 15.45**	**+43 07 36.77**	**8.771**	**4.925 454(1)**	0.036	**LC: Q01234 SC: Q1**
2968811	ASAS 190148+3807.0	19 01 48.21	+38 07 01.99	13.469	14.8854(12)	0.047	LC: Q01234
6437385	ASAS 192000+4149.1	19 20 00.12	+41 49 07.46	11.539	13.6047(7)	0.075	LC: Q01234
8022670	V2279 Cyg	19 18 54.46	+43 49 25.82	12.471	4.125 64(5)	0.189	LC: Q1234
12406908	ROTSE1 J192344.95+511611.8	19 23 44.99	+51 16 11.75	12.354	13.3503(45)	0.015	LC: Q01 SC: Q3.1

δ Scuti stars (three), a slowly pulsating B star (one), long-period variables (seven) and stars with no obvious variations (seven). While this sample is a rich source of flaring, spotted, granulated stars, the detailed investigation of these non-Cepheids is out of scope of this paper. In addition, we inspected all 6300 KASC light curves, but found no Cepheids among them.

Three originally proposed stars were not observed due to technical reasons (position on the CCD chip, brightness/faintness, contamination or pixel number constraints). The large variety of non-Cepheids in our sample indicates that the spatial resolution and photometric accuracy of the ASAS was not adequate to select such relatively faint Cepheids. It further shows that the KIC is clearly not optimal for our purpose.

5 GROUND-BASED FOLLOW-UP

To further confirm or disprove the Cepheid nature of our candidates in Table 1, we employed ground-based multicolour photometry and in some cases spectroscopy. In the case of V1154 Cyg, regular radial velocity (RV) observations and multicolour photometry were scheduled, which helped us to gain more information on the pulsation. In the following, we describe these ground-based follow-up observations and the subsequent scrutinizing classification process on a star-by-star basis.

5.1 Multicolour photometry

Ground-based multicolour observations provide additional information, therefore complementing the space-borne photometry taken in 'white light'. We used the following telescopes to gather $BVR_{\mathrm{C}}I_{\mathrm{C}}$ Johnson–Cousins magnitudes:

(i) Lulin One-meter Telescope (LOT) at the Lulin Observatory (Taiwan)[5]: 1-m Cassegrain-telescope with PI1300B CCD;
(ii) SLT at the Lulin Observatory (Taiwan): 0.4-m RC-telescope with Apogee U9000 CCD;
(iii) Tenagra telescope at the Tenagra II Observatory[6] (USA): robotic 0.8-m RC-telescope with SITe CCD;
(iv) Sonoita Research Observatory (SRO, USA)[7]: 0.35-m robotic telescope with a SBIG STL-1001E CCD.

Observations were performed from 2009 September to 2010 August. All of the imaging data were reduced in a standard way (bias-subtracted, dark-subtracted and flat-fielded) using IRAF.[8] Instrumental magnitudes for the stars in the images were measured using SExtractor (Bertin & Arnouts 1996) with aperture photometry. For the SRO data, a separate photometric pipeline based on DAOPHOT was used, which included analysis of an ensemble of comparison stars. The instrumental magnitudes were transformed to the standard magnitudes using Landolt standards (Landolt 2009). Times of observation were converted to heliocentric Julian day (HJD).

Table 2. Ground-based multicolour photometry of V1154 Cyg and *Kepler* Cepheid candidates. The entire table is available as Supporting Information with the online version of the article.

KIC ID	HJD	Magnitude	Error	Filter	Observer
02968811	245 5103.7700	14.857	0.013	*B*	SRO
02968811	245 5103.7809	14.823	0.013	*B*	SRO
02968811	245 5104.7544	14.797	0.011	*B*	SRO
...	...	...	...	...	...

We gathered between 80–120 frames per target for each passband, excluding KIC 12406908 which was observed only at the TNG and hence had fewer images taken. We have found a small offset between SRO and other *B* data in the case of V1154 Cyg. Fortunately, data were taken in the TNG and SRO very close in time (less than 1 min) twice, allowing us to correct the SRO data by the shift measured in these epochs: $B_{\mathrm{SRO}} - B_{\mathrm{TNG}} = 0.054$. All the (corrected) photometric measurements are available online, while Table 2 shows the layout of the data.

We decomposed the multicolour light curves to derive the widely used Fourier parameters R_{i1} and ϕ_{i1}, as defined by Simon & Lee (1981), which characterize the light-curve shape. The Johnson *V* results are plotted in Fig. 5 along with the Fourier parameters of fundamental-mode (red filled points) and first-overtone (blue open circles) Galactic Cepheids as a function of the pulsational period. As all Galactic Cepheids follow the main Fourier progressions in Fig. 5, a star that lies outside the overall pattern is unlikely to be a Cepheid. We discuss our findings for individual candidates below.

5.2 Spectroscopy

Spectroscopic observations were conducted to measure the RV and derive stellar parameters. We obtained spectra of V1154 Cyg with the Coude–Echelle spectrograph attached to the 2-m telescope of the Thüringer Landessternwarte (TLS) Tautenburg. Spectra cover the region 470–740 nm, the spectral resolution is R = 33 000 and

[5] http://www.lulin.ncu.edu.tw/english/index.htm
[6] http://www.tenagraobservatories.com
[7] http://www.sonoitaobservatories.org
[8] IRAF is distributed by the National Optical Astronomy Observatories, which are operated by the Association of Universities for Research in Astronomy, Inc., under cooperative agreement with the National Science Foundation.

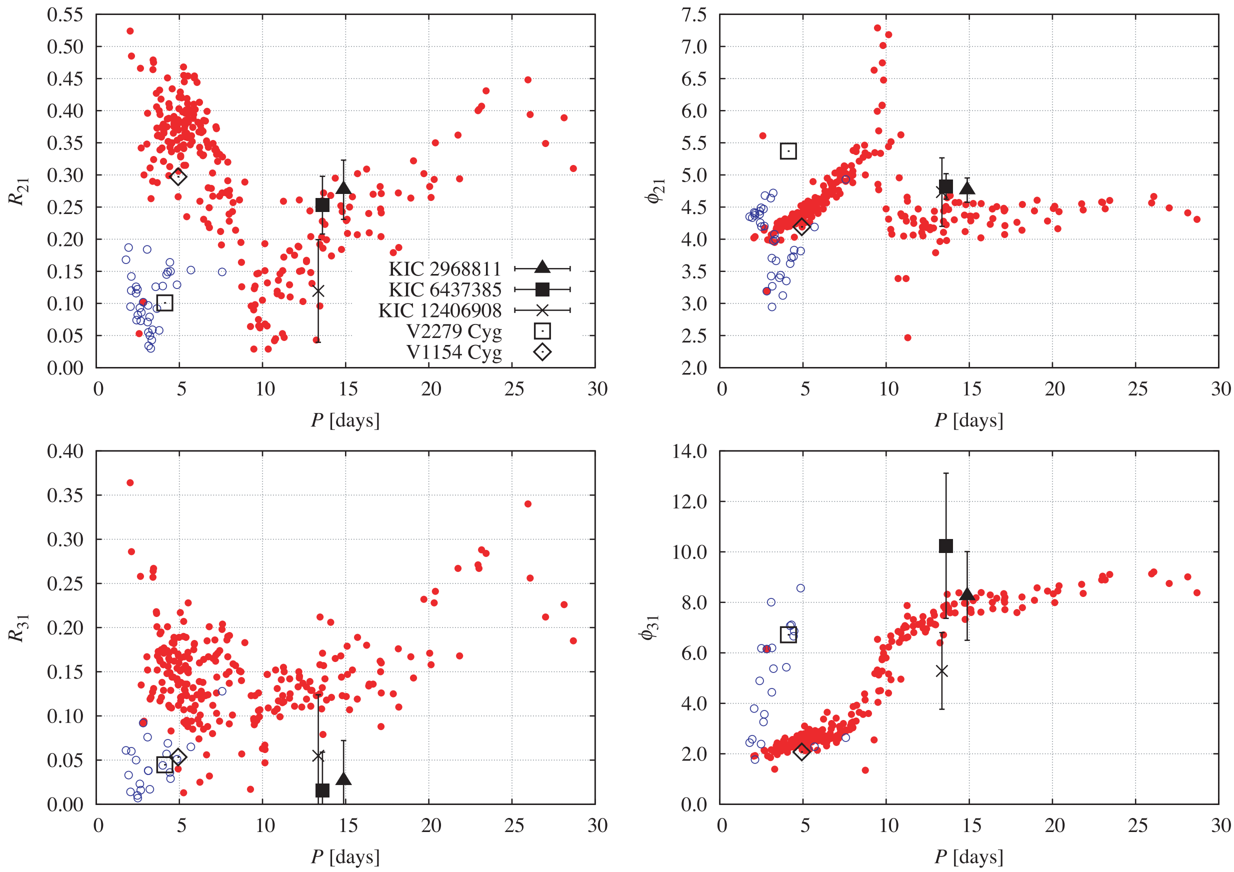

Figure 5. Fundamental-mode (red filled) and first-overtone (blue open symbols) Fourier parameter progressions in the Johnson *V* passband for the Galactic Cepheid sample. V1154 Cyg and other *Kepler* Cepheid candidates are also shown based on their new ground-based Johnson *V* photometry. Error bars for V1154 Cyg and V2279 Cyg are comparable to, or smaller than the symbol size, so these were omitted from the plot.The Galactic Cepheid light curve parameters were compiled from Antonello & Lee (1981), Moffett & Barnes (1985), Antonello & Poretti (1986), Antonello, Poretti & Reduzzi (1990), Mantegazza & Poretti (1992), Poretti (1994) and Antonello & Morelli (1996).

the exposure time was 30 min per spectrum. Spectra were reduced using standard MIDAS packages. The reduction included the removal of cosmic rays, bias and stray light subtraction, flat-fielding, optimum order extraction, wavelength calibration using a Th-Ar lamp, normalization to the local continuum and merging of the orders. Small instrumental shifts were corrected by an additional calibration using a larger number of telluric O_2 lines. In addition, one spectrum of V1154 Cyg was taken on 2007 June 15 at the M. G. Fracastoro station (Serra La Nave, Mt. Etna) of the INAF - Osservatorio Astrofisico di Catania (INAF-OACt). We used the 91-cm telescope and FRESCO, the fiber-fed REOSC echelle spectrograph which allowed us to obtain spectra in the range of 4300–6800 Å with a resolution $R = 21\,000$.

For V2279 Cyg, we made a high-resolution spectrum in a single-shot 1680-s exposure with the 1.5-m telescope at the Fred Lawrence Whipple Observatory (Mt. Hopkins, Arizona) using the Tillinghast Reflection Echelle Spectrograph (TRES) on 2010 September 24. The spectrum is cross-dispersed with a wavelength range of 3860–9100 Å over 51 spectral orders.

5.3 Remarks on individual candidates

In the following, we summarize the *Kepler* light-curve characteristics, the multicolour photometry, the Fourier parameters and the spectroscopic properties of the four Cepheid candidates (see Table 1), before moving to the previously known Cepheid (V1154 Cyg) in Section 6.

(i) *KIC 2968811 = ASAS 190148+3807.0* (P = 14.8854 d). In principle, the light-curve shape matches all the Fourier parameter progressions within the uncertainty, although in the case of ϕ_{21} and R_{31} it is a borderline case (Fig. 5). The amplitude is 0.19 mag in the *Kepler* passband. ‘Shoulders’ or bumps appear on the descending branch (Fig. 6, upper left-hand panel), but they are not present at the beginning of the observations. This effect is frequently seen in spotted stars. The same effect may cause the larger scatter of the folded ground-based multicolour light curves in the first panel of Fig. 7. We note that in the case of a Cepheid in this period range the bump should be present on the ascending branch. By carefully examining the short brightening seen in the *Kepler* light curve, we exclude instrumental or other external origin based on known artefacts discussed in the Kepler Data Release Notes.[9] Taking into account the strong flare events (Fig. 6), we conclude that this object is definitely not a Cepheid.

(ii) *KIC 6437385 = ASAS 192000+4149.1* (P = 13.6047 d). This star shows a similar light curve to KIC 2968811 with an amplitude of 0.09 mag (Fig. 6, upper right-hand panel). Within the uncertainty, the Fourier parameters R_{21} matches the progressions, but R_{31} does

[9] http://archive.stsci.edu/kepler/data_release.html

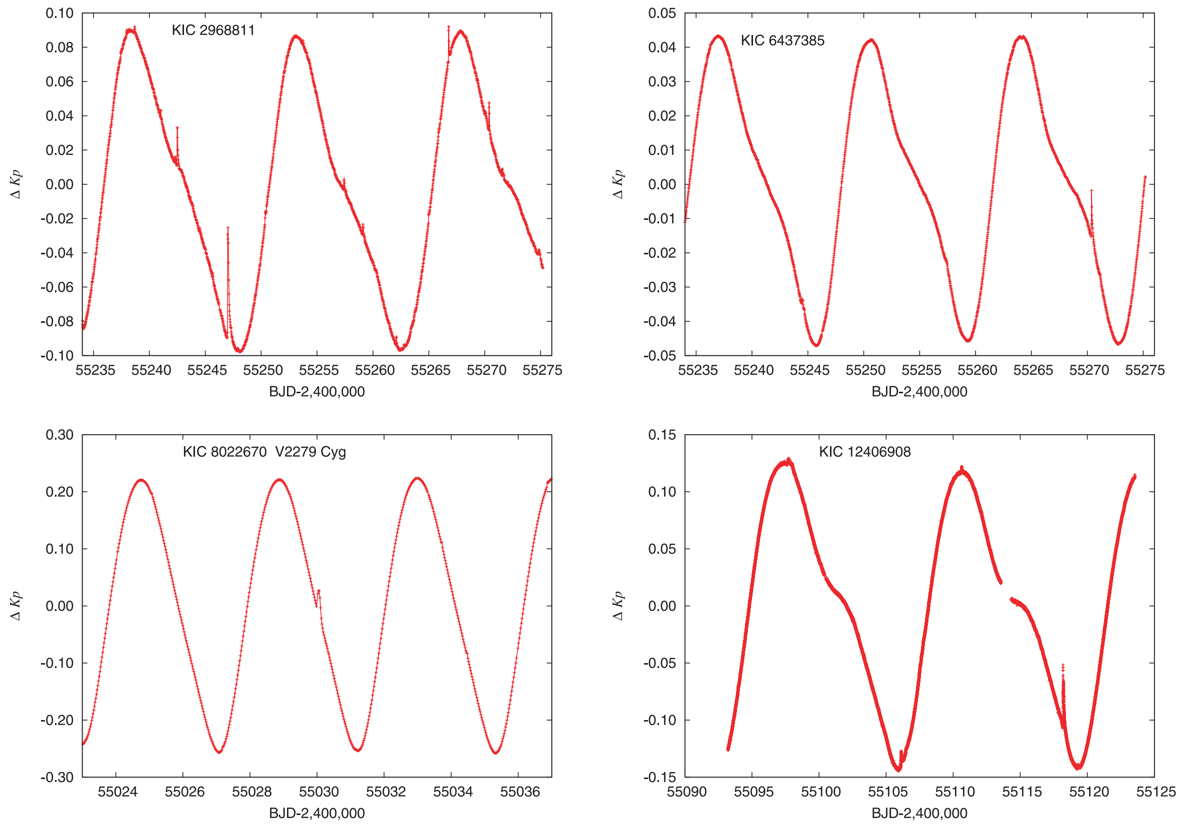

Figure 6. Representative parts of the *Kepler* photometry of four Cepheid candidates (excluding the known Cepheid V1154 Cyg). LC light curves are plotted, except for KIC 12406908 where 1 month of SC data were plotted. The ‘shoulders’ on the descending branches indicate spotted stars and the flares are typical for active stars. These light curves indicate that KIC 8022670 (V2279 Cyg) is the most-promising Cepheid candidate of the four.

not. The phases are close to the phases of the bulk of the Galactic Cepheids (Fig. 5). The B amplitude is smaller than the amplitude measured in V as shown in Fig. 7; this is inconsistent with the Cepheid classification. The light variation shows the same shoulders on the descending branch as in the case of KIC 2968811, while its amplitude and shape are changing throughout the more than 300 d long *Kepler* observations. In addition, several flares can be seen that are intrinsic to the star. One is shown in Fig. 6. Thus, KIC 6437385 is most probably not a Cepheid.

(iii) *KIC 12406908 = ROTSE1 J192344.95+511611.8* (P = 13.3503 d). Interestingly, this variable star exhibits very similar light curve characteristics to the previously discussed objects (Fig. 6, bottom right-hand panel). It has an amplitude of 0.3 mag in the *Kepler* passband. We have too few data points from ground-based observations to put strong constraints on the Fourier parameters, but despite the large uncertainties, this object seems to be slightly off the main location expected for Cepheids (Fig. 5). The ratio of I_C and V amplitudes is 0.74, which is close to, but slightly larger, than the

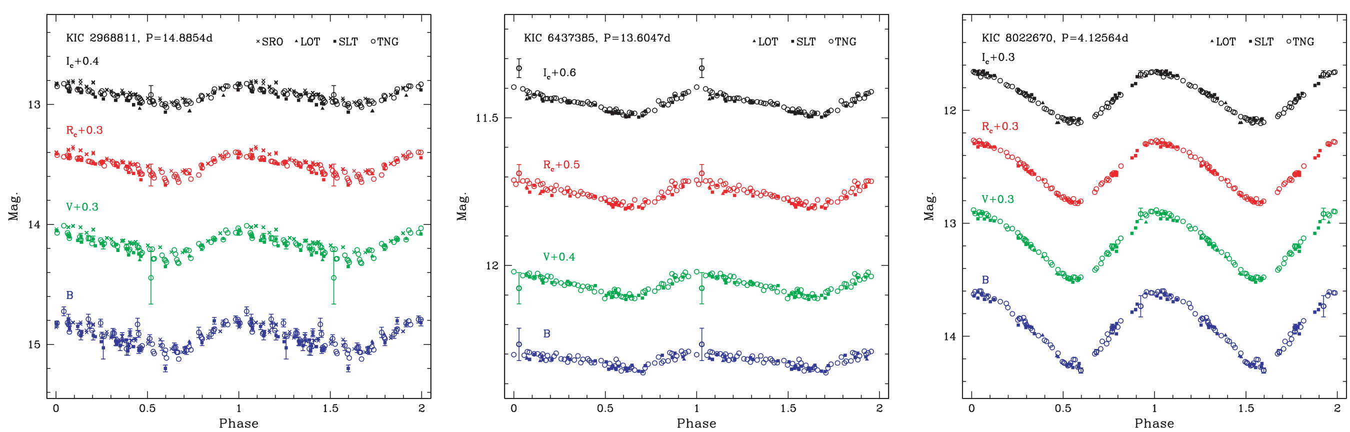

Figure 7. Phased BVR_CI_C Johnson–Cousins phase-folded light curves of three Cepheid candidates taken during the 2010 observing season: KIC 2968811 (left-hand panel), KIC 6437385 (middle panel) and KIC 8022670 (right-hand panel). For clarity, error bars were plotted only for data points with errors larger than 0.02 mag.

standard 0.6. The SC light curves show small short-duration flares at BJD 245 5106.1 and 245 5110.6, and a large one at BJD 245 5118.2 which showed a complex, multipeaked maximum lasting for 7 h. We note that a few outliers were removed from the *Kepler* light curve, which, however, does not influence our conclusions. Based on the observed features, we can safely exclude this star from our Cepheid sample.

(iv) *KIC 8022670 = V2279 Cyg* ($P = 4.125\,64$ d). Based on the space- and ground-based follow-up observations, this star is a strong Cepheid candidate.

We therefore looked into the literature for a more rigorous assessment of whether the Cepheid pulsation is the cause of the observed variability. The variability of this star was revealed by Dahlmark (2000) during a photographic search for variable stars and independently by Akerlof et al. (2000) as a result of the ROTSE project. While Akerlof et al. (2000) classified the star as a Cepheid with a period of 4.122 98 d, Dahlmark (2000) interpreted it as an RS CVn type variable due to its proximity to a known X-ray source detected by the *ROSAT* mission (Voges et al. 1999). This object ROTSE J191853.61+434930.0 = LD 349 was finally designated as V2279 Cyg among the variable stars (Kazarovets et al. 2003).

We first looked at ROTSE-I photometric data retrieved from the NSVS data base (Woźniak et al. 2004), but concluded that this data set does not allow us to unambiguously classify the star. A dedicated photometric project to select Type II Cepheids among the ROTSE-I targets was performed by Schmidt et al. (2007). Based on their two-colour (V, R) photometry, they concluded that V2279 Cyg is a probable Cepheid with a period of 4.117 d. More recently, the photometric survey by Pigulski et al. (2009) resulted in useful data for following the period changes of this star. Additional photometric data are also available from the SuperWASP public archive[10] and the Scientific Archive of the Optical Monitoring Camera (OMC) onboard *INTEGRAL*.[11] Both these archives contain data obtained in a single photometric band and we used these data to investigate the period behaviour of V2279 Cyg.

The *Kepler* light curve of V2279 Cyg seems stable, without any notable light-curve changes (part of the Q2 light curve is plotted in Fig. 6). We only see long-term variations similar in amplitude to what we noted for V1154 Cyg (Fig. 3), which in this case might also just be instrumental effects. What makes V2279 Cyg particularly suspicious is the presence of many flares, one of them is clearly seen at BJD 245 5030.0 in Fig. 6. The (almost) strictly periodic variations and the value of the period are consistent with a rotational modulation.

Multicolour photometry can be decisive in solving this classification problem because Cepheids have characteristic amplitude ratios. Our new photometric data suggest that V2279 Cyg is not a Cepheid. The amplitude of its brightness variation in V is only slightly smaller than the amplitude in the B band: the ratio is about 0.9 instead of the usual value of 0.65–0.70 (Klagyivik & Szabados 2009). Although a bright blue companion star is able to suppress the observable amplitude of the light variations in the B band, the observed amplitude ratio is incompatible with the Cepheid nature even if the star had a very hot companion. R_{21}, R_{31} and ϕ_{31} place it among the first-overtone objects, but ϕ_{21} is very different from both fundamental and first-overtone progressions (Fig. 5).

In the next step, we analyse the cycle-to-cycle variations in the periodicity using the so-called O−C diagram. The O−C diagram

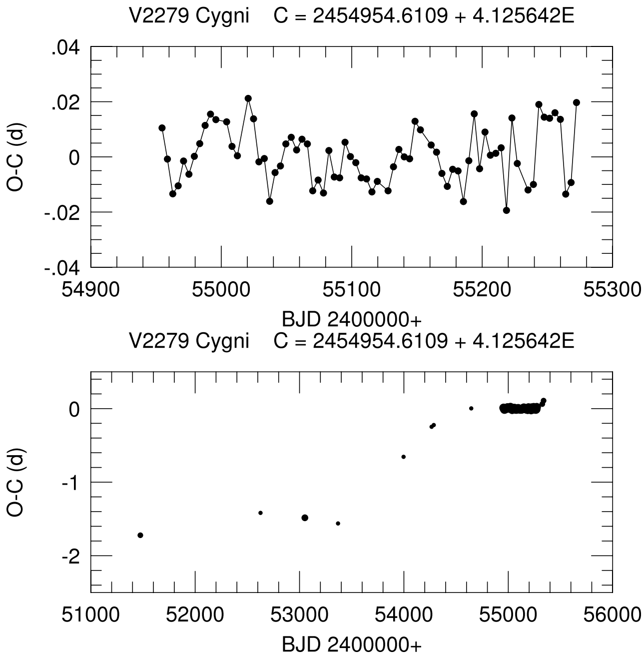

Figure 8. Top panel: O−C diagram of V2279 Cyg for the *Kepler* data. Bottom panel: O−C diagram of V2279 Cyg involving all photometric data. The point size corresponds to the weight assigned to the maxima.

constructed for the moments of brightness maxima is plotted in the top panel of Fig. 8. The zero epoch was arbitrarily chosen at the first maximum in the *Kepler* data set. A least-squares fit to the O−C residuals resulted in the best-fitting period of 4.125 642 d, which is somewhat longer than any formerly published value for V2279 Cyg. We then included all ground-based observations we could find to construct a new O−C diagram using the ephemeris

$$C = \mathrm{BJD}\,(245\,4954.6109 \pm 0.0023) + (4.125\,642 \pm 0.000\,051)E.$$

Table 3 contains the moments of maxima, the corresponding epochs and the O−C residuals of the available observations. We assigned different weights to data from different sources. These weights (between 1–5) correspond to the 'goodness' of the seasonal light curve; a larger number means better coverage and smaller scatter (for *Kepler* data $W = 5$). The period of V2279 Cyg shows large fluctuations during the last decade (see the lower panel of Fig. 8). Our additional ground-based photometric data indicate a very recent change in the period that we will investigate using future quarters of *Kepler* data. We note that the star has a high CI (Table 1), indicating that ∼18 per cent of the measured flux comes form other sources.

Table 3. Sample table for O−C residuals for V2279 Cyg. The entire table is available as Supporting Information with the online version of the article.

JDM$_\odot$ − 240 0000	E	O−C (d)	W	Reference
514 74.9729	−843	−1.7218	2	NSVS
526 26.3311	−564	−1.4177	1	Integral OMC
530 51.2057	−461	−1.4842	3	Schmidt et al.
533 68.6341	−384	−1.7304	1	Schmidt et al.
542 65.3816	−191	−1.2317	1	SWASP
546 45.2207	−75	0.0030	1	SWASP
549 54.6214	0	0.0105	5	*Kepler*
...	...	...	...	...

[10] http://www.wasp.le.ac.uk/public/index.php
[11] http://sdc.laeff.inta.es/omc/index.jsp

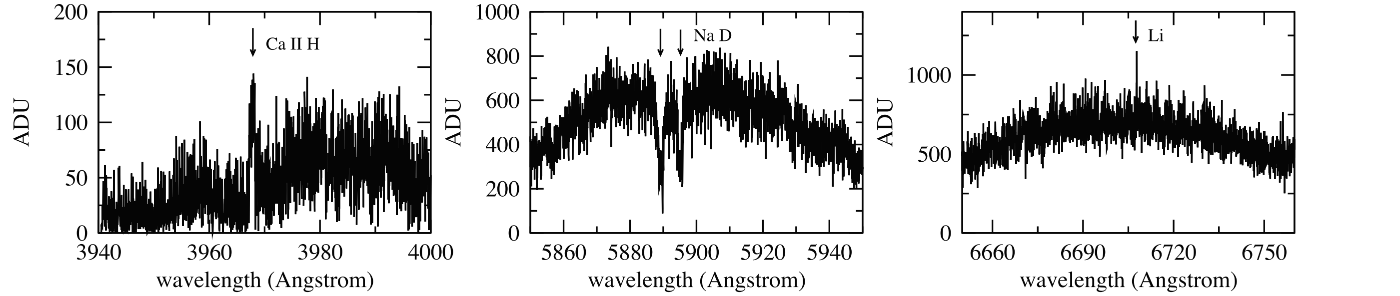

Figure 9. The TRES spectrum of V2279 Cyg. From the left-hand to right-hand panel: zoom in to Ca II H (3968.5 Å), Na D (5890 and 5896 Å) and Li (6708 Å).

The spectrum of V2279 Cyg offers the clearest evidence that this star has been misclassified as a Cepheid. We have plotted three segments of the spectrum taken with the TRES spectrograph in Fig. 9 containing these lines: Ca II H (3968.5 Å), Na D (5890 and 5896 Å) and Li (6708 Å). While the Na D lines are normal, the characteristics of the other two lines do not support a Cepheid nature of V2279 Cyg. The Li (6708 Å) is never seen in emission in Cepheids, while the Ca emission implies chromospheric activity, which is also not a Cepheid characteristic. We fitted theoretical template spectra from the extensive spectral library of Munari et al. (2005) to the spectrum and determined the following atmospheric parameters: $T_{\rm eff} = 4900 \pm 200$ K, $\log g = 3.7 \pm 0.4$, $[M/H] = -1.2 \pm 0.4$ and $v \sin i = 40\,{\rm km\,s^{-1}}$. The resulting parameters are also incompatible with a Cepheid variable, but suggest a cool main-sequence star with moderate rotation.

Summarizing the previous sections, we conclude that all the candidates turned out not to be Cepheids, except the already known Cepheid V1154 Cyg, which we will describe in detail in the following.

6 V1154 Cyg THE ONLY *KEPLER* CEPHEID

In this section, we analyse both *Kepler* data and ground-based follow-up observations of what is apparently the only Cepheid being observed in *Kepler's* FOV.

6.1 Observational data prior to *Kepler*

The brightness variation of V1154 Cyg was discovered by Strohmeier, Knigge & Ott (1963). The Cepheid-type variation and a periodicity somewhat shorter than 5 d were obvious from the photographic magnitudes leading to the discovery. The first reliable light curve based on photoelectric *UBV* observations was published by Wachmann (1976). Further multicolour photoelectric and CCD photometric data were published by Szabados (1977), Arellano Ferro et al. (1998), Ignatova & Vozyakova (2000), Berdnikov (2008) and Pigulski et al. (2009). The last paper contains the data of a dedicated photometric survey of the whole *Kepler* field. Space photometric data of V1154 Cyg are also available from the *Hipparcos* satellite (ESA 1997) and the OMC onboard *INTEGRAL*. None of these previous data can compete with *Kepler* in photometric quality.

In addition, a large number of RV data have been collected on V1154 Cyg by the Moscow CORAVEL team (Gorynya et al. 1998). These data obtained between 1990–96 show a slight change in the mean velocity averaged over the pulsation cycle; thus, Gorynya et al. (1996) suspected spectroscopic binarity of this Cepheid. However, RV data obtained by Imbert (1999) much earlier than the Moscow data and covering a reasonably long time-interval do not indicate binarity.

Molenda-Żakowicz, Frasca & Latham (2008) determined basic parameters for our target: $[Fe/H] = 0.06 \pm 0.07$, spectral type: G2Ib, $T_{\rm eff} = 5370 \pm 118$ K, $\log g = 1.49 \pm 0.34$ and $v \sin i = 12.3 \pm 1.6\,{\rm km\,s^{-1}}$. These parameters are all consistent with a Cepheid and place V1154 Cyg inside the theoretical instability strip presented in Fig. 1. The chemical composition of V1154 Cyg was determined independently by Luck, Kovtyukh & Andrievsky (2006) in a major project of Cepheid spectroscopy. They published a value of $[Fe/H] = -0.10$.

6.2 Multicolour photometry of V1154 Cyg

Fig. 10 shows a multicolour light curve for V1154 Cyg. It contains 114–120 points in each filter obtained with four different telescopes as described in Section 5.1. The amplitudes and amplitude ratios are consistent with V1154 Cyg being a Cepheid, for example, the ratio of the *I* and *V* amplitude is 0.6, which is exactly what is expected. Fig. 5 shows that the average Fourier parameters of V1154 Cyg fit well all the progressions, although in each case they are slightly lower than the main progression.

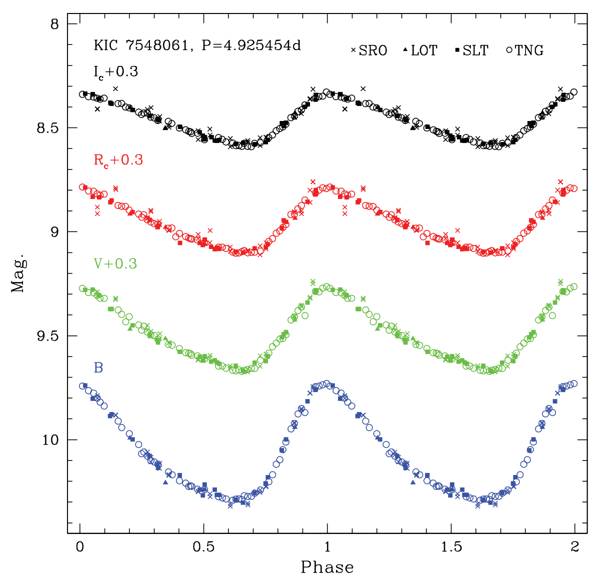

Figure 10. *BVR*$_{\rm C}$*I*$_{\rm C}$ Johnson–Cousins phase-folded light curves of V1154 Cyg taken during the 2010 observing season. Typical errors of the individual photometric points are a few mmag.

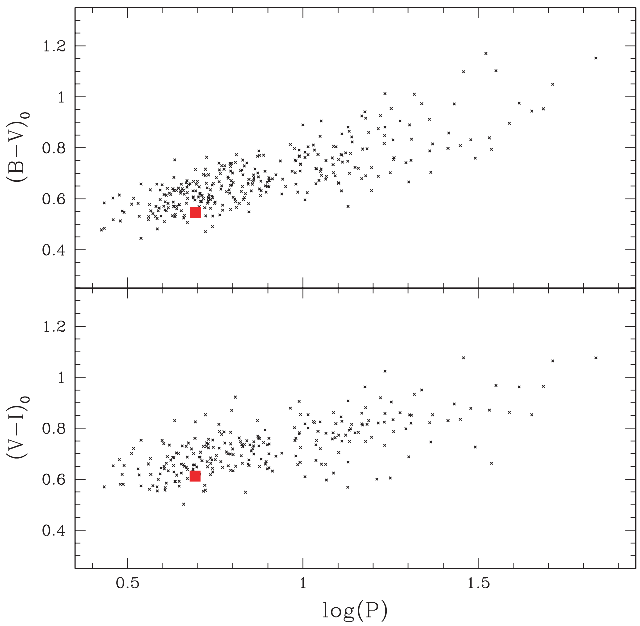

Figure 11. Comparison of the extinction-corrected colours of V1154 Cyg (filled squares) to the Galactic Cepheids adopted from Tammann, Sandage & Reindl (2003) (crosses).

As a check, the colours of V1154 Cyg were compared to other Galactic Cepheids in Fig. 11. The observed colours of $(B-V) = 0.865$ and $(V-I) = 1.021$ were derived from the BVR_CI_C light curves. To correct for extinction, we adopted the colour excess from Fernie et al. (1995)[12] (after removing the systematic trend in the Fernie system using the prescription given in Tammann et al. 2003). The extinction-free colours are $(B-V)_0 = 0.546$ and $(V-I)_0 = 0.612$. As shown in Fig. 11, these colours fit well within the period–colour relations defined by the Galactic Cepheids.

6.3 Analysis of the *Kepler* light curves

With almost a year of continuous data, it is, in principle, possible to study the stability of the light curve of a classical Cepheid over several dozen pulsation cycles. However, because instrumental effects are still present in the data, it is too early to perform such an analysis at least until pixel-level data become available, which would allow the data reduction to be optimized for this particular type of star.

The frequency content of the light curve of V1154 Cyg was investigated with standard Fourier transform methods by applying well-tested software packages: SigSpec (Reegen 2007), Period04 (Lenz & Breger 2005) and MuFrAn (Kolláth 1990). The distorted parts of the LC light curves have been omitted, because their presence causes spurious frequency peaks around the main frequencies. The affected parts are the entire Q0 and BJD = [245 5054.0 − 245 4094.24] in Q2. The frequency spectrum shows the main pulsation frequency at $f_0 = 0.203\,\mathrm{d}^{-1}$ and many harmonics. Two harmonics ($2f_0$ and $3f_0$) are clearly visible in the upper panel of Fig. 12. Pre-whitening with these peaks reveals further harmonics up to the 10th order with very low amplitudes. This is the first time that such high-order harmonics have been detected, underlining the accuracy of the *Kepler* observations. The effect of instrumental artefacts (trends, amplitude variation) is clearly seen in the remaining power around f_0. Apart from that, the frequency spectrum is completely free of additional power at the significance level up to the Nyquist frequency as shown in the lower two panels of Fig. 12.

[12] http://www.astro.utoronto.ca/DDO/research/cepheids/table_colourexcess.html

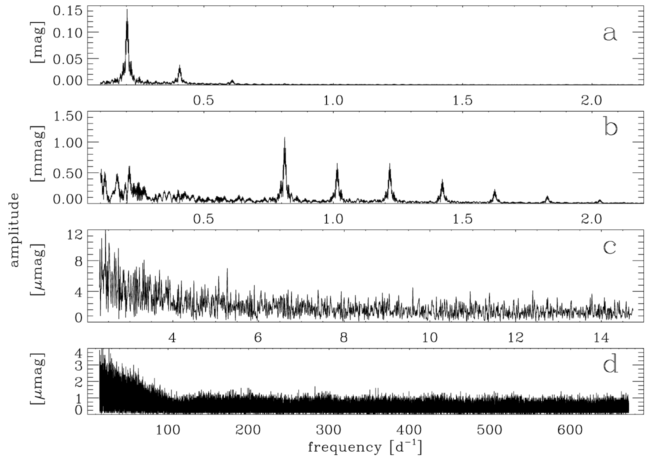

Figure 12. Frequency spectrum of V1154 Cyg based on Q1–Q4 LC data. Panel (a): main pulsational frequency and the first two harmonics. Panel (b): pre-whitened by the three frequency peaks, higher order harmonics emerge up to $10f_0$. The remaining part of the higher frequency range of the spectrum was divided into two for clarity: (panel c) shows the frequency range 2.4–15 d^{-1} and panel (d) comprises the range 15–700 d^{-1} based on Q5 SC data. Note the change in the scale on the vertical axis.

Before finishing this paper, Q5 SC data became available for V1154 Cyg. To investigate the high-frequency range, we used this 94.7-d-long data set and the 33.5-d-long SC data taken in Q1. The two data sets have a very similar frequency content and we chose to plot the Q5 SC frequency spectrum in panel (d) of Fig. 12, because the longer time-base ensures better frequency resolution and higher signal-to-noise ratio (S/N).

The top of the grass of the remaining spectrum is 5 μmag, while the average is 2 μmag in the spectrum up to 50 d^{-1}. Above that the top of the grass of the remaining spectrum decreases to 1.5 μmag and from 100 d^{-1} it remains constant. The average of the remaining peaks is below 1 μmag in this high-frequency range. The residual spectrum shows no signal of any shorter period non-radial pulsation modes or solar-like oscillations.

The frequencies, amplitudes and phases of the detected and identified peaks based on Q1–Q4 LC data are listed in Table 4. The

Table 4. Frequencies, amplitudes and phases of the identified frequency peaks in the frequency spectrum of V1154 Cyg based on Q1–Q4 LC data. The formal uncertainty (1σ) of the amplitudes is uniformly 0.000 024.

ID	Frequency (d^{-1})	σ_f (d^{-1})	Amplitude (mag)	φ phase (rad)	σ_φ (rad)
f_0	0.203 0244	0.000 0002	0.144 984	0.794 350	0.000 027
$2f_0$	0.406 0514	0.000 0010	0.039 291	4.403 636	0.000 097
$3f_0$	0.609 0704	0.000 0041	0.009 880	1.926 416	0.000 385
$4f_0$	0.812 0798	0.000 0375	0.001 090	5.812 189	0.003 496
$5f_0$	1.015 1798	0.000 0668	0.000 611	5.508 786	0.006 232
$6f_0$	1.218 1468	0.000 0683	0.000 598	3.132 366	0.006 361
$7f_0$	1.421 1946	0.000 1077	0.000 379	0.442 772	0.010 040
$8f_0$	1.624 1924	0.000 1820	0.000 224	4.130 455	0.016 973
$9f_0$	1.827 2617	0.000 3652	0.000 112	1.421 814	0.034 039
$10f_0$	2.030 4263	0.000 6842	0.000 060	4.893 997	0.063 769
$11f_0$	2.233 4364	0.000 1591	0.000 026	2.184 016	0.148 302

zero epoch was chosen close to the moment of the first data point, that is, BJD = 245 4954.0. The errors have been estimated from PERIOD04. Searching for only one frequency of the highest amplitude at a time and pre-whitening for it and then repeating the procedure gave practically the same results as searching for all the harmonics simultaneously.

6.4 Behaviour of the pulsation period

This is the first occasion that cycle-to-cycle changes in the pulsation period of a Cepheid can be followed. The O−C analysis of *Kepler* data of V1154 Cyg is published in a separate paper (Derekas et al., in preparation). Here we study the long-term behaviour of the pulsation period.

The computed times of maxima were calculated from the period fitted to the *Kepler* data. One O−C point was derived for the mid-epoch of annual sections for each available photometric time-series taken from the literature. Besides the *Kepler* maxima and available CCD and photoelectric observations, we publish for the first time V1154 Cyg data from digitized Harvard plates and eye estimations from Sternberg Astronomical Institute photographic plates. The passband of these observations is close to Johnson *B*. We also used visual and CCD observations from the AAVSO International Data base. Where both Johnson *B* and *V* data were available at the same epoch, we retained only the *V* maxima.

These data points are listed in the first column of Table 5. Column 2 lists the epoch number ($E = 0$ was arbitrarily taken at the first maximum of the *Kepler* data). Weights were assigned to individual data sets similarly to the case of V2279 Cyg. The weights are listed in Column 4. The final ephemeris was derived by a weighted linear least-squares fit to the preliminary residuals computed from a formerly published (usually slightly incorrect) period value which is an inherent step in the O−C method. No weight was assigned to the photographic normal maxima; these O−C residuals were omitted from the fitting procedure. The O−C residuals in Column 3 have been calculated with the final ephemeris

$$C = \mathrm{BJD}\,(245\,4955.7260 \pm 0.0008) + (4.925\,454 \pm 0.000\,001)E.$$

This period is considered to be more accurate than the one obtained by fitting the frequency and its harmonics. The source of data is given in the last column of Table 5. The O−C diagram is shown in Fig. 13. This plot indicates that the pulsation period has been constant during the last 40 yr. In principle, the moments of the maximum light differ for different passbands. From simultaneous observations, we find a difference of −0.020 d between the *V* and *Kp* maxima in the sense of $V - Kp$, which is neglected in Fig. 13. We note that this does not change our conclusions in any way.

Table 5. Sample table of O−C residuals for V1154 Cyg. The entire table is available as Supporting Information with the online version of the article.

JDM$_\odot$ − 240 0000	*E*	O−C (d)	*W*	Filter	Reference (Instrument)
148 62.215	−8140	−0.3154	0	PG	This work (Harvard)
156 75.172	−7975	−0.0584	0	PG	This work (Harvard)
164 92.860	−7809	0.0043	0	PG	This work (Harvard)
...	...	...	...	...	...
409 62.4929	−2841	−0.0188	3	*V*	Wachmann (1976)
414 94.5033	−2733	0.0426	3	*V*	Szabados (1977)
462 91.8422	−1759	−0.0107	3	*V*	Berdnikov (2008)
...	...	...	...	...	...
549 55.7450	0	0.0185	5	*Kp*	This work (*Kepler*)
549 60.6690	1	0.0170	5	*Kp*	This work (*Kepler*)
549 65.5787	2	0.0014	5	*Kp*	This work (*Kepler*)

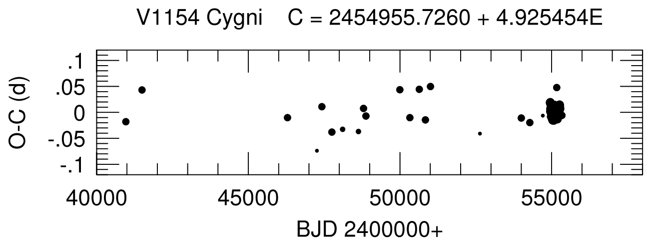

Figure 13. O−C diagram of V1154 Cyg. This plot indicates that the pulsation period has been constant since 1970. The O−C residuals obtained from the *Kepler* data (rightmost clump of points) are analysed in a separate paper (Derekas et al., in preparation).

Table 6. Log of the spectroscopic observations of V1154 Cyg containing the date of observation, the computed RV, the error of the RV, the S/N of the spectrum and the observatory. The exposure time was 30 min in each case.

JDM$_\odot$ (245 0000+)	RV (km s^{-1})	σ (km s^{-1})	S/N	Observatory
4267.4519	−17.22	0.7	60	OACt
5338.5157	8.069	0.033	193	TLS
5359.3851	−14.597	0.053	72	TLS
5376.4405	−1.216	0.006	107	TLS
5376.4621	−0.921	0.006	110	TLS
5378.5110	−1.540	0.006	110	TLS
5381.4465	−0.243	0.007	91	TLS
5381.4681	−0.076	0.007	96	TLS
5389.4482	−15.779	0.046	74	TLS
5393.5050	−7.969	0.019	93	TLS
5397.4266	7.848	0.040	214	TLS
5428.3559	−14.464	0.048	80	TLS
5429.3496	−12.620	0.048	75	TLS
5430.3332	−3.570	0.015	101	TLS
5431.4743	5.302	0.019	141	TLS

6.5 Radial velocities of V1154 Cyg

The suspected spectroscopic binarity of V1154 Cyg can be investigated with the help of the new RV data, most of them obtained with the Tautenburg 2.0-m telescope (see Table 6). Comparison with the data taken from the literature (Gorynya et al. 1998) and Imbert (1999) does not provide a new evidence of spectroscopic binarity, because the γ-velocity (mean RV averaged over a complete pulsational cycle) derived from the new data practically coincides with that obtained from the previous observations – see Fig. 14. Quantitatively, the differences are -0.19 ± 0.30 and -0.15 ± 0.22 km s^{-1} between our new data and data of Gorynya et al. (1998) and Imbert (1999), respectively.

We add that a period derived from all the available RV data is in very good agreement with (less than 2σ from) the photometric period derived in the previous section.

6.6 Pulsation mode of V1154 Cyg

Cepheids pulsate in one of the first three radial modes [fundamental (F), first (O1) and second overtone (O2)] or simultaneously in two or three of them. Some triple-mode Cepheids pulsate in the first three overtones at the same time. From a pulsational and evolutionary

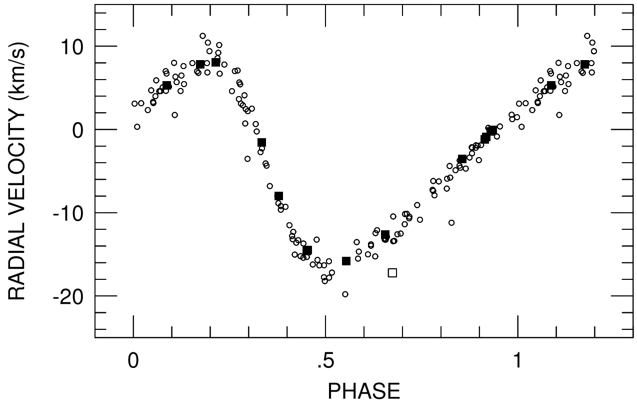

Figure 14. Phased RV data of V1154 Cyg. The open circles denote data obtained by Gorynya et al. (1998) and Imbert (1999), the new Tautenburg data appear as filled squares, while the INAF-OACt spectrum is denoted by an open square.

point of view, it is important to determine the pulsational mode of a monoperiodic Cepheid. Cepheids with pulsational periods similar to V1154 Cyg may pulsate in the fundamental or the first-overtone mode. The usual way of distinction is the use of Fourier parameters that show characteristic progression as a function of period. However, the Fourier parameters of RV curves are indistinguishable for fundamental and first-overtone pulsators with periods around 5 d (see fig. 3 of Baranowski et al. 2009). Light curve Fourier parameters suffer from similar problems. Based on Fig. 5, R_{21} and ϕ_{31} are the most-promising parameters for mode discrimination. However, a closer inspection reveals that there is a 2π difference between ϕ_{31} values of fundamental and first-overtone Galactic Cepheids close to 5 d period; therefore, this particular phase difference is not a good discriminator in the case of V1154 Cyg. R_{21} is higher for F Cepheids and lower for O1 Cepheids. However, it is amplitude-dependent and if we decrease the amplitude of the F Cepheid, then it also goes to zero. V1154 Cyg is not a low-amplitude Cepheid and based on R_{21} alone, it can be classified as a fundamental-mode pulsator. To draw a firm conclusion, we need more pieces of evidence.

Analysis of the first-order phase lag ($\Delta\Phi_1 = \phi_1^{V_r} - \phi_1^{V}$) between the Johnson V light curve and RV may come to the rescue (Ogłoza, Moskalik & Kanbur 2000; Szabó et al. 2007). The phase-lag method is a reliable tool to establish the Cepheid pulsation mode in this pulsation period regime. We used the simultaneous new RV data (Table 6) and Johnson V photometry (Fig. 10 and Table 2) and derived $\Delta\Phi_1 = -0.298 \pm 0.018$, which places our Cepheid firmly among fundamental-mode Cepheids as is clearly seen in Fig. 15.

7 CONCLUSIONS

We described the pre-launch selection of Cepheid candidates within the *Kepler* FOV. Of our 40 candidates, only five remained after inspection of the *Kepler* light curves. Aided by additional ground-based multicolour and spectroscopic observations, we excluded further four stars including V2279 Cyg (KIC 8022670), which is most likely a rapidly rotating K dwarf with flares showing prominent emission lines. Our results show that its previous classification as a Cepheid is not correct. This leaves us with only one star, V1154 Cyg (KIC 7548061), which is a well-known Cepheid.

Kepler has provided one of the most-accurate Cepheid light curves to date. High-order harmonics of the main pulsational mode were detected for the first time up to the 10th harmonic. Reliable investigation of cycle-to-cycle variations in the light curve is currently

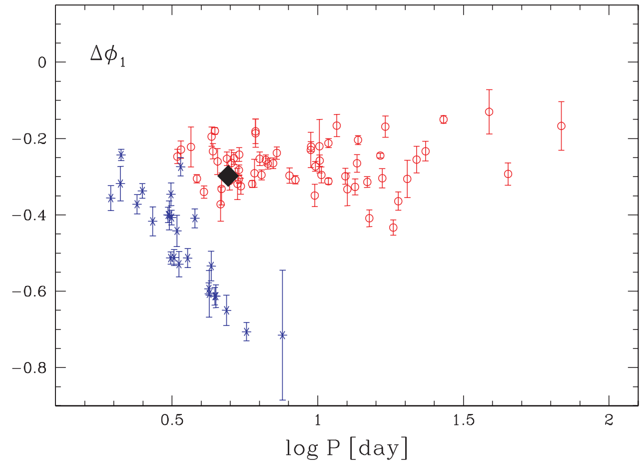

Figure 15. Phase lag of the fundamental-mode (red circles) and first-overtone (blue asterisks) Galactic Cepheids. V1154 Cyg is denoted by a black diamond.

hampered by instrumental effects, but will be investigated as pixel-level data or finally corrected data are available for V1154 Cyg. Period variation is investigated in a separate paper (Derekas et al., in preparation).

New, high-precision RV measurements of V1154 Cyg do not confirm the spectroscopic binarity hypothesized by Gorynya et al. (1996). Measuring the phase lag between simultaneous photometric and RV data of the pulsation allowed us to determine unambiguously that V1154 Cyg is a fundamental-mode pulsator.

An intriguing feature of classical Cepheids is the possible presence of non-radial pulsation modes in the case of a number of first-overtone Cepheids in the Large Magellanic Cloud (Moskalik & Kołaczkowski 2009). Indeed, theoretical computations by Mulet-Marquis et al. (2007) predict the presence of high-order non-radial modes close to and beyond the blue edge of the Cepheid instability strip. Although V1154 Cyg pulsates in the fundamental mode, we have searched for, but have not found any short-period variability (non-radial or stochastically excited modes).

New kinds of investigations will become possible with upcoming years-long *Kepler* data when all instrumental effects are understood. These include analyses of the light-curve variation from cycle to cycle and the detection of low-mass companions through the light-time effect.

ACKNOWLEDGMENTS

Funding for the *Kepler* mission is provided by the NASA's Science Mission Directorate. This project has been supported by the 'Lendület' programme of the Hungarian Academy of Sciences and the Hungarian OTKA grants K83790 and MB08C 81013. Financial support from the ESA (PECS programme No. C98090) is gratefully acknowledged. C-CN thanks the funding from the National Science Council (of Taiwan) under the contract NSC 98-2112-M-008-013-MY3. RS is supported by the Austrian Science Fund (FWF project AP 2120521). We acknowledge the assistance of the queue observers, Chi-Sheng Lin and Hsiang-Yao Hsiao, from the Lulin Observatory. Part of this project is based on data from the OMC Archive at LAEFF, pre-processed by ISDC. We acknowledge with thanks the variable star observations from the AAVSO International Data base contributed by observers worldwide and used in this research. The authors gratefully acknowledge the entire Kepler team, whose outstanding efforts have made these results possible.

REFERENCES

Akerlof C., Amrose S., Balsano R. et al., 2000, AJ, 119, 1901
Antonello E., Lee A. S., 1981, ApJ, 248, 291
Antonello E., Morelli P. L., 1996, A&A, 312, 541
Antonello E., Poretti E., 1986, A&A, 169, 149
Antonello E., Poretti E., Reduzzi L., 1990, A&A, 236, 138
Arellano Ferro A., Rojo Arellano R., González-Bedolla S., Rosenzweig P., 1998, ApJS, 117, 167
Baranowski R. et al., 2009, MNRAS, 396, 2194
Batalha N. M. et al., 2010, ApJ, 713, L109
Berdnikov L. N., 2008, VizieR On-line Data Catalog: II/285
Berdnikov L. N., 2010, in Sterken C., Samus N., Szabados L., eds, Variable Stars, the Galactic Halo and Galaxy Formation. Sternberg Astr. Inst., Moscow
Bertin E., Arnouts S., 1996, A&AS, 117, 393
Blomme J. et al., 2010, ApJ, 713, L204
Borucki W. J. et al., 2010, Sci, 327, 977
Bruntt H. et al., 2008, ApJ, 683, 433
Burki G., Schmidt E. G., Arellano Ferro A., Fernie J. D., Sasselov D., Simon N. R., Percy J. R., Szabados L., 1986, A&A, 168, 139
Dahlmark L., 2000, IBVS, No. 4898
ESA, 1997, Hipparcos Catalogue, ESA SP-1200
Fernie J. D., Evans N. R., Beattie B., Seager S., 1995, IBVS, 4148, 1
Gilliland R. L. et al., 2010a, PASP, 122, 131
Gilliland R. L. et al., 2010b, ApJ, 713, L160
Gorynya N. A., Samus' N. N., Rastorguev A. S., Sachkov M. E., 1996, Astron. Lett., 22, 175
Gorynya N. A., Samus' N. N., Sachkov M. E., Rastorguev A. S., Glushkova E. V., Antipin S. V., 1998, Astron. Lett., 24, 815
Hartman J. D., Bakos G., Stanek K. Z., Noyes R. W., 2004, AJ, 128, 1761
Ignatova V. V., Vozyakova O. V., 2000, Astron. Astrophys. Trans., 19, 133
Imbert M., 1999, A&AS, 140, 79
Jenkins J. M. et al., 2010a, ApJ, 713, L87
Jenkins J. M. et al., 2010b, ApJ, 713, L120
Kazarovets E. V., Kireeva N. N., Samus N. N., Durlevich O. V., 2003, IBVS, 5422
Klagyivik P., Szabados L., 2009, A&A, 504, 959
Koch D. G. et al., 2010, ApJ, 713, L79
Kolenberg K. et al., 2011, MNRAS, 411, 878
Kolláth Z., 1990, Occ. Tech. Notes, Konkoly Obs. No. 1.
Landolt A. U., 2009, AJ, 137, 4186
Lenz P., Breger M., 2005, Commun. Asteroseismol., 146, 53
Luck R. E., Kovtyukh V. V., Andrievsky S. M., 2006, AJ, 132, 902
Mantegazza L., Poretti E., 1992, A&A, 261, 137
Moffett T. J., Barnes T. G., III, 1985, ApJS, 58, 843
Molenda-Żakowicz J., Frasca A., Latham D. W., 2008, Acta Astron., 58, 419
Moskalik P., Kołaczkowski Z., 2009, MNRAS, 394, 1649
Mulet-Marquis C., Glatzel W., Baraffe I., Winisdoerffer C., 2007, A&A, 465, 937
Munari U., Sordo R., Castelli F., Zwitter T., 2005, A&A, 442, 1127
Ogłoza W., Moskalik P., Kanbur S., 2000, in Szabados L., Kurtz D., eds, ASP Conf. Ser. Vol. 203, Phase Lag of Classical Cepheids and RR Lyrae Stars. Astron. Soc. Pac., San Francisco, p. 235
Pigulski A., Pojmański G., Pilecki B., Szczygieł D. M., 2009, Acta Astron., 59, 33
Pojmanski G., Maciejewski G., 2004, Acta Astron., 54, 153
Poretti E., 1994, A&A, 285, 524
Reegen P., 2007, A&A, 467, 1353
Samus N. N., Goranskii V. P., Durlevich O. V., Zharova A. V., Kazarovets E. V., Pastukhova E. N., Hazen M. L., Tsvetkova T. M., 2002, Astron. Lett., 28, 174
Schmidt E. G., Langan S., Rogalla D., Thacker-Lynn L., 2007, AJ, 133, 665
Simon N. R., Lee A. S., 1981, ApJ, 248, 291
Spreckley S. A., Stevens I. R., 2008, MNRAS, 388, 1239
Strohmeier W., Knigge R., Ott H., 1963, Bamberg Veröff., V, Nr. 16
Szabados L., 1977, Commun. Konkoly. Obs. Hung. Acad. Sci., Budapest, No. 70
Szabó R., Buchler J. R., Bartee J., 2007, ApJ, 667, 1150
Szabó R. et al., 2010, MNRAS, 409, 1244
Tammann G. A., Sandage A., Reindl B., 2003, A&A, 404, 423
Voges W. et al., 1999, A&A, 349, 389
Wachmann A. A., 1976, A&AS, 23, 249
Woźniak P. R. et al., 2004, AJ, 127, 2436

SUPPORTING INFORMATION

Additional Supporting Information may be found in the online version of this article:

Table 2. Ground-based multicolour photometry of V1154 Cyg and *Kepler* Cepheid candidates.
Table 3. Table of O−C residuals for V2279 Cyg.
Table 5. Table of O−C residuals for V1154 Cyg.

Please note: Wiley-Blackwell are not responsible for the content or functionality of any supporting materials supplied by the authors. Any queries (other than missing material) should be directed to the corresponding author for the article.

This paper has been typeset from a TEX/LATEX file prepared by the author.

Monthly Notices
of the
ROYAL ASTRONOMICAL SOCIETY

Mon. Not. R. Astron. Soc. **415,** 1220–1227 (2011) doi:10.1111/j.1365-2966.2011.18743.x

The pulsations of PG 1351+489

M. Redaelli,[1⋆] S. O. Kepler,[1] J. E. S. Costa,[1] D. E. Winget,[2] G. Handler,[3] B. G. Castanheira,[1,2,3] A. Kanaan,[4] L. Fraga,[5] P. Henrique,[4] O. Giovannini,[6] J. L. Provencal,[7,8] H. L. Shipman,[7] J. Dalessio,[7] S. E. Thompson,[8,9] F. Mullally,[9] M. M. Brewer,[10] D. Childers,[11] M. E. Oksala,[12] R. Rosen,[13] M. A. Wood,[14] M. D. Reed,[15] B. Walter,[16] W. Strickland,[16] D. Chandler,[16] T. K. Watson,[17] R. E. Nather,[2] M. H. Montgomery,[2] A. Bischoff-Kim,[18] C. J. Hansen,[19] A. Nitta,[20] S. J. Kleinman,[20] C. F. Claver,[21] T. M. Brown,[22] D. J. Sullivan,[23] S.-L. Kim,[24] W.-P. Chen,[25] M. Yang,[25] C.-Y. Shih,[25] X. Zhang,[26] X. Jiang,[26] J. N. Fu,[27] S. Seetha,[28] B. N. Ashoka,[28] T. M. K. Marar,[28] K. S. Baliyan,[29] H. O. Vats,[29] A. V. Chernyshev,[30] P. Ibbetson,[31] E. Leibowitz,[32] S. Hemar,[32] A. V. Sergeev,[33] M. V. Andreev,[33] R. Janulis,[34] E. G. Meištas,[34] P. Moskalik,[35] G. Pajdosz,[35] A. Baran,[36] M. Winiarski,[36] S. Zola,[36,37] W. Ogloza,[36] M. Siwak,[37] Zs. Bognár,[38] J.-E. Solheim,[39] R. Sefako,[40] D. Buckley,[40] D. O'Donoghue,[40] T. Nagel,[41] R. Silvotti,[42] I. Bruni,[42] J. R. Fremy,[43] G. Vauclair,[44] M. Chevreton,[43] N. Dolez,[44] B. Pfeiffer,[44] M. A. Barstow,[45] O. L. Creevey,[46] S. D. Kawaler[47] and J. C. Clemens[48]

[1] *Instituto de Física da Universidade Federal do Rio Grande do Sul, 91501-970 Porto Alegre, RS, Brazil*
[2] *Department of Astronomy and McDonald Observatory, University of Texas, Austin, TX 78712, USA*
[3] *Institut für Astronomie, Universität Wien, Türkenschanzstraβe 17, 1180 Wien, Austria*
[4] *Departamento de Física, Universidade Federal de Santa Catarina, 88040-900 Florianópolis, SC, Brazil*
[5] *Southern Observatory for Astrophysical Research, Casilla 603, La Serena, Chile*
[6] *Departamento de Física e Química, Universidade de Caxias do Sul, 95070-560 Caxias do Sul, RS, Brazil*
[7] *University of Delaware, Department of Physics and Astronomy Newark, DE 19716, USA*
[8] *Delaware Asteroseismic Research Center, Mt Cuba Observatory, Greenville, DE 19807, USA*
[9] *SETI Institute/NASA Ames Research Center, Moffett Field, CA 94035, USA*
[10] *William Jewell College, 500 College Hill Liberty, MO 64048, USA*
[11] *Department of Math and Science, Delaware County Community College, 901 S. Media Road, Media, USA*
[12] *Bartol Research Institute, University of Delaware, Newark, Delaware, USA*
[13] *National Radio Astronomy Observatory, PO Box 2, Green Bank, WV 24944, USA*
[14] *Florida Institute of Technology, Department of Physics and Space Sciences, Melbourne, FL 32901, USA*
[15] *Missouri State University and Baker Observatory, 901 S. National, Springfield, MO 65897, USA*
[16] *Meyer Observatory and Central Texas Astronomical Society, Waco, TX, USA*
[17] *Southwestern University, Georgetown, TX, USA*
[18] *Department of Chemistry, Physics and Astronomy, Georgia College & State University, Milledgeville, GA, USA*
[19] *JILA, University of Colorado, Boulder, CO, USA*
[20] *Gemini Observatory, 670 N A'ohoku PI., Hilo, HI 96720, USA*
[21] *Kitt Peak National Observatory, National Optical Astronomy Observatory, Tucson, AZ, USA*
[22] *Las Cumbres Observatory Global Telescope Network, Inc., 6740 Cortona Drive Suite 102, Santa Barbara, CA 93117, USA*
[23] *Victoria University of Wellington, Wellington, New Zealand*
[24] *Korea Astronomy and Space Science Institute, Daejeon 305-348, Korea*
[25] *Lulin Observatory, National Central University, Taiwan*
[26] *National Astronomical Observatories, Beijing 100012, China*
[27] *Department of Astronomy, Beijing Normal University, Beijing, China*
[28] *Indian Space Research Organization, Airport Road, Vimanapura PO, Bangalore 560017, India*
[29] *Physical Research Laboratory, Ahmedabad 380009, India*
[30] *Astronomical Institute, Astronomicheskaya 33, Tashkent, Uzbekistan*

⋆E-mail: maukeyboard@gmail.com

[31] *Wise Observatory, Tel Aviv University, Tel Aviv, Israel*
[32] *School of Physics and Astronomy and the Wise Observatory, Tel Aviv University, Tel Aviv, Israel*
[33] *Ukranian National Academy of Sciences, Main Astronomical Observatory, Golosiiv, Kiev 022 252650, Ukraine*
[34] *Institute of Theoretical Physics and Astronomy, Vilnius University, Vilnius, Lithuania*
[35] *Copernicus Astronomical Center, Warsaw, Poland*
[36] *Mt Suhora Observatory, Cracow Pedagogical University, Cracow, Poland*
[37] *Astronomical Observatory, Jagiellonian University, ul. Orla 171, 30-244 Cracow, Poland*
[38] *Konkoly Observatory, PO Box 67, H-1525 Budapest XII, Hungary*
[39] *Institute of Theoretical Astrophysics, University of Oslo, NO 0315 Oslo, Norway*
[40] *South African Astronomical Observatory, Observatory 7935, Cape Town, South Africa*
[41] *Institut für Astronomie und Astrophysik, Universitet Tübingen, Sand 1, 72076 Tübingen, Germany*
[42] *INAF Osservatorio Astronomico di Torino, strada dell Osservatorio 20, 10025 Pino Torinese, Italy*
[43] *LESIA, Observatoire de Paris-Meudon, Meudon, France*
[44] *Laboratoire d'Astrophysique de Toulouse-Tarbes CNRS-UMR5572, Université de Toulouse, France*
[45] *Astronomy Department, Leicester University, University Road, Leicester LE1 7RH*
[46] *Instituto de Astrofisica de Canarias, Tenerife, Spain*
[47] *Department of Physics and Astronomy, Iowa State University, Ames, IA 50211, USA*
[48] *Department of Physics and Astronomy, University of North Carolina, Philips Hall, CB 3255, Chapel Hill, NC 27599, USA*

Accepted 2011 March 18. Received 2011 March 15; in original form 2010 September 3

ABSTRACT

PG 1351+489 is one of the 20 DBVs – pulsating helium-atmosphere white dwarf stars – known and has the simplest power spectrum for this class of star, making it a good candidate to study cooling rates. We report accurate period determinations for the main peak at 489.334 48 s and two other normal modes using data from the Whole Earth Telescope (WET) observations of 1995 and 2009. In 2009, we detected a new pulsation mode and the main pulsation mode exhibited substantial change in its amplitude compared to all previous observations. We were able to estimate the star's rotation period, of 8.9 h, and discuss a possible determination of the rate of period change of $(2.0 \pm 0.9) \times 10^{-13}$ s s $^{-1}$, the first such estimate for a DBV.

Key words: stars: evolution – stars: individual: PG 1351+489 – stars: oscillations – white dwarfs.

1 INTRODUCTION

White dwarf stars with spectra dominated by He I lines pulsate when their effective temperatures are between about 30 000 and 22 000 K (see e.g. Beauchamp et al. 1999). These stars, collectively known as DBV, were the first variables to be correctly predicted before their discovery (Winget et al. 1982). There are only 20 DBVs known (Kilkenny et al. 2009; Nitta et al. 2009) and PG 1351+489 is one of them. This star has two determinations for the effective temperature, $T_{\rm eff} = 22\,600$ K, $\log g = 7.9$ using pure He atmosphere and $T_{\rm eff} = 26\,100$ K, $\log g = 7.89$ allowing for unseen H contamination (Beauchamp et al. 1999). Castanheira et al. (2006) estimated from *IUE* spectra the values $T_{\rm eff} = 22\,500 \pm 190$ K, $\log g = 7.60 \pm 0.15$ for pure He and $T_{\rm eff} = 22\,000 \pm 150$ K, $\log g = 7.00 \pm 0.07$ allowing for H contamination. The analysis of the time series photometric data shows one main mode and at least two other normal modes (Winget, Nather & Hill 1987). This is one of the simplest DBV periodogram known.

The study of white dwarfs can contribute to our knowledge about the Galaxy disc and halo (e.g. Winget & Kepler 2008). White dwarf pulsations provide important information about high-energy and high-pressure systems, because the pulsations observed in white dwarfs are their normal modes and depend on their global structure. Also, cooling rates may be measured by the rate of change of period (Winget et al. 1985), because the evolution of a white dwarf is dominated by cooling. As the temperature of a pulsating white dwarf decreases, the depth of the ionization zone increases and longer periods can be excited. Up to now, such a rate of change has been measured for the lukewarm DAVs (Kepler et al. 2005) and for the hot DOVs (Costa & Kepler 2008), but not for DBVs.

PG 1351+489 is a candidate for the first measurement of a DBV cooling rate because its power spectrum is dominated by one mode. The largest amplitude mode, at 489 s, has a peak-to-peak amplitude of 0.16 mag and several harmonics have also been detected (Winget et al. 1987). In addition, two smaller amplitude normal modes have been observed, along with several linear combination frequencies (Alves et al. 2003). In this work we confirm these previous results and provide more precise values for the periods; we also find a new small amplitude mode in the 2009 data and estimate the rotation period for this star. We report the observations of PG 1351+489 during two Whole Earth Telescope (WET) campaigns (Nather et al. 1990) from 1995 and 2009, and discuss a possible rate of change of the main period for this star. A rate of pulsation period change is an evolutionary time-scale, and offers a unique way to look inside a star to measure its internal composition. These rate of period changes constrain models used in cosmochronology, and can even be used to probe for exotic particles like neutrinos and axions.

2 OBSERVATIONS

We obtained ∼170 h of high-speed photometric data from seven different observatories in the WET campaign of 1995 (xcov12), spanning 38 d. There was a 20 d gap between April 5 and April 25, and the coverage was about 40 per cent in the two weeks of intense observation. From the WET campaign of 2009 (xcov27) we obtained only ∼20 h of observations from four observatories, since PG 1351+489 was a tertiary target. We also used four data sets from McDonald Observatory, obtained during the years 1984, 1985, 1986 and 2004. The time base used in this work is the Barycentric Dynamical Time (TDB), or Barycentric Julian Dynamical Date (BJDD), obtained after a conversion from UTC to the barycenter of the Solar system. Table 1 shows the Journal of Observations.

3 ANALYSIS

We began the analysis of PG 1351+489 data looking for pulsation modes in the individual light curves. The peaks in the Fourier transform whose amplitude were above the detection limit of 1/1000 false alarm probability were considered real. For the individual light curves, which consist of equally spaced data, the detection limit was three times the average amplitude, computed by $\langle A\rangle = \sqrt{\Sigma A_i^2/N}$. The main peak of 489 s was present in all the runs. The small amplitude modes were detected only in the longer runs.

Table 1. Journal of observations.

Run	Telescope	Δt (s)	Date (UT)	Begin (UT)	Length (h)
r2957	McDonald 2.1 m	10	1984 May 06	04:04:30	04:25:20
r2961	McDonald 2.1 m	10	1984 May 07	03:20:00	02:36:40
r2962	McDonald 2.1 m	10	1984 May 07	06:28:20	03:54:30
r3006	McDonald 2.1 m	10	1985 February 16	07:20:55	04:15:00
r3007	McDonald 2.1 m	10	1985 February 17	08:28:00	03:44:40
r3015	McDonald 2.1 m	10	1985 March 22	08:15:39	01:28:50
r3019	McDonald 2.1 m	10	1985 March 23	05:29:11	06:06:00
r3025	McDonald 2.1 m	10	1985 March 24	06:24:10	04:47:10
r3072	McDonald 2.1 m	10	1985 June 15	03:44:50	02:19:50
r3077	McDonald 2.1 m	10	1985 June 22	03:40:10	02:26:20
r3080	McDonald 2.1 m	10	1985 June 24	07:37:00	01:47:30
r3142	McDonald 2.1 m	10	1986 April 03	04:04:30	05:07:20
r3144	McDonald 2.1 m	10	1986 April 04	03:54:20	07:25:40
r3149	McDonald 2.1 m	10	1986 April 10	05:37:56	04:21:50
r3150	McDonald 2.1 m	03	1986 April 13	05:23:40	02:50:57
r3151	McDonald 2.1 m	10	1986 April 13	09:21:40	01:46:20
r3168	McDonald 2.1 m	10	1986 June 10	03:36:00	05:10:30
r3170	McDonald 2.1 m	10	1986 June 11	03:38:30	05:12:30
r3172	McDonald 2.1 m	10	1986 June 12	03:36:40	05:31:40
r3173	McDonald 2.1 m	10	1986 June 13	03:36:30	05:07:40
gv0502	Pic du Midi 2.0 m	10	1995 April 02	22:53:07	03:10:10
gv0504	Pic du Midi 2.0 m	10	1995 April 03	22:24:37	01:51:40
gv0506	Pic du Midi 2.0 m	10	1995 April 04	22:09:10	02:44:10
gv0508	Pic du Midi 2.0 m	10	1995 April 05	23:38:50	05:10:40
eml-0002	Wise 1.0 m	10	1995 April 25	18:43:10	05:07:20
eml-0003	Wise 1.0 m	10	1995 April 26	17:55:40	07:24:10
eml-0005	Wise 1.0 m	10	1995 April 27	21:56:40	03:43:10
eml-0006	Wise 1.0 m	10	1995 April 28	18:43:00	01:07:00
eml-0008	Wise 1.0 m	10	1995 April 28	21:06:00	03:55:20
eml-0009	Wise 1.0 m	10	1995 April 29	18:03:00	07:01:00
jebp01	Isaac Newton 2.5 m	10	1995 April 26	00:17:40	05:10:40
jebp02	Isaac Newton 2.5 m	10	1995 April 26	22:58:30	02:07:10
jebp03	Isaac Newton 2.5 m	10	1995 April 27	21:45:00	07:03:50
jebp04	Isaac Newton 2.5 m	10	1995 April 28	23:31:20	05:47:20
jebp05	Isaac Newton 2.5 m	10	1995 April 29	20:54:40	08:26:10
ra360	McDonald 2.1 m	10	1995 April 26	02:40:50	07:59:50
ra361	McDonald 2.1 m	10	1995 April 27	02:29:40	07:25:40
ra362	McDonald 2.1 m	10	1995 April 28	02:39:20	08:03:00
ra363	McDonald 2.1 m	10	1995 April 29	02:35:10	08:35:50
ra364	McDonald 2.1 m	10	1995 April 30	02:31:40	07:58:10
ra367	McDonald 2.1 m	10	1995 May 03	07:29:40	03:37:00
emac-002	Maidanak 1.0 m	10	1995 May 01	20:31:30	01:49:00
emac-003	Maidanak 1.0 m	10	1995 May 01	18:30:00	01:44:10
emac-004	Maidanak 1.0 m	10	1995 May 02	15:54:00	02:49:50
emac-006	Maidanak 1.0 m	10	1995 May 05	16:32:30	05:40:30
emac-008	Maidanak 1.0 m	10	1995 May 06	19:16:00	03:41:50
cfc-202	Mauna Kea 0.6 m	10	1995 May 01	07:47:00	04:24:50
cfc-208	Mauna Kea 0.6 m	10	1995 May 07	08:48:50	04:18:40
rk368	McDonald 2.1 m	10	1995 May 04	02:48:00	06:46:40

Table 1 – *continued*

Run	Telescope	Δt (s)	Date (UT)	Begin (UT)	Length (h)
rk369	McDonald 2.1 m	10	1995 May 06	08:52:40	01:55:30
sjk-0384	BAO 2.16 m	10	1995 May 02	14:22:30	05:10:10
sjk-0385	BAO 2.16 m	10	1995 May 03	14:06:50	05:19:00
sjk-0386	BAO 2.16 m	10	1995 May 04	12:45:00	07:17:00
sjk-0387	BAO 2.16 m	10	1995 May 05	13:24:40	06:00:40
sjk-0388	BAO 2.16 m	10	1995 May 06	16:32:40	03:54:10
an-0015	McDonald 2.1 m	10	1995 May 11	08:03:20	03:03:20
A0876	McDonald 2.1 m	05	2004 May 12	05:54:35	02:34:55
A0900	McDonald 2.1 m	05	2004 June 14	03:06:06	04:01:50
mole090525	Moletai 1.6 m	17	2009 May 25	20:17:08	02:54:32
mole090530	Moletai 1.6 m	17	2009 May 30	20:27:08	02:14:52
naoc090529	China 2.16 m	20	2009 May 29	12:48:11	03:49:00
naoc090530	China 2.16 m	20	2009 May 30	12:38:48	02:04:30
naoc090531	China 2.16 m	20	2009 May 31	12:41:48	01:40:20
pjmo090531	Meyer 0.6 m	30	2009 May 31	04:49:35	03:32:30
teub090524	Tuebingen 0.8 m	30	2009 May 24	21:26:01	04:12:30

The longest data set, acquired in 1995, has the best resolution and signal-to-noise ratio. The detection limit used for the whole 1995 data set was $n\ \langle A\rangle$, where $n = A^{\rm max}_{\rm rand}/\langle A_{\rm rand}\rangle$, and $A^{\rm max}_{\rm rand}$ are the maximum and $\langle A_{\rm rand}\rangle$ are the average amplitudes of the Fourier transform of the randomized light curve, which has no signal, only noise, but the same spacings as the real data. We found $n = 4.3$ using a Monte Carlo simulation method, and $n = 4.12$ using the analytical method described by Scargle (1982). Because the noise increases with decreasing frequency for $f \le 6000$ μHz, the detection limit is a function of frequency.

Run 'emac-002', listed in Table 1 shows a very large phase deviation from the surrounding runs, inconsistent with the rest of the light curve. We assumed a timing mistake occurred and excluded that file from further analysis.

We computed a weighted Fourier transform for the whole 1995 data, shown in Fig. 1. The weights are the inverse of the dispersion in each light curve, (e.g. Handler 2003b; Costa & Kepler 2008). A list of frequencies from our analysis is shown in Table 2.

After pre-whitening the power spectrum of 1995 data by the main peak and its first harmonic, some energy remained around these frequencies (Handler 2003a). Some amount of this energy must be just mathematical artefact: amplitude modulation, real in the star or caused by different sensitivity in the detectors or possible problems in sky subtraction, causes side lobes in a Fourier transform. To search for nearby periodicities to the main pulsation mode in our combined data set, which includes data from different size telescopes, located at different sites, with non-uniform effective wavelength sensitivity, we attempted to minimize the effects of amplitude modulation. We re-normalized each run, from each observatory, by the amplitude average of the main mode estimated from the whole 1995 data set, assuming it remained intrinsically constant over the 38 d of observation.

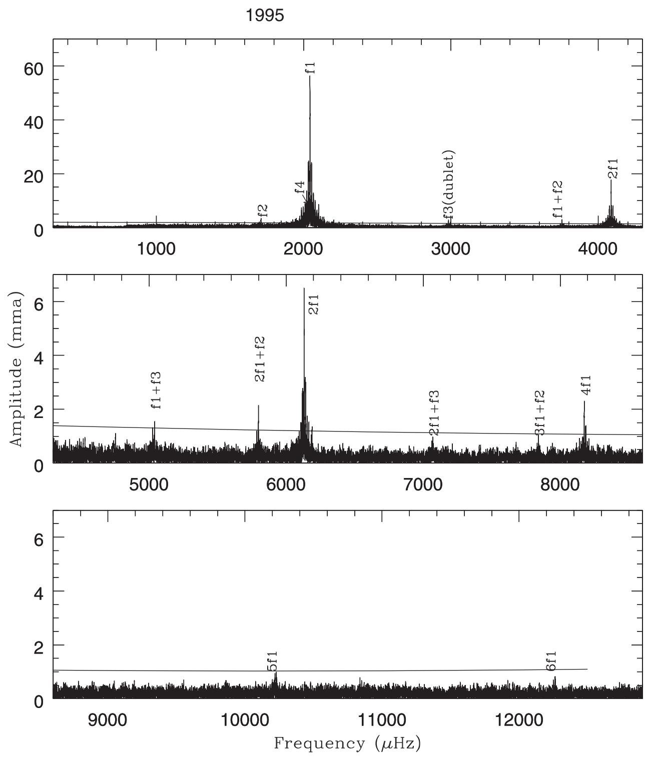

Figure 1. Weighted Fourier transform for 1995 data. The weights are the inverse square of the dispersion in each light curve. The line is the detection limit obtained from the Monte Carlo Simulation. Note the change in the y-axis for the lower panels.

4 ROTATION PERIOD

We found a new peak in the Fourier transform at 2027 μHz. Handler (2003a) analysed a subset of data of four consecutive nights at the 2.5 m Isaac Newton Telescope and pointed out this same interesting result. The original Fourier transform, pre-whitened by the main peak, and the one after re-normalization is shown in Fig. 2. Because this small amplitude mode beats with the main period, it is not easy to resolve it. As the difference of f_1 and this new peak is 16 μHz, the beating period is about 17 h. We need over 10 beating cycles (170 h) to separate these two close frequencies. Fortunately, we obtained more than 260 h in the last two weeks of the 1995 campaign. The doublet at $f_3 = 2982$ μHz has a splitting frequency of 15 μHz and is probably caused by rotation. The observed 16 μHz splitting of the main mode agrees with the splitting of the doublet mode f3, suggesting

Table 2. Frequencies detected in PG 1351+489 during 1995 data.

Frequency (μHz)	Period (s)	Amplitude (mma)	Identification
2043.5919 ± 0.0020	489.334 48 ± 0.000 48	56.36 ± 0.20	f_1
4087.1727 ± 0.0066	244.667 90 ± 0.000 39	17.19 ± 0.20	$2f_1$
6130.744 ± 0.017	163.112 32 ± 0.000 47	6.31 ± 0.20	$3f_1$
8174.315 ± 0.048	122.334 40 ± 0.000 72	2.34 ± 0.20	$4f_1$
10215.05 ± 0.13	97.8947 ± 0.000 13	0.40 ± 0.24	$5f_1$
12298.59 ± 0.46	81.3101 ± 0.0030	0.27 ± 0.27	$6f_1$
1710.337 ± 0.030	584.679 ± 0.010	3.68 ± 0.20	f_2
2982.771 ± 0.041	335.2586 ± 0.0046	2.81 ± 0.20	f_3[1]
3752.14 ± 0.35	266.514 ± 0.025	0.32 ± 0.21	$f_1 + f_2$
5040.885 ± 0.079	198.3778 ± 0.0031	1.44 ± 0.20	$f_1 + f_3$
5797.493 ± 0.050	172.4883 ± 0.0015	2.23 ± 0.20	$2f_1 + f_2$
2027.082 ± 0.023	493.3199 ± 0.0057	4.84 ± 0.20	$f^a{}_1$
1563.390 ± 0.25	639.63 ± 0.10	11.5 ± 1.1	f_4[2]

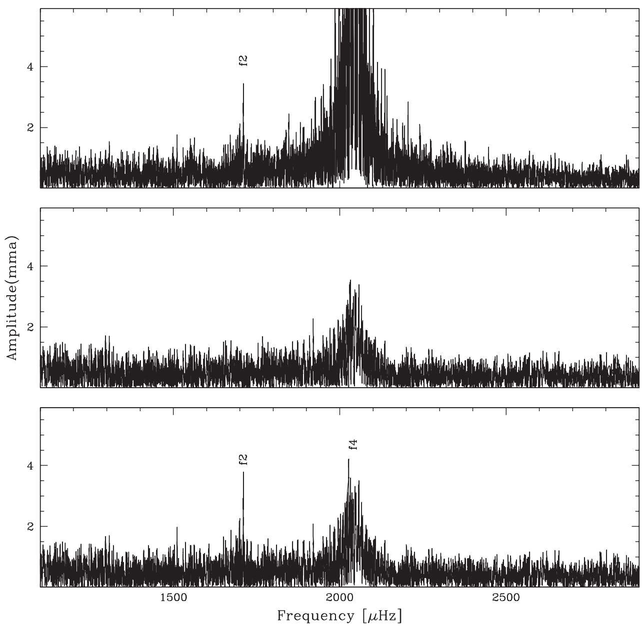

Figure 2. Fourier transforms of 1995 data. The top box shows the whole data FT in a crop of the main peak vicinity. The middle box shows an FT without f_1 and f_2. Some peaks remained nearby the main peak after the prewhitening of f_1 and f_2. Bottom box shows an FT without the main peak for the re-normalized data. We used the main peak amplitude to re-normalize each run, assuming it is constant over the 38 d of observation. A peak at 2027 μHz and $A = 4.43$ mma remained.

that both modes are being rotationally split. The relation between the splitting frequency and the rotation period of the white dwarf depends on the pulsation index ℓ and k (see e.g. Kepler et al. 1995), and is given in the first order by

$$\delta\sigma_{\ell km} = \delta m \Omega_{\rm rot}(1 - C_{\ell \rm km}),$$

where $C_{\ell km}$ is the first-order splitting coefficient, $\delta\sigma_{\ell km}$ is the frequency splitting, δm is the m difference between the components and has a modulus of unity for $\ell = 1$ modes. $\Omega_{\rm rot}$ is the rotation frequency. Using *Hubble Space Telescope* time-resolved spectroscopy, Kepler et al. (2000) found $\ell = 1$ for the main mode. Montgomery (2005) found the same result using a convection model to fit the observed light curve. Even though the asymptotic value for $C_{\ell km}$ is valid only for large k, its value from the models is close to the asymptotic value of $[\ell(\ell + 1)]^{-1}$. Using $\delta\sigma_{\ell km} = 15.5 \pm 0.5$ μHz and $C_{\ell km} = 0.5$, we find a rotation period of 8.9 ± 0.3 h for PG 1351+489. As we have approximately the same splitting at f_1 and f_3, both modes should have the same $\ell = 1$.

The data of 1985 March show a slightly different value for the main peak period, of 489.11 s. The best value found in 1995 data is 489.33 s, which leaves us to speculate that the star became unstable in 1985. The total length of the 1995 March data is ∼50 h giving a resolution of 0.6 μHz, much smaller than the difference in the main mode for 1985 March and 1995, of 10 μHz. Before and after 1985 March the star seems stable, although it changed again in 2009.

The 2009 data surprised us with a different pulsation spectrum (Fig. 3). The main mode shows a small change in period from previous data and its amplitude is reduced by half. At this stage we cannot identify the reason for these changes and need to keep observing PG 1351+489 to determine whether the star reverts to the original set of pulsation modes or maintains this new pulsation spectrum. Another star has shown changes in its periodicities: GD 358, the first DBV detected, showed a remarkable change in its pulsation spectrum in 1996 (Kepler et al. 2003; Castanheira et al. 2005). During that year, the amplitude of all modes changed, the

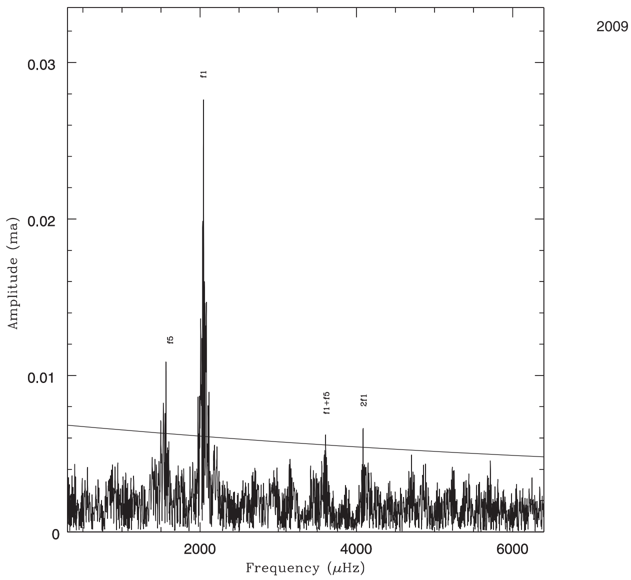

Figure 3. Power spectrum of 2009 data. We got only 20 h of data, but it was enough to see the changes in the star. PG 1351+489 shows a new mode and a decrease to the half of main mode amplitude.

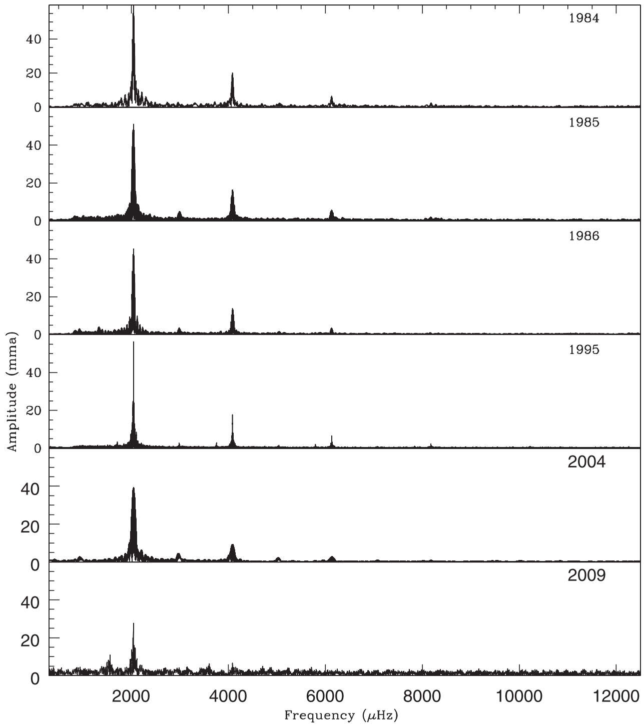

Figure 4. PG 1351+489 yearly Fourier transform on the same scale. Note the changes, especially in 2009.

dominant mode changed and even the shape of its light curve went from non-sinusoidal to sinusoidal. After 1996 their amplitudes returned basically to those of 1994, although the amplitude of all modes still show small changes from year to year (Provencal et al. 2009). Montgomery et al. (2010) show there was a significant change in the convection zone; when the observed amplitude of pulsation of GD 358 is high, the temperature in the heated area increases sufficiently to practically extinguish the convection layer. Robinson, Kepler & Nather (1982) show g-mode pulsations in white dwarf stars are mainly due to temperature changes across the surface of the star. Now we have knowledge of another DBV white dwarf – PG 1351+489 – which changed its pulsation spectrum over a time-scale of years. The fact that we detect at least six harmonics of the main pulsation implies that the intrinsic pulsation amplitude is high, as harmonics represent non-linear effects (Jevtić et al. 2005; Montgomery 2008). The high intrinsic pulsation amplitude possibly affects significantly the convection layers in PG 1351+489, as it does in GD 358.

Detecting as many modes as possible is important to apply seismology to the star, as each mode detected yields an independent constraint on its structure (e.g. Kepler et al. 2003). PG 1351+489 has four pulsation modes known up to now, including the new one detected in 2009. Fig. 4 shows the six amplitude spectra of the yearly data sets.

5 A POSSIBLE ESTIMATE OF $\dot{P}$

The rate of change of a period ($\dot{P} = \mathrm{d}P/\mathrm{d}t$) can be measured directly or indirectly (Costa & Kepler 2008). To do it directly, we must have high rates of change and small uncertainties. Supposing $\mathrm{d}P/\mathrm{d}t \sim 10^{-6}\,\mathrm{s\,yr^{-1}}$, then in 20 yr the period must change $\sim 2 \times 10^{-5}$ s. To measure this small change, the uncertainty in the measured periods must be smaller than $\sim 10^{-5}$ s. To measure $\mathrm{d}P/\mathrm{d}t$ indirectly, we can use the O − C method, which is quadratic in the time-span (e.g. Kepler et al. 1991). This method uses the difference between the times of maxima measured in the light curves and the computed values assuming no significant changes in period, over the number of cycles.

Table 3. Times of maxima for the main mode of PG 1351+489. The 2009 time of maximum was not considered in our analysis of $\mathrm{d}P/\mathrm{d}t$.

Year	$T_{\max}$(BJDD ± s)	P (s)
1984	244 5826.677 079 ± 0.6	489.292 91 ± 0.000 65
1985	244 6112.813 247 ± 0.7	489.316 24 ± 0.000 58
1986 April	244 6523.678 718 ± 0.6	489.302 81 ± 0.000 60
1986 June	244 6591.653 173 ± 0.5	489.2837 ± 0.0026
1995 April	244 9810.461 595 ± 0.9	489.3260 ± 0.0049
1995 May	244 9833.625 895 ± 0.2	489.3345 50 ± 0.000 18
2004	245 3137.751 014 ± 1.4	489.3359 ± 0.000 19
2009	245 6982.358 127 ± 3.2	489.3122 ± 0.025

As discussed, for example, in Kepler et al. (1991), a parabola is fitted to the values of O − C and the quadratic parameter is proportional to the rate of change of period. We assume the periods are changing smoothly in time and short perturbations to the periods do not affect significantly the phase of the pulsations.

Table 3 shows the values for the times of maxima and main period for each chunk of data. To increase the number of independent measurements, we separated the 1986 and 1995 light curves in two chunks each. The phase of the main pulsation for the 2009 data was not used because the star clearly changed in that year.

To apply this method, we assume we do not know the precise value of the period. The cycle count changes significantly when the period changes a little, but we are working with the hypothesis of an unknown period to estimate the secular $\mathrm{d}P/\mathrm{d}t$ for this star. Thus, we must test many different O − C diagrams for many different values of period, following O'Donoghue & Warner (1987). We tested periods from 489.33 to 489.34 s, in steps of 0.000 01 s. For each possible period we found a different O − C set. We chose the smallest S^2 (the normalized sum of the phase differences squared) computed for the O − C values and the fitted parabola. The diagram is shown in Fig. 5. The best values for S^2 are shown in Table 4. The smallest S^2 gives $P = (489.334\,645 \pm 0.000\,023)$ s and $\dot{P} = (2.0 \pm 0.9) \times 10^{-13}\,\mathrm{s\,s^{-1}}$.

6 DISCUSSION

The measurement of the cooling rate of a hot DBV star can be used to estimate the plasmon-neutrino emission rates (Winget et al. 2004). Using the optical spectra determination of effective temperature with pure helium atmospheres, PG 1351+489 is not on the blue edge of the DBV instability strip, hence the plasmon-neutrino emission should not dominate the cooling, except if the star has low mass. Compared to the values calculated by Winget et al. (2004) for such low temperature, but normal mass, the estimate of $\mathrm{d}P/\mathrm{d}t$ we obtain is higher than predicted by the cooling by photon and plasmon-neutrino emission. We call our $\mathrm{d}P/\mathrm{d}t$ an estimate, not a measurement, because the 1985 value is not included; we will discuss these glitches in the next section. Córsico & Althaus (2004) estimate for a 0.5 $\mathrm{M_\odot}$ DB white dwarf model at $T_{\mathrm{eff}} = 22\,100$ K a rate of period change of $\dot{P} = 8.6 \times 10^{-14}\,\mathrm{s\,s^{-1}}$, for their $P = 485$ s mode, with cooling dominated by photon emission. The theoretical value is a factor of 2.3 smaller than that estimated from the observations in this paper.

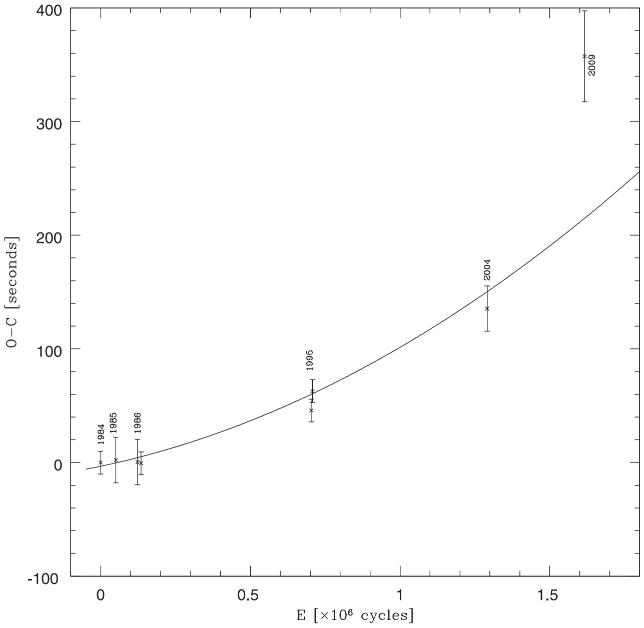

Figure 5. O − C diagram for PG 1351+489. The fitted parabola gives $\dot{P} = (2.0 \pm 0.9) \times 10^{-13}$ s s^{-1} and $P = 489.334\,645 \pm 0.000\,023$ s. The 2009 value was not included in this analysis because the pulsations changed in that year; its value is shown only as a guide. Note we do not include the 489.11 s period and its time of maxima, obtained in 1985.

Table 4. Some values for P and $\dot{P}$ for different O − C diagrams.

S^2 (s ^{2})	P_i(s)	P (s)	$\dot{P}(10^{-13}$ s s$^{-1})$
43.383 7290	489.334 59	489.334 645 ± 0.000 023	2.0 ± 0.9
43.383 7292	489.334 87	489.334 645 ± 0.000 023	2.0 ± 0.9
190.750 3123	489.333 68	489.334 472 ± 0.000 048	−29.2 ± 1.9
190.750 3125	489.333 75	489.334 472 ± 0.000 048	−29.2 ± 1.9
321.933 2478	489.335 67	489.334 818 ± 0.000 063	33.2 ± 2.4

Some pulsation modes have higher amplitude in the core than in the surface layers, while others have the opposite. The core of white dwarf stars represents around 99 per cent of their mass. For those modes with larger amplitudes in the core, the fractional rate of change of their pulsation periods, $\dot{P}/P$, decreases very approximately at the same rate as the star cools, $\dot{T}_{\rm core}/T_{\rm core}$, considering the fractional radius change, $\dot{R}/R$, is around one to two orders of magnitude smaller. For those modes where the surface layer amplitudes dominate, the pulsation periods can change on a much faster time-scale, representative of avoided crossings or changes in the transition layers causing mode trapping. As the masses involved in the surface layers are small, these relatively rapid changes will revert to evolutionary (cooling) time-scales, which are not affected by the surface layer changes. In pulsars, for example, even in the Hulse & Taylor PSR B1913+16, glitches occur, and their rotation behaviour over long time-scales are significantly affected by small-scale irregularities not explicitly accounted for in a deterministic model. Nevertheless, the physically important astrometric, spin and orbital parameters are well determined and well decoupled from the timing noise (Weisberg, Nice & Taylor 2010).

If the estimated $\dot{P}$ value is representative of the stellar cooling and the star has a relatively low temperature, but normal mass, the rate of period change could be used to constrain the axion emissivity. At the low effective temperature determined from pure He models, the energy lost by axion emission is expected to be larger than the energy lost by neutrinos (Kim 2007, fig. 1.2). For an effective temperature of PG 1351+489 as high as $T_{\rm eff} = 26\,000$ K, estimated by Montgomery et al. (2010, fig. 6) non-linear curve fitting, or Beauchamp et al. (1999) if some H contamination is allowed, Córsico & Althaus (2004) estimate $\dot{P} = 1.7 \times 10^{-14}$ s s^{-1}; thus the estimated rate of period change could be reflecting the white dwarf cooling for such a high effective temperature.

Castanheira et al. (2006) determined from *IUE* spectra a surface gravity of $\log g = 7.0 \pm 0.07$, allowing for the presence of unseen atmospheric H, but the external uncertainty in $\log g$ is much larger, because of the weak dependency of DB models on surface gravity. Such a low surface gravity would imply a stellar mass for PG 1351+489 markedly lower than 0.5 $M_\odot$. For such low mass, the neutrino emission could be important even at $T_{\rm eff} = 22\,000$ K (Winget et al. 2004, fig. 1, 0.45 $M_\odot$ white dwarf model).

Unfortunately, we do not have yet a measurement of the cooling rate, because the uncertainty in $\dot{P}$ is relatively high and because our assumption of a stable period cannot be proven. We must continue to observe the star to get a $\dot{P}$ measurement.

The study of the pulsating DB stars can provide new information about their progenitors, possible very late thermal pulse (VLTP) remnants (Althaus et al. 2009). New DB stars have been observed and now we can make good advances to unveil the DB instability strip. It is important to continue observing known DB stars in order to check their pulsation profiles and understand their instabilities while searching for new ones is potentially useful to test theories and improve models.

PG 1351+489 is a very important star to study the cooling rate for DBVs. However, its relatively cool temperature drops it to a secondary choice to measure the plasmon-neutrino emission rate for white dwarfs (e.g. Kim, Winget & Montgomery 2006). We estimate the rotation period of 8.9 ±0.3 h using the splitting frequency of 15.5 ±0.5 μHz we found in the main peak; using this rotation period we deduce the $1.46f_1$ mode has $\ell = 1$ too. We estimate a possible rate of change of period using the O − C method; we found $\mathrm{d}P/\mathrm{d}t = (2.0 \pm 0.9) \times 10^{-13}$ s s $^{-1}$. The high uncertainty in this result is due to the low number of points in the O − C diagram (Fig. 5). Low numbers of points can lead to low confidence statistics, e.g. a negative secular change of PG 1159−035, estimated by Winget et al. (1985), had the best S^2 at that time. Costa, Kepler & Winget (1999) showed the second solution in 1985, a positive $\mathrm{d}P/\mathrm{d}t$ was in fact the correct one when more data were added. As we have no proof of period stability for PG 1351+489, we cannot conclude that the $\dot{P}$ we found represents the evolution of the star. New observations of PG 1351+489 are required in order to improve our chances of estimating the secular changes in the star.

ACKNOWLEDGMENTS

We sincerely thank the referee, Dr Leandro Althaus, for his insightful comments that made this a better paper.

REFERENCES

Althaus L. G., Panei J. A., Miller Bertolami M. M., García-Berro E., Córsico A. H., Romero A. D., Kepler S. O., Rohrmann R. D., 2009, ApJ, 704, 1605

Alves V. M. et al., 2003, Baltic Astron., 12, 33

Beauchamp A., Wesemael F., Bergeron P., Fontaine G., Saffer R. A., Liebert J., Brassard P., 1999, ApJ, 516, 887

Castanheira B. G., Nitta A., Kepler S. O., Winget D. E., Koester D., 2005, A&A, 432, 175
Castanheira B. G., Kepler S. O., Handler G., Koester D., 2006, A&A, 450, 331
Córsico A. H., Althaus L. G., 2004, A&A, 428, 159
Costa J. E. S., Kepler S. O., 2008, A&A, 489, 1
Costa J. E. E., Kepler S. O., Winget D. E., 1999, ApJ, 522, 973
Handler G., 2003a, Baltic Astron., 12, 11
Handler G., 2003b, Baltic Astron., 12, 253
Jevtić N., Zelechoski S., Feldman H., Peterson C., Schweitzer J. S., 2005, ApJ, 635, 527
Kepler S. O. et al., 1991, ApJ, 378, L45
Kepler S. O. et al., 1995, ApJ, 447, 874
Kepler S. O., Robinson E. L., Koester D., Clemens J. C., Nather R. E., Jiang X. J., 2000, ApJ, 539, 379
Kepler S. O. et al., 2003, A&A, 401, 639
Kepler S. O. et al., 2005, ApJ, 634, 1311
Kilkenny D., O'Donoghue D., Crause L. A., Hambly N., MacGillivray H., 2009, MNRAS, 397, 453
Kim A., 2007, PhD thesis, University of Texas at Austin, http://whitedwarf.org/theses/kim.pdf
Kim A., Winget D. E., Montgomery M. H., 2006, Mem. Soc. Astron. Ital., 77, 460
Montgomery M. H., 2005, ApJ, 633, 1142
Montgomery M. H., 2008, Comm. Asteroseismol., 154, 38
Montgomery M. H. et al., 2010, ApJ, 716, 84
Nather R. E., Winget D. E., Clemens J. C., Hansen C. J., Hine B. P., 1990, ApJ, 361, 309
Nitta A. et al., 2009, ApJ, 690, 560
O'Donoghue D., Warner B., 1987, MNRAS, 228, 949
Provencal J. L. et al., 2009, ApJ, 693, 564
Robinson E. L., Kepler S. O., Nather R. E., 1982, ApJ, 259, 219
Scargle J. D., 1982, ApJ, 263, 835
Weisberg J. M., Nice D. J., Taylor J. H., 2010, ApJ, 722, 1030
Winget D. E., Kepler S. O., 2008, ARA&A, 46, 157
Winget D. E., Robinson E. L., Nather R. D., Fontaine G., 1982, ApJ, 262, L11
Winget D. E., Robinson E. L., Nather R. E., Kepler S. O., O'Donoghue D., 1985, ApJ, 292, 606
Winget D. E., Nather R. E., Hill J. A., 1987, ApJ, 316, 305
Winget D. E., Sullivan D. J., Metcalfe T. S., Kawaler S. D., Montgomery M. H., 2004, ApJ, 602, L109

This paper has been typeset from a TEX/LATEX file prepared by the author.

Monthly Notices
of the
ROYAL ASTRONOMICAL SOCIETY

Mon. Not. R. Astron. Soc. **411,** 1204–1212 (2011) doi:10.1111/j.1365-2966.2010.17753.x

Transit timing variation and activity in the WASP-10 planetary system*

G. Maciejewski,[1,2]† D. Dimitrov,[3] R. Neuhäuser,[1] N. Tetzlaff,[1] A. Niedzielski,[2] St. Raetz,[1] W. P. Chen,[4] F. Walter,[5] C. Marka,[1] S. Baar,[1] T. Krejcová,[6] J. Budaj,[7] V. Krushevska,[7,8] K. Tachihara,[9] H. Takahashi[10] and M. Mugrauer[1]

[1]*Astrophysikalisches Institut und Universitäts-Sternwarte, Schillergässchen 2–3, D-07745 Jena, Germany*
[2]*Toruń Centre for Astronomy, N. Copernicus University, Gagarina 11, PL-87100 Toruń, Poland*
[3]*Institute of Astronomy, Bulgarian Academy of Sciences, 72 Tsarigradsko Chausse Blvd, 1784 Sofia, Bulgaria*
[4]*Institute of Astronomy, National Central University, 300 Jhongda Rd, Jhongli 32001, Taiwan*
[5]*Department of Physics and Astronomy, SUNY, Stony Brook, NY 11794-3800, USA*
[6]*Masaryk University, Department of Theoretical Physics and Astrophysics, 602 00 Brno, Czech Republic*
[7]*Astronomical Institute of the Slovak Academy of Sciences, 059 60 Tatranská Lomnica, Slovak Republic*
[8]*Main Astronomical Observatory of National Academy of Sciences of Ukraine, 27 Akademika Zabolotnoho St, 03680 Kyiv, Ukraine*
[9]*National Astronomical Observatory of Japan, ALMA project office, 2-21-1 Osawa Mitaka, Tokyo 181-8588, Japan*
[10]*Gunma Astronomical Observatory, 6860-86 Nakayama, Takayama-mura, Agatsuma-gun, Gunma 377-0702, Japan*

Accepted 2010 September 22. Received 2010 September 22; in original form 2010 July 16

ABSTRACT

Transit timing analysis may be an effective method of discovering additional bodies in extrasolar systems that harbour transiting exoplanets. The deviations from the Keplerian motion, caused by mutual gravitational interactions between planets, are expected to generate transit timing variations of transiting exoplanets. In 2009, we collected nine light curves of eight transits of the exoplanet WASP-10b. Combining these data with those published, we have found that transit timing cannot be explained by a constant period but by a periodic variation. Simplified three-body models, which reproduce the observed variations of timing residuals, were identified by numerical simulations. We have found that the configuration with an additional planet with a mass of $\sim$0.1 M_J and an orbital period of $\sim$5.23 d, located close to the outer 5 : 3 mean motion resonance, is the most likely scenario. If the second planet is a transiter, the estimated flux drop will be $\sim$0.3 per cent and can be observed with a ground-based telescope. Moreover, we present evidence that the spots on the stellar surface and the rotation of the star affect the radial-velocity curve, giving rise to a spurious eccentricity of the orbit of the first planet. We argue that the orbit of WASP-10b is essentially circular. Using the gyrochronology method, the host star was found to be 270 ± 80 Myr old. This young age can explain the large radius reported for WASP-10b.

Key words: planets and satellites: individual: WASP-10b – stars: individual: WASP-10.

1 INTRODUCTION

The analysis of transit timing variations (TTVs) of exoplanets is expected to be an efficient method for discovering additional low-mass planets (Miralda-Escudé 2002; Schneider 2004; Holman & Murray 2005; Agol et al. 2005; Steffen et al. 2007). Many studies have been performed to detect TTV signals but these have resulted only in constraints on the parameters of hypothetical second planets (e.g. Gibson et al. 2009). Recently, Maciejewski et al. (2010) have detected a variation in the transit timing of WASP-3b. They have found that a configuration with a hypothetical second planet with a mass of $\sim 15\,M_\oplus$, located close to an outer 2 : 1 mean motion resonance (MMR), may reproduce the observed TTV signal. Lendl et al. (2010) have found some indications for the TTV for OGLE2-TR-L9b, but no preliminary solution has been proposed.

WASP-10b is an exoplanet, which was discovered by Christian et al. (2009). The mass and radius of the planet have been found to be $2.96^{+0.22}_{-0.17}$ M_J and $1.28^{+0.08}_{-0.09}$ R_J, respectively, larger than the interior models of irradiated giant planets predict. The planet orbits its host star in $\sim$3.09 d at an orbital semimajor axis of $0.0369^{+0.0012}_{-0.0014}$ au. The

*Partly based on observations made with the 0.6- and 2.0-m telescopes of the Rozhen National Astronomical Observatory, which is operated by the Institute of Astronomy, Bulgarian Academy of Sciences, and the 90-cm telescope of the University Observatory Jena, which is operated by the Astrophysical Institute of the Friedrich Schiller University.
†E-mail: gm@astro.uni-jena.de

eccentricity of the orbit has been reported to be $0.059^{+0.014}_{-0.004}$ – a large value for a close-in planet. In the paper reporting on its discovery, Christian et al. (2009) determined the transit depth and duration to be 29 mmag and 2.36 h, respectively.

Johnson et al. (2009, 2010) have redetermined the planet's parameters with a high-precision light curve using the 2.2-m telescope of the University of Hawaii with a photometric precision of 4.7×10^{-4} and a mid-transit time error of 7 s. The mass of the planet has been found to be $3.15^{+0.13}_{-0.11}\,\mathrm{M_J}$ and the planetary radius has turned out to be noticeably smaller (i.e. $1.08 \pm 0.02\,\mathrm{R_J}$). The latter result has not been confirmed by the studies of Krejcová, Budaj & Krushevska (2010) or Dittmann et al. (2010). The first team have found the radius of WASP-10b to be in excellent agreement with the value obtained by Christian et al. (2009), and a similar conclusion has been reached by Dittmann et al. (2010) with no TTV signature detected.

The host star ($V = 12.7$ mag) is a K5 dwarf with an effective temperature of 4675 ± 100 K, located 90 ± 20 pc from the Sun (Christian et al. 2009). Smith et al. (2009) have confirmed the previous evidence that the light curve of WASP-10 exhibits a rotational photometric variability caused by star-spots. The stellar rotation period has been found to be 11.91 ± 0.05 d, in agreement with ∼12 d reported by Christian et al. (2009).

It has been suggested that the presence of an additional small planet could pump the eccentricity of WASP-10b (Christian et al. 2009). This system is therefore a good target for TTV studies.

The order of this paper is as follows. In Section 2, we summarize observations and data reduction. We present the discovery of the periodic TTV in Section 3. We describe the process of identifying and verifying the most likely two-planetary model of the WASP-10 system in Section 4. We present a discussion of the proposed scenario in Section 5. Finally, we give our conclusions in Section 6.

2 OBSERVATIONS AND DATA REDUCTION

We have collected nine light curves of eight transits of WASP-10b during a dedicated international observing campaign involving telescopes worldwide at different longitudes (listed in Tables 1 and 2). The transit on 2009 July 31 was observed with two instruments in different observatories. The telescope diameters of 0.6–2.0 m allowed us to collect photometric data with 1.1–2.7 mmag precision. Observations generally started ∼1 h before the expected beginning of a transit and ended ∼1 h after the event. However, weather conditions and schedule constraints meant that we were not always able to follow this scheme.

Standard IDL procedures (adapted from DAOPHOT) were used for the reduction of the photometric data collected at the National Astronomical Observatory at Rozhen, Bulgaria, and for computing the differential aperture photometry. Using the method of Everett & Howell (2001), several stars (four to six) with photometric precision better than 5 mmag were selected to create an artificial standard star used for differential photometry. Data from the remaining telescopes were reduced with the software pipeline developed for the Semi-Automatic Variability Search sky survey (Niedzielski, Maciejewski & Czart 2003). To generate an artificial comparison star, 30–50 per cent of the stars with the lowest light-curve scatter were selected iteratively from the field stars brighter than 3 mag below the saturation level. To measure instrumental magnitudes, various aperture radii were used. The aperture that was found to produce light curves with the smallest scatter was used to generate a final light curve.

Table 2. The summary of observing runs. ID is the identification of the instrument according to Table 1, N_{exp} is the number of useful exposures, T_{exp} is the exposure time. Dates (UT) are given for the beginning of the night.

Run	Date	ID	Filter	N_{exp}	T_{exp} (s)
1	2009 Jan. 5	1	*R*	254	50
2	2009 Jul. 31	2	*R*	144	60, 80
3	2009 Jul. 31	3	*R*	116	120
4	2009 Aug. 3	3	*R*	122	90
5	2009 Aug. 28	3	*R*	99	90
6	2009 Aug. 31	2	*R*	203	50, 60
7	2009 Sep. 3	3	*R*	105	90
8	2009 Oct. 1	4	*V*	548	15
9	2009 Nov. 17	5	*R*	76	90

3 RESULTS

3.1 Light-curve analysis

A model-fitting algorithm available via the Exoplanet Transit Data base (Poddaný, Brát & Pejcha 2010) was used to derive transit parameters: duration, depth and mid-transit time. The procedure employs the OCCULTSMALL routine of Mandel & Agol (2002) and the

Table 1. A list of the telescopes. FOV is the field of view of the instrument and N_{tr} is the number of observed transits.

ID	Telescope	Observatory and Location	Detector and CCD size	N_{tr} and FOV (arcmin)
1	0.6-m Cassegrain	Astronomical Observatory, N.Copernicus University	SBIG STL-1001	1
		Piwnice near Toruń, Poland	1024 × 1024, 24 µm	11.8 × 11.8
2	0.6-m Schmidt[a]	University Observatory Jena,	CCD-imager STK	2
		Großschwabhausen near Jena, Germany	2048 × 2048, 13.5 µm	52.8 × 52.8
3	0.6-m Cassegrain	National Astronomical Observatory	FLI PL09000	4
		Rozhen, Bulgaria	3056 × 3056, 12 µm	17.3 × 17.3
4	2-m Ritchey-Chrétien	National Astronomical Observatory	PI VersArray:1300B	1
		Rozhen, Bulgaria	1340 × 1300, 20 µm	5.8 × 5.6
5	0.8-m Tenagra II	Tenagra Observatories	SITe	1
		Arizona, USA	1024 × 1024, 24 µm	14.8 × 14.8
6	1.5-m Ritchey-Chrétien	Gunma Astronomical Observatory	Andor DW432	0[b]
		Takayama, Japan	1250 × 1152, 24 µm	12.5 × 11.5

[a]See Mugrauer & Berthold (2010) for details.
[b]No scientific output because of bad weather conditions.

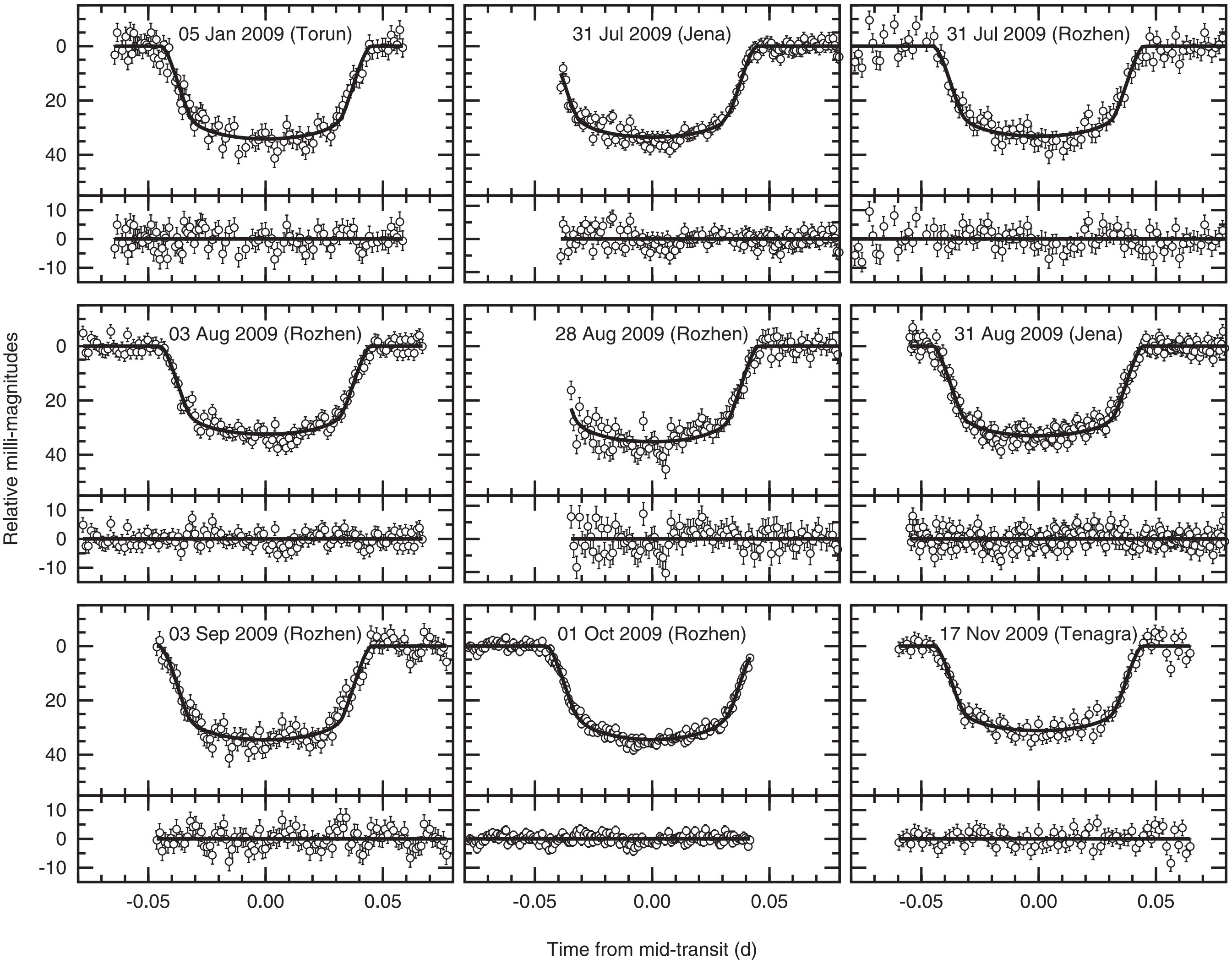

Figure 1. Light curves of WASP-10b transits in individual runs. The best-fitting models are shown as solid lines. The transit on July 31 was observed simultaneously by two observatories.

Levenberg–Marquardt non-linear least-squares fitting algorithm, which also provides uncertainties. As our research was focused on determining mid-transit times, the number of parameters to be fitted could be reduced. An impact parameter $b = a \cos i/R_{*} = 0.299^{+0.029}_{-0.043}$ (where a is the semimajor axis, i is the inclination and R_{*} is the host–star radius) was taken from Johnson et al. (2009) and was fixed during the fitting procedure. We used the linear limb-darkening law of Van Hamme (1993) with the limb-darkening coefficient linearly interpolated for the host star in a given filter. A first- or second-order polynomial was used to remove trends in magnitude or flux. The mid-transit times were corrected from UTC to Terrestrial Dynamical Time (TT) and then transformed into the Barycentric Julian Date (BJD) (Eastman, Siverd & Gaudi 2010). Light curves with best-fitting models and residuals are shown in Fig. 1 and the derived parameters are given in Table 3.

Krejcová et al. (2010) have also published observations and R-band light curves of four complete transit events of WASP-10b. In their analysis, they have focused mainly on the determination of the planet radius and have not studied the mid-transit times, the O − C diagram or TTVs. We determine four mid-transit times for these observations and place them into the context of our data to create a larger sample for TTV analysis. We have used the same method to determine the mid-transit times from their light curves as for all other observations presented here. The corresponding mid-transit times are presented in Table 3.

Across all data sets, two transits on epochs 222 and 232 were observed simultaneously by two different telescopes. The data were reduced with different pipelines and by different teams. The transit on epoch 222 was observed with the 60-cm telescopes in Jena and at Rozhen. The difference in mid-transit times was found to be ∼11 s. The transit on epoch 232 was covered by observations in Jena and by the 50-cm telescope in Stará Lesná in Slovakia (Krejcová et al. 2010). In this case, the discrepancy of timing was found to be ∼18 s. Timing differences are well within the error bars of individual determinations for both transits. This practical test strengthens the reliability of our mid-transit time determinations.

3.2 Detection of a transit timing variation

While determining new linear ephemeris, we noted that a linear fit of the epoch E and orbital period P_{b} of WASP-10b resulted in reduced $\chi^2_{\mathrm{red}} = 13.8$. Individual mid-transit errors were taken as weights in the fitting procedure. Such a high value of χ^2_{red} suggests the existence of an additional signal in the O − C diagram (Fig. 2).

Table 3. Parameters of transit light-curve modelling. T_0 denotes the mid-transit time, T_d is the transit time duration, δ is the depth, σ is the averaged standard deviation of the fit and E is the epoch. The O − C values have been calculated according to the linear part of equation (1) and the best-fitting parameters. The O − C values are given both in days and in uncertainties of the mid-transit times. t_{cad} is the mean cadence of a light curve. The results of reanalysed data from Krejcová et al. (2010) are collected below the horizontal line. BJD times are based on TT.

Run	T_0 BJD$_{TT}$ − 245 0000	T_d (min)	δ (mmag)	σ (mmag)	E	O − C (d)	O − C (T_0 errors)	t_{cad} (s)
1	4837.23116 ± 0.00037	128.9 ± 1.4	34.1 ± 0.8	2.7	155	−0.00030	−0.8	56
2	5044.44427 ± 0.00032	128.9 ± 1.2	33.5 ± 1.1	1.7	222	+0.00069	+2.2	87
3	5044.44415 ± 0.00040	129.1 ± 1.5	33.1 ± 0.7	2.6	222	+0.00057	+1.4	130
4	5047.53696 ± 0.00028	129.4 ± 1.0	32.4 ± 0.5	2.0	223	+0.00066	+2.3	103
5	5072.27861 ± 0.00053	131.1 ± 2.1	35.2 ± 0.8	2.5	231	+0.00056	+1.1	102
6	5075.37129 ± 0.00024	129.2 ± 0.8	33.0 ± 0.7	2.0	232	+0.00053	+2.2	63
7	5078.46485 ± 0.00044	130.4 ± 1.5	34.5 ± 1.1	2.5	233	+0.00137	+3.1	102
8	5106.29681 ± 0.00021	129.8 ± 0.7	34.4 ± 0.7	1.1	242	−0.00115	−5.4	19
9	5152.68923 ± 0.00039	128.8 ± 1.3	33.3 ± 2.4	2.1	257	+0.00051	+1.3	143
	4775.37834 ± 0.00042				135	+0.00125	+2.9	35
	5075.37150 ± 0.00034				232	+0.00073	+2.2	26
	5109.39135 ± 0.00052				243	+0.00068	+1.3	36
	5112.48528 ± 0.00035				244	+0.00189	+5.4	36

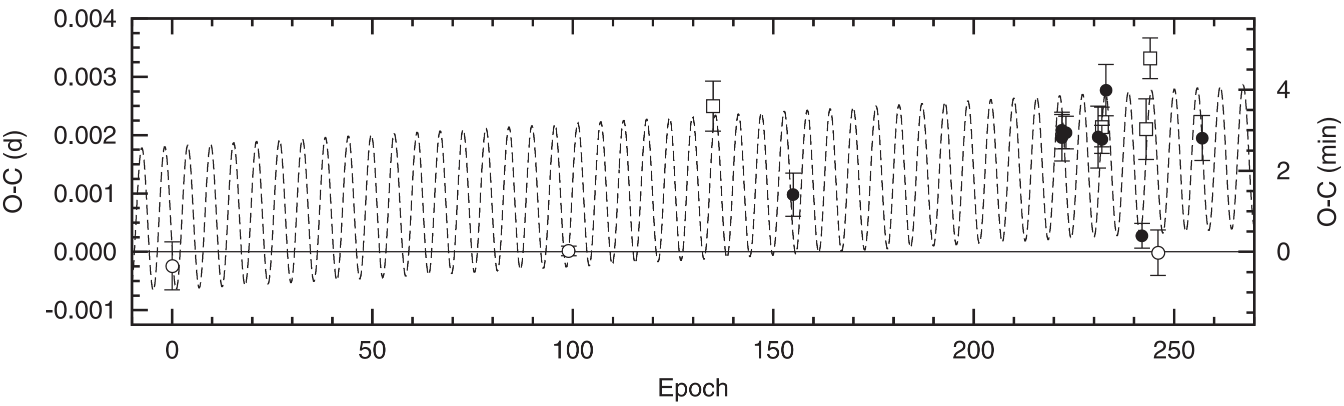

Figure 2. The observation minus calculation (O − C) diagram for WASP-10b, generated for linear ephemeris based on data from the literature (solid line). Open circles denote the data from the literature, taken from Christian et al. (2009), Johnson et al. (2010) and Dittmann et al. (2010). Open squares are based on reanalysed photometry from Krejcová et al. (2010). Filled symbols denote results from our campaign. A significantly better fit may be obtained for the new ephemeris given by equation (1) (dashed line). The 3σ error bars were taken for the mid-transit time reported by Dittmann et al. (2010). Their light curve was not corrected for a linear trend, which is clearly visible in out-of-transit phases (J. Dittmann, private communication). Our tests have shown that this effect significantly affects the accuracy of the mid-transit time.

The Lomb–Scargle periodogram (Lomb 1976; Scargle 1982) of the residuals reveals the existence of two peaks of similar significance and frequencies of 0.175 and 0.183 cycl P_b^{-1} (Fig. 3). For each frequency, an ephemeris was refitted with the linear trend plus a sinusoidal variation in the form:

$$T_b = T_0 + E P_b + A_{ttv} \sin\left(2\pi \frac{E - E_{ttv}}{P^{ttv}}\right) \quad (1)$$

Here, T_0 is the mid-transit time for the initial epoch ($E = 0$), A_{ttv} is the semi-amplitude of the detected TTV, E_{ttv} is the epoch offset of the TTV signal and P^{ttv} is its period. The minimal $\chi^2_{red} = 3.2$ was obtained for $f_1^{ttv} = 0.183$ cycl P_b^{-1} and resulted in $T_0 = 245\,4357.86011 \pm 0.00047$ BJD$_{TT}$, $P_b = 3.0927183 \pm 0.0000021$ d, $A_{ttv} = 0.00120 \pm 0.00036$ d, $E_{ttv} = 1.8 \pm 0.4$ and $P_1^{ttv} = 5.473 \pm 0.012\, P_b$.

The procedure run for $f_2^{ttv} = 0.175$ cycl P_b^{-1} gave $\chi^2_{red} = 4.1$, $P_2^{ttv} = 5.7172 \pm 0.0082\, P_b$ and similar values of T_0 and P_b. In this case, the fit turned out to be poorer, and thus we used the ephemeris based on parameters obtained for P_1^{ttv}.

The ephemeris calculated according to equation (1) (and P_1^{ttv}) is plotted in Fig. 2 with a dashed line. The O − C values, which are used in further analysis, were calculated according to the linear part of equation (1).

To check if a random distribution of data points in the O − C diagram may favour the detected frequencies, 10^5 fake data sets were generated. The original residuals were replaced with random values with a white-noise distribution of the amplitude. Then, the Lomb–Scargle algorithm was run to find a dominant frequency in each fake diagram. Fig. 4 shows a histogram of these frequencies, with the number of bins equal to the square root of the number of data points in the sample. Detected TTV frequencies, f_1^{ttv} and f_2^{ttv}, are not associated with any significant peak in the histogram.

Kipping & Bakos (2010a) have pointed out that the transit phasing, which is the time difference between the expected mid-transit moment and the nearest data point in a light curve, may generate a spurious TTV signal. For example, for a light curve of 60-s cadence, the time difference is expected to be ±30 s (Kipping & Bakos 2010b). Cadences of our individual light curves are in a wide range between 19 and 143 s (see Table 3) with the median value of

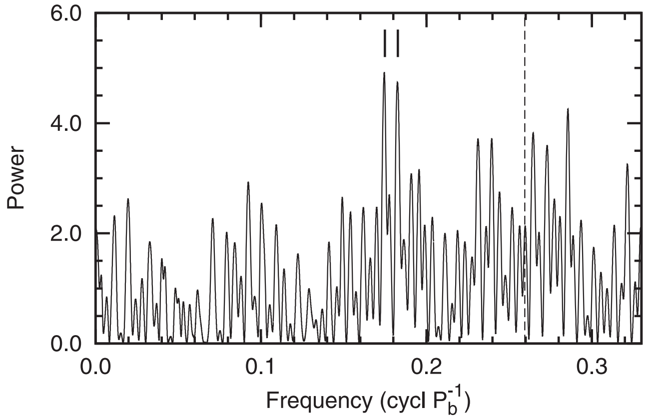

Figure 3. The Lomb–Scargle periodogram generated for the timing residuals plotted in Fig. 2, showing the existence of a periodic signal. The most significant peaks are indicated. The upper limit of the periodogram is determined by the Nyquist frequency for the data set. The vertical dashed line marks the rotational period of the host star (see Section 5).

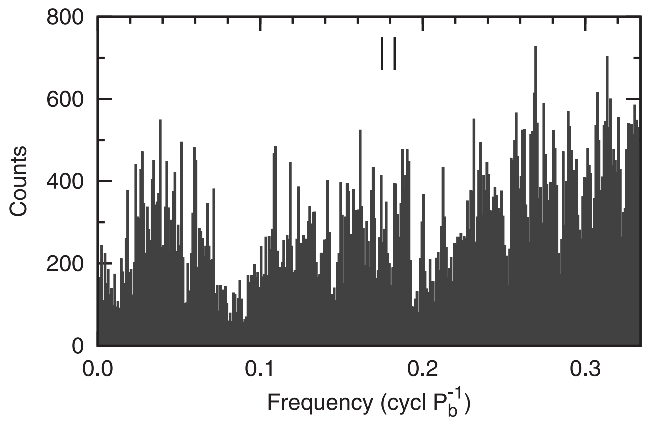

Figure 4. The distribution of dominant frequencies for 10^5 fake O − C diagrams with observed data points replaced by the white noise. The number of bins is equal to the square root of the number of data points in the sample and the width of individual bins is 0.001 cycl P_b^{-1}. Detected TTV frequencies, $f_1^{\rm ttv}$ and $f_2^{\rm ttv}$, are indicated. No significant peak is associated with any of these, which indicates that a spectral window is not a source of detected periodicities.

63 s. This value is ∼ three times smaller than the amplitude of the detected TTV signal. As shown in Fig. 5, no correlation between individual residuals and cadences was detected. A formal least-squares fit to this data set resulted in the correlation coefficient $R = -0.36$, which clearly reveals no correlation at the relevant level. The checks discussed above strengthen the detection of the TTV signal in our data set.

4 TWO-PLANETARY MODEL

The possible non-zero eccentricity postulated by Christian et al. (2009) might potentially have resulted from confusion with a two-planet system in which both planets orbit their host star in circular orbits in an inner 2 : 1 resonance (Anglada-Escude, López-Morales & Chambers 2010). Although we argue later that the eccentricity of WASP-10b is indistinguishable from zero, the case of an inner

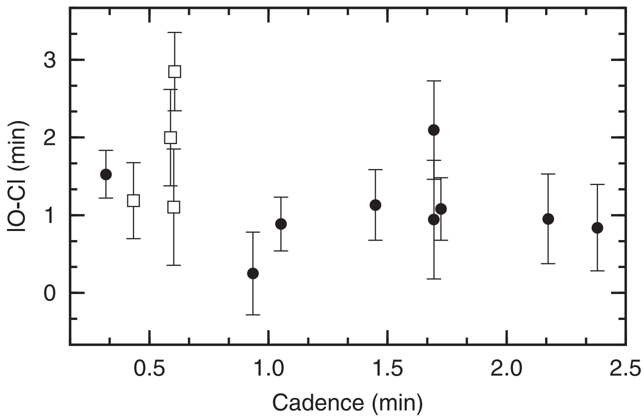

Figure 5. Absolute values of individual residuals in transit timing versus cadence. Symbols denote the same data sets as in Fig. 2. No correlation between both quantities was found.

perturber was considered for the completeness of our analysis.[1] Assuming circular orbits, the mass of the perturbing planet M_c depends on the mass of the outer, more massive transiting planet M_b and its apparent eccentricity e_b (Anglada-Escude et al. 2010). This results in $M_c \approx 0.14\,M_J$ in the WASP-10 system. Such a planet is expected to produce strong gravitational perturbations, which should be visible as the TTVs of WASP-10b. To check this scenario, we have generated synthetic O − C diagrams for WASP-10b in systems with a second planet. Parameters of the transiting planet and its host star were taken from Johnson et al. (2009). Initial circular and coplanar orbits were assumed for both planets. The perturbing planet was put in an orbit with the semimajor axis between 0.0218 and 0.0257 au (±0.0020 au away from the 2 : 1 orbital resonance). Calculations were performed using the MERCURY package (Chambers 1999) employing the Bulirsch–Stoer integrator. Simulations covered 270 periods of WASP-10b (i.e. the time-span covered by observations). No configuration was found to reproduce periodicity close to $P_1^{\rm ttv}$ and $P_2^{\rm ttv}$. The procedure was repeated for the inner 3 : 1 and 3 : 2 MMRs but these cases also brought negative results.

To search for configurations with an outer perturber reproducing $P_1^{\rm ttv}$ and $P_2^{\rm ttv}$, synthetic O − C diagrams were generated with the PTMET code, which is based on perturbation theory (Nesvorný & Morbidelli 2008; Nesvorný 2009). Both planets were put in initial circular orbits. The semimajor axis a_c of the perturber varied between 0.0500 and 0.3000 au in steps of 0.0001 and 0.0002 au for $a_c \le 0.1$ and $a_c > 0.1$ au, respectively. The amplitude of the TTV signal scales nearly linearly with the perturber's mass (Nesvorný & Morbidelli 2008). Thus, M_c was fixed and set equal to $0.3\,M_J$ for the preliminary identification. Each simulation covered 270 periods of WASP-10b. Periodic signals reproducing $P_1^{\rm ttv}$ and $P_2^{\rm ttv}$ were identified close to 5 : 3 and 5 : 2 MMRs for perturber masses of ∼0.1 and ∼$0.5\,M_J$, respectively.

To refine the parameters of a perturbing body, the synthetic O − C diagrams were calculated with the MERCURY code and the Bulirsch–Stoer integrator. The initial parameters of planet c were taken from previous simulations and then refined with the mass varying in steps of $0.05\,M_J$. Each simulation covered 31 000 d (i.e. ∼10 000 periods of WASP-10b). The synthetic O − C diagrams were directly fitted

[1] We do not analyse the scenario with an exomoon orbiting WASP-10b because no transit duration variation, predicted by Kipping (2009), was detected in our data.

Table 4. Outer-perturber solutions that reproduce the observed O − C variation. $P^{\rm ttv}$ indicates which periodicity in the O − C diagram ($P_1^{\rm ttv}$ or $P_2^{\rm ttv}$) is reproduced by a solution, $a_{\rm c}$ denotes the semimajor axis of the perturbing planet, $M_{\rm c}$ is its mass, $P_{\rm c}$ is its orbital period, $K_{\rm c}$ is the expected semi-amplitude of the RV variation and $\chi^2_{\rm red}$ is the lowest value of reduced chi-square for direct model fitting.

No.	$P^{\rm ttv}$	$a_{\rm c}$ (au)	$M_{\rm c}$ ($M_{\rm J}$)	$P_{\rm c}$ (d)	$K_{\rm c}$ (m s^{-1})	$\chi^2_{\rm red}$
1	1	0.0536	0.10	5.2293	14.2	1.5
2	2	0.0539	0.10	5.2647	14.1	2.5
3	2	0.0682	0.55	7.4962	69.1	2.8
4	1	0.0686	0.55	7.5677	68.9	2.8

to observed data by shifting along the time axis and adjusting to the time-span covered by observations. The best-fitting solutions are given in Table 4. The chi-square test favours solution 1, which reproduces $P_1^{\rm ttv}$ with minimal $\chi^2_{\rm red} = 1.5$. This value is significantly smaller than $\chi^2_{\rm red}$ obtained in an analogous way for the remaining configurations. The O − C diagram with solution 1 is presented in Fig. 6, where the residuals are also plotted.

5 SPECTROSCOPIC REANALYSIS AND STELLAR ACTIVITY

To reassess the possible solutions, we have reanalysed the radial-velocity (RV) data published by Christian et al. (2009). We used the SYSTEMIC CONSOLE software (Meschiari et al. 2009). The host star is known to be variable because of stellar rotation and star-spots (Smith et al. 2009). It has been shown that this effect may generate RV variations up to a few hundred m s^{-1} (Hatzes 2002) and mimic a planetary companion on a Keplerian orbit (Desort et al. 2007). We have reanalysed the RV data assuming that WASP-10b has a circular orbit. This has resulted in a best-fitting model with $\chi^2_{\rm red} = 3.9$ and rms = 49.6 m s^{-1}. The periodogram of the residuals (Fig. 7) reveals a periodicity of ∼11.84 d, a value close to the period of stellar rotation $P_{\rm rot} = 11.91 \pm 0.05$ d determined by Smith et al. (2009). The fitting procedure was repeated with an additional sinusoid signal of period $P_{\rm rot}$ and a floating phase and amplitude. The eccentricity of WASP-10b, $e_{\rm b}$, was also allowed to vary. This resulted in a significantly improved model with $\chi^2_{\rm red} = 2.5$ and rms = 31.4 m s^{-1}. The eccentricity was found to be $e_{\rm b} = 0.013 \pm 0.063$ and it is statistically indistinguishable from zero. Therefore, we adopted $e_{\rm b} = 0.0$ in further analysis. This result is not surprising as tidal interactions with the host star are expected to circularize the orbit of the planet (Zahn 1977).

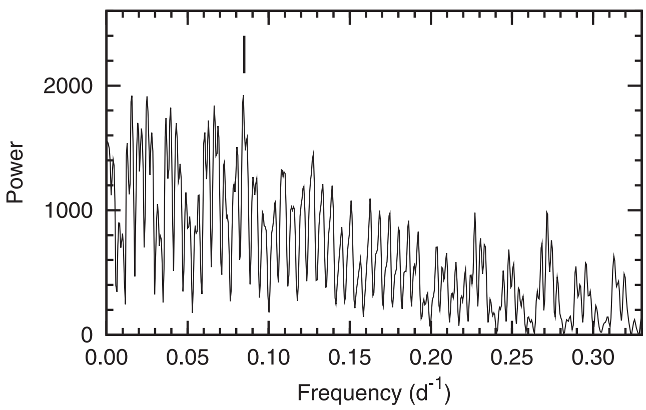

Figure 7. The Lomb–Scargle periodogram for the RV residuals after removing the transiting planet in a circular orbit. A peak corresponding to the stellar rotation is marked.

To check whether the perturbing planet may be hidden in the RV residuals of the model composed of planet b and star-spots, a second planet with physical and orbital parameters as in solutions 1–4 was put into the system. A circular Keplerian orbit of the second planet and coplanarity were assumed for simplicity. We note that only solutions 1 and 2 significantly decrease the rms of the RV model to 24.7 and 22.5 m s^{-1}, respectively. Combining the results of the TTV and RV analyses, we have found solution 1 the most likely. The RV curves are plotted in Fig. 8 for individual components (i.e. WASP-10b, WASP-10c and the star-spot effect).

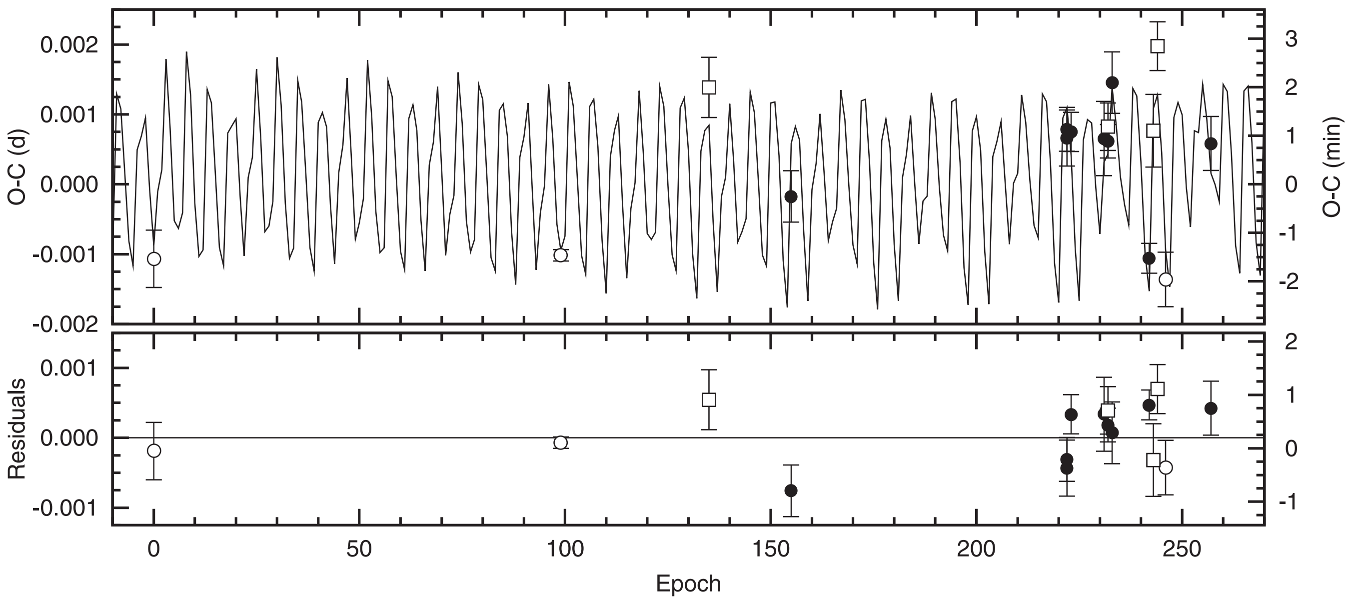

Figure 6. The O − C diagram for WASP-10b with the best-fitting model (solution 1 in Table 4). The mass of the perturber is 0.10 M$_{\rm J}$ and its orbital period is ∼5.23 d. Symbols are the same as in Fig. 2. Residuals are plotted in the bottom panel.

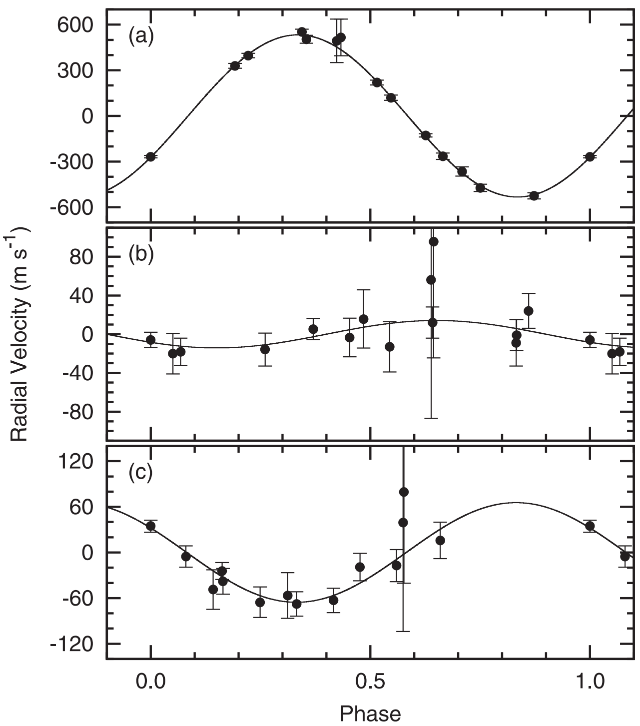

Figure 8. The RV curves after removing the remaining two components for (a) WASP-10b, (b) WASP-10c and (c) the star-spot effect. Data have been taken from Christian et al. (2009). Two points with large error bars were obtained in poor weather conditions and may exhibit systematic errors as a result of scattered moonlight (see, for example, Latham et al. 2010).

The RV semi-amplitude generated by stellar rotation was found to be $\sim$65 m s^{-1}. RV observations by Christian et al. (2009) span from 2007 August to 2008 February and are partially covered by photometric observations from the SuperWASP survey (Pollacco et al. 2006). Smith et al. (2009) determined the amplitude of photometric variation in the 2004 and 2006 seasons only. To find this variation in the 2007 season and to verify determinations from Smith et al. (2009), the analysis of variance method (ANOVA; Schwarzenberg-Czerny 1996) was applied to the WASP-10 light curve, divided into individual seasons. A periodic signal was identified. Then, a sinusoid was fitted to the phased light curve to determine the amplitude. We determined peak-to-peak amplitudes of 20.8 $\pm$ 1.3, 10.4 $\pm$ 1.0 and 8.5 $\pm$ 0.9 mmag for the 2004, 2006 and 2007 seasons, respectively. Our values are similar to the results of Smith et al. (2009), who reported 20.2 and 12.6 mmag for 2004 and 2006, respectively. Desort et al. (2007) have shown that for a G2 V-type star with $v \sin i = 7$ km s^{-1} and a photometric amplitude of 1 per cent (parameters close to those of WASP-10), a spot may produce RV variations with the semi-amplitude of $\sim$70 m s^{-1}. This estimation is consistent with the value determined by us from the RV model analysis.

Stellar spots may affect the transit depth (e.g. Czesla et al. 2009). In our data, we have found that transit depth variation is smaller than the level of 3σ for individual transits, which is thus insignificant. If stellar spots are located along a planet's path projected on to a stellar disc, the shape of the transit may be deformed. This effect may have an influence on determining mid-transit times and may result in a spurious periodic TTV signal (e.g. Alonso et al. 2009). Visual inspection of the photometric residuals (Fig. 1) does not reveal features that could be related to stellar inhomogeneities rather than to red noise. In particular, there are no deviations visible in the light-curve residuals during ingress or egress. Such deformations caused by occulting spots located close to the limb of a stellar disc are expected to generate significant TTV amplitude, even greater than a minute (Miller-Ricci et al. 2008). Furthermore, no peak close to the rotational period of the star was found in the periodogram of the O − C diagram (Fig. 3) and $f_1^{\rm ttv}$ is not an alias of the rotational frequency of the host star (Alonso et al. 2009).

The proposed model of the WASP-10 system (solution 1) was found to be dynamically stable. Simulations were performed with the SYSTEMIC CONSOLE, employing the Bulirsch–Stoer integrator, and covered 10^6 yr with a maximal time-step of 10^{-4} yr. The eccentricity of WASP-10b was found to be close to zero, while the eccentricity of WASP-10c did not exceed 0.05 with a median value of 0.024.

6 AGE OF THE SYSTEM

Given the relatively short rotation period of $\sim$12 d of WASP-10, gyrochronology (Barnes 2007) can roughly yield the age of the star. For a K5 dwarf with $(B - V) = 1.15$ mag (Schmidt-Kaler 1982), we obtain 270 $\pm$ 80 Myr only, suggesting that the star (and the planetary system) is quite young. Christian et al. (2009) estimated the rotational age to be between 600 Myr and 1 Gyr, by comparing the spin period of WASP-10 to stars in Hyades (Terndrup et al. 2000). However, we must note that, according to figs 7 and 8 in Terndrup et al. (2000), there are also Pleiades members of spectral type around K5 (like WASP-10) with $v \sin i$ around 6 km s^{-1} or lower (like WASP-10; Christian et al. 2009). This method shows that it is possible for WASP-10 to have a Pleiades-like young age or an age intermediate between Pleiades and Hyades.

To confirm the relative young age of WASP-10, we have investigated its kinematic properties. The proper motion of WASP-10 is $(\mu_\alpha \cos\delta, \mu_\delta) = (21.4 \pm 2.0, -28.9 \pm 1.0)$ mas yr^{-1} (Zacharias et al. 2003) and its RV is -11.44 ± 0.03 km s^{-1} (Christian et al. 2009), yielding a heliocentric velocity of $(U, V, W) = (-0.3 \pm 0.9, -17.3 \pm 1.7, -8.1 \pm 3.2)$ km s^{-1}. First, we compared the star's spatial velocity with those of known nearby moving groups, including the Pleiades and Hyades (Antoja et al. 2008, e.g. their fig. 5 and table 3; Zhao, Zhao & Chen 2009, e.g. their fig. 2 and table 1). We have found that WASP-10 cannot be associated with any of the moving groups. In fact, it lies in an area in the U–V plane where the star density is low. This may indicate that this star was either formed in isolation (very rare) or was ejected from its parent association.

If WASP-10 was ejected recently, then it might be possible to identify its parent cluster. As stars are ejected most likely soon after cluster formation – as a result of a supernova event in a binary system (e.g. Blaauw 1961) or via dynamical interactions in a dense cluster (e.g. Poveda, Ruiz & Allen 1967) – the age of WASP-10 should be its kinematic age (i.e. it left its parent cluster some hundred Myr ago. For such a long time, it is hardly possible to reconstruct the past trajectory of the system as well as the past trajectory for a potential parent cluster because both the star and the cluster have experienced a complete cycle (or even more) around the Galactic Centre. Considering a time-span up to 1 Gyr, even periodic appearances of close encounters between the star and a cluster could occur. Moreover, it is not unlikely that WASP-10 experienced some perturbations of its path. For these reasons, the parent cluster of WASP-10 might remain unidentified if the star was ejected relatively soon after formation. If, for some reason, WASP-10 was ejected recently, finding its parent cluster could be possible. The system's peculiar spatial velocity is 10 $\pm$ 2 km s^{-1}; the heliocentric velocity was corrected for solar motion and Galactic rotation by applying the local standard of rest

Table 5. Open clusters for which close encounters with WASP-10 were found some Myr in the past. Column 1 gives the cluster designation. Columns 2 and 3 indicate the separation d between WASP-10 and the cluster centre and the radius R of the cluster. Column 4 states the time τ of the encounter (time before present) and column 5 quotes the cluster age as given in Dias et al. (2010). d was derived from three-dimensional Gaussian distributions that can explain the slope of the d distribution (see Tetzlaff et al. 2010a).

Cluster	d (pc)	R (pc)	τ (Myr)	Age (Myr)
Platais 2	0 ± 6	10	13	400
ASCC 123	0 ± 12	6	11	260

from Tetzlaff, Neuhäuser & Hohle (2010b) and a value of $V_{\odot,rot} = 225\,\mathrm{km\,s^{-1}}$. Considering a typical cluster radius of a few parsec, the parent cluster of WASP-10 can be clearly identified if the star system was ejected not earlier than some Myr ago. During 20 Myr, the star travelled about 200 pc. Taking into account the current distance to the Sun of about 100 pc and considering also previous age constraints, we selected open clusters within 300 pc from the Sun, having ages between 100 and 800 Myr (corresponding to the ages of the Pleiades and Hyades, respectively) from the Dias et al. (2010) data base for open clusters, with full kinematics available with the catalogue as well as the Hyades cluster (WEBDA;[2] Mermilliod & Paunzen 2010), 14 clusters in total. We calculated the past orbits of WASP-10 and each cluster in the Galactic potential (Harding et al. 2001) using the epicycle approximation (Lindblad 1959; Wielen 1982). Then, we performed a Monte Carlo simulation varying the distance, proper motion and RV within their confidence intervals to account for their uncertainties. The goal was to find close encounters between WASP-10 and any cluster in the past. Two clusters, for which close encounters with WASP-10 were found (within three times the cluster radius corresponding to approximately 3σ), are listed in Table 5. The cluster radius, the time of the encounter and the age of the clusters are given. If WASP-10 really originated from either Platais 2 or ASCC 123, the star is about 260–400 Myr old, in agreement with our age estimate of 270 ± 80 Myr. It is, of course, more likely that the star is ejected early in the life of a cluster. It is generally not possible to trace WASP-10 backwards reliably for the estimated age of the system.

The young age of the host star may explain the large radius of its planet, WASP-10b. The non-irradiated models by Baraffe et al. (2003), interpolated for such a young 3-$\mathrm{M_J}$ planet, result in a radius of $\sim 1.2\,\mathrm{R_J}$. Irradiation may increase the planetary radius by ~ 10 per cent, compared to non-irradiated models (Baraffe et al. 2003). An analogous procedure based on irradiated planetary models by Fortney, Marley & Barnes (2007) and Baraffe, Chabrier & Bartman (2008) also gives a radius of $\sim 1.2\,\mathrm{R_J}$ for a 300-Myr-old giant planet. This estimate is consistent with the radius of WASP-10b reported by Christian et al. (2009), Dittmann et al. (2010) and Krejcová et al. (2010).

7 CONCLUSIONS

Our investigation indicates that transit timing of WASP-10b cannot be explained by a constant period of the exoplanet. The distribution of data points in the O − C diagram reveals the existence of a periodic signal. We constructed a provisional hypothesis assuming the presence of the third body in the system. Combining the results of three-body simulations and RV measurements, the most likely explanation of the observations is given by a model with a second planet of mass of $\sim 0.1\,\mathrm{M_J}$ and orbital period of ~ 5.23 d.

A reanalysis of RV data shows that WASP-10b orbits its active host star in a circular orbit. The signature of stellar rotation was found in RV measurements. This effect was misinterpreted in previous studies as a non-zero eccentricity of the transiting planet. The second planet would generate wobbling of the host star with the semi-amplitude of $\sim 14\,\mathrm{m\,s^{-1}}$, much less than the RV variation caused by the stellar rotation. Although we managed to distill this weak signal, we emphasize that further simultaneous spectroscopic and photometric observations are needed to study the activity of WASP-10 and to verify the existence of the planet WASP-10c.

WASP-10 has been found to be a relatively young star. Assuming that this finding, which is based on stellar gyrochronology, is correct, then the observed radius of WASP-10b is consistent with theoretical models and no tidal heating is required to match its radius. If planetary gas giants form by gravitational contraction, then young planets should be larger than older ones. If the planets of WASP-10 formed at larger separation than their present location, then migration must have taken place within the young age of the star.

The existence of WASP-10c could be independently confirmed if it is a transiter. Assuming that its radius is $\sim 0.4\,\mathrm{R_J}$ (i.e. similar to exoplanets of similar mass such as HAT-P-11b Bakos et al. 2010 or Kepler-4b Borucki et al. 2010), the expected flux drop during a transit would be ~ 0.3 per cent or even greater if we consider the young age of the system. This could be observable with a large ground-based telescope.

In the proposed model, the ratio of orbital periods of the planets $P_c/P_b = 1.69$ is very close to the 5 : 3 orbital resonance. A significant fraction of known multiplanet systems are in MMRs, mainly in low-order ones. Two planets in wide orbits and trapped in a 3 : 2 MMR were found around HD 45364 by RV measurements (Correia et al. 2009). Planets in the four-planetary system around GJ 581 (Mayor et al. 2009) are very close to 5 : 2 (GJ 581b and c) and 5 : 3 (GJ 581e and b) MMRs (Papaloizou & Terquem 2010). Therefore, we conclude that the architecture of the WASP-10 system would not be completely unusual.

ACKNOWLEDGMENTS

We are grateful to the anonymous referee for remarks and for inspiring us to study the kinematic membership. We thank J. Dittmann for providing the original photometric data. We also thank G. Nowak and T. Eisenbeiss for discussions about stellar spots and gyrochronology. GM acknowledges support from the European Union in the FP6 MC ToK project MTKD-CT-2006-042514. DD acknowledges support from the project DO 02-362 of the Bulgarian Scientific Foundation. RN would like to acknowledge general support from the Deutsche Forschungsgemeinschaft (DFG). GM, RN and AN acknowledge support from the German Academic Exchange Service (DAAD) PPP–MNiSW project 50724260–2010/20011 ‘Eclipsing binaries in young clusters and planet transit time variations’. AN was also supported by the Polish Ministry of Science and Higher Education grant NN 203 510938. NT acknowledges financial support from Carl-Zeiss-Stiftung. SR and CM acknowledge support from the DFG in programmes NE 515/32-1 and SCHR 665/7-1, respectively. TK, JB and VK acknowledge support from the Marie Curie International Reintegration Grant FP7-200297, grant GA ČR GD205/08/H005, the National Scholarship Programme of the Slovak Republic and partly from VEGA 2/0078/10 and VEGA 2/0074/09. A part of this

[2] http://www.univie.ac.at/webda/webda.html

paper is the result of a Polish and Bulgarian Academies of Sciences (PAN/BAN) exchange and a joint research project 'spectral and photometric studies of variable stars'. We have used the Exoplanet Transit Data base (http://var.astro.cz/ETD) and data from the Wide Angle Search for Planets (WASP) public archive in this research. The WASP consortium comprises the University of Cambridge, Keele University, University of Leicester, The Open University, The Queen's University Belfast, St Andrews University and the Isaac Newton Group. Funding for WASP comes from the consortium universities and from the UK's Science and Technology Facilities Council.

REFERENCES

Agol E., Steffen J., Sari R., Clarkson W., 2005, MNRAS, 359, 567
Alonso R., Aigrain S., Pont F., Mazeh T., CoRoT Exoplanet Science Team, 2009, in Pont F. et al., eds, Proc. IAU Symp. 253, Transiting Planets. Kluwer, Dordrecht, p. 91
Anglada-Escude G., López-Morales M., Chambers J. E., 2010, ApJ, 709, 168
Antoja T., Figueras F., Fernández D., Torra J., 2008, A&A, 490, 135
Bakos G. Á. et al., 2010, ApJ, 710, 1724
Baraffe I., Chabrier G., Bartman T. S., Allard F., Hauschildt P. H., 2003, A&A, 402, 701
Baraffe I., Chabrier G., Bartman T. S., 2008, A&A, 482, 315
Barnes S. A., 2007, ApJ, 669, 1167
Blaauw A., 1961, Bull. Astron. Inst. Netherlands, 15, 265
Borucki W. J. et al., 2010, ApJ, 713, 126
Chambers J. E., 1999, MNRAS, 304, 793
Christian D. J. et al., 2009, MNRAS, 392, 1585
Correia A. C. M. et al., 2009, A&A, 496, 521
Czesla A., Huber K. F., Wolter U., Schröter S., Schmitt J. H. M. M., 2009, A&A, 505, 1277
Dias W. S., Alessi B. S., Moitinho A., Lepine J. R. D., 2010, Optically visible open clusters and Candidates, VizieR On-line Data Catalogue, B/ocl (originally published in 2002, A&A, 389, 871)
Dittmann J. A., Close L. M., Scuderi L. J., Morris M. D., 2010, ApJ, 717, 235
Desort M., Lagrange A.-M., Galland F., Udry S., Mayor M., 2007, A&A, 473, 983
Eastman J., Siverd R., Gaudi B. S., 2010, PASP, 122, 935
Everett M. E., Howell S. B., 2001, PASP, 113, 1428
Fortney J. J., Marley M. S., Barnes J. W., 2007, ApJ, 659, 1661
Gibson N. P. et al., 2009, ApJ, 700, 1078
Hatzes A. P., 2002, Astron. Notes, 323, 392
Harding P., Morrison H. L., Olszewski E. W., Arabadjis J., Mateo M., Dohm-Palmer R. C., Freeman K. C., Norris J. E., 2001, AJ, 122, 1397
Holman M. J., Murray N. W., 2005, Sci, 307, 1288
Johnson J. A., Winn J. N., Cabrera N. E., Carter J. A., 2009, ApJ, 692, L100
Johnson J. A., Winn J. N., Cabrera N. E., Carter J. A., 2010, ApJ, 712, L122
Kipping D. M., 2009, MNRAS, 392, 181
Kipping D. M., Bakos G. Á., 2010a, preprint (astro-ph/1004.3538)
Kipping D. M., Bakos G. Á., 2010b, preprint (astro-ph/1006.5680)
Krejcová T., Budaj J., Krushevska V., 2010, preprint (astro-ph/1003.1301)
Latham D. W. et al., 2010, ApJ, 713, L140
Lendl M., Afonso C., Koppenhoefer J., Nikolov N., Henning Th., Swain M., Greiner J., 2010, A&A, 522, 29
Lindblad B., 1959, Handbuch der Physik, Vol. 53. Springer, Berlin, p. 21
Lomb N. R., 1976, Ap&SS, 39, 447
Maciejewski G. et al., 2010, MNRAS, 407, 2625
Mandel K., Agol E., 2002, ApJ, 580, 171
Mayor M. et al., 2009, A&A, 507, 487
Mermilliod J.-C., Paunzen E., 2003, A&A, 410, 511
Meschiari S., Wolf A. S., Rivera E., Laughlin G., Vogt S., Butler P., 2009, PASP, 121, 1016
Miller-Ricci E. et al., 2008, ApJ, 682, 593
Miralda-Escudé J., 2002, ApJ, 564, 1019
Mugrauer M., Berthold T., 2010, Astron. Notes, 331, 449
Nesvorný D., Morbidelli A., 2008, ApJ, 688, 636
Nesvorný D., 2009, ApJ, 701, 1116
Niedzielski A., Maciejewski G., Czart K., 2003, Acta Astron., 53, 281
Papaloizou J. C. B., Terquem C., 2010, MNRAS, 405, 573
Poddaný S., Brát L., Pejcha O., 2010, New Astron., 15, 297
Pollacco D. et al., 2006, PASP, 118, 1407
Poveda A., Ruiz J., Allen C., 1967, Boletin de los Observatorios Tonantzintla y Tacubaya, 4, 86
Scargle J. D., 1982, ApJ, 263, 835
Schmidt-Kaler T., 1982, in Schaifers K., Voigt H. H., Landolt H., eds, Landolt-Bornstein: Numerical Data and Functional Relationships in Science and Technology. Springer, Berlin, p. 19
Smith A. M. S. et al., 2009, MNRAS, 398, 1827
Schneider J., 2004, in Favata F., Aigrain S., Wilson A., eds, Second Eddington Workshop: Stellar Structure and Habitable Planet Finding, ESA SP-538. ESA Publications, Noordwijk, p. 407
Steffen J. H., Gaudi B. S., Ford E. B., Agol E., Holman M. J., 2007, preprint (astro-ph/0704.0632)
Schwarzenberg-Czerny A., 1996, ApJ, 460, 107
Terndrup D. M., Stauffer J. R., Pinsonneault M. H., Sills A., Yuan Y., Jones B. F., Fischer D., Krishnamurthi A., 2000, AJ, 119, 1303
Tetzlaff N., Neuhäuser R., Hohle M. M., Maciejewski G., 2010a, MNRAS, 402, 2369
Tetzlaff N., Neuhäuser R., Hohle M. M., 2010b, MNRAS, in press (doi:10.1111/j.1365-2966.2010.17434.x)
Van Hamme W., 1993, AJ, 106, 2096
Wielen R., 1982, in Landolt-Börnstein, Group VI/2c, Astronomy and Astrophysics. Springer, Berlin, p. 208
Zacharias N., Urban S. E., Zacharias M. I., Wycoff G. L., Hall D. M., Germain M. E., Holdenried E. R., Winter L., 2003, The 2nd US Naval Observatory CCD Astrograph Catalog (UCAC2)
Zahn J.-P., 1977, A&A, 57, 283
Zhao J., Zhao G., Chen Y., 2009, ApJ, 692, 113

This paper has been typeset from a TEX/LATEX file prepared by the author.

PASJ: Publ. Astron. Soc. Japan **63**, 1011–1021, 2011 October 25

Near-Ultraviolet and Visible Spectroscopy of HAYABUSA Spacecraft Re-Entry

Shinsuke ABE
National Central University, 300 Jhongda Road, Jhongli, Taoyuan 32001, Taiwan
shinsuke.avell@gmail.com
Kazuhisa FUJITA
Japan Aerospace Exploration Agency, 7-44-1 Jindaiji-higashi-machi, Chofu, Tokyo 182-8522
fujita.kazuhisa@jaxa.jp
Yoshihiro KAKINAMI
Institute of Seismology and Volcanology, Hokkaido University, Kita 10 Nishi 8, Kita-ku, Sapporo 060-0810
kakinami@mail.sci.hokudai.ac.jp
Ohmi IIYAMA
Osaka Science Museum, 4-2-1 Nakanoshima, Kitaku, Osaka, Osaka 530-0005
Hirohisa KUROSAKI
Japan Aerospace Exploration Agency, 7-44-1 Jindaiji-higashi-machi, Chofu, Tokyo 182-8522
Michael A. SHOEMAKER
Kyushu University, 744 Motooka, Nishi-ku, Fukuoka 819-0395
Yasuo SHIBA and Masayoshi UEDA
Nippon Meteor Society, 43-2 Asuka Habikino Osaka 583-0842
and
Masaharu SUZUKI
GOTO Inc., 4-16 Yazaki-cho, Fuchu, Tokyo 183-8530

(Received 2011 June 23; accepted 2011 August 28)

Abstract

HAYABUSA is the first spacecraft ever to land on and lift off from any celestial body other than the moon. The mission, which returned asteroid samples to the Earth while overcoming various technical hurdles, ended on 2010 June 13, with the planned atmospheric re-entry. In order to safely deliver the sample return capsule, the HAYABUSA spacecraft ended its 7-year journey in a brilliant "artificial fireball" over the Australian desert. Spectroscopic observation was carried out in the near-ultraviolet and visible wavelengths between 3000 Å and 7500 Å at 3–20 Å resolution. Approximately 100 atomic lines such as Fe I, Mg I, Na I, Al I, Cr I, Mn I, Ni I, Ti I, Li I, Zn I, O I, and N I were identified from the spacecraft. Exotic atoms such as Cu I, Mo I, Xe I and Hg I were also detected. A strong Li I line (6708 Å) at a height of $\sim$55 km originated from the onboard Li-Ion batteries. The FeO molecule bands at a height of $\sim$63 km were probably formed in the wake of the spacecraft. The effective excitation temperature as determined from the atomic lines varied from 4500 K to 6000 K. The observed number density of Fe I was about 10 times more abundant than Mg I after the spacecraft explosion. N_2^+ (1^-) bands from a shock layer and CN violet bands from the sample return capsule's ablating heat shield were dominant molecular bands in the near-ultraviolet region of 3000–4000 Å. OH(A–X) band was likely to exist around 3092 Å. A strong shock layer from the HAYABUSA spacecraft was rapidly formed at heights between 93 km and 83 km, which was confirmed by detection of N_2^+ (1^-) bands with a vibration temperature of $\sim$13000 K. Gray-body temperature of the capsule at a height of $\sim$42 km was estimated to be $\sim$2437 K which is matched to a theoretical prediction. The final message of the HAYABUSA spacecraft and its sample return capsule are discussed through our spectroscopy.

Key words: asteroid — atmospheric re-entry — Meteors, meteoroids — spectroscopy

1. Introduction

HAYABUSA, the third engineering space mission of JAXA/ISAS (Japan Aerospace eXploration Agency/Institute of Space and Astronautical Sciences) had several engineering technologies to verify in space (e.g, Kawaguchi et al. 2008). HAYABUSA was launched on 2003 May 9. On 2005 September 12, HAYABUSA arrived at the asteroid (25143) Itokawa. The mission was the first to reveal that Itokawa is a rubble-pile body rather than a single monolithic asteroid among S-class asteroids (Abe et al. 2006; Fujiwara et al. 2006). Finally, the spacecraft performed a landing on Itokawa to collect asteroid samples in 2005 November. Due to a loss of communications, HAYABUSA started an orbit transfer to return to the Earth in 2007 April. The round-trip travel between the Earth and Itokawa with the aid of ion engine propulsion was the first success of its kind in the world (Kuninaka 2008).

On 2010 June 13, the HAYABUSA spacecraft returned to the Earth with the re-entry capsule containing asteroid samples. The sample return capsule was separated at 10:51 UT, which was just 3 hours before the atmospheric re-entry. Due to the failure of all bi-propellant thrusters for orbital maneuvering,

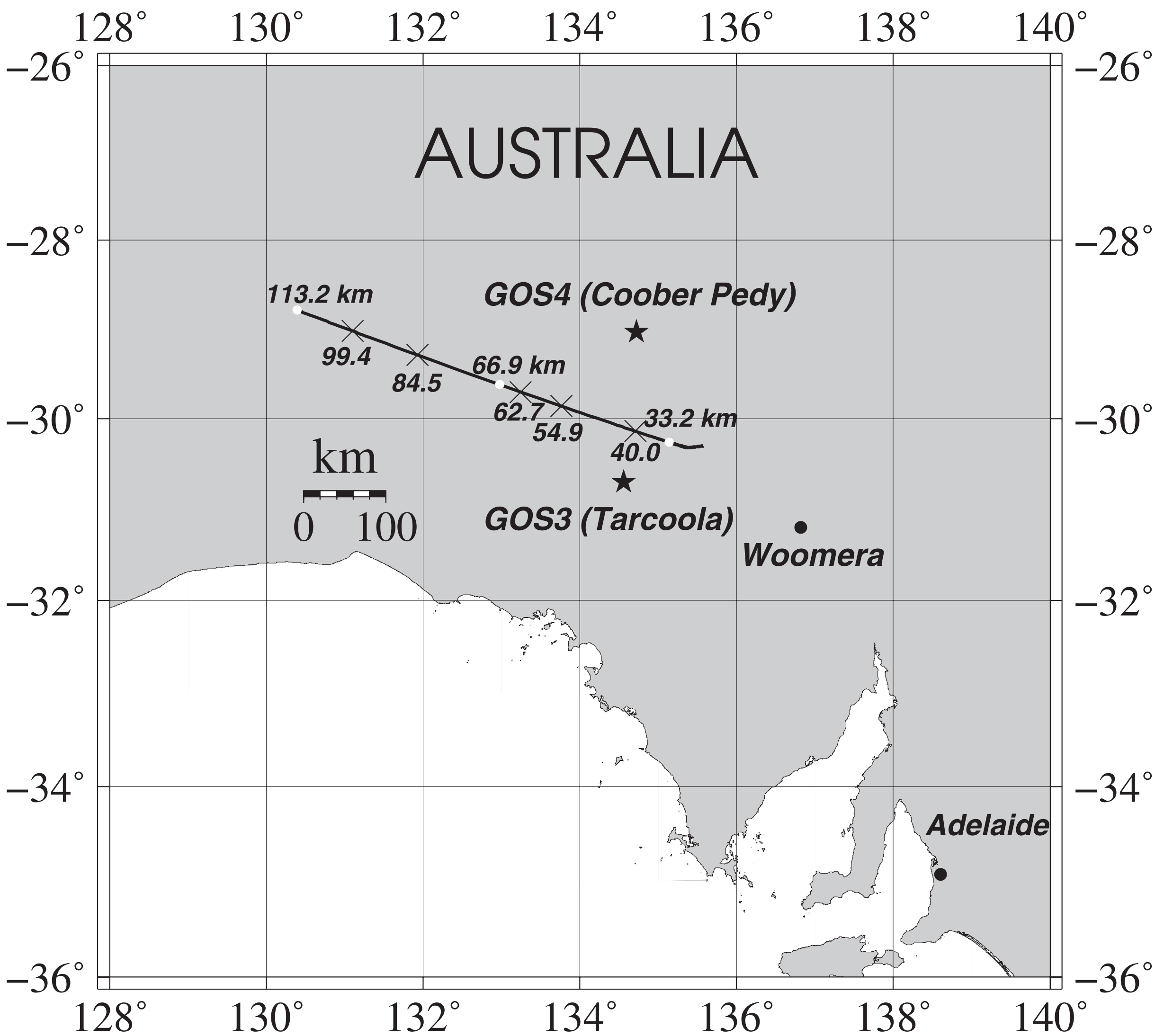

Fig. 1. HAYABUSA trajectory and observation stations in Australia. The HAYABUSA re-entry has flown over and landed on the Woomera Prohibited Area (WPA) where unauthorized people have no admittance. GOS sites were located on the border of the WPA. A thick black line shows the trajectory of sample return capsule in which white dots indicate the heights of beginning (113.2 km), maximum brightness (66.9 km) and the end (33.2 km) detected by our cameras. Several heights at which the spectra were analyzed are indicated by the X marks.

the HAYABUSA spacecraft could not escape from its Earth collision course. Though Japan had several successful experiences with re-entry capsule tests [e.g., RFT-2 (1992), OREX (1994), EXPRESS (1995), HYFREX (1996), and USERS (2003)], the HAYABUSA sample return capsule was the first Japanese re-entry opportunity that entered the Earth's atmosphere directly from an interplanetary transfer orbit with a velocity over $12\,\mathrm{km\,s^{-1}}$. The HAYABUSA sample return capsule and the spacecraft entered the atmosphere at 13:51 UT. The HAYABUSA spacecraft disintegrated in the atmosphere, and the capsule flew nominally and landed approximately 500 m from its targeted landing point.

Spectroscopy of the HAYABUSA re-entry was a golden opportunity to understand (i) the atmospheric influence upon Earth impactors such as meteors, meteorites and meter-sized mini-asteroids, because for such natural bodies the original material, mass, and shape are all unknown (e.g., Ceplecha et al. 1996; Abe 2009); for HAYABUSA, not only these parameters but also the re-entry trajectory were under perfect control, (ii) the hypervelocity impact of large objects that are difficult to reproduce in laboratory experiments, and (iii) the flight environment of re-entry capsules for the utilization of future Japanese sample return missions.

2. Observation and Data Reduction

A ground observation team consisting of 16 members was organized by JAXA (Fujita et al. 2011a). Triangulation observations were coordinated between GOS3 station at Tarcoola (134.55858 E, −30.699114 S, 0.152 km altitude) and GOS4 station at Coober Pedy (134.71819 E, −29.03392 S, 0.224 km altitude) in southern Australia (figure 1). The National Astronomical Observatory of Japan (NAOJ) also made a HAYABUSA observing expedition at Coober Pedy

Table 1. Specifications of spectroscopic and imaging cameras.

Name	Color	Lens	Spectrograph	FOV (H × V)	Pixels	Frame rate
VIS-HDTV	Color	80 mm/F5.6	300/mm*	25°× 17°	1920 × 1080	30 fps
UV-II	B/W	30 mm/F1.2	600/mm†	23°× 13°	720 × 480	29.97 (NTSC)
NCR-550a‡	Color	4.6–60 mm	—	90°–8° diagonal	800 × 412	29.97 (NTSC)
Nikon D300s‡	Color	18–200 mm	—	10° × 7°	1280 × 720	24 fps
WAT-100N§	B/W	25 mm/F0.95	—	15° × 11°	768 × 494	29.97 (NTSC)

* Spectrum resolution = 12 Å (1st order), 6 Å (2nd order), and 3 Å (3rd order).
† Spectrum resolution = 20 Å.
‡ Video data was published on the JAXA digital archive.[1]
§ Video data is used for the trajectory estimation of fragmented HAYABUSA (Shoemaker et al. 2011).

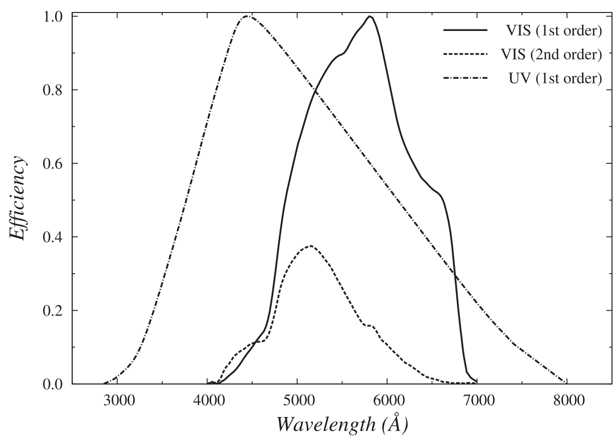

Fig. 2. Efficiency curves of the VIS-HDTV and UV-II spectroscopic cameras. The 1st order spectra are normalized 1.0 at their maximum. The efficiency of the 2nd order of the VIS-HDTV is relative to its 1st order spectrum. The maximum efficiency of the UV-II and the VIS-HDTV's 1st and 2nd orders are 4440, 5804, and 5160 Å, respectively.

(see Watanabe et al. 2011).

Spectroscopy was carried out using two spectrograph systems: a VISual HDTV camera (VIS-HDTV) and an UltraViolet Image-Intensified TV camera (UV-II). An EOS 5D MarkII with lens (f = 80 mm, $F/5.6$) was applied to the VIS-HDTV system equipped with a transmission grating (300 grooves per mm, blazed at 6100 Å). The UV-II system consisted of a UV lens (f = 30 mm, $F/1.2$), a UV image intensifier (ϕ 18-mm photo-cathode: S20), two relay lenses (f = 50 mm, $F/1.4$), and a SONY HDTV Handycam. The UV-II system was equipped with a reflection grating (600 grooves per mm, blazed at 3300 Å). The VIS-HDTV camera obtained the 0th, 1st, and 2nd order spectra in 4000–7000 Å, and the UV-II camera observed the 1st order spectrum in 3000–7500 Å (figure 2). A part of the 2nd order spectrum of the VIS-HDTV was overlapped with the 3rd order spectrum. The specifications of the spectroscopic and imaging cameras are summarized in table 1.

The tracking observations at GOS3 were carried out by S. Abe using co-aligned dual imaging cameras (Nikon D300s and WAT-100N) and the UV-II spectrograph which were mounted on the same hydraulic tripod. Tracking was performed while watching a video monitor taken by WAT-100N (WATEC Inc.). The high-sensitivity television camera, NCR-550a (NEC Corp. & GOTO Inc.), equipped with three 1/2 type EM-CCD (Electron Multiplying CCD) image sensors, was also used to observe the zoomed color TV operated by O. Iiyama. At GOS4, the VIS-HDTV spectroscopy was achieved by Y. Kakinami adopting the same tracking method. Meanwhile, 6 × 7 photographic cameras using a fish-eye lens with a rotating shutter were operated simultaneously at GOS3 by S. Abe and at GOS4 by Y. Kakinami and Y. Shiba. In this paper, the most reliable trajectory (time, height, and velocity) determined by our photographic observation is referred (Borovička et al. 2011). Note that the trajectories derived from different cameras (Shoemaker et al. 2011; Ueda et al. 2011) were comparable to our result and the JAXA prediction. Tracking the capsule was difficult because although there were predictions for the time and point in the sky when the objects would first appear, the capsule moved faster and tracking became more difficult later in flight. In order to track the fast moving HAYABUSA trajectory smoothly, observers were sufficiently trained by using an imitation moving laser pointer on the planetarium dome that was arranged by M. Suzuki. These instrument pointing exercises allowed successful tracking of the HAYABUSA emissions (Abe 2010).

Background and stars were removed by subtracting a median frame shortly before or after the spectrum. After flat-fielding and averaging of the HAYABUSA spectrum, the wavelength was examined carefully using well-known strong atomic lines such as Mg I (5178 Å) and Na I (5893 Å). The pixels were converted to wavelengths with a simple linear function. After more known lines were identified, the wavelength was precisely determined again with regard to the synthetic atomic lines that were convolved by the spectrum resolution (Borovička 1993). On the other, spectra of Venus and Canopus (α Car) were used to calculate the efficiency curves for the VIS-HDTV and UV-II cameras, respectively (figure 2). Table 2 gives trajectories of the HAYABUSA spacecraft (H > 50 km) and the capsule (H < 50 km) compared with detections by our imaging and spectroscopic cameras. The VIS-HDTV spectroscopy was aimed at the HAYABUSA spacecraft (50 < H < 85 km), whereas the UV-II spectroscopy was intended to observe the faint spectrum at the beginning height (H > 80 km) and the capsule spectrum near the terminal height (H < 50 km). Here, we selected some of the best data among a series of spectrum (see figure 12 in Fujita et al. 2011a).

[1] ⟨http://jda.jaxa.jp⟩.

Table 2. Beginning and terminating of light detected by each camera and corresponding trajectory of HAYABUSA and the capsule.

Time UT	Height* (km)	Velocity† ($km\ s^{-1}$)	Event	Cameras (SPectrum or IMage)
13:51:50.1	113.21	12.05	Beginning	WAT-100N (IM)
13:51:53.5	106.17	12.06	Beginning	NCR-550a (IM)
13:51:54.3	104.53	12.06	Beginning	UV-II (SP)
13:51:57.8	97.46	12.06	Beginning	D300s (IM)
13:52:03.9	85.47	12.07	Beginning	VIS-HDTV (SP)
13:52:12.9	68.63	11.95	Explosion	all
13:52:13.6	67.38	11.90	Explosion	all
13:52:13.9	66.85	11.88	Maximum	all
13:52:17.1	61.39	11.57	Explosion	all
13:52:17.2	61.22	11.55	Explosion	all
13:52:19.5	57.53	11.18	Explosion	all
13:52:19.9	56.90	11.10	Explosion	all
13:52:22.7	52.79	10.44	Ending	VIS-HDTV (SP)
13:52:40.2	36.81	3.38	Ending	UV-II (SP)
13:52:42.1	35.98	2.94	Ending	D300s (IM)
13:52:47.4	34.09	2.08	Ending	NCR550a (IM)
13:52:50.6	33.17	1.74	Ending	WAT-100N (IM)

* The trajectory of HAYABUSA and the capsule was obtained by our observation (Borovička et al. 2011).

† The velocity relative to the Earth's center is given (the velocity relative to the surface is about $0.37\ km\ s^{-1}$ lower because of Earth's rotation).

3. Results

3.1. *VIS-HDTV Spectrum in 4000–7000 Å*

Figure 3 shows the VIS-HDTV spectra of the HAYABUSA spacecraft at heights of 84.5, 62.7, and 54.9 km. The estimated absolute magnitude at each height were −7, −12, and −8, respectively. Note that the absolute magnitude is defined as the magnitude an object would have as if placed at the observer's zenith at a height of 100 km. Corresponding color images taken with the NCR-550a and the Nikon D300s were compared. These spectra were not calibrated by the sensitivity curve so that they could be compared with the color as seen by an average human eye as well as with the color images. Identified atoms were indicated on the top of each emission. After the spectral response calibration, the 1st and the 2nd order spectra were obtained (figure 4). Most of the 1st order spectra of the VIS-HDTV and the UV-II during the explosion phase were saturated in their intensities. The 2nd order spectra of the VIS-HDTV, fortunately, were free from saturation and were worthy of close inspection. The absolute flux was estimated using the unsaturated 2nd order spectrum when the maximum magnitude of −12.6 was reached at a height of 66.9 km (Borovička et al. 2011). Identified atoms and molecules using the VIS-HDTV are summarized in table 3.

At a height of 84.5 km, Mg I (5173 and 5184 Å) and Na I (5890 and 5896 Å) emissions were dominant. During the explosion phase, numerous strong emissions were seen in the visible spectrum. Some exotic lines were detected, such as Cu I (5700 and 5782 Å), Mo I (5506 and 5533 Å), Xe I (4624 and 4671 Å), and Hg I (4358 and 5461 Å), which typically could not be seen in a natural meteor spectrum. Note that the "duralumin" of HAYABUSA's structure contains Al, Cu, Mg, and Mn. MoS_2 (molybdenum disulfide) was used as a lubricant in many places of the spacecraft. HAYABUSA's propulsion system operated by accelerating ionized Xe (xenon gas) through a strong electric field, and expelling it at high speed. Of the total 66 kg of xenon gas that was carried on HAYABUSA, there remained about 10 kg at the time of the Earth return. Xe I at 4671 Å was clearly seen in the spectrum (H = 62.7 km) after the main explosion, and disappeared at a lower height (H = 54.9 km). The strong Li I lines (6104 and 6708 Å) at a height of 54.9 km were detected from the spectrum of the HAYABUSA spacecraft. It is most likely that the observed Li I emissions originated from the Li-Ion batteries consisting of 11 prismatic cells with $\sim$6.3 kg total mass onboard the HAYABUSA spacecraft. A series of strong Zn I lines (4680, 4722, and 4811 Å) were detected that was probably originated from the spacecraft. Similar Zn I lines have been seen in a "paint" spectrum of the NASA Stardust capsule due to paint that was applied to the surface of the capsule (Abe et al. 2007a; Jenniskens 2010a).

The continuum spectral profile around 6000 Å at a height of 62.7 km is very similar to published laboratory measurements of the "orange bands" of FeO which have been detected by Jenniskens (2000) and Abe et al. (2005a) in Leonid meteor persistent trains. FeO is the most common molecule observed in the spectrum of bright and relatively slow fireballs (Ceplecha 1971; Borovička 1993). The FeO can be formed during the cooling phase when the temperature drops to 2500–2000 K (Berezhnoy & Borovička 2010), thus it may be emitted in the wake of the HAYABUSA spacecraft. Recently, FeO has been discovered in a terrestrial night airglow spectrum observed with the Odin spacecraft (Evans et al. 2010).

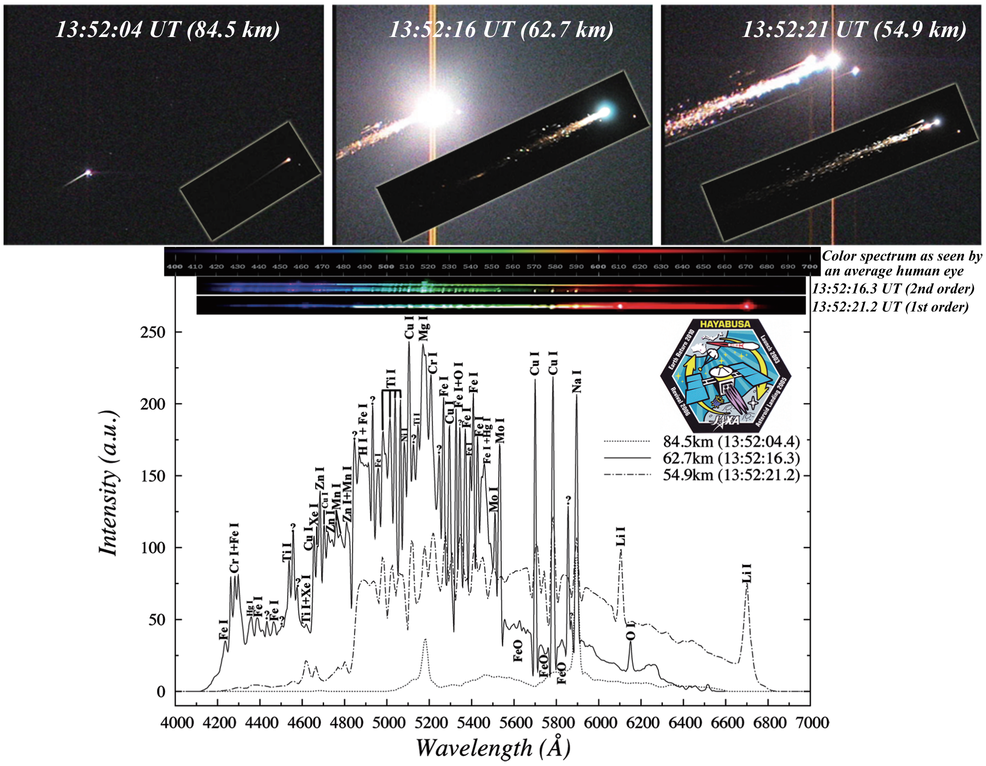

Fig. 3. Visible spectrum of HAYABUSA spacecraft compared with color images taken by the NCR-550a (NEC Corp. & GOTO Inc.) forming a background and the Nikon D300s in a rectangular box. Identified atomic lines are indicated atop each emission. '?' marks are unknown (unidentified) lines. A color spectrum as seen by an average human eye is shown (Nick Spiker).[2]

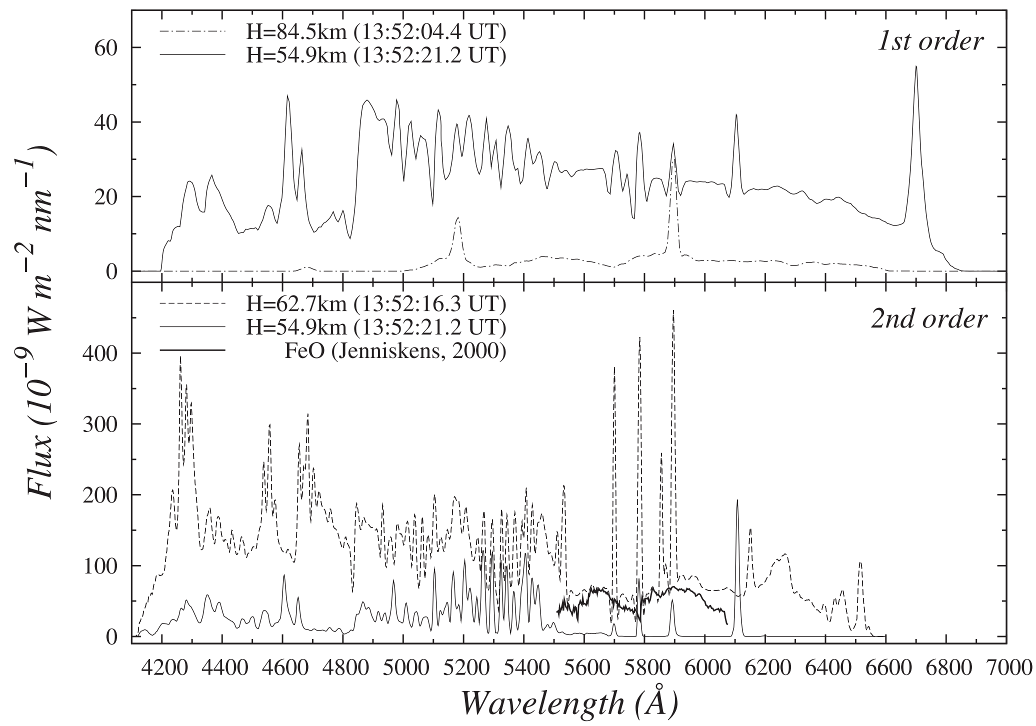

Fig. 4. VIS-HDTV spectra of the HAYABUSA spacecraft in the 1st (upper panel) and in the 2nd (lower panel) order after spectral sensitivity calibration. The 2nd order spectrum was not obtained for H = 84.5 km due to its faintness, while the 1st order spectrum was mostly saturated for H = 62.7 km. The spectral match with the laboratory spectrum of the FeO orange bands (Jenniskens 2000) is superposed. Since the 3rd order is clearly mixed with the 2nd order spectrum below ~6600 Å, the 3rd order spectrum is omitted.

[2] ⟨http://www.repairfaq.org/sam/repspec/⟩.

Table 3. Identification of atoms and molecules in 4200–6800 Å.*

Observed line		Identified line			Observed line		Identified line		
Wavelength (Å)	Intensity	Wavelength (Å)	Element	Multiplet	Wavelength (Å)	Intensity	Wavelength (Å)	Element	Multiplet
4234	10.9	4234	Fe I	152	5081	5.8	5081	Ni I	4
4236	11.0	4236	Fe I	52	5016	9.4	5106	Cu I	1
4256	12.2	4254	Cr I	1	5125	2.7		?	—
4262	29.3	4261	Fe I	152	5146	3.2	5147	Ti I	1
4282	24.7	4272	Fe I	42	5170	8.2	5167	Mg I	2
	24.7	4275	Cr I	1		8.2	5167	Fe I	37
	24.7	4290	Cr I	1		8.2	5173	Mg I	2
4300	19.5	4308	Fe I	42	5184	7.8	5184	Mg I	2
4358	6.1	4358	Hg I	1	5208	7.4	5205	Cr I	7
4388	5.1	4384	Fe I	41		7.4	5205	Fe I	1
4408	2.0	4405	Fe I	41		7.4	5206	Cr I	7
4414	2.0	4415	Fe I	41		7.4	5208	Cr I	7
4434	3.4		?	—	5246	4.6		?	—
4466	2.8	4467	Fe I	350	5268	10.2	5270	Fe I	15
4502	1.6		?	—	5296	11.3	5293	Cu I	1
4538	13.8	4533	Ti I	42	5326	13.8	5328	Fe I	15
4558	19.2		?	—		13.8	5331	O I	12
4575	8.6		?	—	5344	12.2		?	—
4618	1.8	4617	Ti I	4	5370	11.1	5371	Fe I	15
4622	1.6	4624	Xe I	1	5378	3.5	5383	Fe I	1146
4656	14.6	4651	Cu I	1	5394	8.5	5393	Fe I	553
4670	10.2	4671	Xe I	1	5397	4.0	5397	Fe I	15
4684	16.0	4680	Zn I	1	5407	12.6	5404	Fe I	1165
4704	7.3	4705	Cu I	1		12.6	5406	Fe I	15
4724	4.0	4722	Zn I	1	5429	10.0	5430	Fe I	15
4540	1.7		?	—	5448	7.6	5447	Fe I	15
4760	2.6	4754	Mn I	16	5460	8.9	5456	Fe I	15
4762	2.2	4762	Mn I	21		8.9	5461	Hg I	1
4782	1.6	4783	Mn I	16	5488	3.6		?	—
4811	3.6	4811	Zn I	1	5510	6.7	5506	Mo I	1
4822	4.3	4824	Mn I	16	5534	15.5	5533	Mo I	1
4846	12.0		?	—	5702	32.5	5700	Cu I	1
4868	9.3	4861	H I	20	5784	39.8	5782	Cu I	1
4872	9.0	4872	Fe I	318	5856	21.0		?	—
4898	7.0	4891	Fe I	318	5870	4.9		?	—
4912	6.4		?	—	5896	40.2	5890	Na I	1
4932	9.2		?	—		40.2	5896	Na I	1
4958	4.3	4957	Fe I	318	6104	2.2	6104	Li I	2
4982	6.1	4982	Ti I	38	6152	10.0	6156	O I	10
4992	4.7	4991	Ti I	38	6702	4.7	6708	Li I	1
5014	6.4	5014	Ti I	38	5500–6100		FeO	—	
5040	8.6		?	—					

* All atoms except Li I in the table were analyzed from the spacecraft spectrum at a height of 62.7 km (13:52:16 UT). Li I lines resulted from the spacecraft spectrum at a height of 54.9 km (13:52:21 UT). Identified atoms are indicated in the visual spectrum (figure 3). The values for intensities were measured in relative units.

3.2. *UV-II Spectrum in 3000–4000 Å*

Figure 5 shows a series of the UV-II spectra for the spacecraft-capsule mixed at heights between 99.4–82.9 km and for the capsule at heights between 44.7–39.6 km before spectral sensitivity calibration. N_2^+ (1^-) at 3908 Å was a significant band head during the beginning phase, and during the later phase the near-ultraviolet region was filled with N_2^+ (1^-) bands whose band heads were 3880 and 3533 Å. Figure 6 shows the UV-II spectra at heights of 92.5 km and 82.9 km after sensitivity calibration. A scaled 3rd order spectrum obtained using the VIS-HDTV is superposed on this figure. The model spectrum of N_2^+ (1^-) ($B^2\Sigma_u^+ \rightarrow X^2\Sigma_g^+$) system with four bands heads (3300, 3500, 3900, and 4200 Å) caused by different vibrational states were carried out varying the temperatures from 1000 K to 20000 K using the SPRADIAN numerical code (Fujita & Abe 1997). Assuming that a rotation temperature equals to a vibration temperature, N_2^+ (1^-) bands convolved by the spectral resolution (20 Å) were examined (figure 6). The CN violet bands ($B^2\Sigma^+ \rightarrow X^2\Sigma^+$) and a possible contribution of OH band ($A^2\Sigma^+ \rightarrow X^2\Pi$) were also demonstrated

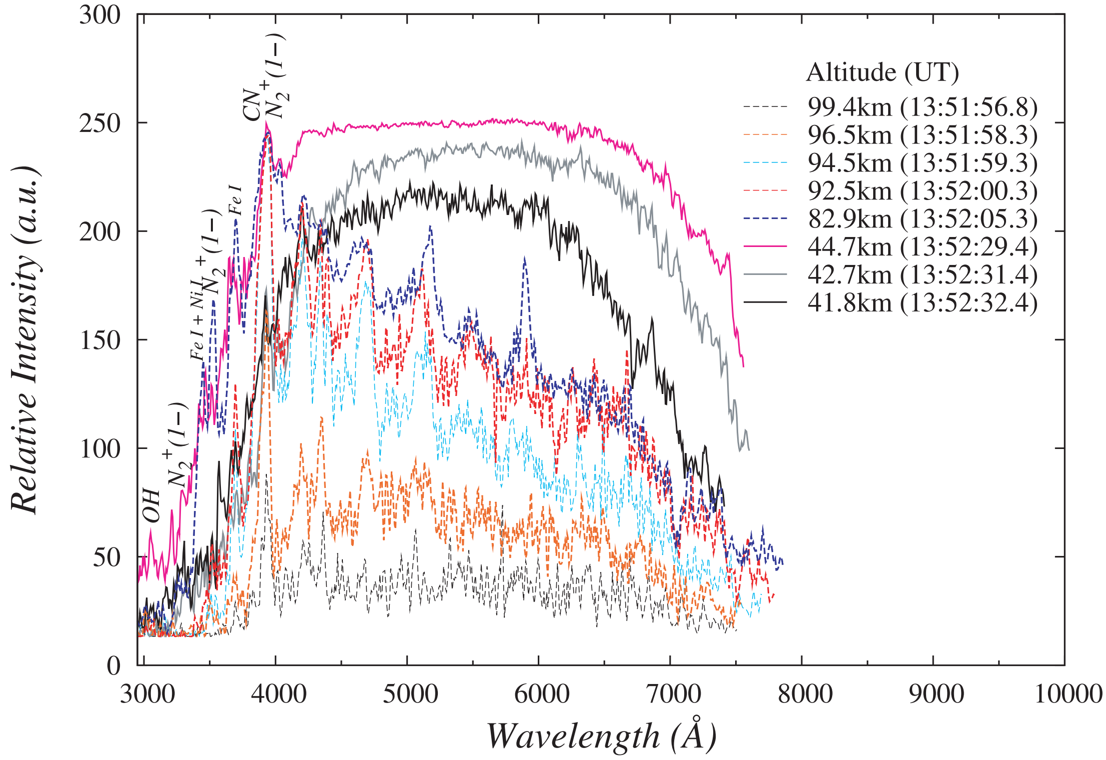

Fig. 5. Time series of the UV-II spectra of HAYABUSA spacecraft (dotted lines) and the re-entry capsule (solid lines) before spectral sensitivity calibration. The saturation in intensity reaches near 250 in this figure. Some important molecular and atomic species below 4000 Å are indicated atop each emissions.

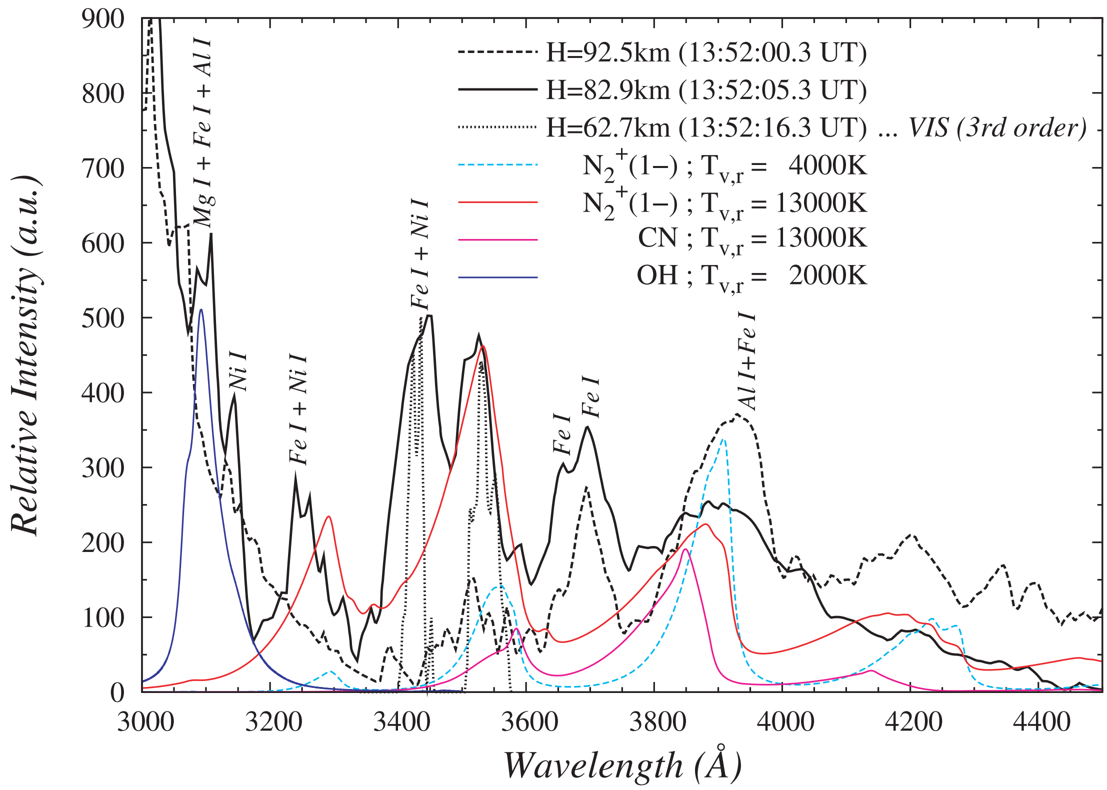

Fig. 6. Selected UV-II spectra of HAYABUSA spacecraft after sensitivity calibration compared. The scaled 3rd order of the VIS-HDTV spectrum without sensitivity calibration is shown in the 3400–3600 Å range. N_2^+ (1$^-$) bands from a shock layer and CN violet bands from an ablating heat shield of a sample return capsule are dominant molecular bands. OH(A–X) band is likely to exist around 3092 Å, but blended with atomic lines. Assuming that a rotation temperature equals to a vibration temperature, the model spectrum of N_2^+ (1$^-$), CN, and OH(A–X) systems are superposed.

Table 4. Identification of atoms and molecules in 3000–4000 Å.*

Identified line		
Band head Wavelength (Å)	Temperature $T_v = T_r$ (K)	Molecule
3092	2000	OH system ($A^2\Sigma^+ \rightarrow X^2\Pi$)
3294	4000	N_2^+ (1^-) system ($B^2\Sigma_u^+ \rightarrow X^2\Sigma_g^+$)
3560	4000	N_2^+ (1^-) system ($B^2\Sigma_u^+ \rightarrow X^2\Sigma_g^+$)
3908	4000	N_2^+ (1^-) system ($B^2\Sigma_u^+ \rightarrow X^2\Sigma_g^+$)
3292	13000	N_2^+ (1^-) system ($B^2\Sigma_u^+ \rightarrow X^2\Sigma_g^+$)
3533	13000	N_2^+ (1^-) system ($B^2\Sigma_u^+ \rightarrow X^2\Sigma_g^+$)
3880	13000	N_2^+ (1^-) system ($B^2\Sigma_u^+ \rightarrow X^2\Sigma_g^+$)
3585	13000	CN violet system ($B^2\Sigma^+ \rightarrow X^2\Sigma^+$)
3849	13000	CN violet system ($B^2\Sigma^+ \rightarrow X^2\Sigma^+$)

Identified line					
Wavelength (Å)	Element	Multiplet	Wavelength (Å)	Element	Multiplet
3020	Fe I	9	3434	Ni I	19
3021	Fe I	9	3441	Fe I	6
3091	Mg I	5	3441	Fe I	6
3092	Fe I	28	3444	Fe I	6
3093	Al I	3	3446	Ni I	20
3093	Al I	3	3648	Fe I	23
3134	Ni I	25	3687	Fe I	21
3226	Fe I	155	3944	Al I	1
3233	Ni I	7	3962	Al I	1
3415	Ni I	19	3969	Fe I	43
3424	Ni I	20			

* Identified atoms here were based on the spacecraft-capsule mixed spectrum at a height of 82.9 km (13:52:05 UT), while molecular bands resulted from the spacecraft-capsule mixed spectra at a height of 92.5 km (13:52:00 UT), 82.9 km (13:52:05 UT), and 62.7 km (13:52:16 UT). Identified atoms and synthetic molecular spectra are shown in the UV-II spectrum (figure 6). The precision of the temperature estimation is about ± 500 K.

in the same way. N_2^+ molecules were originated from the atmospheric gas. CN molecules were produced by a chemical product of ablated carbon atoms from the heat shield of the capsule and atmospheric nitrogen molecules. Both N_2^+ and CN molecules were generated in the shock layer of the body. The derived temperatures of N_2^+ (1^-) bands at heights of 92.5 km and 82.9 km were ~4000 K and ~13000 K, respectively. Though most of CN bands were buried under strong N_2^+ (1^-) bands, a clear CN band head at 3533 Å was detected which is explained by the vibration temperature of ~ 13000 K. The other emission features consisted mainly of Fe I, Mg I, Al I and Ni I. Table 4 gives the identification of atoms and molecules in the range between 3000–4000 Å.

3.3. Gray-Body Spectrum of the Capsule

A black-body is an idealized object with a perfect absorber and emitter of radiation whose emissivity is larger than 0.99. An object which has lower emissivity such as a re-entry capsule is often referred to as a gray-body. The capsule spectrum was well separated from HAYABUSA's fragments below ~45 km in height while N_2^+ (1^-) and CN bands were still strong in the near-ultraviolet region (figure 5). After sensitivity calibration, the gray-body temperature in the wavelengths between 4500–6500 (7000) Å was estimated employing Planck's formula.

Table 5. Gray-body temperature of the sample return capsule.

Time (UT)	Height (km)	Velocity (km s^{-1})	Temperature (K)
13:52:31.35	42.69	6.35	2482 ± 11
13:52:32.35	41.81	5.88	2437 ± 14
13:52:32.99	41.28	5.58	2395 ± 15

The gray-body temperatures of 2482 ± 11, 2437 ± 14, and 2395 ± 15 K were measured at heights of 42.7, 41.8, and 41.2 km, respectively (table 5; figure 5).

4. Discussion

4.1. VIS-HDTV Spectrum in 4000–7000 Å

When the surface temperature of HAYABUSA reached about 2000 K, occurring at a height around 100 km, the spacecraft material started to sublimate from the surface and was surrounded by evaporated vapors. Excited states of atoms of these vapors were gradually de-excited by radiation. HAYABUSA luminosity consisted mostly of radiation of discrete emission spectral lines belonging under the most part to metals and mainly to iron. Ablation particles injected

Table 6. Derived excitation temperature of radiating gas, the column density, and the intensities of identified main neutral atoms.*

Height (km)	84.51	62.72	54.94	54.94
Spectrum order	1st	2nd	1st	2nd
T (K)	6000	6000	4500	4500
Mg I	1.0E+0	1.0E+0	1.0E+0	1.0E+0
Fe I	6.0E−1	1.0E+1	9.0E+0	9.0E+0
Mn I	—	2.0E−1	3.0E−1	3.0E−1
Ti I	< 1.0E−3	2.0E−2	2.0E−2	2.0E−2
Na I	1.2E−2	1.8E−2	1.0E−3	7.0E−4
Cr I	1.2E−2	4.0E−2	4.0E−2	4.0E−2
Li I	—	—	3.2E−3	—
Ni I	< 1.0E+1	1.0E+1	< 1.0E+0	5.0E+0

* The precision of the temperature estimation is about ± 500 K, and that of other parameters is within a factor of 2–3.

into the flow also emitted radiation as a continuum spectrum due to their temperature. Thus, observed atomic spectrum was mixed with thermal continuum and molecular bands. Subtracting these background, excitation temperature and element intensities were estimated under the assumption of a local thermal equilibrium (LTE) condition. Table 6 gives the derived physical quantities.

The excitation temperature was estimated using Fe I and Mg I lines around the 5000–5500 Å wavelength range. The derived excitation temperatures were 6000 K at heights of 84.5 km and 62.7 km, and 4500 K at a height of 54.9 km. These excitation temperatures are comparable to a normal meteor temperature, ∼ 5000 K (e.g, Borovička 1993; Ceplecha et al. 1996; Trigo-Rodriguez et al. 2003) and the excitation temperature range between 5000–6000 K caused by a large bolide (Borovička et al. 1998). Although the ratio of Fe I/Mg I was 0.6 at a height of 84.5 km, the ratio increased to 10 below a height of 62.7 km. Since HAYABUSA was made with much more Fe than Mg, it is likely that iron was conspicuously evaporated during the explosion phase.

Detected Ti I lines seem to originate from fuel and gas tanks, and also bolts with nuts that were made of Ti-6Al-4V. H I line (4861 Å) is possibly present, presumably as a result of the dissociation of N_2H_4 which was used as thruster fuel, meaning that some of the thrusting fuel remained at re-entry. All other elements (Ni, Cr, and Mn) were probably used for constructing the HAYABUSA spacecraft. Though Hg I was identified as the most probable element to explain the presence of lines at 4358 and 5461 Å, details are proprietary information that were not available to the authors. The detected Na I, especially at heights of 62.7 km and 54.9 km, is not likely to have originated from the atmosphere; although Earth's atmosphere contains natural sodium known as the sodium layer at a height of 80–105 km which originated from meteoroids, this sodium is more rare at these low altitudes. Therefore, sodium must have originated from material ablated by the HAYABUSA spacecraft or its capsule. Sodium was also detected by the Stardust capsule at altitudes of 54–48 km (Stenbaek-Nielsen & Jenniskens 2010).

O I and N I are most likely atmospheric lines, or a part of O I and N I arising from the fuel oxidizer, N_2O_4. O I, N I, H I, and Xe I are of high excitation atoms which require either high temperature or a large amount of atoms to be detected. Therefore, these atoms are thought to be excited by the shock layer. On the other hand, typical lines of the high temperature components as seen in the meteor plasma such as Mg II (4481 Å) and Fe II (e.g., 4583, 4923, and 5018 Å) have not been detected in HAYABUSA spectra. The one explanation for the absence of Mg II and Fe II is that the emissions of O I, N I, H I, and Xe I arise promptly from the shock layer in the gas–gas phase, while the ablation of solid Mg and Fe should transform into a gas phase that takes more time than gas–gas transformation because of the low velocity ($\sim 10\,\mathrm{km\,s^{-1}}$) compared with typical meteors ($\sim 40\,\mathrm{km\,s^{-1}}$).

4.2. *UV-II Spectrum in 3000–4000 Å*

The vibration temperature of molecular N_2^+ (1^-) was dramatically changed from 4000 K at a height of 92.5 km to 13000 K at a height of 82.9 km (table 4; figure 6). The observed spectra are a superposition of the post shock plasma radiation which is mixed with a shock layer heating and downward plasma. Thus, it is logical to understand that the high temperature region was induced by a shock layer of the HAYABUSA spacecraft which rapidly grew between 92.5 km and 82.9 km in height. The molecular band of N_2^+ (1^-) was also observed in the spectrum of the Stardust re-entry capsule with a rotational temperature of 15000 K at heights between 71.5 km and 62 km (Winter & Trumble 2011). Interestingly, at a height of 84 km, N_2^+ (1^-) was detected with a vibration temperature of ∼ 10000 K from a −4 magnitude bright fireball of the Leonid meteor shower whose entry velocity was $\sim 72\,\mathrm{km\,s^{-1}}$ (Abe et al. 2005b). The flux of the spacecraft at a height of 62.7 km (−12 absolute magnitude) was about 1600 times brighter than that of the capsule's flux (−4 absolute magnitude at the maximum). Therefore, the N_2^+ (1^-) bands originated from the spacecraft was much stronger than CN bands originated from the capsule in which C was the major erosion product of the Carbon-Phenol heat shield of the capsule as seen by the Stardust capsule (Jenniskens 2010a; Winter & Trumble 2011). Clear C I lines were also observed in the near-infrared spectrum (around 1 μm wavelength) of the Stardust reentry capsule (Taylor & Jenniskens 2010). Note that the vibrational and rotational temperatures of CN violet bands were measured to be 8000 ± 1000 K in the Stardust capsule at a height of 60 km (Jenniskens 2010b). C–N coupling occurs at a higher excited state than a ground state, and then vibration-rotation temperature approaches to the translational temperature. For instance, the estimated translation temperature in the shock layer of the capsule was 11000–13000 K. Hence, the vibration-rotation temperature of ∼ 13000 K for N_2^+ (1^-) and CN is reasonable.

Bright fireballs sometimes leave a self-luminous long-lasting plasma at altitudes of about 80–90 km that is called 'persistent trains'. It is generally believed that the luminosity of persistent trains is fueled by reactions involving O_3 and atomic O, efficiently catalyzed by metals from the freshly ablated meteoroids (e.g., Jenniskens 2000; Abe et al. 2005a). A persistent train was observed at heights between 92 km and to 82 km for about 3 min (Yamamoto et al. 2011). It is reasonable to suppose that sufficient metals were supplied by the ablation of the spacecraft at these heights.

It is important to understand how meteoroids and meteors supply the Earth with space matter including organics and

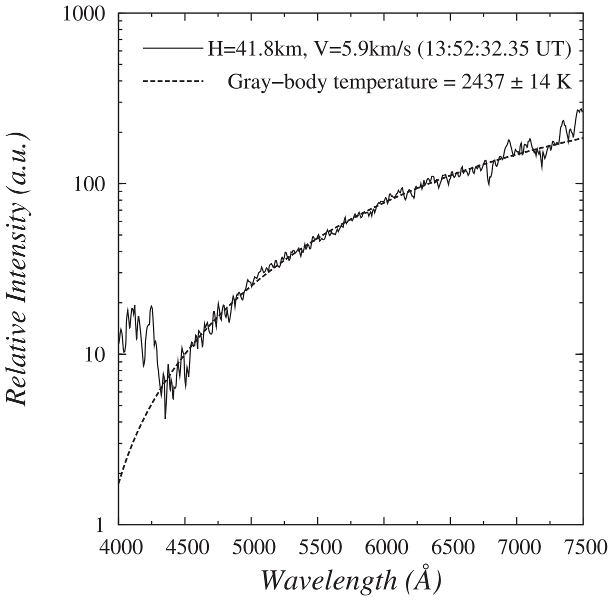

Fig. 7. Gray-body spectra of the sample return capsule at a height of $\sim$42 km. Near-ultraviolet region below 4500 Å is affected by atom and molecule emissions. Thus, Plank's formula was applied to the range between 4500–7000 Å as shown.

water (e.g., Abe et al. 2007b). Meteors represent a unique chemical pathway towards prebiotic compounds on the early Earth and a significant fraction of organic matter is expected to survive. Thus, the investigations of OH(A–X) in the HAYABUSA spectrum is of particular interest. The most likely mechanism for emitting OH(A–X) band in the meteor is caused by the dissociation of water or mineral water in the meteoroid. Our possible detection of OH(A–X) band indicates an Earthly origin caused by the dissociation of water in the upper atmosphere. However, due to blending with other atomic lines such as Mg I, Fe I, and Al I, further spectroscopy with higher resolution and sensitivity around 3090 Å will be needed for further confirmation.

4.3. Gray-Body Spectrum of the Capsule

A continuum consisting of a gray-body emission of the capsule at near-ultraviolet and visible wavelengths was examined. A continuum radiation of the capsule obtained at a height of $\sim$42 km was that of a gray-body at a fitted temperature employing Planck's formula. Our derived temperature from an excellent UV-II data set was 2437 ± 14 K at a height of 41.8 km (figure 7). The surface temperature of 2525 ± 50 K at a height of 41.1 km was estimated based on radiative equilibrium Computational Fluid Dynamics (CFD) (Fujita et al. 2003). Our observed temperature agrees qualitatively with the CFD model prediction. The gray-body temperature observed from NAOJ's team at Coober Pedy resulted in $\sim 2400 \pm 300$ K at a height of $\sim$40.5 km (Ohnishi et al. 2011) which is comparable with our result. Note that dynamical pressure at a height around 40 km was the maximum $\sim$64 kPa (Yamada & Abe 2006). At the GOS3 site, a strong sequence of sonic booms was detected at 13:55:21 UT using a video recorder's microphone which was observed at Tarcoola by Y. Akita and his colleagues. A sonic boom is the sound associated with a shock wave created by the supersonic flight of the capsule. According to this time delay, the shock wave generation point was estimated at a height around 40 km. Considering these fluid conditions, further analysis will be made in a forthcoming paper (e.g., Fujita et al. 2011b).

5. Conclusion

At 13:51:50 UT on 2010 June 13, the HAYABUSA spacecraft appeared as planned in the dark sky over the Australian desert, along with the faint dot of the capsule. The HAYABUSA spacecraft was flying behind the capsule, roughly 1 km above as if he must protect his tiger cub. While the spacecraft burst into many fragments, as if falling into the Milky Way, the capsule became an independent bright fireball wearing an ablative heat shield as its thermal protection system (TPS), as if demonstrating its will to overcome adversity. The planned atmospheric re-entry was perfectly completed. The HAYABUSA spacecraft ended his journey in a brilliant flash of light that provided us a treasure trove of "artificial fireball" data, which has never been observed in a scientific way. Atomic lines such as Fe I, Mg I, Na I, Al I, Cr I, Mn I, Ni I, Ti I, Li I, Zn I, O I, and N I were identified. The excitation temperature ranging from 4500 K to 6000 K was estimated using Fe I and Mg I within the 5000–5500 Å wavelength region, which is similar to a common excitation temperature of meteors and bolides. The identification of emission lines may be inadequate and contain some unknown lines. Exotic atoms such as Cu I, Mo I, Xe I, and Hg I were also identified. The explosion of the spacecraft injected a large amount of iron which increased the density of Fe I. The surprising strong red line during the last flash of the spacecraft was well explained by a Li I line (6708 Å) that was probably caused by explosions of the onboard Li-Ion batteries. A clearly detected FeO band at a height of $\sim$63 km is similar to a common bolide spectrum which is likely to emit in the wake, where the radiation is emitted just behind the body. The alteration in the hot plasma temperature of N_2^+ (1^-) bands (from 4000 K to 13000 K) appears to be the strongest proof that an intense shock layer around the HAYABUSA spacecraft was rapidly formed at heights between 93 km and 83 km. The gray-body temperatures ranging from 2482 K to 2395 K were measured at heights between 42.7 km and 41.2 km that can be explained by the CFD model prediction. Further investigation is required to understand the performance of the TPS. Our experiences will be instructive in observing the planned HAYABUSA-II Earth return mission.

We are thankful to all of the ISAS/JAXA personnel who organized and participated in the recovery operations, especially Jun-ichiro Kawaguchi, Hitoshi Kuninaka, Tetsuya Yamada, Makoto Yoshikawa, Masanao Abe, and Hajime Yano. We are also grateful to all of the JAXA ground observation team members at JAXA, NAOJ, Kochi University of Technology, Kanazawa University, and Nagoya University who assisted in observing at GOS3 and GOS4 stations. We are very grateful to our host family at Tarcoola (Leah, Cameron, Drew and Luke Morgan, and Carol St Clair) for their sincere warmth and kind hospitality. GOTO Inc. and NEC Corp. kindly provided a newly developed high-sensitive EMCCD camera (NCR-550a). Noboru Ebizuka (Nagoya University) designed the UV-II spectroscopic camera with the aid of SHOWA Industry Co., Ltd in Japan. Yuichiro Akita kindly provided recording data of the sonic boom observed at Tarcoola. We express many thanks to Jiří Borovička (Ondřejov observatory) for constructive comments and kind advice. Synthetic spectrum was carried out in part on the general-purpose PC farm at the Center for Computational Astrophysics (CfCA) of NAOJ. Shinsuke Abe is supported by JAXA and the National Science Council of Taiwan (NSC 97-2112-M-008-014-MY3, NSC 100-2112-M-008-014-MY2). *Welcome Back Home "Okaerinasai" HAYABUSA!*

References

Abe, S., et al. 2006, Science, 312, 1344
Abe, S. 2009, in Small Bodies in Planetary Systems, ed. I. Mann et al. (Heidelberg: Springer), 129
Abe, S. 2010, J. Taipei Astron. Museum, 8, 1
Abe, S., Ebizuka, N., Murayama, H., Ohtsuka, K., Sugimoto, S., Yamamoto, M., Yano, H., Watanabe, J., & Borovička, J. 2005a, Earth, Moon, Planets, 95, 265
Abe, S., Ebizuka, N., Yano, H., Watanabe, J., & Borovička, J. 2005b, ApJ, 618, L141
Abe, S., Ebizuka, N., Yano, H., Watanabe, J., & Borovička, J. 2007b, Adv. Space Res., 39, 538
Abe, S., Yamamoto, M., Yano, H., Ebizuka, N., & Watanabe, J. 2007a, Proc. of JAXA/ISAS Solar System Science Symp., 21 (in Japanese)
Berezhnoy, A. A., & Borovička, J. 2010, Icarus, 210, 150
Borovička, J. 1993, A&A, 279, 627
Borovička, J., Abe, S., Shrbený, L., Spurný, P., & Bland, P. A. 2011, PASJ, 63, 1003
Borovička, J., Popova, O. P., Golub', A. P., Kosarev, I. B., & Nemtchinov, I. V. 1998, A&A, 337, 591
Ceplecha, Z. 1971, Bull. Astron. Inst. Czechoslovakia, 22, 219
Ceplecha, Z., Borovička, J., Elford, W. G., Revelle, D. O., Hawkes, R. L., Porubčan, V., & Šimek, M. 1998, Space Sci. Rev., 84, 327
Evans, W. F. J., Gattinger, R. L., Slanger, T. G., Saran, D. V., Degenstein, D. A., & Llewellyn, E. J. 2010, Geophys. Res. Lett., 37, L22105
Fujita, K., et al. 2011, PASJ, 63, 961
Fujita, K., & Abe, T. 1997, ISAS Rep., 669, 1
Fujita, K., Otsu, H., Yamada, T., & Abe, T. 2003, J. Japan Soc. Aeronautical & Space Sci., 51, 419 (in Japanese)
Fujita, K., Suzuki, T., Matsuyama, S., Yamada, T., & Abe, S. 2011, J. Spacecr. & Rockets submitted
Fujiwara, A., et al. 2006, Science, 312, 1330
Jenniskens, P. 2010, J. Spacecr. & Rockets, 47, 718
Jenniskens, P., Lacey, M., Allan, B. J., Self, D. E., & Plane, M. C. 2000, Earth, Moon, Planets, 82/83, 429
Jenniskens, P., Wilson, M. A., Winter, M., & Laux, C. O. 2010, J. Spacecr. & Rockets, 47, 873
Kawaguchi, J., Fujiwara, A., & Uesugi. T. 2008, Acta Astron., 62, 639
Kuninaka, H. 2008, AIP Conf. Proc., 997, 572
Ohnishi, K., Watanabe, J., Sato, M., Ohkawa, T., & Ebizuka, N. 2011, PASJ, 63, 987
Shoemaker, M. A., van der Ha, J. C., Abe, S., & Fujita, K. 2011, J. Spacecraft & Rockets submitted
Stenbaek-Nielsen, H. C., & Jenniskens, P. 2010, J. Spacecr. & Rockets, 47, 884
Taylor, M. J., & Jenniskens, P. 2010, J. Spacecr. & Rockets, 47, 878
Trigo-Rodriguez, J. M., Llorca, J., Borovička, J., & Fabregat, J. 2003, Meteoritics & Planetary Sci., 38, 1283
Ueda, M., et al. 2011, PASJ, 63, 947
Watanabe, J., Ohkawa, T., Sato, M., Ohnishi, K., Iijima, Y., Kagawa, Y., & Tanabe, T. 2011, PASJ, 63, 941
Winter, M. W., & Trumble, K. A. 2011, J. Spacecr. & Rockets, 48, 59
Yamada, T., & Abe, T. 2006, J. Plasma & Fusion Res., 82, 368 (in Japanese)
Yamamoto, M.-Y., Ishihara, Y., Hiramatsu, Y., Kitamura, K., Ueda, M., Shiba, Y., Furumoto, M., & Fujita, K. 2011, PASJ, 63, 971

Publications of the Astronomical Society of the Pacific, **123**:113–124, 2011 January

Forecasting Cloud Cover and Atmospheric Seeing for Astronomical Observing: Application and Evaluation of the Global Forecast System

Q.-Z. Ye,[1]

Department of Atmospheric Sciences, School of Environmental Science and Engineering, Sun Yat-sen University, Guangzhou, China; tom6740@gmail.com

Received 2010 April 14; accepted 2010 November 16; published 2011 January 5

ABSTRACT. To explore the issue of performing a noninteractive numerical weather forecast with an operational global model to assist with astronomical observing, we use the Xu-Randall cloud scheme and the Trinquet-Vernin AXP seeing model with the global numerical output from the Global Forecast System (GFS) to generate 3–72 hr forecasts for cloud coverage and atmospheric seeing, and we compare them with sequence observations from nine sites from different regions of the world with different climatic backgrounds in the period from 2008 January to 2009 December. The evaluation shows that the proportion of prefect forecast of cloud cover forecast varies from ∼50% to ∼85%. The probability of cloud detection is estimated to be around ∼30% to ∼90%, while the false alarm rate is generally moderate and is much lower than the probability of detection in most cases. The seeing forecast has a moderate mean difference (absolute mean difference <0.3″ in most cases) and rms error (0.2″–0.4″ in most cases), compared with the observation. The probability of forecast with <30% error varies between 40% and 50% for the entire-atmosphere forecast and between 30% and 50% for the free-atmosphere forecast for almost all sites, which is in the better cluster among major seeing models. However, the forecast errors are quite large for a few particular sites. Further analysis suggests that the error might primarily be caused by the poor capability of the GFS/AXP model to simulate the effect of turbulence near ground and on a subkilometer scale. Overall, although the quality of the GFS model forecast may not be comparable with the human-participated forecast at this moment, our study has illustrated its suitability for a basic observing reference and has proposed its potential to gain better performance with additional efforts on model refinement.

1. INTRODUCTION

Almost all kinds of ground-based astronomical observations, especially for optical types, are extremely dependent on meteorological condition, so it is no doubt that making the meteorological prediction as precise as possible would significantly help observers to schedule the observation and improve the efficiency of telescope operation. Among all meteorological variables, cloud amount or cloud cover is apparently the dominant factor, while atmospheric/astronomical seeing, sometimes described as the Fried parameter (Fried 1965), is also important.

A climatological study to the annual values of cloud cover and/or atmospheric seeing for a proposed professional observatory is usually done in the site survey prior to the construction (see Walker 1970 and Fuentes & Muñoz-Tuñon 1990 for examples). However, to maximize the observing resources, astronomers not only need to know the approximate percentage of clear nights in a year, but they also wish to know whether the sky will be clear or not in the next few nights. In other words, they expect weather forecasts to be as accurate and precise as possible. However, since astronomical observatories are generally built in distant areas (therefore, with sparse meteorological observations available and less interest from meteorologists), special forecasts that aim at assisting astronomical observation had not been widely practiced until very recent years. Since the end of the 1990s, special forecast services and products based on mesoscale regional numeric models and/or real-time satellite images have been developed at the large professional observatories, such as Mauna Kea Weather Center (MKWC; see Businger et al. 2002 for an overview) and the nowcast model at ESO (Erasmus & Sarazin 2001).

As the operation of high-resolution numeric models would require the ability to perform speedy computation (which is usually only available at large professional observatories), attempts aimed at making direct uses of the model fields from global/continental models were carried out later, such as the Clear Sky Chart[2] that has used the Canadian Meteorological Centre's Global Environmental Multiscale (GEM)[3] since 2002 (Danko 2003) and our 7Timer system[4] that has used the National Centers for Environmental Prediction (NCEP) Global

[1] Current address: Room 404, 12 Huasheng Street, Guangzhou, 510620 China.

[2] See http://cleardarksky.com/csk/.

[3] See http://collaboration.cmc.ec.gc.ca/science/rpn/gef_html_public.

[4] See http://7timer.y234.cn.

Forecast System[5] (GFS) since 2005 (see Sela 1980; Whitaker et al. 2008 for an overview of the model). These direct-from-model forecasts only have decent spatial and vertical resolutions (for a comparison, the spatial resolution of the GFS model is about 40 km, while the regional model operating at MKWC can reach 1 km), but it does not require heavy computation work either; the retrieval of the model fields can be done with an Internet-connected personal computer within a couple of minutes, making it the most favorable (and probably the only) choice when a speedy computer is not available and the demand on forecast precision/accuracy is not critical.

Interestingly, although these services have been put into good use by private, public, and even some professional observatories, there has been no quantitative and systematic understanding of how accurate the model fields are up to now. For example, the only reported estimation of the accuracy of cloud field forecast for a global model was done by Erasmus & Sarazin (2001) from 1992–1993, which suggested that only 15–25% of cloudy nights could be identified with the European Centre for Medium-Range Weather Forecasting model.[6] This is age-old, considering there had been a number of significant upgrades of the global models in the following decade. The forecast for atmospheric seeing, on the other hand, is more complex, since it is related to vertical fine structure of the atmospheric column and is not directly provided as part of the output in any global model. In general, there are two tracks for atmospheric seeing forecast: nowcast track using near-real-time meteorological observation profile combined with a statistical model (such as Murtagh et al. 1995) or the model track using either the derivations of Tatarski's formula (Tatarski 1961; Coulman et al. 1988) or the numeric model proposed by Coulman et al. (1986). The first track is relatively intuitive and is accurate enough on many occasions, but it has a very short forecast range (usually less than 24 hr) and heavily depends on the availability and quality of the observational data; for the second track, one would need to divide the atmospheric column into a good number of layers to gain a numeric simulation that is close enough to the actual situation, which will again require assistance from a speedy computer. In order to solve these shortcomings, Trinquet & Vernin (2006) took advantages from both tracks and introduced a new seeing model called the AXP model. With that model, one only needs to divide the atmospheric column by a number close to that available in most global models, and the consistency from the simulation of the AXP model to the actual situation is satisfying according to the authors. Overall, these direct-from-model forecasts can be a practical solution for the observers without the ability to operate a high-precision regional model of their own, and the job to do is to assess the accuracy of these forecasts.

[5] See http://www.emc.ncep.noaa.gov/GFS/.

[6] See http://www.ecmwf.int/.

We organize this article as follows. In § 2, we briefly outline the technical details of the GFS model used in this study, the Xu-Randall cloud scheme used for cloud simulation, and the AXP model used to derive forecast of atmospheric seeing. In § 3, we describe the observations we used to evaluate the GFS model. Section 4 presents the details and discussions of the evaluation methodology and result, and § 5 gives the concluding remarks of this study.

2. FORECAST

2.1. The NCEP GFS Model

The GFS model provides output in two grids with different spatial resolutions: grid 003 at $1° \times 1°$ and grid 004 at $0.5° \times 0.5°$. To provide the best-possible forecast, we use the latter in our study. Model outputs from the period from 2008 January 1 to 2009 December 31 at three hourly intervals for $0 < \tau \leq 72$ hr at 00Z initialization are retrieved from the National Operational Model Archive & Distribution System (see Rutledge et al. 2006) for evaluation.

The GFS data set contains approximately 140 fields, supplying forecast fields for general meteorological interests (such as temperature, humidity, wind direction and speed, etc.) and for special purpose, including cloud cover fraction on different layers (low, mid, high, convective, and total atmospheric column). Although the atmospheric seeing is not among the output fields, it can be derived indirectly, as all of the required meteorological variables are given.

2.2. Cloud Scheme

In the GFS model, the cloud cover fraction for each grid box is computed using the cloud scheme presented by Xu & Randall (1996), which is shown as equation (1). In this equation, RH is the relative humidity, q^* and q_c are the saturation specific humidity, and $q_{c\,\mathrm{min}}$ is a prescribed minimum threshold value of q_c. Depending on the environmental temperature, q^* and q_c are calculated with respect to water phase or ice phase (F. Yang 2010, private communication). Cloud cover fraction can therefore be calculated for any layer as long as the RH, q^*, and q_c are known and $q_{c\,\mathrm{min}}$ is suitably prescribed. We note that the calculation is done as part of the model simulation at NCEP, so the cloud fields are used as is from the GFS data sets:

$$C = \max\left[\mathrm{RH}^{\frac{1}{4}}\left(1 - e^{-\frac{2000(q_c - q_{c\,\mathrm{min}})}{\min\{\max[((1-\mathrm{RH})q^*)^{\frac{1}{4}},0.0001],1.0\}}}\right), 0.0\right]. \quad (1)$$

The GFS model divides the whole atmospheric column into 26 layers. The total cloud cover for the entire atmospheric column is derived under the assumption that clouds in all layers are maximally randomly overlapped (Yang et al. 2005).

2.3. Seeing Model

The way atmospheric optical turbulence affects astronomical observing is theoretically described by the Kolmogorov-Tatarski turbulence model (Tatarski 1961; Roddier 1981; Tokovinin 2002), which suggested that only one parameter is needed to describe the quality of atmospheric seeing where λ is the wavelength associated with seeing ($\lambda = 5 \times 10^{-7}$ m in most cases) and r_0 is the Fried parameter:

$$\epsilon_0 = 0.98\frac{\lambda}{r_0}. \tag{2}$$

The Fried parameter, r_0, is defined as follows in the direction of zenith (Coulman 1985), where Z_0 is the geopotential height of the observing site, C_N^2 is the refractive index structure coefficient indicating the strength of turbulence associated with the temperature structure coefficient C_T^2, P is the pressure in hectopascals, and T is the temperature in degrees Kelvin:

$$r_0 = \left[0.423\left(\frac{2\pi}{\lambda}\right)^2 \int_{Z_0}^{\infty} C_N^2 dZ\right]^{-\frac{3}{5}}, \tag{3}$$

$$C_N^2 = C_T^2\left(\frac{7.9 \times 10^{-5} P}{T^2}\right)^2. \tag{4}$$

Therefore, with the preceding formulas and suitable inputs, we can derive the total effect of atmospheric turbulence from the integral of $C_N^2(Z)$ for all atmospheric layers:

$$C_T^2 = \frac{T(\mathbf{x}) - T(\mathbf{x} + \mathbf{r})}{|\mathbf{r}|^{\frac{2}{3}}}. \tag{5}$$

There are several ways to derive C_T^2. A theoretical approach is shown as equation (5), where **x** and **r** are the position and separation vectors, respectively. However, in theory, $|\mathbf{r}|$ should be around a few tenths of a meter to precisely describe the effect of turbulence (which is not practical for model simulation, as it would require one to use about 100,000 layers for model simulation). The AXP model uses an alternative approach by considering a simple expression of $C_T^2(h)$ as follows, where the power $p(h)$ adjusts the amplitude of peaks and $A(h)$ connects the level:

$$C_T^2 = \langle C_T^2 \rangle(h)\left[A(h)\frac{d\bar{\theta}}{dz}\right]^{p(h)}. \tag{6}$$

The potential temperature θ in equation (6) can be calculated by Poisson's equation, where T is the absolute temperature of a parcel in degrees Kelvin and P is the pressure of that air parcel in hectopascals:

$$\theta = T\left(\frac{1000}{P}\right)^{0.286}. \tag{7}$$

TABLE 1

LAYERS OF GFS MODEL AND CORRESPONDING ALTITUDE LAYERS

GFS layer (P-coordinate system)	Corresponding altitude (Z-coordinate system)
2 m above ground	2 m above ground
0.995σ[a]	~100 m above ground
30 hPa above ground	~400 m above ground
900–850 hPa	988–1457 m
850–800 hPa	1457–1948 m
800–750 hPa	1948–2465 m
750–700 hPa	2465–3011 m
700–650 hPa	3011–3589 m
650–600 hPa	3589–4205 m
600–550 hPa	4205–4863 m
550–500 hPa	4863–5572 m
500–450 hPa	5572–6341 m
450–400 hPa	6341–7182 m
400–350 hPa	7182–8114 m
350–300 hPa	8114–9160 m
300–250 hPa	9160–10359 m
250–200 hPa	10359–11770 m
200–150 hPa	11770–13503 m
150–100 hPa	13503–15791 m
100–70 hPa	15791–17662 m
70–50 hPa	17662–19314 m
50–30 hPa	19314–21629 m
30–20 hPa	21629–23313 m
20–10 hPa	23313–25908 m

[a] The value 0.995σ stands for the level at 0.995σ in the sigma coordinate system. The sigma coordinate system is a vertical coordinate system being widely used in numerical models. It defines the vertical position as a ratio of the pressure difference between that position and the top of its associated grid.

The authors of the AXP model (Trinquet & Vernin (2006) then statistically determined the values of the three coefficients, $\langle C_T^2 \rangle(h)$, $A(h)$, and $p(h)$, by a vertical spacing of 1 km up to an altitude of 30 km, based on airborne observations from 162 flights at nine sites during 1990–2002. On the other hand, the coordinate system adopted by the GFS model is the P-coordinate system, which divides the atmospheric column by pressure. The vertical spacing of the GFS model over low- and midlevel atmospheres is around 1 km and is roughly compatible with the Z-coordinate system adopted by the AXP model; however, the former becomes too sparse at high-level atmosphere (as illustrated in Table 1). To solve this problem, we set up a degeneracy scheme to allow using the AXP model coefficients in the P-coordinate system by weighting the values according to the correlation between atmospheric pressure and altitude defined by the U.S. Standard Atmosphere, 1976.[7] The transformed coefficients for each pressure layer are given in Table 2. As the output of the GFS model provides fields of temperature and atmospheric pressure for each of its vertical layer, we can align

[7] See http://ntrs.nasa.gov/archive/nasa/casi.ntrs.nasa.gov/19770009539_1977009539.pdf.

TABLE 2

Coefficients for AXP Model and Corresponding GFS Model Layer and Weight

AXP layer	GFS layer and weight	$\bar{P}$	$p(h)$	$A(h)$	$\langle C_T^2 \rangle (h)$
0–50 m above ground	2 m above ground to 0.995σ	$P(h) - 3$ hPa	0.5	1.6E+2	1.4E–2
50–100 m above ground	2 m above ground to 0.995σ	$P(h) - 9$ hPa	0.5	1.6E+2	$4.8\mathrm{E} - 4(h/100)^{-2.6}$
100–1000 m above ground	0.995σ to 30 hPa above ground	$P(h) - 60$ hPa	0.5	1.6E+2	$3.4\mathrm{E} - 5(h/1000)^{-1.1}$
1–2 km	900–850 hPa (50%)	845 hPa	0.3	1.8E+3	5.2E–5
1–2 km	850–800 hPa (40%)	845 hPa	0.3	1.8E+3	5.2E–5
1–2 km	800–750 hPa (10%)	845 hPa	0.3	1.8E+3	5.2E–5
2–3 km	800–750 hPa (50%)	745 hPa	1.3	5.6E+2	4.2E–5
2–3 km	750–700 hPa (50%)	745 hPa	1.3	5.6E+2	4.2E–5
3–4 km	700–650 hPa (60%)	655 hPa	1.7	4.6E+2	2.8E–5
3–4 km	650–600 hPa (40%)	655 hPa	1.7	4.6E+2	2.8E–5
4–5 km	650–600 hPa (20%)	575 hPa	1.7	3.8E+2	2.5E–5
4–5 km	600–550 hPa (70%)	575 hPa	1.7	3.8E+2	2.5E–5
4–5 km	550–500 hPa (10%)	575 hPa	1.7	3.8E+2	2.5E–5
5–6 km	550–500 hPa (60%)	505 hPa	2.6	2.6E+2	1.8E–5
5–6 km	500–450 hPa (40%)	505 hPa	2.6	2.6E+2	1.8E–5
6–7 km	500–450 hPa (30%)	440 hPa	1.1	4.6E+2	1.5E–5
6–7 km	450–400 hPa (70%)	440 hPa	1.1	4.6E+2	1.5E–5
7–8 km	450–400 hPa (20%)	380 hPa	0.8	6.8E+2	1.6E–5
7–8 km	400–350 hPa (80%)	380 hPa	0.8	6.8E+2	1.6E–5
8–9 km	400–350 hPa (10%)	330 hPa	0.6	1.0E+3	1.6E–5
8–9 km	350–300 hPa (90%)	330 hPa	0.6	1.0E+3	1.6E–5
9–10 km	350–300 hPa (20%)	285 hPa	0.3	2.2E+3	1.9E–5
9–10 km	300–250 hPa (80%)	285 hPa	0.3	2.2E+3	1.9E–5
10–11 km	300–250 hPa (40%)	245 hPa	0.5	6.8E+2	2.6E–5
10–11 km	250–200 hPa (60%)	245 hPa	0.5	6.8E+2	2.6E–5
11–12 km	250–200 hPa (80%)	210 hPa	0.7	3.2E+2	3.4E–5
11–12 km	200–150 hPa (20%)	210 hPa	0.7	3.2E+2	3.4E–5
12–13 km	200–150 hPa (100%)	177 hPa	0.6	2.2E+2	4.4E–5
13–14 km	200–150 hPa (50%)	150 hPa	0.1	8.3E+3	4.8E–5
13–14 km	150–100 hPa (50%)	150 hPa	0.1	8.3E+3	4.8E–5
14–15 km	150–100 hPa (100%)	126 hPa	0.2	1.0E+3	5.5E–5
15–16 km	150–100 hPa (80%)	105 hPa	–0.4	3.2E+1	6.5E–5
15–16 km	100–70 hPa (20%)	105 hPa	–0.4	3.2E+1	6.5E–5
16–17 km	100–70 hPa (100%)	88 hPa	–0.3	1.5E+1	8.3E–5
17–18 km	100–70 hPa (70%)	72 hPa	2.5	5.6E+1	1.1E–4
17–18 km	70–50 hPa (30%)	72 hPa	2.5	5.6E+1	1.1E–4
18–19 km	70–50 hPa (100%)	59 hPa	–0.9	2.6E+1	1.1E–4
19–20 km	70–50 hPa (30%)	48 hPa	3.3	3.8E+1	9.5E–5
19–20 km	50–30 hPa (70%)	48 hPa	3.3	3.8E+1	9.5E–5
20–21 km	50–30 hPa (100%)	39 hPa	–1.0	2.6E+1	8.2E–5
21–22 km	50–30 hPa (60%)	31 hPa	1.5	4.6E+1	7.4E–5
21–22 km	30–20 hPa (40%)	31 hPa	1.5	4.6E+1	7.4E–5
22–23 km	30–20 hPa (100%)	24 hPa	–1.9	3.2E+1	7.5E–5
23–24 km	30–20 hPa (30%)	19 hPa	1.3	4.6E+1	8.7E–5
23–24 km	20–10 hPa (70%)	19 hPa	1.3	4.6E+1	8.7E–5
24–25 km	20–10 hPa (100%)	15 hPa	1.1	3.8E+1	1.1E–4
25–26 km	20–10 hPa (100%)	11 hPa	1.5	3.8E+1	1.3E–4

the fields with equations (2), (3), (4), (6), and (7) to derive final ϵ_0 in the form of arcseconds. We refer to this hybrid model as the GFS/AXP model hereafter.

Trinquet & Vernin (2006) reported an accuracy of 58% of the original AXP model forecasts, with error within $\pm 30\%$ of observations. However, as we have modified the model layers to fit the GFS model, some additional errors may have been induced. One may expect two possible sources of errors caused by the degeneracy. The first kind of possible error comes from the layers higher than 10 km. As the GFS model layers with altitude of >10 km have a vertical thickness significantly larger than 1 km, one may suggest that some performance may be lost due to data roughness. However, we argue that the loss of performance for this reason should be minimal, as the high-level atmosphere is much less active than the mid- or low-level atmospheres and contributes minimal turbulence to seeing, compared

TABLE 3

OBSERVING SITES

Site	Location	Elevation (h)	GFS grid elevation	Climate	Data type	Availability	PBL top[a]	$P(h)$[b]
Paranal	−70.40, −24.63	2635 m	919 m	Arid	Cloud, DIMM	2008 Jan 1–2009 Dec 31	3700 m	734 hPa
Mauna Kea	−155.48, +19.83	4050 m	896 m	Highlands	DIMM, MASS	2008 Jan 1–2008 May 31	5100 m	612 hPa
San Pedro Mártir	−115.47, +31.05	2830 m	1038 m	Arid	DIMM, MASS	2008 Jan 1–2008 Aug 31	3800 m	716 hPa
Cerro Tololo	−70.80, −30.17	2200 m	926 m	Arid	MASS	2008 Jan 1–2009 Dec 31	3200 m	775 hPa
Nanshan	+87.18, +43.47	2080 m	2233 m	Semiarid	Cloud	2008 Jan 1–2009 Jul 4	…	…
Lulin	+120.87, +23.47	2862 m	1345 m	Humid subtropical	Cloud	2008 Jan 1–2009 Jul 31	…	…
Cerro Armazones	−70.20, −24.60	3064 m	1997 m	Arid	DIMM, MASS	2008 Jan 1–2009 Sep 30	4100 m	695 hPa
Cerro Pachón	−70.73, −30.23	2715 m	2706 m	Arid	DIMM, MASS	2008 Jan 1–2009 Dec 31[c]	3700 m	727 hPa
Cerro Toloncha	−67.98, −23.93	4480 m	3626 m	Highlands	DIMM, MASS	2008 Jan 1–2008 Sep 30	5500 m	579 hPa

[a] PBL top stands for the upper limit of the PBL adopted in the GFS/AXP model.

[b] $P(h)$ is the atmospheric pressure at the height of the site used in GFS/AXP model, calculated under standard atmosphere.

[c] Ground-based seeing observation from 2008 October 31 to 2009 April 29 only.

with the latter two,[8] so a vertical spacing degeneration from 1 km to 2 km at high-level atmosphere is unlikely to induce error of significance. On the other hand, the degeneracy in planetary boundary layer (PBL), which serves as the second possible source of error, may induce something large. PBL is a layer that is directly influenced by the atmosphere-ground interaction, and it has been shown that the PBL turbulence contributes a major part to the seeing during the night (Abahamid et al. 2004). To improve the model performance at PBL, the AXP model divides the PBL into three sublayers: 0–50 m above ground, 50–100 m above ground, and 100–1000 m above ground. However, the GFS model only provides three near-ground fields, which are at 2 m above ground, 0.995σ (~100 m above ground), and 30 hPa above ground (~400 m). We have to use identical $d\bar{\theta}/dz$ computed from 2 m above ground, 0.995σ for layers of 0–50 m and 50–100 m, and the $d\bar{\theta}/dz$ computed from 0.995σ and 30 mb above ground for layers of 100–1000 m. The ignorance of data at 50 m would almost certainly induce some error. To work around this issue and allow a direct assessment of the GFS/AXP model, we also generate a seeing forecast for free atmosphere only—i.e., with PBL (<100 m in our study) excluded[9]—for our evaluation. The free-atmosphere forecast will be compared with the observations from a multi-aperture scintillation sensor (MASS), which is designed to measure the seeing in free atmosphere (Tokovinin 2002).

[8] Study by Li et al. (2003) suggests the atmosphere beyond 100 hPa (~$15,000$ m) contributes less than 0.01″ to the seeing.

[9] We do not exclude the 100 m–1000 m region in our free-atmosphere seeing forecast, because the MASS instrument used for measurement of free atmosphere seeing considers an altitude of 500 m above ground as the PBL top limit and includes measurements of layers at an altitude as low as 500 m and 1000 m above ground.

3. OBSERVATION

We collect cloud cover and seeing observations for a total of nine sites from central/east Asia, Hawaii, and Central/South America in the period from 2008 January to 2009 December.

TABLE 4

CLOUD COVER FORECAST RESULT FOR PARANAL, NANSHAN, AND LULIN

Category	Paranal	Nanshan	Lulin
30% Threshold			
H	73	715	682
F	443	482	860
M	71	38	14
Z	1411	241	94
Total n	1998	1476	1650
50% Threshold			
H	62	684	670
F	353	386	813
M	82	69	26
Z	1501	337	141
Total n	1998	1476	1650
80% Threshold			
H	44	576	642
F	225	232	734
M	100	177	54
Z	1629	491	220
Total n	1998	1476	1650

TABLE 5
EVALUATION RESULT OF CLOUD COVER FORECAST FOR PARANAL, NANSHAN, AND LULIN

Indicator	Paranal ($n = 1998$)	Nanshan ($n = 1476$)	Lulin ($n = 1650$)
	30% Threshold		
PPF	$0.74^{+0.03}_{-0.02}$	$0.65^{+0.02}_{-0.02}$	$0.47^{+0.01}_{-0.01}$
POD	$0.51^{+0.12}_{-0.07}$	$0.95^{+0.04}_{-0.05}$	$0.98^{+0.01}_{-0.01}$
FAR	$0.24^{+0.04}_{-0.03}$	$0.67^{+0.01}_{-0.01}$	$0.90^{+0.02}_{-0.01}$
FBI	$3.58^{+0.61}_{-0.50}$	$1.59^{+0.03}_{-0.05}$	$2.22^{+0.01}_{-0.03}$
	50% Threshold		
PPF	$0.78^{+0.03}_{-0.02}$	$0.69^{+0.03}_{-0.03}$	$0.49^{+0.02}_{-0.02}$
POD	$0.43^{+0.07}_{-0.04}$	$0.91^{+0.05}_{-0.06}$	$0.96^{+0.03}_{-0.02}$
FAR	$0.19^{+0.03}_{-0.03}$	$0.53^{+0.02}_{-0.01}$	$0.85^{+0.02}_{-0.02}$
FBI	$2.88^{+0.52}_{-0.48}$	$1.32^{+0.04}_{-0.04}$	$2.13^{+0.01}_{-0.02}$
	80% Threshold		
PPF	$0.84^{+0.02}_{-0.03}$	$0.72^{+0.04}_{-0.03}$	$0.52^{+0.02}_{-0.02}$
POD	$0.31^{+0.15}_{-0.10}$	$0.76^{+0.06}_{-0.06}$	$0.92^{+0.05}_{-0.02}$
FAR	$0.12^{+0.05}_{-0.03}$	$0.32^{+0.01}_{-0.01}$	$0.77^{+0.02}_{-0.02}$
FBI	$1.86^{+0.71}_{-0.44}$	$1.07^{+0.06}_{-0.06}$	$1.98^{+0.05}_{-0.05}$

The respective information of each site, including the PBL top limit and $P(h)$, used in the GFS/AXP model is listed in Table 3.

As these observations are all made in sequence with a sampling frequency of around 1–1.5 min, except Nanshan and Lulin (which will be dealt with separately and will be described subsequently), they are first processed to match the time interval of the GFS model output (which is 3 hr). To ensure that the observation is representative in the corresponding interval, we set a minimum data points of 100 for each interval. A sampling frequency of 1–1.5 minutes corresponds 120–180 data points per 3 hr, so the minimum threshold of 100 is reasonable.

As all seeing observations are obtained either by a differential image motion monitor (DIMM) or MASS, they can be used without further reduction, since they give the measurement of ϵ_0 directly. On the other hand, the cloud cover observations from Paranal, Nanshan, and Lulin are obtained with different tools, so they must be reduced to the same definition with the GFS model output before comparing them with the latter. The reduction procedure is described later.

Paranal.—The cloud sensor installed at Paranal determines the sky condition by measuring the flux variation of a star. The sensor graph will suggests a possible cloudy condition when the rms of the flux variation is larger than 0.02.[10]

Nanshan.—For Nanshan, the operation log is used to verify the sky condition. The operation log includes the image sequence log and observer's notes. We divide each night into two parts: evening and morning. A part with roughly $>50\%$ observable time (with images taken and indication of good observing condition from the observer) would be marked as clear; otherwise, it would be marked as cloudy.

[10] See http://archive.eso.org/asm/ambient-server.

Lulin.—A diffraction-limited Boltwood loud Sensor is installed at Lulin to produce sequence observations. The cloud sensor determines the sky condition by comparing the temperature of the sky with ambient ground-level temperature, and a difference threshold of -25°C is set to distinguish clear and cloudy conditions.[11]

4. EVALUATION

4.1. Evaluation of Cloud Cover Forecast

The preliminary result from our companion study suggests that roughly 70% of cloud cover forecasts from the GFS model can achieve an error of less than 30% (Ye & Chen 2010) at 0 hr $< \tau \leq 72$ hr at the grid with spacing of ~300 km. However, the cloud cover observations used in this study are all made at *single geographic points* and are *categorical* (either clear or cloudy), rather than over a grid area and being quantitative. So in order to make comparison between the forecasts and the observations, we first need to simplify the forecast into two categories by setting a spatial threshold that divides cloudy and clear situations. To examine the result sensitivity with different thresholds, we set the threshold at 30%, 50%, and 80%, respectively. Considering that most astronomical observatories are placed at areas with higher chances of being clear rather than cloudy, we should focus on the cloudy event in our study, rather than on the clear event. Thus, the cloudy event is set to be the "yes" statement, and clear is set to be the "no" statement.

We use four indicators to evaluate the performance of the forecast:[12] proportion of perfect forecasts (PPF), probability of detection (POD), false alarm rate (FAR), and frequency bias index (FBI). Let H denote hits (forecasted and observed), let F denote false alarms (forecasted but not observed), let M denote missed (not forecasted but observed), and let Z denote not-forecasted and not-observed situations; we then have

$$\mathrm{PPF} = \frac{H+Z}{H+F+M+Z},$$

$$\mathrm{POD} = \frac{H}{H+M},$$

$$\mathrm{FAR} = \frac{F}{F+Z},$$

and

$$\mathrm{FBI} = \frac{H+F}{H+M}.$$

[11] See http://www.cyanogen.com/downloads/files/claritymanual.pdf.

[12] A more detailed technical document about the application of these four indicators in meteorology may be found at http://www.ecmwf.int/products/forecasts/guide/Hit_rate_and_False_alarm_rate.html.

TABLE 6
MEAN DIFFERENCE AND RMSE OF SEEING FORECAST FOR SAMPLE SITES

Site	Entire atmosphere mean difference[a]	RMSE	Sample n	Free atmosphere mcean difference[a]	RMSE	Sample n
Paranal	−0.09″	0.36″	3630	…	…	…
Mauna Kea	−0.15″	0.26″	34	−0.32″	0.42″	42
San Pedro Mártir	+0.01″	0.45″	326	−0.10″	0.22″	118
Cerro Tololo	…	…	…	−0.24″	0.34″	640
Cerro Armazones	+0.20″	0.34″	776	−0.18″	0.27″	878
Cerro Pachón	+0.46″	0.50″	738	−0.14″	0.27″	928
Cerro Toloncharn	+0.29″	0.40″	298	−0.26″	0.33″	92

[a] Calculated by the mean of forecast minus the mean of observation.

The H, F, M, and Z numbers for each of the three sites are listed in Table 4, and the comparison results between the forecast and observation are shown in Table 5.

As theresult from our companion study has implied that the accuracy declination with the increase of τ is small (rms error [rmse] varies within 5% for τ up to 72 hr) for the GFS model, we see no need to list percentages for each night separately. The percentages given in Table 5 are the average of 0 hr $< \tau \leq 72$ hr, where the uncertainty ranges are denoted by the nights with highest/lowest percentages. The large uncertainty of the FBI of Paranal is caused by small dominators, since the number of false alarms is 5–10 times higher than the number of misses.

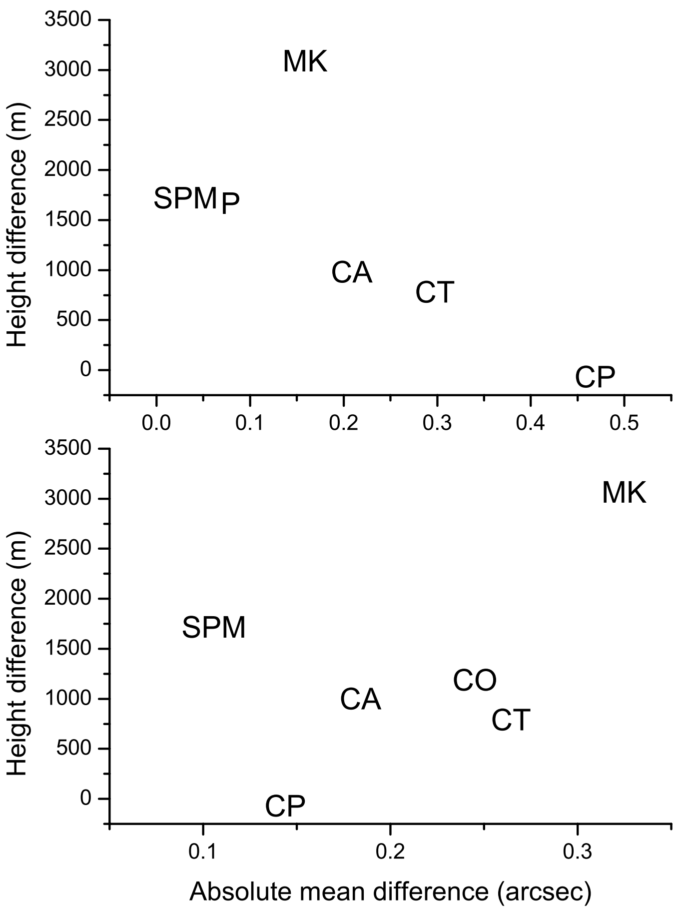

FIG. 1.—Absolute forecast mean errors and the height differences between actual height and GFS grid for all sites for entire atmosphere (*top*) and free atmosphere (*bottom*). Abbreviations are P—Paranal, SPM—San Petro Mártir, MK—Mauna Kea, CO—Cerro Tololo, CA—Cerro Armazones, CT—Cerro Toloncharn, and CP—Cerro Pachón.

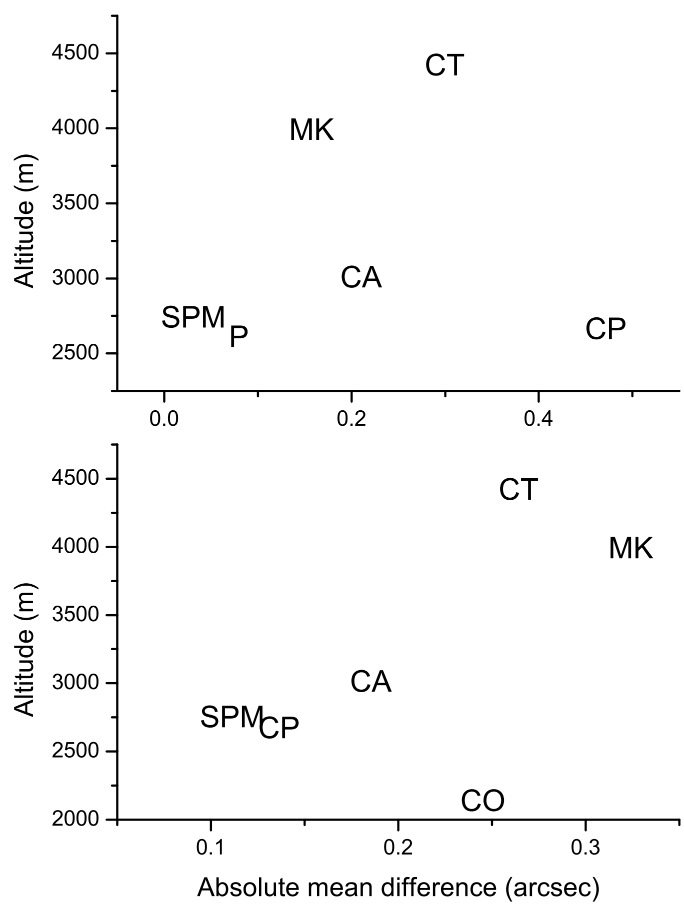

FIG. 2.—Absolute forecast mean error and the altitude of the site for all sites with DIMM observation (*top*) and MASS observation (*bottom*). Abbreviations are P—Paranal, SPM—San Petro Mártir, MK—Mauna Kea, CO—Cerro Tololo, CA—Cerro Armazones, CT—Cerro Toloncharn, and CP—Cerro Pachón.

Although PPF is a biased score, since it is strongly influenced by the more common category, it gives a rough indication about the typical percentage of correct forecasts for one site. A clear feature revealed by Table 5 is the climate dependence of the PPF: arid sites tend to have higher PPF, while humid sites tend to have lower. Generally speaking, the PPF varies from 50% to 85% for the three sites in our sample. As the sites have covered both the extremes of climate type (from arid and humid), it can be considered that this result is relatively representative.

The result revealed by POD is also encouraging. Even for Paranal, the site with an annual cloudy percentage as low as 10% (Ardeberg et al. 1990), the POD can still vary between 20 and 60%, which is better than the 15–25% percentage reported by (Erasmus & Sarazin 2001). We also note that the forecast FAR for Paranal and Nanshan is less than half of the forecast POD, which is far below the human-participated forecasts (for reference, the MKWC forecaster, which can reach a FAR as low as 1%[13]), but is still reasonable for a basic observing reference. We note that the forecast FAR for Lulin is very large; however, considering that Lulin is surrounded by a very complex terrain, where the elevation variation in its assigned grid box is as large as 3500 m, it is not unexpected for a nonideal FAR. Finally, the FBIs for all sites are larger than 1, suggesting the GFS model tends to make more false alarms rather than misses.

4.2. Evaluation of Seeing Forecast

The evaluation of the seeing forecast is relatively easier than that of cloud cover forecast, since the forecasts and observations are in the same definition, and we can simply compare the mean and rmse of the difference between the forecasts and observations (Table 6). The mean errors are computed by averaging the differences between instantaneous forecasts and observations. As the increase of error is small (Δrmse $< \sim 0.05''$) for τ up to 72 hr, we combine forecasts and observations from all three nights into a whole for our study.

As shown in Table 6, either the entire-atmosphere forecast or free-atmosphere forecast has moderate error, compared with the observation; the former tends to slightly overestimate the value and the latter tends to underestimate the value. However, the tendency is severe for the cases such as Cerro Pachón, for which the mean difference reads $+0.46''$. A possible explanation is that many observatories are located in mountainous areas and are actually much higher than the height of their assigned grids in GFS models (the height differences vary from 0–4000 m among our sample, as shown in Table 3); this may produce error in PBL seeing estimation. However, we find no substantial support for this assumption, as there is no significant tendency between the forecast bias and the height difference (Fig. 1). Dramatically, the site with the smallest height difference (Cerro Pachón, with a height difference of 9 m) has the largest mean error ($+0.46''$).

[13] See http://mkwc.ifa.hawaii.edu/forecast/mko/stats/index.cgi?night = 1& fcster = fcsts&var = fog&cut = 2.

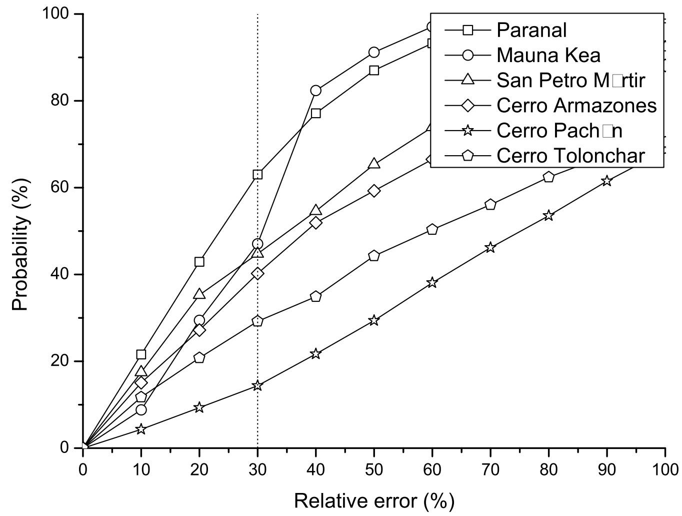

FIG. 3.—Cumulative distribution of relative error of seeing forecast for ground layer plus free atmosphere. Dashed line represents a relative error of 30%. The probability of $<30\%$ forecast error is 63% for Paranal, 47% for Mauna Kea, 45% for San Pedro Mártir, 40% for Cerro Armazones, 14% for Cerro Pachón, and 29% for Cerro Tolonchar. The Mauna Kea curve is quite abnormal, due to the small sample number ($n = 34$), and we estimate that the $<30\%$ forecast error probability is about 15% too low.

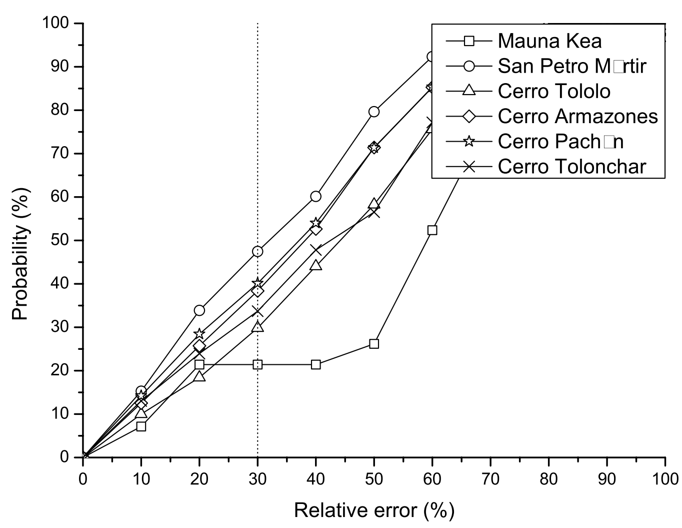

FIG. 4.—Cumulative distribution of relative error of seeing forecast for free atmosphere only. Dashed line represents a relative error of 30%. The probability of $<30\%$ forecast error is 21% for Mauna Kea, 47% for San Pedro Mártir, 30% for Cerro Tololo, 38% for Cerro Armazones, 40% for Cerro Pachón, and 34% for Cerro Tolonchar. The Mauna Kea curve is quite abnormal, due to the small sample number ($n = 42$), and we estimate that the $<30\%$ forecast error probability is about 15% too low.

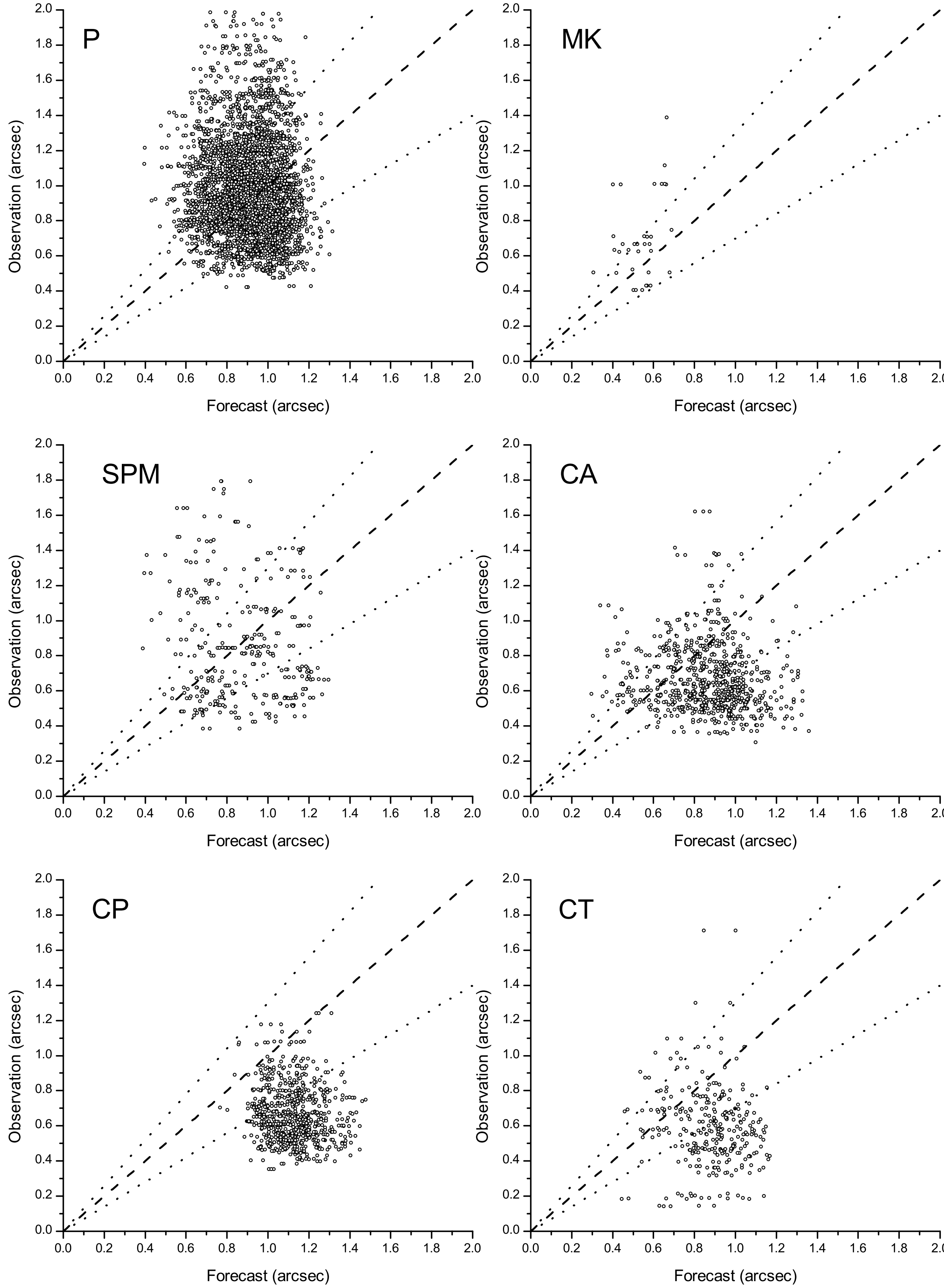

FIG. 5.—Forecast-by-observation figure of entire-atmosphere seeing forecast for Paranal (P), Mauna Kea (MK), San Pedro Mártir (SPM), Cerro Armazones (CA), Cerro Pachón (CP), and Cerro Tolonchar (CT). Dashed line corresponds to the ideal case (slope = 1), and dotted lines are 30% error uncertainty from the ideal case.

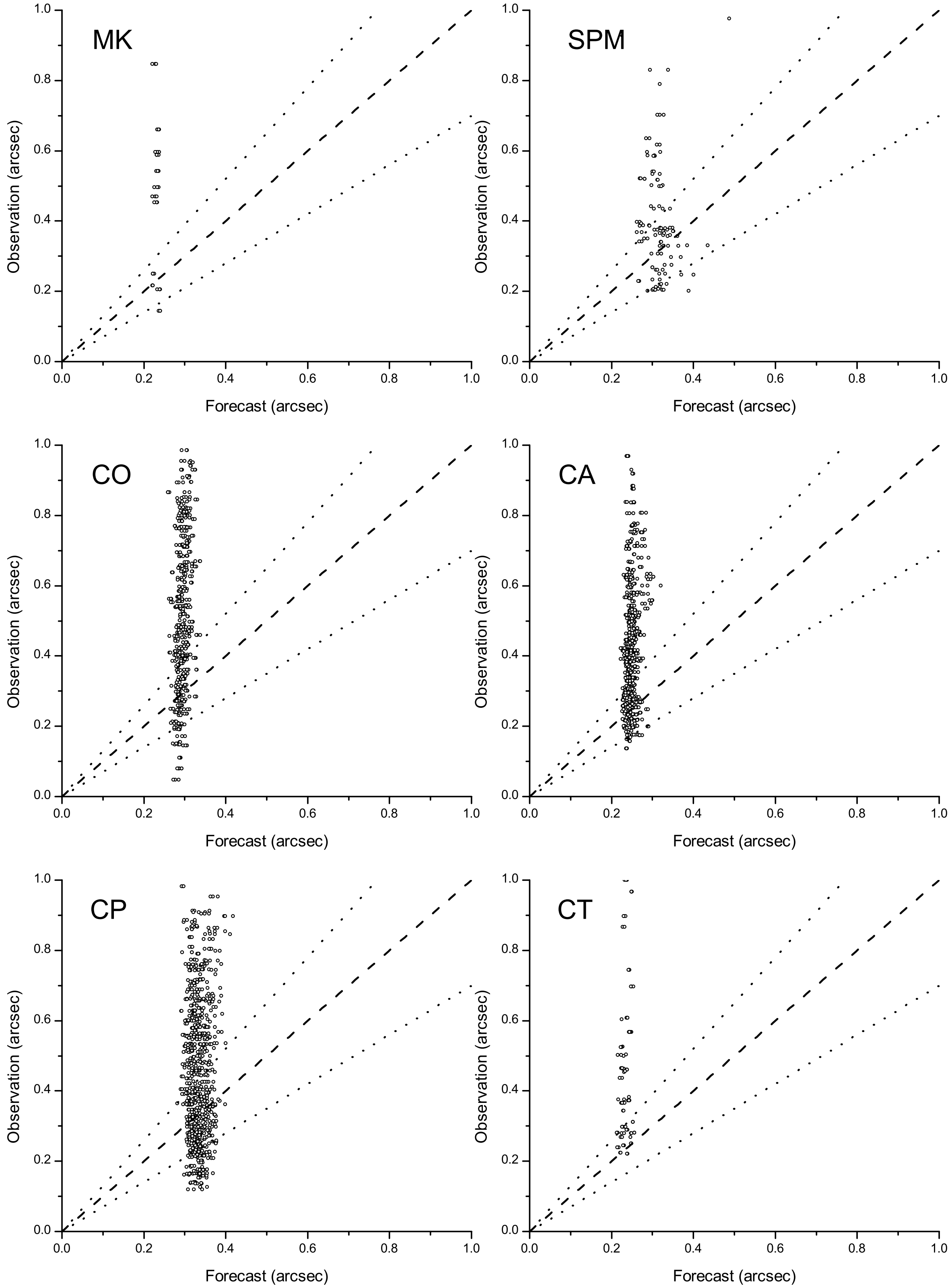

FIG. 6.—Forecast-by-observation figure of free-atmosphere seeing forecast for Mauna Kea (MK), San Pedro Mártir (SPM), Cerro Tololo (CO), Cerro Armazones (CA), Cerro Pachón (CP), and Cerro Tolonchar (CT). Dashed line corresponds to the ideal case (slope = 1), and dotted lines are 30% error uncertainty from the ideal case.

TABLE 7
COMPARISON BETWEEN THE GFS/AXP MODEL VERSUS SEVERAL OTHER MAJOR SEEING MODELS

Model	Forecast lead time	RMSE	$<30\%$ error probability
GFS/AXP	1–3 nights	0.26″–0.50″	Mostly 40–50%
Original AXP[a]	Simultaneous	0.48″	~58%
Vernin-Tatarski[a]	Simultaneous	…	30%
C_N^2 median[a]	Simultaneous	…	41%
Seeing median[a]	Simultaneous	…	45%
Seeing mean	Simultaneous	…	41%
MKWC Forecaster[b]	1–3 nights	0.25″–0.30″	~50%?
MKWC WRF[c]	1 night	0.36″	~50%?[d]

[a] The values of these models are taken from the work of Trinquet & Vernin (2006).
[b] See http://mkwc.ifa.hawaii.edu/forecast/mko/stats/index.cgi?night=1&fcster=fcsts&var=seeing&cut=2.
[c] See http://mkwc.ifa.hawaii.edu/forecast/mko/stats/index.cgi?night=1&fcster=wrf&var=seeing&cut=2.
[d] The probabilities of forecast with $<30\%$ error for the cases of the MKWC forecaster and MKWC WRF model are estimated manually from the plots generated on the MKWC website.

Another equally plausible explanation is the combined effect of the poor consistency between the GFS/AXP model versus the actual C_N^2 variance in PBL and error induced by the layer degeneration of the AXP model for high-altitude areas. In fact, we do find a weak-bias tendency for the free-atmosphere forecast, as shown in Figure 2; the forecast for low-altitude sites tends to be better, and all sites below 3000 m have an absolute mean forecast error below 0.25″. This feature fits the fact that the airborne data used to determine the coefficients in the AXP model only include sites with altitudes up to 2835 m. But generally speaking, no substantial correlation between bias tendency and a unique geographic modeling factor can be identified; therefore, we can only suggest that the bias is caused by a combination effect of some factors.

To give a more comprehensive understanding of the quality of the GFS/AXP forecast, we plot the cumulative distribution of the relative forecast error for each site in Figure 3 (forecast for the entire atmosphere) and Figure 4 (forecast for the free atmosphere only). Let $\hat{\epsilon_0}$ be the forecasted seeing value and let ϵ_0 be the observed seeing value; the relative forecast error $E(\epsilon_0)$ is then calculated by

$$E(\epsilon_0) = \frac{|\hat{\epsilon_0} - \epsilon_0|}{\epsilon_0}.$$

From Figures 3 and 4, we can identify that the probabilities of producing forecast with $<30\%$ error concentrate in 40–50% for the entire-atmosphere seeing forecast and 30–50% for the free-atmosphere seeing forecast. By contrast, Trinquet & Vernin (2006) gave a probability of 58% and 50% for the original AXP model to produce an entire-atmosphere or free-atmosphere forecast with the same quality. Generally speaking, our result is in rough agreement with theirs, although the model's performance is rather unsatisfying on a few particular sites.

In addition to the summarizing table and cumulative distribution figures, we also present the forecast-observation distributions for each site in Figure 5 and Figure 6. We can see that although the statistical values might be satisfying, the forecast-observation distribution figures imply that the correlation between forecast and observation is poor. This is not unexpected, since the study of Cherubini et al. (2009) at MKWC has suggested that one may achieve a good approximation of the actual condition with ~80 vertical layers up to 10 hPa, and so the ~15 layers used in our model may be far from sufficient for a well-correlated distribution. Our assumption is reinforced by the fact that forecasts for free-atmosphere seeing are generally concentrated in a narrow region, despite their mean being close to that of the observation, as shown in Figure 6. This phenomenon implies that turbulence over the subkilometer scale in the vertical direction might be the major contributor to a bad seeing condition in the free-atmosphere region.

Finally, we compare our result with several major models/forecasters (Table 7). The rmse and $<30\%$ error probabilities for the original AXP model, Vernin-Tatarski model, C_N^2/seeing median, and seeing mean are derived by Trinquet & Vernin (2006) with their experimental profile observations. The MKWC Weather Research and Forecasting (WRF) model is initiated with the GFS model output, but the simulation eventually derives output with a final grid spacing of 1 km and a vertical layer number of 40, resulting in a forecast rmse at 0.36″ for the first night. As revealed by Table 7, the rmse uncertainty ranges of GFS/AXP model fall between the mean of MKWC forecaster and the original AXP model, while the $<30\%$ error probability is in the better cluster in all models under most cases. Interestingly, a direct comparison of the GFS/AXP model with the MKWC forecaster over the seeing forecast for the same site (Mauna Kea) even slightly favors the former (0.26″ versus 0.28″ for three-night mean). In short, this result has highlighted the potential of the GFS/AXP model to be a competitive forecast tool once the layer degeneracy and high-altitude issues are solved.

5. CONCLUSION

We have carried out a comprehensive study over the topic of performing automatic numeric forecast of cloud cover and atmospheric seeing with the Global Forecast System, an operational global model. Sequence observations on cloud cover and atmospheric seeing from nine sites from different regions of the world with different climatic backgrounds in the period from 2008 January to 2009 December are used to evaluate the forecast. Although the performance of the model forecast may not be comparable with the human-participated forecast, our study has shown the forecast to be acceptable for a basic observing reference. Our study has also revealed the possibility of gaining better performance from the model with additional efforts on model refinement.

For the cloud cover forecast, we have found that the proportion of perfect forecasts varies from ~50% to ~85% for all three sites we evaluated, including a site located in a subtropical region with a very humid climate (Lulin). In particular, we have found that the model is capable of detecting a significant amount of occurring clouds, and the false alarm rate is moderate. The probability of detection is still measured to be 20–60%, even for sites with very low cloud probability (Paranal).

For the atmospheric seeing forecast, we adopted the AXP model introduced by Trinquet & Vernin (2006). We found that the forecast for the entire atmosphere tends to slightly overestimate the seeing, while the free-atmosphere forecast tends to underestimate it. The rmse for free-atmosphere seeing is smaller (0.22″–0.42″) than that of the entire atmosphere (0.26″–0.50″), but both values can indicate a decent quality of the forecast, compared with the other major models. Further analysis suggests that a major contributor to the forecast error might be the layer degeneracy issue of the hybrid GFS/AXP model. On the other hand, the probability of GFS/AXP forecasts with <30% error varies between 40–50% for the entire-atmosphere forecast and 30–50% for free-atmosphere forecast in most cases, which is in the better cluster among major seeing models. To conclude, our study has suggested a decent performance of the GFS/AXP model that is suitable for basic observing reference. Our study has also suggested that the model has the potential to become a rather useful forecast tool with additional efforts on model refinement.

The author wishes to thank all the people who have given help to this work, particularly to an anonymous reviewer for very constructive comments that led to an advance of this work and to Sisi Chen, Shaojia Fan, Linjiong Zhou, and Johnson Lau for their help from various aspects. The author is very grateful to Chenzhou Cui on behalf of the Large Sky Area Multi-Object Fibre Spectroscopic Telescope (LAMOST) team at National Astronomical Observatory, Chinese Academy of Sciences, who made this work possible by providing excellent long-term resources of server and computing for our 7Timer system since 2005. The author also wishes to thank Mount Nanshan Xingming Observatory, National Central University Lulin Observatory, Cerro Tololo Inter-American Observatory, European Southern Observatory, and the Thirty Meter Telescope (TMT) Site Testing Project for providing and/or granting permission to access and use the astrometeorological observation data from Mount Nanshan, Lulin, Cerro Pachón, Paranal, and the TMT test sites. In addition, the author would like to thank Xing Gao (No. 1 Senior High School of Ürümqi/Xingming Observatory), Hung-Chin Lin (National Central University/Lulin Observatory), Andrei Tokovinin (Cerro Tololo Inter-American Observatory), Edison Bustos (Cerro Tololo Inter-American Observatory), and Felipe Daruich (Gemini Observatory) for providing assistance with obtaining the observational data.

REFERENCES

Abahamid, A., et al. 2004, A&A, 422, 1123
Ardeberg, A., Lundstrom, I., & Lindgren, H. 1990, A&A, 230, 518
Businger, S., McLaren, R., Ogasawara, R., Simons, D., & Wainscoat, R. J. 2002, Bull. Am. Meteorol. Soc., 83, 858
Cherubini, T., Businger, S., & Lyman, R. 2009, in Optical Turbulence: Astronomy Meets Meteorology, Proc. Optical Turbulence Characterization for Astronomical Applications (Hackensack: World Scientific, 196
Coulman, C. E. 1985, ARA&A, 23, 19
Coulman, C. E., André, J.-C., Lacarrère, P., & Gillingham, P. R. 1986, PASP, 98, 376
Coulman, C. E., Vernin, J., Coqueugniot, Y., & Caccia, J.-L. 1988, Appl. Opt., 27, 155
Danko, A. 2003, S&T, 105, 62
Erasmus, D. A., & Sarazin, M. 2001, Proc. SPIE, 4168, 317
Fried, D. 1965, J. Opt. Soc. Am., 55, 1427
Fuentes, F. J., & Muñoz-Tuñon, C. 1990, Ap&SS, 171, 267
Li, S.-X., Fu, Y.-F., Huang, Y.-L., Li, J.-G., & Mao, J.-T. 2003, Acta Astron. Sinica, 44, 431
Murtagh, F., Assem, A., & Sarazin, M. 1995, PASP, 107, 702
Roddier, F. 1981, Prog. Opt., 19, 281
Rutledge, G. K., Alpert, J., & Ebuisaki, W. 2006, Bull. Am. Meteorol. Soc., 87, 327
Sela, J. 1980, Mon. Weather Rev., 108, 1279
Schöck, M., et al. 2009, PASP, 121, 384
Tatarski, V. I. 1961, Wave Propagation in a Turbulent Medium (New York: Dover)
Tokovinin, A. 2002, PASP, 114, 1156
Trinquet, H., & Vernin, J. 2006, PASP, 118, 756
Walker, M. F. 1970, PASP, 82, 672
Whitaker, J. S., Hamill, T. M., Wei, X., Song, Y., & Toth, Z. 2008, Mon. Weather Rev., 136, 463
Xu, K.-M., & Randall, D. A. 1996, J. Atmos. Sci., 53, 3084
Yang, F., Pan, H.-L., Moorthi, S., Lord, S., & Krueger, S. 2005, in Proc. Fifteenth ARM Science Team Mtg., 1, http://www.arm.gov/publications/proceedings/conf15/extended_abs/yang_f.pdf
Ye, Q.-Z., & Chen, S.-S. 2010, J. Atmos. Sci., submitted

Volume Title
ASP Conference Series, Vol. **Volume Number**
Author

Recent Progress of Cepheid Research at National Central University: From *Spitzer* to *Kepler*

Chow-Choong Ngeow

National Central University, 320 Jhongli City, Taoyuan Country, Taiwan

Abstract.
In this presentation I summarize recent work on Cepheid research carried out at the National Central University. The mid-infrared period-luminosity (P-L) relations for Cepheids are important in the *James Webb Space Telescope* era for distance scale work, as the relations have potential to derive the Hubble constant within ∼ 2% accuracy – a critical constraint in the precision cosmology. Consequently, we have derived the mid-infrared P-L relations for Cepheids in the Large and Small Magellanic Clouds, using archival data from the *Spitzer Space Telescope*. *Kepler Space Telescope* is a NASA mission to search for Earth-size and larger planets around Sun-like stars, by observing continuously the stars in a dedicated patch of the sky. As a result, the almost un-interrupted observation is also used for stellar variability and asteroseismological study. However, *Kepler* observations are carried out with a single broad-band filter, hence ground-based follow-up observation needed to complement *Kepler* light curves to fully characterize the properties of the target stars. Here I present the ground-based optical follow-up observations for two Cepheid candidates located within the *Kepler's* field-of-view. Together with *Kepler* light curves, our ground-based data rule out V2279 Cyg being a Cepheid. Hence V1154 Cyg is the only Cepheid in the *Kepler's* field.

1. Introduction

Classical Cepheid variables (hereafter Cepheids) are post main-sequence yellow supergiants. Cepheid masses range from $\sim 3M_\odot$ to $\sim 11M_\odot$ with surface temperatures between $\sim 5000K$ to $\sim 6500K$. Cepheids obey the period-mean density relation, hence their pulsating periods ($1 < P < 100$, where P is period in days) are well correlated with luminosity. This is known as the period-luminosity (P-L) relation, also referred as the Leavitt Law, commonly written in the form of $M_\lambda = a_\lambda \log(P) + b_\lambda$ or $m_\lambda = a_\lambda \log(P) + b_\lambda$. Since Cepheids are evolved pulsating stars, they are ideal laboratories for testing the stellar pulsation and evolution theories. The Cepheid P-L relation is an important rung in the cosmic distance scale ladder that can be used to calibrate a host of secondary distance indicators (for examples, the Tully-Fisher relation, peak brightness of Type Ia supernovae and surface brightness fluctuations). These secondary distance indicators, located well within the Hubble-flow, can then be used to measure one of the most important parameter in modern cosmology – the Hubble constant.

In this proceeding, I will present some recent progress on Cepheid research carried out at the National Central University (NCU), that focused on the following two topics: (a) derivation of the mid-infrared Cepheid P-L relations based on archival data from *Spitzer* observations; and (b) investigation of potential Cepheids located within the *Kepler* field using ground-based follow-up data.

2. Derivation of the Mid-Infrared Cepheid P-L Relation Using *Spitzer* Archival Data

In the era of precision cosmology, it is desirable to independently derive an accurate Hubble constant, This is because degeneracy exists in CMB (cosmic microwave background) anisotropies between the flatness of the Universe and the Hubble constant. Therefore, as stated in Hu (2005):

> "... to test the cosmological constant hypothesis and measure the equation of state of the dark energy at $z \sim 0.4$ - 0.5, the best complement to current and future CMB measurements is a measurement of the Hubble constant that is accurate at the few percent level."

Furthermore, Figures 23 and 24 from Macri et al. (2006) clearly illustrate the improved precision of measured dark energy parameters when the accuracy of Hubble constant is increased. Current systematic errors of Hubble constant measurements based on optical data, using the Cepheid P-L relation as first rung of the distance scale ladder, is $\sim$ 5% to $\sim$ 10% (see the review given in Freedman & Madore 2010). In the near future, it is possible to reduce the systematic error of Hubble constant to $\sim$ 2% from mid-infrared observations from the *Spitzer* and/or next generation *James Webb Space Telescope (JWST)* (Freedman & Madore 2010), taking huge advantage of the fact that extinction is negligible in the mid-infrared (Freedman et al. 2008; Ngeow & Kanbur 2008; Ngeow et al. 2009; Freedman & Madore 2010). The first step toward this goal is to derive and calibrate the Cepheid P-L relation in the mid-infrared.

2.1. The IRAC Band P-L Relations

Prior to 2008, the longest available wavelength for the Cepheid P-L relation is in the *K* band. In 2007, archival data from SAGE (Surveying the Agents of a Galaxy's Evolution) was released, where SAGE is one of the *Spitzer* Legacy programs that map out the Large Magellanic Cloud (LMC) in *Spitzer* IRAC bands[1] (and MIPS bands, see Meixner et al. 2006). Hence, mid-infrared Cepheid P-L relations can be derived by matching the known LMC Cepheids to the SAGE catalog – this has resulted two papers published in 2008 (Freedman et al. 2008; Ngeow & Kanbur 2008). Both papers utilized the SAGE Epoch 1 data matched to different samples of LMC Cepheids: Freedman et al. (2008) matched to $\sim$ 70 Cepheids from Persson et al. (2004) while Ngeow & Kanbur (2008) used the OGLE-II Catalog (Optical Gravitational Lensing Experiment, Udalski et al. 1999) that includes $\sim$ 600 LMC Cepheids.

After the release of SAGE Epoch 1 and 2 data, the IRAC band LMC P-L relations have been updated in Madore et al. (2009) and Ngeow et al. (2009) by averaging the two epochs photometry. Ngeow et al. (2009) also included the $\sim$ 1800 LMC Cepheids from the latest OGLE-III Catalog (Soszynski et al. 2008, with $\sim 3\times$ more Cepheids than OGLE-II Catalog). In addition to LMC, IRAC band P-L relations have also been

[1] The IRAC bands include 3.6μm, 4.5μm, 5.8μm and 8.0μm bands.

derived for SMC Cepheids (see Ngeow & Kanbur 2010, for details) using the publicly available SAGE-SMC data. Finally, IRAC band P-L relations for a small number of Galactic Cepheids that possess independent distance measurements have been presented by Marengo et al. (2010). All together, there are six sets of IRAC band P-L relations for Cepheids in our Galaxy and in Magellanic Clouds. Slopes of these P-L relations are summarized in Figure 1.

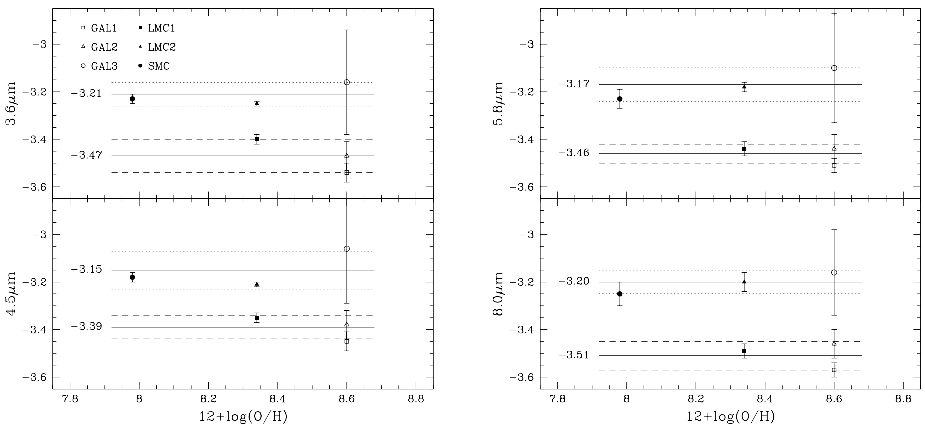

Figure 1. Slopes of the empirical IRAC band P-L Relations from three galaxies. GAL1 and GAL2 were derived from Galactic Cepheids with infrared surface brightness distances using the "old" and "new" *p*-factor, respectively; while GAL3 was based on 8 Galactic Cepheids with *HST* parallax measurements (for more details, see Marengo et al. 2010). LMC1 and LMC2 are the empirical LMC P-L slopes from Madore et al. (2009) and Ngeow et al. (2009), respectively. SMC P-L slopes are adopted from Ngeow & Kanbur (2010). These P-L slopes can be grouped into the "shallow" slopes and "steep" slopes. The Horizontal dashed lines represent the averaged slopes in these two groups, with the values given on the left of these lines. The dashed and dotted lines are the 1σ boundary of the averaged values for the slopes in these two groups, where σ is the standard deviation of the mean values.

As mentioned in Ngeow & Kanbur (2010), these six sets of P-L slopes can be grouped into two groups: one group with "shallow" slopes around −3.18, and another group with "steeper" slopes around −3.46. The expected IRAC band P-L slope can be calculated from $L_\lambda = 4\pi R^2 B_\lambda(T)$, hence $M_{\mathrm{IRAC}} = -5 \times a_R \log(P) + a_T \log(P) +$ constant (where $a_R = 0.68$ is the slope of period-radius relation taken from Gieren et al. 1999). If assumed $B_\lambda(T)$ is constant at long wavelength, then the expected P-L slops is $-5 \times 0.68 = -3.40$. On the other hand, due to Rayleigh-Jean approximation, $B_\lambda(T) \propto T$ at the IRAC band wavelength, then $a_T \sim 0.18$ estimated from color-temperature conversion (for details, see Neilson et al. 2010), the expected P-L slope becomes $-5 \times 0.68 + 0.18 = -3.22$. Both of these expected slopes are close to the averaged slopes in the observed "steep" and "shallow" groups. Finally, these empirical P-L slopes were compared to the slopes from synthetic P-L relations, based on theoretical pulsational models with varying metallicity, in Figure 2. Details of these synthetic P-L relations will be given elsewhere (Ngeow et al. – in preparation). The trends of synthetic P-L slopes with $12 + \log(O/H) > 7.9$ appear to be in agreement to the empirical slopes given in "shallow" group.

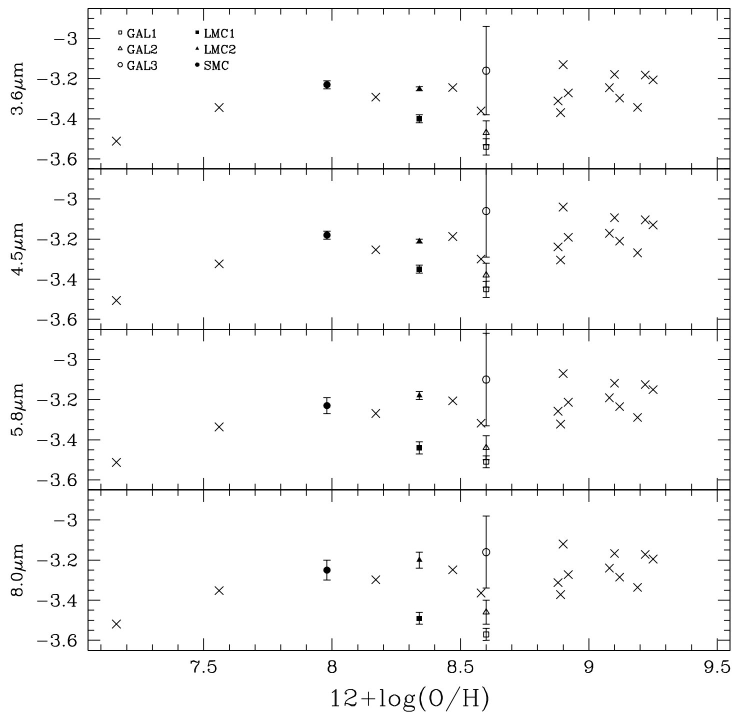

Figure 2. Comparison of the six sets of empirical IRAC band P-L slopes to the synthetic P-L slopes from theoretical models (crosses).

3. Ground-Based Light Curves for Cepheids Located Within *Kepler* Field-Of-View

Kepler is a NASA space mission to search for Earth-like exo-planets using the transit method. Hence, the field-of-view for *Kepler*, with $\sim$ 105deg^2, is constantly pointing toward 19^h22^m:$+44^o30'$. In addition to searching for exo-planets, light curve data from almost un-interrupted observations from *Kepler* are also very useful and valuable for asteroseismic and stellar variability study. Therefore, a consortium called *Kepler* Asteroseismic Science Consortium (KASC)[2] was formed. KASC consists of 14 working groups (WG), and WG7 is dedicated to Cepheids study with *Kepler* data.

Since Cepheids are radially pulsating variable stars with periods longer than a day, it is not necessary to continuously monitor Cepheids in a given night or from different observatories across the globe. These multiple-site observing campaigns, on the other hand, have been practiced for other kinds of variable stars such as short period delta-Scuti stars to investigate, for example, various pulsating modes of these stars. Continuous photometry from *Kepler*, however, offers a great opportunity to study the possible non-radial pulsating modes as suggested by theory (Mulet-Marquis et al. 2007), or even stochastically excited modes, in Cepheids. However, *Kepler* observations are conducted

[2] `http://astro.phys.au.dk/KASC/`

in a customized broad-band filter, and complementary ground-based multi-color photometric and spectroscopic follow-up observations are needed for the Cepheid candidates located within the *Kepler* field-of-view. Detailed investigation of these candidates using both of the *Kepler* light curves and ground-based follow-up data can be found in Szabo et al. (2011), only a brief overview will be presented in this proceeding.

3.1. *BVRI* Follow-Up Observations for Selected Cepheid Candidates

Prior to the launch of *Kepler*, V1154 Cyg was the only Cepheid located in *Kepler's* field, while V2279 Cyg was a strong Cepheid candidate. Several other Cepheid candidates were also selected based on the *Kepler* Input Catalog or other variable stars catalogs (Szabo et al. 2011). Ground-based *BVRI* follow-up observations for these Cepheid candidates were carried out at Lulin Observatory (located at central Taiwan) and Tenagra II Observatory (located in Arizona, USA), mostly from March to August 2010. The author is responsible for the observations from these two observatories, where the telescopes and CCD used are listed in Table 1. Figure 3 shows the distributions of $FWHM$ in *BVRI* band images taken from these telescopes. Data reductions were done based on the following steps:

Table 1. Characteristics of telescopes and CCD for the *BVRI* follow-up observations.

Tel. Abbreviation	Observatory	Aperture [m]	CCD	Pixel Scale ["/pix]
LOT	Lulin Obs.	1.0	PI-1300B	0.52
SLT	Lulin Obs.	0.4	Apogee U9000	0.99
TNG	Tenagra II Obs.	0.8	STIe	0.86

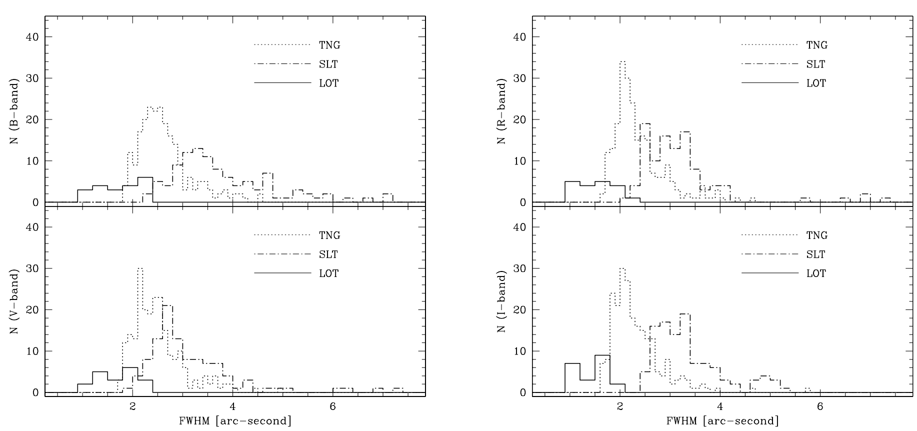

Figure 3. Histograms of the $FWHM$ distributions in *BVRI* bands, separated by the telescopes used.

1. Images were bias-subtracted, dark-subtracted and flat-fielded using *IRAF*[3]. Fringe corrections were applied to the *I* band images from LOT.

2. Astrometric corrections were performed using `astrometry.net` (Lang et al. 2010) and `SCAMP` (Bertin 2006).

3. Instrumental magnitudes were extracted from the images using `SExtractor` (Bertin & Arnouts 1996). These magnitudes were based on `MAG_AUTO` aperture photometry.

4. Observations from Tenagra II Observatory on 12 May 2010 included the Landolt standard fields (Landolt 2009). Instrumental magnitudes from this night were calibrated to the standard magnitudes.

5. Photometry from other nights were relatively calibrated using the calibrated magnitudes from 12 May 2010.

The resulted *BVRI* light curves for two of the candidates, V1154 Cyg and V2279 Cyg, are presented in Figure 4. Additional data were available from Sonoita Research Observatory[4] (Szabo et al. 2011).

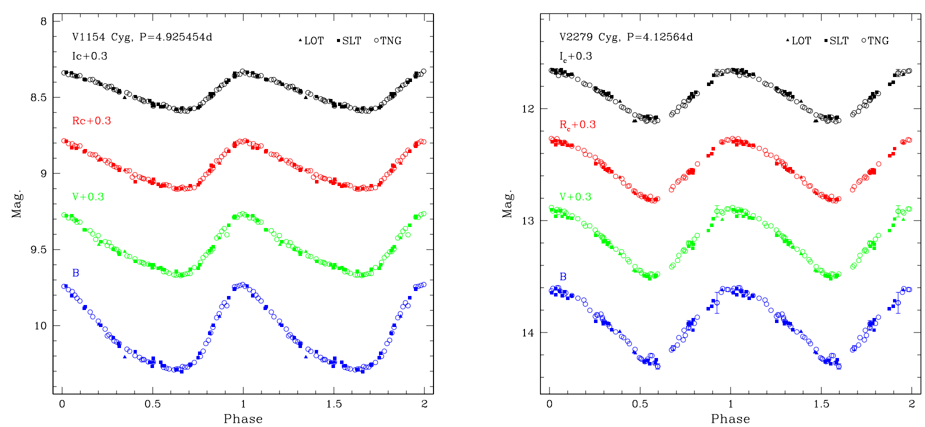

Figure 4. Calibrated *BVRI* light curves for V1154 Cyg (left panel) and V2279 Cyg (right panel). Each light curves contain more than 70 data points.

Light curves of V1154 Cyg from *Kepler* observations resemble a typical sawtooth shape of a Cepheid's light curve (see Figure 4 in Szabo et al. 2011). Frequency analysis of almost continuous *Kepler* light curves for this variable showing a strong peak at the fundamental frequency, with other detectable harmonics in the spectrum (see Figure 12 in Szabo et al. 2011). This suggests that V1154 Cyg pulsates radially in a regular

[3] *IRAF* is distributed by the National Optical Astronomy Observatories, which are operated by the Association of Universities for Research in Astronomy, Inc., under cooperative agreement with the National Science Foundation.

[4] Observations and the data reduction from Sonoita Research Observatory have been taken care by A. Henden.

fashion, without any non-radial or stochastic modes. The *BVRI* light curves of V1154 Cyg also strongly support the Cepheid nature of this variable. Fourier parameters (R_{i1} and ϕ_{i1}), based on the V band light curve, of this Cepheid also fall within the distributions defined by Galactic Cepheids. The phase lag from V band light curve and radial velocity curve confirms that V1154 Cyg is a fundamental mode Cepheid.

Even though the *BVRI* band light curves for V2279 Cyg mimic the light curve of a first overtone Cepheids, Fourier analysis of this variable revealed that this star is not a Cepheid. Furthermore, flares show up in *Kepler* light curves, and the light curve morphology is in agreement with rotational modulation. Additional spectroscopic follow-up observations confirmed that this variable is not a Cepheid. Cepheid nature of other candidates has been ruled out based on *Kepler* light curves and/or *BVRI* light curves, and V1154 Cyg remains the only Cepheid located within the *Kepler's* field.

4. Conclusion

I have presented some recent work on Cepheid research that carried out at NCU. In summary:

- Mid-infrared P-L relations will be important in near future and in *JWST* era with the potential to reduce the systematic error of Hubble constant. Consequently, P-L relations based on Cepheids in Magellanic Clouds have been derived using the archival *Spitzer* data.
- Almost continuous observation from *Kepler* is very valuable for stellar variability and pulsation study. However, ground-based follow-up observations are needed to complement *Kepler* data to fully investigate the variable stars in the *Kepler's* field. Together with *Kepler* light curves, the ground-based follow-up observations for Cepheid candidates confirmed that V1154 Cyg is the only Cepheid located within *Kepler's* field.

Acknowledgments. CCN would like to thank the support from National Science Council under the contract NSC98-2112-M-008-013-MY3. We would also like to thank the collaboration and discussion with Shashi Kanbur, Hilding Neilson, Marcella Marconi, Ilaria Musella, Michele Cignoni, Robert Szabo, Laszlo Szabados, Arne Henden and the *Kepler* Cepheid Working Group. This work is based [in part] on observations made with the *Spitzer Space Telescope*, which is operated by the Jet Propulsion Laboratory, California Institute of Technology under a contract with NASA. Funding for the *Kepler* Mission is provided by NASAs Science Mission Directorate. We acknowledge assistance of the queue observers, Chi-Sheng Lin and Hsiang-Yao Hsiao, from Lulin Observatory, which is operated by the National Central University of Taiwan, and is funded partially by the grant NSC97-2112-M-008-005-MY3. We also acknowledge the variable star observations from the AAVSO International Database contributed by observers worldwide and used in this research.

References

Bertin, E. 2006, in Astronomical Data Analysis Software and Systems XV,, edited by C. Gabriel, C. Arviset, D. Ponz, & E. Solano (San Francisco: Astronomical Society of the Pacific), vol. 351 of ASP Conference Series, 112

Bertin, E., & Arnouts, S. 1996, A&AS, 117, 393
Freedman, W., & Madore, B. 2010, Annual Review of Astronomy and Astrophysics, 48, 673
Freedman, W., Madore, B., Rigby, J., Persson, S. E., & Sturch, L. 2008, ApJ, 679, 71
Gieren, W., Moffett, T., & Barnes, T. III 1999, ApJ, 512, 553
Hu, W. 2005, in Observing Dark Energy, edited by S. C. Wolff, & T. R. Lauer (San Francisco: Astronomical Society of the Pacific), vol. 339 of ASP Conference Series, 215
Landolt, A. 2009, AJ, 137, 4186
Lang, D., Hogg, D. W., Mierle, K., Blanton, M., & Roweis, S. 2010, AJ, 139, 1782
Macri, L. M., Stanek, K. Z., Bersier, D., Greenhill, L. J., & Reid, M. J. 2006, ApJ, 652, 1133
Madore, B., Freedman, W., Rigby, J., Persson, S. E., Sturch, L., & Mager, V. 2009, ApJ, 695, 988
Marengo, M., Evans, N. R., Barmby, P., Bono, G., Welch, D. L., & Romaniello, M. 2010, ApJ, 709, 120
Meixner, M., Gordon, K., Indebetouw, R., & et al. 2006, AJ, 132, 2268
Mulet-Marquis, C., Glatzel, W., Baraffe, I., & Winisdoerffer, C. 2007, A&A, 465, 937
Neilson, H., Ngeow, C.-C., Kanbur, S., & Lester, J. 2010, ApJ, 716, 1136
Ngeow, C.-C., & Kanbur, S. 2008, ApJ, 679, 76
— 2010, ApJ, 720, 626
Ngeow, C.-C., Kanbur, S., Neilson, H., Nanthakumar, A., & Buonaccorsi, J. 2009, ApJ, 693, 691
Persson, S. E., Madore, B., Krzemiński, W., Freedman, W., Roth, M., & Murphy, D. 2004, AJ, 128, 2239
Soszynski, I., Poleski, R., Udalski, A., Szymanski, M. K., Kubiak, M., Pietrzynski, G., Wyrzykowski, L., Szewczyk, O., & Ulaczyk, K. 2008, Acta Astronomica, 58, 163
Szabo, R., Szabados, L., Ngeow, C.-C., & et al. 2011, MNRAS, 413, 2709
Udalski, A., Soszynski, I., Szymanski, M., Kubiak, M., Pietrzynski, G., Wozniak, P., & Zebrun, K. 1999, Acta Astronomica, 49, 223

Proceeding of the 2011 IEEE International Conference on Space Science and Communication (IconSpace)
12-13 July 2011, Penang, Malaysia

The Varying Universe: Participation of NCU in TAOS and Pan-STARRS1 Projects

Chow-Choong Ngeow, Wen-Ping Chen, Daisuke Kinoshita, Yi Chou and Wing-Huen Ip
Graduate Institute of Astronomy, National Central University
300, Jhongda Rd, Jhongli City, Taoyuan County 32001, Taiwan (R.O.C.)
Email: cngeow@astro.ncu.edu.tw

***Abstract*—Time-domain astronomy is an important branch in modern astrophysics, as many celestial objects exhibit variability in time. In the up-coming decade there will be a number of time-domain surveys that will produce huge volume of data available to the astronomical community. In this paper we summarize the participation of National Central University (NCU) in the research of time-domain astronomy. We focus on two projects, the TAOS project and the Pan-STARRS project, at which the NCU has involved heavily in recent years. We also present the follow-up programs for these two main projects – the optical follow-up observations of TAOS variables and the Lulin 2-Meter Telescope and 4-Color Imager aimed to follow-up the Pan-STARRS targets.**

Keywords — Optical astronomy; Time-domain astronomy; Telescope and observatory; CCD detector

I. Introduction

Time-domain astronomy is a major branch in modern astrophysics. Many objects in the Universe show a wide range of variations in time: from nearby asteroids, a large family of variable stars (including, for examples, pulsating variables, binary systems and eruptive stars) to the distant quasars. In addition, transient phenomenon such as supernova explosion and gamma-ray burst afterglow have important implication in modern cosmology. For example, the Type Ia supernova work in 1998 has led to the discovery that our Universe consists of about 76% unknown energy component called the Dark Energy ([1], [2]). In fact, massive time-domain data from multi-wavelength surveys has pushed astronomy to a new direction. Data mining of massive time-domain data can lead to new discovery and enabling new science to be explored. Some examples of the on-going and planned time-domain surveys in astronomy including the All Sky Automated Survey (ASAS, [3]), SuperMACHO ([4]), the Panoramic Survey Telescope & Rapid Response System (Pan-STARRS, [5]), the Optical Gravitational Lensing Survey (OGLE, [6]), the Palomar Transient Factory (PTF, [7]), the SkyMapper ([8]) and Large Synoptic Survey Telescope (LSST, [9]). Note that LSST has be ranked as the first priority in large scale ground-based initiatives in the up-coming decade by the Astro2010 Decadal Survey ([10]). Taiwan has a long history of involvement in time-domain astronomy. In this paper, we summarize two projects, the Taiwan-American Occultation Survey (TAOS, [11]) project and the Pan-STARRS project, together with the associated follow-up programs, at which the National Central University (NCU) has been heavily involved in recent years.

Fig. 1. Two of the TAOS telescopes are shown in front of this image, with enclosure open. The third TAOS telescope can be seen in the upper-left corner (the fourth TAOS telescope is out of this image). The building with dome in the middle of the image is for the 40cm telescope (SLT) at Lulin Observatory. This image is adopted from Lulin Observatory homepage ([18]).

II. The TAOS Project

The TAOS project is an international collaboration project between the institutions in Taiwan, USA and Korea. The aim of TAOS project is to search for Kuiper Belt Objects (KBO) using the stellar Occultation technique. The TAOS project employs four 20-inch wide-field ($F/1.9$, 3 degree-squared field-of-view) telescopes, each equipped with a $2K \times 2K$ CCD from Spectral Instruments, to simultaneously monitor the same patch of the sky. There is a total of 167 fields that TAOS will be continuously monitoring during clear nights. All four TAOS telescopes, which operate automatically, are located at the Lulin Observatory in central Taiwan (see Figure 1). The TAOS project has been continuously taking data since 2005, with billions of stellar photometry acquired by the spring of 2009. A number of papers has been published from the TAOS project (see, for examples, [12], [13], [14], [15], [16], [17]).

A. The TAOS Follow-Up Program

Even though the primary goal of the TAOS project is to detect KBO objects in the outer Solar System ([13]), the dense sampling strategy employed by TAOS can also be used to find variable stars, especially the pulsating variables. In fact, [19] detected 41 δ-Scuti variables in the 2005-2006 observation seasons, and [20] reported 15 new variables and 14 previously known variables found in the TAOS field No. 151.

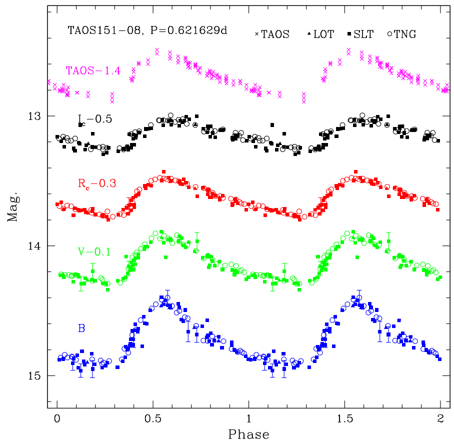

Fig. 2. Calibrated $BVRI$ light curves for a RR Lyrae variable in TAOS-151 field. The TAOS light curve (magenta crosses, taking from the "stare" mode) is included for comparison. For clarity, error-bars are plotted for data points with photometric errors greater than 0.05. Note that the time series information has been folded with the pulsating period, hence the phases from 0 to 1 corresponding to a full cycle of pulsation. LOT=Lulin One-meter Telescope; SLT=Lulin's SLT; TNG=Tenagra II Telescope.

The TAOS observations were conducted using a single broad-band filter. Photometry from the single band filter is good enough for finding variables, determining their periods and provide rough classification of these variables. However, other information, such as the color and extinction, are unknown from the single band observations. As a result, a follow-up program has been carried out to monitor the TAOS variables and construct $BVRI$ light curves for the new variable stars found in the TAOS project. This will enable a wide range of research in astrophysics for the pulsating variables, especially for the Cepheids and RR Lyraes, as well as for other types of variable stars. These include, but not limited to, the calibration of distance scale ladder and constraining stellar pulsation and/or evolution models, beyond the limited information provided from the single broad band light curves. The $BVRI$ light curves can also be used to improve the period determination and classification for the new TAOS variables. The follow-up program utilized the Lulin One-meter Telescope (LOT) and SLT available at Lulin Observatory, supplemented by the observations from the Tenagra II robotic telescope in Arizona, USA. Figure 2 shows the calibrated $BVRI$ light curves for one of the TAOS-151 variables resulted from our follow-up program.

III. The Pan-STARRS1 Project

The Panoramic Survey Telescope & Rapid Response System (Pan-STARRS) aims to patrol the observable sky several times a week to detect variable objects, including near-Earth asteroids, comets, variable stars, supernovae and gamma-ray burst sources. The prototype system (PS1) includes a 1.8-meter telescope, and a 1.4 Giga-pixel orthogonal transfer CCD camera, installed atop of Haleakala in Maui, Hawaii. The complete Pan-STARRS will consist of 4 telescope systems

Fig. 3. Telescope and dome of PS1, taken by Rob Ratkowski, copyright of PS1SC. This image is adopted from [21].

sited on Mauna Kea. PS1 has been operational since May 2010, for a project duration of 3 years. Figure 3 shows the dome of the PS1 telescope. Table I listed the sensitivity in each filters from the PS1 3π steradian survey. PS1 has discovered unusual ultra-luminous supernova SN 2009kf [22] and SN 2010gx [23] from its first year of operation, along with numerous near-Earth asteroids, and Kuiper-belt objects. It is worth to point out that on the night of 29 January, 2011, PS1 discovered record-breaking of 19 near-Earth asteroids in a single night from the same telescope [24].

A. Lulin 2-Meter Telescope for PS1 Follow-Up

Taiwan has geographical advantage for PS1 follow-up observations. It has about same latitude as Hawaii but six hours difference in time zone. As soon as any transient event is discovered by PS1, the follow-up observation can be immediately made in the observatory of Taiwan. Therefore, NCU planned to install a two meter optical telescope at Lulin Observatory. One of the main scientific purposes of this telescope is for PS1 follow-up observations. The construction of the telescope was contracted to Nishimura Optics. The optical system of 2-M Telescope is Ritchey-Chretien type with effective aperture 2000mm in diameter. Its focal ratio of primary mirror is $F/2.2$ and becomes $F/8.0$ after combined with secondary mirror. It has high concentration ability with 80% of light energy being inside 0.4 arcsecond, as well as high mirror surface accuracy ($< 1/15\lambda$). The field of view of the telescope can be as large as 1 degree and the slew rate is able to reach 4 degree/sec. The telescope is Alt-Az mount with total weight of 23 tons and 8664 mm high. Its maximum load for the instrument at Cassegrain focus is 500 kg with maximum size of $2\text{m} \times 2\text{m} \times 2\text{m}$. The construction of the telescope was finished and shipped Taiwan in April 2010 (see Figure 4). It is presently stored in a warehouse to wait for the construction of the building.

In order to realize quick and efficient follow-up observations for PS1, we are developing a 4-color simultaneous imager (see Figure 5). The main scope of this instrument is to provide the opportunities for reliable multi-color photometric measurements in visible wavelength region. Some scientific cases include taxonomic studies of newly discovered asteroids, classifications of supernovae, and characterization of gamma-

TABLE I
THE 5σ SENSITIVITY OF PS1 3π STERADIAN SURVEY.

Filter	Wavelength Range (nm)	Photometric zeropoint (mag)	Sky brightness (mag/arcsec^2)	Exposure time (sec)	Limiting magnitude (mag)
g'	405-550	24.90	21.90	60	23.24
r'	552-689	25.15	20.86	38	22.71
i'	691-815	25.00	20.15	60	22.63
z'	815-915	24.63	19.26	30	21.59
y	967-1024	23.03	17.98	30	20.13

Fig. 4. The performance test of Taiwan 2-Meter Telescope made in March 2010 at Nishimura Opt., Kyoto, Japan.

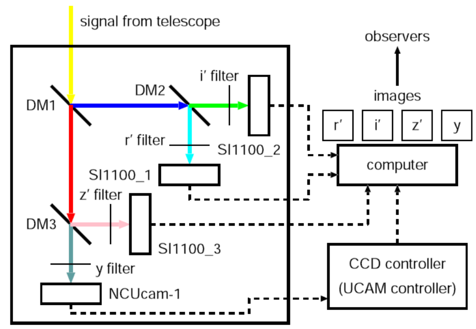

Fig. 5. Schematic diagram for the 4-color imager currently being developed at NCU. Three dichroic mirrors (DM) split the incoming light from the telescope to four CCD cameras, each equipped with different filters. Three SI1000 series CCD cameras are used for $r'i'z'$ bands, while the camera for y band, the NCUcam-1, is being developed by our instrument team. The output of this 4-color imager is the images for the same targets taken simultaneously in four bands.

ray bursts. Dichroic mirrors in the instrument split the beam from the telescope, and images at four different bands are recorded simultaneously by CCD cameras. All of these CCD cameras have 4096×2048 pixels, and each pixel has 15μm in size. For r, i, and z bands, deep depletion CCDs are used. These SI1100 series CCD cameras were purchased from Spectral Instruments. A fully depleted CCD with very thick ($\sim 200\mu$m) depletion layer is used for y band to improve the sensitivity significantly at $\lambda \sim 1\mu$m. This y band camera, called NCUcam-1, is developed by the instrument development team at NCU. A successful CCD drive and image acquisitions using the engineering grade CCD chip were achieved in the laboratory in December 2010. The readout noise was found to be $\sim 5e^-$, and this is acceptable for most cases because the noise contribution from the sky background usually dominates. The science grade CCD chips are scheduled to be delivered at the end of March 2011. A set of filters for the instrument were delivered in February 2011, and the optics part will be delivered in late-April. Assembly of the whole instrument is planned in May to June in 2011. The concurrent control system is now being developed. The observational readiness of the instrument is expected in late-summer or early-autumn of 2011.

IV. CONCLUSION

Two time-domain astronomy survey projects, the TAOS project and the PS1 project, that NCU has been heavily participated are summarized here. We also present short descriptions of the associated follow-up programs for these two projects. Using the telescopes located in Lulin Observatory, the TAOS project has been taking data since 2005. To maximize the TAOS data for variable stars research, a follow-up program has be initiated to observe the TAOS variables in $BVRI$ bands. This follow-up program is still on-going. PS1 is a large scale survey program using a dedicated 1.8-meter telescope located in Hawaii. PS1 officially begin its operation in 2010. To efficiently follow-up the PS1 discovered transients, NCU is planned to install a 2-meter telescope at Lulin Observatory, together with a dedicated 4-color simultaneous imager being developed and built by the instrument team at NCU.

ACKNOWLEDGMENT

The authors acknowledge funding from National Science Council (of Taiwan) under the contract NSC 98-2112-M-008-013-MY3. CCN would also like to thank the financial support from ANGKASA to make this trip become possible.

The PS1 Surveys have been made possible through contributions of the Institute for Astronomy, the University of

Hawaii, the Pan-STARRS Project Office, the Max-Planck Society and its participating institutes, the Max Planck Institute for Astronomy, Heidelberg and the Max Planck Institute for Extraterrestrial Physics, Garching, The Johns Hopkins University, the University of Durham, the University of Edinburgh, Queen's University Belfast, the Harvard-Smithsonian Center for Astrophysics, and the Las Cumbres Observatory Global Telescope Network, Incorporated, the National Central University of Taiwan, and the National Aeronautics and Space Administration under Grant No. NNX08AR22G issued through the Planetary Science Division of the NASA Science Mission Directorate.

REFERENCES

[1] Riess, A. G., Filippenko, A. V., Challis, P., et al., 1998, The Astronomical Journal, Vol. 116, pp. 1009

[2] Perlmutter, S., Aldering, G., Goldhaber, G., et al., 1999, The Astrophysical Journal, Vol. 517, pp. 565

[3] The All Sky Automated Survey homepage. [Online] Available: http://www.astrouw.edu.pl/asas/

[4] SuperMACHO homepage. [Online] Available: http://www.ctio.noao.edu/∼supermacho/

[5] Panoramic Survey Telescope & Rapid Response System homepage. [Online] Available: http://pan-starrs.ifa.hawaii.edu/public/

[6] Optical Gravitational Lensing Survey homepage. [Online] Available:http://ogle.astrouw.edu.pl/

[7] Palomar Transient Factory homepage. [Online] Available: http://www.astro.caltech.edu/ptf/

[8] The SkyMapper homepage. [Online] Available: http://www.mso.anu.edu.au/skymapper/

[9] Large Synoptic Survey Telescope homepage. [Online] Available: http://www.lsst.org/lsst

[10] Committee for a Decadal Survey of Astronomy and Astrophysics; National Research Council, *New Worlds, New Horizons in Astronomy and Astrophysics*. [Online] Available: http://www.nap.edu/catalog/12951.html

[11] The TAOS project homepage. [Online] Available: http://taos.asiaa.sinica.edu.tw/

[12] Lehner, M. J., Alcock, C., Axelrod, T., et al., 2006, Astronomische Nachrichten, Vol. 327, pp.814

[13] Zhang, Z.-W., Bianco, F. B., Lehner, M. J., et al., 2008, The Astrophysical Journal Letters, Vol. 685, pp. L157

[14] Wang, J.-H., Lehner, M. J., Zhang, Z.-W., et al., 2009, The Astronomical Journal, Vol. 138, pp. 1893

[15] Zhang, Z.-W., Kim, D.-W., Wang, J.-H., et al., 2009, Publications of the Astronomical Society of the Pacific, Vol. 121, pp.1429

[16] Bianco, F. B., Zhang, Z.-W., Lehner, M. J., et al., 2010, The Astronomical Journal, Vol. 139, pp. 1499

[17] Lehner, M. J., Coehlo, N. K., Zhang, Z.-W., et al., 2010, Publications of the Astronomical Society of the Pacific, Vol. 122, pp.959

[18] The Lulin Observatory. [Online] Available: http://www.lulin.ncu.edu.tw/

[19] Kim, D.-W., Protopapas, P., Alcock, C., et al., 2010, The Astronomical Journal, Vol. 139, pp. 757

[20] Mondal, S., Lin, C. C., Chen, W. P., et al, 2010, The Astronomical Journal, Vol. 139, pp. 2026

[21] The PS1 Science Consortium. [Online] Available: http://ps1sc.org/index.shtml

[22] Botticella, M. T., Trundle, C., Pastorello, A., et al., 2010, The Astrophysical Journal Letters, Vol. 717, pp. L52

[23] Pastorello, A., Smartt, S., Botticella, M. T., et al., 2010, The Astrophysical Journal Letters, Vol. 724, pp. L16

[24] PS1 News. [Online] Available: http://www.ifa.hawaii.edu/info/press-releases/19asteroids/

Near-Earth Asteroids and Comets

Shinsuke ABE (Institute of Astronomy, National Central University)
阿部 新助 (台灣·國立中央大學天文研究所)
e-mail: *shinsuke.avell@gmail.com*

1. Introduction and Summary

It is of great importance to know the origin and evolution of the solar system. **Asteroids that have survived since the early solar system have experienced numerous collisions that influenced thermal histories and orbital properties. Thus, the physical nature (size, shape, density, composition and orbital distribution) of asteroids is fundamental to understanding how our solar system has been evolved.** Asteroids and comets also represent both a potentially rich resource for future space exploration and a threat to the very existence of humankind on Earth due to impact risks. On the other, meteoroids can be observed during atmospheric entry as a meteor phenomenon. Most meteoroids are weakly bound highly porous chunks of rocky material ejected from parent comets or asteroids. Most of meteors have been treated as cometary origin, while meteorites are usually thought to be associated with asteroids because of mineralogical (spectral class) links. There are over 33,000 meteorites in collections worldwide. However, only about 15 meteorites have been identified with their interplanetary orbits and none of them was associated with known asteroids nor comets. **Near Earth Objects (NEOs) have the advantage of being much more accessible for scientific research and space missions** than small bodies in the outer solar system beyond Jupiter. A study of NEOs will provide crucial evidences to answer the key questions;

(a) What are the main characteristics of near-Earth asteroids; population, sizes, shapes, densities, rotations and orbital evolutions?
(b) How are asteroids and meteorites (and meteor showers) related to each other; orbital evolutions, disruptions, and composition?

The final goal of this research work is to generate **new insights for relations between Near-Earth Asteroids and Meteorites/Meteors**. For this purpose, the orbital distribution of NEOs have been investigated by a comprehensive observation using the world largest sky survey "Pan-STARRS". The disruption phenomena of NEOs to generate "fragmented families" were proposed based on a fact and theories (E. Schunová, M. Granvik, R. Jedicke, G. Gronchi, R. Wainscoat and S. Abe, submitted to *Icarus* in 2012). The meteor/fireball (related with meteorite) were also studied using our established automatic meteor observing system at Lulin and NCU (B.-X. Wu, S. Abe, H.-C. Lin, and C.-S. Lin 2012 *in this volume*) while the properties of NEOs were examined by the in-situ spacecraft missions such as *HAYABUSA*. The C-type asteroid "1999 JU_3", a sample-return target NEO of JAXA's *HAYABUSA-2* mission, have been observed at Lulin (S. Abe et al. 2012 *in prep.*). S. Abe is also deeply involved in an asteroid rover "*MINERVA-II*" and a laser altimeter "*LIDAR-II*" onboard *HAYABUSA-2* spacecraft which will be launched in 2014/2015. A rare phenomenon of the Earth impactor was simulated by using a spacecraft re-entry with the impact speed higher than 12 km/s (S. Abe et al. *PASJ*, 2011). A most likely meteorite-fireball associated with the asteroid Itokawa was identified (K. Ohtsuka, S. Abe et al. *PASJ*, 2011).The spin state and the shape of a comet-asteroid near-Earth transition object, 107P/Wilson-Harrington, was investigated by lightcurve and multiband photometry observations using telescopes in Japan and Lulin (S. Urakawa et al. *Icarus*, 2011). The lightcurve campaign of Jovian Trojan asteroids (JTs) between Lulin (LOT&SLT), Spain and Argentina has succeeded to obtained two long period (~50 hours) JTs (M.D. Melita et al. 2012). Active asteroids (asteroid Phaethon as a parent of Geminid meteor shower) and main belt comets are of importance to know the origin of comets and asteroids (K.-S. Pan & S. Abe 2012 *in prep.*; H. Hsieh et al. *ApJ*, 2012, H. Hsieh et al. *Astron. J.*, 2012).

2. Pan-STARRS all sky survey for finding new Near-Earth Asteroids and Comets

The Panoramic Survey Telescope And Rapid Response System "**Pan-STARRS**" is a project, initiated by the Institute for Astronomy (IfA) University of Hawaii, to repeatedly survey covering three quarters of the entire sky. Since 2010 the prototype single-mirror telescope "P**an-STARRS-1 (PS1)**" has been operating on Mt. Haleakala in Hawaii. Its scientific research program is being undertaken by the PS1 Science Consortium – a collaboration between 10 research organizations in 4 countries including National Central University Taiwan. A major goal of PS1 among 12 key science projects is to discover and characterize Earth-approaching objects, both asteroids and comets, that might pose a danger to our planet.

Pan-STARRS PS1 (1.8m) telescope at Haleakala observatory in Hawaii.

I have been contributing to **Moving Object Processing System "MOPS"** which is the pipeline system to discover, identify and determine the orbit of the NEOs together with other classes of asteroids, comets and distant objects in the solar system (Robert Jedicke, Richard Wainscoat, Larry Denneau, IfA). About 550,000 asteroids were discovered to date and ~9,000 of them are NEOs. In order for an asteroid to be catalogued, the asteroid must be observed by several observatories in different time zones to get better orbital precision. Otherwise it is difficult to find the same object many years into the future and it will be lost. Most of new NEOs are sub-km size that can be observable only when they approach the Earth during a short time period, typically few days to few weeks, due to its faintness. To make a quick follow-up observation, we have established the MOPS Alert System to inform our community of a newly discovered NEO immediately. Since last autumn, PS1 started a dedicated sky survey to detect NEOs efficiently. To contribute PS1 NEO discoveries, NCU team has established our follow-up procedures using TenagraII 32"(~81cm) in Arizona, USA and Lulin 1-m telescope in Taiwan.

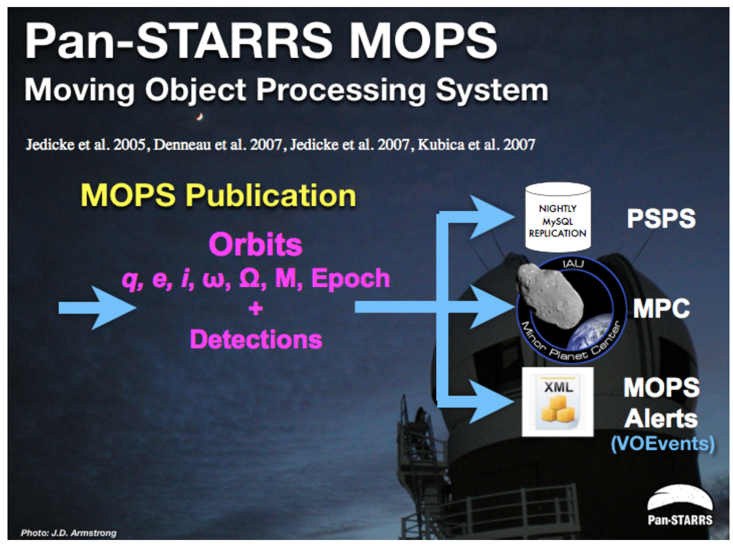

After MOPS detects a NEO candidate, orbital information based on initial orbital determination is distributed by several ways. Follow-up observations are able to turn a NEO candidate into discovery.

– Follow-up of PS1 NEO candidates

Since Pan-STARRS PS1 (*1.8-m*) is not regularly capable of recovering its own NEO candidates, we must rely on the follow-up capabilities of a group of dedicated observers located around the world. PS1 telescope reaches ~22.5 magnitude with exposure time of 60s in V-band while my accessible telescopes, TenagraII 32"(0.81-m) and Lulin 1-m telescopes, with unfiltered exposure time of 60s are able to detect 19 - 21 magnitude objects. In order to detect faint moving object using relatively small telescopes, "shift-and-median" method (e.g., Gladman et al. 1998) is adopted to observe unresolved faint asteroids. The median filter has the advantage of eliminating extremely high noises, such as cosmic rays and hot pixels that remain in an average image. The software algorithm is based on the Omni-directional image shifting at various shift values depending on the motion rate of moving objects. Fainter moving objects are detectable as the number of frames increases. As for 6, 15 and 40 images, the enhancement of the magnitude is estimated to be ~1.0, ~1.5 and ~2.0, respectively. Exposure time is chosen by considering NEOs' moving rate and the seeing size of sky condition (typically ~2.0" at TenagraII/Arizona and ~1.5" at Lulin/Taiwan). Combining with this shift-median method, TenagraII and Lulin 1-m telescopes are able to detect up to 21-22 magnitude that can cover ~50% of NEOs discovered by PS1 telescope (see figure).

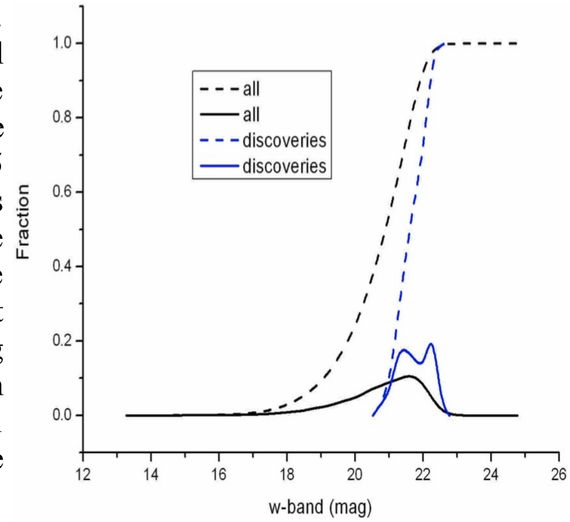

Fraction (solid) and cumulative (dashed) distribution of all asteroid (black) and NEOs (blue).

The total number of newly discovered NEOs detected by PS1 to date (as of 2012 April) was 287 in which 25 objects were **Potentially Hazardous Objects (PHOs)**, a subset of NEOs, closely approach Earth's orbit to within 0.05 AU (~20 Moon distances). PHO collisions to Earth occur infrequently, but the threat is large enough when averaged over time. 7 comets were also discovered by PS1. **Our efforts toward follow-up of PS1 NEO candidates have succeeded in determining their orbits. About 50 of PS1 NEO candidates have been turned into NEO discoveries (4 of them were new comets) by our follow-up observations that were recognized through the Minor Planet Center (MPC) under the International Astronomical Union (IAU)**, for example;

MPEC 2011-Q08 : 2011 QE2 http://www.minorplanetcenter.net/iau/mpec/K11/K11Q08.html
MPEC 2011-N15 : 2011 MD5 http://www.minorplanetcenter.net/iau/mpec/K11/K11N15.html
MPEC 2011-M33 : 2011 MT http://www.minorplanetcenter.net/iau/mpec/K11/K11M33.html
MPEC 2011-H07 : 2011 GX65 http://www.minorplanetcenter.net/iau/mpec/K11/K11H07.html

Follow-up observatories for PS1 NEOs

Observatory	Code	Contact
University of Hawaii 2.2m	568	D. Tholen
Las Cumbres Observatory, Faulkes Telescope North	F65	T. Lister
Las Cumbres Observatory, Faulkes Telescope North	F65	J. D. Armstrong
Cerro Tololo	807	R. Holmes
Spacewatch	291	R. McMillan
Magdalena Ridge Observatory	H01	E. Ryan
Tenagra II, Lulin	926,D35	S. Abe

Our significant contribution to the discovery of NEOs has been encouraged by *NASA NEOO (Near-Earth Objects Observations) program* (selected NASA proposal: R. Wainscoat, R. Jedicke et al. *11-NEOO11-0016*). Since Pan-STARRS is still on-going project until mid-2013, I am continuing my efforts under the support of NSC (*100-2112-M-008-014-MY2*).

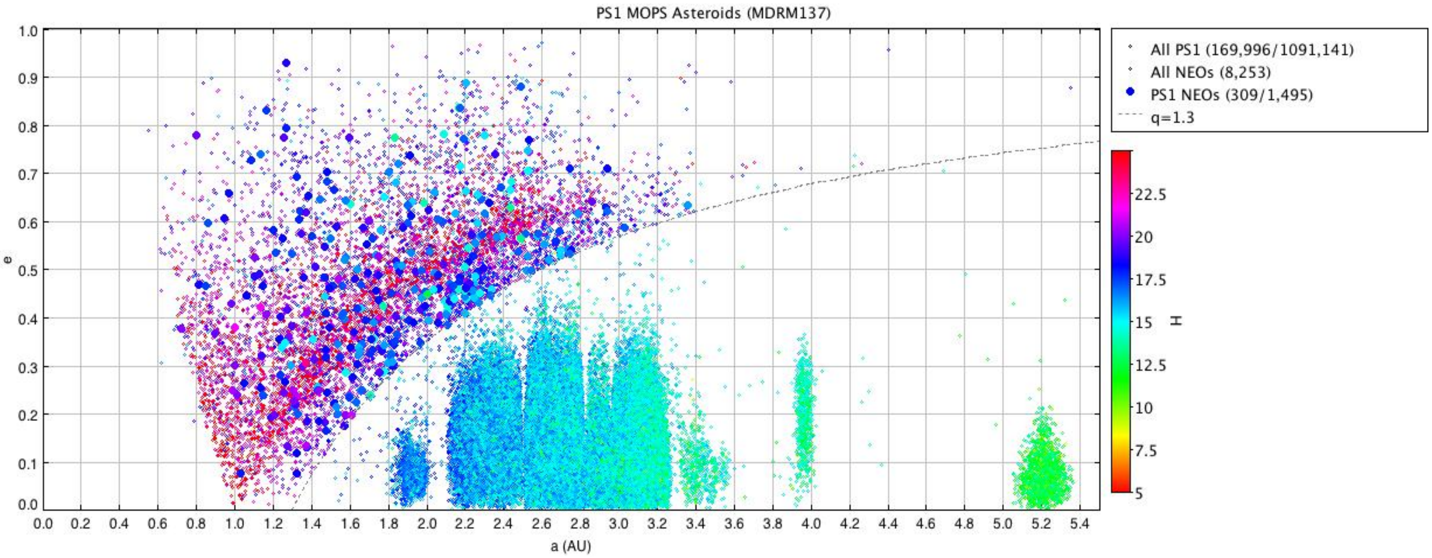

All Pan-STARRS PS1 detected asteroids as of 2012 January plotted against semimajor axis "a" vs eccentricity "e". (Number of objects / number of observations) by PS1 are indicated. The color represents its absolute magnitude "H" which is defined as the apparent V-magnitude if it were 1 AU from both the Sun and the observer at a zero phase angle. PS1 is realized the most capable telescope in the world for discovering NEOs.

Electronic Telegram No. 2790

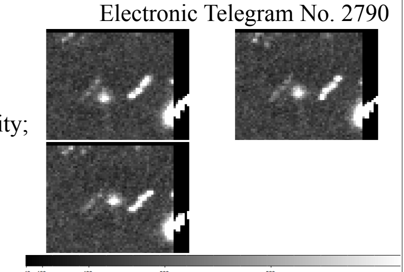

Comet discovery images taken by Lulin 1-m

Central Bureau for Astronomical Telegrams
INTERNATIONAL ASTRONOMICAL UNION
CBAT Director: Daniel W. E. Green; Hoffman Lab 209; Harvard University;
20 Oxford St.; Cambridge, MA 02138; U.S.A.
e-mail: cbatiau@eps.harvard.edu (alternate cbat@iau.org)
URL http://www.cbat.eps.harvard.edu/index.html P
repared using the Tamkin Foundation Computer Network

COMET C/2011 Q1 (PANSTARRS)

Richard Wainscoat, Marco Micheli, Henry Hsieh, and Larry Denneau report the discovery of an apparent comet on images taken with the 1.8-m "Pan-STARRS 1" telescope at Haleakala (discovery observation tabulated below); Wainscoat notes that the object has a distinctly extended point-spread function (PSF), with a core having FWHM approximately 1".2 and nearby stars having a PSF of approximately 1".0 arcsec. **Shinsuke Abe, Institute of Astronomy, National Central University (Jhongli, Taoyuan, Taiwan) writes that follow-up CCD frames taken by H. Y. Hsiao and himself with a 1.0-m f/8 Cassegrain reflector at Lulin Observatory on Aug. 21.7 UT also show an apparent cometary appearance.** After posting on the Minor Planet Center's NEOCP webpage, other CCD astrometrists have also noted cometary appearance. L. Buzzi, Varese, Italy, notes that stacked images taken around Aug. 21.98-22.00 UT with a 0.60-m f/4.6 reflector show a 8" compact coma (red mag 18.7) with a FWHM around 30 percent larger than that of nearby stars; a 30" tail is seen around p.a. 340 deg, but it is difficult to estimate due to background nebulosity in the area. Stacked CCD images taken around Aug. 22.1 by R. Holmes (Ashmore, IL, USA; 0.61-m f/4.0 astrograph; measured by S. Foglia, L. Buzzi, and T. Vorobjov) show the object to have an elongated coma of size 6" x 12" and mag 19.1-19.3, elongated toward p.a. 350 deg, where there is a 20"-long tail.

2011 UT	R.A. (2000)	Decl.	Mag.
Aug. 20.44054	20 48 02.41	+30 21 49.2	20.6

The available astrometry, the following very preliminary parabolic orbital elements by G. V. Williams, and an ephemeris appear on MPEC 2011-Q12.

T = 2012 Oct. 25.931 TT   Peri. = 213.600   Node = 164.968 2000.0   q = 3.19973 AU
Incl. = 67.584

NOTE: These 'Central Bureau Electronic Telegrams' are sometimes superseded by text appearing later in the printed IAU Circulars.

3. Discovery of YORP Asteroid (collaboration with University of Aizu, Seoul National University, and JAXA)

The rotation state of small bodies such as an asteroid is affected by the thermal Yarkovsky-O'Keefe-Radzievski-Paddack (YORP) torque. Owing to asteroids' rotation, YORP is caused by the anisotropic reflection and thermal emissions of sunlight which can be observable as the secular change of the asteroid's rotation period in time. YORP has been measured (1862) Apollo (Kassalainen et al. 2007), (54509) YORP (Lowry et al. 2007; Taylor et al. 2007) and (1620) Geographos (Durech et al. 2008). Lightcurve observation of the near-Earth asteroid (4660) Nereus was carried out using Lulin 1-m telescope in 2010. Using all available photometry covering more than ten years data back to 1997 (Y. Ishibashi et al. 2000) and 2001 (M. Ishiguro et al.), we detected acceleration of the rotation period, -4.2×10^{-16} (rad s^{-2}), caused by the YORP (K. Kitazato, S. Abe et al. 2012 *in prep*).

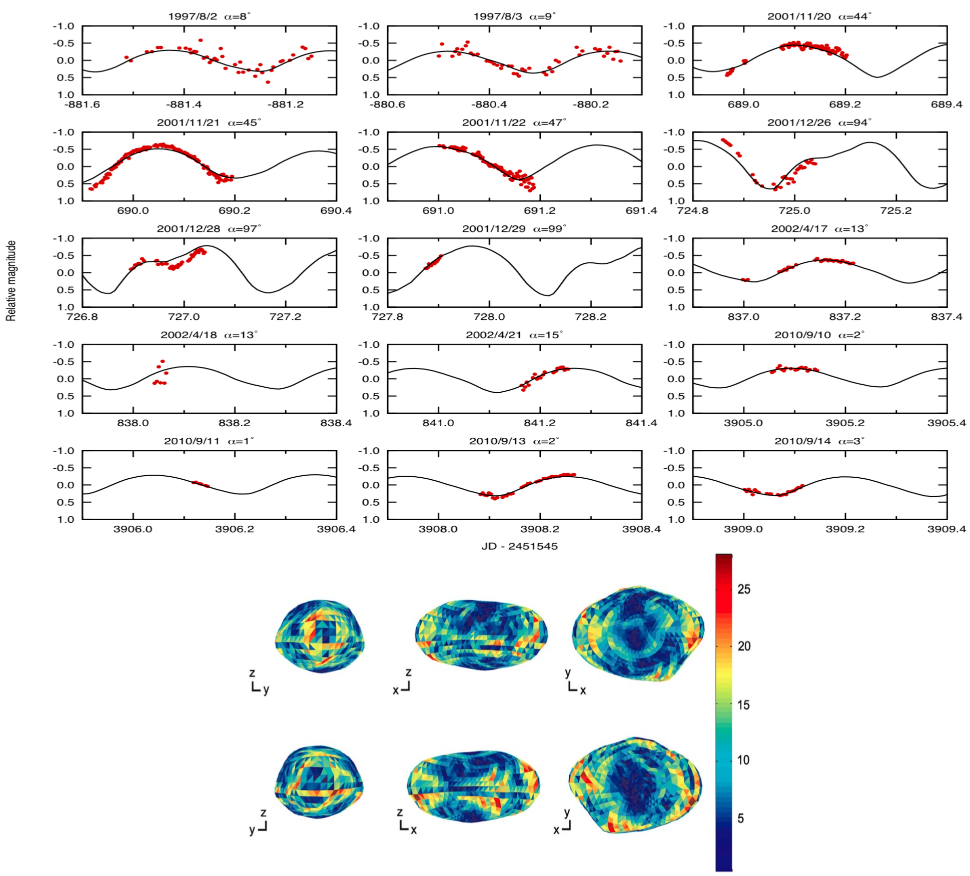

Lightcurve of the near-Earth asteroid (4660) Nereus observed during 2007-2010. The fitted lightcurve (top) is modeled considering the shape model obtained by Arecibo radar (bottom; M. Brozovic et al. 2009). Our observation using Lulin 1-m was accurate enough to measure the YORP effect on Nereus. Note that Nereus was the target of former Japanese HAYABUSA spacecraft, however the target was changed due to delay in launching.

4. Fast rotator of PS1 NEO (collaboration with Bisei Space Guard Center)

2011 XA_3 was discovered by PS1 on Dec 15, 2011. Lightcurve and multiband color observations collaborating with TenagraII/LOT and Japanese BSGC (S. Urakawa) enabled to measure its rotation period and spectral property. Interestingly, 2011 XA_3 is the fast rotator whose rotation period is 0.73 hours with S- and V-type spectral features (S. Abe, S. Urakawa, PS1 ISS team 2012 *in prep.*).

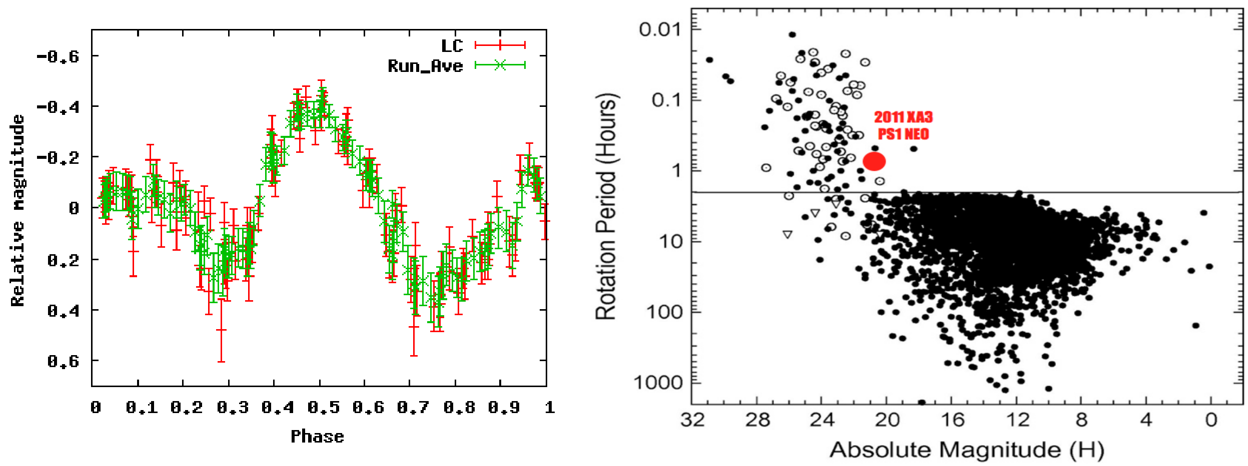

Lightcurve of 2011 XA_3 showed a fast rotating period ~ 0.73 hours (left). The rotation period of 4294 asteroids plotted against absolute magnitude H. Open circles represent data from a survey of small fast rotating NEOs (Hergenrother & Whiteley et al. 2011). The horizontal line (2.0 hours) marks the canonical limit between gravity and strength dominated regions.

5. Lightcurve and Phasecurve of Phaethon (NCU student; Kang-Shian Pan)

Apollo asteroid (3200) Phaethon (1983 TB) classified as F/B-type is thought to be a dormant or an extinct cometary nuclei because (1) Phaethon has been known as the parent of the Geminids which is the most intense meteor shower of the year (e.g. Whipple, 1983) and (2) an brightening enhancement, by a factor of two, during the perihelion passage near 0.14 AU has been reported (Jewitt and Li, 2010). It was also suggested that the Apollo asteroid 155140 (2005 UD) is most likely candidate for being a slitted asteroid that generate a large member of the Phaethon-Geminid stream Complex (Ohtsuka et al. 2006, Jewitt & Hsieh 2006, Kinoshita et al. 2007). Though Phaethon is one of the most important target for the future space missions in the near Earth space to explore water and organics, the spin state and the shape is still under debate (3.604 hours by Meech 1996, 5.1 kilometers in diameter by Green et al. 1985). Time-resolved visible (Johnson-Cousins BVRI) photometric observations of Phaethon were carried out using 0.81-m and 1-m telescopes at Tenagra observatory in US and Lulin observatory in Taiwan, respectively. The rotational period and the surface properties of Phaethon based on color lightcurves taken between 2011 November and 2012 February are analyzing now (K.-S. Pan & S. Abe 2012 *in prep*).

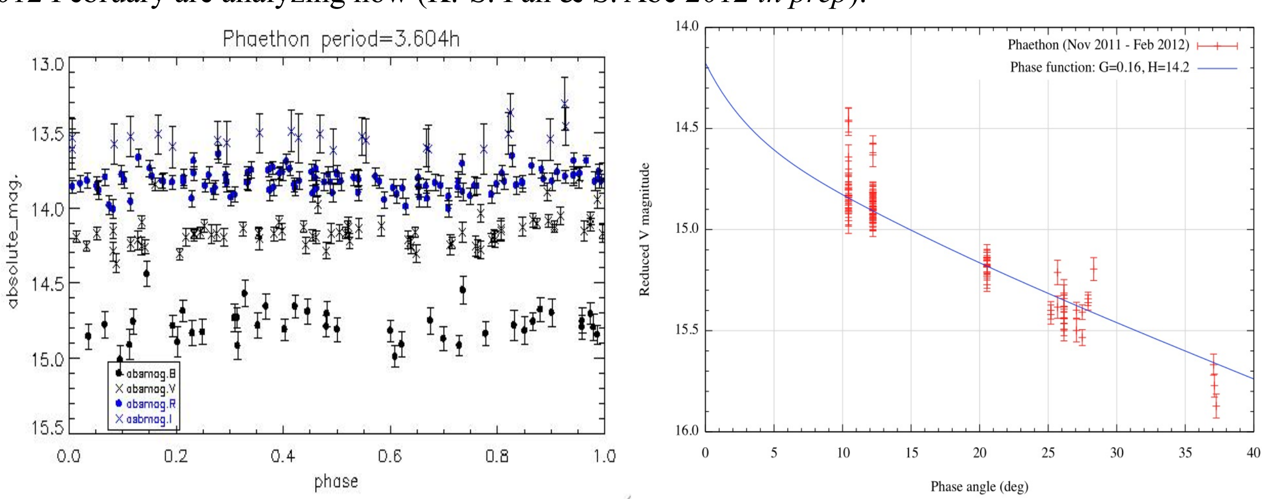

Lightcurve of (3200) Phaethon in B,V,R and I bands with the period of ~3.6 hours (left). Lightcurve in different phase angles were fitted by a phase function (H,G). H is the absolute magnitude and the G is the slope parameter which relates a surge in brightness near opposition. Its value depends on scattering light by particles on the asteroids' surface.

Taiwan Meteor Network

Meteor Observing System at Lulin and NCU

Bing-Xun Wu, Shinsuke Abe, Hung-Chin Lin, Chi-Sheng Lin

Lulin Meteor System (LMS) has started regular observation since December 2009 at Lulin observatory in Taiwan. Three cameras towards north, east, and south are carried out using high sensitive CCD-TV cameras (Watec and Mintron) with wide field of view CCTV lens, which are recorded in video rate controlled by the software UFOCapture. A set of the camera system (NCU Meteor System: NMS) was also installed in NCU campus on August 2010 to make triangulation observations between Lulin and NCU. More than 17,000 meteors has been observed by LMS in which about 2% of meteors were detected by NCU camera. In addition, NCU camera detected 45 unexpected lightning phenomena such as red sprites, elves, blue jets so called Transient Luminous Events (TLEs) which are upper-atmospheric optical phenomena associated with thunderstorms.

Figure1. Meteor cameras installed at Lulin observatory.

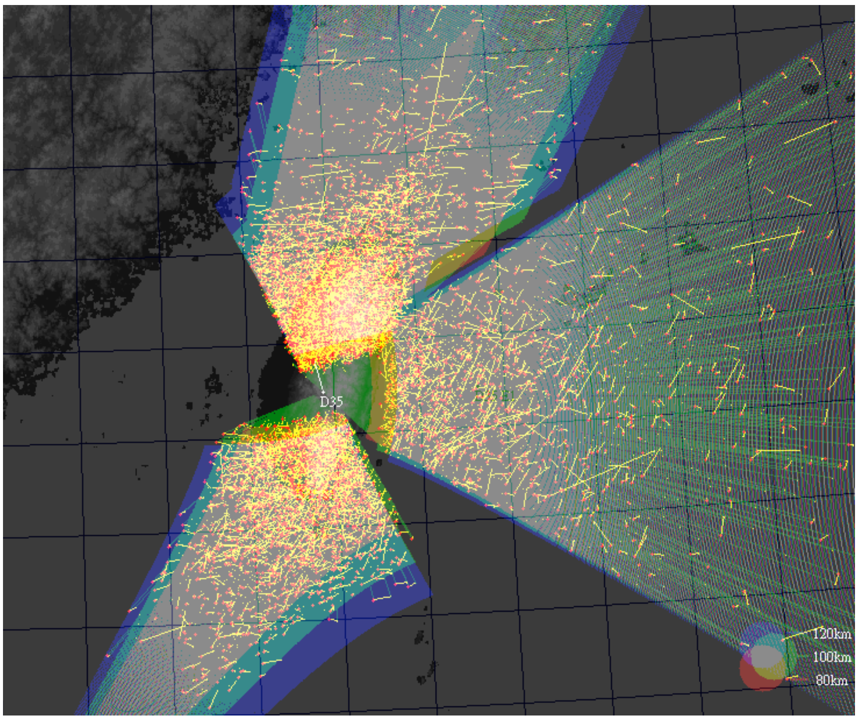

Figure2. Meteor trail map over Taiwan detected by North, South and East cameras at Lulin.

Because of better sky condition at Lulin observatory (high altitude ~2900m and little light pollution), a huge number of meteors were recorded by LMS, while NMS was affected by poor weather condition (especially during winter) and significant light pollution including many fireworks. We have investigated characteristics of meteor showers such as radiant point, velocity distribution, and population (mass) index.

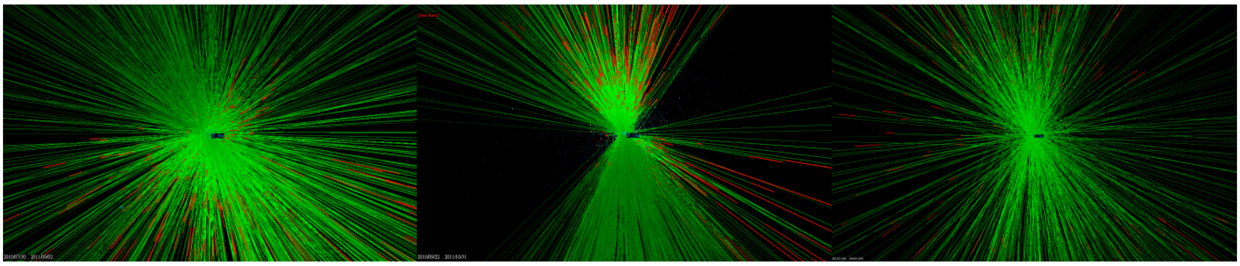

Figure3. (Left to right) Radiant point of Perseids (n=892), Orionids (n=1169), and Geminids (n=495) (): number of meteors, classified by UFOAnalyzer.

Triangulation observations were carried out using cameras at Lulin and NCU. The baseline of tow stations is approximately 170 km. 273 triangulation meteors between two stations were identified so far. With triangulation data, we can study accurate trajectory information on observed meteors. The trajectory (including start and end height, azimuth, distance) can be used to calculate the accurate velocity, radiant point, and interplanetary orbits.

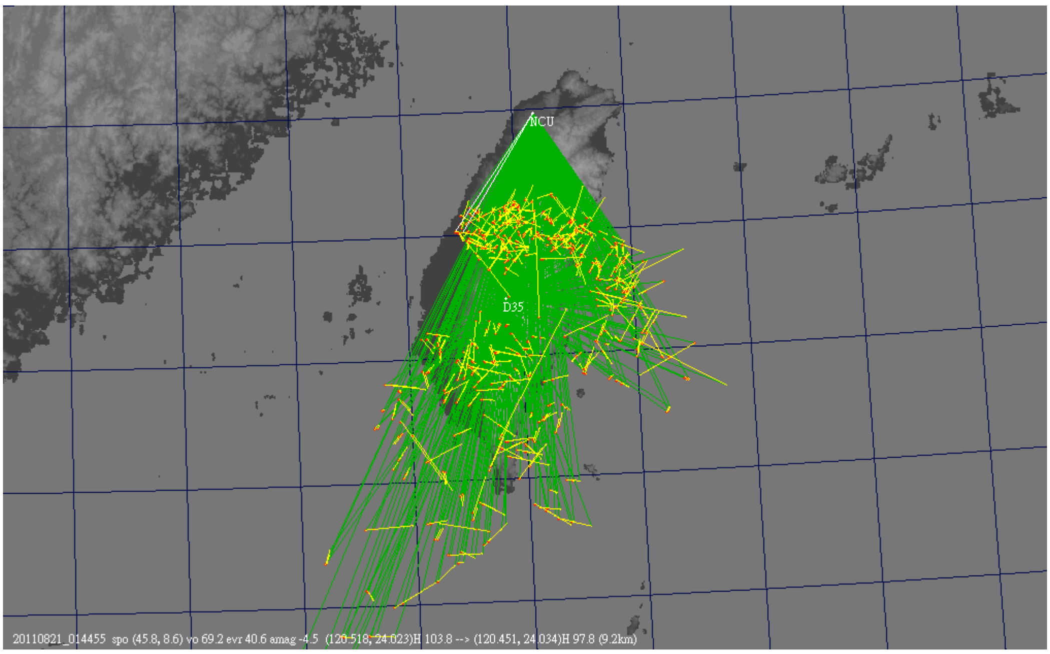

Figure4. Trail map of triangulation meteors between NCU and Lulin

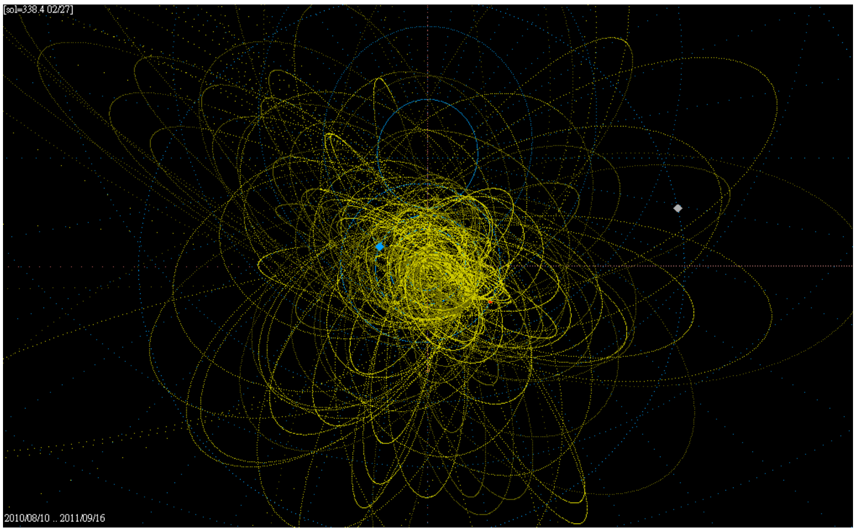

Figure5. Derived interplanetary orbits of all (237 pairs) meteors observed between Lulin and NCU.

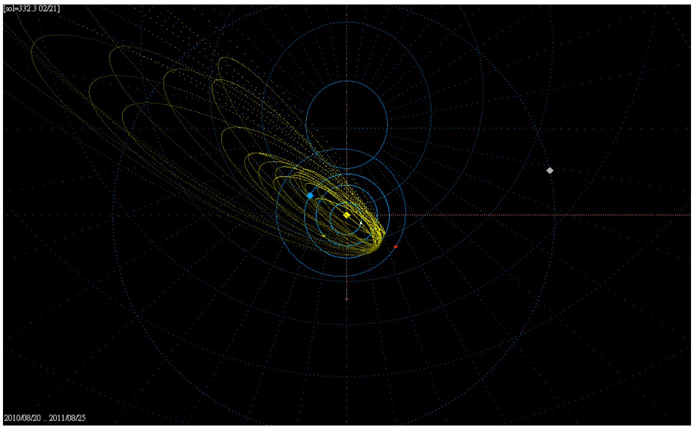

Figre6. Interplanetary orbits of Perseid meteor shower observed between Lulin and NCU.

Most of our data were taken from a single station. Single station data seem to have large errors in their trajectory. To omit such large uncertainty data, we compared “standard sores[2]” of meteor velocity and its trajectory length (angle). Stand score is defined as

$(x - \mu)/\sigma,$

where μ is average of velocity and σ is sample standard deviation.

We picked the samples whose absolute value of standard score is smaller than 1.5, then calculated velocity distribution and population index.

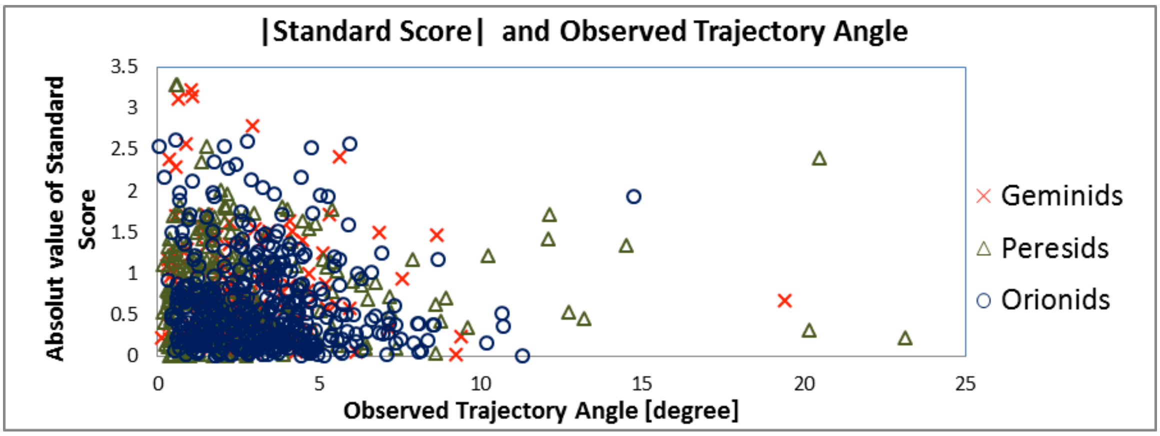

Figure7. Velocity error descried as “Standard Score” plotted against trajectory length of meteors.

From our tentative analysis, the average velocity of Perseids is 66.8 km/s, Orionids is 74.4 km/s , Geminids is 39.5 km/s were obtained. Their velocity distributions are shown in Fig. 8.

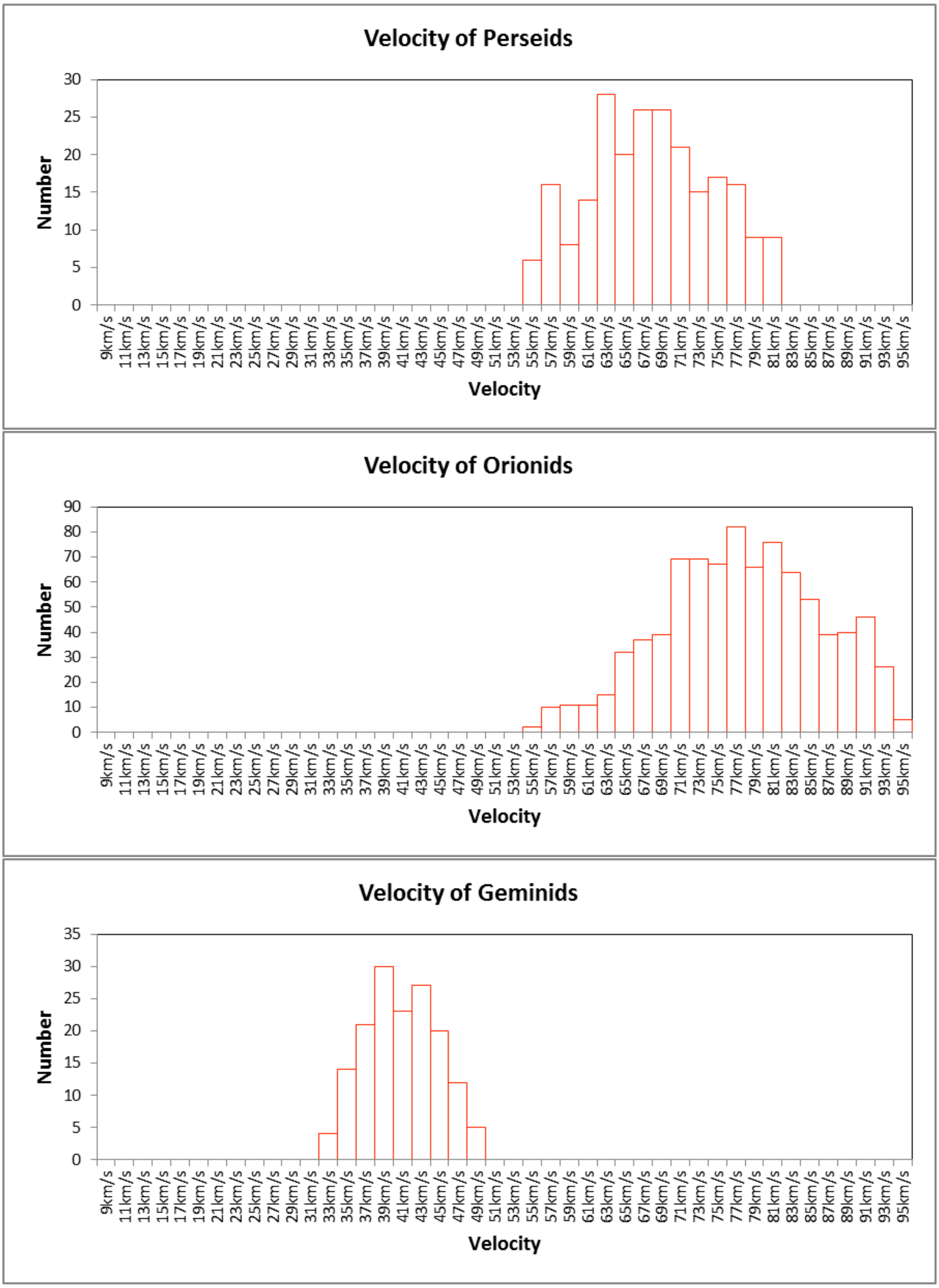

Figure8. Velocity distribution of different meteor showers

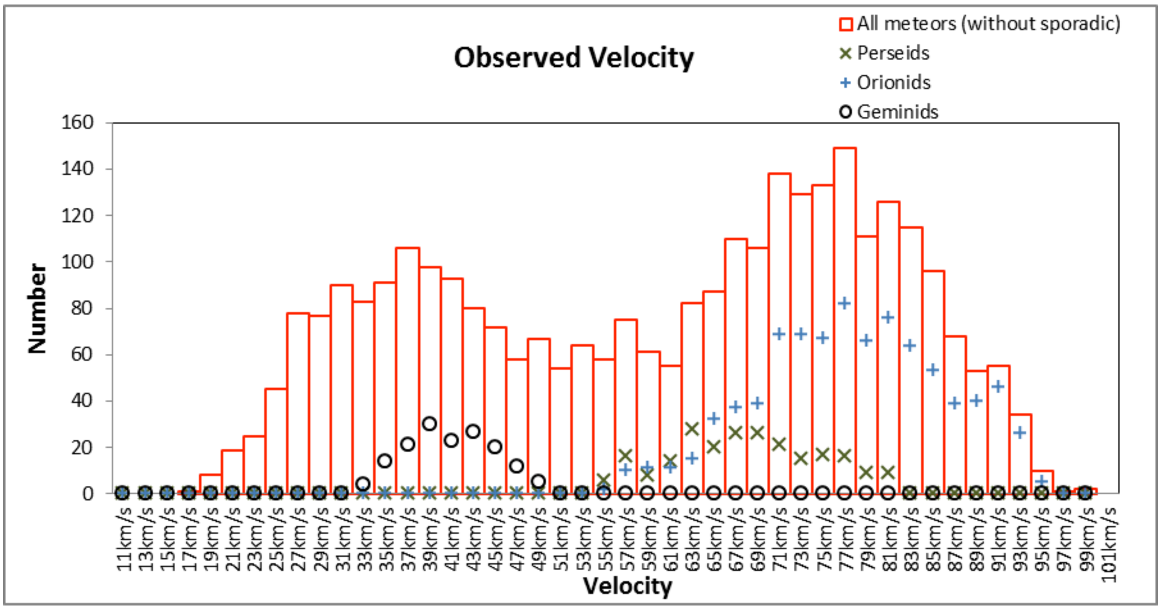

Figure9. Velocity distribution of all meteors (showers and sporadic) and some meteor showers. Basically, the two major velocities can be explained by cometary meteoroids (fast velocity) and asteroidal meteoroids (slow velocity). Some of meteors' speed faster than 72 km/s (Solor system escaping velocity) ssems to be wrong. We should re-analyze and check our data carefully.

The population Index of meteor shower is also very important. Smaller value means more bright meteors.

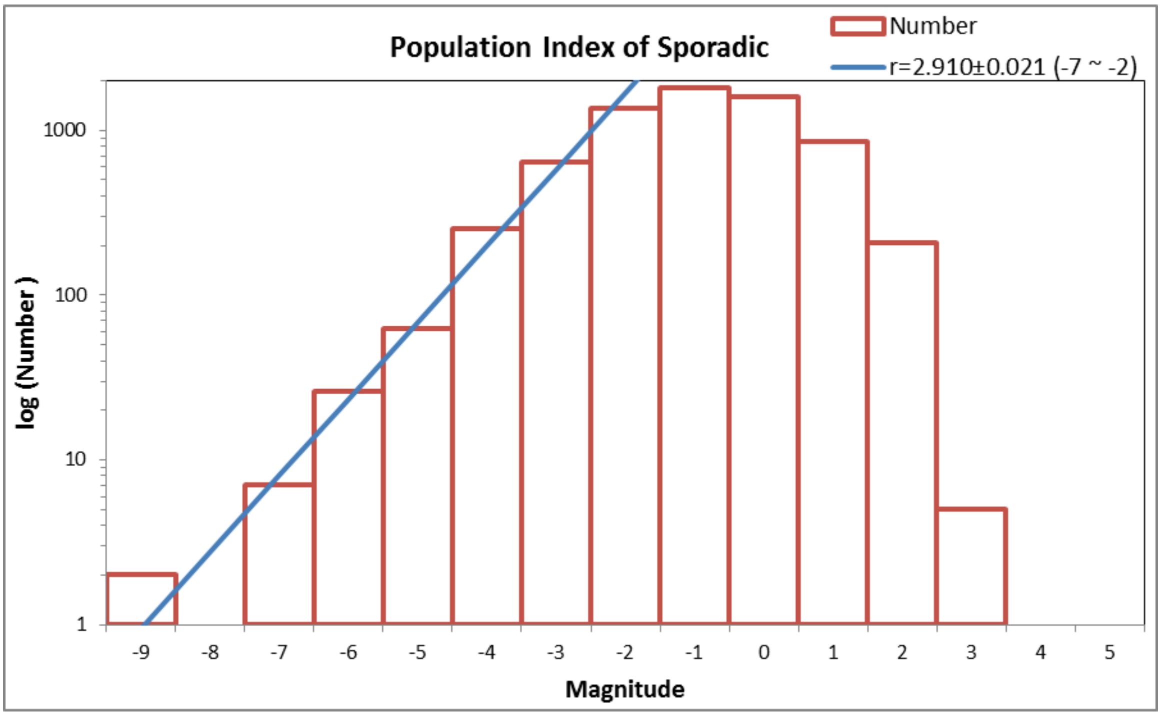

Figure10. Population index of Sporadic

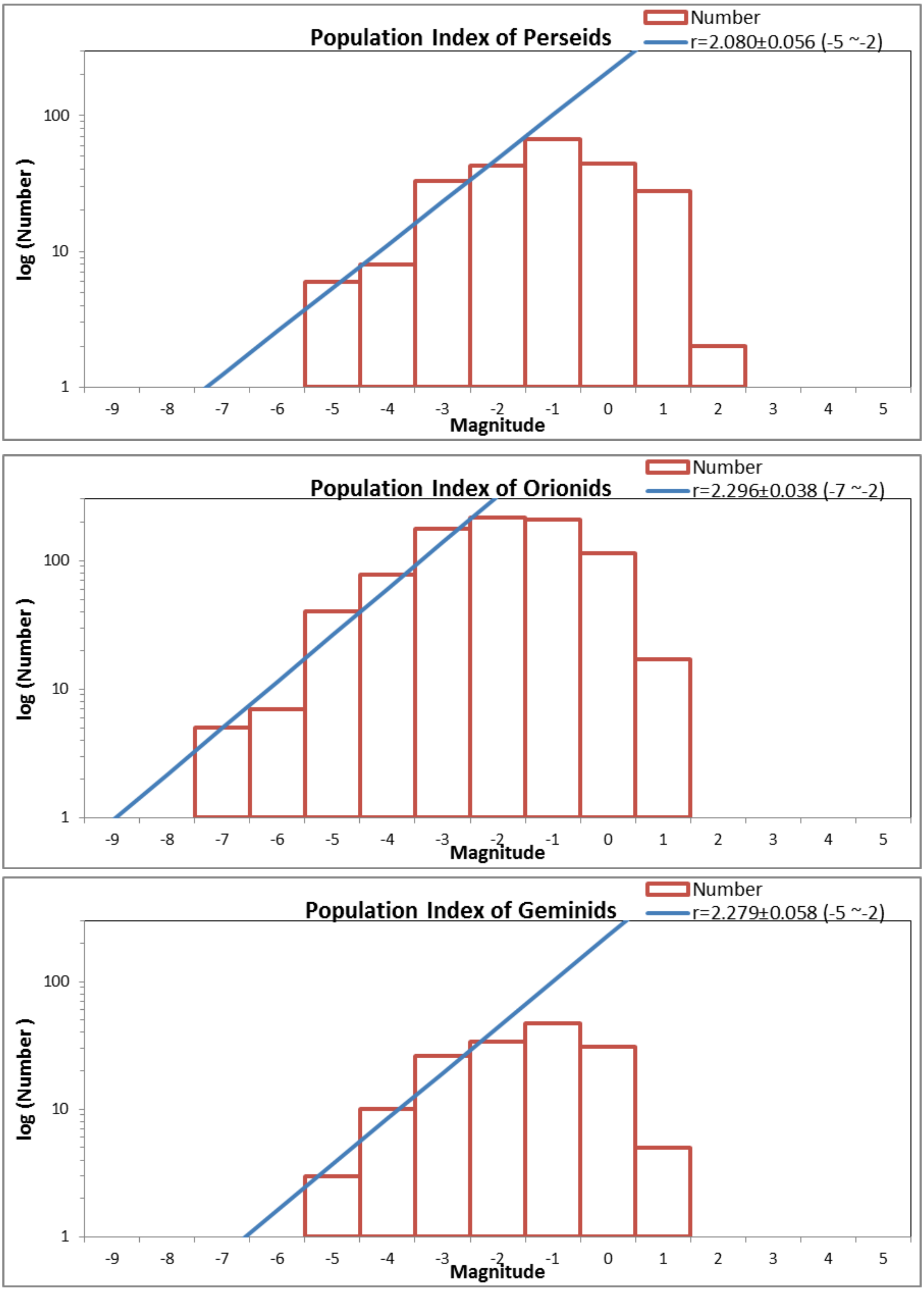

Figure10. Population index of different meteor showers, Perseids (r=2.08), Orionids (r=2.30) and Geminids (r= 2.28). The result suggests that (1) asteroidal meteor shower (Geminids: (3200) Phaethon) contains large fragments as cometary meteor showers (Perseids: 109P/Swift-Tuttle and Orionids: 1P/Halley) have, (2) Brighter meteors in Orionids (66 km/s) and Perseids (59 km/s) are simply due to high atmospheric entry speed because the emission energy is proportional to the forth power of entry speed, while those in Geminids (35 km/s) indicate the existence of larger fragments.

Large thunderstorms are capable of producing other kinds of electrical phenomena called transient luminous events (TLE's). The most common TLE's include red sprites, blue jets, and elves. NCU camera detected unexpected TLE events especially in 2010.

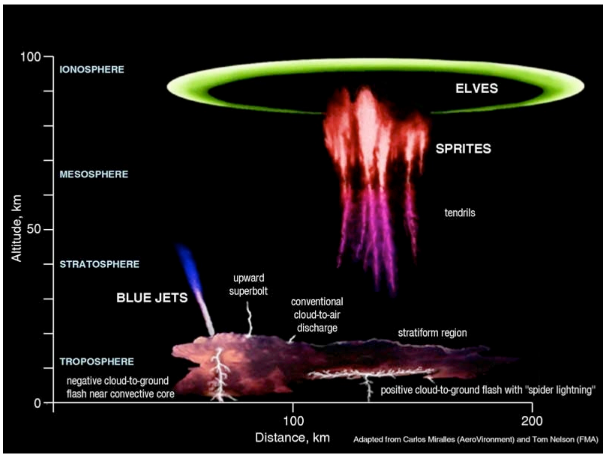

- 107 events were found.
  - NCU_S: 2010/08/21, 2010/08/31, 2010/09/01, 2010/09/07, 2010/09/13, 2010/09/21, 2010/10/16, 2011/06/14, 2011/08/08, 2011/08/25, 2011/08/26, 2011/09/13, 2011/09/27 ……62 events
  - S1: 2010/08/14, 2010/08/21, 2010/08/22, 2010/09/07, 2010/12/25 ……15 events
  - N1: 2010/08/08, 2010/09/30, 2011/05/12, 2011/07/09, 2011/07/13 ……15events
  - E1: 2010/09/28, 2010/10/21, 2011/05/15, 2011/07/09, 2011/08/26 ……15 events
- 3 events can be matched.
  - Lulin S1 - NCU_S： 2010/09/07 22:43:46
    Lulin S1 - NCU_S： 2010/09/07 22:57:26
    Lulin S1 - NCU_S： 2010/09/08 02:55:19

We found 3 transient luminous events were observed from NCU and Lulin cameras. The detailed analysis of the detected TLE's will be submitted soon.

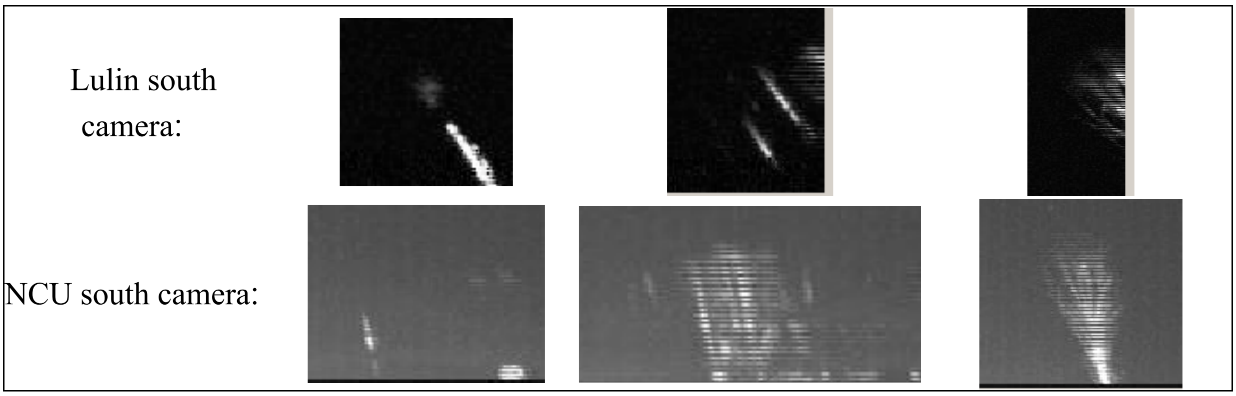

Figure11. Transient luminous events (TLEs).

Ground-Based *BVRI* Follow-Up Observations of the Cepheid V1154 Cyg in *Kepler's* Field

C.-C. Ngeow, R. Szabó, L. Szabados, A. Henden, M.A.T. Groenewegen & the *Kepler* Cepheid Working Group

Abstract The almost un-interrupted observations from *Kepler Space Telescope* can be used to search for Earth-size and larger planets around other stars, as well as for stellar variability and asteroseismological study. However, the *Kepler's* observations are carried out with a single broad-band filter, and ground-based follow-up observations are needed to complement *Kepler's* light curves to fully characterize the properties of the target stars. Here we present ground-based optical (*BVRI*) follow-up observations of V1154 Cyg, the only Cepheid in the *Kepler* field of view, and deriving basic properties of this star.

1 Introduction

V1154 Cyg ($P = 4.925454$ days) is a known Cepheid located within *Kepler's* field-of-view. Analysis of this Cepheid using *Kepler's* light curves has been published in [1] (hereafter S11). Some of the ground based follow-up observations (including optical and spectroscopic observations) can be found in [2, 3] and S11. The aim of this work is to provide further details of the *BVRI* follow-up for V1154 Cyg, to supplement S11. Details of observations and data reduction are given in S11.

2 Results: Basic Properties of V1154 Cyg

BVRI light curve properties and radial velocity measurements from spectroscopic observation suggested V1154 Cyg is a *bona fide* fundamental mode Cepheid. Figure 1 compares our light curves to the light curves presented in [4]. Table 1 summarizes the *BVRI* intensity mean magnitudes and amplitudes (from Fourier fit to the light curves) based on S11 light curves. Baade-Wesselink (BW) surface brightness method was used to derive the distance and mean radius of V1154 Cyg, by combining the published radial velocity (RV) data and available light curves (details of the method can be found in [5]). Figure 2 presents the results of BW analysis. The distance and radius of V1154 Cyg are: $D = 1202 \pm 72 \pm 68$pc, $R/R_{\rm sun} = 23.5 \pm 1.4 \pm 1.3$, the first error is the formal fitting error, the second error is based

C.-C. Ngeow
National Central University, Jhongli City, 32001, Taiwan. e-mail: cngeow@astro.ncu.edu.tw

on a Monte Carlo simulation taking into account the error in the photometry, RV data, $E(B-V)$ and the p-factor ($p = 1.255$ is adopted with a 5% error).

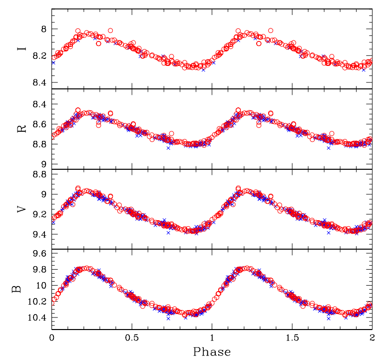

Fig. 1 Comparison of the *BVRI* light curves from S11 (open circles) and Berdnikov (2008, crosses). Note that a correction of $+0.054$ mag needs to be added to S11 *B* band data to bring into agreement between the two light curves.

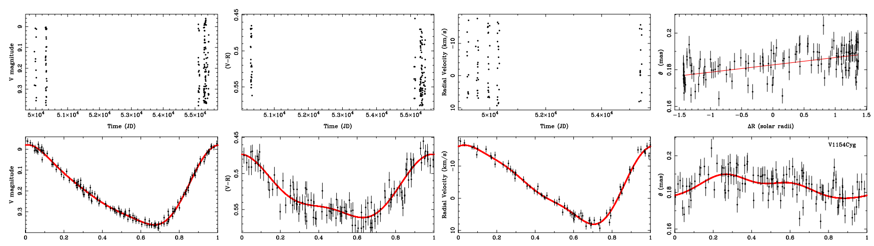

Fig. 2 Results of the BW analysis for V1154 Cyg, including the fitting of V band light curve, $(V-R)$ color curve, RV curve and angular diameters (from left to right).

Table 1 Basic *BVRI* properties of V1154 Cyg.

Band:	B	V	R	I
Intensity mean magnitude	10.107	9.185	8.659	8.168
Amplitude	0.547	0.390	0.314	0.250

Acknowledgements CCN thanks the funding from National Science Council (of Taiwan) under the contract NSC 98-2112-M-008-013-MY3. The research leading to these results has received funding from the European Communitys Seventh Framework Programme (FP7/2007-2013) under grant agreement no. 269194 (IRSES/ASK). This project has been supported by the 'Lendület' program of the Hungarian Academy of Sciences and the Hungarian OTKA grants K83790 and MB08C 81013. R.Sz. was supported by the János Bolyai Research Scholarship of the Hungarian Academy of Sciences.

References

1. Szabó, R., Szabados, L., Ngeow, C.-C., et al. 2011, MNRAS, 413, 2709
2. Molenda-Żakowicz, J., Frasca, A., Latham, D. W. & Jerzykiewicz, M. 2007, Acta Astronomica, 57, 301
3. Molenda-Żakowicz, J., Jerzykiewicz, M. & Frasca, A. 2009, Acta Astronomica, 59, 213
4. Berdnikov, L. N. 2008, VizieR On-line Data Catalog: II/285
5. Groenewegen, M. A. T. 2008, A & A, 488, 25

Comet 213P/Van Ness Monitoring using SLT（編號第 213 號凡尼斯周期彗星的監測）

ZhongYi Lin / IANCU

彗星凡尼斯是一短周期彗星，約 6.6 年回歸一次，這顆彗星在 2005 是美國天文學家(M.E. Van Ness)利用 59 公分望遠鏡發現，發現時彗星只有 17 等。此彗星最近一次回歸是在 2011 年六月 12 日，當時離太陽距離約有 2.12AU。2011 年八月，當這顆平淡無奇的彗星悄悄離開太陽後，一個來自 Gradiff 的 18 歲學生在做他的暑期研究時，卻意外的發現此顆彗星有分裂現象(圖一：除發現彗星分裂現象外，還另發現次彗星的反向彗尾)

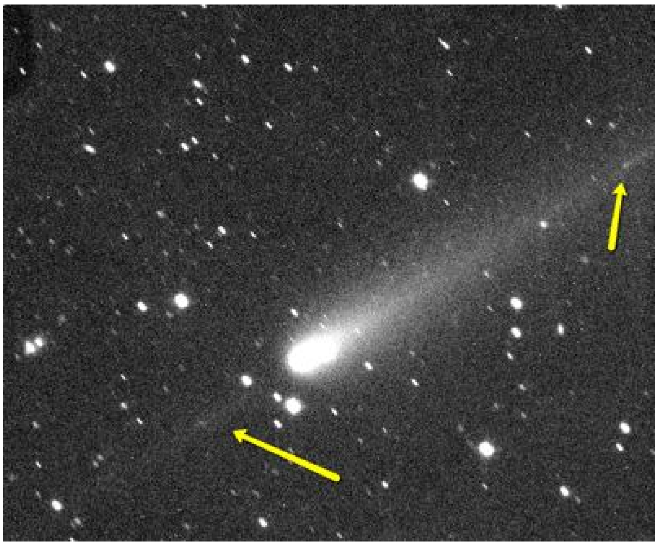

圖一 Comet 213P Van Ness showing the fragments. Source: Faulk Telescope Project

隨後我們立刻使用 SLT 來追蹤此凡尼斯彗星，雖然口徑只有 40 公分，但我們希望利用長期追蹤凡尼斯彗星亮度的變化能提早知道此彗星的分裂！觀測從 2011 年九月初到十月底(圖二)，這段期間我們並沒有看到彗星的亮度有明顯增強，凡尼斯彗星的亮度反而隨著距離的增加漸漸變暗了！

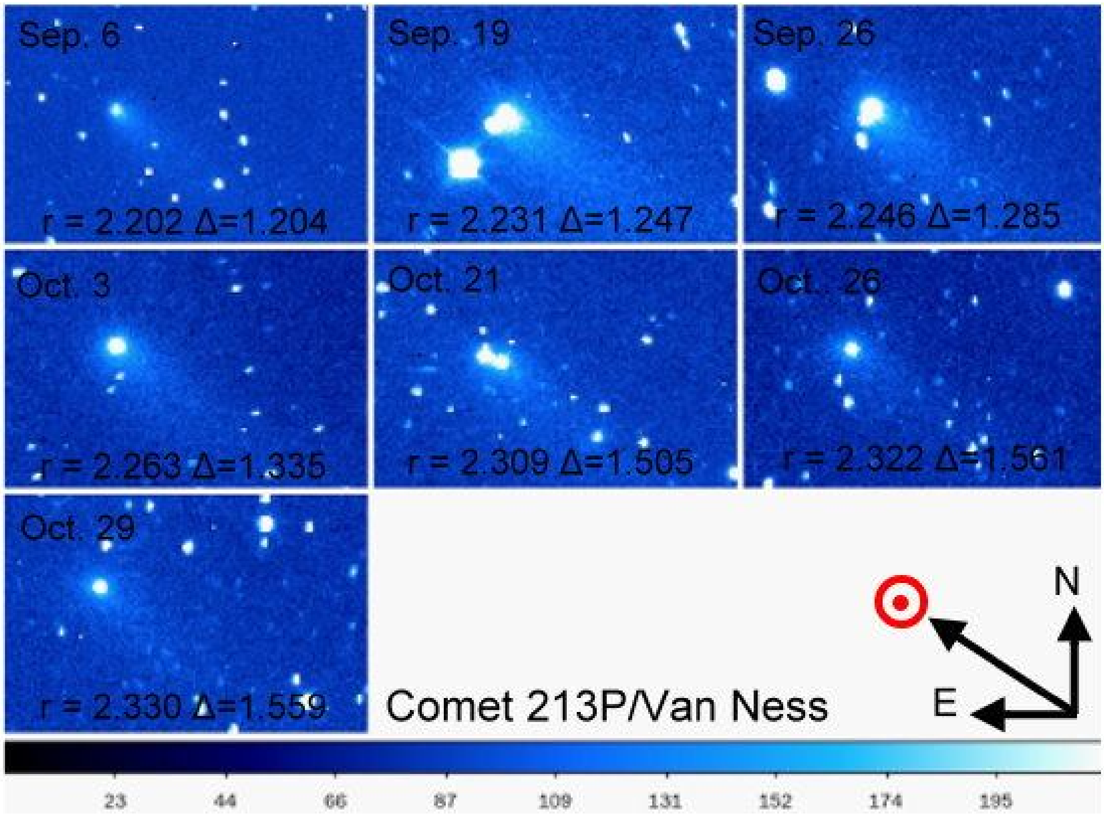

圖二 凡尼斯彗星在鹿林天文台 40 公分望遠鏡從九月初到十月底監測中的影像

Search for Large Amplitude of Jovian Trojan

S. H. Cheng(程劭軒)[1]

[1]InstituteofAstronomy, National Central University, Taiwan, R.O.C

Introjuction

Jovian Trojans are located at Lagrangian points L4 and L5 between the Sun and Jupiter. MPC (Minor Planet Center) estimated now have 5223 Jupiter Trojans, and we have identified 2922 of theem from the Pan-STARRS (ps1-3pi) data set. Trojan asteroids' surface and internal structure are important in understanding the origin and evolution of Jupiter and Jupiter's satellites, because the precursors of Trojans were planetesimals orbiting close to the growing planet (Marzari et al. 2002). Modeling a binary system is the only way to know an asteroid's density and mass and to speculate about an asteroid's internal structure and composition. Mann et al. (2007) estimated 6% to 10% Jovian Trojans should be binaries with large magnitude amplitude.

For this studied, Pan-STARRs has large data set which help to find the cnadidates of binary or elongate shape Trojan asteroids. The target was been detected around 5 times in half year by Pan-STARRs, so the follow-up observation is need.

Observed Method

We used Pan-STARRS 3pi data to find the approximate magnitude variations of Jovian Trojans and selected those which appear to have magnitude variations higher than 0.6 as binary candidates. We have about 30 candidates in the L4 region and a few candidates in the L5 region.

The trojan asteroid's rotation period is about few to ten hours. To cover all of the rotational periods, have two continue nights for each objects at least. But we want to make sure have enough data to fit lightcurve, so we decided three continuous nights for each targets. We assume that Trojans have ten hours for rotation period, and we take 0.1 phase (the 0.1 phase is about half hour) for one exposure. To make sure have enough S/N ratio, the exposure time is 300 seconds for a 19th magitude Trojan.

Finally, We observed two targets in August 25、26 and September 29 of half night, the August 27 and 28 was interrupted by typhoon and September 28 to 30 had cloudy weather.

Observed Result

The Fighre 1 – 6 are the Trojan's lightcurve of single night. X-axis is Modified Julian Date and Y-axis is relative magnitude. The color dots are refer stars to kick out the airmass, and Trojan's relative magnitude is black dot. The refer stars been dispersed by cloudy, like Fig. 03 and 04.

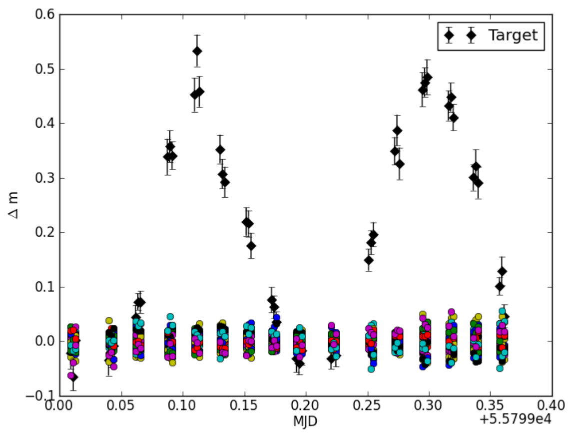

Fig. 01 Date: 2011/08/25, Target: 32467

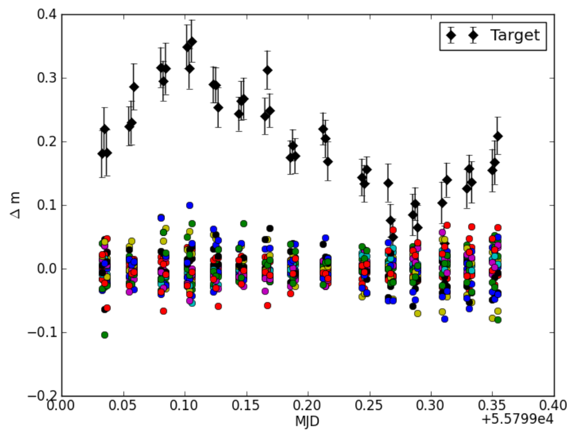

Fig. 02 Date: 2011/08/25, Target: 48373

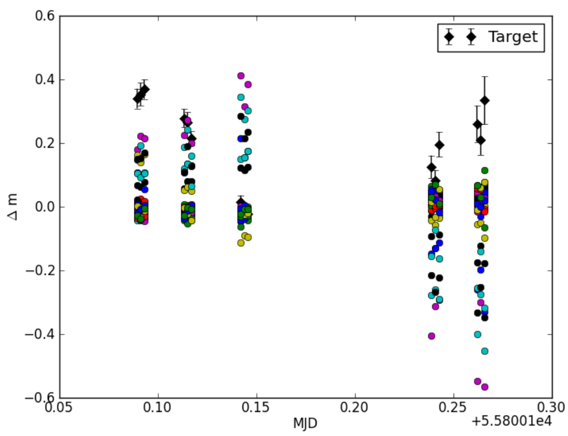

Fig. 03 Date: 2011/08/26, Target: 32467

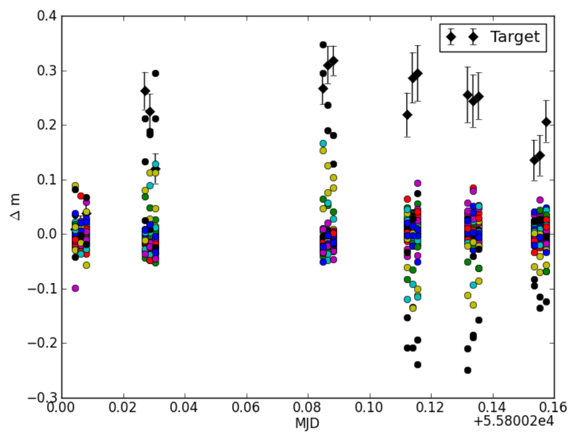

Fig. 04 Date: 2011/08/26, Target: 48373

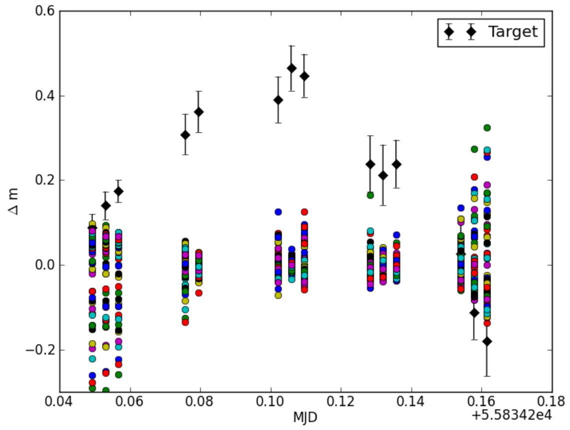

Fig. 05 Date: 2011/09/29 , Target: 20961

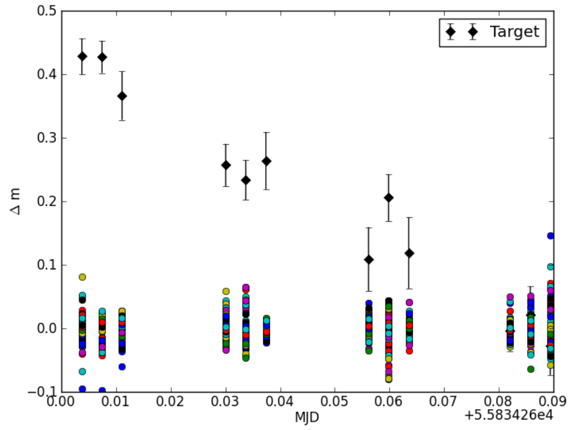

Fig. 06 Date: 2011/09/29 , Target: 35673

Fortunately, I had observed clear lightcurve of 32467 at 2011/08/25. The large amplitude is around 0.593 magnitude. It's almost close 0.6 magnitude. And used Phase Dispersion Minimization (Stellingwerf, 1978) to simulate it period is around 0.3434 day (theta is 0.1031).

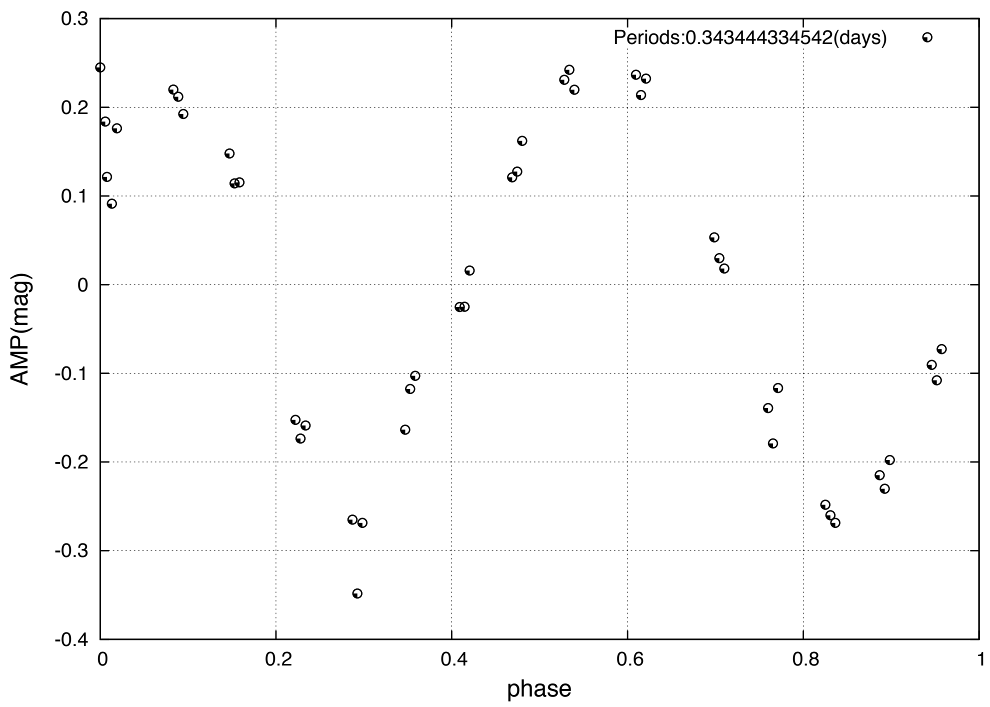

Fig. 07 Rotation phase to resatived magnitude of 32467, was obtained by PDM method.

Reference

1. Marzari, F., Scholl, H., Murray C., Lagerkvist C. 2002, "Origin and Evolution of Trojan Asteroids" Asteroids III, p. 725–738.
2. Mann, R., Jewitt, D., and Lacerda, P. 2007, "Fraction of Contact Binary Trojan Asteroids" ApJ, 134, 1133.
3. Stellingwerf, R. F. 1978, "Period determination using phase dispersion minimization" The Astrophysical Journal, 224: 953-960

Rotationally Resolved Spectroscopic Observations of Asteroids using Lulin One-meter Telescope

Chih-Yang Tai / IANCU

Introduction

Some asteroids are believed to be the parent bodies of meteorites and the asteroid-meteorite interconnection remains an important topic in planetary science. For this reason, we have ran a long-term program in obtaining detailed spectroscopic information of different taxonomic classes of asteroids in various orbital regions. We took observations on LOT (Lulin one-meter telescope) with Hiyoyu spectrometer under different rotation phase. We would like to measure the rotationally resolved surface reflectance visible spectra of a group of asteroids with a view to study the variations of their surface composition and mineralogy.

Observation

Using LOT with Hiyoyu spectrometer attached, we surveyed 12 Asteroids with low resolution grating (R~333) covering visible light (4000A~7500A) during 2010-2011. Though the limiting magnitude of the spectrometer is ~14.5 mag in R-band, in order to achieve the time resolution relative to the rotation period of asteroids, we set R=12.5 as threshold of targets selection. In general, we took one exposure of the target, following by a near-by solar analog exposure to form a cycle. Each night we inserted 4~5 comparison standard lamp in the above procedure. Dome flat-field and dark current are both measured right after each night's observation. Data reduction is showed in Fig 1.

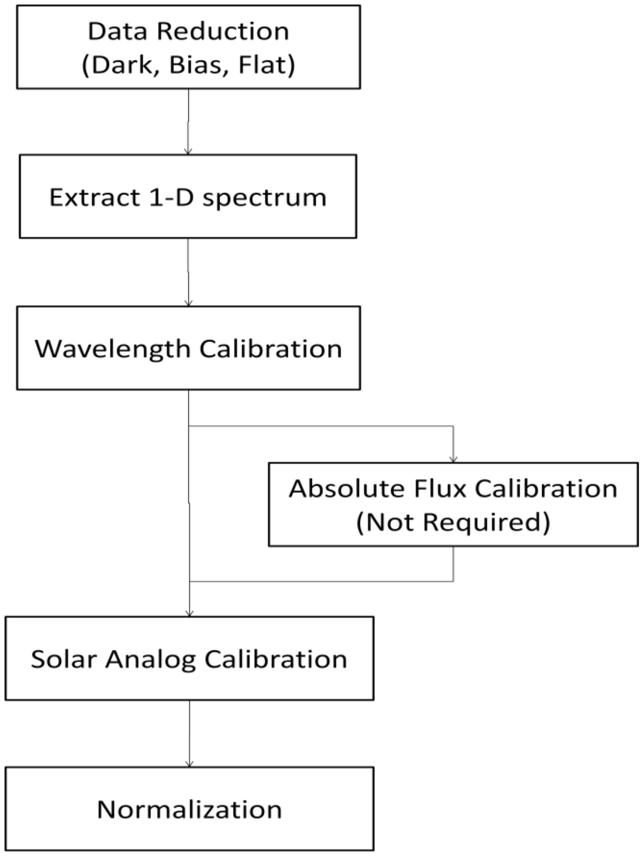

Figure 1. Data reduction flow chart

Discussion

The region near 4000 to 4500 angstroms is affected by atmosphere telluric features. Some spectra were taken under unstable weather and show very different pattern from others. These kinds of data were removed from result figure.
The rest of the data show no significant variation (Fig 2.). This might due to targets selection, because the rotation pole orientation was not considered. Another possibility is that these targets are compositionally homogeneous. Shape is less significant because all spectra were normalized.

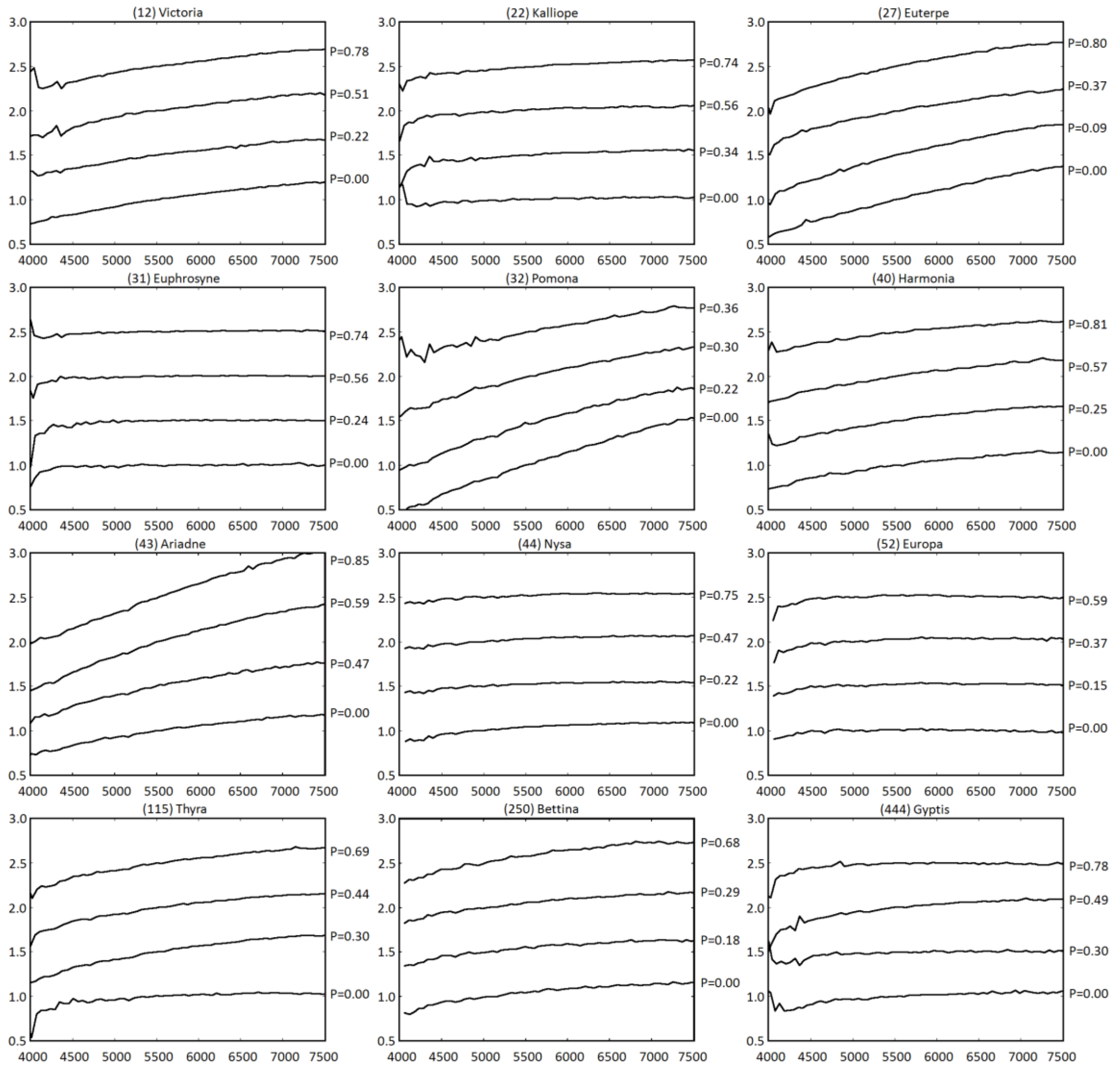

Figure 2. Rotationally resolved spectrum of 12 main belt asteroids. All data relative reflectance were normalized to 1 at 5500 angstroms, and shifted for clearance. Also the data were re-sampled to a lower resolution to focus on the slope variation. The left side Y labels represent relative reflectance, the right side Y labels represent rotational phase relative to a chosen time, X axis represents wavelength in angstroms.

In the future, we will extend this work with focusing on S, V type asteroids and their near infrared features. Pyroxene and Olivine absorption bands are easily found on these taxonomic types. This can help identify meteorites with possible relation with specific types of parent bodies.

Status report on Search for Fragments Caused by Breakup of Titan 3C transtage in the Geostationary Region

Toshifumi Yanagisawa et al

We have performed search observations for fragments caused by breakup of Titan 3C transtage in the geostationary region using the Lulin 1-m Telescope, TAOS telescope and JAXA telescope on October 20th, 21st, and 22nd in 2011. As illustrated in Fig.1, we have applied the orbital debris (OD) modeling techniques to this collaborative observation. The OD modeling techniques can describe debris generation and propagation to define the orbital debris environment. Therefore, the techniques enable us to predict population of debris from the breakup. The predicted debris population specifies effectively when, where and how we should perform observations. The OD modeling techniques also enable us to predict motion of debris in images. The predicted debris motion indicates that debris from the breakup show an own unique and clear trend in motion. Therefore, we can specify effectively and precisely how we should process images of objects in the geostationary region as will be mentioned later. We can also effectively identify their origin without further investigation such as backward propagation of their orbit.

We have also applied effective algorithms for image processing: the stacking method as illustrated in Fig. 2 and the line-identifying technique. Both algorithms have been developed at JAXA to detect faint objects in CCD frames, and validated to work properly with small-aperture telescopes. On an assumption that objects with a seeing size of 0.6 arc-seconds and an albedo of 0.1 are traveling 4.0 arc-seconds every exposure of 3 seconds, therefore, the Lulin 1-m Telescope in combination with the aforementioned algorithms enables us to see tiny fragments down to 6 cm in size (magnitude of 21) with total exposure time of 100 seconds. Such a size of GEO objects has never been detected from the ground-based telescopes.

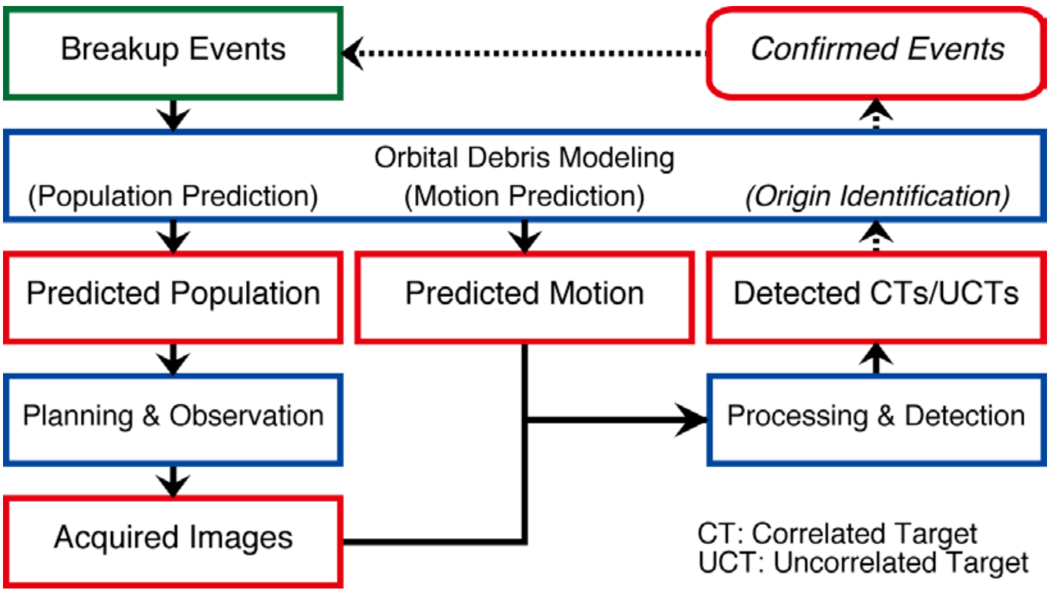

Fig. 1. Sequence of the orbital debris modeling technique

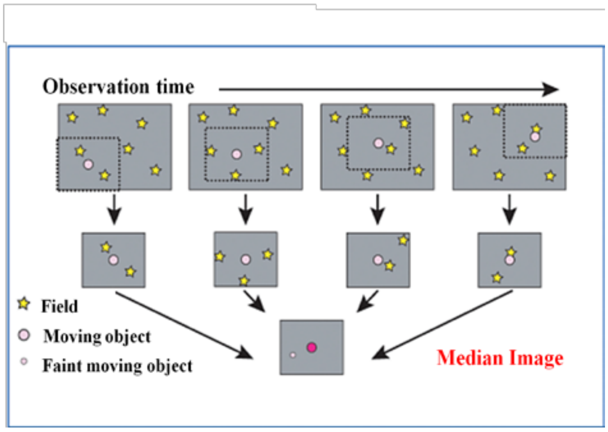

Fig. 2. (a) The concept of the stacking method. Sub-images are cropped from many CCD images to follow the presumed movement of moving objects. Faint objects are detectable by making the median image of these sub-images.

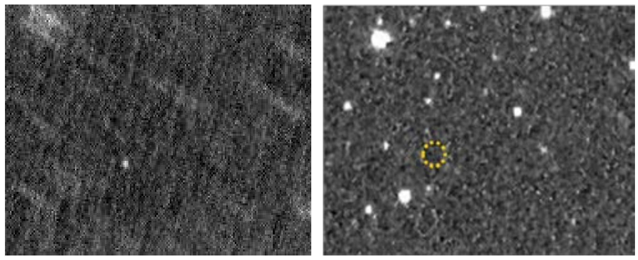

Fig. 2. (b) An asteroid detected by using the stacking method. Left figure shows the final image of the stacking method. Right figure is one of 40 frames used for the method. Detected asteroid must be in the circle but almost invisible.

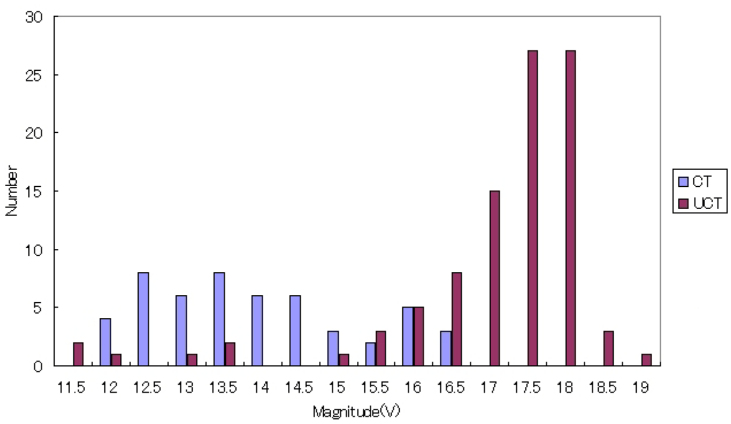

Fig. 3. Brightness distribution of detected objects. Blue and red columns represent cataloged and un-cataloged objects, respectively.

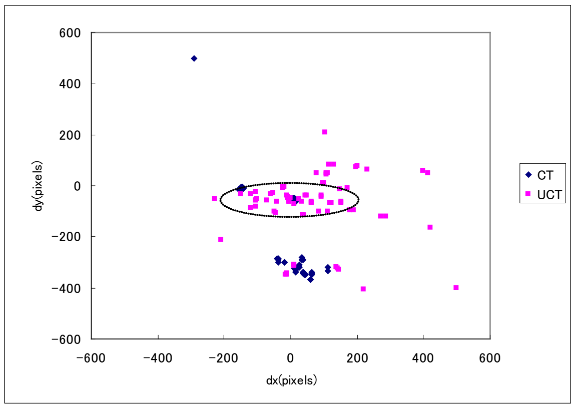

Fig. 4. Motion distribution of detected objects. Blue and pink dots represents cataloged and un-cataloged objects, respectively. Dotted circle may be the fragments caused by the breakup.

Currently, we have completed data analysis of all the data taken with three telescopes. 51 cataloged and 96 un-cataloged objects were detected. Fig.3 and Fig.4 show the brightness and motion distribution of detected objects of this observation. From the motion in Fig. 4, most of un-cataloged objects may be the Titan-related objects. We would like to identify these objects whether they are originated to the breakup with the inverse propagation algorithm and derive size distribution of the fragments which will contribute the breakup model. These results will be presented in upcoming international conferences and published in some academic paper in the near future.

Ground-Based *BVRI* Follow-Up Observations of Two Cepheid Candidates in *Kepler*'s Field

C.-C. Ngeow (NCU, Taiwan), R. Szabo (Konkoly Observatory), L. Szabados (Konkoly Observatory), A. Henden (AAVSO), M. A. T. Groenewegen (Royal Observatory of Belgium) & the Kepler Cepheid Working Group

Introduction

- The *Kepler Space Telescope* (hereafter *Kepler*) is NASA's mission aimed to find Earth size and larger planets around other stars, with almost un-interrupted observation of a 105 deg^2 field near Galactic Plane.

- In addition to finding extra-solar planets, *Kepler's* observation can also be used for asteroseismology and stellar variability studies → goal for ***Kepler* Astroseismic Science Consortium** (http://astro.phys.au.dk/KASC/). There are total of 13 Working Group within KASC, WG #7 is dedicated to Cepheid study.

- Two Cepheid candidates, V1154 Cyg & V2279 Cyg, are located in *Kepler*'s field-of-view. Analysis of these two variables using *Kepler*'s light curves and ground based follow-up data (including *BVRI* light curves and spectroscopy observations) has been published in Szabo et al (2011, MNRAS 413:2709, hereafter S11). The aim of this poster is to provide further details for the *BVRI* follow-up, especially for V1154 Cyg, to supplement S11 paper.

The *BVRI* Follow-Up Observations

- *Kepler's* magnitude system, *Kp*, is based on broad band (430 – 900 nm) transmission of the telescope and detector. Hence, ground-based multi-color (and spectroscopic) follow-up observation is needed to complement the *Kepler's* light curve.
- Time-series observation (more than 3 months) were conducted with the following telescopes:
  I. Lulin One-meter Telescope (LOT) @ Lulin Observatory, Taiwan: 1.00-m Cassegrain telescope with PI1300B CCD.
  II. SLT @ Lulin Observatory, Taiwan: 0.40-m Ritchey-Chretien telescope with Apogee U9000 CCD.
  III. Tenagra telescope (TNG) @ Tenagra II Observatory, Arizona (USA): 0.81-m robotic telescope with STIe CCD.
  IV. Sonoita Research Observatory (SRO) @ Arizona (USA): 0.35-m robotic telescope with SBIG STL-1001E CCD.
- Imaging data process involved the following steps:
  I. Standard IRAF reduction (bias and dark subtracted, flat-fielding).
  II. Cataloging and aperture photometry using SExtractor.
  III. Calibration to standard magnitudes using Landolt standard stars.

Result for V2279 Cyg

- Analysis of *Kepler*'s light curves, *BVRI* light curves and spectroscopic observation shows that V2279 Cyg is NOT a Cepheid. The *BVRI* light curves are shown below.

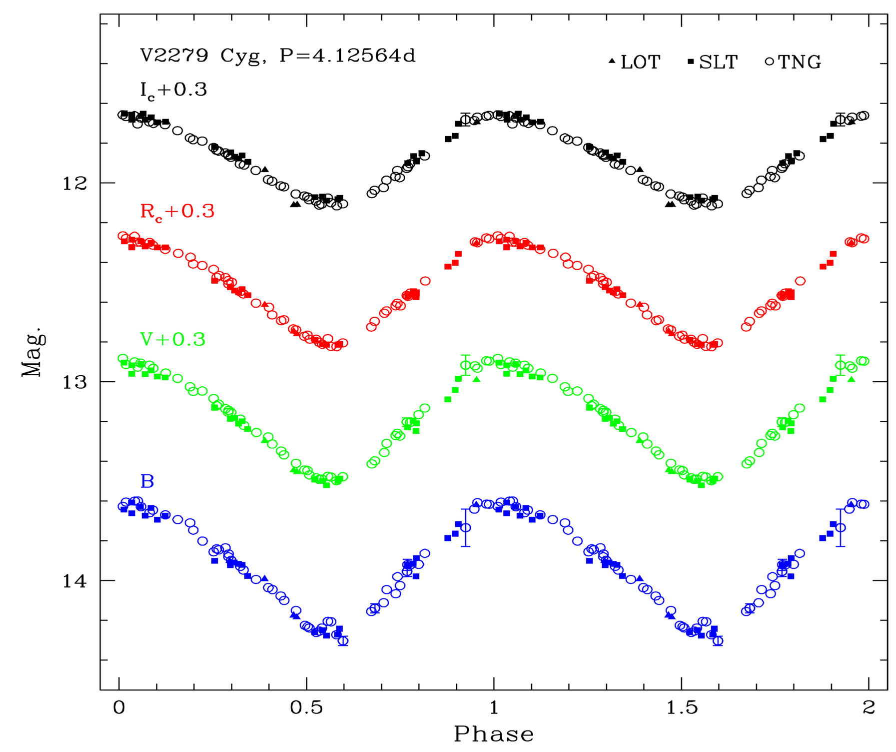

Results for V1154 Cyg

- *BVRI* light curves properties and radial velocity measurement from spectroscopic observation suggested V1154 Cyg is a *bona-fide* fundamental mode Cepheid.

- **Figure 1** shows the *BVRI* light curves from this work (as presented in S11); **Figure 2** compares our light curves to the light curves presented in Berdnikov (2008, VizieR On-line Data Catalog: II/285), note that +0.054 mag need to be added to S11 *B* band data to bring agreement between the two light curves. **Table 1** summarizes the *BVRI* intensity mean magnitudes and amplitudes (from Fourier fit to the light curves) based on S11 light curves.

- Baade-Wesselink (BW) surface brightness method was used to derive the distance and mean radius of V1154 Cyg, by combining the published radial velocity (RV) data and available light curves (details of the method can be found in Groenewegen 2008, A&A 488:25). **Figure 3** presents the results of BW analysis. The distance and radius of V1154 Cyg are: D = 1202 ± 72 ± 68 pc, R/Rsun = 23.5 ± 1.4 ± 1.3, the first error is the formal fitting error, the second error is based on a Monte Carlo simulation taking into account the error in the photometry, RV data, E(B-V) and the p-factor (p = 1.255 is adopted with a 5% error).

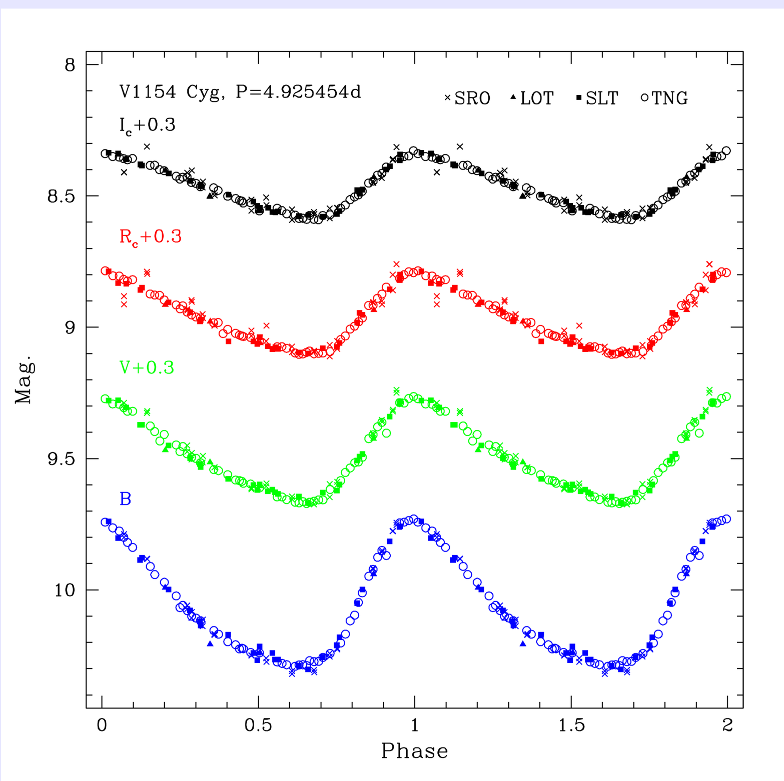

Figure 1: *BVRI* light curves from this work (as in S11).

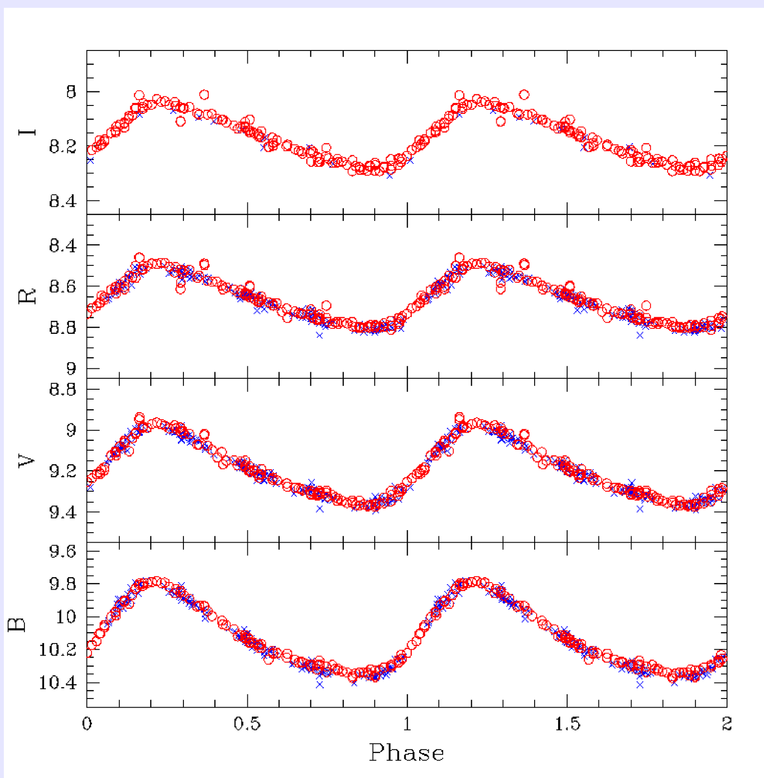

Figure 2: Comparison of the *BVRI* light curves from S11 (open circles) and Berdnikov (2008, crosses)

Band	Intensity Mean Magnitude	Amplitude
B	10.107	0.547
V	9.185	0.390
R	8.659	0.314
I	8.168	0.250

Table 1: Basic *BVRI* properties for V1154 Cyg.

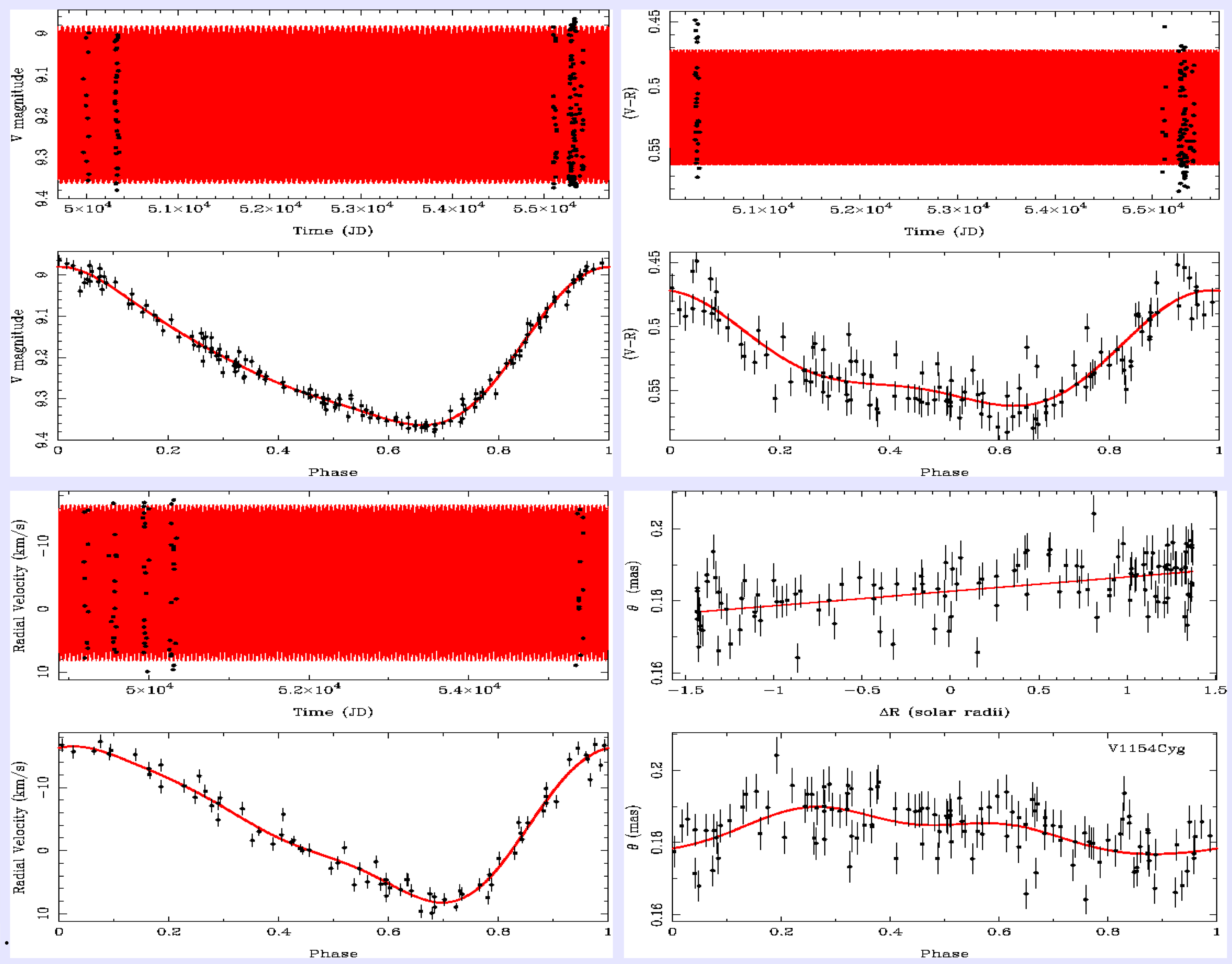

Figure 3: Results of the BW Analysis for V1154 Cyg, including the fitting of *V* band light curve [upper left], *(V-R)* color curve [upper right], RV curve [lower left] and angular diameters [lower right].

CCN thanks the funding from National Science Council (of Taiwan) under the contract NSC 98-2112-M-008-013-MY3. Funding for *Kepler* mission is provided by NASA's Science Mission Directorate.

Moving Needles in a Haystack ~~ Finding Asteroids in Pan-STARRS

Ruo-Lan Jin [1](金若蘭), Dah-Lih You [2](游大立), Shih-Chao Lin [3](林士超)

[1] Taipei First Girls High School , [2]Chang-hua Senior High School , [3]National Dali Senior High School

Between March 28 and May 20, 2011, there is a Pan-STARRS Asteroid Search Campaign using images taken by the 1.8-m PS1 telescope located on Haleakala, Maui, in Hawaii, USA. The campaign is organized by the International Astronomical Search Collaboration (IASC) and in the current campaign draws 32 participating schools from Taiwan, Brazil, Bulgaria, Germany, Poland, Turkey and United States. Each school was paired with an oversea partner to work on the same set of 4-5 images every week. In Taiwan, 3 high schools participated, National Dali Senior High School, Chang-hua Senior High School , and Taipei First Girls High School.

In the campaign, our students competed and collaborated with fellow teammates and with international teams, analyzed the images to make preliminary new identifications of asteroids, and combined local resources to secure the discoveries. Overall, our students excelled, and our efforts were acclaimed by the organizing committee. Students were thrilled about the experience. Here we report our results in the campaign. By the date of May 14 2011, the students of 2nd Pan-STARRS Asteroid Search Campaign have made 267 preliminary Main Belt asteroid (MBA) discoveries plus 22 provisional MBA designations and 1 rare Apollo-class asteroid discovery with an orbit crossing Earth's orbit. Among the 22 provisional MBA discoveries, 3 were discovered independently by students of National Dali High school and 1 was discovered simultaneously by both Chang-Hua Senior High and collaboration school.

More than that National Dali High school’s followed-up observations by Lulin One-meter Telescope made another 3 provisional MBA discoveries! (2011 JF10, 2011 JV12, 2011 JS15)

市立北一女中
沈亮欣, 莊雅淳, 金若蘭,張 瑄, 林孝柔, 黃鈺昕, 蔡佳蓉

國立大里高中
林士超,陳聖丁, 李子駿, 黃義雄, 林學敏, 蔡仲霖 , 林峙宇, 陳琮淯

國立彰化高中
游大立,楊承域, 陳冠綸, 曾泓祥, 趙宥然, 蕭宇泰

本次小行星搜尋活動自2011年3月28日至5月20日舉行，使用美國夏威夷茂宜島1.8米口徑的PS1望遠鏡(右下圖)所攝影像，是國際天文搜尋合作計畫IASC的一部分，請作Isaac, *http://iasc.hsutx.edu* 只要夏威夷茂宜島天氣許可，活動期間每週都會有4~5幅PS1淨化過影像可以下載→ 以Astrometrica 分析天體座標 → 排除CCD熱點，尋找移動天體→ 比對是否為已知的小行星→ 通報IASC進一步研判→發現疑似小行星 (preliminary編號) → 經過再次追蹤，確認為新發現小行星 (MPC會給定provisional編號) ！

＝致謝＝

我們感謝泛星計畫及國際天文搜尋合作計畫提供第一手影像資料給高中生及大學生參與分析，同時我們也感謝中央大學天文研究所陳文屏教授鼓勵我們的學生參與國際性的天文研究活動，讓學生體驗天文學家分析資料的樂趣。同樣的是天體拍攝與分析，不同的是課堂外知識成長與國際視野開展。

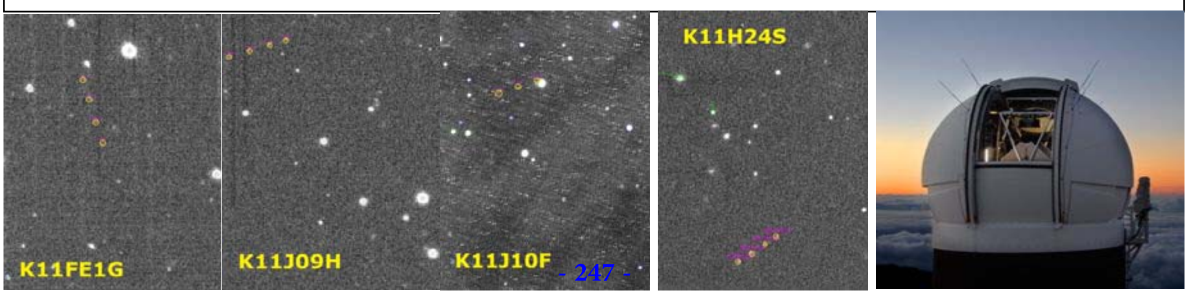

圖說 ：國立大里高中及彰化高中的同學們分析泛星計畫的影像資料找到新的小行星，並且取得臨時編號爲2011FG141(K11FE1G)與2011HS24(K11H24S)。

工作報告

鹿林兩米天文望遠鏡四色同步分光儀器研製工作簡報

A brief of Lulin 2m telescope 4-color simultaneous imager

吳景煌，國立中央大學天文所兩米望遠鏡儀器團隊，31/Mar/2012

一、 簡介：

本所為兩米望遠鏡設計了四色同步分光系統與成像系統。四色的波段分別是：552-689nm(r)、691-815nm(i)、815-915nm(z)以及 967-1024nm(y)，其光學校正、分光部分由日商 Photocoding 公司承製。而其中的 552-689nm(r)、691-815nm(i)與 815-915nm(z)三個波段的相機由美商 Spectral Instruments 公司承製，第四個波段 967-1024nm(y)的相機，則由本所設計 dewar 與介面，並配合日商 Hamamatus 公司的 fully depleted CCD(該 CCD 具有較高的近紅外端 QE)，以及美商 Astro Electronics Technology(AET)公司的 ACS-164 UCAM CCD 資料擷取與控制系統。

目前，四色同步分光系統的光學部分已經完成，第四色(y)相機也已經有了觀測成果，本文將重點說明本儀器團隊在開發四色同步分光系統的現況。

二、 目前進度：

1. **四色同步分光系統：**該系統已經完成，並已進行相機的組裝測試，將再安裝更多的周邊測試。下圖是四色同步分光系統的 3D 示意圖。

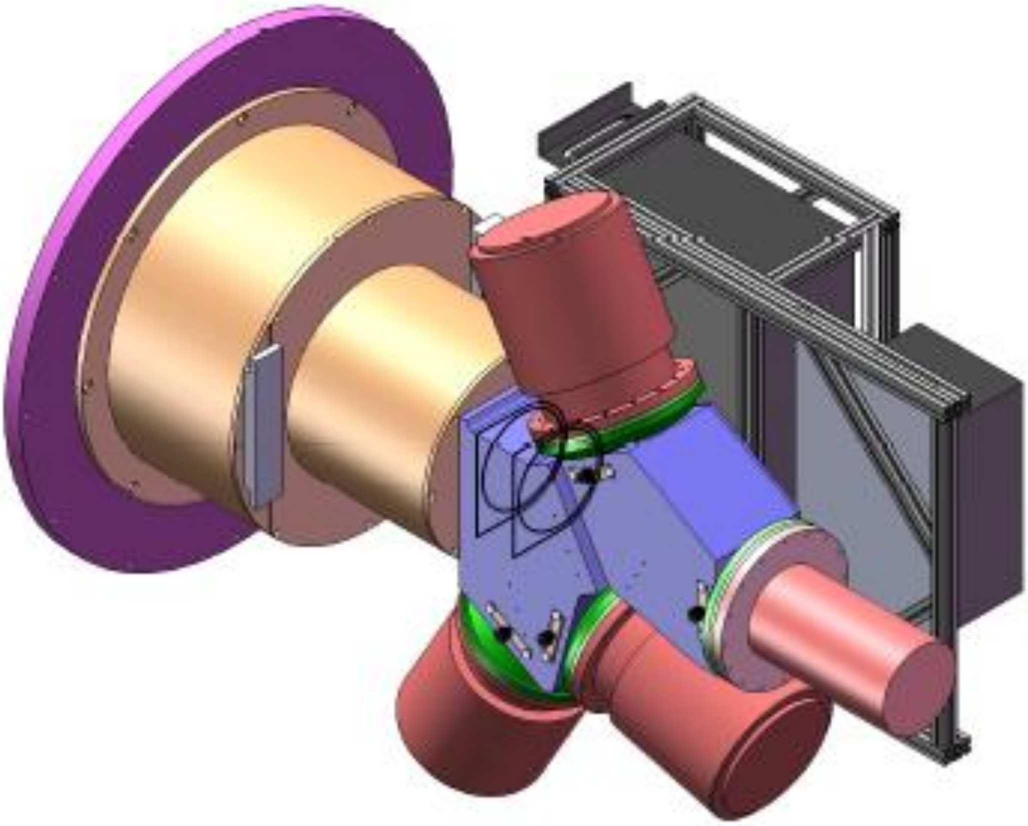

下圖是實際驗收的成品照。

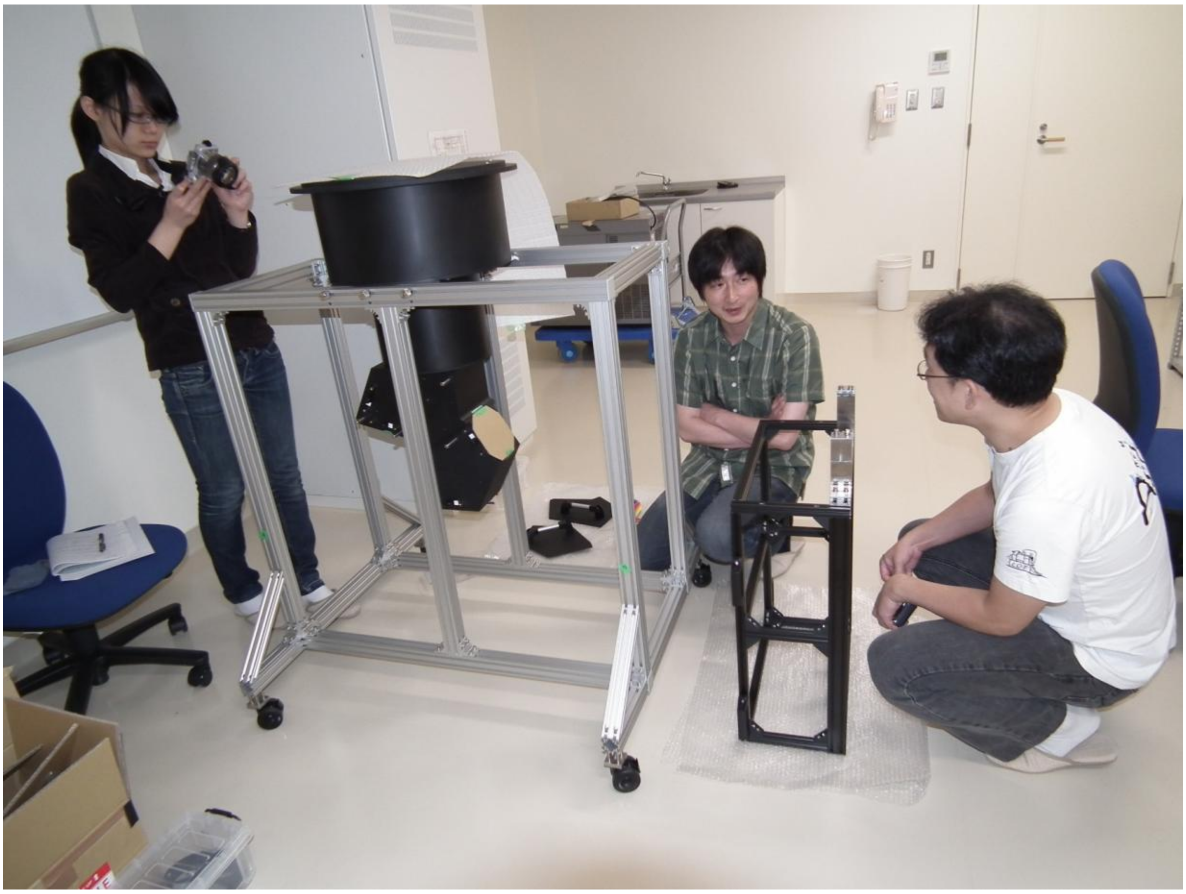

2. y 波段成像系統：本所成功的完成該相機，我們也在鹿林多次觀測，並獲得許多影像如下，大致功能都穩定，唯軟體介面的整合與成像的品質需要再優化。

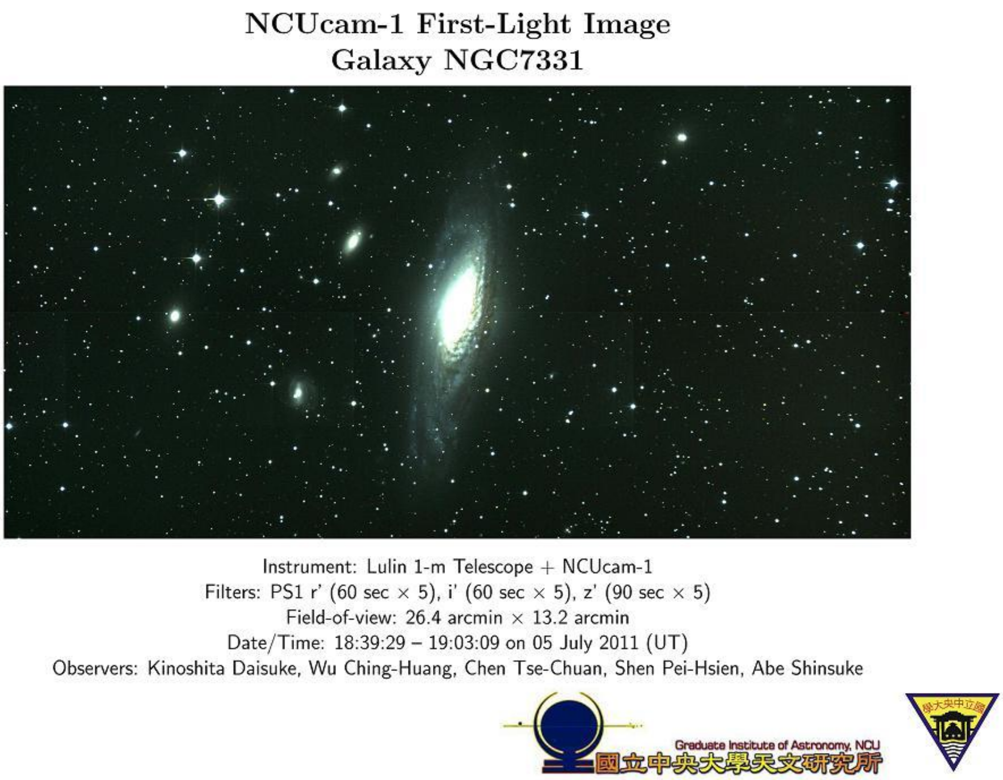

下左圖是 y 波段的照片，可以比對右圖在相同目標時可見光波段的照片。

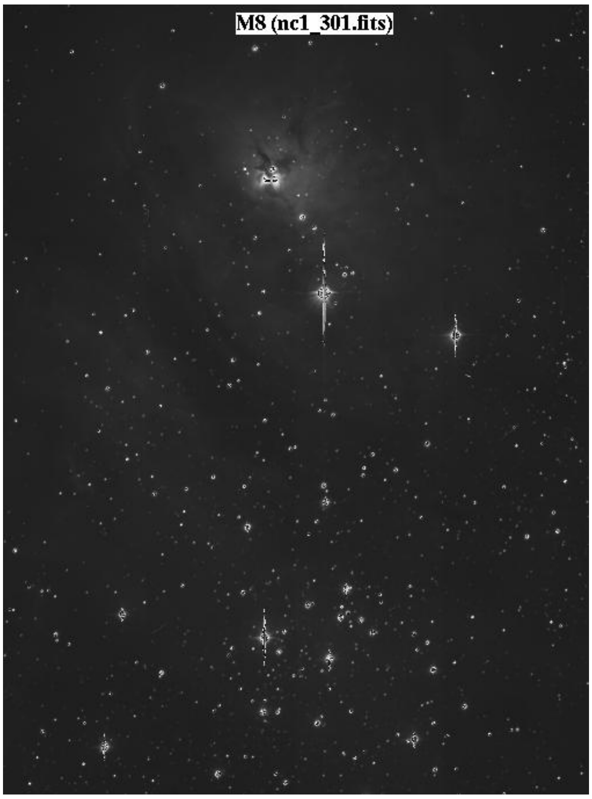

下圖是木下大輔老師(左)與作者(右)拿著 y 波段相機(NCUcam-1)的照片。

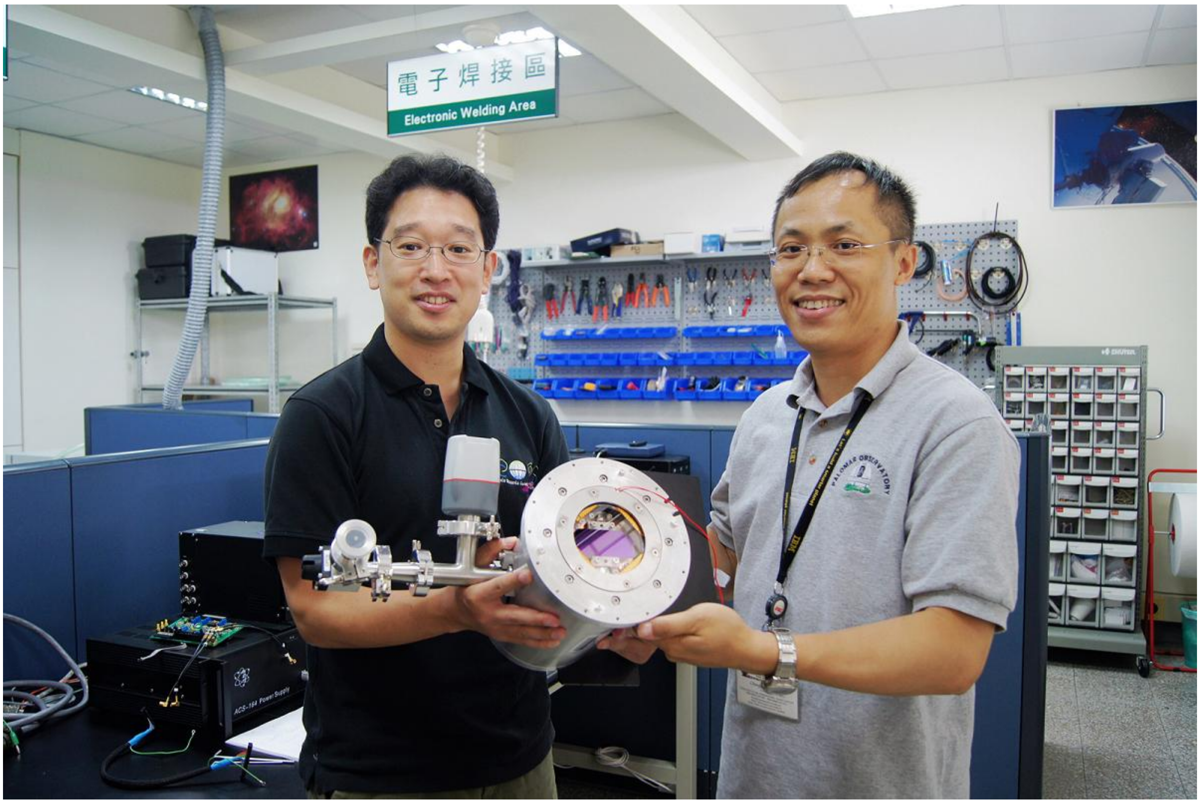

三、 未來計畫：

1. **四色同步分光系統**：預計年底送到夏威夷大學的 UH88 望遠鏡進行合作觀測。

NCUcam-1 CCD Data Reduction Guide

Kinoshita Daisuke

first draft on 11 February 2012
revision on 13 March 2012
second version on 15 March 2012

1 Introduction

This document describes a guideline for the CCD data reduction for the data produced by NCUcam-1 and Lulin 1-m Telescope. The CCD is cooled down to -100°C by the cryocooler and the dark subtraction is not needed. The UCAM CCD controller adds overscan regions for each exposure, and bias subtraction is carried out using the overscan regions. For the data reduction, the use of IRAF (Image Reduction and Analysis Facility) is assumed.

2 Structure of NCUcam-1 FITS data

NCUcam-1 produces a single FITS file for each exposure. The schematic drawing for the structure of NCUcam-1 FITS data is shown in Fig. 1. The CCD chip has four readout channels, and four regions of 512×4096 pixels are read separately. In addition to these four 512×4096 pixels of imaging regions, there are four overscan regions onn the right hand side. The size of each overscan region is 32×4096 pixels. Hence, the size of FITS file is $\{(512 + 32) \times 4\} \times 4096$.

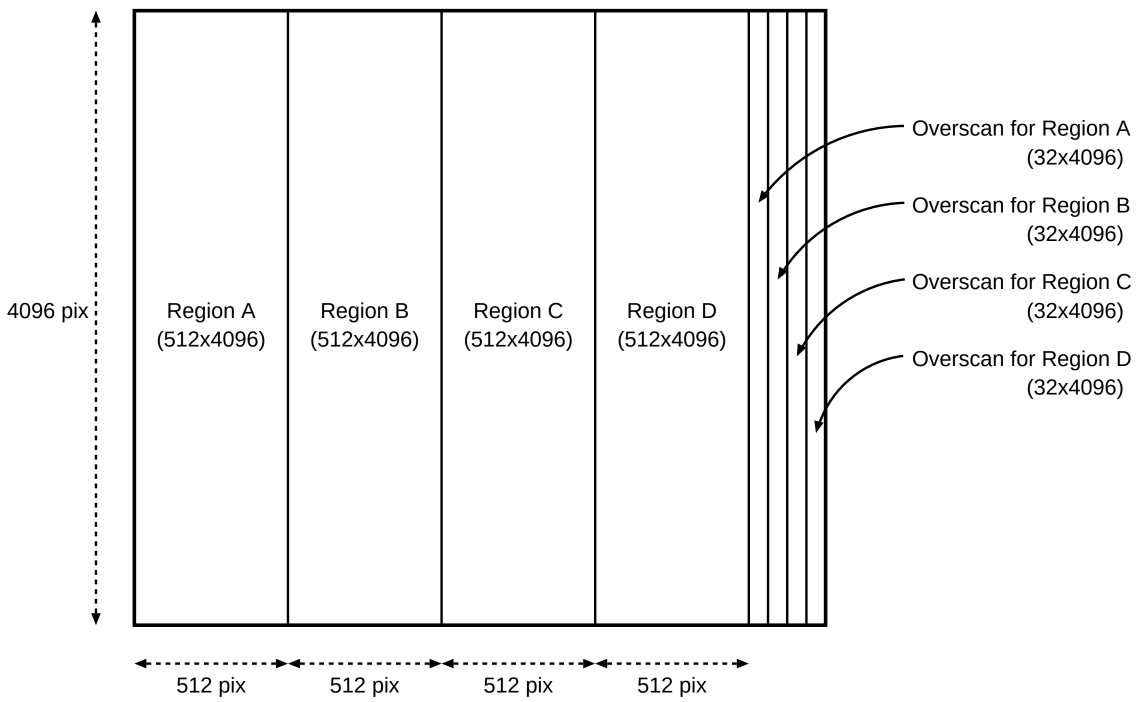

Figure 1: The structure of NCUcam-1 FITS data.

3 Basic idea for CCD data reduction

The CCD data reduction for NCUcam-1 includes the bias subtraction and flatfielding. The basic idea is expressed as

$$reduced(i,j) = \frac{raw(i,j) - bias_{raw}(i,j)}{flat(i,j) - bias_{flat}(i,j)}, \tag{1}$$

where $reduced(i,j)$ is the pixel value of $(x,y) = (i,j)$ in reduced object frame, $raw(i,j)$ is the pixel value of $(x,y) = (i,j)$ in raw object frame, $flat(i,j)$ is the pixel value of $(x,y) = (i,j)$ in raw flatfield frame, and $bias_{raw}(i,j)$ and $bias_{flat}(i,j)$ are the bias value corresponding to $(x,y) = (i,j)$ in raw object frame and flatfield frame, respectively. $bias_{raw}(i,j)$ and $bias_{flat}(i,j)$ are estimated from the overscan region of the raw object frame and flatfield frame. The bias subtracted flatfields are usually normalized.

4 Bias subtraction

To subtract bias using overscan regions, a task `colbias` is used.

```
cl> noao
      artdata.      digiphot.     nobsolete.    onedspec.
      astcat.       focas.        nproto.       rv.
      astrometry.   imred.        observatory   surfphot.
      astutil.      mtlocal.      obsutil.      twodspec.
no> imred
      argus.      crutil.     echelle.    iids.       kpnocoude.  specred.
      bias.       ctioslit.   generic.    irred.      kpnoslit.   vtel.
      ccdred.     dtoi.       hydra.      irs.        quadred.
im> bias
      colbias   linebias
bi> colbias nc1_12345.fits nc1_12345_1.fits bias="[2049:2080,*]" trim="[1:512,*]" \
>>> niterate=5 function=spline3 order=5 median=yes inter-
bi> colbias nc1_12345.fits nc1_12345_2.fits bias="[2081:2112,*]" trim="[513:1024,*]" \
>>> niterate=5 function=spline3 order=5 median=yes inter-
bi> colbias nc1_12345.fits nc1_12345_3.fits bias="[2113:2144,*]" trim="[1025:1536,*]" \
>>> niterate=5 function=spline3 order=5 median=yes inter-
bi> colbias nc1_12345.fits nc1_12345_4.fits bias="[2145:2176,*]" trim="[1537:2048,*]" \
>>> niterate=5 function=spline3 order=5 median=yes inter-
```

Above four commands produce four FITS files of the size of 512 $\times$ 2048. To concatenate those four FITS files, a task `imjoin` is used.

```
cl> imjoin nc1_12345_1.fits,nc1_12345_2.fits,nc1_12345_3.fits,nc1_12345_4.fits \
>>> nc1_12345_o.fits 1
```

The file `nc1_12345_o.fits` is the bias subtracted data. The bias subtraction is applied to all the data obtained, including flatfield frames.

5 Making flatfield

To make a flatfield for each passband, we first combine bias subtracted flatfield frames. It is done by `imcombine`. Here, we assume that ten FITS files from `nc1_12345_o.fits` to `nc1_12354_o.fits` are bias subtracted flatfield frames for r'-band. Then, combined flatfield frame is normalized by `normalize`. Finally, `normflat` is applied to mask negative valued pixels mainly caused by hot and bad pixels.

Here is an example for making r'-band flatfield.

```
cl> ls nc1_1234[5-9]_o.fits nc1_1235[0-4]_o.fits > flat_r.list
cl> imcombine @flat_r.list rawflat_r.fits combine=average \
>>> reject=sigclip scale=median weight=median
cl> normalize rawflat_r.fits
```

```
cl> normflat rawflat_r.fits flat_r.fits minflat=0.7
```

The file `flat_r.fits` is the flatfield for r'-band.

6 Flatfielding

We assume that the FITS file `nc1_12389.fits` is a bias subtracted science frame taken with r'-band filter. To apply flatfielding, a task `imarith` is used.

```
cl> imarith nc1_12389_o.fits / flat_r.fits nc1_12389_of.fits
```

Flatfielding is applied to all the science frames obtained.

7 Successive data analysis

Now, the data are ready for further data analysis to extract quantities you are interested in measuring.

8 A sample script to make flatfields

```
#!/usr/bin/perl

##########################################################################
#                                                                        #
# nc1_makeflat.pl                                                        #
#                                                                        #
#   a Perl script to generate a CL script to make a normalized flatfield #
#   for NCUcam-1                                                         #
#                                                                        #
#   scripted by Kinoshita Daisuke                                        #
#                                                                        #
#   version 1.0: 10 July 2011                                            #
#                                                                        #
##########################################################################

##########################################################################
#                                                                        #
# Parameters                                                             #
#                                                                        #
##########################################################################

#
# minimum exposure time allowed by the shutter
#
$min_exptime = 4.99999999;

#
# minimum and maximum count level for use
#
$min_level =  5000.0;
$max_level = 35000.0;

#
# location of "gethead" command of WCSTools
#
$gethead = "/usr/local/bin/gethead";

#
# location of "imstat" command made by Kinoshita Daisuke
#
$imstat     = "$ENV{HOME}/bin/imstat";
$imstat_opt = '-i 3 -r 300:1700,1500:2500 -s 3.0';
#$imstat_opt = '-i 3 -r 300:1700,1900:2100 -s 3.0';

#
# FITS keywords to be checked
#
$keywords = 'DATA-TYP READ-SPD GAIN EXPTIME FILTER';

#
# IRAF tasks
#
@imarith   = ("images", "imutil", "imarith");
@imcombine = ("images", "immatch", "imcombine");
@colbias   = ("noao", "imred", "bias", "colbias");
@normalize = ("noao", "imred", "generic", "normalize");
@normflat  = ("noao", "imred", "generic", "normflat");
@imjoin    = ("images", "imutil", "imjoin");
@imdelete  = ("images", "imutil", "imdelete");

$imcombine_opt = 'combine=average reject=sigclip scale=median weight=median';
$normflat_opt  = 'minflat=0.7';
$colbias_opt   = 'niterate=5 function=spline3 order=5 median=yes inter-';

#
# current date
#
($sec, $min, $hour, $mday, $mon, $year, $wday, $yday, $isdst) = gmtime (time);
$year += 1900;
$mon += 1;
($current_time) = sprintf ("%04d%02d%02d%02d%02d%02d",
                           $year, $mon, $mday, $hour, $min, $sec);
```

```
#
# name of CL script produced by this script
#
($clscript) = sprintf ("makeflat_%s.cl", $current_time);



###############################################################################
#                                                                             #
# Main routine                                                                #
#                                                                             #
###############################################################################

$NFile = $#ARGV + 1;
$i = 0;

open (CL, ">$clscript") or die "Cannot create a file \"$clscript\": $!\n";

SCANFILES: foreach $fits (@ARGV) {
    printf (STDERR "\033[1M  Progress: %4.1f percent (%d / %d)\n\033[1A",
            $i * 100 / $NFile, $i, $NFile);
    $i++;

    unless ($fits =~ /\.fits$/) {
        print STDERR "The file \"$fits\" is not a FITS file!\n";
        next;
    }

    #
    # Acquiring information from FITS header
    #
    # DATA-TYP READ-SPD GAIN EXPTIME FILTER
    #
    undef $header_info;
    undef @header_info;
    undef %header;
    ($header_info) = `$gethead $keywords $fits`;
    (@header_info) = split (/\s+/, $header_info);
    $header{"datatype"} = $header_info[0];
    $header{"readspd"}  = $header_info[1];
    $header{"gain"}     = $header_info[2];
    $header{"exptime"}  = $header_info[3];
    $header{"filter"}   = $header_info[4];

    ($data_prop) = sprintf ("%s_%s_%s", $header{"filter"},
                            $header{"readspd"}, $header{"gain"});

    #
    # only flatfield with exposure time longer than $min_exptime is used.
    #
    unless ($header{"datatype"} =~ /FLAT/) {
        printf (STDERR
                "\"%s\" is not used: NOT flatfield data\n",
                $fits);
        next SCANFILES;
    }
    if ($header{"exptime"} < $min_exptime) {
        printf (STDERR
                "\"%s\" is not used: exposure time = %8.3f sec\n",
                $fits, $header{"exptime"});
        next SCANFILES;
    }

    #print STDERR "$fits\n";

    # checking mean count of raw flatfield frames
    undef @imstat_results;
    undef $imstat_file;
    undef $imstat_npix;
    undef $imstat_mean;
    undef $imstat_median;
    undef $imstat_stddev;
    undef $imstat_min;
```

```
    undef $imstat_max;
    (@imstat_results) = `$imstat $imstat_opt $fits`;
    ($imstat_file, $imstat_npix, $imstat_mean, $imstat_median,
     $imstat_stddev, $imstat_min, $imstat_max)
        = split (/\s+/, $imstat_results[1]);
    unless ( ($imstat_median > $min_level)
             and ($imstat_median < $max_level) ) {
        printf (STDERR
                "\"%s\" is not used: median count level = %d\n",
                $fits, $imstat_median);
        next SCANFILES;
    }

    #
    # bias subtraction using overscan region
    #
    $fits_ossub = $fits;
    if ($fits_ossub =~ /\//) {
        ($fits_ossub) = ($fits_ossub =~ /\S+\/(\S+)/);
    }
    $fits_ossub =~ s/\.fits/_o.fits/g;
    $ch1 = $fits_ossub;
    $ch1 =~ s/_o\.fits/_1.fits/g;
    $ch2 = $fits_ossub;
    $ch2 =~ s/_o\.fits/_2.fits/g;
    $ch3 = $fits_ossub;
    $ch3 =~ s/_o\.fits/_3.fits/g;
    $ch4 = $fits_ossub;
    $ch4 =~ s/_o\.fits/_4.fits/g;

    undef $task_colbias;
    for ($j = 0; $j <= $#colbias; $j++) {
        if ($j != $#colbias) {
            $task_colbias .= "$colbias[$j]\n";
        } else {
            $task_colbias .= "print \"subtracting bias of $fits using overscan region...\"\n";
            $task_colbias .= "$colbias[$j] $fits $ch1 bias=\"[2049:2080,*]\" trim=\"[1:512,*]\" $colbias_opt\n";
            $task_colbias .= "$colbias[$j] $fits $ch2 bias=\"[2081:2112,*]\" trim=\"[513:1024,*]\" $colbias_opt\n";
            $task_colbias .= "$colbias[$j] $fits $ch3 bias=\"[2113:2144,*]\" trim=\"[1025:1536,*]\" $colbias_opt\n";
            $task_colbias .= "$colbias[$j] $fits $ch4 bias=\"[2145:2176,*]\" trim=\"[1537:2048,*]\" $colbias_opt\n";
        }
    }
    undef $task_imjoin;
    for ($j = 0; $j <= $#imjoin; $j++) {
        if ($j != $#imjoin) {
            $task_imjoin .= "$imjoin[$j]\n";
        } else {
            $task_imjoin .= "$imjoin[$j] $ch1,$ch2,$ch3,$ch4 $fits_ossub 1\n";
        }
    }
    undef $task_imdelete;
    for ($j = 0; $j <= $#imdelete; $j++) {
        if ($j != $#imdelete) {
            $task_imdelete .= "$imdelete[$j]\n";
        } else {
            $task_imdelete .= "$imdelete[$j] $ch1,$ch2,$ch3,$ch4\n";
        }
    }

    print CL "$task_colbias";
    print CL "$task_imjoin";
    print CL "$task_imdelete";

    #
    # making flatfield list
    #
    push ( @{ $flatlist{"$data_prop"} }, $fits_ossub);

    printf (STDERR "\033[1M  Progress: %4.1f percent (%d / %d)\n\033[1A",
            $i * 100 / $NFile, $i, $NFile);
}

foreach $property ( sort keys %flatlist ) {
    ($filter, $readspd, $gain) = split (/_/, $property);
```

```
    ($rawflat) = sprintf ("rawflat_%s.fits", $property);
    ($nflat)   = sprintf ("flat_%s.fits", $property);

    undef $list;
    foreach $file ( @{ $flatlist{$property} } ) {
        $list .= "$file,";
    }
    $list =~ s/,$//;

    undef $task_imcombine;
    for ($j = 0; $j <= $#imcombine; $j++) {
        if ($j != $#imcombine) {
            $task_imcombine .= "$imcombine[$j]\n";
        } else {
            $task_imcombine
                .= "$imcombine[$j] $list $rawflat $imcombine_opt\n";
        }
    }
    undef $task_normalize;
    for ($j = 0; $j <= $#normalize; $j++) {
        if ($j != $#normalize) {
            $task_normalize .= "$normalize[$j]\n";
        } else {
            $task_normalize
                .= "$normalize[$j] $rawflat\n";
        }
    }
    undef $task_normflat;
    for ($j = 0; $j <= $#normflat; $j++) {
        if ($j != $#normflat) {
            $task_normflat .= "$normflat[$j]\n";
        } else {
            $task_normflat
                .= "$normflat[$j] $rawflat $nflat $normflat_opt\n";
        }
    }
    undef $task_imdelete;
    for ($j = 0; $j <= $#imdelete; $j++) {
        if ($j != $#imdelete) {
            $task_imdelete .= "$imdelete[$j]\n";
        } else {
            $task_imdelete
                .= "$imdelete[$j] $list,$rawflat\n";
        }
    }

    printf (CL "print \"creating flatfield for %s-band (read speed = %s, gain = %s)...\"\n",
        $filter, $readspd, $gain);
    print CL "$task_imcombine";
    print CL "$task_normalize";
    print CL "$task_normflat";
    print CL "$task_imdelete";
}

print CL "\n";
print CL "print \"Finished making flatfield!\"\n";
print CL "\n";

close (CL);
```

9 A sample script for data reduction of science frames

```
#!/usr/bin/perl

#########################################################################
#                                                                       #
# nc1_dored.pl                                                          #
#                                                                       #
#   a Perl script to generate a CL script to do bias subtraction and    #
#   flatfielding for NCUcam-1 data                                      #
#                                                                       #
#   scripted by Kinoshita Daisuke                                       #
#                                                                       #
#   version 1.0: 10 July 2011                                           #
#                                                                       #
#########################################################################

#########################################################################
#                                                                       #
# Parameters                                                            #
#                                                                       #
#########################################################################

#
# minimum exposure time allowed by the shutter
#
$min_exptime = 4.99999999;

#
# minimum and maximum count level for use
#
$min_level =  5000.0;
$max_level = 30000.0;

#
# location of "gethead" command of WCSTools
#
$gethead = "/usr/local/bin/gethead";

#
# location of "imstat" command made by Kinoshita Daisuke
#
$imstat     = "$ENV{HOME}/bin/imstat";
$imstat_opt = '-i 3 -r 300:1700,1500:2500 -s 3.0';
#$imstat_opt = '-i 3 -r 300:1700,1900:2100 -s 3.0';

#
# FITS keywords to be checked
#
$keywords = 'DATA-TYP READ-SPD GAIN EXPTIME FILTER';

#
# IRAF tasks
#
@imarith   = ("images", "imutil", "imarith");
@imcombine = ("images", "immatch", "imcombine");
@colbias   = ("noao", "imred", "bias", "colbias");
@normalize = ("noao", "imred", "generic", "normalize");
@normflat  = ("noao", "imred", "generic", "normflat");
@imjoin    = ("images", "imutil", "imjoin");
@imdelete  = ("images", "imutil", "imdelete");

$imcombine_opt = 'combine=average reject=sigclip scale=median weight=median';
$normflat_opt  = 'minflat=0.7';
$colbias_opt   = 'niterate=5 function=spline3 order=5 median=yes inter-';

#
# current date
#
($sec, $min, $hour, $mday, $mon, $year, $wday, $yday, $isdst) = gmtime (time);
$year += 1900;
$mon += 1;
($current_time) = sprintf ("%04d%02d%02d%02d%02d%02d",
                           $year, $mon, $mday, $hour, $min, $sec);
```

```
#
# name of CL script produced by this script
#
($clscript) = sprintf ("dored_%s.cl", $current_time);



############################################################################
#                                                                          #
# Main routine                                                             #
#                                                                          #
############################################################################

$NFile = $#ARGV + 1;
$i = 0;

open (CL, ">$clscript") or die "Cannot create a file \"$clscript\": $!\n";

SCANFILES: foreach $fits (@ARGV) {
    printf (STDERR "\033[1M  Progress: %4.1f percent (%d / %d)\n\033[1A",
            $i * 100 / $NFile, $i, $NFile);
    $i++;

    unless ($fits =~ /\.fits$/) {
        print STDERR "The file \"$fits\" is not a FITS file!\n";
        next;
    }

    #
    # Acquiring information from FITS header
    #
    # DATA-TYP READ-SPD GAIN EXPTIME FILTER
    #
    undef $header_info;
    undef @header_info;
    undef %header;
    ($header_info) = `$gethead $keywords $fits`;
    (@header_info) = split (/\s+/, $header_info);
    $header{"datatype"} = $header_info[0];
    $header{"readspd"}  = $header_info[1];
    $header{"gain"}     = $header_info[2];
    $header{"exptime"}  = $header_info[3];
    $header{"filter"}   = $header_info[4];

    ($data_prop) = sprintf ("%s_%s_%s", $header{"filter"},
                            $header{"readspd"}, $header{"gain"});

    ($flatfield) = sprintf ("flat_%s.fits", $data_prop);

    #
    # only object frames with exposure time longer than $min_exptime is used.
    #
    unless ($header{"datatype"} =~ /OBJECT/) {
        printf (STDERR
                "\"%s\" is not used: NOT object data\n",
                $fits);
        next SCANFILES;
    }
    if ($header{"exptime"} < $min_exptime) {
        printf (STDERR
                "\"%s\" is not used: exposure time = %8.3f sec\n",
                $fits, $header{"exptime"});
        next SCANFILES;
    }
    unless (-e $flatfield) {
        printf (STDERR
                "Sorry! There is no suitable flatfield for FITS file \"%s\"\n",
                $fits);
        next SCANFILES;
    }

    #
    # bias subtraction using overscan region
```

```
#
$fits_ossub = $fits;
if ($fits_ossub =~ /\//) {
    ($fits_ossub) = ($fits_ossub =~ /\S+\/(\S+)/);
}
$fits_ossub =~ s/\.fits/_o.fits/g;
$ch1 = $fits_ossub;
$ch1 =~ s/_o\.fits/_1.fits/g;
$ch2 = $fits_ossub;
$ch2 =~ s/_o\.fits/_2.fits/g;
$ch3 = $fits_ossub;
$ch3 =~ s/_o\.fits/_3.fits/g;
$ch4 = $fits_ossub;
$ch4 =~ s/_o\.fits/_4.fits/g;
$fits_ff = $fits_ossub;
$fits_ff =~ s/_o.fits$/_of.fits/g;

undef $task_colbias;
for ($j = 0; $j <= $#colbias; $j++) {
    if ($j != $#colbias) {
        $task_colbias .= "$colbias[$j]\n";
    } else {
        $task_colbias .= "print \"subtracting bias of $fits using overscan region...\"\n";
        $task_colbias .= "$colbias[$j] $fits $ch1 bias=\"[2049:2080,*]\" trim=\"[1:512,*]\" $colbias_opt\n";
        $task_colbias .= "$colbias[$j] $fits $ch2 bias=\"[2081:2112,*]\" trim=\"[513:1024,*]\" $colbias_opt\n";
        $task_colbias .= "$colbias[$j] $fits $ch3 bias=\"[2113:2144,*]\" trim=\"[1025:1536,*]\" $colbias_opt\n";
        $task_colbias .= "$colbias[$j] $fits $ch4 bias=\"[2145:2176,*]\" trim=\"[1537:2048,*]\" $colbias_opt\n";
    }
}
undef $task_imjoin;
for ($j = 0; $j <= $#imjoin; $j++) {
    if ($j != $#imjoin) {
        $task_imjoin .= "$imjoin[$j]\n";
    } else {
        $task_imjoin .= "$imjoin[$j] $ch1,$ch2,$ch3,$ch4 $fits_ossub 1\n";
    }
}
undef $task_imdelete;
for ($j = 0; $j <= $#imdelete; $j++) {
    if ($j != $#imdelete) {
        $task_imdelete .= "$imdelete[$j]\n";
    } else {
        $task_imdelete .= "$imdelete[$j] $ch1,$ch2,$ch3,$ch4\n";
    }
}

print CL "$task_colbias";
print CL "$task_imjoin";
print CL "$task_imdelete";

#
# flatfielding
#
undef $task_imarith;
for ($j = 0; $j <= $#imarith; $j++) {
    if ($j != $#imarith) {
        $task_imarith .= "$imarith[$j]\n";
    } else {
        $task_imarith .= "$imarith[$j] $fits_ossub / $flatfield $fits_ff\n";
    }
}
undef $task_imdelete;
for ($j = 0; $j <= $#imdelete; $j++) {
    if ($j != $#imdelete) {
        $task_imdelete .= "$imdelete[$j]\n";
    } else {
        $task_imdelete .= "$imdelete[$j] $fits_ossub\n";
    }
}

print CL "print \"flatfielding for $fits...\"\n";
print CL "$task_imarith";
print CL "$task_imdelete";
```

```
    printf (STDERR "\033[1M  Progress: %4.1f percent (%d / %d)\n\033[1A",
            $i * 100 / $NFile, $i, $NFile);
}
```

NCUcam-1 Observing Manual

Kinoshita Daisuke

10 March 2012

1 Introduction

NCUcam-1 is a CCD imager developed at the Institute of Astronomy, National Central University. It is a general purpose optical CCD imager designed, assembled, and tested by the Instrument Development Team[1] It is one of unit cameras for 4-color simultaneous imager for 2-m telescope which is being built at Lulin Observatory. In order to enhance the sensitivity at longer wavelength, a fully depleted CCD chip is equipped for this camera.

2 Before starting the observation

2.1 Login to the computer

First, you need to log in to the computer named "Ying-Hua".

- user name: `ccdev`
- password: Please ask the password to one of the development team members.

2.2 Start a terminal emulator

Start your favourite terminal emulator. For example, start "`xterm`".

2.3 Create a directory for data storage

Then, you need to create a directory for the data produced by NCUcam-1. If you observe on 10 March 2012, then you need to create a new directory named "`/home/ccdev/data/20120310`"

```
% mkdir -p ~/data/20120310
```

2.4 Edit observers' information

The observers names are stored in the file "`/home/ccdev/.obsinfo`". Following is an example of the content of "`.obsinfo`" file.

```
observer = "Kinoshita, Wu, Chen"
prop-id  = "2012A-10"
telescop = "Lulin One-meter Telescope"
observat = "Lulin Observatory, NCU, Taiwan"
longitud = "120:52:25"
latitude = "+23:28:07"
height   = 2862
instrume = "NCUcam-1"
camera   = "NCUcam-1"
detector = "Hamamatsu fully depleted CCD BI11/35/4K2"
focallen = 8000.0
```

[1]Current members of the Instrument Development Team at the Institute of Astronomy, National Central University is Chen Tse-Chuan, Kinoshita Daisuke, Wu Ching-Huang, and Yang Hui-Hsin (in alphabetical order).)

Edit this file using your favourite editor. For example, you may use the visual editor "vi" to edit the file.

```
% vi ~/.obsinfo
```

If the observers are Lin, A.-B. and Huang, C.-D., then change the value of OBSERVER keyword. You must have your own proposal ID for your program, and it may be "2012A-99". After editing, it might be as follows.

```
observer = "Lin, A.-B.; Huang, C.-D."
prop-id  = "2012A-99"
telescop = "Lulin One-meter Telescope"
observat = "Lulin Observatory, NCU, Taiwan"
longitud = "120:52:25"
latitude = "+23:28:07"
height   = 2862
instrume = "NCUcam-1"
camera   = "NCUcam-1"
detector = "Hamamatsu fully depleted CCD BI11/35/4K2"
focallen = 8000.0
```

If you prefer to add more information into FITS header, then you can include more keyword-value pairs to ".obsinfo" file.

2.5 Start CCD control program

To start the CCD control software, type following command on a terminal emulator.

```
% nc1_start &
```

Then, you will see three windows shown in Fig. 1. If you do not see these three windows, please consult to one of development team members.

2.6 Set-up of UCAM CCD Controller

We set up the UCAM CCD Controller using "Instrument" window. When the "Instrument" window comes up, you see "Top Level" panel (Fig. 2). For Top Level panel, there are 4 important parameters. Those are (1) Binning, (2) Gain, (3) Read Speed, and (4) Record / Don't Record.

- Binning
  - Please choose "1" (no binning) for now. 2×2 binning and 4×4 binning modes are not available at this moment.
  - If you choose 2 or 4, then you will not have meaningful data.
  - We are now working on 2×2 binning and 4×4 binning modes. Please wait for a while, if you are willing to use those binning modes.
- Gain
  - Gain 0 setting $\rightarrow \sim 1.0$ e^-/ADU
  - Gain 1 and 2 settings have higher values (~ 2.0 and 3.6 e^-/ADU)
- Read Speed
  - You can choose one from "Fast", "Medium", and "Slow".
  - Default values for "Fast", "Medium", and "Slow" are 1, 4, and 8 μsec sampling per pixel. (These values are defined in "Eng. Level" panel. Users are not expected to change these values.)

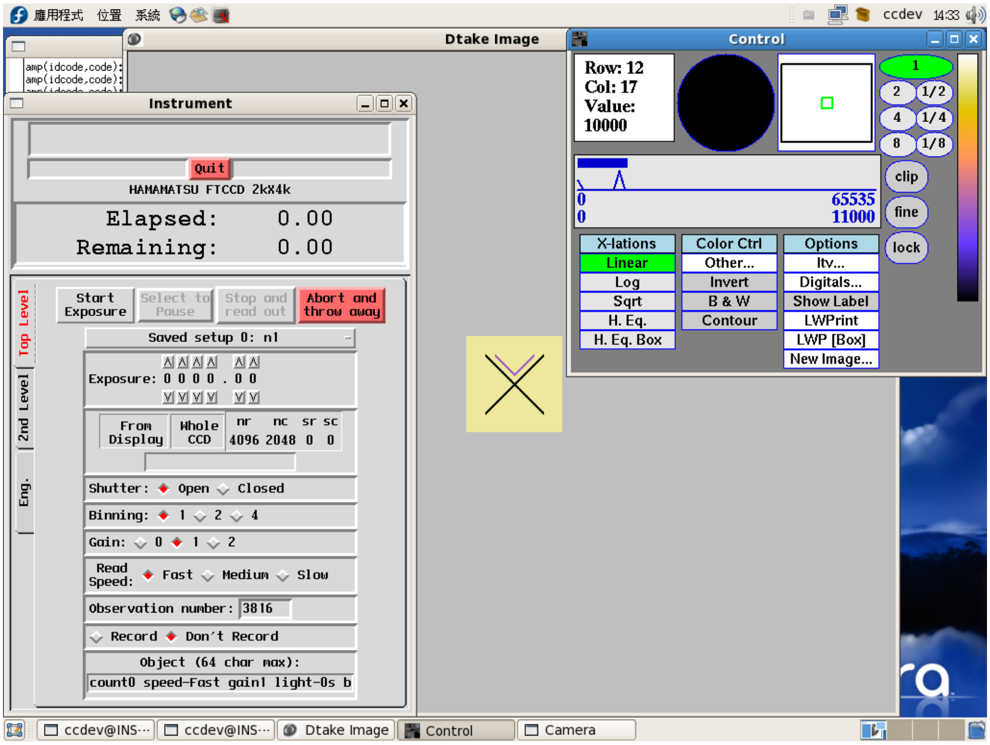

Figure 1: Three windows you see, when you start the CCD control software. Those are “Instrument”, “Control”, and “Dtake Image” windows.

  - Readout times, including erase time, for Fast, Medium, and Slow are $\sim$ 15 sec, $\sim$ 30 sec, and $\sim$ 50 sec, respectively.

- Record / Don't Record
  - When you start the observation, make sure that “Record” is chosen.
  - If “Don't Record” is selected, FITS files are not recorded on hard disk drive.

Next, we check “2nd Level” panel (Fig. 3). If the parameters are set properly, then you will have FITS files stored at `/home/ccdev/data/YYYYMMDD/nc1_NNNN.fits`.

- Directory
  - Change the directory to the one you made.
  - For example, change it to “`/home/ccdev/data/20120310`”, if you observe on 10 March 2012.
- Root
  - Make sure “Root” is “`nc1_`”.
  - The name of FITS files generated starts from “`nc1_`”.
- Suffix
  - Make sure “Suffix” is “`fits`”.
  - The extension of FITS files generated is “`fits`”.
- Select Amplifier
  - Make sure that it is “`x<-- -->x x<-- -->x`”.

“Eng. Level” panel (Fig. 4) is for maintenance activities by the Development Team. Please do not change any parameters here. If you change any of parameters in “Eng. Level” panel, we do not guarantee the proper operation of the instrument.

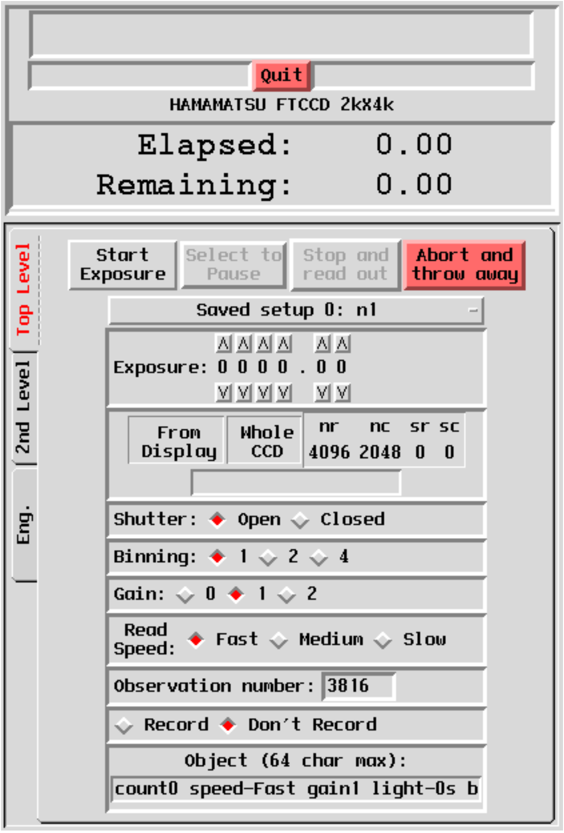

Figure 2: The "Top Level" panel of "Instrument" window of UCAM Controller software. You can set up gain, read speed and other parameters.

2.7 Check of filter table file

Before starting the observation, you need to check the filter table file. The filter table file is located at `/home/ccdev/filters.table`.

Here is an example of the filter table file. For this case, PS1 r', i', z', and Y filters are stored in the first layer in the filter wheel, and no filters are stored in the second layer.

```
0-0    NONE_00
0-1    PS1_r
0-2    PS1_i
0-3    PS1_z
0-4    PS1_y
0-5    NONE_05
1-0    NONE_10
1-1    NONE_11
1-2    NONE_12
1-3    NONE_13
1-4    NONE_14
1-5    NONE_15
```

If there are SDSS g', r', i', and z' filters in the second layer of the filter wheel, then you may edit the file as follows.

```
0-0    NONE_00
0-1    PS1_r
0-2    PS1_i
0-3    PS1_z
0-4    PS1_y
```

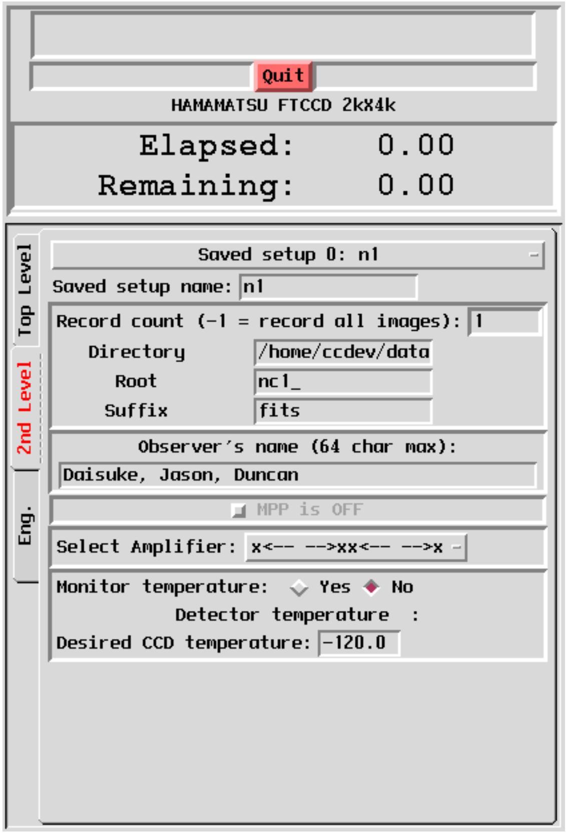

Figure 3: The "2nd Level" panel of "Instrument" window of UCAM Controller software. You can set up the data directory and others.

```
0-5     NONE_05
1-0     NONE_10
1-1     SDSS_g
1-2     SDSS_r
1-3     SDSS_i
1-4     SDSS_z
1-5     NONE_15
```

Please note that the position "0-0" and "1-0" must be kept empty.

3 Operation of NCUcam-1

Now, the operation of NCUcam-1 is described. Table 1 summarizes currently available commands to operate NCUcam-1.

3.1 Filter exchange

To operate the filter wheel, use "nc1_filter" command. If no argument is given to the command, then this command returns name of currently used filter. Following is an example.

```
% nc1_filter

Location of executable file and filter table file:
  Filter Table File = /home/ccdev/filters.table
  Filter Wheel Control Program = /home/ccdev/bin/fwctrl
```

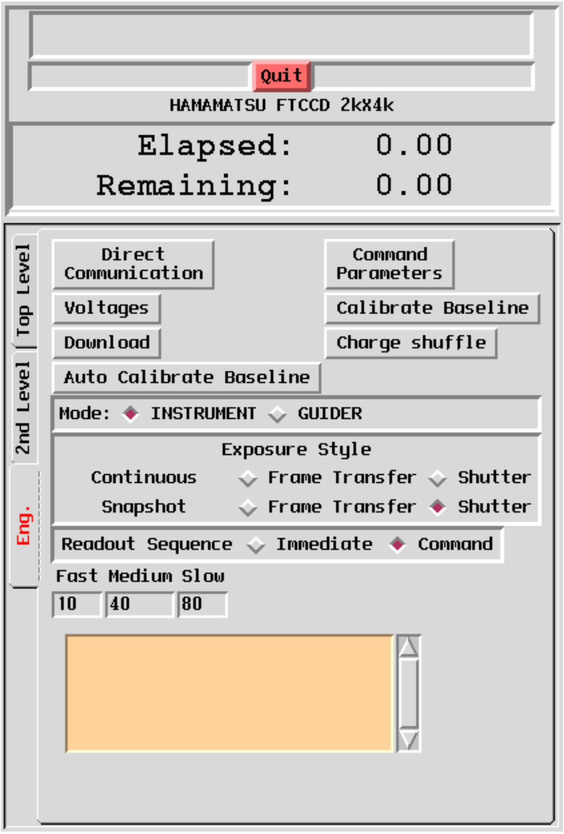

Figure 4: The “Eng. Level” panel of “Instrument” window of UCAM Controller software.

```
Filter Table:
  0-0 = NONE_00
  0-1 = PS1_r
  0-2 = PS1_i
  0-3 = PS1_z
  0-4 = PS1_y
  0-5 = NONE_05
  1-0 = NONE_10
  1-1 = NONE_11
  1-2 = NONE_12
  1-3 = NONE_13
  1-4 = NONE_14
  1-5 = NONE_15


Reply from the filter wheel controller:
  Filter Position = 0-3

PS1_z
```

To exchange the filter, the filter name is given to the command. For example, if you change the filter from PS1_z to PS1_r, then type following command on a terminal emulator.

```
% nc1_filter PS1_r

Location of executable file and filter table file:
  Filter Table File = /home/ccdev/filters.table
  Filter Wheel Control Program = /home/ccdev/bin/fwctrl
```

Table 1: The list of available commands for NCUcam-1 operation.

Command	Short Description
`nc1_bias`	taking bias frames
`nc1_checkdatadir`	checking data directory
`nc1_checkfileroot`	checking file root
`nc1_checkobsnum`	checking sequential number
`nc1_checkreadspeed`	checking read speed
`nc1_checksuffix`	checking suffix of FITS files
`nc1_dark`	taking dark frames
`nc1_ds9`	starting SAOimage DS9
`nc1_exposure`	taking object frames
`nc1_filter`	filter operation command
`nc1_flatfield`	taking flatfield frames
`nc1_start`	starting CCD controller software

```
Filter Table:
  0-0 = NONE_00
  0-1 = PS1_r
  0-2 = PS1_i
  0-3 = PS1_z
  0-4 = PS1_y
  0-5 = NONE_05
  1-0 = NONE_10
  1-1 = NONE_11
  1-2 = NONE_12
  1-3 = NONE_13
  1-4 = NONE_14
  1-5 = NONE_15

Target Filter Position = 0-1
    Destination:      FW0=1, FW1=0
    Current Position: FW0=3, FW1=0
[00] Waiting...
    Destination:      FW0=1, FW1=0
    Current Position: FW0=0, FW1=0
[01] Waiting...
    Destination:      FW0=1, FW1=0
    Current Position: FW0=3, FW1=0
[02] Waiting...
    Destination:      FW0=1, FW1=0
    Current Position: FW0=3, FW1=0

.....

[17] Waiting...
    Destination:      FW0=1, FW1=0
    Current Position: FW0=2, FW1=0
[18] Waiting...
    Destination:      FW0=1, FW1=0
    Current Position: FW0=2, FW1=0
[19] Waiting...
    Destination:      FW0=1, FW1=0
    Current Position: FW0=1, FW1=0
```

```
Reply from the filter wheel controller:
  Filter Position = 0-1

PS1_r
```

3.2 SAOimage DS9

For the quick-look of acquired data, SAOimage DS9 is used. Before taking data, start SAOimage DS9 by typing following command. If you start SAOimage DS9 using this wrapper script, then SAOimage DS9 accepts XPA commands by default.

```
% nc1_ds9 &
```

3.3 Taking bias frames

To take bias frames, you use "nc1_bias" command. Type following command on a terminal emulator, then you will have 5 bias frames.

```
% nc1_bias -n 5
```

3.4 Taking dark frames

To take dark frames, you use "nc1_dark" command. Type following command on a terminal emulator, then you will have 3 dark frames with the exposure time of 300 sec.

```
% nc1_dark -n 3 -t 300
```

3.5 Taking object frames

To take object frames, you use "nc1_exposure" command. Type following command on a terminal emulator, then you will have 2 object frames with the exposure time of 90 sec. The target name of "alpha Lyr" is recorded into the FITS file.

```
% nc1_exposure -n 2 -t 90 -o "alpha Lyr"
```

3.6 Taking flatfield frames

To take flatfield frames, you use "nc1_flatfield" command. Type following command on a terminal emulator, then you will have 10 flatfield frames with the exposure time of 20 sec.

```
% nc1_flatfield -n 10 -t 20
```

3.7 Executing a batch of commands

You can make a simple shell script to execute a series of commands. In this way, a series of commands are executed sequentially by starting a shell script.

For example, you may prepare a shell script with following content. By executing this shell script, you will have 6 FITS files in total.

```
#!/bin/sh

nc1_filter PS1_r
nc1_exposure -n 2 -t 20 -o SA123_456
nc1_filter PS1_i
nc1_exposure -n 2 -t 30 -o SA123_456
```

```
nc1_filter PS1_z
nc1_exposure -n 2 -t 40 -o SA123_456
```

Here is another example for dome flatfield.

```
#!/bin/sh

nc1_filter PS1_r
nc1_flatfield -n 10 -t 15
nc1_filter PS1_i
nc1_flatfield -n 10 -t 20
nc1_filter PS1_z
nc1_flatfield -n 10 -t 30
```

3.8 Focus check

Take images of a star field with different focus offset. For example, set the focus offset to 43.00 and take one image by typing following command.

```
% nc1_exposure -n 1 -t 10 -o "focus offset 43.00"
```

Then, chage the focus offset to 43.50 and take one image by typing following command.

```
% nc1_exposure -n 1 -t 10 -o "focus offset 43.50"
```

You may take 10 images. Then, execute following command to check the best focus position.

```
% nc1red_focus.pl nc1_567[8-9].fits nc1_568[0-7].fits
```

You will see following information on the terminal emulator. For this case, 45.76 is the best focus offset. You also see a figure of the fitted curve.

```
After 18 iterations the fit converged.
final sum of squares of residuals : 127.289
rel. change during last iteration : -1.43491e-10

degrees of freedom (ndf) : 9
rms of residuals      (stdfit) = sqrt(WSSR/ndf)      : 3.76075
variance of residuals (reduced chisquare) = WSSR/ndf : 14.1432

Final set of parameters            Asymptotic Standard Error
=======================            ==========================

a               = 3.60181          +/- 0.752        (20.88%)
b               = 45.7646          +/- 0.1426       (0.3117%)
c               = 3.85475          +/- 1.437        (37.28%)


correlation matrix of the fit parameters:

               a      b      c
a              1.000
b              0.345  1.000
c             -0.639 -0.086  1.000
```

4 If you have a problem...

Please contact to one of the Development Team members, if you have any problem with NCUcam-1.

TRIPOL Set-up and Observing Manual
— How to observe with TRIPOL? —

Kinoshita Daisuke and Chen Tse-Chuan

4 August 2011 (version 2)

1 Introduction

Triple Range Imager and Polarimeter (hereafter, TRIPOL) is an astronomical instrument designed and developed by Prof. Sato Shuji at Nagoya University and his group members. It is a small, light-weight, and versatile instrument for small aperture telescopes.

This document describes (1) how to install TRIPOL, (2) how to set up TRIPOL, and (3) how to observe with TRIPOL.

2 Hardware Installation of TRIPOL

TRIPOL consists of following components:

- 3 SBIG ST-9XEI CCD cameras,
- optics (beam splitters),
- polarizer and wave-plate,
- a PC,
- wave-plate rotator controller,
- cables (USB, network, power),
- AC adapters.

The structure of TRIPOL system is shown in Fig. 1. Fig. 2 shows the optical components in the main body of TRIPOL. We need to (1) connect each component via cables, and (2) plug power-plugs.

For the observation using 1-m telescope at Lulin, the instrument has to be attached to the telescope. Fig. 3 is a photo of TRIPOL attached to 1-m telescope in June 2011. A control PC and AC adapters have to be fixed, Fig. 4 shows a way we fixed these on the side of the telescope in June 2011.

3 Software set-up of TRIPOL

To prepare for the observation, we need to do following steps.

1. Switch on the power of 3 CCD cameras.
2. Switch on the power of the control PC.
3. Set up the network configuration of your PC using DHCP.
4. Log in to the control PC using SSH.
   - `% ssh -X -l observer 192.168.11.90`
   - About the password, please ask Daisuke.
5. Start the server program on the control PC.

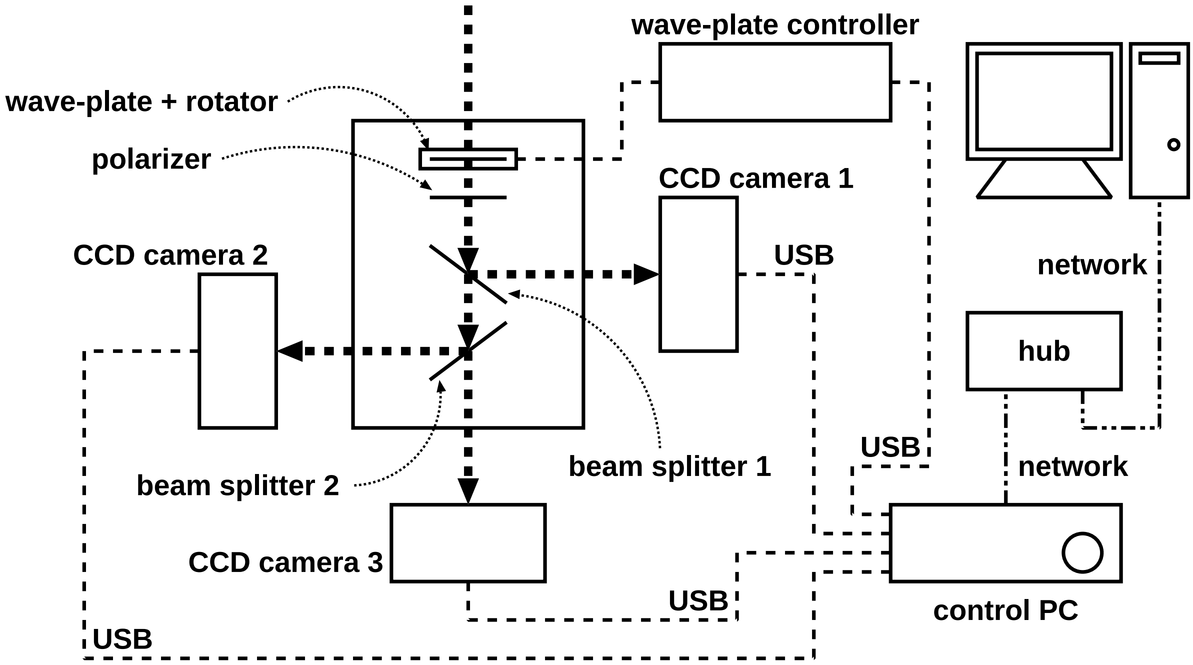

Figure 1: The structure of TRIPOL system.

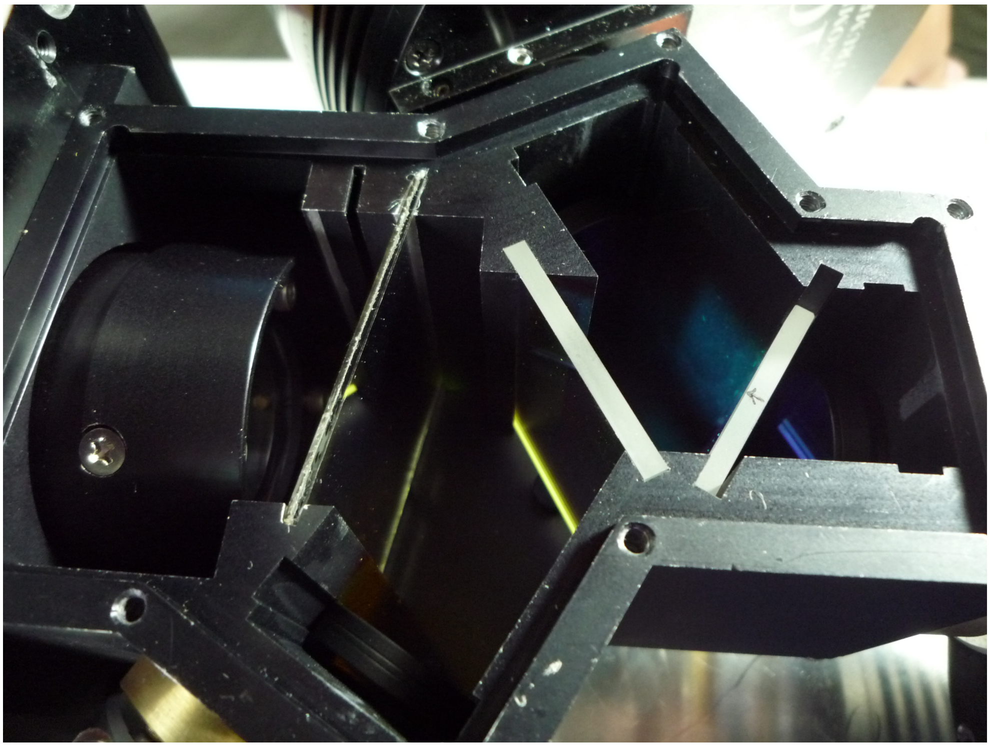

Figure 2: Optical devices in TRIPOL. The photo was taken by Tse-Chuan.

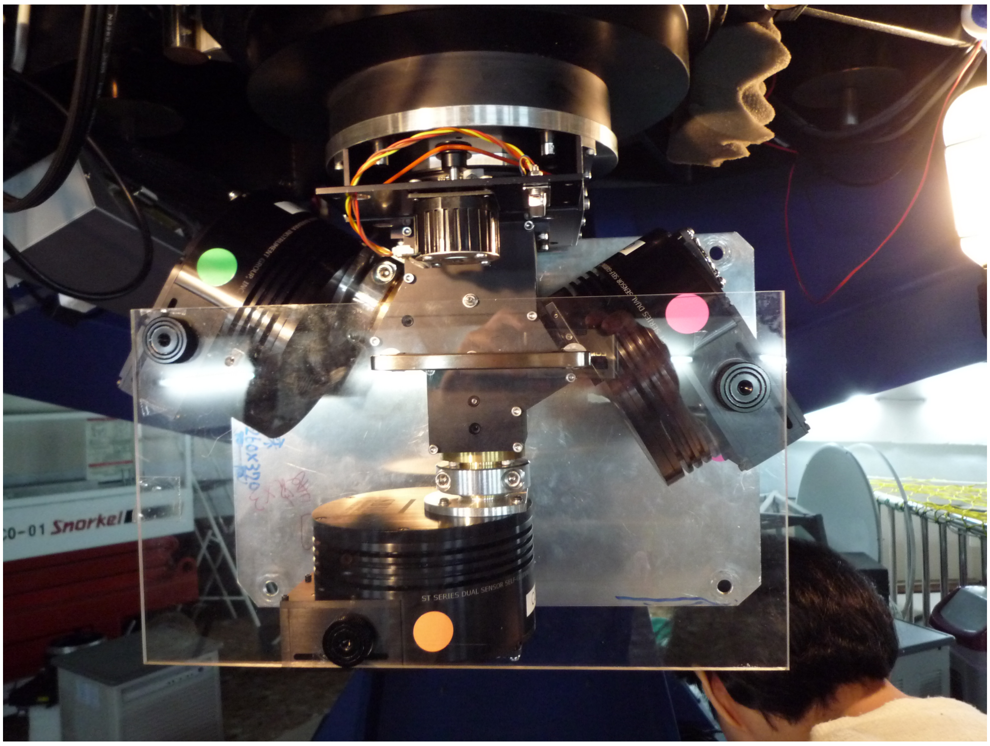

Figure 3: TRIPOL attached to 1-m telescope at Lulin. The photo was taken by Tse-Chuan.

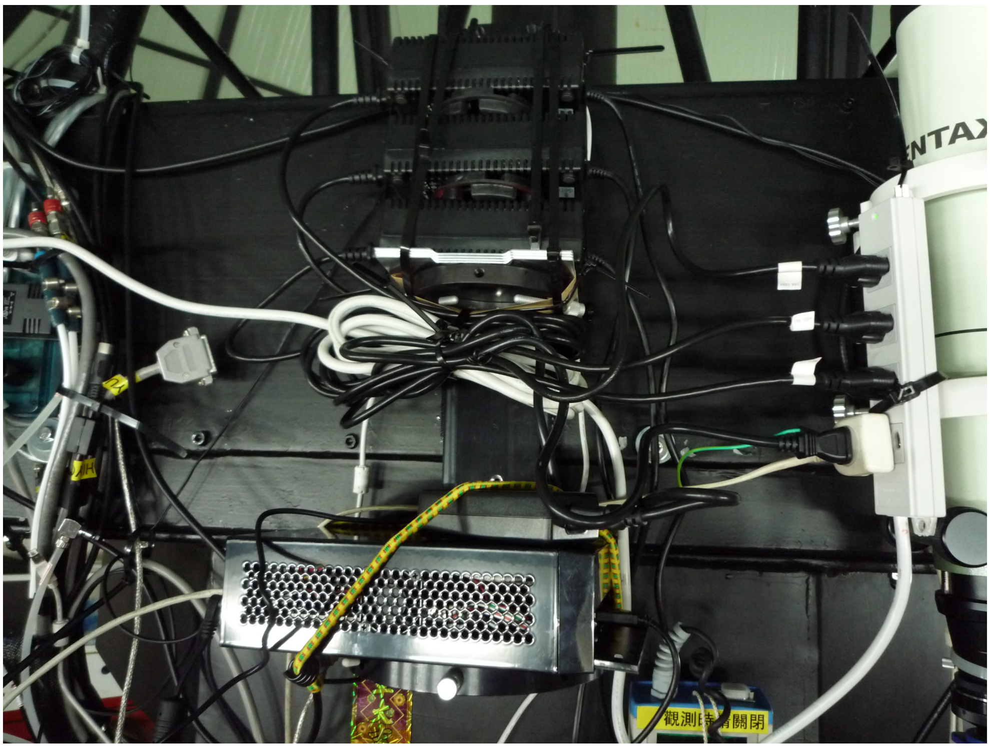

Figure 4: TRIPOL control PC and AC adapters on the side of 1-m telescope. The photo was taken by Tse-Chuan.

- % start_ccd

6. Start SAOimage DS9 program.

   - % start_ds9

7. Set the CCD cooling temperature.

   - % set_temp -10

8. Check the current CCD cooling temperature.

   - % print_temp
   - or % print_temp -s
   - An example of the output of "print_temp -s" command.

   ```
   % print_temp -s
   g: 26.83 -9.79 1 100%
   r: 28.05 -9.79 1 100%
   i: 27.44 -9.79 1 100%
   ```

   - Format: band, current temperature, target temperature, cooling on/off, and cooling load

9. Prepare "target file".

   - Prepare "target file" and place it at the home directory.
   - An example of "target file".

   ```
   HD154445    2000 17 05 32.24 -00 53 31.7
   Hiltner960 2000 20 23 28.44 +39 20 56.1
   VI_Cyg_12   2000 20 32 40.94 +41 14 26.2
   Beta_UMa    2000 11 01 50.47 +56 22 56.6
   BL_Lac      2000 22 02 43.30 +42 16 40.0
   ```

10. Set the observing site specific information.

    - Check site.def file at /usr/local/tripol/site.def.
    - It is currently as follows.

    ```
    observat = 'Lulin' / Observatory Name
    latitude = '+20:28:07' / [deg] Latitude of the Site
    longitud = '120:52:25' / [deg] Longitude of the Site
    height = 2862 / [m] Altitude of the Site
    telesco = 'LOT 1m f8' / Telescope Name
    instrume = 'TRIPOL' / Instrument Name
    ```

    - These information will be added to the FITS file.

11. Other information to add to the FITS file.

    - If you want to add more information in FITS header, you can create a file template.* at /dev/shm.
    - For example, type following command.

    ```
    % echo "observer = 'Kinoshita Daisuke, Chen Tse-Chuan'" > /dev/shm/template.observer
    ```

4 Observation with TRIPOL

1. Check the sequential number for FITS files to be generated.
   - `% counter_check`
   - An example of the output.

     ```
     % counter_check
     /data/110803/rawdata
     25
     ```
   - Next data to be generated are:
     - `/data/110803/rawdata/g110803_0025.fits`
     - `/data/110803/rawdata/r110803_0025.fits`
     - `/data/110803/rawdata/i110803_0025.fits`
2. Set the focus position of the telescope.
   - `% mfocus 12.345`
   - Then, a file `/dev/shm/template.focus` is created.

     ```
     % ls -l /dev/shm/template.focus
     -rw-r--r-- 1 observer observer 23 2011-08-03 16:59 /dev/shm/template.focus
     % cat /dev/shm/template.focus
     focus = 12.345 / focus
     ```
   - Later on, the focus value will be recorded in the data we obtain.
   - If you want to stop recording focus value, then type following command.

     ```
     % mfocus clear
     ```
3. Taking quick-look image without rotating wave-plate.
   - `% TL 6 1`
   - Above command will take 1-sec test exposure, and show the image on SAOimage DS9 after the data acquisition, but does not record the data on the harddisk.
   - Usage:

     ```
     % TL
     usage: TL mode exptime(sec) [object_name] [num]
     ```
   - "mode" is always "6".
4. Taking quick-look image at 4 position angles.
   - `% PTL 1`
   - Above command will take 1-sec test exposure at 4 position angles (0, 45, 22.5, and 67.5 deg), and show the Stokes U and Q.
   - Usage:

     ```
     % PTL
     usage: PTL exptime(sec)
     ```
5. Taking scientific data with wave-plate rotated.
   - Set target name.

     ```
     % point2 target_20110616.list BL_Lac
     ```
   - Before taking image, we need to type "point2" command. Then, the coordinate of the target (RA, Dec) will be recorded in the FITS file.
   - Usage of "point2":

     ```
     % point2
     usage: point2 object_list_file object_name
            point2 clear
     ```

- Start the exposure.

  ```
  % PLo 6 15 BL_Lac 8
  ```

- Above command will take 8 sets of 15-sec exposures. Thus, 96 FITS files (4 positions × 8 sets × 3 cameras) are created in total.
- Usage of "PLo":

  ```
  % PLo
  usage: PLo mode exptime(sec) [object_name] [num]
  ```

6. Taking scientific data without wave-plate rotated.

   - `% Lo 6 30`
   - Above example takes a single 30-sec exposure.
   - Usage of "Lo":

     ```
     % Lo
     usage: Lo mode exptime(sec) [object_name] [num]
     ```

7. Taking dark frames.

   - `% dark 15 30 60 180`
   - Above example will take dark frames of 15-sec, 30-sec, 60-sec, and 180-sec. 10 FITS files will be taken for each exposure time.

8. Taking twilight flatfield.

   - `% twflat -p 10`
   - Above example will take 10 sets of twilight flatfield data with the wave-plate rotated.
   - The exposure time is fixed to 5-sec.

9. How to stop the exposure at the middle of the series of data acqusition?

   - `% xstop`

10. How to shutdown TRIPOL system?

    - Stop the cooling of the CCD cameras.

      ```
      % set_temp 99
      ```

    - Switch off the control PC. (You do not need to type "halt" or "shutdown -h now" command as the root, but you can just push the power switch button of the PC.)
    - Switch off the CCD cameras.

5 Some more information

- The data produced by TRIPOL are stored at the directory `/data/YYMMDD/rawdata` on the control PC. YY, MM, DD are year, month, and day of the observing night.

- The data can be downloaded using `scp` command. Please do not delete original data on the control PC.

- The user interface of TRIPOL system is shown in Fig. 5. We type commands on a terminal, and obtained images are shown on SAOimage DS9.

- Files such as `template.focus`, `template.wpr`, and `template.point` are on the RAM disk (`/dev/shm`), and those files are disappeared when the PC is switched off.

- Data acquisition commands are based on a set of commands developed for IRSF/SIRIUS. If you want to know more about commands like `PLo`, `TL`, and `point2`, then you need to go through the observing manual of "SIRIUS".

- IRSF/SIRIUS Observing Manual:
  http://www.kusastro.kyoto-u.ac.jp/~nagata/Irsf/IRSFmanual.htm
- SIRPOL related documents:
  http://optik2.mtk.nao.ac.jp/~kandori/SIRPOL.html

- A sample of the header part of a FITS file generated by TRIPOL is shown in Table 1.
- About the packing of the instrument, please contact to Chen Tse-Chuan for details.

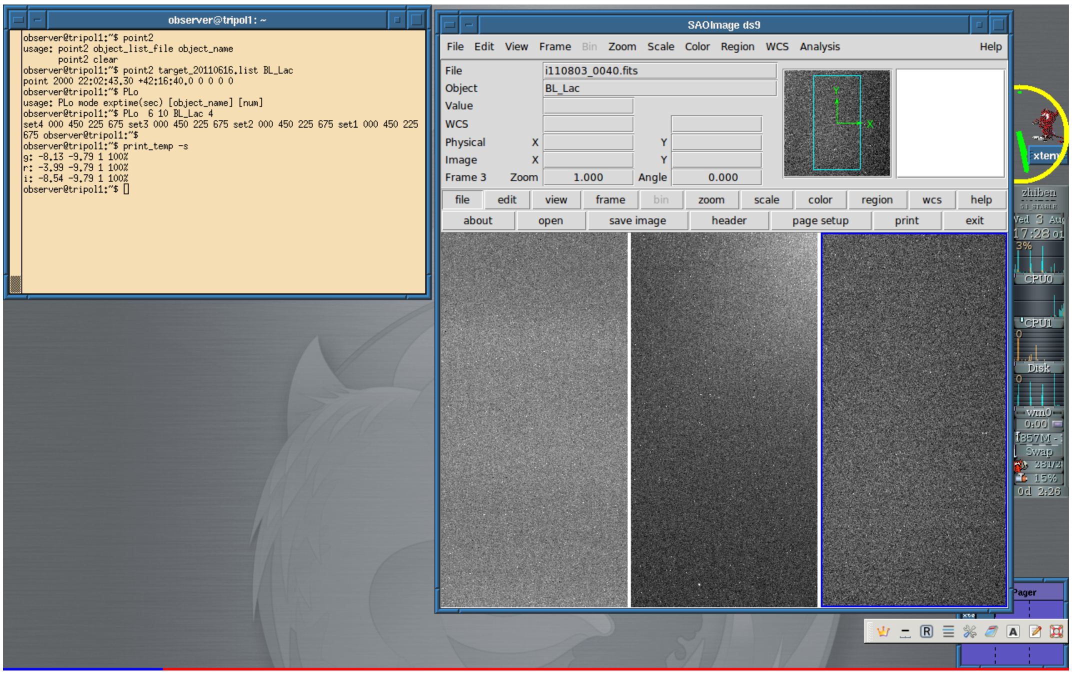

Figure 5: The user interface of TRIPOL.

```
SIMPLE  =                    T / file does conform to FITS standard
BITPIX  =                   16 / number of bits per data pixel
NAXIS   =                    2 / number of data axes
NAXIS1  =                  512 / length of data axis 1
NAXIS2  =                  512 / length of data axis 2
EXTEND  =                    T / FITS dataset may contain extensions
COMMENT   FITS (Flexible Image Transport System) format is defined in 'Astronomy
COMMENT   and Astrophysics', volume 376, page 359; bibcode: 2001A&A...376..359H
BZERO   =                32768 / offset data range to that of unsigned short
BSCALE  =                    1 / default scaling factor
EXPOS   =                 5.00 / [sec] exposure time
XWIDTH  =                  512 / [pixel] image width
YHEIGHT =                  512 / [pixel] image height
XORG    =                    1 / [pixel] image origin X
YORG    =                    1 / [pixel] image origin Y
XBIN    =                    1 / [pixel] X binning
YBIN    =                    1 / [pixel] Y binning
CCDMODE =                  0x0 / ccd readout mode
SHUTTER =                    1 / shutter command 1:open, 2:close
CCD_TEMP=                -9.79 / [degC] ccd temperature
CCD_COOL=                  154 / ccd cooling power, 0 to 255
CAMERA  = 'SBIG ST-9 3 CCD Camera' / camera model
CAM_NO  = '91005855'           / camera serial number
XPIXSZ  =                20.00 / [um] pixel width
YPIXSZ  =                20.00 / [um] pixel height
EGAIN   =                 1.83 / [e-/ADU] typical conversion factor
EXPDATE = '2011-06-17'         / yyyy-mm-dd, local date on ccd controller
EXPSTART= '00:26:01.413'       / hh:mm:ss, exposure start time on controller
EXPEND  = '00:26:06.807'       / hh:mm:ss, exposure  end  time on controller
READSTAR= '00:26:06.807'       / hh:mm:ss, readout start time on controller
READEND = '00:26:07.885'       / hh:mm:ss, readout  end  time on controller
HISTORY  Copy of image g110616_0050.fits rotated 90 degrees
IMROT   = '-r 90   '           / imrot option
OBSERVAT= 'Lulin   '           / Observatory Name
LATITUDE= '+20:28:07'          / [deg] Latitude of the Site
LONGITUD= '120:52:25'          / [deg] Longitude of the Site
HEIGHT  =                 2862 / [m] Altitude of the Site
TELESCO = 'LOT 1m f8'          / Telescope Name
INSTRUME= 'TRIPOL  '           / Instrument Name
OBJECT  = 'VI_Cyg_12'          / Object Name
DATE    = '2011-06-16T16:26:00' / YYYY-mm-ddThh:mm:ss UT
DATE_UTC= '2011-06-16'         / YYYY-mm-dd
TIME_UTC= '16:26:00.824'       / hh:mm:ss
DATE_LT = '2011-06-17'         / YYYY-mm-dd
TIME_LT = '00:26:00.824'       / hh:mm:ss
FOCUS   =               33.289 / focus
EPOCH   = '2000    '           / epoch
RA      = '20:32:40.94'        / hh:mm:ss.s RA (pointing base)
DEC     = '+41:14:26.2'        / dd:mm:ss.s Dec (pointing base)
RA_OFF  =                    0 / [arcsec] Ra offset
DEC_OFF =                    0 / [arcsec] DEC offset
POL-AGL1=                 45.0 / [deg] pol rot angle 1
FILTER  = 'g       '           / Filter Name
ACQSTART= '00:26:00.904'       / data acquisition start time on tripol1
ACQEND  = '00:26:07.897'       / data acquisition  end  time on tripol1
END
```

Table 1: A sample FITS header produced by TRIPOL.

國立中央大學鹿林天文台管理辦法

100年11月1日 天文所所務會議通過
100年12月15日 理學院院務會議通過
100年12月19日 行政會議核備通過

第一條　國立中央大學(以下簡稱本校)鹿林天文台(以下簡稱天文台)為重要之天文及高海拔科學研究基地，為使天文台有效運作，特訂定本管理辦法。

第二條　天文台由管理委員會(以下簡稱管委會)掌管基地及儀器設施運作相關事宜。

第三條　管委會成員共八名，由本校主任秘書、研發長、總務長、理學院院長、地科院長、天文台台長，以及天文所選舉兩位專任(案)教師等組成，並請校長指派其中一名委員擔任召集人。天文所教師委員任期兩年，連選得連任。

第四條　天文台台長由天文所所長兼任，負責依管委會決議綜理儀器運作以及行政庶務管理。

第五條　天文台設駐站主任一名，由本校天文所契僱人員兼任，承台長指示，負責天文台營運管理事務。其下設學術觀測與行政庶務二組，各設組員若干人。

第六條　管委會下設望遠鏡觀測時間分配小組，其成員由台長依照專業考量，邀請校內外專家組成。

第七條　校長得邀請校內外專家學者若干人為天文台諮議委員，評估天文台運作效率與課題成果，並提供天文台未來發展與重要決策之相關建議。

第八條　天文台組織結構圖如下：

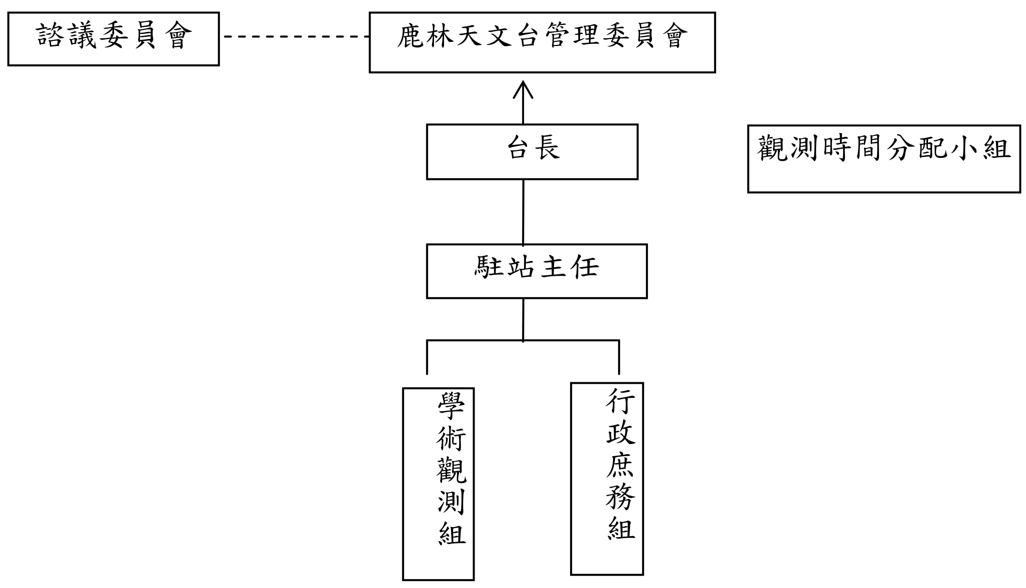

第九條　管委會每年應至少召開一次會議，並得視需要召開臨時會議。

第十條　天文台運作所需相關經費得提計畫向學校申請補助，並得向校外其他單位申請補助及接受外界捐助。

第十一條　因學術研究及教育需要使用天文台相關設施，天文台得依其使用之空間及所需支援收費，收費辦法於管委會通過後公告實行。

第十二條　為推廣天文教育、普及天文知識、提昇國內天文風氣，天文台接受參觀訪問，其辦法另訂之。

第十三條　台長於每年初提出上年度之各項研究、工作及經費報告，交管委會核備。

第十四條　本辦法經天文所所務會議、理學院院務會議及行政會議核備後實施，修正時亦同。

相關報導

《新聞中的科學》 火星上有生物？　好奇號探究竟

【本報記者蔡永彬】

上個月底，美國航空暨太空總署（NASA）從佛羅里達州卡納維爾角發射世界最大、最先進的無人核子動力探測車「好奇號」（Curiosity　），了解火星現在或過去是否適合生命存活。台灣聯合大學系統副校長、中央大學天文研究所教授葉永烜表示，這代表人們始終想知道「我們的後院有沒有生物？」

火星是太陽系 8 大行星（扣掉冥王星）之一，也是除了金星以外，離地球最近的行星。

火星和地球一樣有類似的四季交替，火星上的一天約 24 小時 37 分，幾乎和地球一樣長。每隔 26 個月左右，就會發生一次「火星衝」，此時火星、地球和太陽排列成一直線，火星與地球距離最近；除了讓人們容易觀測火星外，科學家也能利用這個天文現象，把探測器送往火星。

自然科學博物館館長孫維新指出，1877 年義大利天文學家 Giovanni Schiaparelli 觀測火星發現許多「線條」（canali），但傳到美國之後，卻被誤認爲「運河」（canal），讓美國人開始相信「火星上有運河」。1893 年，美國人羅威爾（Percival Lowell）蓋了一座天文台觀測火星，之後甚至宣稱火星上有 500 多條運河，就是火星人開鑿的。

孫維新表示，因爲羅威爾提出的說法，讓有些人以爲火星的環境和地球差不多，也就出現了科幻小說和電影中的「火星人」。

1960 年 10 月，前蘇聯向火星連續發射 2 枚探測器，不過連地球軌道都還沒到就宣告失敗，但這是人類探測火星的開始。

孫維新表示，美國在當時的「水手系列任務」也向著水星、金星和火星而去；1964 年 12　月 28 日「水手 4 號」發射升空，這是有史以來第 1 枚成功到達火星並發回數據的探測器。

水手 4 號從火星表面 9800 公里上空掠過，向地球發回了 21 張照片，它發回的數據顯示火星的大氣密度遠比此前人們認爲的稀薄。孫維新說，這讓人們對火星的夢想破滅了，原來火星又冷、又乾，空氣非常稀薄、沒有運河，當然更沒有火星人。

葉永烜表示，目前最常探測火星的單位除了 NASA 外，還有歐洲太空總署（ESA），「火星很近啦！幾個月就到了。」孫維新表示，NASA　發射的「火星全球測量者號」傳回地球，發現火星南極的冰帽有許多氫，間接代表有大量水冰的可能性，如果真的有水冰，就容易有生命現象了。

原文轉載自【2011-12-19/聯合報/AA3 版/新聞中的科學】

《新聞中的科學》探測小行星　挖礦尋資源

【本報記者蔡永彬】

人類探測火星的歷史，幾乎就是整個人類太空史。台灣聯合大學系統副校長、中央大學天文研究所教授葉永烜指出，探測火星，甚至「行星科學」的主要目的，就是「探究現在、過去有無生物存在」。

葉永烜表示，到目前爲止，人類已經往火星發射過 30 枚以上探測器，然而，前三分之二的探測器幾乎都失敗；最近的便是俄羅斯和中國大陸合作的「火衛一登陸計畫」，因爲太空船推進器發生問題也泡湯了。但是探測火星有「近水樓台」之便，科學家們還是不斷努力。

葉永烜說，2004 年歐洲太空總署（ESA）的火星快車號（Mars Express）確定火星極冠有 85%的乾冰、15%的水冰，後來又在火星大氣層內發現甲烷。甲烷的來源可能是微生物，但也可能是由於地質作用而來，ESA 和美國航空暨太空總署（NASA）都很希望能找到甲烷來源的答案。

除了火星之外，葉永烜說 ESA 的「金星快車」進行順利；但日本在 2010 年 5 月發射的金星太空船，沒有成功進入繞著金星的軌道，宣告任務失敗。目前尚待努力；還有國家想跑到天王星去，但是太遠了，

所需要的時間長，費用也很高，所以有些國家把腦筋動到小行星和衛星上。

葉永烜指出，某些小行星上有稀土金屬等寶貴資源，而且相對來說抵達太陽系中的小行星「相對容易」，所以很多國家都想到小行星上「挖礦」。另外，某些小行星上可能有「氦－3」（氦的一種同位素），可能是未來清潔能源之一；某些小行星可能碰撞地球，精確研究它的動態也很重要。

美國和歐洲的科學家都曾到木星和土星的衛星探勘。葉永烜說，科學家們已經發現土星最大的衛星「泰坦」上「有山有水」；木星的第二大衛星「歐羅巴」表面完全平滑，有科學家認為它很早以前可能是顆「水球」，現在可能還有「地下海洋」甚至生物圈。

原文轉載自【2011-12-19/聯合報/AA3 版/新聞中的科學】

《新聞中的科學》 太陽系外　可能有另一個地球？

【本報記者蔡永彬】

「地球的生物起源和環境是不是很獨特？會有下一個地球嗎？」美國航空暨太空總署（NASA）月初證實，在太陽系之外、距離地球大約 600 光年處有一顆克卜勒 22b（Kepler－22b）行星，表面溫度約 22℃，而且上面可能有水、陸地和大氣，可能可以讓生物存活。

Kepler－22b 體積約為地球的 2.4 倍，每 290 天繞其恆星一周。

台灣聯合大學系統副校長、中央大學天文研究所教授葉永烜指出，地球位於太陽系中的「幸運位置」（habitable zone）：水能以液態存在，大氣溫度也適中（金星太熱、火星太冷）。

葉永烜指出，太空環境是非常「惡毒」的，例如輻射就會影響人體的 DNA，若長期曝露，人們可能已經突變成其他樣子。但他認為「天外有天」，生物圈無所不在，只要有「好運氣」，生物圈就可能形成。

他推測，如果要研究某些星體上是否也有生命，有一項依據是「大氣成份」，因為大氣中的某些成份只會在生命世界上出現。

有些科學家正思考「行星工程」（Planet Engineering）的可能性，也就是「自己創造一個新地球」。葉永烜舉例，我們可以在太空中放許多鏡片、反射陽光，獲取能量來源；如果「暖化過頭」，或許能在極區展開薄膜擋住陽光，稍微減緩影響。

葉永烜說，依目前的科技發展，人類可能在 30 年內有一個「小殖民星球」，但第一批移民者也可能是「敢死隊」，無論是否成功，去了可能就回不來了。

英國物理學家 Stephen Hawking 曾經表示「地球可能在 100 年內『完蛋』，屆時人類只能往太空移民。」葉永烜認為，Hawking 的說法應該只是希望人們不要把地球「弄得不可收拾」，因為目前地球還是我們唯一的答案。

原文轉載自【2011-12-19/聯合報/AA3 版/新聞中的科學】

我學者親赴南極　參與架設微中子天壇

〔記者林曉雲／台北報導〕台灣學術史上頭一遭！台灣大學講座教授陳丕燊，今年前進南極大陸，參加全世界最大的「微中子」天文台打造計畫，未來四年內在南極架設完成的天線探測站，將有四分之一掛上我國國旗，昨天在南極冰層動工，挖了第一個洞。

四年內將架設完成天線探測站

同為計畫負責人聯合大學教授黃明輝表示，二○○二年有一組諾貝爾獎得主，用兩萬噸的水，只看到十個微中子，南極天壇陣列預估可偵測三到五個微中子，達到的效能比目前最好的歐洲大強子對撞機高出十倍以上。

陳丕燊則笑說，這就是科學家想向未知挑戰的原因，當地球上首次捕捉到微中子時，台灣身在其中，因此到南極的每一步都是在創造歷史。

中央大學副校長葉永烜受訪表示，偵測微中子雖然是基礎科學，但因為宇宙間有九十%是看不到的暗

物質，科學家們相信，偵測微中子將可以解開宇宙的秘密。

人在南極的陳丕燊，昨天透過視訊向台灣媒體說明，背景南極只見白雪茫茫。陳表示，當地氣候嚴酷，雖是夏天，戶外氣溫低到零下四十度，剛下飛機就出現高山症，也發生嚴重的缺氧情形，到戶外只要脫下手套，馬上就凍傷。

今年是人類到達南極極頂一百週年，包括美、歐、日及台灣的科學家，進行大型國際合作計畫「天壇陣列」（ARA Observatory），預定在四年內耗資新台幣二．四億元，打造相當於台北市中心大無線電天線陣列。台灣方面由國科會出資六千萬元、廣達副董事長梁次震出資一千多萬元。

南極天文台的望遠鏡，是由埋在海拔三千公尺高的南極極頂冰原中的卅七座天線探測站所組成，以兩公里間隔呈現蜂巢狀六邊形幾何的大面積，傾聽冰層下由極高能宇宙微中子所發出的訊息。

陳丕燊說，因為匆忙出國，只帶了旗杆，忘了帶國旗，但輸人不輸陣，他找來和其他國家插在極頂的國旗尺寸一樣大小的畫布，花十多個小時製作，且為了紀念建國百年和人類登極頂百年，還特地在白日中間寫上「100」，沒想到愛畫畫的興趣，竟能用在南極國旗任務上，當國旗插在極頂上時，非常感動。

原文轉載自【2011-12-13/自由時報/A12 版/生活新聞】

臺灣學者遠征南極　宇宙解密

楊惠芳／臺北報導

臺灣首度參與南極的大型科學研究計畫，打造世界上有史以來最大型的「天壇陣列（ARA）」無線電天線實驗站，要偵測微中子，挑戰人類未知的物理定律。這不但是臺灣學術史上頭一次，能夠參與世界頂尖的科學計畫，更象徵臺灣的科學水準受到世界各國的肯定。

在國科會和廣達副董事長梁次震的支持下，臺大講座教授陳丕燊昨天在南極以電話連線的方式，說明這次計畫，主要將架設三十七座天線實驗站，組成六邊形的望遠鏡陣列，臺灣負責其中的十座，是僅次於美國的第二大主力，預計四年後將完成架設，整個陣列面積將達到八十三平方公里，相當於臺北市中心。參與這項計畫的國家還有美國、德國、比利時、英國和日本等。

目前人在南極的陳丕燊表示，今年正巧是人類到達南極極點的一百周年，來到南極的每一步都在創造紀錄。首次到極頂的陳丕燊表示，南極現在一片白雪茫茫，當地雖是夏天，但氣候嚴苛，戶外氣溫低到零下四十度，剛下飛機就出現高山症，也發生嚴重的缺氧情形，到戶外只要一脫下手套，馬上就會凍傷。

令人感動的是，陳丕燊花了十多個小時製作一面手繪國旗，在青天白日滿地紅的白日中間，寫下象徵建國一百年的「100」圖樣，插在極頂上。

為什麼要那麼辛苦，跑到南極去偵測微中子？中央大學副校長葉永烜表示，主要是因為南極的環境很乾淨，有很大的冰原，可以阻斷各種電波干擾，可以收集到微弱的微中子訊號。因此，科學家是在零下三十度的嚴苛環境架設微中子望遠鏡。

偵測微中子對臺灣的科學有什麼影響？葉永烜說，偵測微中子雖然是基礎科學，短期內看不到明顯的影響，但因為宇宙間有百分之九十都是看不到的暗物質，科學家們相信，偵測微中子將可以解開宇宙的祕密。

聯合大學能源工程學系教授黃明輝說明，過去要偵測微中子非常困難，科學家不斷尋找最省錢的方式。二○○二年的諾貝爾物理獎就是頒給研究微中子天文學的學者，當年日本科學家小柴昌俊的超級神岡探測器需要二十萬噸的海水，才能偵測到十顆微中子，但根據理論，每秒有六十億個微中子穿越人體，顯示要偵測到微中子有多困難。

黃明輝指出，微中子是宇宙早期的反應，可幫助我們了解宇宙的起源。這次建置望遠鏡陣列，預估將可偵測到微中子，只要成功運轉，未來的偵測結果可能改寫人類目前的物理定律。

原文轉載自【2011-12-13/國語日報/1 版/焦點新聞】

小行星命名通過　「桃園」揚名宇宙

【大紀元 2011 年 11 月 23 日訊】（大紀元記者徐乃義台灣桃園報導）中央大學將發現的編號 210030 小行星命名為「Taoyuan」，23 日的全校運動會開幕式中，由蔣偉寧校長頒贈小行星模型給桃園縣長吳志揚，讓「桃園」躍上國際，揚名宇宙。

中大蔣偉寧校長表示，中央大學明年將慶祝在台復校 50 週年，中大民國 57 年從苗栗遷校中壢，讓中大得以在桃園縣奠基，成為縣內最高學府，歷經 40 多年穩健成長，如今已名列世界五百大、前 1%的頂

尖學府。

桃園縣政府以「無償撥用」的方式，提供中大在八德擴大都市計畫 2 公頃土地，發展第二校區。另於觀音撥用 6 公頃土地，共同推動「桃園科學園區」，設置桃科創新育成中心，帶動地方文化經濟繁榮。他上任以來，致力推動中央大學成爲全國最重要大學，也期許「桃園」成爲台灣最重要的城市。

桃園縣長吳志揚表示，中大不但是縣內規模最大，也是歷史最悠久的學府。長期以來與桃園縣政府互動密切，曾有多位學者受邀擔任縣府的重要智庫，協助擘畫縣政藍圖，提供寶貴建言。

獲頒桃園小行星，吳縣長深感榮耀，也心有所感。一來是人類對知識的追求是無窮無盡的，浩瀚的知識可引領我們上天下海、飛天遁地，這說明了「知識就是力量」；其次是如此遙遠的一個星點，觀測者如何發現？這驗證了「天行健，君子以自強不息」這句名言，宇宙萬物都將生生不息地運作，也象徵中大校運和桃園縣運將日益昌隆。「桃園小行星」獲得國際認可，將有助於「桃園」在國際知名度的提昇。

中央大學天文研究所周翊所長表示，桃園小行星是 2006 年 6 月 24 日由中大鹿林天文台楊庭彰與大陸廣州中山大學葉泉志用 40 公分望遠鏡所發現，經國際天文學聯合會(IAU)通過，於今年 6 月 15 日正式命名爲「桃園」(Taoyuan)。

桃園小行星的發現，緣自中央大學鹿林巡天計畫（Lulin Sky Survey，簡稱 LUSS）。該計畫自 2006 年 3 月啓動以來，以 40 公分望遠鏡進行小天體巡天觀測。截至目前爲止，總計發現 800 多顆小行星、1 顆近地小行星 (2007 NL1)和 1 顆彗星(C/ 2007N3 (LULIN))。其中鹿林彗星是台灣首次發現的彗星，爲 2009 年最明亮的彗星，引起全球天文迷之關注。

根據國際天文聯合會小行星中心 (IAU：Minor Planet Center) 的統計資料顯示，鹿林天文台爲亞洲發現小行星最活躍的地點之一，充份展現了台灣人「以小搏大」之精神。 （責任編輯：王正新）

台灣中央大學發現小行星揚名宇宙　取名「桃園」(Taoyuan)

By 彭小樂

台灣國立中央大學 2006 年發現編號 210030 小行星，經認證命名爲桃園「Taoyuan」，桃園小行星位在火星和木星之間的小行星帶，距離地球最近的距離約一點五億公里，繞太陽一圈約三點四年。二 00 六年發現時位在天蝎座，目前則在巨蟹座。

根據中央大學天文研究所周翊所長表示，桃園小行星是在二 00 六年六月二十四日由中大鹿林天文台楊庭彰跟大陸廣州中山大學葉泉志，用四十公分望遠鏡所發現，一般來說國際天文學聯合會(IAU)不會立刻承認，必須要等一個回歸才會承認命名，所以桃園小行星在今年六月正式命名爲「桃園」(Taoyuan)。

周翊所長表示，要在浩瀚的宇宙中發現新天體，除了專業之外，更需要恆心和毅力。中央大學 23 日由校長蔣偉寧將桃園小行星模型頒贈給桃園縣長吳志揚，彰顯「桃園」躍上國際，揚名宇宙。

原文轉載自【2011-11-24/台灣英文新聞】

中大發現小行星　命名「桃園」

【康鴻志／桃園報導】

宇宙中多了顆以「桃園」（Taoyuan）命名的小行星，國立中央大學廿三日舉辦在台復校四十九周年校慶活動，校方感謝桃園縣政府長期大力協助，讓中大得以在桃園縣奠基，成爲名列世界五百大的頂尖學府，特將今年六月中大鹿林天文台發現的編號 210030 小行星向國際天文聯合會（IAU）取得認證，正式命名爲「Taoyuan」。

中大校長蔣偉寧昨天在校慶活動中，頒贈小行星模型給桃園縣長吳志揚，同時宣布宇宙間多一顆以「桃園」命名的小行星。

「桃園小行星」是民國九十五年六月廿四日由中大鹿林天文台楊庭彰與大陸廣州中山大學葉泉志用四十公分望遠鏡所發現，座落於火星和木星之間的小行星帶上，距離地球最近的距離約一.五億公里，

繞太陽一圈約三.四年，當年發現時位於天蠍座，目前則在巨蟹座。

中央大學天文研究所所長周翊表示，當一顆小行星至少四次在回歸中心被觀測到，並精確測定出其運行軌道參數後，它就會得到國際小行星中心給予的永久編號。

中央大學表示，中央大學鹿林巡天計畫（Lulin Sky Survey，簡稱 LUSS），自九十五年三月啓動以來，已經發現八百多顆小行星，當中有十五顆已獲得國際天文聯合會（IAU）認證命名成功，「桃園」就是其中一顆，其他還有「溫世仁」、「鄒族」、「玉山」、「雲門」、「李國鼎」、「小林村」等。

原文轉載自【2011-11-24/中國時報/C1 版/桃竹苗焦點・運動】

新發現小行星　命名桃園

中央大學昨天把新發現的小行星命名為「桃園」，桃園縣長吳志揚說，縣府正全力打造桃園航空城，小行星命名「桃園」，有助於提升國際知名度。

「桃園」小行星介於火星、木星之間，距離地球 1.5 億公里，是全球發現的第 210030 顆小行星，也是第 15 顆以台灣地名、人名或族名命名的小行星，台灣至今發現 800 多顆，觀測科技日益進步，這兩年甚至有高中生找到小行星。　　（圖文：記者羅正明）

原文轉載自【2011-11-24/自由時報/A14 版/桃園焦點】

中大發現小行星！　命名桃園

【記者楊德宜／中壢報導】

中央大學發現編號第廿一萬卅號的小行星，經國際天文學聯合會通過，命名桃園（Taoyuna），桃園縣長吳志揚昨天自校長蔣偉寧手中接過小行星模型，表示桃園不只揚名國際，還揚名宇宙，「希望外星人最早認識台灣的城市是桃園」。

以台灣縣市命名的小行星，有嘉義、南投、高雄等，而以台灣地名命名的還有歸仁、中壢、玉山、鹿林等，另有小行星命名中大、雲門、慈濟、李國鼎等。

中大天文所長周翊說，桃園小行星是民國 95 年 6 月 24 日由中大鹿林天文台研究員楊庭彰、大陸廣州中山大學學生葉泉志，透過 40 公分望遠鏡發現，桃園小行星位於火星、木星之間的小行星帶，距離地球最近距離約 1.5 億公里，繞太陽一圈周期 3.4 年。當年發現位於天蠍座，目前則在巨蟹座。

蔣偉寧說，感謝桃園縣政府大力支持，中大才能在桃縣奠基，如今已是名列世界 500 大、前 1%的頂尖大學，將小行星命名桃園，因為桃園是國門之都，希望桃園縣發展會越來越好，成為台灣最重要的城市。

吳志揚說，很感謝中大以桃園為小行星命名，「桃園小行星存在宇宙 40 億年」，讓他想到「天行健，君子以自強不息」，行星的運作，象徵桃園縣發展能自強不息、永續發展。

周翊說，中大鹿林天文台設在玉山國家公園，是東亞最高的天文觀測點，中大鹿林巡天計畫自民國 95 年 3 月以來，總計發現八百多顆小行星，以及 1 顆近地小行星、1 顆彗星。

蔣偉寧也趁機向吳志揚請命，他說，中大很樂意當桃園縣政府的智庫，希望桃園縣未來規畫捷運路線，務必將中大設置 1 站，「對中大成為一流大學是很關鍵的事」。

原文轉載自【2011-11-24/聯合報/B2 版/桃園綜合新聞】

中央大學發現小行星　命名為桃園「Taoyuan」

中央大學 2006 年發現編號二一 00 三 0 小行星，經認證命名為桃園「Taoyuan」，昨天(23 號) 由校長蔣偉寧將桃園小行星模型頒贈給桃園縣長吳志揚，彰顯「桃園」躍上國際，揚名宇宙。（李明朝報導）

根據中央大學天文研究所周翊所長表示，桃園小行星是在二 00 六年六月二十四日由中大鹿林天文台楊

庭彰跟大陸廣州中山大學葉泉志，用四十公分望遠鏡所發現，一般來說國際天文學聯合會(IAU)不會立刻承認，必須要等一個回歸才會承認命名，所以桃園小行星在今年六月正式命名爲「桃園」(Taoyuan)。

中央大學表示，桃園小行星位在火星和木星之間的小行星帶，距離地球最近的距離約一點五億公里，繞太陽一圈約三點四年。二 00 六年發現時位在天蝎座，目前則在巨蟹座。

周翊所長表示，要在浩瀚的宇宙中發現新天體，除了專業之外，更需要恆心和毅力。
中央大學十一月二十三日由校長蔣偉寧將桃園小行星模型頒贈給桃園縣長吳志揚，彰顯「桃園」躍上國際，揚名宇宙。

原文轉載自【2011-11-24/中廣新聞網】

吳縣長贈送印有「桃園小行星」押花畫作給中央大學感謝將發現的小行星命名爲「桃園」

【中壢訊】爲表達感謝國立中央大學天文所於 2006 年發現編號 210030 小行星，經國際天文學聯合會通過並命名爲「桃園（taoyuan）」，縣長吳志揚 23 日特別前往中大頒贈印有「桃園小行星」押花畫作，希望藉著「桃園小行星」的運行，象徵桃園也能生生不息，持續發展下去。

國立中大 23 日舉行全校運動大會，校長蔣偉寧藉此機會將「桃園小行星」的模型，贈送給吳志揚縣長，而吳縣長也回贈由龜山鄉許巧萍老師以新鮮花材進行乾燥壓製作成以發現「桃園小行星」軌道意象圖爲主軸設計出押花畫作，以感謝中央大學將以小行星命名爲「桃園」。

吳縣長表示，桃園原本就是台灣最棒的縣市，又因縣內有國際機場而馳名國際，如今，中央大學又發現一顆已運行逾 40 億年的小行星並命名爲「桃園」，更讓桃園之名揚名宇宙。

吳縣長說，從中大發現宇宙中的一顆不知名的小行星，讓他學習到兩件事，分別是學習要永遠追求新和，以及古訓「天行健，君子以自強不息」的道理，他期許有了「桃園」這顆小行星，也讓桃園的發展能夠生生不息，永遠持續下去不要間斷。

中大校長蔣偉寧則感謝桃園縣政府長期的支持，特別是吳縣長祖孫三代協助，讓中大在桃園穩健成長，進而名列世界五百大，前 1%的頂尖大學。

中大天文研究所所長周翊表示，這顆被命名爲「桃園（taoyuan）」的小行星，是中大天文所鹿林天文台楊庭彰和大陸廣州中山大學葉泉志，於 2006 年 6 月 24 日以 40 公分望遠鏡發現的，經國際天文學聯合會（iau）通過，並於今年 6 月 15 日正式命名。桃園小行星位於火星和木星之間的小行星帶，距離地球最近的距離約 1.5 億公里，本身的直徑約爲 1-2 公里，繞太陽一圈約 3.4 年，2006 年發現時位於天蝎座，目前在巨蟹座。
(在地生活｜桃竹苗)
出處: 吳縣長贈送印有「桃園小行星」押花畫作給中央大學感謝將發現的小行星命名爲「桃園」

- 楊梅新聞網 - udn 部落格 http://blog.udn.com/yangmei320/5866570#ixzz1ebjB355r

原文轉載自【2011-11-23/楊梅新聞網 - udn 部落格】

中大命名小行星　Taoyuan 贈桃園

記者成志平／桃園報導

爲彰顯「桃園」在臺灣特殊的象徵意義，中央大學將發現的編號 210030 小行星命名爲「Taoyuan」，昨日利用舉行全校運動會開幕式，由校長蔣偉寧頒贈小行星模型給桃園縣長吳志揚，讓「桃園」躍上國際，揚名宇宙。

中央大學校長蔣偉寧說，中央大學明年將慶祝在台復校五十週年，中大民國五十七年從苗栗遷校中壢，受到地方士紳的大力協助，近來非常感謝桃園縣政府以「無償撥用」的方式，提供中大在八德擴大都市計畫 2 公頃土地，發展第二校區；另在觀音撥用 6 公頃土地，共同推動「桃園科學園區」，設置桃科創新

育成中心，帶動地方文化經濟繁榮。

吳志揚表示，中大不但是縣內規模最大，也是歷史最悠久的學府。獲頒桃園小行星，讓他深感榮耀，也心有所感。一來是人類對知識的追求是無窮無盡的，浩瀚的知識可引領我們上天下海、飛天遁地，這說明了「知識就是力量」;其次是如此遙遠的一個星點，觀測者如何發現？這驗證了「天行健，君子以自強不息」這句名言，宇宙萬物都將生生不息地運作，也象徵中大校運和桃園縣運將日益昌隆。

原文轉載自【2011-11-24/青年日報/13 版/桃竹苗地方通訊】

中大發現新行星　命名「桃園」閃耀銀河

【羅安達桃園】

2006 年中央大學鹿林天文台，曾發現一顆小行星，並在今年 6 月 15 日，正式將這顆小行星命名爲「桃園」，23 日中央大學特別頒贈行星模型給桃園縣，央大天文所表示，目前發現的行星，皆以學校所在地命名，未來他們將結合在地客家，以客家最具代表性的人名，當成未來新發現的小行星命名依據，讓客家知名人物能代表台灣躍上國際，揚名宇宙。

開心的從中央大學校長手中，接下小行星「桃園」的模型，桃園縣長吳志揚高興地說，桃園的名聲不只到國際，還揚名宇宙。

桃園縣縣長吳志揚:「這顆行星，因爲是我們中央大學第一個發現的，所以它來命名叫桃園，換句話說，以後有一顆星星名字叫作桃園，這不但是讓桃園世界有名而已，是宇宙知名。」

中央大學鹿林天文台，繼去年 11 月命名小行星「中壢」後，在今年 6 月，也將先前發現的新行星命名爲「桃園」，也通過國際天文聯合會核可，現在浩瀚的宇宙中，已有 2 顆代表桃園的行星閃耀著，天文台技士張光祥表示，這次發現的「桃園」小行星，直徑近似於阿里山的海拔高度，位於火星及木星之間的小行星帶，距離地球約 1.5 億公里遠。

中央大學鹿林天文所技士張光祥:「現在發現小行星，越來越難，因爲發現的越來越小顆，所以要到環境好的鹿林天文台，來發現這些天文現象，這工作就像大海撈針一樣的困難。」

目前中央大學天文所還發現了多顆新行星，除了以桃園縣地名，天文所打算未來以客籍重要人物的姓名來命名。

中央大學鹿林天文所技士張光祥:「像客家文學家鍾理和，還有歌曲的創作鄧雨賢，陸續都會想來做一個發表(命名)。」

鹿林天文台，是目前亞洲發現新行星最活躍的地點之一，這些發現都讓台灣的天文研究，在國際上更發光發熱。　(2011-11-23)

原文轉載自【2011-11-23/客家電視台　CH 17】

天文學者科普演講

台北市立天文科學教育館今天下午 2 時，於館內 1 樓第一演講室舉辦科普演講活動，邀請中央大學大天文所葉永烜教授主講「宇宙線與莫內的荷花池」，可現場報名。
網址：www.tam.gov.tw

原文轉載自【2011-11-21/蘋果日報/A4 版/要聞】

宇宙線與莫內畫　演講

【台北訊】台北市立天文館表示，今天下午 2 時，在館內有場「宇宙線與莫內的荷花池」演講，邀中央大學天文所教授葉永烜擔任主講，演講內容除探討光線與顏色的關係外，還有探討天文觀測問題，歡迎民眾到場聆聽。活動詳情可電洽 28314551。

原文轉載自【2011-11-20/聯合報/B2 版/北市綜合新聞】

北市天文館周日辦天文演講

【聯合晚報／記者嚴文廷／即時報導】 2011.11.18 03:05 pm

台北市立天文館將於 11 月 20 日下午 2 至 4 時舉辦演講，由中央大學天文研究所與太空科學研究所教授葉永烜談「宇宙線與莫內的荷花池」，葉永烜專攻天文，又愛繪畫，這次將從宇宙線談起，帶入宇宙線對生物的影響，以及光線如何呈現這個世界。活動開放電話及現場報名，(02)2831-4551 轉 704。

手機在我手，新聞跟著走　m.udn.com 提供您最豐富的新聞資訊！

原文轉載自【2011-11-18/ 聯合新聞網/生活　即時新聞】

太陽黑子活躍　美麗極光往南移

作者：羅智華

有趣的是，科學家亦透過研究發現，太陽活動的活躍程度也會影響到美麗極光的出現頻率！像是上個月美國中西部如亞特蘭大、喬治亞等地區就出現了如夢似幻的極光蹤影，讓現場目睹的幸運兒莫不驚呼連連。

中央大學天文研究所教授黃崇源表示，極光屬於一種大氣現象，是因為太陽與地球產生交互作用而形成。

他表示，太陽表面會發射出帶電粒子，抵達地球時由於受到地球磁場的牽引而繞至地球南、北極。當這些帶電粒子與地球兩端的空氣分子相互撞擊後，就會產生極光。

黃崇源說，科學家發現，太陽黑子的活躍程度亦和極光出現次數多寡呈現正相關。也就是說，當太陽黑子較為活躍時，就會使得太陽表面發射出大量的帶電粒子；由於這些帶電粒子的數量龐大，所以不見得所有粒子都能被地球磁力線牽引至南北極，部分粒子可能會因此跑到緯度相對較極區低的地帶，因而讓其他非南北兩極的地區也能看見極光的出現。

不過，若沒有機會前往高緯度地區欣賞美麗極光在夜空中搖曳的天文迷也別感到難過。

楊曄群表示，太陽黑子從出現到消失，大約可維持兩周時間，以這次太陽黑子為例，就是六年來最大數量的黑子群，從現在起到下周一前都是適合的觀測時機，為了方便觀賞，台北天文館也特別開放第二觀測室供大眾觀測，現場並有解說人員進行導覽說明，想要躬逢其盛的天文愛好者可把握這次難得的觀測良機。

原文轉載自【2011-11-11/人間福報/遇見科學】

藉超新星揭宇宙奧妙　三天文學家獲諾貝爾獎

作者：羅智華

西元 1609 年，義大利科學家伽利略發明了第一支天文望遠鏡，開啓了人類仰觀蒼穹、進行天文觀測的里程碑。四百年來，人類從抬頭仰望滿天星斗到國際團隊攜手探索宇宙大爆炸源起，一路走來的每個階段都寫下了歷史新頁，隨著觀測工具不斷創新，亦讓天文研究更上層樓，像是今年諾貝爾物理獎就頒給了三位天文物理學家，消息傳出後，讓全球天文迷為之興奮。

這三位得獎者分別是今年 52 歲、現任美國柏克萊加大超新星宇宙計畫主持人波莫特（Saul Perlmutter）、現年 44 歲，現任澳洲國立大學天文學教授施密特（Brian Schmidt）、以及 42 歲的美國約翰霍普金斯大學天文學教授黎斯（Adam Riess）。三人透過超新星的研究而觀測到宇宙以極快速度加速擴張的重要發現，不但改變了天文學家過去對宇宙擴張的看法，也讓他們嘗到獲諾貝爾獎肯定的甜美果實。

瑞典皇家科學院在頌詞中指出，近一百年來，我們已知道宇宙是因一百四十億年前的宇宙大爆炸而擴張，但透過 Saul Perlmutter 等三人對超新星的觀測，則讓我們進一步知道宇宙正加速擴張，這過程就如同我們將一顆球丟向半空中，但我們卻沒看到球因重力吸引而往下掉，反而是加快速度消失於空中，而宇宙的擴張現象就如同這顆球的軌跡般，令人感到驚訝。

不過，大家不免好奇，我們要如何知道宇宙有沒有擴張呢？中央大學天文所教授黃崇源表示，其實三人是藉由觀測 Ia 型超新星發現到宇宙正加速擴張中。他說，一般人印象中的「超新星」大都是發生在重質量星球演化末期的核塌縮型超新星。隨著恆星演化進入末期，星球核心融合產生鐵後，因為缺乏新能量來源，導致無法抵抗外部重力而塌陷成中子星或黑洞，造成星球外層物質向外爆炸，而形成「核塌縮型超新星」爆炸。

然而，Saul Perlmutter 等三人所觀測的 Ia 型超新星成因則不同於「核塌縮型超新星」的演化歷程，黃崇源說，「Ia 型超新星」主要是因白矮星失控的熱核融合而造成恆星的瓦解。由於 Ia 型超新星釋放出的能量十分固定，因此也被用來作爲距離測量的標準值。簡單來說，當科學家了解 Ia 型超新星的實際亮度後，就能從觀測到的 Ia 型超新星亮度來判斷它們的距離究竟有多遠。

研究發現　宇宙正在膨脹中

作者：羅智華

自然科學博物館館長孫維新表示，每個星系大約有一、兩千億顆恆星，平均每三十年就有一顆超新星爆炸，但由於銀河中有很多垃圾、灰塵阻隔，所以人類大約平均三、五百年才能看到超新星爆炸的歷程。

有趣的是，這樣的觀測經驗可不是近代科學家才看得到，孫維新說「早在宋朝，就有人記錄下超新星的爆炸過程」，文史記載北宋仁宗至和元年（西元 1054 年），天空中曾出現一顆連續多日在白晝綻放光亮的星星，引發大家議論紛紛，但回過頭來看，其實這就是恆星爆炸後的超新星。

黃崇源表示，雖然當時的科學家都知道宇宙在擴張，但從過去理論來看，在萬有引力影響下，照理說應該會「拖慢」宇宙的擴張速度。然而，Saul Perlmutter 等三人在 1998 年透過 Ia 型超新星觀測時，卻發現到遙遠星系的超新星亮度比預期來得暗，代表其真實距離比我們原本預期的距離來得遠，意味著宇宙膨脹速度比現在的預估值快上許多，所以三位科學家才會從中得出宇宙正快速擴張中的重大結論。

他指出，透過理論與數據的比較，也發現宇宙不但沒受到重力吸引而降低擴張速度，反而是加速膨脹中；也因此讓我們推測宇宙中存在一種可以讓宇宙加速擴張的黑暗能量（dark energy）。

對普羅大眾來說，我們總認爲宇宙如此浩瀚，要透過現代科學了解宇宙變化似乎是件相當困難的事；但從這三名科學家的研究歷程也彰顯出科學研究致力於「追根究柢」的精神所在。

孫維新表示，天文科學的迷人之處，就在於我們永遠都能在美麗蒼芎中有不同的新發現。當中除了倚賴天文觀測技術與儀器的推陳出新外，最重要就是人類永無止盡的探索欲望，這也是推動科學發展的重要原動力。

原文轉載自【2011-10-14/人間福報/遇見科學】

推翻宇宙等速膨脹　開啓暗物質研究新頁

〔記者湯佳玲／台北報導〕諾貝爾物理獎昨天揭曉，頒發給利用超新星定出距離，計算出宇宙正加速膨脹的三位美籍研究人員，推翻過去宇宙等速膨脹想法，且有九十六%的暗物質與暗能量存在。

國立自然科學博物館館長孫維新解釋，超新星是恆星演化到晚期、燃料用盡後，無法支撐自身整體質量而塌縮往外爆炸，且爆炸亮度比一整個星系還亮。但由於科學家已充分掌握超新星爆炸機制，因此可以當成是標準光源，經由超新星爆炸亮度計算出與地球的距離。而過去科學家利用哈伯望遠鏡發現宇宙膨脹，但一直以爲是等速膨脹，直到分屬兩個競爭陣營的三位諾貝爾獎得主，陸續在一九九八年與一九九九年發現宇宙加速膨脹理論後，科學家才恍然大悟，並意識到宇宙暗能量的存在，也才開啓暗物質與暗能量的天文研究新頁。

中研院天文所助理研究員張慈錦表示，曾經在二〇〇三年至二〇〇六年於美國柏克萊大學進行博士後研究時，與本屆諾貝爾物理獎得主佩爾莫特爾共事過。他當時正在推動大型衛星計畫，利用重力透鏡測量宇宙密度。張慈錦眼中的諾貝爾獎大師，是位非常忙碌、很有活力，深具領導能力、但有點嚴肅的人。孫維新說，二〇〇九年的「科學季：仰望蒼穹四百年特展」中，另一位諾貝爾獎得主施密特即爲第一位邀請來台演說的學者；同年吳健雄科學營也曾邀請他來演講，平易近人、侃侃而談的大師風範，深受學生喜愛。

中央大學天文所教授陳文屏表示，以前人們所認識的宇宙，如電子、原子、元素等一切物質只佔了宇宙的四%；宇宙加速膨脹理論提出後，科學家才發現原來另外還有暗能量與暗物質的存在，而且占據宇

宙的九十六%，未知顯然遠超過目前的已知。陳文屏也說，人類能利用超新星的特別手段，找到宇宙加速膨脹現象，從前以為是神話，現在卻能實際觀測，對人類心智可說是「一件不可思議的事。」

原文轉載自【2011-10-05/自由時報/A5 版/國際新聞】

兩年前　施密特曾來台開講　學者：得獎凸顯人類對宇宙無知

【李宗祐／台北報導】

今年諾貝爾物理獎得主之一施密特曾在二〇〇九年國際天文年應邀到台灣演講。曾與他共事的學者形容，施密特治學嚴謹，但為人和氣，容易相處。國內學界認為，施密特等人獲獎，更凸顯人類對宇宙的「無知」。

中研院天文及天文物理研究所助研究員張錦慈曾在二〇〇三年到二〇〇六年在美國加州大學柏克萊分校與施密特共事。施密特治學嚴謹，做人處世則圓融和氣。

國立自然科學博物館長孫維新在二〇〇九年八月邀請施密特在台灣國際天文年系列活動發表演講，講題就是跟他此次獲獎的有關研究。

中央大學天文研究所教授陳文屏說，施密特等人的研究發現，對人類現在的生活環境沒有特別影響，未來會有什麼影響也不知道。但瑞典皇家科學院頒發諾貝爾物理獎給他們，凸顯人類對宇宙的「無知」，讓人類知道「我們所處的宇宙不像原來想像的那樣！」

原文轉載自【2011-10-05/中國時報/A5 版/話題】

施密特前年來台　解黑暗之惑

【記者蔡永彬、陳幸萱／台北報導】

浩瀚的星空和宇宙美得有如神話故事，人類不斷嘗試更了解它。今年的諾貝爾物理學獎頒給三位天文學家，國立自然科學博物館館長孫維新認為，研究宇宙讓我們了解它的現況和本質，解開人們心中最深沉的疑問。

這三位天文學家透過觀測遙遠的「超新星」，發現宇宙正在加速膨脹。孫維新解釋，超新星是恆星爆炸後「死亡」的過程，人們從它「本來」和「看起來」的亮度，推論出它離我們多遠；再透過星系的光譜，發現這些星系正快速離我們而去，導出宇宙在加速膨脹。

中央研究院天文及天文物理研究所助理研究員張慈錦說，超新星的觀測是最早證明宇宙膨脹的證據。目前天文學家多認為宇宙會膨脹至密度非常小、「很空、很冷」的狀態，星系無法形成、溫度持續下降，一片漆黑。

中央大學天文研究所教授陳文屏表示，依據萬有引力定律，宇宙應該要被「拉回來」才對。為什麼會擴張？陳文屏說，這股「抵抗拉回來的力量」稱作「黑暗能量」，原因不明。

三人中的施密特前年曾來台演講，他當時提到，宇宙中我們了解的物質只有百分之四，黑暗物質、黑暗能量分別占百分之廿四和七十二。

張慈錦說，李斯與波麥特分屬不同的團隊，先後在一九九八、九九年發表類似的研究成果。她在美國柏克萊大學時曾和波麥特共事，「客氣，但比較嚴肅。」對他的印象是「很忙」，一直在推動許多大型計畫。

近十年來，諾貝爾物理獎曾在二〇〇二、〇六年頒給天文、宇宙學研究。

原文轉載自【2011-10-05/聯合報/A10 版/話題】

中央大學觀測天文奇觀地面資料

〔本報訊〕美國航空暨太空總署（NASA）3 月偵測到黑洞吞噬恆星的奇觀，研究成果登上最新的國際期刊自然「Nature」。由於其中地面觀測資料數據部份是中央大學研究團隊提供，中央大學得以列名，該校表示，由天文所提供觀測資料能參與研究，同感興奮與欣慰。

美國航空暨太空總署的衛星（Swift）3 月偵測到黑洞吞噬一顆類似太陽的恆星，以衛星名稱和坐標位置命名爲「Swift J1644+57」。美國賓州州立大學天文及天文物理所教授大衛巴羅斯（David Burrows）領導的跨國研究團隊，對「Swift J1644+57」進行研究，論文成果登上「Nature」。

中央大學表示，中央大學天文研究所助理教授浦田裕次和中央研究院天文與天文物理研究所博士後研究員黃麗錦夫妻檔，透過「東亞伽瑪射線爆觀測網」，結合台灣、中國大陸、日本等地的天文台，提供詳細的「 Swift J1644+57」地面可見光和「紅外光」觀測資料給大衛巴羅斯的團隊，因而在論文中，央大天文所也列名其中。

浦田裕次表示，「Swift J1644+57」是人類首次目睹黑洞吞噬恆星的過程，也是天文界重要里程，這次發現也讓人們對黑洞生長過程有了初步認識。

黃麗錦表示，「觀測不像其他研究，無法事先預期」，因此常處於機動狀態，就怕不小心錯過寶貴資料。爲了天文觀測，經常得從入夜一直連續工作到天亮，期間的辛苦不足爲外人道，但研究成果能對國際社會提供貢獻，也讓她感到欣慰。

原文轉載自【2011-09-04/澎湖時報】

人類首次目睹黑洞「吃掉」恆星

【聯合報／記者蔡永彬／即時報導】 2011.09.01 09:55 pm
美國航空暨太空總署（NASA）近日公布人類史上首次目睹黑洞「吃掉」恆星的過程，這項發現也有台灣的貢獻，成果登上最新一期《Nature》（自然）期刊。
台灣參與這項國際合作計畫的人員是中央大學天文研究所助理教授浦田裕次、中央研究院天文及天文物理研究所博士後研究員黃麗錦夫妻檔。浦田認爲，這次發現將讓人們對於黑洞的生長過程有更多認識。

原文轉載自【2011-09-01/聯合新聞網/要聞　即時新聞　】

天文研究夫妻檔　登上自然期刊

美國航空暨太空總署（NASA）近日公布首度捕捉到黑洞吞噬恆星的天文奇觀，中央大學天文所助理教授浦田裕次和中研院天文所博士後研究員黃麗錦夫妻檔參與了這項計畫。黃麗錦使用中央大學鹿林一米望遠鏡，針對此次伽瑪射線爆餘輝提供觀測數據。兩人在天文研究上產生共同興趣，共結連理，更是學術上的好夥伴，成果登上最新一期「自然」(Nature) 期刊。

NASA 的「雨燕」衛星 (Swift) 於今年 3 月 28 日偵測到天龍座方向發出的異常高能閃焰，來自 39 億光年外的一個星系，顯示星系中心的黑洞正吞噬一顆類似太陽的恆星。多波段觀測結果顯示黑洞質量相當數百萬個太陽質量，且恆星所產生的噴流方向朝向地球，偵測到強烈的伽瑪射線和X射線。 （圖文：記者湯佳玲）

原文轉載自【2011-09-02/自由時報/A14 版/生活新聞】

黑洞吃掉恆星　台學者追蹤發現

【記者蔡永彬】

在浩瀚無垠的太空裡，「黑洞」總是給人神秘色彩。美國航空暨太空總署（NASA）近日公布人類史上首次目睹黑洞「吃掉」恆星的過程，這項發現也有台灣的貢獻，成果登上最新一期「自然」期刊。

台灣參與這項國際合作計畫的人員是中央大學天文研究所助理教授浦田裕次、中央研究院天文及天文物理研究所博士後研究員黃麗錦夫妻檔。黃麗錦表示，浦田和她本來研究「γ（伽瑪）射線爆」現象的成因和原理，他們從 NASA 的「Swift」(雨燕）衛星獲得資訊，再進行觀測。今年 3 月 28 日，衛星偵測到前所未有的「異常高能量閃焰」。

黃麗錦解釋，正常的γ射線爆現象只爆一次就暗下來，但這次卻每天爆、每天爆，「一連持續兩個多月！」這個天文奇觀遠在 39 億光年外，慘遭「吃掉」的「倒楣」恆星編號爲「Swift J1644+57」；浦田和黃麗錦持續追蹤，在紅外光和可見光波段提供許多觀測資料，登上 Nature 期刊讓他們非常興奮。

原文轉載自【2011-09-02/Upaper/3 版/焦點】

NASA 捕捉黑洞吃恆星　台灣有貢獻

【記者蔡永彬／台北報導】

在浩瀚無垠的太空裡，「黑洞」總是給人神秘色彩。美國航空暨太空總署（NASA）近日公布人類史上首次目睹黑洞「吃掉」恆星的過程，這項發現也有台灣的貢獻，成果登上最新一期《Nature》(自然）期刊。

台灣參與這項國際合作計畫的人員是中央大學天文研究所助理教授浦田裕次、中央研究院天文及天文物理研究所博士後研究員黃麗錦夫妻檔。黃麗錦說：「這是人類史上第一次（看到）！很幸運！」浦田認爲，這次發現將讓人們對於黑洞的生長過程有更多認識。

黃麗錦表示，浦田和她本來研究「γ（讀作 gamma、伽瑪）射線爆」現象的成因和原理，他們從 NASA 的「Swift」(雨燕）衛星獲得資訊，再進行觀測。今年三月廿八日，衛星偵測到前所未有的「異常高能量閃焰」；黃麗錦回憶，原本以爲只是一般的γ射線爆現象，她也沒特別留意。

「ㄟ？怎麼又爆一次？」黃麗錦解釋，正常的γ射線爆現象只爆一次就暗下來，但這次卻每天爆、每天爆，「一連持續兩個多月！」這個天文奇觀遠在卅九億光年外，慘遭「吃掉」的「倒楣」恆星編號爲「Swift J1644+57」；浦田和黃麗錦持續追蹤，在紅外光和可見光波段提供許多觀測資料，登上 Nature 期刊讓他們非常興奮。

原文轉載自【011-09-02/聯合報/A8 版/生活】

我國首測得「黑洞吞恆星」

【許敏溶／台北報導】分別在中央大學和中研院任職的夫妻檔，共同參與美國跨國研究團隊的黑洞觀測計劃，率先觀測到可證明黑洞正在吞噬恆星的可見光和紅外光，見證人類首次觀測黑洞吞噬恆星的歷史時刻；該發現日前登上最新一期頂尖學術期刊《自然》(Nature)，浦田裕次和黃麗錦昨都說：「十分欣慰、興奮。」

佐證美衛星發現

由美國賓州州立大學天文及天文物理所教授大衛・伯羅斯領導的跨國研究團隊，利用美國航空暨太空總署「雨燕」衛星，於三月二十八日偵測到距離地球三十九億光年外一個星系出現異常高能閃焰，首度觀測到黑洞正吞噬一顆恆星的過程，以中央大學天文所助理教授浦田裕次和中研院天文所博士後研究員黃麗錦爲主的研究團隊，則率先在發現黑洞吞噬恆星後，提供地面觀測到的可見光和紅外光等資料，佐證「雨燕」的發現，速度領先歐美其他四個團隊。

黃麗錦說，黑洞是恆星爆炸後擠壓成一個質量很大的天體或重力場，因質量大導致引力強，包括光線、物質經過時都會被吞噬，天文學界普遍認爲宇宙中有黑洞存在，但現僅能從銀河系恆星繞著看不見的黑洞運行推論其存在，這次「雨燕」衛星偵測到高能伽瑪射線、X 射線和紫外光，這些都是黑洞吞噬恆星後從中心噴發出的物質，搭配他們團隊發現的可見光和紅外光等資料，證實黑洞吞噬恆星的過程。

學者夫妻：很欣慰

日本籍的浦田裕次說，這是人類首次目睹黑洞吞噬恆星過程，是天文界重要里程；黃麗錦說，觀測不像研究可事先預知結果，常得從入夜工作到天亮，但和先生可互相鼓勵，能有成果十分欣慰。

清華大學天文物理所教授、天文學會前理事長張祥光說，台灣在觀測儀器上不如歐美先進國家，但天文觀測成果不輸人，台灣學者成就值得肯定。

●觀測黑洞吞噬恆星資訊
★參與者：中央大學天文所助理教授浦田裕次和中研院天文所博士後研究員黃麗錦爲主的研究團隊
★成果：美國航空暨太空總署「雨燕」衛星，3 月 28 日偵測到距離地球 39 億光年外一個星系，出現異常高能閃焰，首次觀測到黑洞正在吞噬一顆恆星，台灣的研究團隊領先歐美其他 4 個團隊，率先提供地面觀測到的可見光和紅外光等資料
★重要性：爲人類首次觀測到黑洞吞噬恆星
資料來源：中央大學

原文轉載自【2011-09-02/蘋果日報/A8 版/要聞】

天文教育爲原住民孩童點亮「星」希望

【記者張仟又／桃園縣報導】一群國立中央大學的志工們在今年寒假前往台東縣海端鄉霧鹿國小進行科學深耕教育，希望利用當地光害少的特性，將霧鹿國小打造成一所星光小學。

中央大學課外組行政專員黃裕隆表示，打造星光小學活動共分爲兩個階段，第一階段活動，考量偏遠地區的教學資源缺乏，因此以營隊的方式教學，藉此豐富學童的學習經驗；而第二階段活動，針對參加第一階段活動的國小，進行天文科學深耕的教育訓練，由中央大學偕同天文館工作團隊深入學校，針對教師與學童進行天文延伸教育，並整合當地天然優厚觀星環境，規劃天文觀測活動，讓該校成爲當地天文教育推廣的基地。

今年是星光小學第五班，每年一班，已經舉辦了五年，前面四班都是只由天文館的志工們出隊，包括第一階段的天文館參訪和第二階段的現場教學，今年開始才引進營隊的形式，由自願跟隨天文館志工的大學生們去國小帶營隊。

服務採用分工的方式，天文館的志工負責爲學童解說觀星儀的使用方法、如何使用肉眼觀星，並對當地教師進行天文儀器的教學，希望老師在學會使用儀器後，能讓天文觀測的活動長久持續下去。中大志工則負責帶小隊玩大地遊戲、團康活動、準備午餐、帶晨操和管理秩序，透過玩遊戲的教學方式讓小朋友能學習得更開心。

地球科學系一年級鄭舒尹說：「我覺得很充實，不管是知識方面或是心理都感受到了新的東西流入。服務是件很奇妙的事，不求任何回報，付出的心甘情願，能夠遠離塵囂看看最單純的他們還有自己，我覺得我們彼此都獲得了心靈上的成長。經由星光小學，讓從未有營隊經驗的我們起步，開始了解自己的常處還有值得加強的地方，這不是只是單純的營隊而已，跟著天文館志工們一起活動，讓我學習到了不少野炊的技巧，還有他們廣博的知識，都讓我大感佩服。」

原文轉載自【2011-08-31/生命力新聞】

探索天文 --外星人在哪裡？

作者：文／林琦峰（台北市立天文科學教育館解說員）

夜裡，昂首遙望天際時，你曾經想過地球以外，是否還有外星生命存在嗎？其實，「外星人」的相關話題，一直都是人們所好奇的。從早期好萊塢《外星人 E.T.》電影中，頭大身體圓的 ET；到去年紅極一時《阿凡達》電影中，全身藍色的納美人，這些都深深吸引著民眾的目光，當然也造成民眾，對外星人外型的既有認知，但這其實都只是藝術家對外星人想像而創造出的。如果你問科學家，外星人長怎麼樣？沒有人可以給我們一個答案。但是如果問科學家，有沒有外星生命存在？我想大部分科學家給的答案會是肯定的。

「到底有沒有外星人？」一直是到天文館參觀的小朋友，最常問的問題之一，這個問題同時也縈繞在科學家的腦海之中。近年來，天文學家已經在搜尋外星生命研究中，獲得不少進展！不但在探測火星的機器人傳回捷報，發現那裡極可能曾是水世界。太空船也在木星與土星的衛星發現海洋的蹤跡！

此外，天文學家也發現環繞在其他恆星的行星，甚至還有行星位於適合生命存在的區域。由於這些豐碩的科學成果，台北天文館與國立自然科學博物館「外星人你在哪裡！——尋找外星生命」爲主軸，將介紹宇宙是否處處是生命的樂園，歡迎民眾一同進入外星世界。

地球生命如何發生？生命的原料——有機物質從哪來？這問題始終困擾著我們。在 1950 年代，科學家模擬早期地球環境的密勒——尤列實驗（Miller-Urey experiment），成功地在試管中製造有機物質。但這些年來天文學家發現在隕石中、彗星裡也藏著有機物質，甚至在星雲中看到許多種類的有機物。或許生命的原料來自於宇宙，而我們就是小小星塵！

近年來陸陸續續的太空任務，讓我們發現或許外星生命就住在鄰家。其中，火星是最熱門的地點。科學家已證實遠古的火星是個水世界，甚至微生物還能生存在地底下。在今年年底，美國將有一艘火星機器人好奇號將發射升空，未來它將帶給我們，更多火星的新知識。

此外，氣體行星雖然不容易出現生物，但伽利略與卡西尼太空船分別在探測木衛二、與土衛二時，發現木衛二表面冰層下，可能擁有液態水的海洋，甚至看到土衛二噴泉的現象。基本生命的要素包含空氣、陽光和水，有沒有液態水將是影響生命形成的關鍵之一。因爲水是很好的溶劑，所以人體以及大多數的生物體內都含大量的水。

銀河系擁有約 2 千億顆恆星，宇宙中又有約 1 千億個星系，如此表示宇宙中約有 2x1024 顆恆星。但是在熾熱的恆星上生命不可能生存，所以是否能在其他恆星上找到行星，就成爲尋找外星生命關鍵要素之一。近幾年觀測科技突飛猛進，天文學家已找到數百顆系外行星。如 2009 年 3 月發射的刻卜勒太空船，就是專司尋找系外行星的太空望遠鏡，在短短不到半年，就發現 1 千多顆系外行星的目標。其中，有些行星與其母恆星距離適當，這類的行星極可能和地球一樣發展出生命。目前所發現的系外行星之中，Gliese 581 號星是最適合生命生存。這顆黯淡的紅矮星位於天秤座，距離約 20.4 光年，目前已發現 6 顆行星環繞它。這顆恆星表面溫度僅 3500 度，比太陽低多了，因此適居帶距離母恆星較近。

如果你碰到外星人，你想跟他說什麼？天文學家真的曾向外星人打招呼。1974 年天文學家向武仙座方向的 M13 球狀星團發射的電波信，還在奔馳在星際間。先鋒號與航海家太空船，也攜帶我們的介紹唱片及信，向太陽系外奔馳。

如果這些內容還沒辦法滿足你對外星人的好奇？天文館將於 8 月 27 日下午兩點至四點，舉辦專家演講，邀請中央大學天文研究所教授陳文屏，蒞臨本館現身說法，爲大家帶來精采的「尋找系外生命」演講。

原文轉載自【2011-08-19/人間福報/遇見科學】

11 年一周期太陽黑子進入活躍期

作者：羅智華

美國國家海洋暨大氣總署（NOAA）太空氣象預報中心（SpaceWeather Prediction Center）日前表示，由於受太陽風暴來襲，可能會導致地球衛星通訊設施與全球定位系統、電訊設備受影響，甚至可能發生通訊中斷問題，相關單位需多加注意。

而科學家的「提醒」也讓民眾開始注意到有關太陽風暴的議題，並對其成因和所帶來的影響感到好奇。

對此，中央大學天文所教授黃崇源表示，太陽本身就像是一個巨大的高溫游離氣體，當中的磁力線，會隨著太陽轉速快慢不同而扭曲，導致太陽黑子產生。他表示，其實太陽黑子是太陽磁場的一種表徵、是太陽表面磁場最強的地方，平均每十一年會出現一次活躍周期；當黑子較活躍的時候，會使得太陽表面發射出大量高能帶電粒子（如質子、電子等），而形成所謂的「太陽風暴」。

黃崇源表示，從外觀來看，太陽黑子就像是太陽表面的「黑斑點」，這也是為什麼中國古代會將太陽稱為「金烏」的原因，主要是因為古代人看到金黃太陽表面突然出現了莫名斑點，因而誤以為太陽裡頭住了一群烏鴉，所以才將太陽取名為「金烏」，如今回頭來看，其實這就是所謂的「太陽黑子」。

不過一般人聽到「黑斑點」三個字，可能會以為太陽黑子面積「很迷你」，事實上根據美國大氣海洋局近日來觀測到的好幾群太陽黑子 AR1260、AR1261、AR1263，黑子面積約相當於地球的 5 倍、7 倍與 14 倍；這也是天文學家近年來第一次碰到這麼多群黑子同時出現的情況。

「相較於月亮體積只有地球的 50 分之 1、太陽體積足足是地球的 130 萬倍以上」台北天文科學教育館解說員林琦峰笑著說，正因太陽體積是地球百萬倍，所以即使是太陽表面斑點也「不容小覷」。而隨著大量黑子同時出現，也意味太陽活動愈來愈活躍。

翻開過去的資料來看，加拿大魁的北克省就曾在 1989 年 3 月因太陽風暴導致當地電力突然中斷，斷電時間長達好幾個小時。諸如此類的電訊影響，也讓人不免擔心類似事件是否會「捲土重來」。

對此，林琦峰認為民眾不需太過憂心。因為當帶電粒子從太陽表面四面八方射出到地球時，會因地球磁場與大氣層防護，而減弱帶電粒子的作用。但，對在外太空運行的人造衛星來說，則會因為缺乏大氣層保護而較易受太陽風暴影響、而可能出現衛星電訊設備「秀逗」的情況。

不過，太陽黑子的「活躍」也不盡然只會帶來對通訊設備的「干擾」，它同時也會增加美麗極光的出現頻率。黃崇源表示，這是因為隨著太陽黑子的大量出現，會使太陽發射出大量高能帶電粒子，其中有部分粒子會受地球磁場牽引跑到地球南北極，與極區空氣分子相互碰撞後，就會激發各種波長的可見光，也就是我們所稱的「極光」。

天文館　外星生命特展

【台北訊】

「到底有沒有外星人？」台北市立天文館暑假推出「外星人在哪裡？—尋找外星生命」特展，讓民眾瞭解科學家如何尋找外星生命的進度與方法。

配合特展，31 日及 8 月 27 日下午 2 點至 4 點，舉辦專家講座，分別邀請科普專家眭澔平及中央大學天文所教授陳文屏，為民眾帶來精彩外星人論戰。

原文轉載自【2011-07-24/聯合報/B2 版/北市綜合新聞】

天文相機　台灣首次成功研製

【記者陳幸萱／台北報導】

國立中央大學助理教授木下大輔團隊，成功研製新型數位天文相機「NCUcam-1」，使用對紅外光更敏感的感光元件，可拍到一般相機看不到的天文影像。這是台灣首次在國內開發天文相機。

NCUcam-1 採用新型的天文用科學等級全空乏 CCD 為感光元件，研究團隊表示，傳統的 CCD 只有十五釐米厚，新型 CCD 厚達 200 釐米，對紅外光（波長為一千奈米）靈敏度可達以往三倍以上。

原文轉載自【2011-07-23/聯合報/A17 版/綜合】

中大研製天文相機　穿透五千萬光年

【李宗祐／台北報導】

中央大學天文研究所助理教授木下大輔領導研究團隊突破技術限制，研製完成紅外光靈敏度超越現有傳統設備三倍的「同步分光四色照相儀」，並安裝在鹿林天文台一米口徑天文望遠鏡，成功拍攝到銀河外、距離地球五千萬光年的螺旋星系，創下我國首度自製天文相機在本土觀測的先例。

我國首套自製天文相機在完成測試後，初期暫時搭配鹿林天文台一米望遠鏡執行觀測任務，待建造中的兩米天文望遠鏡完成後，就會安裝到新望遠鏡上，加入美國國務院「泛星計畫」研究團隊，觀測搜尋太空中任何可能撞擊威脅地球的星體（小行星或彗星）。

木下大輔表示，台灣天文學者從國外返台任教後，因肩負「急起直追」的壓力，通常都選擇購買現有儀器協助觀測，但購買儀器很容易，卻無法累積設計、測試、維修、軟體撰寫和資料分析等經驗，更無法培訓兼具機械、光學、電子和資訊工程專長的科學團隊。

從日本到台灣後，木下大輔與儀器工程師吳景煌共同扛起兩米天文望遠鏡建造計畫天文相機自製任務。

負責電路及機構設計組裝的吳景煌，天文相機內部對真空度要求嚴苛，且須在攝氏零下一百度超低溫環境正常運作，都是從未碰過的挑戰。

前後歷經三年半的摸索，終於在七月初研製完成，並利用鹿林天文台一米望遠鏡順利穿雲透霧，成功拍攝到銀河外的螺旋星系ＮＧＣ7 331、礁湖星雲Ｍ８和球狀星團，測試驗證紅外光靈敏度超越現有設備三倍，如鷹眼般敏銳拍攝到可見光看不到的星體。

原文轉載自【2011-07-23/中國時報/A13 版/社會綜合】

歷時 3 年　2 米天文望遠鏡將落腳鹿林

作者：羅智華

不過，要打造一座天文望遠鏡可沒有我們想像中容易！光是磨製鏡片就是一項大工程。中央大學天文所教授黃崇源表示，不同於一般玻璃材質，天文望遠鏡必須要將熱脹冷縮的係數降到最低，因此是採用矽晶玻璃製作。

以 2 米望遠鏡來說，主鏡片是在俄羅斯製作，由於鏡片非一般球面，因此磨製難度更高，得靠「慢工出細活」的點滴醞釀。爲此，他也曾多次飛往俄羅斯監工、爲製作過程把關。

除此之外，望遠鏡鏡片上的鍍膜在歷經一段時間使用後，會容易因接觸空氣導致氧化、造成反射率下降。爲克服這個問題，中大光電所也特別與國際合作開發非球面天文望遠鏡監控技術，以確保鍍膜均勻，讓觀測品質不受影響。

周翊表示，隨著 2 米望遠鏡主體的完工，下一階段將邁入圓頂設計與天文台的打造，預計五年內將在鹿林正式落成，屆時將是東南亞地區海拔最高、觀測位置最佳的天文望遠鏡。

透過 2 米望遠鏡，除了可觀測到銀河系外的天體變化如珈瑪射線爆、超新星、太陽系小天體，也將爲天文搜尋與跟蹤觀測寫下歷史新頁。

未來開始運作後，除了與現有的 1 米望遠鏡相輔相成外，2 米望遠鏡還將會加入「泛星計畫（Pan-STARRS）」的觀測。黃崇源表示，泛星計畫當初是由美國國務院提出，由美國空軍委託夏威夷大學在夏威夷設立望遠鏡，以搜尋太空中可能撞擊地球的天體，爲「保衛地球」肩負起重大使命。

由於「泛星計畫」觀測範圍相當廣闊，加上泛星計畫巡天觀測時間間隔大約是一周左右，若只單靠美國自身之力將難以面面俱到，因此必須和其他地區天文台攜手合作，佈下天羅地網才能進行天體探尋與觀測。

這項計畫除了美國外、也邀請德國、英國等大學研究團隊加入，而台灣鹿林天文台也因具備良好觀測位置而獲邀加入團隊，成爲亞洲國家的唯一成員，替國際天文研究奉獻心力。

2 米望遠鏡小檔案：

作者：羅智華

光學系統：
n 光學型式：Ritchey-Chretien
反射式望遠鏡
n 有效口徑：2000mm
n 焦比：主鏡 F2.2，系統合成 F8
n 角解析率（理論值）：0.07 角秒
（波長：550 nm）
n 集光能力：可將 80%光能量集中
於 0.4 角秒範圍內
n 可用視野：1 度
機械系統：
n 架台型式：經緯台式
n 主鏡重量：2.2 公噸
n 全重：23 公噸
n 全高：8.66 公尺
n 蓋賽格林焦點最大負重：500kg
n 蓋賽格林焦點可附掛最大尺寸：2m×2m×2m

原文轉載自【2011-07-15/人間福報/遇見科學】

以管窺天　伽利略開啓人類仰觀蒼芎新頁

作者：羅智華

西元 1609 年，義大利科學家伽利略運用自製望遠鏡窺探夜空，沒想到竟看見了過去無人見過的月球表面坑洞與群星聚集而成的銀河，這不只是伽利略第一次使用望遠鏡來觀測天象，更開啓人類使用望遠鏡仰望蒼芎的歷史序幕。

台北天文科學教育館解說員林琦峰表示，望遠鏡是進行天文觀測最重要的工具。一般來說，望遠鏡可按接收訊號而分類，像是可接收可見光波段的望遠鏡就稱爲光學望遠鏡（optical telescopes）；而接收無線電波段的則稱爲無線電波望遠鏡（radio telescopes）。以光學望遠鏡來說，又可分爲「光學系統」、「機械裝置」、「電控設備」三大結構，其鏡片則依類型區分爲反射式光學望遠鏡、折射式光學望遠鏡與折反射光學望遠鏡。

很多人對於天文望遠鏡運作原理常感到一頭霧水，其實望遠鏡原理就像我們生活中常使用的照相機一樣，都是仰賴光線來發揮作用。

以反射式望遠鏡爲例，主要是透過有電鍍金屬的凹面玻璃聚焦；再借助另一塊鏡片把觀測影像反射到鏡筒外、藉由目鏡來放大影像。而折射式望遠鏡則是藉光線通過凸透鏡將光線聚集在一個焦點，再借助焦點後端的目鏡將影像放大。

然而，正因宇宙如此浩瀚無垠，四百年來不只吸引天文愛好者想一窺蒼芎之美，更帶動天文望遠鏡發展。除歐、美等國家致力於觀測儀器的推陳出新外，中國、澳洲、印度亦長期投入天體觀測的耕耘。

當然，台灣也沒在天文研究領域中缺席，早在 1999 年，中央大學就在嘉義鹿林設立一個海拔 2862 公尺的天文台，是東南亞最高、也是光害最少的天文觀測點。

鹿林天文台所架設的望遠鏡直徑達 1 米，不僅是東南亞地區發現小行星數量最多的天文台，多年來更參與泛星計畫、中美掩星合作計畫等國際研究、戰績輝煌。

不只如此，爲讓天文觀測看得更遠、更遼闊，中央大學天文所所長周翊表示，中大花了三年時間，終於打造完成直徑達 2 米的大型天文望遠鏡，其集光能力不但是現有一米望遠鏡的 4 倍，觀測範圍更擴大爲 8 倍，將可帶領台灣天文研究更上一層樓。

2 米望遠鏡計畫主要分為望遠鏡主體、圓頂設計、天文台建造、科學觀測儀器等四大主軸，所需經費達 2 億 3 千萬。中央大學校長蔣偉寧表示，這項計畫不只是中央大學「發展國際一流大學及頂尖研究中心計畫」的重要一環，也是許多觀星迷期盼已久的天文夢，未來 2 米望遠鏡運作後，將可提升台灣十倍光學天文觀測能力。對於培養天文研究人才、擴展國際合作視野、開發觀測儀器等面向都有所助益。

原文轉載自【2011-07-15/人間福報/遇見科學】

中央大學打造全台最大望遠鏡

（中央社記者許秩維台北 12 日電）中央大學今天表示，校方歷時 3 年，打造全台最大的 2 米望遠鏡，並獲得企業大力贊助，將於 5 年內在鹿林天文台完成建置，預計可為台灣的光學天文觀測能力提升至少 10 倍。

中央大學下午舉行鹿林 2 米望遠鏡計畫記者會，提供經費贊助的台達電子創辦人鄭崇華也到場聲援，同時代表台達電子文教基金會，協助中央大學成立台達電子年輕天文學者講座。

中央大學表示，1999 年成立鹿林天文台並設置 1 米望遠鏡後，中央大學開始在天文領域嶄露頭角，相繼發現台灣第 1 顆小行星和彗星；現在打造的 2 米望遠鏡，不只是台灣最大的望遠鏡，且使用同步分光四色照相儀和紅外線 CCD 相機，能為台灣光學天文觀測能力提升至少 10 倍。

中央大學表示，在教育部和台達電的經費支持下，預計 2016 年完成 2 米望遠鏡在鹿林天文台的建置，並用來觀測和追蹤美國提出的泛星計畫，搜尋可能撞擊地球的天體，以維持人類永續生存。

鄭崇華表示，自己對天文有濃厚好奇心，在操場看星星的日子為他排遣不少寂寞，心情也變得更開朗，更從中體會人生苦短，不要執著眼前的苦悶；而人類是如此渺小，地球若遭受撞擊可能造成生物滅絕，希望藉由贊助望遠鏡計畫，能及早防範其他天體的撞擊。1000712。

原文轉載自【2011-07-12/華視新聞網】

台灣/中央大學打造全台最大望遠鏡

張達智/整理

中央大學今天表示，校方歷時 3 年，打造全台最大的 2 米望遠鏡，並獲得企業大力贊助，將於 5 年內在鹿林天文台完成建置，預計可為台灣的光學天文觀測能力提升至少 10 倍。

中央社 12 日電，中央大學下午舉行鹿林 2 米望遠鏡計畫記者會，提供經費贊助的台達電子創辦人鄭崇華也到場聲援，同時代表台達電子文教基金會，協助中央大學成立台達電子年輕天文學者講座。

中央大學表示，1999 年成立鹿林天文台並設置 1 米望遠鏡後，中央大學開始在天文領域嶄露頭角，相繼發現台灣第 1 顆小行星和彗星；現在打造的 2 米望遠鏡，不只是台灣最大的望遠鏡，且使用同步分光四色照相儀和紅外線 CCD 相機，能為台灣光學天文觀測能力提升至少 10 倍。

中央大學表示，在教育部和台達電的經費支持下，預計 2016 年完成 2 米望遠鏡在鹿林天文台的建置，並用來觀測和追蹤美國提出的泛星計畫，搜尋可能撞擊地球的天體，以維持人類永續生存。

鄭崇華表示，自己對天文有濃厚好奇心，在操場看星星的日子為他排遣不少寂寞，心情也變得更開朗，更從中體會人生苦短，不要執著眼前的苦悶；而人類是如此渺小，地球若遭受撞擊可能造成生物滅絕，希望藉由贊助望遠鏡計畫，能及早防範其他天體的撞擊。

原文轉載自【2011-07-12/中央日報網路報-教育藝文】

全台最大望遠鏡　鹿林 5 年建置

（中央社記者許秩維台北 12 日電）中央大學今天表示，校方歷時 3 年，打造全台最大的 2 米望遠鏡，並獲得企業大力贊助，將於 5 年內在鹿林天文台完成建置，預計可為台灣的光學天文觀測能力提升至少 10 倍。

中央大學下午舉行鹿林 2 米望遠鏡計畫記者會，提供經費贊助的台達電子創辦人鄭崇華也到場聲援，同時代表台達電子文教基金會，協助中央大學成立台達電子年輕天文學者講座。

中央大學表示，1999 年成立鹿林天文台並設置 1 米望遠鏡後，中央大學開始在天文領域嶄露頭角，相繼發現台灣第 1 顆小行星和彗星；現在打造的 2 米望遠鏡，不只是台灣最大的望遠鏡，且使用同步分光四色照相儀和紅外線 CCD 相機，能為台灣光學天文觀測能力提升至少 10 倍。

中央大學表示，在教育部和台達電的經費支持下，預計 2016 年完成 2 米望遠鏡在鹿林天文台的建置，並用來觀測和追蹤美國提出的泛星計畫，搜尋可能撞擊地球的天體，以維持人類永續生存。

鄭崇華表示，自己對天文有濃厚好奇心，在操場看星星的日子為他排遣不少寂寞，心情也變得更開朗，更從中體會人生苦短，不要執著眼前的苦悶；而人類是如此渺小，地球若遭受撞擊可能造成生物滅絕，希望藉由贊助望遠鏡計畫，能及早防範其他天體的撞擊。1000712

（中央社記者許秩維攝 100 年 7 月 12 日）

原文轉載自【2011-07-12/中央社】

中央大學打造全臺最大 2 米望遠鏡

國立中央大學歷時 3 年，打造全臺最大的 2 米望遠鏡，在教育部、國科會及企業的經費支持下，將於 5 年內在鹿林天文臺完成建置，預計可為臺灣的光學天文觀測能力提升至少 10 倍。中央大學表示，1999 年成立鹿林天文臺並設置 1 米望遠鏡後，相繼發現臺灣第 1 顆小行星和彗星，現在打造的 2 米望遠鏡，不但是臺灣最大的望遠鏡，也使用同步分光四色照相儀和紅外線 CCD 相機，可用來觀測追蹤美國提出的泛星計畫，搜尋可能撞擊地球的天體，以維持人類永續生存。
(2011-07-12 19:13:14 徐詠絮)

原文轉載自【2011-07-12/國立教育廣播電台】

中央大學打造全台最大望遠鏡

（台北十三日電）中央大學昨天表示，校方歷時 3 年，打造全台最大的 2 米望遠鏡，並獲得企業大力贊助，將於 5 年內在鹿林天文台完成建置，預計可為台灣的光學天文觀測能力提升至少 10 倍。

中央大學昨天下午舉行鹿林 2 米望遠鏡計畫記者會，提供經費贊助的台達電子創辦人鄭崇華也到場聲援，同時代表台達電子文教基金會，協助中央大學成立台達電子年輕天文學者講座。

中央大學表示，1999 年成立鹿林天文台並設置 1 米望遠鏡後，中央大學開始在天文領域嶄露頭角，相繼發現台灣第 1 顆小行星和彗星；現在打造的 2 米望遠鏡，不只是台灣最大的望遠鏡，且使用同步分光四色照相儀和紅外線 CCD 相機，能為台灣光學天文觀測能力提升至少 10 倍。

中央大學表示，在教育部和台達電的經費支持下，預計 2016 年完成 2 米望遠鏡在鹿林天文台的建置，並用來觀測和追蹤美國提出的泛星計畫，搜尋可能撞擊地球的天體，以維持人類永續生存。

鄭崇華表示，自己對天文有濃厚好奇心，在操場看星星的日子為他排遣不少寂寞，心情也變得更開朗，更從中體會人生苦短，不要執著眼前的苦悶；而人類是如此渺小，地球若遭受撞擊可能造成生物滅絕，希望藉由贊助望遠鏡計畫，能及早防範其他天體的撞擊。

原文轉載自【2011-07-13/臺灣時報】

中央大學打造全台最大望遠鏡

【中央社台北十二日電】中央大學今天表示，校方歷時三年，打造全台最大的二米望遠鏡，並獲得企業大力贊助，將於五年內在鹿林天文台完成建置，預計可爲台灣的光學天文觀測能力提升至少十倍。

中央大學下午舉行鹿林二米望遠鏡計劃記者會，提供經費贊助的台達電子創辦人鄭崇華也到場聲援，同時代表台達電子文教基金會，協助中央大學成立台達電子年輕天文學者講座。

中央大學表示，一九九九年成立鹿林天文台並設置一米望遠鏡後，中央大學開始在天文領域嶄露頭角，相繼發現台灣第一顆小行星和彗星；現在打造的二米望遠鏡，不只是台灣最大的望遠鏡，且使用同步分光四色照相儀和紅外線 CCD 相機，能爲台灣光學天文觀測能力提升至少十倍。

中央大學表示，在“教育部”和台達電的經費支持下，預計二○一六年完成二米望遠鏡在鹿林天文台的建置，並用來觀測和追蹤美國提出的泛星計劃，搜尋可能撞擊地球的天體，以維持人類永續生存。

鄭崇華表示，自己對天文有濃厚好奇心，在操場看星星的日子爲他排遣不少寂寞，心情也變得更開朗，更從中體會人生苦短，不要執着眼前的苦悶；而人類是如此渺小，地球若遭受撞擊可能造成生物滅絕，希望藉由贊助望遠鏡計劃，能及早防範其他天體的撞擊。

原文轉載自【2011-07-12/澳門日報電子版】

中央大學打造全台最大望遠鏡

（中央社記者許秩維台北 12 日電）中央大學今天表示，校方歷時 3 年，打造全台最大的 2 米望遠鏡，並獲得企業大力贊助，將於 5 年內在鹿林天文台完成建置，預計可爲台灣的光學天文觀測能力提升至少 10 倍。

中央大學下午舉行鹿林 2 米望遠鏡計畫記者會，提供經費贊助的台達電子創辦人鄭崇華也到場聲援，同時代表台達電子文教基金會，協助中央大學成立台達電子年輕天文學者講座。

中央大學表示，1999 年成立鹿林天文台並設置 1 米望遠鏡後，中央大學開始在天文領域嶄露頭角，相繼發現台灣第 1 顆小行星和彗星；現在打造的 2 米望遠鏡，不只是台灣最大的望遠鏡，且使用同步分光四色照相儀和紅外線 CCD 相機，能爲台灣光學天文觀測能力提升至少 10 倍。

中央大學表示，在教育部和台達電的經費支持下，預計 2016 年完成 2 米望遠鏡在鹿林天文台的建置，並用來觀測和追蹤美國提出的泛星計畫，搜尋可能撞擊地球的天體，以維持人類永續生存。

鄭崇華表示，自己對天文有濃厚好奇心，在操場看星星的日子爲他排遣不少寂寞，心情也變得更開朗，更從中體會人生苦短，不要執著眼前的苦悶；而人類是如此渺小，地球若遭受撞擊可能造成生物滅絕，希望藉由贊助望遠鏡計畫，能及早防範其他天體的撞擊。1000712

原文轉載自【2011-07-12/中央社】

鄭崇華捐款協助打造天文望遠鏡

(中央社記者韓婷婷台北 2011 年 7 月 12 日電)

台達電 (2308) 董事長鄭崇華捐助 2000 萬元，協助中央大學鹿林天文台建置台灣最大口徑、歷時 3 年打造的「中央大學鹿林兩米望遠鏡」。

兩米望遠鏡計畫總經費高達 2.3 億，由教育部「發展國際一流大學及頂尖研究中心計畫」補助兩米望遠鏡 8000 萬；國科會補助儀器設備 4000 萬；中央大學自籌 1.1 億，預計 5 年內於海拔 2862 公尺高的鹿林天文台建置完成。

除了台達電子董事長個人捐助 2000 萬元外，台達電子文教基金會也贊助成立「台達電子年輕天文學者講座」，協助培育更多天文後起之秀，爲台灣的天文研究注入新希望。

中央大學校長蔣偉寧表示，兩米望遠鏡計畫為中央大學「發展國際一流大學及頂尖研究中心計畫」的重要指標，將可提升台灣十倍光學天文觀測能力。

長期支持天文環保教育的鄭崇華指出，人類文明的出現跟宇宙形成的時間相比，真是短之又短。而工業發展以來造成環境破壞、天然資源耗竭，溫室氣體過量排放使得全球氣候異常，而且速度之快，遠超乎我們所能想像。

他希望透過對天文研究的支持，讓人類對宇宙的奧妙、地球的珍貴能有更多了解，從而重視「環保節能愛地球」的重要性，追求地球及人類永續的發展。

原文轉載自【2011-07-12/中央社】

鹿林天文台兩米望遠鏡　亞洲海拔最高口徑最大

(蕭照平報導)

中央大學歷時三年，耗資 2.3 億打造的「兩米望遠鏡」組裝完畢，預計在 2016 年，把望遠鏡建置在海拔 2 千 862 公尺的玉山國家公園附近，成為東南亞地勢最高、口徑最大的天文望遠鏡。

中央大學獲得教育部及各界補助，將經費用來打造「兩米望遠鏡」。中央大學天文所所長周翊表示，兩米望遠鏡的集光能力是一米望遠鏡的四倍，所以能夠觀測到更暗的天體。周翊說『如果我們要看更暗的東西，只有造更大的望遠鏡，因為從把光集中在主鏡裡面，再反射聚焦，所以主鏡越大，在同樣時間裡面可以收集到的光就更多。』

雖然世界上有許多十米等級的光學望遠鏡，但在東南亞地區，中央大學建置的「兩米望遠鏡」卻是規模最大、功能最強的一部，因此，成為美國夏威夷大學推動「泛星計畫」亞洲地區的唯一國家。特別的是，天文台位在海拔 2 千 8 百公尺的高山上，寫下東南亞地區，地勢最高的紀錄，因此更凸顯運送的難度。

周翊說『在有路的地方我們當然用車載，沒路的地方，我們會用索道，包括我們建築的材料運輸也是靠索道，到時候望遠鏡也是靠這索道。』周翊表示，整個天文台預計在 2016 年建置完畢，期盼帶領台灣，在全球天文觀測上能有一席之地。

原文轉載自【2011-07-12/中廣新聞網】

美泛星計畫　台灣是亞洲唯一代表

(蕭照平報導)

美國國務院委託夏威夷大學執行泛星計畫，這項計畫除了觀測天體之外，還負責尋找可能撞擊地球的小行星任務。由於台灣近年的天文觀測實力提升，以及地理位置關係，使台灣成為亞洲唯一參與泛星計畫的國家。

中央大學建置「兩米望遠鏡」的主要目的，除了用來觀測天體變化之外，更是用來配合美國國務院提出的泛星計畫，這項計畫美國委託夏威夷大學來執行，目的用來搜尋太空中任何可能撞擊地球的天體。中央大學天文所所長周翊說『它的科學目的很特殊，它就是在巡天，就是在尋找說，有沒有對地球有害的小行星』

這項計畫有美國、德國、英國等大學的研究團隊參加，台灣是亞洲唯一的代表。周翊表示，中央大學建置的鹿林天文台，是世界上最能追蹤天體瞬間變化的天文台，『台灣佔了一個非常好的地理優勢，因為我們跟夏威夷差了六個時區，所以當他第一手資料出現後，台灣是可以做第一個後續觀測』

周翊更強調，2016 年「兩米望遠鏡」在鹿林天文台建置完成後，可望帶來更多天文研究資料，更能凸顯台灣在泛星計畫中的重要性。

原文轉載自【2011-07-12/中廣新聞網】

提昇我 10 倍光學天文觀測力─中大兩米望遠鏡　5 年內鹿林建置

記者李奕縈／臺北報導

我國最大口徑、歷時 3 年打造的「中央大學鹿林兩米望遠鏡」，昨日端出模型與國人見面，預計 5 年內將於海拔 2862 公尺高的鹿林天文臺建置完成。此望遠鏡的設置，除提昇臺灣 10 倍光學天文觀測能力，在拓展國際合作網絡、天文儀器軟硬體開發，以及專業天文人才的養成等，均有莫大助益。

兩米望遠鏡計畫總經費高達 2.3 億元，中央大學校長蔣偉寧表示，這項天文學界引頸期盼的百年大夢，獲臺達電董事長鄭崇華的大力支持，捐款 2 千萬元，另贊助成立「臺達電子年輕天文學者講座」。

原文轉載自【2011-07-13/青年日報/11 版/教育藝文】

台達電鄭崇華捐款 2000 萬　贊助鹿林兩米望遠鏡計畫

記者楊伶雯／台北報導

台灣最大口徑、歷時 3 年打造的「中央大學鹿林兩米望遠鏡」12 日亮相，預計 5 年內在海拔 2862 公尺高的鹿林天文台建置完成，這項天文學界引頸期盼的百年大夢，也獲台達電創辦人暨董事長鄭崇華大力支持，除捐款 2000 萬元外，台達電文教基金會也贊助成立「台達電子年輕天文學者講座」，培育更多天文後起之秀。

中央大學校長蔣偉寧表示，兩米望遠鏡計畫為中央大學「發展國際一流大學及頂尖研究中心計畫」的重要指標，將可提升台灣十倍光學天文觀測能力。此望遠鏡的設置，將對臺灣本土的光學天文觀測能力、拓展國際合作網絡、天文儀器軟硬體開發以及專業天文人才的養成等，有莫大助益。

台灣聯合大學系統副校長、中央大學天文所教授葉永烜表示，科學研究的成長，人才的培育尤其為要。感謝台達電鄭崇華董事長對中大天文所的厚愛，除個人捐資贊助兩米望遠鏡計畫外，台達電文教基金會也將連續 4 年捐出 100 萬元，協助成立「台達電子年輕天文學者講座」，幫助天文所邀請國際間頗有成就的後起之秀，來到台灣短期工作，把天文學最新的發展和國內學界接軌，進一步探索宇宙科學。

鄭崇華指出，「人類文明的出現跟宇宙形成的時間相比，真是短之又短。工業發展以來造成環境破壞、天然資源耗竭，溫室氣體過量排放使得全球氣候異常，而且速度之快，遠超乎我們所能想像。希望透過對天文研究的支持，讓人類對宇宙的奧妙、地球的珍貴能有更多了解，從而重視『環保節能愛地球』的重要性，追求地球及人類永續的發展。」

兩米望遠鏡計畫總經費高達 2.3 億元，由教育部「發展國際一流大學及頂尖研究中心計畫」補助兩米望遠鏡 8000 萬元；國科會補助儀器設備 4000 萬元；中大自籌 1.1 億元，協助天文台建設工程。
原文轉載自【2011-07-12/NOWnews 今日新聞網/頭條新聞】

鄭崇華捐建中央大學鹿林 2 米望遠鏡計畫

【記者柯安聰台北報導】台灣最大口徑、歷時 3 年打造的「中央大學鹿林 2 米望遠鏡」7 月 12 日將正式與國人見面，預計 5 年內於海拔 2862 公尺高的鹿林天文台建置完成。這項天文學界引頸期盼的百年大夢，獲企業家台達電子創辦人暨董事長鄭崇華的大力支持，慨然捐款 2000 萬。同時台達電子文教基金會也贊助成立「台達電子年輕天文學者講座」，培育更多天文後起之秀，為台灣的天文研究注入新希望。

中央大學校長蔣偉寧表示，2 米望遠鏡計畫為中央大學「發展國際一流大學及頂尖研究中心計畫」的重要指標，將可提升台灣 10 倍光學天文觀測能力。此望遠鏡的設置，將對臺灣本土的光學天文觀測能力、拓展國際合作網絡、天文儀器軟硬體開發以及專業天文人才的養成等，有莫大助益。

台灣聯合大學系統副校長、中央大學天文所教授葉永烜表示，科學研究的成長，人才的培育尤其為要。感謝台達電子鄭崇華董事長對中大天文所的厚愛，除了個人捐資贊助兩米望遠鏡計畫外，台達電子文教

基金會亦將連續 4 年捐出 100 萬，協助成立「台達電子年輕天文學者講座」，幫助天文所邀請國際間頗有成就的後起之秀，來到台灣短期工作，把天文學最新的發展和國內學界接軌，進一步探索宇宙科學。

台達電子鄭崇華董事長長期支持天文環保教育，鄭崇華董事長指出，人類文明的出現跟宇宙形成的時間相比，真是短之又短。而工業發展以來造成環境破壞、天然資源耗竭，溫室氣體過量排放使得全球氣候異常，而且速度之快，遠超乎我們所能想像。希望透過對天文研究的支持，讓人類對宇宙的奧妙、地球的珍貴能有更多了解，從而重視『環保節能愛地球』的重要性，追求地球及人類永續的發展。

2 米望遠鏡計畫總經費高達 2.3 億，由教育部「發展國際一流大學及頂尖研究中心計畫」補助兩米望遠鏡 8000 萬；國科會補助儀器設備 4000 萬；中大自籌 1.1 億，協助天文台建設工程。

這項計畫，雖受教育部、國科會和企業的大力支持，但也面臨前所未見的難題。主要因在國土復育和永續發展考量下，台灣的高山近年都被劃爲國土保安用地，除某些明訂項目之外，禁止各種開發和建設，這使得天文台的建置過程中，時程上受到很大挑戰，幸好在立法院跨部會協調下增設法規，最近通過環保署的環境影響評估大會審查，才使得 2 米望遠鏡計畫得以順利進行。

兩米望遠鏡計畫分爲望遠鏡本體、圓頂設計製作、天文台建築、科學觀測儀器等四大範疇。主鏡片在俄羅斯製作，採熱膨脹係數非常低的矽晶玻璃製作。非球面的鏡片磨製困難，需「慢工」才能出細活，爲此，天文所前所長黃崇源曾多次飛往俄國監工。此外，鏡片上的鍍膜在使用一段時間後，會因氧化而使反射率下降，與中大光電所合作開發非球面天文望遠鏡監控技術，維持鍍膜的均勻性和可靠度分析。

中大天文所所長周翊表示，台灣的天文發展最早可追溯至日據時代，當時已有設置天文台的構想，直到 1990 年代，中大因執行教育部學術追求卓越計畫，成立鹿林天文台，設置了 1 米望遠鏡，才開始嶄露頭角。目前世界上有許多 10 米級的光學望遠鏡，台灣如何以 1 個 2 米的望遠鏡，與世界大型望遠鏡一較高下，展現的就是台灣「以小搏大」的精神。

2 米望遠鏡的主要科學目標，是要用來觀測及追蹤「泛星計畫（Pan- STARRS）」發現的特異天體。泛星計畫由美國國務院所提出，透過美國空軍委託夏威夷大學在夏威夷建置望遠鏡，用來搜尋太空中任何可能撞擊地球的天體，以維持人類永續生存的明天。該計畫有美國、德國、英國等大學團隊加入，台灣是亞洲唯一加入的代表。

泛星計畫的巡天觀測時間間隔約爲 1 週，所以極需要與其他天文台連手，針對一些時間變化尺度短暫的天體作密集測量。台灣因地理位置關係，鹿林天文台是世界上最先能追蹤泛星計畫各種瞬間變化的天文台，2 米望遠鏡完工後，可望產出大量的第一手科學成果，對泛星計畫的科學目標有決定性影響。

此外，就本土觀測上，2 米望遠鏡可觀測到銀河系外的天體變化，如珈瑪射線爆、超新星、太陽系小天體的研究，可望開啓國內天文搜尋和跟蹤觀測的新頁。國際接軌上，其集光能力是現有 1 米望遠鏡的 4 倍；而使用「同步分光四色照相儀」讓兩米望遠鏡再提升 4 倍的觀測效率。中大同時自行開發近紅外 CCD 相機，在近紅外線譜段有很高的靈敏度，得以充份發揮兩米望遠鏡功能，帶領台灣在國際天文觀測上佔有一席之地。

2 米望遠鏡計畫的成員，過去 10 年發表超過 100 篇論文，其中多爲有關移動星體與變星的工作，另有 10 餘篇學術研究文章刊登在國際頂尖期刊《自然（Nature）》和《科學（Science）》上，學術能量豐沛，研究成果受到國際矚目。(自立電子報 2011/07/12)

原文轉載自【2011-07-12/自立晚報】

東亞最大兩米望遠鏡　中央大學 2.3 億打造

這座中央大學夢想了十多年，花了三年打造，總計畫 2.3 億，全國最大的「兩米望遠鏡」，未來運轉後，將可提升台灣十倍光學天文觀測能力，從 1999 年，在南投鹿林天文台有了「一米望遠鏡」，創下許多台灣第一紀錄，2002 年發現了第一顆小行星，目前累計發現了約 800 顆，2007 年發現了第一顆鹿林慧星，2007 年發現第一顆近地小行星，未來「兩米望遠鏡」，除了將觀測更多天體變化，也將讓台灣更能與世界接軌。

雖然望遠鏡已經完成，但還要再等五年，才能上得了鹿林山，天文學者說，位在海拔 2862 公尺高的鹿林天文台，是國土保安用地，禁止開發，這座東亞最大的望遠鏡，可能是台灣空前也是絕後的計畫了。

好事多磨，不過對國內天文界來說，有了「兩米望遠鏡」加入觀測，將讓台灣在國際天文觀測上，更有分量。

記者陳姝君謝其文台北報導。

原文轉載自【2011-07-12/公視新聞網 PTS NEWS ONLINE】

鄭崇華：別擔心股票不值錢

【林上祚／台北報導】

歐債危機再起，台股跟著重挫，台達電董事長鄭崇華表示，和世界其他國家比起來，台灣經濟表現其實算很好，台灣民眾應該對自己有信心，不要動輒擔心股票不值錢。

鄭崇華昨日出席中央大學鹿林望遠鏡計畫落成記者會，鄭崇華三年前以個人名義，捐贈中央大學二千萬元，在阿里山鹿林興建天文望遠鏡，鄭崇華說，目前全球科學家都在對小行星進行研究，研究如何讓小行星轉向或毀掉，「當你了解宇宙有這麼浩瀚時，像歐債危機這樣的經濟問題，就顯得小而短暫」。

鄭崇華說，台達電經營四十年，四十年前很多電視機品牌，現在都已經不見了，個人電腦品牌也是一樣，早年的王安、ＩＢＭ都從個人電腦市場退出，他認爲，經營企業就是要不斷採取行動，思考人類下一個階段需要什麼。

對歐債危機，鄭崇華認爲，台灣目前經濟狀況應該算很好，但媒體總是報導一些負面的消息，台灣民眾應該要對自己有信心，不要擔心股票不值錢。

鄭崇華認爲，太陽能等替代性能源，這段期間表現就像「打擺子」一樣，他認爲，歐洲各國政府取消太陽能補助，雖對產業造成影響，但業者不能期待一輩子靠政府補助，日本地震以後，各國對太陽能等替代性能源再度轉趨重視，他對太陽能產業前景仍充滿信心。

原文轉載自【2011-07-13/中國時報/B2 版/投資線上】

全台最大望遠鏡　5 年內建置

【中央社】

中央大學昨天表示，校方歷時 3 年，打造全台最大的 2 米望遠鏡，並獲得企業大力贊助，將於 5 年內在鹿林天文台完成建置，預計可爲台灣的光學天文觀測能力提升至少 10 倍。

中央大學 1999 年成立鹿林天文台，並設置 1 米望遠鏡後，相繼發現台灣第 1 顆小行星和彗星；現在打造的 2 米望遠鏡，不只是台灣最大的望遠鏡，且使用同步分光四色照相儀和紅外線 CCD 相機。

中央大學表示，在教育部和台達電的經費支持下，預計 2016 年完成 2 米望遠鏡在鹿林天文台的建置，並用來觀測和追蹤美國提出的泛星計畫，搜尋可能撞擊地球的天體。

原文轉載自【2011-07-13/Upaper/2 版/焦點】

中央大學打造全台最大望遠鏡

中央大學歷時三年，打造全台最大二米望遠鏡，爲台灣的天文觀測能力提升至少十倍，可搜尋太空中任何可能撞擊地球的天體，預計五年內在鹿林天文台完成這項建制。這個二米望遠鏡可以見到二十一等星（人類肉眼指可見六等星），觀測到銀河系外的天體變化，例如珈瑪射線爆、超新星、太陽系小天體等。原文轉載自【2011-07-13/人間福報/綜合】

鹿林二米望遠鏡計畫

2011/07/13 - DIGITIMES 韓青秀

兩米望遠鏡計畫為中央大學「發展國際一流大學及頂尖研究中心計畫」的重要指標，將可提升台灣 10 倍光學天文觀測能力。

兩米望遠鏡計畫總經費高達新台幣 2.3 億元，由教育部「發展國際一流大學及頂尖研究中心計畫」補助兩米望遠鏡 8,000 萬元；國科會補助儀器設備 4,000 萬元；中大自籌 1.1 億元，協助天文台建設工程。

台達電董事長鄭崇華表示，早年隻身來台讀書，由於假日時格外思念故鄉，故引發他對天文知識的興趣。2009 年全球天文年，鄭崇華擔任星空大使，希望透過對天文研究的支持，讓人類對宇宙奧妙、地球珍貴有更多了解，故此次以個人名義，捐贈新台幣 2000 萬元，贊助中央大學的兩米望遠鏡計畫。

兩米望遠鏡計畫分為望遠鏡本體、圓頂設計製作、天文台建築、科學觀測儀器等 4 大範疇，該計畫主要科學目標，是要用來觀測及追蹤「泛星計畫(Pan- STARRS)」發現的特異天體。

泛星計畫由美國國務院所提出，透過美國空軍委託夏威夷大學在夏威夷建置望遠鏡，用來搜尋太空中任何可能撞擊地球的天體，以維持人類永續生存的明天。該計畫有美國、德國、英國等大學團隊加入，台灣是亞洲唯一加入的代表。

泛星計畫的巡天觀測時間間隔約為 1 週，所以需要與其他天文台聯手，針對一些時間變化尺度短暫的天體作密集測量。台灣鹿林天文台是世界上最先能追蹤泛星計畫各種瞬間變化的天文台，兩米望遠鏡完工後，可望產出大量的第 1 手科學成果，對泛星計畫的科學目標有決定性影響。(韓青秀)

原文轉載自【2011-07-13/科技網】

百年天文大夢　中央大學鹿林兩米望遠鏡計畫啓動

〔鳳凰網記者歸鴻亭台北特稿〕　中央大學今天表示，歷時 3 年打造的全台最大的兩米望遠鏡，將於 5 年內在海拔 2,862 公尺高的鹿林天文台完成建置，預計可為台灣的光學天文觀測能力提升至少 10 倍。

兩米望遠鏡計畫為中央大學「發展國際一流大學及頂尖研究中心計畫」的重要指標，中央大學校長蔣偉寧表示，這項天文學界引頸期盼的百年大夢，獲企業家台達電子創辦人暨董事長鄭崇華支持捐款兩千萬，同時台達電子文教基金會也贊助成立「台達電子年輕天文學者講座」，對發展台灣的天文研究有莫大助益。

蔣偉寧指出，預計 2016 年完成這部兩米望遠鏡在鹿林天文台的建置，並用來觀測和追蹤美國提出的泛星計畫(Pan-STARRS)，搜尋可能撞擊地球的天體任務。由於台灣近年的天文觀測實力提升，以及地理位置關係，使台灣成為亞洲唯一參與泛星計畫的國家。泛星計畫的巡天觀測時間間隔約為 1 週，所以極需要與其他天文台連手，針對一些時間變化尺度短暫的天體作密集測量。台灣因地理位置關係，鹿林天文台是世界上最先能追蹤泛星計畫各種瞬間變化的天文台，2 米望遠鏡完工後，可望產出大量的第一手科學成果，對泛星計畫的科學目標有決定性影響。

不過，蔣偉寧說，這項計畫雖受教育部、國科會和企業的大力支持，但也面臨前所未見的難題，主要因在國土復育和永續發展考量下，台灣的高山近年都被劃為國土保安用地，除某些明訂項目之外，禁止各種開發和建設，這使得天文台的建置過程中，時程上受到很大挑戰，幸好在立法院跨部會協調下增設法規，最近通過環保署的環境影響評估大會審查，才使得 2 米望遠鏡計畫得以順利進行。

中央大學天文所所長周翊表示，台灣的天文發展最早可追溯至日據時代，當時已有設置天文台的構想，直到 1990 年代，中大因執行教育部學術追求卓越計畫，1999 年成立鹿林天文台並設置 1 米望遠鏡後，中央大學開始在天文領域嶄露頭角，相繼發現台灣第 1 顆小行星和彗星；現在打造的 2 米望遠鏡，不只是台灣最大的望遠鏡，且使用同步分光四色照相儀和紅外線 CCD 相機，能為台灣光學天文觀測能力提升至少 10 倍。

周翊說，兩米望遠鏡計畫分爲望遠鏡本體、圓頂設計製作、天文台建築、科學觀測儀器等四大範疇。主鏡片在俄羅斯製作，採熱膨脹係數非常低的矽晶玻璃製作。非球面的鏡片磨製困難，需「慢工」才能出細活，爲此，天文所前所長黃崇源曾多次飛往俄國監工。此外，鏡片上的鍍膜在使用一段時間後，會因氧化而使反射率下降，與中大光電所合作開發非球面天文望遠鏡監控技術，維持鍍膜的均勻性和可靠度分析。

中央大學天文所教授葉永烜也表示，科學研究的成長，人才的培育尤其爲要，「台達電子年輕天文學者講座」可以幫助天文所邀請國際間頗有成就的後起之秀，來到台灣短期工作，把天文學最新的發展和國內學界接軌，進一步探索宇宙科學，爲台灣的天文研究將注入新希望。

鄭崇華則指出，人類文明的出現跟宇宙形成的時間相比，真是短之又短。而工業發展以來造成環境破壞、天然資源耗竭，溫室氣體過量排放使得全球氣候異常，而且速度之快，遠超乎所能想像。希望透過對天文研究的支持，讓人類對宇宙的奧妙、地球的珍貴能有更多了解，從而重視「環保節能愛地球」的重要性，追求地球及人類永續的發展。

國立中央大學鹿林天文台設立於民國 88 年，曾參與計畫包括中美掩星計畫(TAOS)、EAFoN-東亞 Gammy Ray Burst(GRB)觀測網、台灣超新星巡天計畫、美國夏威夷大學天文所及美國空軍合作的泛星計劃(Pan-STARRS)、紅色精靈地面觀測與極低頻無線電波(ELF)偵測系統、亞洲大氣污染物之長程輸送與衝擊研究與中大太空所 airglow imager 與華衛二號 ISUAL 之聯合觀測；2002 年發現台灣第一顆小行星，迄今累計發現約 800 顆，其中有 20 顆已取得永久命名，爲亞洲發現小行星最活躍的地方之一。
頻道:捐贈贊助分類:天文地理

原文轉載自【2011-07-12/鳳凰網鳳凰專題】

中大打造口徑 2 公尺大望遠鏡

台灣天文學界在國際天文觀測上將占一席之地！中央大學在台達電董事長鄭崇華（圖右）的協助下，耗資 2 億 3000 萬元，5 年內將在鹿林天文台打造國內最大的天文望遠鏡，「口徑兩米望遠鏡」預計可提升台灣 10 倍光學天文觀測能力，將用來觀測及追蹤國際合作「泛星計畫」（Pan-STARRS）發現的特異天體，監控太空中可能撞擊地球的天體。

中大校長蔣偉寧（圖左）表示，泛星計畫由美國國務院所提出，透過美國空軍委託夏威夷大學在夏威夷建置望遠鏡，用來搜尋太空中可能撞擊地球的天體，該計畫有美國、德國、英國等大學團隊加入，台灣是亞洲唯一加入的代表。該望遠鏡可觀測到銀河系外的天體變化，例如珈瑪射線爆、超新星、太陽系小天體的研究等。（圖：記者羅沛德／文：記者林曉雲）

原文轉載自【2011-07-13/自由時報/A6 版/生活新聞】

2 米天文望遠鏡　全台最大

【記者鄭語謙／台北報導】

彗星撞地球，台灣來得及應變嗎？中央大學歷時 3 年，打造全台最大的 2 米口徑望遠鏡，爲台灣的光學天文觀測能力提升至少 10 倍，可搜尋太空中任何可能撞擊地球的天體，預計 5 年內在鹿林天文台完成。

中大 1999 年成立鹿林天文台，並設置 1 米望遠鏡後，創下台灣第一個發現小行星和彗星的紀錄，2007 年再度打造 2 米望遠鏡，直到去年正式完工，成爲繼大陸和泰國之後，亞洲第三大的望遠鏡。

中大天文所所長周翊表示，這座 2 米望遠鏡使用「同步分光四色照像儀」和紅外線 CC 相機，一改過去須不斷更換濾鏡才有的效果，集光能力是現有 1 米望遠鏡的 4 倍，可以見到 21 等星（人類肉眼只可見 6 等星），觀測到銀河系外的天體變化，例如珈瑪射線爆、超新星、太陽系小天體等。

這座望遠鏡未來主要用於觀測追蹤美國國務院提出，包含美國、德國、英國等團隊合作的「泛星計畫」，搜尋太空中會撞擊地球天體。

周翊解釋，原泛星計畫的巡天觀測和資料運算結果時間須要一周，現在台灣有 2 米望遠鏡天文觀測台後，可第一手產出科學成果，若有彗星撞擊，台灣也可早一步掌握。

中大校長蔣偉寧表示，2 米望遠鏡計畫是中央大學發展「國際一流大學及頂尖研究中心計畫」重要指標，總經費 2.3 億，已完成造價 0.8 億的望遠鏡，5 年內將完成圓頂設計製作等，經費由教育部頂大計畫、國科會等補助協助建設工程，中大自籌 1.1 億。

原文轉載自【2011-07-13/聯合報/AA4 版/教育】

海王星公轉 164 年　下周二慶生

【張勵德／台北報導】二○○六年冥王星被移出九大行星之列後，太陽系中距離太陽最遠的行星就變成海王星，下周二將是海王星被發現至今，繞行太陽公轉一周的日子，也就是剛好「一個海王星年」，北市天文館昨說，這是人類知道海王星存在後，第一次可幫海王星「過生日」，不妨趁機好好認識海王星。

是地球 58 倍大

海王星是太陽系中體積第四大、質量第三大的行星，體積約是地球的五十八倍，質量約爲地球的十七倍，重力與地球類似。海王星自轉一周約十六小時，繞太陽公轉一周則須一百六十四點七七四年。

台北市立天文館昨指出，海王星在西元一八四六年九月二十三日被發現，主要由氫、甲烷等氣體和冰組成，擁有十三顆衛星。從望遠鏡觀測海王星呈現藍色，是因其大氣中的甲烷吸收了太陽的紅光，反射出藍光。

連續攝影觀看

中央大學天文所教授陳文屏說，海王星的發現過程很有趣。天文學家先確認天王星的存在，但發現其公轉的軌道，與牛頓力學計算出的位置有出入，因此研判可能與另顆不知名的行星產生重力干擾，後來經計算，海王星才被觀測發現；當時英國與法國還爭論誰先發現海王星，最後才同意由雙方共享榮耀。

天文館說，目前海王星每晚十時由東南方升起，日出前位西南方仰角約四十度的天空，但因亮度太低，一般望遠鏡無法觀測，建議民眾透過連續攝影配合星圖，比較容易觀測到。

原文轉載自【2011-07-06/蘋果日報/A6 版/要聞】

周杰倫星　高掛天上紅遍宇宙

【聯合報／記者王郁惠／即時報導】 2011.06.28 09:27 pm

如同周杰倫「愛的飛行日記」歌詞：「找一顆星，只爲你命名」，天上真的有顆星就叫做「周杰倫星」；周杰倫小行星是由兩岸天文愛好者蔡元生、陳韜和林啓生合作發現的，編號 257248；甚至在美國 NASA 官網查詢，即會出現 Chouchiehlun（周杰倫星），周董魅力紅遍國際，更在宇宙發光發熱。

「周杰倫星」於 2009 年由蔡元生、陳韜和林啓生於台灣玉山國家公園的鹿林天文台發現；有些粉絲買星贈偶像，該買賣的星星仍是保有原本的名字，而「周杰倫星」則是目前天文學界由發現者直接命名並獲得公認的天體，若有朝一日出現在科學雜誌中，是直接稱作「周杰倫星」。粉絲猜測發現者應該是周董的粉絲，而杰威爾得知後表示：「謝謝！可能這顆行星也很有創意，很有個性。」

原文轉載自【2011-06-28/聯合新聞網/娛樂追星/即時新聞】

這顆小行星　叫做「周杰倫」

2011 年 06 月 29 日 07:36 蘋果即時

高雄天文學會會員蔡元生、鹿林天文台觀測助理林啓生和大陸天文愛好者金彰偉、陳韜 2 年前共同發現 1 顆小行星，4 人因爲都喜愛周杰倫，觀測星象時多聽周董歌打發時間，且認爲歌曲具教育意義，決定將這顆小行星命名爲「周杰倫」，10 天前已通過「國際行星組織」認證。杰威爾總經理楊峻榮聽聞此事笑說，也許這顆小行星也很有創意、很有個性。

兩岸四名天文愛好者在兩年前發現的小行星，以藝人周杰倫（圖）的名字命名。

原文轉載自【2011-06-29/蘋果日報/即時新聞】

紅到宇宙！　新小行星命名「周杰倫」

〔本報訊〕「周董」魅力無遠弗屆，甚至紅到宇宙去！媒體報導，高雄天文學會會員蔡元生、鹿林天文台觀測助理林啓生和中國天文愛好者金彰偉、陳韜，2009 年共同發現一顆小行星，由於他們都喜愛周杰倫，因此決定將小行星命名爲「周杰倫」（Chouchiehlun），並於日前通過「國際行星組織」認證。

來自兩岸，4 名業餘天文觀察家 2009 年時，觀測發現編號 257248 的新小行星，由於他們都喜愛周杰倫，甚至邊找新的小行星時，還邊聽周杰倫的歌《愛的飛行日記》，因此最後還決定將發現的三顆新小行星中，其中一顆命名爲「周杰倫」。

這顆名爲「周杰倫」（Chouchiehlun）的小行星，因爲是在天文學界中，由發現者直接命名，並獲得「國際行星組織」認證，未來將有可能以「周杰倫星」的名號，出現在科學雜誌上。

報導指出，周杰倫所屬公司杰威爾聽聞此事後，也笑說，「也許這顆小行星也很有創意、很有個性。」

原文轉載自【2011-06-29/自由電子報即時新聞】

星發現　小行星命名「周杰倫」

撰稿•編輯：曾美惠　　新聞引據：中時蘋果日報

兩岸業餘天文觀察家與中央大學合作執行「巡天計畫」，2009 年觀測發現的 257248 號小行星，最近經國際小行星中心審查通過，命名爲「周杰倫小行星」。台灣發現者蔡元生表示，他們都喜歡聽周杰倫的歌，決定以「周杰倫」爲小行星命名。

周董昨天透過杰威爾公司說：「很有創意，也很有個性！」

中央大學鹿林天文台觀測助理蕭翔耀表示，小行星命名通常由發現者決定，但必須提交「國際行星組織」認證，確認是新發現者才能命名。這顆編號 257248 的「周杰倫星」是由高雄天文學會會員蔡元生、鹿林天文台觀測助理林啓生和大陸天文愛好者金彰偉、陳韜等 4 人共同發現。

蔡元生昨表示，「周杰倫星」是在 2009 年 3 月 20 日發現，經一段時日追蹤和確認，才向「國際行星組織」申請認證，並於今年本月中旬審核通過。

蔡元生說，以「周杰倫」爲名，主因他們都是周杰倫的粉絲，中大拍攝的照片都是黑白影像，要從裡面找出新的小行星，過程很無聊。大家就邊找邊聽周杰倫的歌，「愛的飛行日記」更唱出天體搜尋者的浪漫！後來想給小行星取名時，不約而同想到「周杰倫」。

林啓生說，中央大學鹿林天文台過去發現的 20 多顆小行星，分別以「南投」、「高雄」、「玉山」等地名爲小行星命名，而這顆「周杰倫星」是台灣所發現命名的行星中，第一顆以藝人爲名的行星。大陸曾以作家「金庸」、香港也曾以影星「林青霞」、導演「徐克」等名人爲小行星命名。

原文轉載自【2011-06-29/中央廣播電臺新聞頻道】

兩岸 4 人發現　小行星命名「周杰倫」

【徐彩娟、李志展／嘉義報導】兩岸四名天文愛好者在兩年前發現了一顆小行星，因四人都喜歡聽周杰倫的歌《聽媽媽的話》，因此就將這顆小行星命名爲「周杰倫星」，並於十天前通過「國際行星組織」認證，巧合的是，當天恰巧是周杰倫獲金曲獎最佳國語男歌手，讓這顆小行星成了名副其實閃亮「明星」。
喜愛《聽媽媽的話》

周杰倫昨晚在日本大阪舉行歌友會，杰威爾總經理楊峻榮聽聞此事笑說：「謝謝，可能這顆小行星也很有創意、很有個性吧！」

中央大學鹿林天文台觀測助理蕭翔耀表示，小行星命名通常都由發現者決定，但必須提交「國際行星組織」認證，確認是新發現者才能命名。這顆編號 257248 的「周杰倫星」是由高雄天文學會會員蔡元生、鹿林天文台觀測助理林啓生和大陸天文愛好者金彰偉、陳韜等四人共同發現。

蔡元生昨表示，「周杰倫星」是在二〇〇九年三月二十日發現，經一段時日追蹤和確認，才向「國際行星組織」申請認證，於今年本月中旬審核通過。

蔡元生強調，當初他提議以「周杰倫」命名，獲大家一致同意，因爲周杰倫在大陸也很紅；至於爲何會想到周杰倫？蔡元生說，觀察星星的過程十分冗長，甚至會很無聊，但四人都很欣賞周杰倫的歌，尤其是頗具教育意義的歌曲《聽媽媽的話》，所以他就提議以「周杰倫」來命名。
「林青霞」也被命名

林啓生說，中央大學鹿林天文台過去發現的二十多顆小行星，分別以「南投」、「高雄」、「玉山」等地名爲小行星命名，而這顆「周杰倫星」也是台灣所發現命名的行星中，第一顆以藝人爲名的行星。大陸則曾以作家「金庸」、香港也曾以影星「林青霞」、導演「徐克」等名人爲小行星命名。

原文轉載自【2011-06-29/蘋果日報/A4 版/要聞】

「星」發現　小行星以周杰倫命名

【李宗祐、江怡臻／台北報導】

兩岸業餘天文觀察家與中央大學合作執行「巡天計畫」，二〇〇九年觀測發現的二五七二四八號小行星，最近經國際小行星中心審查通過，命名爲「周杰倫小行星」。台灣發現者蔡元生表示，他們都喜歡聽周杰倫的歌，決定以「周杰倫」爲小行星命名。

周董昨透過杰威爾公司說：「很有創意，也很有個性！」

蔡元生說，以「周杰倫」爲名，主因是他們三人都是周杰倫的粉絲，中大拍攝的照片都是黑白影像，要從裡面找出新的小行星，過程很無聊。大家就邊找邊聽周杰倫的歌，《愛的飛行日記》更唱出天體搜尋者的浪漫！後來想給小行星取名時，不約而同想到「周杰倫」。

在此之前，三位天文同好也曾把在同時間觀測發現的二一五〇八〇號小行星命名爲「高雄」，傳爲兩岸佳話。

蔡元生表示，二〇〇九年三月廿日，觀測團隊共發現三顆新小行星，陸續取得國際小行星中心永久編號。稍早有一顆已命名爲「高雄」，目前還有一顆未命名，將委託黃崇源領導的團隊命名。

蔡元生表示，他和另二位發現者陳韜、金彰偉透過網路搜尋「ＳＯＨＯ」衛星傳回太陽表面影像、觀測彗星而結識，進而在二〇〇九年向中央大學鹿林天文台申請參與「巡天計畫」，搜尋可能接近地球的小行星。由中大天文研究所教授黃崇源帶領的研究團隊，利用天文望遠鏡觀測拍攝，再透過網路把影像傳給三人，搜尋新的小行星。

原文轉載自【2011-06-29/中國時報/A8 版/生活新聞】

外太空看周杰倫　巨星紅遍宇宙

生活中心／綜合報導

你知道嗎？天上有一顆星星就叫做「周杰倫星」，2009 年兩岸天文愛好者蔡元生、陳韜和金彰偉，於台灣玉山國家公園鹿林天文台發現 1 顆小行星，因 3 人都喜愛周杰倫，決定將這顆小行星命名爲「周杰倫」。

這顆小行星已於 19 日通過「國際行星組織」認證，當天正好是周杰倫獲得金曲獎最佳國語男歌手獎，也讓這顆小行星成了名副其實的「明星」。周董昨(28)日透過杰威爾公司說，「或許這顆小行星也很有創意、很有個性！」

蔡元生表示，2009 年觀測團隊共發現三顆新的小行星，並陸續取得國際小行星中心永久編號。其中兩顆已分別命名爲「高雄」及「周杰倫」，目前還有一顆尚未命名，將委託中央大學天文研究所教授黃崇源領導的團隊命名。
原文轉載自【2011-06-29/NOWnews 今日新聞網　頭條新聞】

大里高中生發現六顆小行星

記者黃俊昇 / 大里報導

台中市國立大里高中的七位同學，參加國際小行星搜尋計畫，近來一共發現六顆小行星，待確認二至三次週期後，就可擁有命名權，同學們已開始構想命名爲「台灣」、「台中」、「國大里」等。

國立大里高中指出，六千五百萬年前造成恐龍滅絕的原因，可能就是小行星撞擊到地球所引起。科學家因此隨時注意太陽系中的小行星，計算它們是否會撞擊地球。而過去兩個月，全球七個國家三十二所高中的一百多位高中生，加入地球防衛隊，協助找到二十二顆未知小行星，該校與北一女、彰化高中共十八位學生，既競爭又合作，找到其中四顆，交出漂亮成績單。

國立大里高中的蔡仲霖、黃義雄、林峙宇、陳聖丁、李子駸、陳琮淯、林學敏都是高一同學，因爲對天文及科學有濃厚的興趣，他們平常就使用學校天文台及星象教室，這次參加國際小行星搜尋計劃，每週接收美國夏威夷泛星計畫的望遠鏡影像，再利用軟體計算、驗證其運行週期及軌道，再請大學教授指導軌道計算方法。

由於小行星運動速度又快，非常不容易判別，同學自己建立觀測日誌，在活動中共找到三顆小行星，取得臨時編號。另透過中央大學鹿林天文台望遠鏡的追蹤觀測，又幸運的找到三顆小行星。

原文轉載自【2011-05-31/中華日報/A6 版/中部綜合】

7 高一生找到 6 顆小行星　擁命名權

國立大里高中天文社蔡仲霖等 7 名高一生，加入地球防衛隊，協助尋找可能撞上地球的小行星，先後找到 6 顆小行星，並取得臨時編號，待確認 2 至 3 次週期後，就可擁有命名權。7 人異口同聲表示，要命名爲「國大里」，感謝學校及老師用心指導，其他則想命名爲臺灣、台中等名字。

蔡仲霖、黃義雄、林峙宇、陳聖丁、李子駸、陳琮淯、林學敏 7 名同學，因對天文科學很有興趣，平時在林士超老師指導下，利用校內天文台及星象教室，觀察星象變化。這次參與國際小行星搜尋計畫，和全球 7 國、32 所高中的上百位高中生，加入地球防衛隊，利用 2 個月時間，協助找到 22 顆未知小行星。

行星速度快、既小且暗不易掌握，爲尋找小行星，7 名學生每週接收美國夏威夷泛星計畫 1.8 公尺口徑望遠鏡拍攝的影像，再利用軟體計算、驗證其運行週期及軌道。同學更分工合作，每天建立觀測日誌，終於找到 3 顆小行星，並取得臨時編號。後來前往中央大學鹿林天文台利用一米望遠鏡追蹤觀測，又自力找到 3 顆小行星。（記者陳建志）

原文轉載自【2011-05-31/自由時報/A10 版/生活新聞】

大里高中 7 生　發現 6 顆小行星

【記者黃寅／台中報導】

國立大里高中學生參加國際小行星搜尋計畫，成功找到太陽系裡六顆以往未曾被發現的小行星，未來可能擁有命名權，「國大里」是可能的命名選項，學生們的成果受到重視。

總計全球有 7 個國家、32 所高中的一百多位高中生參加這項國際小行星搜尋計畫（IASC，International Astronomical Search Collaboration），並加入所謂的「地球防衛隊」，找尋太陽系中未曾出現的小行星。

學生陳琮淯、林學敏說，他們在兩個月活動期間內，必須每周接收夏威夷泛星計畫（Pan-STARRS）天文台的 1.8 公尺口徑望遠鏡傳來的天文影像，再利用軟體計算、驗證，才能從可疑影像中找到小行星。

學生林峙宇說，六千五百萬年前，恐龍滅絕可能就是小行星撞擊到地球引起，因此找到小行星，並計算它們是否會撞擊地球，具一定的防衛地球意義。

32 所高中，每兩校組成一隊，國大里 7 名學生和夏威夷的茂伊高中搭配成一組，最先找到三顆小行星，並請我國中央大學的鹿林天文台協助確定，接著又從鹿林天文台提供的資料裡另找到三顆，在全體學生找到的 22 顆小行星裡佔最高的比率。

校長游源忠說，蔡仲霖、黃義雄、林峙宇、陳聖丁、李子駸、陳琮淯、林學敏雖僅高一，但平日對天文很有興趣，經常使用學校的天文台及星象教室觀察星象，他們透過觀察星象經常得上網及和國際學者接觸，無論英文、天文知識都迅速增長。

原文轉載自【2011-05-31/聯合報/B2 版/大台中綜合新聞】

恐龍滅絕原因是－小行星撞地球？！科學家覺得有可能

記者林重鎣／台中報導

在 6500 萬年前，造成恐龍滅絕的原因，可能就是小行星撞擊到地球所引起。科學家隨時注意太陽系中的小行星，計算它們是否會撞擊地球。

過去兩個月，全球 7 個國家 32 所高中的一百多位高中生，加入地球防衛隊，協助找到 22 顆未知小行星，其中國立大里高中與北一女中、彰化高中共 18 位高中生，他們既競爭又合作，找到其中 4 顆，交出漂亮成績單！國立大里高中的蔡仲霖、黃義雄、林峙宇、陳聖丁、李子駸、陳琮淯、林學敏都是高一的同學，因爲對天文及科學有濃厚的興趣，他們平常就常使用學校的天文台及星象教室，這次參加國際小行星搜尋計劃(IASC, International Astronomical Search Collaboration)，研讀原文的指引手冊，每週接收美國夏威夷泛星計畫(Pan-STARRS)1. 8 公尺口徑的望遠鏡影像，再利用軟體計算、驗證其運行週期及軌道，再請大學教授指導軌道計算的方法。

由於小行星既小且暗，運動速度又快，非常不容易判別，同學自己建立觀測日誌，共找到三顆小行星，取得臨時編號。令人意外的是在透過中央大學鹿林天文台一米望遠鏡的追蹤觀測中，又幸運地自力找到 3 顆小行星。

國大里指導老師林士超表示：同學利用課餘時間，分工合作完成小行星尋星計劃，爲他們的表現感到驕傲。這些發現的小行星再經過二至三個週期確認後，發現的國立大里高中同學們就可擁有命名權，問到要以什麼名字來爲小行星命名時，7 位同學異口同聲的說：要叫做『國大里』! 以感謝學校提供這麼好的設備，及老師用心的指導。
原文轉載自【2011-05-30/NOWnews【地方新聞】】

尋找小行星　台生表現亮眼

（中央社記者許秩維台北 26 日電）中央大學今天表示，台灣高中生參與「國際天文搜尋聯盟」尋找小行星的活動表現亮眼，在 22 顆取得暫時編號的小行星當中，有 4 顆由台灣團隊所發現，未來將擁有命名權。

中央大學表示，「國際天文搜尋聯盟」(International Astronomical Search Collaboration,IASC）主辦的國際尋找小行星活動，邀請全球 7 個國家的高中學生，利用最先進的泛星計畫所取得的第一手影像，分析比對找出未知小行星，台灣共 10 多名學生參加。

參與計畫的指導教師表示，每個星期泛星計畫釋放出尚未經過科學家分析的影像，學生要利用軟體找出移動天體，要是不在國際小行星中心已知天體的資料庫中，便算初步發現。初步找到的疑似小行星，必須經過後續觀測，驗證其軌道，才能取得暫時編號。

台灣泛星計畫主持人、中央大學天文研究所教授陳文屏表示，主辦單位告訴他，台灣學生在活動期間表現優異，台灣團隊共發現超過 20 個初步驗證的小行星，同時在整個活動結束後，共有 22 顆取得暫時編號的小行星，其中有 4 顆是台灣團隊所發現，未來將擁有命名權。

陳文屏說，台灣學生雖然剛開始因為語言和使用軟體不熟悉，因此較不適應，但中期之後表現漸入佳境，和其他國家相較，表現絲毫不遜色。他也相信，學生很有潛力，只要「告訴孩子跑道在哪，指個方向，他們自己就會跑得又快又穩」。1000526

原文轉載自【2011-05-26/中央社】

尋找小行星　高中生國際發光

(2011/5/27)

楊惠芳／臺北報導

我國高中生參加國際尋找小行星活動，表現亮眼。整個活動結束後，共有二十二顆小行星取得暫時編號，其中有四顆由臺灣團隊發現，未來擁有命名權。北一女等三所高中的師生，預定明天在中華民國天文學年會中，發表這項成果。

這次國際尋找小行星活動由「國際天文搜尋聯盟」主辦，從三月二十八日到五月二十日舉行，共有美國、巴西、德國、波蘭、保加利亞及土耳其等七個國家，總計三十二所高中參加，利用最先進的科技取得第一手影像，進行分析、比對，找出未知的小行星。

中央大學教授陳文屏是臺灣泛星計畫主持人，促成我國高中生參加這次活動。臺灣的十八名學生來自北一女中、彰化高中及大里高中，他們在國際舞臺上既競爭又合作，交出漂亮成績單。

彰化高中教師游大立表示，剛開始活動進行得很不順利，因為軟體操作、郵件來往，全都使用英文，天文知識也不足，學生吃了不少苦頭。後來熟悉工具，逐漸習慣以英文溝通，也學會小組分工合作，才開始發現小行星，不但聯絡天文臺協助後續觀測，也了解更多有關天體運行的知識。

大里高中學生在活動中表現突出。教師林士超說：「學生利用中央大學的鹿林天文臺望遠鏡，進行後續觀測，體會到天體位置誤差、運動快速，以及精確軌道計算的困難。有幾次，在預測的位置，沒有找到原來疑似發現的小行星，卻在影像中另外發現三顆小行星，並取得編號，有柳暗花明的驚喜。」

原文轉載自【2011-05-27/國語日報】

國大里尋星　台中可望成行星名

（中央社記者陳淑芬台中 30 日電）國立大里高中學生參與「國際天文搜尋聯盟」尋找小行星活動，找到多顆小行星，將擁有命名權。學生今天表示，已決定「台中」及「國大里」2 個行星名稱，可望成為行星之名。

國立大里高中 1 年級學生蔡仲霖、黃義雄、林峙宇、陳聖丁、李子駿、陳琮淯、林學敏等人對天文科學興趣濃厚，常使用學校的天文台及星象教室，並參加「國際小行星搜尋計劃」(IASC, InternationalAstronomical Search Collaboration)，尋找到 3 顆行星。

經透過中央大學鹿林天文台望遠鏡的追蹤觀測確認過程中，再幸運地找到另 3 顆小行星。國大里指導老師林士超今天表示，同學利用課餘時間，完成小行星尋星計劃，前後共發現 6 顆行星，令人感到驕傲，經 7 名同學討論，初步已決定「台灣」、「台中」及「國大里」3 個名字。

校方表示，小行星週期約 2 至 3 年，須經過 2 至 3 個週期確認後，發現者就擁有命名權，學生討論後，異口同聲要求取名「國大里」，以感謝學校天文台及星象教室所提供的研究設備及師長的指導。

校方指出，學生表示，想取名「台灣」是希望可讓台灣能登上行星之名，但經了解得知，幾年前即有人以「台灣」命名了；另想取名叫「台中」是因身為台中人，希望讓全世界都知道台中這個地方。1000530

原文轉載自【2011-05-30/中央社】

高中生愛追星

【文／蔡永彬】

國立大里高中的師生團隊參加「國際天文搜尋聯盟」（IASC）活動，一連發現六顆疑似小行星，目前已經取得「暫時編號」，未來還可能獲得「永久編號」和它們的命名權。

中央大學天文研究所教授陳文屏指出，活動期間總共發現廿二顆疑似小行星，其中四顆由台灣學生發現；大里團隊除了包辦三顆外，在請中大鹿林天文台幫他們確認的過程中，又額外找到三顆。
原文轉載自【2011-05-27/聯合報/A6 版/生活】

我高中生　發現 4 顆小行星

〔記者湯佳玲／台北報導〕台灣高中生加入地球防衛隊，協助尋找未知小行星，在二十二顆取得暫時編號的小行星當中，台灣團隊發現四顆，未來擁有命名權，其中有三顆是大里高中發現的。

高中生尋找未知小行星活動由「國際天文搜尋聯盟」主辦，有台灣、美國、巴西、德國、波蘭、保加利亞及土耳其等七個國家參與，利用最先進的泛星計畫所取得的第一手影像，分析比對找出未知小行星。

台灣的高中生團隊共有十八位，分別是來自北一女中的沈亮欣、莊雅淳、張瑄、林孝柔、黃鈺昕、蔡佳蓉；彰化高中楊承域、陳冠綸、曾泓祥、趙宥然、蕭宇泰及大里高中陳聖丁、李子駸、黃義雄、林學敏、蔡仲霖、林峙宇、陳琮淯。

泛星計畫望遠鏡位於美國夏威夷，口徑一．八公尺，配備最先進的電子相機，每個月巡視天空數次，適合用來發現亮度或位置改變的天體，如恆星死亡爆發的超新星，或快速運動的小行星。

大里三顆彰中一顆

初步找到的疑似小行星必須經過後續觀測，驗證其軌道，才能取得暫時編號。在二十二顆新發現的小行星中，大里高中發現三顆、彰化高中發現了一顆。

彰化高中游大立老師敘述：「剛開始進行很不順利，軟體操作、郵件來往全都使用英文，天文的知識也不足，學生們吃了不少苦頭。」北一女中老師金若蘭也說：「要在密密麻麻的星星當中尋找灰暗移動的小天體，簡直就是大海撈針。」

大里高中林士超老師則興奮地說：「我為他們的表現感到驕傲。」初步發現的小行星軌道不詳，需要利用軟體計算未來可能的位置，要再確認並不容易。有些疑似小行星過了很多年以後，才由其他觀測者確認。學生們利用中央大學的鹿林天文台望遠鏡進行後續觀測，「有幾次在預測的位置沒找到原來疑似發現的小行星，卻在影像中另外發現三顆取得編號，真有柳暗花明的驚喜！」

原文轉載自【2011-05-27/自由時報/A8 版/生活新聞】

《探索天文》小王子的故鄉

作者：文／台北市立天文科學教育館解說員林琦峰

小王子是一本法國著名的童話，內容描述一位來自遙遠星球小王子的經歷，小王子遊歷過許多不同的星球，在不同星球中，所遇到的人、事、物，總是讓他感到疑惑不解。故事中敘述小王子出生的星球，與一棟房子相比較，大不了多少，一眼就可以看透，根據判斷應該就是編號 B612 的小行星。

小行星的分布

故事中令我感到興趣的是小王子的故鄉—小行星，依 2006 年 8 月 24 日國際天文聯合會（International Astronomical Union，IAU）決議，太陽系中繞日運動的天體可分為行星、矮行星及太陽系小天體三類。小行星屬於太陽系小天體，自從 1801 年 1 月 1 日，義大利天文學家皮亞齊（Giuseppe Piazzi）發現了編號第 1 號小行星後（Ceres，穀神星現在稱為矮行星），截至 2011 年 3 月分為止，擁有臨時編號的小行星，已經超過 94 萬顆。隨著觀測工具及分析方法的進步，發現太陽系中小行星的分布範圍包含近地小行星（火星軌道內）、主要小行星帶（火星與木星間）、半人馬小行星群（土星與天王星間）、特洛伊小行星（位於行星軌道拉格朗日點上）及庫伯帶小行星（海王星以外）等。當然這些小行星因為體積小、距離遠，所以別說用望遠鏡看只是一顆看不清楚的小光點，更別說想用肉眼看清其真面目。

不可不知的事

雖然小行星觀測不易，但是我們還是要知道，遙遠天空中有幾顆小行星，盡是我們熟悉的台灣地名，包含鹿林、南投、嘉義、高雄及玉山等。

其實小行星的命名有一定的程序，首先在觀測後，可以計算其軌道者，可獲得一個臨時編號；如果該星體可重複被觀測到，並更確定其軌道者，即可擁有一個永久編號，發現者亦可以獲得命名的機會。

就如中央大學在玉山國家公園，設立的鹿林天文台，於 2006 年推出鹿林尋天計畫（Lulin Sky Survey，LUSS），從此台灣開始在尋找小行星領域中嶄露頭角，例如第 145523 號鹿林小行星（Lulin，臨時編號 2006 EM67）及第 145534 號中大小行星（Jhongda，臨時編號 2006 GJ），就是台灣首次命名的小行星，可稱為是台灣之光。

臨時編號的玄機

小行星臨時編號的命名，包含發現的西元年加上兩個英文字母，必要的時候還可以加上數字來排序，其中第一個字母表示發現的月分，以半個月為單位，依英文字母 A 至 Y 排列，其中字母「I」不使用。第二個字母表示在這段時間內發現的次序，按照字母 A 至 Z 排列，字母「I」不使用，排序超過 25 顆後，則從頭排序，並於字母後標上數字，數字表示其循環次數。所以可以透過小行星的臨時編號，推算出其發現的時間。例如臨時編號 2006 EM67 鹿林小行星，表示 2006 月 3 月上半月發現的第 1,687 顆小行星（67*25+12=1,687）。

各位喜歡天文的追星族們，讓我們再來找看看，還有哪些小行星的名稱，是與台灣有關的呢？當然您如果想名留星空，那就請您加入尋星行列。（上）

原文轉載自【2011-04-29/人間福報/遇見科學】

想像力無限上綱　外星人變玄奇

【記者羅智華台北報導】美國聯邦調查局（FBI）日前揭密一批檔案，其中提到有關外星人造訪地球的備忘錄內容，引起國際媒體爭相報導。但後來媒體又報導雖然備忘錄是 FBI 探員所寫，但內容卻不真實，儘管後來被證明是烏龍一場，但依舊引發全球關注，使得外星人議題再度成為沸沸揚揚的討論焦點。

外星球究竟有沒有生命的存在？這個歷久不衰的熱門話題，始終是許多科學家想解開的謎底。對此，長年研究外星生命的中央大學天文研究所物理學系教授陳文屏表示，雖然地球是目前科學家在太陽系中，唯一發現有生命存在的星球，但長年研究天體的他相信，在未知的蒼穹中，仍有可能存在著外星生命。

陳文屏笑著說，說不定在地球人努力尋找外星生命足跡的同時，外星球的生命也在嘗試尋覓其他星球的生命體。從小就對天文感興趣的他也曾想過，如果有一天真有外星人駕著飛碟降落在他面前，自己是否有勇氣跳上飛碟、跟著外星人回外太空。如果是小時候的自己，他可能會不顧一切「SAY YES！」，但現在的他則要先問看看「去了外星球後還能不能回地球」，再決定是否要踏上這趟奇妙的星際旅行。

陳文屏表示，若從科學角度來看，原始生命的形成，必須要在一個溫度、大氣壓力等要素都適合的行星環境中才能順利發展；而「水」則是醞釀生命的重要關鍵，這也是爲什麼，科學家長年來一直積極尋找其他星球上是否有「水」的蹤跡，以藉此推估有沒有外星生命存在，只是迄今，科學家即使透過科技努力在太陽系「趴趴走」，仍尚未找到有生命存在的蛛絲馬跡。但也不能因此就蓋棺論定說，一定沒有外星生命的存在，因爲宇宙中還存在許多未知之事。

「我們不能用未知的科技或知識來解釋人類未知的現象」陳文屏有感而發表示，然而科學的根本精神就是追求真實與證據，我們不能用未知來解釋未知，讓想像力無限上綱，才不會讓外星生命的議題淪爲怪力亂神的無稽之談。

原文轉載自【2011-04-17/人間福報/一周看點】

相信外星人存在　葉永烜：美有所保留

李宗祐／台北報導

美國聯邦調查局（ＦＢＩ）將「一九四七年飛碟墜毀事件」列入備忘錄，被外界解讀爲美國終於承認外星人造訪事實。台灣聯合大學系統副校長葉永烜表示，從科學的角度看，ＦＢＩ的動作很有趣，但ＦＢＩ也不是沒出過錯，美國應公開更多資料，讓科學家研究此事件的真實性；他認爲外星人有可能存在。

葉永烜表示，一九四七年在新墨西哥州羅斯威爾發生的飛碟墜毀事件，一直是科學家好奇的議題，更是科幻小說和電影的熱門題材，真真假假多年來爭議不休。

他說，此次公開的報告到底真假如何，還不知道，「但我看到相關新聞報導之後，覺得很有趣。美國政府在此事件發生後，一直不准科學家碰這些檔案。如果這個事件是真的，美國政府應該有保留一些東西，而不只是照片或文字檔案而已。」

葉永烜笑說，如果ＦＢＩ公開的檔案是真的，或許可促請全球諾貝爾獎得主連署呼籲美國政府開放更多資料、甚至把過去不准科學家碰的東西開放給科學家研究，而不只是公開照片或文字資料。「光看文件資料，很難判斷真假。尤其ＦＢＩ公開的檔案並非科學研究報告，ＦＢＩ也不是沒有出錯過。」

葉永烜指出，到底有沒有外星人存在，科學家的看法相尙紛歧，「我在美國留學期間，一位很有名的天文學者發表有關外星人存在的言論，被我的指導教授罵神經病。」不過，他認爲外星人有可能存在。

葉永烜表示，當地球面臨全球暖化、環境迅速惡化之際，若是能證實真的有外星人的存在，很可能會成爲地球人類的新希望，證實有其他星球可能適合人類生存。或許也可借重外星人的經驗，協助地球解決暖化危機。但一切都要有科學根據，不能以訛傳訛。

原文轉載自【2011-04-12/中國時報/A6 版/生活新聞】

天文迷照過來　2011 年 11 月 8 日大夥追「星」趣

【陳至中／台北報導】
超級月亮之後又會有超級小行星？美國知名網站 space.com 報導，一顆直徑約四百公尺的小行星，將於今年十一月八日和九日「拂」（ whisk）過地球，最靠近時僅僅只有〇・八五個地球、月亮距離。

天文學界認定這顆名爲「2005 YU55」的小行星，不會對地球造成毀滅性的打擊，但畢竟這種「大又近」的小行星，機會相當難得，各地天文台都已積極動員，我國中央大學也考慮舉辦相關活動，邀請民眾共襄盛舉。

科學家估算，其離地球最近的兩個時間，分別是十一月八日夜間十一時二十八分，距離〇・〇〇二一七個天文單位（AU，一 AU 即地球與太陽的平均距離），以及十一月九日上午七時十三分，距離〇・〇〇 一六個天文單位。

「2005 YU55」不會造成世界末日，卻是難得的天文奇觀！天文界預估這種「大又近」的小行星，三十

年才有一次。

中央大學副校長、天文所教授葉永烜表示，小行星靠近地球時，用肉眼就能勉強看見，但在天空中非常小、速度又非常快，建議以天文望遠鏡觀察。

原文轉載自【2011-04-10/中國時報/A5 生活新聞】

太空探索／春天火流星變多　科學家也覺得奇

生活中心／台北報導

春神來了怎知道？除了大家熟知的梅花黃鶯報到、氣溫逐漸回暖之外，還有個徵兆，就是火流星（fireball）也變多了。美國航太總署（NASA）流星體環境中心 Bill Cooke 表示，春天是火流星的季節。由於某種未知的原因，在春分前後的數星期，火流星出現數量增加許多。

在其他季節中，從黃昏到清晨，每個晚上大約可看到約 10 個亮度比金星還亮的「偶發（sporadic）」火流星。地球在太空中運行時，不時會遇上在太空中漂流的小行星或彗星遺留的碎片。然而，春季的火流星數量比其他季節還多了 10~30%左右；而且不僅火流星增加，連落入地球的一般流星體也比較多。科學家知道這種春季火流星增加的現象已經 30 年左右了，卻一直找不出滿意的解釋。事實上，這些科學家想得愈多，就覺得愈奇怪！

在天上有個所謂的「地球向點（apex）」，也就是地球的運動方向。當地球繞太陽公轉一周時，這個地球向點也隨之在天上繞一圈，這圈就是平常所稱的「黃道（Zodiac）」。地球向點通常很明顯，因爲一般偶發流星都似乎是從地球向點向外射出的，就像流星雨的輻射點一樣。假設地球是一輛車，向點就是前擋風玻璃的方向；當車子在鄉間小路往前開動，不小心迎頭撞上的昆蟲就會累積在擋風玻璃上。

每年秋季，地球向點在夜空中的仰角最高，此時一般亮度的偶發流星最多，有時一晚就可見到數十顆。然而，您注意到了嗎？這講的是「秋季」！沒錯，就是秋季。這干春季何事？根本沒辦法解釋春季火流星變多的現象。

西安大略大學（University of Western Ontario）流星體專家 Peter Brown 表示，某些研究人員認爲這可能是沿地球軌道的流星體明顯分布不均所引起的，或許造成火流星的較大流星體剛好在春季到初夏時節比較多。不過，這個概念必須等到更了解這些形成火流星的流星體分布軌道才能證實是與非。

Brown 還表示，與地球向點剛好相反方向的「地球背點（antapex）」在春季夜空的仰角最高，這些偶發火流星會不會來自地球背點？到目前爲止沒有明顯證據顯示地球背點方向有火流星源，但可能是因爲缺乏不同緯度的火流星觀測資料以供分析，所以對此概念的細節還解釋不清楚。

爲了解決這個問題，Cooke 正在美國各地找地方設置流星自動觀測相機，希望成立全天火流星觀測網（All-sky Fireball Network），不僅要捕捉這些火流星的影像，同時要藉由三角測量方式找出流星體的軌道。

國立中央大學天文研究所的阿部新助教授和林宏欽台長，去年也在臺灣成立了流星觀測網，希望研究解開某些流星雨的謎題。這可能得要花上好幾年的時間才能找出答案，在此之前，春季火流星增加是個美麗的謎題，就儘管走出戶外，好好享受這個天上掉下來的禮物吧！(文／引用自臺北天文館之網路天文館網站)
點選以下網址觀看 2009 年 3 月 16 日捕捉到的一顆火流星影片：
http://science.nasa.gov/media/medialibrary/2011/03/31/springfireball.wmv
原文網址: 太空探索／春天火流星變多　科學家也覺得奇 | 頭條新聞 | NOWnews 今日新聞網
http://www.nownews.com/2011/04/06/91-2702516.htm#ixzz1Ip919C5Z

原文轉載自【2011-04-06/NOWnews 今日新聞網】

小行星命名「李國鼎」表彰台灣科技之父

【大紀元 2011 年 01 月 26 日訊】(大紀元記者耿豫仙台北報導)在火星與木星間的小行星帶，在人馬座的

翅膀有顆小行星（行星會隨時移動，被發現時，位置在金牛座），26 日以後它的名字叫「李國鼎」（Likwohting），也就是「台灣科技之父」前總統府資政李國鼎。

在 26 日命名記者會上，中大校長蔣偉寧說，李國鼎對於台灣科技工業的發展貢獻卓著，並博得「科技父」的美譽，他表示，極少數人的貢獻，會隨著時光而更見璀璨。雖未曾與李國鼎有過共事機會，但做中大校長能有如此傑出的校友與有榮焉。

以李國鼎命名的意含，蔣偉寧解釋，第一，李國鼎的風範對於現在的政治人物應有學習之處，另外，希望以其命名，讓中小學生知道，要有第二個李國鼎不太可能，但如果每一個人都致力於想成為李國鼎，台灣就有很大的機會。

對於天上有一顆李國鼎的行星，李國鼎的獨子李永昌感到非常新奇，也很欣慰。相較於其他與會的來賓，談起李國鼎能滔滔不絕 10-20 分欲罷不能的情形相比，李永昌對父親的記憶是「一片空白」，他記憶的父親「很少在家」、「家裏很窮」、「沒什麼訪客」。

無論在工業建設、財經、科技等，都能看到李國鼎推動國家的現代化的貢獻，然而與家人相處的時間極少。從李永昌的身上，就能看到李國鼎對事業和家庭間所分配的輕重。

李國鼎行星(Likwohting)

李國鼎小行星，大小約 2 公里，2010 年經國際天文學聯合會（IAU/CSBN）審議通過，正式命名為「Likwohting 李國鼎」，編號 239611。

2008 年 10 月 23 日在中大鹿林天文台被發現，當時位置在金牛座，火星及木星之間的小行星帶，目前已運行至人馬座的翅膀上。小行星繞太陽一周約 3.48 年，距太陽最接近時約 3.4 億公里，距離最遠時約 3.5 億公里。

發現 800 顆　20 顆命名

中大鹿林天文台以 40 公分望遠鏡進行小天體觀測，截至目前為止，總計發現約 800 顆小行星，其中有 20 顆已取得永久命名，以人命名的有溫世仁、鄭崇華、沈君山、李國鼎，而以地為名有鹿林、嘉義、南投、玉山、中壢，八八水災被淹滅的小林村，編號為 185636「小林村小行星」。

原文轉載自【2011-01-26/大紀元時報首頁　>新聞　>台灣新聞　>正文】

李國鼎小行星　命名通過

再過 2 天，就是「科技教父」李國鼎 101 歲冥誕，為了表彰李國鼎對台灣的貢獻，中央大學今天舉行記者會，對外宣布「李國鼎小行星」經國際天文學聯合會命名通過的好消息。

中央大學昨天在李國鼎故居舉行「李國鼎小行星」命名通過記者會，李國鼎知識促進會理事長王昭明、李國鼎科技發展基金會董事長楊世緘、中央大學校長蔣偉寧、李國鼎兒子李永昌等共同出席見證。

中央大學鹿林天文台在 2008 年 10 月 23 日發現的編號 239611 號小行星，在去年 12 月，經國際天文學聯合會（IAU／CSBN）通過命名為「Likwohting」（李國鼎）。

蔣偉寧表示，李國鼎對台灣經濟發展和資訊推動有傑出的貢獻，表彰感念李國鼎對中華民國的貢獻，期盼透過小行星命名，讓更多人知道；他說，要再出現另一個李國鼎不大可能，但希望所有小朋友都想成為李國鼎，如此台灣就有希望。

原文轉載自【2011-01-27/民眾日報/4 版/綜合新聞】

「李國鼎小行星」　命名通過

記者黃朝琴／臺北報導

為表彰「科技教父」李國鼎對臺灣的貢獻，國立中央大學鹿林天文臺所發現的編號 239611 號小行星，

經國際天文學聯合會（IAU／CSBN）審議通過，正式命名為「Likwohting」（李國鼎），希望有更多人了解李國鼎對國家經濟及科技發展的貢獻。

中央大學昨天舉行記者會，對外宣布「李國鼎小行星」經國際天文學聯合會命名通過的好消息。中大校長蔣偉寧蔣偉寧表示，該校鹿林天文臺在二〇〇八年十月二十三日號發現的這顆小行星，大小估計約二公里，發現時位置在金牛座，目前位於人馬座，繞太陽一周約三點四八年，經國際天文學聯合會（IAU／CSBN）審議通過，正式命名為「Likwohting」（李國鼎），經國際天文學聯合會通過正式命名為「Likwohting」（李國鼎）。

中大鹿林天文臺從九十一年至今已發現約八百顆小行星，過去曾以玉山，還有臺達電創辦人鄭崇華、前清大校長沈君山等命名過小行星，希望透過小行星的命名，表彰具有代表性的臺灣人事物。

李國鼎一九三〇年畢業於中大物理系，是中大校友，一生致力於推動國家現代化，對我國科技工業發展貢獻卓著，博得「科技教父」的美譽，這次李國鼎小行星的命名，希望有更多人了解李國鼎對國家的貢獻，成為中小學生學習的典範。

原文轉載自【2011-01-27/青年日報/6 版/新視界】

表彰科技教父　小行星命名李國鼎

楊惠芳／臺北報導

明天一月二十八日，是「科技教父」李國鼎一百零一歲冥誕，為了表揚他對臺灣的貢獻，國立中央大學將鹿林天文臺發現的編號二三九六一一號小行星，正式命名為「Likwohting 李國鼎」，希望有更多人了解李國鼎對國家經濟和科技發展的貢獻。這項命名已由國際天文學聯合會審議通過。

中央大學校長蔣偉寧表示，大多數人的貢獻，會隨著時光消逝；只有極少數人的貢獻，會隨著時光而更見璀璨。雖然李國鼎已經離開了，但是他仍然影響臺灣整體發展的記憶和經驗，似乎還在大家身邊。希望透過這次小行星的命名，將李國鼎作為中小學學生的學習典範，如果所有學生都想成為李國鼎，臺灣就有希望。

李國鼎是在一九三〇年畢業於中大物理系，是中大校友，一生致力於推動國家現代化，對我國科技工業發展貢獻卓著，有「科技教父」的美譽。

中央大學天文所所長周翊表示，中大鹿林天文臺在二〇〇八年十月二十三日發現這顆小行星，體積大小估計長約兩公里，發現時位置在金牛座，目前位在人馬座，繞太陽一周約需要三點四八年，去年底經國際天文學聯合會通過，正式命名為「李國鼎」。

中大鹿林天文臺到現在，總計已發現約八百顆小行星，過去曾以臺灣的玉山，還有台達電創辦人鄭崇華、前清大校長沈君山等人名，為小行星命名，希望藉此表彰具有代表性的臺灣人事物。

圖說：中央大學校長蔣偉寧（圖中）在李國鼎故居，公布「李國鼎小行星」命名通過的消息。左為李國鼎的兒子李永昌。攝影／楊惠芳

原文轉載自【2011-01-27/國語日報/2 版/文教新聞】

紀念科技之父　小行星命名"李國鼎"

再過兩天，就是國內「科技教父」李國鼎 101 歲的冥誕，為了表彰他對台灣財經界的重大貢獻，中央大學把最近發現的一顆小行星命名為「李國鼎」已經獲得國際天文學聯合會通過。

這顆就是李國鼎小行星。它繞太陽一周大約 3.48 年，最接近太陽時約 3.4 億公里，離太陽最遠時約 3.5 億公里，發現時位置在金牛座，目前移動到人馬座。

鹿林天文台在生態保育良好的玉山，可以杜絕外界的干擾，是很好的觀測地點。目前總計發現約 800 顆小行星、1 顆近地小行星及 1 顆彗星，歷年來也有約 20 顆小行星獲得命名，其中像是以鄭崇華、溫世仁等人名命名，或是以嘉義、南投、中壢等地名來命名，而中央大學鹿林天文台在 2008 年 10 月 23 日發現的這顆編號 239611 號小行星，在去年 12 月，經國際天文學聯合會通過命名為李國鼎。

小行星是目前唯一可由發現者命名，並得到世界公認的天體。發現小行星並經過國際小行星中心確認通過後，就可得到一個國際統一的編號。

記者綜合報導

原文轉載自【2011-01-26/公視新聞網 PTS NEWS ONLINE 科技新聞】

李國鼎小行星　永誌天際

中央社／台北二十六日電

再過兩天，就是「科技教父」李國鼎一〇一歲冥誕，為了表彰李國鼎對台灣的貢獻，中央大學今天舉行記者會，對外宣布「李國鼎小行星」經國際天文學聯合會命名通過的好消息。

中央大學今天在李國鼎故居舉行「李國鼎小行星」命名通過記者會，李國鼎知識促進會理事長王昭明、李國鼎科技發展基金會董事長楊世緘、中央大學校長蔣偉寧、李國鼎兒子李永昌等共同出席見證。

中央大學鹿林天文台在二〇〇八年十月二十三日發現的編號二三九六一一號小行星，在去年十二月，經國際天文學聯合會（IAU／CSBN）通過命名為「Likwohting」（李國鼎）。

蔣偉寧表示，李國鼎對台灣經濟發展和資訊推動有傑出的貢獻，表彰感念李國鼎對中華民國的貢獻，期盼透過小行星命名，讓更多人知道；他說，要再出現另一個李國鼎不大可能，但希望所有小朋友都想成為李國鼎，如此台灣就有希望。

王昭明說，李國鼎對天文非常有興趣，在校期間也寫過很多關於天文的論文。

中央大學天文所所長周翊表示，李國鼎小行星繞太陽一周約三點四八年，最接近太陽時約三點四億公里，離太陽最遠時約三點五億公里，發現時位置在金牛座，目前位於人馬座。

周翊說，鹿林天文台利用有限的經費，在九十五年三月開始的「鹿林巡天計畫（Lulin Sky Survey, LUSS）」，有計畫性觀測小行星，總計發現約八百顆小行星、一顆近地小行星及一顆彗星，其中已有約二十顆小行星獲得永久命名；對於小型望遠鏡的觀測而言，可以說成效卓著。

原文轉載自【2011-01-27/中華日報/A2 版//要聞】

天上有顆小行星　命名李國鼎

【記者林進修)】

仰望蒼穹，今後將多一顆以台灣名人命名的星球。中央大學選在「台灣科技之父」李國鼎 101 歲冥誕前夕，昨天將一顆 2008 年 10 月 23 日發現、編號 239611 的小行星，以「李國鼎」之名命名，李國鼎的兒子李永昌在場見證。

昨天的命名典禮選在台北市泰安街李國鼎故居舉行。中央大學校長蔣偉寧表示，這顆小行星於 2010 年 12 月經國際天文學聯合會確認通過，命名為「李國鼎小行星」(Likwohting)。

蔣偉寧指出，李國鼎是中央大學校友，早年在位於南京的中大物理系就讀時，非常喜歡天文學，生平第一篇論文「太陽運動之絕頂」，正是與天文相關。如今以他之名來命名小行星，表彰並感念他對台灣的不朽貢獻。

中央大學鹿林巡天計畫，透過鹿林天文台的 40 公分望遠鏡，至今已找到 800 多顆小行星，其中 14 顆已正式命名。李國鼎小行星即是顆最新命名的小行星，由蕭翔耀、葉泉志兩名觀測者共同發現。

原文轉載自【2011-01-27/Upaper/2 版/焦點】

李國鼎小行星　表彰科技教父

（中央社記者林思宇台北 26 日電）
再過 2 天，就是「科技教父」李國鼎 101 歲冥誕，為了表彰李國鼎對台灣的貢獻，中央大學今天舉行記者會，對外宣布「李國鼎小行星」經國際天文學聯合會命名通過的好消息。

中央大學今天在李國鼎故居舉行「李國鼎小行星」命名通過記者會，李國鼎知識促進會理事長王昭明、李國鼎科技發展基金會董事長楊世緘、中央大學校長蔣偉寧、李國鼎兒子李永昌等共同出席見證。

中央大學鹿林天文台在 2008 年 10 月 23 日發現的編號 239611 號小行星，在去年 12 月，經國際天文學聯合會（IAU／CSBN）通過命名爲「Likwohting」（李國鼎）。

蔣偉寧表示，李國鼎對台灣經濟發展和資訊推動有傑出的貢獻，表彰感念李國鼎對中華民國的貢獻，期盼透過小行星命名，讓更多人知道；他說，要再出現另一個李國鼎不大可能，但希望所有小朋友都想成爲李國鼎，如此台灣就有希望。

王昭明說，李國鼎對天文非常有興趣，在校期間也寫過很多關於天文的論文。

中央大學天文所所長周翊表示，李國鼎小行星繞太陽一周約 3.48 年，最接近太陽時約 3.4 億公里，離太陽最遠時約 3.5 億公里，發現時位置在金牛座，目前位於人馬座。

周翊說，鹿林天文台利用有限的經費，在 95 年 3 月開始的「鹿林巡天計畫（Lulin Sky Survey, LUSS）」，有計畫性觀測小行星，總計發現約 800 顆小行星、1 顆近地小行星及 1 顆彗星，其中已有約 20 顆小行星獲得永久命名；對於小型望遠鏡的觀測而言，可以說成效卓著。

鹿林天文台站長林宏欽說，鹿林巡天計畫與國外經費充裕的巡天計畫相比，只能算是「小蝦米對大鯨魚」，但重要的是，「在這個世界的舞台上，我們沒有缺席」。1000126

（中央社記者裴禛攝 100 年 1 月 26 日）

原文轉載自【2011-01-26/中央社】

新發現小行星　中大命名爲「李國鼎」

（陳奕華報導）

再過兩天就是台灣「科技教父」－李國鼎先生 101 歲冥誕，爲表彰他對台灣重大貢獻，中央大學將發現編號「239611 號」的小行星，命名爲「李國鼎」（LiKwohting），希望李國鼎先生的貢獻與精神可以繼續流傳下去。

爲表彰李國鼎先生對台灣科技、經濟重大貢獻，中央大學 26 號宣布，李國鼎小行星命名通過國際天文聯合會。

中央大學校長蔣偉寧在記者會上，推崇李國鼎對台灣貢獻，回億起，曾與國鼎先生對談的指導教授，對於李國鼎從天文、地理、經濟到科技侃侃而談、博學的印象深刻，更肯定台灣發展居四小龍之首，另外，提到台達電董事長鄭崇華捐贈中大興建光電大樓，要求命名爲國鼎大樓，以感念國鼎先生營造台灣優質企業環境。蔣偉寧表示，以天下爲己任這樣子的政務官風範，現在社會上幾乎看不到了，希望透過小行星命名活動，將李國鼎先生的貢獻與精神流傳下去。

「我希望能夠讓國鼎先生精神透過媒體與宣導，讓大家關注，甚至進一步透過教育，讓我們的小學生中學生大學生，知道李國鼎先生對國家的貢獻，他的精神不只是精神長流，我想不太可能有第二個李國鼎，但是如果所有小朋友都想要成爲李國鼎，我想台灣就有希望。」

中央大學天文所所長周翊解釋，中大鹿林天文所在 2008 年 10 月 23 號發現標號 239611 號小行星，發現的時候位置在金牛座，目前位在人馬座，大小估計約兩公里，繞太陽一周約 3.48 年，最接近太陽時約 3.4 億公里，離太陽最遠約 3.5 億公里。

原文轉載自【2011-01-26/中廣新聞網】

發現小行星！　中大命名「李國鼎」

生活中心／綜合報導

爲了紀念 2 天後「科技之父」李國鼎的 101 歲冥誕，中央大學今(26)天宣佈，已在去年 12 月經國際天文學聯合會(IAU／CSBN)通過，將 2008 年 10 月 23 日發現的一顆小行星，命名爲「Likwohting」(李國鼎)。

據中央社報導，編號爲 239611 的行星「Likwohting」，是中央大學鹿林天文台在 2008 年發現的，它繞太陽一周約 3.48 年，最接近太陽時約 3.4 億公里，離太陽最遠時約 3.5 億公里，發現時位置在金牛座，目前位於人馬座。

提及李國鼎對台灣的貢獻，中央大學校長蔣偉寧表示，李國鼎先生 1930 年畢業於中大物理系，一生致力於推動國家現代化，對台灣經濟發展和資訊推動有傑出的貢獻，期盼透過小行星命名後，讓更多人了解他的付出，雖然要再出現另一個李國鼎不大可能，「但希望所有小朋友都想成爲李國鼎，如此台灣就有希望。」

自 91 年至今，中大鹿林天文台已發現約 800 顆小行星，目前已有約 20 顆星被永久命名，名稱包括臺達電創辦人「鄭崇華」、前清大校長「沈君山」等人，以及「鄒族」、「玉山」、「雲門」、「中大」等代表性事物，期盼藉此表彰對台灣有所貢獻的人事物。
原文轉載自【2011-01-26/NOWnews 今日新聞網】

天邊有顆星　叫做李國鼎

【文／蔡永彬】

中央大學將二〇〇八年十月廿三日發現的編號 239611 小行星，經國際天文學聯合會通過後，命名「李國鼎（Likwohting）」，表彰校友李國鼎貢獻。發現此行星的蕭翔耀（左），昨天與「李國鼎小行星」模型合影。

原文轉載自【2011-01-27/聯合報/A8 版/綜合】

天上有顆星　叫「李國鼎」

【本報台北訊】仰望蒼穹，今後將多一顆以台灣名人命名的行星。在「台灣科技之父」李國鼎一百齡一歲冥誕前夕，中央大學將一顆二〇〇八年十二月二十三日發現、編號二三九六一一的小行星，命名爲以「李國鼎」（Likwohting）。

中央大學校長蔣偉寧表示，李國鼎是中央大學校友，早年在位於南京的中大物理系就讀時，非常喜歡天文學，生平第一篇論文「太陽運動之絕頂」，正是與天文相關。如今以他之名來命名小行星，表彰並感念他對台灣的不朽貢獻。

李國鼎之子李永昌表示，他父親逝世十年之際，天上竟多了顆以他爲名的星星，不僅相當神奇，也帶給他們家人最大的安慰。

李國鼎小行星是由由蕭翔耀、葉泉志兩名觀測者共同發現，它被發現時，位置在金牛座，目前運行到人馬座。這顆行星位於火星及木星之間的小行星帶，繞著太陽轉，繞太陽一周約三點四八年，距太陽最接近時約三點四億公里，距離最遠時約三點五億公里。

原文轉載自【2011-08-02/人間福報/3 版/綜合／社區】

小行星名「李國鼎」　在天際發光

【台灣醒報記者蔡沛琪台北報導】「如果有很多小朋友都立志成爲李國鼎，台灣就有希望。」中央大學校長蔣偉寧說。在李國鼎 101 歲冥誕前夕，中央大學今天宣布將所發現的 239611 號小行星名爲 Likwohting（李國鼎），未來將有一顆以這位科技教父爲名的小行星，在天際發光。
今天記者會特別選在李國鼎故居舉辦，李國鼎的同事、家人、後輩齊聚ㄧ堂，除了懷念這位台灣經濟舵手，更慶祝李國鼎小行星命名正式通過。

中大天文所教授陳文屏透露，因爲感念李國鼎對台灣的付出，加上李國鼎其實很喜愛天文，還曾前往中國觀測日全食，因此中央大學決定將小行星命名爲李國鼎。

這顆李國鼎小行星是由中央大學鹿林天文台於 2008 年發現，目前位在人馬座，大小估計約兩公里，繞太陽一周約 3.48 年，最接近太陽時約 3.4 億公里，離太陽最遠時約 3.5 億公里。

蔣偉寧回憶李國鼎博學多聞，從天文、地理、經濟到科技都能侃侃而談，而李國鼎以天下爲已任的政

務官風範，更是現代社會難見，希望透過小行星命名活動，流傳李國鼎的貢獻與精神。

「李國鼎一生忠於國家。」曾中風的前行政院秘書長王昭明因爲感念之情，今天抱病前來，他跟隨李國鼎近一甲子，形容李國鼎做事精神令人感佩，從經濟、科技、人文道德著力，對台灣貢獻良多。

「以父親的名字命名小行星，對我們家人是很大的安慰。」李國鼎之子李永昌說，李國鼎一生爲國，和同事相處的時間，恐怕還多過家人。

中央大學鹿林天文所每天觀測小行星，至今已有約 20 顆小行星獲得永久命名，曾以「沈君山」、「鄒族」、「玉山」、「雲門」、「中大」等名稱，命名小行星。

原文轉載自【2011-01-26/台灣醒報】

中大發現小行星　命名李國鼎

中央大學選在「台灣科技之父」李國鼎 101 歲冥誕前夕，將 2008 年發現、編號 239611 的小行星命名爲「李國鼎小行星（Likwohting）」。

中央大學校長蔣偉寧表示，這顆小行星是透過中央大學鹿林天文台，在 2008 年 10 月 23 日由蕭翔耀和葉泉志發現，2010 年 12 月經過國際天文學聯合會確認通過，正式命名爲「李國鼎小行星」。

李國鼎的兒子李永昌表示，他父親逝世 10 年之際，天上竟多了顆以父親爲名的星星，不僅相當神奇，也是家人最大的安慰。

（圖：中央大學提供／文：記者湯佳玲）

原文轉載自【2011-01-27/自由時報/A10 版/生活新聞】

想他，抬頭看　天上有顆小行星　就叫李國鼎

【記者林進修／台北報導】

仰望蒼穹，今後將多一顆以台灣名人命名的星球。中央大學選在「台灣科技之父」李國鼎 101 歲冥誕前夕，今天將一顆 2008 年 10 月 23 日發現、編號 239611 的小行星，以「李國鼎」之名命名，李國鼎的兒子李永昌在場見證。

今天的命名典禮選在台北市泰安街李國鼎故居舉行。中央大學校長蔣偉寧表示，這顆小行星於 2010 年 12 月經國際天文學聯合會確認通過，命名爲「李國鼎小行星」(Likwohting)。

蔣偉寧指出，李國鼎是中央大學校友，早年在位於南京的中大物理系就讀時，非常喜歡天文學，生平第一篇論文「太陽運動之絕頂」，正是與天文相關。如今以他之名來命名小行星，表彰並感念他對台灣的不朽貢獻。

中央大學鹿林巡天計畫，透過鹿林天文台的 40 公分望遠鏡，至今已找到 800 多顆小行星，其中 14 顆已正式命名。李國鼎小行星即是顆最新命名的小行星，由蕭翔耀、葉泉志兩名觀測者共同發現。

李永昌表示，他父親逝世 10 年之際，天上竟多了顆以他爲名的星星，不僅相當神奇，也帶給他們家人最大的安慰。

◎Likwohting
李國鼎行星小檔案
2008 年 10 月 23 日發現，編號 239611 的李國鼎小行星，位於火星及木星之間的小行星帶，繞著太陽轉，繞太陽一周約 3.48 年，距太陽最接近時約 3.4 億公里，距離最遠時約 3.5 億公里，直徑大小約 2 公里。它被發現時，位置在金牛座，目前則運行到人馬座。

原文轉載自【2011-01-26/聯合晚報/A8 版/生活】

感念 K.T.貢獻　小行星命名「李國鼎」

李宗祐／台北報導

明天是台灣「科技教父」李國鼎一〇一歲冥誕，中央大學昨日宣布，國際天文學聯合會已通過將鹿林天文台發現的編號 239611 號小行星，命名爲「Likwohting」（李國鼎），彰顯他對台灣經濟發展的卓越貢獻！

中央大學鹿林天文台已陸續觀測發現八百多顆小行星，十四顆已正式命名，「李國鼎小行星」是該校首度以校友之名命名。這顆小行星於二〇〇八年十月廿三日，由鹿林天文台觀測員蕭翔耀和中國大陸天文愛好者葉泉志在金牛座附近發現，目前位於人馬座。

中大天文研究所長周翊說，「李國鼎小行星」直徑約二公里，繞行太陽一圈約須三・四八年，距離太陽最近約三・四億公里，最遠約三・五億公里。

李國鼎的兒子李永昌昨日應邀出席命名記者會，他表示，父親逝世十年之際，天上多了顆以他爲名的星星，實在很神奇，也帶給家人很大的安慰。李國鼎生前多位門生故舊昨日出席見證，跟隨李國鼎近半個世紀的行政院前書長王昭明已九十一歲高齡，又曾二度中風，昨日出席時仍精神奕奕，兩人情誼令人動容。

中大天文研究所教授兼台灣聯合大學系統副校長葉永烜強調，一個人的價值不在於他擁有多少財富，而是看他「散播」什麼給國家社會。李國鼎就讀中央大學物理系時，立志成爲天文學家，但他後來放棄夢想，卻成就台灣的經濟發展，對國家社會做出更大貢獻。

中大校長蔣偉寧表示，李國鼎雖已辭世，但他對科技產業的貢獻已成爲台灣整體發展的記憶與經驗，活在大家身邊。以「李國鼎」命名國人發現的小行星，正足以表彰感念他對台灣的貢獻。

原文轉載自【2011-01-27/中國時報/A5 版/話題】

科博館長交接　天文學博士孫維新接棒

【陳界良／台中報導】

國立自然科學博物館十七日舉行新、卸任館長交接典禮，卸任館長張天傑將歸建回中興大學任教，由曾在美國太空總署等單位任職的天文學博士孫維新接棒；孫維新表示，未來將引進更多基礎科學的內容，及新穎、有趣的展示方法。

科博館長交接典禮昨在教育部次長陳益興監交下進行，行政院政務委員曾志朗等人均出席；孫維新是美國加州大學洛杉磯分校天文學博士，曾擔任美國太空總署的研究人員，回國後在中央大學、台大任教。

他曾助中央大學建立鹿林山、墾丁天文台，籌辦二〇〇五年世界物理年大型活動；在台大任教期間，他也推動兩岸合作，率學生前往青藏高原建立遠距遙控天文台，獲得台大「教學傑出獎」等肯定，並在前年擔任「全球天文年」台灣總召集人。

孫維新也以活潑、生動的方式向民眾傳遞天文知識，製作天文科學電視影集「航向宇宙深處」，獲頒「金帶獎」等獎項肯定；他表示，接任後將籌劃科博館未來十年發展方向，引進更多基礎科學教育，及國際上新穎的展示方法，讓科博館展現全新風貌。

原文轉載自【2011-01-18/中國時報/C2 版/中彰投新聞】

接掌科博館　孫維新　要讓科學變親和

【記者蔡佳妤／台中報導】

國立自然科學博物館館長昨天交接，台大物理所教授孫維新從卸任館長張天傑手中接過印信，表示「千斤重擔落在身上」；年輕時曾和演藝圈擦身而過的他，是台風極佳的演講高手，希望上任後讓科博館為大眾「解惑」，培養會說故事的人才，深入淺出話科學。

張天傑原為中興大學教授，九十七年接任科博館長，翌年獲得教育部政府服務品質獎。由於他任內曾有遊客爬上館內展示恐龍拍照跌落求償，讓他無時無刻不擔心入館遊客的安全，昨天卸任館長職務後，他打趣說：「以後不用再心驚膽顫了！」

孫維新則說，被告知要接張天傑的棒子時，一度覺得「不知所措」，但很快就想到，除了可延續科博館擅長動物、植物和礦物等領域，他希望再引進自己專長的天文、物理等基礎科學，讓民眾體會天空之美和宇宙之氣。

他說，上任後最重要的目標，是要讓科學教育變得有趣、不再冷冰冰。他想多辦活動、吸引民眾參加，並培養一批會說故事的人，以深入淺出方式解釋科學，讓非理工學生也能聽得懂、產生興趣。

他說，曾有學生告訴他：「學物理前，人生是黑白的；學物理後，人生變成全黑的」，他認為台灣的科學教育還有改革空間，必須想辦法讓學生對科學產生興趣，才能不斷累積知識，「強灌入腦袋的知識，考完試就會忘記」。

除科學教育，孫維新還想讓科博館提供「解惑」的任務。他認為，社會上的怪力亂神太多，他希望針對許多民眾的迷思多辦展覽，例如外星人，他相信偌大宇宙應有外星人，但目前仍沒有足夠證據證明外星人來過地球，科博館就可以科學角度提出公平合理的分析，解釋這些未知現象。

孫維新是美國加州大學洛杉磯分校（ＵＣＬＡ）天文學博士，曾擔任美國太空總署（ＮＡＳＡ）研究員，回國後先後在中央大學、台大任教。

他從小就有演戲天份，小六就被老師選中參加兒童電視劇演出，大學時還擔任國劇社長，曾和劉德凱、歸亞蕾等人同台演出白先勇小說「遊園驚夢」改編的舞台劇。之後有人找他進演藝圈，因不想當武俠明星而婉拒，但這段經歷卻讓他學會把舞台技巧運用在講台上，更吸引學生注意，使他深受學生歡迎，引領許多學生成為天文迷。

教學之外，孫維新也積極參與天文科學教育推廣，常藉寫作和廣電媒體，以深入淺出、活潑生動的方式傳遞天文知識，獲不少獎項。

原文轉載自【2011-01-18/聯合報/A14 版/文化】

葉永烜玉山油畫展　玉山藝廊展出

【大紀元 2010 年 12 月 30 日訊】

(大紀元記者林萌騫台灣南投報導)為慶祝中華民國精彩 100 年，玉山國家公園管理處特別於 30 日上午 11 時，在水里遊客中心玉山藝廊舉辦「江山萬里行之悠然見玉山--葉永烜油畫創作」特展開幕儀式，這項特展的展期將持續 3 個多月，到 100 年 4 月 7 日止。

台灣玉山，目前已晉級為新世界七大自然奇景 28 景點之列，正激烈票選中；為提供遊客更多樣性的認識玉山，玉管處特別規劃藉由油畫的觀點，呈現玉山另一種藝術之美。遊客進入玉山園區前，先在玉管處遊客中心欣賞油畫悠然見玉山美的藝術，心靈美感的提升會有很大的收穫。

玉管處指出，水里遊客中心內「玉山藝廊」展區，從 30 日起展出葉永烜教授「江山萬里行之悠然見玉山油畫創作」，葉教授目前擔任臺灣聯合大學(中央、清大、交大、陽明大學)系統副校長工作，他於 1987 年開始油畫創作，內容包括風景、人物和花卉靜物等作品，希望藉由視覺影像創作增進對大自然藝術品的鑑賞、增加生態藝術涵養。本次葉教授特別精選 16 件玉山地區週邊風采為主軸作品展出，與大眾分享。

本次特展展期將自 99 年 12 月 30 日~100 年 4 月 7 日止，為期 3 個多月，除了呈現中華民國精彩 100 的意涵外，也讓國家公園美學藝術能與國人心靈相契合，玉管處期望社會大眾、學校團體及關切玉山的朋友們，能來參與這場文化藝術的饗宴。

原文轉載自【2010-12-30/大紀元時報首頁>　副刊>　藝術網>　藝術長河>　美術長廊】

油畫木頭創意　玉山國家公園展出

【本報南投訊】國際知名天文學家葉永烜即日起在玉山國家公園展出玉山與台灣寶島油畫創作。

作品包括雲擁玉山、雪封玉山、還有蘭嶼曙光、黃金海峽等十六幅作品，從光影與色彩的千變萬化中，呈現只在台灣這塊寶島特有的時空之旅。

葉永烜教授說：「我覺得太空裡大部分是單調的黑色，二十三年前開始創作油畫，藉著繪畫追色彩的揮灑，描繪生活中的諸多感動，常常帶著相機，捕捉殺那間的感動，化為創作靈感來源，化作永恆的記憶。」

玉山畫廊還邀請魚池鄉貓頭鷹之家女主人李豫婷率創作老師，帶著貓頭鷹創作藝術參展，作品都是利用廢棄的山林樹木樹枝等，以貓頭鷹做主題展現創意的有趣作品，包括小小花博、幸福滿門，還有逗趣的木頭創作，都很有意思。

玉管處長陳隆陞說，為提供遊客更多樣性的認識玉山，藉由油畫的觀點呈現玉山另一種藝術之美；在國家公園生態保育前提下，以廢棄木頭，提供另類的創意巧思。兩項展覽展期都到明年四月七日止。

原文轉載自【2010-12-31/人間福報/7 版/藝文】

天文學家　繪畫玉山新色彩

【記者黃宏璣／南投縣報導】

天文學者透過油畫呈現的玉山與台灣寶島，會是什麼意境？身兼業餘油畫家的中央大學天文學者葉永烜，即日起在玉管處畫廊舉辦玉山之美創作展，至明年 4 月 7 日。

「採星東籬下，悠然見玉山」這則改編陶淵明「飲酒詩」，正可形容葉永烜創作的心情故事，每幅作品都展現科學家眼中特有的玉山光影變化。

葉永烜展出的油畫創作，包括雲擁、雪封玉山，還有蘭嶼曙光、黃金海峽等 16 幅作品，特別強調光影與色彩變化，「我覺得太空裡大部份是單調的黑色，因此藉著繪畫追逐色彩」，葉永烜說，他常帶著相機，捕捉剎那間的感動，這些畫面都成為他創作靈感來源。

縣長李朝卿昨天出席創作展茶會，仔細參觀作品忍不住讚美，「天文學者提供另一個觀賞玉山之美的新視野。」

葉永烜專長慧星與行星大氣研究，去年獲美國太空總署頒給公共服務榮譽勳章，他也是業餘畫家，1996 年受邀在德國 Northeim 地方法院藝文走廊、1997 年在台灣史懷哲紀念醫院辦個展。

自幼喜歡繪畫的葉永烜，早期用畫筆，後來改用畫刀，作品多半呈現印象派畫風，這次展出作品，都是他暑假的最新力作。

原文轉載自【2010-12-31/聯合報/AA4 版/教育】

宇宙有如動物園，裡面住著形形色色的野獸，它們或許凶猛殘暴，或許柔順幽雅，我們一起逛逛吧！

文 / 張光祥

鱟的火星任務 —生命檢測器

圖2 屏東海洋生物博物館所飼養展示的成鱟（鄭宇棋攝）

一個人若從臺灣的平原直登上3000公尺以上大山，生態環境的改變就像從北回歸線到北極圈一樣劇烈，這也造就了寶島臺灣多變的自然環境與極為豐沛的生物資源。臺灣現存極為古老的一種生物《鱟》，將成為全球太空計畫探索外星生命的重要物種。

移民火星是小學生最感興趣的話題

中央大學天文所經常為國小學童辦理天文科普活動，在活動中學童常提問火星生命與移民火星相關問題；有一段對話是很有趣的:如果將來到達火星的第一任務是什麼呢？童言童語的回答是:要建氧氣倉、儲水倉與種樹，我開玩笑地說，要記得於農曆春節，打個電話給老師，小學生馬上天真地問，老師的手機號碼是多少？我說是0910----小朋友立刻抄起電話，我最後補上一句，屆時從火星撥出要加星碼(地球)910----喔！

圖1 小學童參觀中央大學校區天文臺

最近，英國知名天文物理學家史蒂芬．霍金（Stephen Hawking）警告，人類正進入「歷史上越來越危險的時代」，除非在接下來兩個世紀內殖民外太空，不然就將會永遠消失。人類能長存的唯一機會就是搬離地球，而本世紀內最可能移民的星球即是火星。

雖然臺灣目前未參與火星任務，但臺灣現存極為古老的一種生物「鱟」卻可以幫大家圓了這個火星夢，未來NASA計畫將鱟的血液帶上火星，進行生命跡象的探測。鱟將遠赴美國航空暨太空總署NASA，揭開這個令人歎為觀止的太空任務。

鱟有鐵甲武士、活化石的稱號，因一公一母成對生活，又被稱為鴛鴦魚。它的存在最能反映

出潮間帶的健康與否，一處海域如有鱟生活其中，代表該處水域環境純淨。沙質的淺水海域是牠們的棲息地，每一隻鱟魚都要經過十多次的蛻皮才會成體。不過，這些需要十多年長成的鱟魚，現在因為棲息地被破壞以及水的污染，讓鱟魚的數量越來越少，已經瀕臨滅種的危機。根據中央研究院生物多樣性研究中心於2002～2008 年的調查與採集記錄發現，許多原有三棘鱟分佈的地區，鱟被發現的頻率變少、分佈的範圍變小，甚至有些區域已經幾乎不再有鱟的觀察記錄。

但處境危急的鱟卻帶給人類另一種科學價值，鱟因血液特殊，含有內毒螯合酵素，不像其他動物都是帶鐵、呈現紅色，而是帶銅、呈現藍色，遇到細菌中的內毒素會有交結現象，可正確與可溶性蛋白凝固產生反應，廣泛使用在葡萄糖、生理食鹽水細菌檢驗上，鱟血液經過科學證實，可快速檢驗毒素，而美國太空總署火星生物研究計畫，也必須仰賴鱟生物試劑檢驗。

圖 4、LOCAD-PTS：移動式單晶片應用與檢測系統。圖像來源：NASA。

2006年十二月，一種利用鱟的血液特性開發的掌上型細菌探測儀（LOCAD-PTS）首次搭乘太空梭 STS – 116升上太空，在國際太空站裏被科學家們進行測試。LOCAD-PTS的全稱是Lab-On-a-Chip Application Development-Portable Test System，意為“晶片實驗室應用開發-可攜式測試系統”。LOCAD基於四種由鱟的血液裏提取的酶進行工作。首先，少量的酶被注入測試管，並

圖 3、三棘鱟在台灣地區的歷史分佈與目前分佈圖

被烘乾；當液體樣本需要被測試時，將液體導入測試管，其水份使本來乾的酶又恢復活性，如果樣本內含有細菌，其毒性就會啓動酶，進而改變液體樣本的顏色。顏色變化的程度取決於細菌的數量—細菌數量越多，顏色變化越大；反之亦然。由於鱟血液的高度靈敏性，單個細菌的出現就足以引發血液內酶被啓動，使得LOCAD可以被做成這樣小巧玲瓏而又高效率的裝置。傳統的細菌測試方法是讓從病人身上取得血液或尿液樣本在實驗室培養皿內的某種培養基中生長，兩到三天後，可以得到結果，決定感染是由病毒引起，還是由抗生素可以對付的某種細菌或真菌引起。但無論是在載人還是無人的太空計畫中，兩三天的時間都太長了。相比之下，LOCAD只需要5-15分鐘就能給出結果，而且非常精確，即使單個細菌也能被測試出來。

鱟在分類上屬於節肢動物門三棘鱟（Tachypleus tridentatus，Leach， 1891）曾經廣泛地分佈在臺灣本島、澎湖、金門的沙泥海岸，早年與人民的生活密不可分，包括：鱟卵醃醬、如意鱟殼杓、鱟殼炒蚵面、虎頭牌…等，更是潮間帶是否健全的指標；但是，因為人類捕殺、填海造陸、興建海堤、不當地投放消波塊等對鱟棲

地（產卵場等）的破壞，鱟在臺灣本島已經幾乎不見蹤跡，且民間仍然有吃鱟的傳統習慣；目前野生的鱟族群僅零星分佈於金門、澎湖一帶。海峽兩岸之廈門、金門應合作推動對這種有滅絕之虞的珍稀物種積極複育與保護工作。農委會特在澎湖縣成立了一個保育中心。另外在“中央研究院”的生物多樣性研究中心，亦有專研人工繁育的實驗室(如圖5)。最後，衷心期待在未來，我們能幫鱟保存良好的生存空間，並期待鱟能協助人類找到可移民外太空的行星，共同延續生命。

參考資料：

中央研究院生物多樣性研究中心陳章波研究員 陳佳宜助理研究文獻

張光祥: 國立中央大學天文研究所技士

鱟於每天10點餵食一次

稚鱟分組養殖盆

圖5中央研究院生物多樣性研究中心稚鱟養殖實驗室

龍山寺的門柱石刻圖

鹿林天文台、小行星和台灣物理學之父

台灣天文發展雖最早可追溯至日據時代，但是一九九〇年代，中央大學在鹿林山開始籌備建立一米望遠鏡的天文台，才真正起步，而面對世界諸多大型望遠鏡的競爭，鹿林天文台居然成就傲人，嶄露頭角。目前他們準備更上層樓，籌建一具兩米的望遠鏡，發揮「以小搏大」精神，再與世界大型望遠鏡一較高下，他們也將過去發現的一顆小行星，命名為「吳大猷小行星」，一月裡將舉行頒贈儀式。

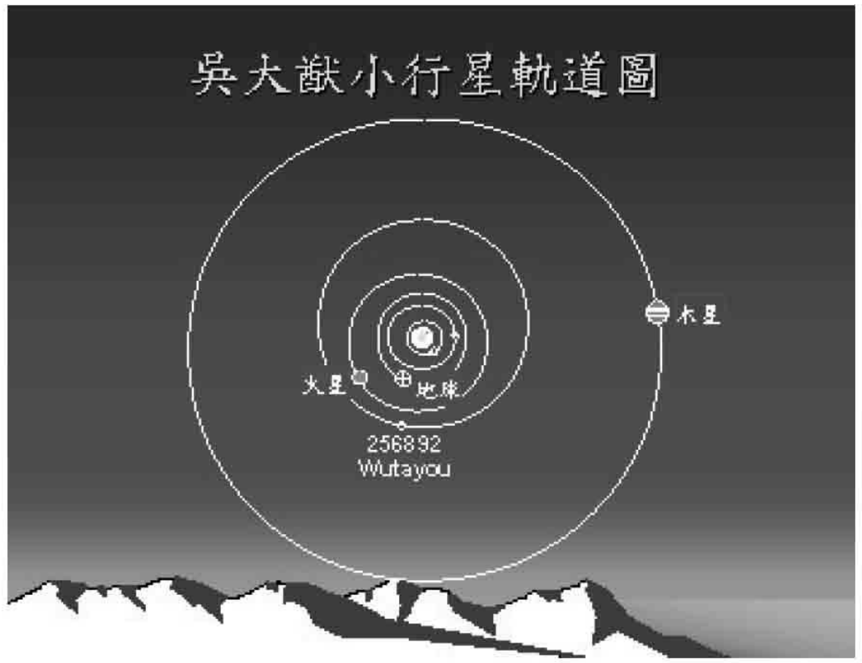

▲吳大猷小行星。

民國八十八年設立的鹿林天文台，本身沒有較大的望遠鏡，歷史也很有限，坐落點也僅海拔兩千八百米的鹿林山前，然而過去十多年，鹿林天文台本身，以及它與世界其他天文觀測機構合作，進行了許多極有創意的天文計劃，可以說將其有限的條件，發揮得淋漓盡致。

在鹿林天文台諸多發現之中，特別令人印象深刻的，是小行星的發現。由二〇〇二年發現第一顆開始，到目前已發現了八百多顆小行星，還發現一顆彗星，以及一顆近地小行星，根據國際天文學聯合會小行星中心的統計資料，鹿林天文台是亞洲發現小行星最為活躍的天文台之一，排名全球第四十七。

小行星是目前唯一可以由發現者命名的天體，其命名並可以得到世界公認。觀測到一顆小行星，通常並不能立刻確定是否為一顆新發現的小行星，因此自己會先給它一個臨時編號。要等到這顆小行星在不同夜晚再被觀測到，並報告國際小行星中心，確認是新發現的小行星之後，才會得到一個國際統一格式的「暫定編號」。

一顆小行星至少要在回歸中觀測到四次，並精確測定其運行軌道的參數，才能夠得到永久編號。小行星的發現者擁有對該星的命名權，在十年內隨時可以行使，但是小行星命名，還須要報經國際天文學聯合會小行星中心和小天體命名委員會審議通過，才能公諸於世，成為該天體的永久名字，並為世界各國公認。

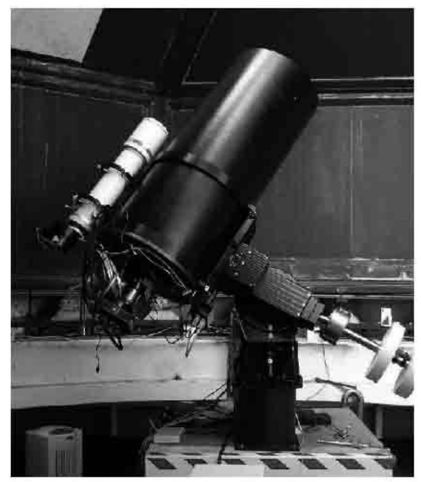
▲以小搏大的鹿林天文台。

相較於近年來國際上提出的大型天文計劃，在傳說中群鹿如林鹿林山上的天文台，可以說是一個規模很小的天文觀測點，但是處身於台灣的群山之中，又鄰近玉山國家公園的無光塵害清朗天空環境，可以說有極佳的觀測優勢。另外台灣接近赤道的低緯度，可以觀測包括南天球天體的廣闊天域，是日本、韓國等高緯度國家所不及，而位處夏威夷大天文台群以西經度的觀測點，也造就鹿林天文台國際觀測上舉足輕重的地位。

但是這個以「鹿」為命的天文台，卻也是一個沒有「路」的天文台，雖然通過環境生態評估而能興建，但由於法規限制，建設至今十餘年，仍然沒有通往鹿林天文台的道路，是世上少數幾個沒有路的天文台。

一個沒有道路到達的天文台，其建設材料和設備運輸的困難，可想而知。過去歷經的三年選址、四年規劃、五年建設，目前還是面臨沒有簡易道路運輸儀器與民生補給品的困境。在這樣一個困境之中，鹿林天文台由二〇〇六年開始的「鹿林巡天計畫」，還是以四十一公分的小型望遠鏡，做出了令人驚豔的成績，和美國的五大巡天計劃相比，雖然設備經費遠遜，是「小

蝦米對大鯨魚」，但是在這個世界的舞台上，「我們沒有缺席！」

未來鹿林天文台將投資兩億三千萬經費，建造兩米的望遠鏡，這項中央大學必須自籌一半費用的天文計劃，未來將成為有多國研究團體之「泛星計畫」的重要成員，一過去輝煌的成就，繼續追尋太空中的未知天體。此一計畫不但在觀測和儀器方面，有很大挑戰，計畫成員過去也已經交出亮麗的成績，發表重要的論文。

一個好的科學計畫，要有好的科學目標，以及好的科學研究成員。也許是這樣的一個原因，他們最近將二〇〇八年發現的二五六八九二小行星，命名為「吳大猷小行星」，紀念和表彰一位傑出的物理科學家。

吳大猷一九三三年在美國密西根大學拿到理論物理學博士，是中國的第三位理論物理學博士，他很快回到北京大學任教。一九三八年以後，吳大猷在對日抗戰期間的昆明西南聯大任教，而一直傳為美談的是，他教出了楊振寧和李政道兩位諾貝爾獎得主。吳大猷自謂不喜競爭，所以在科學上並沒有獲得特別顯赫獎項，但是他最出名的學生楊振寧，也是舉世公認的大物理學家楊振寧認為，吳大猷的物理非常的好。

▲吳大猷盡心於台灣學術。

有一個例子可以證明吳大猷的物理並非泛泛，那就吳大猷在加拿大研究期間，一次邀請英國大物理學家狄拉克（P.A.M.Dirac）往訪，兩人相談甚歡，隨後還有數封私人的信函往還，討論一些物理問題。吳大猷生前對此亦認為是他科學生涯中一件美事，這些信函目前都保存在中研院的資料檔案之中。

一九五八年胡適由美回台出任中央研究院院長，曾經請吳大猷擬定一發展科學的議案，當年就成立了「國家長期發展科學委員會」，一九六二年胡適在中研院院士會議講話時，心臟病發去世，當時蔣介石總統本意於吳大猷接任院長，吳大猷以個性不善與人及家庭原因不能返台，未能應命。

一九六七年吳大猷應請接任科學發展指導委員會主任委員，開始與聞台灣科學政策，後亦兼任國科會主任委員，到一九七三年非主動去職。一九七八年吳大猷自紐約州立大學水牛分校退休，即返回台北長居，一九八三年獲選為中央研究院院長，到一九九四年卸任。

吳大猷在台灣期間，曾經在台大和清華、交大任教，也主持物理科學教科書的編撰，他雖然不喜行政瑣務，但對科學教育和社會文化極為重視，經常在報端雜誌撰文論列，吳大猷見識不凡，文詞直率，難免得罪於人，但是他剛正不阿的學術風範，確實普遍受到社會的肯定，有人認為，他對台灣物理科學有典範人物作用，稱他為「台灣物理學之父」，可說十分允當。

二〇〇〇年吳大猷在臥病年餘後病逝，他的去世，不但是社會少了一位品味卓然的物理學家，他那樣的學人風範，亦益愈難見了。

數理基礎莫輕忽 穩紮穩打研究路

文/ 胡佳伶
蘇羿豪

求學歷程

在小學高年級到中學的這段期間，部分課程開始需要運用邏輯思考，讓我逐漸對科學產生了興趣。就讀師大附中時，因高中物理課程用到的數學工具並不多，且那時候還蠻怕數學的，所以都是勉強過關。直到大學念清華物理系，才發覺數學與物理關係密切，便在暑假自修微積分，慢慢打起了數學和物理的基礎。我在大學的時候了解到學好物理的重要性，於是物理系開的課幾乎都修。當時受到丁肇中等人在1976年獲得諾貝爾獎的影響，對基本粒子物理蠻有興趣，認為粒子物理是最重要的物理，"theory of everything"。雖然那時候比較流行固態物理及超導，但覺得自己對動手實驗不太在行，因而想做理論物理，可是那時候做理論的老師覺得這行發展有限，並不太鼓勵年輕人從事理論物理。因此當時的我還很迷惘，不確定到底要做理論還是實驗。

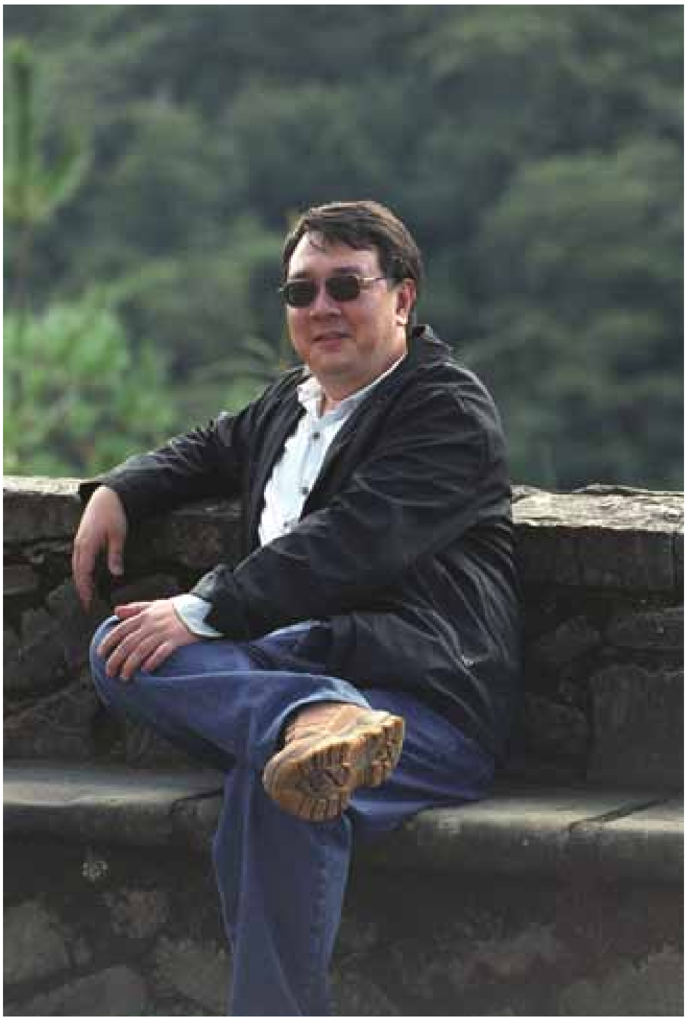

我本來就有出國攻讀研究所的打算，不過一直到大三都還沒有跟老師做過專題，覺得要有研究經驗再出國比較好，所以決定先在臺灣念研究所。剛好看到倪維斗教授在徵人，唯一的條件就是要有耐心，而且倪教授在理論物理的研究相當傑出，正開始要往重力實驗發展，於是我就進了倪老師的實驗室當研究生。

當時我們做的實驗是要測量太陽的重力對實驗裝置產生的力矩，以驗證等效原理。那時候還沒有很好的避震桌，要用沙子來減少震動，但為了避開磁場的影響，所以必須要把沙子裡的鐵吸出來，剛開始就吸了一個暑假的沙子。後來逐漸進入狀況，從倪老師與學長那邊了解到實驗的重要性，也盡量嘗試著將大學課堂上學到的知識，應用在理解發展整個實驗與後續之數據分析上，最重要的是了解究竟什麼是科學研究。

碩士畢業當完兵後，在五專一邊兼課教物理賺生活費，一邊準備申請學校，也考上了公費留學考試。我申請了二十幾家學校，獲得其中三家的入學許可，但之前的迷惘還是沒有解決，依然不知道自己到底要做什麼，即便對粒子物理有興趣，但做理論的老師勸我不要做理論，因為理論和實驗的差距已經很大，所以我選擇進入哈佛大學往粒子物理實驗發展。當時參與了一個在紐約中部康乃爾的高能團隊，但加入了之後發覺跟

想像差異很大，高能實驗的陣容龐大，一個團隊有兩百多人，自覺發揮空間有限，後來便離開了。正在茫然時，恰巧我博士班的指導老師是天文系的教授，想找物理系的學生幫他做儀器，並且希望這個學生對高能實驗有興趣。那時候的我其實希望趕快定下來展開研究工作，就這樣跨入了天文的領域，剛開始也因為對天文還不太熟悉，著實經歷了一段蠻辛苦的時間。做儀器很不容易發表期刊論文，所以指導教授給了我兩個純天文的題目，到現在都還是我的研究主題－這是因為從事了X光雙星的研究之後，覺得很有興趣，並從中獲得了成就感，於是就一直往下鑽研下去。我們做的儀器是一個放在氣球上的X光望遠鏡，在博士生涯去了七次新墨西哥州放氣球，成功了三次。此外，我的工作還包含了儀器的後續進展、分析軟體、資料分析，到我畢業以後，這部望遠鏡也正式退休，在我離開美國前一個月，送著它進倉庫裡。

博士畢業之後開始找工作，我拿的J1簽證，可以留在美國一年半做practical training，實際應用所學。那時候跟指導教授商量，希望留在他那邊做博士後研究，不過他說博士後需做三四年左右才比較可能有點結果出來。另外一方面，我希望做科學的計畫，但他比較看重我對儀器的經驗，最終沒有談攏。於是我就寫信給在清華的指導教授，倪老師很大方地說他有博士後的位置，叫我先回來再說。

九月回台灣之後，先在倪老師那當博士後，也一邊找工作。在那邊先把我之前的論文完成，也指導研究生利用X光波段的天文資料做研究。那時候物理系徵人很多都要有光電、奈米專長，我只投了成大物理、清華天文、中央天文這三所學校。投中央的時候很有趣，之前有到過中央演講，後來看到中央在徵人，趕快寄履歷給當時的所長陳文屏老師，過了幾天再看一下，發現是去年的告示，我就寫信給陳老師說不好意思，沒注意到那是去年的告示，請撤回我的申請。陳老師說不要緊、既來之則安之，又找了我來中央做一次演講，葉永烜老師、陳文屏老師都有再跟我談，隔年八月就加入中央大學。

周翊老師在中央大學天文所高能天文物理實驗室

目前做的天文研究

目前的研究著重於X光雙星的光變行為，研究緻密天體（包含中子星與黑洞）、吸積雙星與吸積盤動力學等天文物理現象。X光雙星中的主星—中子星或黑洞—是大質量恆星演化的終點，對 X 光雙星系統的深入研究，可以讓我們對恆星演化末期的特性有更進一步的了解。

在中子星方面的研究，除了脈衝星外，探討以中子星為主星的X光雙星也是重要的研究手段，天文學家可藉由雙星軌道與吸積盤的運行、X光雙星中的波霎現象、X 光爆發與準週期振盪等現像，來研究中子星的性質與演化。

在黑洞方面的研究，由於黑洞本身不會發出可觀測的電磁輻射，因此我們必須觀察吸積現象所引發出的輻射才能瞭解黑洞性質，X光雙星是目前唯一可用來觀測恆星質量大小黑洞的天體。研究吸積盤運動與雙星之間的關係，可以對緻密星體有更進一步的認知，此外，X光雙星擁有實驗室無法製造的環境，如極大重力場、極強磁場（中子星，10^{8}–10^{13} G）與極高溫（$> 10^{6}$ K），可成為研究基本物理定律（如廣義相對論等）的重要工具。

現在下載archive data已經相當容易，因此我們可以利用最新的觀測資料做研究。X光雙星的光變有的非常快，甚至小於一個毫秒，可以說是所有天文現象中最快的光變，但時間尺度也可以很長，不同的時間尺度代表了不同的物理機制。

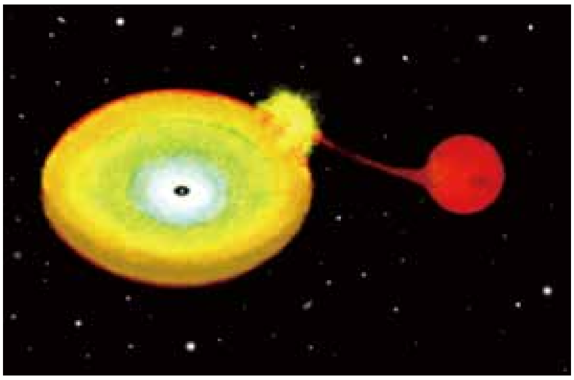

一個X射線雙星X 1916-053的藝術家想像圖。它是由一顆白矮星（右）與一顆中子星（左）組成的雙星系統，當白矮星的物質被吸積到中子星時，由於物質帶有一定大小的角動量，吸積時會形成吸積盤。

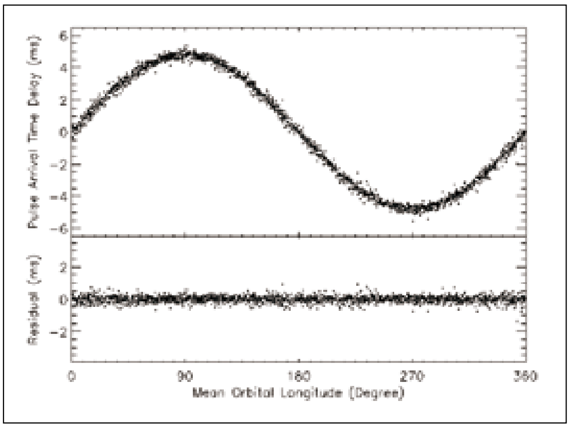

吸積脈衝星 XTE J1807-294 之脈衝由於雙星軌道運動產生的脈衝延遲現象，由此現象可算出以雙星的軌道周期為 40.073601+/-0.000008 分鐘，而中子星之投影軌道半徑為 0.004823+/-0.000005 光秒，就是大約只有 1450 公里左右。下圖為減去其軌道脈衝延遲現象後殘餘數值，可用以檢驗上述分析結果是否正確。

另外羿豪也幫我們開拓了另一個方向，利用光譜的擬合分析去做一些分析研究。

對想念天文所碩班或博班學生的建議

要將數學和物理的基礎打好，這些基本知識會在不經意時發揮功用。比如說我的碩士研究是做重力實驗，好像根本用不著學電動力學。我們的實驗裝置是根據前人的經驗呈三角形對稱的設計，那時候學長就說這樣會讓重力的力矩效應降到八極以下，八極我聽得懂，根據電動力學的概念，偶極、四極、八極的potential和距離的關係，分別是和距離的二次方、三次方、四次方成反比。當降到八極時，potential受距離的影響已經很小了，但我卻不知道為什麼這樣配置就會降到八極以下？但因為我有學過電動力學，我可以自己證明！我不只是know how，我還證明了這句話沒有錯。類似的一個例子，當時這個裝置是由做光學的施宙聰教授設計，雷射光打進來，把CCD擺在凸透鏡的焦點，就可以由偏移測量出角度。但同樣的問題又來了，為什麼要這麼做？我利用幾何光學學過的ray-tracing matrix，就可以導出來的確是這樣沒錯。另一個例子是念博士班的時候要設計一個電路，必須要先做些計算模擬，把電路解出來，最後用到的方法就是數學學到的Green’s function來解微分方程，將它應用到數值模擬上，最後加上可能的noise，預測其response與進一步改善其系統，雖然這些東西在某些人看起來沒甚麼，但我卻做得很有興趣，因為我是完全從我了解的知識出發，因此能掌握所有的細節過程。

現在學的基礎知識，雖然好像對目前的研究看起來沒什麼用，但當你遇到困難，就會需要這些基礎知識發揮作用。做天文可能稍微不一樣，如果你是在做物理的實驗室，你會發現你一天到晚在做的好像不是物理，像我那時候就是在fighting with noise，我的電路裡有noise會影響讀出，一搞就搞掉半年八個月，那時候就會覺得自己物理學的量子力學、電動力學，全都使不上力。其實這些都是做研究必經的訓練過程，碰到困難要想辦法解決，並不是說一開始做研究就要做大學問，就像學剪頭髮，也是要從學徒慢慢做起，先磨刀燒水，看師傅怎麼剪頭髮，過了好幾年才能出師，做研究也是類似的道理。

一句話裡面所隱藏的意義，有著不同基礎的人會有不同的感受。例如剛剛那句「這樣的設計可以讓力矩效應降到八極以下」，完全沒有學過的人只能覆誦這句話，並不懂這句話的妙處在哪；有背景的人就聽得懂這句話背後的內涵，或者是更進一步的證明。我現在常聽到「大家都認為是這樣…」，就繼續跟著前人的方法做，你只

周老師及實驗室成員向剛入學的新生介紹研究內容

周老師及實驗室成員參加物理年會

是know how，you don’t know why。就算以後有了好的工具可以改進流程，你也不知道要怎麼做。如果你具備基礎的知識，便能藉由理性批判的過程，對整個物理和處理的流程有了很深的認識，這樣才有發展的空間。

我開的課「資料分析」，從來不講任何一個套裝軟體，因為這些套裝軟體都會過時。我教的是基本的原理，比如你做curve fitting，為什麼要這樣做，會引發什麼樣的結論，大家會用什麼表示方法，會隱含什麼意義，背後都有一套很深的理論。基礎的東西可能沒那麼簡單，學起來又蠻痛苦的，但是卻很重要。像我念博士班的labmate是天文所的，他們也修物理系開的電動力學、量子力學，有的時候這些課不光只是知識，而是要給你一些想像、思考、解決問題的訓練。

對碩班及博班的期待

用寫字來做個比喻，碩士班就像教小孩寫字，我們會寫好讓他照著描，如果不行的話爸媽會拉著你的手寫；我會看著你的工作進展，不行的時候會插手進來，讓你走到正確的方向。博士班的話，就是告訴你方向在那邊，你得要自己找路，我只是在旁邊看著，非不得以不講話；就像你寫字，我只是就看著你寫，寫不好我就告訴你這裡寫不好，不再給示範。博士班畢業後，就是要自己去找方向。

對出國念博士班的建議

每個人的家庭因素、經濟因素等情況不太一樣，各有各的好處。在國內念的好處是可以繼續原本做的研究，如果表現傑出，在本土學術界的人脈會是很好的延續。現在不少很好的國立大學，也有本土的博士拿到教職。但你也必須很努力，爭取國際的能見度，一旦你有發表論文，跟你研究領域相近的人很快就會來跟你討論。但整體來說國內的資源還是稍嫌不足，國內對學生蠻保護的，在同樣的一個環境待久了，也會比較怠惰。去國外念可以接觸到比較好的環境，你的老師會是世界一流的研究學者，你的同學是來自世界各地的精英，可以知道頂尖的研究，並從中學習。當然這也要經過很多關卡，像是在出國之前，必須把語言能力提升到一個程度，剛開始可能會比較辛苦，要適應當地的氣候、文化、做人做事的方法等等。

中央天文所的優勢與未來期望

中央天文所有優秀的傳統，在一般社會大眾的心裡有比較深刻的印象，現在其他大學也都紛紛成立天文所，有些學生會覺得選校比選系更重要，而其他學校在學生心目中的地位比較好，因此中央天文所也面臨了挑戰。但這是良性的競爭，我們要更努力、做的更好。目前所裡面接了一些大型計畫，藉由這些大型計畫，我們把中央天文所在國際的能見度更加發揚，擴大天文在台

天文所共同慶賀周翊老師結婚的盛大場面

實驗室成員慶祝周老師的生日

周老師私底下其實是個冷面笑匠呢！

灣的研究基礎，培養許多的人才，也希望這些學生可以繼續在學術領域發揮所長，這也是我們努力的方向。

中央天文所對天文推廣教育扮演的角色

世界頂尖的研究機構像是CfA(Havard-Smithsonia Center for Astrophysics)、大型的天文台，也都有在做推廣教育，這是責無旁貸的，像中研院天文所現在也有專人在負責。中央天文所過去也一直有在做天文推廣教育，未來也會繼續。但我希望能夠做到，讓社會知道中央天文所是有尖端研究的，而不是只是單純地散播課本的知識，或是當有科學新聞出來了幫大家解釋。畢竟我們拿了國家社會不少資源，有責任要跟國人報告我們做了哪些研究，獲得了什麼成果，這樣將來社會才會對天文的發展更加支持。

擔任中央天文所所長一年半以來的感想

所長是個服務性的工作，任務是要讓所上事務正常運行，雖然有權分配資源，但更要公平處理事情。我們的所比較小，因此老師們擔的責任也更多，幸運的是所裡的助理幫了很多的忙，老師們也能諒解行政工作不易之處。之前擔任大學物理系學會會長與哈佛大學同學會會長的經驗，也讓我學到「人和」很重要，要比較圓潤，事情才能做通。有些事情會有一定的困難存在，但要努力在現有的資源規範下，發揮最大的效能、推動事情的進展，對於這方面，就像我的研究與教學一樣，仍在學習中。

胡佳伶：現任職於臺北市立天文科學教育館
國立中央天文所碩士班學生
蘇羿豪：國立中央天文所碩士班學生

掩星計畫的推手
—李太楓院士專訪節錄

李太楓院士專長天文及地球科學同位素研究，曾任本所籌備處主任並獲頒多項國際研究獎項與榮譽頭銜。本所掩星計畫，無論是一代（TAOS-1）或二代（TAOS-2），他都是重要的推手。

圖說：利用直升機吊運TAOS望遠鏡至鹿林天文台，在沒有路到達天文台的情況下，大部份設備皆由人力搬運。©中研院天文所

掩星計畫的緣起

李：掩星計畫最早是Charles Alcock博士提出的（註），目的是要觀測太陽系外圍的古柏帶天體（KBO）。然而，觀測很困難，因為掩星過程的光度不是變亮，而是變暗；而且KBO很小，掩星過程很短，平均只有0.2秒。也因為掩星現象極稀少，所以一地點估計至少得擺三台50公分望遠鏡同步監測以減低誤判機率。

三台望遠鏡，美國勞侖斯利福摩國家實驗室率先贊助其一，為了其它兩台，Alcock來到台灣找當時本所籌備處主任魯國鏞籌措經費。臺灣受限於天候條件，重要大型的天文觀測計畫都無法在此進行，掩星計畫是比較可行的題目。於是藉此機會，我們要求將望遠鏡蓋在臺灣。本所與中央大學各認領一台，後來韓國延世大學加入行列，認領了第四台。

掩星計畫的困難

TAOS-1觀測成果未如預期，儀器極限和臺灣天候限制是主要因素。

李：望遠鏡原本計畫放在海拔高、較不受天候或光害干擾的玉山北峰。然而北峰無路可運，搬運儀器有實際上的困難，於是改置中央大學的鹿林前山天文臺。然而當地氣候影響果然很大，鹿林常位處雲層中，溫度很接近露點，是全臺霧氣最大的地方之一。而TAOS望遠鏡的廣角鏡面一旦水氣凝結便無法進行觀測，相對濕度一旦超過85、90%就得關閉遮罩，一年下來可觀測時間只剩2~3個月。此外嘉義那邊來的光害和空氣污染，也提高了觀測的背景雜訊。美方簽約廠商的望遠鏡設計也有瑕疵，聚焦能力不夠，成像銳利度達不到規格，即使我們已經想盡辦法補強，成像效果還是差了將近10倍。

圖說：TAOS成員合照，由右至左：張書豪、溫志懿、陳文屏、王祥宇、Andy Szentgyorgyi之子、Andy Szentgyorgyi、Matt Lehner、李太楓、Tim Norton、賀曾樸、金升光、Charles Alcock、Paula Granados、張智威、嚴萃玲、汪仁鴻、Santiago Torres。©中研院天文所

二代掩星計畫

掩星觀測還是很重要，針對問題進行修正後，二代掩星計畫（TAOS-2）即將上路。

李：TAOS-2是臺灣獨資主導的計畫，新的望遠鏡成像效果將提升200倍。由於臺灣不適合觀測，所以本次地點選在墨西哥大學天文臺。順利的話，三台TAOS-2望遠鏡一年之後便可就定位。而我對TAOS-2主要、也是最後的貢獻就是去和墨西哥人「談判」，之後的研究分析就交棒給其它後進了。

註：Charles Alcock現任哈佛史密松天文物理中心主任

（李太楓院士專訪另有網路完整版，請參閱：http://asweb.asiaa.sinica.edu.tw/。）

紮根本土 放眼世界
—王祥宇博士 談 臺灣的天文儀器研發訓練

～播種～ 從無到有

身為中研院副研究員，本所副所長王祥宇博士是很少數純粹由臺灣本土教育訓練出來，卻站上世界舞台的天文儀器研發學者。王博士在天文所從儀器研發的「一人單位」開始，10年來，他參與的光學或紅外線天文儀器跨國研發計畫，除了加速夏望遠鏡計畫（CFHT，請見100年春季號天聞季報）外，還有昴望遠鏡計畫（包括即將完成的Hyper Suprime Cam計畫與接下來的Prime Focus Spectrometer）、與第一及第二代的TAOS掩星觀測計畫。藉由國際合作，累積經驗、慢慢學習成長，之後把臺灣這邊的實驗室與研發團隊也建立起來了。

圖說：王祥宇博士近照，攝於TAOS-2預定地一墨西哥的Sierra de San Pedro Mártir國家公園。©中研院天文所

～耕耘～ 好，還要更好

誰來研發天文儀器？天文儀器領域的特別之處是涉及很廣，所以做天文儀器的人，人人背景不一、各有所長；縱然如此，大家對儀器一般概念和各設計部位卻仍得全盤認識才行。然而要做這行，即便在外國也沒有標準的訓練流程，那麼在這個領域如何裝備自己呢？首先得要充滿好奇心，就是教導自己「別把每件事都當作理所當然」，同時「不要怕學習新的東西，不要怕提問題」，會主動去想問題，勇於問問題，這樣才能很快地學到更多。

天文研究很重視想像力，天文儀器的開發還需要創新的能力，所以除了充實知識外，王博士表示「動手作的經驗和獨立建構思考能力的培養」也很重要。畢竟有些東西書裡頭不見得會提，或是僅僅以一句話帶過，等實際遇到、做了，才知道原來那句話其實很重要。透過有經驗的人來口頭傳授雖然比較容易上手，但是總是自己重複試誤、思考過後，才能有深刻的印象和經驗。

此外，天文儀器開發的目標是穩定可靠、不會壞，做出來的儀器不會拿去量產，卻會不斷地做修改，所以天文儀器成品要出來之前，都要花很長的時間在解決瑣碎問題。不過王博士認為，做好的東西最後會用在天文研究上，成就感其實是這樣來的。所以他在面試用人時，都會問應徵者是否對天文有興趣，有「興趣」，在這個領域工作才會愉快。再來就是「心態」積不積極的問題了，對自我發展與表現是否有所期許，對工作歸屬是否有認同感和熱情，這些都是在天文儀器領域堅持下去的原動力。

（王祥宇博士專訪網路完整版，請參閱：http://asweb.asiaa.sinica.edu.tw/。）

古柏帶—太陽系的「西伯利亞」

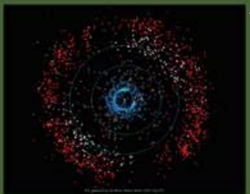

古柏帶（Kuiper Belt）通常是指太陽系內海王星軌道外的冰凍小天體所組成類似小行星帶的結構，盤狀分布在比地球到太陽的距離還遠35倍到1000倍左右的地方。古柏帶的概念最早是在1950年代由艾基渥斯（Kenneth Edgeworth）與古柏（Gerard Kuiper）兩人分別提出，希望能解釋太陽系的行星質量分布，在海王星外邊緣的現象，因此有時也稱為艾基渥斯-古柏帶（Edgeworth-Kuiper Belt）。

盤狀分布的古柏帶和距離更遠並呈球狀分布的彗星雲，也就是歐特雲（Oort Cloud）有所不同。兩者都屬於「海外天體」。在1980年代，透過電腦模擬，葉永烜等人陸續提出需要有一個盤狀分布的彗星帶存在，才能解釋軌道周期約兩百年以下短周期彗星的起源。葉永烜教授解釋，「古柏」原是高齡的參天古木，在此則意謂著，這些天體極可能保存了太陽系誕生初期所形成的最原始物質。

圖說：取自國際天文聯會小行星中心的資料，紅色點主要是分佈在海王星外到50天文單位之間的古柏帶天體。© IAU Minor Planet Center

1992年David Jewitt和Jane Luu兩人發現了冥王星家族之外的第一個古柏帶天體—1992QB1。迄今，已經發現一千多個這類的天體，估計直徑在一百公里以上的總數應該有好幾萬。古柏帶天體依照公轉軌道的特性大致可以分為數種不同的族群，例如：軌道周期與海王星軌道周期有簡單整數比關係的冥王星（Pluto）和小冥王（Plutino）等等。太陽系以外的其他恒星系統也可能有類似古柏帶的結構。（金升光 特稿）

掩星—星際魅影

當某天體被另外一個「視直徑」通常較大天體的全部或部分遮掩時，就可稱為掩星（Occultation）。

嚴格來說，日食應該算是一種標準的掩星。而月食成因是月球被地球的影子遮蔽，所以只能算是「食（Eclipse）」，與掩星並不相同。內行星（水星、金星）遮掩太陽一小部分、行星衛星通過行星盤面和系外行星部分遮掩其母恆星等現象一般皆稱為「凌（Transit）」。不過，以上三者間的界線有時候並不是那麼清楚，當然這可能也因為摻雜了些歷史的因素，例如：食雙星。還有一種「掠掩（Grazing Occultation）」是指月掩星時，沿著月球盤面邊緣不規則的山脈依次遮掩背景星的特殊現象，和日全食時候的倍里珠（Baily's Beads）有異曲同工之妙。

圖說：本圖為小行星掩住背景恆星的假想圖，圖中可見小行星影子落在地球上。如果影子正巧通過觀測站，這個掩星事件就可被偵測到。©中研院天文所

除了日食，月掩星可以算是最容易觀察的掩星現象之一。在馬王堆漢墓出土的帛書之一《天文氣象雜占》就記載有「月食星」的占象，實際上的觀測可能比史前時代就存在了。近代掩星觀測不僅可以研究遮掩天體的細節，例如：月球的山脈山谷、行星的大氣與環、小行星大小形狀等等；也可以研究被遮掩天體的特性，例如：背景星球直徑、是否有其他伴星等等。在天文干涉儀被廣泛應用以前，掩星觀測是從事這類高角解析度天文學研究的重要方法；觀測的波段也不僅限於可見光。例如，著名的活躍星系核3C 273的大小，最初就是透過無線電波段的月掩星觀測來提供線索的。（金升光 特稿）

TO INFINITY AND BEYOND!
航向天際 探索無垠
—宇宙探險幫

圖說：與天文學家對談能增進同學們對科學知識的理解，激發追求卓越的企圖。©中研院天文所

有那個幫會敢把暗物質、暗能量、黑洞、白洞、蟲洞等超級秘境全部搬來，找大家一起去探險嗎？有！那就是本所的「宇宙探險幫」。

儘管報紙新聞標題開玩笑：「中研院搞幫派！」。不過「宇宙探險幫」其實是最天真、最浪漫、最上進的團體活動。天文和物理學家除了會以科學方法來驗證未知事物，看來好像也很喜歡嘗試「撞撞看」的實驗。譬如說：「基本粒子的最小單位到底是什麼」？為了好奇，56個國家用了80億美元去～「撞粒子」。彗星的真面目？不知道？撞看看啊！於是美國NASA發射了「深度撞擊號」太空船去～「撞彗星」。同樣的，為了介紹「天文該怎麼玩」，本所廣邀全國高中以上學子來和我們的天文學家「頭好撞撞」，腦力激盪一下吧。

有機會就來和我們的天文學者互動看看。本所四海一家，有50位來自12國的外籍學者在同一屋簷下工作，而與大家一起探險宇宙的學者中不乏重量級人士，包括本所所長賀曾樸院士、特聘研究員井上允、本院年輕研究員獎得主梅津敬一等人，族繁不及備載。這些學者最熱愛的事之一就是和學生互動。與他們聊過天的同學，都對他們深入淺出的聊天介紹景仰不已。

截至目前已有各方百餘位同學參加過「宇宙探險幫」活動。想組團來宇宙探險幫「頭好撞撞」一下嗎？請上網搜索「宇宙探險幫」報名資訊，本幫與你相約宇宙大世界。　（黃珞文 特稿）

探索 人類視界從所未及之秘境
TAOS掩星觀測計畫

圖說：鹿林天文台，標高2880公尺，位於玉山國家公園。圖中右下角為中大一米望遠鏡（LOT）及控制中心，TAOS及其他計畫的望遠鏡皆散佈於此山頭。左上角為TAOS陣列中的其中一台五十公分望遠鏡©中研院天文所

太陽系的邊陲，冷峻的太空中，存在著一群緩慢繞著太陽的小天體，他們被稱為海王星外天體—Trans-Neptunian Objects（TNO），也常簡稱為海外天體。已知的TNO，主要分布在30天文單位（海王星的所在）至100天文單位的星際之間，這個區域又名古柏帶（Kuiper Belt），位在其中最著名的天體，是從太陽系行星名單被除名的冥王星（Pluto）。此區域內已知最大的兩顆矮行星分別是冥王星和鬩神星（Eris），而最小的TNO直徑約為20公里（視星等約28星等，由哈柏太空望遠鏡發現）。至於更小的天體，受限於距離的遙遠及尺寸大小，天體所反射的太陽光亮度皆無法被目前的大型地面望遠鏡或太空望遠鏡直接觀測到。因此，對於直徑比10公里還小的TNO，其數量、大小和分布，始終仍是個謎團。

於是，TAOS（Taiwanese-American Occultation Survey）掩星觀測計畫誕生了。此計畫利用TNO掩住遙遠背景恆星的方式，來偵測這些約一公里大的小天體，進一步了解古柏帶天體的大小、數量與位置分佈的關係。而藉由研究TNO的大小及數量，也可讓我們了解早期太陽系形成的過程以及TNO在組成上的物理性質。此外，利用掩星觀測推估小天體的空間分布，還可以了解太陽系各大大小小行星在動力學上的演化關係。

海王星外天體在天文學家近二十年的觀測及研究，逐漸揭開了外太陽系形成的面紗。然而隨著觀測儀器的進步，更多難解的問題也一一浮現。包括本所、中央大學、美國史密松哈佛天文物理中心、美國賓州大學、韓國延世大學在內的TAOS掩星計畫團隊，利用設置在鹿林天文台的多台小型望遠鏡協力觀測，試圖補上太陽系形成歷史中這頁遺失的篇章。（張智威 特稿）

全自動與高速測光的極限挑戰
TAOS掩星觀測系統

建構TAOS系統最大的挑戰在於如何實現全自動且高速測光的望遠鏡系統。為了偵測一閃即逝的掩星現象，必須利用三到四台望遠鏡自動觀測同一片星空，以每秒至少五次的速度量測視野中星星的亮度。這在一般的天文觀測中是很少見的。TAOS的控制軟體，是達成此一目標的重要系統。為了達成全自動的目標，TAOS系統中利用許多偵測元件得知望遠鏡以及天候的狀況，控制軟體就是利用這些資訊來決定望遠鏡的動作。

圖說：左上為在網路攝影機同時監看四台望遠鏡的截圖畫面。右上為望遠鏡主鏡支撐機構。下方是以特殊「拉鏈模式」讀取所獲得的影像，圖中由星星拖拉出來的亮線看起來就如同拉鍊般。©中研院天文所

每天日落前，控制系統會依據TAOS氣象儀器的資料決定是否自動開啓系統以及遮罩，讓系統一切就緒。再利用已排定的星場，依據月亮的位置決定觀測的天區。當天空餘光完全黯淡，系統會進行自動對焦，對焦結束後，便開始每秒五次的影像輸出。在每一個天區，這個每秒五次的速率會持續進行觀測1.5個小時，之後再移動至下一個目標天區。每個晴朗的晚上，TAOS會產生超過100GB的資料。

一般天文觀測通常要求的是長時間曝光，影像讀取時間需要好幾秒鐘。對於TAOS的快速系統，我們使用特別的讀取模式，每一次只讀取一小部分影像，以降低影像讀取時間。利用這種方式雖然可以達成5赫茲的取樣速度，但是會造成星星影像重疊以及高背景亮度的問題。針對這個問題，我們利用影像處理的程式來解決。

TAOS系統的開發，包含了許多不同的工程問題，包括光學、機械、電子、軟體以及資料儲存等。這些寶貴的經驗使我們對於正在建造中的TAOS二代（TAOS-2）計畫充滿信心。利用更大的望遠鏡與更快的取樣速度，將可以告訴我們更多太陽系形成歷史的奧秘。（王祥宇 特稿）

「黑洞獵人」即將誕生
—ALMA原型天線 本所成功接收

本所主導的國際合作團隊，前不久從三個競爭隊伍中脫穎而出，爭取到一座12米原型天線。這支天線原本是「阿塔卡瑪大型毫米及次毫米波陣列（簡稱ALMA）」的原型天線。ALMA是目前正在智利興建的巨型電波天文臺計畫，本所是透過日本和美國等合作夥伴，代表臺灣加入這個計畫的。

圖說：本所主導的VLBI團隊成功取得美國國家科學基金會授權免費使用ALMA原型天線。該座天線仍須略加改造，使性能更能適應觀測地點的寒冷氣候。
圖右三胸前掛著相機的是本所特聘研究員井上允（Makoto Inoue）；圖右一是本所法裔電子工程師馬柏翔（Pierre Martin-Cocher）。©中研院天文所

這支原型天線將會結合跨越洲際的「甚長基線干涉儀（Very Long Baseline Interferometry 簡稱VLBI）」，與另外兩個天文計畫—分別是位於夏威夷的「次毫米波陣列」(SMA)，以及位於智利的ALMA—連結成「鐵三角」，在次毫米波段進行更精確、更高解析度的天文觀測。屆時將可提供高達「20微角秒」的解析度（1微角秒=1/3,600,000,000度），相當於從地球可以看到月球上的一枚10元硬幣，這也是目前天文學家所能取得最高的角解析度。

實際上，人類過去從未真正從望遠鏡看到黑洞過，尤其是星系中心的超大質量黑洞。未來透過次毫米波VLBI鐵三角，天文學家不但可以為黑洞拍攝照片，取得存在的直接證據，還可以觀測到黑洞的強重力透鏡效應，對廣義相對論中的「強重力場」進行驗證。此外也能對超大質量黑洞的噴流做進一步研究。這座原型天線本身還可以當作單碟天線使用，能在波長很短的次毫米波或者太赫茲（THz，GHz的一千倍）波段進行很多觀測，研究宇宙中更豐富多樣的主題，包括低溫的星際氣體雲、塵埃密佈的恆星形成區，以及巨大橢圓星系核等。

可讓這個VLBI鐵三角觀測計畫發揮最大效能的最適位址，通常是寒冷、乾燥、高海拔、少光害的地區。本所目前已先於加拿大北部的尤瑞加展開基本測試，接下來打算今夏在鄰近的格陵蘭島「峰頂站臺」基地進行儀器測試。同時，我們也已開始為這支原型天線進行性能升級。

2011暑期學生計畫 火熱上路
—學生心得精選

原本認為這個暑假會是漫長且辛苦的，但進入暑期學生計畫，在許多課程、討論、資料處理中，不知不覺地時間就渡過一半了。在天文所裡認識了很多新朋友，包括來自英國、法國、日本等地的學生。每次跟他們討論事情或聊天，就又學到新的文化與思考模式。

圖說：2011暑期學生活動師生大合照，攝於中研院天文所。©中研院天文所

除了新朋友帶來新的思維，我還從每個禮拜二、四的課程中獲得很多新知識。這種主題式的課程真的讓我受益良多，而且有不清楚的問題馬上可以詢問教授們。並且，我還能跟我的指導教授討論科學、請教問題，教授也常常利用問問題的方式引領我思考，把我錯誤的地方指出來，並刺激我繼續發現那些我從來不知道的事情。除此之外，還有許多善良的學長姐願意幫助我，帶領我探索天文這個未知的領域。

在天文所的這一個月，我發現每個人都很認真地在探討科學，發掘科學。記得第一次參加的小組討論中，有教授跟我們說：不論什麼領域，如果我們想要知道更多的事情，就應該要自己去發掘、尋找，這個尋求知識的過程叫Research。另一位教授也說了同樣的話，他認為應該要自己去尋找問題，並解決問題，在Research的過程中找尋快樂和成就感。我自己在這裡的Research，雖然大部分的時候是感到挫折的，但只要有一點小進展，就會覺得總算邁出一小步，又接近自己的目標一點了。

或許這個暑期學生計畫只有短短兩個月，但我認為帶給我的影響遠超過自己摸索兩年。不論是資料的處理、團體的討論、課堂中的學習、老師的引領，我認為這些對我都非常有幫助。（暑期學生 陳姿穎）

勘誤：夏季號季報—背面宇宙圖
1、「我們所知道的宇宙」右方附圖—「WMAP衛星所偵測推估的宇宙組成比例」：暗能量與暗物質比例誤植，比例74%應是暗能量；22%是暗物質。
2、「宇宙放晴了！」左方電子濃霧插圖：「氫原子核」下方誤植成「氦原子」，應為「氫原子」。

天聞季報編輯群感謝各位閱讀本期內容。本季報由中央研究院天文所發行，旨在報導本所相關研究成果、天文動態及發表於國際的天文新知等，提供中學以上師生及一般民眾作為天文教學參考資源。歡迎各界來信給我們，提供您的迴響、讀後心得、天文問題或是建議指教。

來信請寄至『10617台北郵政23-141號信箱　中央研究院天文所天聞季報編輯小組收』；或是寄至電子信箱：outreach@asiaa.sinica.edu.tw。

發行人＼賀曾樸
執行主編＼陳筱琪
執行編輯＼曾耀寰、蔣龍毅、顏吉鴻
美術編輯＼蔡殷智
發行單位＼中央研究院天文及天文物理研究所
地址＼台北市羅斯福路四段一號天文數學館11樓
電話＼（02）2366-5452
電子信箱＼outreach@asiaa.sinica.edu.tw

背面圖版權所有＼中研院天文所
背面圖圖說＼張智威
背面圖美術製作＼蔡殷智

利用泛星計畫和鹿林一米望遠鏡

觀測極亮可見光天體*SN 2010gx*

文/ 浦田裕次
翻譯/ 莊佳蓉

超新星爆炸是天文學領域裡重要的恆星演化階段，在過程中除了產生現今宇宙的重元素，其所產生的超高動能也是形成星系的關鍵因素。超大質量恆星死亡後的高能量超新星爆炸，所產生的黑洞和相對論性噴流更被天文學家認為與伽瑪射線爆有密切關係，在近期偵測到的超高能伽瑪射線爆（~GeV），恰巧提供了與超新星爆炸有關連的證據。

現今全面性的可見光波段巡天計畫讓我們得以發現了一種新的神秘瞬變天體。這些發現徹底顛覆我們對於恆星爆發的認知，且得到一些十分值得天文學家注意的初步結論。近期發現的可見光波段超亮瞬變天體，可能與黯淡且金屬豐度低的宿主星系有關，而其中的一種成因很可能就像SN 2007bi一樣，被認為是一顆100倍太陽質量的恆星，演化之後因成對不穩定性（pair-instability）所造成的超新星爆炸。這種天體的亮度改變非常快速，而哈柏太空望遠鏡就在對星系團超新星爆炸的搜尋中，找到了這樣一顆不尋常的瞬變天體：SCP 06F6。如圖一所示，SCP 06F6在100天的觀測期中，光度變化呈現對稱，光譜中也存在寬譜線的特性，明顯與宿主星系沒有關聯。這些瞬變天體有著相同的特徵--可見光光度高（絕對星等的峰值約-21到-23，見圖一）、顏色偏藍、缺乏氫和氦的特徵譜線；而這些瞬變天體的亮度甚至比與伽瑪射線爆相關的超新星SN 1998bw還要亮上3-4個星等。近期內，泛星計畫帕洛瑪瞬變天體計畫（Palomar Transient Factory,簡稱PTF)等巡天計畫陸續展開，由於計畫剛剛開始，所以發現此類瞬變天體的事件總數仍然不多。但這些計畫不僅

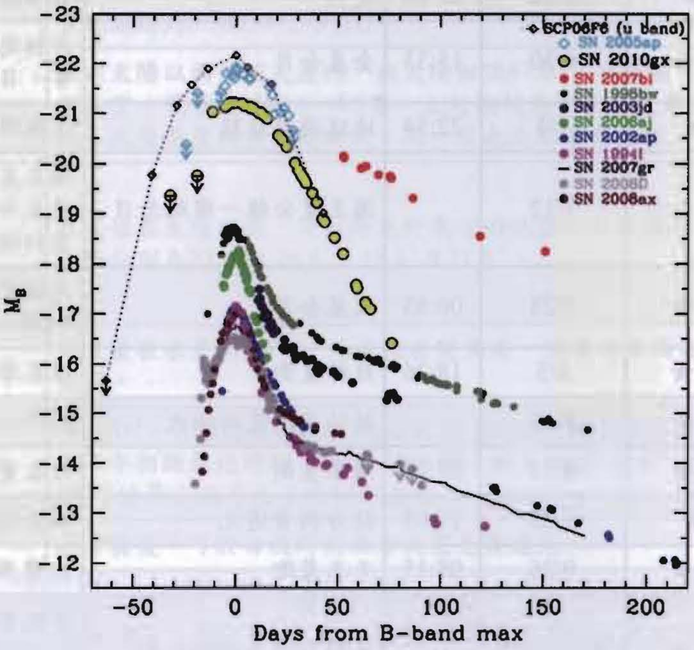

圖 1：SN 2010gx在 B波段絕對星等的光度變化(Vega 系統)和一些非常明亮的事件及標準的Ic型超新星的關係；包括Ic型超新星SNe 1994I, 2002ap, 2006aj, 2003jd, and 1998bw；Ib型超新星SNe 2007gr and 2008D；IIb型超新星SN 2008ax (Pastorello et al 2010)。

配置了廣角的影像設備做系統性觀測，並以此類瞬變星體相似性天體作為重點的目標，因此觀測到的事件數量正在急遽的增加中。

2010年3月13日致力於近地小行星搜尋的卡特林納即時巡天計畫（Catalina Real-time Transient Survey,簡稱CRTS)由天文學者 Mahabal 所領導的團隊宣佈於赤經為11h25m46.71s，赤緯為-08°49'41.4"處發現可見光波段瞬變天體（稱CSS100313，當時星等18.5)，其可見光光譜呈現偏藍、沒有連續光譜的特性且為紅移0.23。幾天後，美國加州理工學院天文學者 Quimby從PTF的觀測也發現了同一個天體，並於3月18日才將此星體命名為PTF10cwr。然而PTF早在3月4日時其實已觀測測過此天區，但當時PTF10cwr暗於望遠鏡的極限星等20.4，因此並未被發現。後來檢視3月5日到16日間的觀測資料，發現PTF10cwr正

在增亮，一直到3月18日才被確認命名。PTF10cwr其可見光光譜與極亮的可見光超新星SN 2005ap非常類似。經過分析，辨認出由大質量超新星爆發所造成的高速爆發而的寬譜線O II，並藉由宿主星系產生的窄譜線估計其距離為z=0.235，並命名為SN 2010gx。

我們從泛星計畫(PS1)的北天大面積巡天（稱3pi巡天）計畫，3月12日到23日的觀測資料中，發現SN 2010gx的光度仍在持續增加。泛星計畫成員之一的英國天文學者Pastorello檢視SDSS巡天計畫的影像檔案，發現SN 2010gx的宿主星系比其他超新星的宿主星系還要暗，且顏色也比其他宿主星系來得藍。此外他確認了紅移量為0.23。並確認Quimby估測的在這個紅移量下，宿主星系的絕對星等在g波段應為-18，這結果顯示SN 2010gx宿主星系的亮度與大麥哲倫星系類似。

圖 2 ：影像中間的藍色的亮點是泛星計畫所發現的光學瞬變星體，此張影像是鹿林一米望遠鏡所拍攝g'、r'、i'三色波段合成的影像。Pastorello博士所領導的團隊，將泛星計畫以及鹿林一米望遠鏡和其他望遠鏡的對這個光學瞬變星體觀測的結果發表於2010的天文物理期刊。台灣參與的人員有中央大學天文所浦田裕次和中研院天文所黃麗錦博士。

不久之後，我透過鹿林一米望遠鏡（LOT）的「超新星後續觀測」計畫進行觀測並取得影像。如圖二所示，LOT成功的偵測到清晰的超亮可見光波段瞬變天體，並利用三個波段（SDSS的 g'、r' 和 i' 波段)的資料製成三色合成影像，影像中央可清楚看見特別亮的藍色物體。同一時間，由英國皇后大學Stephen Smartt教授所率領的泛星計畫瞬變天體團隊也持續利用密集的光譜測量觀測SN 2010gx。分析結果顯示，SN 2010gx早期的光譜與其他同類型的超新星一樣呈現偏藍色的連續譜線，而且有明顯的OII的寬吸收譜線。此外在爆發後25天，出現了Ic型超新星特有的 一Fe II和Si II的寬吸收譜線。換句話說，SN 2010gx與SN 2005ap和SCP 06F6類型的瞬變天體在光度極大值後出現與Ic型超新星類似的特徵，這些無法從目前的超新星爆炸機制學說得到合理的解釋。例如：無法指出晚期的光譜光度是由56Ni所決定、其廣泛的光度變化代表非常大的質量噴出物，以及緩慢的光譜演化有著與Ic型超新星些許的不同。這些初始恆星的性質和光度的來源是有趣且尚未解決的問題，但因為時域巡天計畫的進步，允許天文學家在早期就偵測到這些天體，預計未來將可逐漸完成更多詳細且有系統的研究。

感謝這些瞬變天體的明亮，讓我們可以拿它們作為主要研究高紅移的目標。實際上，令人印象深刻的是泛星計畫已經可以量測到紅移z=1.2的瞬變天體，未來更可預期泛星計畫將可提升到z~2至4，甚至也可利用日本昴星望遠鏡(Subaru)找尋更高紅移的瞬變天體。除了天體本身之外，還可以在最大光度後的數月或數年持續觀測到，因為這些明亮的事件提供穩定的光源照亮她們周圍由氣體和塵埃組成的雲氣；此外也提供了新的機會，可以用高解析度的光譜去探測遙遠的恆星形成區，雖然目前以伽瑪射線爆為基礎研究恆星形成區的這個方法缺乏計劃性和可重複性。未來昴星望遠鏡將建置超廣角（Hyper-Suprime-Cam）相機，並進行計畫性的時域巡天，更可以利用這些瞬變天體事件擴展天文學家對高紅移區域的認識。

《泛星計畫(PS1)臺灣團隊資訊網站: http://www.astro.ncu.edu.tw/~ps1tw/ 》

浦田裕次:國立中央大學天文所助理教授
莊佳蓉:國立中央大學天文所碩士班研究生

Printer-friendly version

Google Search MPC

IAU Minor Planet Center

MPC on Add to circles

MPC Operations Status
Processing (Info)
ECS: Accessible
MPC Status Page

Observer Services (NEOs)
NEO Services Overview
NEO Confirmation
NEO Confirmation (RA order)
NEO Ratings
NEO Page
NEO Observation Planning Aid
NEOChecker
NEOCMTChecker
NEOCP Blog

Observer Services
Services Overview
Minor Planet & Comet Ephem.
Natural Satellite Ephemerides
New Object Ephemerides
MPChecker
CMTChecker
Distant Artificial Satellites
Observing List Customizer
Sky Coverage

Databases
MPC Database
Light Curve Database

Orbital Elements
Orbital Elements Overview
MPCORB
Orbital Elements for Programs
MPCAT
MPCUPDATE

Astrometric Observations
MPCAT-OBS
MPCOBS

Publications
Publications Overview
MPECs
MPC Archive
MPC RSS Feeds
CBAT RSS Feeds

Documentation
Documentation Overview
Tech Info
Minor Body Astrometry
What's New

Lists and Plots
Lists and Plots Overview
Critical-List Minor Planets
Minor Planets
Comets
Animations

General
MPC Blog
Contact Us
Index
Site Map
Search Site

Links
Minor Planet Center
Central Bureau for Astro. Tel.
Cometary Science Archive
International Comet Quarterly
Smithsonian Astro. Obs.

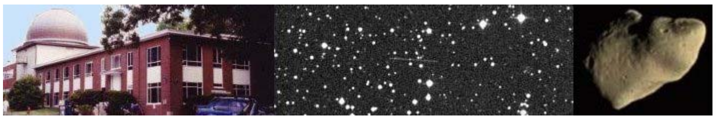

Minor Planet Discovery Sites

The following table lists the total number of discoveries made at each of the most prolific discovery sites, arranged in decreasing order of number of discoveries.

This list was last updated on 2011 Dec. 9.

Rank	Discoveries	Between	Site name
1	129349	1980-2010	Lincoln Laboratory ETS, New Mexico
2	51068	1973-2010	Steward Observatory, Kitt Peak-Spacewatch
3	24755	1960-2010	Palomar Mountain/NEAT
4	17546	1998-2008	Lowell Observatory-LONEOS
5	13072	1973-2010	Catalina Sky Survey
6	12737	1977-2011	Mt. Lemmon Survey
7	6784	1995-2006	Haleakala-AMOS
8	6718	1949-2008	Palomar Mountain
9	5588	1976-2009	European Southern Observatory, La Silla
10	2743	2000-2010	LPL/Spacewatch II
11	2468	1991-2002	Oizumi
12	1800	1975-2007	Siding Spring Observatory
13	1420	2001-2008	Desert Eagle Observatory
14	1398	1995-2001	Visnjan
15	1302	2000-2010	Siding Spring Survey
16	1285	1966-1992	Crimea-Nauchnij
17	1250	1982-2002	Peking Observatory, Xinglong Station
18	1031	1997-2008	Reedy Creek
19	1016	1996-2005	Campo Imperatore-CINEOS
20	949	1960-2010	OAM Observatory, La Sagra
21	920	1996-1999	Caussols-ODAS
22	892	1977-2002	Klet Observatory, Ceske Budejovice
23	823	1891-2007	Heidelberg-Konigstuhl
24	723	1987-2000	Kushiro
25	711	1998-2004	Apache Point-Sloan Digital Sky Survey
26	703	1973-2007	Lowell Observatory, Anderson Mesa Station
27	677	1987-2008	Kitami
28	665	1994-2008	Ondrejov
29	653	1996-2010	Goodricke-Pigott Observatory, Tucson
30	633	1995-2003	Prescott
31	548	1995-2002	Haleakala-NEAT/GEODSS
32	538	1961-1995	Karl Schwarzschild Observatory, Tautenburg
33	497	1999-2003	Fountain Hills
34	452	1995-2010	Bergisch Gladbach
35	426	1982-2007	Kitt Peak
36	360	1994-2010	Crni Vrh
37	347	1978-2006	Cerro Tololo Observatory, La Serena
38	324	1996-2010	WISE
39	321	1993-2000	Nachi-Katsuura Observatory
40	299	1998-2009	Farpoint Observatory, Eskridge
41	296	1925-2009	Uccle
42	284	2004-2010	RAS Observatory, Mayhill
43	273	1992-2008	Mauna Kea
	273	1978-1996	Caussols
45	264	1994-2008	San Marcello Pistoiese
	264	1995-2010	University of Szeged, Piszkesteto Stn. (Konkoly)
47	262	2002-2009	Lulin Observatory
48	261	2000-2010	Bisei Spaceguard Center-BATTeRS
49	257	2004-2006	Apache Point
50	245	1996-2009	George Observatory, Needville